Taku Onishi *Editor*

Theoretical Chemistry for Advanced Nanomaterials

Functional Analysis by Computation and Experiment

Springer

Theoretical Chemistry for Advanced Nanomaterials

Taku Onishi
Editor

Theoretical Chemistry for Advanced Nanomaterials

Functional Analysis by Computation and Experiment

Springer

Editor
Taku Onishi
Hylleraas Centre for Quantum
Molecular Sciences
Department of Chemistry
University of Oslo
Oslo, Norway

Graduate School of Engineering
Mie University
Tsu, Japan

ISBN 978-981-15-0005-3 ISBN 978-981-15-0006-0 (eBook)
https://doi.org/10.1007/978-981-15-0006-0

This Springer imprint is published by the registered company Springer Nature Singapore Pte Ltd.
The registered company address is: 152 Beach Road, #21-01/04 Gateway East, Singapore 189721, Singapore

Preface

This book collects review chapters of theoretical chemistry for advanced nanomaterials from the points of view of both computational and experimental chemistry. It is written for computational and experimental chemists, including undergraduate students, who are working with advanced nanomaterials, where collaboration and interplay between computation and experiment are essential.

This book consists of five parts:

- **Part I Introduction**
- **Part II Computational Approach**
- **Part III Interplay Between Computational and Experimental Approaches**
- **Part IV Experimental Approach**
- **Part V Forthcoming Theoretical Approach**

In Part I, the scientific meaning of nanomaterials is clearly defined. The key point is that nanomaterials stand for not only nanosize materials but also materials with nanoscale functionalities. After the explanation of computational and experimental approaches for functional analysis, nanoscale functionalities are introduced.

Part II: Functional Analysis from Computational Approach

- Hydride Ion Conducting Nanomaterials (Onishi)
- High-κ Dielectric Nanomaterials (Senami et al.)
- Organic Electronics (Yanagisawa et al.)

Part III: Functional Analysis from the Interplay Between Computational and Experimental Approaches

- 0D–3D Carbon-based Nanomaterials (Taioli)
- Oligomers (Timoshkin et al.)
- Carbon Nanomaterials (Lin et al.)
- Sandwich Clusters (Nakajima et al.)

Part IV: Functional Analysis from Experimental Approach
- Silicon Nanomaterials (Hikaru Kobayashi et al.)
- Sodium Ion Conducting Glass Ceramics (Okura et al.)
- Surface Metal Oxides by Plasma-Electrolytic Oxidized Coating (Ustinov et al.)
- Organic Nanochannel (Hirokazu Kobayashi)

Part V: Forthcoming Theoretical Approaches
- Excited States (Bacalis)
- Quantum Dynamics (Hanna et al.)

Finally, I would like to thank Dr. Sinichi Koizumi and the Springer staff. I hope this book facilitates readers' understanding of how to analyze functionalities for advanced nanomaterials.

"Materials development without basic science will face safety problem."

Taku Onishi
May 2019

Contents

About the Editor

Taku Onishi is a Japanese scientist. He graduated from the Faculty of Science, Osaka University, Japan, in 1998, and gained his PhD from the Department of Chemistry, Osaka University, Japan, in 2003. He got a permanent position at the Faculty of Engineering, Mie University, Japan, in 2003. He has been a guest researcher for the Department of Chemistry, University of Oslo, Norway, since 2010. His research covers several research fields such as quantum chemistry, computational chemistry, quantum physics, and material science. In 2017, his book *Quantum Computational Chemistry: Modelling and Calculation for Functional Materials* was published by Springer Nature. He has served on international scientific activities: Member of the Royal Society of Chemistry; Chair of the Computational Chemistry (CC) Symposium; a position on the science committee of the International Conference of Computational Methods in Sciences and Engineering (ICCMSE); a member of the editorial board of *Cogent Chemistry*, the *Journal of Computational Methods in Sciences and Engineering* (JCMSE), and *Cogent Engineering*. He has reviewed many international proceedings, books, and journals in various research fields: *AIP conference proceedings*, *Progress in Theoretical Chemistry and Physics*, *Cogent Chemistry*, *Physical Chemistry Chemical Physics*, *Molecular Physics, Dalton Transaction, The Journal of Physical Chemistry Letters*, *Journal of Computational Chemistry*, *International Journal of Quantum Chemistry*, *Journal of Solid State Chemistry*, *Solid State Ionics*, *Chemistry of Materials*, *Materials Chemistry and Physics*, *Chemical Engineering Journal*, *Chemical Physics*, *ACS catalysis*, *Applied Surface Science*, *Chemical Physics*, *Chemical Physics Letters*, *Chirality*, *Applied Surface Science*, *ACS catalysis*, *Biochimica et Biophysica Acta – Proteins and Proteomics*, *AIP Advances*, *The Journal of Organic Chemistry*, *New Journal of Chemistry,* etc.

About the Corresponding Authors

Chapters 1 and 2

Taku Onishi

Chapter 3

Masato Senami is a theoretical physicist. His interest is broad, from elementary particle to condensed matter.

He received his PhD in 2004 from the Department of Nuclear Engineering, Kyoto University. Following post-doctoral fellowship at the University of Tokyo, he joined the faculty of the Department of Micro Engineering, Kyoto University, in 2007.

Chapter 4

Susumu Yanagisawa received his bachelor and master degrees in engineering and a PhD (2004) in engineering from the University of Tokyo. He was a postdoctoral researcher at the Institute of Scientific and Industrial Research, Osaka University, and in the department of precision science and technology, Osaka University, from 2004 to 2010, and was an assistant professor in the Department of Physics and Earth Sciences, University of the Ryukyus, Japan. Since 2014, he is an associate professor in the Department of Physics and Earthsciences, Faculty of Science, University of the Ryukyus. His research topic covers theoretical investigation on electronic structure of materials or molecules relevant to organic electronics, and the electronic structure methods such as time-dependent density functional (TDDFT) and the GW approximation.

Ikutaro Hamada received a BSc in Engineering from Osaka University and a PhD in Science from Osaka University in 2003. He then joined the Institute of Scientific and Industrial Research, Osaka University, as a postdoctoral researcher, Advance Institute for Materials Science, Tohoku University, in 2009 as an assistant professor, National Institute for Materials Science as a senior researcher in 2013, and currently associate professor in the department of precision science and technology, Graduate School of Engineering, Osaka University. His research interests include electronic structure methods and their application in surfaces and interfaces relevant to energy conversion and heterogeneous catalysis.

Chapter 5

Simone Taioli is presently a senior researcher in the Condensed Matter division of the European Center for Theoretical Studies in Nuclear Physics and Related Areas (ECT_*) in Trento, Italy. He graduated summa cum laude with both a degree (2000) and a PhD (2004) in Nuclear Engineering (University of Bologna) and also earned a second PhD in Physics (University of Trento, 2013). He held academic research positions at University College London, where he dealt with the ab initio simulations of scattering events between electron beams and molecular targets, the study from first principles of the Earth's core and of materials under extreme conditions, and at the University of Sheffield, where he worked on the assessment of the electronic and optical properties of carbon-based materials. From 2015 to 2018 he held joint academic appointments at Charles University in Prague. His research is now focused on the development and application of many-body and Monte Carlo methods in physics and chemistry with particular emphasis in materials science as well as on the relativistic approaches to the beta decay of heavy nuclei, also in astrophysical scenario and for the determination of the neutrino mass to explore the physics beyond the Standard Model.

Chapter 6

Anna V. Pomogaeva studied material science and theoretical solid states physics at Tomsk State University in Russia. She was awarded a PhD in 2009 from Kyushu University of Japan, where she worked at Theoretical Material Lab at the juncture of solid-state physics and quantum chemistry. In 2010–2014 she worked as a postdoc researcher in Radiation Lab, University of Notre Dame, Indiana, USA. The research there was aimed at developing a method for accounting for the effects of solvation in the framework of the continuum solvation model. Since 2014 she works at the Inorganic Chemistry Department of Saint-Petersburg State University, Russia, on projects devoted to the study of donor-acceptor interactions in complexes of inorganic compounds.

Alexey Y. Timoshkin was born in Leningrad, USSR. In 1988–1993 studied chemistry at St. Petersburg State University, Russia (diploma degree in chemistry, 1993). In 1995–1996, on NAFSA/REAP fellowship, he studied computer science at Eastern Connecticut State University, USA (BGS with dean's distinction, 1996). In 1997 he received a Candidate of Science degree in Inorganic chemistry from St. Petersburg State University. In 2001–2002 he was Alexander von Humboldt Research Fellow at Philipps-Universität Marburg, Germany (host Prof. Gernot Frenking). Since 1998 he worked as assistant, associate and now as a full professor at St. Petersburg State University. In 2010 he received the Teaching Excellence award from St. Petersburg State University. He is author and supervisor of the online-course "Inorganic Chemistry: an introduction to the chemistry of the elements" (2017). Since 2017 he is head of the department of Inorganic Chemistry at St. Petersburg State University.

His areas of expertise are main group chemistry, donor-acceptor complexes, Lewis superacids, gas phase thermochemistry, tensimetry, calorimetry, applied quantum chemistry.

He is author or co-author of 178 scientific papers, 1 book chapter and 94 presentations at scientific conferences. Scientific supervisor of 9 diploma, 4 bachelor, 2 master and 2 Candidate of Science Degree theses. Expert of RSF and RAS.

Chapter 7

King-Chuen Lin is a Distinguished Professor of the Department of Chemistry at National Taiwan University and a Distinguished Research Fellow of National Science Council, Taiwan. He received his BS degree in Chemistry from National Taiwan University, Taiwan, his PhD in Chemistry from Michigan State University, USA, and his postdoctoral career began at Cornell University. His research interests are photodissociation and reaction dynamics in gas and condensed phases, atmospheric chemistry, materials designed for sensors and catalysts, and single molecule spectroscopy. He received the Academic Award of Ministry of Education, Taiwan, in 2014, and Richard B. Bernstein Award in International Conference on Stereodynamics, Sep. 2018 in Arosa, Switzerland. He now serves as an Associate Editor for *J. Chin. Chem. Soc.*(Taipei) and a member of the Editorial Board for *Scientific Reports* (Nature publisher), *Journal of Analytical and Bioanalytical Techniques* (Gavin Publishers), and *Journal of Modern Chemical Sciences* (Herald Scholarly Open Access). He has published more than 201 peer-reviewed papers and edited one book on reaction dynamics and chemical kinetics.

Chapter 8

Atsushi Nakajima received BSc, MSc, and DrSc degrees from the University of Tokyo, supervised by Profs. Kozo Kuchitsu and Tamotsu Kondow in 1984,

1986, and 1989, respectively. He was a Research Associate (1989–1994), Assistant Professor (1994–1997), and Associate Professor (1997–2001) in the Department of Chemistry, Keio University. He was promoted to Professor at Keio University in 2001. He has been additionally appointed as Principal Investigator in Keio Institute of Pure and Applied Sciences (KiPAS) (2014–2019). He has been the director general of The Exploratory Research for Advanced Technology (ERATO) research funding program (2009–2015) of the Japan Science and Technology Agency (JST) and a member of the Science Council of Japan since 2006. He has been actively engaged in physical chemistry for and have published in top level journals. His research interests lie in the field of cluster science with methodological developments of soft-landing, photoelectron spectroscopy, ultrafast surface spectroscopy, and large-scale synthesis by pulsed magnetron sputtering, bridging between gas phase clusters and size-selectively deposited clusters. He was awarded prizes for the Chemical Society of Japan (CSJ) award for young chemists, The CSJ Award for Creative Work, and Japan Society for Molecular Science Award in 1995, 2009, and 2018, respectively.

Chapter 9

Hikaru Kobayashi is a Professor of The Institute of Scientific and Industrial Research, Osaka University. He was born in Kyoto, Japan. He received the BE in chemistry from Osaka University in 1979 and the ME (1981) and PhD (1984) in chemistry from Kyoto University, Kyoto, Japan. From 1984 to 1986, he was a Postdoctoral Research Associate in Department of Physics and Astronomy, University of Pennsylvania, PA. From 1986 to 1987, he was a Researcher in Matsushita Electronics Corporation Kyoto Research Center, where he was engaged in LSI wiring and gate oxide technology. From 1987 to 1990, he was a Research Associate in Department of Chemistry, Faculty of Engineering Science, Osaka University, where he was engaged in research on silicon solar cells, surface and interface science of silicon, and low temperature silicon oxidation. From 1990 to 1998, he was an Associate Professor in Department of Chemistry, Faculty of Engineering Science, Osaka University.

Chapter 10

Toshinori Okura completed his doctorate in glass materials science with the theoretical and practical combination of X-ray emission spectroscopy and molecular orbital calculations at the Tokyo Metropolitan University, Tokyo, Japan, in 1990. After his optical study of glass in TOTO Ltd., Kanagawa, Japan, as a researcher, he served the Kogakuin University, Tokyo, Japan, as a research associate in 1993, an assistant professor in 1995, and an associate professor in 2002. He is serving

the University as a professor from 2010. He joined the Massachusetts Institute of Technology, Massachusetts, USA, as a visiting scientist in 1997–1998. He has been a visiting scientist at the University of Tokyo from 2008. He studied the crystallization of glass and designed the Na^+ superionic conducting glass-ceramics. It is expected that this work will lead to the development of novel solid electrolytes. Concurrently, he also studied the immobilization of high-level nuclear waste with new types of phosphate glasses. He won scientific prizes from the Japanese Association of Inorganic Phosphate Chemistry in 2008, the Society of Inorganic Materials, Japan, in 2010, and the International Association of Advanced Materials in 2017 (IAAM medal), respectively, for his great success.

Chapter 11

Elena A. Koblova graduated from the Institute of Physics and Information technologies, Far Eastern Federal University (FEFU) (Vladivostok, Russian Federation) in 2011. In 2016 she received her PhD ("Candidate of Sciences" degree) in condensed matter physics. Since 2011 she has been working as a researcher in the Institute of Chemistry, Far Eastern Branch of the Russian Academy of Sciences (FEB RAS) (Vladivostok, Russian Federation). Her research interests revolve around new functional materials. Her current research focuses on catalytically active and energy-saturated materials. In her work, she takes a combinatorial approach using X-ray photoelectron spectroscopy and quantum-chemical modeling.

Alexander Yu. Ustinov graduated from the Far Eastern State University (FESU) (Vladivostok, Russian Federation) in 1986. In 1990 he received his "Candidate of Sciences" degree and in 1999, "Doctor of Sciences" degree (physics and math), and became a Professor in 2001. His administrative work includes serving as Dean of the Faculty of Physics, FESU (Vladivostok, Russian Federation) from 1999 till 2005, Head of the Department of General Physics, FESU (Vladivostok, Russian Federation) from 2003 to 2011, and Head of the Laboratory of the electronic structure and quantum-chemical modeling, Institute of Chemistry, Far Eastern Branch of the Russian Academy of Sciences (FEB RAS) (Vladivostok, Russian Federation), from 2007 till present. His research interests revolve around composition, electronic structure, and state of elements in various functional materials. He widely uses the method of X-ray photoelectron spectroscopy and develops it for studying advanced materials including magnetic and catalytically active, corrosion resistant, biologically inert, etc.

Oleg L. Shcheka graduated from the Far Eastern State University (FESU) (Vladivostok, Russian Federation) in 1986. He gained his "Candidate of Sciences" degree in 1990, "Doctor of Sciences" degree in 2002, and in the same year became a Professor. His administrative work includes serving as Vice-Director (Research) of

the Institute of Physics and Information Technologies, FESU (Vladivostok, Russian Federation) from 2004 till 2008, Deputy Vice-President (Research and Innovation) of the Far Eastern Federal University (FEFU) (Vladivostok, Russian Federation) from 2011 to 2017 and Vice-President of the Far Eastern State Technical Fisheries University (FESTFU) (Vladivostok, Russian Federation) from 2018 till present. His research interests revolve around X-Ray emission, photoelectron spectroscopy, and electronic structure of the various chemical compounds and solids. He developed new approaches to the electronic theory of heterogeneous catalysis.

Chapter 12

Hirokazu Kobayashi received his PhD in Science from Osaka University in 2005. After postdoctoral research at the Museum of Osaka University, Graduate School of Engineering Science, Osaka University, and Graduate School of Science, Kyoto University, he worked at the College of Humanities and Sciences, Nihon University, as an assistant in 2009–2017. He currently works at Faculty of Arts and Sciences at Fujiyoshida, Showa University, as a lecturer. His research interests comprise molecular dynamics of organic radical in nanospace using electron spin resonance, the design of organic magnets, and thermal analysis of inclusion compounds using TG-DTA. His personal motto is "Confident decision will bring a great success."

Chapter 13

N. C. Bacalis is a Physicist at the University of Athens, Greece. He earned his master's and PhD at the University of Illinois at Urbana-Champaign, USA, doing electronic structure of clusters. He started working at the Research Center of Crete, Greece, doing band structure calculations and electron momentum density and Compton profiles of elemental solids. Since 1987 he has been working at the National Hellenic Research Foundation in Theoretical Chemistry, developing computational methods of electronic structure of atoms using small and concise configuration-interaction wave functions of equivalent accuracy with large standard computations, of diatomic molecules using separable small numerical wave functions also of equivalent accuracy with large standard computations, and of clusters interacting with atoms or small molecules. During the last decade he has developed a minimization principle for excited state saddle points – because the standard methods find a minimum, not the correct saddle point (unless huge – rather incomprehensible – wave functions are used) – using small and concise configuration-interaction wave function of the saddle point excited state, and without using orthogonality to approximate wave functions of lower lying states.

Chapter 14

Gabriel Hanna received his PhD in Chemistry from the University of Toronto in 2006. From 2006 to 2009, he was a postdoctoral fellow at the University of Michigan. In 2009, he joined the Department of Chemistry at the University of Alberta. Currently, he is an Associate Professor at the University of Alberta. His research primarily focuses on the development of mixed quantum-classical methods and their application to chemical problems of fundamental and technological importance.

Part I
Introduction

Chapter 1
Theoretical Chemistry for Advanced Nanomaterials: Computational and Experimental Approaches

Taku Onishi

Abstract Nowadays, functional analysis is getting indispensable to develop advanced nanomaterials. Functional analysis at electron and atomic levels can be performed from both computational and experimental approaches, together with developments of high-performance computers and experimental instruments. In this chapter, after an explanation of the definition of nanomaterial, typical computational and experimental approaches are briefly introduced. Nanomaterials stand for not only nanosize materials but also materials with nanoscale functionality. After an introduction of representative nanosize materials such as organic nanomaterial, cluster and nanoparticle, nanoscale functionalities in perovskites are overviewed. Finally, recent challenges related to advanced nanomaterials are discussed. Especially, nanospace chemistry, hydrogen society in the future, lithium-ion battery safety and replacement of lithium are mentioned.

Keywords Theoretical chemistry · Functional analysis · Nanosize material · Nanoscale functionality · Nanospace chemistry · Battery safety

1.1 Introduction

Computational chemistry and physics enable us to predict molecular and crystal structures for advanced nanomaterials. The functionalities can be revealed by means of further investigations of energetics, structure and electronic state. Since experimental research can be also performed to investigate structure and electronic state, collaborative functional analysis using both computational and experimental approaches is nowadays getting popular.

T. Onishi (✉)
Graduate School of Engineering, Mie University, Tsu, Japan

Hylleraas Centre for Quantum Molecular Sciences, Department of Chemistry, University of Oslo, Oslo, Norway
e-mail: taku@chem.mie-u.ac.jp; taku.onishi@kjemi.uio.no

T. Onishi (ed.), *Theoretical Chemistry for Advanced Nanomaterials*,
https://doi.org/10.1007/978-981-15-0006-0_1

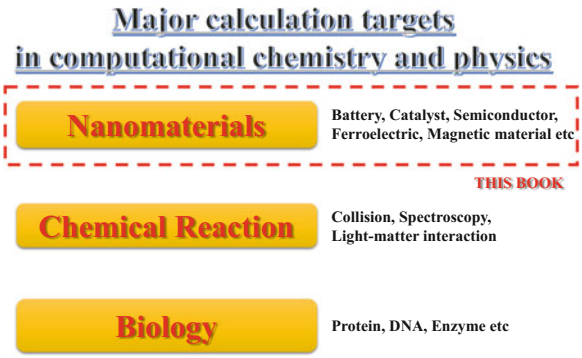

Fig. 1.1 Major calculation targets in computational chemistry and physics

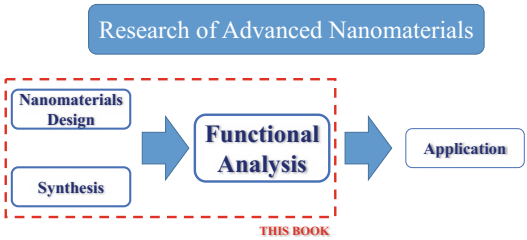

Fig. 1.2 Schematic figure of research of advanced nanomaterials

Every year we have been organising an international symposium on computational chemistry, which is held as main symposium in ICCMSE: International Conference of Computational Methods in Science and Engineering [1–4]. From the viewpoint of calculation targets, computational chemistry and physics are largely classified into three categories: (1) nanomaterials, (2) chemical reaction and (3) biology (See Fig. 1.1). In this book, "Nanomaterials" is mainly focused on.

Figure 1.2 depicts the schematic figure on the research of advanced nanomaterials. Theoretical aspect of nanomaterials science, especially functional analysis, is mainly mentioned in this book. In Chap. 2, nanomaterials design of hydride ion conductor is introduced. In Chaps. 5, 6, 8, 9, 10, 11, and 12, functional analysis for new nanomaterials is also introduced, together with experimental results.

1.2 Definition of Nanomaterial

Nano itself means a unit of length: 1 nm = 10 Å = 10^{-9} m [5]. In a narrow sense, nanomaterial stands only for nanosize material. On the other hand, in a broad sense, it also includes large molecule and bulk. It is because they exhibit *nanoscale functionality*. As shown in Fig. 1.3, nanomaterial can be widely defined as nanosize material or material with nanoscale functionality. In this book, not only nanosize material but also nanoscale functionality is hence mentioned.

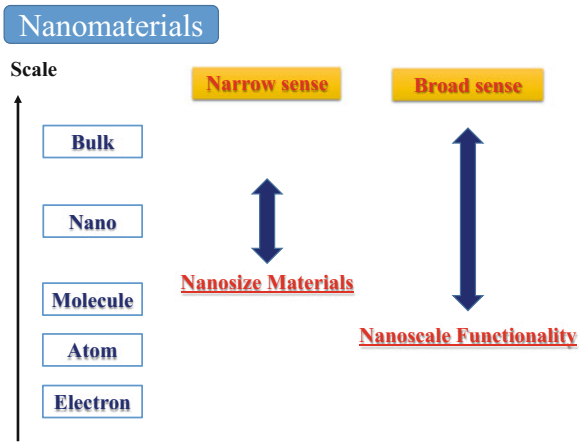

Fig. 1.3 Nanosize materials and nanoscale functionality

1.3 Computation and Experiment

1.3.1 Computational Approach

Energetics, structure and electronic state of nanomaterials can be investigated by performing theoretical calculation. In a quantum mechanical manner, both quantum chemical calculation based on molecular orbital (MO) theory and first principle calculation based on band theory are widely utilised. Schrödinger equation, which is the basis equation of quantum mechanics, is numerically solved in both calculations. Before starting a calculation, two factors must be correctly taken into account.

Two Important Factors

1. *Construction of scientifically reasonable model*
2. *Selection of calculation method*

Note that they strongly depend on considering materials and system. Since a model size is constrained in quantum calculation due to high computational cost, classical mechanics calculation is useful for much larger model and system. For example, dynamical process can be theoretically analysed in molecular dynamics (MD) simulation. However, since quantum effect is neglected, fatal error is sometimes caused in functional analysis. As a solution, quantum mechanical manner is often combined with classical mechanical manner. QM/MM and *ab initio* MD are known to be as typical hybrid method. Note that QM and MM denote quantum mechanics and molecular mechanics, respectively.

It has been widely accepted that density functional theory (DFT) is one of the best methods to solve Schrödinger equation numerically. Figure 1.4 depicts the schematic figure of DFT. Beyond Hartree-Fock (HF), DFT has been recognised as practical and useful method to include strong correlation effect and calculate integrals faster. In DFT calculation, specific functionals must be selected, depending on considering nanomaterials and system. For example, B3LYP, where Becke +

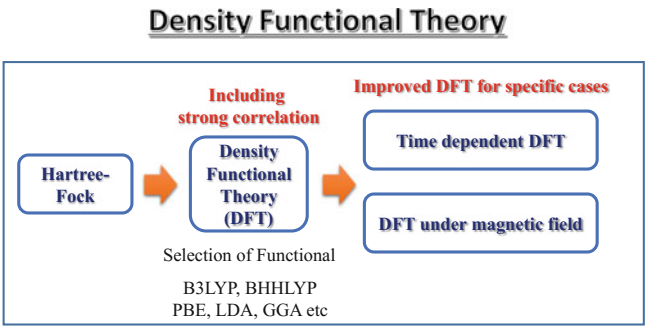

Fig. 1.4 Schematic figure of density functional theory (DFT)

Slater + HF exchange functionals and LYP + VWN5 correlation functionals are included, has been widely recognised as one of the best DFT methods for organics. See Refs [6–9] regarding DFT functional. Though time-dependent DFT (TDDFT) is generally useful for excited state, it often provides unreliable excited state. DFT often fails to estimate dissociation energy and bandgap [10, 11] and exhibits artificial stabilisation of delocalised state (self-interaction error) [11, 12]. It has been still improved to overcome such problems. As a new trail, DFT under strong magnetic field has been recently explored [13, 14]. In Chaps. 2, 4, 6, 7, and 8, DFT calculation results are shown.

In this book, forthcoming theoretical approaches are introduced. In Chap. 3, new theoretical approach based on quantum electrodynamics (QED) [15] is used to discuss dielectric property. In Chap. 13, the theoretical method to estimate excitation energy with low computational cost is introduced. In Chap. 14, quantum dynamical under consideration of nanoscale environment is introduced.

1.3.2 Experimental Approach

As same as theoretical calculations, experimental techniques enable us to characterise nanomaterials at electron and atomic levels (see Fig. 1.5). In X-ray diffraction (XRD), solid structure (lattice constant) can be determined. Both elemental analysis and bonding state analysis of solid surface can be performed by X-ray photoelectron spectroscopy (XPS). In X-ray absorption fine structure (XAFS), charge density of transition metal and bonding distance (atom-atom distance) can be estimated. Elemental analysis is also possible by electron energy loss spectroscopy (EELS). Nanomaterials can be directly observed by scanning electron microscope (STM) and transmission electron microscope (TEM).

To examine molecular vibration (changes of atom-atom distance and angle) in nanomaterials, Fourier transform infrared spectroscopy (FT-IR) and Raman spectroscopy are used. Note that vibration analysis is also possible by MO calculation.

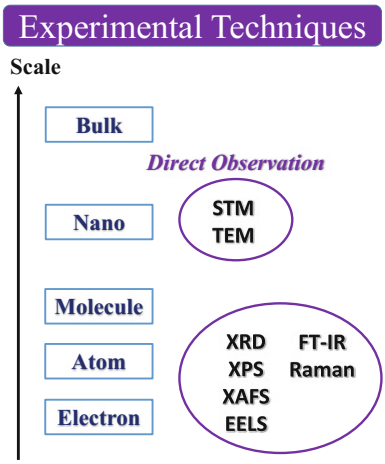

Fig. 1.5 Typical experimental techniques for characterising nanomaterials

To evaluate ion conductivity, alternating current (AC) impedance measurement is popular in the field of solid-state chemistry and physics. As sodium and lithium ions form ionic bonding with other atoms during ion conduction, activation energy for lithium ion and sodium ion conductions can be estimated from Nyquist plot analysis, where electric resistance is divided into three contributions: bulk, grain boundary and electrode interface. However, when conducting ion forms covalent bonding, the analytical manner provides a wrong activation energy [16, 17]. For example, since covalency of hydrogen is variable during proton conduction, the real activation energy cannot be obtained from Nyquist plot analysis. In Chap. 10, AC impedance measurement for sodium-ion conduction is introduced. Electron paramagnetic resonance (EPR) and electron spin resonance (ESR) are applicable to detect spin sources in nanomaterials. Magnetic interactions in nanomaterials are discussed in Chaps. 8 and 12.

1.4 Nanosize Materials

1.4.1 Top-Down and Bottom-Up Approaches

Nanofabrication methods are roughly divided into two: *top-down and bottom-up approaches* [5, 18], as shown in Fig. 1.6. In top-down approach, bulk materials are reduced in nanosize by using nanolithography, etching, etc. On the other hand, in bottom-up approach, atoms or molecules are arranged in nanosize by using microscope, self-assembly, self-organisation, chemical synthesis, etc. Dissociation and aggregation reactions are categorised as quantum interactions. Theoretical analysis at quantum level is hence required to understand the processes.

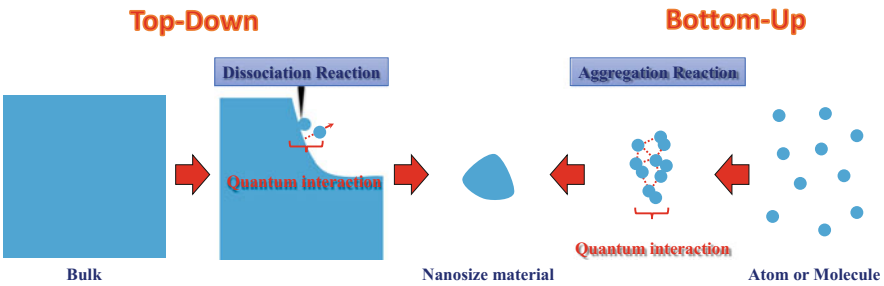

Fig. 1.6 Schematic figure of top-down and bottom-up approaches

Table 1.1 Nanosize materials in this book

Nanosize materials			Chapter
Organic nanomaterials	Carbon nanomaterials	*Fullerene*	Chapter 5 Taioli
		Graphene	Chapter 5 Taioli
			Chapter 7 Lin et al.
	Macromolecule	*Oligomer*	Chapter 6 Timoshkin et al.
Nanoparticle		*Silicon oxide*	Chapter 9 Hikaru Kobayashi et al.
Cluster		*Metal-benzene sandwich*	Chapter 8 Nakajima et al.
		Metal oxide	Chapter 11 Ustinov et al.
Nanospace materials			Chapter 5 Taioli
			Chapter 12 Hirokazu Kobayashi

1.4.2 Organic Nanomaterials

Table 1.1 lists nanosize materials in this book. Since the discovery of carbon nanotube and fullerene [19–21], many researchers have focused on carbon nanomaterials, due to many scientific interests such as nanosize structure itself, superconductivity, application to semiconductor device, storage material, etc. In Chaps. 5 and 7, functional analysis for several carbon nanomaterials is introduced. Note that carbon nanomaterial with nanospace is here categorised as nanospace material. Oligomer can be defined as nanomaterial consisting of relatively small amounts of monomers. In Chap. 6, structure and electronic state of oligomers are introduced.

1.4.3 Cluster

It is roughly regarded that cluster (1 ~ 10 nm) is the aggregation of different atoms, ligands and molecules. For example, Mn_{12}-core cluster is known as cluster magnet [22, 23], which exhibits unique magnetic property different from bulk magnet. Fe_4-core cluster [24] exhibits quantum spin crossover [25, 26]. Iron spin

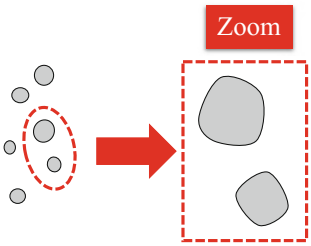

Fig. 1.7 Schematic figure of nanoparticle shape

state is switchable by changing quantum interaction between core and surrounding ligand with external stimulus. We here define such nanoscale quantum interaction as "nano-synchronicity". In Chap. 8, structure and magnetism of sandwich clusters are introduced.

1.4.4 Nanoparticle

Nanoparticle basically tends to keep similar structure with corresponding bulk. It is sometimes called nanopowder or nanocrystal. In principal, it can be expected that chemical reaction on surface is enhanced, due to wide surface area. Since nanoparticle shape and size are not uniform (see Fig. 1.7), bandgap varies in several nanoparticles. In Chap. 9, structure and photoluminescent mechanism are introduced in silicon nanoparticle. In addition, hydrogen molecule production using silicon nanoparticle is introduced.

1.4.5 Plasma Electrolytic Oxidation

Metal alloy surface can be coated with metal oxide, using plasma electrolytic oxidation (PEO) [27–29]. As many types of shape and size are possible (e.g. cluster and nanolayer), PEO has many possibilities to enhance and control nanoscale functionality of metal alloy. In engineering, corrosion and wear resistance of metal alloy have been expected. In Chap. 11, PEO coating on aluminium alloy using nickel and copper is briefly introduced.

1.5 Nanoscale Functionality in Perovskite

As shown in Fig. 1.8, perovskite nanomaterials are classified into two groups. In Next Generation Energy group, they are used as light response nanomaterial, hydrogen storage nanomaterial and ion-conducting nanomaterial for electrode and

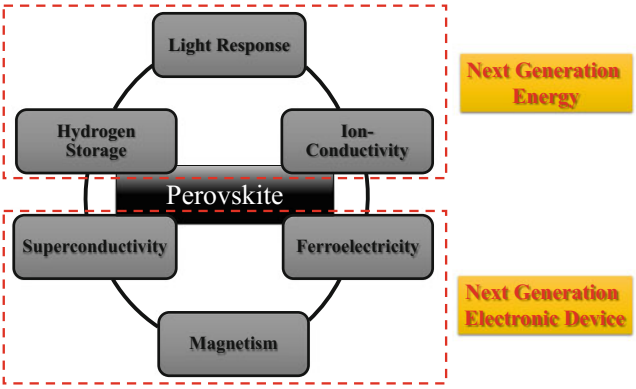

Fig. 1.8 Classification of perovskite nanomaterials: (1) Next Generation Energy; (2) Next Generation Electronic Device

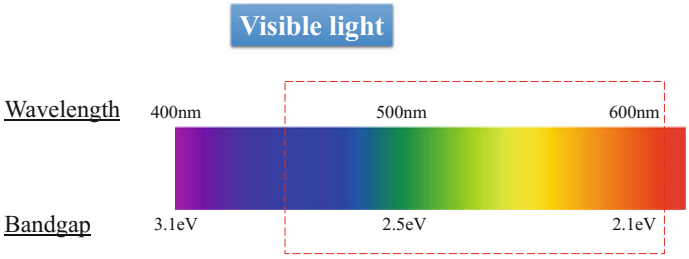

Fig. 1.9 Schematic figure of the relationship between visible light and bandgap

electrolyte in both secondary battery and solid oxide fuel cell (SOFC). On the other hand, in Next Generation Electronic Device group, they are used as ferroelectric, superconductor and magnetic nanomaterial in electronic devices.

1.5.1 Perovskite for Next Generation Energy

1.5.1.1 Light Response Perovskite

It is well known that $SrTiO_3$ perovskite exhibits photocatalytic activity [30]. To obtain the bandgap corresponding to visible light region (see Fig. 1.9), nitrogen and carbon are doped at oxygen site. In undoped case, highest occupied molecular orbital (HOMO) and lowest unoccupied molecular orbital (LUMO) consist of oxygen 2*p* and titanium 3*d* orbitals, respectively. In carbon-doped $SrTiO_3$ perovskite, as Ti–C–Ti type covalent bonding is formed in HOMO, HOMO-LUMO energy difference (bandgap in band theory) varies (see Fig. 1.10). Following the same mechanism, photoluminescent colour [31] is changeable by defect doping. See the details in Ref. [32–34].

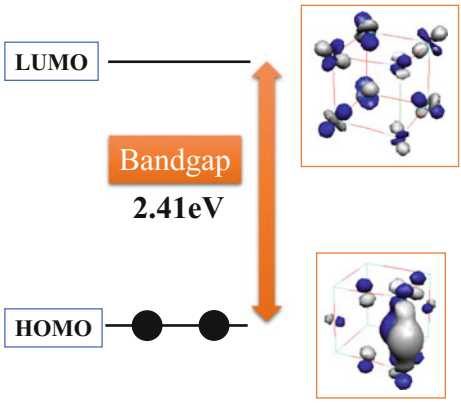

Fig. 1.10 Shapes of HOMO and LUMO and bandgap in carbon-doped $SrTiO_3$ perovskite. BHHLYP calculation was performed for $SrTi_8O_{11}C$ model by using GAMESS [35]. (Reprinted by permission from Springer International Publishing Switzerland, [34], COPYRIGHT (2013). The calculation details are explained in Ref. [34])

1.5.1.2 Ion-Conducting Perovskite

1. *Lithium Ion-Conduction*

Since the discovery of lithium ion-conducting perovskite titanium oxide [36], lithium ion-conducting perovskites have been explored. For example, we demonstrated that lithium ion-conduction occurs in $K_xBa_{(1-x)/2}MnF_3$ perovskite, based on counter cation-vacancy mechanism (see Fig. 1.11) [37–39]. It is noted that counter cation-vacancy is introduced by barium doping at potassium site, due to charge compensation. The activation energy for lithium ion-conduction is 0.27 eV, which is enough small for lithium ion-conduction at room temperature. In such perovskites, conducting lithium ion forms ionic bonding with perovskite framework. It is because lithium 1*s* orbital has no orbital overlap with others.

2. *Oxide Ion-Conduction*

Oxide ion or proton conductor is used for electrode and electrolyte of SOFC. In oxide ion-conducting $LaAlO_3$ perovskite [17, 40], as counter cation forms covalent bonding with conducting oxide ion during the ion conduction (see Fig. 1.12), oxide ion conductivity can be controlled by changing counter cation. The activation energy in strontium-doped $LaAlO_3$ (1.85–2.29 eV) is smaller than undoped case (2.73 eV). It is noted that the doping of different counter cations is required to introduce oxygen vacancy.

3. *Proton-Conduction: Proton-Pumping Effect*

Proton-conducting mechanism [16, 17, 41] is different from oxide ion-conduction. In proton-conducting $LaAlO_3$ perovskite, proton exists as a part of OH, and hydrogen is allocated forward square centre (most stable position). When proton-conduction starts, OH is pumped into square centre: *proton-pumping effect* (see Fig. 1.13). After OH rotation, covalent bonding changes in a diagonal path (OH and OHO covalent bondings) (see Fig. 1.14).

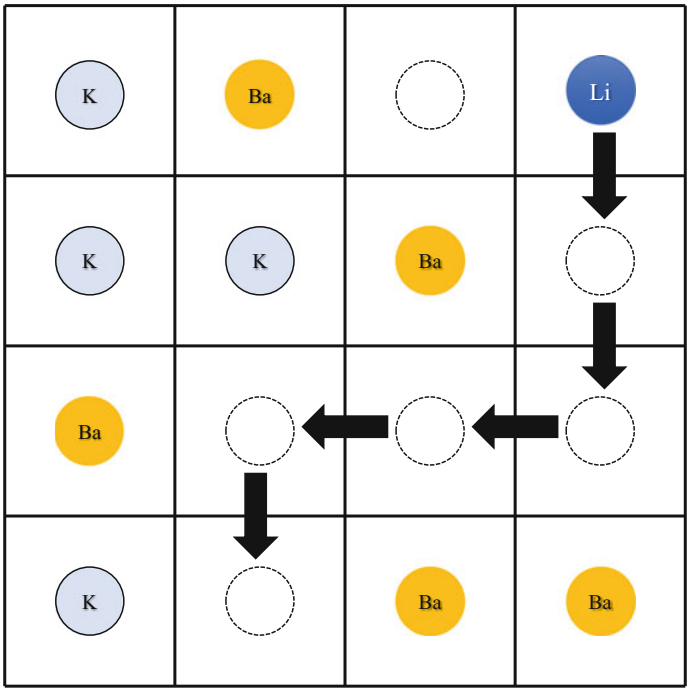

Fig. 1.11 Schematic figure of nanoscale lithium ion-conduction in $K_xBa_{(1-x)/2}MnF_3$ perovskite. (Reprinted by permission from Springer Nature Singapore Pte Ltd., [39], COPYRIGHT (2018). Potassium and barium are fixed within cube, due to large ionic radius. Lithium ion migrates via counter cation-vacancy (dotted circle))

4. *Hydride Ion-Conduction*

Recently hydride ion has attracted much scientific interest, from the viewpoint of fast ion-conduction. We demonstrated that hydride fluctuation occurs in hydride ion-conducting $BaTiO_3$ perovskite [42]. In Chap. 2, hydride ion-conducting mechanism in perovskite fluoride and hydride is overviewed.

1.5.1.3 Hydrogen Storage Perovskite

In metal hydrides, perovskite hydrides and related nanomaterials [43–50], hydrogen storage applicability was experimentally and theoretically investigated. As shown in Fig. 1.15, hydrogen (hydrogen molecule) is released through the dissociation of perovskite hydride. In Chap. 2, chemical bonding between magnesium and hydride ion is explained in $KMgH_3$ perovskite.

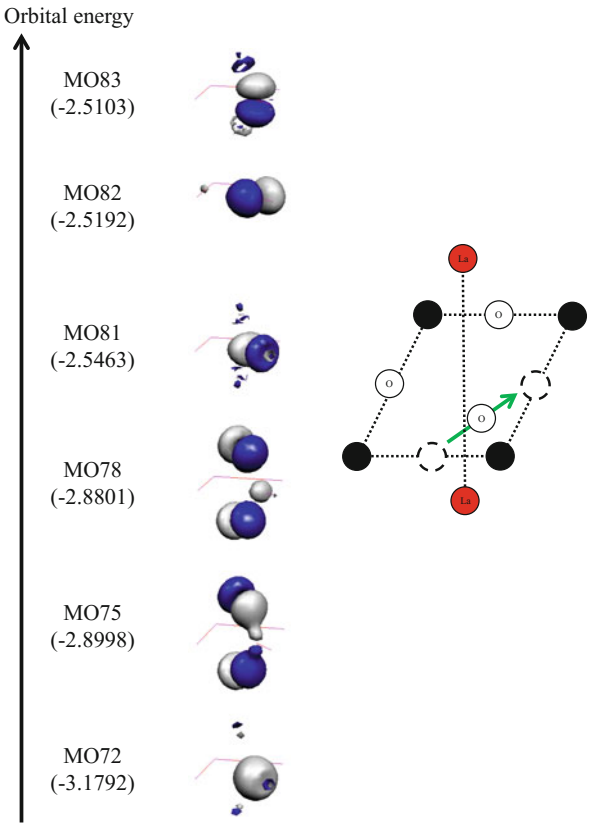

Fig. 1.12 Selected molecular orbitals related to conducting oxide ion in $LaAlO_3$ perovskite. (Reprinted by permission from Springer Nature Singapore Pte Ltd., [17], COPYRIGHT (2018). BHHLYP calculation was performed for $La_2Al_4O_3$ model by using GAMESS [35]. When oxide ion is allocated at diagonal centre, oxide ion forms covalent bonding with both lanthanum atoms)

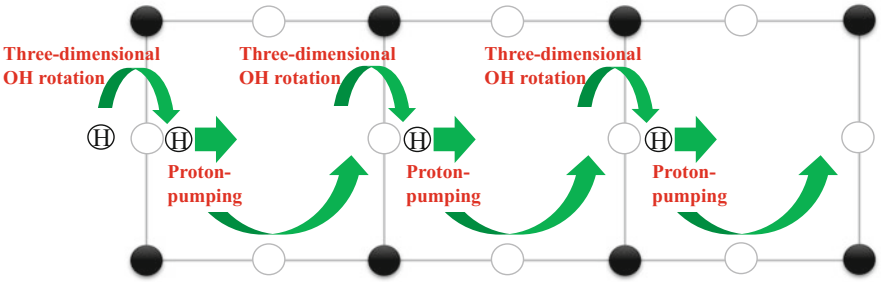

Fig. 1.13 Schematic figure of nanoscale proton-conduction in $LaAlO_3$ perovskite. (Reprinted by permission from Springer Nature Singapore Pte Ltd., [17], COPYRIGHT (2018). Black and white circle denote aluminium and oxygen, respectively)

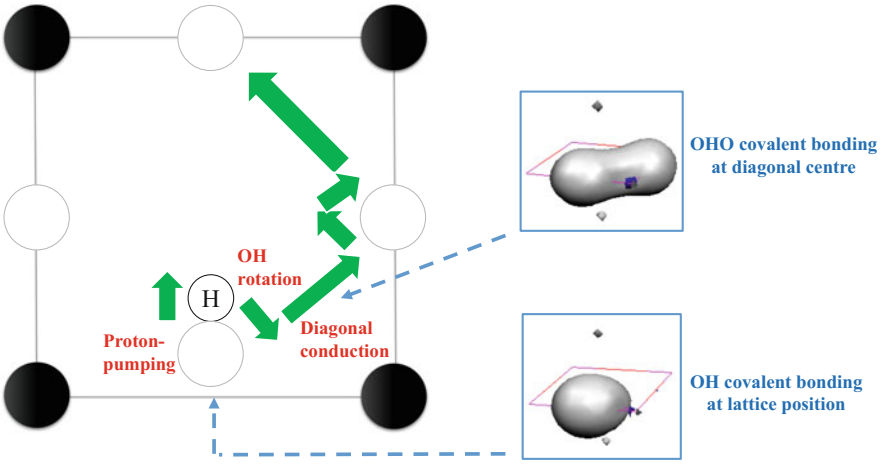

Fig. 1.14 Schematic figure of proton-conduction within Al_4O_4 square in $LaAlO_3$ perovskite. (Reprinted by permission from Springer Nature Singapore Pte Ltd., [17], COPYRIGHT (2018). Black and white circles denote aluminium and oxygen, respectively)

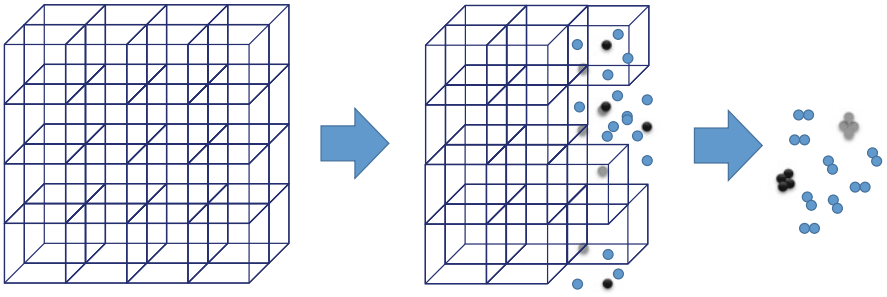

Fig. 1.15 Schematic figure of nanoscale hydrogen release from perovskite hydride. Blue, black and grey spheres denote hydrogen, magnesium and potassium atoms, respectively

1.5.2 Perovskite for Next Generation Electronic Device

1.5.2.1 Ferroelectric Perovskite

Ferroelectric can be applicable to high-performance memory. It is well known that perovskite titanium oxides such as $BaTiO_3$ and $PbTiO_3$ exhibit ferroelectricity [51]. The direction of a nanoscale spontaneous electric polarisation is changeable by applying electric field. As shown in Fig. 1.16, electric polarisation can be reversed by applying an opposite electric field. In present, $PbZr_xTi_{1-x}O_3$ perovskite has been widely utilised as raw material of ferroelectric random access memory (FeRAM).

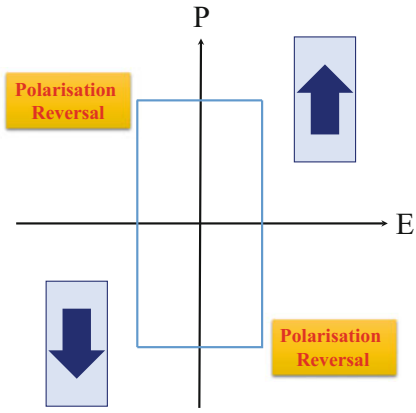

Fig. 1.16 Schematic figure of the relationship between electric polarisation (P) and applied electric field (E)

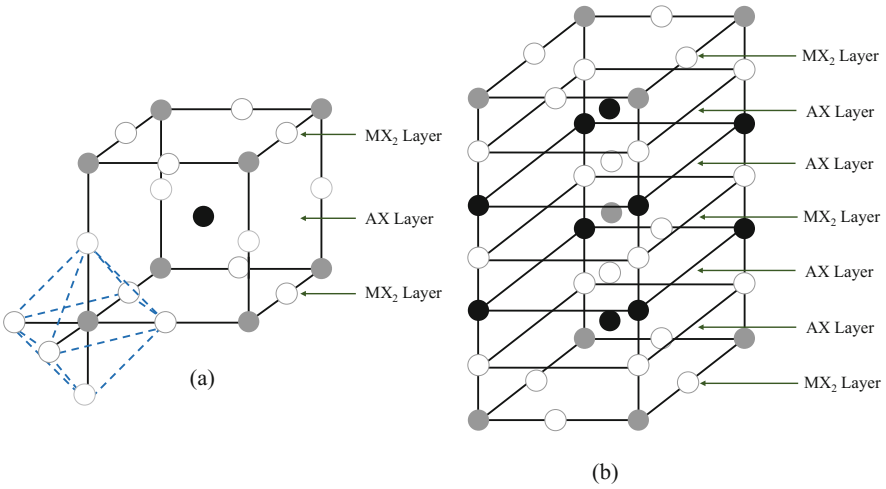

Fig. 1.17 Crystal structures of (**a**) AMX_3- and (**b**) A_2MX_4-type perovskites. A (black circle), M (grey circle) and X (white circle) denote counter cation (K, La, Ba, etc.), metal (Cu, Ni, Mn, Ti, Zr, Mg. etc.) and bridge anion (O, F, H, etc.), respectively

1.5.2.2 Superconductive Perovskite

Since the discovery of high-temperature superconductivity in copper oxide [52], perovskite metal oxides have been explored as high-temperature superconductor [53, 54]. It is noted that in this case, "high-temperature" implies that superconducting transition temperature is higher than ordinary superconductors. Figure 1.17 depicts crystal structures of (a) AMX_3- and (b) A_2MX_4-type perovskites. In La_2CuO_4 perovskite, non-magnetic CuO_2 layer is separated by LaO layers. As shown in Fig. 1.18, there is orbital overlap between copper $3d_{x^2-y^2}$ and oxygen $2p_x$ orbitals in both MOα and MOβ. α spin of oxygen $2p_x$ orbital is cancelled out with β

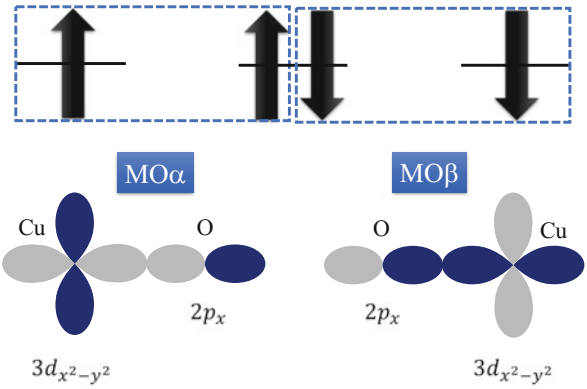

Fig. 1.18 Superexchange interaction between copper atoms via oxygen anion in two-dimensional CuO_2 layer (Cu-O-Cu model)

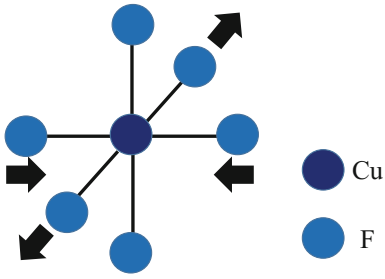

Fig. 1.19 Cu-F shrink and elongation in K_2CuF_4 perovskite

spin of oxygen $2p_x$ orbital. Hence, α spin of left copper $3d_x{}^2{}_{-y}{}^2$ orbital and β spin of right copper $3d_x{}^2{}_{-y}{}^2$ orbital remain: *Superexchange Rule* [55]. When electron or hole is doped in two-dimensional CuO_2 layer together with decreasing temperature, superconductivity appears. Though many superconductor theories were proposed, superconducting mechanism is fully unrevealed.

1.5.2.3 Magnetic Perovskite

1. *Ligand Bonding Effect in Perovskite Fluoride*

Ligand bonding effect [56] is observed in K_2CuF_4 perovskite. Cu-F distance in two-dimensional CuF_2 layer shrinks or elongates, though it is fixed along perpendicular axis (see Fig. 1.19). As the result, orbital overlaps between copper $3d$ and fluorine $2p$ orbitals exist in specific directions (see MO1α and MO2α in Fig. 1.20). In contrast to Cu-O-Cu model, left copper $3d_z{}^2{}_{-y}{}^2$ orbital is not overlapped with bridge oxygen $2p_x$ orbital, though there is overlap between right copper $3d_z{}^2{}_{-x}{}^2$ and bridge oxygen $2p_x$ orbitals. This is why the alternate $3d_z{}^2{}_{-x}{}^2$-type orbital ordering is caused in K_2CuF_4 perovskite.

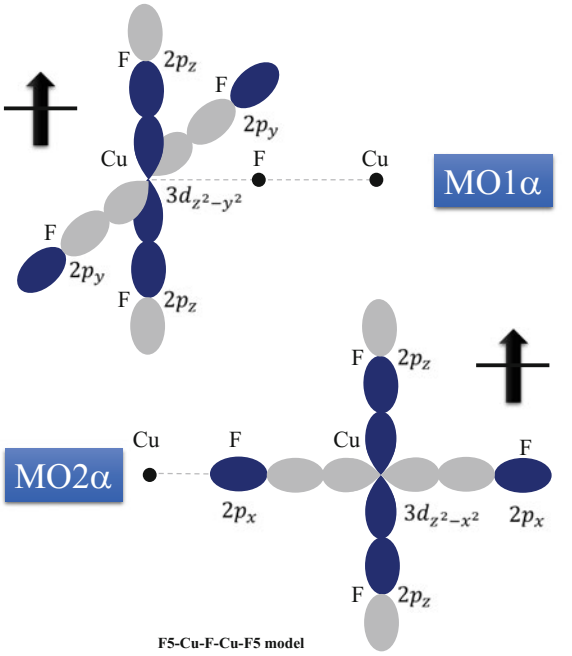

Fig. 1.20 Schematic figure of ligand bonding effect in F5-Cu-F-Cu-F5 model

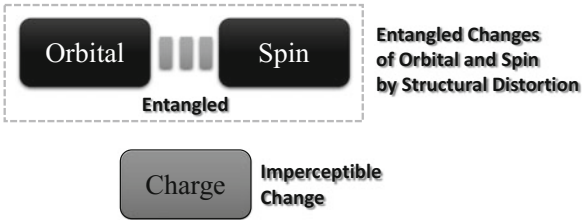

Fig. 1.21 Relationship between orbital, spin and charge in transition metal of insulating perovskite

2. *Orbital Degree of Freedom*

In La_2CuO_4 and K_2CuF_4 perovskites, though the formal charge of copper (+2) is the same, 3*d* electrons occupation pattern is different: *orbital degree of freedom*. Figure 1.21 depicts the relationship between orbital, spin and charge in transition metal of insulating perovskite. It is noted that charge state imperceptibly changes, even if orbital and spin dramatically change by structural distortion. Orbital degree of freedom appears also in $YTiO_3$, $LaVO_3$ and $LaMnO_3$ perovskites [57, 58].

1.6 Challenges

1.6.1 Nanospace Chemistry Towards Nanomachine

Nanospace is defined as nanosize-space, where molecule, atom and ion can be inserted. Though it looks easier to understand insertion process based on classical host-guest chemistry [59], it must be noted that insert-framework interaction is dominated by quantum mechanics. When insert has orbital overlap with framework, covalent bonding is formed. Even if there is no orbital overlap between insert and framework, quantum charge interaction exists. For example, metal organic framework (MOF) [60–63], nanoporous material and inclusion compound have nanospace. Figure 1.22 depicts the schematic figure of "nanospace chemistry". If insertion and release are completely controllable in nanospace, it will work as "nanomachine" [64].

1.6.2 Hydrogen Society and Safety

Hydrogen has been expected as major energy carrier in industry. Figure 1.23 depicts hydrogen society in the future. This energy conversion system is partially in practical use. Hydrogen molecule (H_2) is produced using fossil fuel such as natural gas or using renewable electric energy (via water splitting) [65]. In fuel cell system, electricity is produced through H_2 direct utilisation or natural gas reforming. To use electricity more efficiently, secondary battery system is combined with fuel cell system. Hydrogen can be also extracted via release reaction from hydrogen storage material. Recently, biomass has been also expected in hydrogen production.

In relation to hydrogen society, many nanomaterials have been explored, e.g. catalysts for hydrogen production, hydrogen storage materials, nanomaterials in

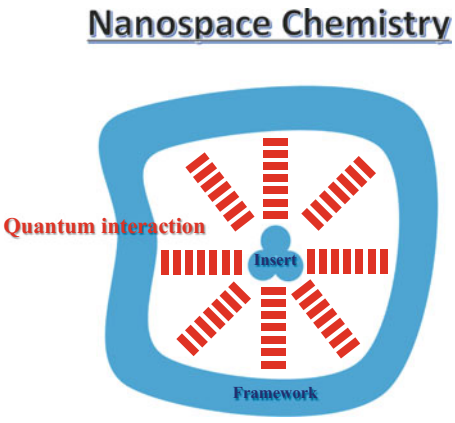

Fig. 1.22 The schematic figure of "nanospace chemistry". Insert-framework interaction is dominated by quantum mechanics (not classical interaction but *quantum interaction*)

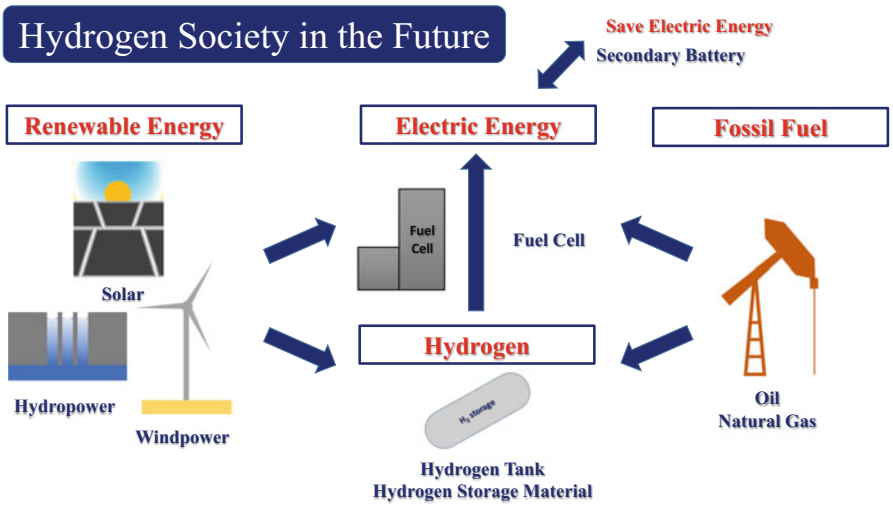

Fig. 1.23 Schematic figure of hydrogen society in the future

SOFC and secondary battery and so on. Except secondary battery materials, there is a possibility of direct contact with hydrogen species (H_2, H^+ and H^-). Pure H_2 is neither explosive nor reactive. However, if the concentration of reactant gas (oxygen molecule, etc.) is over the limit, it exhibits flammability [66]. It is required how to store pure H_2 safely from engineering viewpoint. In proton-conducting perovskite, proton exists as a part of covalent OH or OHO bonding [16, 17]. On the other hand, hydride ion, which exists at lattice position, acts as labile part [67]. In Chap. 2, hydride ion safety is discussed.

1.6.3 Safety of Lithium Ion Battery

Lithium ion battery must be protected against high electric current, internal short circuit, overcharging and overdischarging. It is because the factors cause thermal run-away [68]. Unforeseen and uncontrollable chemical reaction such as gas emission and liquid spillage may occur after thermal run-away.

Let us consider potential hazard of neutral lithium metal in lithium-ion battery. Two possible reactions on lithium ion are considered, when charging lithium ion battery (see Fig. 1.24).

$$Li^+ \rightarrow \left(Li^+\right)_{\text{Inserted}} \tag{1.1}$$

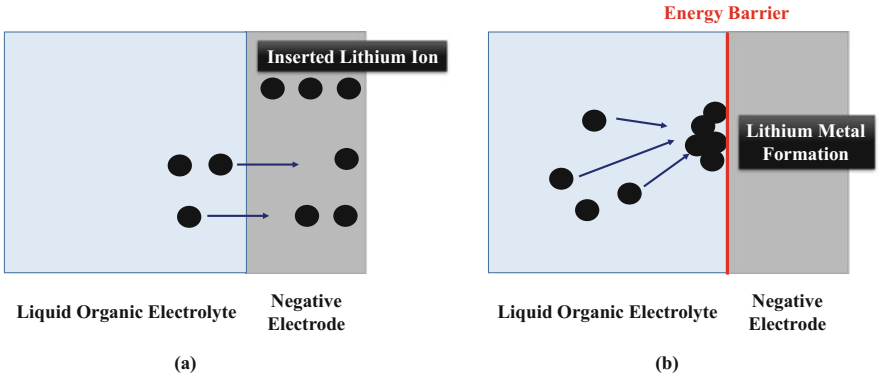

Fig. 1.24 Schematic figures of (**a**) lithium ion insertion to negative electrode and (**b**) lithium metal formation on negative electrode when charging lithium ion battery

$$Li^+ + e^- \rightarrow Li \tag{1.2}$$

where $(Li^+)_{Inserted}$ denotes lithium ion inserted into electrode. After accumulated charging and discharging in liquid organic electrolyte, energy barrier for lithium ion insertion appears, due to structural degradation of negative electrode surface, overcharging, overdischarging and so on. As the result, lithium metal is produced (Eq. (1.2)): *Electrodeposition* [69, 70]. Lithium metal causes following dangerous reactions with water and oxygen molecule (Eqs. (1.3) and (1.4)).

$$2Li + H_2O \rightarrow 2LiOH + H_2 \tag{1.3}$$

$$4Li + O_2 \rightarrow 2Li_2O \tag{1.4}$$

Not only lithium metal produced by electrodeposition but also lithium metal electrode always face the problem after repeated use in severe environment: mechanical and thermal damages (see Fig. 1.25). In large lithium ion battery system for electric vehicle, house and factory, it is much dangerous.

Liquid organic electrolyte itself exhibits flammability. From safety viewpoint of lithium ion battery, *all solid lithium ion battery without using lithium metal electrode* has been much expected. It is noted that no reaction occurs with water and oxygen molecule, when lithium ion is kept inside solid electrodes and electrolyte. Though lithium-oxygen (lithium-air) battery is recognised as theoretical high-performance lithium ion battery [71], it will be difficult for a practical use, due to lithium metal electrode.

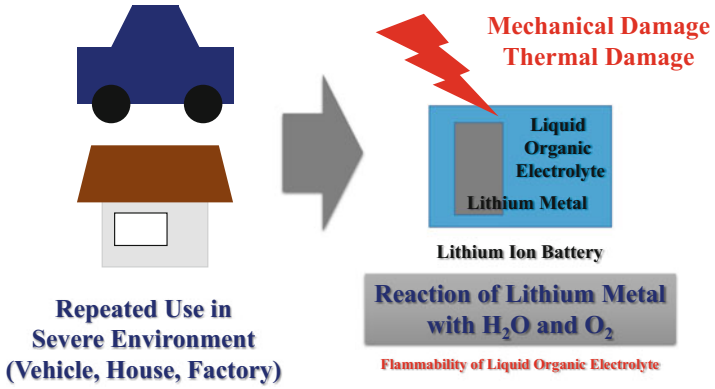

Fig. 1.25 Potential hazard of lithium ion battery using liquid organic electrolyte and lithium metal electrode

1.6.4 Replacement of Lithium: Sodium Ion Battery

As lithium resource is restricted on earth, replacement of lithium ion battery has been explored in secondary battery. One candidate is sodium ion battery, where sodium ion migrates inside electrolyte instead of lithium ion. In sodium-sulphur battery [72, 73], sodium metal, sulphur and β-alumina are used as negative electrode, positive electrode and solid electrolyte, respectively. In spite of utilising solid electrolyte, higher operation temperature (about 280–380 °C) is required. After repeated use, there is possibility that sodium metal may react with water and oxygen molecules. In addition, since β-alumina has a nonstoichiometric structure, sodium ion conductivity is unstable. *Low-temperature operation, replacement of sodium metal electrode and solid electrolyte with high sodium ion conductivity* are desirable, from safety viewpoint of sodium ion battery. In Chap. 10, sodium-ion-conducting glass is introduced. Recently, multivalent ions such as magnesium [74, 75] and calcium [76–78] ions have been also investigated as ion conductor of secondary battery.

1.7 Summary

After an explanation of the definition of nanomaterial, typical computational and experimental approaches to perform functional analysis for advanced nanomaterials were briefly introduced. In addition to introducing representative nanosize materials, nanoscale functionalities such as light response, ion conductivity, hydrogen storage, ferroelectric, superconductivity and magnetism were overviewed. Finally, recent challenges were discussed.

Acknowledgements This work was partially supported by the Research Council of Norway through its Centres of Excellence scheme, project number 262695.

References

1. T. Onishi, in *AIP Conference Proceedings 1702: 090001*, 2015
2. T. Onishi, in *AIP Conference Proceedings 1790: 020001,* 2016
3. T. Onishi, in *AIP Conference Proceedings 1906: 030001*, 2017
4. T. Onishi, in *AIP Conference Proceedings 2040: 020001,* 2018
5. T. Kawai, *Nanotechnology* (Ohmsha, 2002), (In Japanese)
6. Y. Zhao, D.G. Truhlar, Acc. Chem. Res. **41**, 157–167 (2008)
7. C.J. Cramer, D.G. Truhlar, Phys. Chem. Chem. Phys. **11**, 10757–10816 (2009)
8. P.E.M. Siegbahn, M.R. Blomberg, Annu. Rev. Phys. Chem. **50**, 221–249 (1999)
9. D. Rappoport, N.R.M. Crawford, F. Furche, K. Burke, *Encyclopedia of Inorganic and Bioinorganic Chemistry, Approximate Density Functionals: Which Should I Choose?* (Wiley, Hoboken, 2009)
10. A.J. Cohen, P. Mori-Sánchez, W. Yang, Science **321**, 792–794 (2008)
11. A.J. Cohen, P. Mori-Sánchez, W. Yang, Chem. Rev. **112**, 289–320 (2011)
12. M. Lundberg, P.E.M. Siegbahn, J. Chem. Phys. **122**, 224103 (2005)
13. S. Reimann, A. Borgoo, E.I. Tellgren, A.M. Teale, T. Helgaker, J. Chem. Theory Comput. **13**, 4089–4100 (2017)
14. E.I. Tellgren, A. Laestadius, T. Helgaker, S. Kvaal, A.M. Teale, J. Chem. Phys. **148**, 024101 (2018)
15. A. Tachibana, *New Aspects of Quantum Electrodynamics* (Springer Nature, Singapore, 2017)
16. T. Onishi, T. Helgaker, Prog. Theor. Chem. Phys. **27**, (2013), Chapter 14
17. T. Onishi, *Quantum Computational Chemistry – Modelling and Calculation for Functional Materials* (Springer Nature, Singapore, 2018), Chapter 14
18. D. Mijatovic, J.C.T. Eijkel, A. Berg, Lab. Chip. **5**, 492–500 (2005)
19. S. Iijima, Nature **354**, 56–58 (1991)
20. S. Iijima, T. Ichihashi, Nature **363**, 603–605 (1993)
21. H.W. Kroto, J.R. Heath, S.C. O'Brien, R.F. Curl, R.E. Smalley, Nature **318**, 162–163 (1985)
22. K. Takeda, K. Awaga, Phys. Rev. B **56**, 14560 (1997)
23. R. Sessoli, D. Gatteschi, A. Caneschi, M.A. Novak, Nature **365**, 141–143 (1993)
24. D.Y. Wu, O. Sato, Y. Einaga, C.Y. Duan, Angew. Chem. Int. Ed. **48**, 1475–1478 (2009)
25. O. Sato, J. Tao, Y.Z. Zhang, Angew. Chem. Int. Ed. **46**, 2152–2187 (2007)
26. O. Sato, Nat. Chem. **2**, 10–11 (2010)
27. J.A. Curran, T.W. Clyne, Surf. Coat. Technol. **199**, 168–176 (2005)
28. J.A. Curran, T.W. Clyne, Surf. Coat. Technol. **199**, 177–183 (2005)
29. A.L. Yerokhin, L.O. Snizhko, N.L. Gurevina, A. Leyland, A. Pilkington, A. Matthews, J. Phys. D. Appl. Phys. **36**, 2110–2120 (2003)
30. Q.S. Li, K. Domen, S. Naito, T. Onishi, K. Tamaru, Chem. Lett. **3**, 321–324 (1983)
31. D. Kan, T. Terashima, R. Kanda, A. Masuno, K. Tanaka, S. Chu, H. Kan, A. Ishizumi, Y. Kanemitsu, Y. Shimakawa, Nat. Mater. **4**, 816–819 (2005)
32. T. Onishi, *Quantum Computational Chemistry – Modelling and Calculation for Functional Materials* (Springer Nature, Singapore, 2018), Chapter 12
33. T. Onishi, Int. J. Quantum Chem. **108**, 2856–2861 (2008)
34. T. Onishi, Prog. Theor. Chem. Phys. **27**, (2013), Chapter 13
35. M.W. Schmidt, K.K. Baldridge, J.A. Boatz, S.T. Elbert, M.S. Gordon, J.H. Jensen, S. Koseki, N. Matsunaga, K.A. Nguyen, S. Su, T.L. Windus, M. Dupuis, J.A. Montgomery, J. Comput. Chem. **14**, 1347–1363 (1993)
36. Y. Inaguma, J. Ceram. Soc. Jpn. **114**, 1103–1110 (2006)
37. T. Onishi, Polyhedron **28**, 1792–1795 (2009)

38. T. Onishi, Int. J. Quantum Chem. **109**, 3659–3636 (2009)
39. T. Onishi, *Quantum Computational Chemistry – Modelling and Calculation for Functional Material* (Springer Nature, Singapore, 2018), Chapter 13
40. T. Onishi, Int. J. Quantum Chem. **110**, 2912–2917 (2010)
41. T. Onishi, Adv. Quantum Chem. **70**, 31–67 (2015)
42. T. Onishi, in *AIP Conference Proceedings 2040: 020002,* 2018
43. D.P. Broom, *Hydrogen Storage Materials* (Springer Nature, London, 2011), Chapter 2
44. M.B. Ley, L.H. Jepsen, Y.S. Lee, Y.W. Cho, J.M. von Colbev, M. Dornheim, M. Rokni, J.O. Jensen, M. Sloth, Y. Filinchuk, J.E. Jørgensen, F. Besenbacher, T.R. Jensen, Mater. Today **17**, 122–128 (2010)
45. T.K. Mandal, D.H. Gregory, Annu. Rep. Prog. Chem. Sect. A **105**, 21–54 (2009)
46. U. Eberle, M. Felderhoff, F. Schüth, Angew. Chem. Int. Ed. **48**, 6608–6630 (2009)
47. S. Orimo, Y. Nakamori, J.R. Eliseo, A. Züttel, C.M. Jensen, Chem. Rev. **107**, 4111–4132 (2007)
48. P. Ravindran, P. Vajeeston, R. Vidya, H. Fjellvåg, A. Kjekshus, J. Power Sources **159**, 88–99 (2006)
49. O.M. Løvvik, O. Swang, S.M. Opalka, J. Mater. Res. **20**, 3199–3213 (2005)
50. L. Schlapbach, A. Züttel, Nature **414**, 353–358 (2001)
51. T. Onishi, Mol. Phys. **112**, 533–538 (2014)
52. J.G. Bednorz, K.A. Miiller, Z. Phys. B: Condens. Matter. **64**, 189–193 (1986)
53. S. Maekawa, Oyo Buturi. **65**, 334–343 (1996), (In Japanese)
54. S. Maekawa, Oyo Buturi. **75**, 16–25 (2006), (In Japanese)
55. T. Onishi, *Quantum Computational Chemistry – Modelling and Calculation for Functional Material* (Springer Nature, Cham, 2018), Chapter 10
56. T. Onishi, *Quantum Computational Chemistry – Modelling and Calculation for Functional Material* (Springer Nature, Cham, 2018), Chapter 11
57. Y. Tokura, N. Nagaosa, Science **288**, 462–468 (2000)
58. T. Mizokawa, Solid State Phys. **37**, 733–743 (2002), (In Japanese)
59. G.D. Stucky, J.E. Mac Dougall, Science **247**, 669–678 (1990)
60. M. Eddaoudi, D.B. Moler, H. Li, B. Chen, T.M. Reineke, M. O'Keeffe, O.M. Yaghi, Acc. Chem. Res. **34**(4), 319–330 (2001)
61. J.L.C. Rowsell, O.M. Yaghi, Angew. Chem. Int. Ed. **44**, 4670–4679 (2005)
62. H.C. Zhou, J.R. Long, O.M. Yaghi, Chem. Rev. **112**, 673–674 (2012)
63. H.C. Zhou, S. Kitagawa, Chem. Soc. Rev. **43**, 5415–5418 (2014)
64. R.V. Noorden, D. Castelvecchi, Nature **538**, 152 (2016)
65. T. Hamacher, *Hydrogen and Fuel Cell – Technologies and Market Perspectives* (Springer Nature, Berlin, 2014), Chapter 1
66. U. Schmidtchen, R. Wurster, *Hydrogen and Fuel Cell – Technologies and Market Perspectives* (Springer Nature, Berlin, 2014), Chapter 3
67. N. Masuda, Y. Kobayashi, O. Hernandez, T. Bataille, S. Paofai, H. Suzuki, C. Ritter, N. Ichijo, Y. Noda, K. Takegoshi, C. Tassel, T. Yamamoto, H. Kageyama, J. Am. Chem. Soc. **137**, 15315–15321 (2015)
68. D. Lisbona, T. Snee, Process. Saf. Environ. Prot. **89**, 434–442 (2011)
69. D. Aurbach, E. Zinigrad, Y. Cohen, H. Teller, Solid State Ionics **148**, 405–416 (2002)
70. H. Honbo, K. Takei, Y. Ishii, T. Nishida, J. Power Sources **189**, 337–343 (2009)
71. C. Xia, C.Y. Kwok, L.F. Nazar, Science **361**, 777–781 (2018)
72. T. Oshima, M. Kajita, A. Okuno, Int. J. Appl. Ceram. Technol. **1**, 269–276 (2004)
73. R. Okuyama, H. Nakashima, T. Sano, E. Nomura, J. Power Sources **93**, 50–54 (2001)
74. P. Saha, M.K. Datta, O.I. Velikokhatnyi, A. Manivannan, D. Alman, P.N. Kumta, Prog. Mater. Sci. **66**, 1–86 (2014)
75. D. Aurbach, Z. Lu, A. Schechter, Y. Gofer, H. Gizbar, R. Turgeman, Y. Cohen, M. Moshkovich, E. Levi, Nature **407**, 724–727 (2000)
76. A. Ponrouch, C. Frontera, F. Bardé, M.R. Palacín, Nat. Mater. **15**, 169–172 (2016)
77. A. Ponrouch, M.R. Palacín, Curr. Opin. Electrochem. **9**, 1–7 (2018)
78. R.J. Gummow, G. Vamvounis, M.B. Bobby Kannan, Y. He, Adv. Mater. **30**, 1801702 (2018)

Part II
Computational Approach

Chapter 2
Quantum Chemistry in Perovskite Fluoride and Hydride: Nanoscale Hydride Ion Conduction

Taku Onishi

Abstract Hydride ion, which implies negatively charged hydrogen, has recently attracted much scientific attention from the viewpoint of nanoscale fast ion transport. Molecular orbital calculations based on density functional theory were performed for perovskite fluoride and hydride, in order to investigate the hydride ion-conducting mechanism. In hydride ion-doped $KMgF_3$ perovskite, it was found that hydride ion conduction occurs, combined with "competitive fluctuation", which implies that fluorine anion also migrates around local minimum during hydride ion conduction. The activation energy for hydride ion conduction was estimated to be 0.61–0.85 eV. It was also found that hydride ion conduction occurs in $KMgH_3$ perovskite. The activation energy for hydride ion conduction was estimated to be 0.40–0.61 eV. From the viewpoint of structural stability at high temperature, it was concluded that hydride ion-doped $KMgF_3$ perovskite is more favourable than $KMgH_3$ perovskite. In comparison with proton-conducting perovskites, it was concluded that hydride ion conducting perovskites can be utilized as fast ion conductor. Finally, we discuss hydride ion safety and outlook.

Keywords Molecular orbital calculation · Perovskite fluoride · Hydride ion conduction · Competitive fluctuation · Perovskite hydride · Hydrogen storage material

2.1 Introduction

It is well known that perovskites exhibit lithium ion, proton and oxide ion conductivities. Since the discovery of lithium ion conducting perovskite titanium oxides

T. Onishi (✉)
Graduate School of Engineering, Mie University, Tsu, Japan

Hylleraas Centre for Quantum Molecular Sciences, Department of Chemistry, University of Oslo, Oslo, Norway
e-mail: taku@chem.mie-u.ac.jp; taku.onishi@kjemi.uio.no

T. Onishi (ed.), *Theoretical Chemistry for Advanced Nanomaterials*,
https://doi.org/10.1007/978-981-15-0006-0_2

[1], they have been focused on as solid electrolyte of lithium ion battery [2, 3]. In solid oxide fuel cell (SOFC), proton and oxide ion conducting perovskite oxides have been utilized for solid electrolyte, due to stable structure at high operation temperature [4–7].

In proton and hydride ion conducting perovskites, hydrogen atom migrates inside perovskites. Proton and hydride ion conductions can be distinguished from formal charge of hydrogen atom before and after ion conduction: proton (+1) and hydride ion (−1). However, during proton conduction, the real charge density is different from the formal charge (+1). For example, the charge density is close to zero, in proton conducting $LaAlO_3$ perovskite [8]. It is because OH and OHO covalent bondings are formed during proton conduction. Norby et al. indicated the possibility of hydride ion conduction in perovskite titanium oxides [9–11]. Recently, in $BaTiO_3$ perovskite, Kageyama et al. showed that oxygen anion can be replaced by hydride ion [12], and hydride ion acts as labile part [13]. From our previous theoretical calculations, it was found that hydride ion migrates via oxygen vacancy, and fluctuation of hydride ion occurs [14].

Here we focus on perovskite fluoride and hydride, which have a typical perovskite structure [15, 16], since they can be expected as fast ion conducting material. In perovskite fluoride, hydride ion is incorporated by replacing fluorine anion at lattice position [17, 18]. The hydride ion conducting mechanism is explained, from the viewpoints of energetics and bonding.

2.2 Theoretical Approach: Molecular Orbital Calculation and Chemical Bonding Rule

Molecular orbital (MO) calculations based on density functional theory (DFT) were performed for perovskite fluoride and hydride. BHHLYP method, where functionals of Hartree-Fock exchange, Becke exchange and LYP correlation are included, was selected. 6-31G* basis set was used for magnesium, fluorine and hydrogen, combined with MINI basis set for potassium. All calculations were performed by using Firefly program package [19, 20]. The figures of MOs were depicted by MOLEKEL [21]. Chemical bonding property was characterised by using chemical bonding rule [22]. The rule is summarised as below.

Chemical Bonding Rule
For molecular orbitals including outer shell electrons, check whether orbital overlap exists or not.

- With orbital overlap: Covalent.
- Without orbital overlap: Ionic.

2.3 Hydride Ion Conduction in Perovskite Magnesium Fluoride: $KMgF_3$

The crystal structure of $KMgF_3$ perovskite was experimentally investigated from very low temperature to 1200 K. $KMgF_3$ perovskite has a simple cubic structure throughout the temperate range. The lattice parameter (Mg-F-Mg distance) is 3.973 Å [23, 24]. In relation to Jahn-Teller effect [25, 26], optical property and magnetism, transition metals such as Co^{2+} [27], Cu^{2+} [28], Cr^{3+} [29, 30], Ni^{2+} [31, 32], etc. were doped at the lattice position of magnesium. No ion conductivity was previously observed in $KMgF_3$ perovskite [33]. Here we investigate whether hydride ion-doped $KMgF_3$ perovskite exhibits hydride ion conductivity or not, from the viewpoints of energetics and bonding.

2.3.1 Calculation Models

Figure 2.1 depicts the calculation models for $KMgF_3$ perovskite. From our previous MO calculations, it is known that conducting anion migrates along a diagonal line connecting two lattice positions in a cubic perovskite (see arrows in Fig. 2.1). It is because ion conduction via square centre (from F1 to F3) requires larger energy. It is noted that fluorine anion vacancy, which can be introduced by counter cation vacancy or different counter cation doping [3], is required to cause fluorine anion conduction. To take the effect of charge compensation into account, potassium vacancy is also considered.

2.3.2 Fluorine Anion Conduction in Perovskite Magnesium Fluoride

Figure 2.2a, b show the potential energy curves of $K_2Mg_4F_3$ and KMg_4F_3 models, when displacing fluorine anion along the diagonal line. In $K_2Mg_4F_3$ model, local minima are found between midpoint and lattice position ($d = 0.4$ and 2.4 Å), and local maximum is found at the middle ($d = 1.4$ Å). Though the activation energy for fluorine anion conduction is 2.23 eV, the partial activation energy crossing lattice position is much smaller (0.49 eV). It is considered that fluorine anion is displaced till local minimum at room temperature. It is because the partial activation energy is as same as lithium conducting perovskite-type titanium oxides [1], where lithium ion conduction occurs at room temperature. On the other hand, it is considered that high temperature is required when crossing a midpoint. It is because the activation energy is as same as proton conducting perovskite-type oxides [7, 8, 34], where proton conduction occurs at high temperature. The introduction of one potassium vacancy causes one fluorine vacancy, due to charge compensation. In order to investigate the effect, KMg_4F_3 model was also constructed (see Fig. 2.1b).

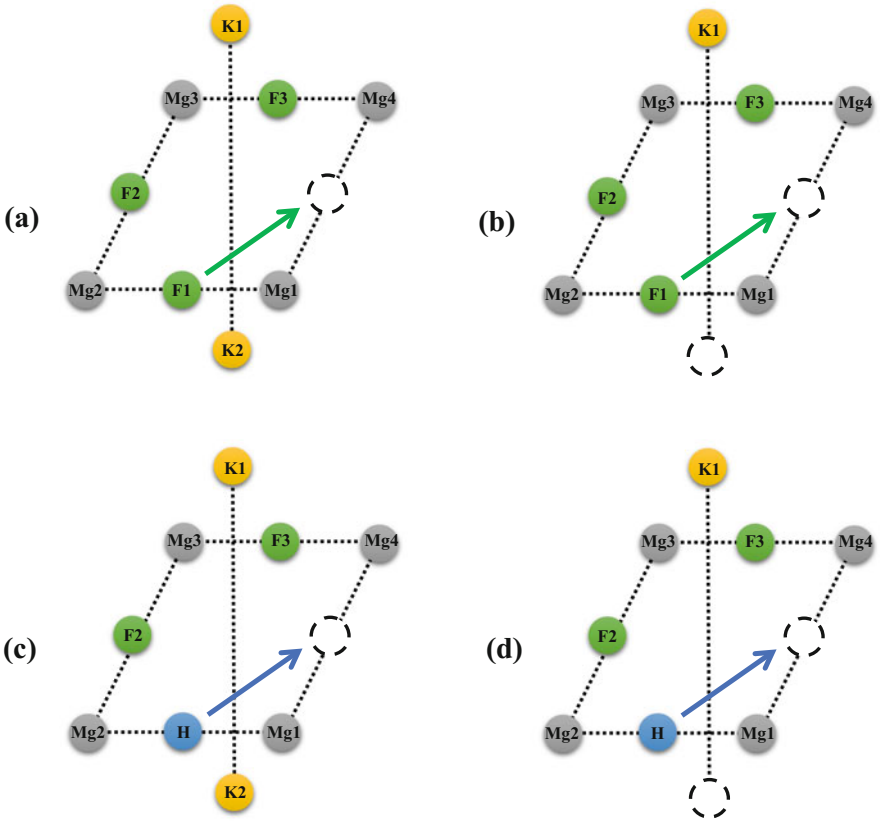

Fig. 2.1 The calculation models for $KMgF_3$ perovskite: (**a**) $K_2Mg_4F_3$, (**b**) KMg_4F_3 with potassium vacancy, (**c**) hydride ion-doped $K_2Mg_4F_2H$, (**d**) hydride ion-doped KMg_4F_2H with potassium vacancy. Note that dotted circle denotes fluorine or potassium vacancy

The figure of potential energy curve in KMg_4F_2H model is similar to $K_2Mg_4F_3$ model. The total and partial activation energies are 2.41 and 0.33 eV, respectively. In $KMgF_3$ perovskite, it is also concluded that no fluorine anion conduction occurs at room temperature, though partial fluorine anion displacement occurs.

Figures 2.3, 2.4, and 2.5 depict the shapes of selected MOs related to fluorine 2*s* and 2*p* orbitals in $K_2Mg_4F_3$ model, at lattice positon, local minimum and local maximum, respectively. At lattice position ($d = 0.0$ Å), F1 (conducting fluorine anion) 2*s* and 2*p* orbitals overlap with F2 and F3 (other fluorine anions) orbitals. In MO36 and MO37, F1 2s orbital overlaps with F3 2*s* orbital. In MO45–MO51, F1 2*p* orbital overlaps with F3 2*p* orbital. Especially in MO45, MO47, MO48 and MO51, F2 2*p* orbital also overlaps with F1 and F3 2*p* orbitals. From chemical bonding rule, it is found that covalent bonding is formed between fluorine anions. MO52 consists of F2 2*p* orbital, though F2 2*p* orbital slightly overlaps with F1 and F3 2*p* orbitals in MO53. In addition, from chemical bonding rule, it is found that ionic

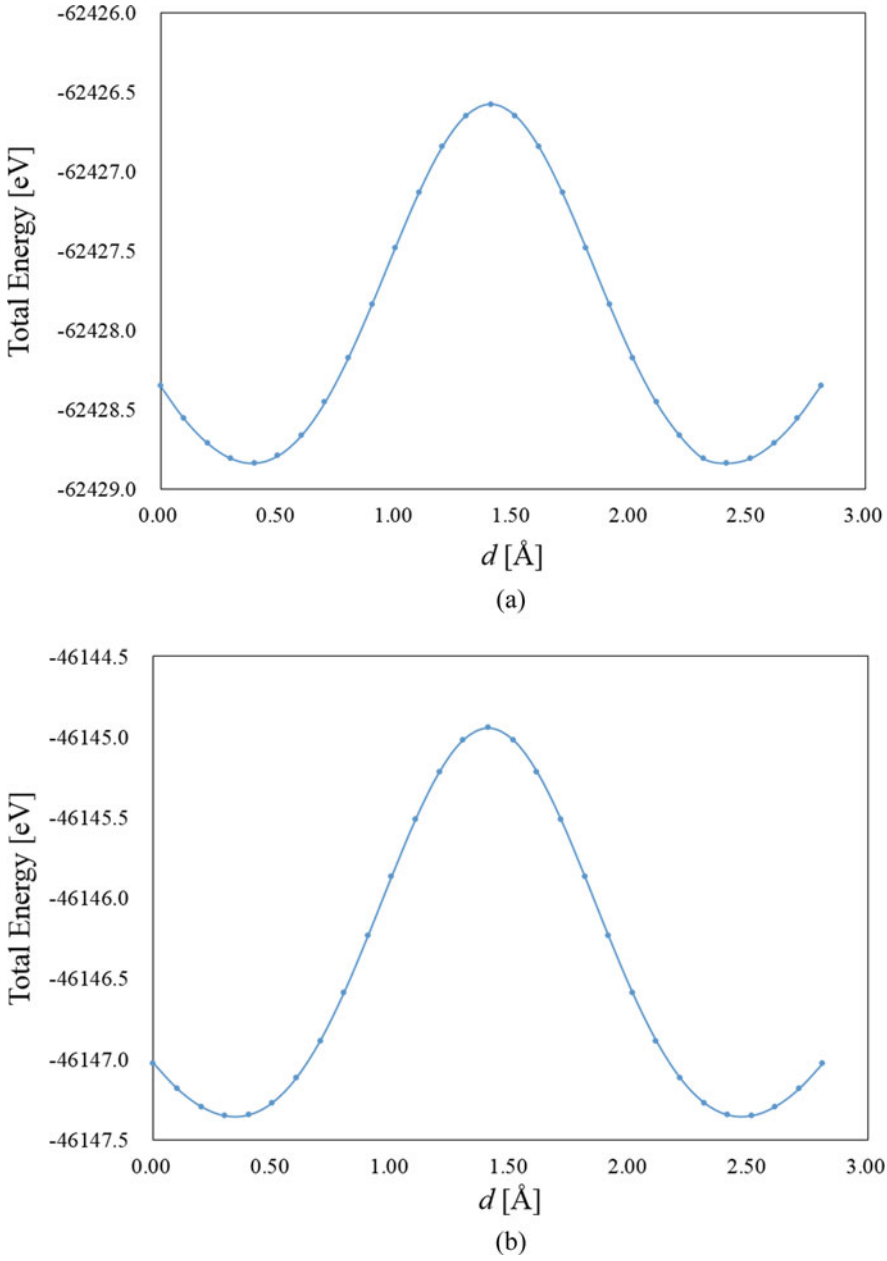

Fig. 2.2 The potential energy curves of (**a**) $K_2Mg_4F_3$ and (**b**) KMg_4F_3 models, when displacing *fluorine anion* along the diagonal line. Note that *d* notes a migration distance from fluorine lattice position (see green arrow in Fig. 2.1a, b)

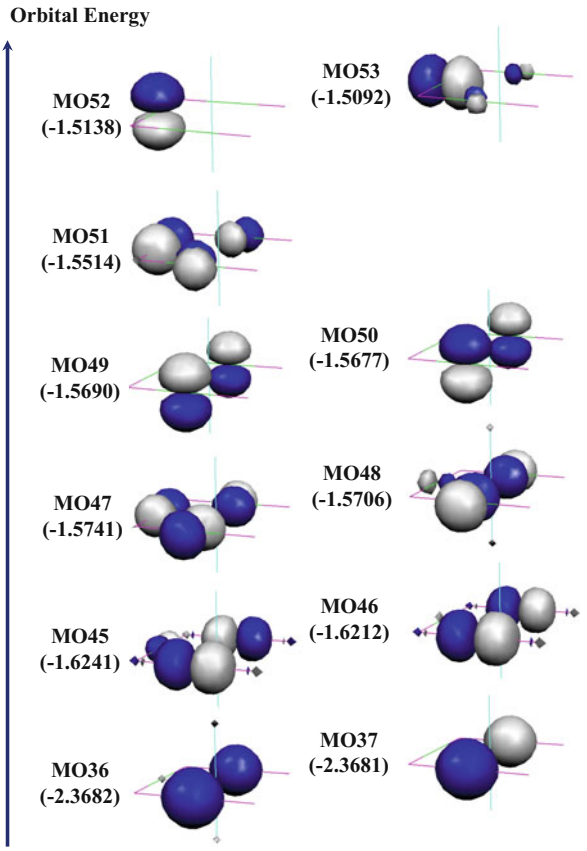

Fig. 2.3 The shapes of selected molecular orbitals related to fluorine 2*s* and 2*p* orbitals (fluorine outer shell orbitals) at lattice position ($d = 0.0$ Å) in $K_2Mg_4F_3$ model. Note that orbital energy is given in parenthesis

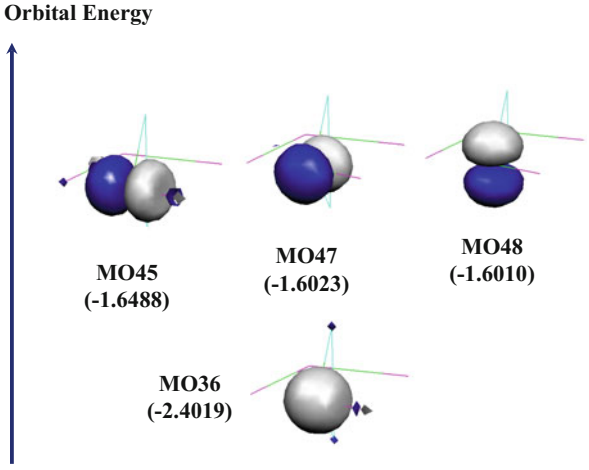

Fig. 2.4 The shapes of selected molecular orbitals related to fluorine 2*s* and 2*p* orbitals (fluorine outer shell orbitals) at local minimum ($d = 0.4$ Å) in $K_2Mg_4F_3$ model. Note that orbital energy is given in parenthesis

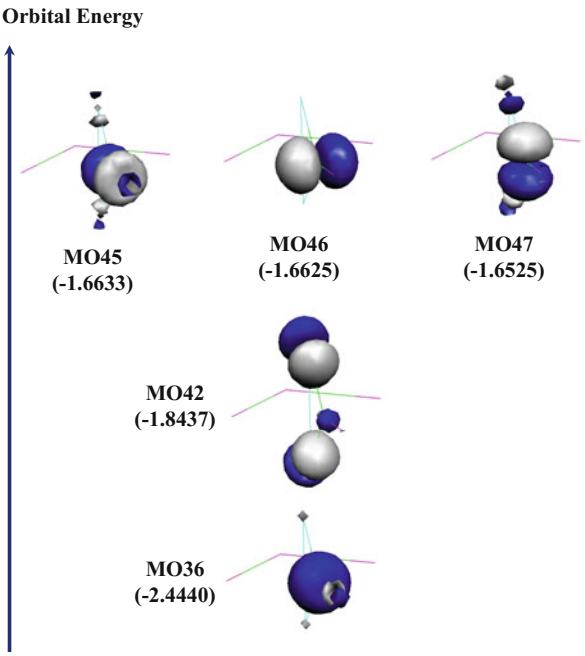

Fig. 2.5 The shapes of selected molecular orbitals related to fluorine 2*s* and 2*p* orbitals (fluorine outer shell orbitals) at local maximum ($d = 1.4$ Å) in $K_2Mg_4F_3$ model. Note that orbital energy is given in parenthesis

bonding is formed between magnesium and fluorine anion, due to no orbital overlap between them. At left local minimum ($d = 0.4$ Å), F1 2*s* and 2*p* orbitals have almost no orbital overlap with other atoms. From chemical bonding rule, it is found that conducting fluorine anion forms ionic bonding with fluorine anions, magnesium and potassium. It is noted that symmetric MOs are given at right local minimum ($d = 2.4$ Å). At local maximum ($d = 1.4$ Å), though F1 2*s* and 2*p* orbitals have no orbital overlap with F2 and F3 orbitals, they overlap with K1 and K2 2*p* orbitals, where $2p_x$, $2p_y$ and $2p_z$ orbitals are hybridized (see MO42, MO45 and MO47 in Fig. 2.5). From chemical bonding rule, it is found that covalent bonding is formed between conducting fluorine anion and potassium.

The shapes of MOs in KMg_4F_3 model are similar to $K_2Mg_4F_3$ model, at lattice position ($d = 0.0$ Å) and local minima ($d = 0.3$ and 2.5 Å). At local maximum, one potassium participates in covalent bonding formation. In Fig. 2.6, the orbital overlaps between conducting fluorine anion, and potassium is smaller than $K_2Mg_4F_3$ model. The larger activation energy crossing a midpoint is due to the smaller covalency.

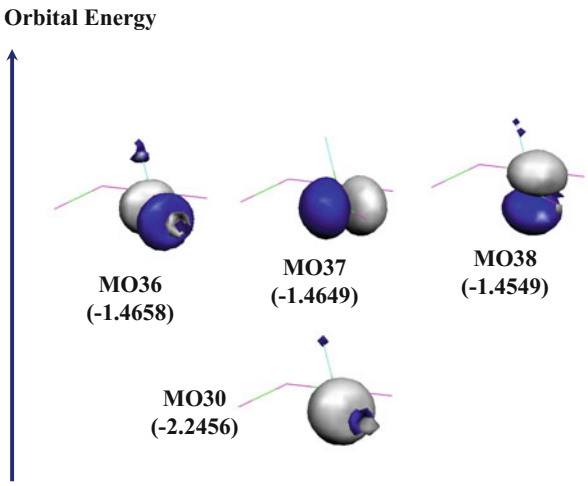

Fig. 2.6 The shapes of selected molecular orbitals related to fluorine 2*s* and 2*p* orbitals (fluorine outer shell orbitals) at local maximum ($d = 1.4$ Å) in KMg_4F_3 model. Note that orbital energy is given in parenthesis

2.3.3 Hydride Ion Incorporation in Perovskite Magnesium Fluoride

We next investigate whether hydride ion, which is incorporated in $KMgF_3$ perovskite, migrates or not. The calculation models used here are $K_2Mg_4F_2H$ and KMg_4F_2H (see Fig. 2.1c, d).

2.3.3.1 Pure Hydride Ion Conduction

Figure 2.7a, b show the potential energy curves of $K_2Mg_4F_2H$ and KMg_4F_2H models, when displacing hydride ion along the diagonal line. In both models, local minima are found: $d = 0.6$ and 2.2 Å ($K_2Mg_4F_2H$ model); $d = 0.5$ and 2.3 Å (KMg_4F_2H model). In $K_2Mg_4F_2H$ model, the activation energy for hydride ion conduction is 0.58 eV, whereas the partial activation energy crossing a midpoint is 0.29 eV. On the other hand, in KMg_4F_2H model, the activation energy for hydride ion conduction is estimated from the total energy difference between midpoint and local minimum (0.45 eV). It is noted that the highest total energy is given at the midpoint.

Figure 2.8a–c depict the shapes of selected MOs related to hydrogen 1*s* orbital in $K_2Mg_4F_2H$ model, at lattice positon, local minimum ($d = 0.6$ Å) and local maximum ($d = 1.4$ Å), respectively. It is noted that MOs at right local minimum ($d = 2.2$ Å) is symmetric to left local minimum ($d = 0.6$ Å). The wave functions of MO49s are expressed as

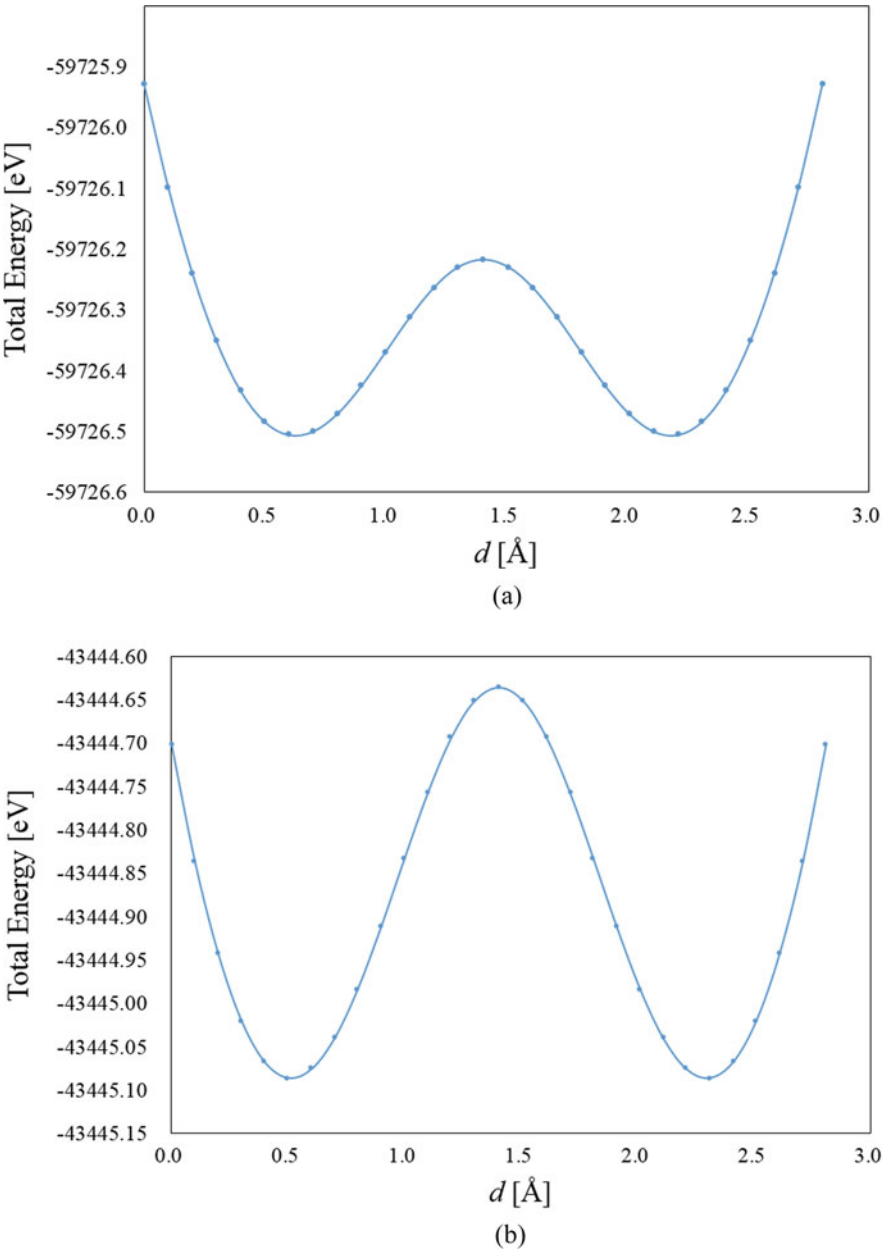

Fig. 2.7 The potential energy curves of (**a**) $K_2Mg_4F_2H$ and (**b**) KMg_4F_2H models, when displacing *hydride ion* along the diagonal line. Note that *d* notes a migration distance from hydrogen lattice position (see blue arrows in Fig. 2.1c, d)

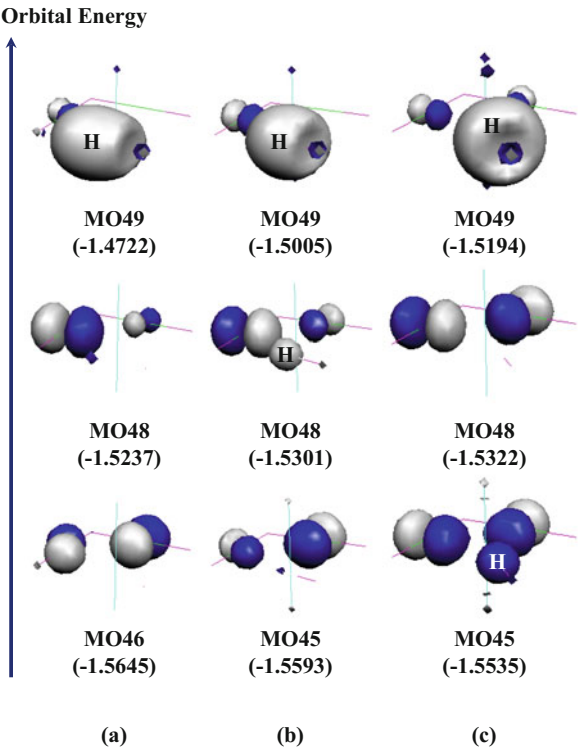

Fig. 2.8 The shapes of selected molecular orbitals related to hydrogen 1*s* orbital at (**a**) lattice position ($d = 0.00$ Å), (**b**) local minimum ($d = 0.6$ Å) and (**c**) local maximum ($d = 1.4$ Å), when displacing *hydride ion* in $K_2Mg_4F_2H$ model. Note that orbital energy is given in parenthesis

$$\Psi_{\mathrm{MO49}}\,(\mathrm{Lattice}) = 0.29\phi_{\mathrm{H}}\left(1s'\right) + 0.52\phi_{\mathrm{H}}\left(1s''\right) - 0.15\phi_{\mathrm{F2}}\left(2px'\right) - 0.12\phi_{\mathrm{F2}}\left(2px''\right) - 0.11\phi_{\mathrm{Mg1}}(2s) + 0.25\phi_{\mathrm{Mg1}}\left(3s'\right) - 0.12\phi_{\mathrm{Mg1}}\left(3px'\right) \tag{2.1}$$

$$\Psi_{\mathrm{MO49}}\,(\mathrm{Min}) = 0.30\phi_{\mathrm{H}}\left(1s'\right) + 0.52\phi_{\mathrm{H}}\left(1s''\right) - 0.23\phi_{\mathrm{F2}}\left(2px'\right) - 0.18\phi_{\mathrm{F2}}\left(2px''\right) - 0.14\phi_{\mathrm{Mg1}}(2s) + 0.22\phi_{\mathrm{Mg1}}\left(3s'\right) - 0.10\phi_{\mathrm{Mg1}}\left(3px'\right) \tag{2.2}$$

$$\begin{aligned}\Psi_{MO49}\,(\mathrm{Max}) = {} & 0.11\phi_{\mathrm{K1}}\,(3pz) - 0.11\phi_{\mathrm{K2}}\,(3pz) \\ & + 0.32\phi_{\mathrm{H}}\left(1s'\right) + 0.53\phi_{\mathrm{H}}\left(1s''\right) \\ & - 0.15\phi_{\mathrm{F2}}\left(2px'\right) - 0.12\phi_{\mathrm{F2}}\left(2px''\right) + 0.15\phi_{\mathrm{F3}}\left(2py'\right) + 0.12\phi_{\mathrm{F3}}\left(2py''\right) \\ & - 0.17\phi_{\mathrm{Mg1}}(2s) + 0.20\phi_{\mathrm{Mg1}}\left(3s'\right)\end{aligned} \tag{2.3}$$

At local maximum, hydrogen 1*s* orbital overlaps with fluorine p, magnesium s and potassium p orbitals. From chemical bonding rule, it is found that hydride ion forms covalent bonding with fluorine anion, magnesium and potassium. At lattice position and local minimum, no potassium p orbital participates in covalent bonding

formation. In MO48 at local minimum and MO45 at local maximum, hydrogen 1*s* orbital overlaps with fluorine 2*p* orbitals. From chemical bonding rule, it is found that covalent bonding related to hydride ion is also formed.

In KMg_4F_2H model, main MOs related to hydrogen 1*s* orbital were MO40s. The wave functions of MO40s are expressed as

$$\begin{aligned}\Psi_{\mathrm{MO40}}\,(\mathrm{Lattice}) = {} & 0.29\phi_{\mathrm{H}}\left(1s'\right) + 0.50\phi_{\mathrm{H}}\left(1s''\right) - 0.16\phi_{\mathrm{F2}}\left(2px'\right) - 0.13\phi_{\mathrm{F2}}\left(2px''\right) \\ & -0.12\phi_{\mathrm{Mg1}}(2s) + 0.26\phi_{\mathrm{Mg1}}\left(3s'\right) - 0.12\phi_{\mathrm{Mg1}}\left(3px''\right)\end{aligned} \tag{2.4}$$

$$\begin{aligned}\Psi_{\mathrm{MO40}}\,(\mathrm{Min}) = {} & -0.30\phi_{\mathrm{H}}\left(1s'\right) - 0.48\phi_{\mathrm{H}}\left(1s''\right) + 0.20\phi_{\mathrm{F2}}\left(2px'\right) + 0.15\phi_{\mathrm{F2}}\left(2px''\right) \\ & + 0.14\phi_{\mathrm{Mg1}}(2s) - 0.27\phi_{\mathrm{Mg1}}\left(3s'\right) + 0.12\phi_{\mathrm{Mg1}}\left(3px'\right)\end{aligned} \tag{2.5}$$

$$\begin{aligned}\Psi_{MO40}\,(\mathrm{Max}) = {} & 0.33\phi_{\mathrm{H}}\left(1s'\right) + 0.46\phi_{\mathrm{H}}\left(1s''\right) \\ & - 0.13\phi_{\mathrm{F2}}\left(2px'\right) - 0.10\phi_{\mathrm{F2}}\left(2px''\right) + 0.13\phi_{\mathrm{F3}}\left(2py'\right) + 0.10\phi_{\mathrm{F3}}\left(2py''\right) \\ & - 0.18\phi_{\mathrm{Mg1}}(2s) + 0.27\phi_{\mathrm{Mg1}}\left(3s'\right) - 0.10\phi_{\mathrm{Mg1}}\left(3px'\right)\end{aligned} \tag{2.6}$$

In Eqs. (2.4) and (2.5), hydrogen 1*s* orbital has similar orbital overlap pattern to MO49s in $K_2Mg_4F_2H$ model. From chemical bonding rule, it is found that covalent bonding is formed between hydride ion, magnesium and fluorine anion. On the other hand, in Eq. (2.6), no potassium participates in covalent bonding formation. It is considered that no covalent bonding formation between hydride ion and potassium at local maximum is one of the reasons why total energy at the midpoint is larger than $K_2Mg_4F_2H$ model.

2.3.3.2 Pure Fluorine Anion Conduction

Let us consider also pure fluorine anion conduction, when fixing hydride ion at lattice position (see Fig. 2.9a). Figure 2.10a, b show the potential energy curves of $K_2Mg_4F_2H$ and KMg_4F_2H models, when displacing fluorine anion along the diagonal line. In both cases, the total energies at right local minima are higher than left local minima, and total energies at initial lattice position are smaller than final lattice position. The total activation energies for fluorine anion conduction are 2.36 eV in $K_2Mg_4F_2H$ model and 2.52 eV in KMg_4F_2H model. The values are too high to cause fluorine anion conduction at room temperature. It is however considered that partial fluorine anion displacement is combined during hydride ion conduction, due to its small energy difference: 0.45 ($K_2Mg_4F_2H$ model) and 0.30 eV (KMg_4F_2H model).

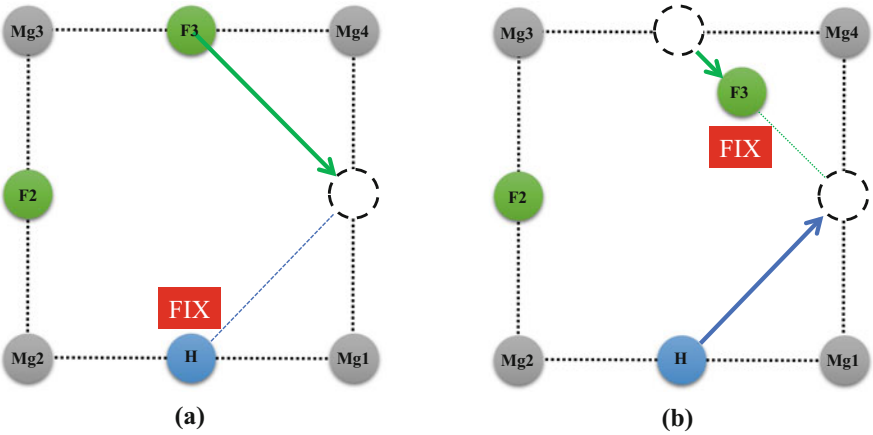

Fig. 2.9 The schematic figures of (**a**) pure fluorine anion conduction and (**b**) hydride ion conduction combined with fluorine anion displacement on two dimensional layers in hydride ion-doped $KMgF_3$ perovskite

2.3.3.3 Competitive Fluctuation of Fluorine Anion

We understood that both hydride ion and fluorine anion migrate on two dimensional layer of hydride ion-doped $KMgF_3$ perovskite. Let us consider the relationship between two competing migrations (hydride ion conduction and fluorine anion displacement).

Figure 2.11 shows the potential energy curves of $K_2Mg_4F_2H$ model, when displacing hydride ion along the diagonal line (see a blue arrow in Fig. 2.9b) and fixing fluorine anion in the diagonal line (see a green arrow in Fig. 2.9b). Since local minimum was given at 0.4 Å in pure fluorine anion conduction, 0.1, 0.2 and 0.4 Å were selected as a fixed distance. Though blue curve (0.4 Å fluorine anion displacement) is lower than other curves at $d = 0.0$ Å, it is the highest at $d = 2.8$ Å. Blue curve has crossing points at 1.3 Å with orange curve (0.2 Å fluorine anion displacement), 1.9 Å with grey curve (0.1 Å fluorine anion displacement) and 2.5 Å with yellow curve (no fluorine anion displacement). Orange curve is lower than grey curve at all distances. From the results, it is concluded that fluorine anion migrates between 0.2 and 0.4 Å in the diagonal line, during hydride ion conduction. The effect is called "competitive fluctuation" (see Fig. 2.12).

Figure 2.13 shows the potential energy curves of KMg_4F_2H model, when displacing hydride ion along the diagonal line and fixing fluorine anion in the diagonal line. Since local minimum was given at 0.3 Å in pure fluorine anion conduction, 0.1, 0.2 and 0.3 Å were selected as a fixed distance. Though blue curve (0.3 Å fluorine anion displacement) is lower than other curves at $d = 0.0$ Å, it is the highest at $d = 2.8$ Å. Blue curve has crossing points at 1.3 Å with orange curve (0.2 Å fluorine anion displacement), 1.9 Å with grey curve (0.1 Å fluorine anion displacement) and 2.4 Å with yellow curve (no fluorine anion displacement).

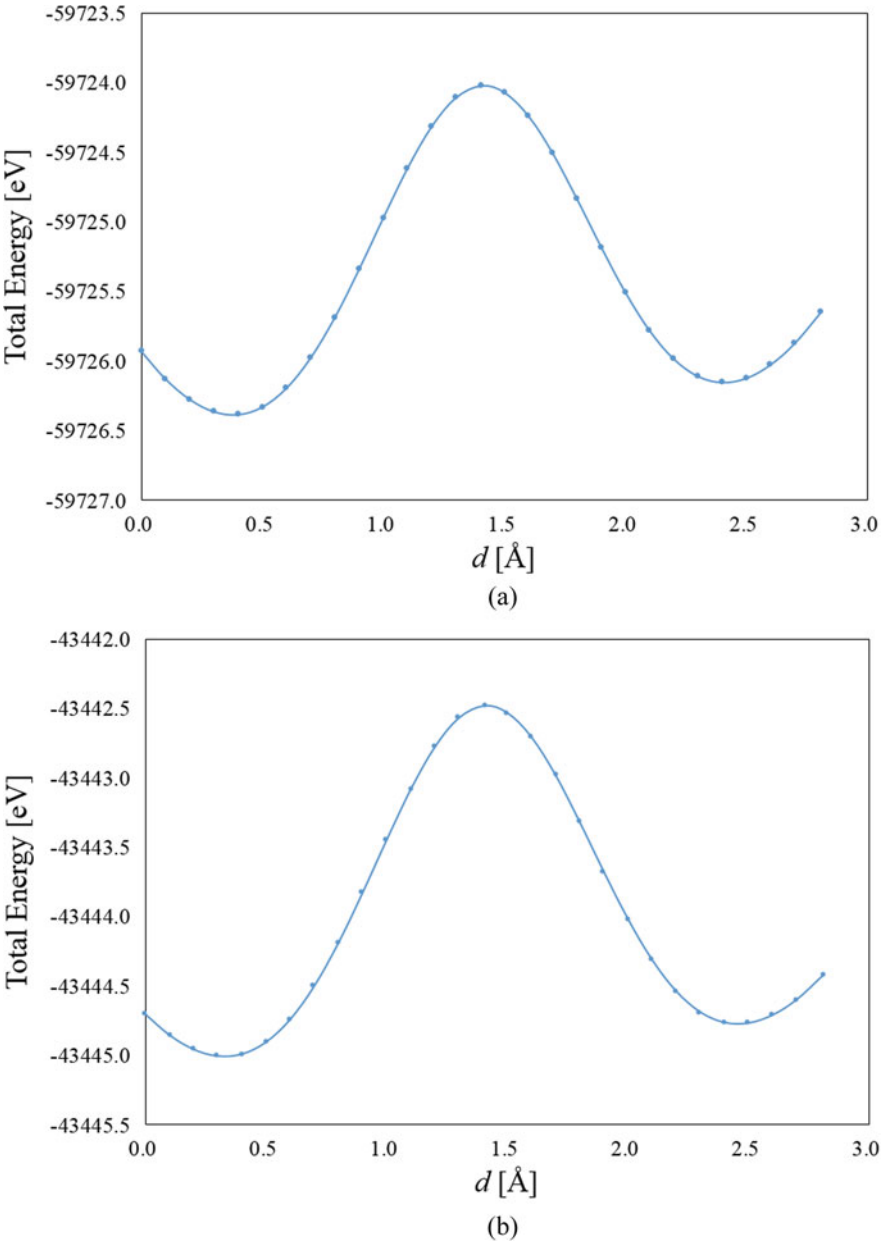

Fig. 2.10 The potential energy curves of (**a**) $K_2Mg_4F_2H$ and (**b**) KMg_4F_2H models, when displacing *fluorine anion* along the diagonal line. Note that *d* notes a migration distance from fluorine lattice position (see a green arrow in Fig. 2.9a)

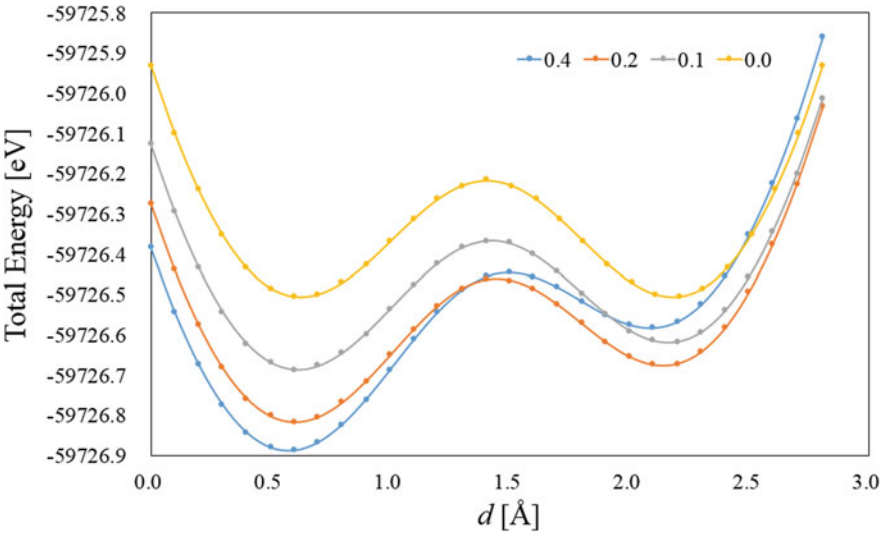

Fig. 2.11 The potential energy curves of $K_2Mg_4F_2H$ model, when displacing hydride ion along the diagonal line and fixing fluorine anion in the diagonal line. Note that *d* notes a migration distance from hydrogen lattice position (see a blue arrow in Fig. 2.9b). Fluorine anion-displacement distances are 0.0, 0.1, 0.2 and 0.4 Å in yellow, grey, orange and blue curves, respectively

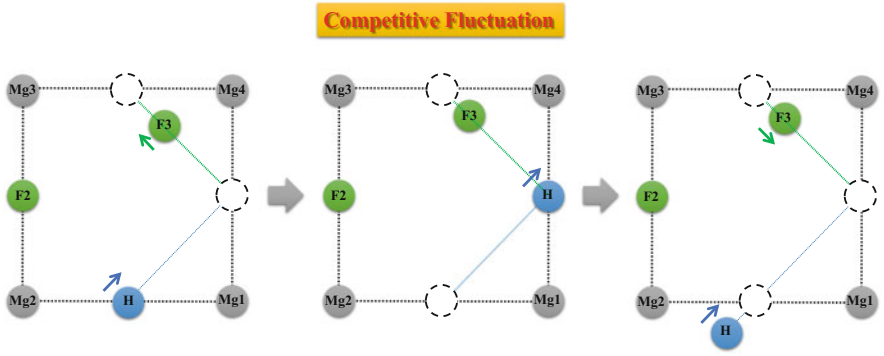

Fig. 2.12 The competitive fluctuation of fluorine anion during hydride ion conduction

Though orange curve is lower than grey curve between 0.0 and 2.4 Å, grey curve is lower than orange curve after the crossing point. From the results, it is concluded that competitive fluctuation occurs between 0.1 and 0.3 Å.

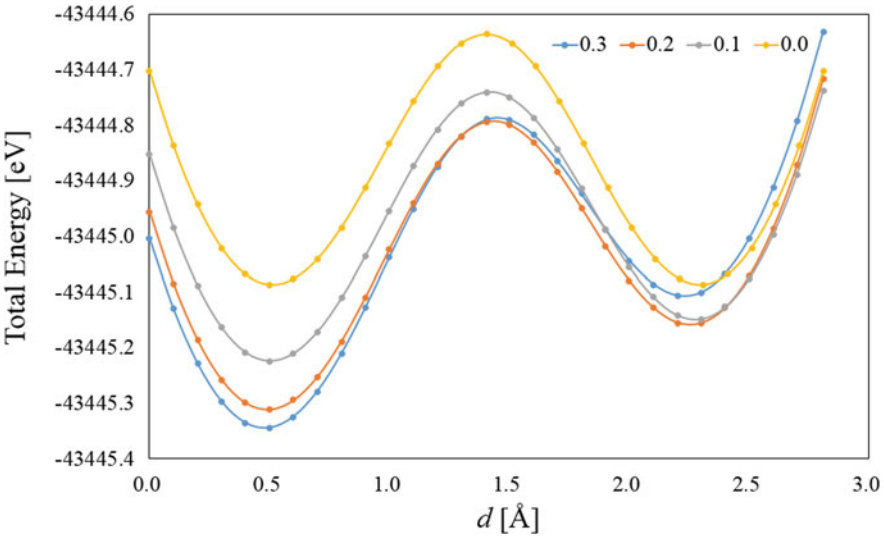

Fig. 2.13 The potential energy curves of KMg_4F_2H model, when displacing hydride ion along the diagonal line and fixing fluorine anion in the diagonal line. Note that *d* notes a migration distance from hydrogen lattice position (see a blue arrow in Fig. 2.9b). Fluorine anion-displacement distances are 0.0, 0.1, 0.2 and 0.3 Å in yellow, grey, orange and blue curves, respectively

2.3.4 Summary

In $KMgF_3$ perovskite, fluorine anion conduction occurs only at high temperature. On the other hand, in hydride ion-doped $KMgF_3$ perovskite, hydride ion conduction occurs at room temperature, combined with "competitive fluctuation" of fluorine anion, which implies that fluorine anion also migrates around local minimum during hydride ion conduction. In $K_2Mg_4F_2H$ model, the activation energy for hydride ion conduction can be estimated to be 0.85 eV, from the total energy difference between left local minimum of blue curve and final lattice position of orange curve. On the other hand, in KMg_4F_2H model, it can be estimated to be 0.61 eV, from the total energy difference between left local minimum of blue curve and final lattice position of grey curve.

2.4 Hydride Ion Conduction in Perovskite Magnesium Hydride: $KMgH_3$

Perovskite magnesium hydride $AMgH_3$ (A = alkali metal such as K, Na, etc.), which has a similar structure with perovskite magnesium fluoride, has been expected as hydrogen storage material, due to light weight and low cost. $KMgH_3$ and

$NaMgH_3$ perovskites have cubic and $GdFeO_3$-type structures, respectively [15, 16]. The experimental lattice parameter of $KMgH_3$ perovskite is 4.023 Å [16]. Though perovskite hydrides are synthesized over 500 K [35], hydrogen molecule is released over 673 K [35–37]. Perovskite hydride cannot be hence utilized for alternative electrolyte of present SOFC. In previous DFT calculations for perovskite hydrides, structural stability, formation enthalpy and luminescence were discussed [16, 38–42]. Here we explore a possibility of hydride ion conduction in $KMgH_3$ perovskite at low temperature, from the viewpoints of energetics and bonding.

2.4.1 Calculation Models

Figure 2.14 depicts calculation models for $KMgH_3$ perovskite. To examine chemical bonding between magnesium and hydride ion in perfect solid state (without defect), $K_2Mg_4H_4$ model was constructed. Since hydrogen vacancy, which can be introduced by counter cation vacancy, is required to cause hydride ion conduction, $K_2Mg_4H_3$ model was constructed. To take the effect of charge compensation into account, potassium vacancy is also considered in KMg_4H_3 model. In $K_2Mg_4H_3$ and KMg_4H_3 models, the hydride ion conduction along the diagonal line is considered, because ion conduction via square centre (from H1 to H3) requires larger energy [7].

2.4.2 Chemical Bonding Between Magnesium and Hydride Ion

Before the investigation of hydride ion conduction, let us examine chemical bonding between magnesium and hydride ion in no defect case. Figure 2.15 depicts the shapes of selected MOs related to hydrogen 1*s* orbitals in $K_2Mg_4H_4$ model. The wave functions of MO39, MO40, MO41 and MO42 are expressed as

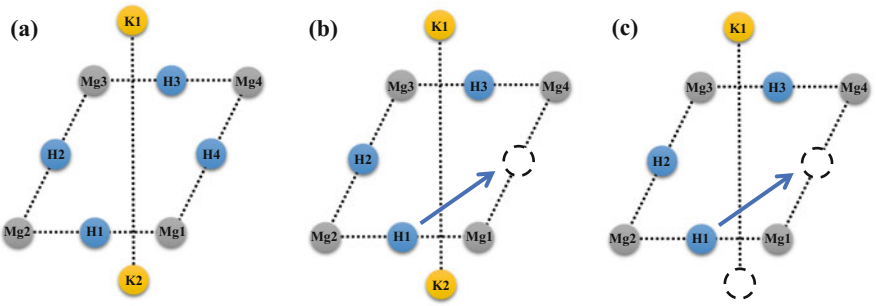

Fig. 2.14 The calculation models for $KMgH_3$ perovskite: (**a**) $K_2Mg_4H_4$, (**b**) $K_2Mg_4H_3$, (**c**) KMg_4H_3 with potassium vacancy. Note that dotted circle denotes hydrogen or potassium vacancy

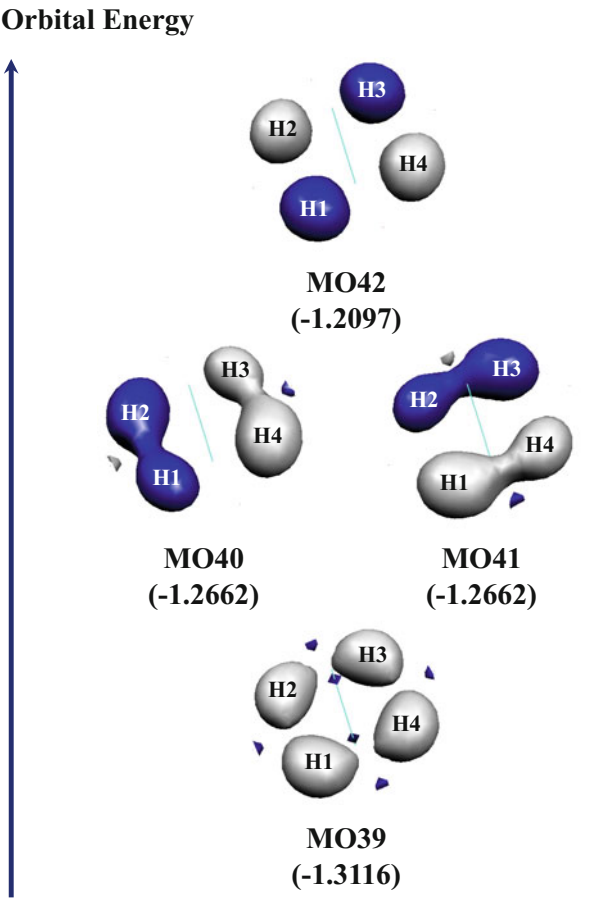

Fig. 2.15 The shapes of selected molecular orbitals related to hydrogen 1*s* orbitals in $K_2Mg_4H_4$ model. The site numbers of hydride ions are also shown. Note that orbital energy is given in parenthesis

$$\begin{aligned}\Psi_{\mathrm{MO39}} = {} & 0.12\phi_{\mathrm{K1}}\left(3pz\right) - 0.12\phi_{\mathrm{K2}}\left(3pz\right) \\ & +0.14\phi_{\mathrm{H1}}\left(1s'\right) + 0.21\phi_{\mathrm{H1}}\left(1s''\right) + 0.14\phi_{\mathrm{H2}}\left(1s'\right) + 0.21\phi_{\mathrm{H2}}\left(1s''\right) \\ & +0.14\phi_{\mathrm{H3}}\left(1s'\right) + 0.21\phi_{\mathrm{H3}}\left(1s''\right) + 0.14\phi_{\mathrm{H4}}\left(1s'\right) + 0.21\phi_{\mathrm{H4}}\left(1s''\right) \\ & +0.13\phi_{\mathrm{Mg1}}\left(3s'\right) + 0.13\phi_{\mathrm{Mg2}}\left(3s'\right) + 0.13\phi_{\mathrm{Mg3}}\left(3s'\right) + 0.13\phi_{\mathrm{Mg4}}\left(3s'\right)\end{aligned} \tag{2.7}$$

$$\begin{aligned}\Psi_{\mathrm{MO40}} = {} & -0.13\phi_{\mathrm{H1}}\left(1s'\right) - 0.24\phi_{\mathrm{H1}}\left(1s''\right) - 0.17\phi_{\mathrm{H2}}\left(1s'\right) - 0.31\phi_{\mathrm{H2}}\left(1s''\right) \\ & +0.13\phi_{\mathrm{H3}}\left(1s'\right) + 0.24\phi_{\mathrm{H3}}\left(1s''\right) + 0.17\phi_{\mathrm{H4}}\left(1s'\right) + 0.31\phi_{\mathrm{H4}}\left(1s''\right) \\ & -0.17\phi_{\mathrm{Mg2}}\left(3s'\right) + 0.17\phi_{\mathrm{Mg4}}\left(3s'\right)\end{aligned} \tag{2.8}$$

$$\Psi_{\mathrm{MO41}} = 0.17\phi_{\mathrm{H1}}\left(1s'\right) + 0.31\phi_{\mathrm{H1}}\left(1s''\right) - 0.13\phi_{\mathrm{H2}}\left(1s'\right) - 0.24\phi_{\mathrm{H2}}\left(1s''\right) - 0.17\phi_{\mathrm{H3}}\left(1s'\right) - 0.31\phi_{\mathrm{H3}}\left(1s''\right) + 0.13\phi_{\mathrm{H4}}\left(1s'\right) + 0.24\phi_{\mathrm{H4}}\left(1s''\right) + 0.17\phi_{\mathrm{Mg1}}\left(3s'\right) - 0.17\phi_{\mathrm{Mg3}}\left(3s'\right) \tag{2.9}$$

$$\Psi_{\mathrm{MO42}} = -0.17\phi_{\mathrm{H1}}\left(1s'\right) - 0.36\phi_{\mathrm{H1}}\left(1s''\right) + 0.17\phi_{\mathrm{H2}}\left(1s'\right) + 0.36\phi_{\mathrm{H2}}\left(1s''\right) - 0.17\phi_{\mathrm{H3}}\left(1s'\right) - 0.36\phi_{\mathrm{H3}}\left(1s''\right) + 0.17\phi_{\mathrm{H4}}\left(1s'\right) + 0.36\phi_{\mathrm{H4}}\left(1s''\right) \tag{2.10}$$

In MO39, H1, H2, H3 and H4 1*s* orbitals are overlapped, and H1, H2, H3 and H4 have one lobe. From chemical bonding rule, it is found that σ-type covalent bonding is formed between hydride ions. MO42 is inversion σ-type covalent bonding to MO39. In MO39, MO40 and MO41, hydrogen 1*s* orbitals slightly overlap with magnesium 3*s* orbitals. From chemical bonding rule, it is also found that slight covalent bonding is formed between hydride ion and magnesium.

2.4.3 Hydride Ion Conduction

Figure 2.16a, b show the potential energy curves of $K_2Mg_4H_3$ and KMg_4H_3 models, when displacing hydride ion along the diagonal line. In $K_2Mg_4H_3$ model, local minima are found between midpoint and lattice position (d = 0.7 and 2.1 Å), and local maximum is found at the midpoint (d = 1.4 Å). The activation energy for hydride ion conduction is 0.61 eV, whereas the partial activation energy crossing a midpoint (local maximum) is 0.23 eV. On the other hand, in KMg_4H_3 model, local minima are found between midpoint and lattice position (d = 0.6 and 2.2 Å), and local maximum is found at the midpoint (d = 1.4 Å). The activation energies crossing a midpoint and lattice position are 0.39 and 0.40 eV, respectively. It is because the total energy at lattice position is almost the same as local maximum.

Figure 2.17 depicts the shapes of selected MOs related to hydrogen 1*s* orbitals in $K_2Mg_4H_3$ model. In MO40s and MO41s, hydrogen 1*s* orbitals are overlapped. From chemical bonding rule, it is found that covalent bonding is formed between hydride ions. The wave functions of MO39s at lattice position, local minimum and local maximum are expressed as

$$\begin{aligned}\Psi_{\mathrm{MO39}}\,(\mathrm{Lattice}) = &- 0.12\phi_{\mathrm{K1}}\,(3pz) + 0.12\phi_{\mathrm{K2}}\,(3pz) \\ &- 0.18\phi_{\mathrm{H1}}\left(1s'\right) - 0.29\phi_{\mathrm{H1}}\left(1s''\right) - 0.13\phi_{\mathrm{H2}}\left(1s'\right) - 0.19\phi_{\mathrm{H2}}\left(1s''\right) \\ &- 0.18\phi_{\mathrm{H3}}\left(1s'\right) - 0.29\phi_{\mathrm{H3}}\left(1s''\right) \\ &- 0.13\phi_{\mathrm{Mg1}}\left(3s'\right) - 0.12\phi_{\mathrm{Mg2}}\left(3s'\right) - 0.12\phi_{\mathrm{Mg3}}\left(3s'\right) \\ &- 0.13\phi_{\mathrm{Mg4}}(3s')\end{aligned} \tag{2.11}$$

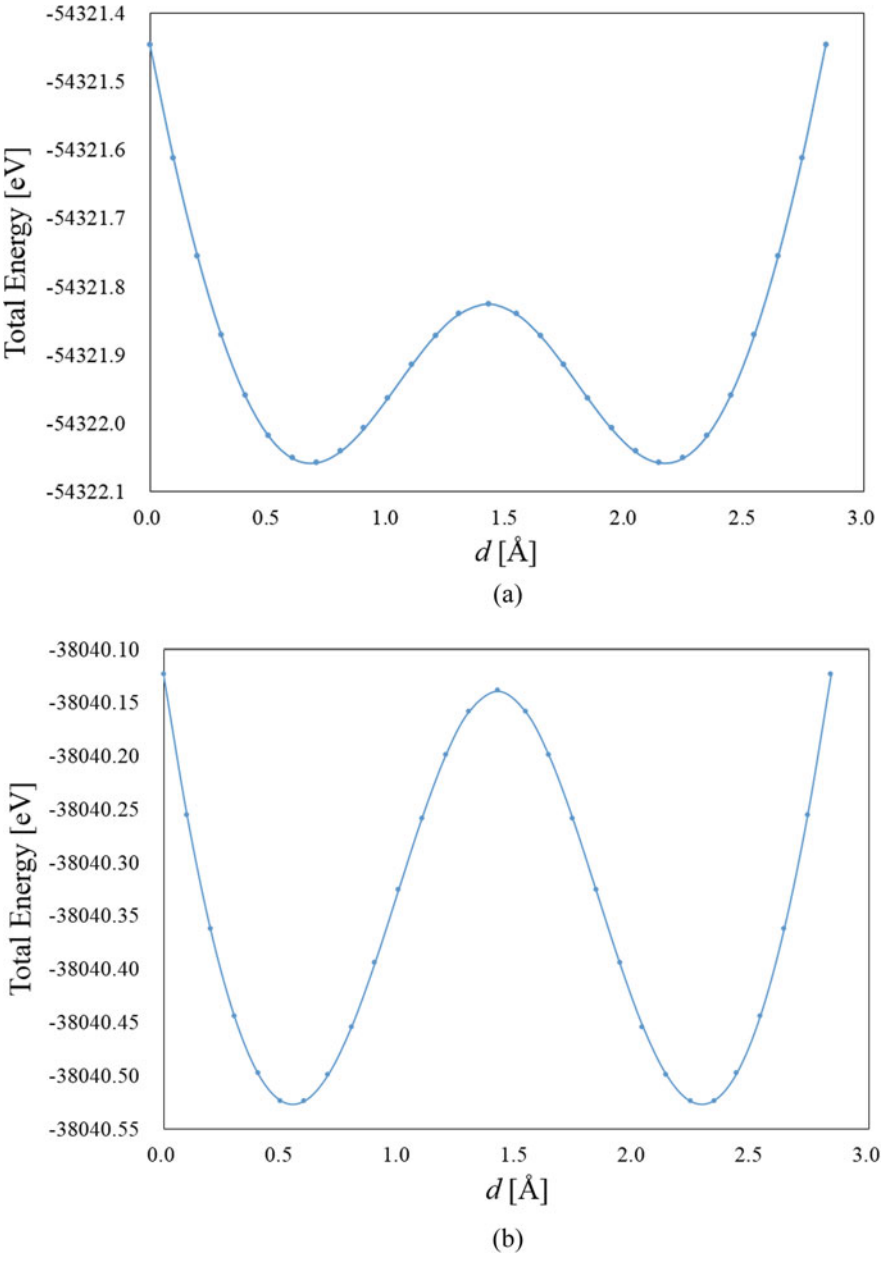

Fig. 2.16 The potential energy curves of (**a**) $K_2Mg_4H_3$ and (**b**) KMg_4H_3 models, when displacing hydride ion along the diagonal line. Note that *d* notes a migration distance from hydrogen lattice position (see blue arrows in Fig. 2.14b, c)

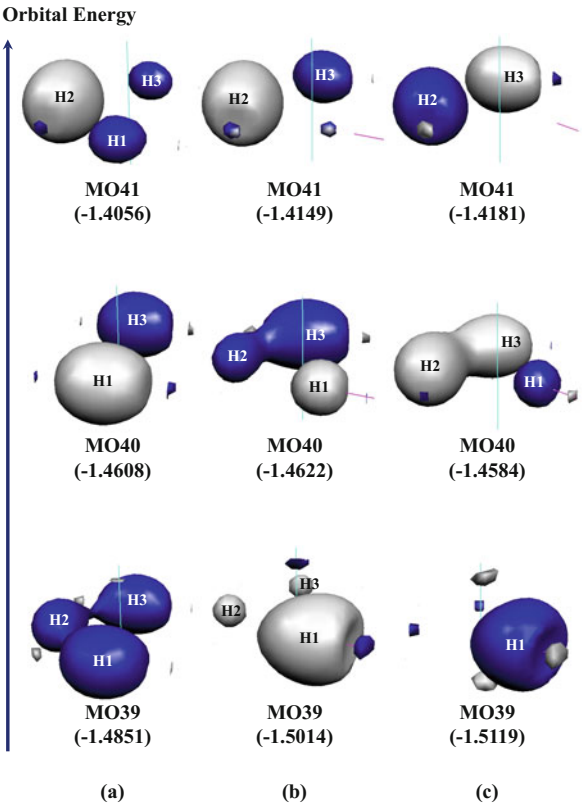

Fig. 2.17 The shapes of selected molecular orbitals related to hydrogen 1*s* orbitals at (**a**) lattice position ($d = 0.0$ Å), local minimum ($d = 0.7$ Å) and local maximum ($d = 1.4$ Å) in $K_2Mg_4H_3$ model. The site numbers of hydride ions are also shown. Note that orbital energy is given in parenthesis

$$\begin{aligned}\Psi_{\mathrm{MO39}}\,(\mathrm{Min}) = & 0.14\phi_{\mathrm{K1}}\,(3pz) - 0.14\phi_{\mathrm{K2}}\,(3pz) \\ & + 0.28\phi_{\mathrm{H1}}\left(1s'\right) + 0.52\phi_{\mathrm{H1}}\left(1s''\right) + 0.13\phi_{\mathrm{H2}}\left(1s''\right) + 0.10\phi_{\mathrm{H3}}\left(1s''\right) \\ & - 0.14\phi_{\mathrm{Mg1}}(2s) + 0.18\phi_{\mathrm{Mg1}}\left(3s'\right) + 0.10\phi_{\mathrm{Mg2}}\left(3s'\right)\end{aligned} \tag{2.12}$$

$$\begin{aligned}\Psi_{\mathrm{MO39}}\,(\mathrm{Max}) = & -0.15\phi_{\mathrm{K1}}\,(3pz) + 0.15\phi_{\mathrm{K2}}\,(3pz) \\ & - 0.32\phi_{\mathrm{H1}}\left(1s'\right) - 0.56\phi_{\mathrm{H1}}\left(1s''\right) \\ & + 0.17\phi_{\mathrm{Mg1}}(2s) - 0.17\phi_{\mathrm{Mg1}}\left(3s'\right)\end{aligned} \tag{2.13}$$

In Eq. (2.11), H1, H2 and H3 1*s* orbitals overlap with potassium 3*p* and magnesium 3*s* orbitals. In Eq. (2.12), H2, H2 and H3 1*s* orbitals overlap with potassium 3*p* orbitals and magnesium 2*s* and 3*s* orbitals, whereas in Eq. (2.13), H1 1*s* orbital overlaps with potassium 3*p* orbitals and magnesium 2*s* and 3*s* orbitals. From chemical bonding rule, it is found that hydride ion forms covalent bonding also with potassium and magnesium in MO39s.

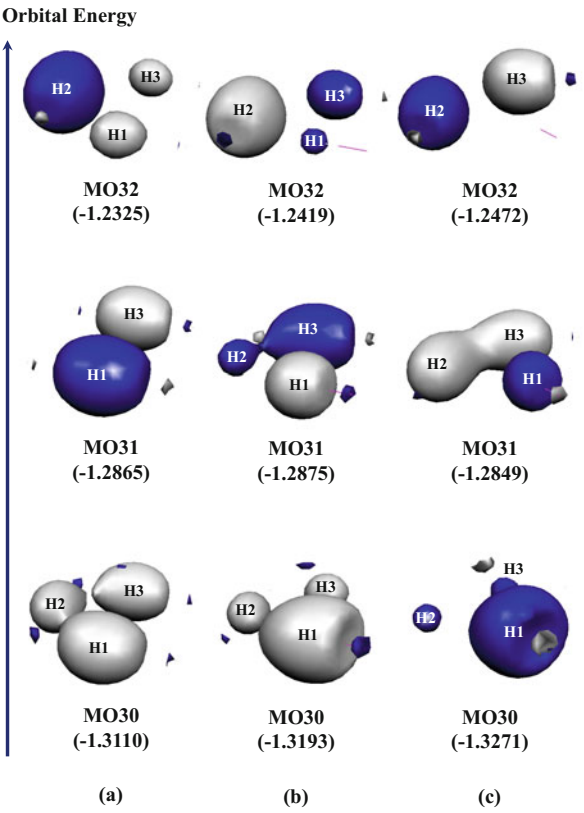

Fig. 2.18 The shapes of selected molecular orbitals related to hydrogen 1*s* orbitals at (**a**) lattice position ($d = 0.0$ Å), local minimum ($d = 0.6$ Å) and local maximum ($d = 1.4$ Å) in KMg_4H_3 model. The site numbers of hydride ions are also shown. Note that orbital energy is given in parenthesis

Figure 2.18 depicts the shapes of selected MOs related to hydrogen 1*s* orbitals in KMg_4H_3 model. In MO31s and MO32s, hydrogen 1*s* orbitals are overlapped as same as MO40s and MO41s of $K_2Mg_4H_3$ model. From chemical bonding rule, it is found that covalent bonding is formed between hydride ions. The wave functions of MO30s are expressed as

$$\begin{aligned}\Psi_{\mathrm{MO30}}\,(\mathrm{Lattice}) = {} & 0.11\phi_{\mathrm{K1}}\,(3pz) \\ & +0.18\phi_{\mathrm{H1}}\left(1s'\right)+0.29\phi_{\mathrm{H1}}\left(1s''\right)+0.13\phi_{\mathrm{H2}}\left(1s'\right)+0.19\phi_{\mathrm{H2}}\left(1s''\right) \\ & +0.18\phi_{\mathrm{H3}}\left(1s'\right)+0.29\phi_{\mathrm{H3}}\left(1s''\right) \\ & +0.14\phi_{\mathrm{Mg1}}\left(3s'\right)+0.14\phi_{\mathrm{Mg2}}\left(3s'\right)+0.14\phi_{\mathrm{Mg3}}\left(3s'\right) \\ & +0.14\phi_{\mathrm{Mg4}}\left(3s'\right)\end{aligned} \tag{2.14}$$

$$\begin{aligned}\Psi_{\mathrm{MO30}}\,(\mathrm{Min}) = {} & 0.12\phi_{\mathrm{K1}}\,(3pz) \\ & + 0.26\phi_{\mathrm{H1}}\left(1s'\right) + 0.43\phi_{\mathrm{H1}}\left(1s''\right) + 0.10\phi_{\mathrm{H2}}\left(1s'\right) + 0.16\phi_{\mathrm{H2}}\left(1s''\right) \\ & + 0.10\phi_{\mathrm{H3}}\left(1s'\right) + 0.16\phi_{\mathrm{H3}}\left(1s''\right) \\ & - 0.12\phi_{\mathrm{Mg1}}(2s) + 0.20\phi_{\mathrm{Mg1}}\left(3s'\right) + 0.13\phi_{\mathrm{Mg2}}\left(3s'\right)\end{aligned} \tag{2.15}$$

$$\begin{aligned}\Psi_{\mathrm{MO30}}\,(\mathrm{Max}) = {} & - 0.14\phi_{\mathrm{K1}}\,(3pz) \\ & - 0.30\phi_{\mathrm{H1}}\left(1s'\right) - 0.47\phi_{\mathrm{H1}}\left(1s''\right) - 0.11\phi_{\mathrm{H2}}\left(1s''\right) - 0.11\phi_{\mathrm{H3}}\left(1s''\right) \\ & + 0.17\phi_{\mathrm{Mg1}}(2s) - 0.22\phi_{\mathrm{Mg1}}\left(3s'\right)\end{aligned} \tag{2.16}$$

In Eq. (2.14), H1, H2 and H3 1*s* orbitals overlap with potassium 3*p* and magnesium 3*s* orbitals. In Eqs. (2.15) and (2.16), H1, H2 and H3 1*s* orbitals overlap with potassium 3*p* orbital and magnesium 2*s* and 3*s* orbitals. From chemical bonding rule, it is found that hydride ion forms covalent bonding also with potassium and magnesium in MO30s. It is considered that higher total energy at a midpoint is due to less covalency between hydrogen and potassium.

2.4.4 Summary

It was concluded that hydride ion conduction occurs at room temperature in $KMgH_3$ perovskite. The activation energy for hydride ion conduction was estimated to be 0.40–0.61 eV. Though the activation energy is smaller than hydride ion-doped $KMgF_3$ perovskite, temperature must be strictly controlled, due to its structural deformation [35–37]. It is concluded that hydride ion-doped $KMgF_3$ perovskite is more favourable than $KMgH_3$ perovskite, from the viewpoint of structural stability at high temperature.

2.5 Hydride Ion Safety and Outlook

In this chapter, hydride ion conducting mechanism in perovskite magnesium fluoride and hydride was revealed. It was found that the activation energies are smaller than proton conducting perovskites: e.g. 0.91–1.78 eV in $LaAlO_3$ perovskite [7, 8]. Hence, it is concluded that hydride ion conducting perovskites can be utilized as fast ion conductor, compared with proton conducting perovskites. Finally, let us discuss also safety and outlook for future engineering application.

2.5.1 Safety of Hydride Ion Conduction

In respect to hydride ion conduction, hydride ion-doped $KMgF_3$ perovskite can be utilized for electrolyte of solid fuel cell, due to small activation energy and structural stability at high temperature. If achieved, it could be called "solid fluoride fuel cell (SFFC)". However, we will face one big concern "hydrogen fluoride generation". Hydrogen fluoride molecule is very harmful for human. If ideal perovskite structure is kept during hydride ion conduction, hydrogen fluoride is not produced. After repeated use of SFFC, nonuniform distorted surface may be formed. For example, hydrogen fluoride may be produced under electron withdrawing environment as shown in Fig. 2.19. This point should be investigated in future experiment.

2.5.2 Safety of Hydrogen Molecule Production Combined with Hydride Ion Conduction

Let us consider the special environment under applied voltage at high temperature. $KMgH_3$ perovskite starts to be dissociated, whereas hydride ion still migrates within remained solid part. It implies that hydrogen migration is accelerated by hydride ion conduction in $KMgH_3$ perovskite (see Fig. 2.20). Thought the synergistic effect on hydrogen molecule production sounds ideal, we must pay attention to rapid hydrogen molecule production in the air. For safety, future experiment should be performed using explosion-proof apparatus.

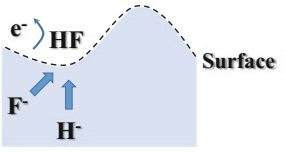

Fig. 2.19 The schematic figure of hydrogen fluoride production on nonuniform distorted surface

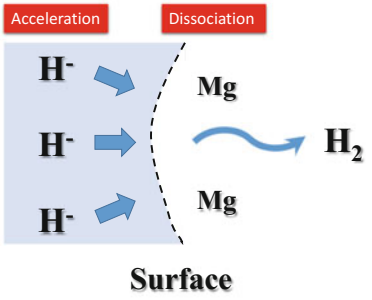

Fig. 2.20 The schematic figure of hydrogen molecule releases on nonuniform distorted surface

2.5.3 AC Impedance Measurement of Hydride Ion Conduction

In general, experimental data, which is obtained by AC impedance measurement, is analysed under assuming that electric resistance is constant in bulk part. It is noted that it is generally divided into three contributions: bulk, grain boundary and electrode interface. However, covalency of hydrogen is changeable during hydride ion conduction. It implies that electric resistance in solid part also varies. Hence, this effect must be taken into account. Otherwise, incorrect activation energy will be given as same as proton conduction [8].

Acknowledgements This work was partially supported by the Research Council of Norway through its Centres of Excellence scheme, project number 262695.

References

1. Y. Inaguma, J. Ceram. Soc. Jpn. **114**, 1103–1110 (2006)
2. M. Yoshino, A. Kozawa, R.J. Brodd, *Lithium-Ion Batteries* (Springer Nature, 2009), Introduction
3. T. Onishi, *Quantum Computational Chemistry* (Springer Nature, Singapore, 2018), Chapter 13
4. T. Norby, M. Widerøe, R. Glöcknera, Y. Larringa, Dalton Trans: 3012–3018 (2012)
5. T. Norby, *Perovskite Oxide for Solid Oxide Fuel Cell* (Springer Nature, Singapore, 2009), Chapter 11
6. T. Ishihara, *Perovskite Oxide for Solid Oxide Fuel Cell* (Springer Nature, Singapore, 2009), Chapter 4
7. T. Onishi, *Quantum Computational Chemistry* (Springer Nature, Singapore, 2018), Chapter 14
8. T. Onishi, Adv. Quantum Chem. **70**, 31–67 (2015)
9. T. Norby, Y. Larring, Solid State Ionics **136–137**, 139–148 (2000)
10. S. Steinsvik, Y. Larring, T. Norby, Solid State Ionics **143**, 103–116 (2001)
11. M. Widerøe, W. Münch, Y. Larring, T. Norby, Solid State Ionics **154–155**, 669–677 (2002)
12. Y. Kobayashi, O.J. Hernandez, T. Sakaguchi, T. Yajima, T. Roisnel, Y. Tsujimoto, M. Morita, Y. Noda, Y. Mogami, A. Kitada, M. Ohkura, S. Hosokawa, Z. Li, K. Hayashi, Y. Kusano, J. Kim, N. Tsuji, A. Fujiwara, Y. Matsushita, K. Yoshimura, K. Takegoshi, M. Inoue, M. Takano, H. Kageyama, Nat. Mater. **11**, 507–511 (2012)
13. T. Yajima, F. Takeiri, K. Aidzu, H. Akamatsu, K. Fujita, W. Yoshimune, M. Ohkura, S. Lei, V. Gopalan, K. Tanaka, C.M. Brown, M.A. Green, T. Yamamoto, Y. Kobayashi, H. Hiroshi Kageyama, Nat. Chem. **7**, 1017–1023 (2015)
14. T. Onishi, in *AIP Conference Proceedings 2040: 020002*, 2018
15. K. Yvon, B. Bertheville, J. Alloys Compd. **425**, 101–108 (2006)
16. K. Klaveness, O. Swang, H. Fjellvåg, Europhys. Lett. **76**, 285–290 (2006)
17. A. Bouamrane, C. Brauer, J.P. Soulié, J.M. Létoffeé, J.P. Bastide, Thermochim. Acta **326**, 37–41 (1999)
18. A. Bouamrane, J.P. Laval, J.P. Soulie, J.P. Bastide, Mater. Res. Bull. **35**, 545–549 (2000)
19. A.A. Granovsky, Firefly version 8, http://classic.chem.msu.su/gran/firefly/index.html
20. M.W. Schmidt, K.K. Baldridge, J.A. Boatz, S.T. Elbert, M.S. Gordon, J.H. Jensen, S. Koseki, N. Matsunaga, K.A. Nguyen, S. Su, T.L. Windus, M. Dupuis, J.A. Montgomery, J. Comput. Chem. **14**, 1347–1363 (1993)
21. U. Varetto, <MOLEKEL 4.3.>; Swiss National Supercomputing Centre. Manno, Switzerland
22. T. Onishi, Adv. Quantum Chem. **64**, 31–81 (2012)

23. M. Rousseau, J.Y. Gesland, J. Julliard, J. Nouet, J. Zarembowitch, A. Zarembowitch, Phys. Rev. B **12**, 1579–1590 (1975)
24. K. Uchino, S. Nomura, K. Vedam, R.E. Newnham, L.E. Cross, Phys. Rev. B **29**, 6921–6925 (1984)
25. T. Onishi, K. Yamaguchi, Polyhedron **28**, 1972–1976 (2009)
26. T. Onishi, *Quantum Computational Chemistry* (Springer Nature, Singapore, 2018), Chapter 11
27. M.D. Sturge, H.J. Guggenheim, Phys. Rev. B **4**, 2092–2099 (1971)
28. P.C. Burns, F.C. Hawthorne, A.M. Hofmeister, S.L. Moret, Phys. Chem. Miner. **23**, 141–150 (1996)
29. M. Mortier, Q. Wang, J.Y. Buzaré, M. Rousseau, B. Piriou, Phys. Rev. B **56**, 3022–3031 (1997)
30. J.L. Patel, J.J. Davies, B.C. Cavenett, H. Takeuchi, K. Horai, J. Phys. C Solid State Phys. **9**, 129–138 (1976)
31. M. Mortier, B. Piriou, J.Y. Buzaré, M. Rousseau, J.Y. Gesland, Phys. Rev. B **67**, 115126 (2003)
32. W.E. Vehse, K.H. Lee, S.I. Yun, W.A. Sibley, J. Luminescence **10**, 149–162 (1975)
33. N.H. Andersen, J.K. Kjems, Solid State Ionics **17**, 143–145 (1985)
34. T. Onishi, T. Helgaker, Prog. Theor. Chem. Phys. **27** (2013), Chapter 14
35. K. Ikeda, Y. Kogure, Y. Nakamori, S. Orimo, Prog. Solid State Chem. **35**, 329–337 (2007)
36. K. Ikeda, Y. Kogure, Y. Nakamori, S. Orimo, Scr. Mater. **53**, 319–322 (2005)
37. K. Komiya, N. Morisaku, R. Rong, Y. Takahashi, Y. Shinzato, H. Yukawa, M. Morinaga, J. Alloys Compd. **453**, 157–160 (2008)
38. P. Vajeeston, P. Ravindran, A. Kjekshus, H. Fjellvåg, J. Alloys Compd. **450**, 327–337 (2008)
39. A. Klaveness, H. Fjellvåg, A. Kjekshus, P. Ravindran, O. Swang, J. Alloys Compd. **469**, 617–622 (2009)
40. M. Fornari, A. Subedi, D.J. Singh, Phys. Rev. B **76**, 214118 (2007)
41. Y. Shinzato, H. Yukawa, M. Morinaga, T. Baba, H. Nakai, Adv. Quantum Chem. **54**, 145–160 (2008)
42. N. Kunkel, A. Meijerink, M. Springborg, H. Kohlmann, J. Mater. Chem. C **2**, 4799–4804 (2014)

Chapter 3
Local Dielectric Constant Density Analysis of High-k Dielectric Nanomaterial

Masato Senami and Akinori Fukushima

Abstract This article reviews progress of recently proposed local dielectric constant and polarizability. Local dielectric constant and polarizability are defined only in the formalism of quantum field theory. These quantities are expected to be good tool to the numerical analysis of nanosize materials. Basis set dependence of these quantities is explained with examples, an atom and a cation. The distribution of local polarizability in molecules is explained for covalent molecules, XH_n (X=C, N, O, F, Si, P, S, Cl, Ge, As, Se, and Br). Particularly, the relation between chemical bond and dielectric property is discussed. Application to practical nanosize materials is introduced for hafnium dioxide, which is the leading candidate for next-generation gate dielectric thin film. Particularly, $HfLaO_x$ model is studied for the purpose of the clarification of the effect of the incorporation of La atoms to HfO_2 on the dielectric properties.

Keywords Quantum field theory · Local polarizability · Local dielectric constant · Hafnium dioxide

3.1 Introduction

The notion of nanotechnology has been started from the lecture by Richard P. Feynman in 1959 [1]. Then technology has been progressed extremely for several decades. In an industrial aspect, some electronic devices are designed and manufactured in a nanometer scale. In laboratory level, molecular computer is studied hard in computational and experimental methods. Properties of these extremely small devices are often dominated by definite local regions in devices: for example, as a

M. Senami (✉)
Department of Micro Engineering, Kyoto University, Kyoto, Japan
e-mail: senami@me.kyoto-u.ac.jp

A. Fukushima
Faculty of Engineering, University of Fukui, Fukui, Japan
e-mail: akinori@u-fukui.ac.jp

T. Onishi (ed.), *Theoretical Chemistry for Advanced Nanomaterials*,
https://doi.org/10.1007/978-981-15-0006-0_3

local region, vacancy, interface, and impurity for condensed matter and functional group and bonding to other molecules for molecular devices.

Gate leakage current through dielectric thin film can be explained by the percolation model [2, 3]. In this model, almost all leakage current flows through defect chain in a film. In other words, observable leakage current for thin films is concentrated on a very restricted region. In another example, benzenedithiol is studied by many groups as prototype for future molecular electronics devices. Experimental measured values of conductance of Au-benzene-1,4-dithiolate-Au junction show very wide range, $10^{-4} - 1[e^2/\hbar]$, [4–9]. This conductance is considered to be heavily dependent on connections between Au atoms in electrodes and sulfur atoms [10–12]. In addition, if π-bonding is broken by adding a functional group, conductance is decreased significantly [13]. Therefore, analysis of a specific local region in a material is important for nanosize device materials.

In Fig. 3.1, the difference between quantum mechanics and quantum field theory is schematically depicted. Particularly, the local description of the equation of

	Equation of motion	Physical quantity
Quantum mechanics	$\frac{d\hat{O}(t)}{dt} = \frac{1}{i\hbar}[\hat{O}(t), \hat{H}] + \frac{\partial \hat{O}(t)}{\partial t}$ Heisenberg equation e. g. spin (Σ) $\frac{\hbar}{2}\frac{d}{dt}\Sigma^i = c\epsilon^{ijk}\alpha^k(p^j + eA^j/c)$	$\langle \hat{O}(t) \rangle = \int d^3\mathbf{r}\psi^\dagger(\mathbf{r})\hat{O}(t)\psi(\mathbf{r})$
Quantum field theory	$\frac{d}{dt}\hat{\Psi}^\dagger(\mathbf{r},t)\hat{O}(t)\hat{\Psi}(\mathbf{r},t)$ $= \left(\frac{d}{dt}\hat{\Psi}^\dagger(\mathbf{r},t)\right)\hat{O}(t)\hat{\Psi}(\mathbf{r},t)$ $+ \hat{\Psi}^\dagger(\mathbf{r},t)\left(\frac{d}{dt}\hat{O}(t)\right)\hat{\Psi}(\mathbf{r},t)$ $+ \hat{\Psi}^\dagger(\mathbf{r},t)\hat{O}(t)\left(\frac{d}{dt}\hat{\Psi}(\mathbf{r},t)\right)$ e. g. spin (Σ) $\frac{\hbar}{2}\frac{\partial}{\partial t}\left(\hat{\Psi}^\dagger\Sigma^i\hat{\Psi}\right)$ $= \left(\frac{i\hbar c}{2}\hat{\Psi}^\dagger\epsilon^{ijk}\alpha^k\hat{D}^j\hat{\Psi} + \text{h.c.}\right)$ $- \frac{\hbar c}{2}\partial_i\left(\hat{\Psi}^\dagger\gamma^5\hat{\Psi}\right)$	Density $\langle \hat{O}(\mathbf{r},t) \rangle$ $= \langle\Phi\|\hat{\Psi}^\dagger(\mathbf{r},t)\hat{O}(t)\Psi(\mathbf{r},t)\|\Phi\rangle$ Total value $\langle \hat{O}(t) \rangle$ $= \int d^3\mathbf{r}\langle\Phi\|\hat{\Psi}^\dagger(\mathbf{r},t)\hat{O}(t)\Psi(\mathbf{r},t)\|\Phi\rangle$

Fig. 3.1 Schematic picture of the difference between quantum mechanics and quantum field theory. The symbol, $\hat{O}$, is an operator and $\hat{H}$ is the Hamiltonian. Wave function in quantum mechanics is denoted by ψ, and field operator is denoted by $\hat{\psi}$

motion has a significant different feature. In quantum mechanics, the time evolution of a physical quantity is given by Heisenberg equation. A physical quantity used in Heisenberg equation of quantum mechanics is given as the inner product defined by the integration over the whole space. Hence, Heisenberg equation in quantum mechanics does not describe the evolution of a physical quantity density in a specific local region. In quantum field theory, the density value of a physical quantity can be treated simply by a field operator and its physical quantity operator. For example, electromagnetic field even in classical field theory can be described as a local density quantity. The time evolution of a physical quantity can be described even for the density in field theory. Therefore, only quantum field theory can explain the behavior of a physical quantity in a local region, and we believe that the analysis in a local region of a device material should be studied based on this theory.

Quantum field theory is consistent with Maxwell's equations, while quantum mechanics is not consistent, as summarized in Fig. 3.2. This is another reason why we should use quantum field theory. For example, quantum mechanics with static Hamiltonian, which is often used in the field of quantum chemistry, cannot dictate dynamical phenomena such as electric current, which is a typical object described in electromagnetism. Dynamical motion of electrons is allowed to be explained by the addition of vector potential to Hamiltonian in a gauge invariant manner. Nevertheless, a simple introduction of vector potential is not sufficient, if we do not include the effect of dynamical motion of electrons on electromagnetic field, which obeys Maxwell's equations. Hence, vector potential and scalar potential should be included so that electromagnetic field is consistent with Maxwell's equations.

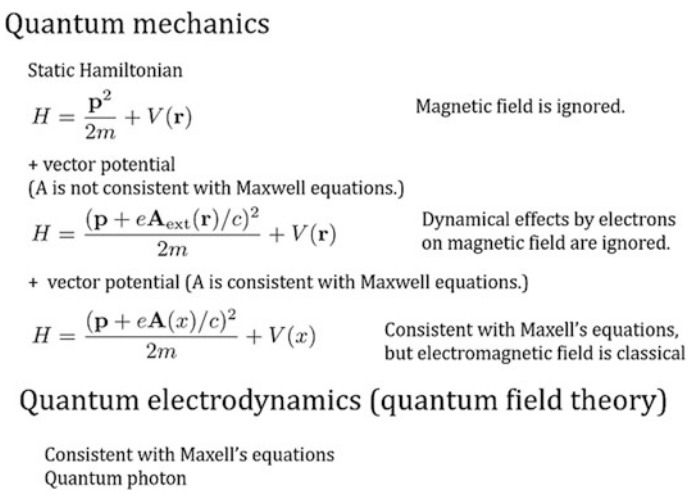

Fig. 3.2 Schematic picture of the consistency with Maxwell's equation and the quantum treatment of electromagnetic field. **p** is the momentum operator, m is the mass of a particle in the system, and V is the potential. **A** is vector potential, and the subscript $_{\text{ext}}$ means that vector potential is treated as an external field and is not affected by the system

This treatment is adopted in some groups and accurate enough for some purpose of researches. However, if quantum property of photon is important for analyses, quantum field theory should inevitably be used. The unified picture of the photon, the electron, and their interactions are only described in quantum field theory.

As a result, we believe that response properties of nanosize devices to electromagnetic fields should be analyzed by using physical quantities based on quantum field theory. For this purpose, local physical quantities based on quantum field theory have been proposed for dielectric constant, conductivity, and spin torque [14–16]. Local quantities for dielectric responses are the topic explained in this article. For conductivity, two types of local conductivity are defined as local counterpart of ordinary conductivity. One is the response to external electric field for a local region, and the other is the response to internal electric field in a local region. These two definitions of local conductivity are mentioned in the next section. Local conductivity is demonstrated in computational approach for nanowire materials and benzenedithiol and its derivatives [13, 17, 18]. By using GaN and silicon nanowire models, internal and external conductivities have been studied [17, 18]. Importance of π-bonding has been studied in comparison between benzenedithiol and its derivatives [13]. For spin torque, the equation of motion of the electron spin is introduced based on quantum field theory, and local description of spin torque is given in this formulation as shown in Fig. 3.1. In local description, in addition to the local counterpart of the ordinary spin torque, new torque term for the electron spin is introduced. This new torque describes a local effect, and this term gives zero if integrated over the whole region. However, this effect is considered to be important. Even for spin steady states, local spin torque does not vanish Heisenberg equation in quantum mechanics, while the equation of motion of the electron spin in quantum field theory gives zero torque state by the cancellation between the spin torque and new torque term even in a local region. This is confirmed in numerical methods for many molecules [19–21]. Hence, quantum field theory should be used for the correct local description of spin torque.

The study of this local physical quantity in quantum field theory started recently, and many things remain to be studied. In this article, we show the formalism of the local dielectric constant and the local polarizability and introduce knowledge derived by recent works. This article is organized as follows. In the next section, definitions of the local dielectric constant and the local polarizability are explained, and some related formulae are introduced, such as the relation with local conductivity tensors. In Sect. 3.3, we explain the internal distribution of the local polarizability in simple molecules, XH_n (X=C, N, O, F, Si, P, S, Cl, Ge, As, Se, and Br). These molecules are typical examples of molecules with covalent bond. It will be seen which electrons in molecules responds to external electric field. In Sect. 3.4, we review the dielectric property of metal oxide for the purpose of the study of hafnium dioxide (HfO_2). Hafnium dioxide has high permittivity (high-k) and hence is often studied for a viewpoint of gate dielectric thin film as insulator in semiconductor devices. In this section, four models are compared and discussed. Four models are two different structures, monoclinic and cubic, of HfO_2, La_2O_3 model, and $HfLaO_x$ model. The $HfLaO_x$ model is investigated for the effect of the

incorporation of La atoms to HfO_2 on the dielectric properties. The last two sections are devoted to the summary of this article and perspective of local dielectric constant and polarizability.

3.2 Theory

In this section, the formalism of dielectric constant density operator is reviewed [14–16]. This operator can parametrize local dielectric constant, which is given as the expectation value of this operator. The ordinary notion of the dielectric constant is based on a concept of a capacitor sandwiched between parallel plates. For a local region in nanosize condensed matter, parallel plates could not be inserted in matter. Hence, it is considered that a system (A), which is a target to study, is embedded in an environmental background medium (M) as depicted in Fig. 3.3, schematically. A local region may be included in both A and M regions, for a particular case. For example, magnetic dipole moment of a nucleus in a system region may be included as a region M.

The electromagnetic scalar field operators for these regions A and M are defined as the integrals of the electric charge density over respective regions,

$$\hat{A}_{0A,M}(x) = \int_{A,M} d^3\boldsymbol{s} \frac{\hat{\rho}(ct, \boldsymbol{s})}{|\boldsymbol{r} - \boldsymbol{s}|}, \tag{3.1}$$

where $x = (ct, \boldsymbol{r})$, c is the speed of light in vacuum, and $\hat{\rho}(x)$ is the charge density operator. The charge density operator is defined as

$$\hat{\rho}(x) \equiv Z_e e \hat{\psi}^\dagger(x)\hat{\psi}(x), \tag{3.2}$$

where $Z_e = -1$ for the electron, e is the elementary electric charge, and $\hat{\psi}(x)$ is the electron field operator. The electromagnetic vector field operators for these regions A and M, which are the rest parts of the four-component vector potential $\hat{A}^\mu$, are defined as the integrals of the transversal component of the electric current density,

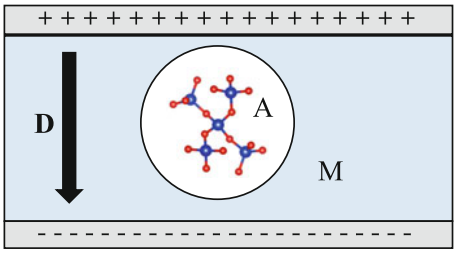

Fig. 3.3 Schematic picture of system A embedded in environment M

$$\hat{\boldsymbol{A}}_{A,M}(x) = \frac{1}{c}\int_{A,M} d^3\boldsymbol{s}\,\frac{\hat{\boldsymbol{j}}_T(u,\boldsymbol{s})}{|\boldsymbol{r}-\boldsymbol{s}|}, \tag{3.3}$$

where $u = t - |\boldsymbol{r}-\boldsymbol{s}|/c$ means the retardation. The electric current density operator is defined as

$$\hat{j}^i(x) \equiv cZ_e e\hat{\bar{\psi}}(x)\gamma^i\hat{\psi}(x), \tag{3.4}$$

where the adjoint field, $\hat{\bar{\psi}} \equiv \hat{\psi}^\dagger\gamma_0$, is often called the Dirac conjugate field, and γ^μ is the gamma matrix. Here and hereafter, Latin indexes span from 1 to 3, and Greek indexes span from 0 to 4, where the zero-th component means the time component of space-time components. This form of the current obeys the Lorentz covariance and hence special relativity. For our purpose in this article, familiar nonrelativistic form of the current is enough, since most dielectric phenomena are nonrelativistic. In non-relativistic theory, the local electric current density operator $\hat{\boldsymbol{j}}(x)$ can be given as,

$$\hat{\boldsymbol{j}}(x) = \frac{Z_e e}{2m_e}\left[-i\hbar\hat{\psi}^\dagger(x)\nabla\hat{\psi}(x) + \frac{e}{c}\hat{\psi}^\dagger(x)\hat{\boldsymbol{A}}(x)\hat{\psi}(x) + h.c.\right], \tag{3.5}$$

where $\hbar$ is the reduced Planck constant.

The four-component electromagnetic gauge field is given as the sum of the contributions from the regions A and M,

$$\hat{A}^\mu(x) = \hat{A}^\mu_A(x) + \hat{A}^\mu_M(x). \tag{3.6}$$

The electric field operator, $\hat{\boldsymbol{E}}(x)$, is known to be defined as

$$\hat{\boldsymbol{E}}(x) = -\mathrm{grad}\hat{A}_0(x) - \frac{1}{c}\frac{\partial}{\partial t}\hat{\boldsymbol{A}}(x). \tag{3.7}$$

The electric field is given by the contributions from the electric displacement density operator $\hat{\boldsymbol{D}}(x)$ of the medium M and the polarization density operator $\hat{\boldsymbol{P}}(x)$ of the system A. These are defined as

$$\hat{\boldsymbol{D}}(x) = -\mathrm{grad}\hat{A}_{0M}(x) - \frac{1}{c}\frac{\partial}{\partial t}\hat{\boldsymbol{A}}_M(x), \tag{3.8}$$

$$\hat{\boldsymbol{P}}(x) = \frac{1}{4\pi}\mathrm{grad}\hat{A}_{0A}(x) + \frac{1}{4\pi c}\frac{\partial}{\partial t}\hat{\boldsymbol{A}}_A(x). \tag{3.9}$$

Therefore, the electric field is cast into another form,

$$\hat{\boldsymbol{E}}(x) = \hat{\boldsymbol{D}}(x) - 4\pi\,\hat{\boldsymbol{P}}(x). \tag{3.10}$$

The electric displacement $\hat{\boldsymbol{D}}(x)$ is considered to be external electric field for the system A. In the original definition [15], $\hat{A}^{\mu}_{\text{radiation}}$ is separately defined in Eq. (3.6), and hence $\hat{A}^{\mu}_{\text{radiation}}$ is explicitly added in this expression (3.10).

In this relation, the polarization of the system A is considered to be linear response to $\hat{\boldsymbol{D}}(x)$,

$$\hat{P}^{i}(x) = \hat{\alpha}^{ij}(x)\hat{D}^{j}(x), \tag{3.11}$$

where $\hat{\alpha}^{ij}(x)$ is the polarizability density tensor operator, which is 3×3 matrix. In this expression, $\hat{\alpha}^{ij}$ is allowed to have time dependence, since $\hat{\alpha}^{ij}$ is known to have dependence of frequency of electric field as well as dielectric constant.

The dielectric constant density tensor operator $\hat{\epsilon}^{ij}(x)$ is the relation between $\hat{\boldsymbol{D}}(x)$ and $\hat{\boldsymbol{E}}(x)$, and the definition is given as

$$\hat{D}^{i}(x) = \hat{\epsilon}^{ij}(x)\hat{E}^{j}(x). \tag{3.12}$$

With Eqs. (3.10) and (3.11), the local dielectric constant density tensor operator is reduced to other form,

$$\hat{\epsilon}^{ij}(x) = \left(\frac{1}{1 - 4\pi\hat{\alpha}(x)}\right)^{ij} \tag{3.13}$$

Physical values of these quantities are derived as expectation values of these operators, which are calculated by using state vector. All the components of the polarizability density tensor and the dielectric constant density tensor are real; the above operators are defined to be Hermitian operators. However, as matrix, these tensors are not Hermitian, and therefore these tensors have three real or one real and two complex values as eigenvalues of these matrices. In almost all cases of ordinary global dielectric constant tensor, tensor is diagonal, and its eigenvalues are only real. Off-diagonal elements of dielectric constant tensor are negligible for large enough materials, since polarization perpendicular to imposed electric field is very small owing to the cancellation among contributions from various positions. However, in a local region of material, dielectric response perpendicular to imposed electric field is not negligible even for amorphous materials and crystals with high symmetry. Hence, off-diagonal elements should not be neglected, and tensor representation of polarizability and dielectric constant is inevitably required for local analysis.

These local dielectric constant and local polarizability should have the same value as the ordinary dielectric constant and polarizability, if regions A and M are chosen to be the same as parallel plate capacitor, and the local dielectric constant and local polarizability are averaged over the whole region of the system A. The averaging way has been proposed in Refs. [22–24], and average values are also useful for the numerical expression of dielectric property of a specific local region as well as the consistency check of these local quantity for ordinary quantities. For a region V whose volume is V, the average of local polarizability is defined as the integration of local polarizability,

$$\langle \alpha_V^{ij}(t) \rangle = \frac{1}{V} \int_V \langle \hat{\alpha}^{ij}(x) \rangle d\boldsymbol{r}. \tag{3.14}$$

The quantity of operator sandwiched by $\langle, \rangle$, which are state vectors, bra and ket, means the expectation value. This definition of the average is reasonable. If the region V is capacitor and the region M is parallel plates, this average corresponds to the polarization induced by the parallel plates over $\boldsymbol{D}$. The average of local dielectric constant is defined as

$$\langle \epsilon_V^{ij}(t) \rangle = \frac{1}{V} \int_V \langle \hat{\epsilon}^{ij}(x) \rangle d\boldsymbol{r}. \tag{3.15}$$

The local dielectric constant and local polarizability are interesting physical quantities by themselves, and moreover, these quantities are important for the representation of the relation between other quantities. In this article, we introduce one example, the relation between local conductivities mentioned in the previous section, and we refer Ref. [25] as another relation, where the variation of Lorentz force density by the change of electric field is given with local dielectric constant. Ordinary electrical conductivity is the linear response of the electric current to electric field between electrodes. A local counterpart of conductivity is the matrix relation of the electric current density of region A to electric displacement of region M. This definition of local conductivity is given as [15, 17, 18]

$$\hat{j}^i(x) = \hat{\sigma}_{\text{ext}}^{ij}(x) \hat{D}^j(x). \tag{3.16}$$

This definition of conductivity corresponds to ordinary conductivity as an average value discussed above. In another definition, we can consider the relation between the local electric current and the electric field $\boldsymbol{E}$,

$$\hat{j}^i(x) = \hat{\sigma}_{\text{int}}^{ij}(x) \hat{E}^j(x). \tag{3.17}$$

These two definition are related through the local dielectric constant as,

$$\begin{aligned} \hat{j}^i(x) &= \hat{\sigma}_{\text{ext}}^{ij}(x) \hat{D}^j(x) \\ &= \hat{\sigma}_{\text{ext}}^{ij}(x) \hat{\epsilon}^{jk}(x) \hat{E}^k(x) \\ &= \hat{\sigma}_{\text{int}}^{ij}(x) \hat{E}^j(x). \end{aligned} \tag{3.18}$$

Before we introduce works using local dielectric constant, some limitation in these works are mentioned. First, the time variation of vector potential in estimate of $\boldsymbol{E}$, $\boldsymbol{D}$, and $\boldsymbol{P}$ is neglected. Only steady states are considered in the works, and it has been reported that effects of vector potential can be negligible even for conductive states where wave packets are prepared by computations based on quantum mechanics [26]. In following sections, system region A is chosen to be a whole cluster model, and electric displacement $\boldsymbol{D}(x)$ is simply assumed to be

homogeneous constant vector $\boldsymbol{D}$. Any definite environmental medium is not set. Here and hereafter, in the expression of expectation values, bra and ket are dropped, and we can discriminate an operator and its expectation value by the existence of the hat symbol "$\hat{}$."

Local polarizability density tensor is calculated by using a finite difference method or coupled perturbed Hartree-Fock (CPHF) method. In both computations of polarization, only electronic contributions are taken into account, and nuclear contributions are not included. First computation of a finite difference method is explained. With six results with different electric displacements, $D^i_{1,2} = 0 \pm \Delta D^i/2 = \pm 0.0001$ [a.u.] ($i = x, y, z$), that is, $\pm D_x, \pm D_y$ and $\pm D_z$, the polarization difference can be calculated as

$$\Delta P^i(x) = P^i(x)|_{+D^j} - P^i(x)|_{-D^j}. \tag{3.19}$$

With these three polarization difference vectors ($j = x, y, z$), local polarizability density tensor is calculated with the expression,

$$\Delta P^i(x) = \alpha^{ij}(x)\Delta D^j. \tag{3.20}$$

By using CPHF method, linear response to external electric field is strictly calculated, though contamination from nonlinear effect was negligible in the above finite difference method. Local polarizability is calculated by CPHF method as follows [18]. Hamiltonian $\boldsymbol{h}$ and density matrix $\boldsymbol{R}$ are expanded with the perturbation parameter, λ, as

$$\boldsymbol{h}(\lambda) = \boldsymbol{h}^{(0)} + \lambda \boldsymbol{h}^{(1)}, \tag{3.21}$$

$$\boldsymbol{R}(\lambda) = \boldsymbol{R}^{(0)} + \lambda \boldsymbol{R}^{(1)} + \cdots. \tag{3.22}$$

The first order Fock matrix $\boldsymbol{h}^{F(1)}$ is given as

$$\boldsymbol{h}^{F(1)} = \boldsymbol{h}^{(1)} + \boldsymbol{G}(\boldsymbol{R}^{(1)}). \tag{3.23}$$

The matrix $\boldsymbol{G}$ is two-electron interaction,

$$G_{pq}(\boldsymbol{R}) = \sum_{r,s} R_{rs} \left([\psi_p \psi_q | \psi_r \psi_s] - [\psi_p \psi_s | \psi_r \psi_q] \right), \tag{3.24}$$

where subscripts p, q, r, s are used for all molecular orbitals (MOs). Then, the first-order CPHF equation is given by

$$(\epsilon_a - \epsilon_i) R^{(1)}_{ai} = -h^{F(1)}_{ai}, \tag{3.25}$$

where ϵ is unperturbed orbital energy, and subscripts a and i are used for virtual and occupied MOs, respectively. In the computation of local polarizability, perturbation parameter is taken for external electric field,

$$\lambda_j \boldsymbol{h}^{(1j)} = \lambda_j D_0 ej, \quad (j = x, y, z) \tag{3.26}$$

and external electric field is considered to be $D_j = \lambda_j D_0 \quad (j = x, y, z)$ with the unit electric field, D_0. With the first-order density matrices $\boldsymbol{R}^{(1x,1y,1z)}$, local polarization $P_i(x)$ can be expanded as

$$P_i(x; \lambda_x, \lambda_y, \lambda_z) = P_i^{(0)}(x) + \lambda_x P_i^{(1x)}(x) + \lambda_y P_i^{(1y)}(x) + \lambda_z P_i^{(1z)}(x) + \cdots, \tag{3.27}$$

and local polarizability tensor α^{ij} is calculated from Eq. (3.11),

$$\begin{aligned} \alpha^{ij}(x) &= \left. \frac{\partial P_i(x)}{\partial D_j} \right|_{D_j=0} \\ &= \left. \frac{\partial P_i(x)}{\partial \lambda_j} \frac{\partial \lambda_j}{\partial D_j} \right|_{D_j=0} \\ &= \frac{P_i^{(1j)}(x)}{D_0}. \end{aligned} \tag{3.28}$$

In this article, eigenvalues and eigenvectors of these tensor are used for the description of 3×3 matrix of α^{ij} and ϵ^{ij}. As explained above, all eigenvalues are real, or only one eigenvalue is real (and two eigenvalues are complex). For the case with three real eigenvalues, eigenvalues are arranged as the descending order. On the other hand, if there are two complex eigenvalues, the first eigenvalue is real one, the second and third eigenvalues are complex. As an exception, the descending order of real part is adopted when we explicitly state the choice of the order. The magnitude of the imaginary part is represented by the argument θ defined as follows,

$$\theta = \sin^{-1}\left[\frac{|\mathrm{Im}(\lambda_i)|}{|\lambda_i|}\right], \tag{3.29}$$

where λ_i is the corresponding eigenvalue. Eigenvalues and eigenvectors of local dielectric constant can easily be calculated by Eq. (3.13).

3.3 Local Dielectric Property of Simple Systems

In this section, we show local dielectric response properties of simple systems, single atom and ion, and molecules, XH_n (X=C, N, O, F, Si, P, S, Cl, Ge, As, Se, and Br), by wave packets based on quantum mechanics computations. These molecules are chosen to be typical examples of covalent molecules. Most results in this section are based on Refs. [27, 28].

Results in this section are useful for the comprehension of local dielectric response property in hafnium dioxide discussed in the next section.

3.3.1 *Dependence of Local Polarizability on Choice of Basis Set*

In this section, local dielectric response property of single atom and ion is discussed for the purpose of clarification of basis set dependence. First, the strong basis set dependence of local polarizability density is shown for hydrogen atom, where an analytical solution of Schrödinger equation is known.

The first eigenvalue of local polarizability density is shown as a function of the distance from the hydrogen nucleus (proton) in Fig. 3.4 [28]. The contraction of basis sets used in this figure is summarized in Table 3.1. Computations of electronic structure were performed by Gaussian 09 program package [29]. With derived electronic structure, CPHF calculations were carried out by the program code developed for this computation. The local polarizability calculated by the analytical solution is shown as a red solid line. Results of smaller basis sets such as double-zeta basis sets are significantly smaller than that of the analytical solution. The choice of larger basis sets than triple-zeta basis sets shows good consistency with the result of the analytical solution.

In Fig. 3.5, the degree of deviation from the analytical solution is shown [28]. The accuracy is not good for the five basis sets from 6-31G** to cc-pVDZ in Table 3.1. For these basis sets, deviations are 40–70% in an atomic region whose radius is

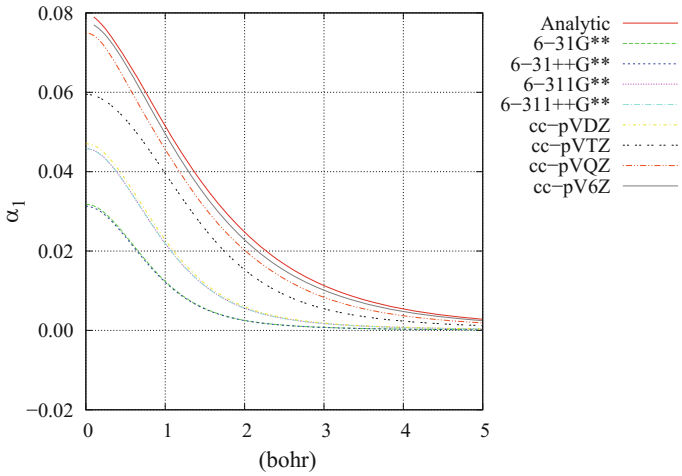

Fig. 3.4 The dependence of local polarizability density on basis set. The horizontal axis means the distance from the hydrogen nucleus

Table 3.1 List of basis sets. The contraction and references are shown

Atom	Basis set	Contraction
H	6-31G** [30, 31]	(4s,1p) – [2s,1p]
	6-31++G** [30–32]	(5s,1p) – [3s,1p]
	6-311G** [33]	(5s,1p) – [3s,1p]
	6-311++G** [32, 33]	(6s,1p) – [4s,1p]
	cc-pVDZ [34]	(4s,1p) – [2s,1p]
	cc-pVTZ [34]	(5s,2p,1d) – [3s,2p,1d]
	cc-pVQZ [34]	(6s,3p,2d,1f) – [4s,3p,2d,1f]
	cc-pV6Z (K.A. Peterson, D.E. Woon, T.H. Dunning Jr., unpublished)	(10s,5p,4d,3f,2g,1h) – [6s,5p,4d,3f,2g,1h]
Hf	LANL2DZ [35–37]	(5s,6p,3d) – [3s,3p,2d]
	LANL2TZ [35–38]	(5s,5p,3d) – [5s,5p,3d]
	Def2-SVP [39, 40]	(7s,6p,5d,1f) – [6s,3p,2d,1f]
	Def2-TZVP [39, 40]	(9s,7p,5d,1f) – [6s,4p,3d,1f]
	Def2-QZVP [39, 40]	(10s,8p,6d,3f,1g) – [7s,5p,4d,3f,1g]
	cc-pVDZ-PP [41]	(8s,7p,6d,1f) – [4s,4p,3d,1f]
	aug-cc-pVDZ-PP [41]	(9s,8p,7d,2f) – [5s,5p,4d,2f]

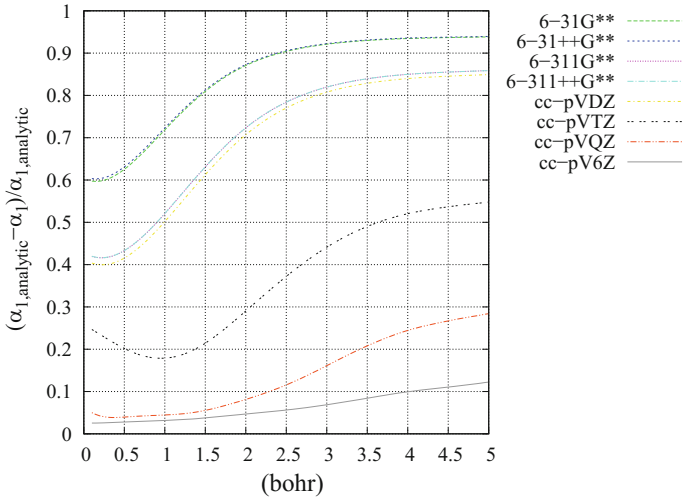

Fig. 3.5 The deviation from the analytical solution. The horizontal axis means the distance from the hydrogen nucleus

taken to be 1 [bohr], and in outer region (>1 [bohr]), deviations reach 50–90%. The reason of the shortage of the accuracy is the lack of the degree of freedom of polarization function. There is only one polarization function for these basis sets. The accuracy becomes worse for outer region from nucleus. This trend is remarkable for smaller basis sets such as double-zeta basis sets, since these basis sets have poor degree of freedom for the change of wave function in outer region. For neutral atoms, the degree of diffuse functions, which are s-type functions, is not important

for the representation of local polarizability density from the comparison between the results of 6-31G** (6-311G**) and 6-31++G** (6-311++G**). The deviation of cc-pVQZ basis set is less than 10 % within 2 [bohr] from the nucleus. The difference between results of cc-pVQZ and cc-pV6Z basis sets is not large, and hence quadruple-zeta basis sets may be the best choice in viewpoints of computational cost and accuracy for hydrogen atom. However, this may be overestimated for other atoms. We consider that this accuracy is heavily dependent on the degree of freedom of nonzero angular momentum orbitals, that is, p, d, f, . . . , types functions, since any s-type function is spherically symmetric and cannot be polarized against electric field. Hence, we consider that smaller basis sets, such as triple-zeta basis sets, are accurate enough to represent the distribution of local polarizability density for atoms with larger atomic number, since basis sets for atoms with large atomic number have the large number of nonzero angular momentum orbitals even for double-zeta basis sets. It is important that this conjecture is confirmed by numerical computations, and, however, this confirmation for neutral single atoms has not been published as far as we know.

In atoms or condensed matter, electrons in some atoms are moved to other regions, so that chemical bonding is formed, such as covalent bond and ionic bond. Particularly, charge transfer between donor and acceptor is larger in ionic bond. Hafnium dioxide discussed in the next section is known to have ionic bond. Hence, next, the basis set dependence of local polarizability is explained for cation, Hf^{4+}, where we assumed simple picture of Hf^{4+} and O^{2-} in HfO_2.

The first eigenvalue of local polarizability density tensor of Hf^{4+} is shown as a function of the distance from the Hf nucleus in Fig. 3.6 [28]. Electronic structure and CPHF computations were performed by Gaussian 09 program package [29] and the program code developed for this computation, respectively. The contraction of basis sets is listed in Table 3.1. These basis sets use pseudo potential for core electrons,

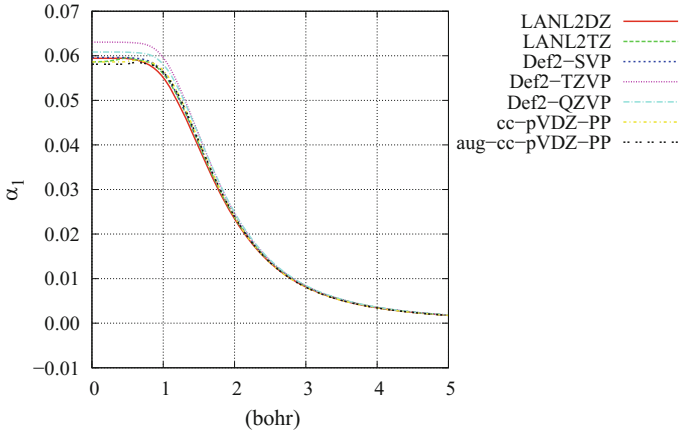

Fig. 3.6 The dependence of local polarizability density of Hf^{4+} on basis set. The horizontal axis means the distance from the Hf nucleus

and the result in inner region (< about 1 [bohr]) should be neglected. Analytical solution for Hf^{4+} is not known, and we judge the accuracy by comparing with results of the largest basis set group. Fortunately, all results are consistent with each other, and basis set dependence is negligible for Hf^{4+}. The response to electric field is small in spite of large electron density, since four valence electrons are removed and rest electrons are significantly stabilized. As a result, it is concluded that the choice of basis sets is not important for cation, Hf^{4+}.

On the other hand, valence electrons are destabilized significantly in anion. Hence, larger basis sets are required for accurate description of local polarizability. However, unfortunately, we cannot confirm this in a numerical method using a single nucleus system, since the highest occupied molecular orbital (HOMO) of O^{2-} has positive energy, and isolated O^{2-} cannot be calculated correctly. Nevertheless, computations of isolated O^{2-} were studied in Ref. [28] for the purpose of the numerical confirmation of strong dependence on the choice of basis sets. It was shown in Ref. [28] that results with larger basis sets have larger polarizability, and diffuse functions are important. This is plausible, since HOMO is not bounded.

As a result, we can summarize the basis set dependence as follows. From the hydrogen result, it is conjectured that triple- or quadruple-zeta basis sets are accurate enough to describe local polarizability density for neutral atoms. For cations, the basis set dependence is small, while a larger basis set is required for anions.

3.3.2 *Local Dielectric Property of Molecules XH_n (X = C, N, O, F, Si, P, S, Cl, Ge, As, Se, and Br)*

In this subsection, we explain results of local dielectric response properties of simple molecules, XH_n (X = C, N, O, F, Si, P, S, Cl, Ge, As, Se, and Br), by wave packets based on quantum mechanics computations. These molecules are chosen to be typical examples of covalent molecules, and these X atoms are elements of group IV–VII in the second to fourth period. Most results in this section are based on Ref. [27]. Results of these simple molecules are used for systematic analysis of local dielectric properties in a molecule. In this subsection, the order of eigenvalues is the descending order of real part.

Wave packets used in this section were computed by ordinary electronic structure computations carried out by GAMESS program package [42]. The cc-pVQZ basis set [34, 43, 44] was chosen, and geometrical optimization computations were performed by Hartree-Fock (HF) method. Singlet spin multiplicity was chosen for all molecules. Configuration interaction single and double (CISD) was adopted for electronic structure computations. This choice is better than the usage of density functional theory (DFT), since the problem of overestimate of dielectric constant is known for DFT [45–49]. Excitation of all electrons in occupied orbitals is taken into account in this CISD computation. Local polarizability was computed by QEDynamics program package [50–55].

In Fig. 3.7, the distributions of eigenvalues and eigenvectors of local polarizability density tensor of H_2O are shown on the plane including O and two H atoms. For two-dimensional representation of distribution of local polarizability density, only

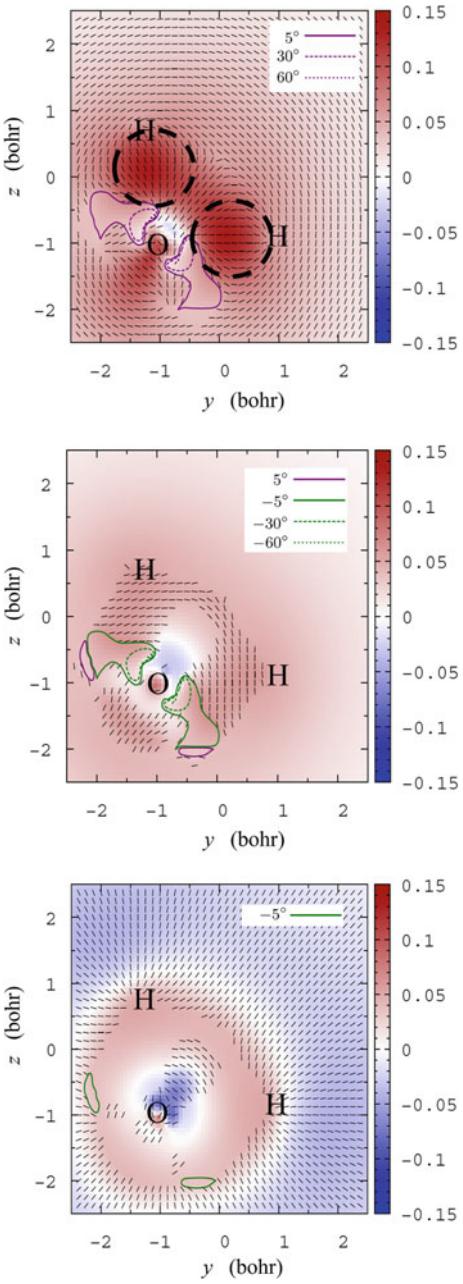

Fig. 3.7 The distribution of eigenvalue and eigenvector of local polarizability density of H_2O. From top, the first, second, and third eigenvalues and eigenvectors are shown. Short lines show directions of corresponding eigenvectors. Eigenvalues are complex in regions enclosed by solid lines. The regions enclosed by bold dashed line show large polarizability density (see text)

one molecule is taken as an example, and common features explained below are also seen for other XH_n molecules. Other results are dropped since those are a little lengthy, and all results of other molecules can be seen in Ref. [27]. The upper, middle, and bottom panels are the first, second, and third eigenvalues and eigenvectors, respectively. Short lines show directions of corresponding eigenvectors. Eigenvalues are complex in regions enclosed by solid lines. In the result of the largest eigenvalue, the first eigenvalue, large polarizability region exists between O and H atoms, which are enclosed by bold dashed line, and the direction of eigenvectors in the region is that of covalent bond of O and H. This directionality shows salient contrast compared to that of HfO_2 discussed in the next chapter, whose bonding is ionic. This directional response is considered to arise from covalent bond. Negative or complex eigenvalues are seen around the oxygen nucleus. In negative eigenvalue regions, the direction of polarization response is opposite to ordinary response. In complex eigenvalue regions, polarization responds to electric field rotationally [18]. This response is not familiar in macroscopic phenomena and originates in combination of electric fields from nuclei and external field. These regions are more outstanding for upper period elements in the periodic table, and similar distribution patterns appear in a same group [27]. These properties explained above arise from the size of a molecule, which correlates with the radius of X atom and the internuclear length between X and H nuclei.

Eigenvalues of local polarizability tensor are shown along internuclear axis of X and H bonding for XH_n (X = C, N, O, F, Si, P, S, Cl, Ge, As, Se, and Br) molecules in Fig. 3.8 (CH_4, NH_3, H_2O, HF), Fig. 3.9 (SiH_4, PH_3, H_2S, HCl), and Fig. 3.10 (GeH_4, AsH_3, H_2Se, HBr). In these figures, top left panels show results of XH_4, top right ones show those of XH_3, bottom left ones show those of H_2X, and bottom right ones show those of HX. In addition to three eigenvalues, the average of eigenvalues is also shown in this figure. Bold dashed line means $\alpha_i = 1/(4\pi) \sim 0.08$. When $\alpha_i = 1/(4\pi)$, the eigenvalue of dielectric constant tensor corresponding to α_i is divergent. For $\alpha_i > 1/(4\pi)$, the corresponding dielectric constant has negative sign. From these figures, large local polarizability density is seen in a region between X and H atoms as seen in Fig. 3.7. This is due to the charge transfer from a region around a nucleus to bonding region. In contrast, local polarizability density is smaller around nuclei for all atoms than bonding region. Electrons around nuclei are bounded strongly by electric field of nuclei, while electrons in bonding region are not strongly trapped by electric field. From the comparison among a same period, the average of local polarizability density is larger for smaller atomic number. The difference of average comes from the difference of the second and third eigenvalues. This is speculated to originate in the X-H internuclear length and other X-H bonding. The peak at a X nucleus is formed by 1s core electrons of the X atom. In Figs. 3.9 and 3.10, multiple peak structure around X nucleus is seen for elements in the third and fourth period. This structure is formed by shell structure of atoms. Inner electrons respond to electric field weakly by strong electric field of a nucleus. Complex eigenvalues around transition region between bonding and X nucleus regions for elements in V and VI groups. The arguments of complex

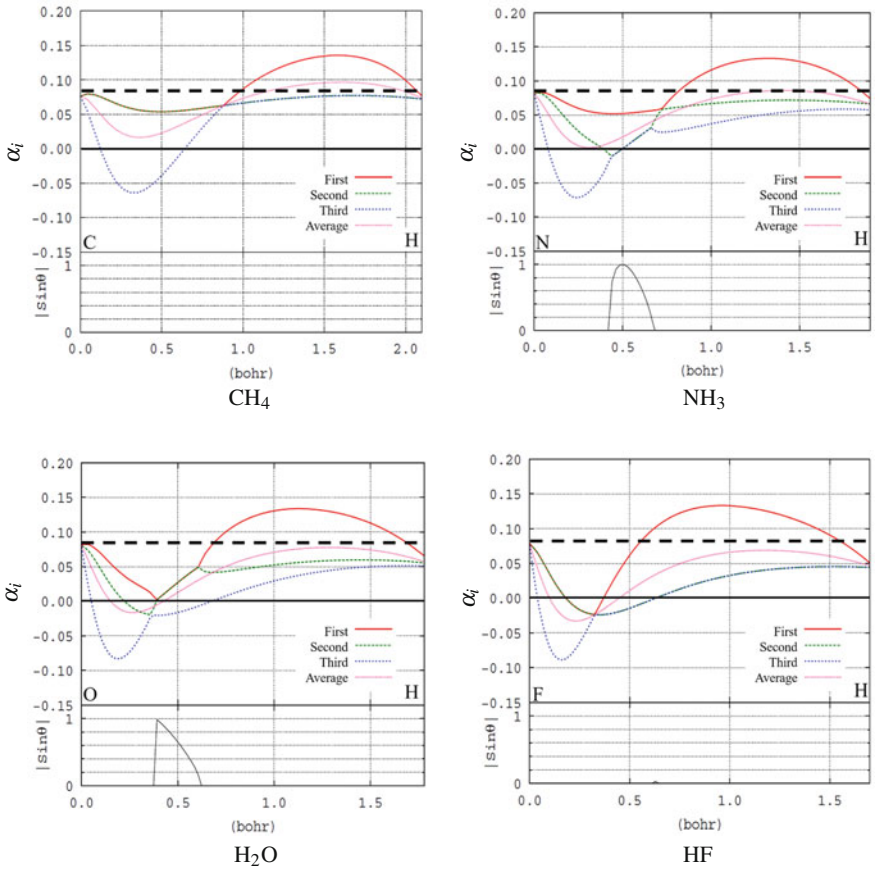

Fig. 3.8 Eigenvalues of local polarizability tensor and their average along internuclear axis of X and H bonding for CH_4, NH_3, H_2O, and HF. Top left panels show results of CH_4, top right ones show those of NH_3, bottom left ones show those of H_2O, and bottom right ones show those of HF. Bold dashed line means $\alpha_i = 1/(4\pi)$

eigenvalues are larger for smaller atomic number both in a same group and in a same period.

The structure of peaks of the average of eigenvalues of local polarizability density tensor is studied in order to see the relation between molecular size and dielectric response. The response to external electric field is maximum at peak positions. Peak positions from X nuclei of XH_n molecules are shown in Fig. 3.11. The peak at a X nucleus is trivial and not included in this figure. Multiple peak structure by core electrons is seen for the third and fourth period X atoms. These peaks (third period 1, fourth period 2, and fourth period 3) are close to X nuclei and within 1 [bohr] and almost independent of atomic number in a same period. Outermost peaks are more distant from X nuclei for larger atomic number in a same group, while in a same

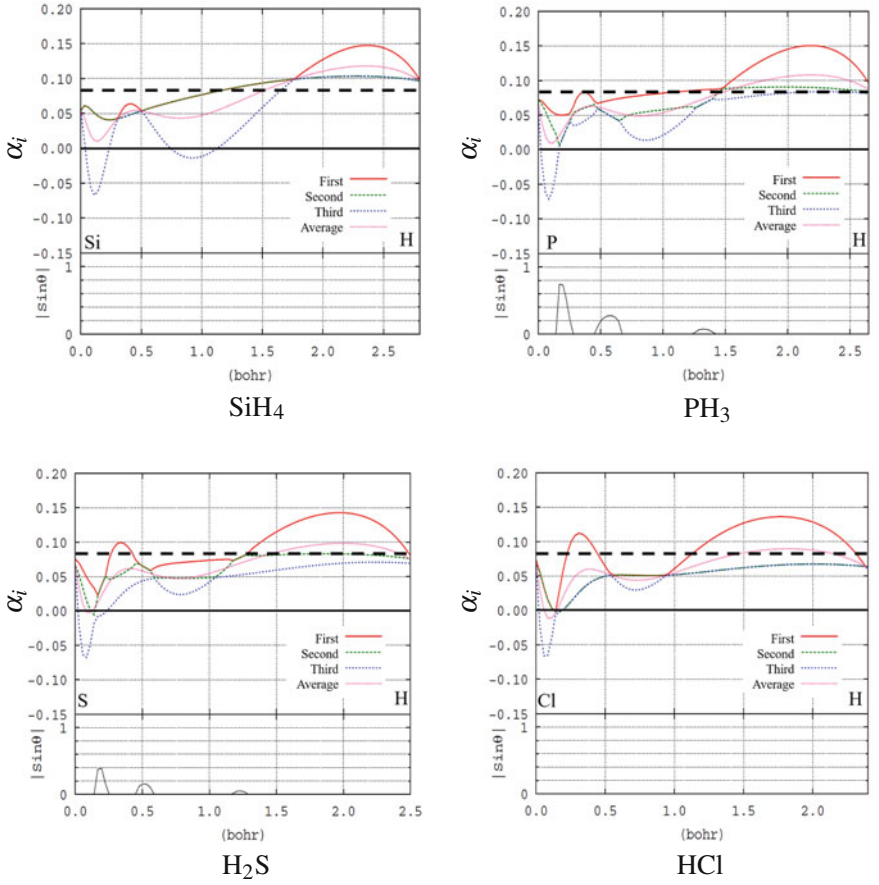

Fig. 3.9 Eigenvalues of local polarizability tensor and their average along internuclear axis of X and H bonding for SiH_4, PH_3, H_2S, and HCl. Top left panels show results of SiH_4, top right ones show those of PH_3, bottom left ones show those of H_2S, and bottom right ones show those of HCl. Bold dashed line means $\alpha_i = 1/(4\pi)$

period, these peaks are closer to the nuclei for larger atomic number. This trend of peaks corresponds to that of internuclear length between X and H atoms.

The distance of peaks from X nuclei over internuclear length between X and H atoms is shown in Fig. 3.12 in order to see the correlation between them. For outermost peaks, this value is about 0.70–0.85. The difference between periods is smaller than that of Fig. 3.11, though values of the second period are somewhat smaller than other periods. In a same period, values are smaller for larger atomic number. The difference of internuclear lengths in a same period is smaller than that of peak positions. Since internuclear lengths are correlated with the strength of covalent bond, the correlation between covalent radius [56] and peak position is shown in Fig. 3.13. Values of outermost peaks are within 0.95–1.15, and this

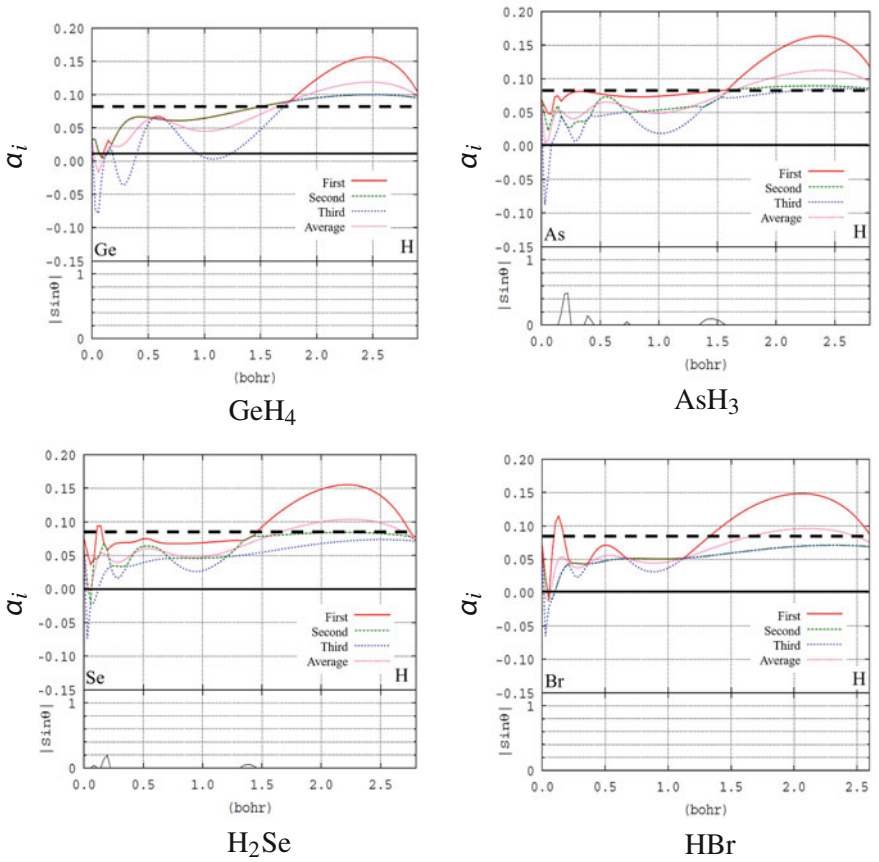

Fig. 3.10 Eigenvalues of local polarizability tensor and their average along internuclear axis of X and H bonding for GeH_4, AsH_3, H_2Se, and HBr. Top left panels show results of GeH_4, top right ones show those of AsH_3, bottom left ones show those of H_2Se, and bottom right ones show those of HBr. Bold dashed line means $\alpha_i = 1/(4\pi)$

parametrization is more close to 1 than that using internuclear length. This also confirms that peak position is dependent on the property of covalent bond.

Next, the correlation between peak positions and atomic radius defined by kinetic energy density [14–16] is shown in Fig. 3.14. The kinetic energy density operator is given as

$$\hat{T}_e(x) = -\frac{\hbar^2}{2m_e}\frac{1}{2}\left(\hat{\psi}^\dagger(x)\hat{\boldsymbol{D}}_e^2(x)\psi(x) + h.c.\right), \tag{3.30}$$

where $\hat{\boldsymbol{D}}_e(x)$ is the covariant derivative, and the expectation value of this operator is denoted by T_e. The surface $T_e = 0$ is proposed to form the surface of an atom or

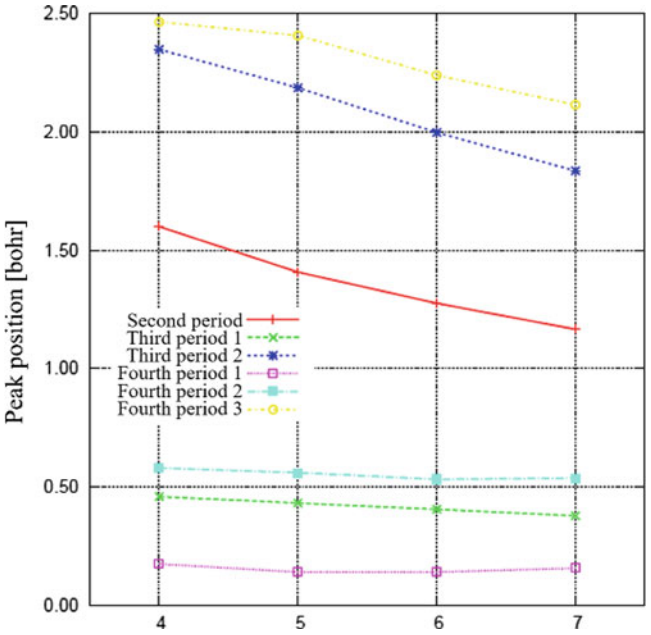

Fig. 3.11 Peak positions of the average of eigenvalues of local polarizability density tensor from X nuclei of XH_n molecules. Horizontal axis means the group of a X atom. Second, third, and fourth periods in the legend means periods of X atoms

a molecule [14–16]. Hence, the radius of the sphere, $T_e = 0$, of an isolated single X atom is adopted as the definitions of atomic radius. Values of outermost peaks are in the region 0.65–0.75 and show strong correlation between these radii and peak positions. The value is most distant from 1 among three parametrizations taken in this article, and, however, both differences between periods and that among a same period are smallest in the three parametrizations. This good property is attributed to good property of kinetic energy density as atomic radius.

In this section, we have seen local dielectric property of molecules with typical covalent bonding systematically. We have shown the distribution pattern of local polarizability density in these molecules. Negative polarizability is seen around X nuclei, and this is due to the complicated response to the combination of nuclear and external electric fields. In addition, complex eigenvalue of polarizability tensor is also seen around X nuclei, and dielectric response is rotational one in this region. Then some relations of local dielectric response to internuclear length, covalent radii, and radii of X atoms are studied, and strong correlation between them is confirmed. Results for simple molecules introduced in this section are useful and applicable for understanding dielectric property of any covalent molecules.

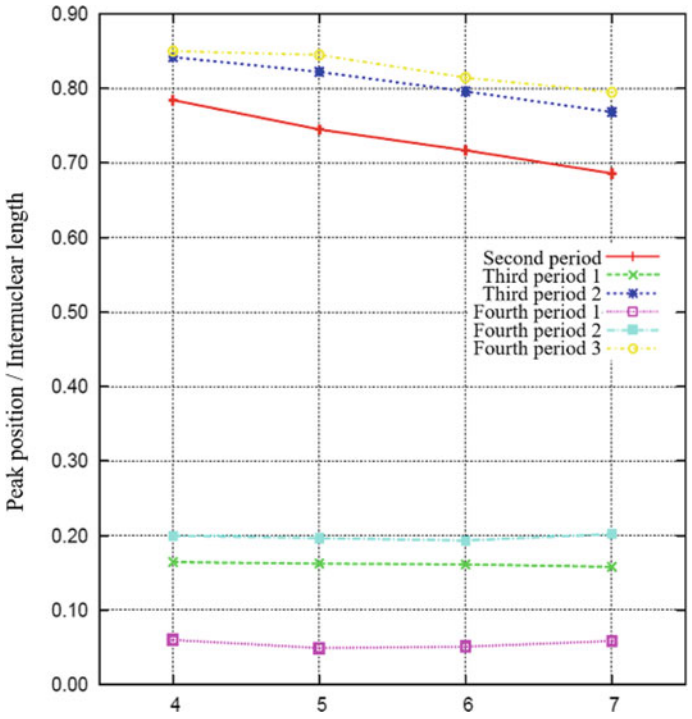

Fig. 3.12 Peak positions in Fig. 3.11 over internuclear length. Horizontal axis means the group of X atom

3.4 Local Dielectric Property of $HfLaO_x$

In this section, we show local dielectric properties of metal oxides used in new insulators for transistors. Among many materials, we focused on hafnium dioxide (HfO_2), which has high permittivity. HfO_2 has two different structures, including monoclinic and cubic. Cubic HfO_2 (c-HfO_2) has a larger dielectric constant than that of monoclinic HfO_2 (m-HfO_2). However, the c-HfO_2 is unstable. Yamamoto et al. [57] reported that the crystal structure changes into the cubic phase by doping La atoms into m-HfO_2. Based on this report, in this study, we employed a $HfLaO_x$ model to analyze the effect of the La atom on the dielectric properties. The details of our work are in Refs. [22–24].

To clarify the effect of La atoms on the dielectric properties, four different models were used, as shown in Fig. 3.15. Red spheres represent O atoms, green spheres represent La atoms, and yellow spheres represent Hf atoms. Figure 3.15a is a m-HfO_2 model, Fig. 3.15b is a La_2O_3 model, Fig. 3.15c is a c-HfO_2 model, and Fig. 3.15d is a $HfLaO_x$ model. All models were rendered by VESTA [58]. These models are made based on their crystal structures. The La_2O_3 has hexagonal unit cell, the m-HfO_2 has a monoclinic unit cell, and the c-HfO_2 has a cubic unit cell. O

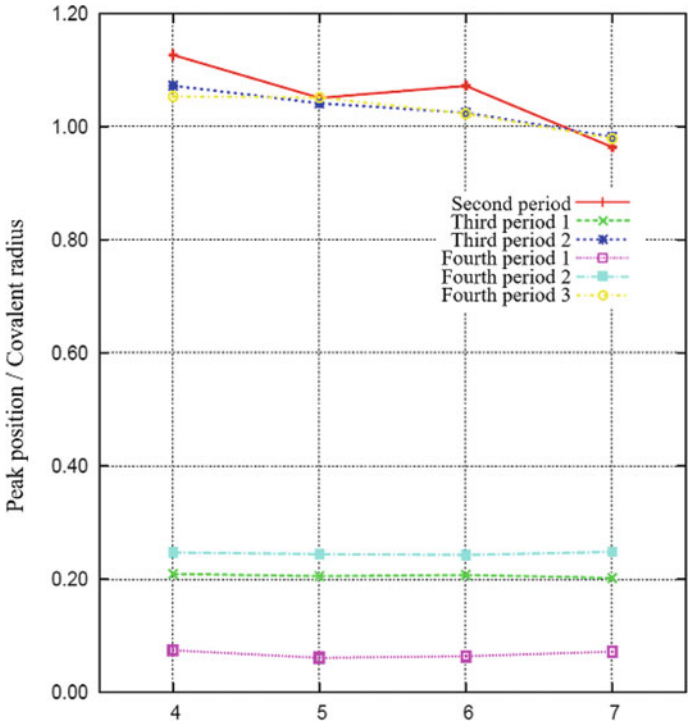

Fig. 3.13 Peak positions of the average of eigenvalues of local polarizability density tensor from X atoms of XH_n molecules. Horizontal axis means the group of a X atom

atoms are at the center of La_2O_3 and m-HfO_2, and the metal atom is at the center of c-HfO_2. In $HfLaO_x$, the center of the model is vacant. Geometry optimization was not conducted for all models. Point charges were placed around models to represent the electronic structure of a bulk system using cluster models. The point charges on the metal atom sites were given a positive charge, while those at the O sites were given a negative charge. The values of these charges were determined again so that the Mulliken charges of the atoms in the analyzed system were uniformly distributed. Accordingly, point charges were set to 0.3 and −0.2 for La_2O_3, 1.0 and −0.5 for m-HfO_2 and c-HfO_2, and 0.6 and −0.3 for $HfLaO_x$. There were 2000 point charges in the La_2O_3 model, 2800 in the m-HfO_2 model, 606 in the c-HfO_2 model, and 560 in the $HfLaO_x$ model. In some quantum chemical calculations, the bonds were terminated by H atoms to suppress the wrong response of dangling bonds. However, in the cases of ionic compounds such as some kinds of metal oxides, using the hydrogen- terminated cluster models results in an underestimation of the dielectric responses [22]. Thus, we employed the method described above.

The HF method was used to derive the electronic state for the polarizability density tensor and dielectric constant density tensor calculations. For basis set functions, LanL2DZ [35–37] was used for La and Hf atoms, and D95* was

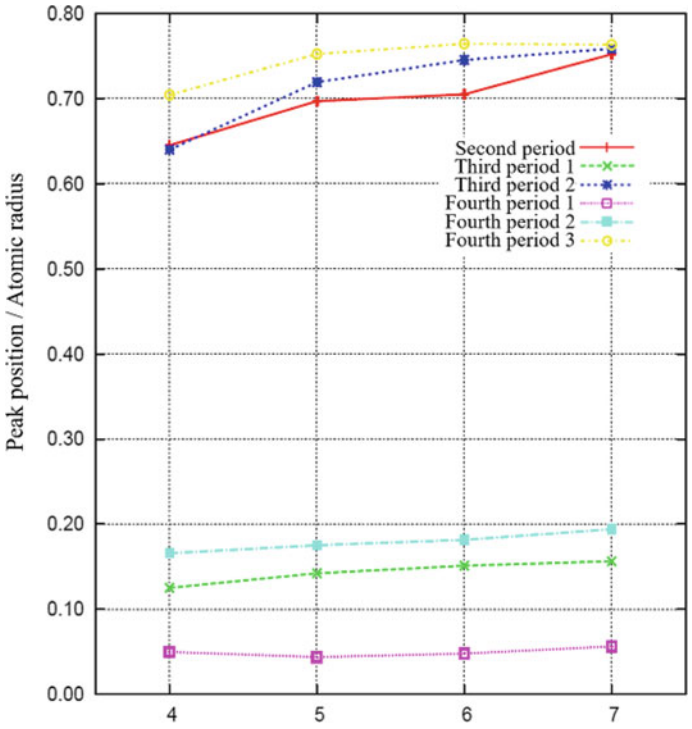

Fig. 3.14 Peak position in Fig. 3.11 over atomic radius, whose definition is explained in the text. Horizontal axis means the group of X atom

used for O atoms [59]. In addition, $4f$ polarization functions were added to that of the La atom, whose exponent coefficients are 0.441 for the LanL2DZ basis set [60]. Computations of the electronic structure were performed using Gaussian 09 program package [29]. Calculation procedures are the same in the case of the small molecules. In this section, we consider only the contribution of electrons to dielectric properties.

First, we focused on the averaged values of the polarizability density tensor and the dielectric constant density tensor according to Eq. (3.14–3.15). We employed a spherical region whose center corresponded to the central O atom, and the radius was equal to the bond length between the central O atom and nearest metal atoms in La_2O_3 and m-HfO_2. In the case of c-HfO_2, the cubic region was employed with its vertices represented with eight O atoms that are nearest to the central Hf atom. In the $HfLaO_x$ model, since the center of the model was vacant, the center of the sphere was the O atom nearest this vacancy, and the radius of the sphere was the distance between the O and La atoms. In this study, the averages of three eigenvalues were employed as indicators, which were $(\alpha_1+\alpha_2+\alpha_3)/3$ and $(\epsilon_1+\epsilon_2+\epsilon_3)/3$, where α_i are the eigenvalues of the polarizability tensor and ϵ_i are the eigenvalues of the dielectric constant tensor. Results are shown in Table 3.2. In the case of polarizability density,

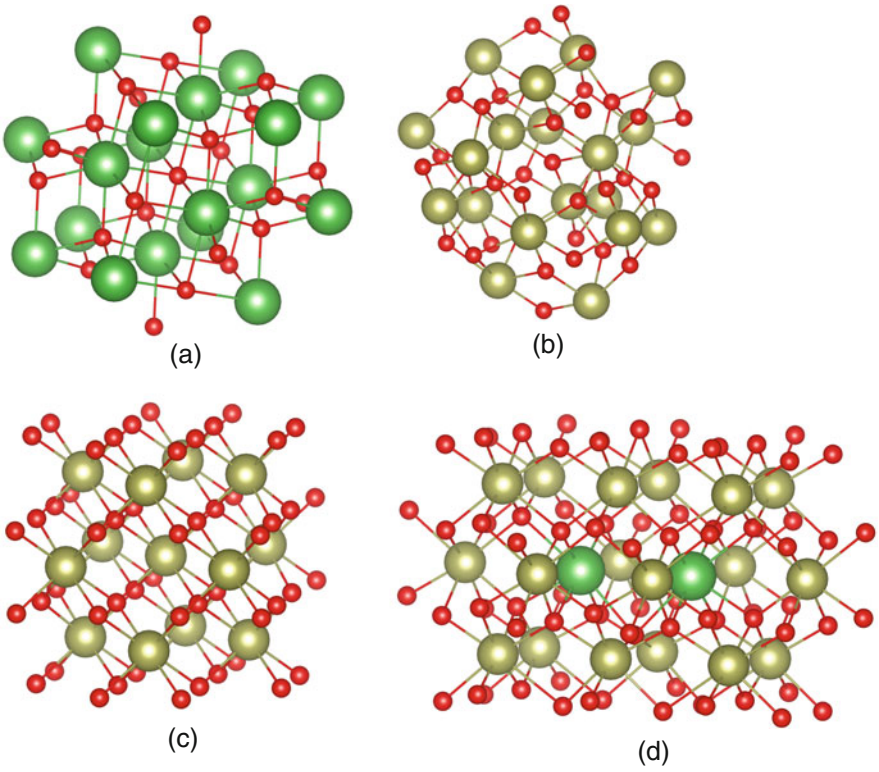

Fig. 3.15 Calculation models. Panel (**a**) is La_2O_3, panel (**b**) is m-HfO_2, panel (**c**) is c-HfO_2, and panel (**d**) is $HfLaO_x$. Red spheres represent O atoms, green spheres represent La atoms, and yellow spheres represent Hf atoms. All models were rendered by VESTA [58]

Table 3.2 The averaged value of the polarizability density tensor and the dielectric constant density tensor around the certain region obtained according to Eq. (3.14–3.15). The definition of the region is in the text

Materials	Polarizability	Dielectric constant
La_2O_3	0.057	4.72
m-HfO_2	0.041	2.40
c-HfO_2	0.058	3.57
$HfLaO_x$	0.047	2.50

the result for $HfLaO_x$ was 0.047, which is smaller than those of La_2O_3 (0.057) and c-HfO_2 (0.058). This value was quite close to that of m-HfO_2 (0.041). In the case of the dielectric constant, the result for $HfLaO_x$ was 2.50, which is smaller than those of La_2O_3 (4.72) and c-HfO_2 (3.57). Similar to the polarizability density, this value is quite close to that of m-HfO_2 (2.40).

We next focused on averaged values in the bond region. In this case, we employed a cylindrical region whose axis corresponded to the bond axis with a radius of 1

Table 3.3 The averaged value of the polarizability density tensor and dielectric constant density tensor between O and metal atoms in $HfLaO_x$ obtained according to Eq. (3.14–3.15). Definition of the cylindrical region is in the text

Bond	Polarizability	Dielectric constant
La−O	0.060	5.88
Hf−O	0.033	2.60

bohr. Results are shown in Table 3.3. The average polarizability density on a La-O bond region was 0.06 and larger than that on the Hf-O bond region (0.03). The same tendency was also observed in the average of the dielectric constant density. At the La-O bond, the average was 5.88 and larger than that on the Hf-O bond (2.60). For both polarizability and dielectric constants, an averaged value between La and O atoms was large.

We focused on the distribution of the polarizability density tensor on a plane with O and metal atoms. Figures 3.16, 3.17, 3.18, and 3.19 show results of La_2O_3, m-HfO_2, c-HfO_2, and $HfLaO_x$, respectively. The color map shows the real parts of the eigenvalues. The black solid line segments show the directions of the eigenvectors. The filled circle shows the pseudopotential of the metal atom. The green line represents the argument of the eigenvalues. Panels (a)–(c) show the first, second, and third eigenvalues, respectively. The values are presented in the descending order of the real parts of the eigenvalues. Panel (d) shows all eigenvalues and their average on the line between the metal and O atoms. In the case of the $HfLaO_x$, panel (d) shows the results between Hf and O atoms, and panel (e) shows results between La and O atoms. Comparing Figs. 3.16 and 3.17, the large polarizability density was distributed almost uniformly in the region in the first eigenvalue. Moreover, the negative value was observed on the bond region in the third eigenvalues of m-HfO_2 (Fig. 3.17c). Eigenvectors of these negative values were parallel to the bond. As shown in panel (d), the large value around $1/4\pi$ was distributed widely in the results of La_2O_3, while it was very restricted around the O atom in the results of m-HfO_2. The dielectric constant density was divergent and changes the sign of the polarizability density at $1/4\pi$. Hence, the regions where the eigenvalues were almost $1/4\pi$ produced divergently large dielectric constant density, and internal polarization was cancelled out with an external electric field. In the case of c-HfO_2 (Fig. 3.18), more complex response was observed compared with m-HfO_2. These results were indicative of the basic response of metal oxides. In panel (d) of Fig. 3.19, the region where first and second eigenvalues were about $1/4\pi$ spread widely. However, in the region between Hf and O atoms, the first eigenvalues were over $1/4\pi$. Moreover, the second eigenvalues between Hf and O atoms were smaller than those between La and O atoms. These make large difference in the cylindrical average presented in Table 3.3. Next, we turned our attention to the distribution of the eigenvalues, as shown in panels (a)–(c). In panel (a), large values in the first eigenvalues were widely observed. The large values of the second eigenvalues can be seen around O, Hf, and La atoms and the bond region between the O atom and

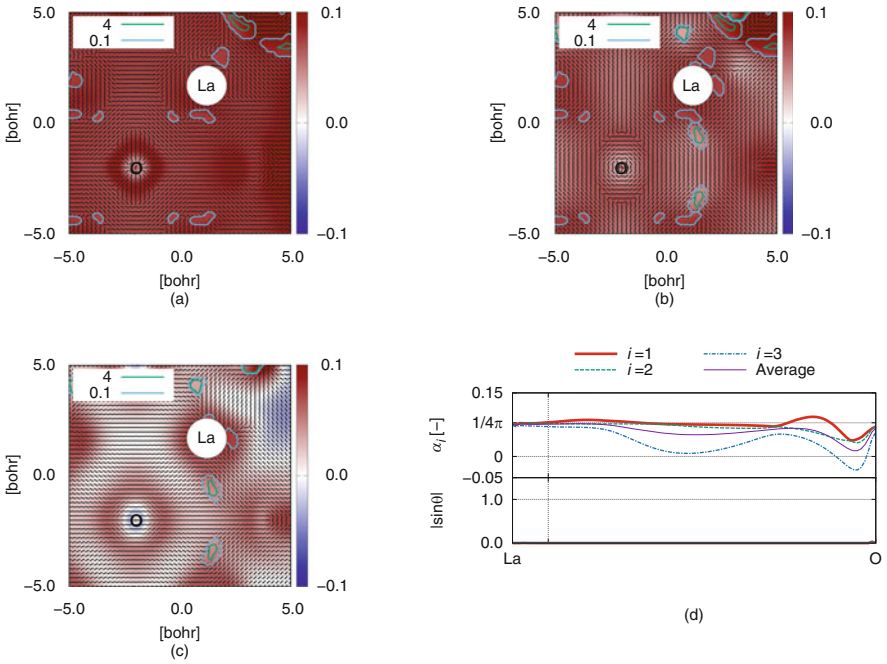

Fig. 3.16 The eigenvalues of the polarizability density tensor of La_2O_3. Panels (**a**)–(**c**) present the results of the first, second, and third eigenvalues ($\alpha_{1,2,3}$) on a plane with the central O atom and a next La atom, respectively. The values are presented in the descending order of the real parts of the eigenvalues. The color map shows the real parts of the eigenvalues, and bold lines represent the contour of the argument, and their units are in degree. The solid black lines show the directions of the eigenvectors. The filled circle shows the pseudopotential of the La atom. Panel (**d**) shows all eigenvalues on the La-O line. The upper part of this panel is the real part of three eigenvalues and their average. The lower part of this panel is the value of sine of the argument. The horizontal dotted line on the upper panel represents $1/4\pi$. The vertical dotted line between the O atom and the La atom shows the boundary of the pseudopotential, and the left region from this line is the inside of the pseudopotential

metal atoms. In other regions far from atoms, smaller values exist. Moreover, in panel (c), the large values were only around La, Hf, and O atoms.

Finally, we focus on the distribution of the dielectric constant density tensor. Figures 3.20, 3.21, 3.22, and 3.23 show results of La_2O_3, m-HfO_2, c-HfO_2, and $HfLaO_x$, respectively. The color map shows the inverse of the real parts of the eigenvalues. The solid line segments show the directions of the eigenvectors. The filled circle shows the pseudopotential of the metal atom. The green line shows the argument of the eigenvalue. Panels (a)–(c) show the first, second, and third eigenvalues, respectively. The values are presented in the descending order of the real parts of the eigenvalues. Panel (d) shows all eigenvalues on the line between the metal and O atoms. In the case of $HfLaO_x$, panel (d) shows results between Hf and O atoms, and panel (e) shows results between La and O atoms. In all models, negative

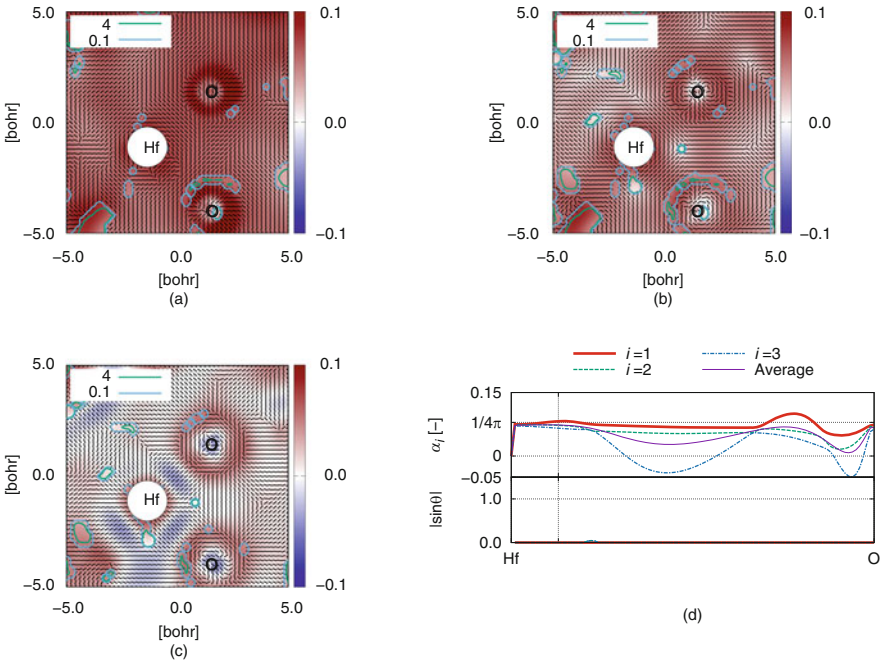

Fig. 3.17 The eigenvalues of the polarizability density tensor of m-HfO_2. Panels (**a**)–(**c**) are the results of the first, second, and third eigenvalues ($\alpha_{1,2,3}$) on a plane with the central O atom and the next Hf atoms, respectively. The values are presented in descending order of the real parts of the eigenvalues. The color map shows the real parts of the eigenvalues, and bold lines represent the contour of the argument, and their units are in degree. The solid black lines show the directions of the eigenvectors. The filled circle shows the pseudopotential of the Hf atom. Panel (**d**) shows all eigenvalues on the Hf-O line. This O atom is the upper one in panels (**a**)–(**c**). The upper part of this panel presents the real part of three eigenvalues and their average. The lower part of this panel is the value of sine of the argument. The horizontal dotted line on the upper panel represents $1/4\pi$. The vertical dotted line between the O atom and the Hf atom shows the boundary of the pseudopotential, and the left region from this line is the inside of the pseudopotential

values can be seen around O atoms. These negative values are due to the large polarizability and decrease in the total dielectric constant. The fact that the large polarizability decreases the dielectric constant is characteristic of local properties. Moreover, a white region can be seen in the third eigenvalues of all models. In this region, the absolute value of the real part of the eigenvalue was less than 1. This indicated that the dielectric constant was less than that of vacuum space. Compared with Figs. 3.20 and 3.21, a large difference can be seen in the third eigenvalues. In the case of m-HfO_2, the region where the dielectric constant was less than the vacuum space was larger than that of La_2O_3. This difference may strongly affect the total dielectric properties.

From dielectric response calculations of high-k oxides, we obtained three basic insights as follows. The first insight is that the large eigenvalues of polarizability

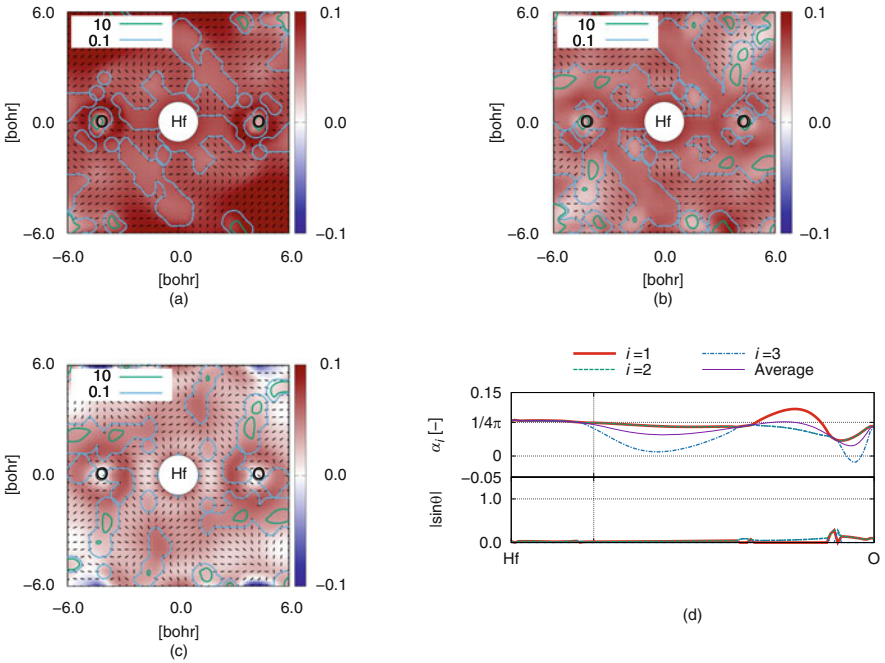

Fig. 3.18 The eigenvalues of the polarizability density tensor of c-HfO_2. Panels (**a**)–(**c**) present the results of the first, second, and third eigenvalues ($\alpha_{1,2,3}$) on a plane with the central Hf atom and the next O atoms, respectively. The values are presented in descending order of the real parts of the eigenvalues. The color map shows the real parts of the eigenvalues, and bold lines represent the contour of the argument, and their units are in degree. The solid black lines show the directions of the eigenvectors. The filled circle shows the pseudopotential of the Hf atom. Panel (**d**) shows all eigenvalues on the Hf-O line. The upper part of this panel is the real part of three eigenvalues and their average. The lower part of this panel is the value of sine of the argument. The horizontal dotted line on the upper panel represents $1/4\pi$. The vertical dotted line between the O atom and the Hf atom shows the boundary of the pseudopotential, and the left region from this line is the inside of the pseudopotential

density tensor over $1/4\pi$ were observed in the surrounding region of the nucleus of the O atom. Due to its large polarizability density, the dielectric constant density tensor has negative eigenvalues. The second one is that in the region where the polarizability density tensor has the negative eigenvalues, one of the eigenvalues of the dielectric constant density tensor shows the negative sign, and this negative eigenvalue may affect the total dielectric constant of the material. At last, doping of La atoms makes the local electric response of HfO_2 more complex compared with pure materials. Focusing the local properties, we can clarify what decreases the total dielectric constant and polarizability, like the negative values of polarizability density and dielectric constant density and may obtain the knowledge to construct new high-k materials.

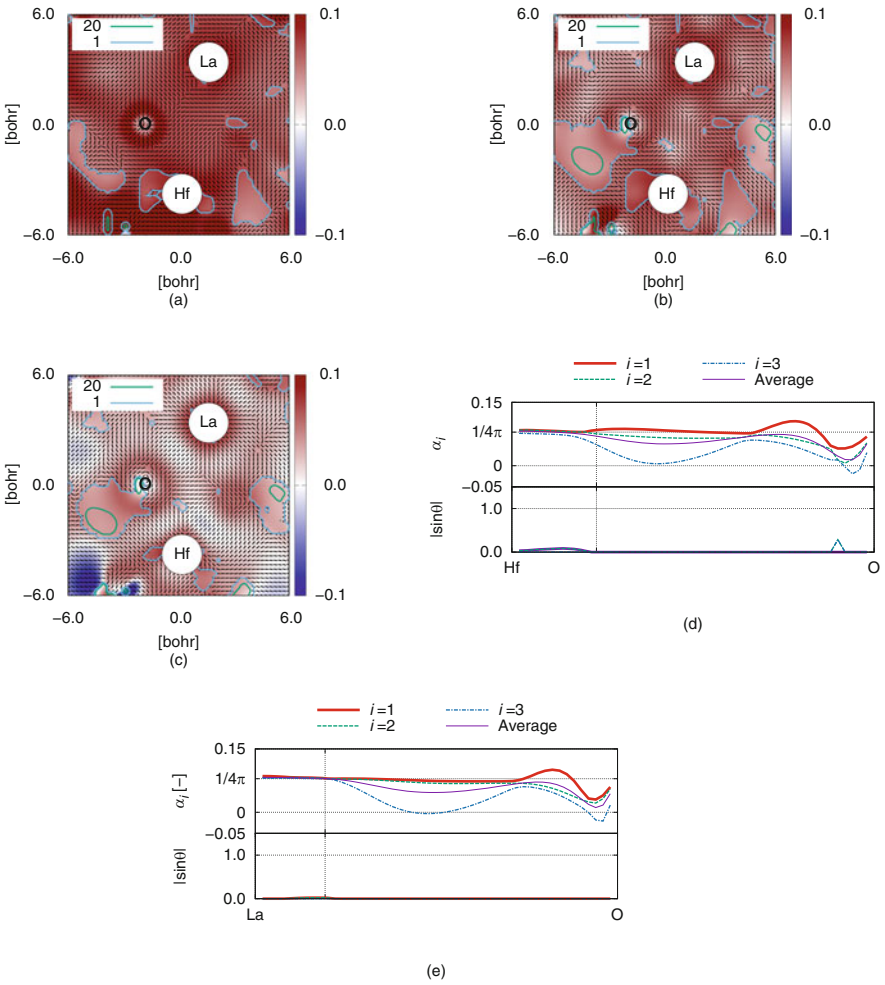

Fig. 3.19 The eigenvalues of the polarizability density tensor of $HfLaO_x$. Panels (**a**)–(**c**) are the results of the first, second, and third eigenvalues ($\alpha_{1,2,3}$) on a plane with the O atom near the central vacancy and the next Hf and La atoms, respectively. The values are presented in descending order of the real parts of the eigenvalues. The color map shows the real parts of the eigenvalues, and bold lines represent the contour of the argument, and their units are in degree. The solid black lines show the directions of the eigenvectors. The filled circles show the pseudopotential of the La and Hf atoms. Panels (**d**) and (**e**) show all eigenvalues on the Hf-O and La-O lines. The upper part of this panel is the real part of three eigenvalues and their average. The lower part of this panel is the value of sine of the argument. The horizontal dotted lines on the upper panels represent $1/4\pi$. The vertical dotted lines between the O atom and the metal atom show the boundary of the pseudopotential, and the left region from this line is the inside of the pseudopotential

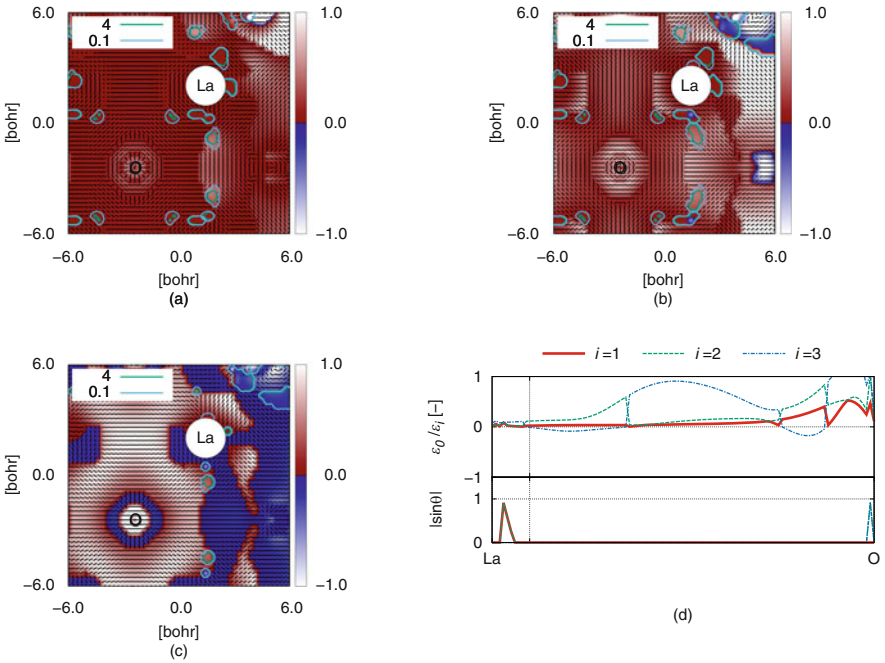

Fig. 3.20 The inverse of the eigenvalues of the dielectric constant density tensor of La_2O_3. Panels (**a**)–(**c**) present the results of the first, second, and third eigenvalues ($\epsilon^{-1}_{1,2,3}$) on a plane with the central O atom and the next La atom, respectively. The values are presented in the descending order of the real parts of the eigenvalues. The color map shows the real parts of the eigenvalues, and bold lines represent the contour of the argument and their units are in degree. The solid black lines show the directions of the eigenvectors. The filled circle shows the pseudopotential of the La atom. Panel (**d**) shows all eigenvalues on the La-O line. The upper part of this panel is the real part of three eigenvalues and their average. The lower part of this panel is the value of sine of the argument. The vertical dotted line between the O atom and the La atom shows the boundary of the pseudopotential, and the left region from this line is the inside of the pseudopotential

3.5 Summary

In this article, local dielectric constant and local polarizability have been explained. These quantities are based on quantum field theory, and formalism of these quantities has been reviewed in this article. For a hydrogen atom and Hf^{4+}, the basis dependence of local polarizability is explained. Triple- or quadruple-zeta basis sets are required for an accurate description of local polarizability density for neutral atoms, while for cations, the basis set dependence is small enough. We have also mentioned that a larger basis set is required for anions. For typical covalent molecules, XH_n (X = C, N, O, F, Si, P, S, Cl, Ge, As, Se, and Br), we have shown the distribution pattern of local polarizability density. Negative and complex eigenvalues of polarizability tensor are seen around X nuclei. These arise from response to the combination of nuclear and external electric fields. We

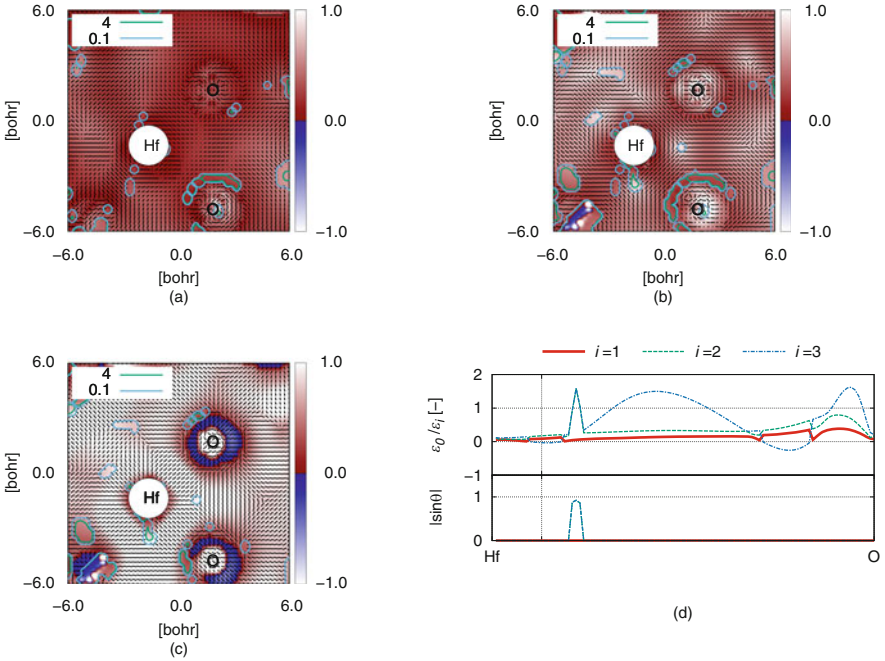

Fig. 3.21 The inverse of the eigenvalues of the dielectric constant density tensor of m-HfO_2. Panels (**a**)–(**c**) present the results of the first, second, and third eigenvalues ($\epsilon^{-1}_{1,2,3}$) on a plane with the central O atom and the next Hf atom, respectively. The values are presented in the descending order of the real parts of the eigenvalues. The color map shows the real parts of the eigenvalues, and bold lines represent the contour of the argument, and their units are in degree. The solid black lines show the directions of the eigenvectors. The filled circle shows the pseudopotential of the Hf atom. Panel (**d**) shows all eigenvalues on the Hf-O line. This O atom is the upper one in panels (**a**)–(**c**). The upper part of this panel is the real part of three eigenvalues and their average. The lower part of this panel is the value of sine of the argument. The vertical dotted line between the O atom and the Hf atom shows the boundary of the pseudopotential, and the left region from this line is the inside of the pseudopotential

have also explained strong correlations of local dielectric response to internuclear length, covalent radii, and radii of X atoms. As an example of application of these quantities to the study of nanomaterial, hafnium dioxide was taken in this article in viewpoints of gate dielectric thin film. Using monoclinic, cubic, and La-doped cubic structures, we have evaluated the dielectric properties around the atoms and the bond regions and clarified the effect of the La doping on the distribution of the dielectric properties. We have shown that large polarizability density that makes the negative eigenvalues of dielectric constant density can be seen around the nucleus of the O atom, and the bond region affects the average dielectric constant strongly. Moreover, we have also clarified that doping of La atoms makes the local electric response of HfO_2 more complex. By focusing the local properties, we may obtain the basic insights to construct new high-k materials.

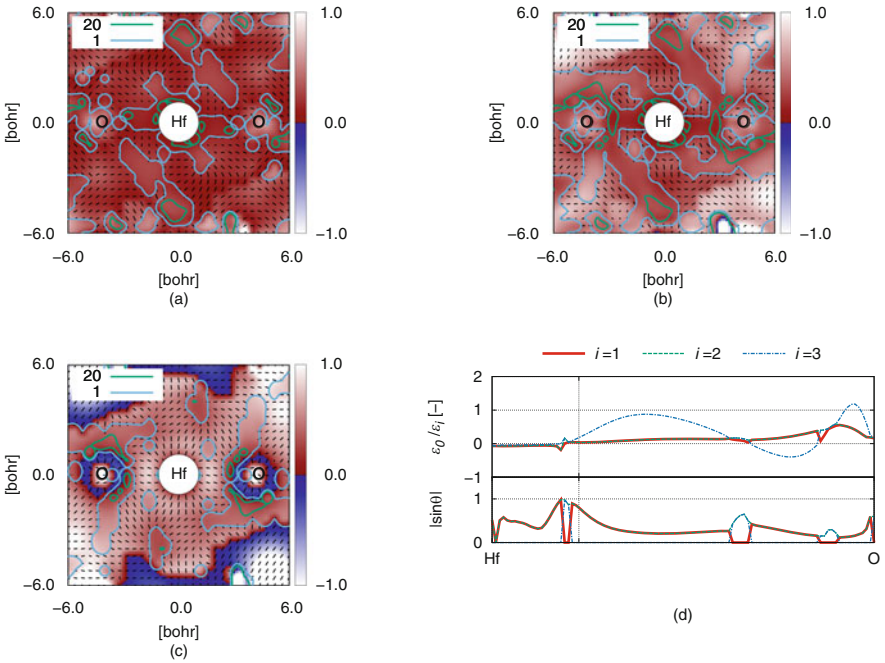

Fig. 3.22 The inverse of the eigenvalues of the dielectric constant density tensor of c-HfO_2. Panels (**a**)–(**c**) present the results of the first, second, and third eigenvalues ($\epsilon^{-1}_{1,2,3}$) on a plane with the central Hf atom and a next O atom, respectively. The values are presented in the descending order of the real parts of the eigenvalues. The color map shows the real parts of the eigenvalues, and bold lines represent the contour of the argument, and their unit is in degree. The solid black lines show the directions of the eigenvectors. The filled circle shows the pseudopotential of the Hf atom. Panel (**d**) shows all eigenvalues on the Hf-O line. The upper part of this panel is the real part of three eigenvalues and their average. The lower part of this panel is the value of sine of the argument. The vertical dotted line between the O atom and the Hf atom shows the boundary of the pseudopotential, and the left region from this line is the inside of the pseudopotential

3.6 Perspective

This analysis approach of the usage of local dielectric constant and local polarizability has been just started, and many subjects remain to be investigated. For example, ordinary dielectric response is known to have the dependence on frequency of electric field, and hence local dielectric constant and local polarizability have also this dependence. However, this dependence has not been studied in any published works. As another important issue, nuclear contribution to dielectric constant is known to be important in hafnium dioxide. The works introduced in this article have not included this contribution, and this important effect remains to be studied.

At last, the formalism of local dielectric constant and local polarizability is based on quantum field theory. However, computations reviewed in this article were performed by electronic structure computations based on quantum mechanics.

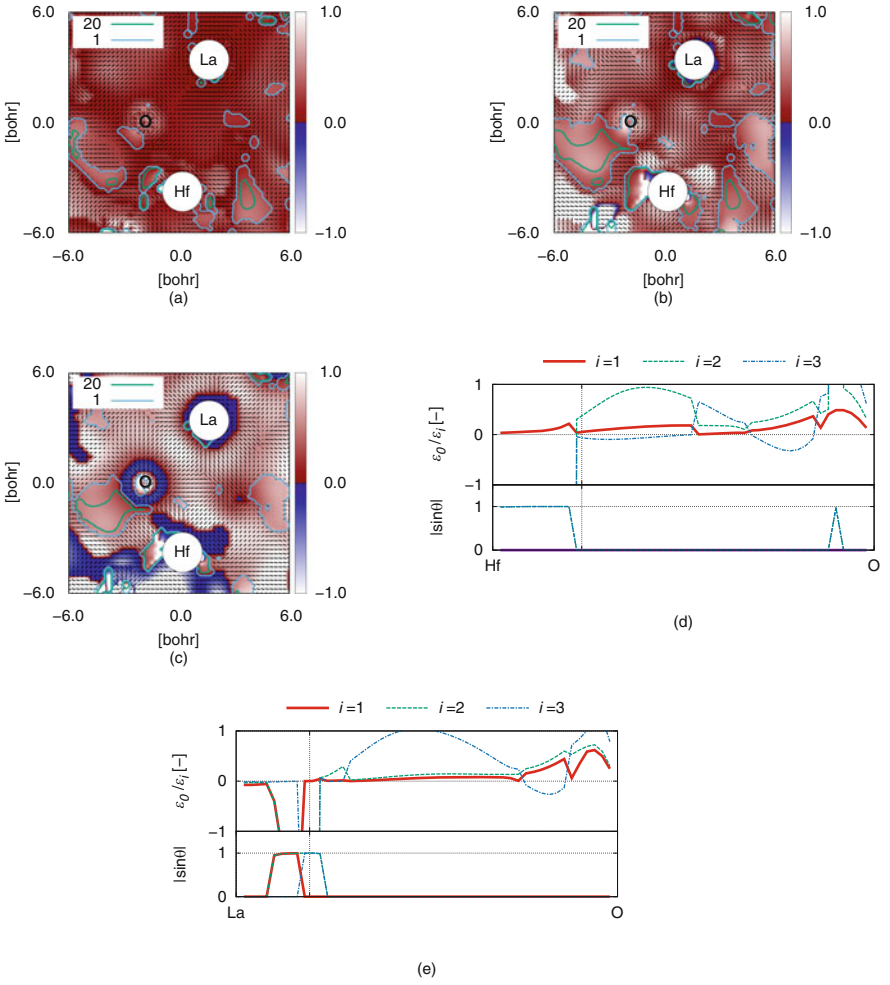

Fig. 3.23 The inverse of the eigenvalues of the dielectric constant density tensor of $HfLaO_x$. Panels (**a**)–(**c**) present the results of the first, second, and third eigenvalues ($\epsilon^{-1}_{1,2,3}$) on a plane with the O atom near the vacancy and the next Hf and La atoms, respectively. The values are presented in the descending order of the real parts of the eigenvalues. The color map shows the real parts of the eigenvalues, and bold lines represent the contour of the argument and their units are in degree. The solid black lines show the directions of the eigenvectors. The filled circles show the pseudopotential of the La and Hf atom. Panels (**d**) and (**e**) show all eigenvalues on the Hf-O and La-O atoms. The upper part of this panel is the real part of three eigenvalues and their average. The lower part of this panel is the value of sine of the argument. The vertical dotted lines between the O atom and the metal atom show the boundary of the pseudopotential, and the left region from this line is the inside of the pseudopotential

Quantum field theory is more correct theory than quantum mechanics. Ideally, electronic structure should be prepared by electronic structure computations based on quantum filed theory, and unfortunately, these computations are not available yet, except for some special cases such as Bethe-Salpeter equation, lattice QCD [61], and NRQED [62]. Some groups are trying to establish electronic structure computation based on quantum field theory [50, 63–69]. This advanced electronic structure computation is hoped to be established in the near future.

References

1. R.P. Feynman, J. Microelectromech. Syst. **1**, 60 (1992)
2. R. Degraeve, G. Groeseneken, R. Bellens, M. Depas, H.E. Maes, Tech. Dig. Int. Electron Devices Meet. 863 (1995). https://doi.org/10.1109/IEDM.1995.499353
3. R. Degraeve, G. Groeseneken, R. Bellens, J.L. Ogier, M. Depas, P.J. Roussel, H.E. Maes, IEEE Trans. Electron Devices **45**, 904 (1998)
4. M.A. Reed, C. Zhou, C.J. Muller, T.P. Burgin, J.M. Tour, Science **278**, 252 (1997)
5. A. Nitzan, M.A. Ratner, Science **300**, 1384 (2003)
6. W. Haiss, C. Wang, I. Grace, A.S. Batsanov, D.J. Schiffrin, S.J. Higgins, M.R. Bryce, C.J. Lambert, R.J. Nichols, Nat. Mater. **5**, 995 (2006)
7. L. Venkataraman, J.E. Klare, I.W. Tam, C. Nuckolls, M.S. Hybertsen, M.L. Steigerwald, Nano Lett. **6**, 458 (2006)
8. Y. Kim, T. Pietsch, A. Erbe, W. Belzig, E. Scheer, Nano Lett. **11**, 3734 (2011)
9. H. Hakkinen, Nat. Chem. **4**, 443 (2012)
10. K. Yokota, M. Taniguchi, M. Tsutsui, T. Kawai, J. Am. Chem. Soc. **132**, 17364 (2010)
11. C.R. Arroyo, E. Leary, A. Castellanos-Gomez, G. Rubio-Bollinger, M. Teresa Gonzalez, N. Agrait, J. Am. Chem. Soc. **133**, 14313 (2011)
12. M. Frei, S.V. Aradhya, M.S. Hybertsen, L. Venkataraman, J. Am. Chem. Soc. **134**, 4003 (2012)
13. Y. Ikeda, M. Senami, A. Tachibana, Trans. Mat. Res. Soc. Jpn. **38**(3), 397 (2013)
14. A. Tachibana, J. Mol. Model **11**, 301 (2005)
15. A. Tachibana, J. Mol. Struct. (THEOCHEM) **943**, 138 (2010)
16. A. Tachibana, *New Aspects of Quantum Electrodynamics* (Springer Nature, Singapore, 2017)
17. M. Senami, Y. Ikeda, A. Tachibana, Jpn. J. Appl. Phys. **50**, 010103 (2011)
18. Y. Ikeda, M. Senami, A. Tachibana, AIP Adv. **2**, 042168 (2012)
19. T. Hara, M. Senami, A. Tachibana, Phys. Lett. A **376**, 1434 (2012)
20. M. Fukuda, M. Senami, A. Tachibana, in *Advances in Quantum Methods and Applications in Chemistry, Physics, and Biology Progress in Theoretical Chemistry and Physics*, vol. 27, chap. 7, eds. by M. Hotokka, E.J. Brändas, J. Maruani, G. Delgado-Barrio (Springer, New York, 2013), pp. 131–139
21. M. Fukuda, K. Soga, M. Senami, A. Tachibana, Int. J. Quant. Chem **116**, 920 (2016)
22. A. Fukushima, Y. Tsuchida, M. Senami, A. Tachibana, Jpn. J. Appl. Phys. **49**, 111504 (2010)
23. A. Fukushima, S. Sugino, Y. Tsuchida, M. Senami, A. Tachibana, Jpn. J. Appl. Phys. **49**, 121504 (2010)
24. M. Senami, Y. Tsuchida, A. Fukushima, Y. Ikeda, A. Tachibana, Jpn. J. Appl. Phys. **51**, 031101 (2012)
25. H. Nozaki, M. Senami, K. Ichikawa, A. Tachibana, Jpn. J. Appl. Phys. **55**, 08PE01 (2016)
26. M. Senami, Y. Ikeda, A. Fukushima, A. Tachibana, Jpn. J. Appl. Phys. **49**, 115002 (2010)
27. M. Senami, Y. Ogiso, T. Miyazato, F. Yoshino, Y. Ikeda, A. Tachibana, Trans. Mat. Res. Soc. Jpn. **38**(4), 535 (2013)
28. F. Yoshino, Master Thesis, Department of Micro Engineering, Kyoto University, Kyoto, 2012

29. M.J. Frisch et al., *Gaussian 09, Revision B. 01* (Gaussian Inc., Wallingford, 2010)
30. W.J. Hehre, R. Ditchfield, J.A. Pople, J. Chem. Phys. **56**, 2257 (1972)
31. P.C. Hariharan, J.A. Pople, Theoret. Chim. Acta **28**, 213 (1973)
32. T. Clark, J. Chandrasekhar, G.W. Spitznagel, P.V.R. Schleyer, J. Comput. Chem. **4**, 294 (1983)
33. R. Krishnan, J.S. Binkley, R. Seeger, J.A. Pople, J. Chem. Phys. **72**, 650 (1980)
34. T.H. Dunning Jr., J. Chem. Phys. **90**, 1007 (1989)
35. P.J. Hay, W.R. Wadt, J. Chem. Phys. **82**, 270 (1985)
36. P.J. Hay, W.R. Wadt, J. Chem. Phys. **82**, 284 (1985)
37. P.J. Hay, W.R. Wadt, J. Chem. Phys. **82**, 299 (1985)
38. L.E. Roy, P.J. Hay, R.L. Martin, J. Chem. Theory Comput. **4**, 1029 (2008)
39. F. Weigend, R. Ahlrichs, Phys. Chem. Chem. Phys. **7**, 3297 (2005)
40. D. Andrae, U. Haeussermann, M. Dolg, H. Stoll, H. Preuss, Theoret. Chim. Acta **77**, 123 (1990)
41. D. Figgen, K.A. Peterson, M. Dolg, H. Stoll, J. Chem. Phys. **130**, 164108 (2009)
42. M.W. Schmidt, K.K. Badridge, J.A. Boatz, S.T. Elbert, M.S. Gordon, J.H. Jensen, S. Koseki, N. Matsunaga, K.A. Nguyen, S. Su, T.L. Windus, M. Dupuis, J.A. Montgomery, J. Comput. Chem. **14**, 1347 (1993)
43. D.E. Woon, T.H. Dunning Jr., J. Chem. Phys. **98**, 1358 (1993)
44. A.K. Wilson, D.E. Woon, K.A. Peterson, T.H. Dunning Jr., J. Chem. Phys. **110**, 7667 (1999)
45. S. Baroni, R. Resta, Phys. Rev. B **33**, 7017 (1988)
46. Z.H. Levine, D.C. Allan, Phys. Rev. B **43**, 4187 (1991)
47. Z.H. Levine, D.C. Allan, Phys. Rev. B **44**, 12781 (1991)
48. Z.H. Levine, D.C. Allan, Phys. Rev. Lett. **63**, 1719 (1989)
49. Z.H. Levine, D.C. Allan, Phys. Rev. Lett. **66**, 41 (1991)
50. M. Senami, K. Ichikawa, A. Tachibana, QEDynamics (2018). https://github.com/mfukuda QED/QEDalpha
51. M. Senami, T. Miyazato, S. Takada, Y. Ikeda, A. Tachibana, J. Phys. Conf. Ser. **454**, 012052 (2013)
52. K. Ichikawa, M. Fukuda, A. Tachibana, Int. J. Quant. Chem. **113**, 190 (2013)
53. K. Ichikawa, M. Fukuda, A. Tachibana, Int. J. Quant. Chem. **114**, 1567 (2014)
54. M. Senami, S. Takada, A. Tachibana, JPS Conf. Proc. **1**, 016014 (2014)
55. M. Fukuda, K. Naito, K. Ichikawa, A. Tachibana, Int. J. Quant. Chem. **116**, 932 (2016)
56. P. Pyykkö, M. Atsumi, Chem. Eur. J. **15**, 186 (2009)
57. Y. Yamamoto, K. Kita, K. Kyuno, A. Toriumi, Appl. Phys. Lett. **89**, 032903 (2006)
58. K. Momma, F. Izumi, VESTA 3 for three-dimensional visualization of crystal, volumetric and morphology data. J. Appl. Crystallogr. **44**, 1272–1276 (2011)
59. C.H. Dunning Jr., P.J. Hay, in *Modern Theoretical Chemistry*, ed. H.F. Schaefer III (Plenum, New York, 1976)
60. K. Doi, Y. Mikazuki, S. Sugino, T. Doi, P. Szarek, M. Senami, K. Shiraishi, H. Iwai, N. Umezawa, T. Chikyo, K. Yamada, A. Tachibana, Jpn. J. Appl. Phys. **47**, 205 (2008)
61. I. Montvay, C. Münster, *Quantum Field on a Lattice* (Cambridge University Press, Cambridge, 1997)
62. W.E. Caswell, G.P. Lepage, Phys. Lett. **167B**, 437 (1996)
63. J. Berges, AIP Conf. Proc. **739**, 3 (2005)
64. F. Hebenstreit, J. Berges, D. Gelfand, Phys. Rev. **D87**, 105006 (2013) and references there's in
65. U.D. Jentschura, Can. J. Phys. **89**, 109 (2011)
66. U.D. Jentschura, J. Evers, Can. J. Phys. **83**, 375 (2005)
67. K.D. Lamb, C.C. Gerry, Q. Su, R. Grobe Phys. Rev. A **75**, 013425 (2007)
68. R.E. Wagner, M.R. Ware, B.T. Shields, Q. Su, R. Grobe, Phys. Rev. Lett. **106**, 023601 (2011)
69. R.E. Wagner, Q. Su, R. Grobe, Phys. Rev. A **88**, 012113 (2013) and references there's in

Chapter 4
Nanoscale First-Principles Electronic Structure Simulations of Materials Relevant to Organic Electronics

Susumu Yanagisawa and Ikutaro Hamada

Abstract Organic molecular materials have attracted considerable attention as a candidate for next-generation flexible electronics in the near future. However, there still remain open questions on fundamental electronic properties such as mechanisms of the carrier transport and barriers for carrier injection at organic-inorganic heterojunctions. In this review, we illustrate the progresses in first-principles electronic structure calculations of the materials for investigation of the atomic- or molecular-scale electronic properties of organic semiconductor materials, which are in general difficult to observe even with present-day experimental techniques. The theoretical studies not only help elucidate the mechanism of the experimental measurement but also may allow us to gain insights into the essences of the materials properties in terms of the electronic structure. Specifically, in this article, we focus on the first-principles theoretical treatment of the geometric configurations of organic semiconductors and their electronic structure at the level beyond the approximation to the density functional theory (DFT) such as the local density (LDA) and generalized gradient approximations (GGA), i.e., the van der Waals-inclusive methods for describing the weak intermolecular interaction in organic solids and the many-body perturbation theory within the GW approximation for treatment of the charged excitation (quasiparticle) and thus the fundamental gap and the band dispersion of the crystals. Here, we illustrate the recent studies on (i) the effect of the molecular configuration on the quasiparticle energy in organic semiconductors, (ii) the energy level alignment at organic-metal interfaces, and (iii) prediction of the charge injection levels at a surface of organic thin film, i.e., the ionization energy and the electron affinity. Further progresses in theoretical

S. Yanagisawa (✉)
Faculty of Science, Department of Physics and Earth Sciences, University of the Ryukyus, Nishihara, Okinawa, Japan
e-mail: shou@sci.u-ryukyu.ac.jp

I. Hamada
Department of Precision Science and Technology, Graduate School of Engineering, Osaka University, Suita, Osaka, Japan
e-mail: ihamada@prec.eng.osaka-u.ac.jp

T. Onishi (ed.), *Theoretical Chemistry for Advanced Nanomaterials*,
https://doi.org/10.1007/978-981-15-0006-0_4

methodologies, being enhanced by rapid progress in computational resource and algorithm, might lead to in silico material simulation or design.

Keywords Organic semiconductors · Intermolecular van der Waals interaction · van der Waals density functional · GW approximation · Organic-metal interfaces · Image potential states

4.1 Introduction

Semiconductors comprised of organic molecules have attracted considerable attention as candidates for next-generation flexible electronics materials. It is believed that organic semiconductor electronics will be competitive against inorganic semiconductors for applications to mechanically flexible, large-area, and low-cost electronics [1]. Some organic-based electronic devices such as organic light-emitting diodes (OLED) are on the market, while other electronics materials such as organic field-effect transistors (OFET) and organic photovoltaics (OPV) are at the stage of a fundamental research. However, there is much room for investigation on the electronic properties of the organic materials, for instance, carrier transport property. Poor knowledge of the transport property in organic solids is contrast to the situation in inorganic semiconductors [2]. More understanding of their basic electronic properties is urgent, which may accelerate development of the next-generation flexible electronics.

Here, we review recent theoretical works with the first-principles electronic structure calculation, i.e., (i) those on the intermolecular van der Waals (vdW) interaction dominating the structural and electronic properties of the organic semiconductor materials and (ii) the effect of the many-body electrons (or the quasiparticle effect) upon the injected charge in the bulk of the organic semiconductors or at the organic-metal interface.

We demonstrate the roles of the first-principles electronic structure calculations which could clarify a relation between the electronic structure and the geometrical configurations. As an example, the impact of the atomic-scale geometric structures on the electronic states is discussed. It was not possible to predict the crystal geometry or the molecular configuration in the unit cell of the organic semiconductor crystals with the density functional theory (DFT) within the local density (LDA) or generalized gradient approximation (GGA), because of the failure of the methodology to describe the intermolecular vdW interaction, which is nonlocal and long-ranged in nature. However, there are more and more methodologies being developed capable of describing the vdW interaction between the constituent organic molecules [3–11].

The quasiparticle energy is essentially related to the barrier for charge injection, i.e., the electronic energy upon charged excitation, and also the interaction between the electron-hole pair upon optical excitation, dominating the optical gap. Fundamental gap and band dispersion of organic molecular solids are becoming accurately

predictable by the first-principles theoretical methods describing the quasiparticle self-energy such as the GW approximation [12].

In this article, we review first-principles electronic structure calculations on

1. Structures of organic semiconductor crystals with the van der Waals (vdW)-inclusive methods
2. Electronic properties of organic-metal interfaces: electronic properties such as energy level alignment and the image potential states
3. Electronic charge (electron or hole) injection level depending on the molecular orientation at the organic crystal surface

In the first topic, we focus on our first-principles study on prediction of the lattice constants and the intermolecular configuration in oligoacene crystals, along with analysis of the band structure and the intermolecular transfer integral [13]. Here, the Wannier functions [14, 15] were derived, allowing us to estimate intermolecular transfer integrals depending crucially on the cell volume or the intermolecular configurations in the crystal. The Wannier functions in organic crystals could be mapped on the crystal Hamiltonian such as the tight-binding Hamiltonian, thus leading to multi-scale real-time simulations of charge carrier transport in organic crystals [16]. In addition to the previous work on naphthalene, anthracene, and tetracene [13], calculation of pentacene and hexacene crystals is demonstrated in this article.

Secondly, the electronic properties induced at the organic-metal interface are discussed. The energy level alignment at the organic-metal interface originating from the rearrangement of the electronic clouds at the interface has attracted considerable attention [17], because of its relevance to barrier for charge injection into an organic layer. To elucidate the experimental measurements using techniques such as photoemission spectroscopy proving the energy levels of the injected hole or electron right at the interface, aid of a reliable theoretical method treating charged excitations (quasiparticles) is necessary. Here, we focus on highly accurate theoretical approaches beyond DFT within the LDA or GGA, such as the many-body perturbation theory within the GW approximation [12, 18]. In addition, we demonstrate our recent theoretical investigation [19] to clarify the electronic nature of the recently reported image potential state of graphite in the presence of an organic overlayer [20].

In the third place, we discuss determination of charge injection levels in organic semiconductor crystals or thin films, mainly based on the GW approximation. The charge injection level relative to the vacuum level, i.e., ionization energy (IE) or electron affinity (EA) of organic semiconductors, crucially affects the charged carrier transport properties. It was practically difficult to predict IE and EA of organic semiconductors using periodic slab models at the GW level of theory, because of the computational cost to meet convergence criteria. Recently, there are theoretical studies at the same level of theory handling the problem [21–23].

Finally, we demonstrate the future aspects of the theoretical methods, both in terms of contribution to elucidation of the novel experimental measurements and room for development of the theoretical methodologies.

4.2 Theoretical Investigations on Electronic Properties of Organic Molecular Materials

4.2.1 Structural Properties: Crystal Geometry and Intermolecular Configuration

4.2.1.1 Crystal Structures Optimized with a Variant of Van der Waal Density Functionals

Geometrical configurations in bulk systems of organic molecular crystals or heterojunctions such as organic-metal electrode and organic-organic interfaces are of importance, in which the atomistic- or molecular-scale geometrical arrangements significantly alter the electronic properties.

The structural properties of organic crystals such as crystal structures and intermolecular geometrical configurations are one of the central issues dominating the electronic properties such as charge transport [24, 25]. Subtle interplay among the intermolecular van der Waals (vdW) forces, the exchange repulsion, and the orbital hybridization leads to a rich variety of polymorphs with different electronic properties. The stability of the polymorphs depends on temperature, and thus attempts are going on to predict (meta-)stable polymorphs of the organic crystals [26]. Nevertheless, first-principles theoretical investigations on electronic structure of the most stable polymorph at 0 K may give us insights into the properties of the materials at not only low temperature but also at room temperature.

Recently proposed vdW-inclusive methods have played roles in prediction of stable crystal structure and molecular configurations, which allows us to discuss the effects of the intermolecular interaction on electronic properties.

Here, we focus on the first-principles theoretical methods that have been successfully applied to organic semiconductor crystals (for a variety of the applications to other molecular aggregates and complexes, see a recent comprehensive review such as Ref. [27]).

The structure and the energetics of an organic crystal could be quite accurately predicted with first-principles methods such as the adiabatic-connection fluctuation-dissipation theorem within the random-phase approximation (RPA) [4, 28, 29], the quantum Monte Carlo [30, 31], and the wave function-based quantum chemistry [32, 33] methods. However, the computational cost involved at present prevents application of the highly accurate methods to organic crystals that are of practical or experimental interest. The vdW-inclusive density functional method, such as the van der Waals density functional (vdW-DF) and its variants [10, 34–39], may be a method of choice, because of its moderate computational cost [40] and its reliability in prediction of structural properties of organic crystals. We employed the revised vdW-DF2 (rev-vdW-DF2), with its reliable prediction of crystal geometries of organic crystals such as rubrene [10] and metal phthalocyanine [41].

We first performed the structural optimizations and determined the stable structures for naphthalene, anthracene, and tetracene crystals (Fig. 4.1) by using

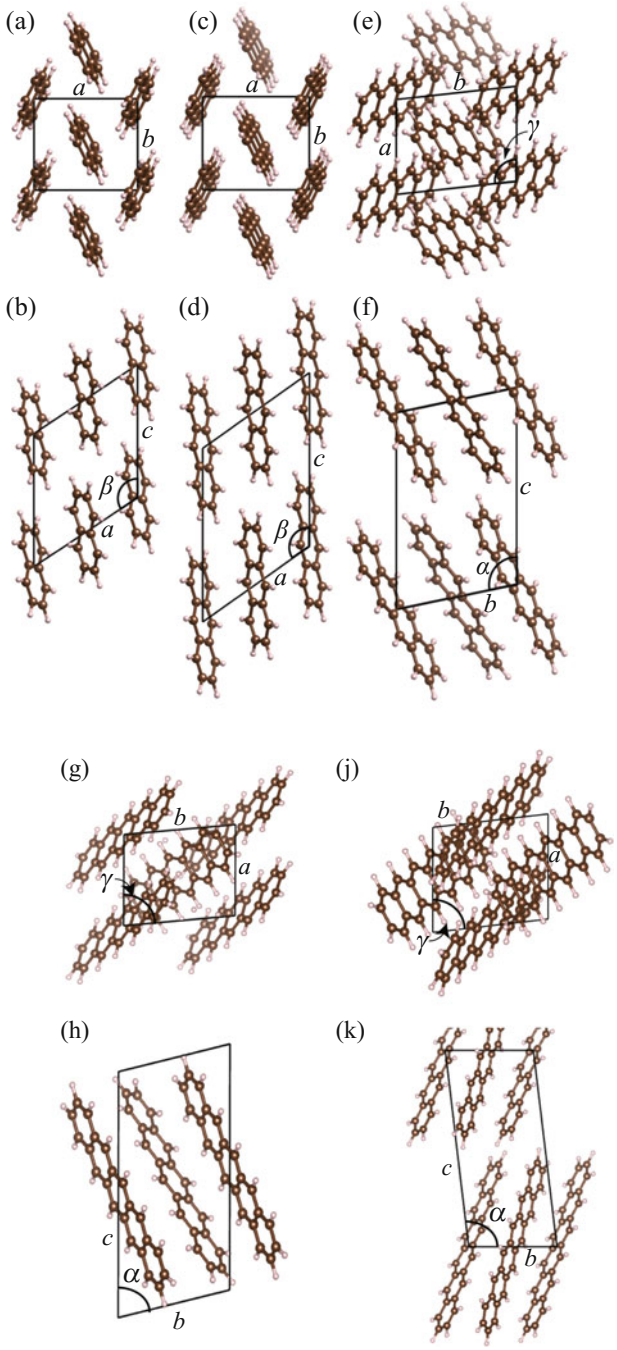

Fig. 4.1 Crystal structures of the single crystals of (**a**), (**b**): naphthalene, (**c**), (**d**): anthracene, (**e**), (**f**): tetracene, (**g**), (**h**): pentacene, and (**j**), (**k**): hexacene [42]. The unit cell consists of the two nonequivalent molecules placed at the corner and center of the cell, which are arranged in a herringbone fashion. For tetracene, the Niggli cell parameters are displayed, for ease of comparison between the crystal geometry obtained in this study and the experimental data (see Table 4.1). (Figure 1(**a**)–(**f**): Reprinted from [13], with the permission of AIP Publishing)

vdW-DF. As the initial structures for the structural optimization, we used the X-ray diffraction data of naphthalene [43] and anthracene [44] with the space group of $P2_1/a$ measured at 295 K and those of tetracene with the $P1$ symmetry reported by Robertson [45, 46]. For additional calculations in this work, we used the X-ray diffraction data of the pentacene crystalline phase obtained by vapor deposition [47]. The crystalline phase has spacing for the ac planes [(001)d spacing] of 1.45 nm [47], and similar spacing has been reported in other experiments of the single crystals [48–50]. Recent theoretical studies [51, 52] showed that with the recent vdW-inclusive method, similar polymorph is more stable than the other experimentally reported polymorphs such as the bulk phase reported by Campbell et al. [53] and the thin film phases [54, 55]. The initial crystal structure of hexacene came from the diffraction data at 123 K of the crystalline phase fabricated with physical vapor transport method [56]. For the total energy calculation, we used the projector augmented-wave (PAW) method [57] as implemented in the Vienna ab initio simulation package (VASP) [58, 59]. The vdW-DF calculations were performed using the Román-Pérez-Soler algorithm [40] implemented by Klimeš et al. [39]. We used the revised vdW-DF2 (rev-vdW-DF2) [10], which uses the revised Becke's exchange functional [60] and the nonlocal correlation for the second version of vdW-DF [37].

We used the kinetic energy cutoff of 1000 eV to expand the wave functions in terms of a plane-wave basis set, along with hardest PAW potentials supplied with the VASP code [61]. The Brillouin zone integration was performed using a $4 \times 4 \times 4$ Monkhorst-Pack (MP) [62] **k**-point set for naphthalene and anthracene, a $4 \times 4 \times 2$ MP **k**-point set for tetracene. In the calculations of pentacene and hexacene in this work, we used a $4 \times 3 \times 2$ and $4 \times 4 \times 2$ **k**-point set, respectively. Cell parameters and internal degrees of freedom were optimized until the forces acting on atoms became smaller than the threshold value of 1.0×10^{-3} eV Å^{-1}. With this setting the cell parameters and lattice energy are estimated to converge within 0.039 Å, 0.49°, and 2.37 Å^3 and 1 meV, respectively. The lattice energy was calculated by subtracting the sum of the total energies of the constituent molecules from that of the molecular crystal.

We also investigated the effect of the zero-point vibrational energy (ZPE) to the equilibrium volume for selected crystals as follows. Starting from the equilibrium crystal structure, the cell volume was varied by ±2% up to ±10%, and at each volume, we performed the fixed volume structural optimization followed by the normal mode analysis at the Γ point to calculate the ZPE contribution to the total energy. We then calculated the total energy with ZPE and fitted it to the Murnaghan [63] equation of state to get the ZPE corrected equilibrium volume.

Table 4.1 displays the resulting lattice constants. Overall, the cell parameters and equilibrium volumes are in reasonable agreement with experimental values in the literature, which were measured at 5−296 K [47, 48, 50, 56, 66, 67]. They are also comparable to other vdW-inclusive methods such as vdW-DF-cx [35],

more elaborated ones such as Tkatchenko-Scheffler vdW correction (TS-vdW) [5], that with the many-body dispersion (MBD) [8], and the exchange-hole dipole moment model with B86b exchange (B86b-XDM) [69, 70]. As for comparison to experiments, the average absolute relative deviations from the experimental values [50, 66, 67] are 0.6% (length) and 0.7% (angle) for naphthalene, 0.5% (length) and 0.02% (angle) for anthracene, and 1.0% (length) and 0.3% (angle) for tetracene. Among the three oligoacene crystals, the maximum absolute relative deviation of the lattice constants of 1.93% was found for b of tetracene crystal, the experimental value of which was measured at 175 K [50].

For pentacene, the absolute relative error from the experimental value measured at 295.5 K [47] is 1.5% (length) and 0.9% (angle) on average, and the maximum absolute relative deviation from experiments is found for b (2.98%). However, if the calculated values are compared to the measurement of the same polymorph at 90 K [48], the maximum absolute relative deviation decreases to 1.07% (b), and the average absolute relative deviations are 0.6% and 0.5% for the cell length and cell angle, respectively. The calculated lattice constants and equilibrium volume are also in good agreement with those predicted with vdW-DF-cx for the same polymorph [52]. In the case of hexacene, the absolute relative deviation from experiments is found to be largest of all the oligoacene crystals, i.e., the averaged deviation of 3.8% and 1.0% for length and angle, respectively, and the maximum deviation of 6.15% is found for length b, in comparison to the experimental values measured at 123 K [56]. The deviation might be diminished if the theoretical result was compared to experiments measured at lower temperature, as demonstrated for pentacene. In addition to that, one should take into account the thermal expansion of the volume at finite temperature, i.e., the vibrational effect of the crystal.

The effect of ZPE to the equilibrium volume was investigated by the fixed volume structural optimization, followed by the normal mode analysis at the Γ point. The ZPE effect was taken into account, while the volume was incrementally varied. The resulting volume of naphthalene and anthracene was reasonably larger than that determined without including ZPE (see Table 4.1). Here, the phonon frequency was calculated by sampling only the Γ-point. The deviation from experiments might decrease if the phonon frequencies in the entire Brillouin zone were taken into account.

The theoretical lattice energies per molecule of the oligoacene crystals, slightly underestimated, are in reasonable agreement with experiments, with the absolute relative deviations (deviations) being 5.2% (0.044 eV) and 8.6% (0.087 eV) for naphthalene and anthracene, respectively. Notice that they are in good agreement with those at the level of RPA with single excitations [29]. Taking into account the calculated lattice energy of the tetracene crystal (-1.383 eV), along with the theoretical vibrational contribution to the sublimation enthalpy of organic crystals ($0.07-0.11$ eV) [64], we estimate the theoretical sublimation enthalpy would be in agreement with the experimental value (-1.409 eV) [68] within 0.14 eV.

Table 4.1 Optimized lattice parameters (a, b, c, α, β, and γ), equilibrium volume (V_0), and lattice energies per molecule (E_b) of the naphthalene and anthracene crystals in the $P2_1/a$ symmetry, tetracene in the $P1$ symmetry, and pentacene single crystal in the $P\bar{1}$ symmetry obtained with rev-vdW-DF2, along with experimental values. The Niggli cell parameters are used for tetracene. (Reprinted from [13], with the permission of AIP Publishing)

	Naphthalene							
	a	b	c	α	β	γ	V_0	E_b
	(Å)	(Å)	(Å)	(deg)	(deg)	(deg)	(Å^3)	(eV)
rev-vdW-DF2[1]	8.012	5.898	8.609	90.00	124.12	90.00	336.8	−0.803
rev-vdW-DF2 (ZPE)[2]	—	—	—	—	—	—	347.2	—
PBE+TS-vdW[3]	8.109	5.884	8.660	90.00	124.05	90.00	342.32	−1.035
PBE+MBD[3]	7.970	5.868	8.570	90.00	123.11	90.00	335.70	−0.905
PBE0+MBD[3]	—	—	—	—	—	—	—	−0.885
B86b-XDM[4]	8.134	5.938	8.699	90.00	124.35	90.00	346.89	−0.784
B86b-XDM[5]	—	—	—	—	—	—	335.8	−0.790
vdW-DF-cx[6]	8.06	5.91	8.75	90.00	124.4	90.00	344.4	−0.92
Expt.	8.080[7]	5.933[7]	8.632[7]	90.00	124.65[7]	90.00	340.4[7]	−0.847[8]
	Anthracene							
	a	b	c	α	β	γ	V_0	E_b
	(Å)	(Å)	(Å)	(deg)	(deg)	(deg)	(Å^3)	(eV)
rev-vdW-DF2[1]	8.339	5.948	11.087	90.00	125.37	90.00	448.40	−1.081
rev-vdW-DF2 (ZPE)[2]	—	—	—	—	—	—	460.8	—
PBE+TS-vdW[3]	8.399	5.943	11.120	90.00	125.21	90.00	453.5	−1.392
PBE+MBD[3]	—	—	—	—	—	—	—	−1.262
PBE0+MBD[3]	—	—	—	—	—	—	—	−1.234
B86b-XDM[4]	8.452	5.985	11.168	90.00	125.43	90.00	460.32	−1.049
B86b-XDM[5]	—	—	—	—	—	—	448.4	−1.054
vdW-DF-cx[6]	8.38	5.96	11.23	90.00	125.6	90.00	456.5	−1.23
Expt.	8.37[9]	6.00[9]	11.12[9]	90.00	125.4[9]	90.00	455.205[9]	−1.168[8]

	Tetracene							
	a	b	c	α	β	γ	V_0	E_b
	(Å)	(Å)	(Å)	(deg)	(deg)	(deg)	(Å^3)	(eV)
rev-vdW-DF2[1]	6.019	7.686	12.489	100.83	99.62	94.36	556.00	−1.383
vdW-DF-cx[6]	6.05	7.69	12.53	100.2	100.1	94.5	561.3	−1.56
PBE+TS-vdW[6]	6.05	7.71	12.53	100.7	99.2	94.3	564.1	—
Expt.	6.0565[10]	7.8376[10]	12.5523[10]	101.2749[10]	99.4529[10]	94.2080[10]	572.968[10]	−1.409[11]
	Pentacene							
	a	b	c	α	β	γ	V_0	E_b
	(Å)	(Å)	(Å)	(deg)	(deg)	(deg)	(Å^3)	(eV)
rev-vdW-DF2[1]	6.268	7.554	14.297	77.51	88.46	84.21	657.56	−1.70
vdW-DF-cx[6]	6.29	7.52	14.35	77.8	88.7	84.1	660.3	−1.92
Expt.[12]	6.265	7.786	14.511	76.65	87.50	84.61	685.49	—
Expt.[13]	6.239	7.636	14.330	76.978	88.136	84.415	661.94	—

(continued)

Table 4.1 (continued)

	Hexacene							
	a	b	c	α	β	γ	V_0	E_b
	(Å)	(Å)	(Å)	(deg)	(deg)	(deg)	(Å^3)	(eV)
rev-vdW-DF2[1]	6.512	7.223	16.140	96.60	91.42	96.42	748.91	−2.02
vdW-DF-cx[6]	6.61	7.05	16.14	95.8	91.5	96.8	743.3	−2.30
Expt.[14]	6.306	7.697	16.480	98.77	91.25	95.81	785.92	—

[1]This work. ZPE is not taken into account
[2]This work. ZPE is included
[3]Ref. [64]
[4]Ref. [7] Lattice energy with ZPE
[5]Ref. [65]
[6]Ref. [52]
[7]Ref. [66] (5 K)
[8]Ref. [64] Experimental sublimation enthalpy with the theoretical ZPE subtracted.
[9]Ref. [67] (16 K)
[10]Ref. [50] (175 K)
[11]Ref. [68] Experimental sublimation enthalpy
[12]Ref. [47] (295.5 K)
[13]Ref. [48] (90 K)
[14]Ref. [56] (123 K)

4.2.1.2 Electronic Structures with the *GW* Approximation

To confirm reliability of the theoretical crystal geometries of the oligoacenes predicted with the vdW-DF method, we investigated the electronic structures for the optimized crystal geometries using the many-body perturbation theory within the *GW* approximation [13]. Here, we considered naphthalene, anthracene, tetracene, and pentacene crystals, of which the experimental fundamental gap or the density of states (DOS) were reported [71–81].

The quasiparticle energy in solids within the *GW* approximation is calculated with [18]

$$E_{n\mathbf{k}}^{\mathrm{qp}} = \epsilon_{n\mathbf{k}}^{\mathrm{DFT}} - \langle \phi_{n\mathbf{k}}^{\mathrm{DFT}} | V_{xc}^{\mathrm{DFT}} | \phi_{n\mathbf{k}}^{\mathrm{DFT}} \rangle + \langle \phi_{n\mathbf{k}}^{\mathrm{DFT}} | \Sigma(E_{n\mathbf{k}}^{\mathrm{qp}}) | \phi_{n\mathbf{k}}^{\mathrm{DFT}} \rangle \,, \tag{4.1}$$

where $\epsilon_{n\mathbf{k}}^{\mathrm{DFT}}$ and $\phi_{n\mathbf{k}}^{\mathrm{DFT}}$ are starting eigenvalues and wave functions, respectively (in general DFT-LDA or DFT-GGA), i.e., a starting mean-field approximation which is to be perturbed by the many-body effect. $\mathrm{V}_{xc}^{\mathrm{DFT}}$ is the corresponding exchange-correlation potential of the mean field, and the self-energy operator $\Sigma(E_{n\mathbf{k}}^{\mathrm{qp}})$ describes all the ingredients of the many-body effect. The self-energy operator, formally obtained as expansion of the self-energy in the Hedin equation to first-order in the screened Coulomb potential W [12], results in formulations computed on numerical grids. For instance, in the *GW* space-time formalism, the self-energy operator is calculated in real space ($\mathbf{r}, \mathbf{r}\prime$) and imaginary time ($i\tau$) [82–84],

$$\Sigma(\mathbf{r}, \mathbf{r}'; i\tau) = iG(\mathbf{r}, \mathbf{r}'; i\tau)W(\mathbf{r}, \mathbf{r}'; i\tau), \tag{4.2}$$

and its diagonal matrix elements are computed, followed by the analytic continuation of the matrix elements to the real frequency axis [82, 83]. G $(\mathbf{r}, \mathbf{r}'; i\tau)$ is the noninteracting Green's function in real space and in imaginary time for propagation of the hole ($\tau > 0$) and the electron ($\tau < 0$), respectively,

$$G(\mathbf{r}, \mathbf{r}'; i\tau) = \begin{cases} i\Sigma_{n\mathbf{k}}^{occ} \phi_{n\mathbf{k}}(\mathbf{r}) \phi_{n\mathbf{k}}^*(\mathbf{r}') \exp(\epsilon_{n\mathbf{k}}\tau) & (\tau > 0), \\ -i\Sigma_{n\mathbf{k}}^{unocc} \phi_{n\mathbf{k}}(\mathbf{r}) \phi_{n\mathbf{k}}^*(\mathbf{r}') \exp(\epsilon_{n\mathbf{k}}\tau) & (\tau < 0), \end{cases} \tag{4.3}$$

constructed from the Kohn-Sham eigenfunctions and eigenvalues, and $\mathbf{k}$ vectors denote those in the first Brillouin zone. The irreducible polarization P within the random-phase approximation is calculated in real space and imaginary time,

$$P(\mathbf{r}, \mathbf{r}'; i\tau) = -2iG(\mathbf{r}, \mathbf{r}'; i\tau)G(\mathbf{r}', \mathbf{r}; -i\tau), \tag{4.4}$$

which is Fourier transformed to $P_{\mathbf{GG}'}(\mathbf{k}; i\omega)$ in reciprocal space. The symmetrized dielectric matrix in reciprocal space $\tilde{\epsilon}_{\mathbf{GG}'}(\mathbf{k}; i\omega)$ is constructed as

$$\tilde{\epsilon}_{\mathbf{GG}'}(\mathbf{k}; i\omega) = \delta_{\mathbf{GG}'} - \frac{4\pi}{|\mathbf{k}+\mathbf{G}||\mathbf{k}+\mathbf{G}'|} P_{\mathbf{GG}'}(\mathbf{k}; i\omega). \tag{4.5}$$

Then, $W(\mathbf{r}, \mathbf{r}'; i\tau)$ is obtained by Fourier transforming to real space and imaginary time the screened Coulomb potential in reciprocal space and imaginary frequency,

$$W_{\mathbf{GG}'}(\mathbf{k}; i\omega) = \frac{4\pi}{|\mathbf{k}+\mathbf{G}||\mathbf{k}+\mathbf{G}'|} \tilde{\epsilon}^{-1}_{\mathbf{GG}'}(\mathbf{k}; i\omega). \tag{4.6}$$

The quantities defined in Eqs. 4.1, 4.2, 4.3, and 4.6 are, practically, calculated only once with the starting eigenvalues and wave functions, i.e., one-shot G_0W_0 calculations.

We performed the electronic structure calculations using the modified version of the GW space-time code [82–84], which enables highly parallelized calculations with thousands of CPU cores. Our perturbative G_0W_0 calculations were based on the norm-conserving pseudopotentials [85] and plane-wave basis set, and the starting wave functions were generated with the Perdew-Burke-Ernzerhof (PBE) [86] functional using the STATE code [87]. To calculate the correlation part of the GW self-energy, we evaluated the full frequency dependence of the dielectric function numerically, and the use of the plasmon-pole model is avoided. On the imaginary frequency/time axis, polarizability, dielectric function, screened Coulomb potential, and self-energy have smoothly decaying tails, which are fitted to simple model functions. The remaining energy/time region around zero is treated numerically. The matrix elements of the correlation self-energy on the imaginary time axis are fitted to a model function, followed by the fast Fourier transform to those on the imaginary frequency axis. Then, they are analytically continued onto the real energy axis [83].

In addition to the G_0W_0 calculation based on the PBE wave functions, we performed the eigenvalue-only self-consistent GW calculations (evGW) [88, 89], to check the starting point dependence [90–95] of the G_0W_0 calculations. In the evGW calculations, we considered only the diagonal part of the self-energy, and only the eigenvalues were updated in constructing the Green's function and the screened Coulomb potential, while we retained the wave functions unchanged (see Eqs. 4.2, 4.3, 4.4, 4.5, and 4.6), assuming that the starting DFT wave functions are close to the true quasiparticle wave functions [18, 96]. We updated the quasiparticle energies of up to the second lowest unoccupied band. To avoid explicitly calculating the quasiparticle energies of the bands whose number exceeds 1000 (see the number of empty states used in the calculation of the Green's function Eq. 4.3, as mentioned below) while retaining the accuracy of the calculated band energies around the conduction band edge, the energies of the higher bands outside the preset energy window were corrected by a scissors-like operation, that is, they were shifted rigidly by $\Delta = E_{m\mathbf{k}} - \varepsilon^{\mathrm{DFT}}_{m\mathbf{k}}$, where $E_{m\mathbf{k}}$, $\varepsilon^{\mathrm{DFT}}_{m\mathbf{k}}$ are, respectively, the quasiparticle energy and the DFT eigenvalue in the highest band m in the preset energy window. Here,

we chose second lowest unoccupied band. We found that five or six iterations were necessary to converge the fundamental gap within 0.01 eV.

For the GW calculations, we transformed the lattice vectors to employ the symmetry points and lines in the Brillouin zone defined in Ref. [97]. We used a $4 \times 3 \times 2$ (naphthalene, anthracene, and pentacene) or a $3 \times 2 \times 4$ (tetracene) Γ-centered **k**-point set, corresponding to the **k**-space mesh sizes of 0.19–0.43 $Å^{-1}$. For naphthalene, anthracene, and tetracene crystal, plane-wave cutoffs of 60 Ry and 24 Ry for the wave function and the dielectric matrix, respectively, were used [13]. For pentacene, we employed plane-wave cutoff of 40 Ry throughout the calculation, that is, for both the wave function and the dielectric matrix. We have found that the convergence of the calculated band gap or band width for the new set of cutoff is similar to that of the cutoff used in Ref. [13]. The number of empty states used in the calculation of the Green's function was 6006 (naphthalene), 5372 (anthracene), 6584 (tetracene), and 5200 (pentacene) bands, which encompass more than 240 eV above the center of the band gap. The convergence of the calculated band gap (band width) with respect to the number of empty states, **k**-point sampling, and plane-wave cutoff is estimated to be within 0.05 (0.01) eV.

Table 4.2 displays the calculated fundamental gap of oligoacene crystals within rev-vdW-DF2 and GW approximations. Figures 4.2a, 4.3a, 4.4a, and 4.5a show the calculated dispersions of the highest occupied (HOMO) and lowest unoccupied molecular orbital (LUMO)-derived bands of the oligoacene single crystals within GW. Because of the self-energy correction, the fundamental gap obtained with the one-shot GW (G_0W_0) was larger than the DFT values by 1.1–1.8 eV. The valence and conduction band widths became larger by the G_0W_0 self-energy correction by 0.05–0.15 eV and 0.04–0.12 eV, respectively [13]. The appreciable increase in band

Table 4.2 Calculated fundamental band gap (E_g) and band width for the HOMO-derived band (W_H) and that for the LUMO-derived band (W_L) of the oligoacene crystals obtained with rev-vdW-DF2 and GW based on the rev-vdW-DF2 optimized structures. The band gap average over the **k**-points in the Brillouin zone is shown in the parenthesis. The unit is eV. (Reprinted from [13], with the permission of AIP Publishing)

	Naphthalene	Anthracene	Tetracene	Pentacene
E_g(rev-vdW-DF2)	2.97	1.89	1.08	1.03
$E_g(G_0W_0)$	4.72 (5.01)	3.37 (3.67)	2.40 (2.75)	2.09 (2.38)
E_g(evGW)	5.70	4.17	3.09	2.68
E_g(Exp.[1])	5.0–5.5	3.9–4.2	2.9–3.4	2.2–2.4
W_H(rev-vdW-DF2)	0.44	0.40	0.44	0.74
$W_H(G_0W_0)$	0.51	0.46	0.49	0.89
W_H(evGW)	0.56	0.50	0.54	0.96
W_L(rev-vdW-DF2)	0.35	0.63	0.65	0.70
$W_L(G_0W_0)$	0.39	0.75	0.73	0.82
W_L(evGW)	0.41	0.78	0.75	0.86

[1] Refs. [71–80]

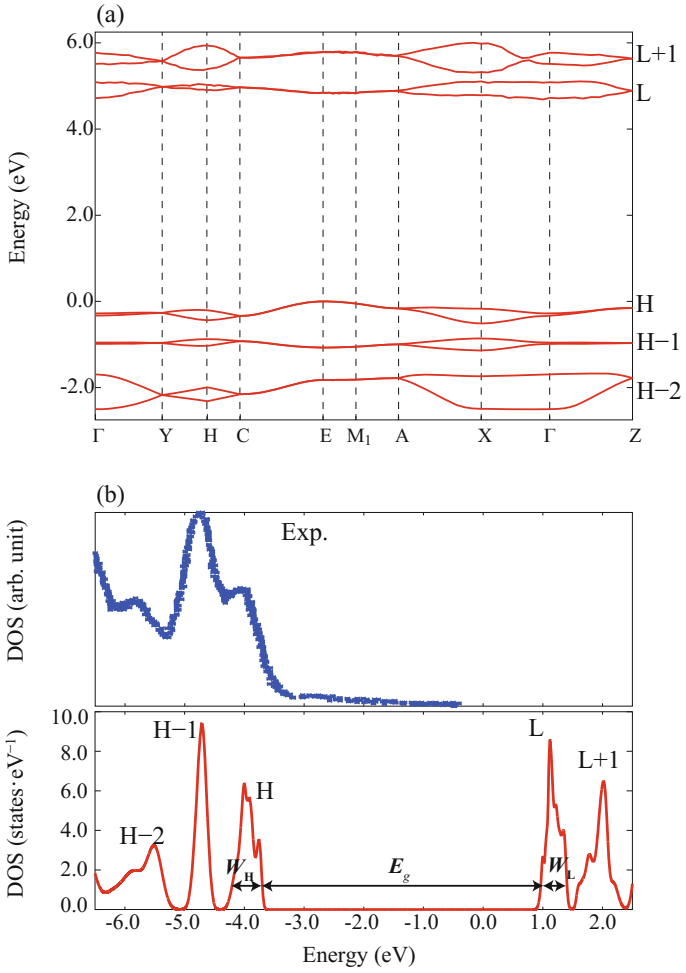

Fig. 4.2 (**a**) The band structure of the naphthalene crystal calculated within the G_0W_0 approximation. The energy zero is set to the top of the highest occupied band. The atomic configurations and the lattice constants are optimized with the rev-vdW-DF2 functional (Table 4.1). We transformed the lattice parameters to adopt the symmetry points and lines in the Brillouin zone defined in Ref. [97], to obtain a' =5.898 Å, b' =7.806 Å, c' =8.012 Å, α' =65.93°, and $\beta' = \gamma'$ =90.0°. The high-symmetry points in the BZ are Γ (0,0,0), Y(0,0,0.5), H(0, 0.361, 0.651), C(0, 0.5, 0.5), E(0.5, 0.5, 0.5), M_1(0.5, 0.639, 0.349), A(0.5, 0.5, 0), X(0, 0.5, 0), Z(0.5, 0, 0) in the unit of the basic reciprocal lattice vectors. (**b**) The density of states (DOS) based on the G_0W_0 band structure. The Gaussian broadening is set to the imaginary part of the self-energy obtained with the G_0W_0 calculation. The symbols such as H, H−1, L, and L+1 denote the molecular orbitals of the constituent molecules such as HOMO, next HOMO, LUMO, and the next LUMO, respectively, which forms the bands. For comparison, the experimental photoemission data (Ref. [81]) is displayed in the upper panel. The theoretical highest peak of the valence band maximum is aligned with that of the experimental photoemission peak by a rigid shift of the band energies. The band widths (W_H and W_L) and band gap (E_g) are indicated by the double-headed arrows for guides to the eyes. (Reprinted from [13], with the permission of AIP Publishing)

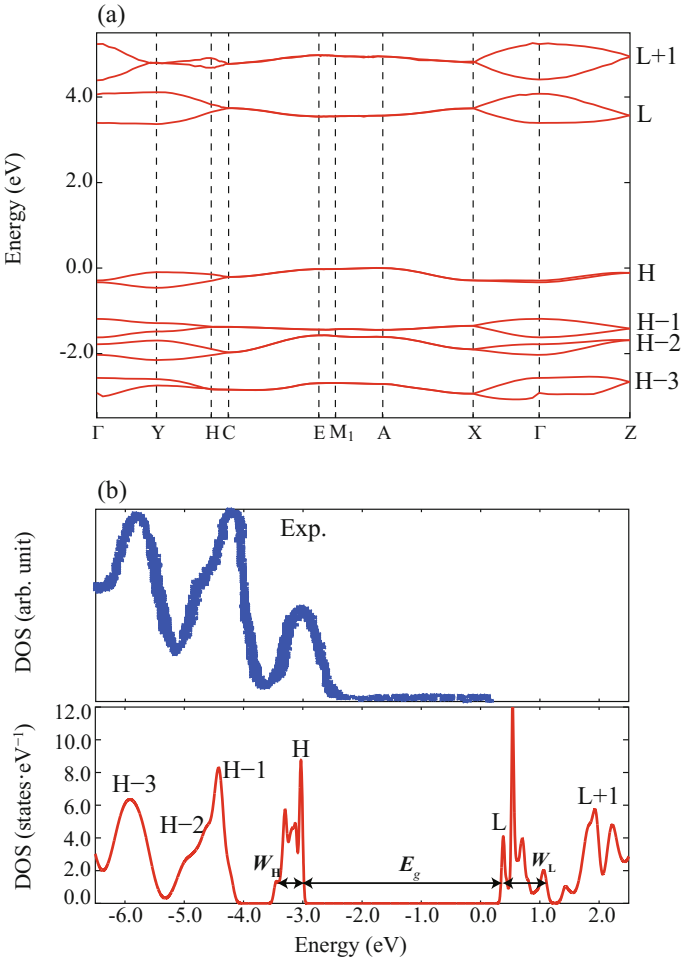

Fig. 4.3 (**a**) The band structure of the anthracene crystal calculated within the G_0W_0 approximation. The energy zero is set to the top of the highest occupied band. The atomic configurations and the lattice constants are optimized with the rev-vdW-DF2 functional (Table 4.1). We transformed the lattice parameters to adopt the symmetry points and lines in the Brillouin zone defined in Ref. [97], to obtain a' =5.948 Å, b' =8.339 Å, c' =9.242 Å, α' =78.00°, and $\beta' = \gamma'$ =90.0°. The high-symmetry points in the BZ are: Γ(0,0,0), Y(0,0, 0.5), H(0, 0.425, 0.598), C(0, 0.5, 0.5), E(0.5, 0.5, 0.5), M_1(0.5, 0.575, 0.402), A(0.5, 0.5, 0), X(0, 0.5, 0), Z(0.5, 0, 0) in the unit of the basic reciprocal lattice vectors. (**b**) The density of states (DOS) based on the G_0W_0 band structure. The experimental photoemission data (Ref. [81]) is displayed. The convention is the same as that in Fig. 4.2. The band widths (W_H and W_L) and band gap (E_g) are indicated by the double-headed arrows for guides to the eyes. (Reprinted from [13], with the permission of AIP Publishing)

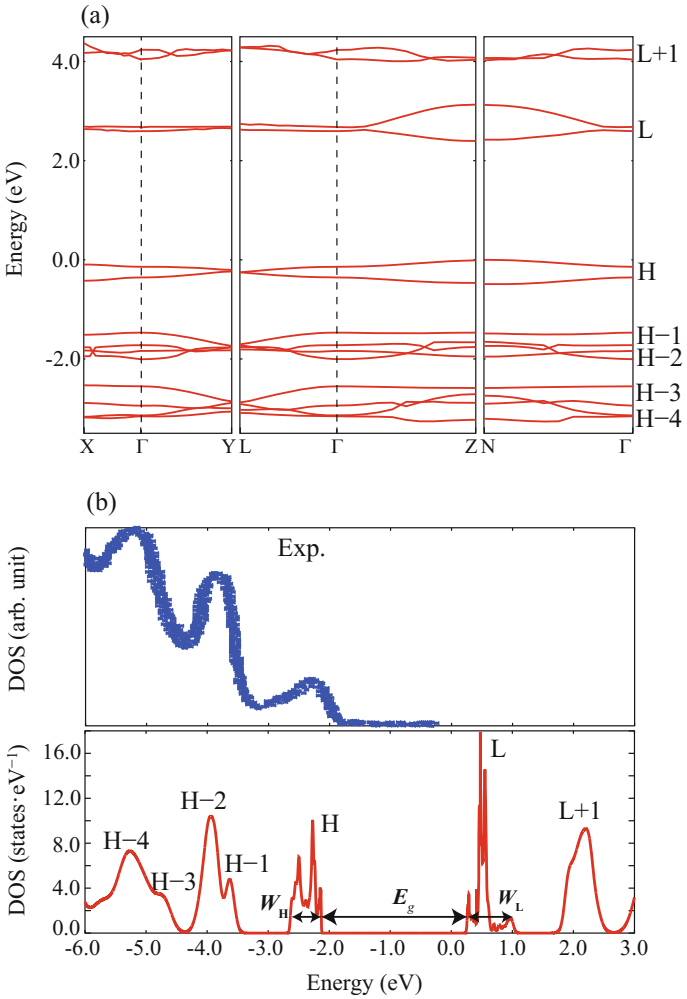

Fig. 4.4 (**a**) The band structure of the tetracene crystal calculated within the G_0W_0 approximation. The energy zero is set at the top of the highest occupied band. The atomic configurations and the lattice constants are optimized with the rev-vdW-DF2 functional (Table 4.1). We transformed the lattice parameters to adopt the symmetry points and lines in the Brillouin zone defined in Ref. [97], to obtain a' =7.686 Å, b' =12.489 Å, c' =6.019 Å, α' =99.62°, β' =94.36°, γ' =100.83°. The high-symmetry points in the BZ are X(0.5, 0, 0), Γ(0,0,0), Y(0, 0.5, 0), L(0.5, 0.5, 0), Z(0, 0, 0.5), N(0.5, 0, 0.5), M(0, 0.5, 0.5), R(0.5, 0.5, 0.5) in the unit of the basic reciprocal lattice vectors. (**b**) The density of states (DOS) based on the G_0W_0 band structure. The experimental photoemission data (Ref. [81]) is displayed. The convention is the same as that in Fig. 4.2. The band widths (W_H and W_L) and band gap (E_g) are indicated by the double-headed arrows for guides to the eyes. (Reprinted from [13], with the permission of AIP Publishing)

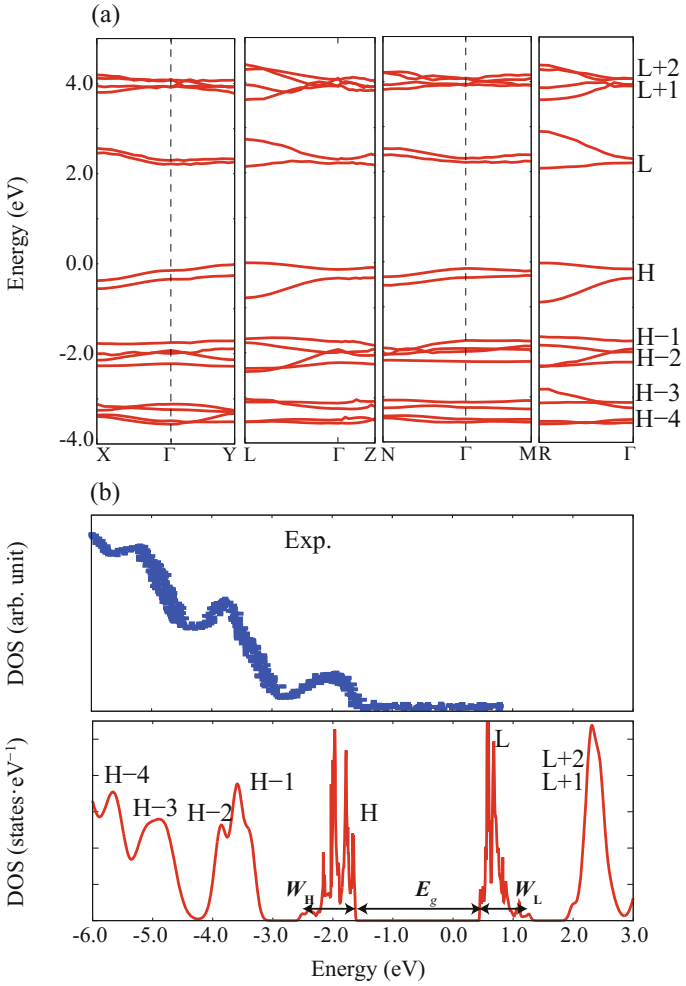

Fig. 4.5 (**a**) The band structure of the pentacene crystal calculated within the G_0W_0 approximation. The energy zero is set at the top of the highest occupied band. The atomic configurations and the lattice constants are optimized with the rev-vdW-DF2 functional (Table 4.1). The lattice parameters to adopt the symmetry points and lines in the Brillouin zone defined in Ref. [97] are the same as those in Table 4.1. The high-symmetry points in the BZ are X(0.5, 0, 0), Γ(0,0,0), Y(0, 0.5, 0), L(0.5, 0.5, 0), Z(0, 0, 0.5), N(0.5, 0, 0.5), M(0, 0.5, 0.5), R(0.5, 0.5, 0.5) in the unit of the basic reciprocal lattice vectors. (**b**) The density of states (DOS) based on the G_0W_0 band structure. The experimental photoemission data (Ref. [81]) is displayed. The convention is the same as that in Fig. 4.2. The band widths (W_H and W_L) and band gap (E_g) are indicated by the double-headed arrows for guides to the eyes

width suggests distribution of the electronic charge density at the intermolecular site, as indicated in Refs. [98–100].

Compared to the fundamental gap estimated with the experimental technique such as photoconductivity, optical absorption, and inverse photoemission measurements [71–80], the theoretical band gap within G_0W_0 is underestimated. The band gap averaged over the **k**-points in the Brillouin zone was also slightly underestimated, which is in line with Ref. [52]. To remove the starting point dependence of the G_0W_0 calculation [90–95], we took partially into account the effect of self-consistency within the eigenvalue-only self-consistent GW (evGW) treatment [88, 89]. As a result, the fundamental gap becomes slightly overestimated, becoming closer to experiments (see Table 4.2) [13]. For pentacene, the gap is in agreement with the recent experimental value measured with the low-energy inverse photoemission spectroscopy (LEIPS) [80]. The band widths slightly increased by the evGW calculation by at most 0.07 eV, independently of the **k**-point.

Figures 4.2b, 4.3b, 4.4b, and 4.5b display the calculated density of states (DOS) in comparison to the experimental photoemission measurement, in which the substrate temperature was kept at 150 K [81]. We calculated the DOS with the Gaussian smearing with the width set to the imaginary part of the self-energy obtained with the G_0W_0 calculation, rather than a uniform broadening. The width or the satellite peak structure of photoemission spectra is, in principle, the imaginary part of the self-energy, i.e., spectral function. Notice that according to Ref. [101], the structures of the organic thin films are similar to those of the single crystal investigated in this study, implying that comparison of the theoretical electronic structures of bulk organic crystals with the experimental photoemission spectra of organic thin films is meaningful. The calculated peak positions of the valence bands derived from HOMO, the next HOMO, the second next HOMO, and so forth, of the constituent molecule, are in agreement with the experimental photoemission spectra of the thin films on Ag(111) [81]. Some shoulder structures are found in the vicinity of the valence band, for instance, H-1 and H-3 DOS peaks in tetracene, which are not resolved in the experimental photoemission spectra. Although there is agreement found between the theoretical DOS and the experiment, factors affecting the experimental photoemission spectra of organic semiconductors such as broadening by temperature effects, instrumental resolution, and other factors causing structural disorder [102] should be taken into account. The incomplete charge screening at the surface was taken into account, when the G_0W_0 DOS of oligoacenes were compared with the experimental data [52]. Furthermore, it was proposed that the electron-phonon coupling and structural disorder should be taken into account to describe the electronic structure of organic semiconductors at finite temperature [103].

As far as the DOS of the unoccupied states are concerned, the inverse photoemission data of 2–3 monolayers of the oligoacenes on Ag(111) were reported [104]. The measured energy difference between the lowest and the second lowest unoccupied π^*-derived peaks was 0.8, 1.1, and 1.7 eV for naphthalene, anthracene, and tetracene, respectively [104]. The theoretical energy difference between the corresponding DOS peaks with G_0W_0 were 0.90, 1.39, and 1.73 eV, respectively, in fair agreement with the experiment.

4.2.1.3 Effects of the Crystal Geometry and the Molecular Configuration

Here, we investigated the impact of the different crystal structures on the electronic structure. For tetracene, theoretical DOS was obtained for the three crystal structures with different lattice constants (Table 4.3). Figure 4.6 displays the theoretical DOS of HOMO- and LUMO-derived bands for the different lattice constants. The calculated band gap and the band widths are summarized in Table 4.4. The experimental crystal geometry determined by the X-ray diffraction measurement [45, 46] and more recent diffraction data measured at 175 K [50] were used. We optimized their internal degrees of freedom with rev-vdW-DF2, while we fixed the

Table 4.3 Lattice constants of the tetracene crystals (Structures I–III) investigated. Structure III corresponds to the fully optimized crystal geometry, whose lattice constants were transformed, as described in the caption of Fig. 4.4. (Reprinted from [13], with the permission of AIP Publishing)

	a(Å)	b(Å)	c(Å)	α(°)	β(°)	γ(°)
Structure I[1]	7.980	12.747	6.140	100.44	92.5	101.92
Structure II[2]	7.837	12.552	6.056	99.45	94.20	101.27
Structure III[3]	7.686	12.489	6.019	99.62	94.36	100.83

[1]Ref. [45, 46, 53]. X-ray diffraction data whose temperature is presumed to be room temperature or higher
[2]Ref. [50]. X-ray diffraction data measured at 175 K
[3]This work

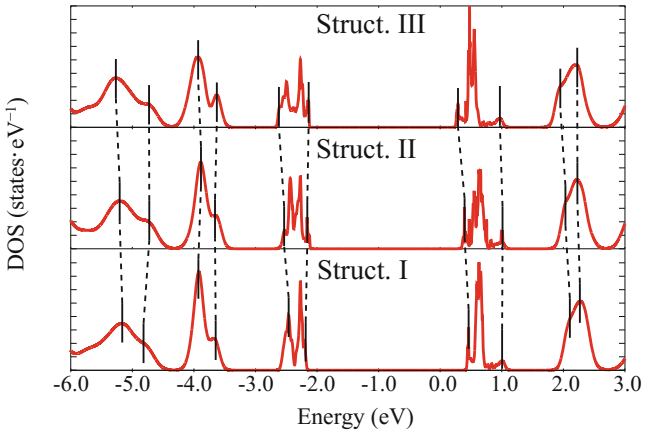

Fig. 4.6 The G_0W_0 densities of states (DOS) of tetracene obtained using different geometries. Structures I and II correspond to those obtained by the X-ray diffraction measurements (Refs. [45] and [50], respectively), where the internal atomic configurations were optimized with rev-vdW-DF2. Structure III was the fully optimized rev-vdW-DF2 structure reported in Table 4.1. The theoretical highest peaks of the valence band maximum in Structures I and II are aligned with that in Structure III. For the ease of comparison, we draw the solid vertical lines for the main peaks in the G_0W_0 DOS, and the states derived from similar molecular orbitals are connected by dashed lines. (Reprinted from [13], with the permission of AIP Publishing)

Table 4.4 Calculated band gap (E_g) and the band width for the HOMO-derived band (W_{H}) and that for the LUMO-derived band (W_{L}) of the tetracene crystal obtained with G_0W_0 and evGW for different structures. I and II denote the structures obtained by the X-ray diffraction experiment in Refs. [45] and [50], respectively, and their internal atomic coordinates were relaxed with their lattice constants fixed. Structure III denotes the one obtained by fully optimizing the cell and internal degrees of freedom, corresponding to the crystal geometry displayed in Table 4.1. E'_g is the molecular fundamental gap plus the polarization effect (see the main text). Unit is eV. (Reprinted from [13], with the permission of AIP Publishing)

Structure	I	II	III
$E_g(G_0W_0)$	2.63	2.50	2.40
$E_g(\mathrm{ev}GW)$	3.31	3.19	3.09
$W_{\mathrm{H}}(G_0W_0)$	0.39	0.45	0.49
$W_{\mathrm{H}}(\mathrm{ev}GW)$	0.44	0.48	0.54
$W_{\mathrm{L}}(G_0W_0)$	0.60	0.66	0.73
$W_{\mathrm{L}}(\mathrm{ev}GW)$	0.64	0.71	0.75
$E'_g(G_0W_0)$	3.12	3.06	3.01
$E'_g(\mathrm{ev}GW)$	3.85	3.79	3.74

lattice constants displayed in Table 4.3. We denote their structures by Structures I and II, for the former and the latter, respectively, and the structure fully optimized with rev-vdW-DF2 is denoted by Structure III.

It is found that the decrease in equilibrium volume from Structure I to III causes the band width to increase: The band width for the HOMO-derived band increases from 0.39 eV for Structure I (598.9 Å^3) to 0.49 eV for Structure III (556.0 Å^3). This is because the overlap between HOMOs of the neighboring molecular sites increases as the cell volume decreases. The result is similar to the change in the theoretical band widths, depending on the lattice constants of a variety of the experimental crystal structures of the organic semiconductors [105].

The fundamental gap also depends on the equilibrium volume. Table 4.4 shows that the band gap is narrowed as the volume decreases from Structure I to III. This is because of the dielectric screening stabilizing the electron or the hole injected into the bulk, which is induced by the surrounding polarization clouds. There is similar trend found in the result obtained at the evGW level of theory, in which the band energies are shifted almost independently of the **k**-points. The different polarization effect could be shown by the fundamental gap plus the polarization effect [80]. That was estimated by adding the halves of the band widths to the fundamental gap: $E'_g = E_g + (W_{\mathrm{H}} + W_{\mathrm{L}})/2$, to remove the effect of the change in the band width. As shown in Table 4.4, the calculated E'_g reasonably decreases as the cell volume increases.

To gain more insights into the effects of the molecular configuration on the electronic structure, we examined the electronic structures in terms of the interaction between the orbitals centered at the molecular sites. We obtained the maximally localized Wannier functions (MLWF) [14, 15] based on the PBE wave function for Structures I–III. We calculated the nearest-neighbor transfer integrals between the HOMOs or between the LUMOs arranged along the unit cell vectors ($t_{\mathrm{a1}} - t_{\mathrm{c1}}$ and

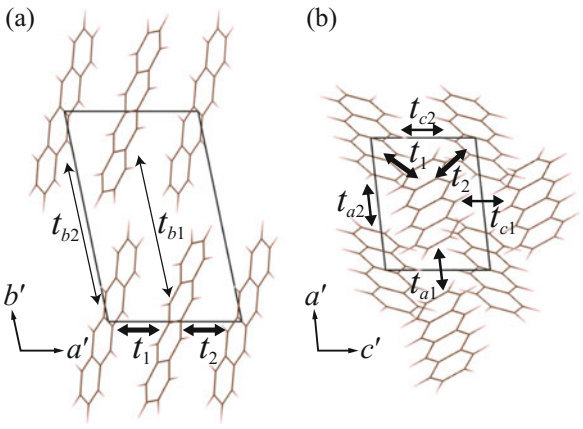

Fig. 4.7 Schematic views of the transfer integral between molecules projected on (**a**) $a'b'$ plane and (**b**) $a'c'$ plane. Conventional unit cell is shown. The unit cell vectors are the same as those defined in Fig. 4.4. (Reprinted from [13], with the permission of AIP Publishing)

$t_{a2} - t_{c2}$) and those along the diagonal directions between the two nonequivalent herringbone-stacked molecules in the cell (t_1 and t_2), which are depicted in Figs. 4.7 and 4.8. In Table 4.5, the transfer integrals for Structures I–III are shown, along with the HOMO- and the LUMO-derived band width determined with the tight-binding approximation. The tight-binding band structure for Structures I–III based on the calculated transfer integrals is displayed in Fig. 4.9.

It is found that the tight-binding band structure is in fair agreement with the first-principles band structure obtained with DFT-PBE. The result is in line with the previous works of oligoacene crystals [106–108]. The transfer integrals along the diagonal paths between the two nonequivalent molecules in the cell (t_1 and t_2) are largest in amplitude, crucially determining the band widths. The magnitudes of t_1 and t_2 for HOMO and LUMO and thus the band width increase from Structures I to III.

The isosurfaces of the MLWF for the two HOMOs and the two LUMOs of the two nonequivalent molecules in the unit cell are displayed in Fig. 4.8. The transfer integral t_1 for HOMO is dominated by the closest antibonding contribution to the interaction between the two HOMOs, resulting in largely positive values (see Table 4.5). On the other hand, t_2 for HOMO is negative, which originates from the closest in-phase bonding interaction. The distance between the molecules is an important factor dominating the transfer integrals and thus the HOMO-derived band widths. Actually, Structure III, with the smallest cell volume, displays the largest band width. In case of the LUMO band, the situations are similar.

However, with their nodal structures as shown in Fig. 4.8, there are competing bonding and antibonding contributions to the transfer integrals. Depending on the intermolecular distance or the molecular orientation angle, the signs of the transfer integrals can switch. The signs of t_1 and t_2 for HOMO switch even when the experimental crystal structures reported in Refs. [45] and [50] are, respectively, relaxed into Structures I and II, with only a minor change in the intermolecular distance or the molecular orientation angle [13]. We also found that the signs of

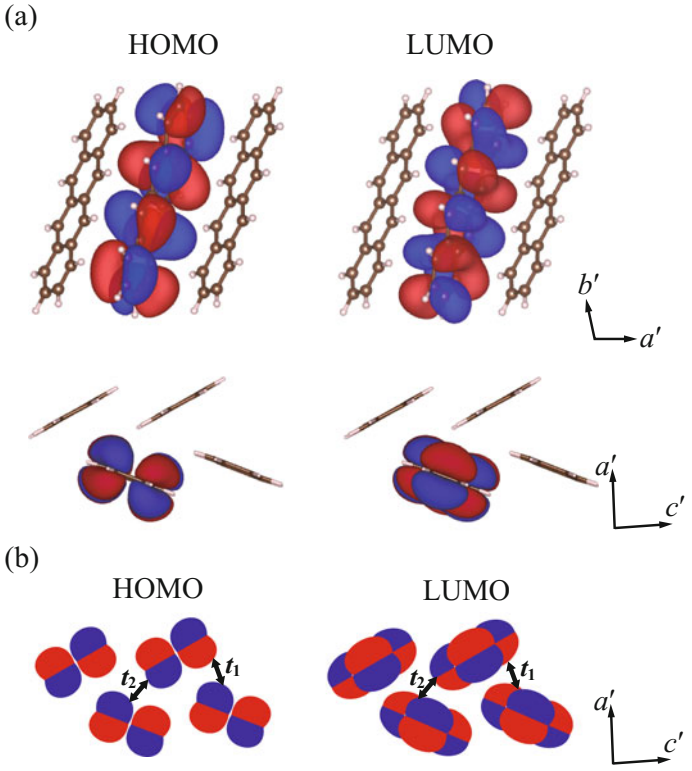

Fig. 4.8 (**a**) Isosurfaces of the maximally localized Wannier functions (MLWFs) corresponding to the HOMO and the LUMO located at one of the two nonequivalent molecules in the unit cell. Different colors (*brightness*) indicate signs of the orbitals. Views from the shortest cell vector c' (*upper*) and those from the longer molecular axis (*lower*) are shown. (**b**) Schematics of the transfer integrals t_1 and t_2 between the MLWFs of the HOMO (*left*) or the LUMO (*right*). The lattice vectors are the same as those defined in Fig. 4.4. (Reprinted from [13], with the permission of AIP Publishing)

the transfer integrals depend on the approximations in the first-principles DFT calculations (PBE or rev-vdW-DF2, in this case). The role of the molecular displacement along the slip direction determining the transfer integral was discussed [109]. In classifying the sign of the transfer integral between the herringbone-like arranged molecules of the pentacene polymorphs, the distance of the molecular slip stepping over the nodes of the molecular orbitals was taken into account [108]. In the present case, the switch of the signs of the transfer integrals t_1 and t_2 does not affect the band structure within the tight-binding approximation [13, 106–108]. Nevertheless, in general, a subtle interplay between the molecular configurations such as distance and angle, and their displacement, and, therefore, the accurate determination of the crystal geometry of organic crystals is crucial for predicting the electronic structure precisely.

Table 4.5 Calculated nearest-neighbor transfer integrals for the HOMO and those for the LUMO of the tetracene crystal obtained with the maximally localized Wannier functions [14, 15] based on the DFT-PBE orbitals. t_{c1} and t_{c2} correspond to the transfer integrals along the shortest unit cell vector, t_{a1} and t_{a2} to those along the second shortest unit cell vector, and t_1 and t_2 to those between the two nonequivalent tetracene molecules as depicted in Figs. 4.7 and 4.8 (t_{b1} and t_{b2} along the longest cell vector are found to be essentially zero). $W_{\mathrm{H}}^{\mathrm{TB}}$ ($W_{\mathrm{L}}^{\mathrm{TB}}$) and $W_{\mathrm{H}}^{\mathrm{PBE}}$ ($W_{\mathrm{L}}^{\mathrm{PBE}}$) denote the HOMO (LUMO)-derived band width within the tight-binding approximation and the first-principles calculation with DFT-PBE, respectively. I and II denote the structures obtained by the X-ray diffraction experiment in Refs. [45] and [50], respectively, and their internal atomic coordinates were relaxed with their lattice constants fixed. Structure III denotes the one obtained by full optimization of the cell and internal degrees of freedom, corresponding to the crystal geometry displayed in Table 4.1. Unit is meV. (Reprinted from [13], with the permission of AIP Publishing)

Structure	I	II	III
	HOMO		
t_{c1}	12.39	11.37	12.15
t_{c2}	−4.72	−6.95	−6.48
t_{a1}	−2.74	−4.33	−5.19
t_{a2}	−2.23	−3.08	−3.22
t_1	16.56	20.45	22.79
t_2	−60.43	−66.54	−78.39
$W_{\mathrm{H}}^{\mathrm{TB}}$	313.35	355.34	411.43
$W_{\mathrm{H}}^{\mathrm{PBE}}$	322.17	370.68	417.33
	LUMO		
t_{c1}	−31.01	−31.10	−33.04
t_{c2}	−11.13	−10.76	−12.10
t_{a1}	−1.55	−1.74	−2.09
t_{a2}	−3.43	−4.09	−4.74
t_1	68.44	73.62	81.07
t_2	−57.38	−67.96	−78.02
$W_{\mathrm{L}}^{\mathrm{TB}}$	510.78	570.12	639.72
$W_{\mathrm{L}}^{\mathrm{PBE}}$	505.09	563.99	629.19

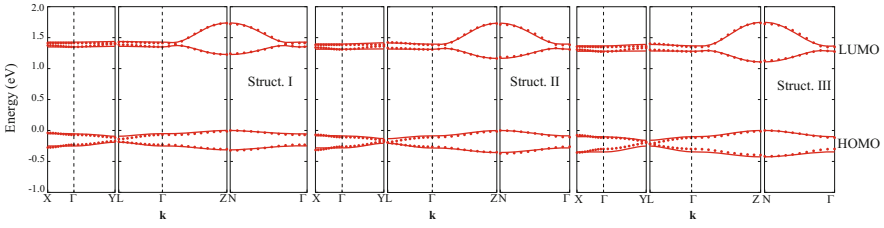

Fig. 4.9 Band structure of the tetracene crystals (Structures I–III). HOMO- and LUMO-derived bands are displayed. Solid lines indicate the band structure within the tight-binding approximation based on the transfer integrals calculated with the maximally localized Wannier functions (see Table 4.5). Dots indicate the band structures obtained with the first-principles DFT-PBE calculation. (Reprinted from [13], with the permission of AIP Publishing)

4.2.2 *Electronic Properties at Organic-Metal Interfaces: Energy Level Alignment and Emergence of the Image Potential-Like States*

The important physical phenomenon crucially affecting the energy level alignment at the interface and thus the charge transport properties [110] is the renormalization of the HOMO-LUMO energy gap induced by the metal surface [111–113]. When a molecule is close to the metal surface, electrons in the metal respond to and screen charged excitations of the molecule. The molecular energy levels at the interface are thus quasiparticle energy levels. As a result, when the molecule is located close to the metal surface, the molecular HOMO and LUMO levels shift closer to the metal Fermi level, and the HOMO-LUMO fundamental gap is narrowed [111–113]. A rigorous theoretical treatment is the many-body perturbation theory within the GW approximation for accurate treatment of the quasiparticle energies at the organic-metal interface [112, 113]. However, the computationally demanding GW treatment hampers its application to periodic systems with hundreds of atoms even with present-day computational resources. That is also the case in treatment of an organic-metal interface by employing a periodic slab model with a vacuum layer along the direction normal to the slab [114]. In addition to the system size tractable, the numerical convergence of the molecular quasiparticle energies and the metal work function can be a problem [114, 115]. The DFT wave functions can be poor approximations to the quasiparticle wave functions for hybridized interfaces, which necessitate diagonalization of the self-energy matrix $\Sigma(\mathrm{E})$ for a better new starting point for the perturbation beyond G_0W_0 or another computational strategy such as evaluation of the self-energy in the basis of the molecular orbitals, which is expected to be diagonal [114].

To avoid the technical issues involved in the GW calculation of the overall interface system, some efforts have been made, for instance, the DFT+Σ approach [112, 116]. For physisorbed systems, with the assumption of weak coupling between the molecule and the metal, the PDOS peaks of an isolated molecule could be shifted by the quasiparticle self-energy correction to HOMO and LUMO energies, along with the gap renormalization upon adsorption on the metal. With DFT+Σ, one adds two corrections denoted by Σ to HOMO-/LUMO-derived levels obtained with DFT within LDA or GGA. First, a difference between HOMO or LUMO energy of an isolated molecule with DFT-LDA or DFT-GGA and that obtained at a highly accurate level of theory such as GW is estimated. Second, the polarization at the surface inducing gap renormalization is corrected based on the classical image charge model $1/4[z - z_0]$, where z is the average height of the molecule on the surface and z_0 is the image plane position. The DFT+Σ method has been successfully employed to predict or elucidate the energy level alignment at organic-metal interfaces with physisorption [112, 117] and to explain the charge transport in molecular junctions where the assumption of weak coupling is reasonable [116].

Overall, however, the representative theoretical works calculating the energy level alignment at organic-metal interfaces within GW or DFT+Σ, despite its

rigorous theoretical background, have been limited to the abovementioned works [112–117]. The computational or numerical difficulty involved, as mentioned above, seems to be a critical limiting factor. Furthermore, determination of the quasiparticle wave functions in a self-consistent manner is necessary in case of a hybridized interface involving appreciable charge transfer at the interface. In terms of the modification of the electronic charge density at a hybridized organic-metal interface in a self-consistent manner, a theoretical methodology within the framework of DFT, such as the optimally tuned range-separated hybrid (OT-RSH), might be a method of choice [118–120].

Unoccupied electronic states at surfaces and interfaces are important as they are relevant to the charge carrier transport in the electronic devices. As such, the image potential state (IPS) is a fundamental electronic state emerging at metal surfaces, which is characterized by a set of Rydberg-like series induced by the Coulombic tail of the potential [121, 122]. Image potential has a form of $V_{\mathrm{im}} = -e^2/4(z - z_0)$, where z_0 is the position of the so-called image plane, the effective position of the surface plane, and the energy levels in the image potential is given by $E_n = -0.85\,\mathrm{eV}/(n + a)^2$ with n and a being the quantum number and the so-called quantum defect, respectively. The IPSs have been shown to exist even for graphitic materials including single-crystal graphite [123], highly oriented pyrolytic graphite [124], carbon nanotube [125], fullerene [126], and fullerite [127]. Double Rydberg states of IPSs are also predicted for freestanding graphene [128] by using the LDA augmented by the image potential tail ("LDA+image tail"), and it was suggested that the IPS is the origin of the interlayer state [nearly free electron (NFE) state] of graphite [129–131]. The double Rydberg states were confirmed for graphene and bilayer graphene on SiC by using the scanning tunneling spectroscopy [132]. Computationally however, it is well-known that the semilocal approximation to the exchange-correlation functional fails to reproduce the image potential, and the dynamic and nonlocal correlation is necessary to describe it accurately. Indeed it has been shown that by using the GW method to evaluate the energy-dependent electron self-energy, an image potential for a metal surface is reproduced [133]. As an alternative, vdW-DF has been used to study graphene and some graphite materials [134], as it contains a dynamical and nonlocal piece of correlation in an approximate manner. In the following, electronic structures of graphitic materials obtained by using vdW-DF are discussed with the emphasis on the IPSs.

In Fig. 4.10, the band structure of graphene obtained by using the rev-vdW-DF2 [10] functional is shown [134]. It is in good agreement with that obtained with the LDA+image tail potential of Ref. [128]. In particular, the low-lying IPS levels agree well (Table 4.6), suggesting that vdW-DF improves the description of graphene's IPS. In order to clarify the role of the nonlocal correlation, calculations without the nonlocal correlation [B86R exchange plus PBE correlation (B86Rx+PBEc) and B86R exchange plus PBEsol correlation (B86Rx+PBEsol$c$)] were performed. It was found that the IPS levels obtained with B86Rx+PBEc and B86Rx+PBEsol$c$ are similar to those with PBE and underestimated, suggesting that the nonlocal correlation plays an important role in describing IPSs accurately. By further analyzing the exchange-correlation potential, it was found that the vdW-DF generates

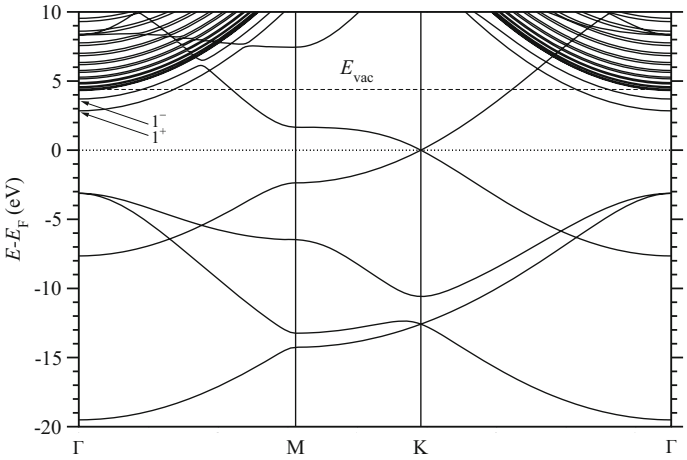

Fig. 4.10 Band structure of graphene obtained by using the rev-vdW-DF2 functional. The origin of energy is the Fermi level (E_F). The symmetry points are $\Gamma = (0, 0)$, $M = (1/2, 0)$, and $K = (1/3, 1/3)$ in the unit of the basic reciprocal lattice vectors. The horizontal dashed line indicates the vacuum level (E_{vac}). The low-lying IPSs corresponding the symmetric (1^+) and antisymmetric (1^-) are indicated by the arrows. (Reprinted from [134], with the permission of AIP Publishing)

Table 4.6 IPS levels of graphene with respect to the Fermi level calculated with rev-dW-DF2 along with those with LDA, PBE, and LDA+image tail ($z_o = 3.0$ Bohr). For comparison those obtained with B86Rx+PBEc and B86Rx+PBEsol$c$ are also shown. IPS levels with respect to the vacuum level are shown in parentheses. The rev-vdW-DF2 lattice constant was used for all the calculations. The unit of the energy level is eV. (Reprinted from [134], with the permission of AIP Publishing)

Method	1^+	1^-	2^+	2^-
rev-vdW-DF2	2.85 (−1.54)	3.70 (−0.69)	4.31 (−0.07)	4.35 (−0.04)
LDA	3.31 (−1.16)	4.25 (−0.23)	4.41 (−0.07)	4.46 (−0.02)
PBE	3.27 (−0.98)	4.03 (−0.22)	4.24 (−0.01)	4.29 (+0.04)
B86Rx+PBEc	3.42 (−0.82)	4.00 (−0.24)	4.18 (−0.06)	4.23 (−0.01)
B86Rx+PBEsol$c$	3.42 (−0.89)	4.05 (−0.25)	4.25 (−0.05)	4.30 (+0.02)
LDA+image tail[a]	2.94 (−1.47)	3.69 (−0.72)	4.16 (−0.25)	4.22 (−0.19)

[a]Ref. [128]

more attractive and longer-range potential than PBE one. It was also found that the exchange potentials used in the improved vdW-DFs such as optB86b-vdW, vdW-DF-cx, and rev-vdW-DF2 are more attractive and longer ranged than PBE

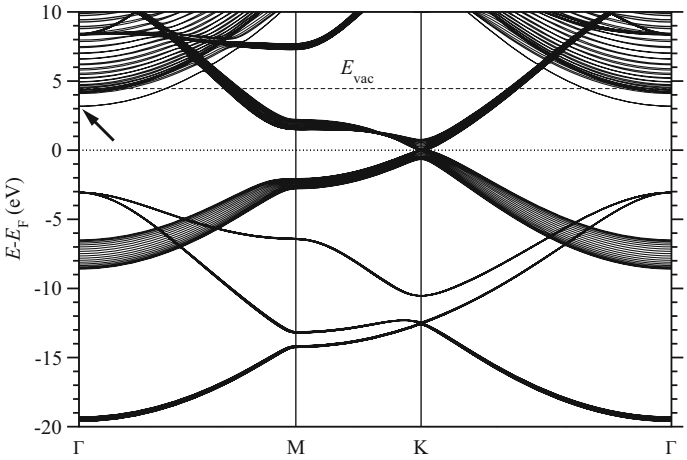

Fig. 4.11 Band structure of the graphite (0001) surface calculated by using rev-vdW-DF2. The origin of energy is E_F. The horizontal dashed line indicates E_{vac}. The lowest IPS is indicated by the arrow. (Reprinted from [134], with the permission of AIP Publishing)

exchange-correlation potential, and the attractive nonlocal correlation further gives more attractive exchange-correlation potential, resulting in the improved description of IPSs.

The band structure of the graphite (0001) surface was also calculated (Fig. 4.11), and the lowest IPS was obtained in the bulk band gap. The position of the lowest ($n = 1$) IPS obtained with rev-vdW-DF2 is 3.18 (-1.28) eV with respect to the Fermi level (vacuum level) and the second lowest ($n = 2$) IPS, 4.18 (-0.28) eV, while the lowest IPS obtained with PBE is 3.61 (-0.69) eV and the second IPS, 4.18 (-0.28) eV. Calculated IPSs with rev-vdW-DF2 are lower (deeper) than the energy of a Rydberg-like series $E_n = -0.85\,\text{eV}/(n+a)^2$ with small quantum defect a reported experimentally, and apparently those with PBE are in better agreement with the experiments. This is presumably because of the error cancellation between the derivative discontinuity and the image potential in PBE. vdW-DF also lacks the derivative discontinuity but gives more attractive nonlocal correlation energy and potential, thereby overestimating the magnitude of the IPS levels. Nevertheless, although the bulk energy gap and the energy levels of the unoccupied orbitals of gas-phase molecules are underestimated, they are described reasonably well on metal surfaces even with semilocal and vdW-DF functionals, and thus we expect the interaction between IPSs and unoccupied molecular orbitals on a metal surface is described fairly well with vdW-DF.

Here it is worth mentioning that there is also a considerable difference in the work function obtained with GGA and vdW-DF: Calculated work functions of graphene are 4.39 eV with rev-vdW-DF2 and 4.25 eV with PBE. Those of graphite are 4.46 eV with rev-vdW-DF2 and 4.30 eV with PBE at the rev-vdW-DF2 optimized geometry, and the former is in better agreement with the experimental value of 4.5–4.7 eV than the latter. Work function predicted by rev-vdW-DF2 is also in good agreement

with that obtained with optPBE-vdW [135]. These results indicate that the nonlocal correlation also affects the electronic structure, although its effect has been thought to be minor [136]. This is in line with the recent work by Ferri et al. [137] using the fully self-consistent Tkatchenko-Scheffler vdW correction [138].

IPSs of metal surfaces functionalized with molecular overlayers have also been investigated [132, 139–142]. Naphthalene on highly oriented pyrolytic graphite (HOPG) is one of prototypical systems for aromatic hydrocarbons physisorbed on a metal surface, and there have been several studies investigating its electronic properties [20, 143–146]. The scanning tunneling microscopy (STM) measurement revealed that the naphthalene overlayer on HOPG forms a superstructure with a tilted adsorption configuration [145]. Furthermore, based on the angle-resolved two-photon photoemission spectroscopy measurement, the authors of Ref. [145] suggested that the lowest IPS behaves almost like a free electron, despite the presence of the molecular overlayer [20].

To gain insights into the nature on the IPS at organic-metal interfaces, DFT calculations were conducted for naphthalene adsorbed on graphene [19]. The rev-vdW-DF2 functional [10] was used to correctly describe the molecule-substrate and the intermolecular interactions, which are typically of the vdW interaction nature. It was found that the naphthalene molecules are stabilized as a superstructure with a periodicity of $(2\sqrt{3} \times 2\sqrt{3})$ with a tilted molecular adsorption geometry, in good agreement with the STM measurement [145]. The band structure of the naphthalene/graphene was calculated (Fig. 4.12), and IPS-like states are found at 2.77 and 3.80 eV with respect to the Fermi level at the Γ point, which are characterized by anisotropic effective mass due to the anisotropic molecular configuration of the naphthalene overlayer. Further, by analyzing the corresponding charge densities of these states as shown in Fig. 4.13, it was found that these IPS-like states are formed

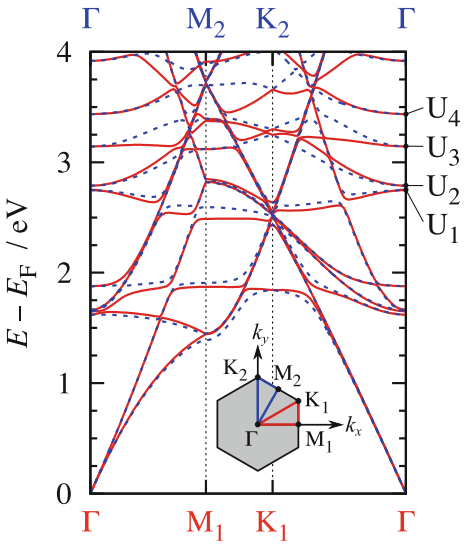

Fig. 4.12 Band structures for the unoccupied states for the naphthalene overlayer on graphene with $(\sqrt{3} \times \sqrt{3})$ periodicity. Energy zero is set to the Fermi level (E_F). The surface Brillouin zone is displayed in the inset

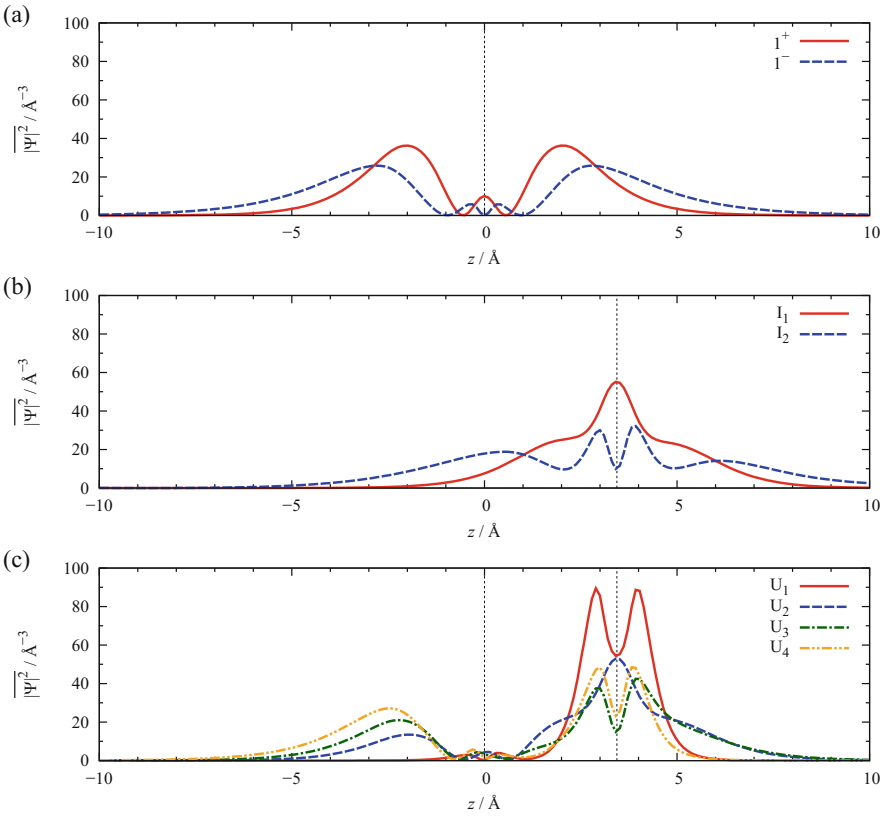

Fig. 4.13 Planer average of charge densities for (**a**) the graphene IPSs with even (1^+) and odd (1^-) parities, (**b**) the IPS-like states of naphthalene with even (I_1) and odd (I_2) parities, and (**c**) the unoccupied states of naphthalene on graphene

by the hybridization of the IPS of graphene and that of naphthalene, which originates from the Rydberg state of naphthalene molecule. In particular, the IPS-like state at 2.77 eV is the bonding state of the lowest IPS of graphene with the even parity and the IPS of naphthalene overlayer, and it was suggested that what is observed in the STM image [20] is this IPS-like state, not the molecular orbital-derived state as suggested before [20]. The results indicate that such "hybrid IPS" can be observed in a variety of systems, as IPS-like states, also known as nearly free electron states, are predicted not only for metal surfaces but also for semiconductors [147, 148], insulators [149, 150], and carbon-based nanostructures [126, 127, 151–157], and further experimental investigation on the IPS of different interfaces is anticipated. Here we stress that to predict the interface IPSs precisely, it is very important to describe the interface structures very accurately, and the use of vdW-DF is decisively important.

4.2.3 Theoretical Determination of the Ionization Energy and Electron Affinity

Energies of the valence and conduction band edges relative to the vacuum level of an organic molecular solid give the ionization energy (IE) and electron affinity (EA), quantities of primary importance leading to the energy levels of the injected or transported electron/hole at the organic-(in)organic heterojunction or inside the organic layer. Essentially, IE and EA are defined as follows:

$$\mathrm{IE} = \epsilon_{\mathrm{vac}} - \epsilon_{\mathrm{H}}, \mathrm{EA} = \epsilon_{\mathrm{vac}} - \epsilon_{\mathrm{L}}, \tag{4.7}$$

where ϵ_{vac} is the vacuum level and ϵ_{H} (ϵ_{L}) is the edge of the highest (lowest) occupied (unoccupied) energy level. Although the definition is straightforward for a molecule in a gas phase, there are physical effects to take into account in case of a molecular solid. The energy of the charge injected into the solid is renormalized: the particle is stabilized by the surrounding polarization clouds with opposite charge. The reduction in energy relative to the gas phase is referred to as polarization energy [158]. The polarization energy is formally described as

$$P^{+} = \mathrm{IE}_{\mathrm{g}} - \mathrm{IE}_{\mathrm{s}}, P^{-} = \mathrm{EA}_{\mathrm{s}} - \mathrm{EA}_{\mathrm{g}}, \tag{4.8}$$

where subscripts s and g denote solid and gas phases, respectively, and P^{+} (P^{-}) is the polarization energy upon injection of hole (electron). P^{+} corresponds to increase in energy of the electron in a solid, leading to reduction in IE relative to that in a gas phase, and vice versa in case of the polarization energy upon electron (P^{-}), resulting in the increased EA. Measurement or quantification of the polarization energy in organic solids dates back to the paper published by Sato, Seki, and Inokuchi in 1981, which was based on the comparison of the photoelectron spectroscopy data between the solid phase and the gas phase [158]. The measured polarization energies upon the injected hole in the solids (P^{+}) were reported to be in the range 0.9–3.0 eV [158]. The sum of the polarization energies $P^{+} + P^{-}$, corresponding to renormalization of the fundamental gap, becomes significant.

The reduced gap in the solid, inherently dielectric response event, may be captured with the theoretical methodologies such as the GW approximation, which describes the screened Coulomb potential based on the frequency-dependent microscopic dielectric function [112, 159]. The weak intermolecular interaction in organic solids may lead us to insights into the electronic nature described by a single molecule surrounded by a dielectric medium of the other molecules. Actually, treatment of a single molecule in the polarizable continuum model (PCM) or the quantum mechanics (QM)/molecular mechanics (MM) treatment gave reasonable estimation of IE and EA as total energy difference between neutral and charged systems obtained at the DFT-GGA level of theory [160, 161].

In photoemission measurements, the energy of the particles injected or extracted at the surface is measured, which is affected by the morphology or the molecular

orientation at the surface. As mentioned in the previous subsection, a rigorous theoretical method describing quasiparticle energy, for instance, GW approximation, requires fairly large computational resources, thus rendering difficult the application of the methodologies to a surface or an interface represented by a periodic slab model with a sufficiently thick vacuum layer.

To circumvent the computational difficulty, it was proposed recently that the electrostatic potential represented by a slab model within DFT-GGA approximation could be aligned to the electrostatic potential determined for a bulk system within the GW approximation [21]. The valence and conduction band edge energies (or HOMO- and LUMO-derived energies) of the bulk determined at the GW level of theory could be shifted according to the electrostatic potential of the surface slab model, for which a well-defined vacuum level could be determined. Overall, the resulting IE and EA are in fair agreement with experiments. The slightly smaller band gap than the experimental values may be ascribed to the different polarization effects in bulk and surface.

According to Ref. [80], $\mathrm{IE_s}$ and $\mathrm{EA_s}$ measured in photoemission or inverse photoemission experiments can be defined as

$$\mathrm{IE_s} = \mathrm{IE_g} - P^+ - \Delta^+, \mathrm{EA_s} = \mathrm{EA_g} + P^- + \Delta^-, \tag{4.9}$$

$$P^+ = E_p^+ + W^+, P^- = E_p^- + W^-, \tag{4.10}$$

where the terms Δ^+ and Δ^- correspond to the width of the valence and the conduction band edges, respectively, which are theoretically estimated with the first-principles band structure calculation. E_p^+ and E_p^- describe the induced polarization upon the injected hole and electron, respectively, which are approximately the same, because they are proportional to the square of the injected charge. On the other hand, W^+ and W^- denote the electrostatic interaction upon the injected hole and electron, respectively, which are different in sign but approximately the same in magnitude, because they are linear functions of the excess charge [162]. The electrostatic interaction W induced upon two-dimensional (2D) periodical arrangement of the molecules could be estimated by the difference in energy level between the isolated gas-phase molecule and the 2D periodically arranged molecules calculated within DFT-LDA or DFT-GGA, given the "nearsightedness" of the local chemical environment of the molecule [163, 164].

The IE and EA of the organic semiconductor thin films were theoretically obtained by adding to the gas-phase IE and EA the electrostatic terms W^+ and W^-, respectively, which are dominated by the long-range electrostatic interaction such as the charge-quadrupole interaction and depend on the surface molecular orientation [165], and the polarization-induced term E_p, which was assumed to be common for the injected hole and charge and thus was estimated as half the fundamental gap difference between the gas phase and the bulk [22]. The result for pentacenequinone, a pentacene derivative, is in agreement with the experimental measurement, demonstrating the molecular orientation crucially affecting the IE

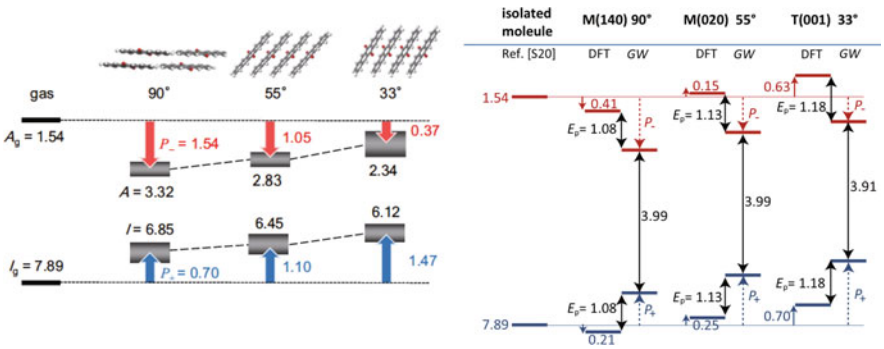

Fig. 4.14 Schematics on theoretical determination of the polarization energies P^+ and P^- (*right panel*) of pentacenequinone, in comparison to the low-energy inverse photoemission spectroscopy (LEIPS) measurement (*left panel*) in Ref. [22]. In the right panel, the solid one-headed arrows indicate the electrostatic term W^+ and W^-, and the double-headed arrows indicate the fundamental gap obtained within GW or the resulting induced polarization effect E_p. (Reprinted figure with permission from [22] Copyright 2018 by the American Physical Society)

and EA of the organic semiconductor [22] (see Fig. 4.14). The theoretical approach might play a role in prediction and tuning of the charge injection levels of organic semiconductors.

The theoretical approaches based on the periodic implementation of the GW approximation give important information on the impacts of the morphology or the molecular orientation at the surface on the charge injection levels. Nevertheless, the screening effect reduced at the surface should be taken into account. The QM/MM-based GW approach was proposed to treat quasiparticle energy of a molecular crystal, with the QM part treating the quasiparticle energy of a single molecule within GW, along with the MM part describing the effect of the surrounding molecules treated with the discrete polarizable model [23]. Based on a Gaussian atomic orbital-based implementation of GW [91] for the QM part, the response of the surrounding medium to the charged excitation of the molecule was described by the charge response model [166]. In addition to the many-body correlation and the polarization effects as taken into account within GW, crystal field effects were included at the stage of the starting DFT calculation, thus leading to the estimation of the charge injection levels relative to the vacuum level [23]. The resulting fundamental gaps of the crystals of pentacene and perfluoropentacene demonstrated the reduced polarization effect at the surface, i.e., the gap enlarged by $\approx 0.2\,\mathrm{eV}$ relative to the bulk. The crystal field effect induced rigid positive (negative) shift of the HOMO and LUMO levels for pentacene (perfluoropentacene), which the authors ascribed to the different charge-quadrupole interaction depending on the macroscopic shape of the surfaces [23, 167].

The results as mentioned above demonstrate that it is becoming possible to extract the physical ingredients dominating the charge injection barrier at an organic semiconductor surface in a quantitative manner.

4.3 Conclusions and Outlook

In this review, we have outlined recent theoretical works on basic electronic properties of organic semiconductors relevant to organic electronic devices with first-principles electronic structure methods. Firstly, we have demonstrated the performances of recently proposed van der Waals (vdW)-inclusive methods in prediction of crystal structures of the oligoacene crystals. It was found that a variant of the vdW density functional (vdW-DF) [10], with its reasonable computational cost being comparative to that of DFT-LDA or DFT-GGA, predicted the lattice constants in good agreement with the experimental values obtained with the diffraction data measured at low temperatures [13]. For the optimized crystal geometries, the many-body perturbation theory within the GW approximation [12, 18] predicted the fundamental band gap and the density of states in agreement with experiments. More importantly, different polarization energies were obtained for the different cell volumes measured at different temperatures, corresponding to the different molecular packing densities and thus the different screenings. Furthermore, based on the maximally localized Wannier functions (MLWF) [14, 15], the impact of the molecular configurations in the unit cell on the transfer integrals between molecules at the neighboring sites was discussed. The result demonstrates the subtle interplay between the intermolecular configurations such as distance and angle, and their displacement, and, therefore, the importance of predicting accurate geometry of organic semiconductor crystals is underscored [13]. Prediction of the crystal geometry of organic semiconductors and calculation of the MLWF, and thus the resulting intermolecular transfer integrals, may lead to multi-scale real-time simulation of the carrier transport in organic crystals [16]. With the aid of the present-day machine learning and artificial intelligence, a theoretical tool for automatic and efficient high-throughput screening of organic semiconductor materials might be realized in the near future.

Secondly, we discussed theoretical treatment of electronic phenomena in organic-metal interfaces. As an example of theoretical study on the interface energy level alignment, we summarized the works based on the GW approximation. GW approximation allows rigorous theoretical treatment of the charged excitation (quasiparticle) at the interface. Actually, there have been works successfully applying the same methodology to the energy level alignment at the physisorbed or hybridized interface. In consideration of the molecular gap renormalization at physisorbed interfaces dominated by the image potential, an approximated approach of adding the image potential effect $1/4z$ to the fundamental gap of an isolated molecule is found to be valid (DFT+Σ) [112, 116, 117]. However, the large computational cost which formally scales as N_{PW}^4 [168], where N_{PW} is the number of plane-wave basis set, the poor convergence of the quasiparticle energies including the work function of the metal, and the effect of self-consistency required [114, 115] critically prohibit one from applying the methodology to organic-metal interfaces in general. In terms of the effect of self-consistency, another formalism within the framework of DFT such as the optimally tuned screened range-separated hybrid (OT-SRSH) can be a method of choice [118–120].

Understanding of unoccupied states including image potential state (IPS) at organic-metal interfaces is of importance, and experimental or theoretical insight into prototype systems such as physisorption of a typical aromatic hydrocarbon on a graphite surface is required. Theoretically, GW approximation is one of the most promising electronic structure methods [169], because of its rigorous description of the long-ranged tail of the (screened) Coulomb potential. However, as far as the authors know, there is no report at present successfully investigating the IPS at organic-metal interfaces based on the same methodology, possibly because of the numerical or technical difficulty, as mentioned above. The approach based on a variant of vdW-DF may be a method of choice at present to gain insights into the IPS at organic-metal interfaces, with its long-range nature of the potential and accuracy in prediction of the interface geometry, along with its reasonable cost almost comparable to DFT-LDA or DFT-GGA [19, 134].

Thirdly, we have outlined recent theoretical approaches for determination of energy levels for charge injection, i.e., ionization energy (IE) and electron affinity (EA), at an organic semiconductor surface, which essentially determines barrier for charge injection. As with the previous topics, GW approximation is promising also for this problem. However, to avoid the numerical or technical difficulties involved in treatment of surfaces and interfaces with the periodic slab, there are some treatments proposed [21, 22], in which the vacuum level is determined based on the calculation of the slab model within DFT-GGA. The approach proposed in Ref. [22] successfully elucidated the dependence of the ionization energy and electron affinity on the surface morphology or the molecular orientation at the surface as measured by the LEIPS technique [170–172]. Nevertheless, in these approaches, the induced polarization effect in the bulk was treated. To be more quantitative in comparison to experimental measurements, the polarization effect on a surface should be taken into account, which is weaker than that in the bulk. A recently proposed approach based on QM/MM, in which IE and EA of a single molecule are treated at the GW level of theory, while the surrounding molecules are treated as continuum of dielectric medium, and thus the macroscopic shape of the surface can be treated within MM [23]. The result demonstrates quantitative treatment of IE and EA taking into account the presence of the organic crystal surface [23]. As far as the theoretical treatment of IE and EA of organic single crystals or thin films is concerned, this treatment may be a method of choice at present.

The first-principles theoretical methods, as outlined in this article, have allowed precise determination or prediction of the intrinsic basic electronic properties of organic semiconductor materials measured or observed in recent well-defined experimental measurements. Compared to the vast amount of database available and the understanding on the electronic properties of inorganic semiconductor materials, there is much room for understanding the basic electronic origin of the materials properties, and there is much need for constructing database for organic semiconductor materials. The roles of the first-principles electronic structure methods as described here, aided by future increase in computational resources and technical development in program codes, will become more and more important for more

understanding on the basic electronic properties and the following construction of a large material database and automatic high-throughput materials screening in the near future.

Acknowledgements This work was supported by Grants-in-Aid for Scientific Research (C) (No. 18K03458), on Innovative Areas "3D Active-Site Science" (No. 26105011) and "Hydrogenomics" (No. 18H05519), and for Fund for the Promotion of Joint International Research (Fostering Joint International Research) (No. 16KK0115) from the Japan Society for the Promotion of Science (JSPS), by "Joint Usage/Research Center for Interdisciplinary Large-scale Information Infrastructures" and "High Performance Computing Infrastructure" in Japan (Project ID: jh180069-NAH), and by the Cooperative Research Program of Network Joint Research Center for Materials and Devices in ISIR, Osaka University. We acknowledge the Supercomputer Center, the Institute for Solid State Physics, the University of Tokyo, and the Cyberscience Center, Tohoku University, for the use of their facilities.

References

1. J.R. Sheats, Manufacturing and commercialization issues in organic electronics. J. Mater. Res. **19**(7), 1974 (2004). https://doi.org/10.1557/JMR.2004.0275
2. M.E. Gershenson, V. Podzorov, A.F. Morpurgo, Colloquium: electronic transport in single-crystal organic transistors. Rev. Mod. Phys. **78**, 973 (2006). https://doi.org/10.1103/RevModPhys.78.973
3. J. Kleis, B.I. Lundqvist, D.C. Langreth, E. Schröder, Towards a working density-functional theory for polymers: first-principles determination of the polyethylene crystal structure. Phys. Rev. B **76**, 100201 (2007)
4. D. Lu, Y. Li, D. Rocca, G. Galli, Ab initio calculation of van der waals bonded molecular crystals. Phys. Rev. Lett. **102**, 206411 (2009)
5. A. Tkatchenko, M. Scheffler, Accurate molecular van der waals interactions from ground-state electron density and free-atom reference data. Phys. Rev. Lett. **102**, 073005 (2009)
6. A. Otero-de-la-Roza, E.R. Johnson, Van der waals interactions in solids using the exchange-hole dipole moment model. J. Chem. Phys. **136**, 174109 (2012)
7. A. Otero-de-la-Roza, E.R. Johnson, Application of the exchange-hole dipole moment (XDM) model to molecular solids. J. Chem. Phys. **137**, 054103 (2012)
8. A. Tkatchenko, J.R.A. DiStasio, R. Car, M. Scheffler, Accurate and efficient method for many-body van der waals interactions. Phys. Rev. Lett. **108**, 236402 (2012)
9. J. Klimeš, A. Michaelides, Perspective: advances and challenges in treating van der waals dispersion forces in density functional theory. J. Chem. Phys. **137**, 120901 (2012)
10. I. Hamada, van der waals density functional made accurate. Phys. Rev. B **89**, 121103(R) (2014)
11. A.M. Reilly, A. Tkatchenko, Role of dispersion interactions in the polymorphism and entropic stabilization of the aspirin crystal. Phys. Rev. Lett. **113**, 055701 (2014)
12. L. Hedin, New method for calculating the one-particle green's function with application to the electron-gas problem. Phys. Rev. **139**, A796 (1965). https://doi.org/10.1103/PhysRev.139.A796
13. S. Yanagisawa, I. Hamada, Determination of geometric and electronic structures of organic crystals from first principles: role of the molecular configuration on the electronic structure. J. Appl. Phys. **121**(4), 045501 (2017). https://doi.org/10.1063/1.4974844
14. N. Marzari, A.A. Mostofi, J.R. Yates, I. Souza, D. Vanderbilt, Maximally localized wannier functions: theory and applications. Rev. Mod. Phys. **84**, 1419 (2012)

15. A.A. Mostofi, J.R. Yates, Y.S. Lee, I. Souza, D. Vanderbilt, N. Marzari, wannier90: a tool for obtaining maximally-localised wannier functions. Comput. Phys. Commun. **178**(9), 685 (2008)
16. C. Motta, S. Sanvito, Charge transport properties of durene crystals from first-principles. J. Chem. Theor. Comput. **10**, 4624 (2014)
17. H. Ishii, K. Sugiyama, E. Ito, K. Seki, Energy level alignment and interfacial electronic structures at organic/metal and organic/organic interfaces. Adv. Mater. **11**, 605 (1999)
18. M.S. Hybertsen, S.G. Louie, Electron correlation in semiconductors and insulators: band gaps and quasiparticle energies. Phys. Rev. B **34**, 5390 (1986). https://doi.org/10.1103/PhysRevB.34.5390
19. S.A. Wella, H. Sawada, N. Kawaguchi, F. Muttaqien, K. Inagaki, I. Hamada, Y. Morikawa, Y. Hamamoto, Hybrid image potential states in molecular overlayers on graphene. Phys. Rev. Mater. **1**(6), 061001 (2017). https://doi.org/10.1103/PhysRevMaterials.1.061001
20. T. Yamada, M. Isobe, M. Shibuta, H.S. Kato, T. Munakata, Spectroscopic investigation of unoccupied states in nano- and macroscopic scale: naphthalene overlayers on highly oriented pyrolytic graphite studied by combination of scanning tunneling microscopy and two-photon photoemission. J. Phys. Chem. C **118**(2), 1035 (2014). https://doi.org/10.1021/jp4097875
21. Y. Kang, S.H. Jeon, Y. Cho, S. Han, Ab initio calculation of ionization potential and electron affinity in solid-state organic semiconductors. Phys. Rev. B **93**, 035131 (2016). https://doi.org/10.1103/PhysRevB.93.035131
22. K. Yamada, S. Yanagisawa, T. Koganezawa, K. Mase, N. Sato, H. Yoshida, Impact of the molecular quadrupole moment on ionization energy and electron affinity of organic thin films: experimental determination of electrostatic potential and electronic polarization energies. Phys. Rev. B **97**, 245206 (2018). https://doi.org/10.1103/PhysRevB.97.245206
23. J. Li, G. D'Avino, I. Duchemin, D. Beljonne, X. Blase, Combining the many-body GW formalism with classical polarizable models: insights on the electronic structure of molecular solids. J. Phys. Chem. Lett. **7**(14), 2814 (2016). https://doi.org/10.1021/acs.jpclett.6b01302
24. J.L. Brédas, J.P. Calbert, D.A. da Silva Filho, J. Cornil, Organic semiconductors: a theoretical characterization of the basic parameters governing charge transport. Proc. Natl. Acad. Sci. U. S. A. **99**, 5804 (2002)
25. V. Coropceanu, J. Cornil, D.A. da Silva Filho, Y. Olivier, R. Silbey, J.L. Brédas, Charge transport in organic semiconductors. Chem. Rev. **107**, 926 (2007)
26. A.M. Reilly, R.I. Cooper, C.S. Adjiman, S. Bhattacharya, A.D. Boese, J.G. Brandenburg, P.J. Bygrave, R. Bylsma, J.E. Campbell, R. Car, D.H. Case, R. Chadha, J.C. Cole, K. Cosburn, H.M. Cuppen, F. Curtis, G.M. Day, R.A. DiStasio Jr, A. Dzyabchenko, B.P. van Eijck, D.M. Elking, J.A. van den Ende, J.C. Facelli, M.B. Ferraro, L. Fusti-Molnar, C.A. Gatsiou, T.S. Gee, R. de Gelder, L.M. Ghiringhelli, H. Goto, S. Grimme, R. Guo, D.W.M. Hofmann, J. Hoja, R.K. Hylton, L. Iuzzolino, W. Jankiewicz, D.T. de Jong, J. Kendrick, N.J.J. de Klerk, H.Y. Ko, L.N. Kuleshova, X. Li, S. Lohani, F.J.J. Leusen, A.M. Lund, J. Lv, Y. Ma, N. Marom, A.E. Masunov, P. McCabe, D.P. McMahon, H. Meekes, M.P. Metz, A.J. Misquitta, S. Mohamed, B. Monserrat, R.J. Needs, M.A. Neumann, J. Nyman, S. Obata, H. Oberhofer, A.R. Oganov, A.M. Orendt, G.I. Pagola, C.C. Pantelides, C.J. Pickard, R. Podeszwa, L.S. Price, S.L. Price, A. Pulido, M.G. Read, K. Reuter, E. Schneider, C. Schober, G.P. Shields, P. Singh, I.J. Sugden, K. Szalewicz, C.R. Taylor, A. Tkatchenko, M.E. Tuckerman, F. Vacarro, M. Vasileiadis, A. Vazquez-Mayagoitia, L. Vogt, Y. Wang, R.E. Watson, G.A. de Wijs, J. Yang, Q. Zhu, C.R. Groom, Report on the sixth blind test of organic crystal structure prediction methods. Acta Crystallogr. B **72**(4), 439 (2016). https://doi.org/10.1107/S2052520616007447
27. J. Hermann, R.A. DiStasio, A. Tkatchenko, First-principles models for van der waals interactions in molecules and materials: concepts, theory, and applications. Chem. Rev. **117**(6), 4714 (2017). https://doi.org/10.1021/acs.chemrev.6b00446. PMID: 28272886
28. J. Klimeš, M. Kaltak, E. Maggio, G. Kresse, Singles correlation energy contributions in solids. J. Chem. Phys. **143**(10), 102816 (2015)

29. J. Klimeš, Lattice energies of molecular solids from the random phase approximation with singles corrections. J. Chem. Phys. **145**(9), 094506 (2016). https://doi.org/10.1063/1.4962188. http://scitation.aip.org/content/aip/journal/jcp/145/9/10.1063/1.4962188
30. K. Hongo, M.A. Watson, R.S. Sánchez-Carrera, T. Iitaka, A. Aspuru-Guzik, Failure of conventional density functionals for the prediction of molecular crystal polymorphism: a quantum monte carlo study. J. Phys. Chem. Lett. **1**(12), 1789 (2010)
31. A. Zen, J.G. Brandenburg, J. Klimeš, A. Tkatchenko, D. Alfè, A. Michaelides, Fast and accurate quantum monte carlo for molecular crystals. Proc. Natl. Acad. Sci. U. S. A. **115**(8), 1724 (2018). https://doi.org/10.1073/pnas.1715434115. http://www.pnas.org/content/115/8/1724
32. J. Yang, W. Hu, D. Usvyat, D. Matthews, M. Schütz, G.K.L. Chan, Ab initio determination of the crystalline benzene lattice energy to sub-kilojoule/mole accuracy. Science **345**(6197), 640 (2014)
33. M. Del Ben, J. Hutter, J. VandeVondele, Forces and stress in second order møller-plesset perturbation theory for condensed phase systems within the resolution-of-identity gaussian and plane waves approach. J. Chem. Phys. **143**(10), 102803 (2015)
34. M. Dion, H. Rydberg, E. Schröder, D.C. Langreth, B.I. Lundqvist, Van der waals density functional for general geometries. Phys. Rev. Lett. **92**, 246401 (2004)
35. K. Berland, P. Hyldgaard, Exchange functional that tests the robustness of the plasmon description of the van der waals density functional. Phys. Rev. B **89**, 035412 (2014)
36. J. Kilmeš, D.R. Bowler, A. Michaelides, Chemical accuracy for the van der waals density functional. J. Phys. Condens. Matter **22**, 022201 (2010)
37. K. Lee, É.D. Murray, L. Kong, B.I. Lundqvist, D.C. Langreth, Higher-accuracy van der waals density functional. Phys. Rev. B **82**, 081101(R) (2010)
38. V.R. Cooper, Van der waals density functional: an appropriate exchange functional. Phys. Rev. B **81**, 161104(R) (2010)
39. J. Kilmeš, D.R. Bowler, A. Michaelides, Van derwaals density functionals applied to solids. Phys. Rev. B **83**, 195131 (2011)
40. G. Román-Pérez, J.M. Soler, Efficient implementation of a van der waals density functional: application to double-wall carbon nanotubes. Phys. Rev. Lett. **103**, 096102 (2009). https://doi.org/10.1103/PhysRevLett.103.096102
41. S. Yanagisawa, K. Yamauchi, T. Inaoka, T. Oguchi, I. Hamada, Origin of the band dispersion in a metal phthalocyanine crystal. Phys. Rev. B **90**, 245141 (2014)
42. The crystal structure for the naphthalene at 5 K was taken from NAPHTA31 in Cambridge Crystallographic database. The structure of anthracene was taken from Ref. [68]. The crystal structure of the tetracene crystal was generated using the atomic coordinates given in Ref. [46]. The pentacene crystalline phase obtained by vapor deposition [48] was taken. The diffraction data measured at 123 K [57] was used for hexacene crystal
43. H.C. Alt, J. Kalus, X-ray powder diffraction investigation of naphthalene up to 0.5 gpa. Acta Crystallogr. B Struct. Crystallogr. Cryst. Chem. **38**, 2595 (1982)
44. R. Mason, The crystallography of anthracene at 95 °K and 290 °K. Acta Cryst. **17**, 547 (1964)
45. J.M. Robertson, V.C. Sinclair, J. Trotter, The crystal and molecular structure of tetracene. Acta Cryst. **14**, 697 (1961)
46. The temperature at which the X-ray diffraction measurement is performed is not clear in Ref. [46]. The cell lengths and the volume of the tetracene crystal ($P\bar{1}$ symmetry) measured at 295 K [54] were slightly smaller. Therefore we presume that the temperature of the measurement in Ref. [46] is 295 K or higher
47. T. Siegrist, C. Kloc, J.H. Schön, B. Batlogg, R.C. Haddon, S. Berg, G.A. Thomas, Enhanced physical properties in a pentacene polymorph. Angew. Chem. Int. Ed. Engl. **40**, 1732 (2001)
48. C.C. Mattheus, A.B. Dros, J. Baas, A. Meetsma, J.L. de Boer, T.T.M. Palstra, Polymorphism in pentacene. Acta Crystallogr. C Cryst. Struct. Commun. **C57**, 939 (2001)
49. C.C. Mattheus, A.B. Dros, J. Baas, G.T. Oostergetel, A. Meetsma, J.L. de Boer, T.T.M. Palstra, Identification of polymorphs of pentacene. Synth. Met. **138**, 475 (2003)

50. D. Holmes, S. Kumaraswamy, A. Matzeger, K.P.C. Vollhardt, On the nature of nonplanarity in the [n]phenylenes. Chem.-Eur. J. **5**, 3399 (1999)
51. S. Yanagisawa, K. Okuma, T. Inaoka, I. Hamada, Recent progress in predicting structural and electronic properties of organic solids with the van der waals density functional. J. Electron Spectros. Relat. Phenomena **204**, 159 (2015). https://doi.org/10.1016/j.elspec.2015.04.007. http://www.sciencedirect.com/science/article/pii/S0368204815000754
52. T. Rangel, K. Berland, S. Sharifzadeh, F. Brown-Altvater, K. Lee, P. Hyldgaard, L. Kronik, J.B. Neaton, Structural and excited-state properties of oligoacene crystals from first principles. Phys. Rev. B **93**(11), 115206 (2016)
53. R.B. Campbell, J.M. Robertson, J. Trotter, The crystal structure of hexacene, and a revision of the crystallographic data for tetracene. Acta Cryst. **15**, 289 (1962)
54. H. Yoshida, N. Sato, Grazing-incidence x-ray diffraction study of pentacene thin films with the bulk phase structure. Appl. Phys. Lett. **89**(10), 101919 (2006). https://doi.org/10.1063/1.2349307
55. S. Schiefer, M. Huth, A. Dobrinevski, B. Nickel, Determination of the crystal structure of substrate-induced pentacene polymorphs in fiber structured thin films. J. Am. Chem. Soc. **129**(34), 10316 (2007). https://doi.org/10.1021/ja0730516
56. M. Watanabe, Y.J. Chang, S.W. Liu, T.H. Chao, K. Goto, M.M. Islam, C.H. Yuan, Y.T. Tao, T. Shinmyozu, T.J. Chow, The synthesis, crystal structure and charge-transport properties of hexacene. Nat. Chem. **4**, 574 (2012). https://doi.org/10.1038/nchem.1381
57. P.E. Blöchl, Projector augmented-wave method. Phys. Rev. B **50**, 17953 (1994)
58. G. Kresse, J. Furthmüller, Efficiency of ab-initio total energy calculations for metals and semiconductors using a plane-wave basis set. Comput. Mater. Sci. **6**, 15 (1996)
59. G. Kresse, D. Joubert, From ultrasoft pseudopotentials to the projector augmented-wave method. Phys. Rev. B **59**, 1758 (1999)
60. A.D. Becke, On the large-gradient behavior of the density functional exchange energy. J. Chem. Phys. **85**, 7184 (1986)
61. We used `C_h` and `H_h` for our vdW-DF calculations
62. H.J. Monkhorst, J.D. Pack, Special points for Brillouin-zone integrations. Phys. Rev. B **13**, 5188 (1976). https://doi.org/10.1103/PhysRevB.13.5188
63. F. Murnaghan, The compressibility of media under extreme pressures. Proc. Natl. Acad. Sci. U. S. A. **30**(9), 244 (1944)
64. A.M. Reilly, A. Tkatchenko, Understanding the role of vibrations, exact exchange, and many-body van der waals interactions in the cohesive properties of molecular crystals. J. Chem. Phys. **139**, 024705 (2013)
65. D.J. Carter, A.L. Rohl, Benchmarking calculated lattice parameters and energies of molecular crystals using van der waals density functionals. J. Chem. Theory Comput. **10**(8), 3423 (2014)
66. S.C. Capelli, A. Albinati, S.A. Mason, B.T.M. Willis, Molecular motion in crystalline naphthalene: analysis of multi-temperature x-ray and neutron diffraction data. J. Phys. Chem. A **110**(41), 11695 (2006). https://doi.org/10.1021/jp062953a
67. S.L. Chaplot, N. Lehner, G.S. Pawley, The structure of anthracene-$d_1 0$ at 16 K using neutron diffraction. Acta Crystallogr. B **38**(2), 483 (1982). https://doi.org/10.1107/S0567740882003239
68. M.V. Roux, M. Temprado, J.S. Chickos, Y. Nagano, Critically evaluated thermochemical properties of polycyclic aromatic hydrocarbons. J. Phys. Chem. Ref. Data **37**(4), 1855 (2008). https://doi.org/10.1063/1.2955570
69. A.D. Becke, E.R. Johnson, Exchange-hole dipole moment and the dispersion interaction revisited. J. Chem. Phys. **127**, 154108 (2007)
70. A.D. Becke, E.R. Johnson, A unified density-functional treatment of dynamical, nondynamical, and dispersion correlations. J. Chem. Phys. **127**, 124108 (2007)
71. N. Geacintov, M. Pope, Low-lying valence band states and intrinsic photoconductivity in crystalline anthracene and tetracene. J. Chem. Phys. **50**(2), 814 (1969)
72. C.L. Braun, G.M. Dobbs, Intrinsic photoconductivity in naphthalene single crystals. J. Chem. Phys. **53**(7), 2718 (1970)

73. H. Baessler, H. Killesreiter, Hot carrier injection into molecular crystals and its relevance to the field dependence of photocurrents. Phys. Status Solidi B **53**(1), 183 (1972)
74. H. Baessler, H. Killesreiter, Bandgap-determination from autoionization data in molecular crystals. Mol. Cryst. Liq. Cryst. **24**(1–2), 21 (1973)
75. A.I. Belkind, V.V. Grechov, Energy levels of polyacene crystals. Phys. Status Solidi A **26**(1), 377 (1974)
76. L. Sebastian, G. Weiser, H. Bässler, Charge transfer transitions in solid tetracene and pentacene studied by electroabsorption. Chem. Phys. **61**, 125 (1981)
77. E.A. Silinsh, V.A. Kolesnikov, I.J. Muzikante, D.R. Balode, On charge carrier photogeneration mechanisms in organic molecular crystals. Phys. Status Solidi B **113**(1), 379 (1982)
78. L. Sebastian, G. Weiser, G. Peter, H. Bässler, Charge-transfer transitions in crystalline anthracene and their role in photoconductivity. Chem. Phys. **75**, 103 (1983)
79. Y. Isono, E. Morikawa, M. Kotani, Two-color pulsed photoconductivity study of naphthalene single crystal: photoionization of singlet exciton. Chem. Phys. Lett. **125**, 344 (1986)
80. H. Yoshida, K. Yamada, J. Tsutsumi, N. Sato, Complete description of ionization energy and electron affinity in organic solids: determining contributions from electronic polarization, energy band dispersion, and molecular orientation. Phys. Rev. B **92**, 075145 (2015). https://doi.org/10.1103/PhysRevB.92.075145
81. M.L.M. Rocco, M. Haeming, D.R. Batchelor, R. Fink, A. Schöll, E. Umbach, Electronic relaxation effects in condensed polyacenes: a high-resolution photoemission study. J. Chem. Phys. **129**(7), 074702 (2008). https://doi.org/10.1063/1.2966356
82. M.M. Rieger, L. Steinbeck, I.D. White, H.N. Rojas, R.W. Godby, The GW space-time method for the self-energy of large systems. Comput. Phys. Commun. **117**, 211 (1999)
83. L. Steinbeck, A. Rubio, L. Reining, M. Torrent, I.D. White, R.W. Godby, Enhancements to the GW space-time method. Comput. Phys. Commun. **125**, 105 (2000)
84. C. Freysoldt, P. Eggert, P. Rinke, A. Schindlmayr, R.W. Godby, M. Scheffler, Dielectric anisotropy in the GW space-time method. Comput. Phys. Commun. **176**, 1 (2007)
85. N. Troullier, J.L. Martins, Efficient pseudopotentials for place-wave calculations. Phys. Rev. B **43**, 1993 (1991)
86. J.P. Perdew, K. Burke, M. Ernzerhof, Generalized gradient approximation made simple. Phys. Rev. Lett. **77**(18), 3865 (1996)
87. Y. Morikawa, H. Ishii, K. Seki, Theoretical study of n-alkane adsorption on metal surfaces. Phys. Rev. B **69**, 041403(R) (2004)
88. C. Faber, P. Boulanger, C. Attaccalite, I. Duchemin, X. Blase, Excited states properties of organic molecules: from density functional theory to the GW and bethe–salpeter green's function formalisms. Phil. Trans. R. Soc. A **372**(2011) (2014)
89. S. Körbel, P. Boulanger, I. Duchemin, X. Blase, M.A.L. Marques, S. Botti, Benchmark many-body GW and bethe-salpeter calculations for small transition metal molecules. J. Chem. Theory Comput. **10**(9), 3934 (2014)
90. C. Rostgaard, K.W. Jacobsen, K.S. Thygesen, Fully self-consistent GW calculations for molecules. Phys. Rev. B **81**, 085103 (2010)
91. X. Blase, C. Attaccalite, V. Olevano, First-principles *GW* calculations for fullerenes, porphyrins, phtalocyanine, and other molecules of interest for organic photovoltaic applications. Phys. Rev. B **83**, 115103 (2011)
92. S. Sharifzadeh, A. Biller, L. Kronik, J.B. Neaton, Quasiparticle and optical spectroscopy of the organic semiconductors pentacene and ptcda from first principles. Phys. Rev. B **85**, 125307 (2012)
93. F. Caruso, P. Rinke, X. Ren, M. Scheffler, A. Rubio, Unified description of ground and excited states of finite systems: the self-consistent *GW* approach. Phys. Rev. B **86**, 081102 (2012)
94. F. Bruneval, M.A.L. Marques, Benchmarking the starting points of the GW approximation for molecules. J. Chem. Theory Comput. **9**(1), 324 (2013)
95. M. Govoni, G. Galli, Large scale GW calculations. J. Chem. Theory Comput. **11**(6), 2680 (2015)

96. W. Luo, S. Ismail-Beigi, M.L. Cohen, S.G. Louie, Quasiparticle band structure of zns and znse. Phys. Rev. B **66**, 195215 (2002)
97. W. Setyawan, S. Curtarolo, High-throughput electronic band structure calculations: challenges and tools. Comput. Mater. Sci. **49**, 299 (2010)
98. S. Yanagisawa, Y. Morikawa, A. Schindlmayr, Homo band dispersion of crystalline rubrene: effects of self-energy corrections within the *GW* approximation. Phys. Rev. B **88**, 115438 (2013)
99. S. Yanagisawa, Y. Morikawa, A. Schindlmayr, Theoretical investigation of the band structure of picene single crystals within the *GW* approximation. Jpn. J. Appl. Phys. **53**, 05FY02 (2014)
100. E.L. Shirley, Many-body effects on bandwidths in ionic, noble gas, and molecular solids. Phys. Rev. B **58**, 9579 (1998)
101. E. Kwon, H. Oikawa, H. Kasai, H. Nakanishi, A fabrication method of organic nanocrystals using stabilizer-free emulsion. Cryst. Growth Des. **7**(4), 600 (2007)
102. N. Ueno, S. Kera, Electron spectroscopy of functional organic thin films: deep insights into valence electronic structure in relation to charge transport property. Prog. Surf. Sci. **83**(10–12), 490 (2008)
103. S. Ciuchi, R.C. Hatch, H. Höchst, C. Faber, X. Blase, S. Fratini, Molecular fingerprints in the electronic properties of crystalline organic semiconductors: from experiments to theory. Phys. Rev. Lett. **108**, 256401 (2012)
104. K.H. Frank, P. Yannoulis, R. Dudde, E.E. Koch, Unoccupied molecular orbitals of aromatic hydrocarbons adsorbed on ag(111). J. Chem. Phys. **89**(12), 7569 (1988). https://doi.org/10.1063/1.455720
105. Y. Li, V. Coropceanu, J.L. Brédas, Thermal narrowing of the electronic bandwidths in organic molecular semiconductors: impact of the crystal thermal expansion. J. Phys. Chem. Lett. **3**(22), 3325 (2012). https://doi.org/10.1021/jz301575u
106. Y.C. Cheng, R.J. Silbey, D.A. da Silva Filho, J.P. Calbert, J. Cornil, J.L. Brédas, Three-dimensional band structure and bandlike mobility in oligoacene single crystals: a theoretical investigation. J. Chem. Phys. **118**(8), 3764 (2003)
107. G.A. de Wijs, C.C. Mattheus, R.A. de Groot, T.T. Palstra, Anisotropy of the mobility of pentacene from frustration. Synth. Met. **139**(1), 109 (2003)
108. H. Yoshida, N. Sato, Crystallographic and electronic structures of three different polymorphs of pentacene. Phys. Rev. B **77**, 235205 (2008)
109. D.A. da Silva Filho, E.G. Kim, J.L. Brédas, Transport properties in the rubrene crystal: electronic coupling and vibrational reorganization energy. Adv. Mater. **17**, 1072 (2005)
110. S.Y. Quek, M. Kamenetska, M.L. Steigerwald, H.J. Choi, S.G. Louie, M.S. Hybertsen, J.B. Neaton, L. Venkataraman, Mechanically controlled binary conductance switching of a single-molecule junction. Nat. Nanotechnol. **4**, 230 EP (2009). https://doi.org/10.1038/nnano.2009.10
111. J.C. Inkson, Many-body effect at metal-semiconductor junctions. II. The self energy and band structure distortion. J. Phys. C Solid State Phys. **6**(8), 1350 (1973). http://stacks.iop.org/0022-3719/6/i=8/a=004
112. J.B. Neaton, M.S. Hybertsen, S.G. Louie, Renormalization of molecular electronic levels at metal-molecule interfaces. Phys. Rev. Lett. **97**, 216405 (2006). https://doi.org/10.1103/PhysRevLett.97.216405
113. J.M. Garcia-Lastra, C. Rostgaard, A. Rubio, K.S. Thygesen, Polarization-induced renormalization of molecular levels at metallic and semiconducting surfaces. Phys. Rev. B **80**(24), 245427 (2009). https://doi.org/10.1103/PhysRevB.80.245427
114. Y. Chen, I. Tamblyn, S.Y. Quek, Energy level alignment at hybridized organic–metal interfaces: the role of many-electron effects. J. Phys. Chem. C **121**(24), 13125 (2017). https://doi.org/10.1021/acs.jpcc.7b00715
115. I. Tamblyn, P. Darancet, S.Y. Quek, S.A. Bonev, J.B. Neaton, Electronic energy level alignment at metal-molecule interfaces with a *GW* approach. Phys. Rev. B **84**(20), 201402 (2011). https://doi.org/10.1103/PhysRevB.84.201402

116. S.Y. Quek, L. Venkataraman, H.J. Choi, S.G. Louie, M.S. Hybertsen, J.B. Neaton, Amine-gold linked single-molecule circuits: experiment and theory. Nano Lett. **7**(11), 3477 (2007). https://doi.org/10.1021/nl072058i
117. D.A. Egger, Z.F. Liu, J.B. Neaton, L. Kronik, Reliable energy level alignment at physisorbed molecule–metal interfaces from density functional theory. Nano Lett. **15**(4), 2448 (2015). https://doi.org/10.1021/nl504863r
118. L. Kronik, T. Stein, S. Refaely-Abramson, R. Baer, Excitation gaps of finite-sized systems from optimally tuned range-separated hybrid functionals. J. Chem. Theory Comput. **8**(5), 1515 (2012). https://doi.org/10.1021/ct2009363
119. R. Baer, E. Livshits, U. Salzner, Tuned range-separated hybrids in density functional theory. Annu. Rev. Phys. Chem. **61**(1), 85 (2010). https://doi.org/10.1146/annurev.physchem.012809.103321
120. Z.F. Liu, D.A. Egger, S. Refaely-Abramson, L. Kronik, J.B. Neaton, Energy level alignment at molecule-metal interfaces from an optimally tuned range-separated hybrid functional. J. Chem. Phys. **146**(9), 092326 (2017). https://doi.org/10.1063/1.4975321
121. P.M. Echenique, J.B. Pendry, The existence and detection of Rydberg states at surfaces. J. Phys. C Solid State Phys. **11**(10), 2065 (1978). http://stacks.iop.org/0022-3719/11/i=10/a=017
122. P.M. Echenique, J.B. Pendry, Theory of image states at metal surfaces. Prog. Surf. Sci. **32**(2), 111 (1989). https://doi.org/10.1016/0079-6816(89)90015-4. http://www.sciencedirect.com/science/article/pii/0079681689900154
123. I.R. Collins, P.T. Andrews, A.R. Law, Unoccupied electronic states of single-crystal graphite by angle-resolved ultraviolet inverse photoemission. Phys. Rev. B **38**, 13348 (1988). https://doi.org/10.1103/PhysRevB.38.13348
124. J. Lehmann, M. Merschdorf, A. Thon, S. Voll, W. Pfeiffer, Properties and dynamics of the image potential states on graphite investigated by multiphoton photoemission spectroscopy. Phys. Rev. B **60**(24), 17037 (1999). https://doi.org/10.1103/PhysRevB.60.17037
125. M. Zamkov, N. Woody, S. Bing, H.S. Chakraborty, Z. Chang, U. Thumm, P. Richard, Time-resolved photoimaging of image-potential states in carbon nanotubes. Phys. Rev. Lett. **93**, 156803 (2004). https://doi.org/10.1103/PhysRevLett.93.156803
126. M. Feng, J. Zhao, H. Petek, Atomlike, hollow-core–bound molecular orbitals of c60. Science **320**(5874), 359 (2008). https://doi.org/10.1126/science.1155866. http://science.sciencemag.org/content/320/5874/359
127. J. Zhao, M. Feng, J. Yang, H. Petek, The superatom states of fullerenes and their hybridization into the nearly free electron bands of fullerites. ACS Nano **3**(4), 853 (2009). https://doi.org/10.1021/nn800834k
128. V.M. Silkin, J. Zhao, F. Guinea, E.V. Chulkov, P.M. Echenique, H. Petek, Image potential states in graphene. Phys. Rev. B **80**(12), 121408 (2009). https://doi.org/10.1103/PhysRevB.80.121408
129. M. Posternak, A. Baldereschi, A.J. Freeman, E. Wimmer, Prediction of electronic surface states in layered materials: graphite. Phys. Rev. Lett. **52**, 863 (1984). https://doi.org/10.1103/PhysRevLett.52.863
130. N.A.W. Holzwarth, S.G. Louie, S. Rabii, X-ray form factors and the electronic structure of graphite. Phys. Rev. B **26**, 5382 (1982). https://doi.org/10.1103/PhysRevB.26.5382
131. T. Fauster, F.J. Himpsel, J.E. Fischer, E.W. Plummer, Three-dimensional energy band in graphite and lithium-intercalated graphite. Phys. Rev. Lett. **51**, 430 (1983). https://doi.org/10.1103/PhysRevLett.51.430
132. S. Bose, V.M. Silkin, R. Ohmann, I. Brihuega, L. Vitali, C.H. Michaelis, P. Mallet, J.Y. Veuillen, M.A. Schneider, E.V. Chulkov, P.M. Echenique, K. Kern, Image potential states as a quantum probe of graphene interfaces. New J. Phys. **12**(2), 023028 (2010)
133. I.D. White, R.W. Godby, M.M. Rieger, R.J. Needs, Dynamic image potential at an al(111) surface. Phys. Rev. Lett. **80**, 4265 (1998). https://doi.org/10.1103/PhysRevLett.80.4265
134. I. Hamada, Y. Hamamoto, Y. Morikawa, Image potential states from the van der waals density functional. J. Chem. Phys. **147**(4), 044708 (2017). https://doi.org/10.1063/1.4995441

135. O. Leenaerts, B. Partoens, F.M. Peeters, A. Volodin, C.V. Haesendonck, The work function of few-layer graphene. J. Phys. Condens. Matter **29**(3), 035003 (2017). http://stacks.iop.org/0953-8984/29/i=3/a=035003
136. I. Hamada, S. Yanagisawa, Pseudopotential approximation in van der waals density functional calculations. Phys. Rev. B **84**, 153104 (2011). https://doi.org/10.1103/PhysRevB.84.153104
137. N. Ferri, A. Ambrosetti, A. Tkatchenko, Electronic charge rearrangement at metal/organic interfaces induced by weak van der waals interactions. Phys. Rev. Mater. **1**, 026003 (2017). https://doi.org/10.1103/PhysRevMaterials.1.026003
138. N. Ferri, R.A. DiStasio, A. Ambrosetti, R. Car, A. Tkatchenko, Electronic properties of molecules and surfaces with a self-consistent interatomic van der waals density functional. Phys. Rev. Lett. **114**, 176802 (2015). https://doi.org/10.1103/PhysRevLett.114.176802
139. M. Shibuta, N. Hirata, T. Eguchi, A. Nakajima, Probing of an adsorbate-specific excited state on an organic insulating surface by two-photon photoemission spectroscopy. J. Am. Chem. Soc. **136**(5), 1825 (2014)
140. M. Shibuta, N. Hirata, R. Matsui, M. Nakaya, T. Eguchi, A. Nakajima, Excitation and relaxation dynamics of two-dimensional photoexcited electrons on alkanethiolate self-assembled monolayers. J. Phys. Chem. C **119**(40), 22945 (2015)
141. M. Shibuta, N. Hirata, T. Eguchi, A. Nakajima, Photoexcited state confinement in two-dimensional crystalline anthracene monolayer at room temperature. ACS Nano **11**(4), 4307 (2017)
142. T. Yamada, M. Shibuta, Y. Ami, Y. Takano, A. Nonaka, K. Miyakubo, T. Munakata, Novel growth of naphthalene overlayer on Cu(111) studied by STM, LEED, and 2PPE. J. Phys. Chem. C **114**(31), 13334 (2010)
143. C. Bondi, P. Baglioni, G. Taddei, Structure of the monolayers of aromatic molecules adsorbed on graphite. Chem. Phys. **96**(2), 277 (1985). https://doi.org/10.1016/0301-0104(85)85091-6. http://www.sciencedirect.com/science/article/pii/0301010485850916
144. U. Bardi, S. Magnanelli, G. Rovida, Leed study of benzene and naphthalene monolayers adsorbed on the basal plane of graphite. Langmuir **3**(2), 159 (1987). https://doi.org/10.1021/la00074a003
145. T. Yamada, Y. Takano, M. Isobe, K. Miyakubo, T. Munakata, Growth and adsorption geometry of naphthalene overlayers on HOPG studied by low-temperature scanning tunneling microscopy. Chem. Phys. Lett. **546**, 136 (2012). https://doi.org/10.1016/j.cplett.2012.08.011. http://www.sciencedirect.com/science/article/pii/S0009261412009128
146. F. Sojka, M. Meissner, T. Yamada, T. Munakata, R. Forker, T. Fritz, Naphthalene's six shades on graphite: a detailed study on the polymorphism of an apparently simple system. J. Phys. Chem. C **120**(40), 22972 (2016). https://doi.org/10.1021/acs.jpcc.6b06702
147. S. Okada, Y. Enomoto, K. Shiraishi, A. Oshiyama, New electron states that float on semiconductor and metal surfaces. Surf. Sci. **585**(3), L177 (2005)
148. M. Kutschera, M. Weinelt, M. Rohlfing, T. Fauster, Image-potential-induced surface state at si (100). Appl. Phys. A **88**(3), 519 (2007)
149. M. Rohlfing, N.P. Wang, P. Krüger, J. Pollmann, Image states and excitons at insulator surfaces with negative electron affinity. Phys. Rev. Lett. **91**(25), 256802 (2003)
150. B. Baumeier, P. Krüger, J. Pollmann, Bulk and surface electronic structures of alkaline-earth metal oxides: bound surface and image-potential states from first principles. Phys. Rev. B **76**(20), 205404 (2007)
151. S. Saito, A. Oshiyama, Cohesive mechanism and energy bands of solid c_{60}. Phys. Rev. Lett. **66**, 2637 (1991). https://doi.org/10.1103/PhysRevLett.66.2637
152. S. Okada, A. Oshiyama, S. Saito, Nearly free electron states in carbon nanotube bundles. Phys. Rev. B **62**, 7634 (2000). https://doi.org/10.1103/PhysRevB.62.7634
153. S. Okada, S. Saito, A. Oshiyama, Energetics and electronic structures of encapsulated C_{60} in a carbon nanotube. Phys. Rev. Lett. **86**, 3835 (2001). https://doi.org/10.1103/PhysRevLett.86.3835
154. T. Miyake, S. Saito, Electronic structure of potassium-doped carbon nanotubes. Phys. Rev. B **65**, 165419 (2002). https://doi.org/10.1103/PhysRevB.65.165419

155. T. Miyake, S. Saito, Quasiparticle band structure of carbon nanotubes. Phys. Rev. B **68**(15), 155424 (2003)
156. E.R. Margine, V.H. Crespi, Universal behavior of nearly free electron states in carbon nanotubes. Phys. Rev. Lett. **96**, 196803 (2006). https://doi.org/10.1103/PhysRevLett.96.196803
157. S. Hu, J. Zhao, Y. Jin, J. Yang, H. Petek, J. Hou, Nearly free electron superatom states of carbon and boron nitride nanotubes. Nano Lett. **10**(12), 4830 (2010)
158. N. Sato, K. Seki, H. Inokuchi, Polarization energies of organic solids determined by ultraviolet photoelectron spectroscopy. J. Chem. Soc. Faraday Trans. **2**, 1621 (1981)
159. S. Refaely-Abramson, S. Sharifzadeh, M. Jain, R. Baer, J.B. Neaton, L. Kronik, Gap renormalization of molecular crystals from density-functional theory. Phys. Rev. B **88**, 081204 (2013). https://doi.org/10.1103/PhysRevB.88.081204
160. J.E. Norton, J.L. Brédas, Polarization energies in oligoacene semiconductor crystals. J. Am. Chem. Soc. **130**(37), 12377 (2008). https://doi.org/10.1021/ja8017797. PMID: 18715006
161. P.K. Nayak, N. Periasamy, Calculation of electron affinity, ionization potential, transport gap, optical band gap and exciton binding energy of organic solids using 'solvation' model and DFT. Org. Electron. **10**(7), 1396 (2009). https://doi.org/10.1016/j.orgel.2009.06.011. http://www.sciencedirect.com/science/article/pii/S1566119909001815
162. N. Sato, H. Inokuchi, E.A. Silinsh, Reevaluation of electronic polarization energies in organic molecular crystals. Chem. Phys. **115**(2), 269 (1987). https://doi.org/10.1016/0301-0104(87)80041-1. http://www.sciencedirect.com/science/article/pii/0301010487800411
163. W. Kohn, Density functional and density matrix method scaling linearly with the number of atoms. Phys. Rev. Lett. **76**, 3168 (1996). https://doi.org/10.1103/PhysRevLett.76.3168
164. D. Deutsch, A. Natan, Y. Shapira, L. Kronik, Electrostatic properties of adsorbed polar molecules: opposite behavior of a single molecule and a molecular monolayer. J. Am. Chem. Soc. **129**(10), 2989 (2007)
165. B.J. Topham, Z.G. Soos, Ionization in organic thin films: electrostatic potential, electronic polarization, and dopants in pentacene films. Phys. Rev. B **84**, 165405 (2011). https://doi.org/10.1103/PhysRevB.84.165405
166. E.V. Tsiper, Z.G. Soos, Charge redistribution and polarization energy of organic molecular crystals. Phys. Rev. B **64**, 195124 (2001). https://doi.org/10.1103/PhysRevB.64.195124
167. J. Li, G. D'Avino, I. Duchemin, D. Beljonne, X. Blase, Accurate description of charged excitations in molecular solids from embedded many-body perturbation theory. Phys. Rev. B **97**, 035108 (2018). https://doi.org/10.1103/PhysRevB.97.035108
168. W.G. Aulbur, L. Jönsson, J.W. Wilkins, in *Quasiparticle Calculations in Solids*, ed. by H. Ehrenreich, F. Spaepen. Solid State Physics, vol. 54 (Academic, 2000), pp. 1–218. https://doi.org/10.1016/S0081-1947(08)60248-9. http://www.sciencedirect.com/science/article/pii/S0081194708602489
169. I.D. White, R.W. Godby, M.M. Rieger, R.J. Needs, Dynamic image potential at an al(111) surface. Phys. Rev. Lett. **80**(19), 4265 (1998). https://doi.org/10.1103/PhysRevLett.80.4265
170. H. Yoshida, Near-ultraviolet inverse photoemission spectroscopy using ultra-low energy electrons. Chem. Phys. Lett. **539–540**, 180 (2012). https://doi.org/10.1016/j.cplett.2012.04.058. http://www.sciencedirect.com/science/article/pii/S000926141200557X
171. H. Yoshida, Measuring the electron affinity of organic solids: an indispensable new tool for organic electronics. Anal. Bioanal. Chem. **406**(9), 2231 (2014). https://doi.org/10.1007/s00216-014-7659-1
172. H. Yoshida, Principle and application of low energy inverse photoemission spectroscopy: a new method for measuring unoccupied states of organic semiconductors. J. Electron Spectros. Relat. Phenomena **204**, 116 (2015). https://doi.org/10.1016/j.elspec.2015.07.003. http://www.sciencedirect.com/science/article/pii/S0368204815001486

Part III
Interplay Between Computational and Experimental Approaches

Chapter 5
Enabling Materials By Dimensionality: From 0D to 3D Carbon-Based Nanostructures

Simone Taioli

Abstract This chapter is aimed at analysing the influence that dimensional scaling exerts on the electronic, optical, transport and mechanical properties of materials using both experiments and computer simulations. In particular, to climb the "dimensional ladder" from 0D to 3D, we analyse a specific set of all-carbon allotropes, making the best use of the versatility of this element to combine in different bonding schemes, such as sp^2 and sp^3, resulting in architectures as diverse as fullerenes, nanotubes, graphene, and diamond. Owing to the central role of carbon in future emerging technologies, we will discuss a variety of physical observables to show how novel characteristics emerge by increasing or decreasing the dimensional space in which particles can move, ranging from the charge transport in semiconductor (diamond) and semimetallic (graphite) samples to the stress-strain characteristics of several 2D carbon-based materials, to the gas absorption and selectivity in pillared structures and to the thermal diffusion in foams. In this respect, our analysis uses ab initio, multiscale and Monte Carlo (MC) methods to deal with the complexity of physical phenomena at different scales. In particular, the response of the systems to external electromagnetic fields is described using the effective dielectric model of the plasma losses within a Monte Carlo framework, while pressure fields are dealt with the ab initio simulation of the stress-strain relationships. Moreover, in this chapter we present recent theoretical and experimental investigations aimed at producing graphene and other carbon-based materials using supersonic molecular beam epitaxy on inorganic surfaces, starting from fullerene precursors. We mostly focus on the computational techniques used to model various stages of the process on multiple length and time scales, from the breaking of the fullerene cage upon impact to the rearrangement of atoms on the metal surface used to catalyse graphene formation. The insights obtained by our computational modelling of the impact and of the following chemical-physical processes underlying the materials growth have been successfully used to set up an

S. Taioli (✉)
European Centre for Theoretical Studies in Nuclear Physics and Related Areas (ECT*), Trento, Italy
e-mail: taioli@ectstar.eu; http://www.ectstar.eu/people/profile/taioli

T. Onishi (ed.), *Theoretical Chemistry for Advanced Nanomaterials*,
https://doi.org/10.1007/978-981-15-0006-0_5

experimental procedure that ended up in the production of graphene flakes by C_{60} impact on copper surfaces.

Keywords Dimensionality · Carbon-based materials · Optical, electronic, andmechanicalproperties · Multiscalesimulations, synthesis, characterization

5.1 Introduction: The Course of Dimensionality

Dimensionality affects dramatically the physical properties of materials owing to the different way that Coulomb repulsion acts upon the electrons in three-dimensional (3D), two-dimensional (2D), one-dimensional (1D), and molecular (0D) structures. Indeed, the presence of constraints on the particle's motion in one or more degrees of freedom leads to remarkable consequences, such as quantum confinement, anisotropic characteristics and new phases. These effects can completely modify the properties that low-dimensional physical systems exhibit with respect to their bulk counterparts.

Additionally, quantum objects do interfere with one another, so that the quantum state of a many-body system is the result of the interaction between its constituent particles. This many-body potential depends on dimensionality and confinement and thus is much more than the simple sum of the interaction between its building blocks. This concept was masterly described by Philip W. Anderson in his article "More is different" [1], where he argues that "the behaviour of large and complex aggregations of elementary particles, it turns out, is not to be understood in terms of a simple extrapolation of the properties of a few particles. Instead at each level of complexity entirely new properties appear…". In this regard, for example, while at angstrom scale it is hard to differentiate between 0D point-like atomic species, such as tantalum or niobium, at 3D macroscale the former is a lustrous transition metal, and the latter undergoes a phase transition to a BCS-type II superconductor at 9.26 K. This means that at the time we reach the microscale, electrons of Nb pair up in Cooper pairs and condensate, transforming the material in a superconductor characterized by zero-resistance conductivity.

While intuitively one may think that increasing the number of degrees of freedom generally results in higher levels of complexity, at odds in physics and chemistry, the curse of dimensionality can act in one or another direction. In this book chapter, we will analyse quite a few examples of this "unconventional" scaling.

For instance, a relative simple approach to describe magnetic materials is provided by the Ising model [2]. This simplified mathematical model of solids represents real systems as made of atomic spins interacting with their neighbours on a lattice and can be used to identify phase transitions. According to the traditional solutions, there is no magnetization in the one-dimensional Ising model in the absence of external magnetic fields, while the two-dimensional square lattice is the simplest statistical problem to show a phase transition. In this respect, while the one-dimensional Ising lattice represents a relatively simple toy model in statistical

mechanics to be solved, the two-dimensional one is highly nontrivial. To date furthermore, the three- or higher-dimensional Ising problems remain unsolved although there exist different approaches related to quantum field theory to tackle this issue.

In more realistic systems, one needs to look no further than studies of the 2D electron gas in semiconductor heterostructures [3] or to the rich physics of graphene [4] and of layered hybrid materials [5] to find examples of remarkable as well often unexpected behaviour of low-dimensional systems. Indeed monolayers, which can be obtained by mechanical exfoliation of bulk crystals, have generally distinctive properties from their bulk counterpart. For example, while bulk MoS_2 in the 2H phase is an indirect band gap semiconductor, MoS_2 monolayer shows a direct band gap.

Moreover, the synthesis of stable cylindrical shapes in several material families, such as nanotubes and nanowires [6], has driven the discovery of completely novel extraordinary thermal, mechanical and electrical properties. Owing to their monodimensional shape, nanotubes and nanowires can be easily integrated in nanoscale devices and used efficiently in electron charge transport and optical excitations with potential applications in nanoelectronics, in composites and functional nanomaterials to enhance their mechanical properties, as well as drug delivers or in photodynamic therapy for cancer cure [7]. Carbon nanotubes in particular [8], owing to the material's exceptional strength and stiffness, have been synthesized with a length-to-diameter ratio of up to $132 \times 10^6 : 1$ [9]. Their electronic and optical properties are determined by the tube's chirality, which is a feature emerging from the 1D geometry inducing an exceptionally high excitonic binding energy [10–12].

By further miniaturizing a device, so to obtain quantum dots (0D) [13], one can observe several phenomena such as the Coulomb blockade due to the strong Coulomb repulsion in charge confinement and the electron tunneling which led to the concept of single-electron transistors [14]. Quantum dots have also been suggested as a possible mean of implementations of qubits for quantum information processing [15].

Another feature of low-dimensional systems is to show energetically discrete molecular-like bands due to confinement and, thus, a sharper density of states (DOS) with respect to higher-dimensional structures. In particular, they exhibit DOS singularities, thus having the potential for superior transport and optical properties with respect to their higher-dimensional counterparts [16]. For example, we sketch the typical DOS of 0D (dots), 1D (wires), 2D (wells) and 3D crystals in left panel of Fig. 5.1, where spikes emerge in the spectrum descending the dimensional ladder.

The fingerprint of dimensionality can be also found in the optical properties of solids. In particular, limiting the discussion to the interband transitions in a semiconductor at zero temperature, a radiation field impinging on a crystal can be absorbed at energies equal to the difference between valence and conduction bands, whereby an electron is excited to a higher energetic level with respect to its ground state. This information is encoded in the energy-dependent absorption coefficient, which in turn is proportional to the imaginary part of the energy-dependent dielectric function $\epsilon(\omega)$ [17]:

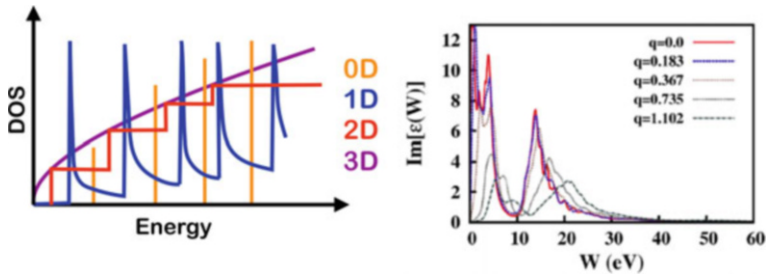

Fig. 5.1 Left panel: bulk 3D material (purple) shows typically continuous DOS, while 1D wires (blue) show van Hove singularities. Right panel: imaginary part of the graphite dielectric function vs. energy (eV) for different momentum transfer q (Å^{-1}) along the ΓL direction, obtained from ab initio simulations. (Reprinted from Ref. [18], Copyright 2017, with permission from Elsevier)

$$\alpha(\omega) = \frac{\omega}{nc}\Im(\epsilon) \tag{5.1}$$

where n is the ordinary refraction index and c is the speed of light in vacuum. The dielectric function is thus a fundamental quantity connecting microscopic observables, such as the band structure of the solid, with macroscopic features, such as the optical properties. The dielectric function is in particular related to the transition probability between a couple of valence and conduction bands, which is proportional to the joint density of states (JDOS) for slowly varying dipole matrix elements [17]. The JDOS provides a measure of the number of allowed optical transitions between the occupied valence and the unoccupied conduction bands separated by photon energy $\hbar\omega$. This is why the JDOS is usually related to the energy-dependent absorption coefficient of Eq. 5.1. Thus, while the DOS counts the number of electronic states at a given energy, the JDOS encloses information on the optical properties, and it is defined as the convolution of the valence and conduction band DOS which are linked by optical transitions. In 3D crystals the JDOS shows four different critical points (maximum, minimum and two saddle points), which tend to have square root singularities. The JDOS in 1D is not a continuous function of energy but presents sharp discontinuous spikes in contrast to three-dimensional materials, showing singularities near the critical points with a behaviour equal to the square root inverse of the energy. At odds, in the two-dimensional case, one identifies three critical points of the JDOS (maximum, minimum and one saddle point), and at the saddle point, the latter is logarithmically divergent, so more easily detectable in experiments where of course these divergences are smoothed out by the electron-electron interactions. In the right panel of Fig. 5.1, we report the optical excitation spectrum for different transferred momenta (proportional to $\Im(\epsilon)$ as by Eq. 5.1) of graphite, which is a quasi-2D materials, where the van Hove singularities are clearly visible.

Dimensionality leaves its signature also in several other observables, such as in plasmon excitations and in the quantum Hall effect in low-dimensional systems.

The former represents a tool for coupling and transferring energy. This mechanism depends on the dimensional scale. Indeed, contrary to ordinary surface plasmons of bulk materials, in low-dimensional structures, plasmon dispersion goes to zero in the long wavelength limit, covering an energy range from terahertz to near infrared. Moreover, in layered materials their in-plane dispersion, such as in the case of transition metal dichalcogenides, can show a negative in-plane plasmon dispersion [19]. Quantum Hall effect in low-dimensional materials, e.g. in graphene, is different from the spin Hall effect found in 3D systems, as it leads to a phase which is topologically distinct from a band insulator [20].

So far, according to the abovementioned Anderson's conjecture, we have shown examples in which the dependence on dimensionality of the particle-particle correlation plays a crucial role. Nevertheless, in some occasions a dimensional change can be enough to modify dramatically the behaviour of physical systems, despite correlation among constituents is switched off.

For example, let us analyse the effect that a dimensional change has on the electronic properties of a system of free (noninteracting) electrons. This model, which is called *Fermi gas*, is appropriate to study the conduction in simple systems, such as alkali and noble metals, even though rigorously the electron motion is also influenced by the periodic potential created by the ions in the lattice. By solving the Schrödinger equation for one electron in a box of edge L where periodic boundary conditions are introduced, a set of discrete energy levels $E_n = \frac{\hbar^2}{2m}(\frac{2\pi n_{x,y,z}}{L})^2 = \frac{\hbar^2}{2m}(k_{x,y,z})^2$ emerge, where $n_{x,y,z}$ is an integer number, m is the electron mass, $\hbar$ is the reduced Plank constant, and $k_{x,y,z}$ is the corresponding wavevector along the three Cartesian directions x, y, z. By neglecting the electron-electron interactions, we can build up the N-electron ground state of the system by accommodating the charges into the allowed one-electron levels starting from the bottom, provided that the same state cannot be occupied by more than two electrons, one with spin up and one with spin down orientation. Indeed, electrons are fermions, following the Fermi-Dirac statistics, and obey the Pauli's exclusion principle. The occupied orbitals are represented by a point in the k-space inside a sphere of radius $k_F = \sqrt{2m\epsilon_F/\hbar^2}$, which is the highest momentum an electron can have within the box. ϵ_F is the Fermi energy, which defines the so-called Fermi sphere, within which all occupied one-electron levels lay. The number of electronic states per unit energy range (DOS, $D(\epsilon)$) in the solid is a quantum observable: for Al, for example, one has $\epsilon_F = 11.6\,\text{eV}$ and $D(\epsilon_F) = 0.39\,(\text{eV atom})^{-1}$.

Furthermore, the kinetic energy of the electron gas increases with temperature, and some energy levels, which were vacant at 0 K, start to be populated. The distribution of electrons among the levels is described by the Fermi distribution function, $f(E) = 1/(\exp^{(\epsilon-\mu)/k_B T} + 1)$, which gives the probability that the energy level E is occupied by fermions. Multiplying the DOS by the latter function, one can obtain the DOS analytic expressions for electrons at temperature T confined in their motion by infinite barriers into (i) a cube box of side L (3D), (ii) a square surface of side L (2D) and (iii) a wire of length L (1D), as follows:

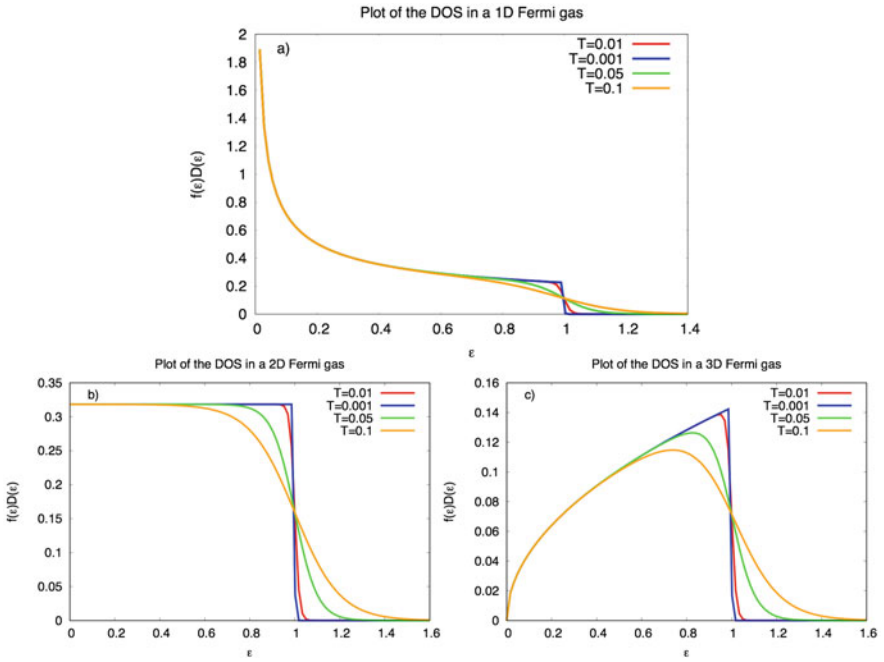

Fig. 5.2 DOS (y-axis) of a free Fermi gas at different temperatures T confined into (**a**) 1D, (**b**) 2D, and (**c**) 3D dimensions vs. energy (x-axis). The electronic levels are populated according to the Fermi distribution function $f(\epsilon) = 1/(\exp^{(\epsilon-1)/T} + 1)$, where the chemical potential $\mu = 1$ is assumed independent of temperature T, and $k_B = 1$. The constant in front of the analytical expression of $D(\epsilon)$ (Eq. 5.2) is assumed equal to 1

$$f(\epsilon)D(\epsilon) = f(\epsilon) \begin{cases} \frac{L^3}{2\pi^2}\left(\frac{2m}{\hbar^2}\right)^{3/2}\epsilon^{1/2}, \ in\ 3D \\ \frac{mL^2}{\pi\hbar^2}, \ in\ 2D \\ \frac{L}{\pi}\left(\frac{2m}{\hbar^2}\right)^{1/2}\epsilon^{-1/2}, \ in\ 1D \end{cases} \tag{5.2}$$

In Fig. 5.2a–c, we report the plots of the DOS for 1D-, 2D- and 3D-confined free Fermi gas at several finite temperatures. Of course, also other quantities derived from the DOS, such as the chemical potential μ, are affected by dimensionality.

While the potential for quantum matter to develop emergent properties is far more striking, nevertheless also classical objects, such as the natural systems, can feel the course of dimensionality and exhibit new classes of behaviour upon dimensional scaling. In particular, the principle that drives the action of systems in nature is the same of quantum objects: behaviour cannot be rationalized as the simple sum of their building block's activity. Nature's great lesson in this regard is that structural solutions of biomaterials at different length scales and dimensions, from nano- to micro- and macro-architectures, are optimized according to hierarchies, in which the building blocks are organized so to "do more with less".

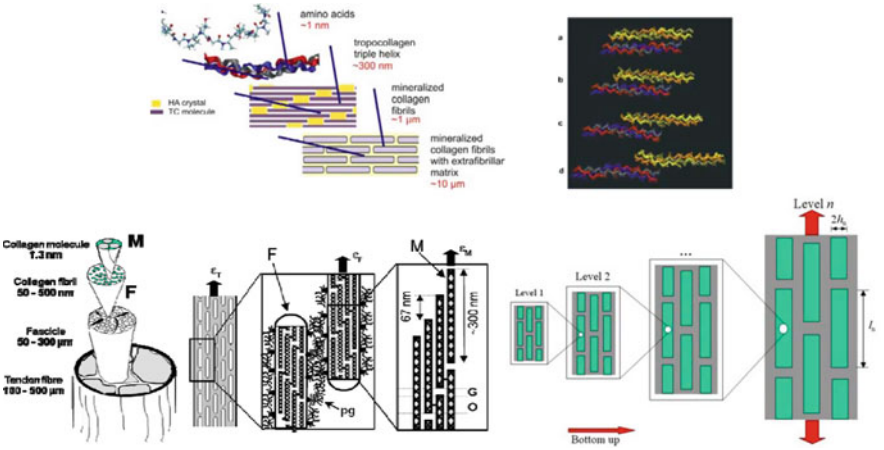

Fig. 5.3 Hierarchical structures of bones and tendons. (Adapted from Refs. [21–24] with permission)

Complex behaviour and functionalities can emerge from the way constituents are assembled or interact with one another, in such a way that the optical or mechanical response of biomaterials to external electromagnetic or force fields is dramatically influenced, or even completely modified, by the presence of these hierarchical levels (see Fig. 5.3 reporting the hierarchical levels present in human tendons). This is of course the result of the basic mechanisms of evolution that nature developed over the years in order to have robust and flaw-tolerant structures for survival. This hierarchical (or dimensional) effect can be seen in many natural systems, e.g. spider silk, gecko feet, lotus flower, bones, tendons (see Fig. 5.3 [21–24]) or butterfly wings to cite a few.

On the other side, even in the realm of real-world technological materials, the electronic, optical and mechanical properties are also affected by dimensionality. One of the most striking examples in this regard is provided by the large family of carbon-based materials. Indeed, carbon is one of the most versatile chemical elements: its relatively small atomic radius and the tetravalent character mean that carbon can easily form covalent bonds with several chemical elements, including itself, also at room conditions. This is the very reason why the number of known chemical compounds constituted of carbon – which is only the 4th most abundant element in the universe by mass after hydrogen, helium and oxygen and only the 15th most abundant in the Earth's crust – is by far higher than the sum of all the others (in excess of 10 million). For example, at odds, silicon is another element in group 14 of the periodic table having also four valence electrons which can bind into both molecular and crystalline compounds. However, due to its atomic radius, 1.5 times larger than that of carbon is too big to fit together into as great a variety of molecules as carbon atoms can.

This remarkable ability of carbon to bind in different ways by sharing from one single to four electrons may lead to the formation of single to triple bonds. This makes for an enormous number of possible bond combinations forming straight chains, such as polymers; rings, such as aromatic hydrocarbons; crystals, such as silicon carbide; and also amorphous phases. The all-carbon materials that carbon can form by binding in different ways are called allotropes of carbon, be those naturally available or man-made. The most common are graphite, diamond, fullerene and amorphous carbon. In this chapter, we will focus on the description of the physical properties of carbon allotropes with the aim to show how the dimensionality leaves its signature on the electronic, optical and mechanical properties of these carbon-based materials. For example, on the one side, graphite is a quasi-two-dimensional material whose distinctive treats are to be opaque, black and sufficiently soft to be used in pencils. Furthermore, graphite is a good electrical conductor. On the other side, diamond is a 3D transparent, hard solid showing low electrical conductivity. Nevertheless, at room conditions, 3D diamond, 1D carbon nanotubes, and 2D graphene have all large thermal conductivities.

In the discussion of these topics, we have made the disputable choice of focussing on the description of structures which grown out of our research activity over the last decade. This includes the fullerenes' family (0D), carbon nanotubes (1D), graphene sheets (2D) and other two-dimensional allotropes, graphite (quasi-2D) as well as diamond and foams (3D) (see Fig. 5.4). This thorough analysis will also show how the investigation of these structures stimulated the development of new computational tools with the ambition to connect first-principles, atomistic,

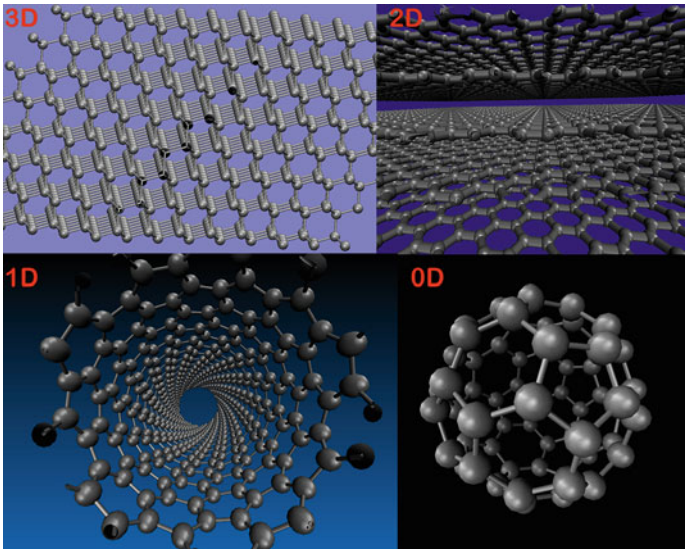

Fig. 5.4 Allotropes of carbon. From left to right: diamond (3D); graphene (2D); nanotubes (1D); and buckyballs (0D)

mesoscopic and continuum models to integrate different levels of simulation for climbing the "dimensional ladder". This approach is not surprisingly called multiscale analysis.

5.2 0D Carbon Materials: The Fullerenes

Pristine C_{60} or buckminsterfullerene is a 0D all-carbon structure (molecule) made of 20 hexagonal and 12 pentagonal faces, with a carbon atom at the vertices of each polygon interconnected by bonds along each edge [25]. This amounts to 60 carbon atom vertices, connected via 90 covalent bonds among single (60) and double (30) bonds. C_{60} resembles a soccer ball (see bottom right panel of Fig. 5.4) and is shaped as a truncated icosahedron. Carbon atoms in C_{60} fullerene are equivalent, and their s and p outer shells are sp^2 hybridized (or almost like that if one refers this hybridization to planar-only geometries). The p orbitals, which are orthogonal to the hypothetical sphere inscribed in the fullerene, form π-type bonds.

While theoretical predictions [26] of the existence and stability of buckminsterfullerene were already put forward, the first isolated and characterized structure belonging to the fullerines' family was synthesized in 1985 by R.F. Curl, H.W. Kroto and R.E. Smalley [27]. Fullerene is the by-product of two synthesis methods, that is, the arc and the combustion methods, and sublimates below 800 °C. They own their name to Buckminster Fuller, an American architect universally known for his innovative design of the geodesic domes shaped as buckyballs.

Nevertheless, some evidence can be found that its geometrical shape was already postulated by Archimedes among his thirteen solids. To the best of author's knowledge, the oldest picture of the fullerene's structure dates back to the Italian renaissance painter and mathematician Piero della Francesca, who drew the shape of C_{60} in his book *Libellus de quinque corporibus regularibus* (see Fig. 5.5a). A further rendition of the truncated icosahedron, ascribed to Leonardo da Vinci, can be found in the book *De Divina Proportione*, written by Luca Pacioli around the end of the fifteenth century (see Fig. 5.5b).

The existence and stability of C_{60} are confirmed by mass spectrometry experiments, which show discrete peaks corresponding to molecules with the exact mass of 30 to 90 carbon atoms (see Fig. 5.6a [28]), making buckminsterfullerene one the most abundant molecules among the fullerenes' family. Furthermore, we report in Fig. 5.6c the relative cohesive energies of carbon architectures at different dimensionality, including linear chains, rings, 2D flakes and fullerenes, which are sketched in Fig. 5.6b. We notice that fullerenes are more stable than rings and planar flakes for $n > 20$, due to the absence of edges with respect to other 2D and 1D structures. Nevertheless, due to the constant positive curvature, which induces stress into the structure, fullerenes are not totally unreactive at odds with the planar sp^2 carbon net of graphene. They have been actually functionalized by several chemical elements, such as hydrogen [31], fluorine, bromine and chlorine [32], both in the

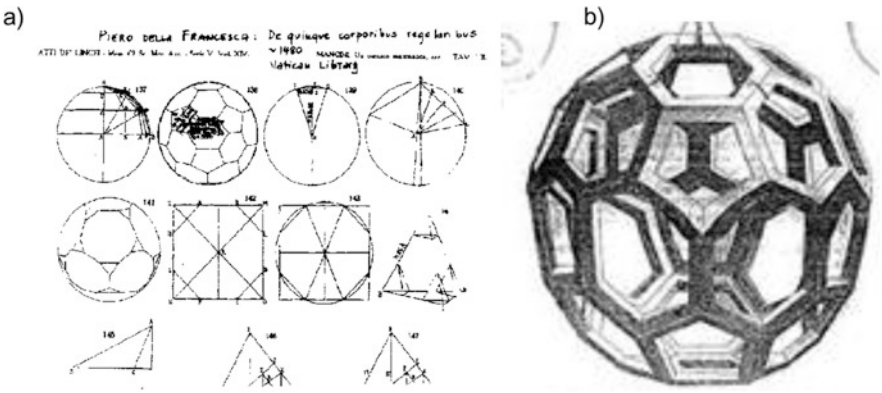

Fig. 5.5 (**a**) Rendition of a truncated icosahedron from the book *Libellus de quinque corporibus regularibus* by Piero della Francesca. (**b**) Fullerene geometry drawn by Leonardo da Vinci found in the *De Divina Proportione* by Luca Pacioli

outer and inner cage; $C_{61}Ph_2$ derivatives were prepared through cyclopropanation for use in organic solar cells [33].

Due to their symmetry, not belonging to the group of the perfect sphere, fullerenes are diamagnetic and display rather high electron affinity, and they do not conduce. At room conditions C_{60} is a semiconductor, with a band gap of about 2.3 eV [34], well reproduced by GW simulations reporting a band gap equal to 2.15 eV [35, 36], showing aromaticity but not "super-aromaticity" (see Fig. 5.7 for band structure and electron spectroscopy characterization). This means that for symmetry reasons, the electrons are not delocalized overall in the molecule whereas localized on the pentagons and the hexagons.

C_{60} usually is found in solid form, with buckyballs arranged in face-centred cubic configurations ($Fm3m$ symmetry group [37]) with lattice constant equal to 1.411 nm, kept together via van der Waals intermolecular forces (see Fig. 5.8). Fullerenes are thus weakly interacting, and the valence bands are only slightly deviated from those of the isolated icosahedral. In Fig. 5.7, we report the electronic structure of the C_{60} cluster (top left panel) and of the fcc solid fullerite (top right panel) [38], along with the photoelectron spectroscopy (PES) and the electron energy-loss spectroscopy (EELS) experimental measurements of thin films of solid C_{60} [39]. We notice that the unique electronic properties of fullerenes have been used to produce molecular rectifiers and transistors that can operate with more than two logical states [40]. Doping with alkali metals leads to compositions such as M_3C_{60} (M can be K, Rb or Cs), called fullerides, which display also superconductive behaviour at low temperature [41].

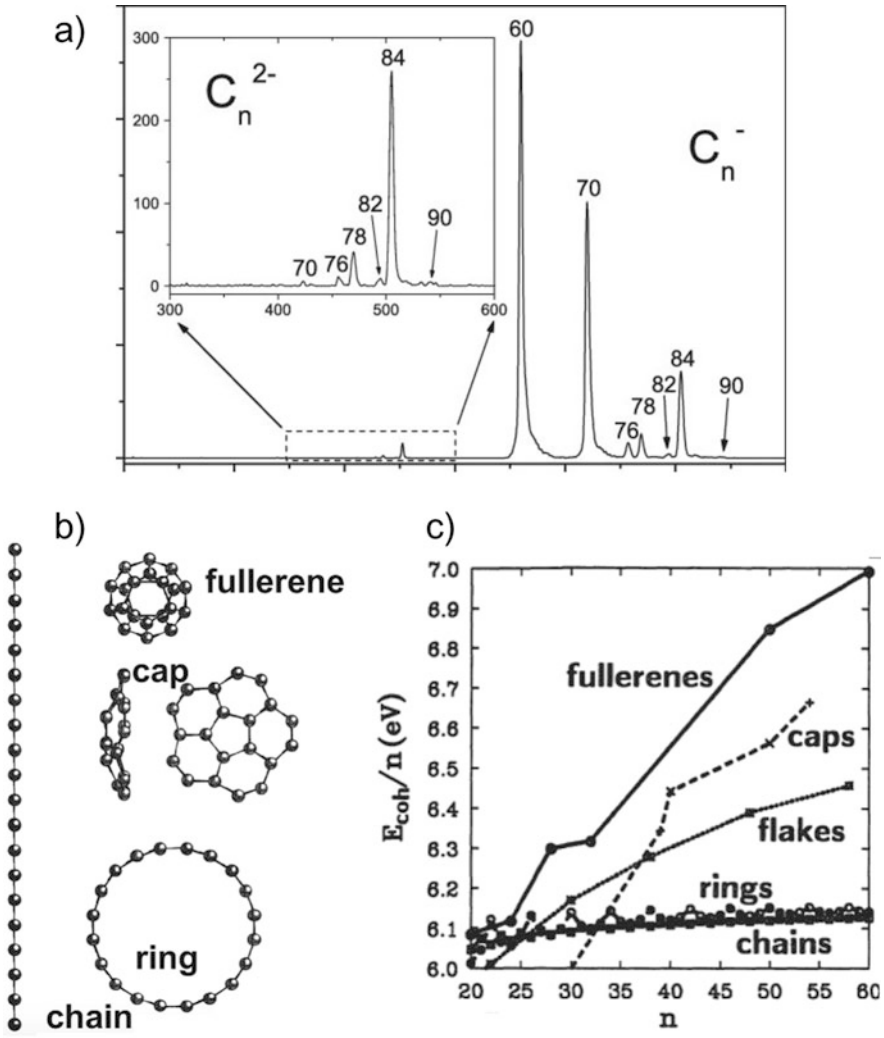

Fig. 5.6 (**a**) Time-of-flight mass spectrum of fullerenes. The mass of C_{60} is 720 amu; (**b**) linear chains, rings, caps and fullerenes structural arrangements; (**c**) binding energy per atom E_{coh}/n in different structural arrangements of C_n. (Panel (**a**) is reproduced from Ref. [28] with the permission of the European Physical Society, while panels (**b**)–(**c**) are reprinted with permission from Refs. [29, 30] Copyright 1991, 1992 by the American Physical Society)

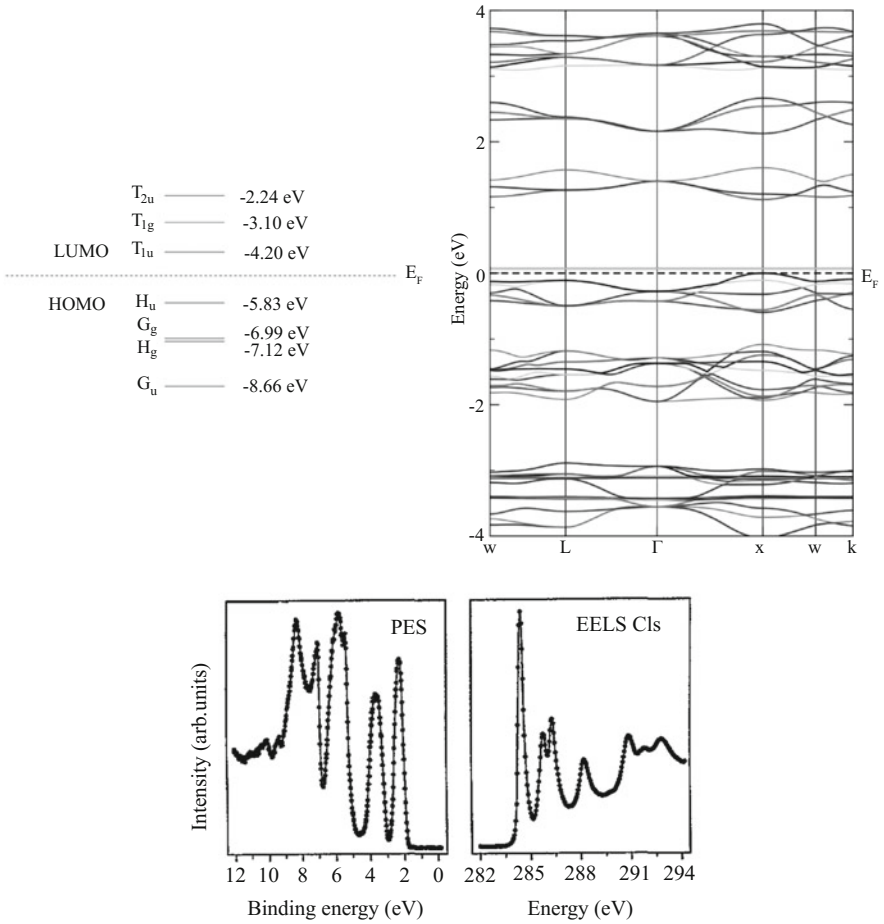

Fig. 5.7 Top panels: electronic structure of the C_{60} molecule (left) and of the pristine fullerite (solid fcc) within PBE-GGA+DFT-D3(vdW). Fermi levels of the two systems are aligned. (Adapted by permission from Springer Nature: [35], COPYRIGHT (2016)). Bottom: photoemission spectrum (left-hand panel, $h\nu = 21.22$ eV) and C 1 s excitation spectrum (right-hand panel) of a thin film of fullerenes. (Adapted from Ref. [39] with permission of UvA-DARE)

5.2.1 Using 0D Carbon Systems to Synthesize 2D Monolayers

The mechanical stability of fullerenes along with their massiveness, compactness and fair reactivity can suggest their use as precursors to initiate the growth of carbon-based materials. In this section we describe a novel experimental method able to grow materials using a kinetically driven approach at temperatures lower than those achieved so far by commonly adopted synthesis techniques.

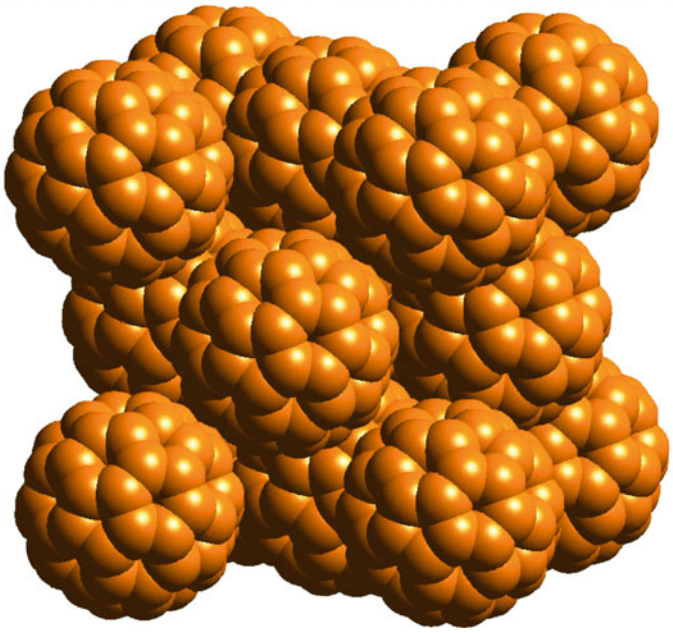

Fig. 5.8 FCC structure of solid C_{60}

In particular, we present recent theoretical and experimental advances on the epitaxy of graphene, when the appropriate molecular bonds are severed by impacting supersonic molecular beam of fullerenes on inorganic surfaces (SuMBE) [42–45]. Furthermore, we show how computational modelling can help our understanding of the various stages of the process on multiple length and time scales, from the breaking of the fullerene cage upon impact to the rearrangement of atoms on the metal surface used to catalyse graphene formation. We notice that the insights obtained by our simulations of the impact and following chemical-physical processes have been successfully used to set up an experimental procedure that ended up in the production of graphene flakes by C_{60} impact on copper surfaces [46].

Graphene is typically synthesized by chemical vapour deposition (CVD) of carbon-rich molecules (usually alkanes, such as propane) on metals [47, 48], such as nickel or copper. On the latter the growth of graphene is known to proceed by surface adsorption as carbon shows low solubility at high temperature [49]. Chemical reactions occurring on the surface are catalysed by the substrate, at temperatures higher than $\simeq$700 °C, and result in bond breaking and rearrangement into a two-dimensional extended structure [49, 50]. Given the presence of hydrogen atoms in the precursors and the relatively high working temperature, this process generally leads to defected hydrogenated graphene. A subsequent thermal treatment at about 1000 °C is finally used to desorb hydrogen, leaving graphene in a highly polycrystalline form.

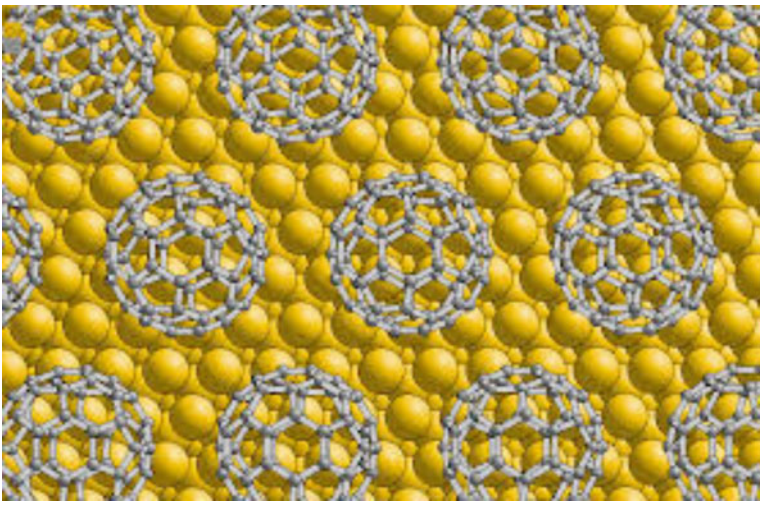

Fig. 5.9 Fullerenes on the top of metallic substrate

At variance, our procedure uses supersonic beams of C_{60} to induce the catalysis. Of course there is no way that by placing fullerenes on the top of a metallic substrate graphene can be formed (see Fig. 5.9). Instead, C_{60} cage must be somehow broken to trigger graphene growth. We remind that fullerenes have the shape of soccer balls, so they can be easily accelerated at intermediate to high kinetic energies (from a few to tens of eV) towards the substrate. On the one side, the high kinetic energy impacts provide the activation energy necessary to initiate graphene sheet formation, so one can avoid the typical shortcomings of CVD, such as the high-temperature dehydrogenation process. On the other side, this kinetic energy regime allows one to avoid crater formation, surface spreading and sputtering upon collision events.

Following this remarkably simple idea of bombarding a silicon substrate with buckyballs travelling at supersonic speeds (C_{60} kinetic energy = 35 eV), we were able to grow silicon carbide (3C-SiC) nanocrystalline islands (about 10 nm wide) with a completely relaxed lattice at room temperature (RT) using H_2 as carrier gas [42–45]. SiC island formation was also obtained at 800 K for a C_{60} kinetic energy (KE) of 20 eV using He as carrier gas. These experimental evidences show that (i) the chemical-physical mechanisms underlying SiC synthesis are kinetically driven and triggered by C_{60} cage disruption occurring above a KE threshold; (ii) SuMBE is a promising technique able to reduce drastically the growth temperature and increase the structural order.

5.2.1.1 Experimental Results

The experimental activity was focussed on synthesizing nanostructured carbon-based materials, such as silicon carbide (3C-SiC) [42–44] and graphene [46, 49, 50], using C_{60} fullerene supersonic beams impinging on metallic or semiconductor substrates aiming at room temperature (RT) growth conditions (see Fig. 5.10a). SuMBE makes use of two types of devices: one for producing a highly energetic beam of C_{60} molecules and the other for characterizing the growing film by in situ electron spectroscopy techniques. The apparatus is self-contained within a UHV chamber (base pressure = 7.0×10^{-11} mbar) and consists of a quartz tube in which an inert carrier gas, usually He or H_2, is seeded with highly diluted (below 0.1% in number of the mixture) organic molecules sublimated by Joule heating. Figure 5.11a shows a layout of the instrumentation under consideration.

In the case of graphene growth by SuMBE, the two major issues to take into account are the substrate type and the fullerene KE able to trigger the cage

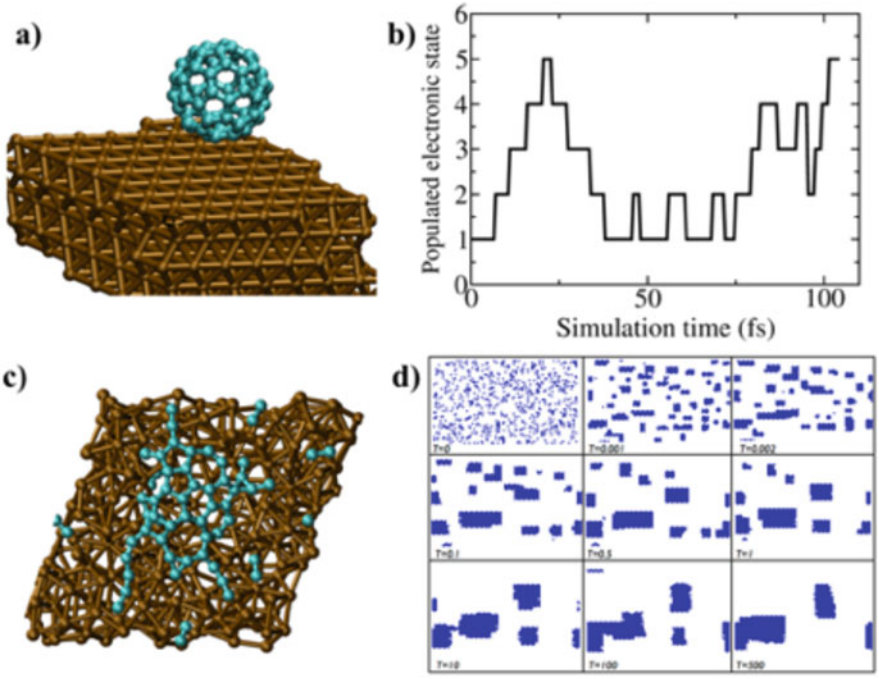

Fig. 5.10 (**a**) Representation of the system studied. A C_{60} molecule (cyan) and the Cu(111) surface (brown). (**b**) Time-dependent populated electronic state vs. simulation time. In particular, we report the first six electronic excited states (labelled from 1 to 6) above the ground state (labelled by 0) visited during a simulation of fullerene impact onto the Cu(111) surface. (**c**) Early stage investigations of graphene formation by metadynamics. (**d**) Kinetic Monte Carlo simulations of graphene flakes formation and merging by carbon diffusion on the Cu(111) surface. (Adapted from Refs. [46, 50])

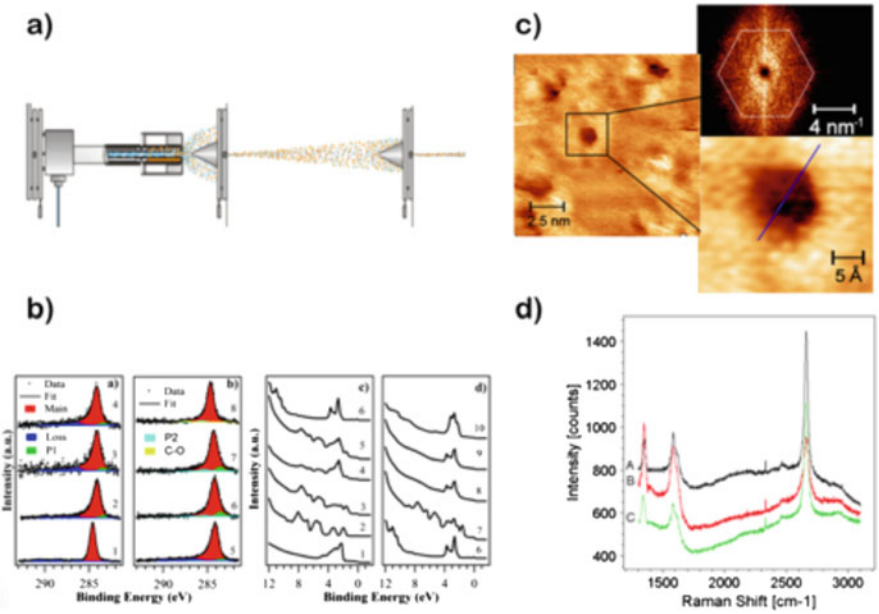

Fig. 5.11 (**a**) Schematic drawing of an apparatus for SuMBE deposition; (**b**) XPS and UPS measured spectra. Left panel: C1s CL from C_{60} film deposited at RT by SuMBE on Cu poly at KE = 15 eV (panels 1 and 2) and Cu(111) at KE = 35 eV (3, 4) with thickness: (1) 20 nm; (2) 1 ML; (3) 0.3 ML; (4) 0.6 ML.; C1s CL from C_{60} 1 ML films deposited at RT for KE = 35 eV, after thermal annealing at 425 °C (5), 645 °C (6), 795 °C (7). C1s emission from commercial single-layer graphene on Cu foil is shown for comparison (8). Right panel: VB on Cu poly (1); VB analysis of C_{60} films deposited by SuMBE on Cu poly at RT for KE=15 eV (2–3) and Cu(111) at KE = 35 eV (4, 5) with thickness: (2) 20 nm; (3) 1 ML, after annealing a 20 nm film at 400 °C; (4) 0.3 ML; (5) 0.6 ML. VB on Cu(111) (6); VB from C_{60} 1 ML film deposited at RT with KE = 35 eV, after thermal annealing at 425 °C (7), 645 °C (8), 795 °C (9). VB from a commercial graphene single layer on Cu foil (10) is shown for comparison. (**c**) STM analysis, showing few nm extended graphene-like domains after annealing at 645 °C a C_{60} 1 ML on Cu(111). (**d**) Raman analysis of C_{60} 1 ML on Cu(111) after annealing at 645 °C. A, B, C represent Raman spectra acquired in different regions of the sample. (Adapted from Ref. [46])

disruption. The main steps generally undertaken for synthesizing graphene via SuMBE (or also SiC thin films for which this technique was initially successfully used) are the following:

- **Surface preparation.** Several (up to 40) argon ion sputtering (0.5 keV) cycles and annealing of the copper substrate (T > 700 °C for obtaining optimal LEED diffraction pattern) to expunge contaminants, such as oxygen, sulphur or adventitious carbons.
- **Carrier gas choice.** C_{60} KE can be tuned by changing the carrier gas from He (lower KE) to H_2 (higher KE), being the KE inverse proportional to the carrier gas mass; furthermore, using noble gases a strong interaction with the substrate

leading to adsorption of the carrier gas is avoided. C_{60} internal dynamics is frozen unlike ordinary heating that dramatically increases the molecular vibrations.
- **Aerodynamical acceleration.** The highly diluted C_{60} plus carrier gas mixture fluxes via isentropic expansion out of the injection cell into vacuum through a nozzle (see Fig. 5.11a). Fullerene KE can be tuned not only by changing the carrier gas but also modifying the seeding parameters, such as the source temperature and the gas inlet pressure. In this way C_{60} KEs of 10–15 eV using He carrier gas can be achieved, while up to 30–40 eV using H_2.
- **Collimation** of the diluted mixture towards the copper reconstructed surface. The substrate temperature can be increased as well from RT conditions.
- **Thermal activated growth** of graphene islands by increasing the substrate temperature to 645 °C.

To our surprise, we found out that the substrate temperature must be raised to synthesize graphene islands as C_{60} high-energy deposition on Cu, even at the highest KE reachable by SuMBE, does not lead to immediate C_{60} cage rupture at variance with SiC growth on silicon (as confirmed by our nonadiabatic molecular dynamics simulations that find a KE cage breaking on copper higher than 40 eV). It seems that the excess of energy made available by C_{60} supersonic impacts is spent for rearranging fullerene positions in a very stable 4×4 pattern on the copper surface, which eventually induces a tighter interaction characterized by charge transfer between a number of carbon atoms of the organic molecule with the directly facing copper adatoms [51]. This covalent interaction at the C_{60}-Cu interface, following the 4×4 reconstruction, leaves its signature in our in situ core-level analysis, resulting in a spectral shift of about -0.5 eV and in the emergence of a new feature with respect to films deposited by standard MBE technique, at variance characterized by C_{60} clustering. These spectral characteristics, present at all beam KEs, at any surface coverage from 0.3 to 1 equivalent monolayers (ML), without remarkable differences for temperatures up to 445 °C, have been interpreted as the proof of a significant deformation, operated by the impinging C_{60} molecules, of the copper superficial layers into a cup shape with removal of a number of copper adatoms and formation of stable bonds with those surrounding the deformed or partially broken cage.

Moreover, we did not find evidence of C_{60} cage rupture by SuMBE deposition on single- or polycrystal copper in all range 10 to 40 eV, changing the carrier gas, even increasing the substrate temperature during the C_{60}-Cu collision up to 565 °C. Nevertheless, the 4×4 rearrangement of fullerenes on the copper surface induced by the collision creates favourable conditions for cage unzipping via thermally activated processes.

In fact, high-energy 4×4 deposition on single- or polycrystal substrates kept at RT, followed by a temperature increase to 550 °C (645 °C) when using He (H_2) as carrier gas, resulted in a dramatic change of the C_{60} typical spectral patterns (as seen in Fig. 5.11b). In particular, the main peak in the C1s core-level spectrum, not compatible with the presence of unbroken C_{60}, shows the typical asymmetry of defected graphene nano-islands, while the valence spectrum loses all the features

reported for the MBE deposited C_{60} film. Finally, the KVV Auger signal intensity from carbon is not depleted with respect to the copper one by increasing the temperature up to 800 °C, meaning that the grown species is stable and not volatile. Most importantly, evidence of fullerene cage disruption under these conditions has been found independently of the carrier gas used and of copper surface coverage from 0.3 to 1 ML.

The ultimate evidence of the presence of defected nanometric graphene islands on the copper substrate is confirmed by both STM measurements and Raman spectroscopy, reported in Fig. 5.11c, d, respectively.

These findings point towards a graphene growth model, in which the excess of energy provided by the C_{60} translational KEs does not lead immediately to C_{60} cage break and to the activation of kinetically driven chemical-physical mechanisms; rather, at odds with the case of SiC synthesis, this energy is used to enhance surface mobility and C_{60} diffusion, regardless of the carrier gas used for the expansion. Moreover, after fullerenes find their optimal hosting sites by lattice distortion of the copper surface owing to this increased mobility and tighten their interaction by forming covalent bonds with the inorganic substrate, chemical-physical processes that change the material topological and electronic properties can be thermally activated by raising the substrate temperature, eventually leading to the C_{60} cage break. The increase of temperature can of course enhance the catalytic action of copper as well as contribute to activate nonlinear excitations of vibrational motion and to desorb physisorbed species above the first C_{60} ML.

5.2.1.2 Computational Modelling: Breaking the Fullerene Cage

In this section, we report the principal computational results and modelling tools that have been used to model the physical-chemical processes leading from C_{60} impacts onto metallic surfaces to the early stages of graphene formation. A very similar theoretical and computational framework could be used to model the interaction with other surfaces commonly used in graphene synthesis, such as nickel, or to understand, and thus control, the growth of other carbon-based nanoclusters. However, due to the possible formation of nickel carbide species, we opted for single- or polycrystal copper substrates for which the chemical-physical mechanisms underlying graphene growth turned out to be very similar.

Previous calculations based on empirical or semiempirical interaction potentials [52, 53], aimed at investigating the stability of C_{60} molecules upon impact on silicon surfaces, indicate that KEs of several hundred of eV are required to observe cage rupture. However, this result was in sheer contrast with our experiments [42, 43], showing SiC formation on the surface of silicon for impinging KEs of $\simeq$ 35 eV at RT conditions. A detailed analysis of fullerene cage breaking conditions upon impact on the silicon substrate at different levels of accuracy (and corresponding different computational costs), using both classical and Born-Oppenheimer (BO) ab initio molecular dynamics (AIMD), confirmed these previous findings. Indeed, no cage breaking was observed for fullerene initial KEs lower than 300 eV, even

using first-principles molecular dynamics based on density functional treatment of the electronic motion [43].

While this conclusion is expected when using classical molecular dynamics, whereby atoms are treated as hard spheres interacting through a pair-wise potential, making this model not capable of treating out-of-equilibrium conditions where bonds are breaking and forming, it is surprising when electronic motion is explicitly treated from first-principles. However, a critical reassessment of the validity of the BO approximation – that is the assumption that the electrons at every instant collapse into their ground state configuration – suggests that the electronic and nuclear motion are intimately intertwined, due to the short time scales involved in the molecule-surface collision.

Indeed, computer simulations allowing electron hopping between several excited states, calculated by time-dependent density functional theory (TDDFT), indicate that C_{60} cage breaking can indeed occur for impact KEs of the order of 35 eV. Figure 5.10b shows the progressively higher-energy surfaces visited by the electrons during the simulation of a fullerene molecule approaching the silicon surface. Due to the high-energy impact occurring in the timespan of a few femtoseconds, electrons cannot relax fast enough to the ground state relative to the instantaneous configuration of the nuclei. Thus, the forces acting on the nuclei during molecular dynamics simulation must be calculated on the pure adiabatic surfaces populated at the present time step. These gradients can be very different from the BO ground state ones, leading to a highly dissociative path. Therefore, the cage disruption cannot be accurately modelled at the measured KE if not by adopting a nonadiabatic description of the impact. A similar behaviour was observed in the case of fullerene molecules breaking upon impact on copper surfaces: we found out that one needs to include excited-state dynamics in the description of the system in order to accurately describe the processes involved in the collision and correctly estimate the cage rupture energy threshold [46].

Similarly to what occurs with semiconducting silicon surfaces, even in the case of collision with copper surface, C_{60} cage breaking is observed for KEs slightly higher than 40 eV. Unfortunately, this KE is marginally too high for SuMBE. In the experimental section, we have seen indeed that in order to synthesize graphene islands, we need to raise the substrate temperature up to 645 °C after the impact.

It is worth noticing that the significant computational requirements of excited-state simulations prevent following the system's dynamics on time scales much larger than several hundred femtoseconds in a reasonable time frame. Thus, one needs to go beyond first-principles simulations and use multiscale approaches to model the chemical-physical processes underlying graphene growth. Rearranging the atoms to synthesize graphene, C_{60} high-energy impacts on Cu and cage breaking are the first two steps towards graphene growth on the substrate. In particular, the energy released in the impact is absorbed by the distortion of the surface and dissipates via phonon excitations. The system quickly reaches a regime where excited-state dynamics is quenched and its evolution, thus, can be followed by methods based on the validity of the BO approximation, notably density functional theory (DFT).

Nevertheless, even if the computational cost of DFT calculations is much lower with respect to nonadiabatic molecular dynamics, the comparatively large time scale on which atomic rearrangement is expected to take place, typically of the order of seconds, is still prohibitive for first-principles simulations. In order to speed up the calculation, we thus use enhanced sampled techniques, such as metadynamics, or multiscale approaches, such as kinetic Monte Carlo (KMC) [50, 54]. In particular, we introduce a fictitious force coupled to a collective coordinate describing the number of carbon-carbon bonds that drives the system towards the formation of a carbon net, if clustering is energetically favourable. To carry out these calculations, we used the Vienna Ab initio Simulation Package (VASP) [55, 56]. Long-time metadynamics simulations provide a clear indication that the system, after cage rupture, tends to rearrange towards the formation of graphene. Furthermore, we were able to show that formation mechanisms are effective only above a critical carbon atom density on the surface, as shown in Fig. 5.10c.

Still, the time scale of graphene growth is much longer than can be modelled by metadynamics, in which electronic motion is explicitly included. Furthermore, by adopting this approach, we lose information on the actual time frame, as common in accelerated molecular dynamics methods. In this respect, the very long time scale dynamics, of the order of seconds, leading to graphene island formation and merging, is most effectively studied by means of KMC simulations [50]. Within this approach, nudged-elastic band simulations (NEB) using BO ground state DFT at RT are performed to calculate reaction activation energies and relevant transition rates (assuming Boltzmann-distributed occupation of the states) for carbon atom diffusion between adsorption sites on the copper surface, as well as the energy variation upon carbon-carbon bond formation. Once the rates and energies of all possible reactions and site jumps occurring on the copper surface are known, the KMC method is capable to follow the various stages leading to graphene production. Figure 5.10d shows the progressive creation and clustering of graphene flakes on the Cu surface after diffusion and merging of initially separated carbon atoms. This multiscale study pointed out the existence of a critical carbon density on the surface for successful graphene growth, in good agreement with our BO-DFT simulations of the early growth stages (see Fig. 5.10c) [50].

Finally, we notice that the kinetic energy threshold for projectile breaking can in principle be estimated also by a continuum mechanical model (CM) [57]. The kinetic energy threshold for projectile breaking in a CM is assumed proportional to the object volume V, where the proportionality constant is the product of the mechanical strength of the projectile and the ratio of the projectile and target densities. The threshold velocity for breakup at temperature T would then be given by:

$$\frac{1}{2}Mv^2 + \frac{1}{2}k_{\mathrm{B}}TnN = \frac{\rho_n}{\rho}\sigma_f V \tag{5.3}$$

where M is the mass of C_{60}, σ_f is the mechanical strength of the fullerene, ρ_n is its density, $\rho = 8960\,\mathrm{kg/m^3}$ is the copper density, $N = 60$ is the number of

atoms, $n = 3$ are the internal degrees of freedom per atom and k_B is the Boltzmann constant. Since in the SuMBE approach the rotational and vibrational degrees of freedom of C_{60} result frozen, the second term in the left-hand side of Eq. 5.3 can be neglected. Assuming σ_f of the order of the mechanical strength of carbon nanotubes [58] ($\simeq$50 GPa), the threshold kinetic energy of C_{60} breakup would be estimated $\simeq$40 eV. This value is in good agreement with our ab initio nonadiabatic simulations.

5.3 2D Carbon-Based Materials: Graphene and Its Low-Density Allotropes

The large interest expressed over the last decade in graphene, the bi-dimensional allotropic form of carbon, is largely determined by the honeycomb-shaped sp^2 carbon net from which it derives its unique electronic and mechanical properties [11, 12, 18, 47, 48, 59–65], such as unexpectedly high opacity for a thin atomic monolayer, high electron mobility at room temperature, with reported values in excess of 15,000 $cm^2\,V^{-1}\,s^{-1}$, and breaking strength over 100 times bigger than a hypothetical steel film of the same thickness [4]. Furthermore, pristine graphene differs from most three-dimensional materials being a semimetal or a zero-gap semiconductor, in which electrons and holes behave like Dirac fermions due to the linear dispersion in the vicinity of the six corners of the Brillouin zone, where valence and conduction bands touch upon.

Despite some concern raised about the stability of suspended monolayers owing to the theoretical prediction that a 2D lattice is unstable upon thermal fluctuations [66, 67], graphene was synthesized in 2004 by K. Novoselov and A. Geim [68], who managed to cleave out single-atom-thick crystallites from bulk graphite. Due to its properties, graphene finds application in a variety of fields, including electronic devices (transistors, sensors, batteries, transparent conductive coatings for solar cells, OLEDs, high frequency devices), nanocomposites (to make lighter aircraft, or embedded in plastics to conduct electricity, or again in sports equipment) or in medicine (such as in artificial cell membranes). Thus, despite the difficulties in synthesizing high-quality large-area graphene sheets [46, 49, 50], its great promises and achievements in the fields of materials science motivate the large scientific and technological efforts that the scientific community is pursuing.

Nevertheless, the importance of graphene goes beyond its own specific characteristics, as it represents the paradigm of a new class of bi-dimensional materials obtained from layered structures, such as transition metal dichalcogenides (TMDs) [69], silicene [70], germanene, the monolayer form of black phosphorous [71, 72] and boron nitride.

In this section, due to the large amount of reviews [4] and books [73] on the physics of graphene, we will only use graphene as a fundamental texture to deal with some novel carbon allotropes at lower density. In particular, we discuss the possibility to introduce interesting features in bi-dimensional all-carbon materials, keeping the planar structure and the sp^2-net of graphene. In this regard, one of the

most striking properties of graphene is its Young's modulus to density ratio, possibly the highest achieved so far. We discuss here a systematic method for finding novel energetically stable structures characterized by sp^2-hybridized carbon atoms with decreasing density but almost unchanged specific mechanical characteristics with respect to graphene. In this way, lower structural weight could be achieved which is an important request, e.g. in aerospace applications.

5.3.1 Structure Search Method

The geometry of graphene can be generated by using the two-dimensional packing of congruent discs touching each other in three points under the following constraints (for further details, see [74]):

- No two discs overlap;
- Each disc is in contact with at least another disc;
- For any choice of two discs in the packing, there is always a path connecting them through mutual contacts;
- Angles between the segments connecting two disc centres must be smaller than π rad (local stability);

With these constraints in place, one can search for novel structures with specific characteristics comparable to graphene and also for the least dense arrangement of discs in the plane which is an important issue on its own.

5.3.1.1 Graphene and Graphene Daughter

The packing of graphene, reproduced in the left-hand side of Fig. 5.12a, has a density equal to $\pi/(3\sqrt{3}) \sim 0.6046$ and can be used to create the graphene net, reported in the left panel of Fig. 5.12b, by positioning a carbon atom at the centre of each disc. One can generate a novel architecture by replacing each disc in the graphene packing with three discs having a radius $\frac{1}{1+2/\sqrt{3}}$ smaller than that of graphene, which leads to a less dense packing $\pi(7\sqrt{3}) - 12 \sim 0.390675$, as shown in the right panel of Fig. 5.12a. This process is known as "augmentation" [75], and the "*graphene daughter*" obtained by applying this procedure is reported in the right panel of Fig. 5.12b (called gr11 in [76]).

5.3.1.2 Tilene Parent and Tilene

By considering tilings with polygons having a number of sides larger than triangles, one can obtain the packing associated with, e.g. the square-octagon tiling. In the left panel of Fig. 5.13a, we show the tiling and in the left panel of Fig. 5.13b the

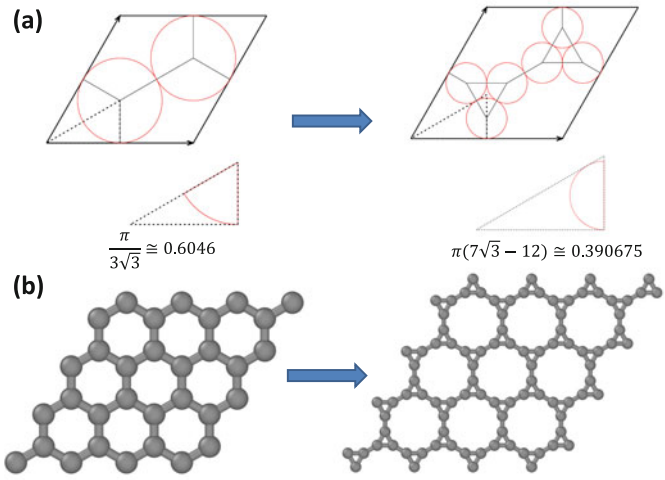

Fig. 5.12 (**a**) Graphene (left) and graphene daughter (right) unit cells. The latter can be obtained by using the two-dimensional packing of congruent discs, represented in the figure by red circles, touching each other. The centres of the nearest neighbour red discs, where carbon atoms lay, are connected by black lines representing the carbon bonds. (**b**) 4×4 supercells of graphene (left) and graphene daughter (right)

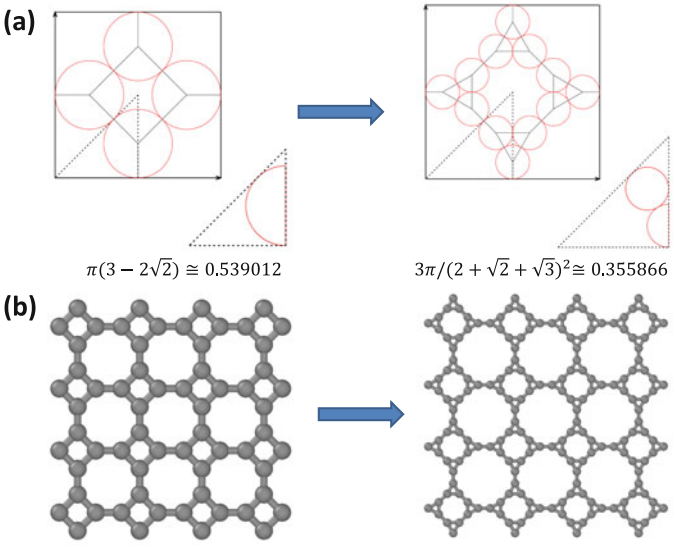

Fig. 5.13 (**a**) Tilene parent (left) and tilene (right) unit cells. The latter can be obtained by using the two-dimensional packing of congruent discs, represented in the figure by red circles, touching each other. The centres of the nearest neighbour red discs, where carbon atoms lay, are connected by black lines representing the carbon bonds. (**b**) 4×4 supercells of tilene parent (left) and tilene (right)

corresponding net of carbon atoms of "*tilene parent*" (octagraphene in [76]). Its packing factor is lower than graphene and equal to $\pi(3-2\sqrt{2}) \sim 0.539012$. Its augmentation, carried out under the constraints discussed in Sect. 5.3.1, leads to the lesser dense packing equal to $3\pi/(2+\sqrt{2}+\sqrt{3})^2 \sim 0.355866$ shown in the right panel of Fig. 5.13a. The resulting structure, called "*tilene*", is reported in the right panel of Fig. 5.13b.

5.3.1.3 Flakene Parent and Flakene

In the left panel of Fig. 5.14a, we report the trihexagonal tiling of the plane, obtained via regular polygons with the largest rings achieving a density equal to $\pi(2/\sqrt{3}-1) \sim 0.486006$. The resulting geometry filled with carbon atoms, called "*flakene parent*" (C_{64} graphenylene in [76]), is reported in the left panel of Fig. 5.14b. Its augmentation, shown in the right-hand side of Fig. 5.14a, shows a 24-sided polygon tiling with density equal to $3\sqrt{3}\pi/(20+3\sqrt{3}+6\sqrt{7}+2\sqrt{21}) \sim 0.324951$. The corresponding allotropic form, obtained by filling the discs at their centres by carbon atoms, is reported in the right panel of Fig. 5.14b, and we call it "*flakene*". We claim that the latter is one of the sp^2 structures with lowest density ever studied which agree to the locally jammed packing conditions.

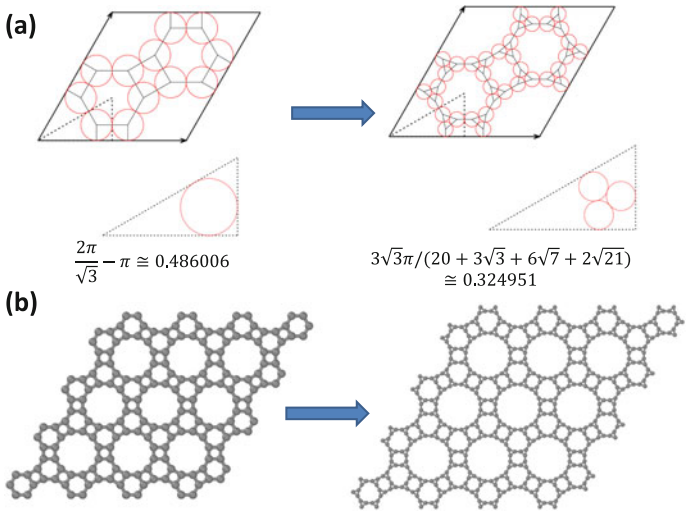

Fig. 5.14 (**a**) Flakene parent (left) and flakene (right) unit cells. The latter can be obtained by using the two-dimensional packing of congruent discs, represented in the figure by red circles, touching each other. The centres of the nearest neighbour red discs, where carbon atoms lay, are connected by black lines representing the carbon bonds. (**b**) 3×3 supercells of flakene parent (left) and flakene (right)

5.3.1.4 Liskene

Other carbon structures can be designed by relaxing the constraint of having only three-coordinated carbon atoms. A first example is given in Fig. 5.15a, b where we report the top and side views of pentagraphene [77], which has $four$ three-coordinated and two four-coordinated vertices. At variance with previous tilings, the plane is not filled using congruent discs, which reflects the fact that one cannot tile the plane by congruent pentagons. The resulting structure is not planar and is characterized by different bond lengths owing to the sp^2-sp^2 or sp^2-sp^3 hybridization. By applying the augmentation procedure to the pentagonal tiling, we obtain a planar three-coordinated structure that we name "*liskene*", which is shown in Fig. 5.16a. This daughter architecture is again a three-coordinated system with a density lower than the parent. In Fig. 5.16b we show the DFT optimized geometry of this geometrical tiling.

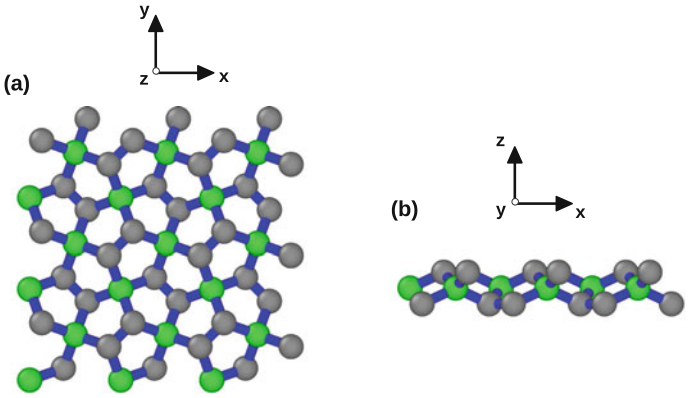

Fig. 5.15 (**a**) Top view of a 3×3 pentagraphene super cell; (**b**) side view of a 3×3 pentagraphene super cell. The sp^3-hybridized carbon atoms are reported in green colour, while in grey scale, we find the sp^2-hybridized carbon centres

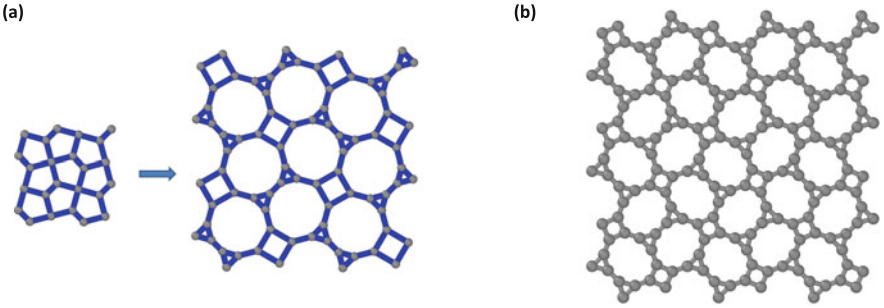

Fig. 5.16 (**a**) Augmentation of the Cairo pentagonal tiling. (**b**) 3×3 supercell of liskene after performing DFT minimization

5.3.2 Electronic Properties of 2D All-Carbon-Based Materials

Here we discuss the electronic band structure and the stress-strain characteristics of the father and daughter structures obtained by the space tiling and augmentation procedures previously introduced. Further details on computer simulations and methods can be found in Ref. [74].

In Table 5.1 we report the energy per atom and the cohesive energies. Graphene has a cohesive energy equal to 7.74 eV (experimental value is 7.6 eV [78, 79]) and still results the most energetically stable bi-dimensional allotrope of carbon. In general, with the notable exception of pentagraphene for which the out-of-plane geometry daughters into a planar sp^2 net, we observe that daughter architectures are characterized by lower stability along with lower density. While we notice that the loss of stability is not significant, as the energy difference between the less stable material (flakene) and graphene is of the order of 0.7%, the density is almost two times lower than that one of graphene (see the first column of Table 5.1).

Furthermore, we present the band structures alongside the relevant DOSs for the seven structural arrangements described in this section. Generally, we observe that moving from father to daughter in the case of graphene (Figs. 5.17 and 5.18), tilene (Figs. 5.19 and 5.20), flakene (Figs. 5.21 and 5.22) and pentagraphene (Figs. 5.23 and 5.24), a narrow band close to the Fermi level (reported as horizontal red lines in the figures) appears, increasing the metallic character of the parent structures. We argue that the appearance of an almost flat band can be the signature of geometrical and, thus, orbital frustration, similarly to the kagome lattice. These frustrated geometries pay the way also to the creation of strongly-correlated materials.

Table 5.1 First column: structure type. Second column: surface density. Third and fourth columns report the total energy per atom with respect to graphene and the cohesive energy per atom obtained upon structural optimization, respectively. With the exception of pentagraphene, all structures are planar, and each carbon atom is three-coordinated. In the table the following abbreviations were used: p. = parent, d. = daughter, dir. = direct gap, indir. = indirect gap

Structure	Density (atoms/Å^2)	Energy ([eV]/atom)	Cohesive energy ([eV]/atom)	Type	Bandgap [eV]
Graphene	0.379	0	7.7404	Semi-met.	0 (dir.)
Graphene d.	0.256	0.9882	6.7523	Metal	–
Tilene p.	0.336	0.5186	7.2219	Metal	–
Tilene	0.233	1.0765	6.6640	Metal	–
Flakene p.	0.301	0.6395	7.1009	Semi-met.	0.043 (dir.)
Flakene	0.212	1.1071	6.6334	Metal	–
Pentagraphene	0.452	0.9044	6.8361	Semicond	2.23 (ind.)
Liskene	0.297	0.7789	6.9615	Semicond	0.36 (ind.)
Liskene d.	0.247	1.0506	6.6897	Semicond	0.46 (ind.)

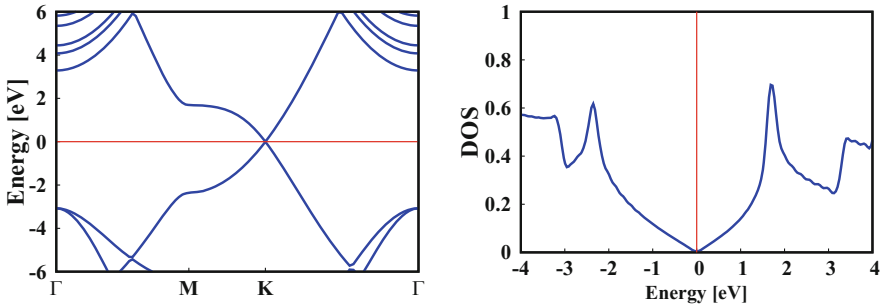

Fig. 5.17 Band structure (left) and DOS (right) of graphene. Fermi level is shifted to zero and reported as an horizontal red line in the left-hand side (bands) and as a vertical red line in the right-hand side (DOS) of the figure

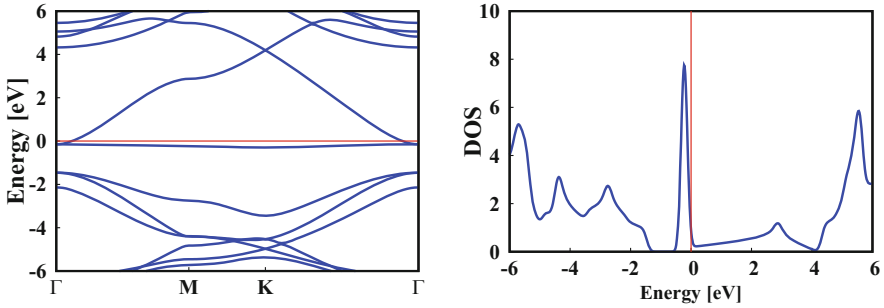

Fig. 5.18 Band structure and DOS of graphene daughter. Fermi level is shifted to zero and reported as a horizontal red line in the left-hand side (bands) and as a vertical red line in the right-hand side (DOS) of the figure

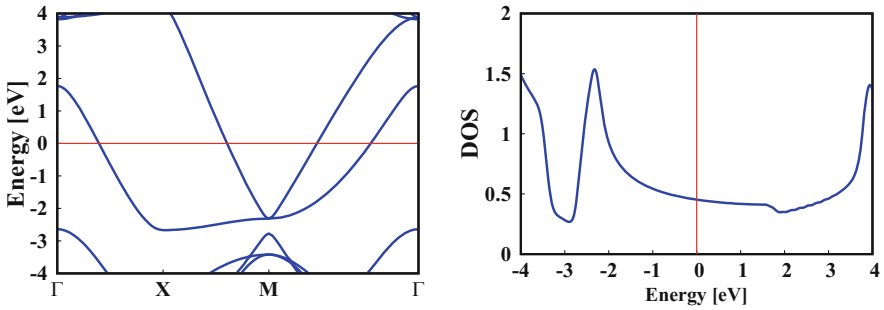

Fig. 5.19 Band structure and DOS of tilene parent. Fermi level is shifted to zero and reported as a horizontal red line in the left-hand side (bands) and as a vertical red line in the right-hand side (DOS) of the figure

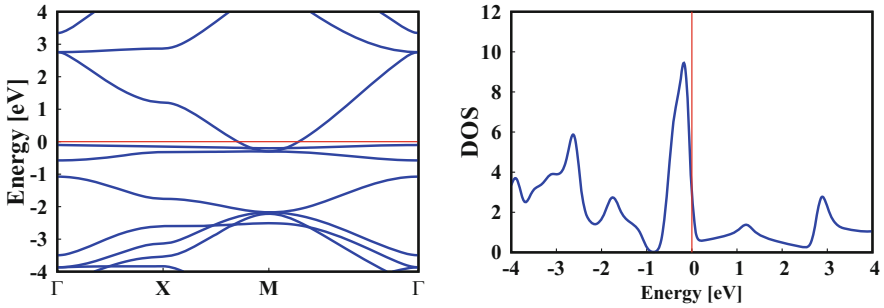

Fig. 5.20 Band structure and DOS of tilene. Fermi level is shifted to zero and reported as a horizontal red line in the left-hand side (bands) and as a vertical red line in the right-hand side (DOS) of the figure

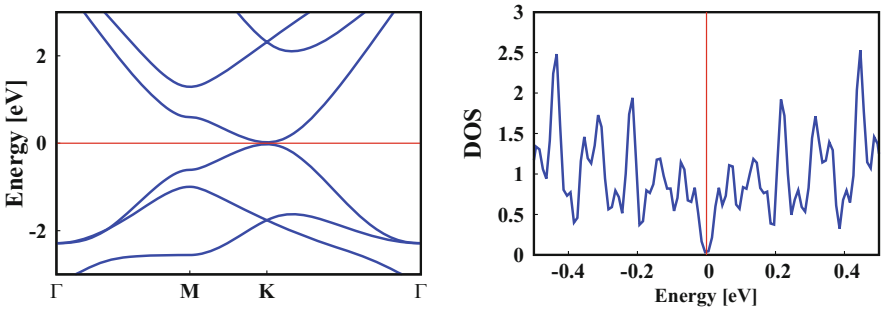

Fig. 5.21 Band structure and DOS of flakene parent. Fermi level is shifted to zero and reported as a horizontal red line in the left-hand side and as a vertical red line in the right-hand side of the figure. In this case we report for the DOS only the zoom near the Fermi energy which is obtained with a Fermi function smeared with a Gaussian of 0.0136 eV width in order to resolve the very low energy band gap

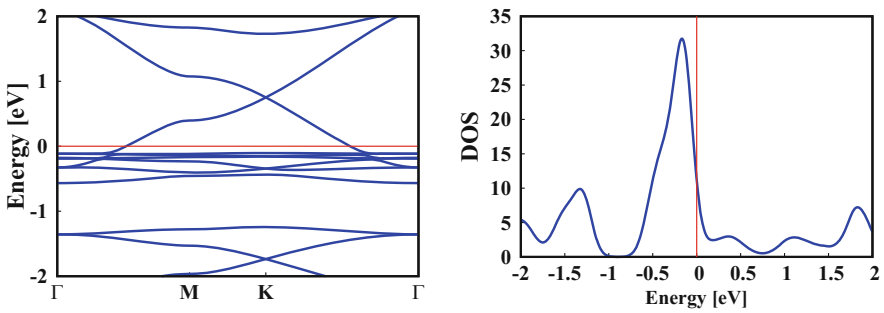

Fig. 5.22 Band structure and DOS of flakene. Fermi level is shifted to zero and reported as a horizontal red line in the left-hand side (bands) and as a vertical red line in the right-hand side (DOS) of the figure

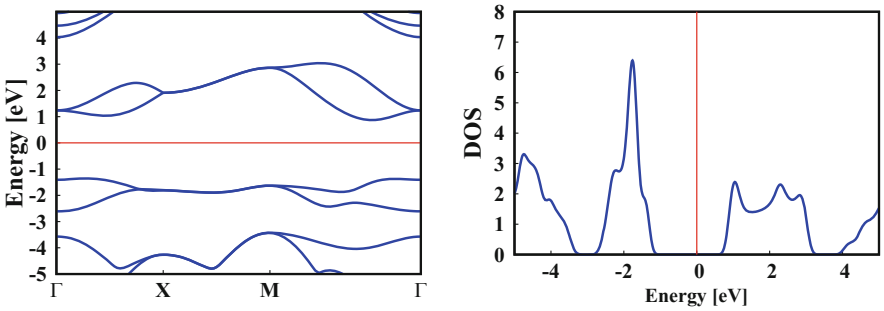

Fig. 5.23 Band structure and DOS of pentagraphene. Fermi level is shifted to zero and reported as a horizontal red line in the left-hand side (bands) and as a vertical red line in the right-hand side (DOS) of the figure

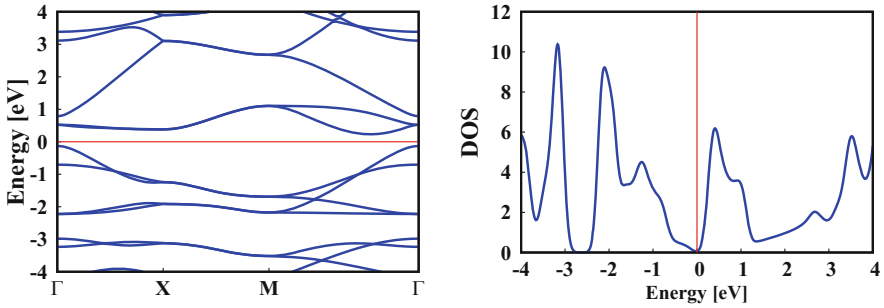

Fig. 5.24 Band structure and DOS of liskene. Fermi level is shifted to zero and reported as a horizontal red line in the left-hand side (bands) and as a vertical red line in the right-hand side (DOS) of the figure

5.3.3 *Mechanical Properties of Two-Dimensional All-Carbon Materials*

To assess the mechanical properties of the daughter and parent structures, one can carry out the ab initio simulations of the elastic stiffness tensor **C**, which in linear approximation represents the proportionality constants between stress and strain, $\boldsymbol{\sigma} = \boldsymbol{\varepsilon}\mathbf{C}$, where $\boldsymbol{\varepsilon}$ is the six-component strain vector and $\boldsymbol{\sigma}$ is the stress tensor. We remind in passing that the Hook's law may be written in tensor notation as $\sigma_i = C_{ij}\epsilon_j$ where $i, j = 1, \ldots, 6$ label the corresponding directions xx, yy, zz, yz, zx and xy, respectively. The first subscript identifies the direction in which the stress is measured, while the second one identifies the direction orthogonal to the plane on which the stress is acting. Since $\sigma_{ij} = \sigma_{ji}$ the independent stress components are six.

The elastic constants C_{ij} can be obtained as follows:

$$C_{ij} = \frac{\partial^2 F}{\partial \varepsilon_i \partial \varepsilon_j} \tag{5.4}$$

where in harmonic approximation (neglecting the thermal electronic contribution) the density function F can be expressed as:

$$F = F_0 + \frac{1}{2} F^{(2)} \varepsilon^2 + o(\varepsilon^3) \tag{5.5}$$

where F_0 and $1/2F^{(2)}\varepsilon^2$ are the static energy of the system and the lattice vibrational contribution, respectively. From the knowledge of the elastic constants, the Young's modulus E, which measures the material stiffness, and the Poisson's ratio ν, which measures the material tendency to expand perpendicularly to the direction of compression, can be computed as $E = (C_{11}^2 - C_{12}^2)/C_{11}$ and $\nu = C_{12}/C_{11}$, respectively.

In Table 5.2 we report the Poisson's ratio and the Young's modulus of all the 2D carbon allotropes discussed in this chapter with some other DFT values found in the literature [76, 80]. We remind that here we deal with two-dimensional structures where the specific mechanical properties should be referred to the area rather than the volume, at odds with the usual approach in 3D solids. Thus, ρ_A is the area density, and the quantities divided by ρ_A, such as E_A/ρ_A, must be understood per area density. The Young's modulus E, in particular, is a measure of the response to tensile or compressive loading and usually is measured in N/m^2 because the load is meant to be applied to an orthogonal cross section of the 3D solid. However, in 2D materials, such as graphene, the load is applied to a thin, in principle, monodimensional stripe because the orthogonal cross section of a two-dimensional solid is a line. Thus, the Young's modulus is measured as a force per unit length (N/m) rather than per unit area, and in order to distinguish this case from the 3D

Table 5.2 The columns report, respectively, the 1D (E_A) and 2D (E, thickness $t = 0.314$ nm) Young's modulus, Poisson's ratio (ν) and area-specific Young's modulus (E_A/ρ_A) of the parent and daughter carbon structures. To evaluate the accuracy of our simulations, we report a comparison with data in the literature where available. In the table the following abbreviations were used: p. = parent, d. = daughter

	E_A (N/m)	E (TPa)	ν	E_A/ρ_A (10^{-3} Nm kg^{-1})
Graphene	340	1.14	0.154	1.79
[76]	349		0.17	
Graphene d.	89.6	0.30	0.631	0.70
[76]	92.6		0.64	
Tilene p.	288	0.96	0.150	1.70
[80]	306		0.13	
Tilene	78.6	0.26	0.607	0.67
Flakene p.	205	0.69	0.263	1.36
[76]	210		0.27	
Flakene	38.6	0.13	0.746	0.36
Liskene	138	0.46	0.508	0.93
Liskene d.	93.1	0.31	0.517	0.75

case, we call it E_A. Of course one can define also the usual Young's modulus E by introducing a fictitious thickness t which for graphene is conventionally chosen equal to the intra-planar distance in solid graphite (0.335 nm). We also remind that at variance with a stable, isotropic, linear elastic 3D material where the bounds on Poisson's ratio are $-1 < \nu < 1/2$, for 2D materials, one can have $-1 < \nu < 1$ [81]. Furthermore, we notice that the Poisson's ratio of tilene, flakene and liskene shows that these materials are almost incompressible.

The most significant quantity to be compared with graphene is of course the specific modulus, that is, the Young's modulus divided by the mass density. In particular, dealing with a bi-dimensional material one can assess the Young's modulus E per area density ρ_A, E/ρ_A. We report this quantity in the last column of Table 5.2. We notice that graphene presents the biggest specific modulus among the materials studied here. Flakene, in particular, displays the lowest density among the investigated structures and shows a major drop in both the absolute and specific elastic moduli, which are from eight to five times lower than graphene. Nevertheless, while we do not find a material outperforming the specific properties of graphene in this respect and, thus, we do observe that the augmentation is only partially an advantageous route to follow in order to increase the specific modulus of graphene-like materials, the difference in the specific Young's modulus is less remarkable than for the absolute values, with the exception of flakene.

In Fig. 5.25 we report the specific biaxial modulus ($E_{bi} = C_{11} + C_{22}$) of the low-density carbon allotropes versus area density. The drop of flakene mechanical characteristics suggests that there is a threshold to the decrease of the density of these carbon-based planar materials, below which the mechanical properties are significantly depleted. Thus, the idea of decreasing the density, retaining the specific mechanical characteristics, can be pursued only to some extent at least as far as the Young's modulus is concerned.

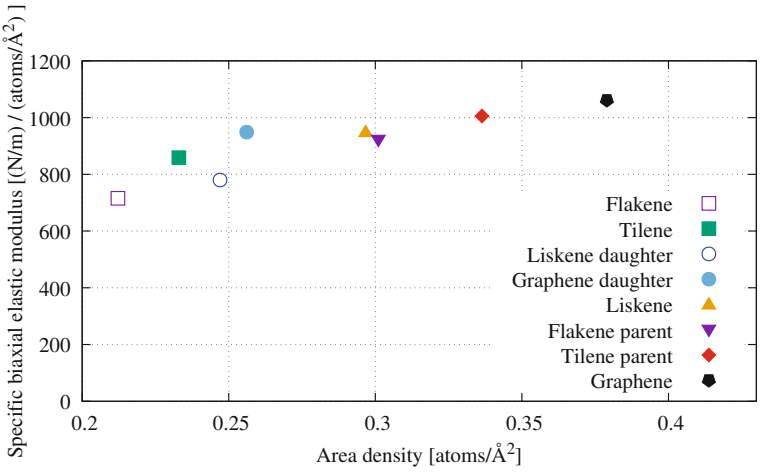

Fig. 5.25 Specific biaxial elastic modulus versus area. (Adapted from Ref. [74])

Further information on the mechanical properties of the graphene-based low-density structures can be obtained by analysing the stress-strain curves from which several quantities can be obtained, such as the absolute fracture strain, tensile strength and toughness.

In Fig. 5.26 we plot the stress-strain curves of these parent and daughter structures along the Cartesian directions x, y, which represent the zig-zag and armchair directions of graphene ribbon, or along the 45° direction owing to the unit cell symmetry of tilene and liskene. The stress-strain characteristics show (i)

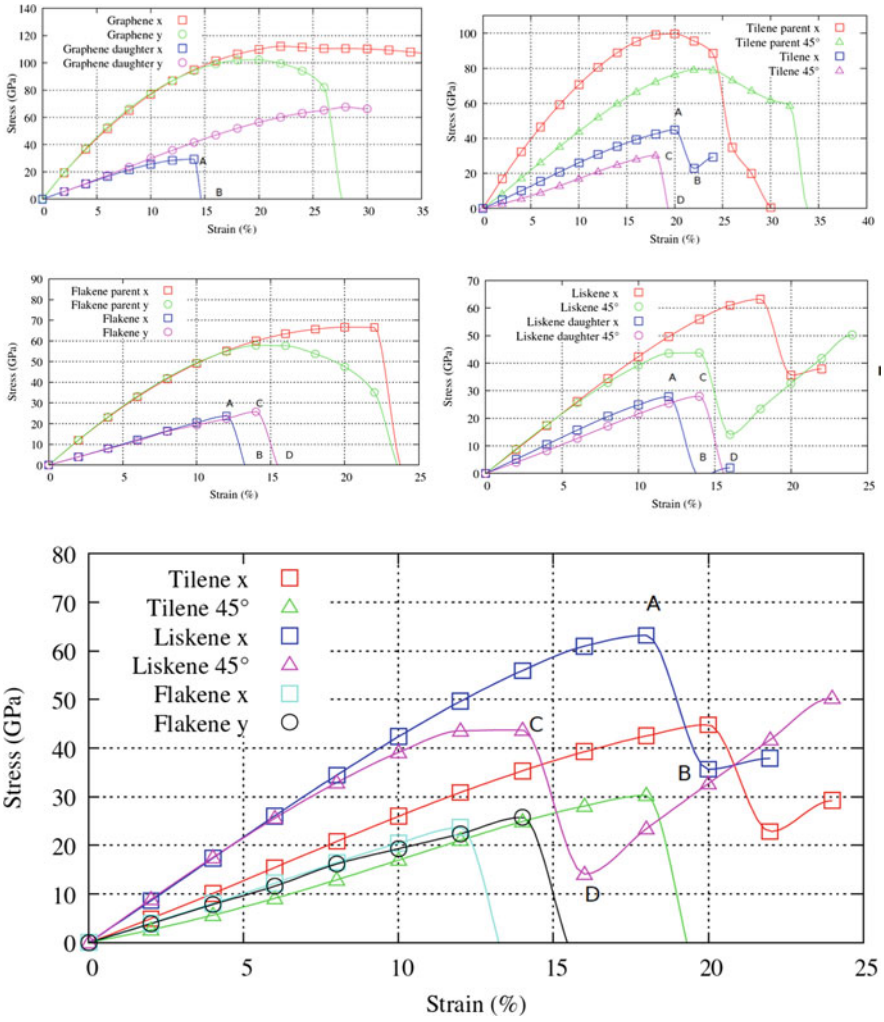

Fig. 5.26 Stress-strain curves of parent and daughter structures along the x-direction (or zig-zag), the y-direction (or armchair) and 45° (diagonal). The differently coloured lines represent the best fits to the ab initio data. (Adapted from Ref. [74])

the anisotropic response of these structures under uniaxial loading along different directions, which results in a nonlinear, hyperelastic constitutive equation; (ii) the significant depletion of the absolute mechanical response from parent to daughter architectures, with a strong decrement in toughness, yield and ultimate strengths (see also Table 5.3); and (iii) that the mechanical response is basically determined by the reaction of triangular (tougher) or square (softer) shapes in the structures.

As a final remark, we point out that the picture so far described concerning the absolute values slightly changes when we look at the specific properties reported in the last two columns of Table 5.3. Indeed, the specific ultimate strength of our novel 2D structures is comparable to graphene or even higher than the latter in the case of the tilene parent. Nevertheless, the trend of the specific toughness, which measures the ability of a material to absorb energy before fracture, is overwhelmingly favourable to graphene with respect to the other structures.

Table 5.3 Fracture strain (first column), strength (second column), strength $\times t$ (third column) and toughness$\times t$ (fourth column) of the parent and daughter planar structures alongside the specific strength and specific toughness (fifth and sixth columns). The conventional thickness of the graphenic materials is considered to be $t = 3.35$ Å. In the table the following abbreviations were used: p. = parent, d. = daughter

	Loading direction	Fracture strain (%)	Strength (GPa)	Strength $\times t$ (N/m)	Toughness $\times t$ ($J\,m^{-2}$)	Specific strength ($MNm\,kg^{-1}$)	Specific toughness ($MJ\,kg^{-1}$)
Graphene	x	>35	112	37.5	>9.83	49.7	> 13.0
	y	26–28	102	34.2	6.51	45.2	8.61
Graphene d.	x	18–20	29.3	9.81	0.83	19.2	1.62
	y	>30	67.7	22.6	>3.63	44.3	> 7.11
Tilene p.	x,y	24–26	99.6	33.4	5.55	49.7	8.27
	45°	32–34	79.1	26.5	5.68	39.5	8.47
Tilene	x,y	20–22	44.8	15.0	1.66	32.3	3.57
	45°	18–20	30.3	10.2	0.92	21.9	1.97
Flakene p.	x	22–24	66.7	22.3	3.37	37.2	5.61
	y	22–24	57.9	19.4	3.01	32.3	5.02
Flakene	x	12–14	23.6	7.92	0.49	18.7	1.16
	y	14–16	25.8	8.63	0.63	20.4	1.49
Liskene	x,y	18–20	63.2	21.2	2.19	35.8	3.70
	45°	14–16	43.8	14.7	1.27	24.7	2.14
Liskene d.	x,y	12–14	27.8	9.32	0.59	18.5	1.20
	45°	14–16	28.0	9.37	0.68	19.0	1.37

5.4 Graphene Pseudospheres

Graphene is a versatile material, which can be arranged in the shape of stripes (nanoribbons), rolled nanotubes or piled up in the direction orthogonal to its plane (graphite). So, it is a legitimate thinking to search for other shapes.

In this respect, Beltrami's pseudosphere, named after the Italian mathematician Eugenio Beltrami who first devised this hyperbolic shape, is a surface of revolution characterized by constant negative Gaussian curvature. Thus, it represents the negative counterpart of the sphere which, at odds, is characterized by constant positive curvature. A Beltrami's pseudosphere can be realized by using carbon (see Fig. 5.27) [82] and represents a portion of the Lobachevsky geometry on a real surface. Its counterpart can be also realized using carbon and is represented by the previously discussed fullerene shape.

Graphene pseudospheres are carbon-based energetically stable molecular structures, which (i) correspond to a non-Euclidean crystallographic group, namely, a loxodromic subgroup of $SL\,(2,\mathbb{Z})$, and (ii) have an unavoidable singular boundary, where planar graphene meets the "trumpet" (see Fig. 5.27).

We devise that owing to its unique electronic properties, a graphene monolayer arranged in a pseudosphere shape can be used to realize a realistic analogue of a quantum field in a curved space-time and thus can be used to test certain scenarios of the physics of curved space-times, e.g. the Hawking-Unruh effect [83]. The latter states that the ground state of an inertial observer is seen in thermodynamic equilibrium with a nonzero temperature by a uniformly accelerating observer. Thus,

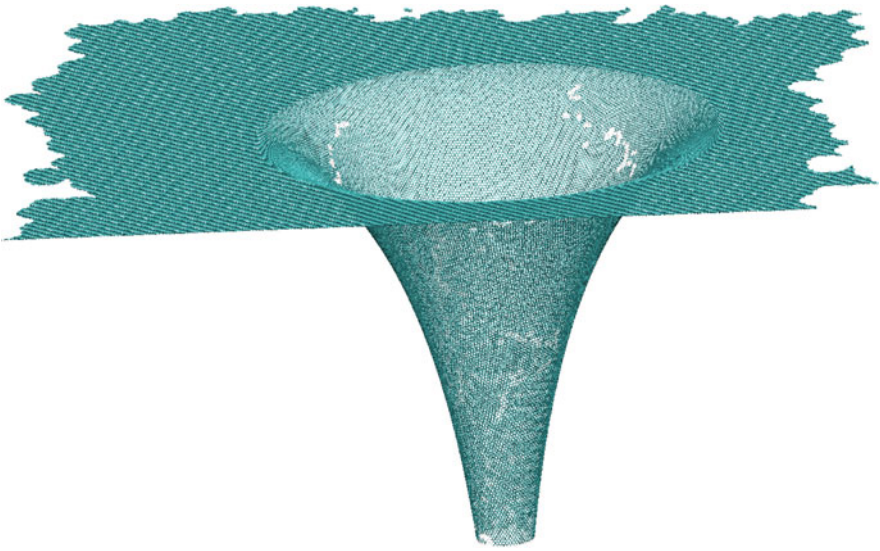

Fig. 5.27 A graphene pseudosphere

a quantum fields in a space-time with a horizon should exhibit a thermal character. This effect is closely related to the local density of states (LDOS) of the graphene pseudosphere, which could be possibly considered as a black hole analogue. Indeed, one can show that by solving the Dirac equation in a continuum space-time, the LDOS has the following analytic behaviour [83]:

$$\rho(E,u,r) = \frac{1}{(\hbar v_F)^2} \frac{\exp^{(-2u/r)}}{\exp^{E/(k_B T_0 \exp^{u/r})} - 1} \tag{5.6}$$

where $T_0 = (\hbar v_F)^2 \exp^{u/r} \rho(0,u,r)$ defines the Hawking temperature, u is the hyperbolic coordinate along the pseudosphere axis, k_B is the Boltzmann constant, v_F is the Fermi energy and r is the pseudosphere maximum radius (event horizon). We remind that the Hawking temperature is the temperature to which black holes, acting as perfect blackbodies, radiate. The electromagnetic radiation, owing to quantum effects, is emitted at a temperature inversely proportional to the mass of the black hole. Only electrons with an energy $E = \hbar v_F / r$, which represents the intrinsic energy scale associated to the pseudosphere, have a long enough wavelength to experience the whole curved surface; hence their contribution to the LDOS is important. We notice that for a graphene pseudosphere with a radius $r = 0.1\,\mu\text{m}$, the Hawking temperature is about 13 K.

5.5 1D Carbon-Based Materials

Carbon nanotubes (CNTs) are graphitic sheets rolled in hollow cylinders with walls made by hexagonal carbon rings (see Fig. 5.4). They often form large bundles and are capped by domed structures at their termination. Two types of CNTs have been synthesized: single-wall carbon nanotubes (SWCNTs or simply CNTs), consisting of a single rolled layer of graphene, and multiwall carbon nanotubes (MWCNTs), made by multiple graphene layers telescoped about one another. CNTs were first isolated and characterized by Iijima in 1991 [8].

CNTs inherit from graphene some of its unique physical and chemical properties, such as structural rigidity, flexibility, strength, and ideal thermal conductivity. Owing to these intrinsic features, 1D all-carbon nanomaterials found a wide variety of applications in molecular electronics and in semiconducting device technologies, such as FET, electrodes, power cables, fibres, composites, actuators, sensors and biosensors [6]. Furthermore, due to their small size and biocompatibility, CNTs express great potential in the emerging field of nanomedicine, e.g. for implantable applications for continuous monitoring of clinically relevant analytes, including glucose, or in food industry and environmental sciences. Finally, due their hollow, curved shape and the large surface/volume ratio, CNTs can be easily doped and functionalized, e.g. using carboxyl (COOH) and/or hydroxyl (OH) groups, to acquire the desired electronic, optical or adsorption properties. At odds with

graphene, however, the electronic properties of single CNTs depend on their chirality. The nanotube chirality is defined by the specific and discrete chiral angles at which graphene sheets are rolled. In particular, the chirality is identified by a couple of numbers (n, m), which define a vector $(C_h = na_1 + ma_2)$ in an infinite graphene sheet that describes how to "roll up" the graphene sheet to make the nanotube. The nanotube diameter $(d = (n^2 + m^2 + nm)^{1/2})$, its density, lattice structure and the electronic characteristics, such as the conductance, depend only on the chirality indexes (n, m). A SWNT is considered metallic, with conductivity showing rectification or ohmic characteristics, if the fraction $(n - m)/3$ is an integer value. Otherwise, the nanotube is semiconducting, with variable energy gaps ranging from a few meV to a few tenths of an eV. In this section we will investigate the electronic properties of small semiconductor CNTs using high-level accuracy many-body perturbation theory. In particular, we use the GW approximation, which assumes that the self-energy of a many-body electron system can be assessed by keeping only the lowest order term in the expansion of the self-energy in powers of the screened interaction W. By doing so the self-energy is written as the product of G, the one-body Green's function, and W, the screened Coulomb interaction [84].

5.5.1 The GW Method for CNTs

Recently, Umari and coworkers have developed a method for performing accurate and well-converged GW calculations in large simulation cells based on reduced basis sets for expressing the polarizability operators [85] and on Lanczos's chains for avoiding sums over unoccupied one-particle states [86]. This scheme, which will be revised in this section, was used for investigating the dependence of electronic band gaps with respect to the tube diameter for a number of semiconducting single-wall zig-zag CNTs, with diameters ranging from 0.56 to 1.27 nm [11, 12].

Beyond the independent electron approximation, the electronic states in a strongly interacting system can be described through a quasi-particle picture in which the behaviour of the bare electron is strongly renormalized by the presence of the other electrons of the system. On the experimental side, this quasi-particle behaviour can be probed via direct and inverse photoelectron spectroscopy. On the theoretical side, MBPT and, in particular, the G_0W_0 approximation [87] represent a rather simple, though accurate approach for addressing quasi-particle calculations on large systems. The G_0W_0 approach allows one to apply many-body perturbative corrections to a starting DFT calculation. Within this method, the quasi-particle energy level E_i for the i-th Kohn-Sham state is obtained from the solution of the following self-consistent one-variable equation:

$$E_i = \epsilon_i + \langle \psi_i | \, \Sigma_c \left(E_i \right) | \psi_i \rangle - \langle \psi_i | \, V_{xc} \, | \psi_i \rangle + \langle \psi_i | \, \Sigma_x \, | \psi_i \rangle \, , \tag{5.7}$$

where ψ_i is the i-th Kohn-Sham eigenstate, ϵ_i the eigenenergy, V_{xc} is the exchange and correlation potential and Σ_c and Σ_x are the correlation and exchange parts

of the self-energy operator, respectively. In this approach, Σ_c is found from the convolution of the one-body Green's function G_0, obtained from DFT calculations, with the correlation part of the screened Coulomb potential W_0^c, obtained at random-phase approximation level (RPA [84]):

$$\Sigma_c\left(\mathbf{r}, \mathbf{r}'; \omega\right) = \frac{1}{2\pi} \int d\omega' G_0\left(\mathbf{r}, \mathbf{r}'; \omega + \omega'\right) W_0^c\left(\mathbf{r}, \mathbf{r}'; \omega'\right). \tag{5.8}$$

Despite the apparent simplicity of this approach, its application requires a considerably larger effort than the starting DFT calculation. In fact, the evaluation of operators, such as G_0 and W_0^c, at many frequencies contains the sum over a large (in principle infinite) number of unoccupied Kohn-Sham states, resulting in a convergency very difficult to be achieved [88]. The approach developed by Umari et al. overcomes these drawbacks by expanding the polarizability and the screened Coulomb interaction operators through a reduced (optimal) basis set [85], which allows us to obtain overall good accuracy. Furthermore, within this method we avoid the sum over unoccupied states by a Lanczos' chains approach [86].

5.5.2 *Band Gap of Model CNTs*

Here, we show the application of this method to the calculations of the electronic band gap of a selected number of semiconducting single-wall zig-zag CNT with chirality indices equal to (7,0), (8,0), (10,0), (11,0), (13,0) (14,0), (16,0). Computational details can be found in Ref. [11], while here we summarize the main results. DFT calculations were performed within the local-density approximation (LDA) [89] using norm-conserving pseudopotentials with single-particle orbitals and charge densities expanded in plane waves. The calculations of the electronic band gaps of the selected CNTs neglect the excitonic effects due to the electron-hole pair formation. Within this approximation, the electronic band gap, usually indicated as E_{11}, corresponds to the energy difference relative to the van Hove singularities appearing in the density of electronic states below and above the Fermi level. The energy difference relative to the gap between the second singularities above and below the Fermi level is referred to as E_{22} (see top panel of Fig. 5.28). However, we remember that experimental measurements of the band gap performed through optical spectroscopies record fluorescence lines that include the correlated motion of electrons and holes, which affects strongly the spectrum. Indeed, in a semiconductor, where excitonic effects are not negligible, the exciton binding energy E_b strongly renormalizes the "electronic or fundamental band gap" E_g, that is, $E_{opt} = E_g - E_b$. Thus, there is a distinction between the optical band gap, which represents the threshold value for photons to be absorbed, and the "electronic or fundamental band gap", which represents the threshold value for creating an electron-hole pair that is not bound together. Therefore, experimental band gaps are dramatically renormalized by this effect and one rather measures

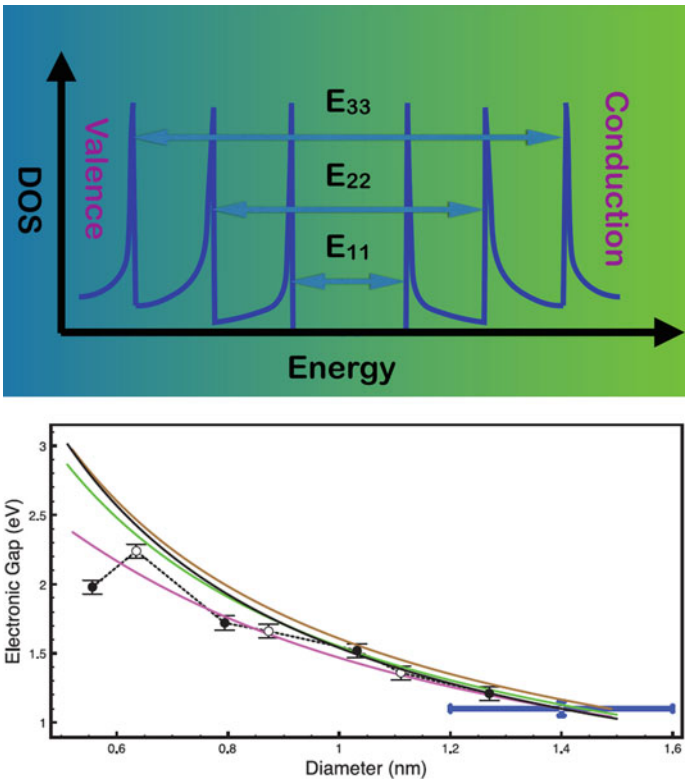

Fig. 5.28 Top panel: scheme of the electronic transitions in semiconductor CNTs. Bottom: electronic band gaps for semiconducting CNT of diameter d_t, corresponding to optical transitions. Full black circles: GW results for mod1 zig-zag CNT. White circles: GW results for mod2 zig-zag CNT. The error bars refer to the total estimated accuracy of the GW energy levels with the dashed black line guiding the eye. Black line: fit of GW results for large CNT (see text). Theoretical estimates for semiconducting CNT as by: Eqs. 5.9 (green line), 5.10, and 5.11 for zig-zag CNT of mod1 (purple line) and mod2 (brown line) species. The experimental STS measurement of Ref. [91] is reported together with error bars (blue line). (Adapted from Ref. [11])

the energies of the lowest (E_{1A_2}) and of the second lowest (E_{2A_1}) optically active exciton states and their difference. We remind that E_{1A_2}, E_{2A_1} label the excitonic states by $n\Gamma$, where $n-1$ is the number of nodes in the hydrogenic function that represents the exciton and provides a physically grounded guess to the ordering in which the different exciton states might appear (higher n corresponds to higher excitonic states), and Γ labels its irreducible representation. For example A_1 is the totally symmetric representation of the symmetry group of the chiral nanotubes [90]. Moreover, in some specific zig-zag small diameter CNTs, such as the (7,0) and (8,0) CNTs, the band gap corresponding to the optically active excitons may be even energetically higher than the minimum energy semiconducting band gap. As such, the experimental values of the electronic band gap do not match the calculated ones.

In principle, scanning tunneling spectroscopy (STS) could give a direct measure of electronic band gaps. However, in such a case screening effects arising from the metal substrate on which the CNT is dispersed become important. A model of these screening effects was tried, but the final error bars are quite large [91]. Therefore, accessing to electronic band gaps usually relies both on optical measurement and theoretical modelling.

The edges for fluorescence emission have been measured for several CNTs, and the dependence on the tube diameter has been fitted with model functions [92, 93]. For example, Dukovic et al. [93] reports the following behaviour for the optical first emission gap E_{op}^{11}:

$$E_{\text{op}}^{11} = \frac{1.11}{d_t + 0.11}\text{eV} \tag{5.9}$$

where the diameter d_t is expressed in nm. A further formula relating the electronic gap vs. CNT diameter is obtained by Weisman and Bachilo [92] as follows:

$$\begin{aligned} E_{\text{op}}^{11}(\text{mod1}) &= \frac{1.241 * 10^3\,\text{eV}}{157.5 + 1066.9 d_t} - \frac{0.0957\,[\cos(3\alpha)]^{1.374}}{d_t^{2.272}} \\ E_{\text{op}}^{11}(\text{mod2}) &= \frac{1.241 * 10^3\,\text{eV}}{157.5 + 1066.9 d_t} + \frac{0.04307\,[\cos(3\alpha)]^{0.886}}{d_t^{2.129}} \end{aligned} \tag{5.10}$$

where α is the chiral angle [94] and $mod(n - m, 3) = 1$ (mod1 species, such as the (7,0), (10,0), (13,0) and (16,0) CNTs) or $mod(n - m, 3) = 2$ (mod2 species, such as the (8,0), (11,0) and (14,0) CNTs). For zig-zag CNTs one has $\alpha = 0$.

By solving a model electron-hole Hamiltonian [95], which delivers exciton binding energies in agreement with accurate GW-Bethe-Salpeter calculations [96], the semiconducting CNT binding energy $E_{1A_2}^{\text{bind}}$ for the lowest $1A_2$ exciton can be expressed as:

$$E_{1A_2}^{\text{bind}} \approx \frac{0.55}{d_t}\text{eV} \tag{5.11}$$

The electronic band gap E^{11} can thus be obtained by Eqs. 5.10 and 5.11 as:

$$E^{11} = E_{\text{op}}^{11} + E_{1A_2}^{\text{bind}} \tag{5.12}$$

In Table 5.4 we report the calculated band gaps relative to optically allowed electronic transitions for the CNTs under investigation. In the (7,0) and (8,0) CNTs, the fundamental electronic band gap refers to transitions that are not optically allowed. We note that our calculated value of the fundamental gap for the (8,0) CNT, equal to 1.80 eV, is in good agreement with previous GW calculations from Spataru and coworkers [10] giving 1.75 eV and from Kang et al. [97] giving 1.51 eV. The calculated gap for the (8,0) CNT relative to optically allowed transitions (2.24 eV)

Table 5.4 Electronic band gaps from LDA and GW calculations for the semiconducting zig-zag CNTs under investigation with chirality indices (m,n) (first column). The gaps are relative to optically allowed transitions. When the electronic band gap for optically allowed transitions differs from the fundamental electronic band gap, we have reported also the latter in parenthesis

(m,n)	LDA (eV)	GW(eV)
(7,0)	0.16	1.98 (1.47)
(8,0)	0.5	2.24 (1.80)
(10,0)	0.80	1.72
(11,0)	0.95	1.66
(13,0)	0.65	1.52
(14,0)	0.74	1.36
(16,0)	0.56	1.21

is in good agreement with the value of 2.54 eV from Spataru et al. [10] and with the value of 2.14 eV previously found by Taioli et al. with a preliminary version of the method here used [12].

Furthermore, our calculated value of the fundamental electronic gap for the (7,0) CNT is 1.47 eV, which is higher than the value of 0.60 eV reported in a previous study by Miyake et al. [98] and the value of 1.22 eV obtained by Taioli et al. [12]. The latter values are reported for the case of zig-zag semiconducting CNT for both mod1 and mod2 species. We note that a good agreement of our calculated GW electronic gaps with the previous estimates is found for the investigated diameter sizes, excluding the (7,0) CNT. In this case, curvature effects due to the small size of the CNT become important and σ and π states mix into hybrids with partly sp^2 and sp^3 character. It should be noted that LDA results, not reported in this figure, are far from the theoretical/experimental lines as one can see in Table 5.4. The GW results for the largest CNTs are also in excellent agreement with the STS measurement of the electronic gap by Lin et al. [91] for the case of 1.4 nm diameter CNT.

Nevertheless, CNTs used in electronic devices have of course diameters larger than those studied here. It is thus interesting to extrapolate our GW results to obtain a model electronic gap-diameter function. To this goal, we fitted our GW results for CNT larger than 1.0 nm with the simple relation $E^{11} = \frac{a}{d_t}$ pointing towards a closed gap in the large diameter limit as expected from zero-gap graphene. We find a value $a = 1.54\,\text{eV}\times\,\text{nm}$.

5.6 3D Carbon-Based Structures

As a last step into the "dimensional ladder", we finally discuss a number of properties of all-carbon 3D architectures, notably the charge transport in diamond and graphite, and the mechanical and thermal properties of carbon foams.

5.6.1 Two Case Studies: Transport Properties of Diamond and Graphite

First we consider the electron transport properties from reflection electron energy-loss spectroscopy (REELS) measurements of diamond and graphite films. Indeed, while graphene and other 2D materials are considered the most promising replacements of silicon in future electronics [99], difficulties in finding scalable, cheap and safe techniques to grow high-quality graphene sheets currently hamper the hypothetical potential of this 2D material. Furthermore, in order to use graphene in microelectronic applications, a band gap must be opened [47, 48]. In this regard, other naturally occurring allotropic forms of carbon, such as diamond and graphite, could be used as viable candidates for an all-carbon electronics.

For example, diamond, owing to several ideal characteristics, such as large thermal conductivity, high charge mobility, wide band gap, optical isotropic structure and robustness, can be considered also a competitor in the carbon-based revolution for enhancing the performances of electronic devices. On the other side, graphite is the most stable naturally occurring carbon allotrope, characterized by a layered architecture with both strong in-plane sp^2-bonds, comparable in cohesive energy to those found in diamond, and weak interplanar bonds that make it soft and malleable as well as anisotropic to external perturbations. Furthermore, graphite shows optimal heat, large electrical conductivity and high strength and stiffness even above 3000 °C.

5.6.1.1 The Dielectric Response of Materials

The study of charge transport in solids is of paramount importance in several applications, ranging from materials characterization via electron microscopy and spectroscopy to the production of optimally designed electronic devices by controlling the energy transfer scattering processes that occur in different energy ranges [100–102].

In this regard, we notice that the analysis of the collision events taking place within a solid is based on the accurate assessment of the frequency-dependent dielectric function, which links microscopic properties, such as the band structure of solids, to macroscopic features that are the direct outcome of spectroscopic experiments, such as the absorption coefficient, the surface impedance or the electron energy loss. Indeed, the dielectric function $\epsilon(W, q)$, where W is the energy loss and q the transferred momentum, provides access to the full electronic excitation spectrum of the material in both energy and momentum space. Furthermore, we observe that the dielectric function is the only material property necessary to assess the inelastic cross sections. In particular, the real part of the dielectric function $\Re[\epsilon]$ describes the screening (i.e. the polarizability) of the medium, while the imaginary part $\Im[\epsilon]$ the absorption. In general, single-electron excitations, such as excitons, interband excitations and core-hole ionizations, are connected to the maxima of

$\epsilon(W, q)$, while collective many-electron excitations (plasmons), which are typical of the condensed phase, are related to the minima of $\epsilon(W, q)$, which usually appear if the two conditions $\Im[\epsilon(W, q)] \ll 1$ and $\Re[\epsilon(W, q)] = 0$ occur. From the knowledge of $\epsilon(W, q)$, one can calculate observables of paramount importance for designing novel optical and electronic devices, such as inelastic mean free path, stopping power, plasmons and secondary electron spectra.

To compute the dielectric function dependence on the energy and transferred momentum, one can proceed along three different routes [18]. First, one may use a semiclassical approach, whereby one assumes the knowledge of the long wavelength or optical limit of the dielectric function ($q \rightarrow 0$); this information is usually provided by experimental measurements of optical absorption [103], transmission electron energy-loss experiments [104, 105] or ab initio simulations [106]. To go beyond the optical limit, one can extend the dielectric response to finite momenta by using a Drude-Lotentz (DL) model. In this approach, the dielectric function is approximated by a number of damped harmonic oscillators with frequencies equal to the plasmon frequencies obtained by fitting experimental data [107, 108] and a friction-type force to simulate general dissipative processes; this extension of the dielectric response to finite momenta with the DL functions represents the most accurate approach available [109]. The second viable approach concerns the ab initio calculation of the dielectric response for vanishing momentum transfer and then its extension to finite momenta by a DL model. Finally, one could assess the dispersion law of the dielectric function at finite momentum q by using a full ab initio (AI) approach, based on time-dependent density functional simulations [110] in the linear-response regime (LR-TDDFT) [111–113].

The so-derived dielectric functions are used as input for a Monte Carlo description of the inelastic scattering probability to calculate the energy loss of electrons along their path within the solid. The comparison between our simulated and recorded REELS allows us to assess the impact that external tuneable parameters and semiclassical assumptions might have on the accuracy of simulated spectral line shapes for the characterization of 3D carbon-based materials.

Frequency- and Momentum-Dependent Dielectric Function

The microscopic representation of electromagnetic fields in interaction with periodic crystals can be described in terms of the microscopic dielectric function $\epsilon_{\mathbf{G},\mathbf{G}'}(\mathbf{q}, W) = \epsilon(\mathbf{q} + \mathbf{G}, \mathbf{q} + \mathbf{G}', W)$, where $\mathbf{G}$ and $\mathbf{G}'$ are the lattice vectors in the reciprocal space, while $\mathbf{q}$ is the transferred momentum contained in the first Brillouin zone. The relation between the latter quantity, which is usually the outcome of ab initio simulations, and the experimentally measurable macroscopic dielectric function is the following [114, 115]:

$$\epsilon(\mathbf{q}, W) = \left[\epsilon^{-1}_{\mathbf{G}=0,\mathbf{G}'=0}(\mathbf{q}, W)\right]^{-1} \tag{5.13}$$

where the $G = G' = 0$ limit results in an average over the unit cell of the corresponding microscopic quantity, which can exhibit rapid oscillations at the atomic level.

The dielectric function provides access to the differential inelastic scattering cross section σ_{inel}, since [116]:

$$\frac{d\sigma_{\text{inel}}}{dW} = \frac{1}{\rho\pi a_0 T}\int_{q_-}^{q_+}\frac{dq}{q}\text{Im}\left[-\frac{1}{\epsilon(q,W)}\right] \tag{5.14}$$

where a_0 is the Bohr radius, ρ the atomic density of the target material, q is the transferred momentum and the integration limits are $q_- = \sqrt{2m}(\sqrt{T} - \sqrt{T-W})$ and $q_+ = \sqrt{2m}(\sqrt{T} + \sqrt{T-W})$. Equation 5.14 states that at a given incident electron energy and scattering angle, the negative inverse of the imaginary part of the dielectric function is the electron energy loss in a transmission experiment, which is defined as follows:

$$\text{ELF} = \text{Im}\left[-\frac{1}{\epsilon(\mathbf{q},W)}\right] \tag{5.15}$$

This quantity is called the energy-loss function (ELF) and depends only on the material specific properties. At variance, the inelastic scattering cross section is also a function of the incident electron beam kinetic energy. Finally, the total electron mean free path λ is given by [117]:

$$\lambda = \frac{1}{\rho(\sigma_{\text{el}} + \sigma_{\text{inel}})} \tag{5.16}$$

where σ_{inel} is the total inelastic mean free path, obtained by integrating Eq. 5.14 over the energy range, and σ_{el} is the elastic scattering cross section. In general, the momentum transferred by electrons upon collision is neither negligible nor constant in different energy ranges, and the material dispersion relation (E vs. $\mathbf{q}$) shows generally a non-flat behaviour. Thus, one needs to evaluate the dielectric function also out of the optical limit before calculating the expression in Eq. 5.15.

First, we notice that Eq. 5.15 is obtained under the assumptions of validity of the first-order Born approximation, which works for sufficiently fast, point-like, particles weakly deflected by potential scattering. These requirements turn out to be met when the incident particle kinetic energy is $T\,(\text{eV}) \gg 13.6Z^2 \simeq 490\,\text{eV}$, which is the typical situation of valence electrons [118]. Nevertheless, we will show applications of Eq. 5.15 also to slow (up to a few tens of eV) secondary electron emission.

Second, we observe that to invert the dielectric matrix in Eq. 5.15, one needs also to assess the dependence on finite momentum transfer $\mathbf{q}$. In this regard, we now revise the two different approaches that have been devised to this purpose; these are the DL and the full AI models.

Drude-Lorentz Model

Within the DL model, the material response to an applied uniform external electromagnetic field is approximated by considering the target screening electrons as harmonic oscillators of frequency $\omega_n = \frac{E_n}{\hbar}$, where E_n is the plasmon energy. Charge oscillations are damped via a damping term Γ_n, which introduces friction-like forces affecting the oscillatory harmonic motion.

Outside the optical domain, the ELF is extrapolated to nonvanishing momenta by using a quadratic dispersion law [109, 118, 119], which basically assumes that the valence electrons in the solid can be considered as a noninteracting homogeneous gas. The plasmon energy is expanded to second order in q as follows:

$$E_n(q \neq 0) = E_n(q = 0) + \frac{\hbar^2 q^2}{2m} \tag{5.17}$$

The ELF is finally expressed as a sum over all oscillators of q-dependent generalized DL functions with a full-width-half-maximum Γ_n [118, 120, 121]:

$$\mathrm{Im}\left[-\frac{1}{\epsilon(q, W)}\right] = \sum_n \frac{A_n \Gamma_n W}{(E_n^2(q) - W^2)^2 - (\Gamma_n W)^2} \tag{5.18}$$

where A_n is the oscillator strength of the nth-oscillator which are obtained by fitting procedures of optical data. We remind that the f-sum rule must be exactly satisfied by the Drude dielectric function [122].

Ab Initio Simulations

The dielectric function of materials can be also obtained from ab initio simulations using a TDDFT approach in the linear-response (LR-TDDFT) approximation [111].

In LR-TDDFT simulations, one aims at calculating the polarization function $\chi(\mathbf{r}, t, \mathbf{r}', t')$ relating the perturbation of the density δn at $(\mathbf{r}, t)$ due to a small change of the external potential δv_{ext} at $(\mathbf{r}', t')$:

$$\delta n(\mathbf{r}, t) = \int dt' \int d^3 r' \chi(\mathbf{r}, t, \mathbf{r}', t') \delta v_{\mathrm{ext}}(\mathbf{r}', t') \tag{5.19}$$

The many-body response function $\chi(\mathbf{r}, t, \mathbf{r}', t')$ can be obtained by the independent particle polarizability $\chi_{KS}(\mathbf{r}, t, \mathbf{x}, \tau)$ via a Dyson-type equation as follows:

$$\chi(\mathbf{r},t,\mathbf{r}',t') = \chi_{\mathrm{KS}}(\mathbf{r},t,\mathbf{r}',t')\Big\{\int d\tau \int d^3x \int d\tau' \int d^3x' \\ \chi_{\mathrm{KS}}(\mathbf{r},t,\mathbf{x},\tau)\Big[\frac{\delta(\tau-\tau')}{|\mathbf{x}-\mathbf{x}'|} + f_{\mathrm{xc}}(\mathbf{x},\tau,\mathbf{x}',\tau')\Big] \\ \chi(\mathbf{x}',\tau',\mathbf{r}',t')\Big\} \tag{5.20}$$

where $f_{\mathrm{xc}}(\mathbf{r},t,\mathbf{r}',t') = \frac{\delta v_{\mathrm{xc}}(\mathbf{r},t)}{\delta n(\mathbf{r}',t')}\Big|_{n_{\mathrm{gs}}(\mathbf{r},t)}$ is the energy-dependent exchange-correlation kernel. The independent particle response function χ_{KS} is calculated usually by solving the standard Kohn-Sham equations. As for static DFT, the time-dependent exchange-correlation potential is unknown. Thus, calculations of $\chi(\mathbf{r},t,\mathbf{r}',t')$ usually rely on the so-called adiabatic local-density approximation (ALDA) in which the time dependence of the functional is neglected [110]. However, in systems where excitonic effects are expected to have a strong influence on spectral features due to an ineffective electronic screening, e.g. in insulators such as diamond, the use of a bootstrap kernel [125] that includes effects beyond the RPA is necessary.

Assuming translational invariance, the ELF can be computed inserting Eq. 5.13 into Eq. (5.15). The inversion procedure can be cumbersome for large basis sets and large k-point grids. Thus, wherever possible the most viable option is to assess the microscopic dielectric matrix by inverting only the head of the matrix, which means to neglect the off-diagonal elements ($\epsilon_{\mathbf{G},\mathbf{G}'}(\mathbf{q},W)$, $\mathbf{G},\mathbf{G}' \neq 0$) for all $\mathbf{q}$ [115]. These off-diagonal terms include the fluctuations of the fields on atomic scale, called the local field effects (LFE). Nevertheless, for highly inhomogeneous or strongly locally polarizable systems, such as in the case of diamond and graphite, strong microscopic local fields can exist, and thus LFE can play a significant role in the description of the dielectric properties [126], particularly at small wavelengths, to the point of invalidating even qualitative results. This is the case, for example, of our 3D carbon-based materials, and, thus, we will include LFE in our analysis. With the inclusion of the LFE, one can show that the dielectric function in reciprocal space is [127]:

$$\epsilon^{-1}_{\mathbf{G},\mathbf{G}'}(\mathbf{q},W) = \delta_{\mathbf{G},\mathbf{G}'} + v^{s}_{\mathbf{G},\mathbf{G}'}(\mathbf{q})\chi_{\mathbf{G},\mathbf{G}'}(\mathbf{q},W) \tag{5.21}$$

where $v^{s}_{\mathbf{G},\mathbf{G}'}(\mathbf{q}) = \frac{4\pi e^2}{|\mathbf{q}+\mathbf{G}||\mathbf{q}+\mathbf{G}'|}$ is the Fourier transform of the Coulomb potential and $\chi_{\mathbf{G},\mathbf{G}'}(\mathbf{q},W)$ is the microscopic polarizability.

ELFs and Related Observables of Diamond and Graphite

While for computational details we refer to Ref. [64], using LR-TDDFT we calculated the ELFs of diamond and graphite according to Eq. 5.15. In the top panels of Fig. 5.29, we report the ELFs of diamond (left) and of graphite (right) in comparison to the Drude-Lorentz approach (black lines).

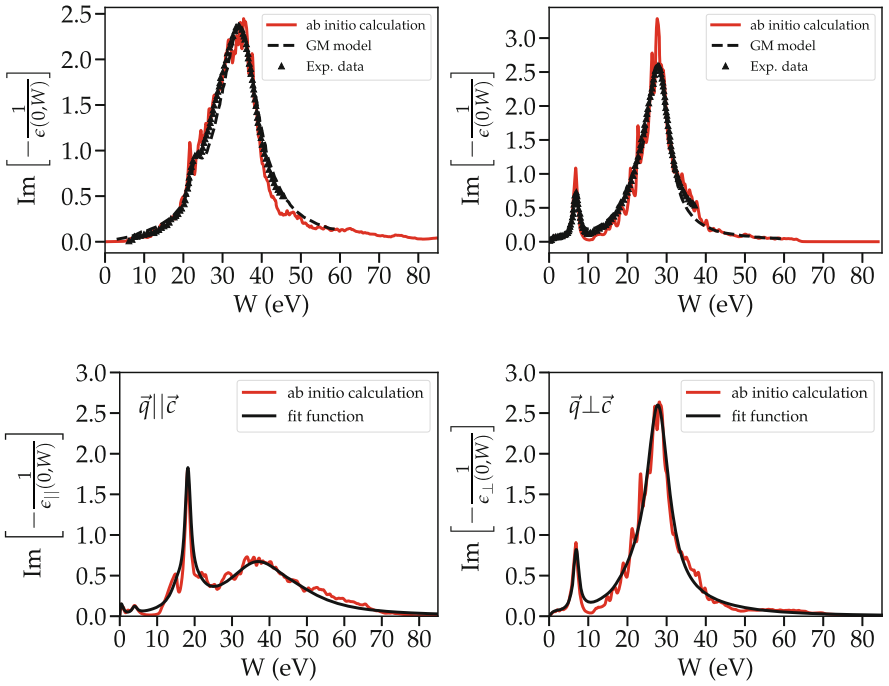

Fig. 5.29 Top panels: Comparison between the ELF of diamond (left) and graphite (right) in the optical limit obtained from AI simulations (continuous red curve), experimental data from Refs. [104] and [105] (black triangles) and fit obtained with the model of Garcia-Molina et al. [123] (dashed black line). Bottom panels: ELF of graphite from AI simulations along the direction $q||c$ (left) and $q \perp c$ (right). (Adapted from Refs. [18] and [64])

Nevertheless, in the case of graphite, one should also take into account the anisotropic structure. This can be achieved by calculating the inverse of the total inelastic mean free path $\Lambda_{inel} = \lambda_{inel}^{-1}$ and the energy loss W as a linear combination along the two directions, respectively, orthogonal ($\perp$) or parallel ($||$) to the vector $\boldsymbol{c}$ pointing towards the direction orthogonal to the graphite plane, as follows [64]:

$$\Lambda_{inel} = f\cos^2(\theta)\Lambda_{||} + [(1-f) + f\sin^2(\theta)]\Lambda_{\perp} \tag{5.22}$$

$$W = f\cos^2(\theta)W_{||} + [(1-f) + f\sin^2(\theta)]W_{\perp} \tag{5.23}$$

where f is an anisotropy parameter in the range $[0:1]$ determined so to obtain the best agreement between theoretical and experimental spectra and θ is the angle between $\boldsymbol{c}$ and $\boldsymbol{q}$. This parameter is put in place to favour the electron motion in the planar direction ($q \perp c$).

In the bottom panels of Fig. 5.29, the contributions to the ELFs of graphite are resolved in the direction parallel $q||c$ (left) and perpendicular $q \perp c$ (right) to the graphite plane obtained from AI simulations (and relevant fits). Finally, in Fig. 5.30 we report the parallel (left panel) and orthogonal (right panel) contributions to the

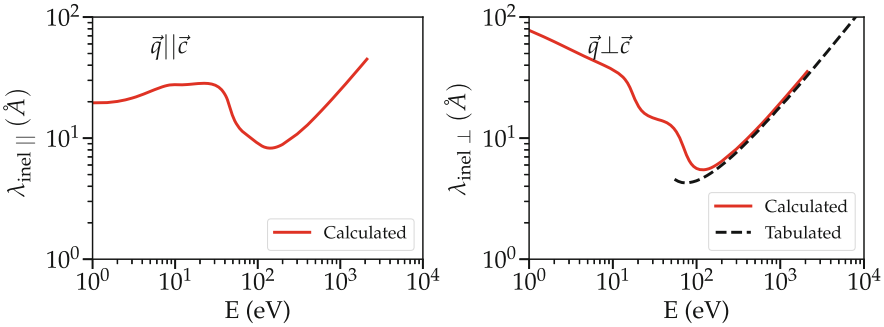

Fig. 5.30 Inelastic mean free path along the parallel (left panel) and orthogonal (right panel) directions of the transferred momentum $\boldsymbol{q}$ in graphite. For $\boldsymbol{q} \perp \boldsymbol{c}$, the calculated values are compared with the data by Tanuma et al. (dashed lines) [124]. (Adapted from Ref. [64])

inelastic mean free path in graphite. These quantities are then used as input to a Monte Carlo approach of the charge transport within solids.

5.6.1.2 Theory of Monte Carlo Simulations

The transport of electrons within a material can be simulated by a classical MC approach, assuming that the non-relativistic electron beam wavelength is small with respect to interatomic separation [118] and that the scattering cross sections for the different processes occurring within materials are known.

At this level the target is assumed to be semi-infinite, homogeneous and amorphous, the latter conditions supporting the assumption of incoherent scattering between different events. In our transport model, we consider a monoenergetic N-electron beam impacting on the target with kinetic energy T and angle of incidence θ with respect to the surface normal.

Electrons can undergo elastic and inelastic scattering. The scattering is usually elastic when electrons scatter nuclei with far heavier mass, and only a trajectory change by an angle θ is recorded. In this case, the elastic cross section σ_{el} is calculated by using the Mott theory, which is based on the solution of the Dirac equation in a central field [117]. In contrast, inelastic scattering processes resulting in both an energy loss W and a directional change θ are mainly due to electron-electron interactions.

Our MC algorithm proceeds by assuming that the path travelled by a test charge between two subsequent collisions is Poisson-distributed, so that the cumulative probability that the electron goes a distance Δs before colliding is given by:

$$\Delta s = -\lambda \cdot \ln(r_1) \tag{5.24}$$

The random numbers r_1, as well as all random numbers employed in our MC simulations, are sampled in the range [0,1] with a uniform distribution. A second

random number r_2 is compared with the elastic ($p_{\text{el}} = \frac{\lambda_{\text{el}}}{\lambda\text{el}+\lambda\text{inel}}$) and inelastic ($p_{\text{inel}} = 1 - p_{\text{el}}$) scattering probabilities to determine whether the scattering is elastic ($r_2 < p_{\text{el}}$) or inelastic ($r_2 \geq p_{\text{el}}$). The algorithm to determine which move is accepted or refused resembles the Bortz-Kalos-Lebowitz kinetic Monte Carlo approach [128] rather than the typical Metropolis algorithm.

The outcome of an elastic interaction is given by the trajectory deflection of an angle θ' with respect to the direction before the collision, which can be computed by equalizing the following cumulative elastic probability with a third random number r_3:

$$P_{\text{el}}(\theta', T) = \frac{1}{\sigma_{\text{el}}} 2\pi \int_0^{\theta'} \frac{d\sigma_{\text{el}}}{d\theta} d\theta = r_3 \tag{5.25}$$

On the other hand, inelastic processes are dealt with by computing the inelastic scattering probability as:

$$P_{\text{inel}}(W, T) = \frac{1}{\sigma_{\text{inel}}} \int_0^{W} \frac{d\sigma_{\text{inel}}}{dW'} dW' = r_4 \tag{5.26}$$

As customary in electronic transport MC calculations, the maximum energy loss corresponds to half of the kinetic energy of the incident electron, to comply with the indistinguishability principle of identical particles. To determine the energy loss W, we generate a database of P_{inel} values for different W and T, and we equalize the integral in Eq. 5.26 to a random number r_4.

Eventually, scattered electrons can be ejected from the target. This ejection can be assessed by a quantity that is called the secondary emission yield (δ). The latter is given by the ratio between the number of secondary electrons emitted from the target material and the number of electrons of the primary beam. The assessment of the secondary electron spectral features is particularly important in imaging techniques [129, 130]. In their way out of the solid, the electrons lose further energy to overcome the potential barrier E_{A} (electron affinity or work function) at the surface of the material. This process can be modelled as scattering by a potential barrier. Thus, the transmission coefficient can be computed as follows:

$$t = \frac{4\sqrt{(1 - E_{\text{A}}/(T \cdot \cos^2\theta'_z))}}{(1 + \sqrt{(1 - E_{\text{A}}/(T \cdot \cos^2\theta'_z))})^2} \tag{5.27}$$

where t represents the probability that the electron leaves the sample's surface and θ'_z is the incident angle with respect to the surface normal. Finally, by comparing this transmission coefficient with a random number r_5, electrons are (or are not) emitted into the continuum with a kinetic energy lowered by the work function E_{A} whenever $t \geq r_5$ ($t < r_5$). By definition, emitted electrons emerging with kinetic energies below 50 eV are called secondary electrons. The Monte Carlo routines used

for performing these simulations are embedded in the in-house developed code suite *SURPRISES* [131–133].

5.6.1.3 Monte Carlo Simulations of Energy-Loss Spectra and Secondary Electron Yield

Diamond

To compare our experimental REELS data of diamond with the three different models of ELF presented above, we performed Monte Carlo (MC) simulations following the scheme reported in Sect. 5.6.1.2. In our MC simulations, diamond crystals are approximated by a homogeneous system with density 3.515 g/cm^3 [123]. Thus, in our simulations we assume that the ELF is almost similar in all directions, and thus we can retain our simulated ELF along the ΓL direction only for calculating the energy-loss spectra. The band gap of diamond was set equal to 4.16 eV. The electron beam direction is orthogonal to the target surface, and the initial kinetic energy ranges from 250 to 2000 eV. The number of impinging electrons is 10^9.

First, we notice that in our treatment we define more generally as backscattered electrons those beam electrons that are reflected back out of the specimen after both elastic and inelastic collisions. In Fig. 5.31 spectra of backscattered electrons simulated in terms of the three different models of the ELF are compared with our REELS experimental data. Simulated and experimental spectra present the σ plasmon peak at ∼35 eV, related to the four valence electrons of the equivalent covalently bonded carbon atoms. This finding is in agreement with the ELF function in the top left panel of Fig. 5.29, showing a maximum at about the same energy.

Furthermore, the two-plasmon excitation at higher energy (∼70 eV) in the experimental spectrum is also present in our MC simulations. We observe that while the MC simulations carried out using the dispersion law of Eq. 5.17 show a blue shift with respect to experimental data, the use of a full AI approach results in a better

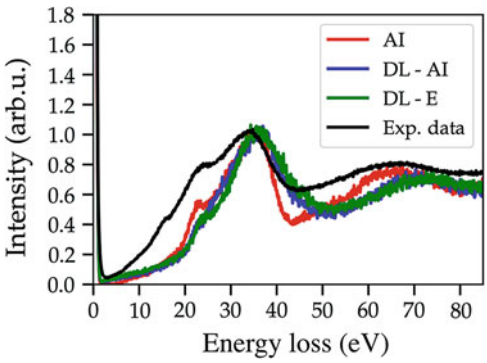

Fig. 5.31 REELS of diamond: experimental data are reported in black, while simulated results using the three different dielectric models are sketched in red (AI), blue (DL-AI) and green (DL-E). Electron beam kinetic energy is 1000 eV. Data are normalized with respect to the σ plasmon peak. (Adapted from Ref. [18])

agreement with experiments. We can conclude that at least in the case of insulators, due to the strongly inhomogeneous electron density and, thus, to the complexity of the dielectric response, the DL model is quantitatively less accurate than a full AI approach in the prediction of the experimental REELS. This behaviour worsens at higher transferred momenta, where particle-hole excitations, rather than collective plasma excitation, come into play. Single-particle excitations generally cannot be well described by a simple RPA or by the DL model of the ELF, while TDDFT AI simulations are also able to take into account these spectral features.

Graphite

Highly oriented pyrolytic graphite (HOPG) crystals were considered to have a density of 2.25 g/cm^3 [123]. The band gap was set equal to 0.06 eV according to our DFT calculations. MC simulations of REELS were carried out using the three different approaches to the calculation of the ELF mentioned above, with a number of electrons in the beam equal to 10^9. Initially, only the in-plane component of the energy-loss function was dealt within the calculation (i.e. we considered the component of the momentum transfer only along the graphite layers). In Fig. 5.32 we report the MC REELS simulations compared to our experimental measurements (black line).

We notice that our MC simulations reproduce both the π (due to the collective excitation of valence electrons in the π band) and the $\pi + \sigma$ (due to collective excitation of all valence electrons) plasmon peaks. These findings are in agreement with the ELF function in the top right panel of Fig. 5.29, showing maxima at about the same energies. While the results of the simulations show good agreement with experimental data independently of the ELF model, nevertheless, using the ab initio calculated ELF at finite momentum transfer, a third peak around 60 eV can be found. This peak corresponds to two-plasmon excitation, and its presence is less

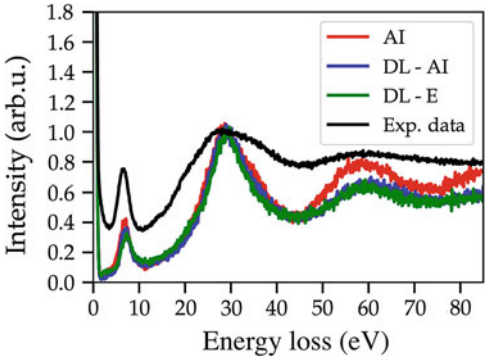

Fig. 5.32 REEL of graphite: experimental data are reported in black, while simulations using the three different models are sketched in red (AI), blue (DL-AI) and green (DL-E). Electron beam kinetic energy is 1000 eV. Data are normalized with respect to the $\pi + \sigma$ plasmon peak. (Adapted from Ref. [18])

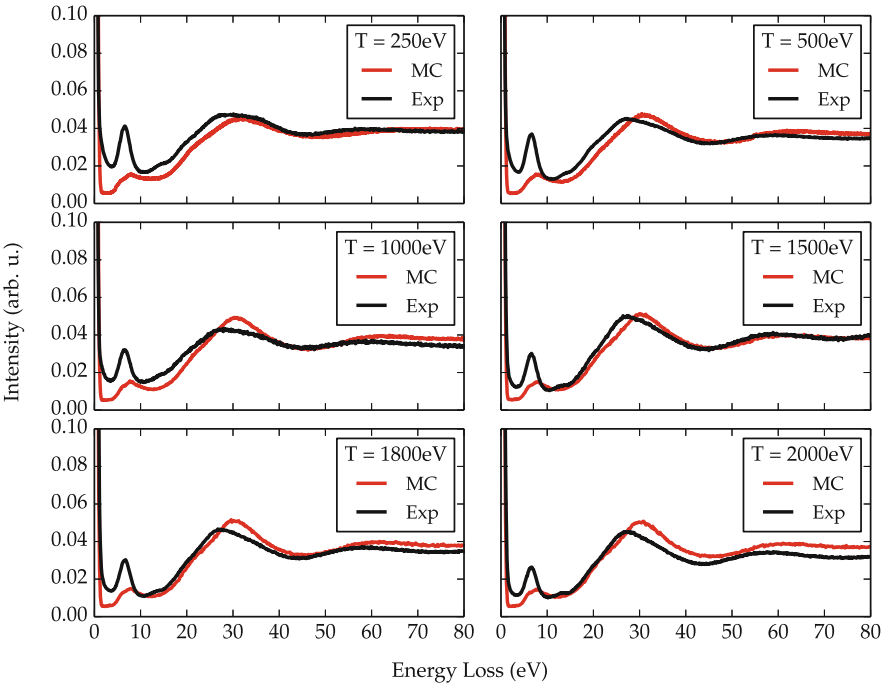

Fig. 5.33 REELs of HOPG for several primary beam kinetic energies. Red lines show simulated spectra, while black curves report our experimental data [18]. The results are normalized at a common area of the elastic peak. (Adapted from Ref. [64])

apparent by adopting DL models. Indeed, in DL models the RPA approximation describes the system as composed of free electrons; in the case of graphite, the electrons populating the π bands are delocalized, and they behave as almost-free electrons. For this reason, the π plasmon peak is prominent in all three spectra. The discrepancies found in the energy-loss spectral features recommend the use of AI approaches for the extension of the ELF out of the optical region, in order to deal accurately with the electronic motion inside the material.

Furthermore, we performed REEL spectra MC simulations at several primary beam kinetic energies for a value of the anisotropy parameter $f = 0.6$, which provides the best agreement between experimental and calculated REELS (see Fig. 5.33). This anisotropic model is consistent with the higher tendency of the electrons to move along the graphite planes rather than across the planes.

Finally, the assessment of secondary electron (SE) spectra and yield is crucial in imaging techniques. SE emission from graphite was thus assessed by MC simulations, using a kinetic energy of the incident beam ($N = 10^6$) equal to 1000 eV. In Fig. 5.34 we compare our MC calculations with the acquired experimental spectra.

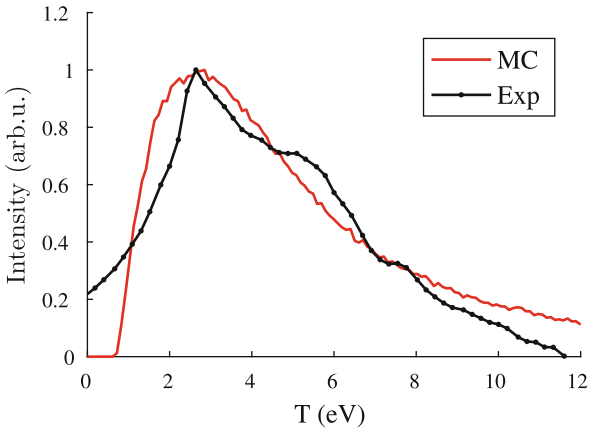

Fig. 5.34 Secondary electron spectra of HOPG. Black line represents experimental data, while in red we report the theoretical spectrum. The data are normalized to a common height of the secondary electron emission peak. (Adapted from Ref. [64])

5.6.2 Graphite for Armour Technologies

The study of ballistic properties of layered two-dimensional materials upon the hypervelocity impacts is an important topic for the protection of structures and devices from the penetration of highly energetic projectiles [61]. In particular, in this section we describe the impact of C_{60} molecules on graphite.

While the critical penetration energy of monolayer membranes can be determined using monolayers, the synergistic behaviour of multilayered structures, such as graphite, depends dramatically on the interface characteristics (e.g. adhesive strength). Indeed, in some occasions, the layer coupling may not be effective. This effect can be expressed using the following energy absorption scaling law:

$$\frac{K_{abs}(N)}{N} = K \times N^{\alpha} \tag{5.28}$$

where K is a constant. A scaling exponent $\alpha > 0$ indicates a synergistic behaviour in which single layers interact to mutually enhance their specific contribution. On the other hand, for $\alpha = 0$, the total absorbed energy is the mere sum of single-layer contributions, whereas for $\alpha < 0$ a suboptimal behaviour is identified in which increasing the number of layers leads to worse or inefficient interlayer coupling.

At the nanolevel, we find by impinging C_{60} fullerene on graphite samples that a synergistic interaction between the graphene layers emerges, whereby an optimal number of layers, between 5 and 10, can be identified demonstrating that few-layered 2D material armours possess impact strength even higher than their monolayer counterparts. In Fig. 5.35 we report the representation of the optimal number of layers, which corresponds to both the maximum specific energy absorption by strain and the inversion in the sign of the scaling exponent of Eq. 5.28.

These results provide fundamental understanding for the design of ultralight weight multilayer armours using enhanced 2D material-based nanocomposites.

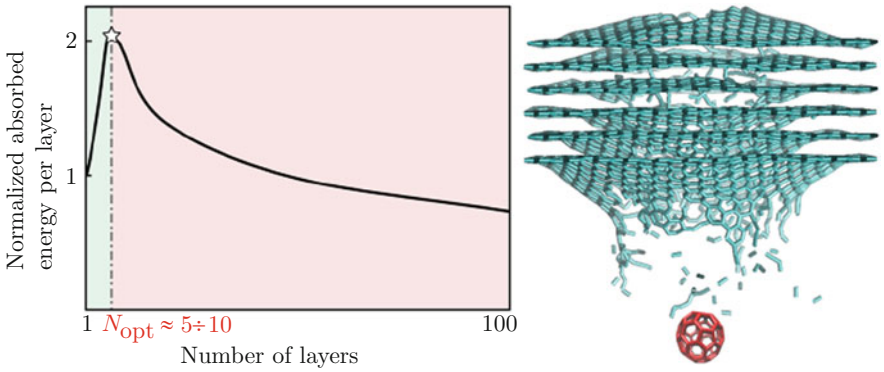

Fig. 5.35 Representation of the optimal number of layers, which corresponds to both the maximum specific energy absorption by strain and the inversion in the sign of the scaling exponent of Eq. 5.28. (Adapted from Ref. [61])

5.6.3 Other 3D Carbon Materials: Foams and Graphene Frameworks

5.6.3.1 Graphene Foams

Graphene foams are all-carbon 3D structures made by big fullerenes connected through carbon nanotubes (see top panels of Fig. 5.36), so they possibly represent relics of the mechanical and thermal properties of graphene. Recently, they have attracted interest for their possible use as electrochemical storage devices, in wearable electronics, in chemical sensing and as impact energy absorbers [63, 65].

In particular, one can assess the mechanical and thermal performances of foams characterized by increasing mass density and decreasing average pore size. In the bottom panels of Fig. 5.36, we show the mechanical performances under compression for regular (bottom left) and random (bottom right) foams. Regular foams are nanotruss networks characterized by some degree of crystallinity with face-centred cubic geometry (these are shown in the top left panel of Fig. 5.36). It is worthwhile noticing that the mechanical response of regular foams to loading depends on the ratio between the nanotube and the sphere diameters (see bottom left panel of Fig. 5.36). In the case of random foams, where pore positions and dimensions are random (see top right panel of Fig. 5.36), the higher-density foams show the typical slope change in the stress-strain curve at 5–10% strain, moving from linear elasticity to bending stress plateau, and lower density foams display a quasilinear behaviour up to 35% strain (see bottom right panel of Fig. 5.36). We conclude that in both crystalline and random foams, we observe the typical elastic deformation regime under compression, with a specific Young's modulus significantly increasing with a decreasing average pore size. Nevertheless, some of these nanotruss networks present a negative Poisson's ratio in compression, like re-entrant foams. Furthermore, for nanotruss network, at 5–8% strain, the stress is

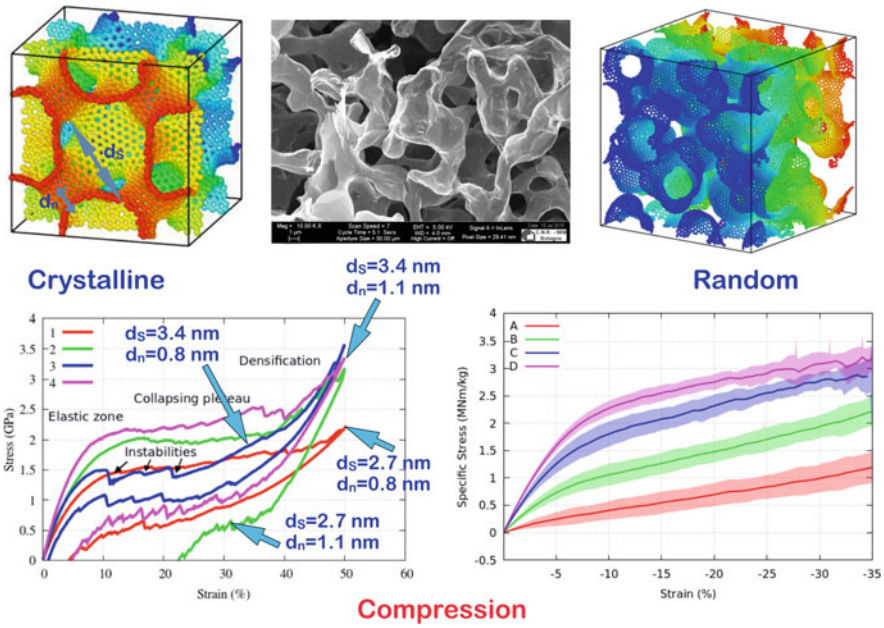

Fig. 5.36 Top panels: crystalline and random graphene-like foams. Bottom panels: stress-strain curves of crystalline (left) and random (right) foams with different sphere (d_s) and tube (d_n) diameters in compressive regime. Middle: electron microscopy image of a graphene random foam (courtesy of CNR-IMM Bologna, Italy). (Adapted from Refs. [63, 65])

in the range 90–130 MNm kg^{-1}, while for random foams at the same strain, the values are in the range 3.9–36.6 MNm kg^{-1}. This makes clear that regular foams are mechanically stiffer than the random ones.

Finally, owing to the interest of using foams as a mean for achieving thermal resistance, we assess the thermal conductivity of the random foams using the equilibrium Green-Kubo approach [134, 135]. According to this formalism, the equilibrium thermal conductivity k can be calculated as follows:

$$k = \frac{V}{3K_B T^2} \int_0^\infty \langle \boldsymbol{J}(0) \cdot \boldsymbol{J}(t) \rangle dt \tag{5.29}$$

where V is the volume of the simulation cell, t is the correlation time, K_B is the Boltzmann constant and $\boldsymbol{r}$ identifies the particle positions. The heat current $\boldsymbol{J}$, appearing in Eq. 5.29, is defined by:

$$\boldsymbol{J} = \frac{1}{V}\Big(\sum_i E_i \boldsymbol{v}_i + \frac{1}{2} \sum_{i<j} (\boldsymbol{F}_{ij} \cdot (\boldsymbol{v}_i + \boldsymbol{v}_j) \boldsymbol{r}_{ij}) \Big) \tag{5.30}$$

where $\boldsymbol{v}$ is the velocity of a particle, $\boldsymbol{r}_{ij}$ and $\boldsymbol{F}_{ij}$ are the distance and force between the particles i and j and E_i is the total energy per atom. The first term in the

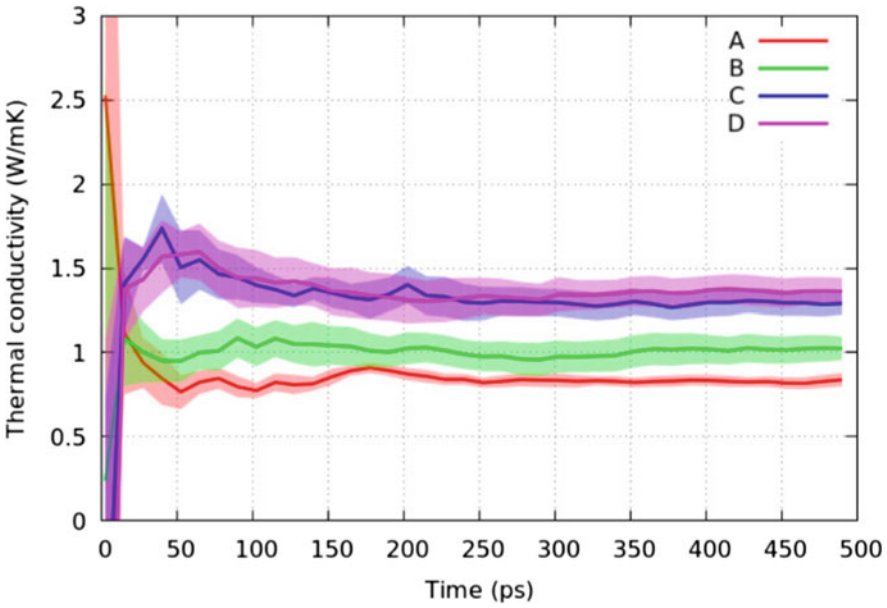

Fig. 5.37 Time averaged vs. simulation time of the four random foam families calculated as by Eq. 5.29. The asymptotic values after 300 ps provide the thermal conductivity of the samples. The shaded area for each relevant curve represents half of the standard deviation. (Adapted from Ref. [63])

right-hand side of Eq. 5.30 corresponds to convection while the second term to conduction. The integrand in the expression 5.29 of the thermal conductivity is the heat current autocorrelation function (HCACF). While foam thermal conductivity is affected by both connectivity and defects, nevertheless we obtain similar values for all the investigated families. The thermal conductivity, reported in Fig. 5.37, is comparable to that of glass, thus higher than materials typically used as thermal insulators, such as polyurethane rigid foams.

5.6.3.2 Pillared Graphene

Pillared Graphene Frameworks (PGF) are a novel class of microporous materials made by graphene sheets separated by organic spacers [136, 137]. One of their main features is that the pillar type and density can be chosen to tune the capacity of the material to, e.g. adsorb gases or separate gas mixtures. Pillars are typically made by organic rigid molecules, containing carbon and/or nitrogen (see top panels of Fig. 5.38). In general, the pillar density plays the most important role in determining gas adsorption rather than the chemical typology of the spacers. In the low-pressure regime ($\lesssim$10 bar), the amount of gas adsorbed is an increasing function of pillar density. At higher pressures the opposite trend is observed. This effect is

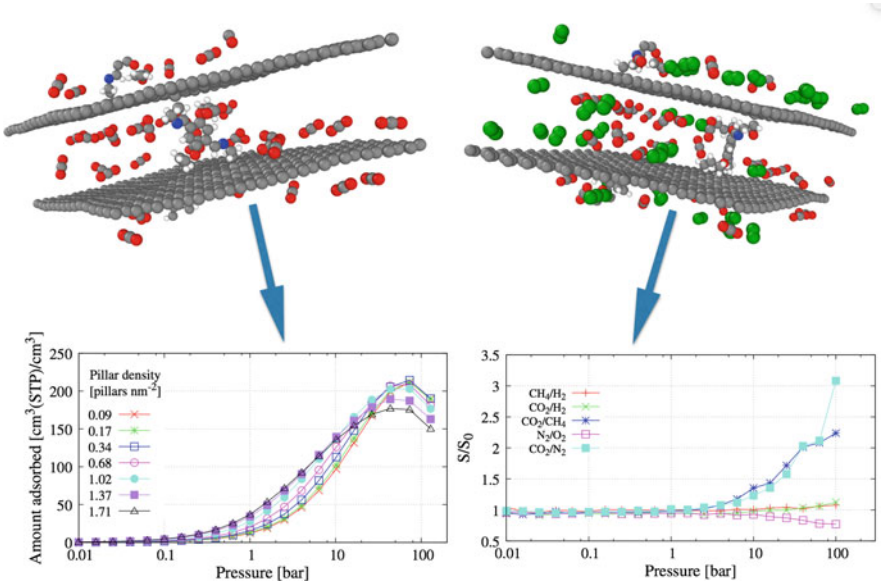

Fig. 5.38 Top: typical PGFs with nitrogen and organic based pillars. Bottom left: Volumetric adsorption isotherms of CH_4 at $T = 298$ K in PGF. Bottom right: Selectivity for gas mixtures at $T = 298$ K, normalized with respect to the zero-pressure limit value of selectivity (S_0). (Reproduced by adapting figures from Ref. [136])

clearly visible in the bottom left panel of Fig. 5.38, where the volumetric uptake of CH_4 vs. pressure is plotted. Other than adsorption, PGF can be used to sieve gas binary mixture, such as CH_4/H_2, CO_2/H_2 and CO_2/N_2. The dynamic of the mixture passing through the pillared structures can be simulated by assessing the diffusion coefficients taking into account the framework flexibility that is essential in assessing the dynamical properties of the adsorbed gases. Good performance for the gas separation in mixtures was found with values comparable to those of metal-organic frameworks (MOFs) and zeolites (ZIFs) [138, 139]; see bottom right panel of Fig. 5.38.

5.7 Conclusions and Future Outlook

The first goal of this chapter was to demonstrate the impact that dimensionality has in the emergence of novel properties at nanoscale. Climbing up the "ladder of dimensionality", from 0D to 3D, we discussed a variety of systems using several all-carbon-based materials as role models of our analysis.

In particular, we used fullerene, the spherically shaped 0D carbon allotrope, accelerated to supersonic velocities to demonstrate the factual possibility to synthe-

size graphene sheets at low temperature via our in-house SuMBE growth technique. While we did not succeed for technological limitations to lower the working temperature down to room conditions at variance with the case of SiC growth, however SuMBE was capable of synthesizing a fairly even coating of graphene-like material in a single layer at 645 °C using H_2 as carrier gas. This temperature is remarkably smaller than that of other widely used approaches, such as CVD (in excess of 900 °C), MBE of C_{60} on Ru(0001) (725 K for the cage thermal break and 1200 K for complete monolayer formation) [140] or on noble metals (1050 K) [141]. Graphene nano-islands, even according to our metadynamics simulations, are not made of regular hexagons, like in pristine graphene, but also contain pentagons, which come from the original buckyball structures. We notice that this characteristic is potentially useful, because the pentagonal defects introduce a band gap into the material, something materials scientists have longed hoped to create in graphene. Although at this stage we believe that our results represent a proof of principle, the technique looks interesting, not least because it produces relatively high-quality films and could also be applied using a wide range of materials as a substrate, such as semiconductors and insulators avoiding the graphene layer transfer from the growth substrate to different substrates for producing high-end electronic devices.

We then discussed a systematic approach for generating bi-dimensional all-sp^2 carbon allotropes, aiming at decreasing the density of graphene without depleting its unique mechanical properties. This method proceeds by augmenting the number of congruent discs under the constraint of local stability. The daughter structures share the common drawbacks of having lower stability and smaller cohesive energy than graphene, while their density is reduced by 45% with respect to graphene. In particular, we conclude that (i) flakene may represent the least dense possible architecture among the families of bi-dimensional all-sp^2 carbon allotropic forms under the local stability constraints; (ii) the augmentation increases the metallicity character of the daughter structures with respect to parent ones; (iii) while the absolute stress-strain characteristics are definitely depleted by augmentation, also a threshold exists below which one cannot reduce further the density without a considerable performance loss of the specific mechanical properties; (iv) tilene parent displays a specific strength higher than graphene; and (v) finally, graphene presents one of the highest specific modulus ever found, and the quest for finding a better replacement in mechanical engineering applications is still open.

Graphene can be also rolled in the shape of nanotubes, and we have showed, using a GW approach based on the expansion of the polarizability operator in an optimal basis, how the electronic band gap of semiconducting CNTs evolves by increasing the tube size. This approach allows one to avoid the explicit sum over the unoccupied states while allowing for good accuracy. We showed that an accurate estimate of the excitation binding energies can be achieved by coupling optical measurements with theoretical modelling [93, 95]. We extrapolated the gap vs. diameter function for large dimensions showing that this dependence can be modelled by $E_{\text{gap}} = 1.54\ \text{eV} \times \text{nm}$. This relation is found to be in good agreement with a recent direct measurement of the electronic gap performed via STS for the case of 1.4 nm diameter CNT [91].

In the 3D case of study, we assessed the frequency-dependent dielectric response and energy-loss functions of diamond and graphite in two ways: a full ab initio approach, in which we carry out time-dependent density functional simulations in linear response for different momentum transfers, and a semiclassical model, based on the Drude-Lorentz extension to finite momenta of the optical dielectric function. We conclude that ab initio calculated dielectric functions lead to better agreement with measured energy-loss spectra compared to the widely used Drude-Lorentz model. This discrepancy is particularly evident for insulators and semiconductors beyond the optical limit ($\mathbf{q} \neq 0$), where single-particle excitations become relevant. Furthermore, we show that the behaviour of the energy-loss function obtained at different accuracy levels has a dramatic effect on other physical observables, such as the inelastic mean free path and the stopping power in the low energy ($<100\,\mathrm{eV}$) regime and thus on the accuracy of MC simulations of REEL spectra. Thus, the major point of this work is to show that an accurate treatment of the electron-electron correlations beyond the random-phase approximation of the homogeneous Fermi gas is necessary to increase the overall accuracy of the simulations to be compared with REEL experiments. We also discuss a theoretical approach for taking into account the anisotropic structure of HOPG in the Monte Carlo simulations of charge transport. The anisotropic description of the dielectric response is achieved by linearly combining the contributions to the inverse inelastic mean free path and energy losses along the two main orthogonal directions identifying the layered crystalline structure of graphite. Monte Carlo simulated spectra, obtained with our anisotropic approach, are compared with acquired experimental data of reflection electron energy loss and secondary electron spectra, showing a good agreement. These findings validate the idea of the importance of considering properly weighted interplanar and intra-planar interactions in the simulation of electron transport in layered materials.

Furthermore, we discussed the mechanical behaviour of single and multilayer graphene armours subjected to hypervelocity impacts of fullerene molecules, due to their outstanding mechanical stability. The investigation of the interlayer synergy between adjacent layers at the nanoscale determines that an optimal number of layers, between 5 and 10, emerges that maximizes also the specific energy dissipation under impact. These results suggest that multilayer 2D material-based armours should be structured and optimized at the nanolevel, not relying on the mere high-specific mechanical properties of the constituent materials.

Finally, we studied the mechanical properties of nanotruss networks and of random foams, as a further example of 3D materials based on carbon. In this respect, we conclude that nanotruss networks and random foams may represent exceptional candidates for porous, flexible and high-strength materials. Basically they inherit the marvellous mechanical properties of the parent material, graphene, adding a third bearing stress dimension. In applications to gas adsorption and sieving, other convenient 3D architectures are represented by the PGFs. Our results show that the density of pillars dramatically affects the adsorption rather than the pillar type as, under saturation conditions, the increase of pillar density results in a sensible decrease of the amount of gas adsorbed.

After having discussed the marvellous properties that carbon nanomaterials acquire by moving up the dimensionality ladder, we believe meaningful to provide an outlook about the foreseeable impact that over the next decades carbon-based materials can have in defining the reach and applications of nanotechnology. Indeed, the versatility of carbon to make bonds with itself and also other chemical elements with different hybridization levels represents the most striking feature which allows to use it in different technological scenarios. In the last three decades, starting from the discovery of fullerenes, carbon nanotube (CNT), graphene and other 2D materials, we have been flush with novel ideas and innumerable attempts to find the killer applications for these remarkable nanostructures. For example, nearly two decades of research in graphene fundamental properties have landed potential influence on longer-lasting batteries, more efficient solar cells, transparent and wearable faster electronics, novel LCD and OLED display panels, data storage devices as well as novel approaches to electrochemical sensing in medicinal technologies or to reinforcing composite matrices to enhance their mechanical properties. Significant breakthrough in our everyday life can also come from the revival of CNT-based technologies, such as in the production of transparent electrodes due to their high conductivity, which allows the construction of ultra-thin films (1–100 nm). Additionally, one can exploit CNTs for solving environmental issues due to their promising catalytic properties, such as in pollution remediation, and energy-related problems, such as in the search for alternative energy sources to replace the use of fossil fuels or the production of H_2 via water splitting due to the large number of active adsorption sites.

Nevertheless, we notice that so far, despite the many worldwide efforts to advance carbon-based technology by using CNT or graphene, very few real-world applications benefit from the potential that these materials display. This still missing carbon revolution to replace silicon as the material of the future electronics seems to be due to factors such as mass production and sample quality. For example, the requirement of large-area, defect-free, grain boundary-free, monocrystalline graphene to date has not been yet achieved. Furthermore, the question of whether CNTs and graphene are the right choices for mechanical reinforcement still remains largely unanswered, basically due to adhesion issues at the interface. Nevertheless, with the great deal of interest in carbon-based technologies, it would not be surprising if the first commercially available applications could be already found in the next decade timeframe. Still, we believe that what makes CNTs and graphene so special is beyond their technological applications, as they represent a paradigm of a new class of mono- and bi-dimensional materials, whose discovery and study clearly date from its synthesis. Furthermore, the electrical conductivity, the electronic structure and the optical properties of carbon-based materials can be easily tuned by heteroatom doping in order to adjust their electron mobility, charge transfer capacity and optical response. For example, due to the potential applications as a basic unit of a quantum computer, in quantum cryptography, spintronics and masers, recently nitrogen-vacancy centre (N-V centre) in diamond gained a lot of attention in the scientific community. Indeed, its most investigated and potentially useful property is photoluminescence, which can be easily detected from an individual N-V centre.

Electron spins localized at N-V centres can be manipulated at room temperature by applying magnetic or electric fields, resulting in sharp resonances in the intensity and wavelength of the photoluminescence. These resonances can be rationalized in terms of quantum entanglement, spin-orbit interaction and Rabi oscillations and analysed using advanced quantum optics theory.

As a final remark, we strongly believe that there is a great need for research and development of new technologies involving the reduction of environmental impacts, seeking the use of renewable raw and low-cost materials. In this regard, carbon-based nanomaterials, such as ultra-thin carbon films, can play a major role [142].

Acknowledgements S.T. acknowledges invaluable discussions with several colleagues who helped him to develop the methods described in this chapter and to carry out the computational modelling presented. In particular, we mention Dr. M. Azzolini, Dr. M. Dapor, Dr. G. Garberoglio, Dr. T. Morresi, Dr. A. Pedrielli, prof. N. Pugno and Dr. S. Simonucci. This chapter is basically the outcome of a decade-long collaboration with all of them.

References

1. P.W. Anderson, More is different. Science **177**, 393–396 (1972)
2. G. Gallavotti, *Statistical Mechanics*. Texts and Monographs in Physics. (Springer, Berlin, 1999)
3. C.G. Smith, Low-dimensional quantum devices. Rep. Prog. Phys. **59**, 235–282 (1996)
4. A.H. Castro Neto, F. Guinea, N.M.R. Peres, K.S. Novoselov, A.K. Geim, The electronic properties of graphene. Rev. Mod. Phys. **81**, 109–162 (2009)
5. K.S. Novoselov, A. Mishchenko, A. Carvalho, A.H. Castro Neto, 2D materials and van der Waals heterostructures. Science **353**, 461–472 (2016)
6. P.J. Burke, Nanotubes and nanowires. (World Scientific, Singapore, 2007)
7. T. Morresi, M. Timpel, A. Pedrielli, G. Garberoglio, R. Tatti, R. Verucchi, L. Pasquali, N. Pugno, M.V. Nardi, S. Taioli, A novel combined experimental and multiscale theoretical approach to unravel the structure of SiC/SiO_x core/shell nanowires for their optimal design. Nanoscale **10**, 13449–13461 (2018)
8. S. Iijima, Helical microtubules of graphitic carbon. Nature **354**, 56–58 (1991)
9. X. Wang, Q. Li, J. Xie, Z. Jin, J. Wang, Y. Li, K. Jiang, S. Fan, Fabrication of ultralong and electrically uniform single-walled carbon nanotubes on clean substrates. Nano Lett. **9**, 3137–3141 (2009)
10. C.D. Spataru, S. Ismail-Beigi, L.X. Benedict, S.G. Louie, Excitonic effects and optical spectra of single-walled carbon nanotubes. Phys. Rev. Lett. **92**, 077402 (2004)
11. P. Umari, O. Petrenko, S. Taioli, M.M. De Souza, Communication: electronic band gaps of semiconducting zig-zag carbon nanotubes from many-body perturbation theory calculations. J. Chem. Phys. **136**, 181101 (2012)
12. S. Taioli, P. Umari, M.M. De Souza, Electronic properties of extended graphene nanomaterials from *GW* calculations. Phys. Status Solidi (B) **246**, 2572–2576 (2009)
13. R.C. Ashoori, Electrons in artificial atoms. Nature **379**, 413–419 (1996)
14. W.G. Van der Wiel, S. De Franceschi, J.M. Elzerman, T. Fujisawa, S. Tarucha, L.P. Kouwenhoven, Electron transport through double quantum dots. Rev. Mod. Phys. **75**, 1–22 (2002)
15. A. Imamoglu, Are quantum dots useful for quantum computation? Phys. E Low Dimens. Syst. Nanostruct. **16**, 47–50 (2003)

16. L. Van Hove, The occurrence of singularities in the elastic frequency distribution of a crystal. Phys. Rev. **89**, 1189–1193 (1953)
17. F. Bassani, G. Pastori Parravicini, *Electronic States and Optical Transitions in Solids* (Pergamon Press, Oxford/New York, 1975)
18. M. Azzolini, T. Morresi, G. Garberoglio, L. Calliari, N.M. Pugno, S. Taioli, M. Dapor, Monte Carlo simulations of measured electron energy-loss spectra of diamond and graphite: role of dielectric-response models. Carbon **118**, 299–309 (2017)
19. P. Cudazzo, M. Gatti, A. Rubio, Interplay between structure and electronic properties of layered transition-metal dichalcogenides: comparing the loss function of $1T$ and $2H$ polymorphs. Phys. Rev. B **86**, 075121 (2012)
20. C.L. Kane, E.J. Mele, Quantum spin hall effect in graphene. Phys. Rev. Lett. **95**, 22680 (2005)
21. H. Gao, Application of fracture mechanics concepts to hierarchical biomechanics of bone and bone-like materials. Int. J. Fract. **138**, 101–137 (2006)
22. H. Yao, H. Gao, Multi-scale cohesive laws in hierarchical materials. Int. J. Solids Struct. **44**, 8177–8193 (2007)
23. M.J. Buehler, S. Keten, T. Ackbarow, Theoretical and computational hierarchical nanomechanics of protein materials: deformation and fracture. Prog. Mater. Sci. **53**, 1101–1241 (2008)
24. R. Puxkandl, I. Zizak, O. Paris, J. Keckes, W. Tesch, S. Bernstorff, P. Purslow, P. Fratzl, Viscoelastic properties of collagen: synchrotron radiation investigations and structural model. Philos. Trans. R. Soc. Lond. B **357**, 191–197 (2001)
25. M.S. Dresselhaus, G. Dresselhaus, P.C. Eklund, Science of fullerenes and carbon nanotubes (Academic Press, San Diego, 1996)
26. D.E.H. Jones, Hollow molecules. New Sci. **32**, 245 (1966)
27. H.W. Kroto, J.R. Health, S.C. O'Brien, R.F. Curl, R.E. Smalley, C60: Buckminsterfullerene. Nature **318**, 162–163 (1985)
28. A. Lassesson, N. Walsh, F. Martinez, A. Herlert, G. Marx, L. Schweikhard, Formation of fullerene dianions in a Penning trap. Eur. Phys. J. D At. Mol. Opt. Plasma Phys. **34**, 73–77 (2005)
29. D. Tomànek, M.A. Schluter, Growth regimes of carbon clusters. Phys. Rev. Lett. **67**, 2331–2334 (1991)
30. C.J. Brabec, E.B. Anderson, B.N. Davidson, S.A. Kajihara, Q.-M. Zhang, J. Bernholc, D. Tomànek, Precursors to C_{60} fullerene formation. Phys. Rev. B **46**, 7326–7328 (1992)
31. Z. Yufeng, K. Yong-Hyun, A.C. Dillon, M.J. Heben, S.B. Zhang, Hydrogen storage in novel organometallic buckyballs. Phys. Rev. Lett. **94**, 155504 (2005)
32. C.E. Housecroft, A.G. Sharpe, Chapter 14: the group 14 elements, in *Inorganic Chemistry*, 3rd edn. (Pearson, London, 2008)
33. N.S. Sariciftci et al., Semiconducting polymer-buckminsterfullerene heterojunctions: diodes, photodiodes, and photovoltaic cells. Appl. Phys. Lett. **62**, 585–587 (1993)
34. F. Tran, P. Blaha, Accurate band gaps of semiconductors and insulators with a semilocal exchange-correlation potential. Phys. Rev. Lett. **102**, 226401 (2009)
35. S. Jalali-Asadabadi, Electronic structure of crystalline buckyballs: fcc-C_{60}. J. Electron. Mater. **45**, 339–348 (2016)
36. E.L. Shirley, S.G. Louie, Electron excitations in solid C_{60}: energy gap, band dispersions, and effects of orientational disorder. Phys. Rev. Lett. **71**, 133–136 (1993)
37. K.H. Michel, J.R.D. Copley, D.A. Neumann, Microscopic theory of orientational disorder and the orientational phase transition in solid C_{60}. Phys. Rev. Lett. **68**, 2929–2932 (1992)
38. S. Saito, A. Oshiyama, Cohesive mechanism and energy bands of solid C_{60}. Phys. Rev. Lett. **66**, 2637–2640 (1991)
39. M.S. Golden, M. Knupfer, J. Fink, J.F. Armbruster, T.R. Cummins, H.A. Romberg, M. Roth, M. Sing, M. Schmidt, E. Sohmen, The electronic structure of fullerenes and fullerene compounds from high-energy spectroscopy. J. Phys. Condens. Matter **7**, 8219 (1995)
40. J.R. Pinzón, A. Villalta-Cerdas, L. Echegoyen, Fullerenes, carbon nanotubes, and graphene for molecular electronics, in *Unimolecular and Supramolecular Electronics*, vol. 312 (Springer, Berlin/Heidelberg, 2012), pp. 127–74

41. O. Gunnarson, *Alkali-Doped Fullerides Narrow-Band Solids with Unusual Properties* (World Scientific, Singapore, 2004)
42. R. Verucchi, L. Aversa, M.V. Nardi, S. Taioli, S. a Beccara, D. Alfè, L. Nasi, F. Rossi, G. Salviati, S. Iannotta, Epitaxy of nanocrystalline silicon carbide on Si(111) at room temperature. J. Am. Chem. Soc. Commun. **134**, 17400–17403 (2012)
43. S. Taioli, G. Garberoglio, S. Simonucci, S. a Beccara, L. Aversa, M. Nardi, R. Verucchi, S. Iannotta, M. Dapor, D. Alfè, Non-adiabatic ab initio molecular dynamics of supersonic beam epitaxy of silicon carbide at room temperature. J. Chem. Phys. **138**, 044701 (2013)
44. L. Aversa, S. Taioli, M.V. Nardi, R. Tatti, R. Verucchi, S. Iannotta, The interaction of C_{60} on Si(111) 7×7 studied by supersonic molecular beams: interplay between precursor kinetic energy and substrate temperature in surface activated processes. Front. Mater. **2**, 46 (2015)
45. S. Taioli, M. Dapor, N.M. Pugno, New frontiers in multiscale modelling of advanced materials. Front. Mater. **2**, 71 (2015)
46. R. Tatti, L. Aversa, R. Verucchi, E. Cavaliere, G. Garberoglio, N.M. Pugno, G. Speranza, S. Taioli, Synthesis of single layer graphene on Cu(111) by C_{60} supersonic molecular beam epitaxy. RSC Adv. **6**, 37982–37993 (2016)
47. D. Haberer, D. Vyalikh, S. Taioli, B. Dora, M. Farjam, J. Fink, D. Marchenko, T. Pichler, K. Ziegler, S. Simonucci et al., Tunable band gap in hydrogenated quasi-free-standing graphene. Nano Lett **10**, 3360–3366 (2010)
48. D. Haberer, L. Petaccia, M. Farjam, S. Taioli, S. Jafari, A. Nefedov, W. Zhang, L. Calliari, G. Scarduelli, B. Dora et al., Direct observation of a dispersionless impurity band in hydrogenated graphene. Phys. Rev. B **83**, 165433 (2011)
49. S. Taioli, A. Paris, L. Calliari, Characterization of pristine and functionalized graphene on metal surfaces by electron spectroscopy, in *Graphene Science Handbook: Size-Dependent Properties*, vol. 5 (CRC Press/Taylor & Francis Group, Boca Raton, 2016), pp. 269–285
50. S. Taioli, Computational study of graphene growth on copper by first-principles and kinetic Monte Carlo calculations. J. Mol. Mod. **20**, 1–13 (2014)
51. G. Xu, X.-Q. Shi, R.Q. Zhang, W.W. Pai, H.T. Jeng, M.A. Van Hove, Detailed low-energy electron diffraction analysis of the (4×4) surface structure of C_{60} on Cu(111): seven-atom-vacancy reconstruction. Phys. Rev. B **86**, 075419 (2012)
52. G. Galli, F. Mauri, Large scale quantum simulations: C_{60} impacts on a semiconducting surface. Phys. Rev. Lett. **73**, 3471–3474 (1994)
53. X. Hu, K. Albe, R.J. Averback, Molecular-dynamics simulations of energetic C_{60} impacts on (2×1)–(100) silicon. Appl. Phys. **88**, 49–54 (2000)
54. A. Paris, S. Taioli, Multiscale investigation of oxygen vacancies in TiO_2 anatase and their role in memristor's behavior. J. Phys. Chem. C **120**, 22045–22053 (2016)
55. G. Kresse, J. Hafner, Ab initio molecular dynamics for liquid metals. Phys. Rev. B **47**, 558–561 (1993)
56. G. Kresse, J. Hafner, Ab initio molecular-dynamics simulation of the liquid-metal–amorphous-semiconductor transition in germanium. Phys. Rev. B **49**, 14251–14269 (1994)
57. A. Carpinteri, N.M. Pugno, One-, two- and three-dimensional universal laws for fragmentation due to impact and explosion. J. Appl. Mech. **69**, 854–856 (2002)
58. Z. Slanina, E. Osawa, Average bond-dissociation energies of fullerenes. Fullerene Sci. Technol. **5**, 167–175 (1997)
59. M.J. Allen, V.C. Tung, R.B. Kaner, Honeycomb carbon: a review of graphene. Chem. Rev. **110**, 132–145 (2010)
60. E.P. Randviir, D.A.C. Brownson, C.E. Banks, A decade of graphene research: production, applications and outlook. Mater. Today **17**, 426–432 (2014)
61. S. Signetti, S. Taioli, N.M. Pugno, 2D material armors showing superior impact strength of few layers. ACS Appl. Mater. Interfaces **9**, 40820–40830 (2017)
62. E. Lepore, F. Bosia, F. Bonaccorso, M. Bruna, S. Taioli, G. Garberoglio, A.C. Ferrari, N.M. Pugno, Spider silk reinforced by graphene or carbon nanotubes. 2D Mater. **4**, 031013 (2017)
63. A. Pedrielli, S. Taioli, G. Garberoglio, N.M. Pugno, Mechanical and thermal properties of graphene random nanofoams via molecular dynamics simulations. Carbon **132**, 766–775 (2018)

64. M. Azzolini, T. Morresi, K. Abrams, R. Masters, N. Stehling, C. Rodenburg, N.M. Pugno, S. Taioli, M. Dapor, Anisotropic approach for simulating electron transport in layered materials: computational and experimental study of highly oriented pyrolitic graphite. J. Phys. Chem. C **122**, 10159–10166 (2018)
65. A. Pedrielli, S. Taioli, G. Garberoglio, N.M. Pugno, Designing graphene based nanofoams with nonlinear auxetic and anisotropic mechanical properties under tension or compression. Carbon **111**, 796–806 (2017)
66. L.D. Landau, E.M. Lifshitz, *Statistical Physics* (Pergamon, Oxford, 1980)
67. R.E. Peierls, Bemerkungen über Umwandlungstemperaturen. Helv. Phys. Acta **7**, 81–83 (1934)
68. K.S. Novoselov, A.K. Geim, S.V. Morozov, S.V. Dubonos, Y. Zhang, D. Jiang, Room-temperature electric field effect and carrier-type inversion in graphene films. arXiv:cond-mat/0410631 (2004)
69. C. Tan, H. Zhang, Two-dimensional transition metal dichalcogenide nanosheet-based composites. Chem. Soc. Rev. **44**, 2713–2731 (2015)
70. P. Vogt, P. De Padova, C. Quaresima, J. Avila, E. Frantzeskakis, M.C. Asensio, A. Resta, B. Ealet, G. Le Lay, Silicene: compelling experimental evidence for graphenelike two-dimensional silicon. Phys. Rev. Lett. **108**, 155501 (2012)
71. X. Chen, Q. Yang, R. Meng, J. Jiang, Q. Liang, C. Tan, X. Sun, The electronic and optical properties of novel germanene and antimonene heterostructures. J. Mater. Chem. C **4**, 5434–5441 (2016)
72. L. Matthes, O. Pulci, F. Bechstedt, Massive Dirac quasiparticles in the optical absorbance of graphene, silicene, germanene, and tinene. J. Phys. Condens. Matter. **25**, 395305 (2013)
73. H. Aoki, M. Dresselhaus (eds.), *Physics of Graphene* (Springer, Berlin, 2014)
74. T. Morresi, A. Pedrielli, R. Gabbrielli, N.M. Pugno, S. Taioli, Structural, electronic and mechanical properties of all-sp^2 graphene allotropes: the specific strength of tilene parent is higher than that of graphene and flakene has the minimal density. arXiv:1811.01112 [cond-mat.mtrl-sci] (2018)
75. W. Fischer, E. Koch., Homogeneous sphere packings with triclinic symmetry. Acta Crystallogr. Sect. A **58**, 509–513 (2002)
76. H. Sun, S. Mukherjee, M. Daly, A. Krishnan, New insights into the structure-nonlinear mechanical property relations for graphene allotropes. Carbon **110**, 443–457 (2016)
77. S. Zhang, J. Zhou, Q. Wang, X. Chen, Y. Kawazoe, P. Jena, Penta-graphene: a new carbon allotrope. PNAS **112**, 2372–2377 (2015)
78. Y.J. Dappe, R. Oszwaldowski, P. Pou, J. Ortega, R. Pérez, F. Flores, Local-orbital occupancy formulation of density functional theory: application to Si, C, and graphene. Phys. Rev. B **73**, 235124 (2006)
79. I.A. Pasti, A. Jovanović, A.S. Dobrota, S.V. Mentus, Atomic adsorption on pristine graphene along the periodic table of elements – from PBE to non-local functionals. Appl. Surf. Sci. **436**, 433–440 (2018)
80. X.L. Sheng, H.-J. Cui, F. Ye, Q.-B. Yan, Q.-R. Zheng, G. Su, Octagraphene as a versatile carbon atomic sheet for novel nanotubes, unconventional fullerenes, and hydrogen storage. J. Appl. Phys. **112**, 074315 (2012)
81. F. Thorpe, I. Jasiuk, Proc. Math. Phys. Sci. **438**, 531–544 (1992)
82. S. Taioli, R. Gabbrielli, S. Simonucci, N.M. Pugno, A. Iorio, Lobachevsky crystallography made real through carbon pseudospheres. J. Phys. Condens. Matter. **28**, 13LT01 (2016)
83. A. Iorio, G. Lambiase, The Hawking-Unruh phenomenon on graphene. Phys. Lett. B **716**, 334–337 (2012)
84. M.M. Riegera, L. Steinbeck, I.D. White, H.N. Rojas, R.W. Godby, The GW space-time method for the self-energy of large systems. Comput. Phys. Commun. **177**, 211–228 (1999)
85. P. Umari, G. Stenuit, S. Baroni, Optimal representation of the polarization propagator for large-scale GW calculations. Phys. Rev. B **79**, 201104(R) (2009)
86. P. Umari, G. Stenuit, S. Baroni, GW quasiparticle spectra from occupied states only. Phys. Rev. B **81**, 115104 (2010)

87. M.S. Hybertsen, S.G. Louie, Electron correlation in semiconductors and insulators: band gaps and quasiparticle energies. Phys. Rev. B **34**, 5390–5413 (1986)
88. C. Friedrich, M.C. Müller, S. Blügel, Band convergence and linearization error correction of all-electron *GW* calculations: the extreme case of zinc oxide. Phys. Rev. B **83**, 081101R (2011)
89. J.P. Perdew, A. Zunger, Self-interaction correction to density-functional approximations for many-electron systems. Phys. Rev. B **23**, 5048–5079 (1981)
90. E.B. Barros, A. Jorio, G.G. Samsonidzef, R.B. Capazc, A.G. Souza Filhoa, J.M. Filhoa, G. Dresselhaus, M.S. Dresselhaus, Review on the symmetry-related properties of carbon nanotubes. Phys. Rep. **431**, 261–302 (2006)
91. H. Lin, J. Lagoute, V. Repain, C. Chacon, Y. Girard, J.-S. Lauret, F. Ducastelle, A. Loiseau, S. Rousset, Many-body effects in electronic bandgaps of carbon nanotubes measured by scanning tunnelling spectroscopy. Nat. Mat. **9**, 235–238 (2010)
92. R.B. Weisman, S.M. Bachilo, Dependence of optical transition energies on structure for single-walled carbon nanotubes in aqueous suspension: an empirical kataura plot. Nano Lett. **3**, 1235–1238 (2003)
93. G. Dukovic, F. Wang, D. Song, M.Y. Sfeir, T.F. Heinz, L.E. Brus, Structural dependence of excitonic optical transitions and band-gap energies in carbon nanotubes. Nano Lett. **5**, 2314–2318 (2005)
94. R. Saito, G. Dresselhaus, M.S. Dresselhaus, *Physical Properties of Carbon Nanotubes* (Imperial College Press, London, 1998)
95. J. Deslippe, M. Dipoppa, D. Predergast, M.V.O. Moutinho, R.B. Capaz, S.G. Louie, Electron-hole interaction in carbon nanotubes: novel screening and exciton excitation spectra. Nano Lett. **9**, 1330–1334 (2009)
96. M. Rohlfing, S.G. Louie, Electron-hole excitations and optical spectra from first principles. Phys. Rev. B. **62**, 4927–4944 (2000)
97. W. Kang, M.S. Hybertsen, Enhanced static approximation to the electron self-energy operator for efficient calculation of quasiparticle energies. Phys. Rev. B **82**, 195108 (2010)
98. T. Miyake, S. Saito, Quasiparticle band structure of carbon nanotubes. Phys. Rev. B **68**, 155423 (2003)
99. P. Avouris, Z. Chen, V. Perebeinos, Carbon-based electronics. Nat. Nano. **2**, 605–615 (2007)
100. M. Dapor, Mermin differential inverse inelastic mean free path of electrons in polymethylmethacrylate. Front. Mater. **2**, 27 (2015)
101. S. Taioli, S. Simonucci, L. Calliari, M. Dapor, Electron spectroscopies and inelastic processes in nanoclusters and solids: theory and experiment. Phys. Rep. **493**, 237–319 (2010)
102. S. Taioli, S. Simonucci, A computational perspective on multichannel scattering theory with applications to physical and nuclear chemistry. Annu. Rep. Comput. Chem. **11**, 191–310 (2015)
103. Y. Li, A. Chernikov, X. Zhang, A. Rigosi, H.M. Hill, A.M. van der Zande, D.A. Chenet, E.-M. Shih, J. Hone, T.F. Heinz, Measurement of the optical dielectric function of monolayer transition-metal dichalcogenides: MoS_2, $MoSe_2$, WS_2, and WSe_2. Phys. Rev. B **90**, 205422 (2014)
104. J. Daniels, C.V. Festenberg, H. Raether, K. Zeppenfeld, *Optical Constants of Solids by Electron Spectroscopy*. Springer Tracts in Modern Physics, vol. 54 (Springer, Berlin, 1970), pp. 77–135
105. H. Raether, Excitation of plasmons and interband transitions by electrons, vol. 88 (Springer, Berlin, 1980)
106. S. Baroni, R. Resta, Ab initio calculation of the macroscopic dielectric constant in silicon. Phys. Rev. B **33**, 7017–7021 (1986)
107. M. Dapor, G. Garberoglio, L. Calliari, Energy loss of electrons impinging upon glassy carbon, amorphous carbon, and diamond: comparison between two different dispersion laws. Nucl. Instrum. Methods Phys. Res. B **352**, 181–185 (2015)
108. M. Dapor, L. Calliari, M. Filippi, Computational and experimental study of π and $\pi + \sigma$ plasmon loss spectra for low energy ($<1000\,\mathrm{eV}$) electrons impinging on highly oriented pyrolitic graphite (HOPG). Nucl. Instrum. Methods Phys. Res. B **255**, 276–280 (2007)

109. R. Garcia-Molina, I. Abril, I. Kyriakou, D. Emfietzoglou, Inelastic scattering and energy loss of swift electron beams in biologically relevant materials. Surf. Interface Anal. **49**, 11–17 (2017)
110. E. Runge, E.K.U. Gross, Density-functional theory for time-dependent systems. Phys. Rev. Lett. **52**, 997–1000 (1984)
111. C.A. Ullrich, *Time-Dependent Density Functional Theory: Concepts and Applications*. Oxford Graduate Texts (Oxford University Press, Oxford, 2012)
112. G. Onida, L. Reining, A. Rubio, Electronic excitations: density-functional versus many-body Green's-function approaches. Rev. Mod. Phys. **74**, 601–659 (2002)
113. L. Hedin, New method for calculating the one-particle green's function with application to the electron-gas problem. Phys. Rev. **139**, A796–A823 (1965)
114. S.L. Adler, Quantum theory of the dielectric constant in real solids. Phys. Rev. **126**, 413–420 (1962)
115. N. Wiser, Dielectric constant with local field effects included. Phys. Rev. **129**, 62–69 (1963)
116. R.H. Ritchie, Plasma losses by fast electrons in thin films. Phys. Rev. **106**, 874–881 (1957)
117. M. Dapor, *Electron–Beam Interactions with Solids* (Springer, Berlin, 2003)
118. H. Nikjoo, S. Uehara, D. Emfietzoglou, *Interaction of Radiation with Matter* (CRC Press/Taylor & Francis Group, Boca Raton, 2012)
119. H. Nikjoo, D. Emfietzoglou, T. Liamsuwan, R. Taleei, D. Liljequist, S. Uehara, Radiation track, DNA damage and response–a review. Rep. Prog. Phys. **79**, 116601 (2016)
120. M. Dapor, Energy loss of fast electrons impinging upon polymethylmethacrylate. Nucl. Instrum. Methods Phys. Res. B **352**, 190–194 (2015)
121. F. Yubero, S. Tougaard, Model for quantitative analysis of reflection-electron-energy-loss spectra. Phys. Rev. B **46**, 2486–2497 (1992)
122. E. Shiles, T. Sasaki, M. Inokuti, D.Y. Smith, Self-consistency and sum-rule tests in the Kramers-Kronig analysis of optical data: applications to aluminum. Phys. Rev. B **22**,1612–1628 (1980)
123. R. Garcia-Molina, I. Abril, C.D. Denton, S. Heredia-Avalos, Allotropic effects on the energy loss of swift H^+ and He^+ ion beams through thin foils. Nucl. Instrum. Methods Phys. Res. B **249**, 6–12 (2006)
124. S. Tanuma, C.J. Powell, D.R. Penn, Calculations of electron inelastic mean free paths. IX. Data for 41 elemental solids over the 50 eV to 30 keV range. Surf. Interface Anal. **43**, 689–713 (2011)
125. S. Sharma, J. Dewhurst, A. Sanna, E.K.U. Gross, Bootstrap approximation for the exchange-correlation kernel of time-dependent density-functional theory. Phys. Rev. Lett. **107**, 186401 (2011)
126. S. Waidmann, M. Knupfer, B. Arnold, J. Fink, A. Fleszar, W. Hanke, Phys. Rev. B **61**, 10149–10153 (2000)
127. J. Harl, The linear response function in density functional theory: optical spectra and improved description of the electron correlation. Ph.D. thesis, Universitat Wien (2008)
128. A.B. Bortz, M.H. Kalos, J.L. Lebowitz, A new algorithm for Monte Carlo simulation of Ising spin systems. J. Comput. Phys. **17**, 10–18 (1975)
129. M. Dapor, *Transport of Energetic Electrons in Solids*, 2nd edn. (Springer, Berlin, 2017)
130. M. Dapor, Role of the tail of high-energy secondary electrons in the Monte Carlo evaluation of the fraction of electrons backscattered from polymethylmethacrylate. Appl. Surf. Sci. **391**, 3–11 (2017)
131. S. Taioli, S. Simonucci, M. Dapor, Surprises: when ab initio meets statistics in extended systems. Comput. Sci. Discov. **2**, 015002 (2009)
132. S. Taioli, S. Simonucci, L. Calliari, M. Filippi, M. Dapor, Mixed ab initio quantum mechanical and MonteCarlo calculations of secondary emission from SiO_2 nanoclusters. Phys. Rev. B **79**, 085432 (2009)
133. S. Taioli, A bird's eye view on the concept of multichannel scattering with applications to materials science, condensed matter, and nuclear astrophysics. Front. Mater. **2**, 71 (2015)

134. M.S. Green, Markoff random processes and the statistical mechanics of time-dependent phenomena. II. Irreversible processes in fluids. J. Chem. Phys. **22**, 398–413 (1954)
135. R. Kubo, Statistical-mechanical theory of irreversible processes. I. General theory and simple applications to magnetic and conduction problems. J. Phys. Soc. Jpn. **12**, 570–586 (1957)
136. A. Pedrielli, S. Taioli, G. Garberoglio, N.M. Pugno, Gas adsorption and dynamics in pillared graphene frameworks. Microporous Mesoporous Mater. **257**, 222–231 (2018)
137. G. Garberoglio, N.M. Pugno, S. Taioli, Gas adsorption and separation in realistic and idealized frameworks of organic pillared graphene: a comparative study. J. Phys. Chem. C **119**, 1980–1987 (2014)
138. A. Battisti, S. Taioli, G. Garberoglio, Zeolitic imidazolate frameworks for separation of binary mixtures of CO_2, CH_4, N_2 and H_2: a computer simulation investigation. Microporous Mesoporous Mater. **143**, 46–53 (2011)
139. G. Garberoglio, S. Taioli, Modelling flexibility in metal–organic frameworks: comparison between density-functional tight-binding and universal force field approaches for bonded interactions. Microporous Mesoporous Mater **163**, 215–220 (2012)
140. L. Lu, P.S.E. Yeo, C.W. Gan, P. Wu, K.P. Loh, Transforming C_{60} molecules into graphene quantum dots. Nat. Nanotechnol. **6**, 247–252 (2011)
141. N. Swami, H. He, B.E. Koel, Polymerization and decomposition of C_{60} on Pt(111) surfaces. Phys. Rev. B **59**, 8283–8291 (1999)
142. E.P. Randviir, D.A.C. Brownson, C.E. Banks, A decade of graphene research: production, applications and outlook. Mater. Today **17**, 426–432 (2014)

Chapter 6
Group 13–15 Needle-Shaped Oligomers and Nanorods: Structures and Electronic Properties

Anna V. Pomogaeva and Alexey Y. Timoshkin

Abstract Synthetic approaches, structures, and reactivity of group 13–15 needle-shaped oligomers have been reviewed. Computational studies reveal that needle-shaped oligomers are more stable than fullerene-like isomers for all 13–15 pairs. Formation of such oligomers in the gas phase is energetically favorable and feasible from the thermodynamic point of view. However, many competitive reaction pathways are kinetically possible which leads to cascade of reactions and different reaction products. A systematic study of the various effects of structural variations on the electronic properties of Ga-N-based nanorods has been performed. On the basis of DFT computations, we demonstrate that terminal groups have a crucial impact on the electronic properties of the rod-shaped $[RGaNH]_{3n}$ (R=H, CH_3) oligomers. Oligomers capped with GaR and NH groups adopt almost periodic structure in which terminal groups affect only the very edges of the oligomer. The band gap energy of the $[HGaNH]_{3n+1}$ is defined by states localized at the different ends of the oligomer. The value of the band gap is converging fast with increase of n, and for $n = 38$ it is about 93% of the value of the band gap of the $[HGaNH]_{3\infty}$ polymer. In contrast, termination of the $[HGaNH]_{3n}$ rod-shaped oligomer by saturation of dangling bonds with H or CH_3 groups destroys the periodic pattern and increases the number of states, localized at the ends of the oligomer. This way of termination is characterized by systematic change in structural parameters of the oligomer and near exponential decrease of the band gap energy with the oligomer length. The band gap energy for the rod-shaped oligomer of 10 nm of length ($n = 38$) amounts to only 27% of the value for the band gap of the $[HGaNH]_{3\infty}$ polymer. Substitution of Ga atoms by Al and In has also been considered. Absorption spectra undergo a red shift if Ga atoms are replaced by In atoms and a small blue shift if Ga atoms are replaced by Al atoms. The effect of electron-donating and electron-withdrawing terminal groups (H, CH_3, F, CF_3) on a dipole moment and energy gap values is found to be significant. The band gap energy of long tube-shaped Ga-N-based oligomers can be tuned within 2 eV

A. V. Pomogaeva · A. Y. Timoshkin (✉)
Institute of Chemistry, St. Petersburg State University, St. Petersburg, Russia
e-mail: a.y.timoshkin@spbu.ru

T. Onishi (ed.), *Theoretical Chemistry for Advanced Nanomaterials*,
https://doi.org/10.1007/978-981-15-0006-0_6

by changing the substituents at the ends of the oligomer. A combined effect of all considered factors, substituent groups variations, rod's elongation, and the way of ends' termination, can help to vary energy gap of the $[HGaNH]_{3n}$ rod-shaped oligomer within the range 1–7 eV. Potential applications and further directions are also discussed.

Keywords 13–15 compounds · Ga-N · Oligomers · Reaction mechanisms · DFT · Electronic properties

6.1 Introduction

In past decades, chemistry of oligomeric group 13–15 compounds has grown dramatically due to their importance as precursors for semiconductor materials. Group 13–15 binary compounds are prospective materials for microelectronics, solar cell elements, light-emitting diodes, UV photodetectors, high electron mobility transistors, and ceramic materials [1–3]. Among 13–15 binary compounds, the gallium nitride stands out due to its unique properties and applications [4–6]. The simplest architectures of interest here are one-dimensional (1D) nanorods or whiskers. One-dimensional nanopatterning of Ga-N surface results in significant enhancement (by 40–60%) of the light output of Ga-N-based LEDs [7]. Production of one-dimensional 13–15 architectures is an important task. Oligomer and 1D polymer compounds are excellent precursors for the 13–15 materials. In 1990 only several 13–15 oligomer compounds have been experimentally known, mostly amido- and iminoalanes [8]. Since then, the rapid developments in oligomer 13–15 chemistry have been the topic of numerous books and reviews [9–22].

Among the many possible structures of 13–15 oligomers, the needle-shaped or rod-like compounds attracted special attention. These compounds can be considered as a product of subsequent oligomerization of $[RMYR']_3$ trimeric rings, which can be either saturated with R,R' substituents or capped by MR and YR' groups, resulting in *open* and *closed* oligomers, respectively (M = Al, Ga, In; Y = N, P, As; R,R' = H, halogens, or organic substituents). Their structures are schematically shown in Fig. 6.1 on the example of $[MeGaNH]_{3n+1}$.

It was computationally predicted that with the increase of the oligomerization degree, these compounds become more stable than fullerene-like clusters for all 13–15 pairs [23, 24].

The key oligomerization degrees of *closed* $[RMYR']_m$ oligomers are 4, 7, 10, 13, 16, etc., and they can be written as $[RMYR']_{3n+1}$, where n – number of trimeric $[RMYR']_3$ rings. The drum-type hexamer $[RMYR']_6$ is a product of dimerization of two trimeric $[RMYR']_3$ rings.

Formation of oligomeric compounds in the gas phase at high temperatures was proposed on the basis of the computational study of $AlCl_3$-NH_3 system in 1997 [25] based on experimental observations of 13–15 nanoparticle formation in CVD processes [26–30]. Experimental in situ mass spectrometry (MS) monitoring

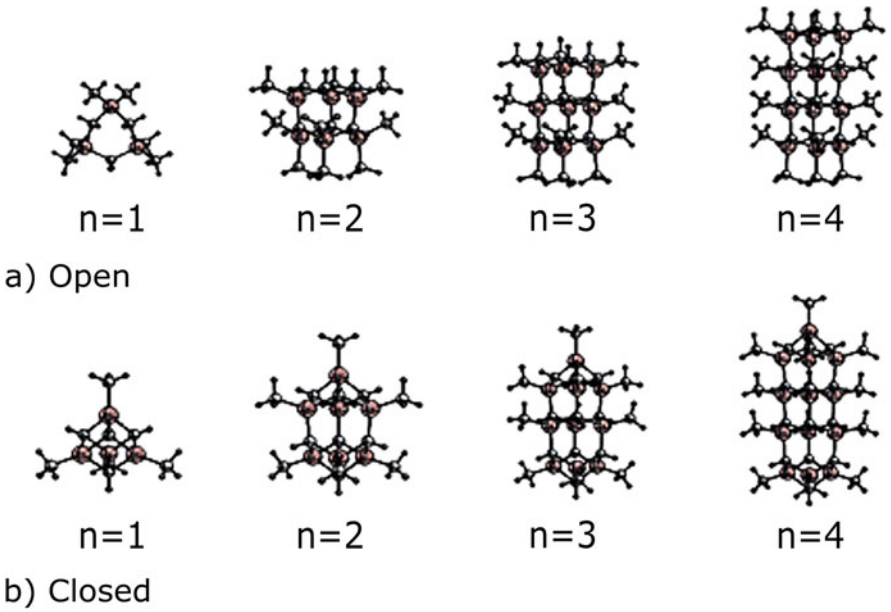

Fig. 6.1 Structures of (**a**) *open* $Me_3[MeGaNH]_{3n}H_3$ and (**b**) corresponding *closed* $[MeGaNH]_{3n+1}$ needle-shaped oligomers with one, two, three, and four $[MeGaNH]_3$ rings

of Ga-N MOCVD from trimethylgallium and ammonia suggested formation of $[Me_2GaNH_2]_n$ oligomers, most probably with $n = 3$ [31]. Dimeric $[Me_2GaNH_2]_2$ species have also been observed [32, 33]. Laser-assisted reactivity studies between trimethylgallium or trimethylaluminum and ammonia at low temperatures by Demchuk and Koplitz [34–37] provided mass spectrometry evidence of formation of larger oligomeric molecules, containing up to 6 aluminum and gallium atoms. Indirect measurements pointed out the formation of species containing as many as 80 gallium atoms [38]. These experimental findings confirmed our 1997 hypothesis [25] concerning the gas phase oligomer formation and opened the field for the extensive computational studies of 13–15 amido [39–41] and imino [42–50] compounds, as well case studies for G-aN CVD from organometallic $Ga(CH_3)_3NH_3$ [51–53] and inorganic $GaCl_3NH_3$ [54, 55] precursors.

In this review, in Sect. 6.2 we will discuss synthetic approaches to 13–15 needle-shaped oligomers, review their experimental structures, and briefly present results of computational studies of reaction mechanisms for generation of 13–15 needle-shaped compounds.

In Sect. 6.3, structures and electronic properties of Ga-N-based rod-like oligomers and related compounds will be discussed in detail based on results of our recent comprehensive computational studies [56–59]. Possible directions for future research are also outlined.

The following abbreviations are used: Me, methyl; Et, ethyl; Pr, propyl; Bu, butyl; Hx, hexyl; Ph, phenyl; Xyl, -C_6H_3-2,6-Me_2; Cp, cyclopentadienyl; py, pyridine; Mes, mesityl (2,4,6-trimethylphenyl or –C_6H_2-2,4,6-Me_3); Mes*, 2,4,6-tri-*tert*-butylphenyl (–C_6H_2-2,4,6-$^tBu_3$); Dipp, 2,6-diisopropylphenyl (-C_6H_3-2,6-$^iPr_2$); Ad, adamantyl; THF, tetrahydrofuran; r.t., room temperature; ALD, atomic layer deposition; CVD, chemical vapor deposition; MOCVD, metal organic CVD; LED, light-emitting diode; UV, ultraviolet; MO, molecular orbital; CO, crystal orbital; AO, atomic orbital; PBC, periodic boundary condition; BZ, Brillouin zone; HOMO, highest occupied MO; LUMO, lowest unoccupied MO; (TD)DFT, (time-dependent) density functional theory; GGA, generalized gradient approximation; TS, transition state; and PDOS, partial density of states.

6.2 13–15 Needle-Shaped Oligomers: Experimental and Computational Studies

6.2.1 Synthetic Methods of Production of Needle-Shaped 13–15 Compounds

Thermal activation is the first method employed for the synthesis of imino compounds [60–62], and it remains one of the major synthetic methods for their generation. Wiberg [60] demonstrated that thermolysis of group 13 alkyls MR_3 with ammonia results in the stepwise elimination of RH and formation of amido and imino compounds and finally the bulk group 13 metal nitride (MN). These reactions in case of $AlMe_3$ are given in Scheme 6.1.

Decomposition of Me_3AlNH_3 in the condensed phase (Scheme 6.1) proceeds slowly at 60–70 °C with evolution of one mole of methane per mole of adduct and formation of oligomeric amido compounds [62]. Further heating results in formation of imino polymers (ca 150–200 °C) and finally amorphous AlN at ca 500 °C [62]. Prolonged heating at elevated temperatures increases crystallinity of the material. However, in the original works of Wiberg [60], oligomer imino compounds $[RMNR']_n$ have not been isolated and identified due to their insolubility in common organic solvents.

For the controlled synthesis of well-defined imino compounds, use of primary amines NH_2R' instead of ammonia is necessary to prevent the last RH elimination

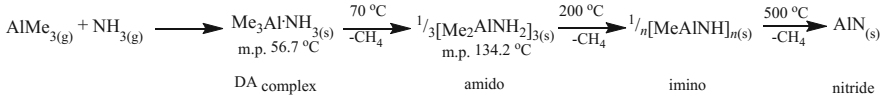

Scheme 6.1 Reaction sequence for the thermal decomposition of the trimethylaluminum-ammonia adduct in the condensed phase

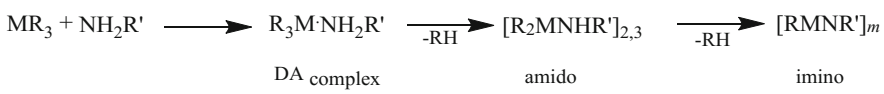

Scheme 6.2 Synthetic approach to imino compounds by thermal decomposition of DA complexes

step. Reaction between R_3M and NH_2R' initially produces the donor-acceptor complex $R_3M{\cdot}NH_2R'$, which upon thermolysis produces amido and afterwards imino compounds (Scheme 6.2). The oligomerization degree *m* for the generated compounds strongly depends on the bulkiness of the substituents R and R′ [12, 13, 15]. More bulky substituents yield lower oligomerization degree.

Since thermal activation requires elevated temperatures, undesirable side reactions may accompany the desired reaction pathway yielding by-products, generally due to the activation of C-H bonds [63]. For example, reaction between $AlMe_3$ and NH_2Mes^* results in metallation of ^{t}Bu group of the Mes* [63–65], while reaction between $AlCp_3$ and NH_2Dipp yields $[CpAlNDipp]_2$ ring [66]. Analogous metallation of ^{t}Bu group of Mes* was observed upon thermal decomposition of $Et_2GaNHMes^*$ [67]. Reaction between $GaMe_3$ and $NH(CH_2Ph)_2$ also resulted in orthometallated compound with 65% yield [68]. In order to reduce by-side reactions, low pressures are often used. Thus, thermolysis of solid amido compounds was carried out at mild conditions (130 °C, 10^{-2} Torr) for 12–36 days to afford desirable cubanes [69].

The reaction pathway presented in Scheme 6.1 may be generalized to all group 13–15 element derivatives, as was shown by Beachley and Coates [70]. Reactions of Me_3M with YH_2R (M = Al,Ga,In; Y = P,As; R = Me,Ph) results in evolution of circa two moles of methane (1.86–2.02) and formation of the colored involatile polymeric materials $[MeMYR]_n$ [70]. In the case of Ga derivatives, elimination of methane was not complete; it varied from 1.41 to 1.94 even at elevated (circa 200 °C) temperatures. This result is in agreement with observation of P-H and As-H stretching vibrations in all IR spectra of gallium-containing polymers. No such absorptions were present in the spectra of Al and In polymers. Unfortunately, no further characterization and isolation of the $[MeMYR]_n$ compounds were performed.

Despite of this example, the general use of thermal activation methods for phosphorus- and arsenic-containing compounds is limited due to their low thermal stability and formation of by-products. In such a case, methathesis reactions can be used instead. Thus, reaction between organometallic group 13 halides RMX_2 and doubly lithiated group 15 species Li_2YR' yields desired oligomer species $[RMYR']_n$ (R′=SiR′′$_3$) [71–73]:

$$2X_2MR + 2Li_2YSiR''_3 = 4LiX + \left[RMYSiR''_3\right]_2$$

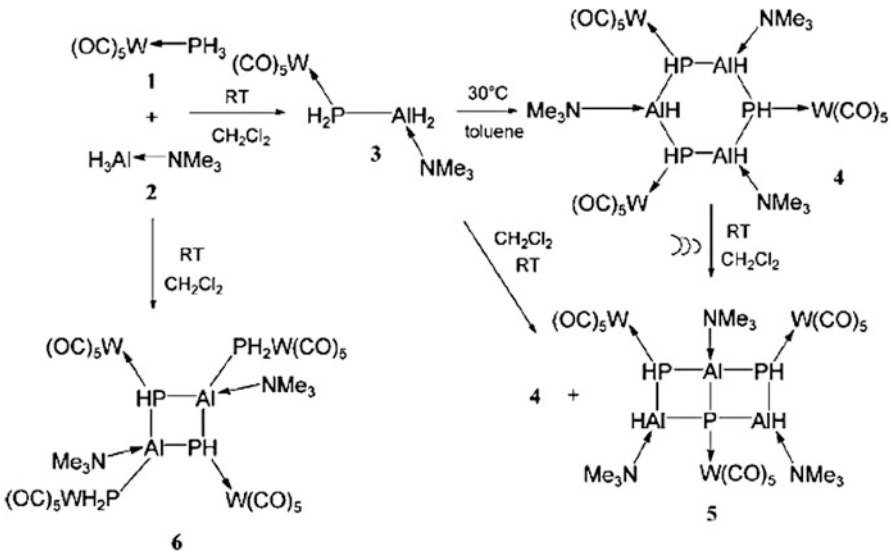

Scheme 6.3 Synthetic approach to donor-acceptor stabilized Al-P oligomer compounds. From [74] Copyright © 2009 by John Wiley Sons, Inc. (Reprinted by permission of John Wiley & Sons, Inc.)

Use of the Lewis acid/base stabilization concept allowed to produce cyclic trimer $\{W(CO)_5\}_3[HAlPH]_3\{NMe_3\}_3$ by H_2 elimination from the monomeric $W(CO)_5{\cdot}H_2AlPH_2{\cdot}NMe_3$. The elimination is controlled by fine tuning the temperature and solvent conditions. Elimination of one mole of H_2 from $\{W(CO)_5\}_3[HAlPH]_3\{NMe_3\}_3$ results in the ladder compound 5 (Scheme 6.3) [74].

Instead of primary amines, tertiary amines, phosphines, and arsines, containing easily removable functional groups can be also utilized in elimination reactions. For example, such substituents as $SiMe_3$ [73] and $SnMe_3$ [75] are easy leaving groups. Thus, thermolysis of $[(Me_2GaN(^iBu)SnMe_3)]_2$ at 160°C resulted in $SnMe_4$ elimination with formation of hexamer $[MeGaN^iBu]_6$ [75]. Reaction between $GaCl_3$ and $As(SiMe_3)_3$ in the presence of the Lewis acid P^tBu_2Me leads to the donor-acceptor stabilized dimeric compound $[ClGaAsSiMe_3]_2{\cdot}2P^tBu_2Me$ with liberation of $ClSiMe_3$ [73].

Instead of MR_3 derivatives, hydridic derivatives $LiAlH_4$ or $NaAlH_4$ can be used as starting compounds in reaction with NH_2R in hydrocarbon solvents [76]. Such reaction pathway allows to obtain soluble hydridic polyiminoalanes $[HAlNR]_n$ which were characterized by NMR spectroscopy [77, 78]. These hydridic $[HAlNR]_n$ compounds can be further functionalized by substitution of the H atoms to other groups. Thus, substitution by Cl [79], Br [80, 81], F [82], Me [83], Et [83], -C≡CR [80, 81], and $CpFeC_5H_4C{\equiv}C$- [84] groups has been carried out. It should be noted that this route provides access to compounds with oligomerization degrees,

not accessible by the elimination route. As an example, reactions of $[HAlN^iPr]_6$ with $AlMe_3$ and $AlEt_3$ produce methyl- and ethyl-substituted hexamer species $[MeAlN^iPr]_6$ and $[EtAlN^iPr]_6$, respectively. In contrast, direct reaction between $AlMe_3$ or $AlEt_3$ and $NH_2{}^iPr$ resulted in tetramers $[MeAlN^iPr]_4$ and $[EtAlN^iPr]_4$ [85].

HCl, $HgCl_2$, and $TiCl_4$ were used to obtain partially or fully chlorinated poly(N-alkyliminoalanes), starting from the corresponding hydride derivatives [79].

$$[HAlNR]_n + n\ HCl \xrightarrow{Et_2O} [ClAlNR]_n + nH_2$$

$$[HAlNR]_n + {}^n/_2 HgCl_2 \xrightarrow{Et_2O} [ClAlNR]_n + {}^n/_2 Hg + {}^n/_2 H_2$$

$$[HAlNR]_n + n\ TiCl_4 \xrightarrow{n-heptane} [ClAlNR]_n + n\ TiCl_3 + {}^n/_2 H_2$$

A series of Cl- and Br-substituted compounds was obtained by substitution from $[HAlNCH_2Ph]_6$ [80, 81, 84]. Roesky was able to introduce six ferrocene units $CpFeC_5H_4C{\equiv}C$ as substituents to form very bulky hexamer compound $[CpFeC_5H_4C{\equiv}CAlNCH_2Ph]_6$ [84]. One of the drawbacks of such an approach is incompleteness of the substitution reaction. Thus, only partial substitution of H by F atoms was achieved by treating heptamer compound $[HAlNCH_2(1\text{-}Ad)]_7$ with Me_3SnF. Resulting product has an empiric formulae $[F_{0.32}H_{0.68}AlNCH_2(1\text{-}Ad)]_7$ [82]. Reaction of $[HAlNR]_4$ with $ZpCp_2Me_2$ leads to stepwise substitution of H into Me groups, forming $[Me_{0.22}H_{0.78}AlNR]_4$, $[Me_{0.5}H_{0.5}AlNR]_4$, and finally $[MeAlNR]_4$ [83].

Series of substitution reactions have been performed for the $[HAlNR]_n$ compounds (n=4,6,8) by Nöth and Wolfgardt, resulting in full or partially substituted compounds $X_mH_{n\text{-}m}[AlNR]_n$ (X=D,Cl,Br,I) [86, 87]. Mechanism of a hydrogen/deuterium exchange via formation of intermediates with pentacoordinate aluminum was discussed in work [87].

Despite numerous successful examples, the application of substitution reactions is limited due to undesired side processes, one of which is a cage degradation to form amido compounds [79]. Cage degradation reaction was observed upon interaction of PhSH with $[HAlNCH_2(C_4H_3S)]_6$, producing amido compound $[(PhS)_2AlNHCH_2(C_4H_3S)]_2$ instead of the desired $[PhSAlNCH_2(C_4H_3S)]_6$ [81]. Computational studies suggest that both substitution reactions of $[HAlNR]_n$ and cage degradation reactions with formation of amido compounds $[H_2AlNR_2]_m$ are thermodynamically favorable and therefore can proceed concurrently [47].

Polyalkyliminoalanes can be also produced in one-pot reaction between aluminum and primary amines in hydrogen atmosphere [88]:

$$Al + RNH_2 = {}^1/_n[HAlNR]_n + \frac{1}{2}H_2$$

This reaction is activated by metallic sodium, $NaAlH_4$, or $[HAlNR]_6$. Since such reaction requires excess of molecular hydrogen, it was assumed that the first step is in situ generation of AlH_3. Reaction of $LiAlH_4$ with NH_3RCl has also been used to generate iminoalanes [89]:

$$LiAlH_4 + NH_3RCl = {}^1/_n[HAlNR]_n + 3\ H_2 + LiCl$$

Direct reduction of nitriles RCN by $AlH_3 \cdot NMe_3$ also results in the formation of iminoalanes [89]:

$$AlH_3 \cdot NMe_3 + RCN + {}^1/_n[HAlNCH_2R]_n + NMe_3$$

Similar approach was used by Roesky for the synthesis of various hexamer compounds [80], which were used as a starting materials for the functionalization by substitution reactions [80, 81, 84].

It should be also noted that reaction between MR_3 and YH_3 is one of the major methods in production of 13–15 binary materials in CVD processes [90–92], which occurs at high temperatures. In the condensed phase chemistry, it has been mostly used for the production of iminoalanes.

6.2.2 *Structural Features and Reactivity of Needle-Shaped Oligomers*

6.2.2.1 Tetramers

Formally, several isomers are possible for the $[RMYR']_4$ composition, but the cubane-type structures in which both metal and pnictogen centers adopt coordination number 4 (Fig. 6.2a) are the most stable [50]. The metal-metal bonded isomer with Al_4 tetrahedral core $Al_4(NRR')_4$ (Fig. 6.2b) is also structurally characterized [93]. Structural properties of the experimentally known more than forty 13–15 cubanes have been discussed in [20]. Uhl [11] reviewed the hydrazine-based compounds, which possess M_4N_8 core with five-membered rings, which formally corresponds to the $[RMYR']_4$ composition.

Coordination number 4 both on metal and pnictogen centers makes cubanes relatively stable species. Thus, $[^i PrInPSiPh_3]_4$ is relatively stable toward alcoholysis but unstable with respect to photolysis and electrochemical oxidation [95]. Many of cubane clusters are volatile compounds and can be purified by vacuum sublimation. Structures of cubane-type clusters are usually highly symmetric with equal M-Y bond distances in the M_4Y_4 cube.

Despite coordination number 4 on metal center, metal atoms in cubanes are able to participate in donor-acceptor interactions. Thus, each In atom in [MeIn(THF)N(4-C_6H_4F)]$_4$ is coordinated to THF molecule [96], which may result from the larger atomic radius of indium. $[HAlN^iPr]_4$ forms solid adduct with

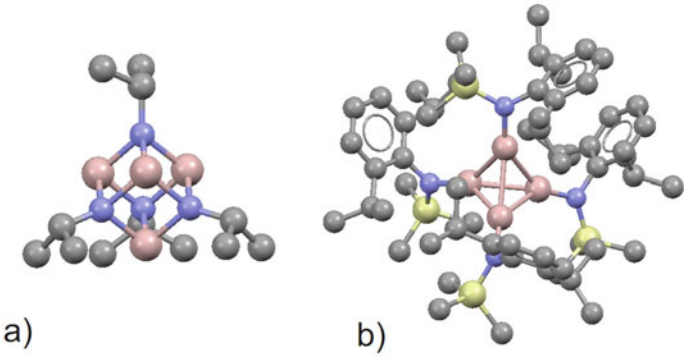

Fig. 6.2 Structures of $[RMYR']_4$ tetramers on the example of (**a**) cubane-type $[HAlN^iPr]_4$ cluster tetrakis(μ^3-isopropylimido)-tetrahydrido-tetra-aluminium [94] and (**b**) tetrahedral cluster tetrakis((N-(2,6-Di-isopropylphenyl)trimethylsilylamino)-aluminium(I)) $Al_4(NRR')_4$ [93]. Aluminum atoms are colored in pink, nitrogen in blue, silicon in yellow, and carbon in gray. Hydrogen atoms are omitted for clarity

1,2-diisopropyldiazene molecule ^{i}PrN=N^{i}Pr, but this adduct decomposes upon sublimation to give pure $[HAlN^iPr]_4$ cubane (Fig. 6.2a) [94].

It was supposed that interaction of weakly M-Y bonded cubanes with strong Lewis bases will result in opening of the M_4Y_4 cage, yielding ladder-type structures. Tensimetry study of interaction of phosphorus-containing cubane-type clusters $[RMPR']_4$ (M = Ga, In) toward pyridine showed that M_4P_4 core is stable and does not react with Py, although computations show that process is energetically favorable at low temperatures [97].

Nevertheless, several group 13–15 ladder compounds of $[ClMYR]_4D_2$ composition are known and structurally characterized [98–100]. They are formed when donor-acceptor interactions with Lewis base D prevent formation of $[ClMYR]_n$ cages due to much lower M-Y bond energies in P-, As-, and Sb-containing cubanes [43]. Upon the removal of donor molecules, closure of ladder structure to tetramer or hexamer is expected. Indeed, when synthesis of $[ClAlPSi^iPr_3]_4{\cdot}2OEt_2$ (Fig. 6.3) was carried out in absence of OEt_2, hexameric compound $[ClAlPSi^iPr_3]_6$ was formed [98].

Mixed metal ladder compounds are also known. Molecular structure of $[(ClGa)_2(BPh)_2(N^tBu)_4]$ with $Ga_2B_2N_4$ core (Fig. 6.3c) was reported in work [101]. Analogous indium compound with $In_2B_2N_4$ core incorporates bissolvated lithium chloride molecule in the indium complex, resulting in coordination number 5 on In center.

Mixed group 13 element and mixed pnictogen tetramers are not yet experimentally realized. $[(M_xM'_yM''_z)Y_4]H_8$ and $[M_4(Y_xY_yY_z)]H_8$ ($x+y+z=4$; M,M′,M″=Al,Ga,In; Y,Y′,Y″=N,P,As) compounds were computationally studied in [44]. Their structural parameters resemble those of individual cubanes. The

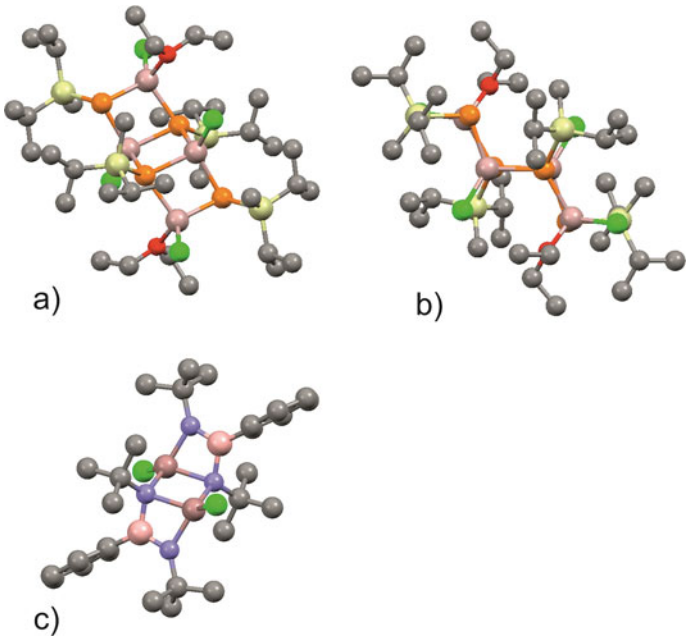

Fig. 6.3 Structures of ladder compounds on the example: $[ClAlPSi^{i}Pr_3]_4 \cdot 2OEt_2$ (**a**) front view; (**b**) side view; (**c**) mixed element ladder $[(ClGa)_2(BPh)_2(N^{t}Bu)_4]$. Group 13 element atoms are colored in pink, phosphorus in orange, nitrogen in blue, silicon in yellow, chlorine in green, and carbon in gray. Hydrogen atoms are omitted for clarity

process of generation of mixed cubanes is predicted to be thermodynamically favorable at higher temperatures [44].

Computational studies also suggest that existence of donor-acceptor stabilized "naked" cubanes $D_4[MY]_4A_4$ (D-Lewis base; A-Lewis acid, M=B-Ga; Y=N-As) is thermodynamically feasible [48].

In these compounds (Scheme 6.4, upper right corner), the functional groups R are substituted by donor and acceptor molecules. The proposed reaction pathway to these compounds from the donor and acceptor stabilized hydrides is shown on Scheme 6.4. Computations predict that Al-N- and Al-P-based cubanes are the most stable [48]. Indeed, use of this synthetic approach allowed Bodensteiner et al. [74] to produce dimeric, trimeric, and ladder-type Al-P compounds (Scheme 6.3, *vide supra*). In the structure of the ladder compound, middle aluminum (Al3) and phosphorus (P2) atoms lost hydrogens and remain stabilized by donor NMe_3 and acceptor $W(CO)_5$ molecules (Fig. 6.4).

It should be noted that in case of amines as Lewis bases instead of ladder compounds of $[XAlNMe]_4 \cdot 2NMe_3$ composition, their formal isomers and adamantane-type cages are realized. Reaction of primary amine NH_2Me with amidoalanes $HXAlNMe_2$ (X=H,Cl,Br,I) results in hydrogen evolution and formation of

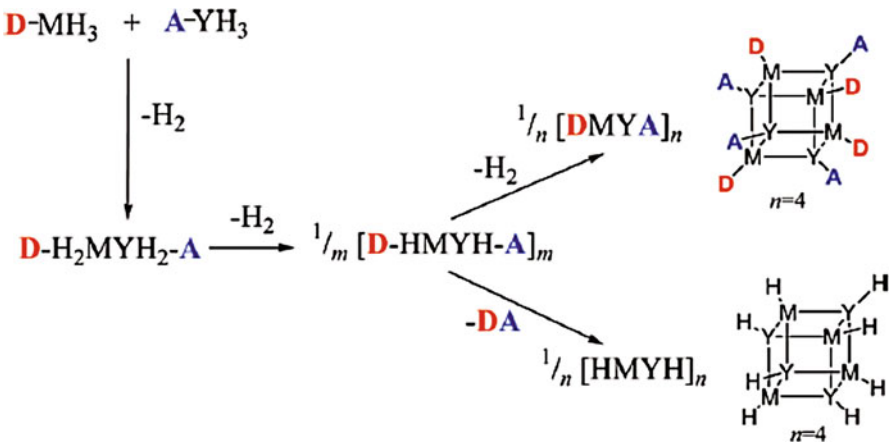

Scheme 6.4 Reaction pathways, leading to DA stabilized cubanes and higher oligomers according to [48]. (Reprinted with permission from [48]. Copyright 2009 American Chemical Society)

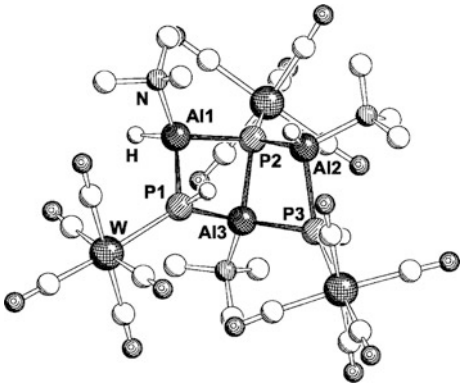

Fig. 6.4 Molecular structure of donor-acceptor stabilized ladder $(NMe_3)_3[(HAl)_2AlP(PH)_2]\{W(CO)_5\}_3$ compound. (From [74] Copyright © 2009 by John Wiley Sons, Inc. Reprinted by permission of John Wiley & Sons, Inc.)

adamantane-type $[(AlX)_4(NMe_2)_4(NMe)_2]$ cages [102, 103]. In these compounds the Me groups of amine nitrogen are transferred to the nitrogen atoms of the cluster core (Fig. 6.5).

Analogous gallium compound $[(GaPh)_4(NH^iBu)_4(N^iBu)_2]$ which also features adamantane-type structure has been prepared by reaction of $[PhGa(NMe_2)_2]_2$ with $NH_2{}^iBu$ [104]. Noteworthy, that in the chemical ionization mass spectrum at ca 310 °C, the base peak was assigned to $[PhGaN^iBu]_4$, suggesting that conversion of adamantane-type to cubane-type structure occurs at elevated temperatures. Formation of Ga_4-containing species was also evidenced in chemical ionization mass spectrum of $[^nHxGa(NMe_2)_2]_2$ at 300 °C [105].

Computational studies of the products of interaction of $[HGaNH]_4$ with one and two ammonia molecules suggest that formation of adamantane-type $[(GaH)_4(NH_2)_4(NH)_2]$ cage is energetically very favorable at low temperatures.

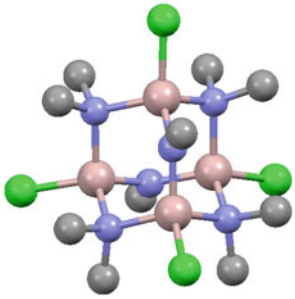

Fig. 6.5 Molecular structure of $[(AlCl)_4(NMe_2)_4(NMe)_2]$ compound with adamantane core [103]. Aluminum atoms are colored in pink, nitrogen in blue, chlorine in green, and carbon in gray. Hydrogen atoms are omitted for clarity

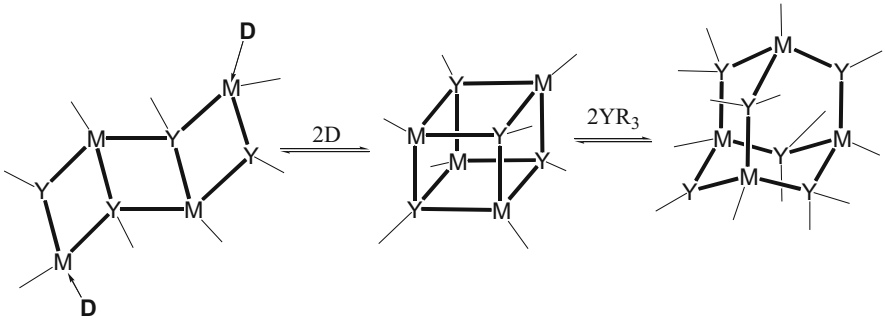

Scheme 6.5 Relationship between the ladder, cubane, and adamantine-type structures. (Reprinted from [20], Copyright (2005), with permission from Elsevier)

At temperatures higher than 440 °C, liberation of extra ammonia and conversion to cubane structure is predicted to be thermodynamically favorable [53].

The relationship between the cubane, ladder, and adamantine-type structures is summarized on the Scheme 6.5 [20].

Formation of tetramer cubic imino compounds from amido compounds supposedly proceeds with formation of *open* or "broken cube" compounds as intermediates. NMR studies of iminoalanes evidence the existence of the amido-imino broken cube intermediate $[(AlH_2)(NHR)(AlH)_3(NR)_3]$ [77, 78, 89]. The optically active amido-imino compound was prepared with R=-CH(Ph)Me, and its catalytical properties have been discussed [106]. "Broken cube" $[In_3Br_4(N^tBu(NH^tBu)_3]$ compound was isolated as a by-product of synthesis of cubane $[BrInN^tBu]_4$ [107].

6.2.2.2 Heptamers and Decamers

Compared to cubanes, structurally characterized heptamers are rare [20]. The cage of the heptamer can be viewed as an insertion of additional M_3Y_3 ring in M_4Y_4 cubane cluster. Heptamer $[HAlPSiMe_2(C^iPrMe_2)]_7$ [108] (Fig. 6.6) was crystallized and structurally characterized from the solution, which contained mostly hexamers. Attempt to produce $[FAlNCH_2(1\text{-}Ad)]_7$ by substitution route from

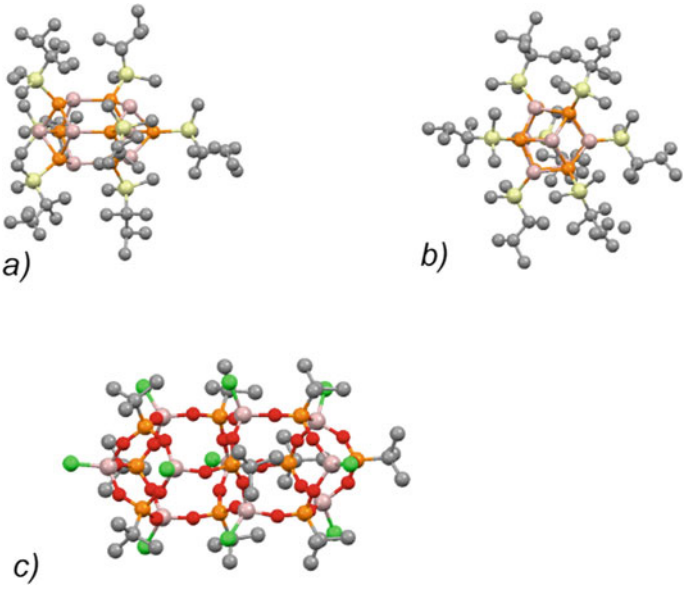

Fig. 6.6 Structure of needle-shaped heptamer on the example $[HAlPSiMe_2(C^iPrMe_2)]_7$ [108] (**a**) side view and (**b**) top view and (**c**) structure of the oxidized decamer $[ClAlPO_3Me]_{10}$ [109]. Aluminum atoms are colored in pink, phosphorus in orange, silicon in yellow, chlorine in green, oxygen in red, and carbon in gray. Hydrogen atoms are omitted for clarity

$[HAlNCH_2(1\text{-Ad})]_7$ was unsuccessful. Full substitution was not achieved, resulting in compound $[F_{0.32}H_{0.68}AlNCH_2(1\text{-Ad})]_7$ [82].

The needle-shaped structure of oxidized decamer $[ClAlPO_3Me]_{10}$ (Fig. 6.6c) is also noteworthy [109], since it reflects the stability of needle-shaped structural motif.

Needle-shaped heptamer with Ga_7N_7 core $[PhGaNMe]_7$ was synthesized by thermolysis of $[Ph_2GaNHMe]_2$ and structurally characterized [110]. The reactivity leading to tetrameric and heptameric Ga-N-based compounds with adamantane-type cores is presented in Scheme 6.6 [104]. Decomposition of adamantane-type amido-imino compound $[(GaPh)_7(NHMe)_4(NMe)_5]$ at 340 °C leads to heptamer $[PhGaNMe]_7$, as indicated by chemical ionization mass spectrometry studies [104].

Computational studies of heptamer compounds $[HAlNH]_7$ and $[RGaNH]_7$ (R=H,Me) were performed in works [53, 111, 112]. Mixed element heptamer clusters $[(HM)_k(HM')_l(NH)_7]$ (M, M′ = B, Al, Ga and k + l = 7) and $[(HGa)_7(YH)_m(Y'H)_n]$ (Y,Y′ = N, P, As and m + n = 7) have been computationally studied by Mohajeri and Ebadi [113].

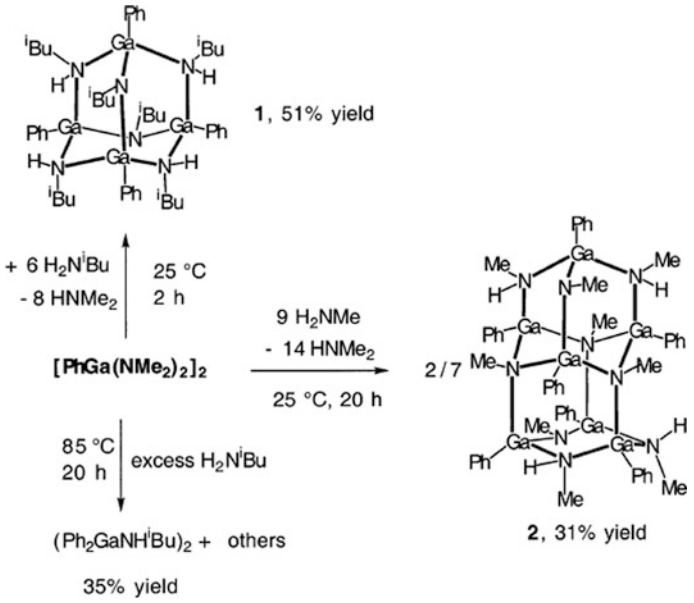

Scheme 6.6 Reactions leading to Ga-N-based needle-shaped compounds with adamantane-type cores. (Reprinted with permission from [104]. Copyright 2002 American Chemical Society)

6.2.2.3 Higher Oligomers and Polymers

It is well known that less bulky substituents favor formation of high oligomers and polymers. In fact, polymeric species were predominant in first synthetic works but were poorly characterized. Formation of polymeric compound $[ClAlNMe]_n$ from $AlEt_2Cl$ and NH_2Me was observed in 1961 [61]. It was noted that in rapid pyrolysis of $[AlEt_2Cl(NH_2Me)]$ at 160 °C, the solid product had intermediate, "amido-imino" composition $[(EtClAlNMeH)(ClAlNMe)]_x$. Prolonged heating at 210–220 °C resulted in white, nonvolatile highly polymeric solid material $[ClAlNMe]_n$ insoluble in benzene, carbon tetrachloride, pentane, and heptane. Two- and three-dimensional network structures were suggested for the structure of $[ClAlNMe]_n$ [61].

Reaction of $LiAlH_4$ with NH_4X resulted in polymeric $[HAlNH]_n$, which was converted to microcrystalline AlN at 950 °C [114]. Slightly off-white $[HGaNH]_n$ solid with m.p. >270 °C was produced by the reaction of cyclotrigallazane $[H_2GaNH_2]_3$ with ammonia at 150 °C [115, 116] or, alternatively, by the reaction of $[HGa(NMe_2)_2]_2$ with excess of ammonia at room temperature [117]. Analogous reaction of $[HGa(NMe_2)_2]_2$ with excess of NH_2Me resulted in $[HGaNMe]_n$ polymers [117]. It was proposed that gallazane-based adducts $[H_2GaNH_2(NH_3)]$ equilibrate via a ligand redistribution reaction and that the formation of $[HGaNH]_n$ results from NH_3 elimination from a diaminogalliumhydride $[HGa(NH_2)_2]$ [115].

In earlier study [118], cyclotrigallazane $[H_2GaNH_2]_3$ was found to decompose with evolution of H_2 and ammonia and formation of the polymeric product, insoluble in Et_2O. Pyrolysis of this product at 300–600 °C yields Ga-N. Several possible structures were proposed for $[HGaNH]_n$ imino gallanes; authors [115] concluded that the best candidate is the planar hexagonal network. Considered alternatives included a molecular cluster that is large enough to be insoluble, or more complex (perhaps microporous) solid-state structure [115].

In 2005, synthesis and characterization of series of $[(RGaNH)_3]_n$ oligomers have been performed by Kormos et al. using reactions of $[RGa(NMe_2)]_2$ with ammonia at high pressures at 150 °C (R=Me,Et,Bu,Hx) [119]. X-ray powder diffraction results are in agreement with needle-shaped arrangement of Ga_3N_3 rings (Fig. 6.7).

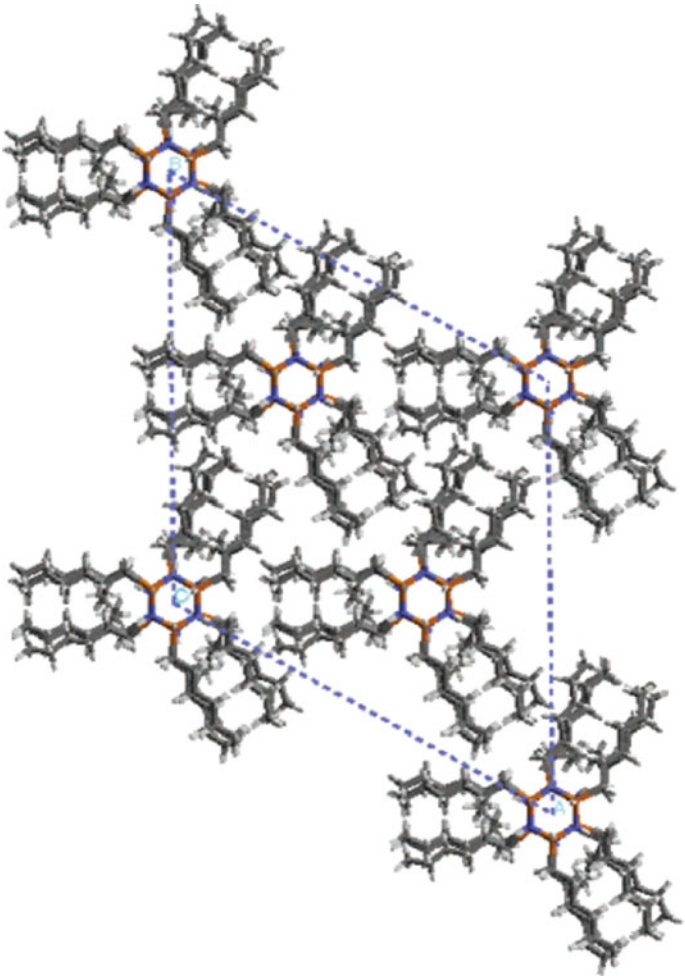

Fig. 6.7 Packing of $H_3[(HxGaNH)_3]_{12}H_3$ along c axis (top view on the rod, which is aligned to c axis). (Reprinted with permission from [119]. Copyright 2005 American Chemical Society)

Formation of incomplete needle-shaped decamer structure $[(InMe)_9(As^tBu)_8(OH)_2]2.5THF$ was reported by Neumüller [120]. Intermediate formation of zinc-blende InP cluster fragments, with external faces terminated by residual In-^{t}Bu and P-H groups, was discussed in [96]. Formation of polymeric material $[ClInPSiMe_3]_n$ was observed in reaction of $InCl_3$ with $P(SiMe_3)_3$ at 150 °C [121]. On further heating (650 °C), polymeric material was converted to InP. Insoluble residues of $[^t BuGaYH]_n$ (Y=P,As) have been produced by reaction of Ga^tBu_3 and YH_3 [122]. No further characterization of oligomers/polymers has been made.

Computational studies indicate that formation of gas phase needle-shaped clusters from the corresponding hydrides

$$MH_3 + YH_3 = {}^1/_n[HMYH]_n + 2H_2$$

is favorable thermodynamically for all 13–15 pairs even at high temperatures [45, 53].

Stability of the needle-shaped (Fig. 6.8a, c, e) *versus* fullerene-like (Fig. 6.8b, d, e) isomers of $[HGaNH]_n$ (n=10,13,16) was discussed in [53]. Needle-like isomers are predicted to be more stable compared to fullerene-like cage structures, and their stability increases with the increase of the oligomerization degree n [53]. This result has been generalized for all $[HMYH]_n$ compounds (M=Al,Ga,In;

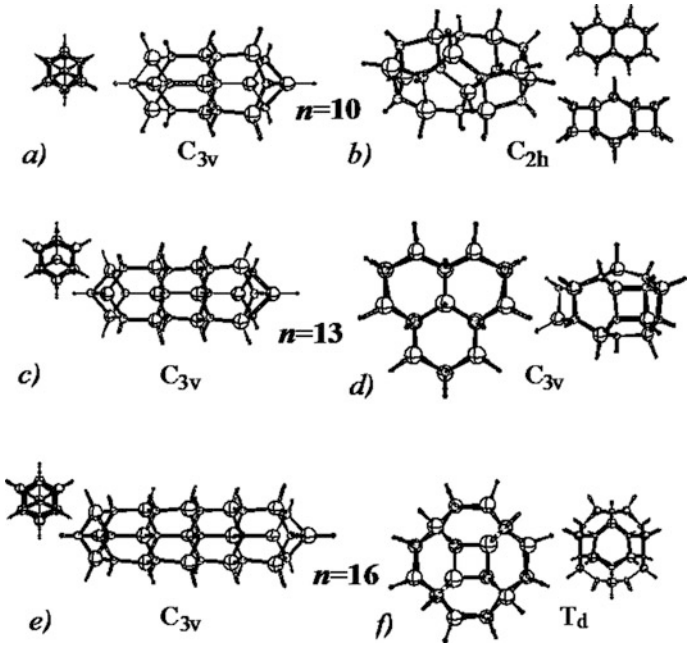

Fig. 6.8 Structures of needle-shaped and fullerene-like $[HMYH]_n$ isomers. (Reprinted with permission from [23]. Copyright 2005 American Chemical Society)

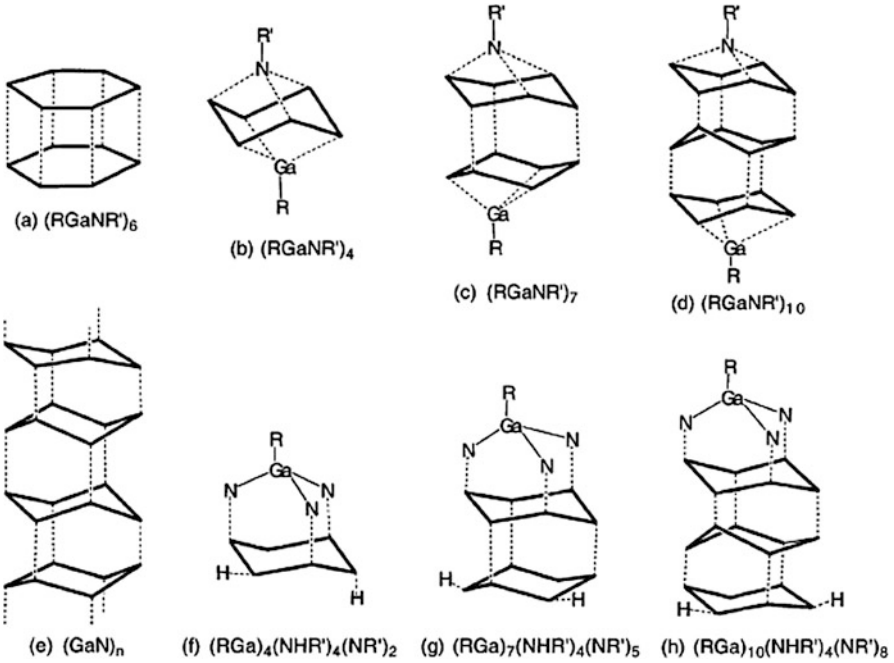

Scheme 6.7 Relationship between Ga-N-based compounds with Ga_3N_3 unit: hexamer imino compound (**a**); needle-shaped imino compounds (**b–d**); hexagonal Ga-N (**e**); adamantane-type amido-imino compounds (**f–h**). (Reprinted with permission from [104]. Copyright 2002 American Chemical Society)

Y=N,P,As) [23, 24]. High stability of needle-shaped oligomers allowed to propose a mechanistic pathway for their formation, which involves subsequent condensation of $[H_2MYH_2]_3$ amido trimers [20]. Relationship between compounds of different structural types, based on Ga_3N_3 cycles, is shown in Scheme 6.7 [104].

6.2.3 Reaction Pathways to 13–15 Needle-Shaped Compounds

Possible reaction pathways leading to needle-shaped oligomers will be considered on the example of reaction between trimethylalane and ammonia. Leitner, Steiskal, and Sofer note that "Lewis acid–base adduct $Me_3Al{\cdot}NH_3$ formation and the subsequent methane elimination leading to the trimeric amide $[Me_3AlNH_2]_3$ is the dominant reaction pathway for Al-containing species at low temperatures and atmospheric pressure" [123]. However, gas phase chemistry involved in needle-shaped oligomer formation is not well understood at present time. Initial methane elimination reactions from $AlMe_3NH_3$ adduct have been considered by Tachibana and co-workers [124, 125]. In more detail, initial reactivity between $AlMe_3$ and NH_3

as well as reactions of monomeric Me_2AlNH_2 with excess of $AlMe_3$ and ammonia has been computationally studied by Lisovenko et al. [126]. It was shown that the TS for the first methane elimination from the Me_3AlNH_3 complex is the highest point on the reaction pathway and the only one lying above the isolated $AlMe_3$ and NH_3. Subsequent stepwise substitution of methyl groups in $AlMe_3$ by amido groups NH_2 is exothermic, and despite the sizable activation energies of the intermediate steps, the overall reaction profile is essentially downhill. It was also shown [126] that formation of $[Me_2AlNH_2]_2$ dimer is very favorable thermodynamically and affordable kinetically. This dimer can rearrange to the trimer $[Me_2AlNH_2]_3$, which is a smallest *open* needle cluster and a potential candidate for the growth of needle-shaped $Me_3[MeAlNH]_{3n}H_3$ oligomers.

Enthalpy of the dimer-trimer equilibrium reaction $[Me_2AlNH_2]_2 = 2[Me_2AlNH_2]_3$ is -38 kJ mol^{-1} according to temperature-dependent NMR studies in benzene-d_6 solution [127]. Since rearrangement of $[Me_2AlNH_2]_2$ dimer to $[Me_2AlNH_2]_3$ trimer is exothermic in solution, formation of trimeric species is also expected. Indeed, trimeric $[Me_2AlNH_2]_3$ has been synthesized and characterized by Interrante et al. [128] and successfully used as single source precursor to AlN. Numerical simulations of processes in MOCVD reactors [129] and thermodynamic analysis of gas phase reactions [123] underline the importance of oligomeric species in the chemical reactivity model. In 2003, trimeric $[Me_2AlNH_2]_3$ was identified as one of the important intermediates in AlN formation by X-ray powder diffraction [130]. Vaporization and gas phase thermal decomposition of the deuterated analog $[Me_2AlND_2]_3$ were monitored by time-of-flight mass spectrometry [131, 132]. Dimeric and trimeric molecules $[Me_2AlND_2]_{2,3}$, deuterated methane CH_3D, and oligomers with a pentameric structure were detected in the vapor [132]. Experimental mass spectrometry observations reveal formation of cluster compounds in the gas phase upon laser irradiation of $AlMe_3$–NH_3 mixtures at low (below room) temperatures [34–36].

Reaction energy profiles starting from trimers $[Me_2AlNH_2]_3$ and leading to hexamer amido-imino $[Me_9Al_6N_6H_9]$ and imino $[MeAlNH]_6$ compounds have been computationally explored by Davydova et al. at B3LYP/def2-SVP, B3LYP-D3/def2-TZVPP//B3LYP/def2-SVP, and M06-2X/def2-TZVPP//B3LYP/def2-SVP levels of theory [133]. Three alternative reaction pathways of transformations of cyclic $[Me_2AlNH_2]_3$ have been explored (Figs. 6.9, 6.10, and 6.11). Activation energies for the first methane elimination are very close both for mono- and bimolecular reaction pathways (Figs. 6.9 and 6.10). Intermolecular methane elimination is always exothermic, while intramolecular methane elimination steps are endothermic. Thus, generation of $[MeAlNH]_6$ from $[Me_2AlNH_2]_3$ at low temperatures is expected to proceed via a bimolecular pathway. Formation of $[Me_9Al_6N_6H_9]$ from two $[Me_2AlNH_2]_3$ trimers is expected to be less favorable, as it involves higher barriers and lower endothermicity.

Alternative Al-N bond breaking pathway was also considered. Obtained results show that the energy required for Al-N bond breaking in cyclic $[Me_2AlNH_2]_3$ (185 kJ mol^{-1}) is of the same order as the activation energy (183 kJ mol^{-1}) for the first (limiting) step of methane elimination (both for mono- and bimolecular

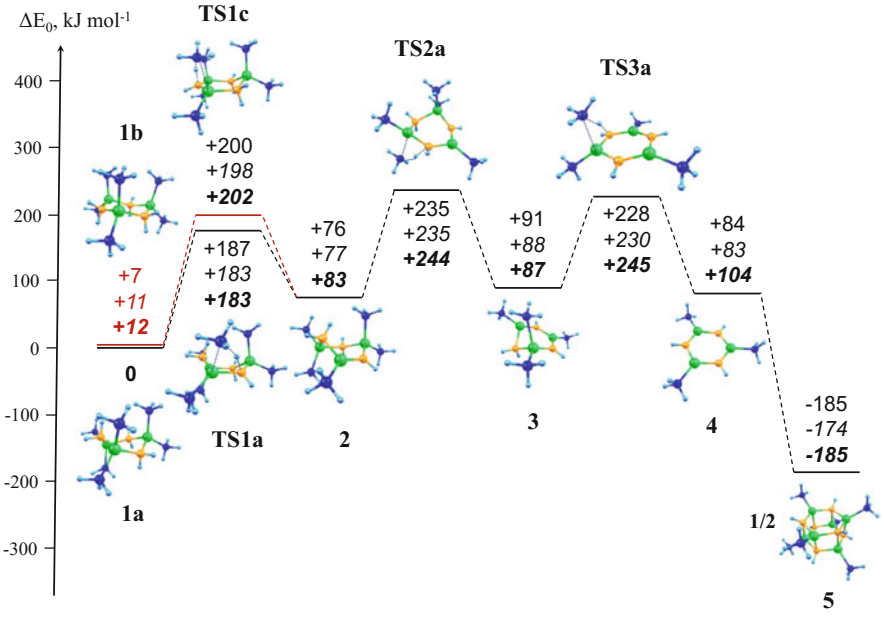

Fig. 6.9 Reaction profile for monomolecular reaction of $[Me_2AlNH_2]_3$ to $[MeAlNH]_3$ with its subsequent dimerization to $[MeAlNH]_6$. Relative energies (in kJ mol^{-1}) with respect to $[Me_2AlNH_2]_3$. B3LYP/def2-SVP (normal text), B3LYP-D3/def2-TZVPP//B3LYP/def2-SVP (in italics), and M06-2X/def2-TZVPP//B3LYP/def2-SVP (in bold) levels of theory. Aluminum atoms are in green, nitrogen in yellow, carbon in blue, hydrogen in cyan. (From [133] Copyright © 2014 by John Wiley Sons, Inc. Reprinted by permission of John Wiley & Sons, Inc.)

mechanisms) [133]. Thus, dissociative and associative reaction pathways are competitive. Low-temperature/high-pressure conditions will favor bimolecular pathway, while at high temperatures either intramolecular methane elimination or Al-N bond breaking dissociative pathways will be operational. Gibbs energy diagram (Fig. 6.12) indicates that transition states for all three considered pathways have similar energy and thus the pathways may operate concurrently.

Thus, formation of larger needle-shaped oligomers via interaction of $[Me_2AlNH_2]_3$ trimers appears to be feasible. The obtained quantitative results can be used to facilitate gas phase chemical reactivity modeling in 13–15 MOCVD processes.

In conclusion, needle-shaped $[RMYH]_n$ oligomers are known laboratory species, which are used as precursors to 13–15 binary materials. However, these compounds also may have their own applications. The electronic properties of *open* and *closed* needle-shaped oligomers will be considered in detail in the third section of the present chapter.

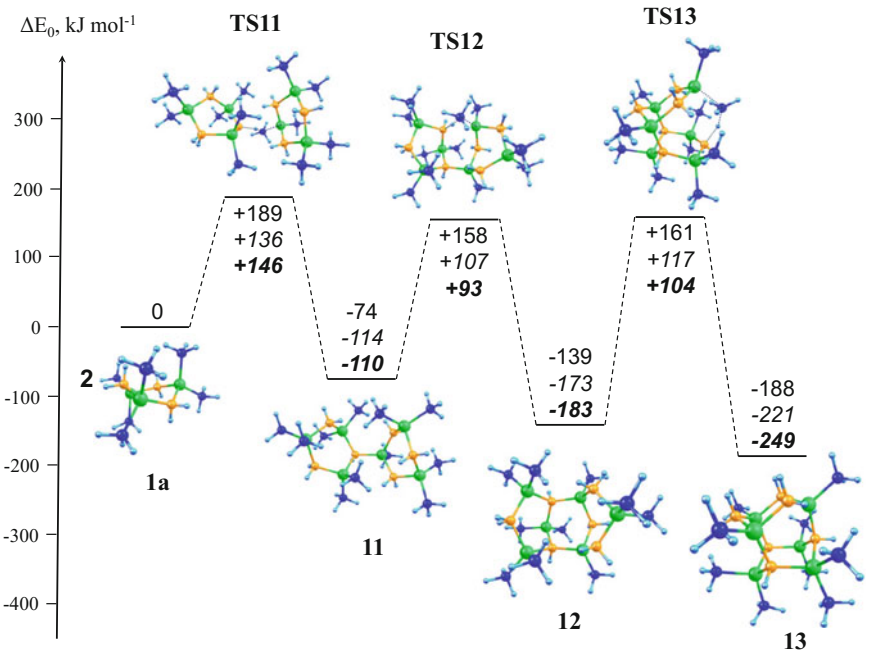

Fig. 6.10 Reaction profile for bimolecular reaction of $[Me_2AlNH_2]_3$ to $[Me_9Al_6N_6H_9]$. Relative energies (in kJ mol^{-1}) with respect to two isolated $[Me_2AlNH_2]_3$. B3LYP/def2-SVP (normal text), B3LYP-D3/def2-TZVPP//B3LYP/def2-SVP (in italics), and M06-2X/def2-TZVPP//B3LYP/def2-SVP (in bold) levels of theory. Aluminum atoms are in green, nitrogen in yellow, carbon in blue, hydrogen in cyan. (From [133] Copyright © 2014 by John Wiley Sons, Inc. Reprinted by permission of John Wiley & Sons, Inc.)

6.3 Electronic Properties of Ga-N-Based Needle-Shaped Oligomers

6.3.1 Background of Ga-N-Based Needle-Shaped Oligomers

Confinement effect of nanoscaled semiconducting systems provides a link between properties of bulk semiconductors and those of discrete molecules. It makes nanoparticles attractive as fundamental building blocks for extremely small circuits. Polarization properties of semiconducting quantum dots [134], generation of entangled photons [135, 136], and decoupling of quantum effects on excitation make nanoparticles widely applicable in physical, chemical, and medical nanoengineering [137].

One-dimensional nanostructures, like nanowires and nanotubes, have their own unique properties [138]. Ga-N-based nanosystems are among the most popular for nanoengineering due to their high chemical and temperature stability. Ga-N-

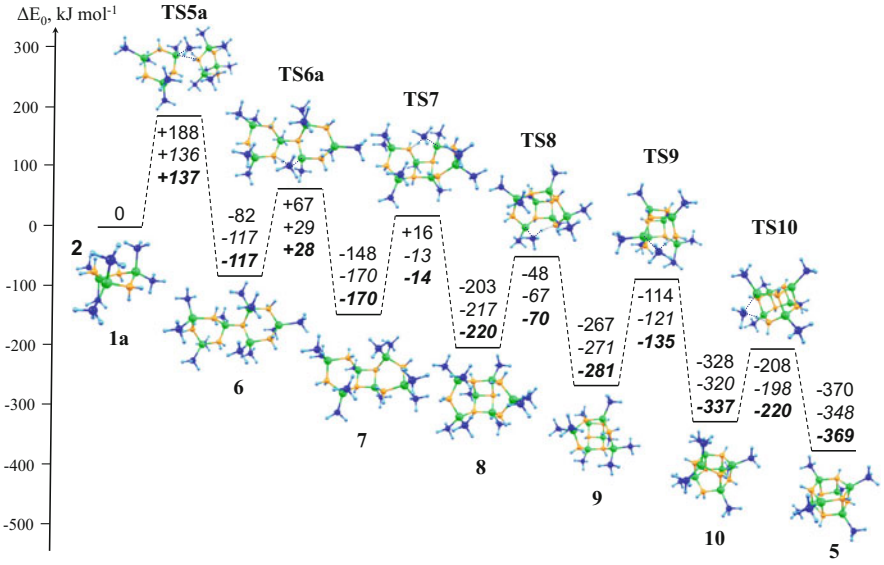

Fig. 6.11 Reaction profile for bimolecular reaction of $[Me_2AlNH_2]_3$ to $[MeAlNH]_6$. Relative energies (in kJ mol^{-1}) with respect to two isolated $[Me_2AlNH_2]_3$. B3LYP/def2-SVP (normal text), B3LYP-D3/def2-TZVPP//B3LYP/def2-SVP (in italics), and M06-2X/def2-TZVPP//B3LYP/def2-SVP (in bold) levels of theory. Aluminum atoms are in green, nitrogen in yellow, carbon in blue, hydrogen in cyan. (From [133] Copyright © 2014 by John Wiley Sons, Inc. Reprinted by permission of John Wiley & Sons, Inc.)

based semiconducting nanorods can serve as channels for charge carriers with polarization-dependent conductivity [139] with variety of applications as light-emitting diodes [140], transistors, UV sensors, lasers [141], and piezotronic devices [142].

Chemical vapor deposition technique is one of the most popular ways for the production of high-purity semiconducting materials [92, 143]. Experimental studies show possibilities for obtaining nanoparticles directly in the gas phase [144]. It opens inexpensive way for the manufacture of one-, two-, and three-dimensional 13–15 nanoarchitectures. Energetics of the gas phase chemical reactions leading to the formation of 13–15 nanorods is summarized in the review [22]. Spontaneous needle-shaped cluster formation has been reported in gas phase during the chemical vapor deposition of group 13–15 materials [145].

Size dependence of properties of nanorods and sensibility of the properties to subtle structural variations leads to immense design freedom for creating functional elements of nanoscaled devices. However, experimentally obtained nanoparticles typically are different in size and/or structure. Thus, understanding of properties of particular types of nanoobjects in a great extend relies on theoretical investigation and computer simulation.

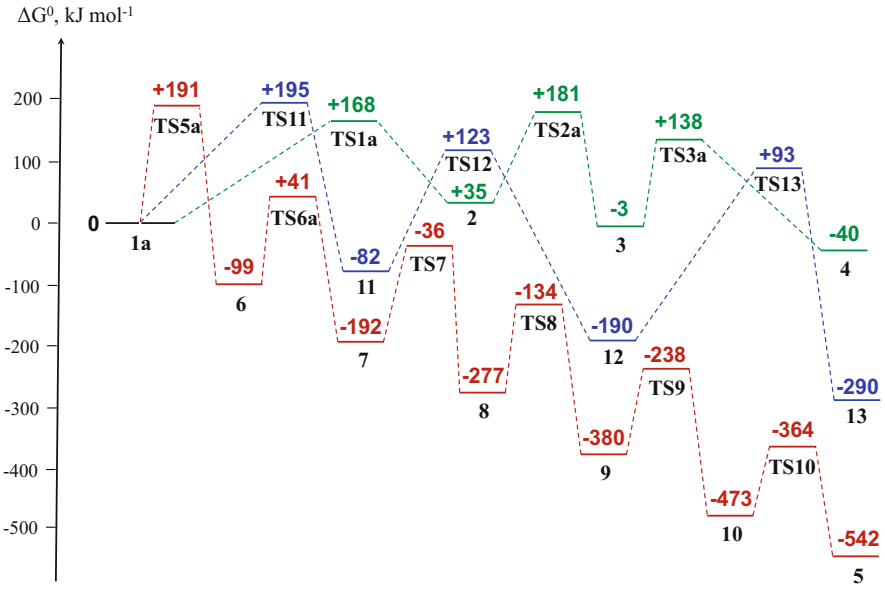

Fig. 6.12 Gibbs energy (in kJ mol^{-1}) reaction profiles for considered pathways. Monomolecular pathway (green); bimolecular pathway for $[MeAlNH]_6$ formation (red); and bimolecular pathway for $[Me_9Al_6N_6H_9]$ formation (blue). M06-2X/def2-TZVPP//B3LYP/def2-SVP level of theory (thermal corrections and entropies are at B3LYP/def2-SVP level of theory). (From [133] Copyright © 2014 by John Wiley Sons, Inc. Reprinted by permission of John Wiley & Sons, Inc.)

A potentially interesting subclass of Ga-N-based nanostructures is oligomeric clusters composed of $[HGaNH]_3$ rings with the wurtzitic arrangement of the Ga-N backbone. The rod-shaped oligomers are energetically more favorable than cage-like isomers or three-dimensional structures [21, 23, 24, 45, 146–148]. High polarizability of the rod-shaped oligomers along with tunable band gap makes them promising charge carriers under an external electric field or under strength. Such oligomer compounds were theoretically predicted [53], and, soon, family of $[RGaNH]_n$ (R= H, CH_3, C_2H_5, C_4H_9, C_6H_{13}) rod-like compounds was synthesized in ammonia solution [119].

Possible pathways for adjusting the band gap in such compounds include variations in size, shape, substituents, dopant effects, and terminal effects. In the present review, we summarize results of comprehensive computational studies of how different factors affect structural and electronic properties of Ga-N-based rod-like oligomers. Schematic view of the considered rod-like oligomers is shown in Fig. 6.13. The building block of oligomers is the chair-shaped $[RGaNH]_3$ ring, where R is hydrogen atom or methyl group.

In the present chapter, we will summarize results of computational studies of electronic properties of rod-like $[RMNH]_{3n}$ clusters of group 13 metals M=Al, Ga,

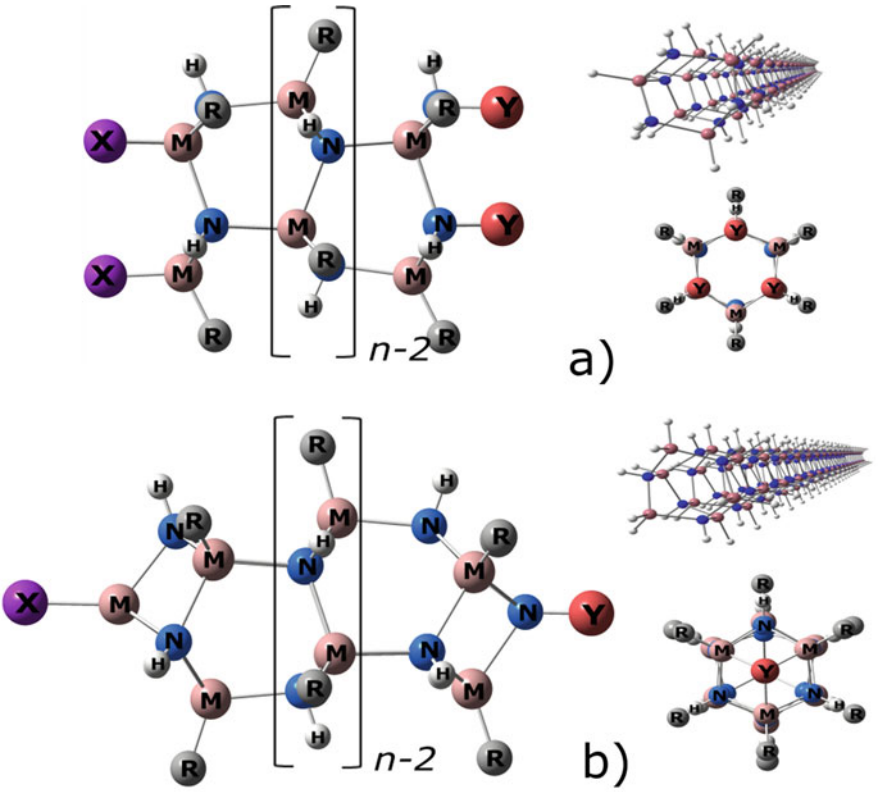

Fig. 6.13 Schematic representation of *open* oligomer $X_3[RMNH]_{3n}Y_3$ (**a**) and *closed* oligomer $XM[RMNH]_{3n}NY$ (**b**) Perspective views (right side) are given for the longest considered rods on the example of hydrogen-substituted derivatives (R=X=Y=H)

and In. Two types of rod termination have been considered. Tube-like structures will be referred below as *open* oligomers (Fig. 6.13a). In *open* oligomers three dangling bonds at the each end are terminated by 3X/3Y functional groups. Needle-shaped structures, where the three dangling bonds at the ends are capped by addition of GaX and NY groups, will be called *closed* oligomers (Fig. 6.13b). The terminal groups considered are X=H, CH_3 and Y=H in parts 3.3–3.4 of the present review and X,Y=CH_3, H, F, CF_3 in the part 3.5.

We will test the performance of computational methods, explore the influence of the length of the rod-like oligomer on the example of clusters with Ga-N backbone, and reveal the influence of terminal groups on the electronic properties of oligomers.

6.3.2 Analysis of Computational Approaches

6.3.2.1 Choice of the Level of the Theory of the Computational Method

Nowadays, DFT is a common approach for theoretical studies of molecular systems. Many exchange-correlation functionals are available, and the choice of the functional for the particular application must be justified. Computations [47] on cubane cluster $[HAlNH]_4$ that could be considered as the smallest *closed* oligomer $[HAlNH]_{3n+1}$ with $n = 1$ showed the reliability of B3LYP/TZVP approach compared to the results obtained at CCSD(T)/cc-PVTZ level of theory. However, results of a systematic study [149] of several exchange-correlation functionals indicate that for extended metal-containing systems, including 13–15 semiconductor materials, B3LYP [150, 151] optimized lattice constants for Ga-containing compounds are overestimated by 0.6–2.2% with respect to experimental values, while those obtained with nonempirical hybrid PBE0 [152] or HSSE [153] functionals provide the lattice constants within 0.9% from the experimental values. Test computations have been performed to compare the performance of different DFT methods against the CCSD [154] method for geometry optimization on the example of $[RGaNH]_4$ cubanes with R=H, CH_3. The LDA correlation functional VWN5 [155] and hybrid GGA, B3LYP, PBE0, and HSSE methods, were considered.

A series of def-2 basis sets developed for all elements by Weigend and Ahlrichs [156], equally efficient for DFT, HF, and post-HF computational levels, were chosen. In the following, we will omit def-2 when indicating the used basis set. Split-valence basis plus set of polarization functions (SVP), triple-zeta (TZV), corresponding basis with additional polarization functions (TZVP), and quadruple zeta (QZVP) valence quality basis sets (for the $[HGaNH]_4$ compound only) were tested.

Selected structural parameters obtained using these various methods are shown in Table 6.1. The influence of basis set on Ga-N distances is rather small, Ga-N bond lengths agree with each other within 0.004 Å for each DFT method and within 0.008 Å for CCSD method. N-Ga-N angle varies within maximum 0.29° in all cases. Moreover, the cancelation of errors results in good agreement between the results obtained with relatively small SVP basis set and nearly complete QZVP basis set for all DFT methods.

The difference in performance of different DFT methods is more profound. While PBE0 and HSSE optimized geometries are very similar, optimized distances at VWN5 level of theory are shorter by about 0.015 Å, and distances at B3LYP level are longer by about 0.016 Å, compared to values obtained using PBE0 and HSSE methods. Optimized valence angles at VWN5, PBE0, and HSSE levels of theory are similar and smaller by more than 0.3° compared to B3LYP values. Substitution of H atoms by CH_3 groups on Ga atoms increases Ga-N distances by about 0.005 Å and only slightly affects N-Ga-N angles. CCSD geometry optimization yields results somewhat intermediate between those obtained with B3LYP and PBE0 methods. B3LYP/SVP Ga-N bond length in $[HGaNH]_4$ is 2.001Å, and it is less

Table 6.1 Distances (Å) and angles (degrees) of $[RGaNH]_4$ cubane clusters optimized at different levels of theory

Method	Basis set	$[HGaNH]_4$		$[CH_3GaNH]_4$	
		Ga-N	N-Ga-N	Ga-N	N-Ga-N
CCSD	TZVP	1.989	87.49	1.994	87.50
	QZVP	1.997	87.76	–	–
B3LYP	SVP	2.001	87.64	2.005	87.60
	TZV	2.003	87.46	2.008	87.46
	TZVP	2.004	87.52	2.009	87.52
	QZVP	2.003	87.61	2.008	87.59
VWN5	SVP	1.969	88.10	1.972	88.09
	TZV	1.972	87.81	1.977	87.85
	TZVP	1.973	87.94	1.976	87.88
	QZVP	1.971	88.00	1.975	87.95
PBE0	SVP	1.986	87.97	1.989	87.94
	TZV	1.987	87.76	1.992	87.81
	TZVP	1.988	87.88	1.992	87.82
	QZVP	1.987	87.98	1.991	87.92
HSSE	SVP	1.987	87.91	1.990	87.88
	TZV	1.989	87.73	1.993	87.76
	TZVP	1.989	87.83	1.993	87.77
	QZVP	1.988	87.92	1.992	87.88

overestimated with respect to 1.997 Å at CCSD/QZVP level than Ga-N distances obtained with other DFT functionals. Similarly, N-Ga-N angles at B3LYP/SVP level differ from CCSD/QZVP by only about 0.12° that is slightly smaller compared to other DFT methods. Overall, the computations show that bond lengths and bond angles optimized at the B3LYP/SVP level of theory have smaller deviation from the benchmark CCSD/QZVP results than other considered functionals (probably due to fortunes cancelation of errors between incompleteness of the basis set and the electron correlation treatment).

Additionally, computations for selected long oligomers were performed at PBE0/SVP, B3LYP/SVP, and B3LYP/TZVP levels of theory in order to ensure that the reliability of the chosen B3LYP/SVP computational approach remains valid with the elongation of the oligomer. It was found that PBE0 functional reproduces elongation effects qualitatively similar to B3LYP method. For example, in case of geometry optimization of $H_3[HGaNH]_{30}H_3$, Ga-N bond lengths at PBE0 level are shorter than at B3LYP level by about 0.015−0.019 Å. The values of the band gap energy computed at PBE0 level are by circa 0.6 eV larger than computed at B3LYP level for a wide range of the oligomers of different lengths.

The average difference in Ga-N bond lengths computed using TZVP and SVP basis sets (circa 0.002 Å) is the same for $H_3[HGaNH]_9H_3$ and $H_3[HGaNH]_{30}H_3$ compounds. Thus, we conclude that the error does not increase notably with the elongation of the oligomer. A difference in the reaction energies of formation of $H_3[HGaNH]_{3n}H_3$ from GaH_3 and NH_3 calculated using TZVP and SVP basis sets is about 1% of the value obtained using the TZVP basis set, irrespective of the

oligomerization degree. In absolute value the difference is 10.2 kcal mol^{-1} for $n = 10$. The HOMO-LUMO gaps of $H_3[HGaNH]_{3n}H_3$ obtained using the TZVP basis set are by 0.27 eV ($n = 3$) and by 0.20 eV ($n = 10$) smaller than the values obtained using the SVP basis set. In general, HOMO-LUMO energies are sensitive to the particular choice of DFT method. It was found that a choice of PBE0 instead of B3LYP causes an increase of the HOMO-LUMO gap value of about 0.55 eV, while the overall tendencies in the changes in the HOMO-LUMO gap upon the rod elongation are qualitatively similar.

Thus, in the following discussion, geometries of all compounds were fully optimized at the B3LYP/SVP level of theory. All electron basis sets were applied for all atoms except for In, where effective core potential (ECP-28 core AOs 1*s* to 3*d*) [157] is used to reflect the varying degree of separation between core and outer shells. The vibrational frequency computations were performed to verify that obtained structures are true minima on their respective potential energy surfaces. The same level of theory was used to evaluate the characteristic features of the ground state electronic structure.

Computations of excitation spectra required additional testing on the reliability of computational methods. TDDFT method is highly popular tool to estimate excitation energies of rather complicated systems [158]. Time-dependent response theory is used to reduce electronic excitations to ground state properties. It considers a molecule in its ground state to be a subject of a periodic perturbation by uniform electric field. The perturbation theory in this case operates with frequency-dependent one-particle density matrix. The excitation energies are obtained as eigenvalues of an electronic Hessian which may be imagined as the matrix of second derivatives of the electron energy with respect to the electronic degrees of freedom.

Efficiency of TDDFT calculations with B3LYP, PBE0, M06 [159], and HSSE functionals was tested against the benchmark EOM-CCSD [160, 161] calculations on the example of $[HGaNH]_4$. Effect of diffusion functions extension to TZVP and QZVP basis sets was studied by considering augmented TZVPD and QZVPD basis sets developed by Rappoport and Furche [162]. Energies of several low-lying singlet states calculated at different levels of theory are provided in Table 6.2.

The results show that all TDDFT methods underestimate excited state values with respect to the values obtained at EOM-CCSD level. An underestimation of valence excitation energies by TDDFT methods is often attributed to so-called self-interaction problem of semi-local DFT functional [163]. The larger the basis set, the greater is the underestimation in the obtained values of energy for the tested compound. Thus, the smallest tested basis set, TZVP, provides the best agreement with the benchmark EOM-CCSD/TZVPD computations for any of the considered DFT functional.

It was found that excitation energies computed with PBE0 functional are in better agreement with EOM-CCSD/TZVPD results. In case of PBE0/TZVP level, the correct order of three- and twofold degenerate levels is preserved (see Table 6.2). The error is less than 0.01 eV for the lowest triply degenerate spin-singlet state and is smaller than 0.06 eV for higher singlet states.

Table 6.2 Excitation energies (in eV) to low-lying excited (singlet) states of $[HGaNH]_4$ at different levels of theory

Electronic state									
Method	Basis set	1	2	3	4	5	6	7	8
EOM-CCSD	TZVPD	6.318	6.318	6.318	6.368	6.368	6.506	6.506	6.506
PBE0	TZVP	6.314	6.314	6.316	6.316	6.316	6.447	6.447	6.447
	QZVP	6.193	6.193	6.199	6.199	6.199	6.301	6.301	6.301
	TZVPD	6.120	6.120	6.128	6.128	6.128	6.227	6.227	6.227
	QZVPD	6.095	6.095	6.103	6.103	6.103	6.197	6.197	6.197
HSSE	TZVP	6.258	6.258	6.259	6.259	6.259	6.383	6.383	6.383
	QZVP	6.143	6.143	6.147	6.147	6.147	6.245	6.245	6.245
	TZVPD	6.075	6.075	6.082	6.082	6.082	6.176	6.176	6.176
	QZVPD	6.052	6.052	6.058	6.058	6.058	6.148	6.148	6.148
M06	TZVP	6.177	6.177	6.179	6.179	6.179	6.301	6.301	6.301
	QZVP	5.779	5.779	5.809	5.809	5.809	5.855	5.855	5.855
	TZVPD	5.618	5.618	5.625	5.625	5.625	5.678	5.678	5.678
	QZVPD	5.554	5.554	5.563	5.563	5.563	5.614	5.614	5.614
B3LYP	TZVP	6.101	6.101	6.112	6.112	6.112	6.218	6.218	6.218
	QZVP	5.976	5.976	5.989	5.989	5.989	6.070	6.070	6.070
	TZVPD	5.903	5.903	5.919	5.919	5.919	5.997	5.997	5.997
	QZVPD	5.874	5.874	5.889	5.889	5.889	5.963	5.963	5.963

All computations discussed in this chapter were performed using Gaussian 09 program package [164]. PDOS for a chosen fragment was computed using GaussSum code [165].

6.3.2.2 Band Structure Computation Method

Periodicity is an essential property of bulk semiconductors, and band structure is an important characteristic of their electronic properties. Being intermediates between molecules and bulk crystals, semiconducting nanoparticles also exhibit periodic properties in structural as well as in electronic features. It is a common approach treating nanorods within PBC [166–169]. PBC approximation allows to study the effect of surface dangling bonds [167, 170]. It was found that the band gaps of Ga-N [167] or GaAs [171] nanorods are ruled by surface states and do not change with the diameter of the nanorods according to the trend dictated by the quantum confinement effect. However, the PBC approach is difficult to be used for studying structures with local defects and substituents, and it is not applicable for studying the effect of dangling bonds at the terminal edges of nanorods.

On the other hand, the edge effects for rather short nanorods can be studied using ab initio methods. Investigation of finite size carbon nanotubes shows that terminal effects have strong impacts on the vibrational frequencies [172], and the study of finite graphene nanoribbons shows that the gap defined by the end-localized states

decreases exponentially as a function of the ribbon length [173]. It is expected that terminal effects should be profound in the case of 13−15 nanorods grown in [0001] direction, where alternation of atoms of group 13 and 15 sublayers provides polarization of the nanorods along the main axis and produces high interface charge densities.

The good choice of simultaneous study of edge effects and periodic properties of oligomer at the same level of theory is a method of extracting a band structure from the conventional computations of long but finite size oligomer of more or less regular structure [174, 175]. It is a method of mapping of MOs on reciprocal space which allows building of the band structure of the polymer without applying PBC during computations. The extracting of the $[HGaNH]_{3\infty}$ polymer properties from B3LYP/SVP computation of the finite $GaX[HGaNH]_{3n}NY$ oligomers allows a direct comparison of their electronic structures. It gives a unique ability to track edge effects provided by different types of termination of the finite oligomers. All details of the method one can find elsewhere [174, 175] and here we provide only the core idea of it.

MO of an oligomer built by periodically repeated molecular units could be written as a linear combination of AOs:

$$\psi^{MO} = \sum_{j,r} C_{jr}^{MO} \chi_j^r \tag{6.1}$$

where χ_j^r is the r^{th} atomic function of the j^{th} unit. If the oligomer is long enough and MO is periodically delocalized along the chain, it is similar to the CO of the corresponding polymer. Thus, for such MOs wave vectors k of the related Bloch functions are to be mapped. In order to identify k for the MO, it is projected onto real linear combinations of AOs that correspond to model Bloch functions:

$$\begin{aligned} X_q^r &= \sum_j C_{jr}^{MO} \sum_{j'} \sin\left(\tfrac{\pi j' q}{M+1}\right) \left\langle \chi_j^r | \chi_{j'}^r \right\rangle \\ Y_q^r &= \sum_j C_{jr}^{MO} \sum_{j'} \cos\left(\tfrac{\pi j' q}{M+1}\right) \left\langle \chi_j^r | \chi_{j'}^r \right\rangle \end{aligned} \tag{6.2}$$

The integer q is related to the wave vector in the first BZ through:

$$k = \frac{q}{M+1}\frac{\pi}{a}, \quad q = 1, 2, \ldots M, \quad 0 < k < \frac{\pi}{a} \tag{6.3}$$

where a is the length of the unit cell and M is the number of repeated units in the oligomer. k value is assigned for each delocalized MO by looking for the maximum of the quantity:

$$R_q = \sqrt{\left(X_q^r\right)^2 + \left(Y_q^r\right)^2} \tag{6.4}$$

as a function of q.

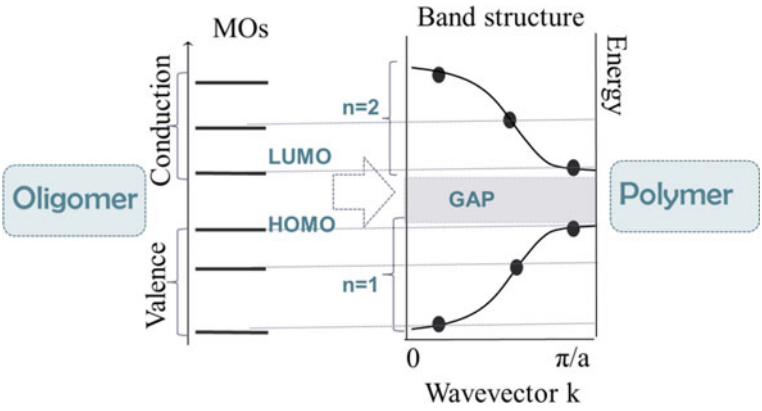

Fig. 6.14 Schematic representation of mapping of MOs of an oligomer on reciprocal space of the first BZ of the polymer

The overall procedure is schematically shown in Fig. 6.14. For any MO of long but finite oligomers, including HOMO and LUMO, one can find a value q, at which the value R_q (Eq. 6.4) will be maximal. Thus, the energy of the MO can be associated with the value of wave vector k. MOs of the same nature (e.g., σ or π states of the same point group symmetry) belong to the same crystal band n. The longer the oligomer, that is, the more periodic cells it contains, the more k values will correspond to the same band n, the more smoothly the k values will change from 0 to π/a. Since k cannot be 0 or π/a if M is a finite number (Eq. 6.3), the band gap can be obtained by extrapolation to the edges of the BZ of bands containing HOMO and LUMO, respectively.

It should be stressed that this procedure is meaningful only for MOs well delocalized along the chain. MOs localized at the ends of the oligomer are not localized in BZ. The degree of localization of a MO could be estimated considering distribution along the chain of the electronic density for the particular unit cell:

$$Q_l^{MO} = \sum_{r,r'} C_{r,l}^{MO} \left\langle \chi_i^r | \chi_i^{r'} \right\rangle C_{r',l}^{MO} \tag{6.5}$$

where l refers to the number of the unit cell and the particular MO is considered to be edge-localized if the average number of the Q value over three central units is vanishing.

The efficiency of the method was demonstrated in previous works both for simple organic polymeric systems, like polyacetylene, poly-paraphenylene [174], and polybutatriene [176], and for complex systems like single wall (4,4) carbon, boron nitride, and mixed nanotubes [175, 177, 178], one-dimensional periodic associations of benzo-2,1,3-chalcogendiazoles [179], and organometallic polymers like *meso-meso*-linked metalloporphyrins of Mg, Zn, and Ni [180].

In the following discussion, we will distinguish between the HOMO-LUMO gap and the bandgap, which is obtained by extrapolation to the edges of BZ of bands, obtained by mapping of MOs on reciprocal space. We should note that in case of long periodic oligomer in which HOMO and LUMO are well delocalized, HOMO-LUMO gap and bandgap could be close numerically but are not the same.

6.3.3 *Small Open $(CH_3)_3[CH_3MNH]_9H_3$ and Closed $[CH_3MNH]_{10}$ Mixed Metal Oligomers (M = Al, Ga, In)*

It is natural to start the consideration from clusters of relatively small size. On the one hand, cluster of three trimeric $[RMNH]_3$ rings is a minimal unit for which the term "nanorod" is appropriate; on the other hand, these oligomers are small enough to be studied comprehensively in detail with R=CH_3 and different metal atom. Methyl substituents are interesting because the alkyl-substituted derivatives of the needle-shaped Ga-N clusters are experimentally known [119]. In this section we provide a direct comparison of electronic properties of *open* $(CH_3)_3[CH_3MNH]_{3n}H_3$ and *closed* $[CH_3MNH]_{3n+1}$ mixed metal oligomers with $n = 3$ (M = Al, Ga, In) [56, 57].

6.3.3.1 Structures of Mixed Metal Oligomers

Table 6.3 provides selected structural parameters for $[CH_3MNH]_{10}$ and $(CH_3)_3[CH_3MNH]_9H_3$ (M = Al, Ga, In) oligomers. The specified bond lengths and angles are indicated in Fig. 6.15.

Binary *closed* oligomers possess C_{3v} point group, while *open* ones are C_3 symmetric. Three terminal methyl groups in *open* oligomers are almost free rotors; thus, the global minimum is shallow with respect to the mutual orientation of the hydrogen atoms of the methyl groups. Terminal CH_3 groups are rotated by 8.8°, 17.6°, and 23.6° for M = Al, Ga, and In, respectively. For the mixed metal oligomers, it was found that the rotation angle θ_{Me} of the terminal methyl groups depends only on the type of the closest metal atom.

M-N bond lengths vary significantly over the oligomer core for both *closed* and *open* oligomers. M-N distances in the middle of M_3N_3 rings are by 0.01–0.02 Å shorter than those in the outmost rings. Considering the middle M_3N_3 rings, one can notice that M-N bond lengths are slightly shorter and both M-N-M and N-M-N angles are slightly larger for *closed* oligomers than for *open* ones. M-N bond lengths between M_3N_3 rings are generally shorter than ones within rings. M-N bonds connecting the end's MCH_3 group with the first ring are among the longest.

Al-N bond lengths are about 3% shorter, and In-N bond lengths are about 10% longer than respective Ga-N distances. Similar trends in bond lengths are observed for bulk wurtzitic Al/Ga/In nitride structures [181]. Our computations indicate that

Table 6.3 Selected M-N bond lengths (Å) and bond angles (deg) of binary oligomers

Parameter (ring number)	$[CH_3MNH]_{10}$			$(CH_3)_3[CH_3MNH]_9H_3$		
	M=Al	M=Ga	M=In	M=Al	M=Ga	M=In
RM–N	1.939	2.004	2.216			
d⊥(1)	1.938	1.998	v2.212	1.968	2.030	2.246
d‖ (1–2)	1.932	1.990	2.203	1.896	1.945	2.15
d⊥(2)	1.933	1.987	2.200	1.951	2.013	2.232
d‖ (2–3)	1.922	1.983	2.193	1.881	1.931	2.13
d⊥(3)	1.943	2.001	2.216	1.968	2.028	2.252
M–NH	1.937	2.001	2.210			
ϕ_M (1)	88.1	87.0	90.1	98.9	98.5	97.6
ϕ_M (2)	102.1	102.0	102.0	99.5	99.6	98.8
ϕ_M (3)	103.0	102.8	102.7	99.3	98.5	97.0
ϕ_N (1)	118.6	119.2	121.0	116.6	116.8	117.0
ϕ_N (2)	115.0	115.8	117.8	113.0	113.8	115.6
ϕ_N (3)	89.2	91.0	93.8	117.7	118.5	121.3
θ_{NMNM} (1)	74.5	75.3	76.8	64.6	65.1	65.7
θ_{NMNM} (2)	62.6	61.8	60.8	67.5	66.6	65.7
θ_{NMNM} (3)	83.6	82.5	80.8	63.0	63.0	61.9
θ_{Me}[a]	180.0	180.0	180.0	171.2	162.4	156.4

Adapted by permission from Springer Nature: Springer [56], COPYRIGHT (2014)
[a]θ_{Me} dihedral angle shows rotation of CH_3 group relative to the first ring (see Fig. 6.15), value of 180° corresponds to C_{3v} point group

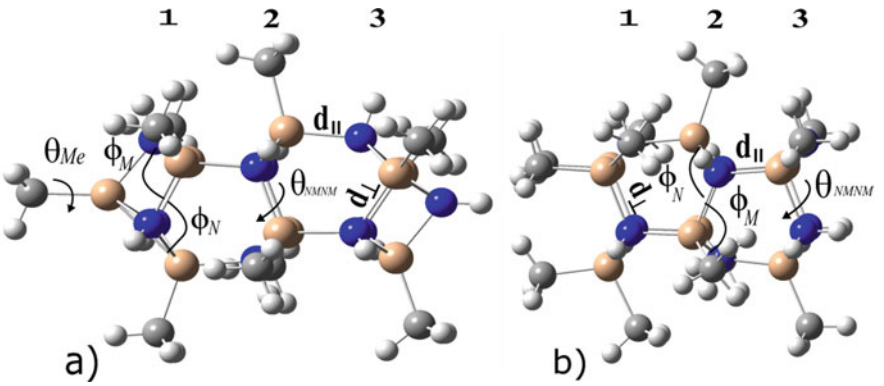

Fig. 6.15 Ring numbering and designation of structural parameters of oligomers. (**a**) $[CH_3MNH]_{10}$; (**b**) $(CH_3)_3[CH_3MNH]_9H_3$

this trend holds both for binary and mixed oligomers and it does not depend on the position of substituted atom.

Overall, we conclude that unlike similar nitrogen clusters [182], optimized geometry of the Ga-N-based oligomer rod is strongly affected by a type of terminal

groups. Irrespective to the group 13 metal M, the middle M_3N_3 ring in *closed* oligomers is rather "flat" compared with a bent chair shape in the *open* oligomer.

Middle M_3N_3 rings of the *closed* oligomers have larger N-M-N and M-N-M angles and shorter M-N bonds.

Since both types of oligomers can be simultaneously generated at the experimental conditions, it is of interest if they can be distinguished by IR spectroscopy. Computed gas phase IR spectra of *closed* $[CH_3MNH]_{10}$ and *open* $(CH_3)_3[CH_3MNH]_9H_3$ (M=Al, Ga, In) oligomers are shown in Fig. 6.16. The spectra are qualitatively similar for compounds with different metal atoms, but there are some specific features that are helpful to distinguish between *closed* and *open* structures. The *open* oligomer has two neighboring fingerprint bands associated with

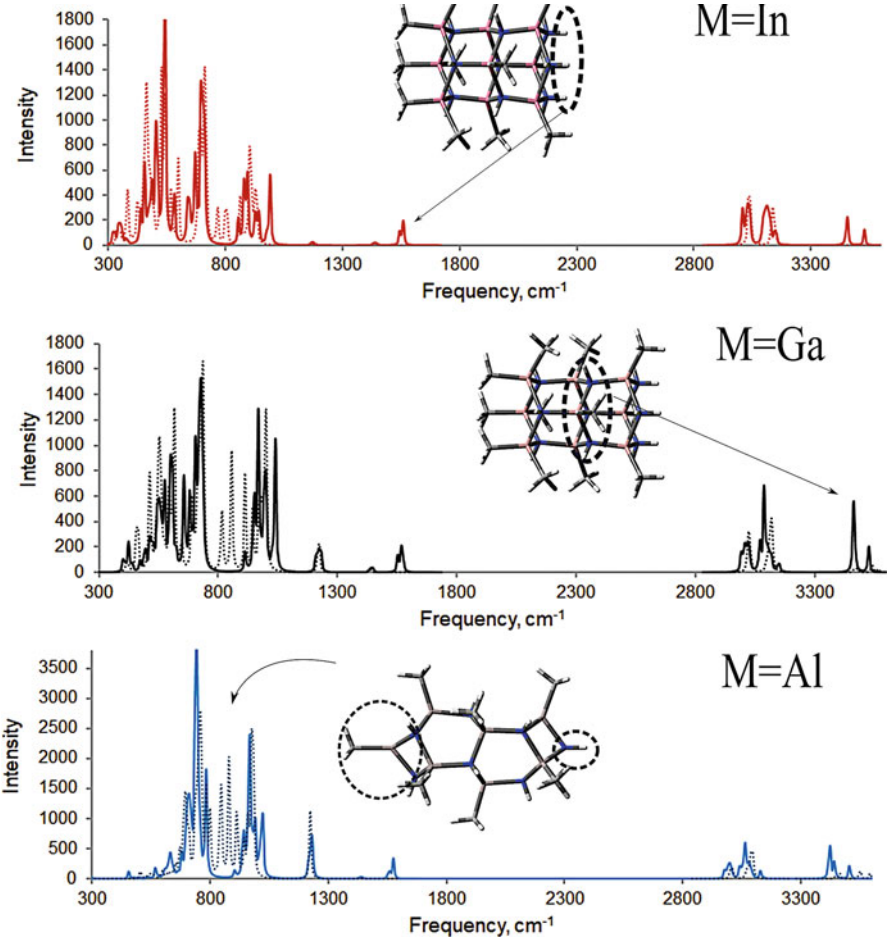

Fig. 6.16 Computed IR spectra of $[CH_3MNH]_{10}$ (*dashed line*) and $(CH_3)_3[CH_3MNH]_9H_3$ (*solid line*)

H-N-H scissoring in the terminal ring. The characteristic frequencies are similar for M=Al, Ga, and In. The values are 1556 and 1575 cm^{-1} for M=Al, 1554 and 1571 cm^{-1} for M=Ga, and 1546 and 1559 cm^{-1} for M=In. On the other hand, NH-M deformation frequencies on the end's rings of *closed* oligomer give intensive bands at 845 and 880 cm^{-1} for M=Al; 814 and 856 cm^{-1} for M=Ga; 803, 863, and 880 cm^{-1} for M=In. IR spectrum of the *open* oligomer has a clear gap in this region. Additional difference is observed in the highest frequency modes. Stretching of NH bonds of the middle ring of the *open* oligomer makes contributions to the intense modes near 3420, 3465, and 3453 cm^{-1} for M=Al, Ga, and In, respectively. The intensive peaks near 1200–1500 cm^{-1} and 2800–3300 cm^{-1} are similar for *closed* and *open* oligomers and related to the different methyl group vibrations (stretching and bending). Similar differences in IR spectra of *open* and *closed* oligomers are observed for the other related binary and mixed metal compounds. Thus, computations suggest the IR spectroscopy may be useful to distinguish between *open* and *closed* oligomers.

6.3.3.2 Effect of Group 13 Metal on the Electronic Structure of Mixed Metal Oligomers

Group 13 nitride bulk semiconductors have direct band gaps, ranging from 0.7 eV (InN) to 6.2 eV (AlN) with 3.4 eV for Ga-N. Our computations reveal that *closed* oligomer compounds $[CH_3MNH]_{10}$ have HOMO-LUMO gaps of 6.79, 6.30, and 4.95 eV for Al, Ga, and In, respectively. These results are in line with earlier results obtained for the heptamer clusters [113] at B3LYP/6−311+G* level of theory. *Open* oligomers exhibit significantly narrow gaps: 5.19, 5.00, and 4.12 eV or Al, Ga, and In, respectively. Effect of subsequent substitution of Ga by Al and In atoms on the electronic properties was also studied. In Table 6.4, energy gaps of Ga binary and mixed oligomers are presented. The substituted Al_3N_3/In_3N_3 rings are located in different positions with ring numbering in accordance with the order given in Fig. 6.15.

Table 6.4 HOMO-LUMO gap, ΔE (eV) and dipole moments, μ (D) of mixed metal oligomers

Substituted ring	$[CH_3MNH]_{10}$				$(CH_3)_3[CH_3GaNH]_9H_3$			
	Ga→In		Ga→Al		Ga→In		Ga→Al	
	ΔE	μ	ΔE	μ	ΔE	μ	ΔE	μ
0	6.30	1.78	6.30	1.78	5.00	14.45	5.00	14.45
1	5.76	1.55	6.38	2.28	4.94	13.11	4.99	15.94
2	5.69	1.56	6.45	2.02	4.74	14.19	5.04	14.26
3	5.47	3.13	6.49	0.77	4.23	15.64	5.12	13.55

Adapted by permission from Springer Nature: Springer [56], COPYRIGHT (2014)

It was found that the closer the In atoms are located to the NH/H_3-capped end, the greater is the reduction of the energy gap. The closer the Al atoms are located to the NH/H_3-capped end, the bigger is the HOMO-LUMO difference.

The importance of electrostatic interaction in *open* rods has been noticed in early study [167]. Dipole moments μ of studied compounds are given in Table 6.4. The direction of the vector is from the GaR/R_3-capped end of the oligomer to the NH/H_3-capped end. There is almost linear dependence of the dipole moments on the position of substituted rings for *open* oligomers. Replacement of Ga atoms by Al or In atoms in the middle rings of the *open* oligomer has very minor effect on the dipole moment. For *closed* oligomers, the position of the substituent in the vicinity of the N-capped end plays a predominant role in the value of the dipole moment. Dipole moments of the *open* oligomers are more than an order of magnitude larger than that of *closed* ones. Values of dipole moments for *closed* oligomers are 2.66, 1.78, and 1.50 D for Al, Ga, and In, respectively. For *open* oligomers, respective values are 14.75, 14.45, and 14.07 D. However, there is no simple linear correlation between the value of dipole moment and the decrease of the HOMO-LUMO gap energy.

The dependences of energies of HOMO, LUMO, and energy gap values from the number of the Al/In atoms in mixed metal oligomers are shown in Fig. 6.17. N is a number of Ga atoms substituted by Al (shown by black marks) or In (shown by empty marks) atoms. The leftmost side of the figures (N = 0) corresponds to the binary $[CH_3GaNH]_{10}$ (triangles) and $(CH_3)_3[CH_3GaNH]_9H_3$ (circles) compounds. Gallium atoms are one by one substituted by Al or In atoms, starting from the capping CH_3Ga group of the *closed* oligomer and followed by the gallium atoms

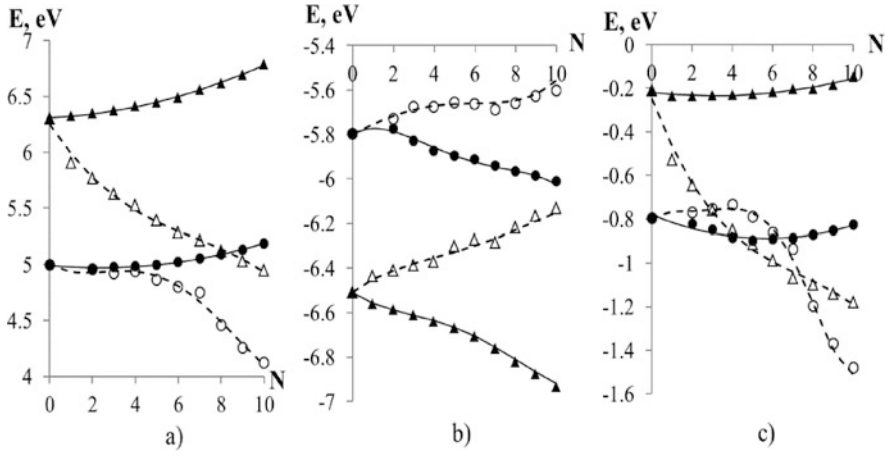

Fig. 6.17 The HOMO-LUMO gap energy (**a**), energies of HOMO (**b**), energies of LUMO (**c**) of *closed* (triangles) and *open* (circles) mixed metal oligomers. N is a number of Ga atoms, substituted by Al (black markers) or In (empty markers) atoms. Lines drawn are to guide the eye only. (Adapted by permission from Springer Nature: Springer [56], COPYRIGHT (2014))

of the first, second, and third Ga_3N_3 rings. The rightmost side (N = 10) represents energy values of *closed* and *open* binary Al and In oligomers. There is a monotonous increase of the HOMO-LUMO gap with increasing the number of Al atoms and rather sharp reduction of energy gap upon introduction of In atoms. The energies of HOMOs increase almost linearly with increasing a number of In atoms; the effect is more pronounced for the *closed* oligomers. The LUMO energies are only slightly affected by introduction of Al atoms but significantly decrease when the Ga atoms are replaced by In atoms.

To get insight into this behavior, let us consider the nature of the HOMOs and LUMOs in more detail (see MOs in Fig. 6.18). HOMOs and LUMOs of M=Al, Ga, and In are qualitatively similar. For C_{3v} and C_3 symmetric structures, HOMO is a degenerate state of E irreducible representation of these point groups.

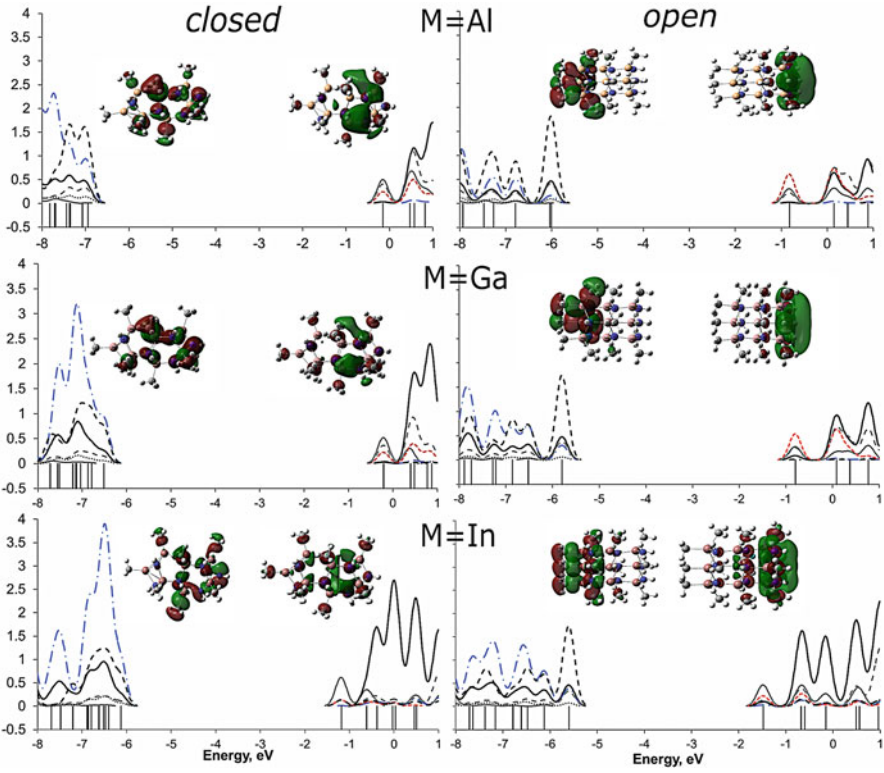

Fig. 6.18 Electronic states (vertical lines) and PDOS of binary *closed* $[CH_3MNH]_{10}$ (left) and *open* $(CH_3)_3[CH_3MNH]_9H_3$ (right) [M = Al, Ga, and In] oligomers. PDOS lines represent contributions of *p* (black) and *s* (gray) states of metal elements. Black dotted lines represent *d* states of metal atoms. Contributions from methyl groups *p* (black) and *s* states (gray) are shown by dashed line, from nitrogen by blue dot-dashed and from N-bonded hydrogens by red short-dashed lines. HOMO and LUMO are shown for the each oligomer. (Adapted by permission from Springer Nature: Springer [56], COPYRIGHT (2014))

LUMO belongs to totally symmetric irreducible representation. Note that in case of *open* oligomers, HOMO and LUMO are strongly localized on the different ends of the rod. The orbitals are more delocalized in case of *closed* oligomers. We should note also that besides HOMO/HOMO−1 (for *open* rods) and LUMO (for all rods), HOMO−2, HOMO−3, HOMO−4, LUMO+1, and LUMO+2 are also end localized in *open* oligomers, while HOMO−2, HOMO−3, and LUMO+3 are localized at the end of the rod for *closed* oligomers.

Figure 6.18 presents electronic states and PDOS analysis for the energy states in vicinity of HOMO-LUMO gaps. The highest occupied states of the oligomers are predominantly *p* orbitals, and the lowest unoccupied states are predominantly *s* orbitals. For highest occupied states of the *closed* oligomers, the largest contribution comes from the *p* states of nitrogen atoms, and it increases with increasing of atomic radius of metal element. In contrast, HOMOs of the *open* oligomers have larger contribution from *p* states of metal atoms, and major contribution comes from *p* states of carbon atoms of terminal methyl groups. There is some contribution from metal *d* states to the highest occupied states. Unlike *closed* oligomers, in the *open* ones, HOMO is localized and easily distinguished in PDOS. Note a difference in the nature of the lowest unoccupied state. For both *open* and *closed* oligomers, LUMO consists of *s* states of metal atoms and N-bonded hydrogens with the portion of metal contribution increasing in order Al < Ga < In. However, in case of *open* oligomers, the hydrogen atoms at the ends of the rod play the major role in electronic structure of LUMO. *s* states of LUMO of *closed* oligomers are delocalized over the whole molecule. In case of indium compounds, *s* orbitals of In have the major contribution to LUMO.

It is worth to mention that research on three-dimensional Ga-N nanodots and Ga-N nanowires [183] suggests valence band to be predominantly of nitrogen *p* orbitals and the lowest unoccupied states are of Ga *p* (nanowires) and Ga *s* and *p* orbitals (nanodots).

From the observations above, it is understandable that substitution of gallium atoms at the end where the LUMO is localized should have a more profound effect on the electronic structure than substitution at the opposite, $(CH_3)_3$ capped side. It is more important in case of replacement of Ga with In atoms because of predominant role of indium *s* orbitals on the LUMO.

From the results obtained for the small rod-shaped clusters ($n = 3$), it is expected that change in the nature of the terminal groups on the ends of the oligomer will significantly influence the electronic structure of *open* oligomer.

6.3.3.3 Excitation Spectra

Absorption spectra of *closed* and *open* oligomers with $n = 3$ generated from vertical excitation energies with transition dipole moment are presented in Fig. 6.19. Test computations indicate that PBE0 hybrid DFT functional is better suited for excitation spectra treatment than B3LYP (see Table 6.2). Thus, in further discussion we will refer to the results of PBE0/TZVP TDDFT computations. However, please

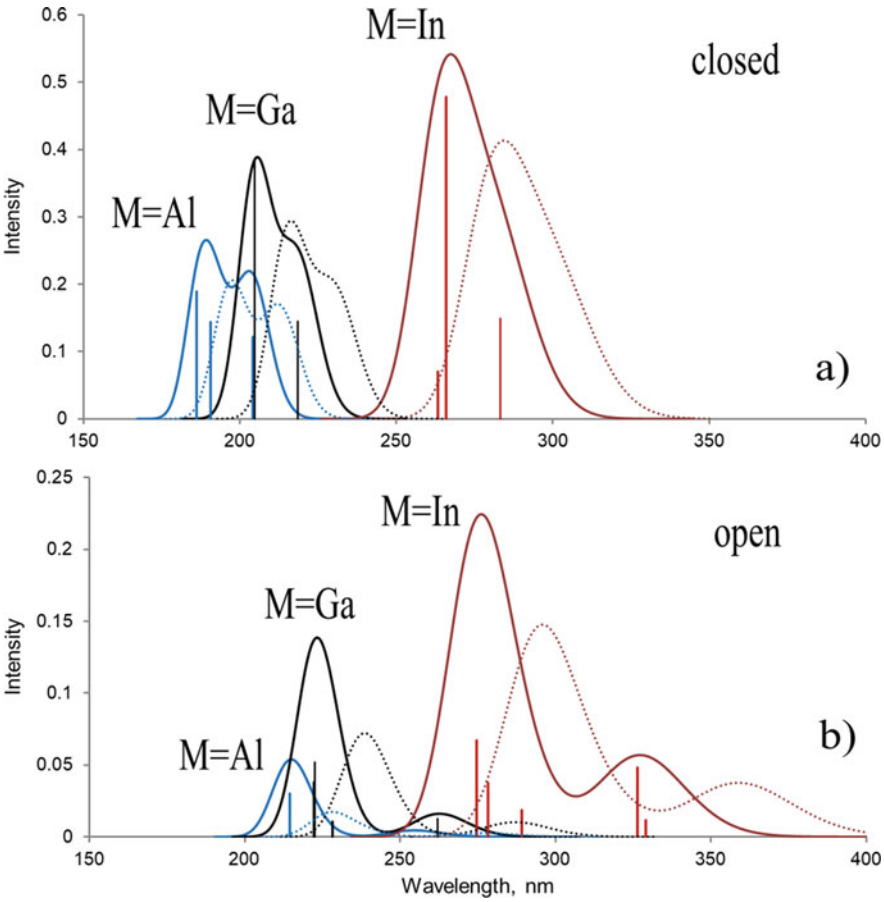

Fig. 6.19 UV excitation spectra of $[CH_3MNH]_{10}$ (**a**) and $(CH_3)_3[CH_3MNH]_9H_3$ (**b**) for M = Al (blue), Ga (black), and In (red) calculated with PBE0/TZVP (lines) and B3LYP/TZVP (dotted lines) levels. Straight lines denote vertical excitations, and their height corresponds to the oscillator strength. (Adapted by permission from Springer Nature: Springer [56], COPYRIGHT (2014))

note that B3LYP/TZVP results are qualitatively similar. As can be seen from Fig. 6.19, at B3LYP level of theory, all spectra are shifted toward the lower energies but have shapes and relative intensities similar to the spectra at PBE0 level.

It was found that spin-triplet states do not contribute to the low-lying optical transitions; thus, only data for the spin-singlet states are presented. Changes in excitation energies upon the structural changes are similar to the ones found for the energy gaps. There is a red shift in absorption spectra for binary compounds from Al to Ga and from Ga to In, and there is a red shift from *closed* to *open* oligomers. In the latter case, the shift of peak's maxima is about 66 nm for Al, 57 nm for Ga, and 8 nm for In binary compounds. Energies of absorption maxima for the *closed* oligomers are 6.6 eV (Al), 6.0 eV (Ga), and 4.6 eV (In); respective values for the

open oligomers are 4.8, 4.7, and 4.5 eV. Energies of the lowest singlet states are 6.1, 5.7, and 4.3 eV for the *closed* Al, Ga, and In binary compounds, respectively. The corresponding values for the *open* oligomers are 4.8, 4.7, and 3.8 eV. These values are larger than the corresponding B3LYP data by about 0.2–0.3 eV.

The intensity of the absorption for the *open* rods is significantly smaller than the one for the *closed* rods. Two absorption peaks are distinguished in the spectra. These two intensive peaks are separated by about 40 nm for Ga and Al and by about 50 nm for In in case of *open* oligomers and only by 13–18 nm in case of *closed* oligomers. In case of $[CH_3InNH]_{10}$, these two peaks are essentially merged into a single, wide absorption band.

For all binary compounds, HOMO/HOMO−1 → LUMO transition makes the greatest contribution (more than 90%) to the lowest spin-singlet state S1. For *open* $(CH_3)_3[CH_3MNH]_9H_3$ oligomers, oscillator strengths of excitation into the S1 state are very small: 0.012, 0.004, and 0.001 for M=In, Ga, and Al, respectively. *Open* oligomers have also low-lying S2 state in the immediate vicinity of S1 state (it differs by about 1–4 nm from the S1 state). For all oligomers, S2 state is predominantly (~99%) the HOMO−2 → LUMO transition; the S2 oscillator strengths are 0.048, 0.013, and 0.003 for In, Ga, and Al *open* oligomers, respectively.

The absorption band with the largest intensity for the each compound is associated with a group of states which have more complex composition. Spin-singlet states with the largest oscillator strength for the *closed* oligomers are fully symmetric (A_1) and for Ga and In binary compounds correspond mostly to HOMO−4 → LUMO excitation (more than 90%). In case of $[CH_3AlNH]_{10}$, main contribution to the state is HOMO−7 → LUMO (50%) and HOMO−6 → LUMO (19%). These transitions occur from the delocalized MOs to the end-localized LUMO.

For *open* oligomers, two adjacent states, which are very close in energy (they are indistinguishable in Fig. 6.19), have the largest oscillator strengths: 0.067 and 0.063 for In, 0.052 and 0.038 for Ga, and 0.030 and 0.017 for Al. One of these states has the largest contributions from HOMO−2 → LUMO+3, HOMO−1 → LUMO+1, and HOMO → LUMO+2 transitions. The composition of the other adjacent state is more complex, and it is different for Al, Ga, and In oligomers.

Experimental spectra obtained for solid powder $[RGaNH]_n$ compounds R=H (Fig. 6.20a) and R=CH_3 (Fig. 6.20b) also reveal absorption in the ultraviolet range [119]. The absorption maximum for $[CH_3GaNH]n$ powder is about 280 nm, i.e., red-shifted compared with our calculated spectra (Fig. 6.19). It is not clear what kinds of oligomers, *open* or *closed*, are dominant in the powder samples studied experimentally [119]. The range of lengths of oligomers in experimental samples is also unknown. Taking into account red shift in excitation energies for the oligomers upon elongation, it was suggested [119] that oligomers of intermediate length (n=10–12) are prevail in the experimentally studied samples.

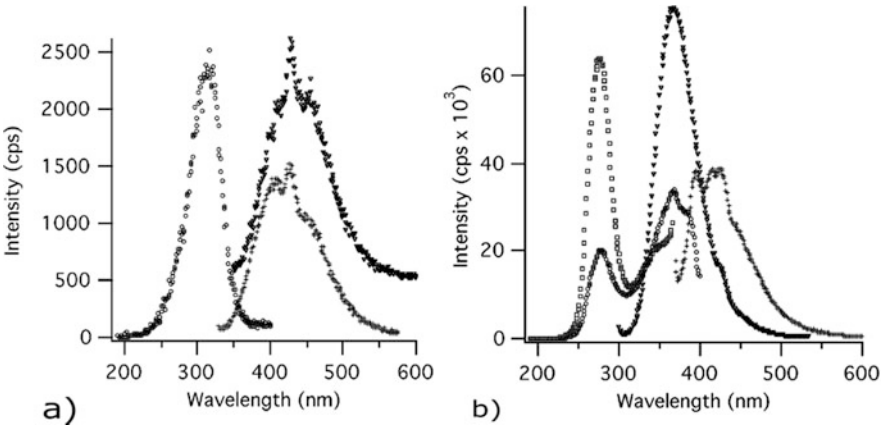

Fig. 6.20 Experimental photoluminescence spectra of $[RGaNH]_n$ powder, R=H (**a**), R=CH_3 (**b**); (▼) emission spectrum with λ_{ex} = 320 nm (R=H) and λ_{ex} = 275 nm (R=CH_3); (+) emission spectrum with λ_{ex} = 320 nm (sample exposed to air for 1 week) (R=H) and λ_{ex} = 345 nm (R=CH_3); (□) excitation spectrum with λ_{obs} = 390 nm (R=CH_3); (○) excitation spectrum with λ_{obs} = 430 nm (R=H) and λ_{obs} = 425 nm (R=CH_3). (Reprinted with permission from [119]. Copyright 2005 American Chemical Society)

6.3.4 Size Effect: The Elongation of the $[RGaNH]_n$ Oligomers

In this section we demonstrate that the type of termination of rod-shaped $[RGaNH]_{3n}$ oligomers [*open* (Fig. 6.13a) versus *closed* (Fig. 6.13b)] significantly affects structural and electronic properties of not only short but even long oligomers.

The existence of edges violates a periodic pattern of the rod-shaped oligomeric structure and changes its properties compared to the properties of the ideal polymeric rod. All edge effects are expected to disappear in the center of the long oligomer. Thus, the comparison of different ways of oligomer's termination necessary involves an investigation of how extended is the impact of the terminal groups. First, we will discuss how intense are structural changes caused by termination of *open* and *closed* oligomers of different length. After that we will compare the electronic structure of the infinite $[HGaNH]_{3\infty}$ polymer with those of long (*circa* 10 nm of length) *open* and *closed* hydrogen-containing oligomers. Finally, we will discuss thermodynamic aspects of the elongation of *open* and *closed* rod-shaped oligomers [58].

6.3.4.1 The Effect of the Rod Termination on the Structural Properties

All considered oligomers remain rod-shaped upon geometry optimization. There is a profound difference in structural parameters of *open* and *closed* oligomers. Figure 6.21 shows distribution of Ga-N bond lengths along the main axis for

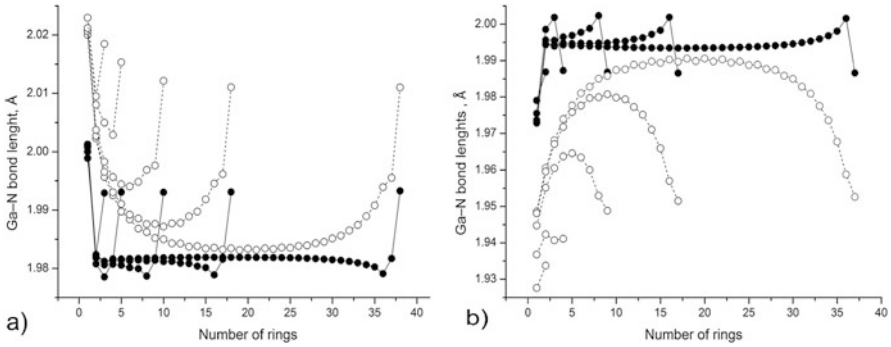

Fig. 6.21 Distribution of Ga-N bond lengths in $[HGaNH]_{3n+1}$ oligomers of different lengths (n = 3, 5, 10, 18, 38). Intra-ring (**a**) and interring (**b**) Ga-N bond's lengths of *closed* (filled circles) and *open* (empty circles) oligomers. Lines are drawn to guide the eye only. (Reprinted with permission from [58]. Copyright 2015 American Chemical Society)

the selected compounds. Hydrogen-containing *open* $H_3[CH_3MNH]_9H_3$ and *closed* $[HGaNH]_{3n+1}$ oligomers with n = 2, 5, 10, 18, and 38 are chosen for comparison. The $[HGaNH]_3$ rings are numbered in the figure starting from the N-terminated end of the oligomer. Ga-N bond lengths within $[HGaNH]_3$ rings are shown on Fig. 6.21a. The Ga-N axial bonds, connecting the neighboring rings, are aligned with the main axis of the oligomer; their lengths are given in Fig. 6.21b.

For *closed* oligomers, Ga-N bond lengths are essentially constant along the rod. The difference in the Ga-N bond lengths of oligomers with n = 10, 18, and 38 is small (below 0.001 Å at the center of the rod). Capping by terminal GaH and NH groups affects Ga-N bond lengths near the very edges of the oligomer, while the internal structure is almost undisturbed. Except for the outmost units, the Ga-N bond lengths in $[HGaNH]_{3n+1}$ are constants within 0.007 Å starting with n = 10. Thus, *closed* oligomers of length longer than ~3 nm ($n \geq 10$) may legitimately be regarded as periodic with a unit cell of a constant length. The value of the unit cell obtained for the longest *closed* oligomer is 5.34 Å.

For *open* oligomers the effect of the terminal groups is more pronounced. The Ga-N bond lengths gradually vary from ring to ring along the oligomer. For *open* oligomers with $n \geq 10$, the Ga-N bond lengths distribution is almost symmetric with respect to the central unit of the oligomer. Both *open* and *closed* oligomers are supposed to have identical geometry in the infinite limit. Nevertheless, even for $[HGaNH]_{3n}$ oligomers of about 10 nm of length (n = 38), the different terminal groups cause a notable difference in respective Ga-N bond lengths even in the central part of the oligomer. Obviously, in case of *open* oligomers, periodic approximation is not appropriate even for the relatively long oligomers. Similar tendencies are found for other structural parameters as well. Intra-ring Ga-N-Ga and N-Ga-N angles as well as N-Ga-N-Ga dihedral angles also gradually change along the rod (Fig. 6.22). There are sharp changes in these parameters near the very edges of the *closed* oligomers. Except for the outmost units, in *closed* oligomers

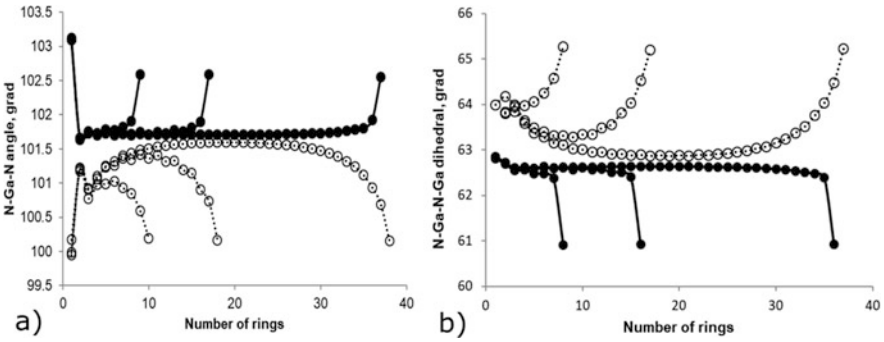

Fig. 6.22 Distribution of valence N-Ga-N (**a**) and dihedral N-Ga-N-Ga (b) interring angles in $[HGaNH]_{3n+1}$ *closed* (filled circles) and *open* $H_3[HGaNH]_{3n}H_3$ (empty circles) oligomers of different lengths ($n = 10, 18, 38$). Lines are drawn to guide the eye only

the angles vary within 0.3° along the oligomer. In the middle rings of the longest *closed* oligomer, Ga-N-Ga is 115.3°, N-Ga-N is 101.7°, and N-Ga-N-Ga is 62.6°. Corresponding values for the longest *open* oligomer are 115.2°, 101.6°, and 62.8°. In the case of the *open* oligomers, except for rather sharp deformations near the very edges of the rods, the Ga-N-Ga and N-Ga-N angles monotonically decrease from the center toward the edges by about 1.5° (see Fig. 6.22a), and N-Ga-N-Ga dihedral angles smoothly increase from the center toward the edges by about 2.5° (Fig. 6.22b). In general, *open* structures in the center have flatter and smaller Ga_3N_3 rings than at the edges. The closer to the edges, the tighter the Ga_3N_3 rings are joined. With the exception of the very edge and with a good approximation, it can be said that all Ga_3N_3 rings in long *closed* oligomers are essentially the same and they are evenly distributed with respect to the center of oligomer.

Systematic changes in structural parameters were also reported for the short $H_3[BN]_{3n}H_3$ rod-shaped oligomers ($n \leq 10$) [184], where authors pointed out monotonic changes in interring B-N bond lengths.

Comparison of inter- and intra-ring Ga-N bond lengths reveals that for all *closed* oligomers, interring Ga-N bonds, except those in the outmost rings, are longer than intra-ring bonds. The former converge to the value of 1.993 Å and the later converge to the value of 1.981 Å. In the *open* oligomers, interring bonds are always shorter, and intra-ring bonds are always longer than those in *closed* oligomers. In contrast to *closed* oligomers, for the *open* oligomers, there is a qualitative change in trends of inter- and intra-rings Ga-N bond lengths upon oligomer elongation. In *open* oligomers with $n < 25$, all interring Ga-N bonds are shorter than intra-ring bonds. Starting from $n = 25$, the Ga-N bond lengths between the central rings become longer than the Ga-N bond lengths within the rings. For about half of $[HGaNH]_3$ units in the central part of the longest considered *open* $H_3[HGaNH]_{3n}H_3$ oligomer ($n = 38$), the interring bond lengths are longer than the intra-ring Ga-N bond lengths. For the rest of the oligomer, the opposite situation is observed: the interring Ga-N bonds are shorter than the intra-ring Ga-N bonds.

For both *closed* and *open* oligomers, there is a contraction of interring Ga-N bond lengths (Fig. 6.21b) as well as expansion of the intra-ring Ga-N bond lengths (Fig. 6.21a) toward the edges of the rod. For *closed* oligomers of all lengths, the contraction near the Ga-capped edge of the rod is 0.007 Å (~0.3%) from the interring Ga-N bond lengths of 1.993 Å at the center of the oligomer. The contraction near the N-capped edge of the oligomer is 0.02 Å (~1.0%). In *open* oligomers, the contraction of the interring Ga-N bond lengths is somewhat larger (up to 0.04 Å, 2%) and depends on the length of the oligomer. These structural changes are quantitatively similar to those predicted for the contraction of surface Ga-N bond lengths in hydrogen-substituted Ga-N nanorods with diameters up to 3.5 nm studied at PBC level [183]. The expansion of intra-ring Ga-N bond lengths in *closed* nanorods near the Ga-capped edge is 0.011 Å ~ 0.6%, and near the N-capped edge is 0.019 Å (~1.0% relative the bond lengths at the center of the rod). For *open* oligomers, the expansion is also length-dependent and amounts up to 0.04 Å (2% relative to the bond lengths at the center of the oligomer).

Methyl-substituted oligomers within considered lengths with $n \leq 9$ demonstrate the same tendencies as hydrogen-substituted analogs. All structural parameters of the methyl-substituted oligomers are very similar, with Ga-N bond lengths being slightly longer (within 0.005 Å) and N-Ga-N angles being slightly smaller (within 1°) than related parameters in the hydrogen-substituted oligomers of the same length and the same type of termination.

Overall, the impact of the terminal groups is found to be surprisingly large. Quite large oligomers, with 19 equivalent structural units (38 $[HGaNH]_3$ rings) and differences only in the terminal groups, coincide in their geometrical parameters only in a small section (about 10 $[HGaNH]_3$ rings) in the central part of the rod. Moreover, the needle-shaped (*closed*) oligomers exhibit comparative regularity in the geometric parameters of the $[HGaNH]_3$ units, with the exception of those closest to the edges. The tube-like (*open*) oligomers are monotonically compressed from the center to the edges. Such significant difference in structural characteristics of *open* and *closed* oligomers results in pronounced differences in their electronic properties.

6.3.4.2 Band Structure of $[RGaNH]_n$ Polymer and Electronic Structure of Finite Size Oligomers

It was stressed above (Sect. 6.3.4.1) that oligomers with a *closed* type of termination maintain periodicity, that is, all structural parameters of neighboring $[HGaNH]_3$ repeating units are almost equivalent. The exception is the outmost GaH and NH units whose influence on the electronic structure is supposed to be rather local. The $[HGaNH]_{115}$ oligomer has 19 repeating units $[HGaNH]_6$ and capping GaH and NH groups. More than 15 equivalent unit cells of an oligomer are generally enough to extract band structure of the related polymer from the finite oligomer calculation [174]. Indeed, except for a limited number of localized states, MOs of the *closed* oligomer with $n = 38$ are found to be properly delocalized along the chain. In Fig. 6.23a circles show positions of these delocalized MOs in the first BZ of $[HGaNH]_{3\infty}$

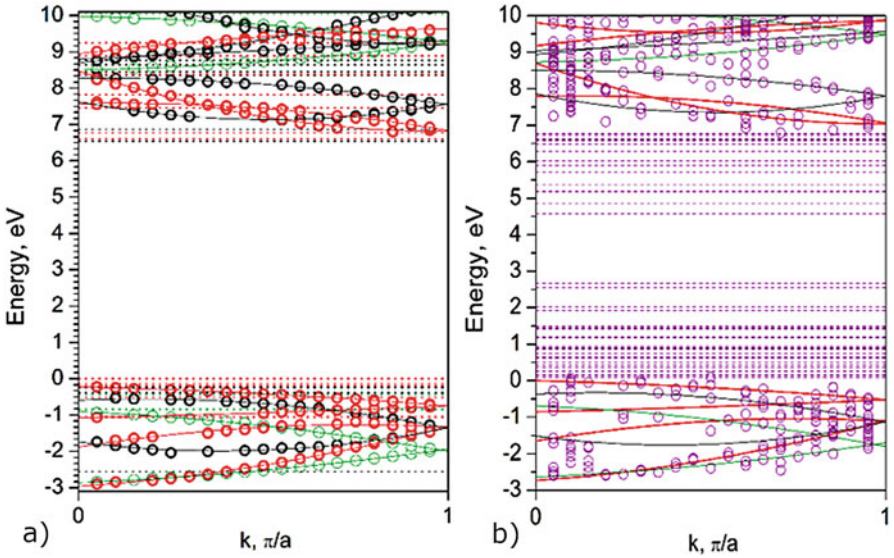

Fig. 6.23 MOs (circles) of *closed* $[HGaNH]_{115}$ (**a**) and *open* $H_3[HGaNH]_{114}H_3$ (**b**) oligomers projected on reciprocal space. Lines indicate the band structure of $[HGaNH]_{3\infty}$ polymer obtained from $[HGaNH]_{115}$ oligomer calculations. Dotted lines show energies of localized MOs. Black, red, and green colors refer to A_1, E, and A_2 symmetries. Purple color is used to show results for the *open* oligomer. (Reprinted (adapted) with permission from [58]. Copyright 2015 American Chemical Society)

polymer. The pattern obtained by projection of the MOs on the reciprocal space allows to draw the polymer's bands easily. The lines in Fig. 6.23 present the band structure of the $[HGaNH]_{3\infty}$ polymer. Particular bands of the polymer, $\varepsilon_n(k)$, are obtained by interpolation/extrapolation to the edges of BZ by the quadratic fit of the MOs in the first BZ. The question of crossing versus avoiding crossing of bands is resolved based on the shape of the curve obtained for $\varepsilon_n(k)$ versus k [175]. Few unphysical bands crossing near the very edges of the BZ seen in Fig. 6.23 are caused by the inaccuracy of the extrapolation associated with a relatively small number of unit cells in the oligomer.

If all MOs of the $[HGaNH]_{115}$ oligomer were properly delocalized, each band $\varepsilon_n(k)$ would have exactly 19 circles arranged strictly along the line. Some displacements in positions of MOs within a band $\varepsilon_n(k)$ as well as "missed" circles are caused by the deviation in phase and energies of the real MOs of the finite oligomer with relaxed structure compared to the orbitals of perfectly periodic polymer. One can see in Fig. 6.23a that some bands have more "missed" circles than the others, that is, these bands are more affected by the type of termination, reflecting violation of the periodicity in the relaxed structure. For example, A_2 bands are affected less than A_1 or E bands within the shown range of energies. The highest valence band and the lowest conduction band are the most affected. Both of them

belong to E symmetry of C_{3v} point group and have p-nature. States of the valence band have the main contribution from N atoms, and states of the conduction band have the main contribution from Ga atoms. Similar conclusions about the nature of valence and conductive bands were made on the basis of PBC computations of the band structure of Ga-N nanowires with diameters of 0.9−2.8 nm [167].

It is interesting that the band gap of the $[HGaNH]_{3\infty}$ polymer is clearly indirect, with the bottom of the conduction band laying near (but not exactly at) the edge of BZ with $k = \pi/a$. Contributions of individual atomic orbitals to the lowest unoccupied delocalized MO of $[HGaNH]_{115}$ consistently change sign from one unit cell to another. The bulk Ga-N is a direct band gap semiconductor. However, it is known that stress applied to a unit cell of a bulk material via doping or strain applied to the one-dimensional nanostructures [185, 186] can cause a switching from direct to indirect band gap. Recent research of GaAs nanowires grown in the [0001] direction [187] demonstrated the phenomenon of transition from direct to indirect band gap when the diameter of the GaAs nanowire becomes smaller than ~28 Å. Obviously, the same effect takes place in the case of Ga-N nanowires. While wider Ga-N nanowires have the direct band gap [167], the thinnest $[HGaNH]_{3n+1}$ rod-shaped polymer has a conduction band with minimum shifted from the Γ point toward the edge of BZ with $k = \pi/a$.

The band gap of the $[HGaNH]_{3\infty}$ polymer is found to be about 7.0 eV, that is, significantly larger than 3.4 eV of the band gap of bulk Ga-N or the band gaps 3–4 eV, obtained for Ga-N nanowires with diameters of 0.9−2.8 nm by pseudopotential DFT computations with PBC [167]. However, the actual energy gap of the finite $[HGaNH]_{3n+1}$ oligomer is defined by localized states situated in the band gap rather than in the top of valence and in the bottom of conductive bands. It is interesting that elongation of the $[HGaNH]_{3n+1}$ does not lead to delocalization of HOMOs and LUMOs over the oligomer. Thus, $[HGaNH]_{3n+1}$ oligomers differ from the similar rods of group 14 elements [119, 188], unsaturated $(BN)_{3n}$ rods [184], and model nitrogen nanoneedles [182]. In Fig. 6.24, HOMOs and LUMOs are shown for *closed* and *open* oligomers. The structure with $n = 9$ is chosen to compare the orbitals of hydrogen- and methyl-substituted oligomers that will be discussed later. Elongation up to $n = 38$ of the hydrogen-substituted oligomers does not reduce the degree of localization of the MOs. In case of the *closed* $[HGaNH]_{115}$ oligomer, about 92% of the electronic density of HOMO is distributed over the two unit cells of the oligomer near the Ga-capped edge (Fig. 6.24a). LUMO of this oligomer is about 91% localized on the unit cell near the N-capped edge (Fig. 6.24b).

MOs which are localized in the real space cannot be localized in the reciprocal space of the BZ. Thus, energy positions of HOMO, LUMO, and other edge-localized MOs of the $[HGaNH]_{115}$ oligomer are shown by the dashed lines in Fig. 6.23a. Most of these states are located in the band gap near the top of valence band and near the bottom of the conduction band. Similar to states of valence band of the $[HGaNH]_{3\infty}$ polymer, HOMO of the $[HGaNH]_{115}$ oligomer is doubly degenerate, with a major contribution of *p* orbitals of N atoms, with some contributions from *s* orbitals of H atoms. LUMO is formed mainly by *s* orbitals of Ga atoms. The presence of the localized states in the spectrum of the finite oligomer reduces the

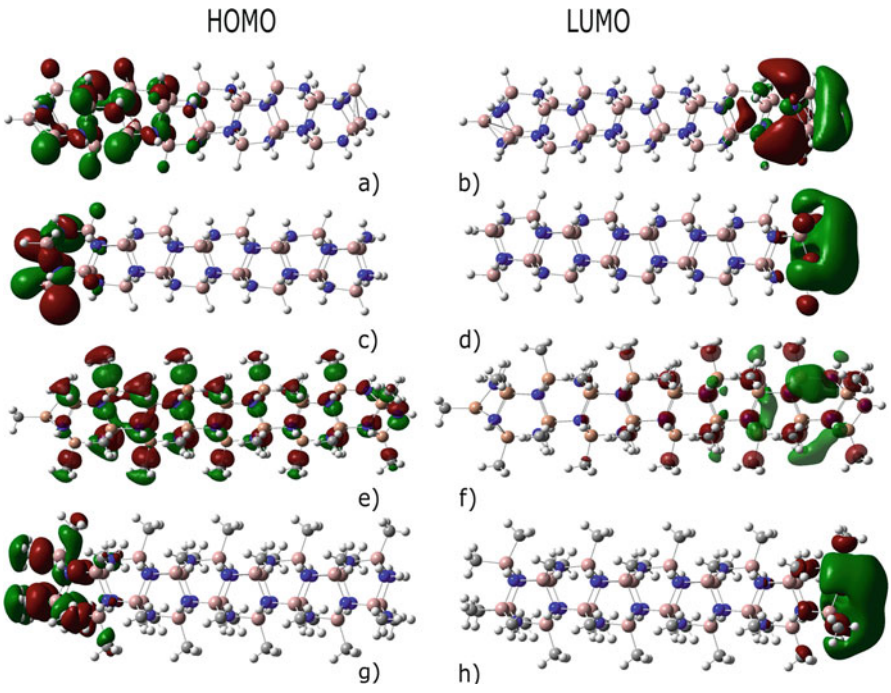

Fig. 6.24 MOs of *closed* $[RGaNH]_{3n+1}$ (**a**, **b**, **e**, **f**) and *open* $R_3[RGaNH]_{3n}H_3$ (**c**, **d**, **g**, **h**) oligomers with $n = 9$; R=H (a–d), or R=CH_3 (e–h). HOMOs are shown on the left side; LUMOs are on the right side. (Reprinted (adapted) with permission from [58]. Copyright 2015 American Chemical Society)

energy gap from 7.0 to 6.54 eV. Moreover, the LUMO of the polymer belongs to the fully symmetric representation of the C_{3v} point group. Thus, HOMO-LUMO transition in the finite oligomer means $E-A_1$ symmetry transition rather than E−E transition, like in $[HGaNH]_{3\infty}$ polymer, and should involve the intramolecular charge transfer from the Ga-capped to the N-capped edge.

In contrast to *closed* oligomers, the electronic structure of the *open* oligomers is drastically different. It is impossible to extract the band structure of $[HGaNH]_{3\infty}$ polymer form MOs of the *open* oligomer with $n = 38$. In Fig. 6.23b, we provide results of projecting of MOs on the reciprocal space and comparison of these results with the results for the *closed* oligomer with the same number of $[HGaNH]_3$ rings. The lack of periodicity, that is, the significant difference in structural parameters of neighboring repeated units in the *open* oligomer, leads to significant localization of MOs; thus, in most of the cases, it is impossible to assign a proper k value for a particular MO. Many MOs are localized at the very edges of the oligomer as well as at different $[HGaNH]_3$ rings at some distance from the edges. These localized MOs of the $H_3[HGaNH]_{114}H_3$ have energies deep inside the band gap of the $[HGaNH]_{3\infty}$ polymer. HOMO and LUMO of the oligomer are similar to those of *open* oligomers with $n = 9$ presented in Fig. 6.24c, d. The nature of the orbitals is similar to HOMOs

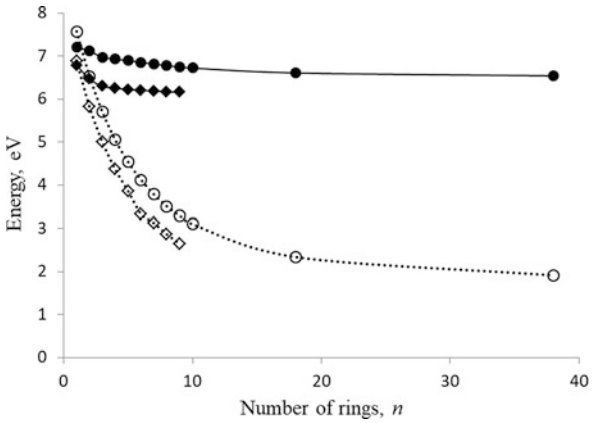

Fig. 6.25 HOMO-LUMO gaps of *closed* $[RGaNH]_{3n+1}$ (black marks) and *open* $R_3[RGaNH]_{3n}H_3$ (empty marks) oligomers of different lengths (n = number of $[RGaNH]_3$ rings). Circles refer to R=H and rhombs refer to R=CH_3. Lines are drawn to guide the eye only. (Reprinted (adapted) with permission from [58]. Copyright 2015 American Chemical Society)

and LUMOs of the *closed* oligomers, but the energies of the states are significantly different. HOMO has much higher, and LUMO has much lower energy than the states of the *closed* oligomer with the same $n = 38$. The HOMO-LUMO gap of the $H_3[HGaNH]_{114}H_3$ oligomer is only 1.91 eV.

Now let us consider the confinement effect for the *open* and *closed* oligomers. Figure 6.25 presents the HOMO-LUMO energy gap for $[RGaNH]_{3n}$ oligomers as a function of number of $[HGaNH]_3$ rings n. One can see that for *open* oligomers the HOMO-LUMO energy gap is much stronger dependent on n. The value of the HOMO-LUMO gap for *closed* $[HGaNH]_{3n}$ oligomers slightly decreases for small n but reaches some plateau with the oligomer elongation. The value of HOMO-LUMO gap could be considered converged for *closed* oligomers with $n \geq 10$. The difference in the HOMO-LUMO gap values between *closed* oligomers with $n = 10$ and 38 is only about 0.18 eV.

The energy gap in *open* oligomers monotonically decreases with the increasing of the length of the oligomer. Up to $n = 10$, the decrease is exponential. For longer oligomers there is a tendency to saturate the value of the HOMO-LUMO gap. However, even for the longest considered oligomer ($n = 38$, ~10 nm of length), the value of HOMO-LUMO gap is not yet converged. Thus, it is expected that, for longer *open* oligomers, the HOMO-LUMO gap could be significantly less than 1.9 eV obtained for the oligomer with $n = 38$.

The decrease of the gap in *open* oligomers is equally provided by monotonic decrease of the LUMO energies and monotonic increase of the HOMO energies, while the decrease of the gap in *closed* oligomers is mainly (~94%) provided by the lowering of the LUMO energies.

Figure 6.25 demonstrates that for methyl-substituted oligomers, there is a nearly constant decrease (the average values are 0.69 and 0.62 eV for *open* and *closed* oligomers, respectively) of the HOMO-LUMO gap compared to the hydrogen-substituted oligomers of the same length. This allows to predict HOMO-LUMO gaps of methyl-substituted oligomers based on the computations for the hydrogen-substituted analogs. HOMO and LUMO of the *open* methyl-substituted oligomers

(Fig. 6.24g, h) obviously have the same origin as the orbitals of *open* hydrogen-substituted oligomers (Fig. 6.24c, d). The only difference is observed for the HOMO, where in methyl-substituted oligomers *p* orbitals of C atoms make a significant contribution. However, HOMO and LUMO of the *closed* methyl-substituted oligomers (Fig. 6.24e, f) are different from those of *closed* hydrogen-substituted analogs (Fig. 6.24a, b). While LUMO is semilocalized near the N-capped edge of the oligomer, the HOMO is delocalized along the oligomer. Thus, it is supposed that for the long but finite methyl-substituted oligomers $[CH_3GaNH]_{3n+1}$, HOMO energy will coincide with the top of the valence band of the $[CH_3GaNH]_{3\infty}$ polymer, and LUMO will be located only slightly below the bottom of the conduction band.

Taking into account that methyl-substituted oligomers exhibit the constant red shift in the energy spectrum compared to hydrogen-substituted analogs, one can estimate that *open* methyl-substituted oligomers with the length of about 10 nm will have the energy gap less than 1.4 eV. Although numerical values of the energy levels obtained with DFT approach are not totally reliable, the qualitative behavior is expected to be valid. Values of band gap change drastically upon the change of terminal groups; they are also strongly dependent on the length of the oligomer.

6.3.4.3 Thermodynamic Characteristics of the Oligomer Elongation

It is of interest to compare relative energetic favorability of *open* and *closed* oligomers. It was found [53] that formal capping process, that is, termination of the $H_3[HGaNH]_{3n}H_3$ oligomer by reaction with NH_3 and GaH_3 with formation of $[HGaNH]_{3n+1}$ and release of five molecules of H_2 is exothermic, and the exothermicity increases with the increase of the oligomerization degree. One can compare an energy associated with the attachment of each additional ring of *open* and *closed* oligomers by considering energetic characteristics of formal reactions leading to the oligomer of a particular length (processes 6.6 and 6.7).

$$3n\mathrm{GaR_3} + 3n\mathrm{NH_3} = R_3[\mathrm{RGaNH}]_{3n}\mathrm{H_3} + (6n-3)\,\mathrm{RH} \tag{6.6}$$

$$(3n+1)\,\mathrm{GaR_3} + (3n+1)\,\mathrm{NH_3} = [\mathrm{RGaNH}]_{3n+1} + (6n+2)\,\mathrm{RH} \tag{6.7}$$

Both standard enthalpies and standard Gibbs energies of the reactions (6.6) and (6.7), with R=H or CH_3, are linear functions of the number of trimeric $[HGaNH]_3$ rings *n*. These reactions are exothermic and exergonic, and favorability of cluster formation increases with increase of *n*. Entropy change in these reactions is unfavorable, but it remains approximately constant upon elongation of the rod.

Let us compare ΔH° and ΔG° of reactions of *open* (6.6) and *closed* (6.7) oligomer formation with $n \leq 10$. The differences between processes (6.7) and (6.6) are the reaction (6.8) of formal capping of the *open* oligomers:

$$\mathrm{GaR_3} + \mathrm{NH_3} + \mathrm{R_3}[\mathrm{RGaNH}]_{3n}\mathrm{H_3} = [\mathrm{RGaNH}]_{3n+1} + 5\,\mathrm{RH} \tag{6.8}$$

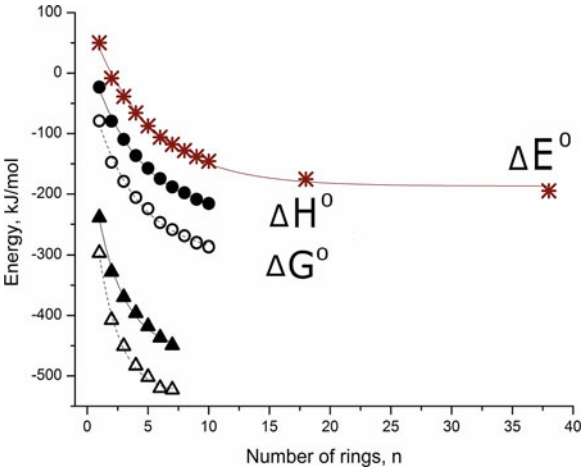

Fig. 6.26 Difference in thermodynamic characteristics of reactions of formation of *open* and *closed* $[RGaNH]_{3n}$ oligomers as a function of number of trimeric $[RGaNH]_3$ rings *n*: standard enthalpies $\Delta_{(6.8)}H°$ (white marks), standard Gibbs energies $\Delta_{(6.8)}G°$ (black marks), and total energies $\Delta_{(6.8)}E°$ (stars) in kJ mol^{-1}; R=H (circles); and R=CH_3 (triangles). Lines represent an exponential fit. (Reprinted (adapted) with permission from [58]. Copyright 2015 American Chemical Society)

The difference between the values of Gibbs energies of formation of *closed* and *open* oligomers is always negative, indicating thermodynamic favorability of *closed* oligomers. Both $\Delta_{(6.8)}H°$ and $\Delta_{(6.8)}G°$ are exponentially decreasing with addition of each $[RGaNH]_3$ ring both for hydrogen-substituted and methyl-substituted oligomers (Fig. 6.26).

The $\Delta_{(6.8)}E°$ for hydrogen-substituted *closed* and *open* oligomers of all considered lengths ($n \leq 38$) is also presented in Fig. 6.26. It follows the same trend as differences in enthalpies and free energies. Thus, for the long $[HGaNH]_{3n+1}$ oligomers, the *closed* oligomers are expected to be preferable by about ~209 kJ/mol compared to the *open* analogs.

On the other hand, the study of the *open* oligomers [119] indicates that the electric dipole moment aligned exactly along the main axis is a driving force for the new $R_3Ga_3N_3H_3$ ring attachment. Indeed, the dipole moment, directed from the Ga to N edges of the oligomer, linearly increases with the number of rings *n* of the $[HGaNH]_{3n}$ oligomers (Fig. 6.27). Linear fitting for the *open* oligomers results in the equation: $\mu = (10.36 \pm 0.14)n - (21.1 \pm 1.9)$ (values in Debye, $R^2 = 0.995$).

The capping of the oligomer by GaH and imino groups partly compensates the axial electric field; thus, the value of the dipole moments of the *closed* oligomers increases to much lesser extent: $\mu = (1.58 \pm 0.01)n - 2.7 \pm 0.2$ ($R^2 = 0.997$).

Dipole moments of methyl-substituted oligomers are similar to those of hydrogen-substituted analogs: for *open* methyl-substituted oligomers

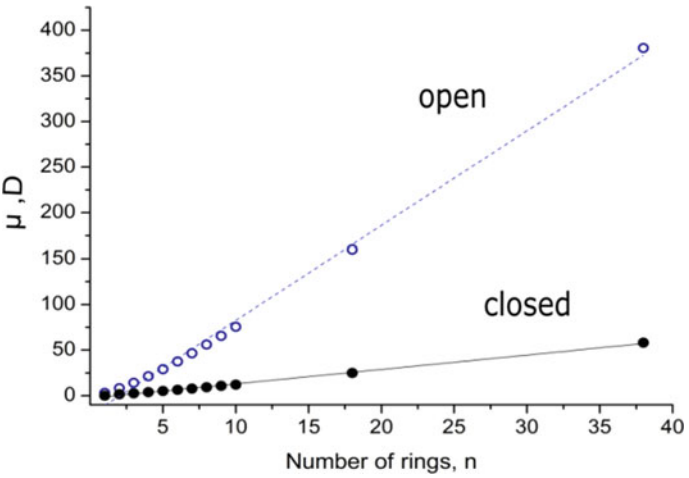

Fig. 6.27 Dipole moments μ, Debye of *closed* (black circles) and *open* (blue circles) $[HGaNH]_{3n}$ oligomers as a function of *n*. Lines drawn are linear fit. (Reprinted (adapted) with permission from [58]. Copyright 2015 American Chemical Society)

$$\mu = (8.54 \pm 0.21)\, n - (9.8 \pm 1.2) \quad \left(R^2 = 0.993\right)$$

and for *closed* methyl-substituted oligomers

$$\mu = (0.77 \pm 0.01)\, n - (0.59 \pm 0.06) \quad \left(R^2 = 0.998\right).$$

Competition of the processes of oligomer formation, favorability of the growth of *open* rod-shaped oligomers, and favorability of the capping reaction can lead to the coexistence of *open* and *closed* oligomers of different lengths. It should be taken into account that the high polarizability of the oligomers can also lead to a formation of some supramolecular aggregates in the condensed phase. Knowledge of actual distribution of different oligomers requests theoretical study of the kinetics of the oligomerization processes in the gas phase as well as experimental studies.

6.3.5 *The Effect of Terminal Substituents on the Electronic Properties of Oligomers*

The strong influence of the terminal groups at the oligomer ends on its electronic properties opens a way for fine tuning of the HOMO-LUMO gap by the variation of only terminal substituents. In this section, we demonstrate that the variation

Table 6.5 Standard enthalpies ΔH^0_{298} (in kcal/mol) of the formal reactions of "capping" $X_3[HGaNH]_{3n}Y_3$ oligomers with XGa and NY groups (process 6.8)

X	H	H	H	H	CH_3	CH_3	CH_3	CH_3
Y	H	CH_3	F	CF_3	H	CH_3	F	CF_3
n = 3	−26.2	−74.4	−150.1	−62.8	−49.5	−97.7	−173.1	−85.6
n = 10	−51.6	−99.6	−180.0	−93.7	−75.8	−123.8	−204.3	−118.1
X	F	F	F	F	CF_3	CF_3	CF_3	CF_3
Y	H	CH_3	F	CF_3	H	CH_3	F	CF_3
n = 3	34.1	−14.0	−91.2	−4.3	−37.7	−85.8	−163.0	−76.2
n=10	13.3	−34.7	−115.1	−28.6	−57.3	−105.6	−186.0	−99.8

of electron donor/electron acceptor properties of terminal substituents allows one to adjust the HOMO-LUMO gap to cover a wide spectral range [59]. *Closed* $XGa[HGaNH]_{3n}NY$ and *open* $X_3[HGaNH]_{3n}Y_3$ (X, Y=CH_3, H, F, CF_3) oligomers (see Fig. 6.13) have been considered as the smallest oligomeric clusters ($n = 3$), as well as rods of about 10 nm in length ($n = 38$) and also oligomers of some intermediate length ($n = 10$). Several oligomers with $n = 2$, 4, and 6 have been considered to evaluate the distribution of partial charges.

It was shown in Sect. 6.3.4.3 that the stability of $[RGaNH]_{3n}$ increases linearly with the elongation of the oligomer. The introduction of the substituents on the oligomer ends does not change this trend. *Closed* oligomers in general are energetically more favorable than the *open* oligomers. Reactions of capping of *open* rods are exothermic for all X and Y pairs with the exception of X=F and Y=H.

$$X_3[HGaNH]_{3n}Y_3 + GaH_3 + NH_3 = XGa[HGaNH]_{3n}NY + 2HX + 2HY + H_2 \quad (6.9)$$

The standard enthalpies of the formal reaction for oligomers of two different lengths are given in Table 6.5. The exothermicity of capping reactions increases with the increase of the oligomerization degree.

As has been comprehensively shown by Kormos et al. [119], the relative displacement of nitrogen N_3 and gallium Ga_3 planes provides a non-zero, 2.9 D, dipole moment of the cyclotrigallazane ring $H_3[H_2GaNH_2]_3H_3$ that increases up to 69.3 D upon the elongation up to $H_3[H_2GaNH_2]_{27}H_3$ due to the increase of the distance between the oppositely charged ends. For the following analysis, we calculated ESP charges [189] that are fitted to the electrostatic potential and constrained them to reproduce the dipole moment μ. Results are given in Figs. 6.28 and 6.29.

The dipole moment in considered oligomers is usually directed from the negative charge accumulated near the Ga-saturated end of the oligomer to the positive charge accumulated near the N-saturated end. In Fig. 6.28 the ESP charge distribution and dipole moments are shown for *open* oligomers with CH_3/CH_3 and CH_3/CF_3 terminal groups for comparison. In case of methyl substituents on both sides, the dipole moment is always directed from Ga-saturated end toward N-saturated

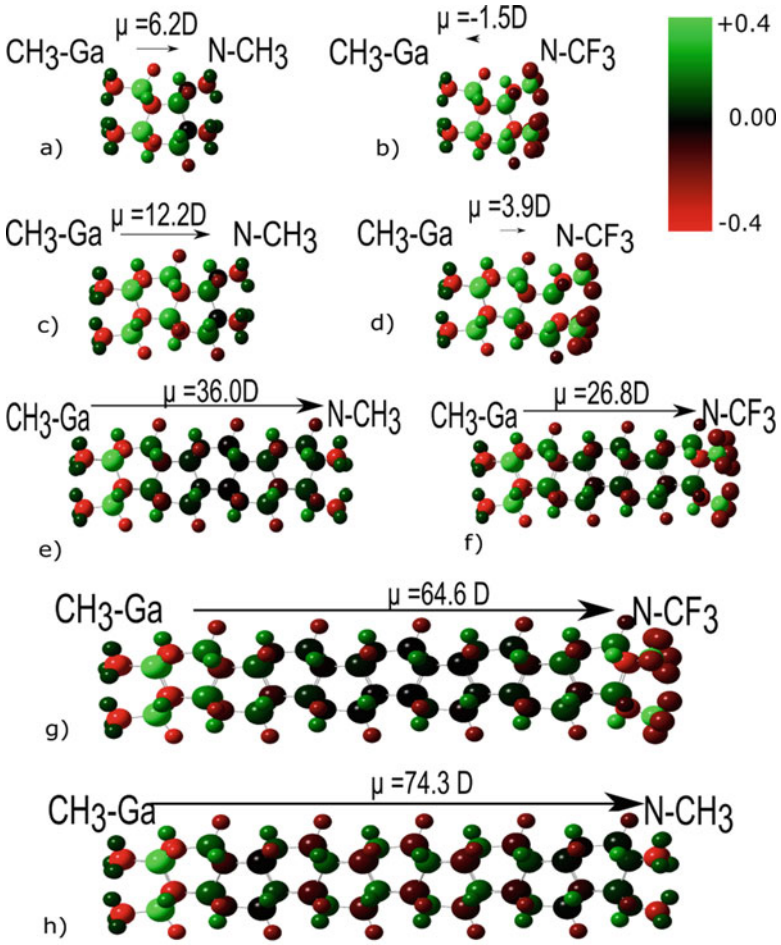

Fig. 6.28 Dipole moment vectors and ESP charge distribution over atoms in *open* $X_3[HGaNH]_{3n}Y_3$ oligomers with n=2 (**a**, **b**), 3 (**c**, **d**), 6 (**e**, **f**), 10 (**g**, **h**) and with terminal groups $X=CH_3$, $Y=CH_3$ (a,c,e,h) and $X=CH_3$, $Y=CF_3$ (b,d,f,g)

end, $\mu > 0$ for all oligomers and dipole moment increases with the increase of the length of the oligomer (Fig. 6.28 a, c, e, h). However, if CH_3 groups are replaced by the electron-withdrawing CF_3 groups on N-saturated end (Fig. 6.28 b, d, f, g), it significantly reduces the dipole moment. For the smallest rod-shaped $(CH_3)_3[HGaNH]_6(CF_3)_3$ compound, electrophilicity of the CF_3 groups overcomes the charge separation caused by displacement of Ga_3 and N_3 planes, and the dipole moment has small negative value, $\mu = -1.5$ D (Fig. 6.28b).

The effect is more pronounced in case of *closed* $XGa[HGaNH]_9NY$ oligomers. If X=H or CH_3 and Y=F or CF_3, the electron-withdrawing power of the F and CF_3 groups overcomes the electrostatic field provided by the spatial separation of

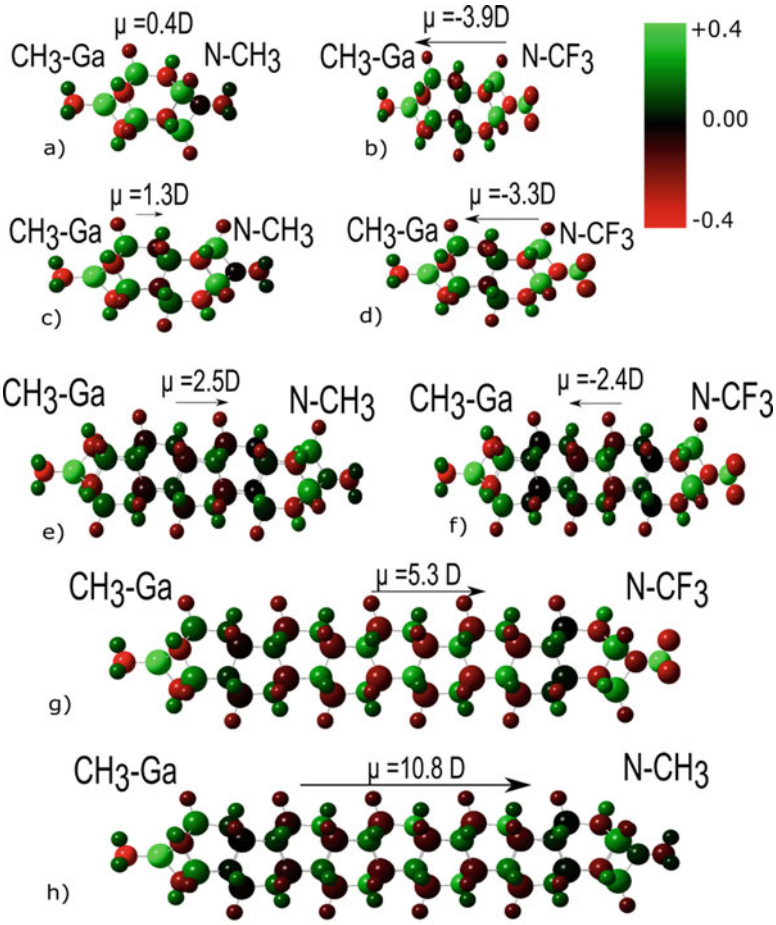

Fig. 6.29 Dipole moment vectors and ESP charge distribution over atoms in closed $XGa[HGaNH]_{3n}NY$ oligomers with n=2 (**a**, **b**), 3 (**c**, **d**), 6 (**e**, **f**), 10 (**g**, h) and with terminal groups $X{=}CH_3$, $Y{=}CH_3$ (a,c,e,h) and $X{=}CH_3$, $Y{=}CF_3$ (b,d,f,g)

gallium and nitrogen planes. This leads to the change in the direction of the dipole moment for compounds with $n \leq 6$. As an example, in Fig. 6.29, the ESP charge distribution and dipole moments are shown for *closed* oligomers with CH_3/CH_3 and CH_3/CF_3 end substituents. In methyl substituent *closed* oligomers, one outmost Ga-CH_3 and N-CH_3 groups (Fig. 6.29 a, c, e, h) cause significantly smaller dipole moments, 0.4, 1.3, 2.5, and 10.8 D in *closed* oligomers against 6.2, 12.2, 36.0, and 74.3 D in *open* oligomers for $n = 2$, 3, 6, and 10, respectively. Consequently, the replacement of N-CH_3 with N-CF_3 group (Fig. 6.29 b, d, f, g) has larger effect and alters the dipole moment direction for the number of small *closed* oligomers. One

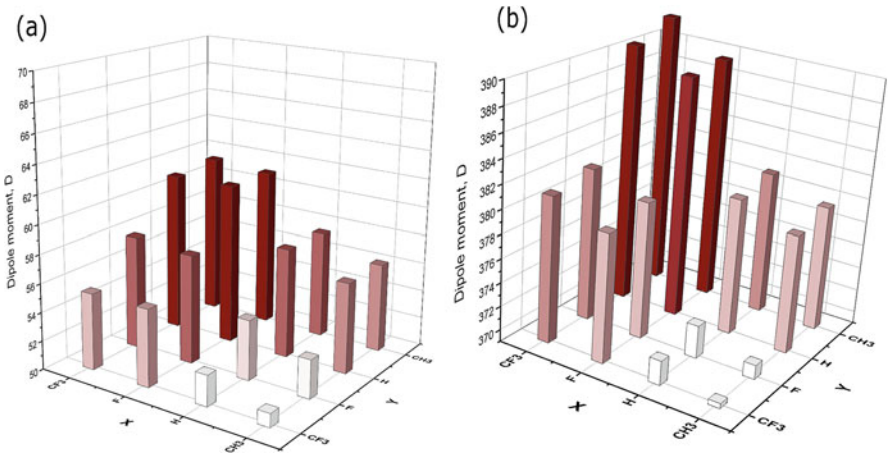

Fig. 6.30 Dipole moments of *closed* XGa[HGaNH]$_{114}$NY (**a**) and *open* X$_3$[HGaNH]$_{114}$Y$_3$ (**b**) oligomers. Reproduction of material from PCCP (Physical Chemistry Chemical Physics). (Reproduced from Ref. [59] with permission from the PCCP Owner Societies)

can see that $\mu = -2.4$D for $n = 6$ (Fig. 6.29f), $\mu = -3.3$D for $n = 3$ (Fig. 6.29d), and $\mu = -3.9$ for $n = 2$ (Fig. 6.29b).

In general, the dipole moments of the oligomers increase linearly with the increase of the oligomer lengths, although some small nonlinearity is noticeable for *open* types of oligomers of shorter lengths. The dipole moment values of the longest ($3n = 114$) oligomers are given in Fig. 6.30.

Capping of the H$_3$[HGaNH]$_{3n}$H$_3$ oligomer by terminal XGa and NY groups significantly (by 317–330 D) reduces the dipole moment (Fig. 6.30a) not only because the Ga-terminated end has only one XGa group instead of three in *open* oligomers but also due to the different chemical environment around the Ga atom. In *closed* oligomers terminal Ga atom is bonded with one X group and three N atoms, but in *open* oligomers each terminal Ga atom is bonded to one X group, one H, and two N atoms. It leads to an overall decrease of the charge at the Ga-terminated end in *closed* oligomers. For example, the ESP charge in the outermost Ga atom of CH$_3$Ga[HGaNH]$_6$NCH$_3$ is about 0.478, while the charge of each Ga atom in the outermost plane in (CH$_3$)$_3$[HGaNH]$_6$(CH$_3$)$_3$ is 0.515. Values of the sum of partial charges in the vicinity of Ga- and N-terminated ends for several *open* and *closed* oligomers are presented in Table 6.6. Partial charge accumulated on the Ga-terminated end in *open* oligomers is more than three times larger than the one on XGa groups in *closed* oligomers.

For the longest considered oligomers with $n = 38$, the dipole moment calculated per monomeric HGaNH unit varies from 3.24 (X=CH$_3$,Y=CF$_3$) to 3.44 D (X=CF$_3$, Y=CH$_3$) for *open* and from 0.44 (X=CH$_3$, Y=CF$_3$) to 0.54 D (X=CF$_3$, Y=CH$_3$) for *closed* oligomers.

Table 6.6 Group partial electrostatic charges in the vicinity of the opposite ends of oligomers $(CH_3)_3[HGaNH]_{3n}Y_3$ and $CH_3Ga[HGaNH]_{3n}NY$ with Y=CH_3 or CF_3

	$(CH_3)_3[HGaNH]_{3n}Y_3$				$CH_3Ga[HGaNH]_{3n}NY$			
n\group	$(CH_3GaH)_3$	$(NHCF_3)_3$	$(CH_3GaH)_3$	$(NHCH_3)_3$	CH_3Ga	NCF_3	CH_3Ga	NCH_3
2	1.65	−1.34	1.58	−0.56	0.29	−0.37	0.30	−0.09
3	1.55	−1.10	1.43	−0.43	0.28	−0.35	0.27	−0.07
4	1.43	−0.94	1.38	−0.24	0.26	−0.32	0.24	−0.03
6	1.27	−0.84	1.16	−0.17	0.26	−0.29	0.23	0.01
10	1.21	−0.79	1.13	−0.07	0.25	−0.24	0.27	0.00
38	1.24	−0.68	1.23	−0.00	0.21	−0.29	0.21	0.03

Substituents X and Y change the dipole moment by donating/withdrawing the electron density to/from the neighboring Ga or N atoms. The electron-withdrawing ability decreases in row CF_3 > F> H> CH_3 [190]. Our results for the distribution of dipole moment values over different combinations of terminal groups (Fig. 6.30) are in accord with such a trend. The oligomer with a CF_3 group on the gallium atom (X) and a CH_3 group on the nitrogen atom (Y) has the maximal dipole moment in the case of both *closed* (Fig. 6.30a) and *open* (Fig. 6.30b) rods. F or CF_3 terminal groups on the gallium and H or CH_3 groups on the nitrogen atoms result in similar values of the dipole moments. In contrast, H or CH_3 groups attached to terminal Ga atoms along with F or CF_3 groups attached to terminal N atoms provide small dipole moments. The oligomer with X=CH_3 and Y=CF_3 has the smallest dipole moment. Combinations of X=F/CF_3 with Y=F/CF_3 or X=H/CH_3 with Y=H/CH_3 provide intermediate values of the dipole moment.

Let us compare atomic charge distribution for the combination X=CH_3 and Y=CF_3, which provides the smallest dipole moments for the fixed n (with the reversal of the dipole moment vector in the case of the shortest oligomers), with oligomers with methyl substituents on both ends. Partial charges accumulated at opposite ends (the outermost Ga and N planes with the conjunct substituents) are provided in Table 6.6. The CH_3-substituted N-terminated end is essentially neutral, while F atoms along with N atoms of the outermost plain accumulate significant negative charge that counterpoises or even overcomes the negative charge accumulated at CH_3 groups of the Ga-terminated end. In all cases, the partial charges on the negatively and positively charged ends decrease with the elongation of the oligomer. The NCF_3 group of *closed* oligomers loses about 0.09 ē when the oligomerization degree increases from n = 2–38. For the *open* oligomers, three N-CF_3 groups lose altogether more than 0.5 ē when n increases from 2 to 6 in $(CH_3)_3[HGaNH]_n(CF_3)_3$. The respective change in the charge of three Ga-CH_3 groups in $(CH_3)_3[HGaNH]_{3n}(CH_3)_3$ is about 0.4 ē. Thus, notable charge transfer between opposite ends occurs in short oligomers. It depends on the particular substituents and affects oligomers with length up to about 14 Å (n < 6).

The HOMO and LUMO of the rod-shaped *open* oligomers are strictly localized at the ends of the molecules. Figure 6.31a shows the HOMO and LUMO of $(CH_3)_3[HGaNH]_{30}F_3$ as an example. The HOMO is almost entirely localized at

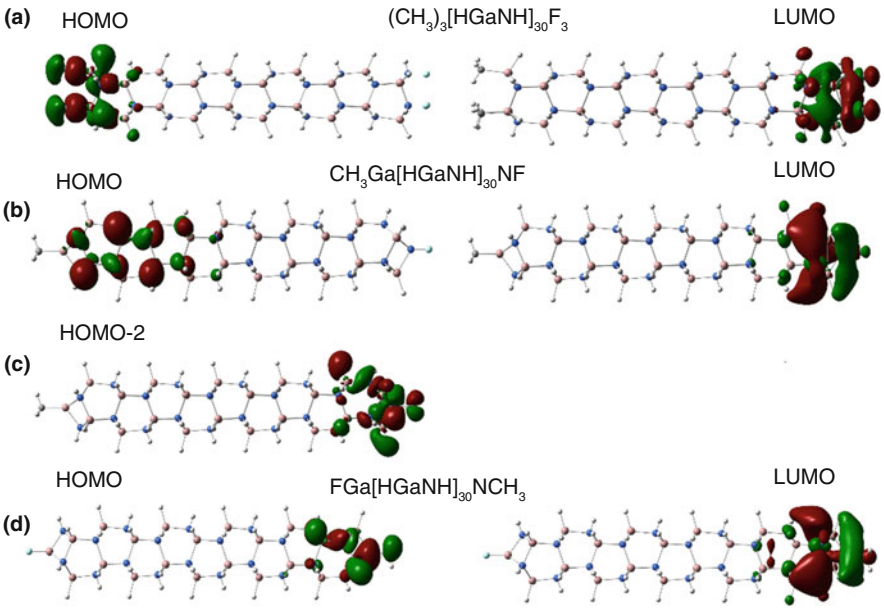

Fig. 6.31 MOs of selected oligomers. Blue color refers to N, pink to Ga, white to H, gray to C, and light blue to F atoms

the gallium-terminated end in long oligomers, and the LUMO is almost entirely localized at the nitrogen-terminated end. It should be noted that all other occupied orbitals with energy within at least 2 eV below the HOMO are also localized at the Ga-terminated end.

Likewise, all unoccupied orbitals with energy within at least 2 eV higher than the LUMO are localized at the N-terminated end. It is expected that the HOMO energy will be sensitive to the X substituent while the LUMO energy will depend on the Y substituent.

In *closed* oligomers, the LUMO of A_1 symmetry is strongly localized at the N-terminated end (Fig. 6.31b), but the HOMO of E symmetry is more delocalized and does not extend over the terminal group at the Ga-terminated end, having major contribution from N atoms (see also Figs. 6.18 and 6.24). In the most of the considered *closed* oligomers with $n = 10$, the HOMO is moderately localized in the vicinity of Ga-terminated end as shown for $CH_3Ga[HGaNH]_{30}NF_3$ in Fig. 6.31b. However, there are MOs in the vicinity of the HOMO which are localized at the N-terminated end. For example, in Fig. 6.31c the *p*-type HOMO-2 of $CH_3Ga[HGaNH]_{30}NF_3$ is shown which is localized at the terminal F and adjacent N atoms. The energy difference between HOMO and HOMO-2 is below 0.1 eV. Thus, the HOMO-2-LUMO energy difference is similar to the HOMO-LUMO energy difference, while HOMO-2-LUMO transition does not involve an end-to-end intramolecular charge transfer. A similar situation is observed for other *closed*

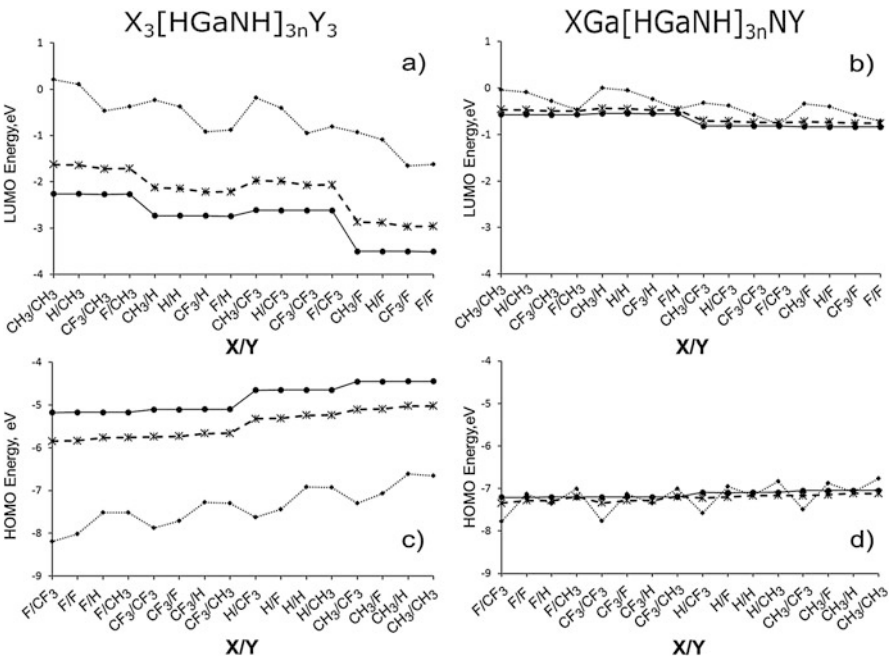

Fig. 6.32 Energies of LUMO (**a**, **b**) and HOMO (**c**, **d**) for *open* $X_3[HGaNH]_{3n}Y_3$ (a, c) and *closed* $XGa[HGaNH]_{3n}NY$ (b, d) oligomers with $n = 3$ (dotted line), $n = 10$ (dashed line), and $n = 38$ (solid line) for different combinations of X/Y substituents. Reproduction of material from PCCP (Physical Chemistry Chemical Physics). (Reproduced from Ref. [59] with permission from the PCCP Owner Societies)

oligomers with intermediate length ($n = 10$). In some cases (X=CF_3, Y=F; X=CF_3, Y=CH_3; X=H, Y=CH_3; X=F, Y=CH_3; X=F, Y=F), the occupied molecular orbital localized at the N-terminated end shifts to somewhat higher energy than the one localized at the Ga-terminated end and becomes the HOMO (see Fig. 6.31d).

Figure 6.32a, b shows the energies of LUMOs for *open* and *closed* oligomers. The estimation of electronegativities of functional groups based on core-ionization energies [191] implies that the CF_3 group is significantly less electronegative than F. It correlates with the trend in the LUMO energies. The lowest energy of the LUMO corresponds to Y=F for both *closed* and *open* oligomers with $n = 10$ or $n = 38$; for *open* oligomers Y=CF_3 yields much higher LUMO energies (Fig. 6.32a). The difference in LUMO energies between Y=F and Y=CF_3 is circa 0.9 eV in *open* oligomers with $n = 38$ or $n = 10$. The difference in LUMO energies between Y=CH_3 and Y=H in *open* oligomers with n = 38 or n = 10 is *circa* 0.5 eV.

In the case of *closed* oligomers (Fig. 6.32b), if they are long enough to neglect the influence of terminal groups at opposite ends ($n = 10$ or 38), there is no difference between Y=F and Y=CF_3, or Y=H and Y=CH_3. The only factor lowering the LUMO energy (by ~0.3 eV compared to Y=H or Y=CH_3) is the presence of fluorine atoms (Y=F or Y=CF_3) in substituents at the nitrogen-terminated end.

The HOMO energies of long oligomers (Fig. 6.32c, d) increase in the order $X = F < CF_3 < H < CH_3$. The effect of terminal substituents on the HOMO energies is less pronounced than on the LUMO energies. The largest difference in the energies between long *open* oligomers ($n = 10$ or 38) with $X = F$ and $X = CH_3$ of is ~0.65 eV (Fig. 6.32c). For long needle-shaped oligomers (Fig. 6.32d), the difference does not exceed 0.16 eV. It correlates with the observation that terminal groups in the Ga-terminated end of long *closed* oligomers do not contribute to the HOMO (see Fig. 6.31b). The elongation of *open* oligomers has a drastic effect on the HOMO and LUMO energies (see Fig. 6.32). The average downshift of LUMO energies of *open* rods is ~0.58 eV (Fig. 6.32a) with elongation from $n = 10$–38. The respective upshift for the HOMO energies is ~0.62 eV (Fig. 6.31a).

As expected, X substituents do not influence the energy of LUMO, and Y substituents do not influence the HOMO energies for oligomers with $n = 10$ or 38. However, the substituents play a significant role in molecules with $n = 3$ where the opposite ends of the molecule are close enough to interact with each other. For any particular substituents at the nitrogen atom, LUMO energies decrease in the order of substituents at the gallium atom (X) as $CH_3 > H > CF_3 > F$ for *closed* and as $CH_3 > H > F > CF_3$ for *open* oligomers with $n = 3$. On the other hand, for any particular substituent at the gallium atom, HOMO energies of oligomers with $n = 3$ increase with changing Y substituents in order $CF_3 < F < H < CH_3$ for *open* and as $CF_3 < H < F < CH_3$ for *closed* oligomers. On the whole, for short oligomers the substituents Y at the nitrogen-terminated end have a larger effect on the energies of HOMO and LUMO and, consequently, the HOMO-LUMO gap values, than the substituents X at the gallium-terminated end.

Electronic energies and partial density of states in the vicinity of HOMO-LUMO gaps of $F_3[HGaNH]_{114}F_3$ and $(CH_3)_3[HGaNH]_{114}(CH_3)_3$ oligomers are given in Fig. 6.33. At such a length (*circa* 10 nm), the terminal substituents do not affect the opposite ends of the rod. Thus, the PDOS in the vicinity of the HOMO and LUMO of the oligomers with the smallest ($X{=}CH_3$ and $Y{=}F$) and the largest ($X{=}F$ and $Y{=}CH_3$) energy gaps are expected to be the same as the respective local PDOS shown in Fig. 6.33a, b.

The estimated band gap of the $[HGaNH]_\infty$ polymer, extrapolated from the oligomer computations, is circa 7.0 eV. Finite *open* oligomers have a number of localized states within the band gap of the parent polymer. These states are clearly seen in the energy spectra shown in Fig. 6.33 as spatially separated levels in the vicinity of the HOMO-LUMO gap in contrast to nearly continuous spectra in valence and conductivity bands. Most of the HOMOs exhibit density distribution over the N atoms near the Ga-terminated end, while lower unoccupied states have the main contribution from the Ga atoms near the N-terminated end. The contribution of terminal groups is noticeable not only in HOMO and LUMO states but also deeper in the spectrum. F substituents produce a relatively sparse spectrum of lower unoccupied localized states which results in the maximal downshift of the LUMO energy (Fig. 6.33a). By withdrawing electrons from N atoms, F substituents induce vacant orbitals of the lowest energy which result in lower LUMO energies.

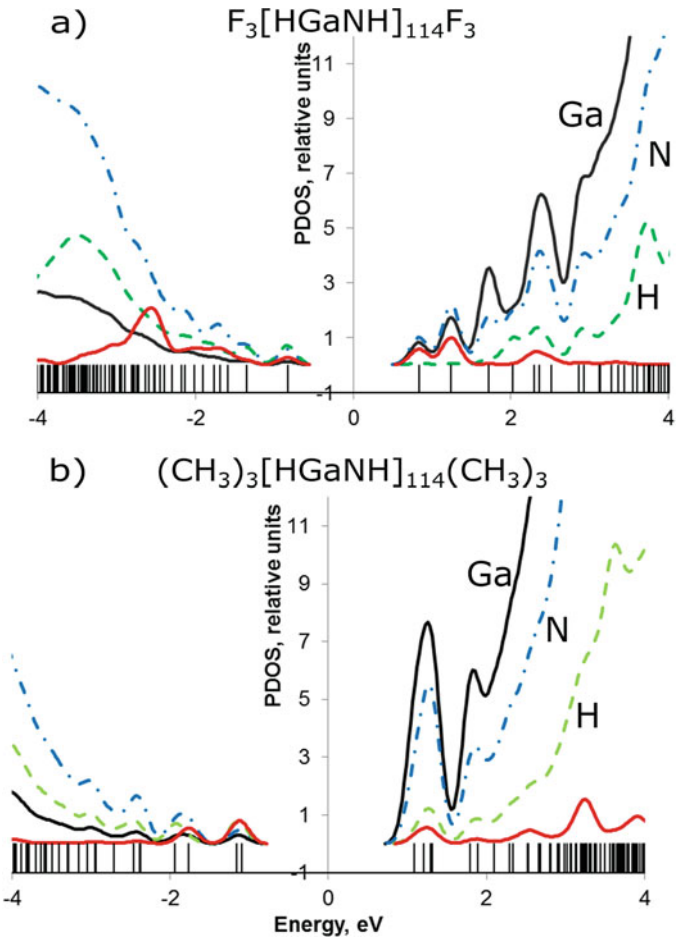

Fig. 6.33 PDOS of $F_3[HGaNH]_{114}F_3$ (**a**) and $(CH_3)_3[HGaNH]_{114}(CH_3)_3$ (**b**) Contributions from Ga atoms are shown by black lines, from N atoms by blue dash-dotted lines, and from backbone H atoms by green dashed lines, and contributions from terminal groups (F or CH_3) are presented by red lines. For drawing this figure, the middle of the energy gap is chosen as the zero energy. Reproduction of material from PCCP (Physical Chemistry Chemical Physics). (Reproduced from Ref. [59] with permission from the PCCP Owner Societies)

In contrast, methyl substituents produce a relatively sparse spectrum of the highest occupied molecular orbitals (Fig. 6.33b).

The values of HOMO-LUMO gaps for all considered oligomers with $n = 38$ are shown in Fig. 6.34. In all cases, the smallest HOMO-LUMO gap corresponds to the oligomer with a methyl group at the Ga atom and fluorine at the nitrogen atom. The largest values of the HOMO-LUMO gap correspond to strong electron-withdrawing substituents (F, CF_3) at the terminal Ga atoms and electron-donating groups (CH_3) at the terminal N atoms. Thus, substituents which reduce the dipole

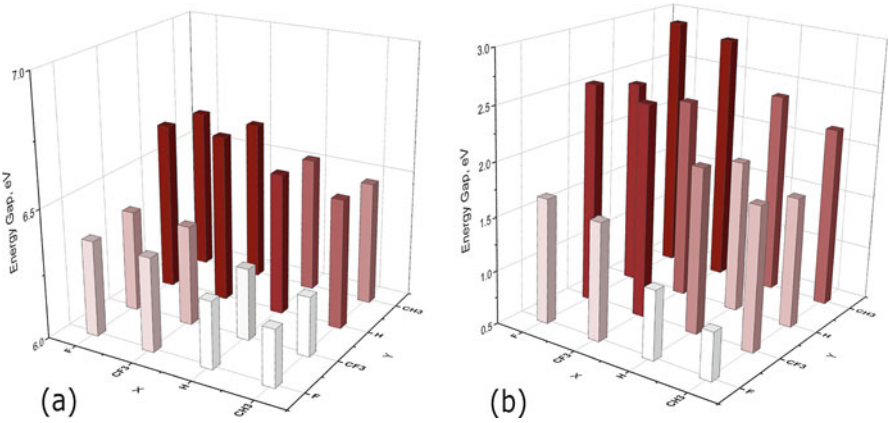

Fig. 6.34 HOMO-LUMO gaps of *closed* XGa[HGaNH]$_{114}$NY (**a**) and *open* X$_3$[HGaNH]$_{114}$Y$_3$ (**b**) oligomers with different substituents X and Y. Reproduction of material from PCCP (Physical Chemistry Chemical Physics). (Reproduced from Ref. [59] with permission from the PCCP Owner Societies)

moment of the system (Fig. 6.30) reduce the energy gap as well (Fig. 6.34). The HOMO-LUMO gap values of *closed* oligomers vary within circa 0.4 eV depending on terminal groups (Fig. 6.34a). The change is much more pronounced in the case of *open* oligomers (Fig. 6.34b); the HOMO-LUMO gap varies from 0.94 to 2.91 eV. It should be noted that the change in the HOMO-LUMO gap value is smaller in the case of shorter oligomers. Depending on substituents, the HOMO-LUMO gap of *open* oligomers changes within 1.83 eV (from 2.22 to 4.05 eV) for $n = 10$ and within 1.33 eV (from 5.23 to 6.56 eV) for $n = 3$.

6.4 Conclusions

Synthetic approaches, structures, and reactivity of group 13–15 needle-shaped oligomers have been reviewed. It is demonstrated that such compounds exist both in the condensed phase and may be formed in situ directly in the gas phase upon CVD processes. Computational studies reveal that such needle-shaped oligomers are more stable than fullerene-like isomers for all 13–15 pairs. Nitrogen-containing oligomers are more stable compared to their heavier P- and As-containing analogs. Formation of such oligomers in the gas phase is energetically favorable and feasible from the thermodynamic point of view. However, many competitive reaction pathways are kinetically possible which leads to cascade of reactions and different reaction products. Electronic properties of the needle-shaped rods can be finely tuned in broad range by variation of way of termination, substituents on terminal atoms, and the length of the oligomer.

From the results, presented and discussed above, it is clear that the way of termination of nanorods plays an important role in the controlling of their electronic properties. Electronic properties of the *open* (tube-like) and *closed* (needle-shaped) Ga-N-based nanorods are completely different. This holds both for the short and long (at least up to 10 nm of length) rod-like oligomers.

All the $[RGaNH]_{3n+1}$ oligomeric rods have a charge polarization with a dipole moment directed from the Ga-terminated end toward N-terminated end. The dipole moment of *open* oligomers is much greater than for the *closed* ones. Since the dipole moment is a driving force of oligomerization process [119], the growth of *open* rod-shaped oligomers is energetically more favorable. On the other hand, the capping reaction is energetically favorable as well. Thus, the coexistence of *open* and *closed* oligomers of different lengths is possible from the thermodynamic point of view.

Our study of the finite $[RGaNH]_{3n+1}$ oligomers, with $n \leq 38$, showed that saturation of dangling bonds at the polarized ends of the oligomers by H atoms or methyl groups leads to monotonic changes in structural $[RGaNH]_3$ units of the oligomer. In the case of the *open* oligomers, Ga-N bond lengths along the main axis monotonously decrease, and Ga-N bond lengths perpendicular to the main axis monotonously increase from the center to the ends of the oligomer. In the case of *closed* oligomers, polarization is partially compensated by capping of the rod ends by GaR and NH groups; the structural differences are observed only for the outmost $[RGaNH]_3$ rings.

Band structure of the infinite polymer obtained from computations of *closed* oligomers with length ~10 nm demonstrates that majority of MOs are delocalized. Band structure of the $[HGaNH]_{3\infty}$ polymer, extracted from the computations of $[HGaNH]_{115}$ oligomer, exhibits indirect band gap. However, the actual band gap energy of the finite oligomer is formed by end-localized states where HOMO is localized at GaH-capped end and LUMO is localized at the NH-capped end. The polarized states can provide local attractors for holes and electrons [192]. These localized MOs reduce the energy gap of the finite *closed* oligomer by ~0.46 eV compared to the band gap of the polymer (7.0 eV). The value of the HOMO-LUMO gap moderately depends on the oligomer length, and it converges to 6.54 eV for oligomers with $n \geq 10$. Oligomers with *open*-type termination exhibit greater changes in electronic structure with respect to the band structure of the infinite polymer. Multiple localized MOs of the $H_3[HGaNH]_{114}H_3$ oligomer have energies within the band gap of the $[HGaNH]_{3\infty}$ polymer. HOMO and LUMO of *open* oligomers are strongly localized at the opposite ends of the oligomer. The HOMO-LUMO gap of the *open* oligomers (with the exception for the smallest oligomers) is significantly narrower than the gap of the *closed* oligomers with the same n. The gap decreases dramatically with elongation of the oligomer. For oligomers with a length of about 10 nm, the band gap energy of the *open* oligomer is less than 30% of the band gap of the *closed* oligomer, and the band gap value (1.9 eV) is not yet converged in case of $H_3[HGaNH]_{114}H_3$ oligomers.

Excited state calculations for small clusters ($n = 3$) predict a dominance of HOMO → LUMO transition in the lowest excited states both for *closed* and *open* rods. While the probability of the transition is higher for the *closed* oligomers, the

lowest singlet states have lower energy values for the *open* rods, which lead to a red shift in the absorption spectra of *open* oligomers comparing with *closed* one oligomers.

The predicted profound difference in electronic properties between *open* and *closed* rod-shaped oligomers can help to identify the type of termination of the oligomeric rod in the experimental studies.

We also tracked the effects of changing the metal atom and substituents on terminal groups on the electronic properties of the Ga-N-based nanorods. Substitution of Ga atoms by Al moderately increases energy gaps for both *closed* and *open* oligomers. Substitution of Ga by In atoms effectively reduces the energy gap in both cases. However, for *closed* oligomers, the metal substitution is the most efficient in positions closer to the metal-terminated end of the rod, while for *open* oligomers the metal substitution near the amido-terminated end of the rod has a predominant effect.

Substitution of H atoms by CH_3 groups on metal centers does not lead to a qualitative difference in electronic and structural properties of the $[RGaNH]_{3n+1}$ oligomers but results in a constant shift in quantitative characteristics, such as decrease of HOMO-LUMO gap by 0.6 eV for *closed* and by 0.7 eV for *open* oligomers with respect to values for the hydrogen-substituted rods.

It was found that for the *open* oligomers, the molecular orbital energy values of end-localized states are highly sensitive to a particular terminal group. This, along with a variation of the length of the oligomer, allows adjusting the HOMO-LUMO gap to cover a wide spectral range. For example, the elongation of $F_3[HGaNH]_{3n}(CH_3)_3$ from $n = 3$–38 reduces the HOMO-LUMO gap from 6.5 to 2.9 eV, the elongation of $(CH_3)_3[HGaNH]_{3n}F_3$ from $n = 3$–38 reduces the HOMO–LUMO gap from 5.2 to 0.9 eV, and the change from $F_3[HGaNH]_{3n}(CH_3)_3$ to $(CH_3)_3[HGaNH]_{3n}F_3$ reduces the HOMO-LUMO gap from 2.9 to 0.9 eV in the case of $n = 38$ and from 6.5 to 5.2 eV in the case of $n = 3$.

For the long oligomers, where the influence of the substituents at the opposite end of the rod is negligible, HOMO-LUMO gap values decrease in the order $F > CF_3 > H > Me$ for the substituents on the Ga atom. The order of substituents on the nitrogen atom, which contributes to the corresponding reduction of the gap, is as follows: $F < CF_3 < H < CH_3$. Qualitatively, this trend is observed both for open and *closed* oligomers, but in the latter case, the influence of the substituents on band gap energy values is much less pronounced.

The HOMO-LUMO transition in long *open* oligomers requires a relatively small energy change (which could be as low as 0.9 eV for X=CH_3, Y=F in oligomers of *circa* 10 nm of length) but involves an intermolecular end-to-end charge transfer. In contrast, in *closed* oligomers the transitions occur only at the nitrogen-terminated end of the oligomer and require a large energy change (at least 6.3 eV for $n = 38$, X=CH_3, Y=F). Overall, we conclude that the type of termination (*open* or *closed*) has the largest effect on the electronic properties of $[HGaNH]_{3n}$ oligomers. The elongation and variation of substituents on the terminal groups have comparable effects on the HOMO-LUMO gap and can be effectively combined for fine tuning

of the energy gap to a desirable value within 1–7 eV range. These features make these compounds promising targets for the practical applications.

6.5 Future Directions

Since the Ga-N-based rod-shaped compounds possess intriguing electronic properties for their practical use, the reliability of their synthesis and isolation becomes the key issue for the future experimental works. It is highly desirable to selectively synthesize arrays of pre-oriented Ga-N-based oligomers. One of the approaches to achieve this goal may be the atomic layer deposition (ALD) technique. In contrast to CVD, in ALD the deposition reaction is split in two steps, and the precursor materials are introduced into the reaction volume separately, step by step [193, 194]. During each reaction step, one new layer of group 13 or group 15 atoms is formed; the repetition of reaction cycles using subsequent introduction of $GaMe_3$ and ammonia precursors leads to gallium nitride [195, 196]. After each cycle, the reaction vessel is purged by inert gas to remove unreacted compounds and avoid the stoichiometry loss.

To force the formation of needle-shaped oligomers in ALD process, a template approach, based on organic cycles with three amido groups, which are connected to the polymer backbone, is suggested. This approach is schematically shown on Scheme 6.8. The functionalized polymer, having a cycle with three amido groups NHR, reacts with $GaMe_3$, forming an initial Ga_3N_3 ring, which can be expanded only in one direction by subsequent reaction steps with ammonia and $GaMe_3$. This approach may allow to make the arrays of arranged Ga-N-based nanorods.

Moreover, this approach can be easily expanded in order to produce functionalized or mixed metal rod-shaped oligomers. Thus, using primary amines NH_2R instead of ammonia on each reaction step will allow to introduce different functional groups R to the backbone of the oligomer. Use of other group 13 precursors instead of $GaMe_3$ (e.g., $AlMe_3$ or $InMe_3$) will allow to controllably produce the subsequent M_3N_3 rings with different group 13 metals. Thus, the template-based

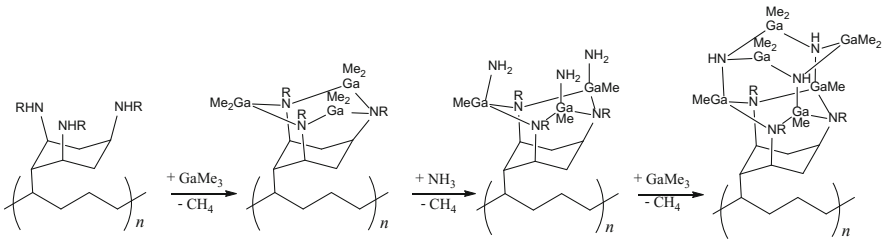

Scheme 6.8 Initial stages for proposed template synthesis of rod-shaped Ga-N-based oligomers on the functionalized polymeric matrix

ALD approach in our opinion is potentially very powerful tool to controllably produce the functionalized rod-shaped 13–15 oligomers.

Another important issue which is of interest to both theoreticians and experimentalists is to study how the functionalization of rod-shaped 13–15 oligomers with photoactive, luminescent, red-ox, or other functional groups will affect the properties of the constructed multipurpose composite functional materials. Thus, we believe that expansion of chemistry of rod-shaped 13–15 oligomers will be beneficial and highly rewarding both from fundamental and applied point of view.

Acknowledgments Authors thank Resource Center Computer Center of SPSU for the computer time. This research was supported by SPSU grants 12.50.1563.2013 and 12.38.255.2014.

References

1. A.C. Jones, P. O'Brien, *CVD of Compound Semiconductors: Precursor Synthesis, Development and Applications* (VCH, Weinheim, 1997)
2. S.P. DenBaars, Proc. IEEE **85**, 1740 (1997)
3. W.M. Chen, E. O'Reilly, A. Forchel, C.W. Tu (eds.), *N-Containing III-V Semiconductors: Fundamentals and Applications. European Materials Research Society Symposia Proceedings*, (Elsevier, Amsterdam, 2003), p. 136; Solid State Electron. **4**7, 385(2003)
4. J. Emsley, Chem. World **1**(3), 30 (2004)
5. F. Medjdoub, *Gallium Nitride (GaN): Physics, Devices, and Technology* (CRC Press, Boca Raton, 2017)
6. G. Meneghesso, M. Meneghini, E. Zanoni (eds.), *Gallium Nitride-enabled High Frequency and High Efficiency Power Conversion* (Springer, Cham, 2018)
7. H.-G. Hong, S.-S. Kim, D.-Y. Kim, T. Lee, J.-O. Song, J.H. Cho, C. Sone, Y. Park, T.-Y. Seong, Appl. Phys. Lett. **88**, 103505 (2006)
8. M. Veith, Chem. Rev. **90**(1), 3 (1990)
9. F.C. Sauls, L.V. Interrante, Coord. Chem. Rev. **128**, 193 (1993)
10. C.J. Carmalt, Coord. Chem. Rev. **223**, 217 (2001)
11. W. Uhl, *Structure and Bonding*, vol 105 (Springer-Verlag, New York, 2003), p. 42
12. M. Cesari, S. Cucinella, *The Chemistry of Inorganic Homo- and Heterocycles*, vol 1 (Academic Press, London, 1987), p. 167
13. G. Dozzi, S. Cucinella, A. Mazzei, T. Salvatory, Inorg. Chim. Acta **15**, 179 (1975)
14. G. H. Robinson (ed.), *Coordination Chemistry of Aluminum* (VCH, New York, 1993)
15. A. J. Downs (ed.), *Chemistry of Aluminum, Gallium, Indium and Thallium* (Chapman & Hall, New York, 1993)
16. C. E. Housecroft (ed.), *Comprehensive Organometallic Chemistry*, vol 1 (Pergamon, London, 1995)
17. I. Haiduc, *The Chemistry of Inorganic Ring Systems* (Wiley-Interscience, London, 1970)
18. I. Haiduk, T.F. Edelmann, *Supramolecular Organometallic Chemistry* (Wiley-VCH, Weinhiem, 1999)
19. S. Aldridge, T. Downs (eds.), *The Group 13 Metals Aluminium, Gallium, Indium and Thallium. Chemical Patterns and Peculiarities* (Wiley & Sons Ltd, 2011), p. 726. https://doi.org/10.1002/9780470976548
20. A.Y. Timoshkin, Coord. Chem. Rev. **249**, 2094 (2005)
21. A.Y. Timoshkin, Russ. J. Phys. Chem. A **81**, 515 (2007)
22. A.Y. Timoshkin, H.F. Schaefer, J. Phys. Chem. C **112**, 13816 (2008)
23. A.Y. Timoshkin, H.F. Schaefer, Inorg. Chem. **44**, 843 (2005)

24. A.Y. Timoshkin, Russ. J. Inorg. Chem. **50**, 1232 (2005)
25. A.Y. Timoshkin, H.F. Bettinger, H.F. Schaefer, J. Am. Chem. Soc. **119**, 5668 (1997)
26. P.C. Sercel, W.A. Saunders, H.A. Atwater, K.J. Vahala, R.C. Flagan, Appl. Phys. Lett. **61**, 696 (1992)
27. K.J. Vahala, W.A. Saunders, C.S. Tsai, P.C. Sercel, T. Kuech, H.A. Atwater, R.C. Flagan, J. Vac. Sci. Technol. B **11**, 1660 (1993)
28. H.J. Kim, Y. Egashira, H. Komiyama, Appl. Phys. Lett. **59**, 2521 (1991)
29. H.J. Kim, Y. Egashira, H.J. Komiyama, Chem. Vap. Depos. **1**, 20 (1992)
30. Y. Egashira, H.J. Kim, H.J. Komiyama, Am. Ceram. Soc. **77**, 2009 (1994)
31. A. Thon, T.F. Kuech, Appl. Phys. Lett. **69**, 55 (1996)
32. B. Atakan, Phys. Stat. Sol. A **176**, 719 (1999)
33. J. Schäfer, A. Simons, J. Wolfrum, R.A. Fischer, Chem. Phys. Lett. **319**, 477 (2000)
34. A. Demchuk, J. Porter, A. Beuscher, A. Dilkey, B. Koplitz, Chem. Phys. Lett. **283**, 231 (1998)
35. A. Demchuk, J. Porter, B. Koplitz, J. Phys. Chem. A **102**, 8841 (1998)
36. A. Demchuk, S. Simpson, B. Koplitz, Electrochem. Soc. Proc. **13**, 389 (2001)
37. A. Demchuk, S. Simpson, B. Koplitz, J. Phys. Chem. A **107**, 1727 (2003)
38. A. Demchuk, *Private Communication to A.Y Timoshkin*, (2001)
39. A.Y. Timoshkin, A.V. Suvorov, H.F. Schaefer, Russ. J. Gen. Chem. **71**, 10 (2001)
40. A.Y. Timoshkin, in *Chemtracts*, (Inorganic-Chemistry-**18**, 619 (2005))
41. A.Y. Timoshkin, Russ. J. Inorg. Chem. **59**, 1152 (2014)
42. A.Y. Timoshkin, Electrochem. Soc. Proc. **13**, 25 (2001)
43. A.Y. Timoshkin, G. Frenking, Inorg. Chem. **42**, 60 (2003)
44. A.Y. Timoshkin, Solid State Electron. **47**, 543 (2003)
45. A.Y. Timoshkin, Inorg. Chem. Commun. **6**, 274 (2003)
46. A.Y. Timoshkin, Phosphorous Sulfur Silicon Relat. Elem. **179**, 707 (2004)
47. A.Y. Timoshkin, H.F. Schaefer, Inorg. Chem. **43**, 3080 (2004)
48. A.Y. Timoshkin, Inorg. Chem. **45**(17), 8145 (2009)
49. C. Trinh, A.Y. Timoshkin, G. Frenking, J. Phys. Chem. A **113**, 3420 (2009)
50. A.Y. Timoshkin, H.F. Schaefer, J. Phys. Chem. A **114**, 516 (2010)
51. A.Y. Timoshkin, H.F. Bettinger, H.F. Schaefer, J. Phys. Chem. A **105**, 3240 (2001)
52. A.Y. Timoshkin, H.F. Bettinger, H.F. Schaefer, J. Phys. Chem. A **105**, 3249 (2001)
53. A.Y. Timoshkin, H.F. Schaefer, J. Am. Chem. Soc. **126**, 12141 (2004)
54. A.Y. Timoshkin, H.F. Bettinger, H.F. Schaefer, Inorg. Chem. **41**, 738 (2002)
55. A. Kovacs, Inorg. Chem. **41**, 3067 (2002)
56. A.V. Pomogaeva, A.Y. Timoshkin, Theor. Chem. Accounts **133**(10), 1572 (2014)
57. A.A. Oranskaya, A.V. Pomogaeva, A.Y. Timoshkin, AIP Conf. Proc. **1653**, 20083 (2015)
58. A.V. Pomogaeva, A.Y. Timoshkin, J. Phys. Chem. C **119**, 16475 (2015)
59. A.V. Pomogaeva, A.Y. Timoshkin, Phys. Chem. Chem. Phys. **18**, 19859 (2016)
60. G. Bahr, in *FIAT Review of WWII German Science, 1939–1946, Vol. 24; Inorganic Chemistry, Part II*, Dieterichsche Verlagsbuchhandlung, ed. by W. Klemm, (FRG, Wiesbaden, 1948), p. 155
61. A.W. Laubengayer, J.D. Smith, G.G. Ehrlich, J. Am.Chem.Soc. **83**, 542 (1961)
62. F.C. Sauls, W.H. Hurley Jr., L.V. Interrante, P.S. Marchetti, G.E. Maciel, Chem. Mater. **7**, 1361 (1995)
63. K.M. Waggoner, P.P. Power, J. Am. Chem. Soc. **113**, 3385 (1991)
64. P.P. Power, J. Organomet. Chem. **400**, 49 (1990)
65. P.B. Hitchcock, H.A. Jasim, M.F. Lappert, H.D. Williams, Polyhedron **9**, 245 (1990)
66. J.D. Fischer, P.J. Shapiro, G.P.A. Yap, A.L. Rheingold, Inorg. Chem **35**, 271 (1996)
67. S.J. Schauer, C.H. Lake, C.L. Watkins, L.K. Krannich, Organometallics **15**, 5641 (1996)
68. O.T. Beachley Jr., D.B. Rosenblum, M.R. Churchill, D.G. Churchill, L.M. Krajkovski, Organometallics **18**, 2543 (1999)
69. D.M. Choquette, M.J. Timm, J.L. Hobbs, T.M. Nicholson, M.M. Olmstead, R.P. Planalp, Inorg. Chem. **32**, 2600 (1993)
70. O.T. Beachley, G.E. Coates, J. Chem. Soc. **1965**, 3241 (1965)

71. H. Hope, D.C. Pestana, P.P. Power, Angew. Chem. **103,** 726 (1991); Angew. Chem. Int. Ed. Engl. **30**, 691 (1991)
72. A.H. Cowley, R.A. Jones, M.A. Mardones, J. Ruiz, J.L. Atwood, S.G. Bott, Angew. Chem. **102**, 1169 (1990)
73. C. von Hänisch, Z. Anorg. Allg. Chem. **627**, 68 (2001)
74. M. Bodensteiner, U. Vogel, A.Y. Timoshkin, M. Scheer, Angew. Chem. Int. Ed. **48**, 4629 (2009)
75. K. Schmid, M. Niemeyer, J. Weidlein, Z. Anorg. Allg. Chem. **625**, 186 (1999)
76. S. Cucinella, G. Dozzi, A. Mazzei, T. Salvatori, J. Organomet. Chem. **90**, 257 (1975)
77. C. Busetto, S. Cucinella, T. Salvatori, Inorg.Chim. Acta **26**, L51 (1978)
78. C. Busetto, M. Cesari, S. Cucinella, T. Salvatori, J. Organomet. Chem. **132**, 339 (1977)
79. S. Cucinella, T. Salvatori, C. Busetto, A. Mazzei, J. Organomet. Chem. **108**, 13 (1976)
80. N.D. Reddy, H.W. Roesky, M. Noltemeyer, H.-G. Schmidt, Inorg.Chem **41**, 2374 (2002)
81. N.D. Reddy, S.S. Kumar, H.W. Roesky, D. Vidovic, J. Magull, M. Noltemeyer, H.-G. Schmidt, Eur. J. Inorg. Chem. **2003**, 442 (2003)
82. Y. Peng, J. Rong, D. Vidovic, H.W. Roesky, T. Labahn, J. Magull, M. Noltemeyer, H.-G. Schmidt, J. Fluor. Chem. **125**, 951 (2004)
83. C.J. Harlan, S.G. Bott, A.R. Barron, J. Chem. Soc. Dalt. Trans. **1997**, 637 (1997)
84. S.S. Kumar, N.D. Reddy, H.W. Roesky, D. Vidovic, J. Magull, R.F. Winter, Organometallics **22**, 3348 (2003)
85. S. Cucinella, T. Salvatori, C. Busetto, M. Cesari, J. Organomet. Chem. **121**, 137 (1976)
86. H. Nöth, P. Wolfgardt, Z. Naturforsch. **31b**, 697 (1976)
87. H. Nöth, P. Wolfgardt, Z. Naturforsch. **31b**, 1201 (1976)
88. S. Cucinella, G. Dozzi, C. Busetto, A. Mazzei, J. Organomet. Chem. **113**, 233 (1976)
89. S. Cucinella, T. Salvatori, C. Busetto, G. Perego, A. Mazzei, J. Organomet. Chem. **78**, 185 (1974)
90. G.B. Stringfellow, *Organometallic Vapor Phase Epitaxy: Theory and Practice* (Academic Press, New York, 1989)
91. G.B. Stringfellow, *Organometallic Vapor Phase Epitaxy*, 2nd edn. (Academic Press, New York, 1998)
92. H. O. Pierson (ed.), *Handbook of Chemical Vapor Deposition: Principles, Technology and Applications*, 2nd edn. (William Andrew publishing, LLC, New York, 2000), p. 482
93. M. Schiefer, N.D. Reddy, H.W. Roesky, D. Vidovic, Organometallics **22**, 3637 (2003)
94. W. Uhl, J. Molter, B. Neumüller, Chem. Eur. J. **7**, 1510 (2001)
95. D.A. Atwood, A.H. Cowley, R.A. Jones, M.A. Mardones, J. Organomet. Chem. **449**, C1 (1993)
96. C. Schnitter, S.D. Waezsada, H.W. Roesky, M. Teichert, I. Usón, E. Parisini, Organometallics **16**, 1197 (1997)
97. A.Y. Timoshkin, I.V. Kazakov, C. von Hänesch, Russ. J. Gen. Chem. **79**, 1067 (2009)
98. C. von Hänisch, F. Weigend, Z. Anorg. Allg. Chem. **628**, 389 (2002)
99. C. von Hänisch, Z. Anorg. Allg. Chem. **629**, 1496 (2003)
100. C. von Hänisch, P. Scheer, B. Rolli, Eur. J. Inorg. Chem. **2002**, 3268 (2002)
101. T. Chivers, C. Fedorchuk, G. Schatte, M. Parvez, Inorg. Chem. **42**, 2084 (2003)
102. H. Nöth, P. Wolfgardt, Z. Naturforsch. **31b**, 1447 (1976)
103. U. Thewalt, I. Kawada, Chem. Ber. **103**, 2754 (1970)
104. B. Luo, W.L. Gladfelter, Inorg. Chem. **41**, 6249 (2002)
105. J.A. Jegier, B. Luo, C.E. Buss, W.L. Gladfelter, Inorg. Chem. **40**, 6017 (2001)
106. R. Annunziata, G. Borgogno, F. Montanari, S. Quici, S. Cucinella, J. Chem. Soc. Perkin Trans. **1981**, 113 (1981)
107. T. Grabowy, K. Merzweiler, Z. Anorg. Allg. Chem. **626**, 736 (2000)
108. M. Driess, S. Kuntz, C. Monsé, K. Merz, Chem. Eur. J. **6**, 4343 (2000)
109. D. Wulff-Molder, M. Meisel, Z. Kristallogr. New Cryst. Struct. **213**, 353 (1998)
110. B. Luo, W.L. Gladfelter, Inorg. Chem. **41**, 590 (2002)
111. H. Wu, C. Zhang, X. Xu, F. Zhang, Q. Zhang, Chin. Sci. Bull. **46**, 1507 (2001)

112. X.-H. Xu, H.-S. Wu, F.-Q. Zhang, C.-J. Zhang, Z.-H. Jin, J. Mol. Struct. **542**, 239 (2001)
113. A. Mohajeri, M. Ebadi, J. Phys. Chem. A **116**, 4678 (2012)
114. J.F. Janik, R.T. Paine, J. Organomet. Chem. **449**, 39 (1993)
115. J.A. Jegier, S. McKernan, W.L. Gladfelter, Inorg. Chem. **38**, 2726 (1999)
116. J.A. Jegier, S. McKernan, W.L. Gladfelter, Chem. Mater. **10**, 2041 (1998)
117. B. Luo, W.L. Gladfelter, J. Organomet. Chem. **689**, 666 (2004)
118. J.F. Janik, R.L. Wells, Inorg. Chem. **36**, 4135 (1997)
119. B.L. Kormos, J.A. Jegier, P.C. Ewbank, U. Pernisz, V.G. Young Jr., C.J. Cramer, W.L. Gladfelter, J. Am. Chem. Soc. **127**, 1493 (2005)
120. E. Iravani, A. Dashti-Mommertz, B. Neumüller, Z. Anorg. Allg. Chem. **629**, 1136 (2003)
121. T. Belgardt, S.D. Waezsada, H.W. Roesky, H. Gornitzka, L. Häming, D. Stalke, Inorg. Chem. **33**, 6247 (1994)
122. A.H. Cowley, P.R. Harris, R.A. Jones, C.M. Nutt, Organometallics **10**, 652 (1991)
123. J. Leitner, J. Steiskal, Z. Sofer, Phys. Stat. Sol. C **0**, 133 (2002)
124. A. Tachibana, O. Makino, S. Tanimura, H. Tokunaga, N. Akutsu, K. Matsumoto, Phys. Stat. Sol. A **176**, 699 (1999)
125. M. Ikenaga, K. Nakamura, A. Tachibana, K. Matsumoto, J. Cryst. Growth **936**, 237 (2002)
126. A.S. Lisovenko, K. Morokuma, A.Y. Timoshkin, J. Phys. Chem. A **119**, 744 (2015)
127. F.C. Sauls, L.V. Interrante, Z. Jiang, Inorg. Chem. **29**, 2989 (1990)
128. L.V. Interrante, L.E. Carpenter, C. Whitmarsh, W. Lee, G.A. Slack, Mater. Res. Soc. Proc. **73**, 359 (1986)
129. E. Mesic, M. Mukinovic, G. Brenner, Comput. Mater. Sci. **31**, 42 (2004)
130. R. Dinnebier, J. Müller, Inorg. Chem. **42**, 1204 (2003)
131. C.C. Amato, J.B. Hudson, L.V. Interrante, Appl. Surf. Sci. **54**, 18 (1992)
132. C.C. Amato, J.B. Hudson, L.V. Interrante, Mater. Res. Soc. Proc. **282**, 611 (1993)
133. E.I. Davydova, G. Frenking, A.Y. Timoshkin, Chem. Phys. Chem. **15**, 2774 (2014)
134. A. Lundskog, C.-W. Hsu, K.F. Karlsson, S. Amloy, D. Nilsson, U. Forsberg, P.O. Holtz, E. Janzen, Light Sci. Appl. **3**, 1 (2014)
135. P. Michler, A. Kiraz, C. Becher, W.V. Schoenfeld, P.M. Petroff, L. Zhang, E. Hu, A.A. Imamoglu, Science **290**, 2282 (2000)
136. W.B. Gao, P. Fallahi, E. Togan, J. Miguel-Sanchez, A. Imamoglu, Nature **491**, 426 (2012)
137. D. Bera, L. Qian, T.-K. Tseng, P.H. Holloway, Materials **3**, 2260 (2010)
138. J. Hu, T.W. Odom, C.M. Lieber, Acc. Chem. Res. **32**, 435 (1999)
139. S. Han, W. Jin, D. Zhang, T. Tang, C. Li, X. Liu, Z. Liu, B. Lei, C. Zhou, Chem. Phys. Lett. **389**, 176 (2004)
140. M. Tchernycheva, P. Lavenus, H. Zhang, A.V. Babichev, G. Jacopin, M. Shahmohammadi, F.H. Julien, R. Ciechonski, G. Vescovi, O. Kryliouk, Nano Lett. **14**, 2456 (2014)
141. J.C. Johnson, H.-J. Choi, K.P. Knutsen, R.D. Schaller, P. Yang, R.J. Saykally, Nature Mater. **1**, 106 (2002)
142. Z.L. Wang, Nano Today **5**, 540 (2010)
143. I.M. Watson, Coord. Chem. Rev. **257**, 2120 (2013)
144. H.Y. Sohn, T. Ryu, *Nanopowders and Nanocoatings: Production, Properties and Applications* (Nova Science Publishers, Inc, Hauppauge, 2011), pp. 147–178
145. J. Zheng, Y. Yang, B. Yu, X. Song, X. Li, ACS Nano **2**, 134 (2008)
146. A.J. Karttunen, M. Linnolahti, T.A. Pakkanen, J. Phys. Chem. C **112**, 10032 (2008)
147. H. Wang, H.S. Wu, J.F. Jia, Chin. J. Chem. **24**, 731 (2006)
148. A. Schaumloffel, M. Linnolahti, A.J. Karttunen, T.A. Pakkanen, Chem. Phys. Chem. **8**, 62 (2007)
149. J. Paier, M. Marsman, G. Kresse, J. Chem. Phys. **127**, 024103 (2007)
150. A.D. Becke, J. Chem. Phys. **98**, 5648 (1993)
151. P.J. Stephens, F.J. Devlin, C.F. Chabalowski, M.J. Frisch, J. Phys. Chem. **98**, 11623 (1994)
152. C. Adamo, V. Barone, J. Chem. Phys. **110**, 6158 (1999)
153. J. Heyd, G.E. Scuseria, M. Ernzerhof, J. Chem. Phys. **118**, 8207 (2003)
154. G.E. Scuseria, C.L. Janssen, H.F. Schaefer, J. Chem. Phys. **89**, 7382 (1988)
155. S.H. Vosko, L. Wilk, M. Nusair, Can. J. Phys. **58**, 1200 (1980)

156. F. Weigend, R. Ahlrichs, Phys. Chem. Chem. Phys. **7**, 3297 (2005)
157. B. Metz, H. Stoll, M. Dolg, J. Chem. Phys. **113**, 2563 (2000)
158. D. Escudero, A. Laurent, D. Jacquemin, Time-dependent density functional theory: A tool to explore excited states, in *Handbook of Computational Chemistry*, ed. by J. Leszczynski, A. Kaczmarek-Kedziera, T. Puzyn, M. G. Papadopoulos, H. Reis, M. K. Shukla, (Springer, Cham, 2017)
159. Y. Zhao, D.G. Truhlar, Theor. Chem. Accounts **120**, 215 (2008)
160. J.F. Stanton, R.J. Bartlett, J. Chem. Phys. **98**, 7029 (1993)
161. M. Kallay, J. Gauss, J. Chem. Phys. **121**, 9257 (2004)
162. D. Rappoport, F. Furche, J. Chem. Phys. **133**, 134105 (2010)
163. F. Furche, D. Rappoport, Theor. Comput. Chem. **16**, 93 (2005)
164. M.J. Frisch, G.W. Trucks, H.B. Schlegel, G.E. Scuseria, M.A. Robb, J.R. Cheeseman, G. Scalmani, V. Barone, B. Mennucci, G.A. Petersson, et al., *Gaussian 09, Revision B.01* (Gaussian, Inc, Wallingford, 2009)
165. N.M. O'Boyle, A.L. Tenderholt, K.M. Langner, J. Comput. Chem. **29**, 839 (2008)
166. W. Liu, Q. Jiang, J. Comput. Theor. Nanosci. **7**, 2225 (2010)
167. D.J. Carter, M. Puckeridge, B. Delley, C. Stampfl, Phys. Rev. B: Condens. Matter Mater. Phys. **77**, 115349 (2008)
168. M.-H. Tsai, Z.-F. Jhang, J.-Y. Jiang, Y.-H. Tang, L.W. Tu, Appl. Phys. Lett. **89**, 203101 (2006)
169. Q. Wang, Q. Sun, P. Jena, Phys. Rev. Lett. **95**, 167202 (2005)
170. H. Shu, X. Chen, Z. Ding, R. Dong, W. Lu, J. Phys. Chem. C **115**, 14449 (2011)
171. M. Rosini, R. Magri, ACS Nano **4**, 6021 (2010)
172. T. Yumura, D. Nozaki, S. Bandow, K. Yoshizawa, S. Iijima, J. Am. Chem. Soc. **127**, 11769 (2005)
173. M. Ijäs, M. Ervasti, A. Uppstu, P. Liljeroth, J. van der Lit, I. Swart, A. Harju, Phys. Rev. B **88**, 075429 (2013)
174. A. Pomogaeva, B. Kirtman, F.L. Gu, Y. Aoki, J. Chem. Phys. **128**, 074109 (2008)
175. A. Pomogaeva, M. Springborg, B. Kirtman, F.L. Gu, Y. Aoki, J. Chem. Phys. **130**, 194106 (2009)
176. A. Pomogaeva, F.L. Gu, B. Kirtman, Y. Aoki, AIP Conf. Proc. **963**, 118–121 (2007)
177. A. Pomogaeva, M. Springborg, B. Kirtman, AIP Conf. Proc. **1504**, 563 (2012)
178. O. Loboda, F.L. Gu, A.V. Pomogaeva, M. Makowski, Y. Aoki, AIP Conf. Proc. **1504**, 544 (2012)
179. A. Pomogaeva, F.L. Gu, A. Imamura, Y. Aoki, Theor. Chem. Acta **125**, 453 (2010)
180. L.K. Yan, A. Pomogaeva, F.L. Gu, Y. Aoki, Theor. Chem. Accounts **125**, 511 (2010)
181. H. Morkoç, *Handbook of Nitride Semiconductors and Devices*, vol 1 (Wiley-VCH Verlag GmbH & Co. KGaA, Berlin, 2008)
182. J.L. Wang, G.H. Lushington, P.G. Mezey, J. Chem. Inf. Model. **46**, 1965 (2006)
183. D.J. Carter, M. Puckeridge, B. Delley, C. Stampfl, Nanotechnology **20**, 425401 (2009)
184. E. Simon, P.G. Mezey, Theor. Chem. Accounts **131**, 1097 (2012)
185. G. Signorello, E. Lörtscher, P.A. Khomyakov, S. Karg, D.L. Dheeraj, B. Gotsmann, H. Weman, H. Riel, Nat. Commun. **5**, 1 (2014) (and refs therein)
186. Y. Duan, L. Qin, L. Shi, G. Tang, H. Shi, J. Appl. Phys. **110**, 103712 (2011)
187. A. Copple, N. Ralston, X. Peng, Appl. Phys. Lett. **100**, 193108 (2012)
188. J.L. Wang, P.G. Mezey, J. Chem. Inf. Model. **46**, 801 (2006)
189. U.C. Singh, P.A. Kollman, J. Comput. Chem. **5**, 129 (1984)
190. W.A. Sheppard, J. Am. Chem. Soc. **84**, 3072 (1962)
191. J.E. True, T.D. Thomas, R.W. Winter, G.L. Gard, Inorg. Chem. **42**, 4437 (2003)
192. S. Gemming, T. Kunze, K. Morawetz, V. Pankoke, R. Luschtinetz, G. Seifert, Eur. Phys. J. Spec. Top. **177**, 83 (2009)
193. T. Kääriäinen, D. Cameron, M.-L. Kääriäinen, A. Sherman, *Atomic Layer Deposition: Principles, Characteristics, and Nanotechnology Applications*, 2nd edn. (John Wiley & Sons, Inc, New York, 2013)

194. H. Yu, T. Duan (eds.), *Gallium Nitride Power Devices*, 1st edn. (Pan Stanford, Singapore, 2017)
195. C. Ozgit, I. Donmez, M. Alevli, N. Biyikli, J. Vac. Sci. Technol. A **30**, 01A124 (2012)
196. S. Banerjee, A.Y. Kovalgin, Abstracts of AiMES Meeting 2018, G02-0988.. https://ecs.confex.com/ecs/aimes2018/webprogram/Paper113495.html

Chapter 7
Computational and Experimental Analysis of Carbon Functional Nanomaterials

Pitchaimani Veerakumar, Namasivayam Dhenadhayalan, and King-Chuen Lin

Abstract Density functional theory (DFT) as one of molecular simulation techniques has been widely used to become rapidly a powerful tool for research and technology development for the past three decades. In particular, the DFT-based theoretical and fundamental knowledge have shed light on our understanding of the fundamental surface science, catalysis, sensors, materials science, and biology. Oxygen, nitrogen, boron, phosphorus, and sulfur are the most common heteroatoms introduced on the functional carbon nanomaterials surface with different surface functionalities. This book chapter aims to provide a pedagogical narrative of the DFT and relevant computational methods applied for surface chemistry, homogeneous/heterogeneous catalysis, and the fluorescence-based sensing properties of carbon nanomaterials. We overview several representative case studies associated with energy and chemicals production and discuss relevant principles of computationally driven carbon nanomaterials design.

Keywords Carbon nanomaterials · Density functional theory · Graphene · Catalysis · Sensors · Carbon dots

7.1 Introduction

In recent years, the computational techniques developed for studying the chemical interactions, transformations, and mechanism of the reactions are often based on density functional theory (DFT) [1]. Recent research into the heterogeneous catalysis, a key pathway for the interaction of active metal catalysts in solid supports involving the bond-formation or bond-cleavage reaction or decomposition mechanism, is a subject of considerable debate [2]. This is because of selectivity of

P. Veerakumar · N. Dhenadhayalan · K.-C. Lin (✉)
Department of Chemistry, National Taiwan University, Taipei, Taiwan

Institute of Atomic and Molecular Sciences, Academia Sinica, Taipei, Taiwan
e-mail: kclin@ntu.edu.tw

T. Onishi (ed.), *Theoretical Chemistry for Advanced Nanomaterials*,
https://doi.org/10.1007/978-981-15-0006-0_7

the reaction, tunability of the catalyst, and the choice of solvent toward reactivity and selectivity, etc. which play vital roles in catalysis [3]. The electronic structure calculations by DFT are useful for characterizing the chemical and physical properties of bare and functionalized materials [4, 5]. As such, many graphene-based nanomaterials and related catalysis have been explored and designed with implementation of the classes.

Plane-wave density functional theory (DFT) is a powerful tool for gaining insight into bulk and surface structures at accurate, atomic level. The delocalized nature of the plane-wave basis set hinders the application of many powerful post-computation analysis approaches, many of which rely on localized atom-centered basis sets [6]. Traditionally, this gap has been bridged via projection-based techniques from a plane-wave to atom-centered basis. Many numerical methods have been developed to solve plane-wave DFT. It has been popularly classified as three methods including Gaussian basis set methods, linear-augmented-plane-wave (LAPW) methods, and pseudopotential plane-wave (PSPW) methods. All three methods can be made very accurate and have been capable of predicting structures, frequencies, and energetics for a wide class of compounds [7]. However, the current consensus in the quantum chemistry and condensed matter physics communities reflects that only the first two of these three methods are straightforward to apply for first-row transition metals. It would be beneficial for PSPW methods to work well for these systems, because Gaussian basis set and LAPW methods lack certain capabilities. In particular, PSPW methods can perform ab initio molecular dynamics extremely efficiently and treat unit cells up to a few hundred atoms. Another advantage of PSPW methods is their transferability from molecules to surfaces to solids. In contrast, Gaussian-based methods have different basis set requirements for gas and solid phase applications, complicating the transferability of these methods [8]. Plane-wave DFT calculations were usually performed using commercially available programs such as VASP [9], SIESTA [10], CASTEP [10], ABINIT [11], and Quantum ESPRESSO [12] program packages.

Recently, the modern density functional theory is molecular orbital DFT (like valence bond and molecular orbital theory) as a very efficient additional tool in the arsenal of computational methods rather than a perfectly different theory, which is used orthogonal to traditional approaches [13]. A wave function for a single electron is called a molecular orbital (MO). The MO with spatial and spin coordinates are called spin orbitals and are products of a spatial orbital and a spin function. The lowest unoccupied molecular orbital (LUMO) in DFT has as much meaning in describing electron addition as the highest occupied molecular orbital (HOMO) in describing electron removal [14]. Molecular orbital DFT calculations were performed using Gaussian [15], ADF [16], and TURBOMOLE [17] program packages, to investigate important atomic and molecular properties as well as some selected areas of application.

The DFT results over graphene-based catalysts have been widely used for determining the rate-limiting step [18], active sites [19], adsorption and activation mechanisms [20], activation energy [21], and catalytic pathways [22], which cover almost all catalysis-related topics. Perhaps one of the most illustrious examples

that showcase the development of DFT methodology is a direct non-oxidative conversion of methane to ethylene, aromatics, and H_2 [23]. Obtaining accurate information on the energetics for these processes is challenging. Advanced quantum chemical methods with faster computers are enabling the prediction of accurate energetics of chemical transformations of the larger molecules involved in the processes [24].

The chemical interactions and transformations at the gas-solid, liquid-solid, and gas-liquid interfaces are facilitated by the solid or liquid surface form the basis of the advanced functional catalysis that drives the production of many value-added chemicals [25, 26]. Recently, one approach to circumventing ongoing challenges is through the use of metal-free catalysts as substitutes. Although organocatalysts have been effective in this role [27], carbon-based catalysts derived from graphite, graphene (Gr), or graphene oxides (GO) and other similar materials may serve as useful alternatives [28]. It has been reported that graphene-based catalysts can also work in oxidation of aryl and alkyl alcohols [29, 30], hydrochlorination [31], nitrobenzene reduction [32], and so on. In addition, other applications of graphene materials in catalysis may contain hydrogenation (HYD), hydrodesulfurization (HDS), hydrodenitrogenation (HDN), hydrocracking (HCR), hydrodeoxygenation (HDO), and hydrodechlorination (HDCl). Beyond the exploration of its novel fundamental reactivity, the use of GO as a catalyst is attractive from a practical perspective, owing to the abundance of natural carbon sources, the catalyst's low density, extensive chemical functionalization, hydrophilicity, low cost, and ease for preparation [33]. For deeply understanding the reaction processes, it is strongly suggested to combine DFT computational results with experimental observation. On the other hand, the graphene catalysts co-doped with two or three heteroatoms were also extended [34]. For instance, Zhao et al. reported a universal strategy to synthesize an N-P-O co-doped free-standing three-dimensional (3D) graphene through a one-pot red phosphorus-assisted "cutting-thin" technique [35]. The DFT calculations verified that the enhancement of charge delocalization should be beneficial for the electrochemical applications [36, 37]. We will introduce the DFT computations in this section to rationalize experimental results in graphene-based catalysis, due to their extensive applications when combined with the related characterization techniques [38, 39].

In this chapter, we comprehensively summarized the theoretical chemistry for graphene-based nanomaterials by computation methods covering active surface sites and surface defect structure analysis, binding ability determination, and reaction mechanism investigation. We reviewed the advantages/disadvantages and challenges and further provided key information to catalysis community on how to adopt suitable computation methods for their research. In addition, the electronic and sensing properties of fluorescent carbon nanomaterials are reviewed from a theoretical perspective.

7.2 Density Functional Theory

Density functional theory (DFT) is primarily a theory of the electronic structure of atoms, molecules, and solids in their ground states, in which the electronic density distribution n(r) plays the central role. It is one of the standard computational tools in the condensed matter, chemistry, and biochemistry in both academia and industry [40]. Up to now, the DFT is presently the most successful and also the most promising approach to compute the electronic structure of materials. It provides the description of electronic structure (i.e., structure prediction) and enables to calculate the optical properties, total energies (thermodynamics and kinetics), and forces of materials under very general conditions [41]. The theory was extensively applicable for atoms, molecules, solids, nuclei, and quantum as well as classical fluids [42]. In its original formulation, the DFT provides the electron density which plays a key role in describing the ground state properties of a material. Later on in the field of chemistry, the DFT is employed to predict a great variety of molecular properties including molecular structures, vibrational frequencies, atomization energies, ionization energies, electric and magnetic properties, reaction paths, etc. [43]. The original DFT has been generalized to deal with many different situations: spin-polarized systems, multicomponent systems such as nuclei and electron-hole droplets, free energy at finite temperatures, superconductors with electronic pairing mechanisms, relativistic electrons, time-dependent phenomena and excited states, bosons, molecular dynamics, etc. [44]. For example, the energies of the functional group and the interaction of carbon dioxide were investigated by DFT calculations with the use of the $DMol^3$ code [45] and selection of generalized gradient approximation (GGA-PBE) by Perdew, Burke, and Ernzerhof (PBE) [46]. The atomic orbital was described using double numeric polarization (DNP) basis set, which is comparable to 6-31G (d,p). The van der Waals correction was further taken into account [47]. The type of core processing is set up using a DFT half-core pseudopots (DSPP) specifically designed for $DMol^3$ calculations [48]. The real-space orbital global cutoff radius is 3.7 Å. The convergence threshold parameters for the optimization are 10^{-5} Hartree (energy), 2×10^{-3} Hartree (gradient), and 5×10^{-3} Hartree (displacement) [49].

Since the 1960s, the DFT was introduced in two seminal papers by the authors Hohenberg-Kohn and Kohn-Sham, and its citation is soon up to ~4000 (1964) ~9000 (1965). The annual paper collections dealing with the DFT application are shown in Fig. 7.1 [50]. Note that the relatively small number of publications before 1990 by no means implies that important work was not being carried out. It was a very well-established computational technique, and "density functional" or other designations are named in many applications. Remarkably, the number of publications per year (1975–2014) on topics ("density functional" or "DFT") is listed, according to the Web of Science Core Collection (February 2015). The inset shows data near 1990 on an expanded scale [51]. Obviously, it shows the dramatic increase in the number of publications on the topics "density functional" and density functional theory "(DFT)" in recent years. DFT was promptly incorporated into

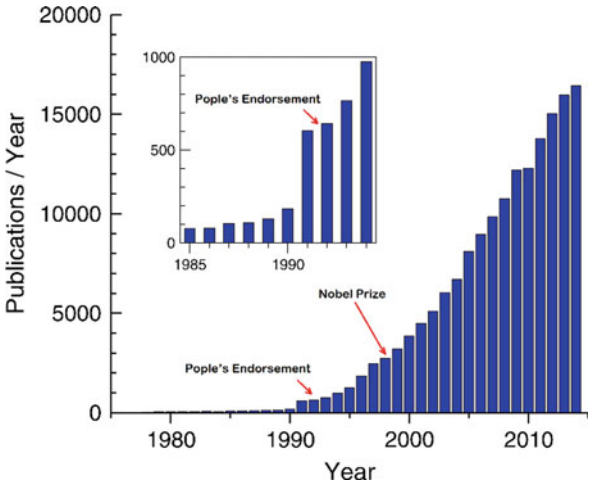

Fig. 7.1 Number of papers that mention DFT as found by the Web of Science. (Reproduced with Ref. [51]. with permission from the American Physical Society)

Pople's widely used Gaussian computer program, and, with this endorsement, the popularity of DFT calculations among chemists began to grow exponentially (see Fig. 7.1). Accordingly, when the Nobel Chemistry Committee decided it was time to honor quantum chemistry with a Prize, it was not difficult for them to split the award between John Pople and Walter Kohn.

7.3 Graphene-Based Functional Nanomaterials

As reported, the pristine graphene (Gr) is a defect-free and stable material composed of a single two-dimensional (2D) layered sheet of polycyclic, hexagonally arranged, sp^2-bonded aromatic carbon [52–54]. However, the production of monolayer graphene may yield by-product of few-layer graphene (FLG) which contains a number of stacked sheets of pristine Gr (usually less than 10). For effective catalytic reactions, fabrication of irregularities and/or defects in the structure of pristine Gr is required. The way to generate irregular structure of pristine Gr was by replacement of some carbon atoms with either sulfur, nitrogen, or other dopants (e.g., phosphorus and boron) [55]. Then, the activity of Gr catalysts was enhanced significantly after dopants were doped on the surface. Figure 7.2a, b show the structures of pristine Gr and heteroatom-doped Gr. As a highly oxidized form of pristine Gr, graphene oxide (GO) is produced by the chemical oxidation of graphite, followed by the exfoliation of single monolayer sheets, and its structure is shown in Fig. 7.2c [56]. The model chemical structural of GO has six-membered benzene rings along with several functionalities such as hydroxyl, carboxyl, epoxy, and ketone, which are represented in different color. Conversely, the aromaticity of the pristine Gr can be partially reestablished by the reduction of GO to yield reduced graphene oxide (RGO) which still contains some residual oxygen as well as the defects both on the

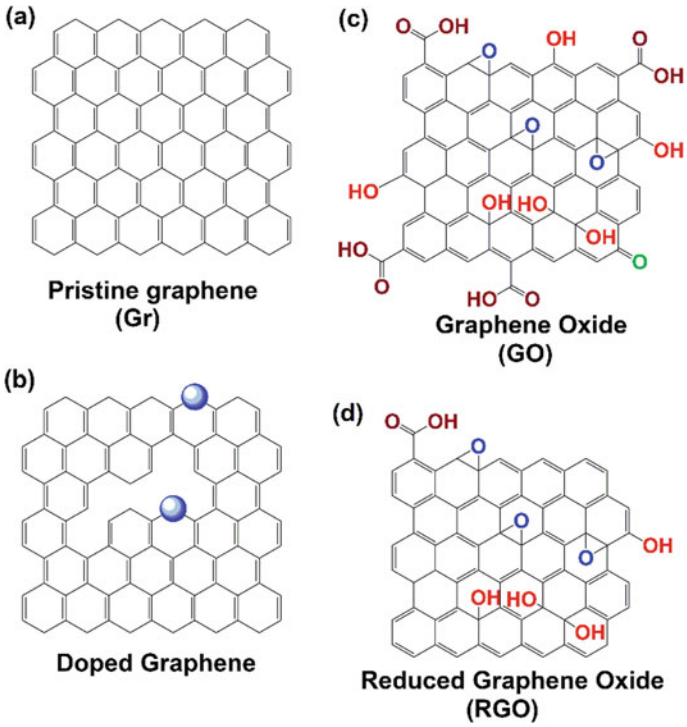

Fig. 7.2 Pristine graphene and graphene-derived solids. (Reproduced from Ref. [52] with permission from the American Chemical Society)

basal plane and at the edges of sheets, as displayed in Fig. 7.2d. The heteroatom-doped graphene or GOs act as catalyst support, in which both the irregularities and residual O-containing groups play a vital role during reaction mechanism in organic transformations and other reactions.

7.3.1 Active Sites of Graphene-Based Metal-Free Catalysts

Generally, graphene-based materials have been widely studied the field of metal-free catalysis due to the outstanding electronic, thermal, and mechanical properties [57]. The unprecedented features of metal-free catalysts, which are believed to account for their superior catalytic performance, have been studied by computation methods. The perfect pure graphene essentially exhibits very low catalytic activities, because of the low density of states around the Fermi level, but it is active at the defects and edges [58]. An effective way is to reduce the lateral size in order to increase the active edges. Nevertheless, in-plane structure of graphene bears a very low chemical activity, which may be apparently enhanced by doping different heteroatoms such

as O, N, B, S, P, and their corresponding functional groups [59]. Catalytic active sites on graphene carbon nanomaterials may be generated by tuning electronic structures. Several approaches are reported. First of all, introducing intrinsic defects and the edge topological structures [60] may facilitate the electron transfer which is beneficial to the conductivity and catalytic activity of carbon nanomaterials. Therefore, to enhance the catalytic activities is probable by optimizing the topology through the charge density analysis on these defective carbon materials by DFT methods. Doping atoms in graphene-based nanomaterials is an alternative approach, based on which carbon atoms are substituted by heteroatoms, such as N, P, and B, or bonded with heteroatoms (O, S, Se, Cl, Br, and I) on carbon surfaces or edges [61]. Such an atomic replacement results in distinct difference of electronegativity, thus leading to localization of, the charge and spin densities and enhancement of the catalytic activities. The active sites are located at the carbon atoms nearby the dopant or at edges, or dopant atom itself. The DFT calculations verified that doping heteroatom (N, O, B, S, Cl, P, Cl, Br, and I) in graphene remarkably changed the charge density and spin density distributions on the doped carbon materials and consequently enhanced their catalytic and electrocatalytic properties [62, 63]. Carboxyl (-COOH), carbonyl (-C=O), and hydroxyl (–C-OH) containing oxygen functional group exhibited the synergistic effect of edge defects on graphene to enhance catalytic activities [64]. The final approach is to physically adsorb organic molecules on graphene or hybrid structure of N-doped graphene [62]. Defects on carbon materials can induce the electron transfer between the organic molecule and the graphene or between the graphitic carbon nitride (g-C_3N_4) and the doped graphene [60]. However, the DFT calculation shows that an electron transfer occurs from graphene sheets to the adsorbed tetracyanoethylene (TCNE) molecules. In addition, the carbon atoms with higher charge density can generate the catalytic active sites due to the electron transfer from the graphene to TCNE molecule [64].

The oxygen functionalities for GO can be introduced via chemical oxidation. These oxygen functionalities with acidic and oxidative nature render GO to function as a solid acid or green oxidant. Besides, the edges or defect sites in GO are found to carry carboxylic acids, quinones, and aromatic CH, as well as the spin electrons. The resulting quinone and diol redox sites play the role as active sites in carbon materials for oxygen-activation reactions. In addition, the amphiphilic character of GO should be advantageous for acting as a phase-transfer catalyst in oil-water biphasic systems [65]. The potential different active sites of graphene scaffold are displayed in Fig. 7.3 [66].

In order to alter the identities of the N moieties, the content of graphitic N species, pyridinic N centers, and pyrrolic N moieties could be tuned through annealing of GO with various N-rich precursors such as ammonia, polyaniline, or polypyrrole, thereby making this process more suitable for practical applications, and the schematic diagram is shown in Fig. 7.4 [67].

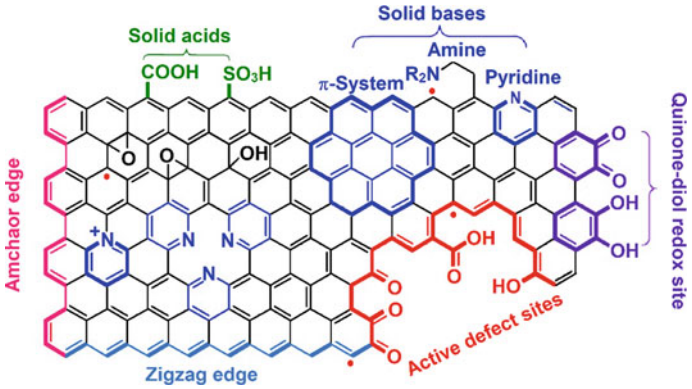

Fig. 7.3 Schematic representation of catalytic active graphene sites on the edges, defects, heteroatoms, and groups. (Reproduced from Ref. [66] with permission of the American Chemical Society)

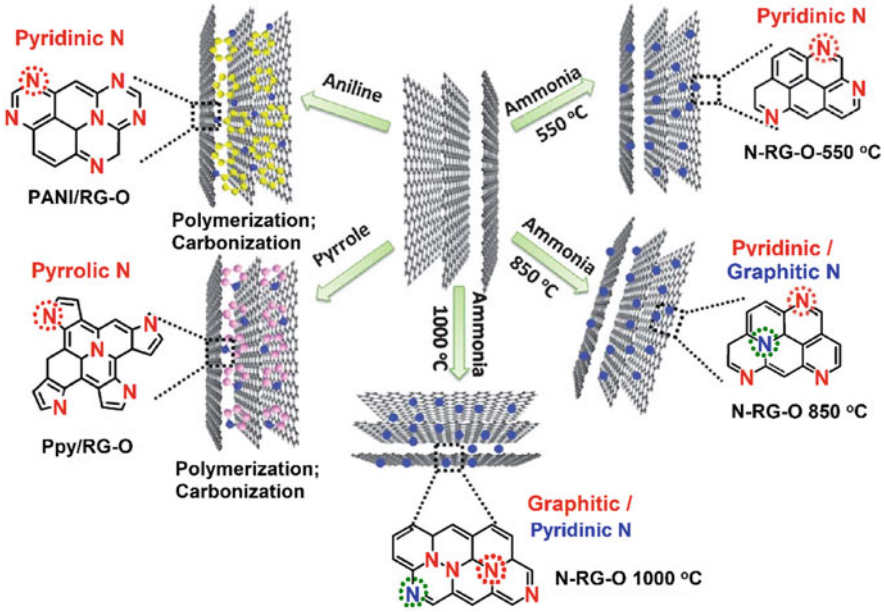

Fig. 7.4 Schematic diagram for the preparation of N-graphene with different N states. (Reproduced from Ref. [67] with permission of the Royal Society Chemistry)

7.3.2 Oxidation Reactions

Currently, the GO with oxygen-containing functional groups is applied to efficiently catalyze the oxidative reactions for value-added chemicals [33, 68]. Therefore, GO can be considered as a green oxidant to oxidize substituted cis-stilbenes to their corresponding diketones [69, 70]. On the other hand, a proton source is necessary

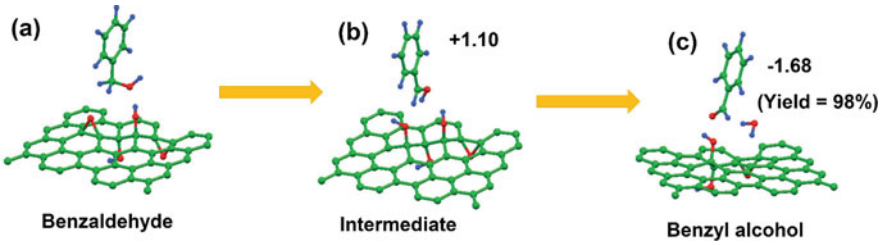

Fig. 7.5 Optimized atomic structures for the (**a**) initial, (**b**) intermediate, and (**c**) final steps of benzyl alcohol oxidation over GO with the initial coverage of epoxy and hydroxyl groups, in which 12.5% of the carbon atoms are on the material's basal plane. The total energy of the reactions is reported in eV. (Reproduced from Ref. [29] with permission of Wiley-VCH)

when GO and RGO are treated as supports for the preparation of bifunctional catalysts. Gomez-Martínez et al. [56] demonstrated that a proton can be generated by the dissociation of sulfonyl groups, i.e., ($-SO_3H \rightarrow SO_3- + H^+$). Although less efficiently, proton can also be donated by carboxylic and hydroxyl groups present on the surface of GO and RGO. The carboxylic acid functionalized GO (GO–CO_2H) few-layers are able to catalyze the pinacol rearrangement and the direct nucleophilic substitution of allylic alcohols. In most cases, GO functionalization is the best way to achieve the performance in oxidation reactions. According to the DFT and experimental results, Boukhvalov et al. [29] have proposed that epoxide functional group may play a role in the metal-free oxidation reactions (Fig. 7.5). For example, benzyl alcohol oxidation (Fig. 7.5a) initiates the reaction, followed by hydrogen transfer from -CH_2 group of benzyl alcohol to GO surface as intermediate (Fig. 7.5b) and terminated with ring opening of epoxide group on the GO surface. This process appears to be energetically favorable pathway. Moreover, the DFT model calculations exhibit the relevant reactivity, mechanisms, and total energies for such an oxidation reaction reported experimentally (Fig. 7.5c).

7.3.3 Oxidative Dehydrogenation

Metal-free graphene shows interesting catalytic properties also in oxidative dehydrogenation (ODH) [71–73], in particular, the selective gas-phase oxidation of acrolein (C_3H_4O) to acrylic acid ($C_3H_4O_2$) [74]. Figure 7.6 displays the reaction mechanism proposed for the oxidation of C_3H_4O on the graphitic carbon surface. Along a rectangular section of a planar graphene sheet with a hole defect illustrates the sp^2 carbon acting as a bifunctional catalyst in the active domain which is terminated by arbitrarily positioned oxygen functionalities. Hence, O_2 adsorbs dissociatively at the (0001) surface to form mobile epoxy groups, feasibly migrating to the prismatic edge sites [75]. The C_3H_4O adsorbed at the nucleophilic oxygen sites, i.e., the ketones/quinones, initiates its oxygenation by epoxy oxygen atoms

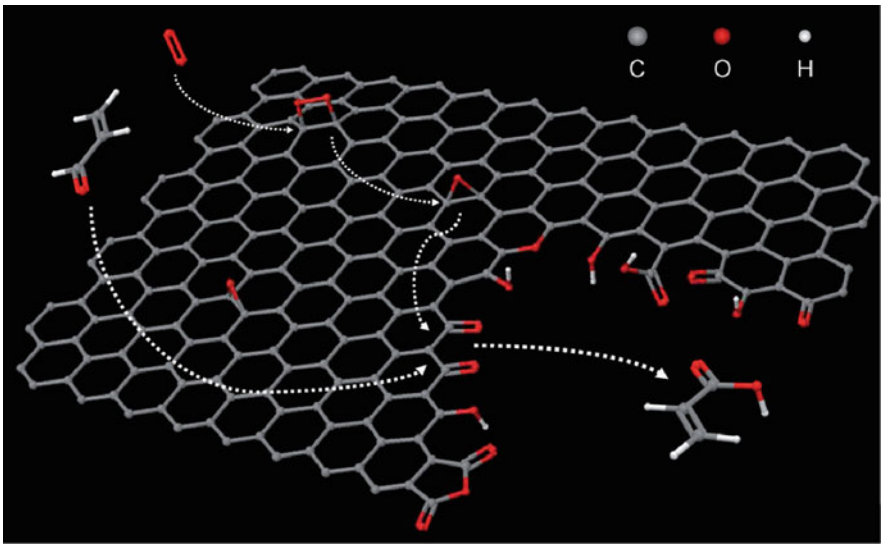

Fig. 7.6 Reaction pathway proposed for the oxidation of C_3H_4O at the graphitic carbon surface. (Reproduced from Ref. [74] with permission of the Wiley-VCH)

to form acrylic acid. Ni et al. [76] showed that graphite-like nitrogen and Stone-Wales defect nitrogen with higher concentration of nitrogen may decrease the dissociation barrier by 0.2 eV more efficiently than pyridine-like nitrogen, due to partial occupation of π_* orbitals and change of work functions.

Tang and Cao [77] showed that the epoxy groups on the GO surface provided active sites around which the -OH groups remarkably enhanced the C–H bond activation of propane (Fig. 7.7). However, high catalyst loading is required for the widespread application of GO in these oxidative reactions. The DFT calculations were performed on the oxidative dehydrogenation of propane over GO. In Fig. 7.7, the pathways denoted by the red and blue lines are associated with two different GO structures including one epoxide group (GO10) and one added to neighboring OH at the opposite side with respect to other oxygen groups on GO10 (GO20), respectively. Figure 7.7 also shows all energies (kcal mol^{-1}) with respect to propane adsorbed onto GO and the optimized configurations (distances in Å) of the initial, transition, and final states.

7.3.4 Friedel-Crafts Reaction

Very recently, a low GO loading has been demonstrated to promote effectively site-selective allylic alkylation of thiophenes with alcohols under mild reaction conditions (Fig. 7.8) [78].

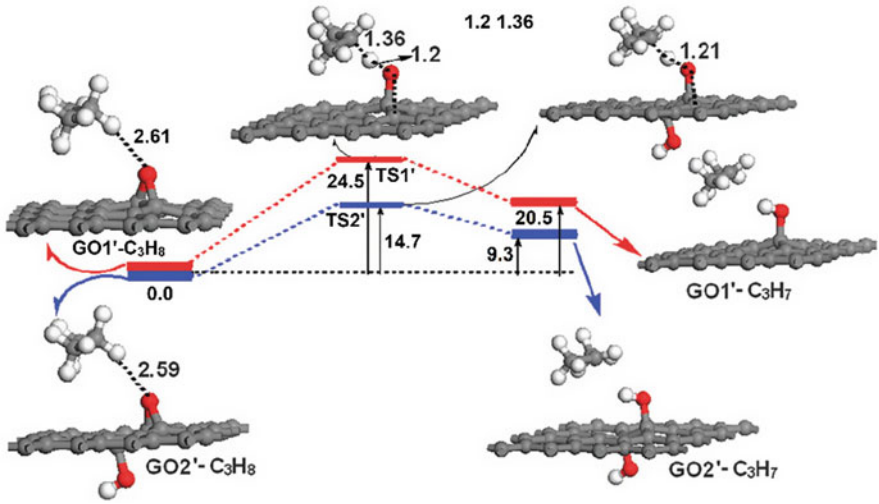

Fig. 7.7 Relative energy profiles for the first H abstraction from CH_2 of propane on GO. (Reproduced from Ref. [77] with permission from the Royal Society of Chemistry)

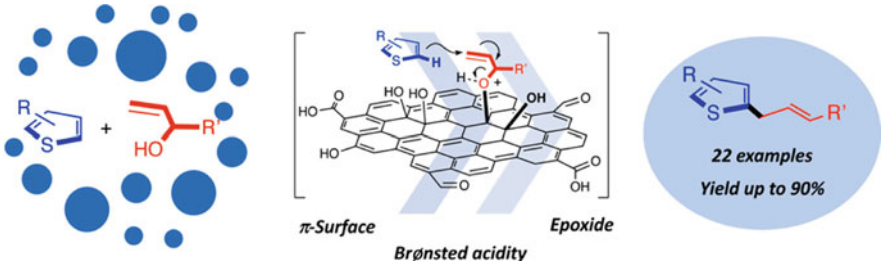

Fig. 7.8 GO-based Friedel-Crafts-type alkylation of alkenes. (Reproduced from Ref. [78] with permission from the American Chemical Society)

The stoichiometric amounts of styrene oxides were carried out intentionally as a control experiment to verify the potential role of the oxiranes moieties present in the GO surface on the reaction mechanism. Such a mechanism justifies the spectroscopic observation by XPS showing the overall increase of alcoholic moieties versus the oxirane ones. The reaction mechanism contains a three-step process, as depicted in Fig. 7.9a. In step 1 the allylic alcohol grafts to the GO surface, followed by an S_N1 mechanism in which the epoxide ring on the GO surface releases a proton to form an unstable oxonium unit that opens without overcoming any barrier ($\mathbf{R_x}$). The proton source could rely on the intrinsic Brønsted acidity of GO. The next step undergoes a reactive α-carbocation in which a nucleophilic attack occurs by the allylic alcohol (**Ts1**). From this picture, the GO π-system plays a crucial role in stabilizing the carbocation generated by the epoxide ring opening event. The compensation effect can be explained probably based on the transition

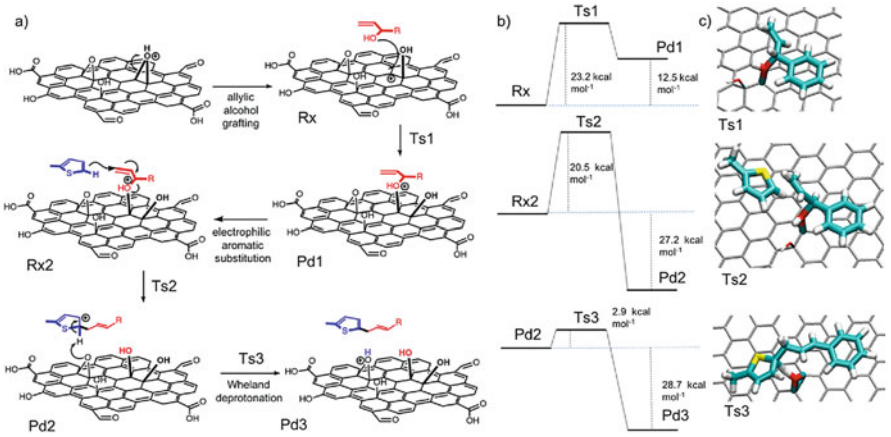

Fig. 7.9 (**a**) Schematic representation of the reaction mechanism; (**b**) energy profiles for the three steps; (**c**) 3D representation of the identified transition states. (Reproduced from Ref. [78] with permission from the American Chemical Society)

state theory of chemical reactions, in which the energy levels are given in Fig. 7.9b. The concerted reaction of the GO π-system and the functional groups present in the 2D-material are marked, consistent with experimental observations. The resulting protonated allyl ether may undergo a Friedel-Crafts-type allylic alkylation yielding the observed allyl-thiophene (**Pd1**). In step 2, a concerted mechanism is followed, showing the α-carbon of the 2-methyl-thiophene attacks the allylic position (**Ts2**), inducing a reorganization of the π-system (Fig. 7.9c). The leaving O−H group remains grafted on the GO surface (**Pd2**). The deprotonation of the Wheland-like intermediate (**Ts3**) is the final step which is a fast process with a calculated barrier of only 2.9 kcal mol^{-1}carried out by other epoxide groups on the GO surface.

7.3.5 Oxidative Coupling

In the chemical catalysis, Loh and coworkers demonstrated this mechanism by the oxidative coupling of amines using porous ba-GO as a metal-free catalyst [79]. The "ba-GO" was denoted, when the base reduction followed by acid reprotonation steps were involved in the preparation of GO under reflux conditions. It was resulted from a sequential base and acid treatment of GO prepared by Hummers' method. Given only 5.0 wt% loading of the carbocatalyst, the imine reached a 98% yield under solvent-free, atmospheric conditions, which is as comparable or even superior to that based on transition metal catalysts. The low catalyst loading is superior to most of the catalysis reaction involving GO catalyst. The dramatically enhanced catalytic activity was contributed to the synergistic effect of the unique functionalities along the edge defects that were created during the base-acid treatment, specifically the

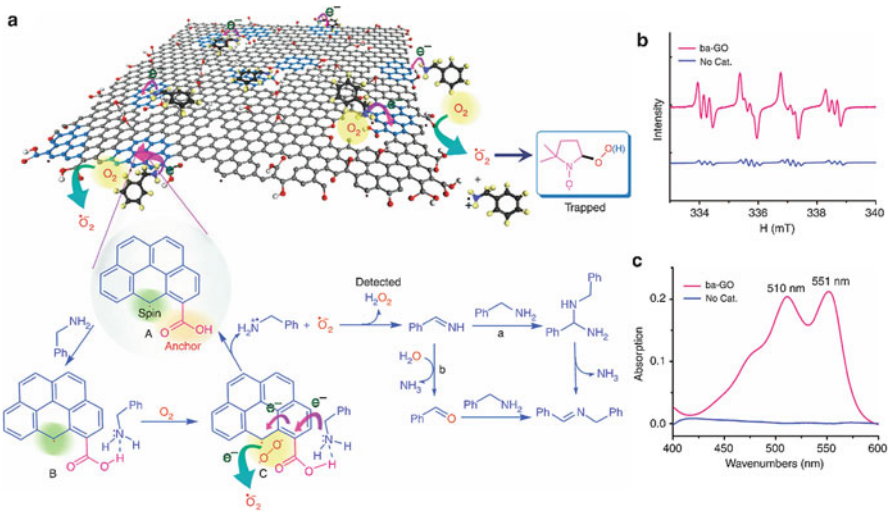

Fig. 7.10 Proposed mechanism of ba-GO-catalyzed oxidative coupling of primary amines. (Reproduced from Ref. [79] with permission of Springer Nature)

unpaired electrons and carboxylic acid (-COOH) groups (Fig. 7.10). The base treatment may generate a large amount of nanoholes and their associated edge defects on the basal planes of GO. These edge sites with unpaired electrons behave as the active catalytic sites which enhance the kinetic rates for the trapping and activating molecular oxygen by a sequence of electron transport and reduction steps to superoxide radical ($\bullet O_2$), which acted as the oxidant in this catalytic reaction. The following three designed experiments supported the proposed hypothesis. Firstly, electron paramagnetic resonance (EPR) is employed to measure the localized spins created at the edge of ba-GO. Secondly, comparable catalytic reaction is carried out to inspect if the catalytic activity decreased upon selectively blocking the unpaired electrons via a diazonium coupling reaction. Finally, in situ spin-trapping EPR experiment is conducted to trap the in situ formed radicals. The carboxyl anionic groups can be obtained by the acid treatment to position along the edges to carboxylic acid groups, which produced a synergistic effect for the coupling reaction. These carboxylic groups may act as hydrogen bonding sites to the amines and facilitate proton transfer reactions due to acidic properties. Further, the base reduction eliminated the hydroxyl groups from the GO and thus changed the dynamics of water solvation layer around GO, allowing more amount of reactants into the catalytic sites. The solvent-free and metal-free catalysis with low catalyst loading is an ideal model for practical application such as industrial-relevant carbocatalysts. The RGO as metal-free catalysts were also demonstrated in oxidative desulfurization reactions using molecular oxygen as the terminal oxidant [80].

The RGO catalyst was demonstrated to be capable of effectively removing a broad range of sulfur-containing compounds from fuels with excellent reusability. The studies on X-ray photoelectron spectroscopy (XPS), chemical titration method, and a series of comparative experiments revealed that carbonyl groups played a crucial role during the oxidation process. The RGO with defects in such as vacancies is beneficial to the catalytic performance because carbonyl groups could be generated in situ on these defects under the reaction conditions. Although the carbonyl groups were not directly involved in the generation of ROS, their electron-withdrawing properties reduce the electron population of the carbon atoms at their adjacent positions, which facilitates absorption and activation of molecular oxygen. The strongly adsorbed oxygen molecules may then convert to super-oxygen anion radicals (RGO–OO–•). Meanwhile, the sulfur-containing substrates turn into sulfur-centered cation radicals, which react with the negative charged radicals of RGO–OO–• to generate sulfones as the final products.

7.3.6 C–H Bond Activation

Transition metals and organometallic complexes were employed traditionally to catalyze the C−H bond activation [81]. Recently, cheap metal-free catalysts have emerged as promising candidates for this transformation. Gao and coworkers reported that N-doped Gr plays a major role in the work on sp^2 C−H activation that covers the selectivity for the oxidation of arylalkanes in aqueous phase, affording high value-added products for biomedical applications [82]. The N-doped sp^2 hybridized carbon was prepared through a chemical vapor deposition (CVD) process with acetonitrile vapor as the N source with 8.9% N content. DFT calculation suggested that the nitrogen atoms are not able to host the peroxide species because of the high negative charge of nitrogen. Both the electronic charge and spin density on the *o*-carbons are superior positions for the adsorption of reactive oxygen species such as peroxide. Both C K-edge and N K-edge X-ray absorption spectroscopy (XAS) were used to study N-doped carbon catalysts before and after TBHP (*t*-BuOOH) and ethylbenzene treatment, clearly revealing that the graphitic nitrogen dopant modulated the electronic structure of sp^2 carbon material. The intensities of density of states near the Fermi level for the adjacent ortho-carbon are much stronger than those of undoped graphene carbon, which gives the nitrogen-neighboring carbon a metal-like d-band electronic structure.

In 2016, an inexpensive, metal-free GO catalyst used for the C–H bond arylation of benzene enables the formation of bi-aryl compounds in the presence of aryl iodides [83]. The oxygen functional groups in these GO sheets and the addition of KOtBu are essential for the observed catalytic activity. The DFT calculations on reactions with various model compounds confirmed that these negatively charged oxygen atoms promote the overall transformation by stabilizing and activating K^+ ions, which in turn facilitate the activation of the C-I bond, [as benzyl alcohol was a particularly active model system]. Based on DFT calculations, a GO nanopore was

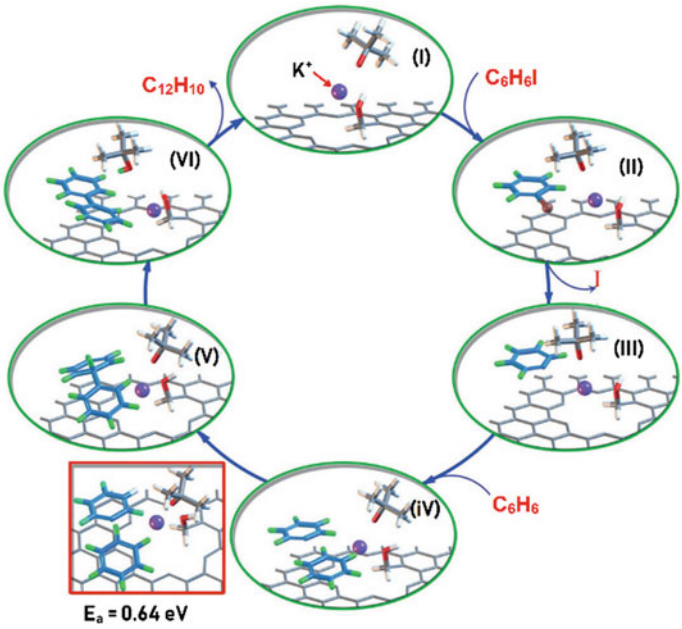

Fig. 7.11 Mechanism proposed for the GO-catalyzed arylation reaction. (Reproduced from Ref. [83] with permission of the Wiley-VCH)

focused (the edge of graphene; Fig. 7.11). The interaction between KOtBu and Gr is very weak without hydroxy groups. Instead, as shown in Fig. 7.11, K^+ can strongly interact with oxygen species at the edge of a Gr nanopore (**I**; the adsorption energy, E_{ad}, is −0.96 eV). The distance between a K^+ ion and the oxygen atom of an ether OtBu moiety is 2.53 Å, whereas the distance between K^+ and a hydroxy oxygen atom is 2.57 Å. At the same time, the π-π interactions between the π system of Gr and that of iodobenzene (C_6H_5I) enable the adsorption of the latter on the same graphene surface (**II**, $E_{ad} = -0.97$ eV) [84]. The charge of the immobilized K^+ ion is 0.89 eV owing to the electron transfer between K and the oxygen group, which is beneficial to the subsequent activation of C_6H_5I. Indeed, the iodine-carbon bond of C_6H_5I can be easily activated by attack of a K^+ ion, which leads to the formation of a C_6H_5 radical. The benzene radical is stabilized by the π system of Gr and the positively charged hydrogen atoms (**III**; $E_{ad} = -1.29$ eV). This intermediate then reacts with adsorbed benzene (**IV**; $E_{ad} = -0.76$ eV) with a moderate activation energy (0.64 eV). After proton transfer, biphenyl is formed (VI). In addition, the Gr π system also greatly facilitates the overall reaction as the aromatic coupling partners are adsorbed.

7.3.7 *Reduction of Nitro Compounds*

Nitroaromatic compounds (NACs) are widely utilized as pesticides, explosives, and synthesis intermediates, [85, 86] causing environmental pollution. The electron-withdrawing effect of the nitro groups and the stability of the benzene ring lead to the recalcitrance of the NACs through either chemical reduction [87] or oxidative degradation [88]. Pal et al. found that 4-nitrophenol (Nip) may be reduced to 4-aminophenol (Amp) by sodium borohydride ($NaBH_4$) in the presence of N-doped graphene (NG), in which the N-doping greatly enhanced catalytic activity [89]. The activity was related to the surface area of the catalysts. Recently, Kong group [90] reported the NG synthesis and its catalytic behavior in the reduction of Nip to Amp (Fig. 7.12a). The catalytic procedure of this reaction was described in Fig. 7.12b. Nip ions adsorb initially on the active sites of NG in solution, and then the adsorbed Nip ions can desorb into water to reach equilibrium. There are a limited number of active sites such that only the carbon atoms next to the doped N atoms can be activated. The adsorption of Nip ions is much faster than its desorption ($k_1 >> k_2$), so that the number of Nip ions absorbed on NG sheets is not determined by their concentration, but by the number of active sites on NG, which will lead to the pseudo-zero-order reaction. The desorption rate of Amp k_4 is very fast during the course of reaction. In contrast, the active sites in metallic catalysts are abundant, and the adsorption rate and desorption rate are comparable so that the amount of adsorbed Nip ions are highly dependent on their concentration, which could lead to pseudo-first-order reaction.

The DFT calculations have also been performed to simulate the adsorption configuration of Nip ion on this metal-free catalyst according to the XPS and in

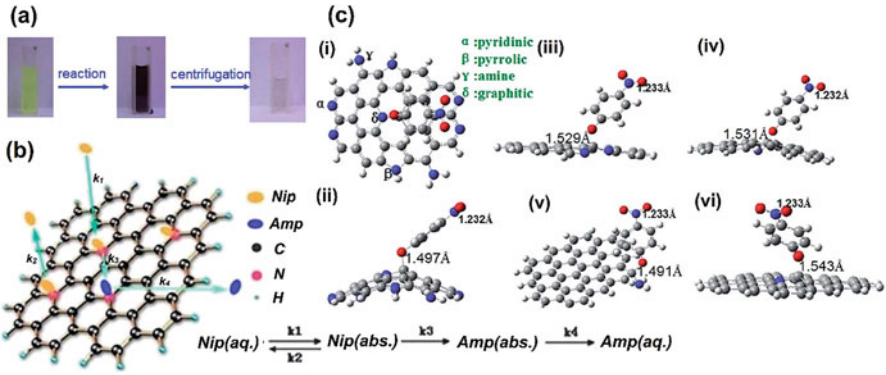

Fig. 7.12 (**a**) Optical photos of the color change during the reaction, (**b**) catalytic process of the reduction of Nip on the surface of NG, and (**c**) the optimized structures of Nip ions adsorbed on NG: (*i*) top view and (*ii*) side view; Nip ions adsorbed at the (*iii*) pyridinic, (*iv*) pyrrolic, (*v*) amine, and (*vi*) graphitic NG. The separated distances and the N–O bond length of nitro group for each model have been marked directly in the corresponding figures. (Reproduced from Ref. [90] with permission of the Royal Society of Chemistry)

situ FTIR results. Only the carbon atom near the doped N atom could be activated to catch Nip ions owing to its weaker conjugation compared to the other carbon atoms. It reflects that the number of active sites on the Gr surface was much smaller than those of metallic nanoparticles. Therefore, the adsorption process of Nip ions on the surface of NG, appearing a different reaction kinetics, was more pivotal than in the cases of metals. Furthermore, the active sites of NG were positively charged owing to the large electronegativity of doped N atoms, so that Nip ions preferred to combine with Gr sheet via the hydroxyl group. Based on the Mulliken analysis, it had a charge of −0.450 electrons, more negatively charged than the −0.246 electrons of the -NO_2 group. This was in agreement with the decrease of O–H vibration of the in situ FTIR results. Interestingly, the XPS data show that there are four kinds of N atoms with a ratio of 4 (pyridinic):2 (pyrrolic):2 (amine):1 (graphitic) acting as the catalytic active site as shown in Fig. 7.12c(i). The NG sheet shows intense distortions, and the Nip ion could combine with the carbon atom (next to the doped N atom) of the NG tightly, with the C–O bond distance at 1.497 Å (Fig. 7.12c(ii)). Together with the strong adsorption energy as mentioned above, it is concluded that the N-doping can indeed improve the adsorption ability of NG, which will contribute to the catalytic properties. The graphitic N atom is at the center of the surface while the others are at the edge. As such, the adsorption of Nip ions both at the center and edge should be considered. Each kind of these doped N atoms was calculated individually, and the results are illustrated in Fig. 7.12c(iii–vi). As expected, every configuration induces strong adsorption of the Nip ions onto NG, showing significantly enhanced adsorption energies with their small separated distances at the interface ca. 1.5 Å. The N–O bond lengths of the nitro group have also been calculated and marked in Fig. 7.12. Moreover, only the carbon atoms next to the doped N atoms on NG surface can be activated, serving as the active sites. As expected, all four kinds of the doped N atoms are beneficial to the adsorption and activation of Nip, contributing to the catalytic reduction reaction.

Li et al. recently reported that reduced graphene oxide (RGO) mediates the reductive transformation of biological NACs by electrochemically active bacteria, such as *Escherichia*, *Desulfovibrio*, and *Enterobacter*, which had been detected in both sludge and sludge-RGO systems [91]. The reduction of nitrobenzene (NB) results shows that RGO could increase the rate by an approximate onefold by mixed culture with glucose (electron donor). The influence of the surface properties of RGO on biological NACs removal was further elucidated. When RGO was used as metal-free catalyst with limited oxygen moieties on the surface of RGO such as quinone groups, the NB transformation rate was decreased, whereas nitrogen-doped RGO framework exhibited a positive effect as well as enhanced reduction rate. Indeed, RGO can absorb NB and form π-π interactions with aromatic rings, which resulted in the electron transfer to NB. Additionally, RGO could mediate direct interspecies electron transfer (DIET) and activate NB molecules. In recent years, it was suggested that DIET is an alternative mechanism for electron exchange through biological electrical connections [92], in contrast to interspecies hydrogen/formate electron transfer. Liu et al. reported that activated carbon promoted DIET [93]. RGO was also expected to accelerate DIET between microbes, which might be favorable

for nitroreductase to accept electrons. Here, RGO plays the role of "extended nanowire." The activation of NB by Gr has been proposed using DFT calculations, and the unsaturated carbon atoms at the edges of Gr and defects on Gr might possess catalytic activity [87].

7.4 Porous Carbon-Based Functional Nanomaterials

Porous carbon materials including traditional activated carbons (ACs), carbon nanotubes (CNTs), ordered mesoporous carbon (OMCs), carbon black (CBs), nanofibers (NFs), and recently emerged novel structured carbons synthesized by hard and soft templating methods have been widely used in a variety of applications [94]. Due to their high specific surface areas, micro−/mesoporous structure, tunable pore size, electronic conductivity, excellent accessibility to active sites, enhanced mass transport and diffusion. These properties make them a special and unique choice for various applications in divergent fields such as energy storage, fuel cells, adsorption/separation, heterogeneous catalysts, catalyst supports, photocatalysis, CO_2 capture, electrochemical sensors, and so forth [95–97]. However, to improve their catalytic properties, surface modification, heteroatom doping, chemical activation, and defects on graphic layers are necessary and have been extensively investigated [98–100]. It is well known that various surface groups, impurities and surface irregularities (i.e., surface heterogeneity), as well as fine pores of different sizes and shapes (i.e., structural heterogeneity) will contribute to the reaction mechanisms. An uneven distribution of functional groups creates surface heterogeneity. Another reason for heterogeneity is the presence of heteroatoms (commonly O, N, and S). However, the emission resulting from graphene has been attributed to C-oxygen-, C-nitrogen-, and/or C-sulfur-related localized states [101]. To induce ripples on the graphene surface can probably alter the local electrical and optical properties of graphene; thus, modified ripple engineering can be used for various applications [102]. Among the elements of complexity are the high surface area resulting from an intricate pore structure, significant differences in the physicochemical parameters among the heterogeneous surface sites, the occurrence of partial delocalization of the π-electrons, and the ability of certain surface sites to react with water and other solvents [103]. Some authors suggest that the distribution of the functional groups on the surface of ACs depends on pore size. The surface area is characterized among microporous materials (<2 nm), mesoporous materials with pore diameter between 2 and 50 nm, and nonporous or macroporous materials with pore diameter >50 nm [104]. The surface reactions of carbon nanomaterials are generally initiated from reactions of C atoms at the edges of the layers or at other lattice defects or reactions of functional groups that are bound to such C atoms. Surface reactions based on carbon as metal-free catalysts are of particular interest. The catalytic performance is significantly increased with an increase in the number of surface oxygen groups present, which are responsible for the enhancement in reaction rate, higher catalytic performance, and yield of the products [105]. Metal-

organic frame work (MOF)-derived ACs, as the other major form of porous carbon, are primarily made of graphitic sheets with regular order and possess extremely high surface areas and large pore volumes which make them extremely promising candidates for applications such as catalyst supports and adsorbents. Due to the presence of favorable pore geometries and volumes, ACs have been used in the areas of gas separation and storage, water purification, electrochemistry, and catalysis [106].

The catalytic behavior of carbon materials depends on their surface properties and unsaturated carbon atoms at the edges of the graphene layers and in basal plane defects that can easily react with oxygen, water, or nitrogen compounds, originating surface groups such as those represented schematically in Fig. 7.13 [107].

These functional groups can be used to metal-free catalysts or catalyst precursors or for subsequent functionalization and so on. In addition, they may be active sites for specific catalytic reactions [108]. Among the oxygenated groups, carboxylic acids and anhydrides, lactones, lactols, and phenols are acidic, while carbonyl and ether groups are neutral or may form basic structures (quinone, chromene, and pyrone groups). The carbon π electrons in the basal planes also contribute to the basicity of the carbon material, affecting its adsorption and catalytic properties [109].

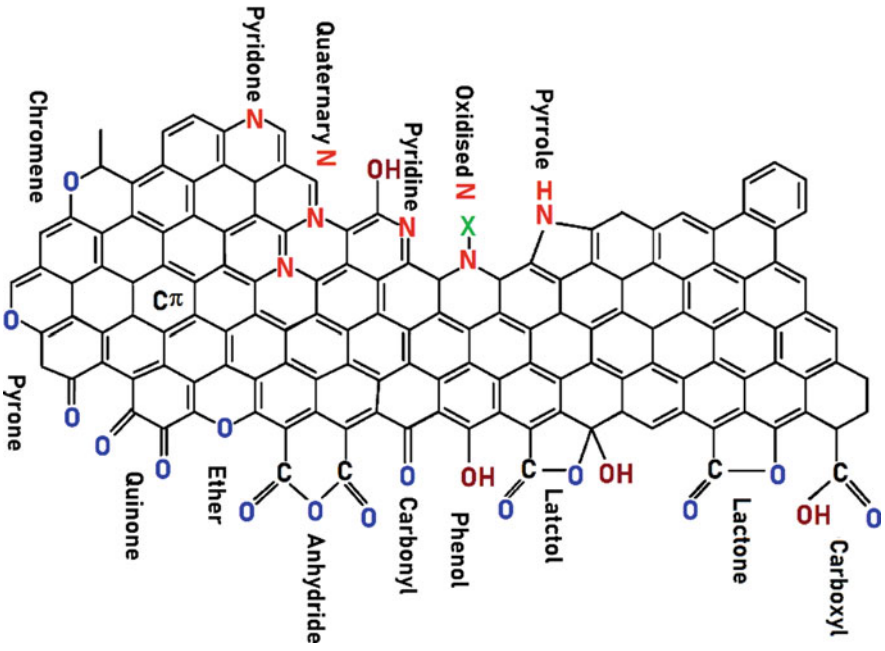

Fig. 7.13 Surface groups on carbon layers. (Reproduced from Ref. [107] with permission of Elsevier)

Recently, PCs have long been used as catalysts in organic transformations such as oxidation phenol [110], ODH of ethylbenzene [111], and anaerobic biotransformation of nitroanilines [112]. But the considerable modification in the porous structure of bare carbon materials, as well as the possibility of chemical and structural changes, offers new opportunities to use the PC materials in many different chemical reactions [113].

Carbon gels (CGs) are obtained by carbonization of organic gels produced by the sol-gel polycondensation of organic monomers such as resorcinol and formaldehyde, as first described by Pekala [114]. It exhibits high porosity and surface area, narrow pore size distributions, and randomly oriented pores, which have been reported as catalysts for quite a large variety of reactions. For instance, CGs functionalized with sulfonic acid groups are active acid catalysts for the esterification of acetic acid with ethanol [115]; N-doped carbon xerogels were used for oxidation of NO [116] and in the degradation of organic pollutants by advanced oxidation processes [117].

Black carbons (BCs) are carbonaceous materials composed of single and stacked polyaromatic sheets in a highly disordered arrangement. These sheets can be functionalized along the edges with hydroxyl (-OH), carboxyl (-COOH), keto (>C=O), or other functional groups. The textural properties such as surface area, pore volume, and pore size were dependent on the source material and conditions of synthesis [118]. It consists of spherical graphite particles (less than 50 nm diameter) with 0.35 nm interplanar spacing. The N_2 gas adsorption measurements reveal high surface area (typically, more than 50 $m^2\ g^{-1}$), high porosity (0.1–0.2 $cm^3\ g^{-1}$), and small pore size, i.e., below approximately 20 Å, with small porosity in the range 4–10 Å. They are most commonly used catalyst support in various environmental applications due to its high surface area (250 $m^2\ g^{-1}$) and low cost [119].

Recent studies have demonstrated that black carbons (BCs) could significantly accelerate the abiotic reduction of NACs in the presence of reductants, after their strong sorption to the NACs [120, 121]. It is well known that the pathway of NB reduction involves three successive two-electron transfer and protonation steps [122].

$$\text{Ar-NO}_2 \xrightarrow[-\text{H}_2\text{O}]{2e^- 2H^+} \text{Ar-NO} \xrightarrow{2e^- 2H^+} \text{Ar-NHOH} \xrightarrow[-\text{H}_2\text{O}]{2e^- 2H^+} \text{Ar-NH}_2$$

In addition, the DFT method was applied to calculate the sequences of electron and proton (H^+) for the reduction of NB to aniline [123]. However, the reductions of trifluralin (TF) and pendimethalin (PDM) seem to be more complex with competing reduction pathways, because there are two nitro groups on the benzene rings. Gong et al. reported the results combining the quantum-mechanical DFT calculation with experimental findings to elucidate the abiotic reduction mechanism of two nitro groups in TF and PDM [124]. They displayed the most plausible pathways and calculated energy profiles for reduction of TF and PDM in Figs. 7.14a and 7.15a, respectively.

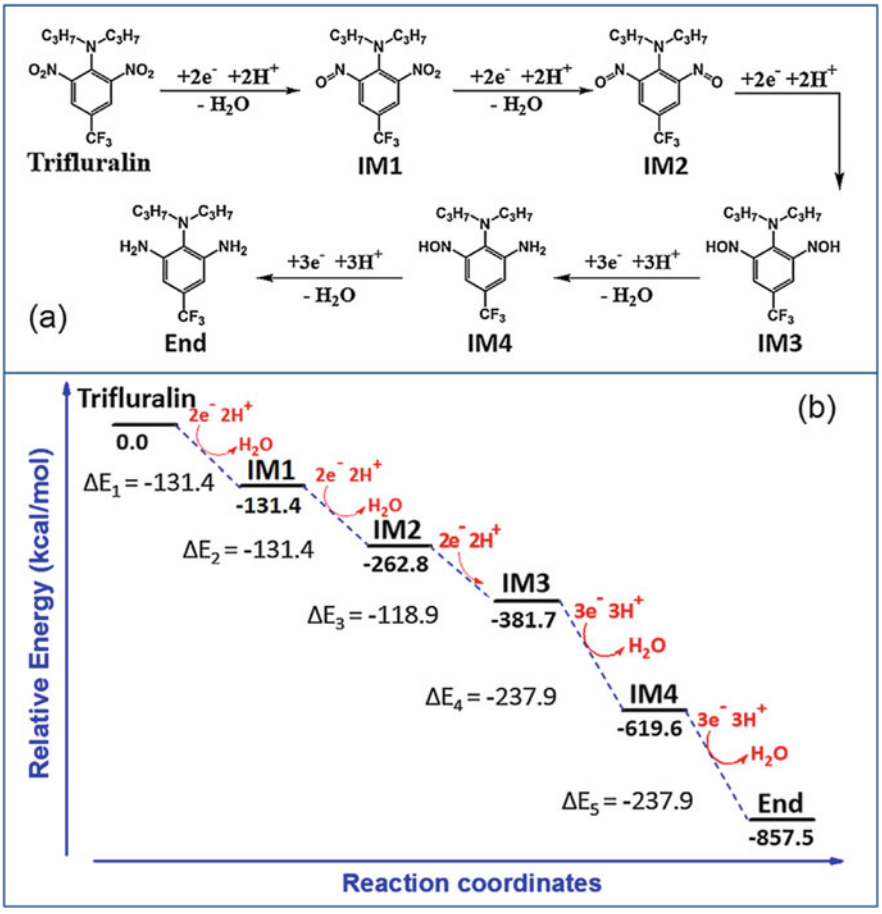

Fig. 7.14 Schematic representation (**a**) and calculated relative energy profiles (**b**) for abiotic reduction of TF. (Reproduced from Ref. [123] with permission of Elsevier)

While inspecting the energy profiles, the reduction of TF and PDM to their corresponding 2-NH_2 products is thermodynamically favorable, because the ΔE value of each step is negative (Figs.7.14b and 7.15b). The reduction intermediates and end products were identified, and the mass spectrum matched the results of detected species. It was noted that not all of the intermediates could be identified probably due to their instability. However, we can find evidence from the calculated quantum chemical properties of the reactants and transformation products. Thus, BCs could promote the abiotic reduction of TF and PDM by sulfides in the anoxic sediments, plausibly by accelerating the transfer of electron and atomic hydrogen from sulfides to dinitroaniline herbicides [124].

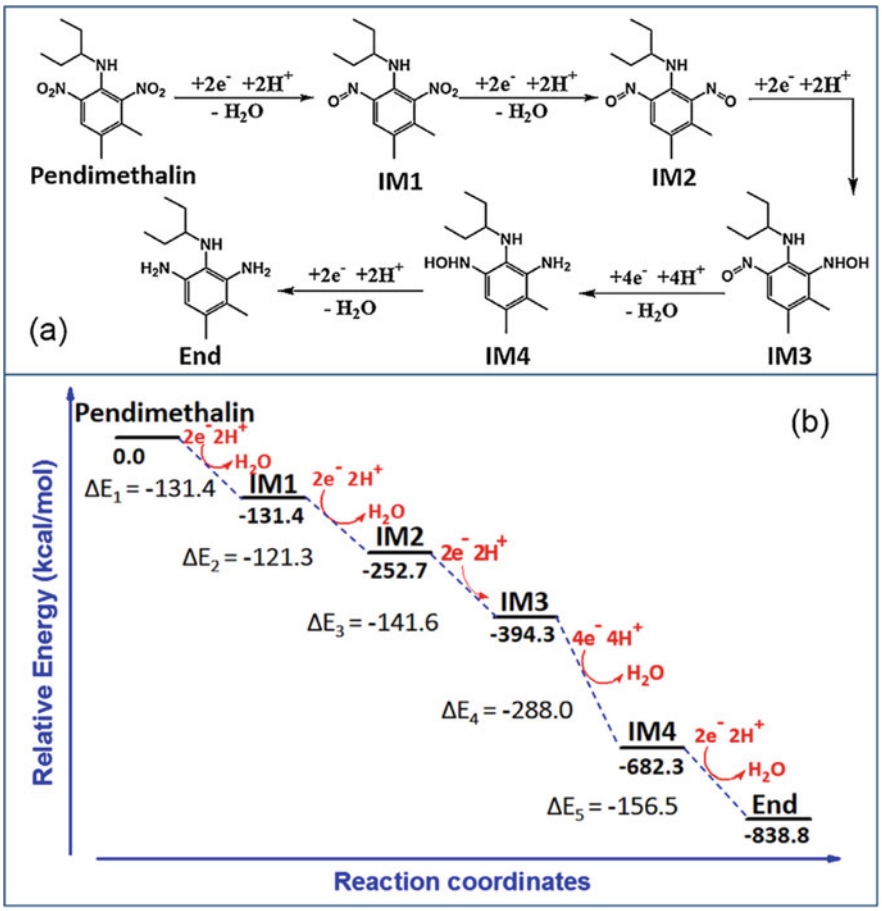

Fig. 7.15 Schematic representation (**a**) calculated relative energy profiles, and (**b**) for abiotic reduction of PDM. (Reproduced from Ref. [123] with permission from of Elsevier)

7.5 DFT Analysis for Structural, Fluorescence, and Sensing Properties of Fluorescent Carbon Nanomaterials

Carbon nanomaterials are one of the emergent advanced nanomaterials, due to their unique physicochemical properties, thereby showing promising performance in diverse applications [125–128]. These appeared in different structures including carbon nanotubes (CNTs), carbon dots (C-dots), graphene, graphene quantum dots (GQDs), graphene oxide (GO), fullerene, carbon nanohorns (CNHs), and carbon nano-onions (CNOs) which have been explored for potential applications in the field of chemistry and biology (Fig. 7.16) [125–128]. The carbon nanomaterials are mainly classified based on their dimensions such as zero-dimensional (0D),

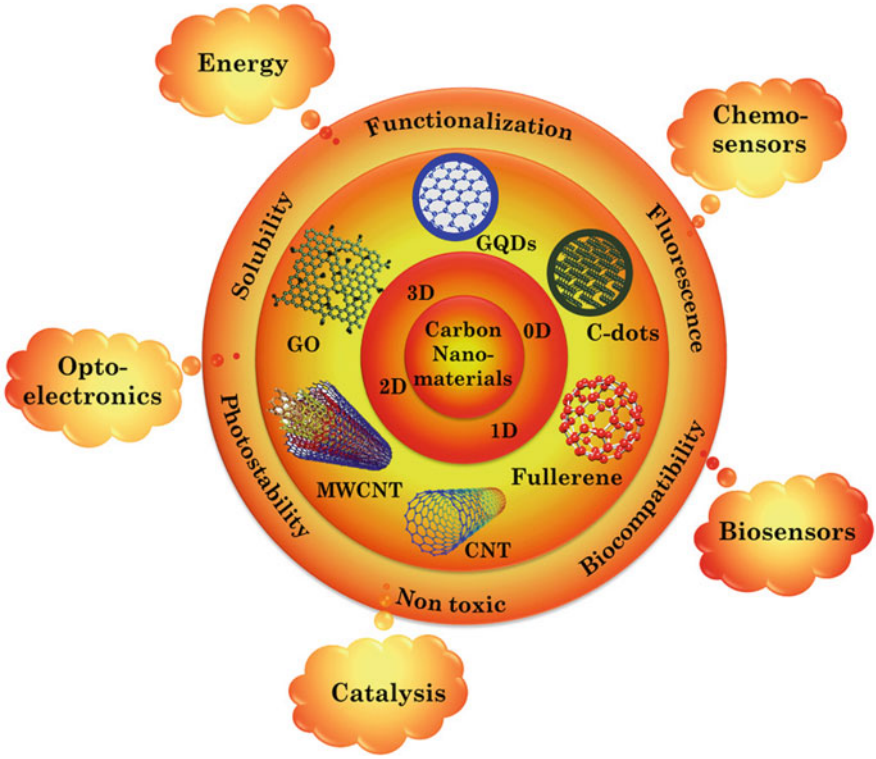

Fig. 7.16 Schematic representation of carbon nanomaterials

one-dimensional (1D), two-dimensional (2D), and three-dimensional (3D) nanostructures. The 0D materials have no dimensions with nanosize range which is considered as a spherical in shape including C-dots, fullerene, and GQDs. The 1D materials (CNTs) have one dimension outside of nanomateric size range (1–100 nm), whereas 2D materials (graphene and GO) possess two dimension lying in a nanosize. Generally, the bulk materials are known to be 3D materials which are composed of individual blocks with the size of nanometer scale (1–100 nm) or more. The 3D materials such as diamond and graphite have all dimensions in macroscale. This dimension-based classification is greatly dependent on the electron movement along the dimensions in the nanomaterials. For instance, electrons in 0D materials are entrapped in a dimensionless space, while electrons move along the x-axis in 1D materials. Similarly, 2D and 3D materials have electron movement along the x-y-axis and x-, y-, and z-axes, respectively. The 0D nanomaterials possess well-defined and quantized energy levels compared to those of other dimensional materials. Because the electron mobility is confined in 0D nanomaterials, the motion of randomly moving electrons is restricted to specific energy levels resulting in the increase of band gap of materials.

Diamond consists of sp^3-hybridized carbons, where the purely covalent chemical bonds extend three-dimensionally. Diamond is known as an electrically insulator due to lack of π electrons. On the other hand, the graphene is a 2D single layer of graphite and known to be very strong conductive material, because the graphene consists of sp^2 bonds. Structurally, a graphene sheet is a single layer of carbon atoms packed into 2D honeycomb lattice structure, whereas the CNTs are considered as rolled-up graphene sheet and their edges of the sheet joint together to form a seamless cylinder. In the case of 0D nanomaterials, GQDS are formed by the cutting a graphene monolayer into the small spherical molecules with the size of below 20 nm. These GQDS are mainly composed of sp^2 hybridized carbon atoms and crystalline in nature. In contrast, the C-dots composed of sp^3 hybridized carbon atoms predominantly with the various combinations of graphitic and turbostratic carbons. Moreover, the C-dots exhibit amorphous nature of their carbogenic cores. Recently, the C-dots and GQDs are getting much popularity among the 1D and 2D carbon nanomaterials. They can be synthesized from diverse kind of carbon precursors including organic molecules (citric acid, carbohydrates derivatives, etc.) and biomolecules (proteins, amino acids, etc.) with facile method and in shorter time. Another important feature is that C-dots and GQDs have photoluminescence property inherently as well as they can be tuned by chemical surface functionalization.

The applications as fluorescence sensors have been extensively studied by using these carbon nanomaterials due to their inherent fluorescence properties and non-toxicity. Among these nanocarbons, the single- and two-dimensional (1D and 2D) materials such as CNTs, graphene, and GO were served as sensing platform. The zero-dimensional (0D) materials like GQDs and C-dots are emerging as promising fluorescence sensing probe in consequence of several unique features including strong fluorescence with tunability, high photostability, smaller in size, ease to be functionalized, biocompatibility, and non-toxicity. Due to these advantages, the GQDs and C-dots materials were widely utilized as a fluorescent sensing probe in chemical and biosensors. The most important feature is that these materials exhibit non/less-toxicity in nature which enhances the potential in their sensor application.

7.5.1 Structural and Fluorescence Analysis of Graphene Quantum Dots and Carbon Dots

Firstly, Suda et al. have prepared the nanometer-size carbon particles on a Si substrate using plasma-assisted pulsed laser deposition (PLD) method [129]. The prepared carbon nanoparticles were in an amorphous state with sp^3 and sp^2 carbon components. Then in 2006, Sun et al. reported the photoluminescence carbon nanoparticles which were then named as “carbon dots” [130]. They observed strong excitation wavelength-dependent fluorescence (Fig. 7.17) which is ascribed to the emissive surface defects caused by the surface passivation of C-dots with organic molecules such as diamine-terminated oligomeric poly-(ethylene glycol)

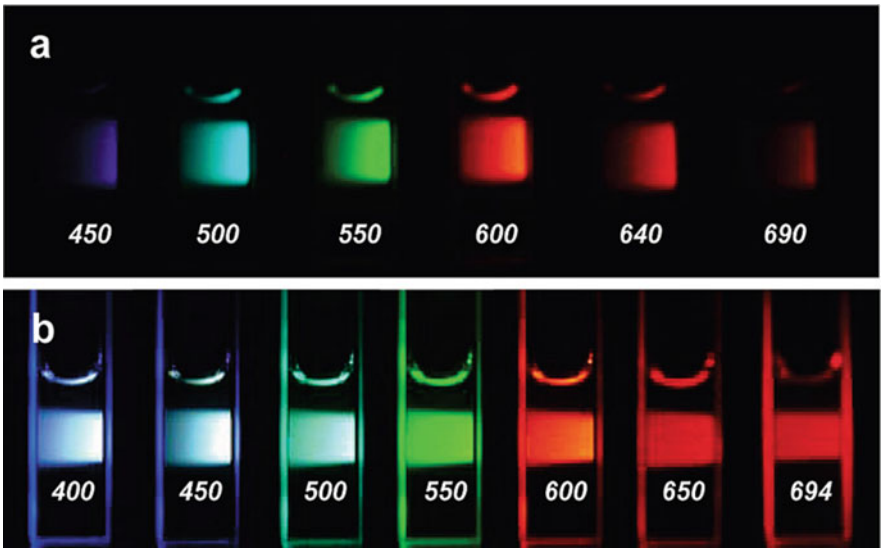

Fig. 7.17 Aqueous solution of the PEG_{1500N}-attached carbon dots (**a**) excited at 400 nm and photographed through band-pass filters of various wavelengths and (**b**) excited at the indicated wavelengths and photographed directly. (Reproduced from Ref. [130] with permission of the American Chemical Society)

(PEG_{1500N}) and poly(propionylethyleneimine-*co*-ethyleneimine) (PPEI-EI). On the other hand, Pan et al. in 2010 first synthesized the fluorescent functionalized GQDs from graphene sheets using hydrothermal method [131]. They have proposed that the luminescence originates from free zigzag sites with a carbene-like triplet ground state described as $\sigma^1\pi^1$. Recently, many research groups have extensively studied the fluorescence properties of C-dots and GQDs and proposed the mechanisms for multi-emissions by experimental observations [132–137]. However, the mechanisms are still not completely understood, because fluorescence properties are highly sensitive to several factors including size and shape of particles, carbon precursor, heteroatom doping, nature of the capping agent, experimental conditions, defects sites, etc. With the aid of theoretical calculations and modelling which provide precise details about the fluorescence properties of C-dots and GQDs, it becomes possible to investigate the influence of each abovementioned factor on the fluorescence properties of materials.

Time-dependent density functional theory (TDDFT) for response properties and excited states, which is a prerequisite to compute electronic spectra and related quantities like dispersion effects on polarizabilities and optical rotation [138–140]. Initially, SK et al. have demonstrated the systematic theoretical investigations of tunable photoluminescence properties of GQDs by regulating its size, shape, edge configuration, functional groups, and defects by using DFT and TDDFT calculations (Gaussian 09 package, B3LYP/6-31G(d) level) [141]. As shown in Fig. 7.18a, the emission wavelengths were linearly dependent on the increasing size of the GQDs,

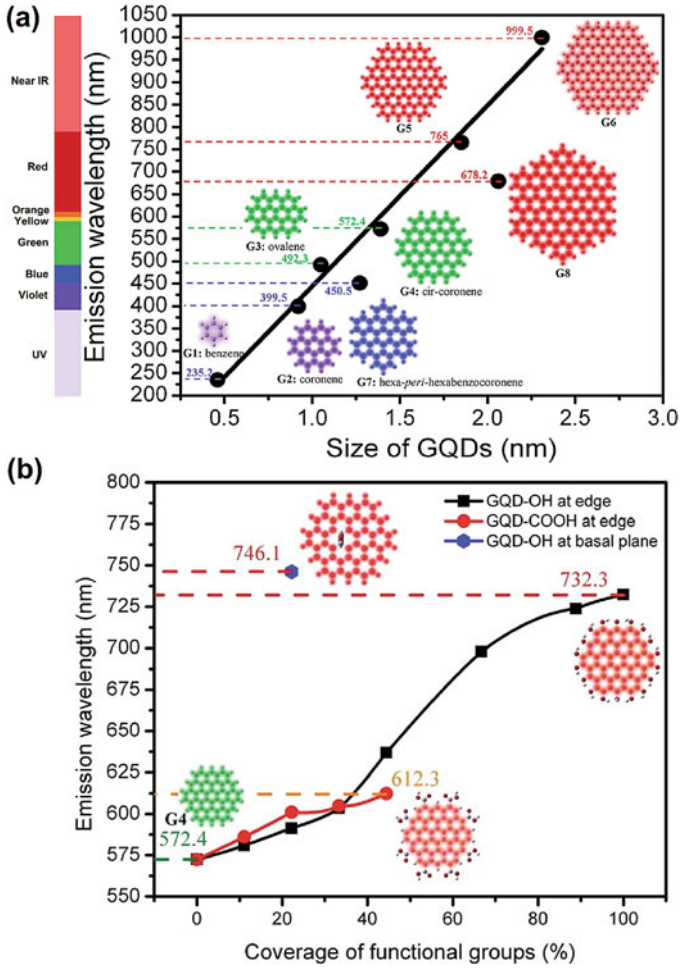

Fig. 7.18 (**a**) Calculated emission wavelength (nm) using TDDFT method in vacuum as a function of the diameter of GQDs. The solid line is the linear fitting of zigzag-edged GQDs (G1–G6). The indicated diameter is the average of the horizontal and vertical dimensions. (**b**) Emission wavelength of oxidized GQD (G4) as a function of the coverage of –OH and –COOH groups. (Reproduced from Ref. [141] with permission of the Royal Society Chemistry)

indicating that the entire visible light emissions (400–770 nm) may be covered by the diameter of GQD while varying from 0.89 to 1.80 nm. The red shift of the emission wavelength, as the size increases, is due to the decrease in band gap resulting from π-electron delocalization [141]. Moreover, such a band gap reduction may also be caused by the fabrication of functional groups (Fig. 7.18b). Graphene with either zigzag or armchair edges may influence the fluorescence of GQDs; for instance, the 1.27 and 2.06 nm armchair-edged GQDs emit at blue-shifted wavelength of ~450.5 and 678.2 nm, respectively, whereas the zigzag-edged GQDs

emit at red-shifted wavelength of ~551 and 872 nm, respectively. The observed results are well related to experimental results reported by Kim et al. supporting the observed blue- and red-shift emission based on the armchair- and zigzag-edged configuration of GQDs [142]. Furthermore, the pyridinic and pyrrolic N-doping on GQDs causes slight blue shift of emission wavelength in a concentration-dependent behavior. Previously, Jin et al. reported the band gap tuning of GQDs through the charge effect of functional groups using DFT analysis with the atomic orbital-based $Dmol^3$ software package [143]. The band gap was predicted to decrease for the functionalization of GQD with one amine group, and further decrease with increase of the number of amine groups (Fig. 7.19a), due to the increased electron density in a GQD-$(NH_2)_n$. As shown in Fig. 7.19b, the energy levels for HOMO state of GQD

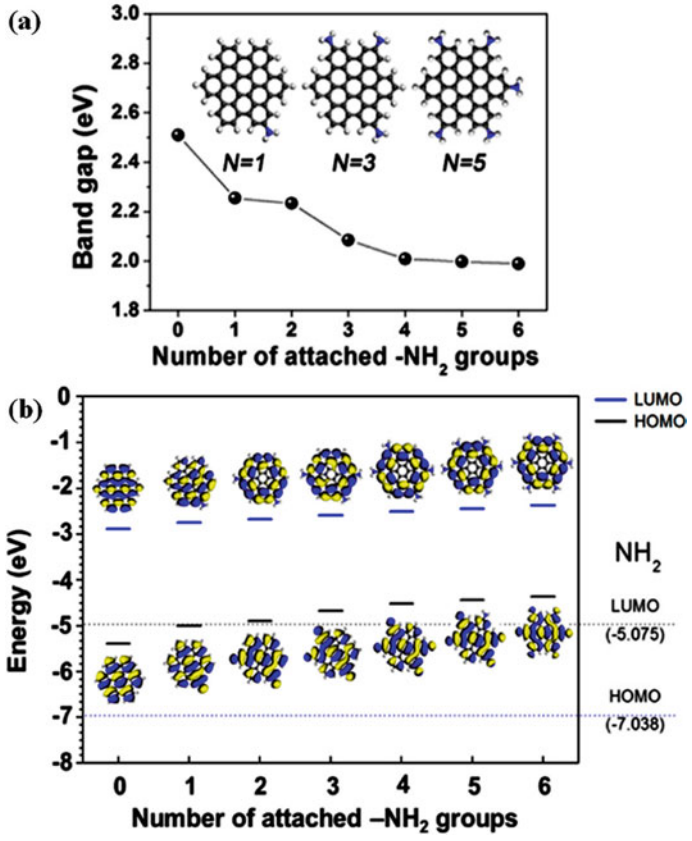

Fig. 7.19 (**a**) Band gap change of GQD-$(NH_2)_n$ as function of the number of attached NH_2 groups (inset images are optimized configuration of GQD-$(NH_2)_n$), (gray, C; white, H and blue, N atom), and (**b**) HOMO and LUMO energy levels of GQDs-$(NH_2)_n$. black and blue lines indicate HOMO and LUMO levels of GQDs-$(NH_2)_n$, respectively. The dotted lines denote the HOMO and LUMO energy level of NH_2. Insets describe HOMO and LUMO isosurface of each system (the isovalue is 0.01 e/Å3). (Reproduced from Ref. [143] with permission of the American Chemical Society)

and the LUMO state of amine group are almost identical, though the energy level of the GQD HOMO state becomes gradually higher than the amine LUMO state as a result of increasing number of NH_2 groups which leads to the difference in the band gap of GQD [143].

Similar to GQDs, the fluorescence of C-dots is originated from the diverse factors such as quantum confinement effect, carbon core effect, surface states, defect/trap sites, and heteroatom/element doping [132–136]. Even so, it was verified that the multi-emission of C-dots was predominated by the carbon core and surface states. The shorter wavelength emissions are mainly due to the recombination of electron-hole pairs in the carbon core, whereas the longer wavelength emissions originate from the surface states [132]. The carbon core in C-dots is mainly composed of sp^2 carbon clusters in the amorphous state. To understand the fluorescing mechanism originated from carbon core, Zhu et al. have analyzed the carbon core structure where the Gaussian 09 package (B3LYP/6-31G(d)) was used to optimize the electronic structures and calculate the energies of frontier molecular orbitals [144]. They used two different model compounds of fused aromatic rings (FARs) and cyclo-1,4-naphthylenes with different C-dots microstructure corresponding to graphitized carbon core (class I) and disordered carbon core (class II), respectively. The energy gaps between the HOMO and LUMO for the class I were calculated to be 2.82 and 1.63 eV for FAR-19 (1.2 nm) and FAR-61 (2.2 nm), respectively. But the inverse trend was calculated for the class II to be 2.80 and 3.46 eV for CN-8 (1.5 nm) and CN-16 (2.7 nm), respectively. From these calculation data regarding the size-dependency of C-dots fluorescence, it can be concluded that for the C-dots with a graphitized core, the smaller the size of the core, the higher the PL energy, while an inverse trend is observed for C-dots with an amorphous core.

Apart from the carbon core, the fluorescence was controlled by the surface states caused by the surface passivation with small organic molecules. The functional groups possess different energy levels leading to the various emissive states on the surface. Upon excitation of functionalized C-dots at certain excitation wavelength, the domination of surface emissive states generally generates fluorescence at the longer wavelength as compared to the fluorescence emitted by carbon core. Dhenadhayalan et al. have studied the effect of surface functional groups (-COOH and $–NH_2$) on the fluorescence of C-dots using time-resolved fluorescence spectroscopy techniques [132]. The surface functional groups are capable of regulating the multi-fluorescence behavior based on the electron-withdrawing and -donating properties of functional groups. The electron transfer takes place from the carbon core to surface domain by the presence of $-$COOH on the surface and vice versa for the case of $-NH_2$ present on the surface. Hola et al. have reported the red-shifted emission for the carboxylic functionalized C-dots [145]. Further, they have analyzed coronene derivatives as a model system to understand the influence of functional groups using TDDFT computation. The maximum emission of functionalized coronene (tricarboxylcoronene, ester of tricarboxylcoronene) was calculated to red shift with respect to that of coronene, as a result of an extension of π-conjugated electrons system. Moreover, upon the addition of carboxyl groups, the electrostatic potential surfaces show a shift of charge toward the edge. This

significant contribution of electrostatic interactions of the surface carboxyl groups greatly influences the role of C-dots acting as surface emissive traps. Similarly, the fluorescence of *para*-substituted anilines functionalized C-dots was controlled to emit at longer wavelength with very narrow spectral width by creating a new energy levels [146].

Different from surface functionalization, the metal/element doping is another important factor to influence the fluorescence properties of C-dots. For instance, Hola et al. have reported graphitic nitrogen triggers red fluorescence in carbon dots accompanied by the results of DFT and TDDFT calculations [147]. The five different pyrene-based models were used for DFT studies which contained carboxyl and hydroxyl groups on the surface and also two graphitic nitrogen inside the pyrene structure as shown in Fig. 7.20. The absorption spectra were computed using the TDDFT with the range-separated hybrid ωB97xD exchange-correlation functional

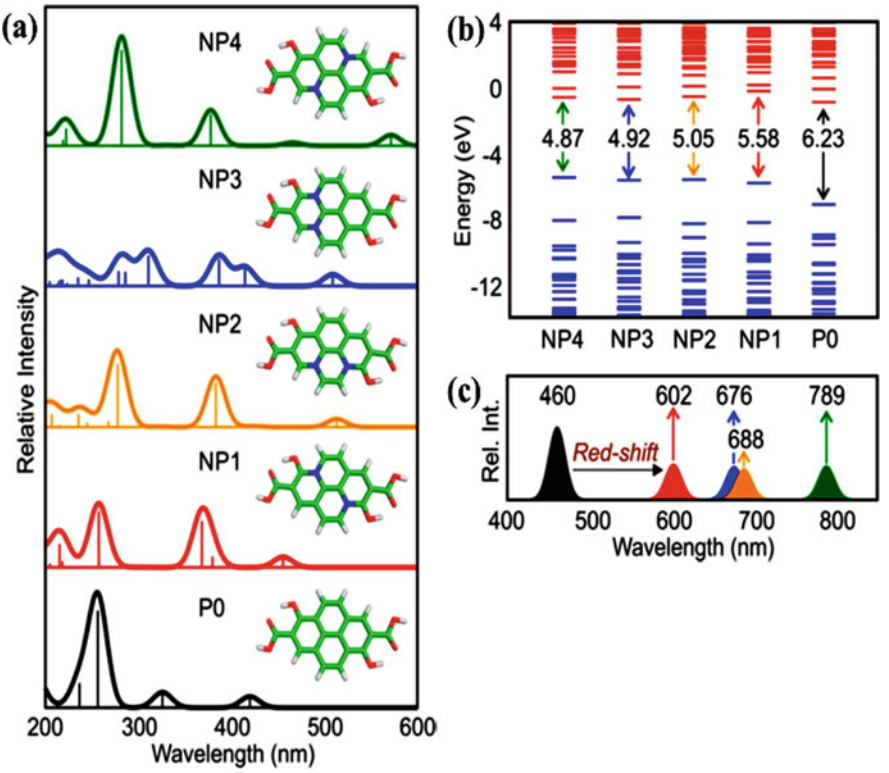

Fig. 7.20 (**a**) Calculated UV-vis absorption spectra for the N-doped models (NP1–NP4) and nitrogen-free system (P0) of the same size: carbon (green), hydrogen (white), oxygen (red), and nitrogen (blue). (**b**) Relative energy levels of the occupied (blue) and unoccupied (red) molecular orbitals of the same structures. (**c**) Model fluorescence spectra of the nitrogen-doped systems NP1 (red), NP2 (orange), NP3 (blue), and NP4 (green) and nitrogen-free system P0 (black). (Reproduced from Ref. [147] with permission of the American Chemical Society)

and 6-31+G(d) basis set. The DFT calculations suggested that the existence of graphitic nitrogen into the carbon core resulted in red-shifted absorption with respect to undoped system which is due to the transition into the second excited singlet state ($S_0 \rightarrow S_2$). Moreover, the differences between the HOMO and LUMO band gap, as shown in Fig. 7.20b, clearly indicate narrowing of the HOMO-LUMO gap in the nitrogen-doped systems and also create mid gap states within the original gap of the undoped system. Consequently, the red-shift fluorescence (above 600 nm) was observed for nitrogen-doped systems (Fig. 7.20c), and the red shift extent gradually increases as increasing amount of graphitic nitrogen in carbon core.

Xu et al. reported the Zn-doped C-dots with a high fluorescence quantum yield (32.3%). The ab initio studies were investigated to understand the involvement of molecular orbitals in the fluorescence process [148]. They have employed two well-established DFT-based ab initio methods including the plane-wave projector-augmented wave method as implemented in the Vienna ab initio simulation package (VASP) and the orthogonalized linear combination of atomic orbital (OLCAO) method. The notable twist in the C-dots structure was observed due to incorporation of Zn on the C-dots surface, as shown in Fig. 7.21a–c, and the Zn dopant may lift up the C-dots surface to move the electronic wave function distribution to the lower side (Fig. 7.21d–e). Moreover, the HOMO and LUMO are loading on the same lower part of C-dots leading to feasible charge transfer from LUMO to HOMO as a result of the binding of Zn with oxygen atoms on the C-dots surface. Then, they have calculated the electronic density of states for Zn-doped C-dots as shown in

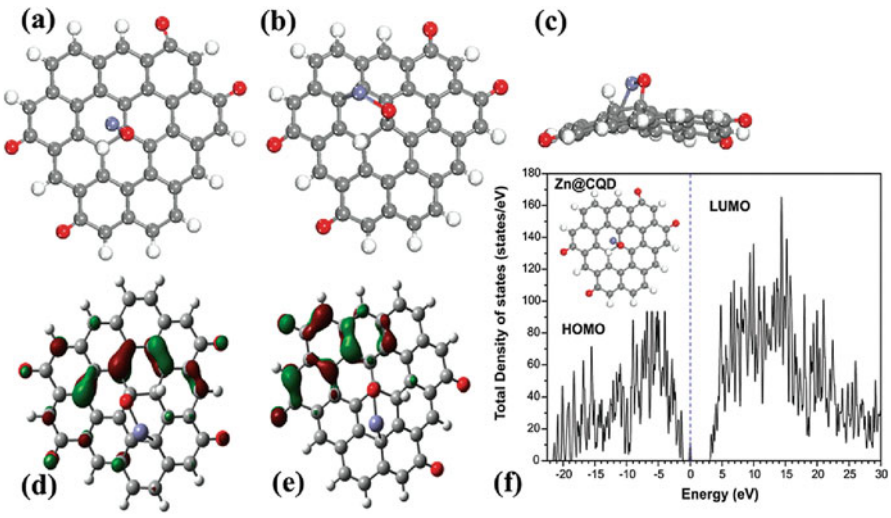

Fig. 7.21 The schematic structure and calculated frontier orbitals for Zn-doped C-dots, with C, H, and O indicated as gray, white, and red spheres. (**a**) Top view of the unrelaxed structure; (**b**) top view of the relaxed structure; (**c**) side view of the relaxed structure; (**d**) HOMO; (**e**) LUMO of Zn-doped C-dots; and (**f**) total density of states of Zn-doped C-dots. (Reproduced from Ref. [148] with permission of the Royal Society Chemistry)

Fig. 7.21f. The Zn-induced state was observed in the middle of the band gap which indicates that the dangling bonds of ionic Zn act as an energy gradient. Due to this intermediate state, the electrons or holes can efficiently move to the surface of C-dots which enhances the charge transfer, thereby resulting in the higher fluorescence quantum yield.

7.5.2 Sensing Analysis of Graphene Quantum Dots and Carbon Dots

The design and fabrication of new fluorescent chemosensors have been developed enormously since successful synthesis of carbon nanomaterials last decade [149–153]. There are two fundamental moieties which merged to obtain the fluorescent chemosensor, composed of the recognition site and the fluorescence signaling source. It is possible to develop a specific fluorescent sensor by switching these two moieties, thereby yielding a strong stable fluorescence signal with high specificity and enhancing the ability for detection of analyte. Generally, the fluorescent sensor materials should have multiple features such as ease for preparation and functionalization, high quantum yield with tunable absorption and fluorescence properties, reliable photostability, non-toxicity, and capability of sensing an analyte at lower detection limit. The GQDs and C-dots exhibit aforementioned unique merits and deserve a wide attention for the application of prospective sensors. To date, the GQDs and C-dots have been extensively utilized as a fluorescence sensing probes to detect analytes including inorganic metal cations and anions, nitro explosives, pesticides, drugs, toxic organic molecules, and important biomolecules based on the fluorescence turn-on and/or turn-off mechanisms. A diverse form of chemical functionalization of these nanomaterials is required in order that their functional properties might be involved in the detection of analytes. Indeed, a variety of analytes could be detected selectively by simply tuning the different functional groups on the surface of nanomaterial. The process of surface functionalization is of crucial importance to impart desired properties to nanomaterials for their applications. The functionalization of nanomaterials can be achieved through either covalent or noncovalent modification techniques. Rich functional groups including carboxylic, amine, alcohol, and thiol groups and also functional small molecules can attach on the surface of nanomaterials to improve their optical properties by controlling the energy gap and electronic properties. Moreover, formation of metal/element doping (N, S, transition metals, etc.) and composites/hybrids (with noble nanoparticles, metal oxides, etc.) with nanomaterials were applied to enhance their inherent properties to expand the application range.

For instance, the S-doped GQDs show the improved electronic properties and surface chemical reactivities compared with that of GQDs, and thereby can be used as an efficient fluorescent probe for highly selective and sensitive detection of Fe^{3+}, reported by Li et al. [153]. The DFT calculations (B3LYP/6-31G*) that the

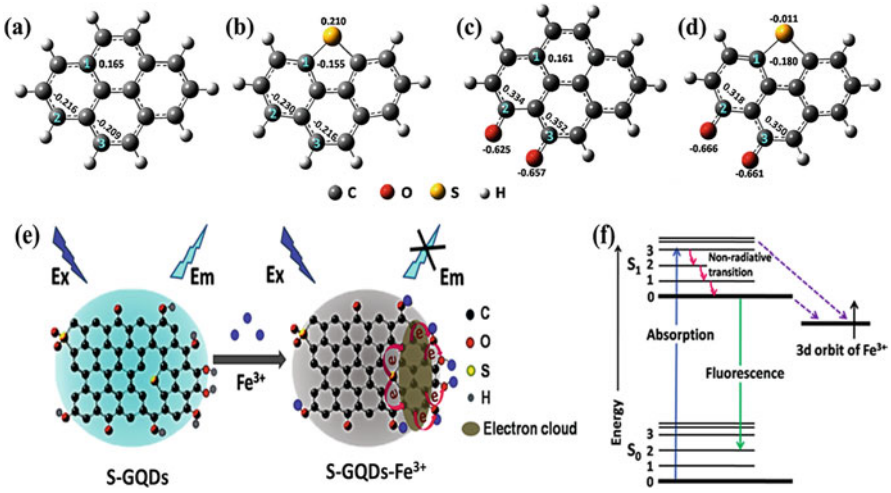

Fig. 7.22 The theoretical models of (**a**, **c**) GQDs and (**b**, **d**) S-GQDs. (**e**) Fluorescence quenching mechanism of the S-GQDs in the presence of Fe^{3+} and (**f**) the electron transfer process from S-GQDs to Fe^{3+}. (Reproduced from Ref. [153] with permission of the American Chemical Society)

electronic density of GQDs was effectively modulated due to doping of S atoms into the conjugated carbon skeleton of GQDs. As shown in Fig. 7.22a–d, four models of GQDs (a, c) and S-GQDs (b, d) were implemented, and the charge density of the representative atoms are shown in black numbers. The S atom directly bonded with C(1) atom enhances the electron density significantly due to the electron-donating ability of S atom, such that the electron densities of C(2) and C(3) atoms increased (Fig. 7.22a, b) as compared with those of undoped GQDs. In contrast, the electron densities of O atoms might increase while bonded to C(2) and C(3) atoms (Fig. 7.22c, d), due to its electron-withdrawing ability thereby enhancing surface electron densities along with S atoms. Therefore, Fe^{3+} ions were efficiently coordinated with phenolic hydroxyl groups on the edge of S-GQDs (Fig. 7.22e) and the electrons transferred from the excited state of S-GQDs to the half-filled 3*d* orbits of Fe^{3+} (Fig. 7.22f), resulting in the fluorescence quenching of S-GQDs.

The detection of chemical explosives has become important issue due to their impact on the environment pollution [154]. The explosives do not have fluorescent properties, and thus the fluorescence-based explosive sensors still dominated over other sensing techniques. The GQDs and C-dots have been used as fluorescence probe to sensing the chemical explosives with high sensitivity and selectivity. According to the experimental results, the sensing mechanism such as photo-induced electron transfer, fluorescence resonance energy transfer, inner filter effect, and intermolecular charge transfer for the fluorogenic detection of explosives was proposed based on the change in the fluorescence properties [154]. Indeed, to understand the accurate sensing mechanism, theoretical studies are needed to integrate the electronic structures. Ju et al. have proved that there were two

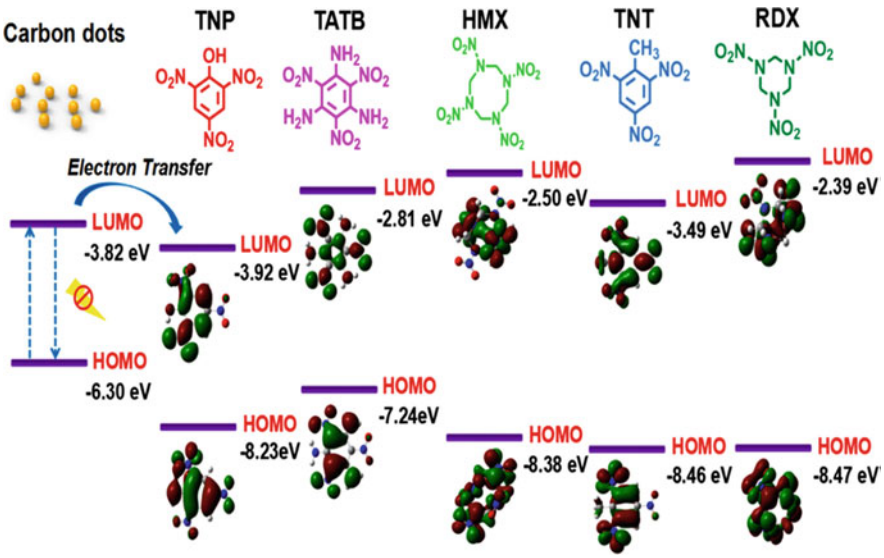

Fig. 7.23 HOMO and LUMO energy levels of C-dots and nitro explosives. (Reproduced from Ref. [155] with permission of the Royal Society Chemistry)

kinds of electron transfer based detection of 2,4,6-trinitrophenol (TNP) using C-dots as fluorescent probe through theoretical calculations along with spectroscopic studies [155]. As shown in Fig. 7.23, the HOMO and LUMO energy levels were calculated for C-dots and various nitro explosives using the B3LYP/6-31G-(d,p) method (Gaussian 09). The obtained results show that the LUMO levels of C-dots ($E_{LUMO} = -3.82$ eV) are higher than that of TNP ($E_{LUMO} = -3.92$ eV) which facilitates the electron transfer from the LUMO of C-dots to the LUMO of TNP resulting in the fluorescence quenching of C-dots. On the other hand, the respective electron transfer is not feasible to other explosives due to a higher LUMO energy level than that of C-dots. Thus, the high sensitivity and selectivity of CDs toward TNP can be ascribed to their efficient ET. Moreover, the theoretical studies confirmed that two kinds of electron transfer processes involve in the detection of TNP such as proton transfer-assisted and hydrogen-bond interaction-assisted electron transfer.

7.6 Conclusions

Since the rapid development in the number of studies related to the applications of functionalized graphene-based metal-free heterogeneous catalysis, rather than attempting to summarize all the progress achieved to date, we discuss the role of metal-free graphene and its derivatives with particular emphasis on the influence of

defects and functional groups on their interaction with catalytic phases, as well as the advantages of structures in the electron/mass transfer process. Additionally, we provide a comprehensive summary on the contribution of edges/defects, functional groups, and doping structures to the intrinsic catalytic properties of graphene-based metal-free catalysts.

Recently, the fluorescence mechanism of GQDs and C-dots has been extensively resolved by experiments with some theoretical calculations. The fluorescence properties of GQDs and C-dots turn out to be sensitive to their size, defects, edge configuration, surface functional groups, heteroatom/element dopant, etc. The DFT calculations are significantly helpful with the understanding about the fluorescence properties of GQDs and C-dots. However, restricted to complicated involvement of several factors, there is a room left for further investigation to gain better theoretical understanding of fluorescence properties which could assist to design and develop new advanced functional nanomaterials as well as enhance their applications.

7.7 Outlook

This book chapter highlights the important developments of functional carbon nanomaterials for these most distinguished organic transformations by using DFT methods. Notably, DFT is widely used in structure prediction, defects, phase stability, property prediction, and screening for many industrially and biologically important reactions. Thanks to the effective efforts of scientists and researchers in DFT-related fields, much progress has been achieved in the direction of the synthesis and characterization of these functional carbon nanomaterials and their applications to various organic transformations. Among these materials, the porous carbon materials have been the main choice for carbon nanomaterials in catalytic applications, because of their special physiochemical properties, including large surface area and pore volumes, active sites, low toxicity, and chemically modifiable surfaces. The application of DFT in functional carbon nanomaterial-related chemistry helps design catalytically across a range of homogeneous and heterogeneous catalysts. A variety of surface functional groups can be generated upon the bonding or doping of heteroatoms such as N, O, P, S, B, etc., to defects in metal-free carbon catalysts. Although focusing on electrostatic environmental effects may open new routes toward the rational optimization of efficient catalysts, much more predictive capacity is required with theoretical methods to have a transformative impact in their computational design as well as fulfill the concept of sustainable chemistry which should be the main objectives for future research and development (R&D). Moreover, in that context significant stimulation and progress may also be expected from virtual exploration and massive in DFT for the field of functional carbon nanomaterials in near future.

Apart from the utilization of carbon nanomaterials in the fields of catalysis and chemosensors, nowadays the usage of nanomaterials in biosensor has gained a great importance and explored for point-of-care applications. The unique inherent prop-

erties of carbon nanomaterials especially 0D of C-dots and GQDs, 1D of CNTs, and 2D of graphene have extensively employed toward the development of biosensors. When applying carbon nanomaterials with biomolecules, a significant improvement can be achieved in characteristics of biosensors such as high selectivity and sensitivity, biocompatibility, non-toxicity, and fast response. The biomolecules including proteins, DNA, antibody, and enzyme can be easily associated with functionalized carbon nanomaterials through covalent and/or electrostatic interactions. Due to the strong specificity of carbon nanomaterials with biomolecules, they provide an excellent advantage for biosensors by detecting a specific target biomolecules with higher sensitivity. The other important characteristics of carbon nanomaterials are low toxicity, good biocompatibility, as well as superior resistance to photobleaching which make them good candidates for the development of biosensors.

From the viewpoint of fluorescence experiments, the interaction between the carbon nanomaterials (GQDs and C-dots) and biomolecules occurs via due to the hydrophobic and/or electrostatic interaction, and the corresponding sensing mechanism proposed is based on the fluorescence change. However, understanding the precise role of carbon nanomaterials in interacting with the biomolecules still need to be discovered. Thus there is a good reason for further development of fluorescence carbon nanomaterial-based biosensors. As such a future trend is to better understand the relation between the probe and analyte, and the sensing mechanism. In addition to experiments, the theoretical simulation studies will play a major role in future to potentially solve the issues related to fundamental understanding about the fluorescence of carbon nanomaterials, sensing mechanism, etc. To achieve this goal, the integrating theoretically the complete structure of GQDs and C-dots is necessary in accordance with the core moiety, size, shape, and functional groups, so that it can help to predict the accurate interaction between the sensing materials and biomolecules from a theoretical perspective. The sensing performance would be significantly improved by regulating the properties of sensing materials including size, shape, functional groups, electronic structures, optical absorption and emission, and redox properties. The information from the theoretical aspects can be aid to design the new and unique materials to sensing the specific biomolecules with higher selectivity and sensitivity. We believe that theoretical simulation and modelling studies of fluorescence-based biosensors will have a promising future.

References

1. L.A. Curtiss, P.C. Redfern, K. Raghavachari, Assessment of Gaussian-3 and density-functional theories on the G3/05 test set of experimental energies. J. Chem. Phys. **123**, 124107 (2005)
2. R.K. Raju, A. Ramraj, I.H. Hillier, M.A. Vincent, N.A. Burton, Carbohydrate-aromatic pi interactions: A test of density functionals and the DFT-D method. Phys. Chem. Chem. Phys. **11**, 3411–3416 (2009)

3. P. Liu, Y. Zhao, R. Qin, S. Mo, G. Chen, L. Gu, D.M. Chevrier, P. Zhang, Q. Guo, D. Zang, B. Wu, G. Fu, N. Zheng, Photochemical route for synthesizing atomically dispersed palladium catalysts. Science **352**, 797–801 (2016)
4. J.K. Nørskov, M. Scheffler, H. Toulhoat, Density functional theory in surface science and heterogeneous catalysis. MRS Bull. **31**, 669–674 (2006)
5. J.K. Norskov, T. Bligaard, J. Rossmeisl, C.H. Christensen, Towards the computational design of solid catalysts. Nat. Chem. **1**, 37–46 (2009)
6. B.D. Dunnington, J.R. Schmidt, A projection-free method for representing plane-wave DFT results in an atom-centered basis. J. Chem. Phys. **143**, 104109 (2015)
7. E.J. Bylaska, M. Valiev, R. Kawai, J.H. Weare, Parallel implementation of the projector augmented plane wave method for charged systems. Comput. Phys. Commun. **143**, 11–28 (2002)
8. E.J. Bylaska, Plane-wave DFT methods for chemistry. Annu. Rep. Comput. Chem. **13**, 185–228 (2017)
9. R. Das, N. Dhar, A. Bandyopadhyay, D. Jana, Size dependent magnetic and optical properties in diamond shaped graphene quantum dots: A DFT study. J. Phys. Chem. Solids **99**, 34–42 (2016)
10. V. Cantatore, I. Panas, Communication: Towards catalytic nitric oxide reduction via oligomerization on boron doped graphene. J. Chem. Phys. **144**, 151102 (2016)
11. H.R. Jiang, T.S. Zhao, L. Shi, P. Tan, L. An, First-principles study of nitrogen-, boron-doped graphene and co-doped graphene as the potential catalysts in nonaqueous Li-O_2 batteries. J. Phys. Chem. C **120**, 6612–6618 (2016)
12. L. Ferrighi, M. Datteo, C. Di Valentin, Boosting graphene reactivity with oxygen by boron doping: Density functional theory modeling of the reaction path. J. Phys. Chem. C **118**, 223–230 (2014)
13. R.G. Parr, W. Yang, *Density-Functional Theory of Atoms and Molecules* (Oxford University Press, Oxford, 1989)
14. W. Koch, M.C. Holthausen, *A Chemist's Guide to Density Functional Theory* (Wiley-VCH, New York, 2001)
15. Q. Liu, Z.S. Li, S.L. Chen, Metal-embedded graphene as potential counter electrode for dye-sensitized solar cell. Ind. Eng. Chem. Res. **55**, 455–462 (2016)
16. X. Chen, F. Li, N. Zhang, L. An, D. Xia, Mechanism of oxygen reduction reaction catalyzed by Fe(Co)-Nx/C. Phys. Chem. Chem. Phys. **15**, 19330–19336 (2013)
17. W.B. Schneider, U. Benedikt, A.A. Auer, Interaction of platinum nanoparticles with graphitic carbon structures: A computational study. ChemPhysChem **14**, 2984–2989 (2013)
18. J. Kang, J.S. Yu, B. Han, First-principles design of graphene based active catalysts for oxygen reduction and evolution reactions in the aprotic Li-O_2 battery. J. Phys. Chem. Lett. **7**, 2803–2808 (2016)
19. S. Navalon, A. Dhakshinamoorthy, M. Alvaro, M. Antonietti, H. García, Active sites on graphene-based materials as metal-free catalysts. Chem. Soc. Rev. **46**, 4501–4529 (2017)
20. X. Duan, Z. Ao, L. Zhou, H. Sun, G. Wang, S. Wang, Occurrence of radical and nonradical pathways from carbocatalysts for aqueous and nonaqueous catalytic oxidation. Appl. Catal. B **188**, 98–105 (2016)
21. J. Vazquez-Arenas, G. Ramos-Sanchez, A.A. Franco, A multiscale model of the oxygen reduction reaction on highly active graphene nanosheets in alkaline conditions. J. Power Sources **328**, 492–502 (2016)
22. S. Mussell, P. Choudhury, Density functional theory study of iron phthalocyanine porous layer deposited on graphene substrate: A Pt-free electrocatalyst for hydrogen fuel cells. J. Phys. Chem. C **120**, 5384–5391 (2016)
23. X. Guo, G. Fang, G. Li, H. Ma, H. Fan, L. Yu, C. Ma, X. Wu, D. Deng, M. Wei, D. Tan, R. Si, S. Zhang, J. Li, L. Sun, Z. Tang, X. Pan, X. Bao, Direct, nonoxidative conversion of methane to ethylene, aromatics, and hydrogen. Science **344**, 616–619 (2014)

24. R.S. Assary, P.C. Redfern, J.R. Hammond, J. Greeley, L.A. Curtiss, Computational studies of the thermochemistry for conversion of glucose to levulinic acid. J. Phys. Chem. B **114**, 9002–9009 (2010)
25. L.A. Curtiss, P.C. Redfern, K. Raghavachari, Gaussian-4 theory using reduced order perturbation theory. J. Chem. Phys. **127**, 124105 (2007)
26. G.I. Csonka, A.D. French, G.P. Johnson, C.A. Stortz, Evaluation of density functionals and basis sets for carbohydrates. J. Chem. Theory Comput. **5**, 679–692 (2009)
27. S. Bertelsen, K.A. Jørgensen, Organocatalysis-after the gold rush. Chem. Soc. Rev. **38**, 2178–2189 (2009)
28. O. Mohammadi, M. Golestanzadeh, M. Abdouss, Recent advances in organic reactions catalyzed by graphene oxide and sulfonated graphene as heterogeneous nanocatalysts: A review. New J. Chem. **41**, 11471–11497 (2017)
29. D.V. Boukhvalov, D.R. Dreyer, C.W. Bielawski, Y.-W. Soon, A computational investigation of the catalytic properties of graphene oxide: Exploring mechanisms by using DFT methods. ChemCatChem **4**, 1844–1849 (2012)
30. V.S. Jeyaraj, M. Kamaraj, V. Subramanian, Generalized reaction mechanism for the selective aerobic oxidation of aryl and alkyl alcohols over nitrogen-doped graphene. J. Phys. Chem. C **119**, 26438–26450 (2015)
31. B. Dai, K. Chen, Y. Wang, L. Kang, M. Zhu, Boron and nitrogen doping in graphene for the catalysis of acetylene hydrochlorination. ACS Catal. **5**, 2541–2547 (2015)
32. H. Yang, X. Cui, X. Dai, Y. Deng, F. Shi, Carbon-catalysed reductive hydrogen atom transfer reactions. Nat. Commun. **6**, 6478 (2015)
33. D.R. Dreyer, C.W. Bielawski, Carbocatalysis: Heterogeneous carbons finding utility in synthetic chemistry. Chem. Sci. **2**, 1233–1240 (2011)
34. X. Wu, Z. Xie, M. Sun, T. Lei, Z. Zuo, X. Xie, Y. Liang, Q. Huang, Edge-rich and (N, S)-doped 3D porous graphene as an efficient metal-free electrocatalyst for the oxygen reduction reaction. RSC Adv. **6**, 90384–90387 (2016)
35. Y. Zhao, S. Huang, M. Xia, S. Rehman, S. Mu, Z. Kou, Z. Zhang, Z. Chen, F. Gao, Y. Hou, N-P-O co-doped high performance 3D graphene prepared through red phosphorous-assisted "cutting-thin" technique: A universal synthesis and multifunctional applications. Nano Energy **28**, 346–355 (2016)
36. H. Wang, K. Sun, F. Tao, D.J. Stacchiola, Y.H. Hu, 3D honeycomb-like structured graphene and its high efficiency as a counter-electrode catalyst for dye-sensitized solar cells. Angew. Chem. Int. Ed. **52**, 9210–9214 (2013)
37. D. Deng, L. Yu, X. Pan, X. Wang, X. Chen, P. Hu, L. Sun, X. Bao, Size effect of graphene on electrocatalytic activation of oxygen. Chem. Commun. **47**, 10016–10018 (2011)
38. D. Deng, K.S. Novoselov, Q. Fu, N. Zheng, Z. Tian, X. Bao, Catalysis with two-dimensional materials and their heterostructures. Nat. Nanotechnol. **11**, 218–230 (2016)
39. F. Yang, D. Deng, X. Pan, Q. Fu, X. Bao, Understanding nano effects in catalysis. Natl. Sci. Rev. **2**, 183–201 (2015)
40. W. Koch, M.C. Holthausen, *A Chemist's Guide to Density Functional Theory* (Wiley VCH, Weinheim, 2001)
41. W. Kohn, Nobel lecture: Electronic structure of matter–wave functions and density functionals. Rev. Mod. Phys. **71**, 1253 (1998)
42. R.O. Jones, O. Gunnarsson, The density functional formalism, its applications and prospects. Rev. Mod. Phys. **61**, 689 (1989)
43. P. Veerakumar, P. Thanasekaran, K.-L. Lu, K.-C. Lin, S. Rajagopal, Computational studies of versatile heterogeneous palladium catalyzed Suzuki, Heck, and Sonogashira coupling reactions. ACS Sustain. Chem. Eng. **5**, 8475–8490 (2017)
44. V.V. Welborn, L.R. Pestana, T. Head-Gordon, Computational optimization of electric fields for better catalysis design. Nat. Catal. **1**, 649–655 (2018)
45. B. Liu, H. Li, X. Ma, R. Chen, S. Wang, L. Li, The synergistic effect of oxygen-containing functional groups on CO_2 adsorption by the glucose–potassium citrate-derived activated carbon. RSC Adv. **8**, 38965–38973 (2018)

46. G. Lim, K.B. Lee, H.C. Ham, Effect of N-containing functional groups on CO_2 adsorption of carbonaceous materials: A density functional theory approach. J. Phys. Chem. C **120**, 8087–8095 (2016)
47. S. Grimme, Semiempirical GGA-type density functional constructed with a long-range dispersion correction. J. Comput. Chem. **27**, 1787–1799 (2006)
48. X. Wang, Y. Liu, X. Ma, S.K. Das, M. Ostwal, I. Gadwal, K. Yao, X. Dong, Y. Han, I. Pinnau, Soluble polymers with intrinsic porosity for flue gas purification and natural gas upgrading. Adv. Mater. **29**, 1605826 (2017)
49. P. Geerlings, F. De Proft, W. Langenaeker, Conceptual density functional theory. Chem. Rev. **103**, 1793–1874 (2003)
50. A. Zangwill, The education of Walter Kohn and the creation of density functional theory. Arch. Hist. Exact Sci. **68**, 775–848 (2014)
51. R.O. Jones, Density functional theory: Its origins, rise to prominence, and future. Rev. Mod. Phys. **87**, 897–923 (2015)
52. E. Furimsky, Graphene-derived supports for hydroprocessing catalysts. Ind. Eng. Chem. Res. **56**, 11359–11371 (2017)
53. B.C. Thompson, E. Murray, G.G. Wallace, Graphite oxide to graphene. Biomaterials to bionics. Adv. Mater. **27**, 7563–7582 (2015)
54. Z. Huang, H. Zhou, W. Yang, C. Fu, L. Chen, Y. Kuang, Three-dimensional hierarchical porous nitrogen and sulfur-codoped graphene nanosheets for oxygen reduction in both alkaline and acidic media. ChemCatChem **9**, 987–996 (2017)
55. I. Shimoyama, Y. Baba, Thiophene adsorption on phosphorus and nitrogen-doped graphites: Control of desulfurization properties of carbon materials by heteroatom doping. Carbon **98**, 115–125 (2016)
56. M. Gomez-Martínez, A. Baeza, D.A. Alonso, Pinacol rearrangement and direct nucleophilic substitution of allylic alcohols promoted by graphene oxide and graphene oxide CO_2H. ChemCatChem **9**, 1032–1039 (2017)
57. H. Ahmad, M. Fan, D. Hui, Graphene oxide incorporated functional materials: A review. Compos. Part B **145**, 270–280 (2018)
58. S. Ren, P. Rong, Q. Yu, Preparations, properties and applications of graphene in functional devices: A concise review. Ceram. Int. **44**, 11940–11955 (2018)
59. M. Sun, J. Li, Graphene oxide membranes: Functional structures, preparation and environmental applications. Nano Today **20**, 121–137 (2018)
60. L. Zhang, Q. Xu, J. Niu, Z. Xia, Role of lattice defects in catalytic activities of graphene clusters for fuel cells. Phys. Chem. Chem. Phys. **17**, 16733–16743 (2015)
61. Z. Zhao, M. Li, L. Zhang, L. Dai, Z. Xia, Design principles for heteroatom-doped carbon nanomaterials as highly efficient catalysts for fuel cells and metal–air batteries. Adv. Mater. **27**, 6834–6840 (2015)
62. Y. Zheng, Y. Jiao, Y. Zhu, L.H. Li, Y. Han, Y. Chen, A. Du, M. Jaroniec, S.Z. Qiao, Hydrogen evolution by a metal-free electrocatalyst. Nat. Commun. **5**, 3783 (2014)
63. C.J. Paez, A.L.C. Pereira, J.N.B. Rodrigues, N.M.R. Peres, Electronic transport across linear defects in graphene. Phys. Rev. B–Condens. Matter Mater. Phys. **92**, 045426 (2015)
64. L. Zhang, Z. Xia, Mechanisms of oxygen reduction reaction on nitrogen-doped graphene for fuel cells. J. Phys. Chem. C **115**, 11170–11176 (2011)
65. G.L. Tian, M.Q. Zhao, D. Yu, X.Y. Kong, J.Q. Huang, Q. Zhang, F. Wei, Nitrogen-doped graphene/carbon nanotube hybrids: In situ formation on bifunctional catalysts and their superior electrocatalytic activity for oxygen evolution/reduction reaction. Small **10**, 2251–2259 (2014)
66. C.L. Su, K.P. Loh, Carbocatalysts: Graphene oxide and its derivatives. Acc. Chem. Res. **46**, 2275–2285 (2013)
67. L. Lai, J.R. Potts, D. Zhan, L. Wang, C.K. Poh, C. Tang, H. Gong, Z. Shen, J. Lin, R.S. Ruoff, Exploration of the active center structure of nitrogen-doped graphene-based catalysts for oxygen reduction reaction. Energy Environ. Sci. **5**, 7936–7942 (2012)

68. B.F. Machado, P. Serp, Graphene-based materials for catalysis. Catal. Sci. Technol. **2**, 54–75 (2012)
69. D.R. Dreyer, H.P. Jia, C.W. Bielawski, Graphene oxide: A convenient carbocatalyst for facilitating oxidation and hydration reactions. Angew. Chem. Int. Ed. **49**, 6813–6816 (2010)
70. H.P. Jia, D.R. Dreyer, C.W. Bielawski, C-H oxidation using graphite oxide. Tetrahedron **67**, 4431–4434 (2011)
71. X.Y. Sun, P. Han, B. Li, S.J. Mao, T.F. Liu, S. Ali, Z. Lian, D.S. Su, Oxidative dehydrogenation reaction of short alkanes on nanostructured carbon catalysts: A computational account. Chem. Commun. **54**, 864–875 (2018)
72. X. Liu, B. Frank, W. Zhang, T.P. Cotter, R. Schlögl, D.S. Su, Carbon-catalyzed oxidative dehydrogenation of n-butane: Selective site formation during sp^3-to-sp^2 lattice rearrangement. Angew. Chem. Int. Ed. **50**, 3318–3332 (2011)
73. L. Roldan, A.M. Benito, E. Garcıa-Bordeje, Self-assembled graphene aerogel and nanodiamond hybrids as high performance catalysts in oxidative propane dehydrogenation. J. Mater. Chem. A **3**, 24379–24388 (2015)
74. B. Frank, R. Blume, A. Rinaldi, A. Trunschke, R. Schlögl, Oxygen insertion catalysis by sp^2 carbon. Angew. Chem. Int. Ed. **50**, 10226–10230 (2011)
75. O.V. Khavryuchenko, B. Frank, A. Trunschke, K. Hermann, R. Schlögl, Quantum-chemical investigation of hydrocarbon oxidative dehydrogenation over spin-active carbon catalyst clusters. J. Phys. Chem. C **117**, 6225–6234 (2013)
76. S. Ni, Z. Li, J. Yang, Oxygen molecule dissociation on carbon nanostructures with different types of nitrogen doping. Nanoscale **4**, 1184–1189 (2012)
77. S.B. Tang, Z.X. Cao, Site-dependent catalytic activity of graphene oxides towards oxidative dehydrogenation of propane. Phys. Chem. Chem. Phys. **14**, 16558–16565 (2012)
78. L. Favaretto, J. An, M. Sambo, A.D. Nisi, C. Bettini, M. Melucci, A. Kovtun, A. Liscio, V. Palermo, A. Bottoni, F. Zerbetto, M. Calvaresi, M. Bandini, Graphene oxide promotes site-selective allylic alkylation of thiophenes with alcohols. Org. Lett. **20**, 3705–3709 (2018)
79. C. Su, M. Acik, K. Takai, J. Lu, S.-J. Hao, Y. Zheng, P. Wu, Q. Bao, T. Enoki, Y.J. Chabal, K.P. Loh, Probing the catalytic activity of porous graphene oxide and the origin of this behaviour. Nat. Commun. **3**, 1298 (2012)
80. Q. Gu, G. Wen, Y. Ding, K.-H. Wu, C. Chen, D. Su, Reduced graphene oxide: A metal-free catalyst for aerobic oxidative desulfurization. Green Chem. **19**, 1175–1181 (2017)
81. R.H. Crabtree, A. Lei, Introduction: CH activation. Chem. Rev. **117**, 8481–8482 (2017)
82. Y. Gao, G. Hu, J. Zhong, Z. Shi, Y. Zhu, D.S. Su, J. Wang, X. Bao, D. Ma, Nitrogen-doped sp^2-hybridized carbon as a superior catalyst for selective oxidation. Angew. Chem. Int. Ed. **52**, 2109–2113 (2013)
83. Y. Gao, P. Tang, H. Zhou, W. Zhang, H. Yang, N. Yan, G. Hu, D. Mei, J. Wang, D. Ma, Graphene oxide catalyzed C-H bond activation: The importance of oxygen functional groups for biaryl construction. Angew. Chem. Int. Ed. **55**, 3124–3128 (2016)
84. J.H. Yang, Y.J. Gao, W. Zhang, P. Tang, J. Tan, A.H. Lu, D. Ma, Cobalt phthalocyanine–graphene oxide nanocomposite: Complicated mutual electronic interaction. J. Phys. Chem. C **117**, 3785–3788 (2013)
85. P. Veerakumar, P. Thanasekaran, K.-C. Lin, S.-B. Liu, Well-dispersed rhenium nanoparticles on three-dimensional carbon nanostructures: Efficient catalysts for the reduction of aromatic nitro compounds. J. Colloid Interface Sci. **506**, 271–282 (2017)
86. X.X. Chen, B.L. Chen, Macroscopic and spectroscopic investigations of the adsorption of nitroaromatic compounds on graphene oxide, reduced graphene oxide, and graphene nanosheets. Environ. Sci. Technol. **49**, 6181–6189 (2015)
87. Y.J. Gao, D. Ma, C.L. Wang, J. Guan, X.H. Bao, Reduced graphene oxide as a catalyst for hydrogenation of nitrobenzene at room temperature. Chem. Commun. **47**, 2432–2434 (2011)
88. T. Lv, S.B. Wu, H. Hong, L. Chen, R.J. Dong, Dynamics of nitrobenzene degradation and interactions with nitrogen transformations in laboratory-scale constructed wetlands. Bioresour. Technol. **133**, 529–536 (2013)

89. N. Pradhan, A. Pal, T. Pal, Silver nanoparticle catalyzed reduction of aromatic nitro compounds. Colloids Surf. A Physicochem. Eng. Asp. **196**, 247–257 (2002)
90. X. Kong, Z. Sun, M. Chen, C. Chen, Q. Chen, Metal-free catalytic reduction of 4-nitrophenol to 4-aminophenol by N doped graphene. Energy Environ. Sci. **6**, 3260–3266 (2013)
91. L. Li, Q. Liu, Y.-X. Wang, H.-Q. Zhao, C.-S. He, H.-Y. Yang, L. Gong, Y. Mu, H.-Q. Yu, Facilitated biological reduction of nitroaromatic compounds by reduced graphene oxide and the role of its surface characteristics. Sci. Rep. **6**, 30082 (2016)
92. Z.M. Summers, H.E. Fogarty, C. Leang, A.E. Franks, N.S. Malvankar, D.R. Lovley, Direct exchange of electrons within aggregates of an evolved syntrophic coculture of anaerobic bacteria. Science **330**, 1413–1415 (2010)
93. F. Liu, A.-E. Rotaru, P.M. Shrestha, N.S. Malvankar, K.P. Nevin, D.R. Lovleya, Promoting direct interspecies electron transfer with activated carbon. Energy Environ. Sci. **5**, 8982–8989 (2012)
94. L. Borchardt, Q.-L. Zhu, M.E. Casco, R. Berger, X. Zhuang, S. Kaskel, X. Feng, Q. Xu, Toward a molecular design of porous carbon materials. Mater. Today **20**, 592–610 (2017)
95. J.L. Figueiredo, Functionalization of porous carbons for catalytic applications. J. Mater. Chem. A **1**, 9351–9364 (2013)
96. D.S. Su, J. Zhang, B. Frank, A. Thomas, X. Wang, J. Paraknowitsch, R. Schlçgl, Metal-free heterogeneous catalysis for sustainable chemistry. ChemSusChem **3**, 169–180 (2010)
97. M.R. Benzigar, S.N. Talapaneni, S. Joseph, K. Ramadass, G. Singh, J. Scaranto, U. Ravon, K. Al-Bahily, A. Vinu, Recent advances in functionalized micro and mesoporous carbon materials: Synthesis and applications. Chem. Soc. Rev. **47**, 2680–2721 (2018)
98. S. Xiaoyan, W. Rui, S. Dangsheng, Research progress in metal-free carbon-based catalysts. Chin. J. Catal. **34**, 508–523 (2013)
99. J. Wang, H. Liu, X. Gu, H. Wang, D.S. Su, Synthesis of nitrogen-containing ordered mesoporous carbon as a metal-free catalyst for selective oxidation of ethylbenzene. Chem. Commun. **50**, 9182–9184 (2014)
100. I. Matos, M. Bernardo, I. Fonseca, Porous carbon: A versatile material for catalysis. Catal. Today **285**, 194–203 (2017)
101. S.S. Barton, M.J.B. Evans, E. Halliop, J.A.F. Macdonald, Acidic and basic sites on the surface of porous carbon. Carbon **35**, 1361–1366 (1997)
102. A. Stergiou, N. Karousis, D.T. Dimitratos, Metal-Free Functionalized Carbons in Catalysis Synthesis, Characterization and Applications, in *Non-covalent Methodologies for the Preparation of Metal-Free Nanocarbons for Catalysis*, (The Royal Society of Chemistry, Cambridge, 2018), pp. 29–66;. ISBN 978-1-78262-863-7
103. P. Serp, B. Machado, *Nanostructured Carbon Materials for Catalysis* (The Royal Society of Chemistry, Cambridge,. ISSN 1757–6725, 2015)
104. M. Naderi, Chapter 14: Surface Area: Brunauer–Emmett–Teller (BET), in *Progress in Filtration and Separation*, ed. by S. Tarleton, (Academic, London, 2015), pp. 585–608
105. P. Tang, G. Hu, M. Li, D. Ma, Graphene-based metal-free catalysts for catalytic reactions in the liquid phase. ACS Catal. **6**, 6948–6958 (2016)
106. X. Li, J. Zhang, W. Li, MOF-derived nitrogen-doped porous carbon as metal-free catalysts for acetylene hydrochlorination. J. Ind. Eng. Chem. **44**, 146–154 (2016)
107. J.L. Figueiredo, M.F.R. Pereira, The role of surface chemistry in catalysis with carbons. Catal. Today **150**, 2–7 (2010)
108. A. Rey, M. Faraldos, A. Bahamonde, J.A. Casas, J.A. Zazo, J.J. Rodrıguez, Role of the activated carbon surface on catalytic wet peroxide oxidation. Ind. Eng. Chem. Res. **47**, 8166–8174 (2008)
109. G. Wen, S. Wu, B. Li, C. Dai, D.S. Su, Active sites and mechanisms for direct oxidation of benzene to phenol over carbon catalysts. Angew. Chem. Int. Ed. **54**, 4105–4109 (2015)
110. Q. Wei, H. Fan, F. Qin, Q. Ma, W. Shen, Metal-free honeycomb-like porous carbon as catalyst for direct oxidation of benzene to phenol. Carbon **133**, 6–13 (2018)

111. L.F. Wang, J. Zhang, D.S. Su, Y.Y. Ji, X.J. Cao, F.S. Xiao, Simple preparation of honeycomb-like macrostructured and microporous carbons with high performance in oxidative dehydrogenation of ethylbenzene. Chem. Mater. **19**, 2894–2897 (2007)
112. L. Pereira, R. Pereira, M.F.R. Pereira, M.M. Alves, Effect of different carbon materials as electron shuttles in the anaerobic biotransformation of nitroanilines. Biotechnol. Bioeng. **113**, 1194–1202 (2016)
113. D.S. Su, S. Perathoner, G. Centi, Nanocarbons for the development of advanced catalysts. Chem. Rev. **113**, 5782–5816 (2013)
114. R.W. Pekala, Organic aerogels from the polycondensation of resorcinol with formaldehyde. J. Mater. Sci. **24**, 3221–3227 (1989)
115. R.P. Rocha, M.F.R. Pereira, J.L. Figueiredo, Carbon as a catalyst: Esterification of acetic acid with ethanol. Catal. Today **218–219**, 51–56 (2013)
116. J.P.S. Sousa, M.F.R. Pereira, J.L. Figueiredo, NO oxidation over nitrogen doped carbon xerogels. Appl. Catal. B **125**, 398–408 (2012)
117. R.P. Rocha, J. Restivo, J.P.S. Sousa, J.J.M. Órfão, M.F.R. Pereira, J.L. Figueiredo, Nitrogen-doped carbon xerogels as catalysts for advanced oxidation processes. Catal. Today **241**, 73–79 (2015)
118. B. Xing, J.J. Pignatello, Sorption of Organic Chemicals, in *Encyclopedia of Soils in the Environment*, ed. by D. Hillel, (Elsevier, Oxford, 2005), pp. 537–548
119. T.W. Kirchstetter, T. Novakov, Controlled generation of black carbon particles from a diffusion flame and applications in evaluating black carbon measurement methods. Atmos. Environ. **41**, 1874–1888 (2007)
120. X.D. Yu, W.W. Gong, X.H. Liu, H.Y. Bao, The reductive mechanism of nitrobenzene catalyzed by nine charcoals in sulfides solution. Sci. China Chem. **55**, 1–7 (2012)
121. H. Amezquita-Garcia, E. Razo-Flores, F. Cervantes, J. Rangel-Mendez, Activated carbon fibers as redox mediators for the increased reduction of nitroaromatics. Carbon **55**, 276–284 (2013)
122. R.P. Schwarzenbach, P.M. Gschwend, D.M. Imboden, *Environmental Organic Chemistry* (Wiley, Hoboken, 2005)
123. W. Gong, X. Liu, S. Xia, B. Liang, W. Zhang, Abiotic reduction of trifluralin and pendimethalin by sulfides in black-carbon-amended coastal sediments. J. Hazard. Mater. **310**, 125–134 (2016)
124. S.Y. Oh, P.C. Chiu, Graphite-and soot-mediated reduction of 2,4-dinitrotoluene and hexahydro-1,3,5-trinitro-1,3,5-triazine. Environ. Sci. Technol. **43**, 6983–6988 (2009)
125. X. Yu, H. Cheng, M. Zhang, Y. Zhao, L. Qu, G. Shi, Graphene-based smart materials. Nat. Rev. Mater. **2**, 17046 (2017)
126. A.J. Clancy, M.K. Bayazit, S.A. Hodge, N.T. Skipper, C.A. Howard, M.S.P. Shaffer, Charged carbon nanomaterials: Redox chemistries of fullerenes, carbon nanotubes, and graphenes. Chem. Rev. **118**, 7363–7408 (2018)
127. A. Narita, X.-Y. Wang, X. Feng, K. Mullen, New advances in nanographene chemistry. Chem. Soc. Rev. **44**, 6616–6643 (2015)
128. V. Georgakilas, J.N. Tiwari, K.C. Kemp, J.A. Perman, A.B. Bourlinos, K.S. Kim, R. Zboril, Noncovalent functionalization of graphene and graphene oxide for energy materials, biosensing, catalytic, and biomedical applications. Chem. Rev. **116**, 5464–5519 (2016)
129. Y. Suda, T. Ono, M. Akazawa, Y. Sakai, J. Tsujino, N. Homma, Preparation of carbon nanoparticles by plasma-assisted pulsed laser deposition method—Size and binding energy dependence on ambient gas pressure and plasma condition. Thin Solid Films **415**, 15–20 (2002)
130. Y.-P. Sun, B. Zhou, Y. Lin, W. Wang, K.A.S. Fernando, P. Pathak, M.J. Meziani, B.A. Harruff, X. Wang, H.F. Wang, P.J.G. Luo, H. Yang, M.E. Kose, B.L. Chen, L.M. Veca, S.-Y. Xie, Quantum-sized carbon dots for bright and colorful photoluminescence. J. Am. Chem. Soc. **128**, 7756–7757 (2006)
131. D. Pan, J. Zhang, Z. Li, M. Wu, Hydrothermal route for cutting graphene sheets into blue-luminescent graphene quantum dots. Adv. Mater. **22**, 734–738 (2010)

132. N. Dhenadhayalan, K.-C. Lin, R. Suresh, P. Ramamurthy, Unravelling the multiple emissive states in citric-acid-derived carbon dots. J. Phys. Chem. C **120**, 1252–1261 (2016)
133. L. Wang, S.-J. Zhu, H.-Y. Wang, S.-N. Qu, Y.-L. Zhang, J.-H. Zhang, Q.-D. Chen, H.-L. Xu, W. Han, B. Yang, H.-B. Sun, Common origin of green luminescence in carbon nanodots and graphene quantum dots. ACS Nano **8**, 2541–2547 (2014)
134. H. Ding, S.-B. Yu, J.-S. Wei, H.-M. Xiong, Full-color light-emitting carbon dots with a surface-state-controlled luminescence mechanism. ACS Nano **10**, 484–491 (2016)
135. X.M. Wen, P. Yu, Y.R. Toh, X.T. Hao, J. Tang, Intrinsic and extrinsic fluorescence in carbon nanodots: Ultrafast time-resolved fluorescence and carrier dynamics. Adv. Opt. Mater. **1**, 173–178 (2013)
136. S. Zhu, Y. Song, X. Zhao, J. Shao, J. Zhang, B. Yang, The photoluminescence mechanism in carbon dots (graphene quantum dots, carbon nanodots and polymer dots): Current state and future perspective. Nano Res. **8**, 355–381 (2015)
137. G. Yang, C. Wu, X. Luo, X. Liu, Y. Gao, P. Wu, C. Cai, S.S. Saavedra, Exploring the emissive states of heteroatom-doped graphene quantum dots. J. Phys. Chem. C **122**, 6483–6492 (2018)
138. M.E. Casida, T.A. Wesolowski, Generalization of the Kohn–Sham equations with constrained electron density formalism and its time-dependent response theory formulation. Int. J. Quantum Chem. **96**, 577 (2004)
139. T.A. Wesolowski, Hydrogen-bonding-induced shifts of the excitation energies in nucleic acid bases: An interplay between electrostatic and electron density overlap effects. J. Am. Chem. Soc. **126**, 11444 (2004)
140. J. Neugebauer, On the calculation of general response properties in subsystem density functional theory. J. Chem. Phys. **131**, 084104 (2009)
141. M.A. Sk, A. Ananthanarayanan, L. Huang, K.H. Lim, P. Chen, Revealing the tunable photoluminescence properties of graphene quantum dots. J. Mater. Chem. C **2**, 6954–6960 (2014)
142. S. Kim, S.W. Hwang, M.-K. Kim, D.Y. Shin, D.H. Shin, C.O. Kim, S.B. Yang, J.H. Park, E. Hwang, S.-H. Choi, G. Ko, S. Sim, C. Sone, H.J. Choi, S. Bae, B.H. Hong, Anomalous behaviors of visible luminescence from graphene quantum dots: Interplay between size and shape. ACS Nano **6**, 8203–8208 (2012)
143. S.H. Jin, D.H. Kim, G.H. Jun, S.H. Hong, S. Jeon, Tuning the photoluminescence of graphene quantum dots through the charge transfer effect of functional groups. ACS Nano **7**, 1239–1245 (2013)
144. B. Zhu, S. Sun, Y. Wang, S. Deng, G. Qian, M. Wang, A. Hu, Preparation of carbon nanodots from single chain polymeric nanoparticles and theoretical investigation of the photoluminescence mechanism. J. Mater. Chem. C **1**, 580–586 (2013)
145. K. Hola, A.B. Bourlinos, O. Kozak, K. Berka, K.M. Siskova, M. Havrdova, J. Tucek, K. Safarova, M. Otyepka, E.P. Giannelis, R. Zboril, Photoluminescence effects of graphitic core size and surface functional groups in carbon dots: COO^- induced red-shift emission. Carbon **70**, 279–286 (2014)
146. W. Kwon, S. Do, J.-H. Kim, M.S. Jeong, S.-W. Rhee, Control of photoluminescence of carbon nanodots via surface functionalization using para-substituted anilines. Sci. Rep. **5**, 12604 (2015)
147. K. Hola, M. Sudolska, S. Kalytchuk, D. Nachtigallova, A.L. Rogach, M. Otyepka, R. Zboril, Graphitic nitrogen triggers red fluorescence in carbon dots. ACS Nano **11**, 12402–12410 (2017)
148. Q. Xu, Y. Liu, R. Su, L. Cai, B. Li, Y. Zhang, L. Zhang, Y. Wang, Y. Wang, N. Li, X. Gong, Z. Gu, Y. Chen, Y. Tan, C. Dong, T.S. Sreeprasad, Highly fluorescent Zn-doped carbon dots as Fenton reaction-based bio-sensors: An integrative experimental–theoretical consideration. Nanoscale **8**, 17919–17927 (2016)
149. Y. Dong, J. Cai, X. You, Y. Chi, Sensing applications of luminescent carbon based dots. Analyst **140**, 7468–7486 (2015)
150. H. Sun, L. Wu, W. Wei, X. Qu, Recent advances in graphene quantum dots for sensing. Mater. Today **16**, 433–442 (2016)

151. H. Zhang, H. Zhang, A. Aldalbahi, X. Zuo, C. Fan, X. Mi, Fluorescent biosensors enabled by graphene and graphene oxide. Biosens. Bioelectron. **89**, 96–106 (2017)
152. A.P. Demchenko, M.O. Dekaliuk, Novel fluorescent carbonic nanomaterials for sensing and imaging. Methods Appl. Fluoresc. **1**, 042001 (2013)
153. S. Li, Y. Li, J. Cao, J. Zhu, L. Fan, X. Li, Sulfur-doped graphene quantum dots as a novel fluorescent probe for highly selective and sensitive detection of Fe^{3+}. Anal. Chem. **86**, 10201–10207 (2014)
154. X. Sun, Y. Wang, Y. Lei, Fluorescence based explosive detection: From mechanisms to sensory materials. Chem. Soc. Rev. **44**, 8019–8061 (2015)
155. B. Ju, Y. Wang, Y.-M. Zhang, T. Zhang, Z. Liu, M. Li, S.X.-A. Zhang, Photostable and low-toxic yellow-green carbon dots for highly selective detection of explosive 2,4,6-trinitrophenol based on the dual electron transfer mechanism. ACS Appl. Mater. Interfaces **10**, 13040–13047 (2018)

Chapter 8
Electronic Properties of Transition Metal-Benzene Sandwich Clusters

Tsugunosuke Masubuchi and Atsushi Nakajima

Abstract Organometallic clusters composed of transition metal atoms and benzene molecules have been topics of great interest from both fundamental and technological points of view. In this chapter, we review the progress in the physical chemistry of transition metal-benzene clusters. The intrinsic properties of transition metal-benzene clusters as a function of cluster size are investigated by gas-phase experiments, often in combination with quantum chemical calculations. In particular, vanadium-benzene clusters denoted V_nBz_m, showing magic numbers at $m = n + 1$, n, and $n - 1$, are characterized to possess multiple-decker sandwich structures, where vanadium atoms and benzene molecules are alternately piled up. Moreover, the discovery of such multiple-decker formation is a cornerstone in bottom-up approaches of molecular magnetism. The interplay of mass spectrometry, laser spectroscopies, and density functional calculations reveals that multiple-decker V_nBz_m clusters exhibit monotonic increase in magnetic moment with the number of layers. Anion photoelectron spectroscopic studies allow direct observations of the geometric and electronic structures of sandwich clusters and their anions. Major progress in this direction includes the recent characterization of tilted multiple-decker sandwich cluster anions composed of manganese atoms and benzene molecules. The sandwich clusters with high-spin characteristics will hopefully be exploited as building blocks in advanced electronic and magnetic nanomaterials via controlled assembly.

T. Masubuchi
Department of Chemistry, Faculty of Science and Technology, Keio University, Kohoku-ku, Yokohama, Japan

State Key Laboratory of Molecular Reaction Dynamics, Dalian Institute of Chemical Physics, Chinese Academy of Sciences, Dalian, China

A. Nakajima (✉)
Department of Chemistry, Faculty of Science and Technology, Keio University, Kohoku-ku, Yokohama, Japan

Keio Institute of Pure and Applied Sciences (KiPAS), Keio University, Kohoku-ku, Yokohama, Japan
e-mail: nakajima@chem.keio.ac.jp

T. Onishi (ed.), *Theoretical Chemistry for Advanced Nanomaterials*,
https://doi.org/10.1007/978-981-15-0006-0_8

Keywords Sandwich complexes · Multiple-decker sandwich clusters · Mass spectrometry · Photoionization spectroscopy · Anion photoelectron spectroscopy · Molecular magnetism

8.1 Introduction

It was 60 years ago that Feynman [1] delivered a famous lecture named "There's Plenty of Room at the Bottom," where he proposed a concept of designing functionalities by taking full advantage of the properties of things on a small scale. In 1962, Kubo [2] theoretically inferred that physicochemical properties of such small materials are different from those in bulk because of discrete energy levels of electrons. Since then, nanoscale materials have been important subjects in both basic and applied sciences. Among them, clusters consisting of up to about 1000 atoms have been extensively studied as they exhibit unexpected geometric and electronic properties that are scaled as a function of cluster size [3].

In recent decades, indeed, metal clusters and molecular clusters have attracted great attention as novel nanoscale materials of finite multifunctional systems. For metal clusters, spectroscopic and theoretic studies have revealed the size-dependent electronic properties of metal-insulator transition [4] and the electron shell structures based on jellium model [3, 5], the latter of which were discussed also from the viewpoint of mimicking shell model of nucleus [5]. As well as physical properties, chemical properties of size-specific reactivity of the metal clusters have been greatly explored as cluster catalysts [6]. On the other hand, molecular clusters have been extensively studied as the aggregates of weak van der Waals forces or hydrogen bond network, revealing microscopic solvation dynamics [7], coexisting phases [8], and electronic evolution of organic semiconductors [9].

However, studies on hybridized clusters between metal atoms and molecules, organometallic clusters, are limited, although organometallic molecular complexes such as an archetypal complex of ferrocene and ligated metal cluster compounds have been well known [10]. In particular, organometallic cluster formation can facilitate to control the dimensionality of the geometric structure through local metal-ligand interaction [11]. Since a low-dimensional structure of organometallic clusters synergistically exploits the chemical and physical features of metal atoms and organic molecules, leading to a dramatic change in their confinement behavior, functional properties such as charge transfer, conductivity, and electron spin arrangement can be designed by selecting an appropriate organic ligand which optimizes the characteristics of the metal atoms.

Sandwich clusters, consisting of metal atoms and planar ring ligands, are typical organometallic clusters, whose metal-ligand interactions are of fundamental interest due to their unique structures and electronic properties [11]. In this chapter, we focus on transition metal-benzene sandwich clusters. Followed by a general introduction on organometallic sandwich compounds, we explain gas-phase synthesis and characterization studies to probe the structures of transition metal-benzene clusters.

These studies are intended to understand how the structures of metal-benzene clusters are governed by the constituent metal atoms or molecules as well as the cluster size. Then, we refer to joint experimental and theoretical studies, including our recent works, for vanadium-benzene and manganese-benzene clusters and their anions. A special emphasis is put on their electronic and magnetic properties, which are characterized and understood from a nanoscopic point of view.

8.2 Preparation and Structures of Transition Metal-Benzene Sandwich Clusters

8.2.1 Early Studies on Sandwich Complexes

The discovery of ferrocene, a typical metallocene consisting of a Fe(II) atom and two cyclopentadienyl (C_5H_5 = Cp) ligands [12], is counted as a milestone in organometallic chemistry. Chemical, magnetic, and X-ray crystallographic characterizations revealed the sandwich structure of ferrocene, where the iron atom is η^5-bound to both the Cp ligands [13–14]. From the viewpoint of molecular orbital theory, the interaction of the Fe atom and the Cp ligands is shown in Fig. 8.1. In the following way, Lauher and Hoffmann [15] described the kinetic and thermodynamic stability of ferrocene. The *p* orbitals of the two Cp ligands produce three sets of approximately degenerate orbitals: a low-lying filled pair of a_{1g} and a_{2u} symmetry, a filled set of e_{1g} and e_{1u} symmetry, and an unoccupied pair of antibonding orbitals of e_{2g} and e_{2u} symmetry. When these orbitals interact with the Fe 3*d* orbitals, the resultant molecular energy levels of ferrocene are understood in terms of symmetry matching. The e_{1g} orbitals of the Cp ligands strongly interact with the Fe $3d_{yz}$ and $3d_{zx}$ orbitals, yielding a pair of bonding and antibonding orbitals, each of which is doubly degenerate. The a_{1g}, a_{2u}, and e_{1u} orbitals could interact but are much less combined with the Fe 4*s* or 4*p* orbitals that are too high in energy. The $3d_z{}^2$, $3d_{xy}$, and $3d_x{}^2{}_{-y}{}^2$ orbitals of the Fe atom thus remain essentially nonbonding. Ferrocene thus fulfills the 18-electron rule by filling its bonding and nonbonding orbitals. In fact, other metallocenes that do not satisfy the 18-electron rule, such as cobaltocene, $CoCp_2$ [16], are basically less stable than ferrocene.

Besides the metallocene family, bis(benzene)chromium, $CrBz_2$ (Bz = C_6H_6) [17], and bis(cyclooctatetraene)uranium, $U(COT)_2$ (COT = C_8H_8), called uranocene [18], are well-known sandwich compounds (Fig. 8.2). Their molecular orbital interactions between the metal and ligands are described in the same manner as that for ferrocene [19–20]. Bis(benzene)vanadium, VBz_2, was also prepared by the similar (Fischer-Hafner) method that was used for $CrBz_2$, but it was much more immediately oxidized in air than $CrBz_2$ [21]. Likewise, sandwich complexes that do not satisfy the 18-electron rule are difficult to be synthesized in the condensed phase. Another interesting derivative is a triple-decker sandwich complex of Ni atoms and Cp ligands, $[Ni_2Cp_3]^+$ (Fig. 8.2) [22]. Chemical synthesis of multiple-decker sandwich compounds, however, often requires appropriate ligands to stabilize such

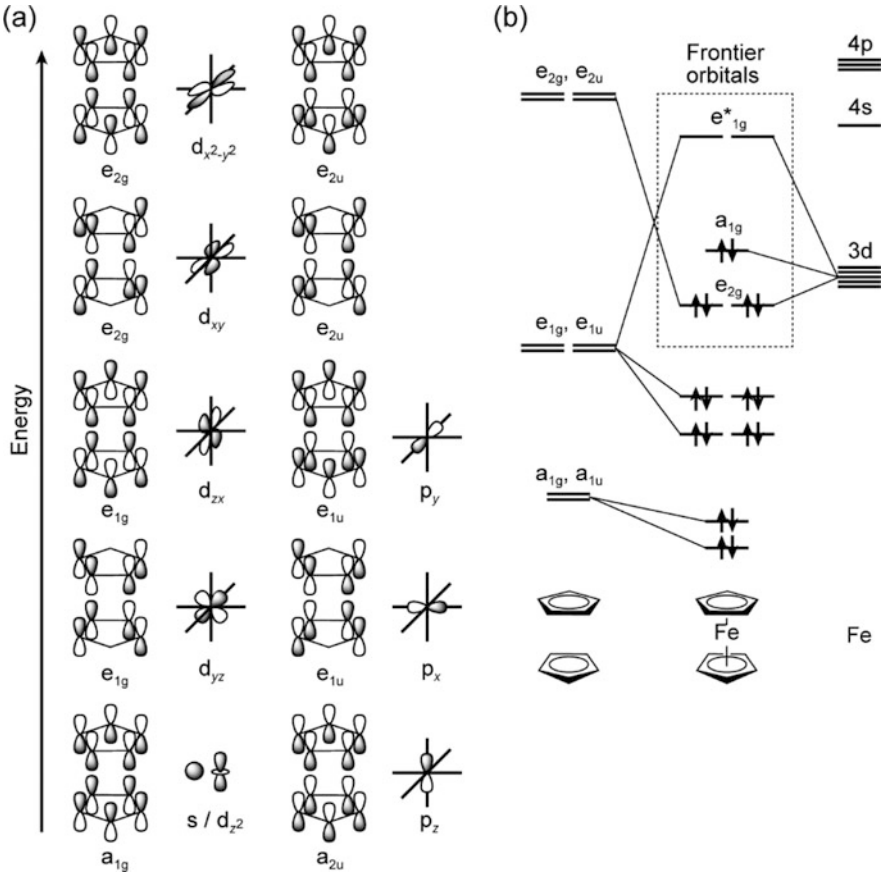

Fig. 8.1 (**a**) Symmetry matching of the molecular orbitals of the Cp ligands with the atomic orbitals of the Fe atom in ferrocene. The e_{2u} orbitals of the Cp ligands do not match with any orbitals of Fe. (**b**) Schematic molecular orbital diagram for ferrocene. The unoccupied e_{*1g} orbitals of ferrocene have antibonding character

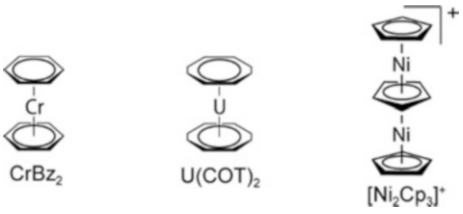

Fig. 8.2 Sandwich structures of $CrBz_2$, $U(COT)_2$, and $[Ni_2Cp_3]^+$

structures, as demonstrated in the early study that yielded up to hexa-decker sandwich complexes by using boron heterocycles instead of Cp [23]. More synthetic attempts on sandwich compounds have been detailed in the former reviews [24–25], and then we do not intend to introduce such contributions in this chapter.

8.2.2 *Gas-Phase Synthesis of Organometallic Complexes*

The development of vacuum techniques has enabled the direct synthesis of difficult-to-form complexes from vaporized materials. Followed by the synthesis of C_3 dicarbene from carbon vapor [27], Timms built the vacuum apparatus depicted in Fig. 8.3 in order to produce a variety of organometallic complexes. In the vacuum apparatus, transition metals were vaporized by the electric heating wire and allowed to react with gaseous organic reagents sprayed from a burette [26, 28]. The early efforts include the synthesis of several sandwich complexes such as bis(benzene)ruthenium, $RuBz_2$ [29], and triple-decker $Cr_2(1,3,5\text{-mesitylene})_3$ [30] in this way. In these studies, NMR spectroscopy was used for the structural characterization. Importantly, this gas-phase synthesis of sandwich compounds benefits from its oxygen- and solvent-free conditions that can avoid unwanted dissociation of the reaction products.

The recent advent of the laser vaporization method combined with molecular beam techniques has opened up a different aspect of organometallic chemistry. The laser vaporization method enables atoms, dimers, and various clusters (consisting of up to 1000 atoms) to be produced in considerably higher density in a short period [31]. When the laser vaporization products adiabatically expand into a vacuum with high-pressure carrier gas of helium (or other rare gases), they are allowed to form well-collimated, thermalized cluster beams that are ideal for studying their thermodynamic and kinetic properties [32–35]. Duncan and co-workers [36] produced the clusters of silver and aluminum ions with benzene by

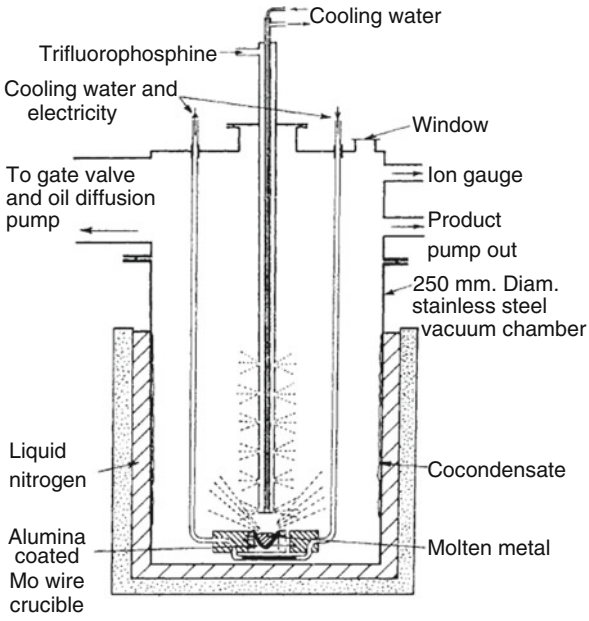

Fig. 8.3 Schematic view of a vacuum apparatus for the gas-phase synthesis of organometallic complexes presented by Timms. (Reproduced from Ref. [26] with permission from the Royal Society of Chemistry)

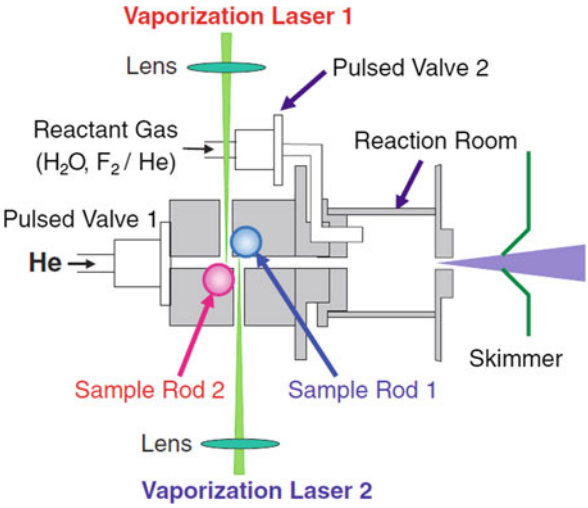

Fig. 8.4 Schematic view of a dual-laser vaporization cluster source which has two sample rods, two pulsed valves, and a reaction room. (Reproduced from Ref. [45] with permission from the Chemical Society of Japan)

means of laser vaporization and studied their photoinduced dissociation. Armentrout and co-workers [37–38] examined collision-induced dissociation of silver-benzene and first-row transition metal-benzene cluster ions. These works provided reliable thermodynamic data of the vibrational modes and dissociation energies for the clusters, which contributed to the understanding of the bonding nature between the metal atom and the benzene ligands.

In the laser vaporization method, cluster size and composition are controllable in a wide range, depending on the choice of the target material, laser fluence, carrier gas pressure, and the volume of the reaction room (sometimes called "waiting room"), where the metal vapor and the gaseous reactants are mixed in the presence of the carrier gas [39–40]. Kaya, Nakajima, and co-workers [41–42] built a dual-laser vaporization cluster source depicted in Fig. 8.4, equipped with a couple of pulsed valves, which enabled the production of clusters containing multiple elements and/or gaseous ligands. Using this cluster source, Hoshino et al. [43] synthesized polynuclear clusters of multiple vanadium atoms and benzene molecules denoted V_nBz_m and examined their structures with mass spectrometry. Interestingly, the photoionization mass spectrum in Fig. 8.5 indicated that these V-Bz neutrals were populated by magic number clusters with $m = n + 1$, each of which has one Bz molecule in excess. The chemical probe experiment showed that V_nBz_{n+1} were inert upon exposure to carbon monoxide (CO) while V_nBz_n and V_nBz_{n-1} absorbed 3 and 6 CO molecules, respectively. Since CO is regarded as a two-electron donor, three CO molecules are equivalent to one Bz ligand. Compared to V_nBz_{n+1}, it was thus thought that the addition of 3 and 6 CO molecules correspond to the lack of one and two exterior Bz molecules in the structures of V_nBz_n and V_nBz_{n-1}, respectively. These magic number behavior and reactivity suggested that V_nBz_{n+1} clusters exhibit a multiple-decker sandwich structure in which V atoms and Bz molecules are piled up alternately (see Fig. 8.5), while V_nBz_n and V_nBz_{n-1} were deduced

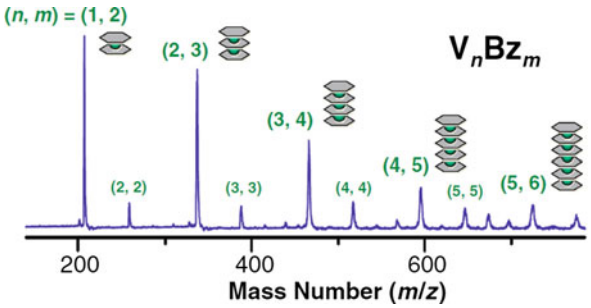

Fig. 8.5 Photoionization mass spectrum for V_nBz_m clusters. Each V_nBz_m is expressed as (n, m). The predominant peaks have magic numbered compositions of $(n, n + 1)$, and most of the minor peaks are assigned to the (n, m) clusters. Proposed structures for $(n, n + 1)$ clusters are also shown. (Reproduced from Ref. [45] with permission from the Chemical Society of Japan)

to be one- and two-end open sandwich clusters, respectively. The multiple-decker structures of cationic clusters of $V_nBz_{n+1}^+$ have later been confirmed by Bowers and co-workers with ion mobility measurements [44].

8.2.3 *Mass Spectroscopic Characterization of Transition Metal-Benzene Sandwich Clusters*

To gain detailed insights into the bonding scheme of V_nBz_{n+1} clusters, it is a good idea to address a question of how such multiple-decker sandwich formation is dependent on metal elements and ligands. To answer this question, Kurikawa et al. [46–48] synthesized a series of metal-benzene clusters, M_nBz_m, from first-row transition metals M (= Sc to Cu), and the cluster formation of these clusters was studied in the same manner as was employed for V_nBz_m clusters. For Co_nBz_m clusters, photoionization mass spectroscopy revealed that, in the series of the abundant clusters, the number of Co atoms increased one by one, whereas the number of Bz molecules did not necessarily increase with the cluster size (Fig. 8.6g). Namely, every n had a specific maximum number of Bz molecules adsorbed (m_{max}). The magic number clusters such as $(n, m) = (1, 2)$, $(2, 3)$, $(3, 3)$, $(4, 4)$, $(5, 4)$, and $(6, 4)$ did not react with ammonia molecules. However, most of these clusters cannot be expressed as $(n, n + 1)$ and thus are unlikely to take a sandwich structure. It was deduced that they exhibit a so-called "rice-ball" structure, where the Co_n core is surrounded by the Bz molecules, as depicted in Fig. 8.7b [46–47]. A similar mass spectral trend (in m_{max}) was seen for the Bz complexes of other late transition metals of Fe and Ni, while Sc_nBz_m and Ti_nBz_m were distributed over the $(n, n + 1)$ composition (see Fig. 8.6). Thus, the following two types of structures are concerned with transition metals M: the multiple-decker sandwich structure is characteristic of the complexes for early transition metals (M = Sc to V), whereas

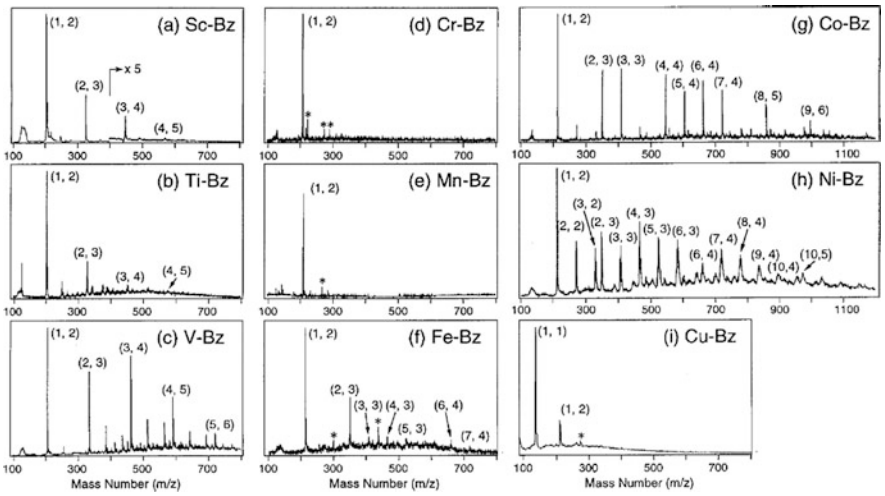

Fig. 8.6 Photoionization mass spectra for M_nBz_m clusters (M = 3*d* transition metals: (**a**) Sc, (**b**) Ti, (**c**) V, (**d**) Cr, (**e**) Mn, (**f**) Fe, (**g**) Co, (**h**) Ni, and (**i**) Cu). Each M_nBz_m is expressed as (*n*, *m*). The asterisks denote the contamination peak of oxide. (Reprinted with permission from Ref. [48]. Copyright 1999 American Chemical Society)

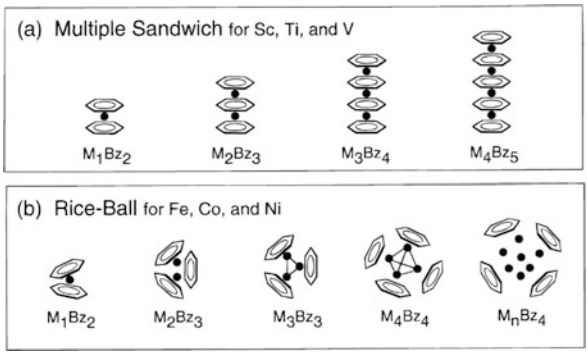

Fig. 8.7 (**a**) Proposed structures for early transition metals for Sc, Ti, and V; multiple sandwich. (**b**) Proposed structures for late transition metals from Fe to Ni; rice-ball. (Reprinted with permission from Ref. [48]. Copyright 1999 American Chemical Society)

the rice-ball structure is formed for late transition metals (M = Fe to Ni). Cr, Mn, and Cu belong to neither of the two metal groups: they did not produce any larger clusters than mononuclear MBz_2 in the reaction with Bz (see Fig. 8.6d, e, i) [48].

To probe basic concepts underlying the metal-ligand interactions, transition metal-fullerene (C_{60}) cluster ions, $M_n(C_{60})_m^+$ (M = Sc, Ti, V, Cr, Mn, Fe, Co, and Ni), were prepared by means of laser vaporization and studied with mass spectrometry [11, 49–53]. Among the transition metals studied, Nakajima et al. [51, 53] found that $M_n(C_{60})_m^+$ with M = Sc, Ti, and V were populated by (*n*, $n + 1$) and (*n*, *n*) clusters, which did not form a carbonyl complex. It was proposed that the structures of the predominant clusters are chain-like multiple dumbbell or ring structures (Fig. 8.8), analogous to multiple-decker sandwich clusters. In

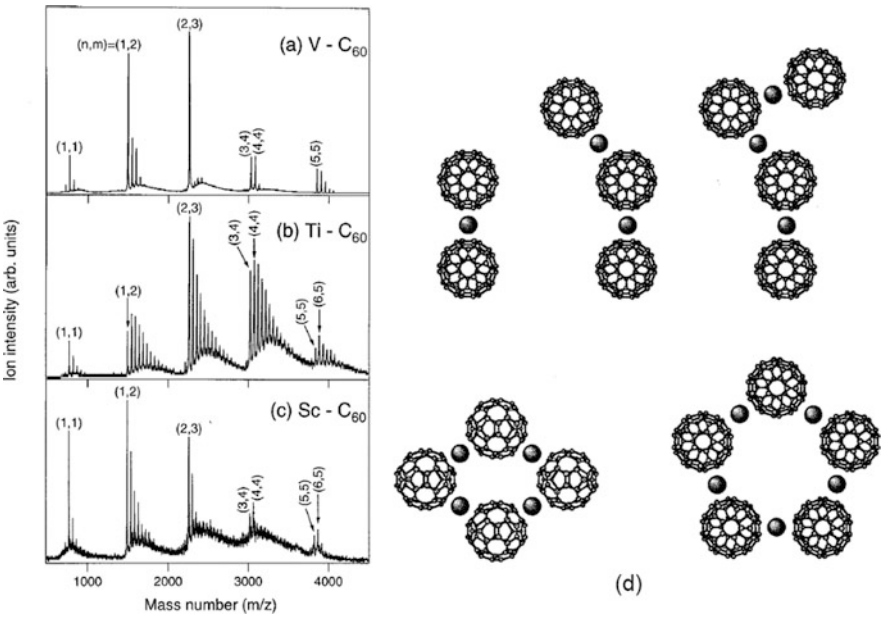

Fig. 8.8 Left: typical photoionization mass spectra of (**a**) $V_n(C_{60})_m$, (**b**) $Ti_n(C_{60})_m$ and (**c**) $Sc_n(C_{60})_m$. Right: (**d**) proposed dumbbell and ring structures for $M_n(C_{60})_m$ (M = Sc, Ti and V). (Reprinted with permission from Ref. [11]. Copyright 2000 American Chemical Society)

contrast, $M_n(C_{60})_m^+$ with the other metals exhibited a different mass feature. Nagao et al. [52] proposed that $Co_4(C_{60})_4^+$ exhibit a face-centered tetrahedron structure (Fig. 8.9) that is again analogous to the rice-ball structure of Co_4Bz_4. Such face-centered structures are thought to be prevalent in $M_n(C_{60})_m^+$ where M = Cr, Fe, Co, and Ni [11, 53]. Metal-coronene ($C_{24}H_{12}$) clusters, $M_n(C_{24}H_{12})_m$, have also attracted much interest, as their ions consisting of various metals were investigated. Pozniak and Dunbar [54] studied the reactivity of more than 20 metal ions toward coronene and classified these ions into 2 groups depending on whether the reaction led to the (1, 2) formation. Many of the transition metals such as Sc^+, Ti^+, Cr^+, Mn^+, Fe^+, Ni^+, and Cu^+ allowed yielding $M(C_{24}H_{12})_2^+$ that was deduced to be a sandwich complex. Duncan and co-workers [55–57] conducted photodissociation measurements on $Fe_n(C_{24}H_{12})_m^+$ and $Cr_n(C_{24}H_{12})_m^+$ and evidenced possible sandwich structures for these cluster ions, including the multiple-decker $Cr_2(C_{24}H_{12})_3^+$ cluster. $V(C_{24}H_{12})_2^-$ and $Ti(C_{24}H_{12})_2^-$ anions were also assigned to be sandwiches [58]. Nakajima, Kaya, and co-workers studied vanadium complexes with substituted benzene, $V_n(\text{arene})_m$ (arene = toluene, $C_6H_5CH_3$, and fluorobenzene, C_6H_5F) [59] and their mononuclear anions $V(\text{arene})_m^-$ ($m = 1, 2$) [60], as well as $Sc(C_6H_5CH_3)_m^-$ ($m = 1, 2$) [61], and demonstrated that the arene's electron-donating or electron-withdrawing property shifts the energy levels of its valence orbitals that affect the production efficiency of these clusters. Although

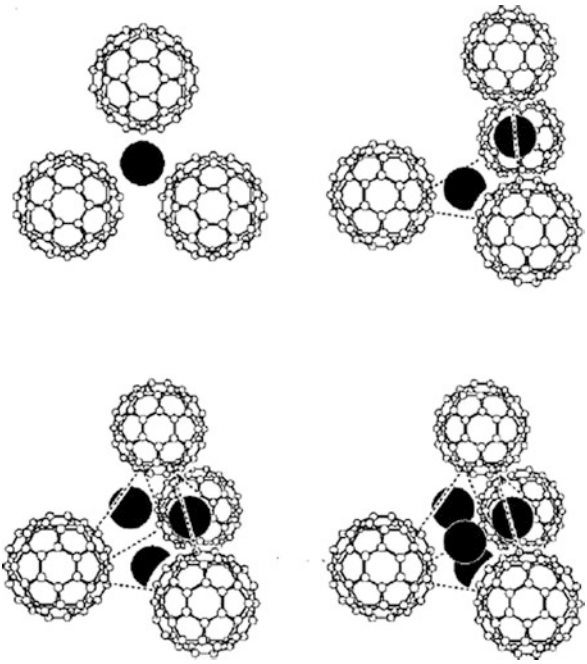

Fig. 8.9 Proposed face-centered structures for $M_n(C_{60})_m$ (M = Cr, Fe, Co, and Ni). (Reprinted with permission from Ref. [11]. Copyright 2000 American Chemical Society)

electrostatic interactions might partly contribute to the bonding of the ion-molecule complexes, these studies reinforced that the orbital interactions between the metal *d* and Bz π electrons are responsible for the M-Bz bonding in the M_nBz_m clusters.

It is then postulated that the stability of the M-Bz sandwich formation is balanced by the antibonding character resulting from the orbital interactions. The simplest examples are mononuclear MBz_2 clusters, the structures of which are described with the 18-electron rule in the same manner as those of metallocenes. While $CrBz_2$ satisfies the 18-electron rule by filling its bonding (e_{2g}) and nonbonding (a_{1g}) orbitals, MBz_2 clusters with the late transition metals of M = Mn to Ni violate the rule due to the excess 3*d* electrons that should occupy the antibonding orbitals with e^*_{1g} symmetry. It is known that such extra electrons in the e^*_{1g} orbitals induce a Jahn-Teller instability which may distort the sandwich structure from the highest (D_{6h} or D_{6d} in case of MBz_2) symmetry to a lower one to remove the degeneracy [20]. This effect lowers the M-Bz binding energy compared to that of a M-M bond in case of multinuclear complexes, leading to the rice-ball formation for the late transition metals rather than the multiple-decker sandwich formation. In the rice-ball structures, m_{max} is governed not only by electronic but also by geometric factors, and it is basically lower than the value expected from the total number of valence electrons, as the steric hindrance between Bz molecules becomes more crucial at large *n* [48].

In contrast, all the transition metals of M = Sc to Cr allow MBz_2 complexes which have no more than 18 valence electrons, but the production efficiency of

the multiple-decker sandwich clusters is quite metal-dependent, as depicted in Fig. 8.6. Yasuike et al. [62] demonstrated that the sandwich formation is affected not only by a thermodynamic but also by a kinetic factor, where the formation process governs the reactivity rather than the thermodynamic stability of the reaction products does. In particular, the spin multiplicity of the system has been proven to be an important guideline in understanding the reactivity of transition metal ions [63]. They carried out quantum chemical calculations to determine the most preferable spin states for reactant and product clusters in the cluster growth process of $M_nBz_{n+1} + M \rightarrow M_{n+1}Bz_{n+1}$ ($n = 1, 2$), where M = Ti, V, and Cr. According to the calculation results, both $CrBz_2$ and Cr_2Bz_2 preferred a singlet state, whereas the ground state of a Cr atom is septet [64]. This means that multiple-step nonadiabatic (i.e., spin-flip) transitions are needed for the growth from $CrBz_2$ to Cr_2Bz_2 as the overall reactant system ($CrBz_2 + Cr$) does not conserve its total spins during the reaction. By contrast, the calculation results estimated the lowest-energy state of V_2Bz_2 to be either a singlet or triplet, which is close in energy to each other. VBz_2 was determined to be a doublet while the ground state of a V atom is a quartet [64]. Therefore, spin flipping is not required for the transition from $VBz_2 + V$ to the triplet-state V_2Bz_2. The reaction barrier arising from the spin conservation rule explains the absence of Cr_2Bz_2 and larger clusters, while the efficient production of V_nBz_{n+1} is likely due to spin conservation in the cluster growth process.

8.3 Electronic and Magnetic Properties of Transition Metal-Benzene Sandwich Clusters

8.3.1 Physical Properties of Low-Dimensional Materials

It has been known that properties of materials which have low-dimensional (i.e., zero-, one-, and two-dimensional, hereafter 0D, 1D, and 2D, respectively) structures are different from those of three-dimensional (3D) materials such as bulk materials [65]. For instance, fullerenes, carbon nanotubes, and graphene (Fig. 8.10) are regarded as typical low-dimensional materials that are distinguished from graphite. There has been tremendous interest in extraordinary electron motion and resulting unique electronic properties originating from the low dimensionality of these materials. In fact, conductivity of carbon nanotubes has been a stimulating subject, since it was shown that nanotubes with a certain chirality (i.e., degree of twist) exhibit dramatically high conductivity [66–67]. It is understood that electron transport in the nanotubes is an anisotropic phenomenon in which different periodic boundary conditions are applied depending on the chirality [68]. Likewise, low-dimensional magnetism has gathered continuous attention since the discovery of the first single-molecule magnet (SMM), which exhibited magnetic hysteresis of a pure molecular origin [69]. Mn-containing SMMs have been studied for decades because the high-spin ($3d^5 4s^2$) configuration of a Mn atom is advantageous

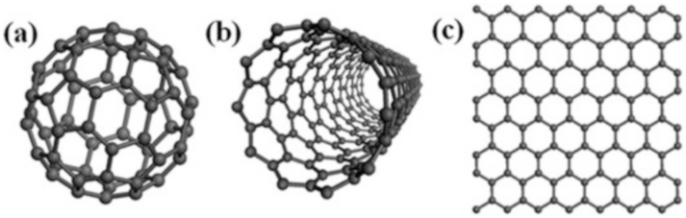

Fig. 8.10 Typical structures of (**a**) fullerene, (**b**) carbon nanotube, and (**c**) graphene as representatives for 0D, 1D, and 2D materials, respectively. (Reproduced from Ref. [79] with permission from the Royal Society of Chemistry)

for maximizing the spin multiplicity of SMMs. However, it is noted that better performing SMMs, with a large energy barrier to magnetic relaxation, require not only a high-spin ground state but also a large magnetic anisotropy. Such SMMs have often been achieved by strategic choices of bridging ligands that induce effective exchange interactions with a large anisotropy in the metal-ligand system [70–73]. Recently, 1D polymer chains called single-chain magnets (SCMs) have been demonstrated to show magnetic properties analogous to those of 0D SMMs [74–75]. These electronic and magnetic properties of low-dimensional materials have also motivated lots of studies aimed at their technological applications for molecule-based semiconductors [76], spintronics devices [77–78], energy storage media [76], high-density information storage devices [77], and so on.

8.3.2 Low Dimensionality of Transition Metal-Benzene Sandwich Clusters

The design of functional nanomaterials benefits more and more from a bottom-up approach that utilizes clusters as building blocks. Dimensionality plays an important role in defining the properties of nanomaterials. The controlled assembly of clusters facilitates the fabrication of materials with tailored dimensionality, that is, with tailored functionality [45, 80–81]. In order to explore, identify, and tune the functionality via the bottom-up approach, on the other hand, it is essential to understand the intrinsic properties of clusters themselves.

At this point, transition metal-Bz sandwich clusters can be ideal building blocks for low-dimensional functional nanomaterials. For instance, mononuclear MBz and MBz_2 clusters are regarded as motifs for organic surface-supported metal atoms, the magnetic moments of which have been of great interest [82]. Pandey et al. [83–84] calculated magnetic moments for MBz and MBz_2 complexes (M = Sc-Ni) and showed that the first and second Bz molecules differently interact with the electrons of the M atom. According to the calculation result, some MBz complexes (M = Sc, Ti, and V) have a high magnetic moment. The second Bz addition quenches the

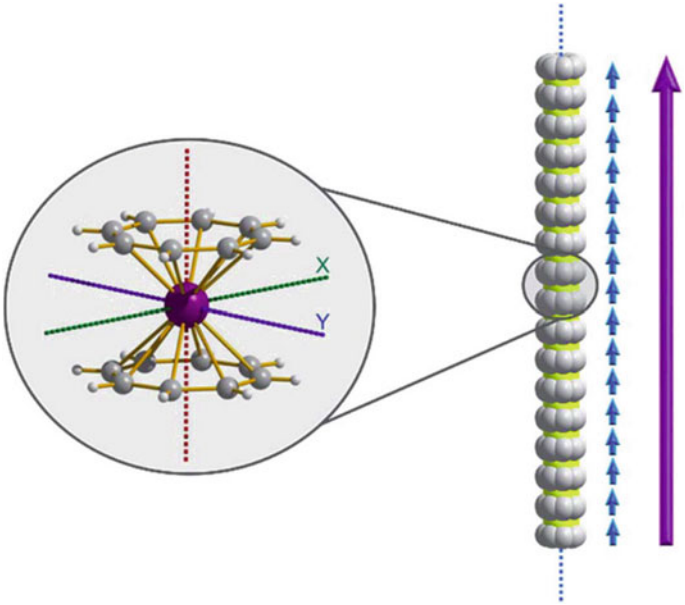

Fig. 8.11 A hypothesized chain-like arrangement of $M(COT)_2$ monomers with uniaxial magnetic anisotropy, illustrating the concept of modular design of SCMs. The axial anisotropy of each monomer is depicted as blue vectors, and the vector addition of the monomeric axial anisotropies yields the net axial anisotropy (purple). (Reproduced from Ref. [86] with permission from the Royal Society of Chemistry)

electron spins of MBz, and one unpaired electron remains in the odd-electron systems of $ScBz_2$ and VBz_2. Indeed, the electron paramagnetic resonance (EPR) measurement by Elschenbroich et al. [85] confirmed that VBz_2 derivatives which have an interannular bridge are paramagnetic with a spin multiplicity of $2S + 1 = 2$. Moreover, multiple-decker sandwich clusters can be viewed as single atomic chains, where an important question should be addressed how the electron spins of each metal atom interact with those of each other. It is hypothesized that a modular design of SCMs may be feasible if each $M(COT)_2$ monomer with uniaxial magnetic anisotropy is aligned along with the primary (z) axis (Fig. 8.11) [86]. The Stern-Gerlach experiment [87] carried out by Miyajima et al. [88–90] provided direct insights into magnetic properties of multiple-decker sandwich clusters. Importantly, the experiment reported that the magnetic moments of V_nBz_{n+1} monotonically increased with increasing cluster size (Fig. 8.12). In contrast, the magnetic moments of Co_nBz_m clusters, measured in the same manner, showed a quenching effect with increasing n and m [91]. This difference somewhat illustrates that the multiple-decker formation can stabilize the ferromagnetic ordering of the electron spins contained on metal atoms.

Recent advances in theoretical chemistry and computer resources have allowed computations of geometric and electronic structures of even large, multinuclear

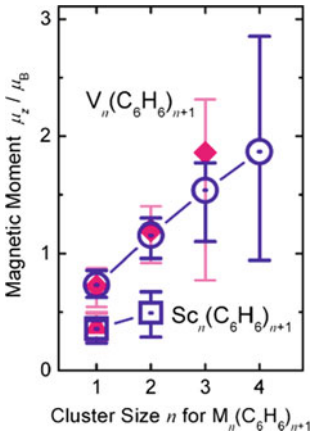

Fig. 8.12 Magnetic moments μ_z for V_nBz_{n+1} clusters measured by the Stern-Gerlach experiment. Those for Sc_nBz_{n+1} are also plotted. Open circles/squares indicate the magnetic moments determined at ~150 K, whereas filled diamonds indicate the magnetic moments at room temperature. (Reprinted with permission from Ref. [90]. Copyright 2007 American Chemical Society)

transition metal-Bz clusters. Kandalam et al. [92] employed density functional theory (DFT) to optimize the structures for V_nBz_{n+1} clusters up to $n = 3$. Upon comparison of the total energies between the sandwich and rice-ball V_2Bz_3 clusters, they confirmed that the sandwich formation was lower in energy than the rice-ball cluster at any possible spin multiplicity. In addition, the simulated spin multiplicities of V_nBz_{n+1} ($n = 1$–3) exhibited a linear increase, in agreement with the experiment described above. Shortly after this work, Wang et al. [93] extended calculations up to V_5Bz_6 and confirmed the size evolution of magnetic moment in this size range. They also reported that, regardless of cluster size and the position of the atom, each V atom possesses a magnetic moment of slightly larger than 1 Bohr magneton (μ_B). In contrast, each Bz molecule has a small negative magnetic moment. This counterbalancing illustrates that not only VBz_2 but also each VBz unit has a magnetic moment of 1 μ_B, resulting in the size-dependent increase of the total magnetic moment. On the other hand, rice-ball Co_nBz_m clusters such as $(n, m) = (3, 3)$ and (4, 4) have been calculated to have antiferromagnetic nature [94], which does not contradict their small magnetic moments determined in the experiment [91]. Furthermore, various infinite sandwich wires composed of metal atoms and arene molecules have been theoretically investigated [95–105]. Particularly, early works simulated the density of states in the V-Bz wire and proposed that the V-Bz wire is a half-metallic ferromagnet [95–99], where only one spin channel is metallic owing to the insulating band gap in the opposite spin channel (see Fig. 8.13). Such half metallicity of the sandwich wires has made metal-organic sandwich complexes promising candidates for organic spintronics, where the spin-polarized signal can be mediated and controlled by organic molecules in a 1D wire form. It should be noted that, in terms of their electronic and magnetic properties, organic half metals are especially useful for organic spintronics, because 100% spin polarization transportation is then available.

Despite the successes of these computational studies, it should be emphasized that, for many theories including the widely used DFT, there is still room for

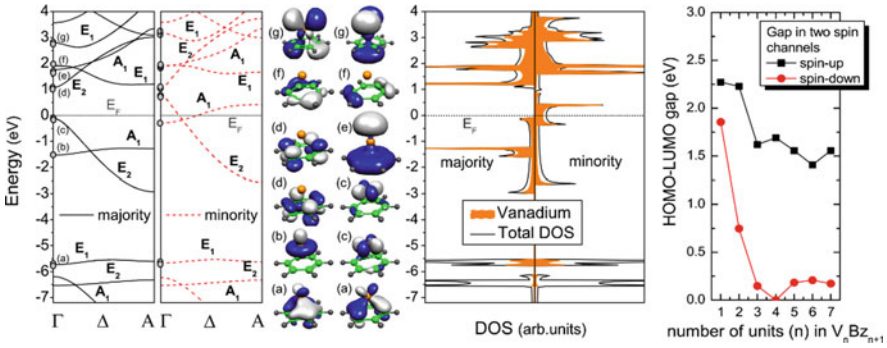

Fig. 8.13 The calculated spin-resolved band structure (left plot) and the DOS (plot in the middle) of the V-Bz wire in the ferromagnetic phase. The labels at the band structure refer to crystalline orbitals of the wire calculated for the Γ point, which are depicted on the right of the plot. The right panel shows values of the HOMO-LUMO gap in two spin channels for V_nBz_{n+1} as a function of n. (Reproduced from Ref. [97] with permission from the American Physical Society)

improvement in the reliability of magnetic moments and other spin-dependent properties [106–108]. In fact, the DFT methods for even small organometallic systems have the specific problem that the spin multiplicity of a global minimum structure depends on the employed functional. Recently, the quantum Monte Carlo (QMC) method has offered accurate calculations for spin-dependent properties of VBz [106] and V_nBz_{n+1} ($n = 1$–3) [109] systems. Such higher-level theories, however, are much computationally demanding and are not universally applicable when compared to the DFT. Here, combining computational methods with experiments is an effective approach. Quantum chemical calculations provide various kinds of simulated action spectra that are structure- and electronic state-dependent. Through the comparison between simulated and experimental spectra, the correctness of the calculations can be verified within a reasonable level of theory. In this way, the calculation results, which show the same fingerprints as the experiments do, give information on plausible structures and electronic and magnetic properties.

For the electronic and magnetic characterization of transition metal-Bz sandwich clusters, notable progress has indeed been made by joint experimental and theoretical studies. The details and outcomes of these studies are described in the following subsections.

8.3.3 Laser Spectroscopic Studies of Transition Metal-Benzene Sandwich Clusters

Among physical quantities that give direct insights into the valence electronic structure of a molecule, ionization energy (IE) and electron affinity (EA) are of particular importance. IE reflects the energy level of the highest occupied

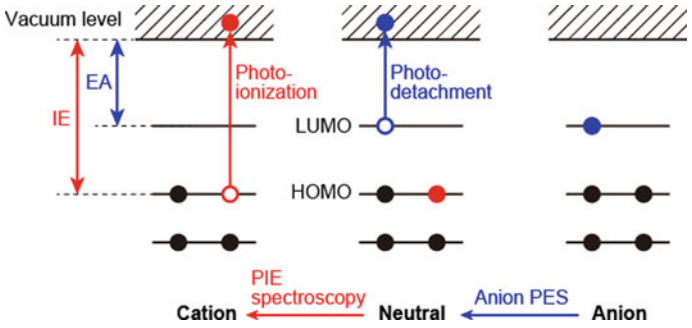

Fig. 8.14 Schemes of photoionization efficiency (PIE) spectroscopy and anion photoelectron spectroscopy (PES). Filled circles represent electrons that occupy valence orbitals. The HOMO and LUMO stand for those of the neutral state. For simplicity, the neutral is a singlet state with a closed-shell configuration, and it is assumed that there is no significant relaxation of the electronic structure during the electronic transitions

molecular orbital (HOMO), whereas EA is related to the energy level of the lowest unoccupied molecular orbital (LUMO). Experimental IE and EA values for a cluster are accessible by gas-phase laser spectroscopies. Photoionization efficiency (PIE) spectroscopy measures PIE as a function of photon energy. The PIE curve exhibits an onset whose energy gives the IE value for the neutral. Anion photoelectron spectroscopy (PES) estimates the binding energy of the excess electron of an anion by measuring the kinetic energy of the photoelectron (photodetached electron, PE). Within the limits of Koopmans' theorem, the observed photoelectron originates from the LUMO of the neutrals, which is occupied for the corresponding anions, so the EA of the neutral is obtained in this way. The energetic relationship between IE and EA is depicted in Fig. 8.14, along with the schemes of PIE spectroscopy and anion PES.

The PIE curves have been measured for V_nBz_{n+1} sandwich clusters with up to $n = 5$, showing that the IE monotonically decreased with increasing cluster size, as depicted in Fig. 8.15 [43, 110]. For larger clusters with $n \geq 4$, the PIE measurements also determined second lowest IEs that reflect the ionization from the next HOMO (HOMO – 1). The second lowest IEs exhibited a similar decrease seen for the lowest IEs [110]. Yasuike and Yabushita [111] employed the extended Hückel molecular orbital method to compute electronic structures of V_nBz_{n+1} clusters. Like those of ferrocene, the valence orbitals computed for V_nBz_{n+1} are classified into three types in terms of symmetry matching. dδ orbitals, which are combinations of the $3d_{xy}$ or $3d_{x^2-y^2}$ orbitals of V atoms and their symmetry-matching π orbitals of Bz molecules, form a quasi-band electronic structure as shown in Fig. 8.16, resulting in a monotonic decrease in IE with an increasing number of n. Importantly, the calculated IEs for V_nBz_{n+1} agreed well with the experimental values from the PIE spectra, thus reinforcing the theory employed in the calculations. In a general sense, such IE decrease has been known as a common phenomenon in multiple-decker

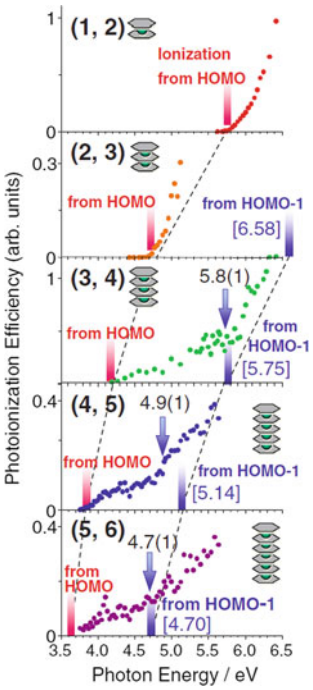

Fig. 8.15 Photoionization efficiency (PIE) spectra of V_nBz_m for $(n, m) = (1, 2)$ to (5, 6). The first onset corresponds to the ionization energy (IE) for removing an electron from the HOMO. As well as the first onset, a second ionization onset was observed as the change of slope in the PIE curves of (3, 4), (4, 5), and (5, 6) to be 5.8 ± 0.1, 4.9 ± 0.1, and 4.7 ± 0.1 eV, respectively. The second onsets represent second lowest IE that can be explained by ionization processes from the next HOMO (HOMO – 1). The onsets predicted by the quasi-band electronic structure are also shown in brackets. (Reproduced from Ref. [45] with permission from the Chemical Society of Japan)

structures of M_nBz_{n+1} (M = Sc, Ti, and V) [48], as it was not observed for other species such as Co_nBz_m that prefers a rice-ball structure at large n [46–48].

On the other hand, Judai et al. [60–61] conducted their pioneering works by applying anion PES to transition metal-arene complex anions. A magnetic bottle-type PE spectrometer was used in their experimental setup (shown in Fig. 8.17), as PEs can be collected at high efficiency in this method. Their PE spectra for mononuclear VBz^- and derivatives, $V(arene)^-$ (arene = toluene, $C_6H_5CH_3$, and fluorobenzene, C_6H_5F), taken with 355 nm (3.49 eV) laser radiation, are shown in Fig. 8.18. In the figure, the horizontal axis corresponds to electron binding energy (EBE), which is defined as EBE = $h\nu$ – EKE, where $h\nu$ is a photon energy of the detachment laser and EKE is an electron kinetic energy. Each arrow indicates the threshold binding energy, which corresponds to the upper limit of EA. The binding energy at each peak center represents a vertical detachment

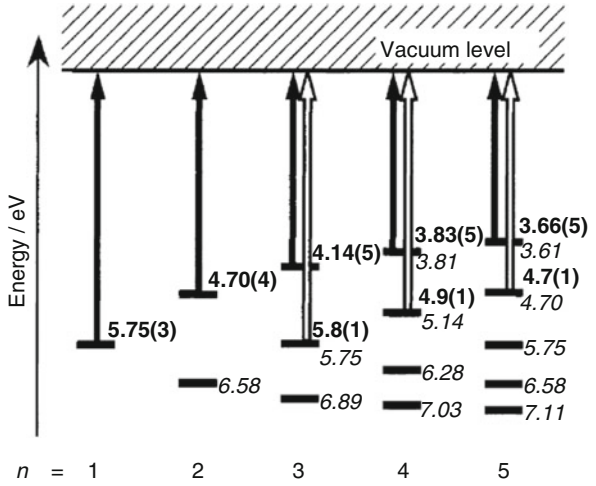

Fig. 8.16 Quasi-band electronic structure of valence orbitals of V_nBz_{n+1}. Bold-faced numbers indicate experimental values in eV with uncertainties in parentheses; 5.75(3) represents 5.75 ± 0.03 eV. Calculated values obtained by the simple Hückel model are given in italics. Solid and open arrows indicate the lowest and the second lowest ionization processes from each HOMO and HOMO – 1, respectively. They also correspond to the ionization processes observed in the PIE spectra of Fig. 8.15, respectively. (Reprinted with permission from Ref. [110]. Copyright 2002 American Chemical Society)

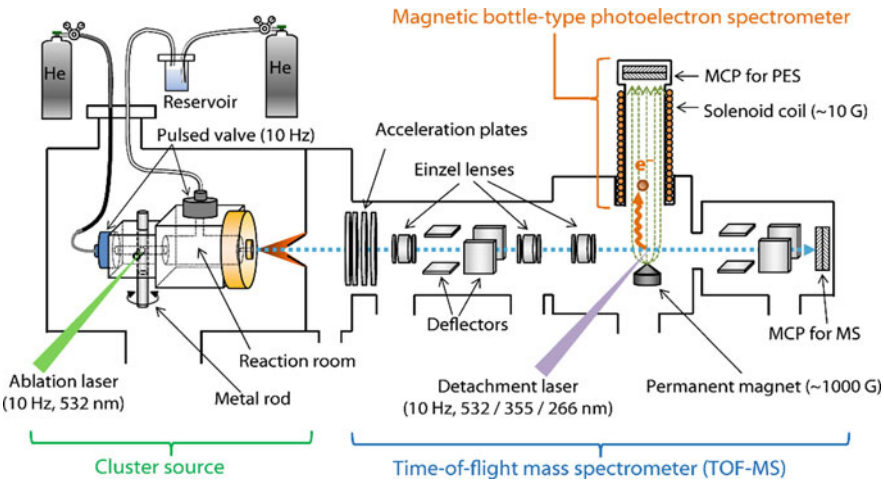

Fig. 8.17 An experimental setup for anion PES equipped with a time-of-flight mass spectrometer for metal-organic cluster anions. Lasers, valves, and high-voltage electronic pulses are controlled by a digital delay generator

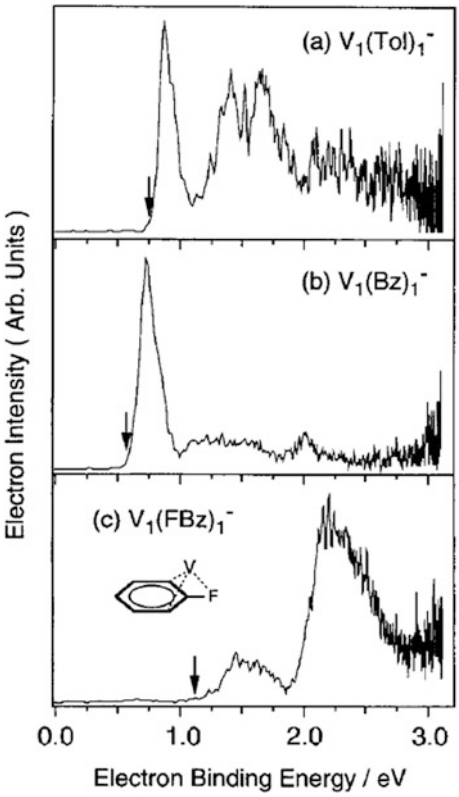

Fig. 8.18 Anion PE spectra of (**a**) $V(C_6H_5CH_3)^-$, (**b**) VBz^-, and (**c**) $V(C_6H_5F)^-$ taken with 355 nm (3.49 eV) radiation. Vertical arrows indicate onset energies. In (**c**), the presumed structure for $V(C_6H_5F)^-$ is shown. (Reprinted from Ref. [60] with permission from Elsevier)

energy (VDE), at which the geometry of the cluster anion is unchanged during the photodetachment process. The broadness of the peak reflects the Franck-Condon overlap between the vibrational ground state of the anion and that of the corresponding neutral. For example, the sharp and intense peaks in Fig. 8.18a, b show that $V(C_6H_5CH_3)^-$ and VBz^-, respectively, do not significantly change their structures upon photodetachment. This spectral feature is often ascribed to possible photodetachment from a nonbonding orbital electron at the anionic state. Indeed, the molecular orbital diagram of VBz^- showed that the HOMO of the anion is a nonbonding orbital with a_1 symmetry [60]. By contrast, $V(C_6H_5F)^-$ exhibited a broad feature in its PE spectrum (Fig. 8.18c). It is thus conceivable that its structure (see the inset of Fig. 8.18c) may be somewhat different from the half-sandwich structures of VBz^- and $V(C_6H_5CH_3)^-$. Another interesting feature is the lack of VBz_2^- in the mass spectrum. The molecular orbital theory showed that both of the HOMO and LUMO of VBz_2 are nonbonding orbitals. The absence of VBz_2^- is thus ascribed to the negative EA of VBz_2, meaning that the excess electron does not lower the energy of VBz_2^-.

8.3.4 *Joint Anion Photoelectron and Computational Studies of Vanadium-Benzene Sandwich Clusters and Their Anions*

The interplay between anion PES and theory, as described in Sect. 8.3.3, is especially powerful to study clusters both at anionic and neutral states. However, applications of this method for transition metal-Bz sandwich clusters were somewhat limited due to difficulty in preparing anions of the transition metal-Bz clusters. Despite their successful work on VBz^-, Judai et al. did not investigate multinuclear $V_nBz_m^-$ anions. Their mass spectrum (Fig. 8.19a) showed some dehydrogenation products with no presence of $V_nBz_m^-$ with $n \geq 2$ and $m \geq 2$.

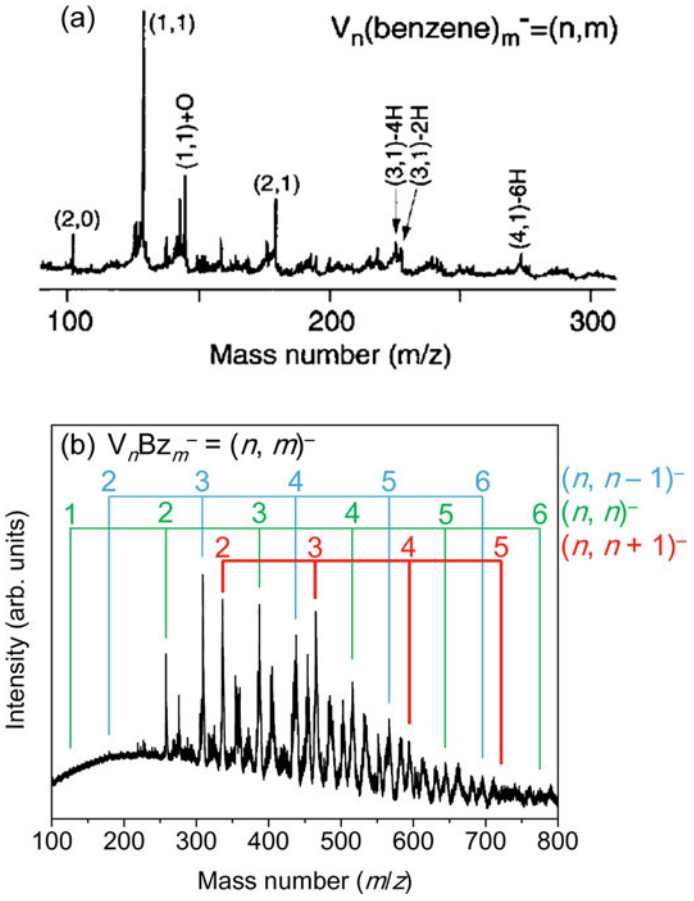

Fig. 8.19 Mass spectra of $V_nBz_m^-$ cluster anions measured by (**a**) Judai et al. [60] and (**b**) Masubuchi et al. [113] The maximum stagnation pressures of He carrier gas used for cluster production were 10 bar and 50 bar for (**a**) and (**b**), respectively. (**a**) was reprinted from Ref. [60] with permission from Elsevier and (**b**) from Ref. [113] with the permission of AIP Publishing

The dehydrogenation channels may be characteristic of transition metal-Bz cluster ions as they have also been found in the reaction of V_n^+ with deuterated benzene (C_6D_6), where deuterium-poor clusters $V_nC_6D_k^+$ ($k = 0, 2, 4$) were detected [112]. Nevertheless, we recently succeeded in the gas-phase synthesis of $V_nBz_m^-$ anions without dehydrogenated species [113]. In the mass spectrum of Fig. 8.19b, the peaks of $V_nBz_m^-$ are denoted by the notation $(n, m)^-$, and the number above each peak indicates the number of V atoms, n. $V_nBz_{n+1}^-$ ($n \geq 2$) and some other kinds of anions such as $V_nBz_{n-1}^-$ ($n \geq 2$) and $V_nBz_n^-$ ($n \geq 1$) are the most abundant, though the other peaks are assigned to $V_nBz_m^-$ combined with oxygen or water molecules. We adopted a high-pressure Even-Lavie pulsed valve [114] to load He carrier gas at a stagnation pressure of 50 bar, which is approximately five times higher than that in the former experiments (~10 bar at maximum). The Even-Lavie valve is known to generate cold molecules whose rotational temperature is even lower than 1 K [114]. It is thus reasonable that such high pressure promotes further cooling down of $V_nBz_m^-$ anions to avoid unwanted dehydrogenation.

The joint anion PE and computational method was first employed for Bz-rich the anionic series of $V_nBz_{n+1}^-$ ($n \geq 2$), henceforth $(n, n+1)^-$ [113]. The question in this study was whether $V_nBz_{n+1}^-$ anions exhibit multiple-decker structures with high-spin characteristics in common with the corresponding neutrals. The PE spectra for $(n, n+1)^-$ ($n = 2$–5), taken with various photon energies, are shown in Fig. 8.20. The 532 nm spectra in Fig. 8.20a–d, having a better resolution at a particular EBE than that with larger photon energy, exhibit a monotonic increase of EA with increasing cluster size, as indicated by the vertical arrows. On the other hand, the EAs of $(n, n+1)$ ($n = 1$–5) were calculated by means of the DFT, where all the possible spin multiplicities of the neutrals and anions were assessed. The EA of VBz_2 was calculated to be negative, in agreement with the work by Judai et al. [60] Moreover, the calculated EAs at $n = 2$–5, marked by the vertical lines in Fig. 8.20a–d, showed the best matches with the experimental EAs when the lowest-energy $V_nBz_{n+1}^-$ anions were featured by monotonically increasing spin multiplicities denoted as $2S + 1 = n$.

The DFT calculations also give optimized geometries, molecular orbital energy levels, and HOMO and LUMO pictures of the neutrals and anions, as displayed in Fig. 8.21a, b, respectively. For the neutrals, both the HOMOs and LUMOs belong to the minority spin. At $n = 1$–3, the HOMOs are degenerate dδ orbitals, while the LUMOs are nonbonding dσ orbitals that are mostly composed of the $3d_z^2$ orbitals of the V atoms. At $n = 4$ and 5, on the other hand, the Jahn-Teller effect lowers the D_{6h} symmetry of the multiple-decker structure, as described previously by Wang et al. [93] This also removes the degeneracy of the dδ orbitals. Because of their close energies, the dδ and dσ orbitals are hybridized, making the orbital pictures a bit complicated. However, this minor effect does not change the persistent multiple-decker formation with the ferromagnetic spin ordering even at larger n. For the anions, the comparison between Fig. 8.21a, b reveals that, except mononuclear singlet $(1, 2)^-$, the $(n, n+1)^-$ anions have ferromagnetic multiple-decker sandwich structures similarly to the corresponding $(n, n+1)$ neutrals. The excess electron occupies a dσ orbital for $n = 1$–3, a hybridized orbital consisting of dδ and dσ for

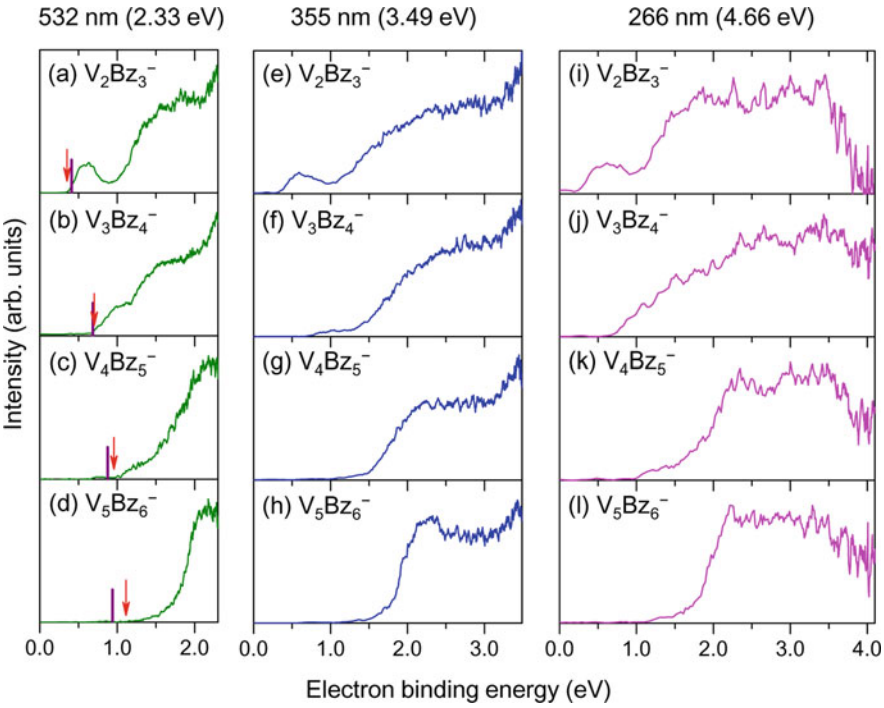

Fig. 8.20 Anion PE spectra of $V_nBz_{n+1}^-$ ($n = 2$–5) clusters taken with (**a**–**d**) 532 nm (2.33 eV), (**e**–**h**) 355 nm (3.49 eV), and (**i**–**l**) 266 nm (4.66 eV) radiation. Vertical arrows indicate the onsets of the spectra corresponding to the 532 nm spectra, while vertical lines indicate the calculated adiabatic EA values of the neutral species. (Reprinted from Ref. [113], with the permission of AIP Publishing)

$n = 4$, and again a dσ orbital for $n = 5$, all of which are delocalized along with the V atoms one-dimensionally. Importantly, for both the neutrals and anions, both the HOMOs and LUMOs belong to the minority spin, and the HOMO-LUMO gap with the majority spin is much larger than that with the minority spin irrespective of n, as plotted in the insets of Fig. 8.21. Our results not only are consistent with the former studies which have theoretically discussed the neutral V_nBz_{n+1} system [93, 97–98] but also include new experimental insights into the anionic system that can be produced during electron transport. Taken together, it can be expected that, when carrying current through a V_nBz_{n+1} cluster coupled to two electrodes, only one direction of spin will be transportable in the V_nBz_{n+1} system, hopefully leading to future spintronic applications of these sandwich clusters.

The unique electronic characteristics of $(n, n+1)^{0/-}$ (neutral and anion) clusters, as described above, originate from their one-dimensional structures. Thus, it would be interesting to determine whether eliminating Bz would change the multiple-decker sandwich structures and, more importantly, the electronic properties of such clusters. Therefore, we also acquired anion PE spectra of $V_nBz_n^-$ ($n = 1$–5),

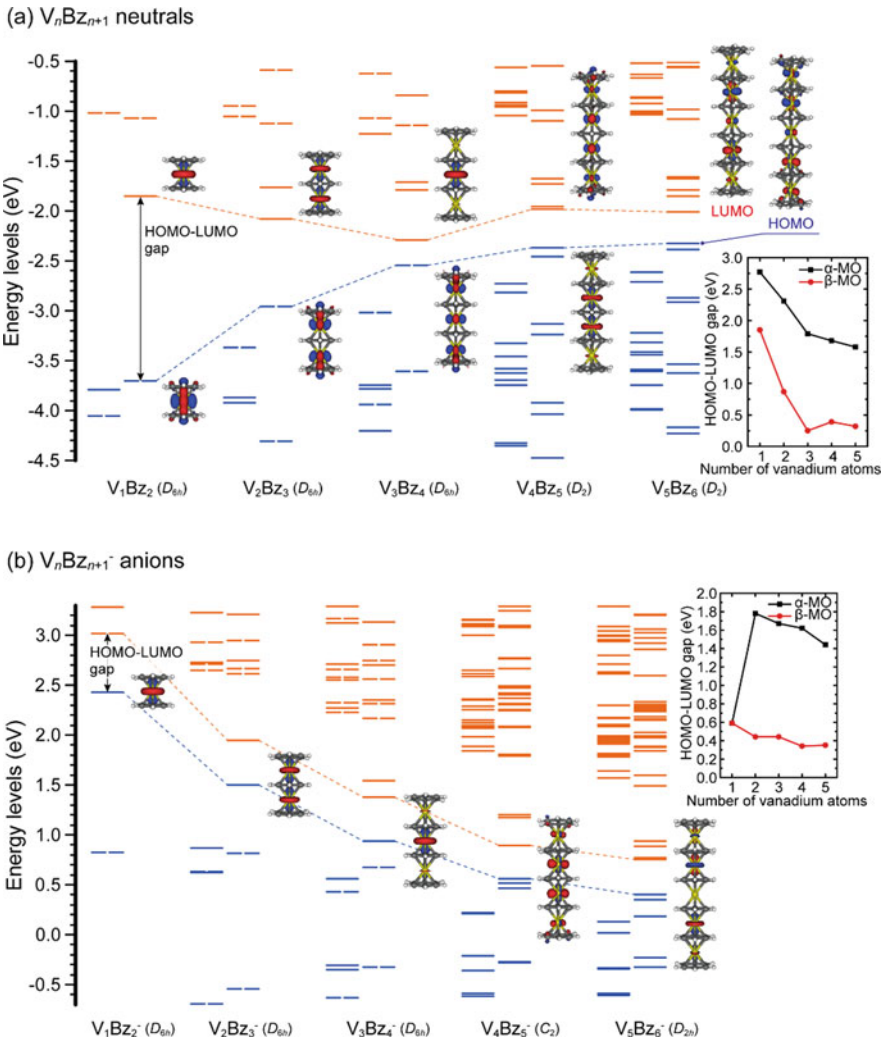

Fig. 8.21 The molecular orbital energy levels and the HOMOs and LUMOs of the lowest-energy geometries of (**a**) V_nBz_{n+1} neutrals and (**b**) $V_nBz_{n+1}^-$ anions ($n = 1$–5). The α (majority spin)-MO (left) and β (minority spin)-MO (right) are separately depicted for each cluster. The values of the HOMO-LUMO gaps in the two spin directions as a function of n is shown in the inset. (Reprinted from Ref. [113], with the permission of AIP Publishing)

henceforth $(n, n)^-$, and $V_nBz_{n-1}^-$ ($n = 2$–5), denoted as $(n, n-1)^-$. The EA for each cluster was obtained in the same manner as those for $(n, n+1)$ and plotted against n in Fig. 8.22. It can clearly be seen from the figure that, in the range of $n \geq 3$, the EAs for (n, n) and $(n, n-1)$ monotonically increased with increasing n and converged on the EA of $(n, n+1)$. Taken into account that the monotonic

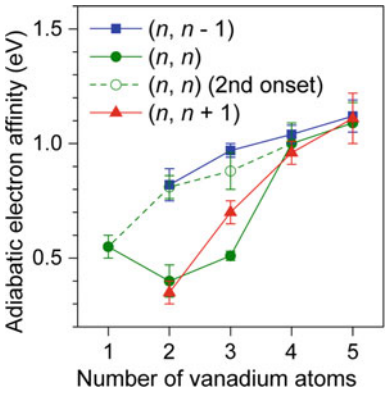

Fig. 8.22 Experimental EAs for V_nBz_m ($n = 1$–5, $m = n - 1$, n, and $n + 1$) as a function of n. The threshold energies of the second peaks in the PE spectra for V_2Bz_2 and V_3Bz_3 were determined by Gaussian fitting and are called the "second onset" and marked using open circles (°) connected with a dashed line. The connecting lines are provided to guide the eye. (Reprinted from Ref. [115], with the permission of AIP Publishing)

increase in the EA for $(n, n + 1)$ is attributable to the delocalized orbital along with the V atoms formation, EA would only be a function of n if the same number of V atoms were stacked alternately in a sandwich fashion. Indeed, similar AEAs were found for the clusters with $n = 4$ and 5 and different m values, thus suggesting that $(n, n - 1)^{0/-}$ and $(n, n)^{0/-}$ can also have one-dimensional sandwich structures with similar electronic configurations.

At $n = 1$–3, on the other hand, EA is dependent on both n and m. The non-monotonic variation in the EA between the (1, 1), (2, 2), and (3, 3) clusters was of particular interest because it implied that there may be structural isomers of these clusters. Figure 8.22 also indicates "second onsets" for (2, 2) and (3, 3), obtained by deconvoluting the PE spectra (for $(2, 2)^-$ shown in Fig. 8.23a, b) through a Gaussian fitting technique. Interestingly, the second onsets do not hint at possible excited states but at the presence of higher-lying isomers of the anions, as they disappeared under a different experimental (Bz-poor) condition (Fig. 8.23b). In fact, our DFT calculations found three and two isomers for (2, 2) and its anion, respectively, as displayed in Fig. 8.23c, d. The dimer sandwiches **1** and **4** have the lowest spin states, while the alternating sandwiches **2**, **3**, and **5** favor high-spin multiplicities that originate from the V atoms. Comparison between experimental and calculated EAs and VDEs assigned the first and second peaks, labeled (i) and (ii) in the PE spectrum of Fig. 8.23a, to **4** and **5**, respectively, showing the coexistence of the two isomers for $(2, 2)^-$. It is conceivable that, due to their "packed" structures, the non-alternating sandwich clusters such as **1** and **4** could limit their growth process, making alternating sandwiches major at larger n. The multiple-decker sandwich formation of $V_nBz_m{}^{0/-}$ regardless of $m = n + 1$, n, and $n - 1$ could extend its technological use because $V_nBz_{n+1}{}^{0/-}$ clusters do not lose their electronic and magnetic character via elimination/modification of their terminal Bz molecules.

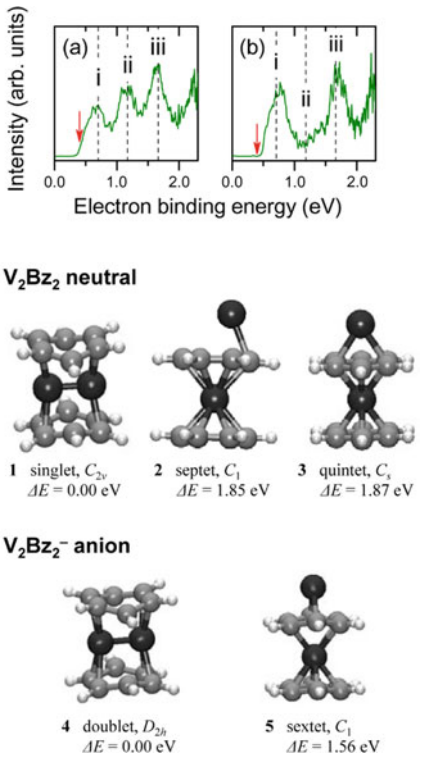

Fig. 8.23 (**a**, **b**) show PE spectra for $V_2Bz_2^-$ acquired using 532 nm radiation under relatively benzene-poor and benzene-rich conditions, respectively. The EBEs at the vertical arrows and the dashed lines (labeled *i–iii*) correspond with the experimental EAs and VDEs, respectively. The amount of Bz introduced into our apparatus could be qualitatively controlled by changing the pulse duration (by controlling the pulsed valve). (**c**, **d**) display low-lying isomers of the V_2Bz_2 and its anionic clusters, respectively, with their spin states, symmetries, and relative energies. (Reprinted from Ref. [115], with the permission of AIP Publishing)

8.3.5 *Multiple-Decker and Ring Sandwich Formation of Manganese-Benzene Cluster Anions*

In Sects. 8.3.3 and 8.3.4, we described our research on the electronic and magnetic characteristics of $V_nBz_m^{0/-}$ ($m = n - 1$, n, and $n + 1$) multiple-decker sandwich clusters. Our finding further motivates such characterization of multiple-decker sandwich clusters containing different metal atoms. Indeed, several theoreticians have predicted that an infinite Mn-Bz sandwich wire would have half metallicity that surpasses that of a V-Bz wire [96, 100]. However, several transition metals (M = Cr, Mn, and Cu) had never produced any larger clusters than mononuclear MBz_2 in the reaction with benzene, as stated in Sect. 8.3.3. Nevertheless, we reported a joint anion PES and theoretical study on $Mn_nBz_m^-$ cluster anions, hereafter denoted $(n, m)^-$ [116]. In this subsection, we unveil unprecedented structures and electromagnetic properties of $(n, n)^-$ cluster anions, which in turn are quite different from those predicted in the former studies [96, 100].

In order to produce $(n, m)^-$ anions, we used the same laser vaporization source as described in Sect. 8.3.4. Figure 8.24 shows the mass spectrum for produced anions, indicating that various $(n, m)^-$ anions were generated without dehydrogenation. It is understood that efficient cooling in clustering reactions led to the complete $(n, m)^-$

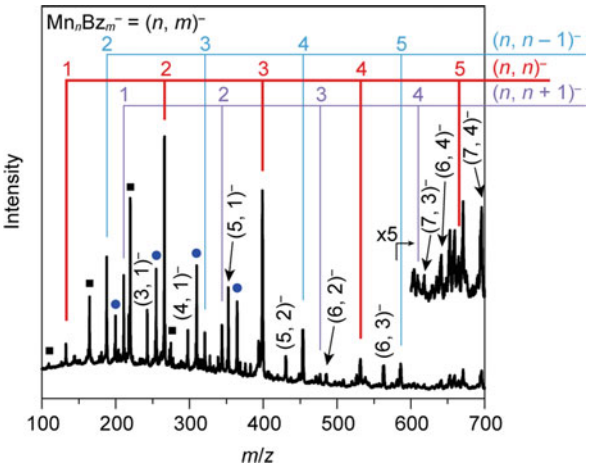

Fig. 8.24 Mass spectrum of $Mn_nBz_m^-$. The peak assignments for $(n, m)^- = (n, n-1)^-$, $(n, n)^-$, and $(n, n+1)^-$ are indicated with vertical lines. Several dominant $(n, m)^-$ clusters with $m \leq n-2$ are also labeled. Coexistent naked Mn_n^- clusters and incomplete Mn-Bz cluster anions are marked by ■ and •, respectively. (Reproduced from Ref. [116] with permission from the Royal Society of Chemistry)

formation, as we discussed for the case of $V_nBz_m^-$ clusters. Anion PE spectra taken for $(n, n)^-$ clusters (n = 1–5) are displayed in Fig. 8.25a. Our DFT calculations revealed unprecedented tilted sandwich structures for all $(n, n)^-$ studied (see **1**, **2a**, **3a**, **4**, and **5** in Fig. 8.25b) in contrast to linear sandwich chains assumed in the former studies [96, 100]. The PE spectra can be assigned to the tilted clusters though isomers **2b** and **3b** could also contribute to the spectra for n = 2 and 3, as were seen in the case of V_2Bz_2 and V_3Bz_3. Interestingly, the tilted form exhibits size evolution of its spin multiplicity that is even higher than that of $V_nBz_{n+1}^{0/-}$; for example, $Mn_5Bz_5^-$ (**5**) has a spin state of $2S + 1 = 17$, while multiple-decker $V_5Bz_6^-$ is a quartet. Such high-spin states of $Mn_nBz_n^-$ are accounted for by three unpair electrons (i.e., 1 dσ and 2 dπ electrons) in each Mn(η^6-Bz) unit that is further η^2-bound to each other in the structures of **3a**, **4**, and **5**.

The tilted sandwich structures of $Mn_nBz_n^-$ addressed another question whether or not the size evolution of the $Mn_nBz_n^-$ is terminated at the finite number n, in contrast to the linear V-Bz system. Indeed, a couple of ring-structured $Mn_{18}Bz_{18}^{-/0}$ were computationally anticipated as it was estimated from the extrapolation of the structures **3a**, **4**, and **5** that cyclization of $Mn_nBz_n^-$ occurs at n = 18. Our structure optimization of $Mn_{18}Bz_{18}$ starting from a C_{18h} geometry obtained a neutral structure with perfect C_{18h} symmetry, as shown in Fig. 8.26a, when assuming a spin state of $2S + 1 = 55$. This structure has a pretty large negative spin density ($\rho_s = -0.52$) for each Bz and the positive spin density of $\rho_s = 3.52$ per a Mn atom. Likewise, the anionic $Mn_{18}Bz_{18}^-$ was determined to be C_2 symmetric with a spin state of $2S + 1 = 54$. In both cases, the calculations on the neighboring spin states found higher energies or even met convergence problems within C_{18h} or C_2 symmetry. In fact, the spin state of the anionic $Mn_{18}Bz_{18}^-$ is well consistent with the extrapolation from those of $Mn_nBz_n^-$ (n = 1–5), as shown in Fig. 8.26b.

We further highlight the unique electromagnetic properties of $Mn_{18}Bz_{18}$ cluster. The valence orbitals in the majority (α) spin part of the neutral $Mn_{18}Bz_{18}$ are

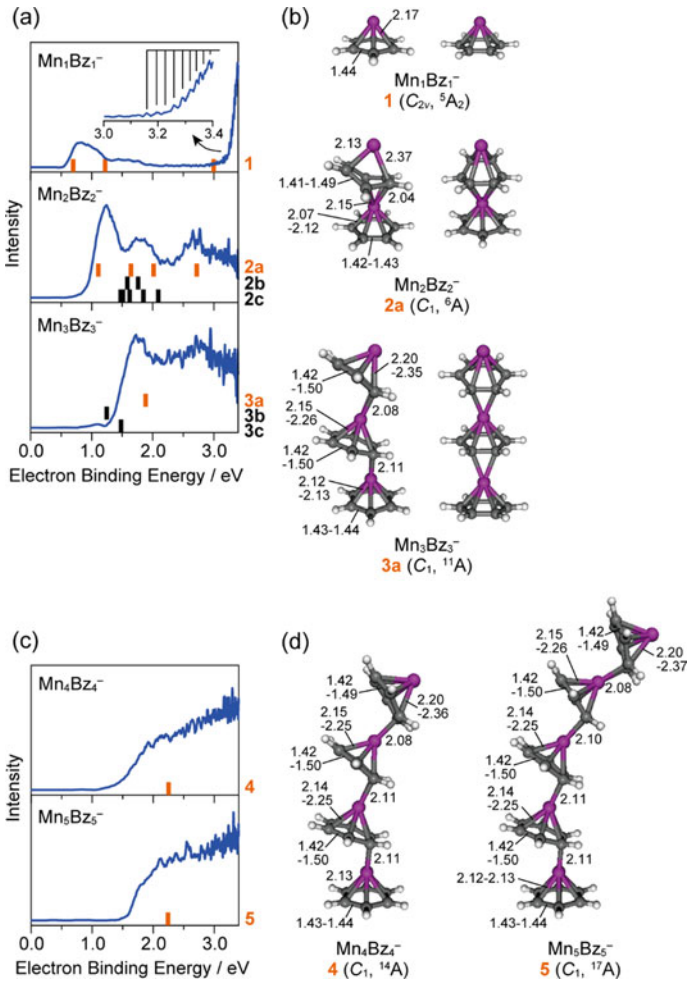

Fig. 8.25 (**a**) Anion PE spectra for $Mn_nBz_n^-$ ($n = 1$–5) taken with 355 nm (3.49 eV) radiation. The calculated VDEs of the plausible structures are indicated below the spectra with vertical bars. Bold-faced labels right to the VDE bars are denoted to identify the structures. (**b**) The most plausible structures for $Mn_nBz_n^-$ ($n = 1$–5) with their symmetries and electronic states. Typical bond lengths are indicated in Å. (Reproduced from Ref. [116] with permission from the Royal Society of Chemistry)

displayed in Fig. 8.27a. The α-HOMO has a delocalized bonding character and can be divided into contributions from the α-HOMOs of each quartet-state MnBz unit (inset of Fig. 8.27a). The degenerate α-HOMO − 1 and α-HOMO − 2, and other orbitals (6 sets of degenerate and 1 nondegenerate) with the α spin are isomorphous to the α-HOMO. Interestingly, each delocalized $Mn_{18}Bz_{18}$ orbital allows us to define the number of its orbital nodes k, analogously to π conjugated hydrocarbon

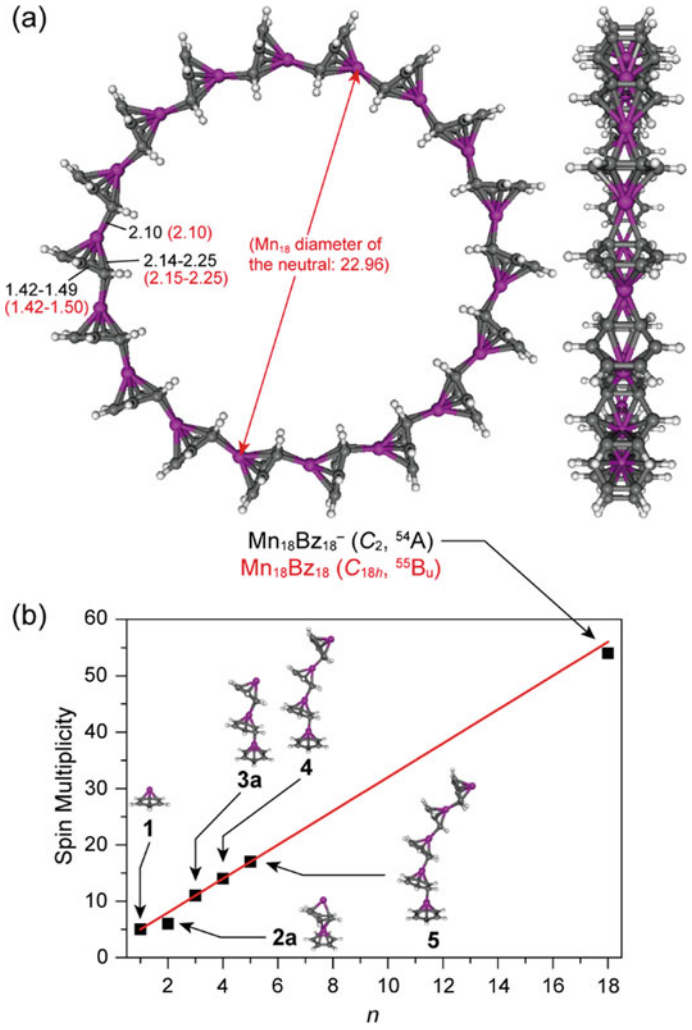

Fig. 8.26 (**a**) Top and side views of the optimized structures for $Mn_{18}Bz_{18}^{-/0}$ ring clusters with their symmetries and electronics states. Typical bond length are indicated in Å (those of the neutral are given in parentheses). (**b**) Side-dependent spin multiplicities of $Mn_nBz_n^-$ ($n = 1$–5 and 18). The linear extrapolation of the spin multiplicities for tilted multiple-decker sandwich structures is expressed by the red line. (Reproduced from Ref. [116] with permission from the Royal Society of Chemistry)

systems. Compared to [18]annulene ($C_{18}H_{18}$), which has an 18-membered ring structure with 18π electrons (Fig. 8.27b), particularly unusual for $Mn_{18}Bz_{18}$ is that the smaller number of nodes is rather associated with the energetically higher orbital.

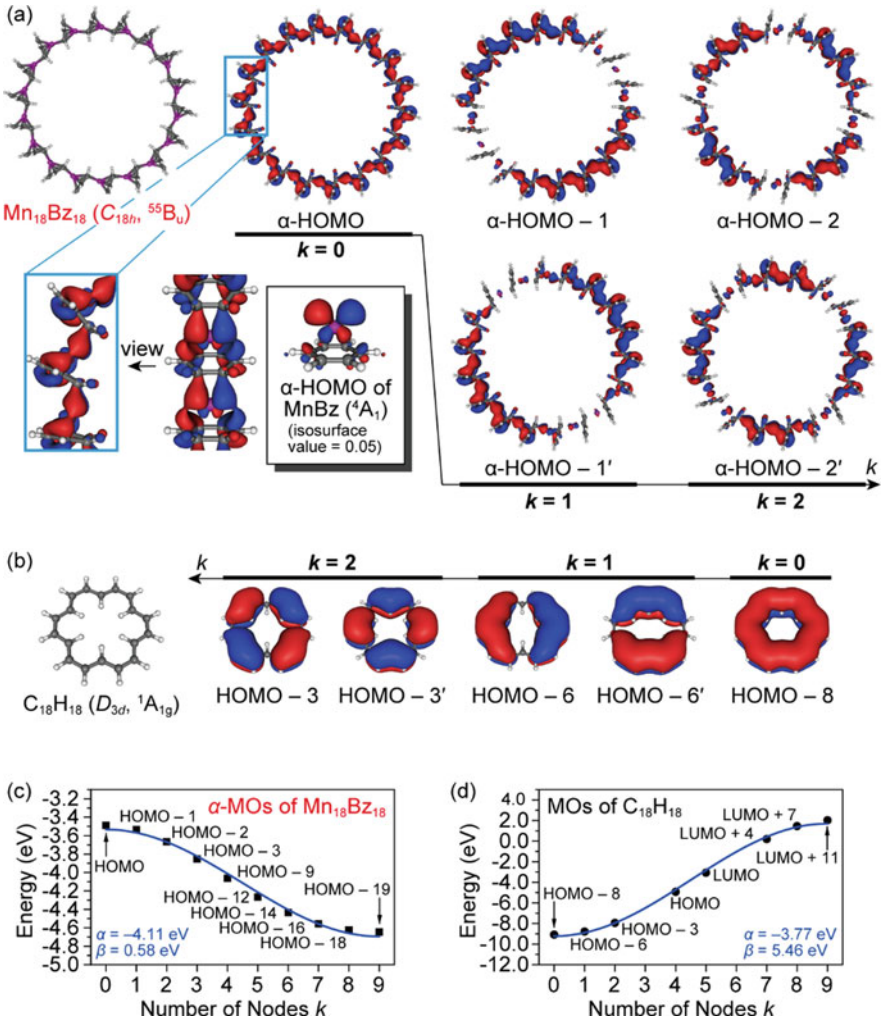

Fig. 8.27 (**a**) Valence orbital pictures in the majority (α) spin part of the neutral $Mn_{18}Bz_{18}$ cluster. The number of nodes k is given for each delocalized orbital. Inset shows top and side views of the partially magnified α-HOMO. The isosurface value of 0.01 was adopted unless otherwise noted. (**b**) Orbital pictures of [18]annulene ($C_{18}H_{18}$) with an isosurface value = 0.01, having the same k values as depicted in (**a**) for comparison. (**c**) Orbital energies plotted against k for the $Mn_{18}Bz_{18}$ α-HOMO and lower-lying isomorphous orbitals, and (**d**) those for the $C_{18}H_{18}$ orbitals composed of delocalized π electrons. Blue curves are obtained by a curve-fitting analysis using Eq. (8.1). (Reproduced from Ref. [116] with permission from the Royal Society of Chemistry)

For an intelligible explanation of such delocalized electron systems, we use a simple Hückel model: for cyclic conjugated systems, each molecular orbital energy ε_k is given as

$$\varepsilon_k = \alpha + 2\beta \cos\left(\frac{2\pi}{N}k\right) \qquad \left(0 \leq k \leq \frac{N}{2}\right) \tag{8.1}$$

where the Hückel parameters α and β are employed. The number of basis functions N is set to 18 in both cases of $Mn_{18}Bz_{18}$ and $C_{18}H_{18}$, in which fragment (or atomic) orbitals of each MnBz and C are treated, respectively. To apply this model, orbital energies were plotted against k and fit by Eq. (8.1); namely, the plots for the $Mn_{18}Bz_{18}$ α-HOMO and lower-lying isomorphous orbitals are shown in Fig. 8.27c. The same analysis was done for the $C_{18}H_{18}$ orbitals as plotted in Fig. 8.27d. From the figure, the simple Hückel model can describe the $Mn_{18}Bz_{18}$ plot but claims a positive β which contrasts the conventional cases (with a negative β) as demonstrated for $C_{18}H_{18}$. Taken into consideration that β in general is not significantly affected by two-electron repulsive interactions, the positive β of $Mn_{18}Bz_{18}$ may originate from its strong intra-atomic exchange interactions within the Mn $3d$ electrons. In fact, former studies [90, 111, 117] have explained that the intra-atomic exchange interactions within the metal $3d$ orbitals induce localized positive and negative spin densities on each metal atom and Bz molecule, respectively. The ferromagnetic spin ordering of multiple-decker V_nBz_{n+1} is stabilized by this spin localization, and that of $Mn_{18}Bzn_{18}{}^{-/0}$ may also be explained in the same manner. Although to date it has not been characterized experimentally, $Mn_{18}Bz_{18}$, having the planar (i.e., 2D) ring structure, could be exploited for applications in future nanoscale electronics and spintronics.

8.4 Conclusions and Outlook

In this chapter, we first wrote a brief history of organometallic sandwich complexes starting from the discovery of ferrocene. We then described enormous contributions on the gas-phase synthesis and spectroscopic characterization for transition metal sandwich complexes. Our particular focus among them was on the formation and electromagnetic properties of transition metal-benzene sandwich clusters. In the reaction with benzene, early transition metals (Sc, Ti, and V) form multiple-decker metal-benzene sandwich clusters, where metal atoms and benzene molecules are piled up alternately. This multiple-decker formation was confirmed by means of laser spectroscopies and quantum chemical calculations. The multiple-decker clusters of V_nBz_{n+1} exhibit a linear increase of their magnetic moment with increasing the cluster size. The interplay between anion photoelectron spectroscopy and theoretical calculations revealed that such magnetic behavior is attributed to the ferromagnetic spin ordering of $3d$ electrons localized at each metal atom. Interestingly, these unique structural and electronic features of V_nBz_{n+1} do not change either upon electron attachment which generates the corresponding anions ($V_nBz_{n+1}{}^-$) or, in case of $n \geq 4$, even upon elimination of a terminal benzene

molecule that yields $V_nBz_m^{0/-}$ ($m = n - 1$ and n). Furthermore, we described our recent research that studied a new family of manganese-benzene cluster anions, $Mn_nBz_n^-$, which were found to exhibit unprecedented multiple-decker structures with a tilted Mn-Bz stacking and a monotonically increasing behavior of their high-spin multiplicities.

Lastly, we herein refer to several studies that are aimed at the controlled assembly of transition metal-benzene sandwich clusters. For the functionalization of such clusters, a promising route is to assemble the clusters on surfaces with certain hierarchical nanostructures and tailored dimensionality. However, the fabrication of cluster-based assemblies on surfaces requires a deposition technique that allows clusters to be deposited softly onto a surface, as clusters may be dissociated upon impact. In addition, a deep understanding of the cluster-surface interaction is crucial because cluster structures are often perturbed by a strong interaction with surfaces. To this end, Judai et al. [60, 118] adopted a soft-landing technique to deposit VBz_2^+ cluster cations into a low-temperature Ar matrix with precise control of deposition energy. The Ar matrix was chosen as it is known to serve as a buffer dissipating the kinetic energy of the projectile clusters and keeping the cluster largely intact [119–120]. Nagaoka et al. later deposited VBz_2^+ [121], $V_2Bz_3^+$ [122], and $Cr(aniline)_2^+$ cations [123] onto alkanethiolate self-assembled monolayers (SAMs). Infrared reflection absorption spectroscopy (IRAS) confirmed that, on both the substrates, the deposited clusters are neutralized and maintain sandwich structures. While the use of Ar matrix is limited to cryogenic temperature conditions, SAMs can support the sandwich clusters even at room temperature. In addition, the sandwich clusters can be highly oriented on the SAMs. Very recently, Huttmann et al. [124] synthesized europium-cyclooctatetraene (Eu-COT) nanowires on a graphene substrate, where the nanowires are found to be lying parallel to each other. Scanning tunneling spectroscopy (STS) and low-temperature X-ray magnetic circular dichroism (XMCD) revealed that the Eu-COT wire is a ferromagnetic insulator [125]. These immobilization methods, together with spectroscopic applications and theoretical approaches, can readily provide a direct route to investigate the low-dimensional functionality of transition metal-benzene sandwich clusters on a substrate. As such, functionalized sandwich clusters will open up possibilities for exploiting themselves as new building blocks in future molecular electronics and spintronics.

Acknowledgments We are grateful to Prof. S. Yabushita (Keio University), Dr. T. Iwasa (Hokkaido University), and Prof. K. Kanoda (The University of Tokyo) for fruitful discussion. This work is partly supported by the program of Exploratory Research for Advanced Technology (ERATO) in Japan Science and Technology Agency (JST) entitled with "Nakajima Designer Nanocluster Assembly Project" and by JSPS KAKENHI of Grant-in-Aids for Scientific Research (A) Grant Number 15H02002. The computations were partly performed using Research Center for Computational Science, Okazaki, Japan.

References

1. R.P. Feynman, There's plenty of room at the bottom. Caltech Eng. Sci. **23**, 22–36 (1960)
2. R. Kubo, Electronic properties of metallic fine particles. I. J. Phys. Soc. Jpn. **17**, 975–986 (1962)
3. W.A. de Heer, The physics of simple metal clusters: Experimental aspects and simple models. Rev. Mod. Phys. **65**, 611–676 (1993)
4. B. von Issendorff, O. Cheshnovsky, Metal to insulator transitions in clusters. Annu. Rev. Phys. Chem. **56**, 549–580 (2005)
5. M. Brack, The physics of simple metal clusters: Self-consistent jellium model and semiclassical approaches. Rev. Mod. Phys. **65**, 677–732 (1993)
6. U. Heiz, U. Landman (eds.), *Nanocatalysis* (Springer, Berlin, 2007)
7. H. Haberland (ed.), *Clusters of Atoms and Molecules II: Solvation and Chemistry of Free Clusters, and Embedded, Supported and Compressed Clusters* (Springer, Berlin, 1994)
8. B.M. Smirnov, R.S. Berry, *Phase Transitions of Simple Systems* (Springer, Berlin, 2008)
9. M. Mitsui, A. Nakajima, Photoelectron Spectroscopy of Organic Clusters, in *Handbook of Nanophysics*, (CRC Press, Boca Raton, 2010)
10. R.H. Crabtree, *The Organometallic Chemistry of the Transition Metals*, 5th edn. (Wiley, Hoboken, 2016)
11. A. Nakajima, K. Kaya, A novel network structure of organometallic clusters in the gas phase. J. Phys. Chem. A **104**, 176–191 (2000)
12. T.J. Kealy, P.L. Pauson, A new type of organo-Iron compound. Nature **168**, 1039–1040 (1951)
13. G. Wilkinson, M. Rosenblum, M.C. Whiting, R.B. Woodward, The structure of iron Biscyclopentadienyl. J. Am. Chem. Soc. **74**, 2125–2126 (1952)
14. E.O. Fischer, W. Pfab, Cyclopentadien-Metallkomplexe, ein neuer Typ metallorganischer Verbindungen. Z. Naturforsch. B **7**, 377–379 (1952)
15. J.W. Lauher, R. Hoffmann, Structure and chemistry of bis(cyclopentadienyl)-MLn complexes. J. Am. Chem. Soc. **98**, 1729–1742 (1976)
16. E.O. Fischer, R. Jira, Di-cyclopentadienyl-kobalt(II). Z. Naturforsch. B **8**, 327–328 (1953)
17. E.O. Fischer, W. Hafner, Di-benzol-chrom. Z. Naturforsch. B **10**, 665–668 (1955)
18. A. Streitwieser, U. Müller-Westerhoff, Bis(cyclooctatetraeny1)uranium (Uranocene). A new class of sandwich complexes that utilize atomic f orbitals. J. Am. Chem. Soc. **90**, 7364 (1968)
19. N. Rösch, A. Streitwieser Jr., SCF-Xα scattered-wave MO study of thorocene and uranocene. J. Organomet. Chem. **145**, 195–200 (1978)
20. E.L. Muetterties, J.R. Bleeke, E.J. Wucherer, T. Albright, Structural, stereochemical, and electronic features of arene-metal complexes. Chem. Rev. **82**, 499–525 (1982)
21. E.O. Fischer, H.P. Kögler, Über Aromatenkomplexe von Metallen, IX. Di-Benzol-Vanadin(O). Chem. Ber. **90**, 250–255 (1957)
22. A. Salzer, H. Werner, A new route to triple-decker sandwich compounds. Angew. Chem. Int. Ed. **11**, 930–932 (1972)
23. W. Siebert, 2,3-Dihydro-1,3-diborole-metal complexes with activated C-H bonds: Building blocks for multilayered sandwich compounds. Angew. Chem. Int. Ed. **24**, 943–958 (1985)
24. H. Werner, New varieties of sandwich complexes. Angew. Chem. Int. Ed. **16**, 1–9 (1977)
25. M. Munakata, L.P. Wu, G.L. Ning, A new type of multilayer system–silver(I) complexes of polycyclic aromatic compounds. Coord. Chem. Rev. **198**, 171–203 (2000)
26. P.L. Timms, Chemistry of transition-metal vapours. Part I. reactions with trifluorophosphine and related compounds. J. Chem. Soc. A **1970**, 2526–2528 (1970)
27. P.S. Skell, L.D. Wescott, Chemical properties of C3, a dicarbene. J. Am. Chem. Soc. **85**, 1023–1023 (1963)
28. R. Middleton, J.R. Hull, S.R. Simpson, C.H. Tomlinson, P.L. Timms, Chemistry of transition-metal vapours. Part III. Formation of complexes with arenes, trifluorophosphine, and nitric oxide. J. Chem. Soc. Dalton Trans. **1**, 120–124 (1973)

29. P.L. Timms, R.B. King, Preparative applications of metal vapours obtained by evaporation of metal powders from coated filaments : A new preparation of dibenzene-ruthenium and observation of its limiting N.M.R. spectrum. J. Chem. Soc. Chem. Commun. **22**, 898–899 (1978)
30. W.M. Lamanna, Metal vapor synthesis of a novel triple-decker sandwich complex: (η_6-mesitylene)$_2$(μ-η_6:η_6-mesitylene)Cr_2. J. Am. Chem. Soc. **108**, 2096–2097 (1986)
31. R.E. Smalley, Laser studies of metal cluster beams. Laser Chem. **2**, 167–184 (1983)
32. P.M. Holland, A.W. Castleman, The thermochemical properties of gas-phase transition metal ion complexes. J. Chem. Phys. **76**, 4195–4206 (1982)
33. H. Higashide, T. Kaya, M. Kobayashi, H. Shinohara, H. Sato, Reactions of benzene clusters with metal ions as studied by the laser ablation—Molecular beam method: Observation of clustered complex ions $M(C_6H_6)_n^+$ ($n \geqslant 2$) and fragment complex ions $M(C_6H_6)(C_XH_Y)^+$ with $X \leqslant$ and $Y \leqslant 4$. Chem. Phys. Lett. **171**, 297–302 (1990)
34. C.S. Yeh, K.F. Willey, D.L. Robbins, J.S. Pilgrim, M.A. Duncan, Photodissociation spectroscopy of Mg^+H_2O. Chem. Phys. Lett. **196**, 233–238 (1992)
35. F. Misaizu, M. Sanekata, K. Fuke, S. Iwata, Photodissociation study on $Mg^+(H2O)_n$, n=1–5: Electronic structure and photoinduced intracluster reaction. J. Chem. Phys. **100**, 1161–1170 (1994)
36. K.F. Willey, P.Y. Cheng, K.D. Pearce, M.A. Duncan, Photoinitiated charge transfer and dissociation in mass-selected metalloorganic complexes. J. Phys. Chem. **94**, 4769–4772 (1990)
37. Y.-M. Chen, P.B. Armentrout, Collision-induced dissociation of $Ag(C_6H_6)^+$. Chem. Phys. Lett. **210**, 123–128 (1993)
38. F. Meyer, F.A. Khan, P.B. Armentrout, Thermochemistry of transition metal benzene complexes: Binding energies of $M(C_6H_6)x^+$ ($x = 1, 2$) for M = Ti to Cu. J. Am. Chem. Soc. **117**, 9740–9748 (1995)
39. S. Maruyama, L.R. Anderson, R.E. Smalley, Direct injection supersonic cluster beam source for FT-ICR studies of clusters. Rev. Sci. Instrum. **61**, 3686–3693 (1990)
40. P. Milani, W.A. de Heer, Improved pulsed laser vaporization source for production of intense beams of neutral and ionized clusters. Rev. Sci. Instrum. **61**, 1835–1838 (1990)
41. A. Nakajima, T. Kishi, T. Sugioka, Y. Sone, K. Kaya, Mass distributions of aluminum negative cluster ions and their binary cluster ions mixed with a carbon atom. Chem. Phys. Lett. **177**, 297–300 (1991)
42. S. Nonose, Y. Sone, K. Onodera, S. Sudo, K. Kaya, Structure and reactivity of bimetallic cobalt-vanadium (Co_nV_m) clusters. J. Phys. Chem. **94**, 2744–2746 (1990)
43. K. Hoshino, T. Kurikawa, H. Takeda, A. Nakajima, K. Kaya, Structures and ionization energies of sandwich clusters (V_n(benzene)$_m$). J. Phys. Chem. **99**, 3053–3055 (1995)
44. P. Weis, P.R. Kemper, M.T. Bowers, Structures and energetics of $V_n(C_6H_6)_m^+$ clusters: Evidence for a quintuple-decker sandwich. J. Phys. Chem. A **101**, 8207–8213 (1997)
45. A. Nakajima, Study on electronic properties of composite clusters toward nanoscale functional advanced materials. Bull. Chem. Soc. Jpn. **86**, 414–437 (2013)
46. T. Kurikawa, M. Hirano, H. Takeda, K. Yagi, K. Hoshino, A. Nakajima, K. Kaya, Structures and ionization energies of cobalt-benzene clusters (Co_n(benzene)$_m$). J. Phys. Chem. **99**, 16248–16252 (1995)
47. T. Kurikawa, H. Takeda, A. Nakajima, K. Kaya, Structures and stabilities of 3d-transition metal-benzene organometallic clusters. Z. Phys. D **40**, 65–69 (1997)
48. T. Kurikawa, H. Takeda, M. Hirano, K. Judai, T. Arita, S. Nagao, A. Nakajima, K. Kaya, Electronic properties of organometallic metal−benzene complexes [M_n(benzene)$_m$ (M = Sc−Cu)]. Organometallics **18**, 1430–1438 (1999)
49. Y. Huang, B.S. Freiser, Synthesis of Bis(buckminsterful1erene)nickel cation, $Ni(C_{60})_2^+$, in the gas phase. J. Am. Chem. Soc. **113**, 8186–8187 (1991)
50. Y. Basir, S.L. Anderson, Interaction of Mn^+ and Mn_2^+ with C_{60}. Exohedral and endohedral metal-fullerene bonding. Chem. Phys. Lett. **243**, 45–48 (1995)

51. A. Nakajima, S. Nagao, H. Takeda, T. Kurikawa, K. Kaya, Multiple dumbbell structures of vanadium–C_{60} clusters. J. Chem. Phys. **107**, 6491–6494 (1997)
52. T. Kurikawa, S. Nagao, K. Miyajima, A. Nakajima, K. Kaya, Formation of cobalt-C_{60} clusters: Tricapped $Co(C_{60})_3$ unit. J. Phys. Chem. A **102**, 1743–1747 (1998)
53. S. Nagao, T. Kurikawa, K. Miyajima, A. Nakajima, K. Kaya, Formation and structures of transition metal-C_{60} clusters. J. Phys. Chem. A **102**, 4495–4500 (1998)
54. B.P. Pozniak, R.C. Dunbar, Monomer and dimer complexes of coronene with atomic ions. J. Am. Chem. Soc. **119**, 10439–10445 (1997)
55. J.W. Buchanan, J.E. Reddic, G.A. Grieves, M.A. Duncan, Metal and multimetal complexes with polyaromatic hydrocarbons: Formation and photodissociation of Fe_x-$(Coronene)_y$ cations. J. Phys. Chem. A **102**, 6390–6394 (1998)
56. J.W. Buchanan, G.A. Grieves, J.E. Reddic, M.A. Duncan, Novel mixed ligand sandwich complexes: Competitive binding of iron with benzene, coronene, and C_{60}. Int. J. Mass Spectrom. **182–183**, 323–333 (1999)
57. N.R. Foster, G.A. Grieves, J.W. Buchanan, N.D. Flynn, M.A. Duncan, Growth and photodissociation of Cr_x-$(Coronene)_y$ complexes. J. Phys. Chem. A **104**, 11055–11062 (2000)
58. M.A. Duncan, A.M. Knight, Y. Negishi, S. Nagao, K. Judai, A. Nakajima, K. Kaya, Photoelectron spectroscopy of $V_x(Coronene)_y$ and $Ti_x(Coronene)_y$ anions. J. Phys. Chem. A **105**(44), 10093–10097 (2001)
59. M. Hirano, K. Judai, A. Nakajima, K. Kaya, Effect of ring substituents on formation rates for vanadium-arene clusters. J. Phys. Chem. A **101**, 4893–4899 (1997)
60. K. Judai, M. Hirano, H. Kawamata, S. Yabushita, A. Nakajima, K. Kaya, Formation of vanadium-arene complex anions and their photoelectron spectroscopy. Chem. Phys. Lett. **270**, 23–30 (1997)
61. K. Judai, Y. Nakamura, M. Tachibana, Y. Negishi, A. Nakajima, K. Kaya, Photoelectron spectroscopy of scandium-arene complex anions. Chem. Lett. **30**, 114–115 (2001)
62. T. Yasuike, A. Nakajima, S. Yabushita, K. Kaya, Why do vanadium atoms form multiple-decker sandwich clusters with benzene molecules efficiently? J. Phys. Chem. A **101**, 5360–5367 (1997)
63. P.B. Armentrout, Electronic state-specific transition metal ion chemistry. Annu. Rev. Phys. Chem. **41**, 313–344 (1990)
64. C.E. Moore, *Atomic Energy Levels* (National Bureau of Standards, Washington, DC, 1949)
65. J. Hu, T.W. Odom, C.M. Lieber, Chemistry and physics in one dimension: Synthesis and properties of nanowires and nanotubes. Acc. Chem. Res. **32**, 435–445 (1999)
66. J.W. Mintmire, B.I. Dunlap, C.T. White, Are fullereue tubules metallic? Phys. Rev. Lett. **68**, 631–634 (1992)
67. R. Saito, M. Fujita, G. Dresselhaus, M.S. Dresselhaus, Electronic structure of chiral graphene tubules. Appl. Phys. Lett. **60**, 2204–2206 (1992)
68. J.W.G. Wildöer, L.C. Venema, A.G. Rinzler, R.E. Smalley, C. Dekker, Electronic structure of atomically resolved carbon nanotubes. Nature **391**, 59–62 (1998)
69. D. Gatteschi, R. Sessoli, J. Villain, *Molecular Nanomagnets* (Oxford University Press, New York, 2006)
70. G.S. Papaefstathiou, A. Escuer, C.P. Raptopoulou, A. Terzis, S.P. Perlepes, R. Vicente, Defective double-cubane, tetranuclear manganese (II) and cobalt (II) complexes with simultaneous $\mu_{1,1}$-azido and μ-O bridges. Eur. J. Inorg. Chem. **6**, 1567–1574 (2001)
71. C. Dendrinou-Samara, M. Alexiou, C.M. Zaleski, J.W. Kampf, M.L. Kirk, D.P. Kessissoglou, V.L. Pecoraro, Synthesis and magnetic properties of a metallacryptate that behaves as a single-molecule magnet. Angew. Chem. Int. Ed. **42**, 3763–3766 (2003)
72. D.E. Freedman, W.H. Harman, T.D. Harris, G.J. Long, C.J. Chang, J.R. Long, Slow magnetic relaxation in a high-spin iron(II) complex. J. Am. Chem. Soc. **132**, 1224–1225 (2010)
73. F. Habib, O.R. Luca, V. Vieru, M. Shiddiq, I. Korobkov, S.I. Gorelsky, M.K. Takase, L.F. Chibotaru, S. Hill, R.H. Crabtree, M. Murugesu, Influence of the ligand field on slow magnetization relaxation versus spin crossover in mononuclear cobalt complexes. Angew. Chem. Int. Ed. **52**, 11290–11293 (2013)

74. R. Clérac, H. Miyasaka, M. Yamashita, C. Coulon, Evidence for single-chain magnet behavior in a Mn^{III}-Ni^{II} chain designed with high spin magnetic units: A route to high temperature metastable magnets. J. Am. Chem. Soc. **124**, 12837–12844 (2002)
75. W.-X. Zhang, R. Ishikawa, B. Breedlove, M. Yamashita, Single-chain magnets: Beyond the Glauber model. RSC Adv. **3**, 3772–3798 (2013)
76. R.H. Baughman, A.A. Zakhidov, W.A. de Heer, Carbon nanotubes—The route toward applications. Science **297**, 787–792 (2002)
77. M.H. Jo, J.E. Grose, K. Baheti, M.M. Deshmukh, J.J. Sokol, E.M. Rumberger, D.N. Hendrickson, J.R. Long, H. Park, D.C. Ralph, Signatures of molecular magnetism in single-molecule transport spectroscopy. Nano Lett. **6**, 2014–2020 (2006)
78. L. Bogani, W. Wernsdorfer, Molecular spintronics using single-molecule magnets. Nat. Mater. **7**, 179–186 (2008)
79. L. Ma, A.H.C. Hart, S. Ozden, R. Vajtaia, P.M. Ajayan, Spiers memorial lecture advances of carbon nanomaterials. Faraday Discuss. **173**, 9–46 (2014)
80. S.N. Khanna, P. Jena, Assembling crystals from clusters. Phys. Rev. Lett. **69**, 1664–1667 (1993)
81. S.A. Claridge, A.W. Castleman Jr., S.N. Khanna, C.B. Murray, A. Sen, P.S. Weiss, Cluster-assembled materials. ACS Nano **3**, 244–255 (2009)
82. P. Gambardella, S. Rusponi, M. Veronese, S.S. Dhesi, C. Grazioli, A. Dallmeyer, I. Cabria, R. Zeller, P.H. Dederichs, K. Kern, C. Carbone, H. Brune, Giant magnetic anisotropy of single cobalt atoms and nanoparticles. Science **300**, 1130–1133 (2003)
83. R. Pandey, B.K. Rao, P. Jena, J.M. Newsam, Unique magnetic signature of transition metal atoms supported on benzene. Chem. Phys. Lett. **321**, 142–150 (2000)
84. R. Pandey, B.K. Rao, P. Jena, M.A. Blanco, Electronic structure and properties of transition metal-benzene complexes. J. Am. Chem. Soc. **123**, 3799–3808 (2001)
85. C. Elschenbroich, E. Schmidt, R. Gondrum, B. Metz, O. Burghaus, W. Massa, S. Wocadlo, Metal π complexes of benzene derivatives. Germanium in the periphery of Bis(benzene)vanadium and Bis(benzene)chromium. Synthesis and structure of new heteram-etallocyclophanes. Organometallics **16**, 4589–4596 (1997)
86. J.M. Frost, K.L.M. Harriman, M. Murugesu, The rise of 3-d single-ion magnets in molecular magnetism: Towards materials from molecules? Chem. Sci. **7**, 2470–2491 (2016)
87. W. Gerlach, O. Stern, Das magnetische Moment des Silberatoms. Z. Phys. A **9**, 353–355 (1922)
88. K. Miyajima, A. Nakajima, S. Yabushita, M.B. Knickelbein, K. Kaya, Ferromagnetism in one-dimensional vanadium-benzene sandwich clusters. J. Am. Chem. Soc. **126**, 13202–13203 (2004)
89. K. Miyajima, M.B. Knickelbein, A. Nakajima, Stern-Gerlach studies of organometallic sandwich clusters. Eur. Phys. J. D. **34**, 177–182 (2005)
90. K. Miyajima, S. Yabushita, M.B. Knickelbein, A. Nakajima, Stern-Gerlach experiments of one-dimensional metal-benzene sandwich clusters: $M_n(C_6H_6)_m$ (M = Al, Sc, Ti, and V). J. Am. Chem. Soc. **129**, 8473–8480 (2007)
91. M.B. Knickelbein, Magnetic moments of bare and benzene-capped cobalt clusters. J. Chem. Phys. **125**, 044308-1–044308-7 (2006)
92. A.K. Kandalam, B.K. Rao, P. Jena, R. Pandey, Geometry and electronic structure of $V_n(Bz)_m$ complexes. J. Chem. Phys. **120**, 10414–10422 (2004)
93. J. Wang, P.H. Acioli, J. Jellinek, Structure and magnetism of V_nBz_{n+1} sandwich clusters. J. Am. Chem. Soc. **127**, 2812–2813 (2005)
94. X. Zhang, J. Wang, Structural, electronic, and magnetic properties of Co_n(benzene)$_m$ complexes. J. Phys. Chem. A **112**, 296–304 (2008)
95. M.M. Rahman, H. Kasai, E.S. Dy, Theoretical investigation of electric and magnetic properties of benzene–vanadium sandwich complex chain. Jpn. J. Appl. Phys. **44**, 7954–7956 (2005)
96. H. Xiang, J. Yang, J.G. Hou, Q. Zhu, One-dimensional transition metal−benzene sandwich polymers: Possible ideal conductors for spin transport. J. Am. Chem. Soc. **128**, 2310–2314 (2006)

97. V.V. Maslyuk, A. Bagrets, V. Meded, A. Arnold, F. Evers, M. Brandbyge, T. Bredow, I. Mertig, Organometallic benzene-vanadium wire: A one-dimensional half-metallic ferromagnet. Phys. Rev. Lett. **97**, 097201-1–097201-4 (2006)
98. Y. Mokrousov, N. Atodiresei, G. Bihlmayer, S. Heinze, S. Blügel, The interplay of structure and spin-orbit strength in the magnetism of metal-benzene sandwiches: From single molecules to infinite wires. Nanotechnology **18**, 495402-1–495402-12 (2007)
99. H. Weng, T. Ozaki, K. Terakura, Theoretical analysis of magnetic coupling in sandwich clusters $V_n(C_6H_6)_{n+1}$. J. Phys. Soc. Jpn. **77**, 014301-1–014301-9 (2007)
100. L. Shen, S.-W. Yang, M.-F. Ng, V. Ligatchev, L. Zhou, Y. Feng, Charge-transfer-based mechanism for half-metallicity and ferromagnetism in one-dimensional organometallic sandwich molecular wires. J. Am. Chem. Soc. **130**, 13956–13960 (2008)
101. L. Zhou, S.-W. Yang, M.-F. Ng, M.B. Sullivan, V.B.C. Tan, L. Shen, One-dimensional iron−cyclopentadienyl sandwich molecular wire with half metallic, negative differential resistance and high-spin filter efficiency properties. J. Am. Chem. Soc. **130**, 4023–4027 (2008)
102. L. Wang, Z. Cai, J. Wang, J. Lu, G. Luo, L. Lai, J. Zhou, R. Qin, Z. Gao, D. Yu, G. Li, W.N. Mei, S. Sanvito, Novel one-dimensional organometallic half metals: Vanadium-cyclopentadienyl, vanadium-cyclopentadienyl-benzene, and vanadium-anthracene wires. Nano Lett. **8**, 3640–3644 (2008)
103. X. Zhang, M.-F. Ng, Y. Wang, J. Wang, S.-W. Yang, Theoretical studies on structural, magnetic, and spintronic characteristics of sandwiched Eu_nCOT_{n+1} (n = 1-4) clusters. ACS Nano **3**, 2515–2522 (2009)
104. X. Zhang, Z. Tian, S.-W. Yang, J. Wang, Magnetic manipulation and half-metal prediction of one-dimensional bimetallic organic sandwich molecular wires $[CpTM_1CpTM_2]_\infty$ (TM_1 = Ti, Cr, Fe; TM_2 = Sc−Co). J. Phys. Chem. C **115**, 2948–2953 (2011)
105. X. Zhang, J. Han, Y. Liu, J. Wang, Structural, electronic, and magnetic properties of one-dimensional organic bimetal-naphthalene sandwich nanowires. J. Phys. Chem. C **116**, 5414–5419 (2012)
106. L. Horváthová, M. Dubecký, L. Mitas, I. Štich, Spin multiplicity and symmetry breaking in vanadium-benzene complexes. Phys. Rev. Lett. **109**, 053001-1–053001-5 (2012)
107. K.P. Kepp, Consistent descriptions of metal–ligand bonds and spin-crossover in inorganic chemistry. Coord. Chem. Rev. **257**, 196–209 (2013)
108. M. Kepenekian, J.-P. Gauyacq, N. Lorente, Difficulties in the ab initio description of electron transport through spin filters. J. Phys. Condens. Matter **26**, 104203-1–104203-8 (2014)
109. L. Horváthová, R. Derian, L. Mitas, I. Štich, Quantum Monte Carlo study of one-dimensional transition-metal organometallic cluster systems and their suitability as spin filter. Phys. Rev. B Condens. Matter **90**, 115414-1–115414-5 (2014)
110. K. Miyajima, K. Muraoka, M. Hashimoto, T. Yasuike, S. Yabushita, A. Nakajima, K. Kaya, Quasi-band electronic structure of V_n(benzene)$_{n+1}$ clusters. J. Phys. Chem. A **106**, 10777–10781 (2002)
111. T. Yasuike, S. Yabushita, Ionization energies and bonding scheme of multiple-decker sandwich clusters: $M_n(C_6H_6)_{n+1}$. J. Phys. Chem. A **103**, 4533–4542 (1999)
112. M.R. Zakin, D.M. Cox, R.O. Brickman, A. Kaldor, Benzene C-D bond activation by free vanadium cluster cations. J. Phys. Chem. **93**, 6823–6827 (1989)
113. T. Masubuchi, K. Ohi, T. Iwasa, A. Nakajima, Experimental and theoretical studies on the electronic properties of vanadium-benzene sandwich cluster anions, $V_nBz_{n+1}^-$ (n = 1-5). J. Chem. Phys. **137**, 224305-1–224305-9 (2012)
114. U. Even, J. Jortner, D. Noy, N. Lavie, C. Cossart-Magos, Cooling of large molecules below 1 K and He clusters formation. J. Chem. Phys. **112**, 8068–8071 (2000)
115. T. Masubuchi, T. Iwasa, A. Nakajima, Experimental and theoretical studies of the structural and electronic properties of vanadium–benzene sandwich clusters and their anions: $V_nBz_n^{0/-}$ (n = 1–5) and $V_nBz_{n-1}^{0/-}$ (n = 2–5). J. Chem. Phys. **141**, 214304-1–214304-8 (2014)
116. T. Masubuchi, T. Iwasa, A. Nakajima, Multiple-decker and ring sandwich formation of manganese–benzene organometallic cluster anions: $Mn_nBz_n^-$ (n = 1–5 and 18). Phys. Chem. Chem. Phys. **18**, 26049–26056 (2016)

117. A. Goto, S. Yabushita, Theoretical study on the spin states and intra-cluster spin relaxation of the one-dimensional metal–benzene sandwich clusters: $M_2(C_6H_6)_3$ (M = Sc, Ti, V). Chem. Phys. Lett. **454**, 382–386 (2008)
118. K. Judai, K. Sera, S.-i. Amatsutsumi, K. Yagi, T. Yasuike, S. Yabushita, A. Nakajima, K. Kaya, A soft-landing experiment on organometallic cluster ions: Infrared spectroscopy of V(benzene)$_2$ in Ar matrix. Chem. Phys. Lett. **334**, 277–284 (2001)
119. H.-P. Cheng, U. Landman, Controlled deposition, soft landing, and glass formation in nanocluster-surface collisions. Science **260**, 1304–1307 (1993)
120. K. Bromann, C. Félix, H. Brune, W. Harbich, R. Monot, J. Buttet, K. Kern, Controlled deposition of size-selected silver nanoclusters. Science **274**, 956–958 (1996)
121. S. Nagaoka, T. Matsumoto, E. Okada, M. Mitsui, A. Nakajima, Room-temperature isolation of V(benzene)$_2$ sandwich clusters via soft-landing into *n*-Alkanethiol self-assembled monolayers. J. Phys. Chem. B **110**, 16008–16017 (2006)
122. S. Nagaoka, T. Matsumoto, K. Ikemoto, M. Mitsui, A. Nakajima, Soft-landing isolation of multidecker V_2(benzene)$_3$ complexes in an organic monolayer matrix: An infrared spectroscopy and thermal desorption study. J. Am. Chem. Soc. **129**, 1528–1529 (2007)
123. S. Nagaoka, K. Ikemoto, K. Horiuchi, A. Nakajima, Soft- and reactive-landing of Cr(aniline)$_2$ sandwich complexes onto self-assembled monolayers: Separation between functional and binding sites. J. Am. Chem. Soc. **133**, 18719–18727 (2011)
124. F. Huttmann, N. Schleheck, N. Atodiresei, T. Michely, On-surface synthesis of sandwich molecular nanowires on graphene. J. Am. Chem. Soc. **139**, 9895–9900 (2017)
125. F. Huttmann, N. Rothenbach, S. Kraus, K. Ollefs, L.M. Arruda, M. Bernien, D. Thonig, A. Delin, J. Fransson, K. Kummer, N.B. Brookes, O. Eriksson, W. Kuch, T. Michely, H. Wende, Europium cyclooctatetraene nanowire carpets: A low-dimensional, organometallic, and ferromagnetic insulator. J. Phys. Chem. Lett. **10**, 911–917 (2019)

Part IV
Experimental Approach

Chapter 9
Si Nanopowder for Photoluminescence and Hydrogen Generation Materials

Yuki Kobayashi and Hikaru Kobayashi

Abstract Si nanopowder fabricated from Si swarf using the beads milling method exhibits two kinds of photoluminescence (PL), green-PL and blue-PL. Green-PL arises from band-to-band transition of Si nanopowder with band-gap enlarged by the quantum confinement effect. Blue-PL, on the other hand, is attributable to adsorbed 9,10-dimethylanthracene (DMA) impurity in hexane because the structure of the observed PL spectra is nearly identical to that of DMA solvent. The peaked PL spectra arise from vibronic interaction of DMA, and nearly the identical separation energies between the neighboring peaks correspond to the vibrational energy of DMA in the electronic ground-state. The PL intensity of DMA is enhanced by 60,000 times due to adsorption of DMA on Si nanopowder. For excitation photon energies higher than 4.0 eV, new peaks appear in the energy region higher than the (0, 0) band, attributable to transition from vibrational excited-states.

Si nanopowder reacts with water in the neutral pH region between 7 and 9. The hydrogen generation rate strongly depends on pH, while pH doesn't change after the reaction. Si nanopowder reacts with OH^- ions, generating hydrogen, SiO_2, and electrons in the SiO_2 conduction band. Electrons are accepted by water molecules, generating hydrogen and OH^- ions. Since OH^- ions act as a catalyst, the hydrogen generation rate greatly increases with pH. The generated hydrogen volume vs. the reaction time follows a logarithmic relationship, indicating that migration of OH^- ions through the SiO_2 layer is the rate-determining step. The hydrogen generation reaction stops when the SiO_2 thickness reaches to $\sim$5 nm.

Keywords PL enhancement · Vibrational excited-state · Neutral water · Hydroxyl ions · Internal hydrogen generation · Oxidative stress

Y. Kobayashi · H. Kobayashi (✉)
Institute of Scientific and Industrial Research, Osaka University, Ibaraki, Osaka, Japan
e-mail: h.kobayashi@sanken.osaka-u.ac.jp

T. Onishi (ed.), *Theoretical Chemistry for Advanced Nanomaterials*,
https://doi.org/10.1007/978-981-15-0006-0_9

9.1 Photoluminescence From Si Nanostructures

9.1.1 Introduction

Si is a nonpoisonous material, and thus, its photoluminescence (PL) phenomenon is applicable to biology [1]. PL from Si nanoparticles is attributed to (i) intrinsic band-to-band transition [2, 3] and (ii) extrinsic transition involving states such as defect states in an oxide layer [3, 4]. For case (i), the PL energy depends on the size of Si nanoparticles because the band-gap energy strongly depends on the size due to the quantum confinement effect [5, 6]. For example, the energy shift of the PL peaks by oxidation of Si nanoparticles results from case (i) because oxidation decreases the size of Si nanoparticles by the formation of SiO_2 [2, 3]. For case (ii), on the other hand, the PL energies are less dependent or independent of the nanoparticle size [3, 4].

Trave et al. [6] fabricated Si nanoparticles by the laser pyrolysis method and found that the PL intensity of as-deposited nanoparticles was weak, but it increased after thermal oxidation at temperatures between 700 and 1000 °C accompanied by blue shift to the wavelength region between 800 and 900 nm. Kang et al. [2] showed that using the oxidation method which could control the size of Si nanoparticles, the PL emission color could be varied in the wide wavelength range between red and blue. For Si nanoparticles produced using the pulsed laser ablation method in liquid, a PL peak was observed at ∼500 nm [7] or 450 and 600 nm [8]. Si nanoparticles which exhibited PL were also formed by the use of the laser ablation method in helium gas [9]. Si nanoparticles of ∼3 nm size were fabricated by implantation of Si^+ ions onto SiO_2, and the PL peak was observed in the 750∼950 nm wavelength region [10]. Si nanoparticles embedded in silicon oxide were formed by the rf co-sputtering method, and their PL spectra were greatly changed by heat treatment up to 1100 °C [8]. Using ball-milling of graphite and SiO_2 powder, Si nanoparticles with PL emission in the broad wavelength region between 650 and 900 nm were fabricated [11]. For Si nanoparticles fabricated using ball milling of graphite and SiO_2 powder, broad PL spectra were observed in the wavelength region between 650 and 900 nm [12].

Several researchers investigated effects of adsorbates on Si nanoparticles on PL behavior. Ryabechikov et al. [13] showed that adsorption of alkyl groups caused blue shift of the PL peak accompanied with broadening of the peak and attributed the phenomenon to prevention of energy transfer from small to large Si nanoparticles by adsorption. For phenyl-passivated Si nanoparticles in hexane, Imamura et al. [14] reported three-peaked PL spectra (∼3.52, ∼3.68, and ∼3.85 eV) which did not depend on excitation photon energies. Fang et al. [15] observed enhancement of PL from adsorbed porphyrin on Ag nanoparticle-covered Si surfaces and attributed the enhancement to the resonant excitation by local surface plasmons and to the increased radiative decay rate. We observed peaked structure in the PL spectra for Si nanopowder in hexane and attributed it to 9,10-dimethylanthracene (DMA) adsorbed on the surface by which the PL intensity was greatly enhanced [16, 17].

9.1.2 Experiments

Si swarf generated during slicing of Si ingots by use of the fixed-abrasive wire saw method was used as a starting material. After cleaning with organic solvent to remove coolant and other organic species, Si swarf was milled with a ball mill apparatus followed by beads milling with zirconia beads [16–19]. For one-step beads milling, 0.5 μm diameter beads were used, while for two-step beads milling, subsequent milling was performed with 0.3 μm beads. The following two different methods were employed for production of green-PL and blue-PL Si nanopowder: To obtain green-PL Si nanopowder, fabricated nanopowder was etched with an HF solution, followed by centrifugation and filtration, and then, it was immersed in ethanol. For fabrication of blue-PL Si nanopowder, milled swarf was filtered using a Teflon membrane filter, followed by immersion in hexane solvent.

Transmission electron micrography (TEM) measurements were performed using an EM-3000F (JEOL) microscope with 300 keV incident electrons. X-ray diffraction (XRD) measurements were carried out by use of a Rigaku SmartLab diffractometer. Photoluminescence (PL) spectra were recorded using a Hitachi High-Technologies Corporation F-7000 spectrometer. Ultraviolet and visible light (UV-Vis) absorption spectra were measured by use of a JASCO V-570 spectrometer. Time-dissolved PL measurements were carried out using a HORIBA DeltaFlex photometer.

9.1.3 Results and Discussion

9.1.3.1 Structure of Si Nanopowder

Figure 9.1a shows the TEM micrograph of Si nanopowder fabricated by the one-step beads milling method from Si swarf. The TEM observation was performed after etching with an HF solution to remove amorphous SiO_2. Many crystallites with polygonal shapes and sizes less than 10 nm are clearly observed.

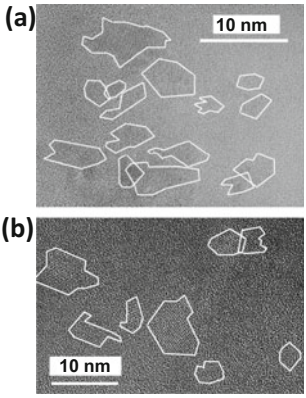

Fig. 9.1 TEM micrographs of Si nanopowder fabricated from Si swarf using the following beads milling methods: (**a**) one-step milling, (**b**) two-step milling

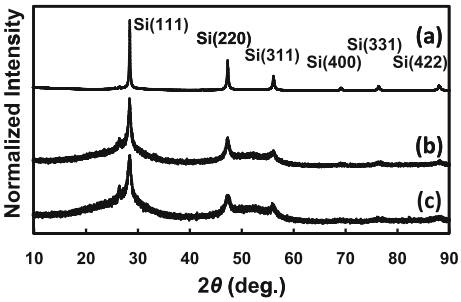

Fig. 9.2 XRD patterns of Si swarf before (**a**) and after beads milling using the following methods: (**b**) one-step milling, (**c**) two-step milling

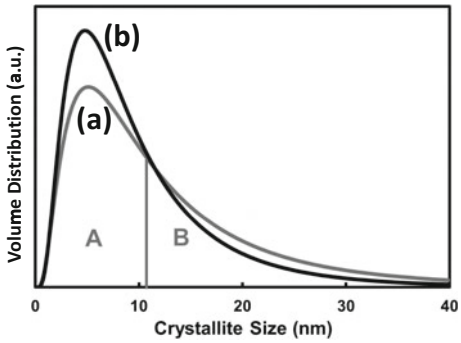

Fig. 9.3 Volume distribution of the crystallite size of Si nanopowder fabricated from Si swarf using the following methods: (**a**) one-step beads milling, (**b**) two-step beads milling

Figure 9.2 shows the XRD patterns of Si swarf before (pattern a) and after one-step (pattern b) and two-step (pattern c) beads milling. The intense peaks at 28.4, 47.5, and 56.2° are attributable to (111), (220), and (311) orientations of Si nanopowder. After beads milling, all the diffraction peaks due to Si observed before milling are present with nearly the same intensity ratio, but the widths of the peaks are considerably increased, indicating that the average crystallite sizes are greatly decreased.

From the analysis of the shape of the Si(111) XRD peak, the volume distribution of Si nanopowder (i.e., distribution of the volume of Si nanoparticles vs. the diameter assuming the spherical shape) obtained using the theoretical diffraction line profile from spherical crystallites with lognormal size distribution (SLN profile) method [20] is shown in Fig. 9.3. For one-step milling, the maximum of the volume distributions (i.e., mode diameter) is present at 5.2 nm. The median diameter for the volume distribution (i.e., the vertical line by which two regions, A and B, is divided into the same areas) is estimated to be 10.5 nm and the average diameter to be 13.2 nm. For two-step milling, the mode diameter, the median diameter, and the average diameter are determined to be 4.8, 8.4, and 10.2 nm, respectively.

9.1.3.2 Photoluminescence from Si Nanopowder

Figure 9.4 shows the photos of the solutions containing blue-PL and green-PL Si nanopowders, observed under 365 nm black light irradiation. Si nanopowder was

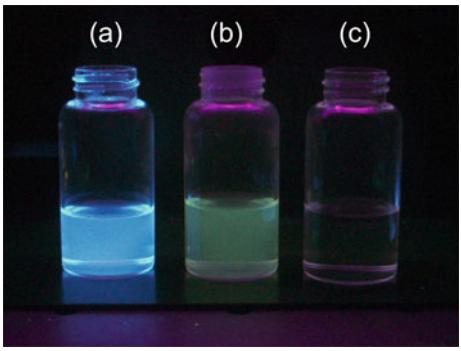

Fig. 9.4 Photos of Si nanopowder in the following solvents under black light irradiation: (**a**) Si nanopowder without HF etching in hexane, (**b**) Si nanopowder with HF etching in ethanol. Photo c is for hexane without Si nanopowder

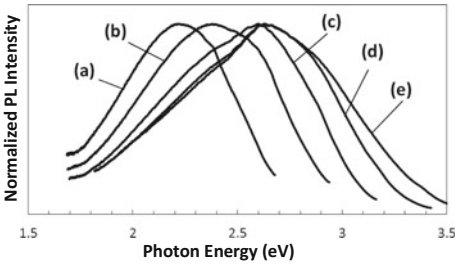

Fig. 9.5 PL spectra of green-PL Si nanopowder in ethanol with HF etching observed under the following excitation energies: (**a**) 2.76 eV, (**b**) 3.02 eV, (**c**) 3.26 eV, (**d**) 3.54 eV, (**e**) 3.76 eV

fabricated using the one-step beads milling method from Si swarf. It is clearly seen that PL color strongly depends on the treatments carried out after fabrication of Si nanopowder. Si nanopowder without HF etching in hexane shows blue-PL (Fig. 9.4a) while that with HF etching in ethanol exhibits green-PL (Fig. 9.4b). It is noted that hexane without Si nanopowder doesn't show PL (Fig. 9.4c).

Green-Photoluminescence-Emitting Si Nanopowder

Figure 9.5 shows the PL spectra for green-PL Si nanopowder. Only one broad peak is observed in the spectra, and the peak maximum shifts in the higher energy direction by an increase in the excitation photon energy. The width of the peak increases with the excitation energy (i.e., incident light energy). It should be noted that Si nanopowder includes various size crystallites as shown in Fig. 9.3. With low excitation energy, only large size Si crystallites with narrow band-gap energies are excited, followed by low energy PL (Fig. 9.6a). With high excitation energy, on the other hand, smaller Si nanopowder with higher band-gap energies can also be excited, and thus, higher energy PL is exhibited (Fig. 9.6b). The broader structure of the PL spectra results from wider distribution of PL-emitting Si nanopowder with various band-gap energies, e.g., 2.2 eV band-gap for 2.4 nm diameter and 1.7 eV for 4.5 nm diameter [5, 6].

Figure 9.7 shows the PL spectra for one-step beads milled Si nanopowder (spectrum a) and two-step milled Si nanopowder (spectrum b). The maximum of the PL peak for one-step beads milled Si nanopowder is located at 2.60 eV while that for two-step beads milled Si nanopowder is present at 2.91 eV. Since two-step

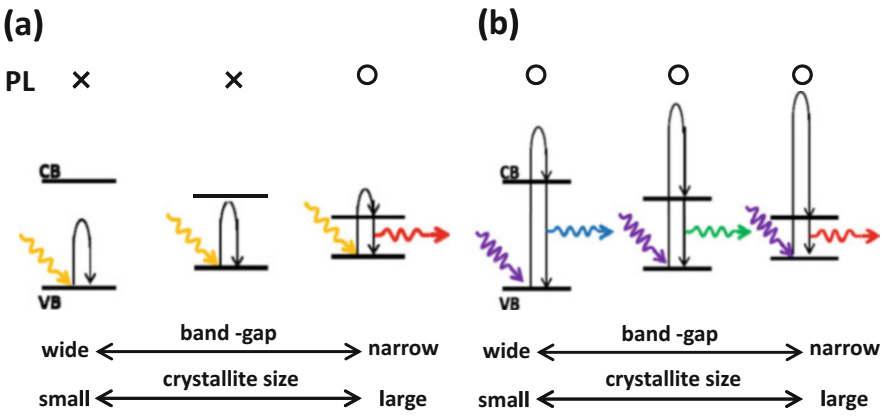

Fig. 9.6 Schematics to explain the relationship between the PL characteristics and the excitation energy: (**a**) low excitation energy, (**b**) high excitation energy

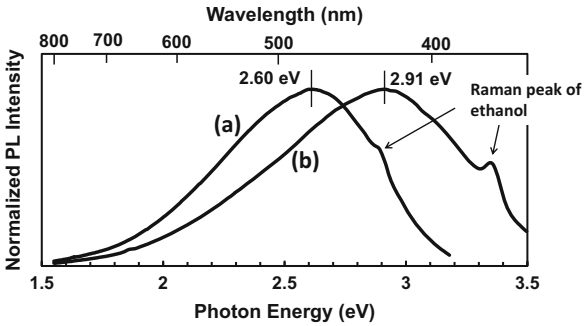

Fig. 9.7 PL spectra for green-PL Si nanopowder fabricated with the following methods: (**a**) one-step beads milling, (**b**) two-step beads milling

beads milled Si nanopowder possesses higher band-gap energies due to the quantum confinement effect, this result also gives the evidence that green-PL arises from band-to-band transition of Si nanopowder.

Assuming the free electron model for valence and conduction bands of Si nanopowder and using the indirect band-gap energy, $E_{\mathrm{g,\,indi}}$, and direct band-gap energy, $E_{\mathrm{g,\,di}}$, the absorption coefficient, α, is written as

$$\alpha^2 \propto \mathrm{h}\nu - E_{\mathrm{g,di}}, \tag{9.1}$$

$$\alpha^{1/2} \propto \mathrm{h}\nu - E_{\mathrm{g,indi}}, \tag{9.2}$$

where $\mathrm{h}\nu$ is the incident photon energy. The plots for green-PL Si nanopowder using Eq. (9.1) and (9.2) are shown in Fig. 9.8a and b, respectively.Both the plots aren't

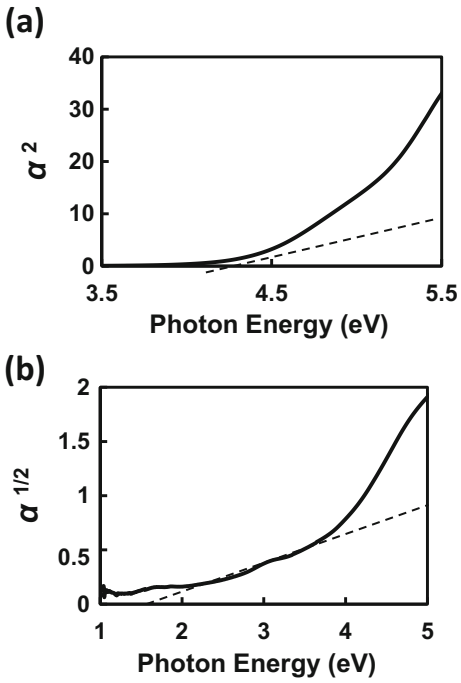

Fig. 9.8 Plots for estimation of the band-gap energies of Si nanopowder: (**a**) α^2 vs. $h\nu$ (α, absorption coefficient; $h\nu$, photon energy) plot for estimation of indirect band-gap energy, (**b**) $\alpha^{1/2}$ vs. $h\nu$ plot for estimation of the direct band-gap energy

linear but curves with the curvature increasing with the energy. These nonlinear plots result from presence of Si nanopowder with various sizes (cf. Fig. 9.3). From the intercept of the plot with the energy axis, the minimum of the indirect band-gap energy of Si nanopowder is determined to be 1.3 eV, which corresponds to the diameter of 6∼8 nm [21]. On the other hand, the minimum of the direct band-gap energy is estimated to be 4.1 eV (cf. direct band-gap energy of crystalline Si: 3.4 eV [22]).

Blue-Photoluminescence-Emitting Si Nanopowder

Figure 9.9 shows the PL spectra of blue-emission Si nanopowder fabricated by the one-step milling method. Four peaks are clearly observed at 2.54, 2.72, 2.91, and 3.10 eV, and these peak energies don't change at all by changing the excitation photon energy from 3.17 eV (spectrum a) to 3.50 eV (spectrum c). This result indicates that blue-PL arises from a single source. The PL spectra of Si nanopowder coincide with that of DMA (spectrum d). These results show that PL emission results from adsorbed DMA on Si nanopowder surfaces. (Low concentration DMA is present in hexane as an impurity.) The PL emission is attributable to $\pi - \pi_*$ transition of DMA and the peaked structure to the vibronic bands with the total symmetric breathing vibrational mode [23].

Figure 9.10 shows the PL spectra of hexane containing Si nanopowder before (spectrum a) and after (spectrum b) addition of an HNO_3 plus HF solution. The HNO_3 plus HF solution dissolves Si nanopowder [24], and after addition,

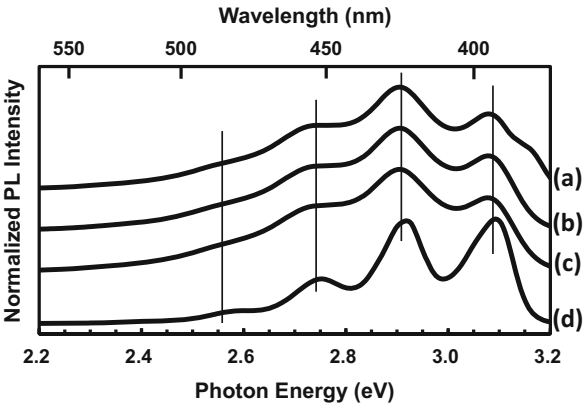

Fig. 9.9 PL spectra of blue-PL Si nanopowder observed with the following excitation energies: (**a**) 3.17 eV, (**b**) 3.35 eV, (**c**) 3.50 eV. Spectrum d is for free DMS molecules for comparison

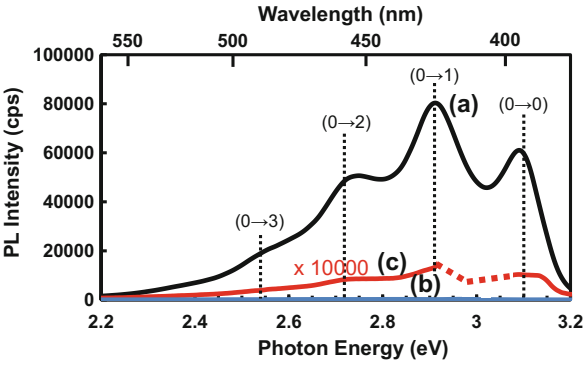

Fig. 9.10 PL spectra for blue-PL Si nanopowder fabricated using the one-step beads milling method before (**a**) and after (**b**) addition of an HNO_3+HF solution. Spectrum c is 10,000 times enlargement of spectrum b

the PL intensity greatly decreases, indicating that adsorption of DMA on Si nanopowder greatly enhances the PL intensity. The low intensity PL observed after addition of HF+HNO_3 is probably due to undissolved Si nanopowder stabilized by adsorbed DMA. The PL intensity of a DMA-containing hexane solution without Si nanopowder don't change at all by addition of HF plus HNO_3, showing that the HF+HNO_3 solution doesn't react with DMA (i.e., no chemical reaction). Spectrum c is observed after concentration of DMA in hexane solutions by 10,000 times by evaporation. Comparison of spectrum a with spectrum c demonstrates that the PL intensity of DMA is enhanced by ~60,000 times by the presence of Si nanopowder.

Figure 9.11 shows the absorption spectra of blue-PL Si nanopowder in hexane. For both the spectra, the absorption background due to hexane solvent is subtracted. In the presence of Si nanopowder in hexane (spectrum a), the peaked structure is observed, and it is attributed to absorption by DMA adsorbed on Si nanopowder. The peaked structure in the absorption spectrum due to adsorbed DMA disappears by addition of an HF+HNO_3 solution in hexane containing Si nanopowder (spectrum b), clearly showing that the peaked structure arises from DMA adsorbed on Si nanopowder, but not from free DMA dissolved in hexane. It is confirmed that the

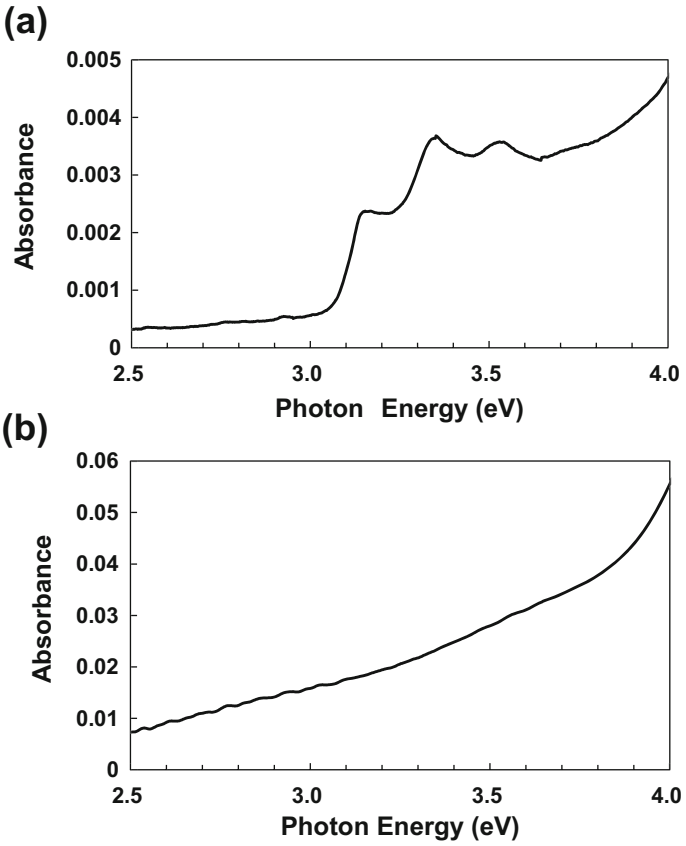

Fig. 9.11 Absorption spectra for the following specimens: (**a**) blue-PL Si nanopowder in hexane, (**b**) after addition of an HNO_3+HF solution to specimen a

absorption spectrum of hexane containing DMA without Si nanopowder doesn't change at all by addition of the HF+HNO_3 solution.

The peaked structure in the absorption spectra results from transition to the electronic excited-state with various vibrational states. The peaks at 3.153, 3.341, and 3.530 eV are due to (0,0), (1,0), and (2,0) bands. (For both the PL spectra and the absorption spectra, (l, m) denotes transition between the l-th vibrational state of the electronic excited-state and the m-th vibrational state of the electronic ground-state.) The separated energy for these peaks of 0.19 eV is ∼0.02 eV higher than that observed without Si nanopowder. This result indicates that adsorbed DMA in the excited-state has a slightly higher C–C bond energy, possibly leading to a shorter C–C bond length than that of free DMA.

The shortened C–C bond length in the exited-state results in an increase in the difference in the bond length between the excited- and ground-states. The PL spectrum of free DMA molecules has a (0,0) peak with the highest intensity

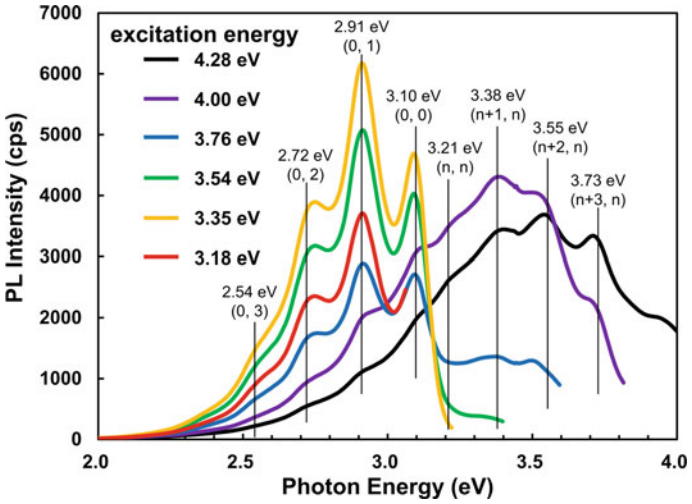

Fig. 9.12 PL spectra for blue-PL Si nanopowder in hexane observed with various excitation photon energies between 3.18 and 4.28 eV

(spectrum d in Fig. 9.9), which results from the nearly identical C–C bond lengths of DMA in the electronic ground- and excited-states. On the other hand, the PL spectra of DMA adsorbed on Si nanopowder possess the (0,1) peak with the highest intensity (spectra a∼c in Fig. 9.9). This result is in accordance with the above consideration that the C–C bond length of adsorbed DMA in the excited-state is shorten.

Figure 9.12 shows the PL spectra of blue-PL Si nanopowder in hexane, i.e., DMA-adsorbed Si nanopowder, observed with various excitation energies. With the excitation energies higher than 3.76 eV, PL peaks with energies higher than the (0,0) band are observed at 3.21, 3.38, 3.55, and 3.73 eV, i.e., nearly the constant energy separation, in a broad peak. The energies of the sharp peaks remain constant by changing the excitation photon energy, while the broad peak shifts toward the higher energy with an increase in the excitation energy. The broad peak is attributed to band-to-band transition of Si nanopowder, similar to the case of green-PL (Figs. 9.5 and 9.7).

Each neighboring PL peak is separated by 0.17∼0.18 eV, which is nearly identical to that observed in the absorption spectrum (Fig. 9.11). These PL peaks with energies higher than the (0,0) energy are attributable to transitions from the vibrational excited-states, and thus, the separation energy corresponds to the vibrational energy in the electronic excited-state, i.e., the same as that observed in the absorption spectra. The transition from the vibrational excited-states most probably results from an increased probability of the transition between the electronic excited-state and the ground-state, in analogy to electronic transition observed in absorption spectrum b of Fig. 9.11.

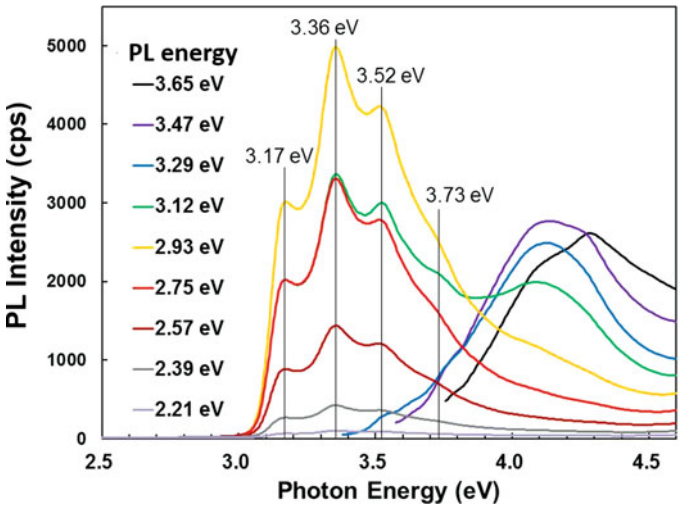

Fig. 9.13 PL excitation spectra for blue-PL Si nanopowder in hexane observed at various PL energies between 2.21 and 3.65 eV

Figure 9.13 shows the PL excitation spectra for blue-PL Si nanopowder in hexane. The excitation spectra are measured by scanning the incident photon energy with the PL energy fixed, and thus, they correspond to absorption which causes PL emission at the fixed PL energy. For the PL energies between 2.39 and 2.93 eV, i.e., transitions from the vibrational ground-state, peaked structure is observed, showing that absorption by adsorbed DMA causes the PL peaks. In the higher energy region, on the other hand, broad structure is present with no vibronic bands. The broad structure is attributable to absorption by Si nanopowder, indicating that the PL peaks with energies higher than the (0,0) peak result from band-to-band excitation of Si nanopoweder.

Figure 9.14 shows the time-dependent PL intensity measured at 2.91 eV (curve a) and 3.35 eV (curve b). The PL intensity at 3.35 eV for DMA without Si nanopowder is shown in curve c for reference, and in this case, the PL lifetime is determined to be 5.0 ns. The PL lifetime measured at 2.91 eV which corresponds to the (0, 1) transition of DMA, on the other hand, is much shorter, i.e., 0.97 ns. Considering that the pulse width of incident light is 0.75 ns, the real lifetime is estimated to be 0.62 ns for DMA with Si nanopowder and 4.9 ns for DMA without Si nanopowder. The short lifetime results from the high PL transition probability, indicating that the interaction of DMA with Si nanopowder greatly increases the PL transition probability.

The PL energy for curve b (3.35 eV) corresponds to the (n+1, n) PL band overlapped with the more intense band-to-band transition of Si nanopowder. The lifetime considering the pulse width is estimated to be 3.1 ns, indicating that the lifetime of electron-hole pairs in Si nanopowder is much longer than the PL lifetime arising from adsorbed DMA of 0.62 ns.

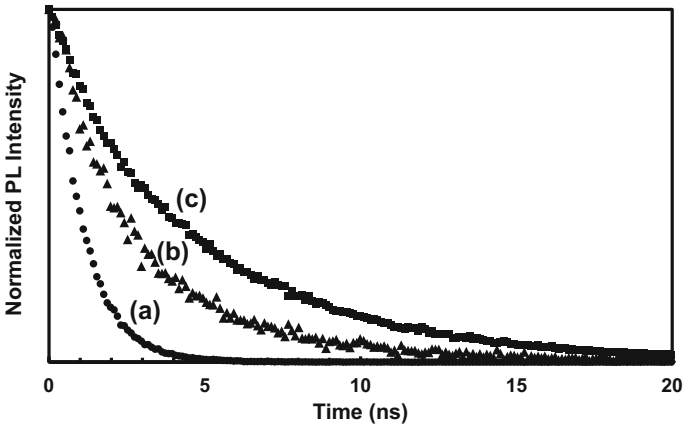

Fig. 9.14 Time-dependent PL intensity for blue-PL Si nanopowder in hexane measured with the following excitation photon energies: (**a**) 2.91 eV, (**b**) 3.35 eV. Curve c is for DMA-containing hexane without Si nanopowder

Photoluminescence Enhancement for DMA by Adsorption on Si Nanopowder
The absorption bands due to DMA appear in the presence of Si nanopowder in hexane, while they aren't observed in the absence of Si nanopowder (cf. Fig. 9.11). This result clearly shows that the light absorption probability is greatly increased by adsorption on Si nanopowder. Therefore, the PL enhancement is partly attributable to an increased light absorption probability.

The transition probability from the ground-state to the excited-state is greatly enhanced by adsorption of DMA on Si nanopowder as described above. Therefore, it is quite likely that the transition probability from the excited-state to the ground-state is also increased by the adsorption. The PL intensity is proportional to the product of the light absorption probability and the PL emission probability, leading to the great enhancement by ~60,000 times by adsorption of DMA on Si nanopowder (cf. Fig. 9.10).

The PL intensity, I_g, for transitions from vibrational ground-state of the electronic excited-state is proportional to the number of electrons, n_e, in the vibrational ground-state and the rate constant, k_r, for radiative transition. Considering the PL enhancement factor by Si nanopowder of 60,000, we have

$$I_g \propto {n_e}^1 {k_r}^1 = 60,000 {n_e}^0 {k_r}^0, \tag{9.3}$$

where superscripts 0 and 1 denote the values without and with Si nanopowder, respectively. For ${n_e}^0$ and ${n_e}^1$, we have the following differential equations:

$$\frac{\mathrm{d}{n_e}^0}{\mathrm{d}t} = -\left({k_r}^0 + {k_{\mathrm{nr}}}^0\right) t, \tag{9.4}$$

$$\frac{\mathrm{d}{n_e}^1}{\mathrm{d}t} = -\left({k_r}^1 + {k_{\mathrm{nr}}}^1\right)t, \tag{9.5}$$

where k_{nr} is the rate constant for non-radiative transition. Since the PL lifetime is inversely proportional to the total rate constant, we have

$$4.9 : 0.62 = \frac{1}{{k_r}^0 + {k_{\mathrm{nr}}}^0} : \frac{1}{{k_r}^1 + {k_{\mathrm{nr}}}^1}. \tag{9.6}$$

Considering the quantum efficiency of 0.42 and 0.45 for PL in the absence and presence of Si nanopowder, respectively, we have

$$\frac{{k_r}^0}{{k_r}^0 + {k_{\mathrm{nr}}}^0} = 0.42, \tag{9.7}$$

$$\frac{{k_r}^1}{{k_r}^1 + {k_{\mathrm{nr}}}^1} = 0.45. \tag{9.8}$$

Using Eqs. (9.6), (9.7), and (9.8), we have

$${k_r}^1 = 8.5{k_r}^0. \tag{9.9}$$

Therefore, using Eq. (9.3), ${n_e}^1$ is given by

$${n_e}^1 = 7.1 \times 10^3 {n_e}^0. \tag{9.10}$$

The above consideration can lead to the following conclusion. The PL intensity is increased by adsorption on Si nanopowder for the following two reasons: (i) an increase in the number of electrons in the electronic excited-state (~7100 times enhancement) and (ii) an increase in the rate constant for radiative transition (~8.5 times enhancement). The increased number of electrons in the excited-state results from the increased transition probability which in turn results from a great increase in the dynamic dipole moment by adsorption and/or enhancement of wave function of DMA by adsorption, i.e., surface resonance state [25].

Photoluminescence Mechanism

The excitation spectra with the PL energies lower than 3.12 eV clearly possess vibronic bands (Fig. 9.13), indicating that adsorbed DMA molecules are directly excited. In the excitation spectra for the PL energies higher than 3.29 eV, on the other hand, a broad structure is dominant. The peak energy of the broad structure shifts in the higher energy direction with the PL energy. It should be noted that for excitation with energies higher than 3.76 eV, the PL vibronic bands from vibrational excited-states are observed (cf. Fig. 9.12). This result demonstrates that for PL emission from vibrational excited-states, incident light is absorbed

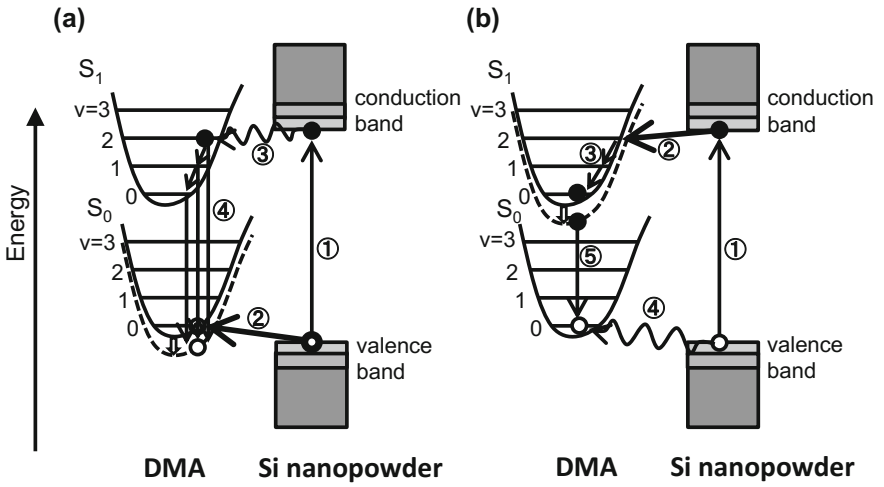

Fig. 9.15 Mechanism of blue-PL emission involving generation of electron-hole pairs in Si nanopowder by incident light, followed by electron and hole transfer to adsorbed DMA with the following order: (**a**) a photo-generated hole transfers to DMA first, (**b**) a photo-generated electron transfers to DMA first

by Si nanopowder. Therefore, it can be concluded that for PL emission from the vibrational excited-states, electron-hole pairs are generated in Si nanopowder, and they transfer to adsorbed DMA, followed by recombination.

The lifetime of photo-generated electron-hole pairs (3.1 ns) is much longer than the PL lifetime (0.62 ns), and therefore, a photo-generated electron and a hole transfer to adsorbed DMA separately. We consider the case where a photo-generated hole in Si nanopowder moves to adsorbed DMS first, and then an electron moves to DMA. In this case, the hole is captured by the potential of the electronic ground-state of DMA. The ground-state with a positive charge is stabilized due to solvation (Fig. 9.15a). Immediately when an electron is captured by a potential of the electronic excited-state, transition from the electronic excited-state to the ground-state occurs. Due to the high transition probability, transition from the vibrational excited-state to the electronic ground-state proceeds. Since solvation lowers the potential energy of the ground-state, the transition energy is increased by solvation, leading to a blue shift of the PL peaks.

For the opposite case, an electron generated in Si nanopowder transfers to adsorbed DMA first, followed by transfer of a hole to DMA (Fig. 9.15b). An electron is captured in the electronic excited-state of DMA, and in this case, internal relaxation to the vibrational ground-state proceeds before electronic transition because of the absence of a hole in the electronic ground-state. There is enough time for solvation of adsorbed DMA with the electron in the electronic excited-state to proceed before a hole transfers to DMA (Fig. 9.15b). Due to solvation, the potential energy of the electronic excited-state is lowered. When a hole transfers to DMA, it is captured in the vibrational ground-state of the electronic ground-

state. Immediately after a hole is captured, electronic transition of the electron in the electronic excited-state occurs, resulting in PL emission. Because of lowering of the potential energy for the temporary captured electron (i.e., the potential of the excited-state), the PL energy decreases, in contrast to the case where a hole transfers to DMA first. The above consideration clearly shows that the PL energy for case a in Fig. 9.15 increases by solvation, while that for case b decreases. This consideration is verified by observation of two (0, 0) bands (or one (0,0) band and one (n, n) band) separated by 0.11 eV. Each solvation energy is likely to be approximately a half of the energy difference of the two (0, 0) bands, i.e., ~55 meV.

The (0, 0) PL band for case a and the (n, n) band for case b are located at 3.10 and 3.21 eV, respectively. The (0, 0) band in the absorption spectra is observed at 3.15 eV, i.e., the average energy between the (0, 0) and (n, n) PL bands. In the case of light absorption, both the initial and final states are in neutral charge states, and therefore, solvation doesn't occur. Therefore, the transition energy is between that for the ground-state-stabilized case (case a) and the excited-state-stabilized case (case b).

The intensity ratios of the PL peaks due to transitions from the vibrational ground-states, i.e., (0, 0), (0, 1), (0, 2), and (0, 3) bands, are nearly independent on the excitation energy. This is because after complete internal relaxation, transition from the vibrational ground-state proceeds, and in this case, the PL intensity is determined by the individual Franck-Condon factors which don't depend on the excitation energy. On the other hand, the intensity ratios of the PL peaks due to transitions from the vibrational excited-states strongly depend on the incident photon energy. To explain this phenomenon, we consider the case where an electron enters the x-th vibrational state of the electronic excited-state. The n-th PL band contains various transitions, (l, m), which satisfy the following equation:

$$\mathrm{l} - \mathrm{m} = \mathrm{n}. \tag{9.11}$$

The transition rate, $R_{\mathrm{l,\,m}}$, is given by the product of the transition probability, $P_{\mathrm{l,\,m}}$, and the number of electrons in the l-th vibrational state, N_l:

$$\mathrm{R_{l,m}} = P_{\mathrm{l,m}} N_l. \tag{9.12}$$

N_l is given by

$$N_l = N_x\,(1 - a_x)\,(1 - a_{x-1}) \cdot \cdots \cdot (1 - a_{l+1}) = N_x \prod_{x}^{l+1} (1 - a_x)\,, \tag{9.13}$$

where N_x is the number of electrons transferred from Si nanopowder to the x-th vibrational state of the electronic excited-state, and a_j expresses the transition probability from the j-th vibrational states to various vibrational states of the electronic ground-state which probability is proportional to the sum of the Franck-Condon factors:

$$a_j \propto \sum_m F_{\mathrm{j,m}}, \tag{9.14}$$

where $F_{\mathrm{j,\,m}}$ is the Franck-Condon factor for the (j, m) transition. The term, $\prod_{j=x}^{l+1}\left(1-a_j\right)$, in Eq. (9.13) expresses the probability that an electron transferred from Si nanopowder to the x-th vibrational state of adsorbed DMA relaxes to the l-th vibrational state without electronic transition. Therefore, we have

$$\mathrm{R_{l,m}} \propto F_{\mathrm{l,m}} \prod_j^{n-l+1}\left(1-a_j\right) = F_{\mathrm{l,m}} P_{\mathrm{l,m}} N_x \prod_x^{l+1}(1-a_x)\,. \tag{9.15}$$

The intensity of the n-th band, I_n, is proportional to the sum of the transition rates over l which satisfies Eq. (9.11):

$$I_n \propto N_x \sum_l F_{l,l-n} \prod_j^{n-l+1}\left(1-a_j\right) = N_x \sum_l P_{l,,m} \prod_x^{l+1}(1-a_x)\,. \tag{9.16}$$

Equation (9.16) clearly shows that the PL intensity of the n-th band (i.e., (a+n, a), $a = 0.1{,}2{,}3\cdot\ \cdots$) depends not only on the Franck-Condon factor for the (n, 0) transition, $F_{n,\,0}$, (i.e., $a = 0$), but also other Franck-Condon factors. When the incident photon energy is varied, the vibrational energy state, x, to which a photo-generated electron in Si nanopowder transfers, is changed, leading to a change in the PL intensity, I_n. Therefore, the PL bands whose intensities depend on the excitation energy support the transition from vibrational excited-states.

9.2 Hydrogen Generation from Si Nanopowder by Reaction with Water

9.2.1 Introduction

Reactive oxygen species (ROS) are generated in the body for various reasons, e.g., metabolism [26], UV irradiation [27], and environmental pollution [28]. Among ROS, hydroxyl radicals (OH radicals) possess the highest oxidation-reduction potential, i.e., the highest oxidation power. Oxidation of cells, DNA [29], lipid [30], etc., (i.e., oxidative stress) causes various diseases such as Alzheimer's disease [31, 32], Parkinson's disease [31, 33], chronic kidney failure [34], cancer cell proliferation [35], atopic dermatitis [36], cutaneous senility [37], etc. Hydrogen reacts with OH radicals to form water molecules, and thus hydrogen can prevent oxidative stress-induced diseases.

Although Si bulk doesn't strongly react with water in the neutral pH region between 7 and 9, Si nanopowder with sizes less than ~30 nm does, leading to

generation of hydrogen molecules [38–40]. Therefore, oral administration of Si is expected to prevent oxidative stress-induced diseases.

To prevent oxidative stress-induced diseases by elimination of OH radicals generated in the body without side effects, the following three requirements should be satisfied: (i) a large amount of reducing species is present in the body, (ii) the concentration of reducing species is always maintained high, and (iii) reducing species reacts only with OH radicals among ROS. Requirement (i) arises from the high reactivity of OH radicals, which easily attack and oxidize cells, and therefore, hydrogen is necessary to react with OH radicals before they damage cells. Requirement (ii) results from continuous generation of OH radicals in the body due to mitochondrial respiratory metabolism. Other ROSes possess physiological functions such as immunity, and therefore, their elimination may cause side effects. Hydrogen reacts only with the most reactive OH radicals among ROSes (requirement iii), and therefore, no side effects arise by hydrogen.

Hydrogen-rich water may have effects to prevent oxidation stress-induced diseases. However, the saturated hydrogen concentration in water is only 1.6 ppm at room temperature, and even in the case of the saturated concentration, only 18 mL hydrogen gas dissolves in 1 L water. The hydrogen concentration in hydrogen-rich water is usually much lower because hydrogen easily diffuses to air even when it is contained in a container. Moreover, in 1 h, the hydrogen concentration in every organ returns to the initial values before intake of hydrogen-rich water [41]. Therefore, the effects of intake of hydrogen-rich water on oxidative stress-induced diseases seem to be limited.

Polyphenol [42, 43], vitamin C [44], and vitamin E [45] can eliminate OH radicals. However, their reducing power is too strong to react with other ROSes. Therefore, taking a large amount of these species may cause side effects. Moreover, keeping a high concentration of these species in the body continuously is almost impossible.

We have demonstrated that the above three requirements can be satisfied with intake of Si composition, as explained below.

9.2.2 Experiments

Si nanopowder was fabricated from Si powder (Koujundo Chemical Laboratory, Si Powder ca. 5 μm) by use of the beads milling method with 0.5 mmΦ zirconia beads, unless otherwise noted. Fabricated Si nanopowder was etched in a 5wt% HF solution for 10 min at room temperature, followed by immersion in ethanol to make the surface hydrophilic.

For the reaction with water in the neutral pH region between 7 and 9, the generated hydrogen volume was obtained by measuring the hydrogen concentration in water using a TOA DKK DH-35A potable dissolved hydrogen meter, while that generated by the reaction with strong alkaline solutions was determined just by measuring the volume after subtraction of the volume of water vapor.

Fourier transform infrared absorption (FT-IR) spectra were measured using a JASCO FT/IR-6200 spectrometer. X-ray photoelectron spectroscopy (XPS) measurements were performed by use of a KRATOS AXIS-165x spectrometer with an Mg Kα radiation source in which photoelectrons were collected in the surface-normal direction. SEM measurements were carried out using a JOEL JSM-6335F microscope.

9.2.3 Results and Discussion

9.2.3.1 Reaction of Si Nanopowder with Strong Alkaline Solutions

Figure 9.16 shows the hydrogen volume generated by the reaction of Si nanopowder with strong alkaline solutions having pH higher than 12.9 at room temperature. The total amounts of generated hydrogen are 1589 mL/g for the pH 13.9 solution, 1530 mL/g for the pH 13.4 solution, and 972 mL/g for the pH 12.9 solution. The maximum hydrogen generation rate in the case of the reaction with pH 13.9 solution is 351 mL/min.g. This hydrogen generation rate corresponds to ∼10,000 times that for photocatalytic hydrogen generation using efficient photocatalysts such as Ta_3N_5/SiO_2 which respond to visible light [46]. Using the 1 g photocatalyst under AM1.5 100 mAW/cm^2 irradiation, generation of 1,500 mL hydrogen requires more than 1.5 years. In the case of Si nanopower, ∼1.500 mL hydrogen can be generated in a few minutes although the reaction is irreversible.

We consider the following reaction mechanisms for hydrogen generation by the reaction of Si nanopowder with water:

$$\mathrm{Si} + 2\mathrm{H_2O} \rightarrow \mathrm{SiO_2} + 2\mathrm{H_2O}, \tag{9.17}$$

$$\mathrm{Si} + 2\mathrm{OH^-} + 2\mathrm{H_2O} \rightarrow \mathrm{H_2SiO_4}^{2-} + 2\mathrm{H_2}. \tag{9.18}$$

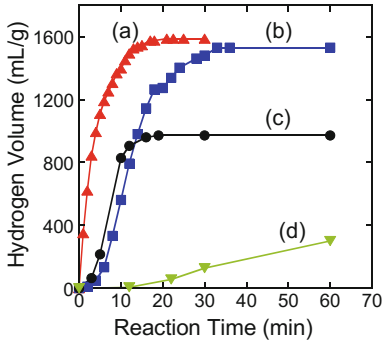

Fig. 9.16 Hydrogen volume generated by the reaction of Si nanopowder with alkaline solutions at room temperature having following pHs: (**a**) 13.9, (**b**) 13.4, (**c**) 12.9, (**d**) 12.1

Both the reactions generate 2 M hydrogen from 1 M Si, i.e., 1712 mL hydrogen at room temperature from 1 g Si. Reaction (9.17) doesn't consume OH^- ions, while reaction (9.18) does, resulting in a decrease in pH. Therefore, the reaction ratio, i.e., the hydrogen volume generated by reaction (9.18) divided by the total generated hydrogen volume, can be estimated from the decrease in pH. This ratio is estimated to be 1.0 for pH 13.4 and 13.9 solutions, 0.58 for pH 12.9 solutions, and 0.12 for pH 12.1 solutions. By reaction (9.18), soluble $H_2SiO_4^{2-}$ ions are formed, and thus, all Si atoms in Si nanopowder can react with OH^- ions because no materials to prevent the reaction with OH^- ions are present on the Si surface. For reaction (9.17), on the other hand, SiO_2 with low solubility is formed on the surface, and when the SiO_2 thickness reaches a certain value, the hydrogen generation stops because of the migration-limited mechanism. (For reaction (9.17), OH^- ions are the migrating species through SiO_2 as explained below.) We have observed that when the SiO_2 thickness reaches to ~5 nm, the hydrogen generation reaction stops. The decrease in the volume of generated hydrogen with a decrease in pH can be explained by this migration-limited mechanism.

1589 mL/g hydrogen generated by the reaction with pH 13.9 solutions is 93% of the stoichiometric value of 1712 mL/g at room temperature. This small difference is attributable to the presence of a silicon oxide layer on Si nanopowder before the hydrogen generation reaction, i.e., 7wt% Si is already oxidized before the reaction.

972 mL/g hydrogen is generated by the reaction with the pH 12.9 solutions, which is equal to 61% hydrogen generated by the reaction with 13.9 solutions, and therefore, unreacted Si is estimated to be 39% that before the reaction. The weight of SiO_2 formed by the hydrogen generation reaction is estimated to be 1.22 g from initial 1 g Si nanopowder. Assuming that Si nanopowder before the reaction possesses spherical shape with the 23.4 nm diameter (i.e., the average diameter before the reaction), the diameter of unreacted Si nanopowder is estimated to be 17.1 nm. From the diameter of unreacted Si nanopowder, its weight, and the weight of formed SiO_2, the thickness of formed SiO_2 is estimated to be 5.1 nm, in good agreement with that estimated from XPS measurements, i.e., 4.8 nm.

9.2.3.2 Reaction of Si Nanopowder with Neutral Water

Si nanopowder was produced from Si powder for hydrogen generation experiments with neutral water. The size of Si nanopowder is larger than that produced from Si swarf, i.e., for one-step milling, the mode diameter, the median diameter, and the average diameter are 6.6, 14.0, and 23.4 nm, respectively, and those for two-step milling are 5.8, 9.6, and 13.8 nm, respectively.

Figure 9.17 shows the hydrogen volume generated by the reaction with water in the neutral pH region vs. the reaction time. Even in the case of the reaction with ultrapure water of pH 7.0, Si nanopowder generates hydrogen (plot a), but the hydrogen generation rate is low, i.e., 0.026~0.047 mL/min.g. The hydrogen generation rate increases by the reaction with tap water having pH 7.4 (plot b). The hydrogen generation rate further increases by increases of pH to 8.0 (plot c) and 8.6

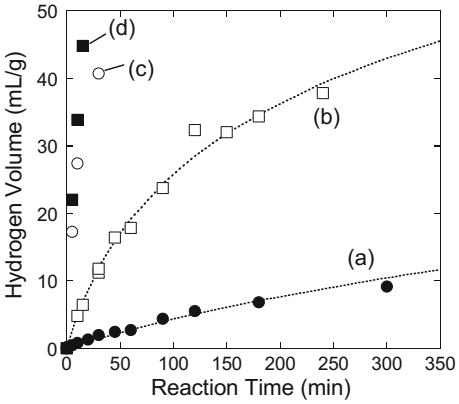

Fig. 9.17 Hydrogen volume generated from Si nanopowder vs. the reaction time for the reaction with water having following pHs: (**a**) 7.0 (ultrapure water), (**b**) 7.4 (tap water), (**c**) 8.0, (**d**) 8.6

(plot d). The initial hydrogen generation rates for pH 7.4, 8.0, and 8.6 solutions are higher by approximately 10, 50, and 100 times than that for ultrapure water of pH 7.0. On the other hand, the change in pH observed after the hydrogen generation reaction is much lower than that calculated assuming that OH^- ions are consumed for the hydrogen generation reaction. (The slight pH change is due to dissolution of CO_2 in the air to the solutions during the hydrogen generation reaction.) From these results, the most probable reaction schemes are written as

$$Si + 2OH^- \rightarrow SiO_2 + H_2 + 2e, \tag{9.19}$$

$$2H_2O + 2e \rightarrow 2OH^- + H_2. \tag{9.20}$$

In reaction (9.19), Si reacts with OH^- ions, forming SiO_2, H_2, and electrons most probably in the SiO_2 conduction band. Electrons transfer to the SiO_2 surface, and water molecules accept them, resulting in the formation of OH^- ions and H_2. OH^- ions are consumed in reaction (9.19) but generated in reaction (9.20), and therefore, after the overall reaction (reaction (9.17) = reactions (9.19) + (9.20)), the concentration of OH^- ions, i.e., pH, doesn't change. The reaction rate for reaction (9.19) is much lower than that for reaction (9.20), and therefore, the total reaction rate greatly increases with the concentration of OH^- ions.

If reaction (9.19) was the rate-determining step for hydrogen generation reaction, then the reaction rate should be proportional to the square of the concentration of OH^- ions. However, the initial reaction rates for the reaction with pH 7.4, 8.0, and 8.6 solutions are approximately 10, 50, and 100 times that for ultrapure water of pH 7.0. It is very likely that even in the early reaction stage, a silicon oxide layer is present on Si nanopowder, and migration of OH^- ions through the oxide layer is the rate-determining step, as explained below.

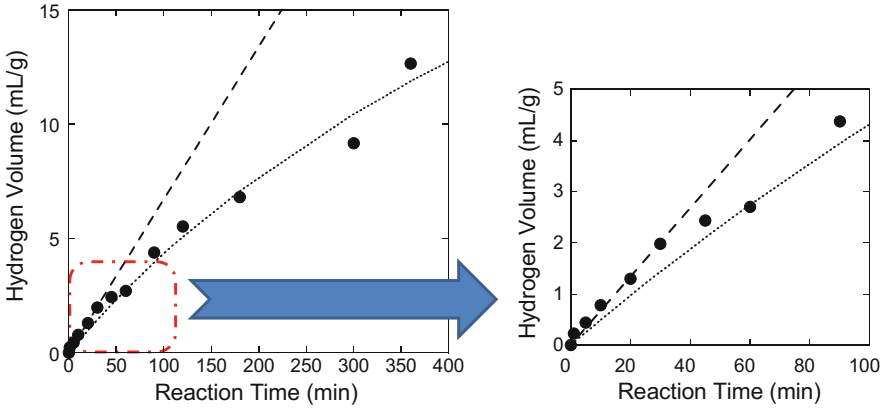

Fig. 9.18 Hydrogen volume generated from Si nanopower vs. the reaction time for the reaction with ultrapure water. The dashed and dotted lines show the calculated curves for the reaction-limited and migration-limited mechanisms

Figure 9.18 shows the generated hydrogen volume vs. the reaction time for the reaction of Si nanopowder with ultrapure water of pH 7.0 at room temperature. The observed plot is well expressed by the curve calculated with the following procedure: Si nanopowder is assumed to possess spherical shape with the initial diameter, r_0, and the diameter changes to $r_1(t)$ by the hydrogen generation reaction. The weight of an SiO_2 overlayer, W_{ox}, is simply written as

$$W_{ox} = \frac{4\pi}{3}\left({r_o}^3 - {r_1}^3\right) D_{Si}\frac{60}{28}, \tag{9.21}$$

where D_{Si} is the density of Si nanopowder. Using the SiO_2 thickness, l_{ox}, W_{ox} is given by

$$W_{ox} = \frac{4\pi}{3}\left[(r_1 + l_{ox})^3 - {r_1}^3\right] D_{ox}, \tag{9.22}$$

where D_{ox} is the density of silicon oxide. The hydrogen volume generated from unit weight Si nanopowder, V_{H_2}, is given by

$$V_{H_2} = \frac{4\pi}{3}\left[\left(r_1 + l_{ox}\right)^3 - {r_1}^3\right] D_{ox}\frac{3}{4\pi {r_0}^3 D_{Si}}C_0 = \frac{\left[\left(r_1 + l_{ox}\right)^3 - {r_1}^3\right]}{{r_0}^3}\frac{D_{ox}}{D_{Si}}C_0, \tag{9.23}$$

where C_0 is a constant.

When anions are the moving species through SiO_2 and their migration is the rate-determining step, the relationship between the SiO_2 thickness, l_{ox}, and the reaction time, t, is given by [47]

$$l_{ox} = \frac{kT}{C_1} \ln \frac{C_1 C_2 (t + t_0)}{kT} - \frac{W}{C_1}, \tag{9.24}$$

where W is the activation energy for migration of anions, and C_1 and C_2 are constants. Using Eqs. (9.23) and (9.24), the relationship between the generated hydrogen volume, V_{H_2}, and the reaction time, t, can be calculated, and the result is shown by the dotted line in Fig. 9.18.

In cases where the reaction at the Si/SiO_2 interface is the rate-determining step, the relationship between the SiO_2 thickness, l_{ox}, and the reaction time, t, is simply given by

$$l_{ox} = Ct, \tag{9.25}$$

where C is a constant. Using Eqs. (9.23) and (9.25), the relationship between V_{H_2} and t can be obtained, and the calculated curve is shown by the dashed line in Fig. 9.18. The experimental plot in the initial reaction stage and the subsequent stage is well fitted by the dashed line and the dotted line, respectively. This result shows that in the initial reaction stage, interfacial reaction is the rate-determining step, and in the subsequent stage, anions, i.e., OH^- ions, are the migrating species, and the migration of OH^- ions through SiO_2 is the rate-determining step. The rate-determining step changes from the interface reaction to migration of OH^- ions across silicon oxide at the generated hydrogen volume between 2.0 and 2.2 mL/g. In the case of the reaction with pH 8.0 and 8.6 solutions (plots c and d in Fig. 9.17), this volume of hydrogen is generated in a few minutes, showing that the rate-determining step changes to migration in the very early reaction stage.

For reaction (9.19), OH^- ions move inward, while for reaction (9.20), electrons move outward. This mechanism in which negative charges transfer in the opposite direction is likely to decrease the activation energy for migration of OH^- ions which is the rate-determining step. By this decrease in the activation energy, the hydrogen generation reaction proceeds easily at room temperature, resulting in the formation of the thick silicon oxide layer of ~5 nm thickness. It should be noted that in the case of thermal oxidation of crystalline Si, formation of a ~5 nm SiO_2 layer requires temperatures above 700 °C [48].

Figure 9.19 shows the hydrogen volume generated by the reaction of HF-etched Si nanopowder with ultrapure water vs. the reaction time for two different crystallite sizes. The hydrogen generation rate for smaller crystallite size Si nanopowder produced by the two-step beads milling method (average crystallite size: 13.8 nm) is 1.4~1.5 times higher than that for the larger crystallite size Si nanopowder (average crystallite size 23.4 nm). The surface area estimated from the average crystallite size is 190 m^2/g for the two-step beads milled Si nanopowder and 110 m^2/g for the one-step beads milled Si nanopowder. The ratio of the hydrogen generation rate of 1.4~1.5 between the two-step and one-step beads milled Si nanopowders is in reasonable agreement with the ratio of the surface area estimated from the average crystallite sizes. Si nanopowder forms agglomerate as is evident from the SEM micrograph (Fig. 9.20). The average sizes of Si agglomerates for one-step

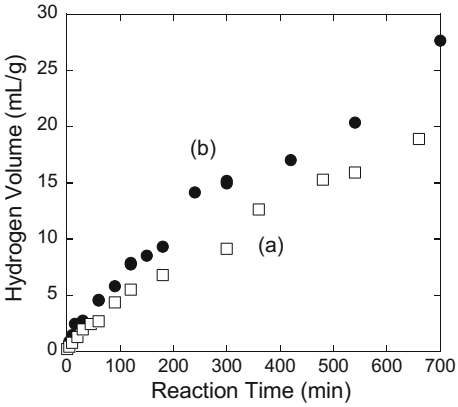

Fig. 9.19 Hydrogen volume vs. the reaction time for the reaction of Si nanopowder fabricated by the following methods with ultrapure water: (**a**) one-step beads milling (average crystallite diameter: 23.4 nm), (**b**) two-step beads milling (average crystallite diameter: 13.8 nm)

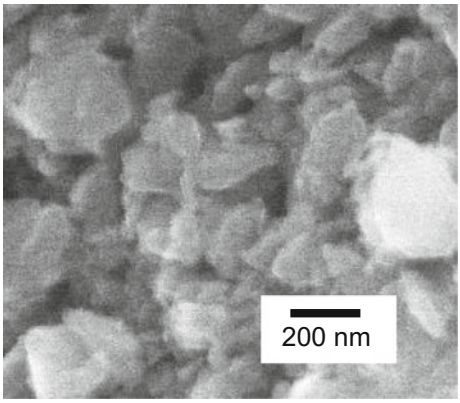

Fig. 9.20 SEM micrograph of Si nanopowder fabricated by the one-step beads milling method

and two-step beads milled Si nanopowers determined from dynamic light scattering measurements are nearly the same, i.e., 128 and 134 nm, respectively. These results show that the hydrogen generation rate strongly depends on the crystallite size but not on the size of agglomerate.

The thickness of the silicon oxide layer formed on Si nanopoweder by the reaction with water is estimated from XPS spectra in the Si 2p region (Fig. 9.21). The peak at 99∼100 eV is due to Si nanopowder, and the broader peak centered at 103∼105 eV is attributable to silicon oxide [49, 50]. After HF etching (spectrum a), the peak due to silicon oxide is very weak, and the thickness of the oxide layer is thought be less than 0.3 nm. When the hydrogen generation reaction stops after the reaction with pH 8.0 solutions for 24 h, the thickness of the silicon oxide layer can be estimated assuming a cylindrical shape with the radius, R, the same as the height. (Although Si nanopowder possesses polygonal shape (cf. Fig. 9.1.), assumption of cylindrical shape is thought not to cause a serious error in estimation of the silicon oxide thickness.) In this case, the oxide thickness, l_{ox}, is estimated using the following equation [51]:

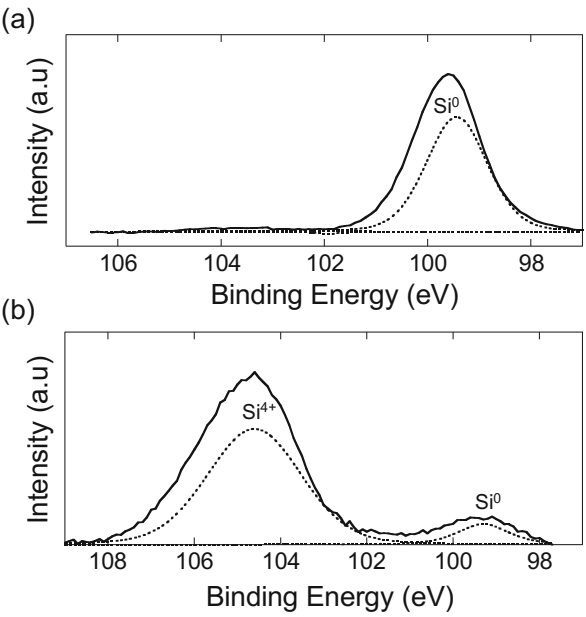

Fig. 9.21 XPS spectra in the Si 2p region for Si nanopowder fabricated by the one-step beads milling method: (**a**) after etching with an HF solution, (**b**) after the reaction of specimen a with the pH 8 solution for 24 h

$$\frac{I_{ox}}{I_{Si}} = \frac{N_{ox}\sigma_{ox}\lambda_{ox}}{N_{Si}\sigma_{Si}\lambda_{Si}} \frac{(R-l_{ox})^2\left[1-\exp\left(\frac{l_{ox}}{\lambda_{ox}}\right)\right]+l_{ox}\,(2R-l_{ox})\left[1-\exp\left(-\frac{R}{\lambda_{ox}}\right)\right]}{(R-l_{ox})^2\exp\left(-\frac{l_{ox}}{\lambda_{ox}}\right)\left[1-\exp\left(-\frac{R-l_{ox}}{\lambda_{Si}}\right)\right]}, \tag{9.26}$$

where I is the area intensity of the XPS peak; N, σ, and λ are the number density of Si atoms, the photoemission cross-section, and the photoelectron mean free path, respectively; and subscripts, *ox* and *Si*, denote the values for silicon oxide and Si, respectively. The radius, R, is assumed to be 11.7 nm which is a half of the average diameter determined from XRD measurements. In this estimation, the following values are adopted: $\lambda_{ox} = 2.9$ nm for Mg Kα (1254 eV) radiation, $\lambda_{Si} = 2.5$ nm, and $\frac{\sigma_{ox}}{\sigma_{Si}} = 1.1$ [52, 53]. Using Eq. (9.26), the silicon oxide thickness after the hydrogen generation reaction stops (spectrum b) is determined to be 4.8 nm.

Figure 9.22 schematically shows the mechanism of hydrogen generation from Si nanopowder. OH^- ions are adsorbed on the silicon oxide surface. OH^- ions migrate through a silicon oxide layer (step 1) enhanced by electrical field induced by adsorbed OH^- ions. Si atoms at the Si/silicon oxide interface react with OH^- ions, leading to generation of hydrogen, silicon oxide, and electrons in the conduction band of the silicon oxide layer (step 2). Electrons in the conduction band move outward to the silicon oxide surface (step 3), and then, electrons are accepted by water molecules, generating OH^- ions and hydrogen (step 4). Namely, OH^- ions move inward, while electrons move outward, which is likely to decrease the activation energy of inward migration of OH^- ions, i.e., the rate-determining

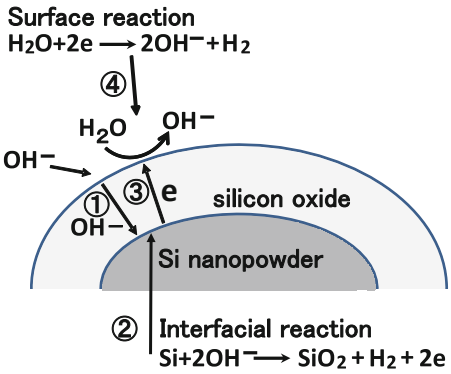

Fig. 9.22 Schematic mechanism of the reaction of Si nanopowder with water in the neutral pH region

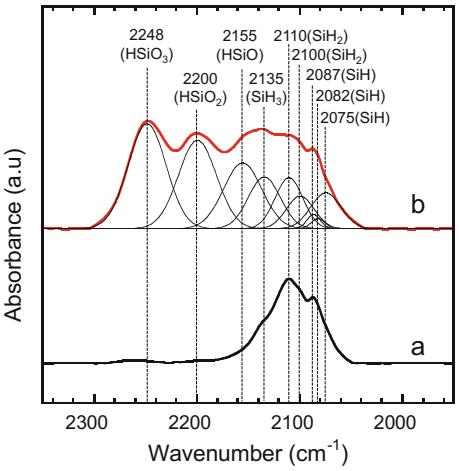

Fig. 9.23 FT-IR spectra in the Si-H stretching vibrational region for HF-etched Si nanopowder: (**a**) just after etching with the HF solution, (**b**) after the reaction of specimen a with ultrapure water for 24 h

step for the hydrogen generation reaction from Si nanopowder, and therefore, the reaction proceeds at room temperature.

The initial reaction of HF-etched Si nanopowder with ultrapure water is investigated using FT-IR spectroscopy (Fig. 9.23). HF-etched Si nanopowder exhibits three peaks in the Si-H stretching vibrational region (spectrum a), and they are attributed to SiH (2087 cm^{-1}), SiH_2 (2110 cm^{-1}), and SiH_3 (2155 cm^{-1}) [54, 55]. After reaction with ultrapure water for 24 h at room temperature (spectrum b), new peaks appear at 2158, 2200, and 2248 cm^{-1}, which are attributable to HSiO, $HSiO_2$, and $HSiO_3$ species, respectively [56, 57], and the peaks due to SiH, SiH_2, and SiH_3 are still present. These results show that OH^- ions attack Si back bonds to form Si-O bonds, but they don't attack Si-H bonds. Nearly the same energy differences between the HSiO and $HSiO_2$ peaks and between the $HSiO_2$ and $HSiO_3$ peaks show that only one species with one hydrogen atom (i.e., HSiO, $HSiO_2$, and $HSiO_3$, but not H_3SiO, H_2SiO, and H_2SiO_2) is included in each Si-H stretching vibrational peak.

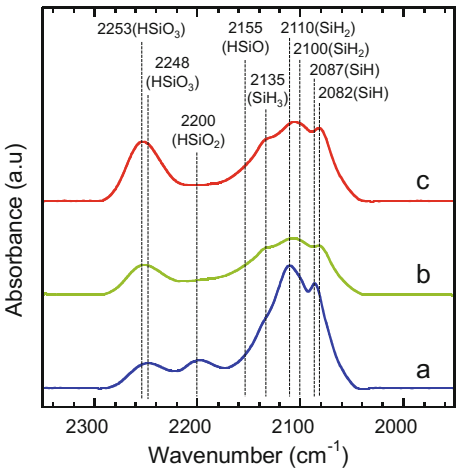

Fig. 9.24 FT-IR spectra in the Si-H stretching vibrational region for HF-etched Si nanopowder after the reaction with pure heavy water for the following periods: (**a**) 10 min, (**b**) 3 h, (**c**) 24 h

In the case of the reaction with pure D_2O (Fig. 9.24), a strong $HSiO_3$ peak is observed even after 10 min reaction, but the intensity of the peak due to $HSiO_2$ is much weaker (spectrum a), and after 3 h reaction, the intensity of the $HSiO_3$ peak increases, while the $HSiO_2$ peak disappears almost completely (spectrum b). This result is in strong contract to the reaction with H_2O where $HSiO_2$ species is present even after the reaction for 24 h (spectrum b in Fig. 9.23). This difference can be explained by the local reaction to form two-dimensional agglomerate-like structure in the case of the surface reaction with D_2O, while the reaction proceeds more uniformly on the surface for the reaction with H_2O.

The peak due to $HSiO_3$ shifts from 2248 (cf. spectrum a for 10 min reaction) to 2253 cm^{-1} (spectrum c for 24 h reaction) with the reaction time for the reaction with D_2O, while such a shift doesn't occur in the case of the reaction with H_2O. This shift is most probably attributable to an increase of the charge on Si atoms [58]. Namely, the Si-H bonds become stronger as the reaction proceeds locally. For the reaction with H_2O, on the other hand, the reaction proceeds uniformly, and such a change in the charge state doesn't occur.

After the reaction with D_2O, vibrational peaks are observed in the Si-D stretching vibrational region (Fig. 9.25), indicating that replacement of H atoms to D atoms proceeds on the surface. Peaks appear at 1516, 1525, and 1549 cm^{-1}, and they are most probably attributable to SiD, SiDH, and $SiDH_2$ species, respectively. The replacement probability after 24 h reaction (spectrum c) is estimated to be 37%, and therefore, the probabilities of formation of SiD_2 and SiD_2H (or SiD_3) are likely to be much lower than those of SiDH and $SiDH_2$, respectively.

Although the intensity of the Si-H peak is lower than that of Si-H_2 peak before the reaction with D_2O (spectrum a in Fig. 9.23), the intensity of the Si-D peak is higher than that of the Si-DH peak after the reaction with D_2O. This result indicates that Si-H bonds in Si-H species are weaker than those in Si-H_2 species, resulting

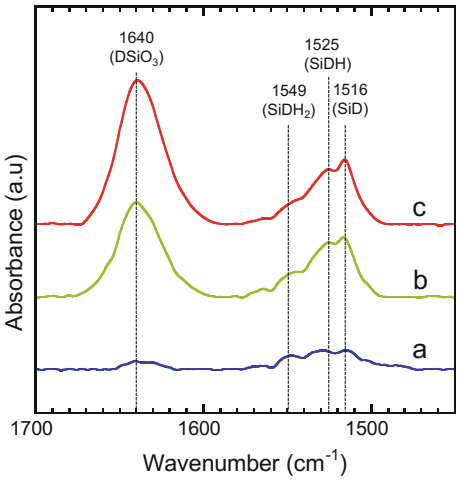

Fig. 9.25 FT-IR spectra in the Si-D stretching vibrational region for HF-etched Si nanopowder after the reaction with pure heavy water for the following periods: (**a**) 10 min, (**b**) 3 h, (**c**) 24 h

in the higher replacement probability. This result is in accordance with the higher frequency of the Si-H_2 vibrational peak than that of the Si-H peak.

After the reaction with D_2O for 3 h (spectrum b), a strong peak due to $DSiO_3$ is observed at 1640 cm^{-1}, while no peak due to $DSiO_2$ is present. This result also indicates the formation of agglomerate-like structure which consists of $DSiO_3$ and $HSiO_3$.

9.3 Conclusion

Si nanopowder is fabricated by use of the beads milling method. Fabricated Si nanopowder has the following PL and hydrogen generation characteristics:

1. Si nanopowder etched with an HF solution and immersed in ethanol shows green-PL. The PL energy depends on the excitation photon energy, and it is attributed to band-to-band transition of Si nanopowder whose band-gap is enlarged by the quantum confinement effect.
2. Si nanopowder which isn't etched with HF and immersed in hexane exhibits blue-PL. The PL energy is independent of the excitation photon energy, and it is attributed to transition of DMA adsorbed on Si nanopowder.
3. The intensity of blue-PL is enhanced by ~60,000 times due to adsorption of DMA on Si nanopowder. The PL intensity is increased by adsorption on Si nanopowder for the following two reasons: (i) an increase in the number of electrons in the electronic excited-state (~7100 times enhancement) and (ii) an increase in the rate constant for radiative transition (~8.5 times enhancement).

4. For blue-PL arising from excitation with energies higher than 3.76 eV, PL peaks with energies higher than the (0,0) band are present, and they are attributed to transition from vibrational excited-states.
5. The excitation spectra show that blue-PL results from the two different mechanisms: (i) excitation of adsorbed DMA and (ii) band-to-band transition of Si nanopowder, followed by transfer of photo-generated electrons and holes to DMA. For mechanism (ii), a photo-generated electron and a hole transfer to DMA separately, resulting in two (0,0) bands.
6. Only when a photo-generated hole transfers to DMA first, followed by electron transfer, transition from vibrational excited-states occurs.
7. Si nanopowder easily reacts with strong alkaline (pH>13) solutions, and almost stoichiometric amount of hydrogen (i.e., ∼1700 mL/g) is generated in a few minutes.
8. Si nanopowder reacts with water in a neutral pH region between 7 and 9 to generate hydrogen. In this case, the hydrogen generation rate markedly increases with pH of the solution, while pH doesn't change by the reaction. In the first reaction stage, Si nanopowder reacts with OH^- ions, generating hydrogen, silicon oxide, and electrons in the conduction band of silicon oxide, while in the second reaction stage, electrons are accepted by water molecules to form hydrogen and OH^- ions.
9. In the very early hydrogen generation reaction stage (less than 2.2 mL/g hydrogen generation), the surface reaction is the rate-determining step, and then, migration of OH^- ions through a silicon oxide layer becomes the rate-determining step.
10. The hydrogen generation reaction stops when a ∼5 nm silicon oxide layer is formed on Si nanopowder.
11. The hydrogen generation rate strongly depends on the crystallite size of Si nanopowder, but it doesn't depend on the size of its agglomerate.

9.4 Outlook

Si is a nontoxic material, and its medical application is expected. We have proposed two kinds of medical application of Si nanopowder, i.e., (i) photoluminescence material and (ii) internal hydrogen generation material. For application (i), Si nanopowder can be applied to life cell imaging, e.g., to detect cancer cells. Si nanopowder, especially, blue-PL Si nanopowder, can give much stronger PL than conventional dyes and is more stable, especially, high photostability, both of which make the application easier and more effective.

For various diseases, oxidation stress is one of the largest factors to cause diseases. Hydrogen generation in the body can decrease oxidative stress, and therefore, it can prevent various oxidative stress-induced diseases. Moreover, for apparently healthy persons, i.e., persons who don't suffer from diseases but on whom addition of a tiny factor causes diseases, a decrease of oxidative stress can

make them really healthy. The decrease of oxidative stress by internal hydrogen generation can also retard aging, which can extend health life expectancy.

Si-based agent which can generate a high amount of hydrogen in bowels is now being developed in our laboratory. Contrary to conventional medicines, Si-based agent isn't absorbed in the body, but only hydrogen generated from the agent is absorbed. Therefore, a medicine with great medical effects but without any side effects is expected to be developed using Si-based agent.

References

1. N. O'Farrell, A. Houlton, B.R. Horrocks, Int. J. Nanomed. **1**, 451 (2006)
2. Z. Kang, Y. Liu, C.H.A. Tsang, D.D.D. Ma, X. Fan, N.-B. Wong, S.-T. Lee, Adv. Mater. **21**, 661 (2009)
3. X.P. Zhu, T. Yukawa, M. Hirai, T. Suzuki, H. Suematsu, W. Jiang, K. Yatsui, Appl. Surf. Sci. **242**, 256 (2005)
4. M. Inada, H. Nakagawa, I. Umezu, A. Sugimura, Mater. Sci. Eng. **B101**, 283 (2003)
5. L. Mangolini, J. Vac. Sci. Technol. B **31**, 020801 (2013)
6. O.B. Gusev, A.N. Poddubny, A.A. Prokofiev, I.N. Yassievich, Semiconductors **47**(2), 183–202 (2013)
7. Z. Gu, X.-Y. Chen, Q.-D. Shen, H.-X. Ge, H.-H. Xu, Polymer **51**, 902 (2010)
8. E. Fazio, F. Barreca, S. Spadaro, G. Currò, F. Neri, Mater. Chem. Phys. **130**, 418 (2011)
9. K. Watanabe, K. Sawada, M. Koshiba, M. Fujii, S. Hayashi, Appl. Surf. Sci. **197–198**, 635 (2002)
10. L. Nikolova, R.G. Saint-Jacques, C. Dahmoune, G.G. Ross, Surf. Coat. Technol. **203**, 2501 (2009)
11. P.T. Huy, V.V. Thu, N.D. Chien, C.A.J. Ammerlaan, J. Weber, Physica B **376–377**, 868 (2006)
12. C. Lam, Y.F. Zhang, Y.H. Tang, C.S. Lee, I. Bello, S.T. Lee, J. Crystal Growth **220**, 466 (2000)
13. Y.V. Ryabchikov, S.A. Alekseev, V. Lysenko, G. Bremond, J.-M. Bluet, J. Nanopart. Res. **15**, 1535 (2013)
14. M. Imamura, J. Nakamura, S. Fujimasa, H. Yasuda, H. Kobayashi, Y. Negishi, Eur. Phys. J. D **63**, 289 (2011)
15. Y.C. Fang, Y. Zhang, H.Y. Gao, L.G. Chen, B. Gao, W.Z. He, Q.S. Meng, C. Zhang, Z.C. Dong, Appl. Surf. Sci. **285P**, 572 (2013)
16. T. Matsumoto, M. Maeda, H. Kobayashi, Nanoscale Res. Lett. **11**, 7 (2016)
17. M. Maeda, T. Matsumoto, H. Kobayashi, Phys. Chem. Chem. Phys. **19**, 21856 (2017)
18. T. Matsumoto, M. Maeda, J. Furukawa, W.-B. Kim, H. Kobayashi, J. Nanopart. Res. **16**, 2240 (2014)
19. M. Maeda, K. Imamura, T. Matsumoto, H. Kobayashi, Appl. Surf. Sci. **312**, 39 (2014)
20. T. Ida, S. Shimazaki, H. Hibino, H. Toraya, J. Appl. Cryst. **36**, 1107 (2003)
21. G. Conibeer, Silicon nanocrystals, Pavesi and R. Turan (eds.), Wiley-VCH Verlag GmbH & Co. KGaA, Weinheim, pp. 555–561, 2010.
22. J.P. Wilcoxon, G.A. Samara, P.N. Provencio, Phys. Rev. B **60**, 2704 (1999)
23. K. Ohno, Chem. Phys. Lett. **53**, 571 (1978)
24. A. Henβge, J. Acker, C. Müller, Talanta **68**, 581 (2006)
25. K. Oura, VG. Lifshits, AA. Saranin, AV. Zotov, and M. Katayama, Surface Science, Springer, Berlin/Heiderberg/New York, p. 267, 2003.
26. D.R. Johar, L.H. Bernstein, Diab. Res. Clin. Pract. **126**, 222 (2017)
27. K. Takeshita, C. Chi, H. Hirata, M. Oho, T. Ozawa, Free Radic. Biol. Med. **40**, 876 (2006)

28. B. Shao, L. Mao, N. Qu, Y.-F. Wang, H.-Y. Gao, F. Li, L. Qin, J. Shao, C.-H. Huang, D. Xu, L.-N. Xie, C. Shen, X. Zhou, B.-Z. Zhu, Free Radic. Biol. Med. **104**, 54 (2017)
29. J.B. Jeong, E.W. Seo, H.J. Jeong, Food Chem. Toxicol. **47**, 2135 (2009)
30. Y. Hayashi, Y. Ueda, A. Nakamura, H. Yokojyama, Y. Mitsuyama, H. Ohya-Nishiguchi, H. Kamada, Brain Res. **941**, 107 (2002)
31. T. Jian, Q. Sun, S. Chen, Prog. Neurobiol. **147**, 1 (2016)
32. J. Li, C. Wang, J.H. Zhang, J.M. Cai, Y.P. Cao, X.J. Sun, Brain Res. **1328**, 152–161 (2010)
33. A. Yoritaka, M. Takanashi, M. Hirayama, T. Nakahara, S. Ohta, N. Hattori, Mov. Disord **28**, 836 (2013)
34. O. Boutaud, L.J. Roberts II, Free Radic. Biol. Med. **51**, 1062 (2011)
35. A. Kagawa, K. Katsura, M. Mizumoto, Y. Tagawa, Y. Masiko, Mater. Sci. Forum **706–709**, 520 (2012)
36. Y.S. Yoon, M.E. Sajo, R.M. Ignacio, S.K. Kim, C.S. Kim, K.J. Lee, J. Biol. Pharm. Bull. **37**, 1480 (2014)
37. S. Kato, Y. Saitoh, K. Iwai, N. Miwa, J. Photochem. Photobiol. B Biol. **106**, 24 (2012)
38. Y. Kobayashi, S. Matsuda, K. Imamura, H. Kobayashi, J. Nanopart. Res. **19**, 176 (2017)
39. K. Imamura, Y. Kobayashi, S. Matsuda, T. Akai, H. Kobayashi, AIP Adv. **7**, 085310 (2017)
40. Y. Kobayashi, K. Imamura, T. Matsumoto, H. Kobayashi, J. Elect. Eng. **68**, 17 (2017)
41. C. Liu, R. Kurokawa, M. Fujino, S. Hirano, B. Sato, X.-K. Li, Sci. Rep. **4**, 5485 (2014)
42. G.K.B. Lopes, H.M. Schulman, M. Hermes-Lima, Biochim. Biophys. Acta **1472**, 142 (1999)
43. S. Ozgová, J. Heřmánek, I. Gut, Biochem. Pharmacol. **66**, 1127 (2003)
44. D.D. Kitts, Trends Food Sci. Technol. **8**, 198 (1997)
45. E. Niki, Free Radic. Biol. Med. **66**, 3 (2014)
46. X. Liu, L. Zhao, K. Domen, K. Takanabe, Mater. Res. Bull. **49**, 58 (2014)
47. D.D. Eley, P.R. Wilkinson, Proc. R. Soc. London Ser. A **254**, 327 (1960)
48. A. Atkinson, Rev. Mod. Phys. **57**(2), 437 (1985)
49. F.J. Himpsel, F.R. McFeely, A. Taleb-Ibrahimi, J.A. Yarmoff, G. Hollinger, Phys. Rev. B **38**, 6084 (1988)
50. H. Kobayashi, T. Ishida, Y. Nakato, H. Tsubomura, J. Appl. Phys. **69**, 1736 (1991)
51. O. Renault, R. Marlier, N.T. Barrett, E. Martinez, T. Baron, M. Gely, B. De Salvo, Surf. Interface Anal. **38**, 486 (2006)
52. H. Kobayashi, Asuha, O. Maida, M. Takahashi, H. Iwasa, J. Appl. Phys. **94**, 7328 (2003)
53. M.F. Hochella Jr., A.H. Carim, Surf. Sci. **197**, L260 (1988)
54. A.I. Belogorokhov, S.A. Gavrilov, P.K. Kashkarov, I.A. Belogorokhov, Phys. Status Solidi A **202**, 1581 (2005)
55. Y.H. Ogata, T. Tsuboi, T. Sakka, S. Naito, J. Porous Mater. **7**, 63 (2000)
56. Y. Kato, T. Ito, A. Hiraki, Jpn. J. Appl. Phys. **27**, L1406 (1988)
57. X.H. Sun, S.D. Wang, N.B. Wong, D.D.D. Ma, S.T. Lee, Inorg. Chem. **42**, 2398 (2003)
58. G. Lucovsky, Solid State Commun. **29**, 571 (2017)

Chapter 10
New Na^+ Superionic Conductor Narpsio Glass-Ceramics

Toshinori Okura and Kimihiro Yamashita

Abstract This review article describes a series of studies on glass-ceramic Na^+ superionic conductors with the $Na_5YSi_4O_{12}$ (N5)-type structure and with a $Na_{3+3x-y}R_{1-x}P_ySi_{3-y}O_9$ composition, where R is a rare earth element. In the crystallization of N5-type glass-ceramics, its relatives ($Na_3YSi_3O_9$ (N3)- and $Na_9YSi_6O_{18}$ (N9)-type glass-ceramics) structurally belonging to the family of $Na_{24-3x}Y_xSi_{12}O_{36}$ were found to crystallize as the precursor phase at low temperatures. In order to produce N5 single-phase glass-ceramics, the concentration of both phosphorus and rare earth was found important. The meaning of the composition was evaluated by kinetic study on the phase transformation of metastable N3 or N9 phases to stable N5 phase with Na^+ superionic conductivity. The possible combinations of x and y became more limited for the crystallization of the superionic conducting phase as the ionic radius of R increased, while the Na^+ conduction properties were more enhanced in the glass-ceramics of larger R. These results are discussed in view of the structure and the conduction mechanism. Also discussed were the microstructural effects on the conduction properties, which were dependent upon the heating conditions of crystallization. These effects were understood in relation to the grain boundary conduction properties as well as the transmission electron microstructural morphology of grain boundaries. Recent research into the effects of microstructure on conduction properties and microstructural control of Na^+ superionic conducting glass-ceramics is also introduced. The optimum conditions for crystallization are discussed with reference to the conduction properties and the preparation of crack-free N5-type glass-ceramics. The effects of substituting Si with other elements exhibiting tetrahedral oxygen coordination and substituting Y with various rare earth elements are also

T. Okura (✉)
Department of Applied Chemistry, School of Advanced Engineering, Kogakuin University, Tokyo, Japan
e-mail: okura@cc.kogakuin.ac.jp

K. Yamashita
Institute of Biomaterials and Bioengineering, Tokyo Medical and Dental University, Tokyo, Japan
e-mail: yama-bcr@tmd.ac.jp

T. Onishi (ed.), *Theoretical Chemistry for Advanced Nanomaterials*,
https://doi.org/10.1007/978-981-15-0006-0_10

discussed in the context of the ionic conductivity of these N5-type glass-ceramics. In addition, results on the improvement in superconductivity by Na^+ ion implantation and control of the structure by bias crystallization of glasses in an electric field are presented.

Keywords Superionic conductor · Glass-ceramics · Crystallization · Microstructure · Ion implantation · Bias crystallization

10.1 Introduction

The use of glass-making processing is favorablefor the fabrication of Na^+ conducting electrolyte tubes, which has been the key to the technological development of 1 MW Na/S secondary battery plants. However, the processing technique cannot be applied to well-known β- and β″-aluminas (e.g., $NaAl_{11}O_{17}$ and $NaAl_5O_8$) and Nasicons ($Na_{1+x}Zr_2P_{3-x}Si_xO_{12}$) because their high inclusion of Al_2O_3 or ZrO_2 brings about the inhomogeneous melting or crystallization of glasses. Alternatively, Nasicon-like glass-ceramics were synthesized using a composition with lower content of ZrO_2 (mNa$_2$O·xZrO$_2$·yP$_2$O$_5$·(100−m−x−y)SiO$_2$ [m = 20, 30 mol %]). However, the conductivities (σ) attained were, at most, as high as $\sigma_{300} = 2 \times 10^{-2}$ S/cm at 300 °C with the activation energies (E_a) of ca. 30 kJ/mol [1]. These low conductivities were attributed to the crystallization of the poorly conductive rhombohedral phase in these Nasicon-like materials [1]. $Na_5YSi_4O_{12}$ (N5), which comprises 12-$(SiO_4)^{4-}$-tetrahedra-membered skeleton structure (Fig. 10.1) [2, 3], is another Na^+ superionic conductor with $\sigma_{300} = 1 \times 10^{-1}$ S/cm and $E_a = 25$ kJ/mol [4–7]. A pioneering work on N5-type glass-ceramics was performed by Banks et

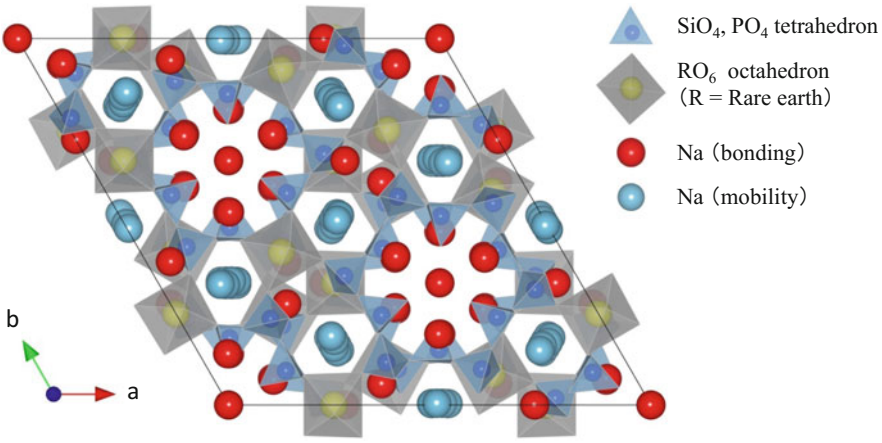

Fig. 10.1 Crystal structure of $Na_5YSi_4O_{12}$ [4]. Reprinted from Solid State Ionics 285 (2016) 143, Copyright 2016, with permission from Elsevier

al. on the family of N5-type materials by substituting Y with Er, Gd, or Sm [8]. However, their results were not completely satisfactory because of the relatively lower conductivities of $\sigma_{300} < 2 \times 10^{-2}$ S/cm than the reported values of N5 [8]. This discrepancy may possibly have arisen from the occurrence of a less conductive metastable phase during crystallization [9], as discussed below.

Contrary to the results of Banks et al., we obtained glass-ceramics where $\sigma_{300} = 1 \times 10^{-1}$ S/cm and $E_a = 20$ kJ/mol [10]; these compounds were based on the phosphorus-containing N5-type materials discovered in the Na_2O-Y_2O_3-P_2O_5-SiO_2 system [10]. These N5-type materials, in addition to $Na_3YSi_3O_9$ (N3)-type materials [11–13], were obtained with the composition formula originally derived for N3-type solid solutions and expressed as follows [14]:

$$Na_{3+3x-y}Y_{1-x}P_ySi_{3-y}O_9 \ (x < 0.6, \quad y < 0.5) \tag{10.1}$$

With the aim of searching for more conductive glass-ceramic N5-type materials, the verification of the validity of the general composition

$$Na_{3+3x-y}R_{1-x}P_ySi_{3-y}O_9 \ (R = \text{a rare earth element}) \tag{10.2}$$

for the synthesis of other types of rare earth N5-type glass-ceramics was studied first. Formula 2 is rewritten with formula 3 according to the formula N5.

$$Na_{4(3+3x-y)/3}Y_{4(1-x)/3}P_{4y/3}Si_{4(3-y)/3}O_{12} \tag{10.3}$$

In relation to previous works [10, 14], formula 2 was employed in this work, and formula 3 is referred to in the results. The trivalent ions employed here for R^{3+} were Sc^{3+}, In^{3+}, Er^{3+}, Gd^{3+}, Sm^{3+}, Eu^{3+}, Nd^{3+}, La^{3+}, and Y^{3+}. These results are to be interpreted in terms of the effect of the rare earth ions on the crystallization of the N5-type phase in glasses [15–20].

Interestingly, in the course of the fundamental studies on the glass-ceramics $Na_{3+3x-y}R_{1-x}P_ySi_{3-y}O_9$, we have found the crystallization of those N3- and $Na_9YSi_6O_{18}$ (N9)-type phases as the precursors in the glasses [21]. These are the analogues to the silicates N3 and N9 [10, 22] and therefore are the same members of the family of $Na_{24-3x}Y_xSi_{12}O_{36}$ [12] as N5. Although we had also successfully synthesized those materials by the solid-state reactions of powders with the above composition of various sets of the parameters x and y [10, 22], the metastability of those precursor phases had not been noticed in the synthesis. It has been observed that such precursor phases were transformed to the Na^+ superionic conducting phase on specimens with appropriate sets of x and y. The present review paper deals with the thermodynamic and kinetic studies on the phase transformation of metastable phases to the stable phase with Na^+ superionic conductivity. The superiority of our present materials to the other silicate N5 will also be detailed based on the kinetic results.

The microstructure of a glass-ceramics, including neck growth among grains as well as grain size, is generally affected by the crystallization process [23]. As

the abovementioned devices utilize the dc conduction properties of Na^+ superionic conductors, another aim was to study the microstructural effects on the conduction properties of a whole glass-ceramic [24–28]. Special attention was paid to the analysis of grain boundary properties using the Na_2O-Y_2O_3-P_2O_5-SiO_2 system. For the analysis of grain boundary properties, as discussed below, composition dependences on the conductivity of sodium silicophosphate glasses containing Y_2O_3 were also introduced in the Na_2O-Y_2O_3-P_2O_5-SiO_2 system. For convenience, the present materials are abbreviated as Narpsio, taken from the initials of the Na_2O-R_2O_3-P_2O_5-SiO_2 system.

10.2 Materials

10.2.1 Glasses and Glass-Ceramics

We successfully produced the Narpsio family by the following methods: (i) solid-state reactions of powders [10, 22], (ii) sol-gel method [19, 29], and (iii) crystallization of glasses [30]. In considering practical applications such as Na/S batteries, the present Narpsio materials may be expected to show advantages over the aluminas, both in lowering the heat treatment temperatures and in fabricating various shapes because of the ease of glass-making. The latter point closely depends on the glass-ceramic processing technology.

Precursor glasses were prepared from reagent-grade oxides of anhydrous Na_2CO_3, R_2O_3 (R = Y, Sc, In, Er, Gd, Sm, Eu, Nd, La), $NH_4H_2PO_4$, and SiO_2; the mechanically mixed powders according to formula 2 or appropriate compositions shown below were melted at 1350 °C for 1 h after calcination at 900 °C for 1 h. The melts were quickly poured into a graphite cylinder and then annealed at 500 °C for 3 h, giving Narpsio glasses. The composition parameters studied were in the range of $0.2 < x < 0.6$ and $0 < y < 0.5$ of formula 2. As shown below, grain boundary conduction properties are discussed in relation to the properties of glasses. For the evaluation of the composition dependence of conductivity in Na^+ conducting glasses, various sodium-yttrium silicophosphate glass specimens with different atomic ratios of Na/(P+Si) and Na/Y were also prepared.

Crystallization was carried out according to a previous report [14]; bulk glasses were heated at a rate of 75 °C/h to a temperature approximately 50 °C above the glass transition point, which had been determined in advance by differential thermal analysis (DTA). This pretreatment was performed in order to obtain homogeneous nucleation [23]. After annealing for 1 h, the specimens were heated at temperatures of 800–1100 °C, depending on the composition, for 0.5 to 72 h, and thereafter slowly cooled in a furnace with a decreasing rate of 150 °C/h to room temperature. These quenched glasses or glass-ceramic specimens were polished with 0.5 μm diamond paste and thereafter subjected to conductivity measurements.

For the description of a specific Narpsio, *R* of the term will be replaced, respectively, with Y, Sc, In, Er, Gd, Sm, Eu, Nd, and La as Y-Narpsio, Sc-Narpsio, In-Narpsio, Er-Narpsio, Gd-Narpsio, Sm-Narpsio, Eu-Narpsio, Nd-Narpsio, and La-Narpsio for Y_2O_3, Sc_2O_3, In_2O_3, Er_2O_3, Gd_2O_3, Sm_2O_3, Eu_2O_3, Nd_2O_3, and La_2O_3, respectively.

10.2.2 Characterization

10.2.2.1 AC Impedance Measurement

Ionic conductivities were evaluated by the complexim pedance method on cylindrical glasses or glass-ceramics, typically 15 mm in diameter and 2 mm in thickness. Electrodes were prepared by sputtering of gold on polished surfaces. The applied ac field ranged from 5 to 10 MHz in frequency. The temperature dependence of the conductivity was measured similarly at several temperatures ranging from room temperature to 350 °C. The complex impedance or admittance loci of glass and glass-ceramics were analyzed by an equivalent circuit (Fig. 10.2), which was experimentally found to comprise one and two semicircles in Narpsio glasses and glass-ceramics, respectively. The two intercepting points on the real axis are interpreted as the resistance of the crystallized grains ($R_{G(c)}$) and the total resistance

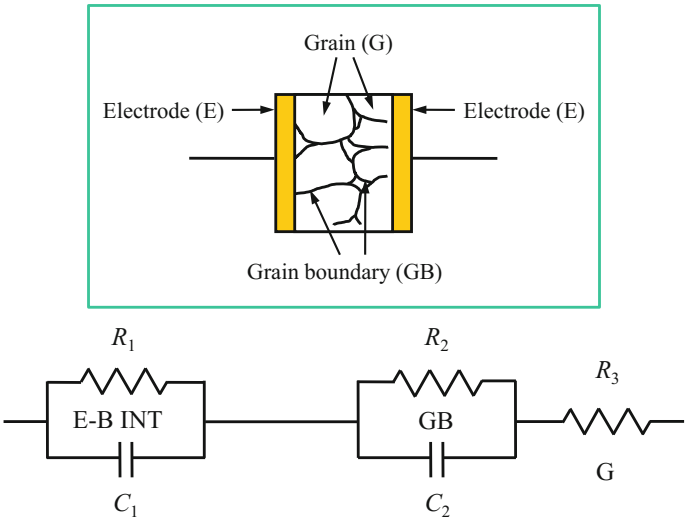

Fig. 10.2 Equivalent circuit employed for the admittance analysis. E-B INT, GB, and G represent the electrode-bulk interface, grain boundaries, and grains, respectively, and (R_1, C_1), (R_2, C_2), and R_3 are their resistances and capacitances [30]. Reprinted by permission from Springer Nature: Springer J. Electroceram. 24 (2010) 83, COPYRIGHT (2010)

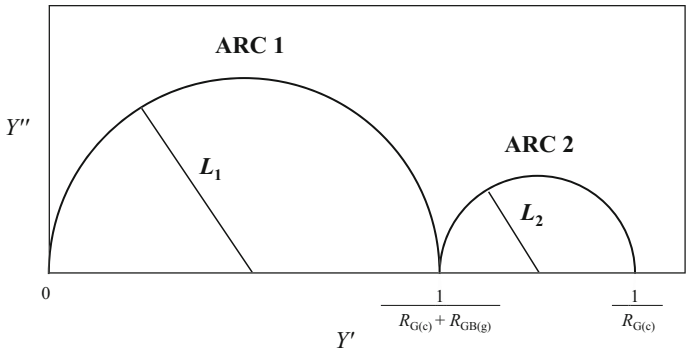

Fig. 10.3 Idealized diagram of complex admittance for glass-ceramics, in which arc 1 (ARC 1) and arc 2 (ARC 2) are related to the crystallized grains (G(c)) and remaining glasses (GB(g)). L_1, L_2, $R_{G(c)}$, and $R_{GB(g)}$ are, respectively, the radii of arcs 1 and 2 and the resistances of G(c) and GB(g) [30]. Reprinted by permission from Springer Nature: Springer J. Electroceram. 24 (2010) 83, COPYRIGHT (2010)

of the grains and remaining glassy grain boundaries ($R_{GB(g)}$). Assume the complex admittance diagram shown in Fig. 10.3, where the parameters L_1 and L_2 are set here as the radii of the two arcs 1 and 2. Those parameters are related to one another as follows:

$$L_1 \propto 1/\left(R_{G(c)} + R_{GB(g)}\right) \tag{10.4}$$

and

$$L_2 \propto \left(1/R_{G(c)}\right) - 1/\left(R_{G(c)} + R_{GB(g)}\right) \tag{10.5}$$

Then,

$$L_2/L_1 = R_{GB(g)}/R_{G(c)} \tag{10.6}$$

Therefore, in an ideal glass-ceramic where residual glass would have negligible influence on the total, arc 2 would be much smaller than arc 1, because $L_2/L_1 \rightarrow 0$.

10.2.2.2 X-Ray Diffraction

The form of the powder X-ray diffraction (XRD) data obtained from a material will depend upon the crystal structure it adopts. This structure is delineated by the lattice type, crystal class, unit cell parameters, and the distribution of the various ion and molecule types within the unit cell. The number and positions, in terms of 2θ, of the reflections depend upon the cell parameters, crystal class, lattice type, and

wavelength used to collect the data, while peak intensity depends upon the types of atoms present and their positions.

As a result of the enormous range of different structures which materials adopt, nearly all crystalline solids have a unique powder X-ray diffraction pattern in terms of the positions of the observed reflections and the peak intensities. In mixtures of compounds, each crystalline phase present will contribute to the powder diffraction pattern in its own unique set of lines. The relative intensity of line sets from mixtures will depend on the amount present and the ability of a structure to scatter X-rays.

The crystalline phases of glass-ceramic specimens were identified by XRD. The lattice parameters of the N5-type hexagonal unit cell were calculated by a least-squares method using the XRD peaks of (054), (044), (134), (440), and (024).

10.2.2.3 Scanning Electron Microscope and Transmission Electron Microscope

A recent and very useful research tool is a scanning electron microscope (SEM). The surface of a specimen to be examined is scanned with an electron beam, and the reflected (or backscattered) electron beam is collected and then displayed at the same scanning speed on a cathode ray tube (CRT). The image on the screen that may be photographed represents the surface features of the specimen. The surface may or may not be polished and etched but must be electrically conductive. A very thin metal surface coating must be applied to the nonconductive material. Magnifications in the range of 10 times to 50,000 times are also possible, and there is also a very great depth of field. Ancillary equipment allows qualitative and semiquantitative analysis of the elemental composition of highly localized surface areas.

The image seen with a transmission electron microscope (TEM) is formed by an electron beam passing through the specimen. Details of the internal microstructural features are accessible for observation. The contrasts in the image are caused by the differences in beam scattering or diffraction occurring between the various elements of the microstructure or defect. Since the solid materials are highly absorptive to the electron beams, the specimen to be examined must be prepared in the form of a very thin foil. This allows a significant fraction of the incident beam to penetrate the specimen. The transmitted beam is projected onto a fluorescent screen or a photographic film so that the image can be seen.

Glass-ceramics of Y^{3+}-containing Narpsio were subjected to SEM and TEM for microstructural analysis. Electron diffraction and compositional analyses were also performed to characterize the structure of the grain boundary.

10.2.2.4 Arrhenius Plot and Kissinger Plot

In chemical kinetics, an Arrhenius plot displays the logarithm of a reaction rate constant (ln k, ordinate axis) plotted against inverse temperature (1/T, abscissa axis). Arrhenius plots are often used to analyze the effect of temperature on the

rates of chemical reactions. For a single rate-limited thermally activated process, an Arrhenius plot gives a straight line, from which the activation energy can be determined. The temperature dependence Arrhenius plots were presented based on the calculated conductivity values of grains and grain boundaries of the Narpsio glass-ceramics.

Apparent activation energies for crystallization (crystal growth) were determined by employing the non-isothermal-modified Kissinger methods [31, 32] in which some characteristics of the crystallization peak determined by DTA were monitored as a function of heating rate or temperature. The following relationship was then applied.

$$\ln\left(\frac{\alpha^n}{{T_0}^2}\right) = -\frac{\mathrm{E}m}{\mathrm{R}T_0} + const.,$$

where α is the heating rate, T_0 is the peak crystallization temperature at a given heating rate, E is the apparent activation energy, R is the gas constant, and m and n are numerical factors which depend on the crystallization mechanism (m depends on the dimensionality of crystal growth). When bulk crystallization occurs with an increasing number of nuclei (i.e., the number of nuclei is inversely proportional to the heating rate), $m = 3$ and $n = 4$ (indicating three-dimensional growth of crystals). In this study, the parameters m and n were assumed to be 3 and 4, respectively, because bulk glasses were heated to a temperature above ca. 50 °C of T_g in order to obtain homogeneous nucleation.

10.3 Phase Stability and Transformation

10.3.1 Composition Dependence of Precursor and High-Temperature-Stable phases

Figure 10.4 shows the composition dependence of both the precursor phases and the high-temperature-stable phases of glass-ceramic Y-Narpsio on the maps of phosphorus-yttrium (P-Y, Fig. 10.4a), yttrium-sodium (Y-Na, Fig. 10.4b), and phosphorus-sodium (P-Na, Fig. 10.4c), where the variables on the abscissas and ordinals are expressed with the composition parameters $1 - x$, y, and $3 + 3x - y$ for yttrium, phosphorus, and sodium, respectively. As reported before [10, 21], N3- and N9-type Y-Narpsio glass-ceramics can be crystallized as the high-temperature-stable phases at the regions of higher yttrium content [Y] ($1 - x >$ approximately 0.8) and rather lower [Y] ($1 - x <$ approximately 0.55), respectively, in the phosphorus content [P]-[Y] relation.

Concerning the precursor phases, only either N3- or N9-type Y-Narpsio was found in any composition, and N5-type Y-Narpsio was difficult to crystallize from glasses at low temperatures. It is also seen in the P-Y map (Fig. 10.4a) that, under a given [P] (< 0.6), a composition with a higher [Y] gives N3-type Y-Narpsio (open

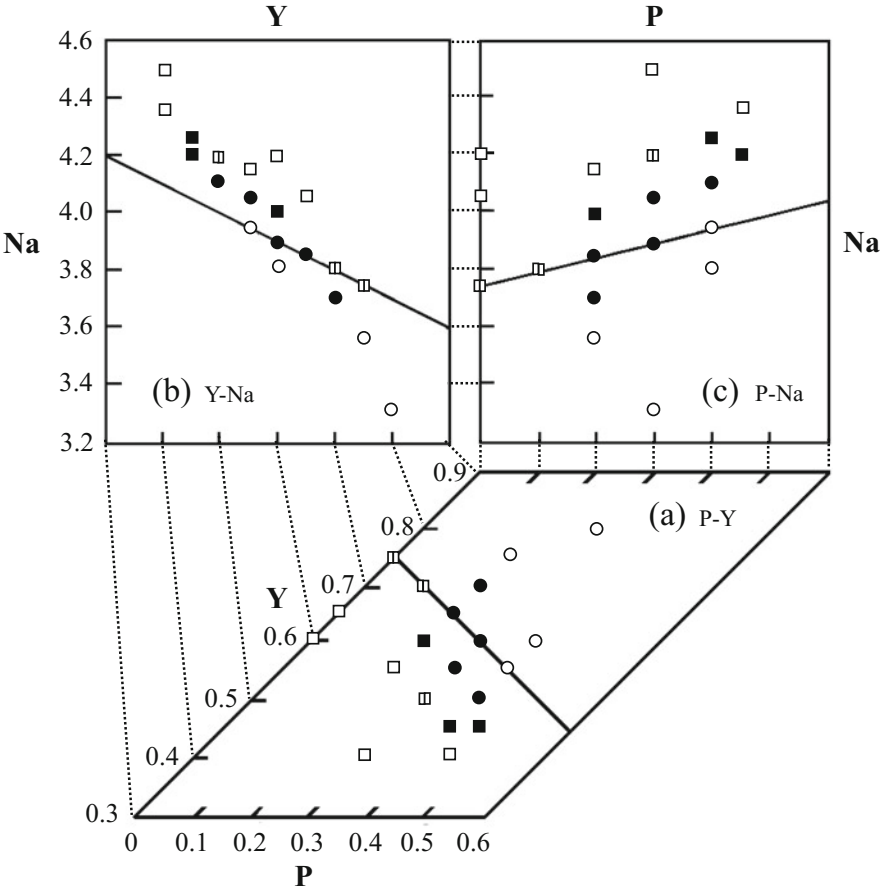

Fig. 10.4 Composition dependence of precursor (pp) and high-temperature-stable phases (sp) of glass-ceramic Narpsio on P-Y (**a**), Y-Na (**b**), and P-Na (**c**) maps, where precursor phases N3 and N9 are shown with circles and squares, respectively. High-temperature-stable phases are shown in such a way that solid marks means that N5-Narpsio is the stable and open marks indicate that the precursor phases are also stable even at high temperatures [30]. Mixed phases are also shown: open circle pp = sp = N3; filled circle pp = N3, sp = N5; open square pp = sp = N9; filled square pp = N9, sp = N5; open split square pp = N9, sp = N9 + N5. Reprinted by permission from Springer Nature: Springer J. Electroceram. 24 (2010) 83, COPYRIGHT (2010)

circles) as the precursor phase, whereas lower [Y] results in N9-type phase (open squares). The values of [Y] dividing the regions allowed for N3- and N9-type Y-Narpsio glass-ceramics decreased with increasing [P], and the boundary seems to locate slightly apart from the deduced line of $[Y] = 0.75 - 0.5[P]$ [10] shown with the solid line. Around the boundary region, N5-type Y-Narpsio can be obtained as the stable phase at high temperatures (solid circles or squares). In the Y-Na or P-Na relations (Fig. 10.4b and c), the region where N5-type Y-Narpsio can be found

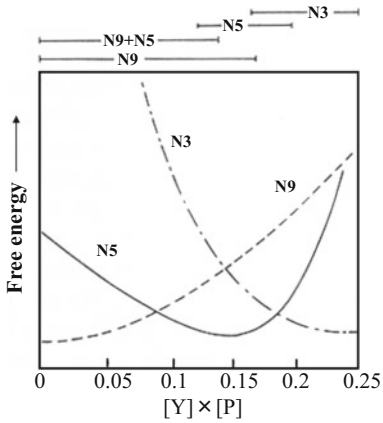

Fig. 10.5 Schematic figure of composition ([Y]×[P]) dependence of free energy of N5-, N3-, and N9-type Y-Narpsio [30]. Reprinted by permission from Springer Nature: Springer J. Electroceram. 24 (2010) 83, COPYRIGHT (2010)

as the high-temperature-stable phase is found under approximately 3.6 < sodium content [Na] < 4.3. The effect of sodium content seems insignificant, because the value of [Na] is subordinately determined as [Na] = 6 − 3[Y] − [P] (=3 +3 $x - y$) depending on the contents of both yttrium and phosphorus.

The above results may suggest that the [P]-[Y] relation dominates the region which is allowed for each Y-Narpsio at high temperatures. Considering this inference, we calculated the products of [P] × [Y] for all the specimens. The values of [P] × [Y] were as follows (shown in Fig. 10.5): 0.16–0.25 for single-phase N3-type Y-Narpsio, 0.14 for mixed phases of N3- and N5-type Y-Narpsio, 0.12–0.20 for single-phase N5-type Y-Narpsio, 0–0.14 for the mixed phases of N5- and N9-type Y-Narpsio, and 0–0.17 for single-phase N9-type Y-Narpsio, respectively. It was therefore deduced (Fig. 10.5) that the free energy of formation (ΔG_f) of N9-type Y-Narpsio would be the lowest in a lower region of [P] × [Y], N5-type Y-Narpsio may have the lowest ΔG_f in a medium [P] × [Y] region, and a higher [P] × [Y] would lower the ΔG_f of N3-type Y-Narpsio.

For a specimen in which N5-type Y-Narpsio is the stable phase at high temperatures, the aspect such as Fig. 10.6a would be illustrated in that ΔG of N3- or N9-type Y-Narpsio would be much smaller than that of N5-type Y-Narpsio near the crystallization temperature (T_c), and the value of N5-type Y-Narpsio would be lowered much less than of the two. Figure 10.6b indicates the aspect that ΔG of N3- or N9-type Y-Narpsio is stable.

10.3.2 Kinetic Effects of Composition on the Phase Transformation

The kinetic effects of composition on the phase transformation are shown in Fig. 10.7, which compares the phase transformation rates of specimens

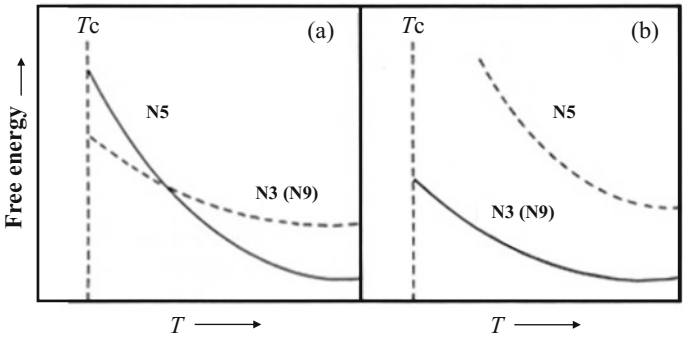

Fig. 10.6 Schematic figures of temperature dependence of free energy change of N5- and N3- or N9-type Y-Narpsio in the cases assuming N5- (**a**) and N3- (**b**) or N9-type (**b**) Y-Narpsio as the high-temperature-stable phase, where *T*c is the crystallization temperature [30]. Reprinted by permission from Springer Nature: Springer J. Electroceram. 24 (2010) 83, COPYRIGHT (2010)

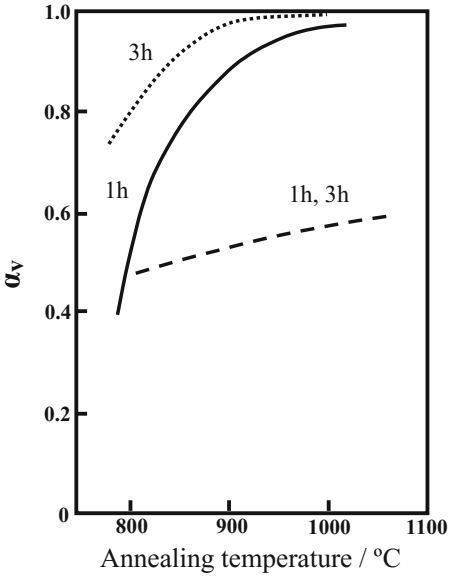

Fig. 10.7 Comparison of phase transformation rate (α_v) between specimens $Na_{3.9}Y_{0.6}P_{0.3}Si_{2.7}O_9$ (1 h-annealing, (—); 3 h-annealing, (· · ·)) and $Na_{3.75}Y_{0.65}P_{0.3}Si_{2.7}O_9$ (1 h, 3 h-annealing, (- - -)) [30]. Reprinted by permission from Springer Nature: Springer J. Electroceram. 24 (2010) 83, COPYRIGHT (2010)

$Na_{3.9}Y_{0.6}P_{0.3}Si_{2.7}O_9$ and $Na_{3.75}Y_{0.65}P_{0.3}Si_{2.7}O_9$. The transformation rate (α_v) of a precursor phase to the stable N5 phase was determined as the weight ratio of N5-type Y-Narpsio in a glass-ceramic specimen. The value of α_v was experimentally obtained from the relationship between the weight ratio and the XRD intensity ratio, which had been determined previously by XRD intensity measurement on specimens with a given weight ratio of N5-type Y-Narpsio to metastable phases. It is seen that the composition $Na_{3.9}Y_{0.6}P_{0.3}Si_{2.7}O_9$ is superior to the other, for

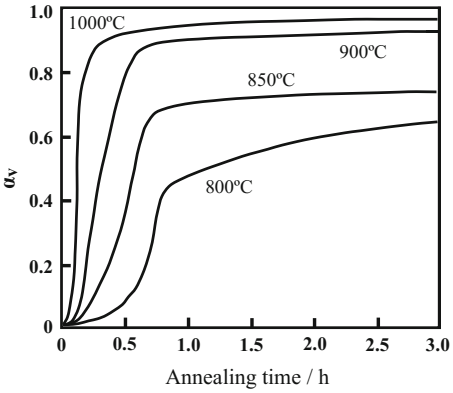

Fig. 10.8 Phase transformation rate (α_v) of N3- to N5-type Y-Narpsio on the specimen $Na_{3.9}Y_{0.6}P_{0.3}Si_{2.7}O_9$ [30]. Reprinted by permission from Springer Nature: Springer J. Electroceram. 24 (2010) 83, COPYRIGHT (2010)

Table 10.1 Kinetic parameters of phase transformation of N3- to N5-type Y-Narpsio of $Na_{3.9}R_{0.6}Si_{2.7}O_9$ [30]

Annealing temp. (K)	Avrami modulus n	ln k
1073	2.61	−20.7
1123	1.94	−14.6
1173	1.39	−9.54
1223	0.75	−4.41

Reprinted by permission from Springer Nature: Springer J. Electroceram. 24 (2010) 83, COPYRIGHT (2010)

the N5 single-phase Y-Narpsio was difficult to obtain in the latter specimen. In specimen $Na_{3.9}Y_{0.6}P_{0.3}Si_{2.7}O_9$, a glass-ceramic of N5 single-phase Y-Narpsio was easily obtained at a temperature higher than 900 °C for only 3 h. The composition $Na_{3.75}Y_{0.75}Si_3O_9$ (or $Na_5YSi_4O_{12}$) was inferior in the same respect.

Figure 10.8 shows the kinetic characteristics of phase transformation of the metastable phase of N3- to N5-type Y-Narpsio of specimen $Na_{3.9}Y_{0.6}P_{0.3}Si_{2.7}O_9$ at various temperatures. The transition rates, α_v, of the silicophosphate Y-Narpsio were much higher than those of the $Na_{3.75}Y_{0.75}Si_3O_9$ silicate material.

The results shown were analyzed with the Avrami empirical equation, $\alpha_v = 1 - \exp(-kt^n)$, where k is the rate constant and n is a constant. The data on α_v obtained at the initial and intermediate stages gave a linear relationship between $\ln(\ln(1 - \alpha_v)^{-1})$ and $\ln(t)$ with a correlation coefficient of more than 0.99. The Avrami parameter and rate constants obtained are summarized in Table 10.1. Based on the Arrhenius relationship (Fig. 10.9), $k = A\exp(-E_v/RT)$ with E_v as the activation energy and constants A and R, where the k values which increased with increasing temperature, we obtained an activation energy of 1.2×10^3 kJ/mol, suggesting that the phase transformation could be rather difficult to take place. An addition of phosphorus and the excess sodium seem effective to the promotion of the phase transformation.

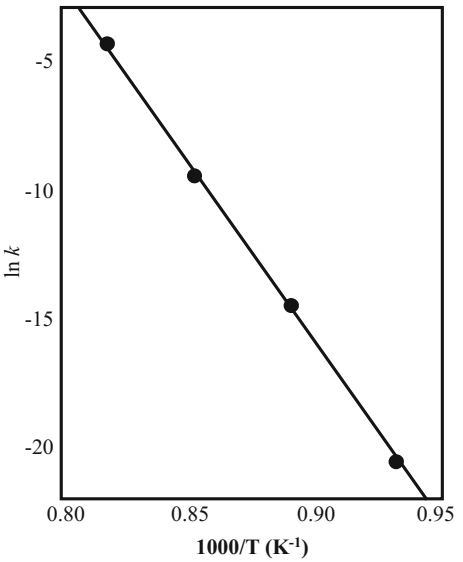

Fig. 10.9 Arrhenius-type plot of ln k with 1000/T of specimen $Na_{3.9}Y_{0.6}Si_{2.7}O_9$ [30]. Reprinted by permission from Springer Nature: Springer J. Electroceram. 24 (2010) 83, COPYRIGHT (2010)

10.4 Effects of Microstructure on Conduction Properties

10.4.1 Crystallization and Phase Diagram

As expected from the previously reported results on Y-Narpsio [9], the crystallization of the superionic conducting N5-type phase took place, depending both on the contents of [R] and [P], at temperatures of 800–1000 °C in most Narpsio glasses of Er to Sm, except for scandium and lanthanum Narpsio glasses. The N5 single-phase region was wider for Narpsio of smaller R but was limited at the [P] $\approx$ 0 region. The effect of phosphorus substitution for Si is important in the crystallization of N5-type phase. Composition 7

$$Na_{3.9}R_{0.6}P_{0.3}Si_{2.7}O_9 \tag{10.7}$$

was experimentally shown as the most appropriate composition for the crystallization of N5-type phase.

The relationship between the ionic radius of R^{3+} (r_R) and the hexagonal lattice parameters of N5-type single phase is consistent with the previous report [4] on $Na_5RSi_4O_{12}$ (R = Sc–Sm) in the tendency that both lattice parameters increased with increasing r_R. The elongation of these lattice axes is attributed to the octahedral coordination of R^{3+} with the O^{2-} of SiO_4- or PO_4-tetrahedra of the 12-membered rings. The local structure around R^{3+} ions is to be further discussed below in relation to conduction properties. On the formation of N5-type single phase, the incorporation of excess sodium ions [$4(3 + 3x - y)/3 - 5 = (12x - 4y - 3)/3$ in

composition 3] and substitution of rare earth ions [$1 - 4(1 - x)/3 = (4x - 1)/3$] must be accounted for in view of the N5-type crystal structure.

Banks et al. [8] have reported the values of σ_{300} as 5×10^{-3} to 1×10^{-2} S/cm for glass-ceramic $Na_5RSi_4O_{12}$ (R = Er, Y, Gd, Sm), which are as low as those of the mixed-phase Narpsio specimens. The single-phase N5-type glass-ceramic was not obtained in the present work. Based on the above crystallization analysis, their glass-ceramic specimens are reasonably considered to suffer from phase inhomogeneity brought about by insufficient annealing. The formation of N5-type structure from the precursor glasses is a matter of crystallization kinetics, because single-phase N5 has been synthesized in single crystal [2, 3, 33] or polycrystalline [6, 7, 11] form based on the composition of N5. It is noted here that the precursor phases identified were N3- or N9-type. Both N3 and N9 are considered to form isostructural [12, 21, 34] with $Ca_3Al_2O_6$ [35] to be comprised of the skeleton structure of six-membered SiO_4-tetrahedra rings [14]. It is generally known that phosphorus pentoxide acts as a nucleating agent in the formation of glass-ceramics. It is therefore presumed at present that the substitution of an asymmetric PO_4-tetrahedron has a weakening effect on the bonding of the skeleton structure of 6-membered SiO_4-tetrahedra rings, resulting in the tendency to form the stable 12-membered structure.

10.4.2 Conduction Properties of Crystalline Grains

The complex impedances and admittances of the measured Narpsio glass-ceramics consisted of two semicircles below 300 °C. The two intercepting points on the real axis are interpreted as the resistance of the crystallized grains (R_G) and the total resistance of grains and remaining glassy grain boundaries (R_{GB}). Figure 10.10 shows examples of the temperature dependence Arrhenius plots based on the calculated conductivity values of grains and grain boundaries of the glass-ceramics Y-Narpsio ($Na_{3.9}Y_{0.6}P_{0.3}Si_{2.7}O_9$) and Sm-Narpsio ($Na_{3.9}Sm_{0.6}P_{0.3}Si_{2.7}O_9$), in which the geometrical ratios of thickness-to-surface area for grains were also used for convenience for those of grain boundaries, because of their undefinable shapes. Table 10.2 summarizes the measured conductivities (σ_{300}) and the calculated activation energies (E_a) assigned for grains of the glass-ceramics with composition 7 of Sc to La, regardless of whether their crystalline phases are N5-type or not. The conductivities, σ_{300}, of single-phase Narpsio specimens of Er to Sc range from 4×10^{-2} to 1×10^{-1} S/cm; in accordance the E_a falls in the range of 23–27 kJ/mol. In contrast, the mixed-phase Narpsio of Sc and In showed much smaller σ_{300} of 3×10^{-3} with an E_a of 35–40 kJ/mol, whereas non-Narpsio glass-ceramics with unknown or mixed phases showed much lower conductivities of 1×10^{-5} to 1×10^{-4} S/cm with an E_a of 55–58 kJ/mol.

The tendency of the conduction properties in single-phase Narpsio specimens is consistent with the reported result measured on the corresponding polycrystalline

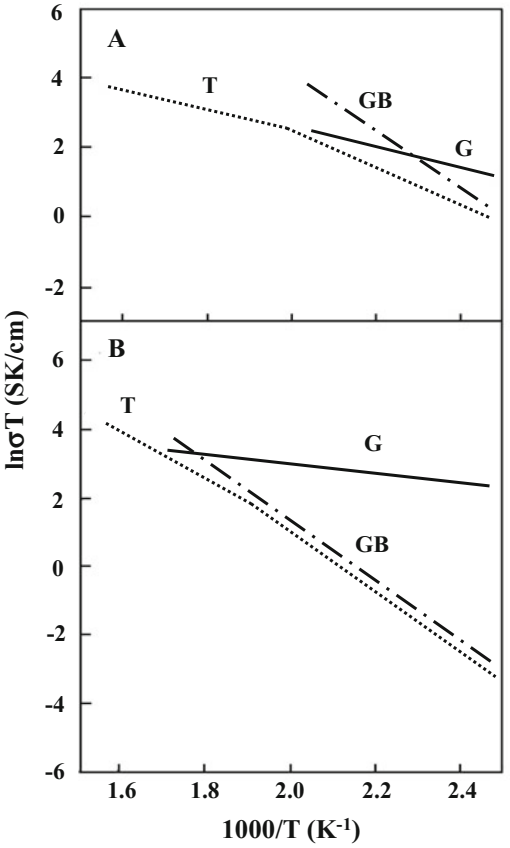

Fig. 10.10 Arrhenius plots of the conductivities of grains (G), grain boundaries (GB) and the total bulk (T) of the glass-ceramic $Na_{3.9}Y_{0.6}P_{0.3}Si_{2.7}O_9$ (A) and $Na_{3.9}P_{0.3}Sm_{0.6}Si_{2.7}O_9$ (B) [30]. Reprinted by permission from Springer Nature: Springer J. Electroceram. 24 (2010) 83, COPYRIGHT (2010)

Table 10.2 Conduction properties of various Narpsio glass-ceramics with composition $Na_{3.9}R_{0.6}Si_{2.7}O_9$ [30]

R^{3+} (ions)	Ea kJ•mol^{-1}	Conductivity (σ_{300}) S•cm^{-1}	Crystalline phase
Sc	35.3	3.2×10^{-3}	N5-type + unknown
In	39.8	3.1×10^{-3}	N5-type + unknown
Er	26.9	3.6×10^{-2}	N5-type
Y	26.6	6.6×10^{-2}	N5-type
Gd	23.0	1.3×10^{-1}	N5-type
Eu	24.4	5.2×10^{-2}	N5-type
Sm	20.9	6.3×10^{-2}	N5-type
Nd	55.1	2.2×10^{-5}	Unknown
La	57.8	1.6×10^{-4}	Unknown

Reprinted by permission from Springer Nature: Springer J. Electroceram. 24 (2010) 83, COPYRIGHT (2010)

$Na_5RSi_4O_{12}$ [4]: σ increased with increasing r_R. Previous works have proposed a mechanism whereby rare earth ions, octahedrally coordinated with the non-bridging oxide ions of the 12-membered rings of silica tetrahedra, work to expand the conduction paths for Na^+ ions along the c-axis [4, 33], which could explain the observed dependence of E_a on r_R in this work.

10.4.3 Structure and Conduction Properties of Grain Boundaries

As R_{GB} decreases rapidly with increasing temperature because of high $(E_a)_{GB}$ to a comparable value with R_G at 300 °C (Fig. 10.10), the total conductivities ($R_G + R_{GB}$) are dominated by grain boundary conductivity. The grain size-dependence of σ_{300} is therefore explained by the decrease in the number of poorly conductive grain boundaries with increasing grain size.

The conduction properties of grain boundaries were strongly dependent on the annealing conditions, although those of the grains were little changed by the annealing temperature and time. Glass-ceramics are generally composites consisting of crystallized grains and small amounts of residual glass (< 1%) [23]. To compare the properties of grain boundaries with those of glasses, the conduction properties of sodium-yttrium silicophosphate glasses with various compositions were measured. Unlike glass-ceramics, the impedance loci of glasses were comprised of one arc, which indicates that there is no polarization arising from microstructural inhomogeneity. Based on the intercepting points on the horizontal axis, the composition dependence of the conduction properties of σ_{300} and E_a was evaluated. The value of σ_{300} ranged from 1×10^{-4} to 5×10^{-3} S/cm, and E_a increased from 53 to 67 kJ/mol with [Na] or [Na]/[Y]. These results are also in good agreement with those reported for the glasses in the Na_2O-Y_2O_3-SiO_2 system [36]. The values of $(E_a)_{GB}$ of the specimens annealed below 950 °C for shorter times correspond to those in the range of glasses, strongly suggesting that their grain boundaries are a glassy matrix. The abovementioned dependence of $(E_a)_{GB}$ on sodium oxide content [Na_2O] is explained by the well-known tendency that the conduction properties of glasses are improved by increasing [Na_2O], which provides the increase in carrier Na^+ ions. The ratio of [Na]/[Y] is also an important parameter for the conduction properties [36], showing an effect on the conduction properties similar to [Na_2O].

In order to identify the structure of the grain boundaries of the specimen ($Na_{3.9}Y_{0.6}P_{0.3}Si_{2.7}O_9$) annealed at 800 °C for 0.5 h, TEM analysis was performed both on grains and grain boundaries. The results in Fig. 10.11 show clear electron diffraction on grains, but not on grain boundaries. This confirms that the grain boundaries are amorphous. Compositional analyses were also performed; however, [Na] was difficult to determine because of the evaporation by electron ablation. It was also observed that the glassy phase was condensed at triple points enclosed by grains and that the neck growth among the grains was well developed. Thus, it is

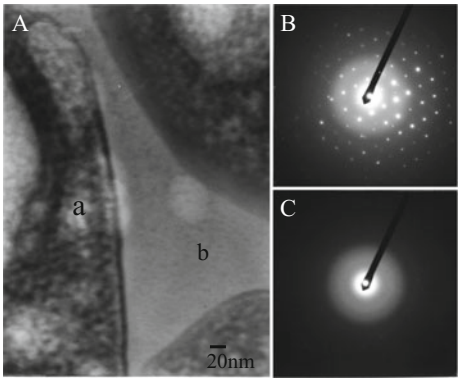

Fig. 10.11 TEM micrograph of glass-ceramic specimen ($Na_{3.9}Y_{0.6}P_{0.3}Si_{2.7}O_9$) annealed at 800 °C for 0.5 h (**a**) and the electron diffraction patterns on the spots a (**b**) and b (**c**) in Fig. 11A [18]. Reprinted with permission from J. Electrochem. Soc., 143, (1996) 2180. Copyright 1996, The Electrochemical Society

reasonable to consider that the grain boundaries annealed at lower temperatures are amorphous, whereas those annealed at higher temperatures for longer periods of time are poorly conductive crystalline compounds in the specimens.

10.5 Microstructural Control of Glass-Ceramic Narpsio Conductors

10.5.1 Preparation of Crack-Free $Na_5YSi_4O_{12}$-Type Glass-Ceramics Containing Large Sm^{3+} Ions: Crystallization Conditions and Ionic Conductivities [15–17]

A number of glass-ceramics of the phosphorus-containing N5-type Na^+ superionic conductors have been prepared by the crystallization of glasses with the composition formula 2, where it was found that the identity of *R* strongly influences the glass crystallization and its conduction properties. To date, polycrystalline N5-type Narpsio compounds have been prepared using Sc, Y, Gd, or Sm as the *R* component. In such compounds, the ionic radius of *R*, which is coordinated to six oxygen atoms, strongly affects the phase crystallization. In addition, the reported results for the silicate ceramics show that the conductivity of N5-type Narpsio increases with an increasing ionic radius of *R*, thereby giving the order Sm-Narpsio > Gd-Narpsio > Y-Narpsio > Sc-Narpsio. However, this order has not always held true in glass-ceramics. Although the majority of Narpsio compounds have been obtained as crack-free bulky glass-ceramics (15 mm diameter and 5 mm thickness), the cracking of Sm-Narpsio during crystallization has proven difficult to prevent. Furthermore, crack-free Gd-Narpsio, which contains relatively large Gd^{3+} ions, was found to be the most conductive; however, Sm-Narpsio, which contains the largest *R* ions, exhibited a lower conductivity than Y-Narpsio, which contained only medium Y^{3+}

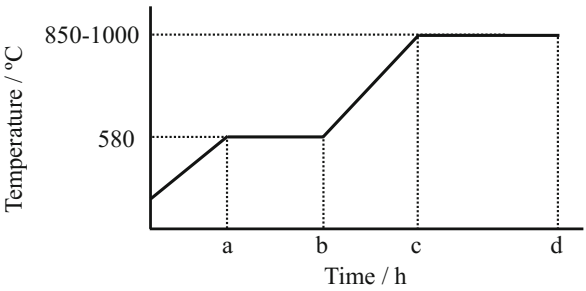

Fig. 10.12 Temperature/time program for the production of the Sm-Narpsio glass-ceramics [17]. Reprinted from J. Ceram. Soc. Jpn. 111 (2003) 257, Copyright 2003

	a-b	b-c	c-d
(A)	1	7	17
(B)	3	8	10
(C)	6	8	5

a-b : Nucleation c-d : Crystal growth

ions. In the study discussed herein, N5-type Sm-Narpsio ionic conductors were prepared by the crystallization of the corresponding glasses, and the optimum conditions for crystallization are discussed in this review with reference to the conduction properties and the preparation of crack-free N5-type glass-ceramic Sm-Narpsio.

Samples were prepared according to the desired composition $Na_{3+3x-y}Sm_{1-x}P_ySi_{3-y}O_9$, and the temperatures employed for nucleation and crystallization of the glass specimens were selected based on the results of DTA. Figure 10.12 shows the temperature/time program employed for preparation of the Sm-Narpsio glass-ceramics. The corresponding N5-type Sm-Narpsio ionic conductors were then produced successfully following the crystallization of these glasses. Although the glass samples heated using program (A) broke during crystallization, and the glass-ceramic Sm-Narpsio obtained using pattern (B) cracked easily during crystallization, the majority of Sm-Narpsio compounds prepared using pattern (C) were obtained as crack-free bulky glass-ceramics. However, it should be noted that the glass samples broke during crystallization when a crystallization heating time of > 5 h was employed. Figure 10.13 shows the phase-composition diagram of the samples crystallized at 900 °C using pattern (C). As indicated, crystallization of the N5 single-phase glass-ceramic Sm-Narpsio was strongly dependent on the concentrations of both *R* and P (or *x* and *y* in the composition parameters) and on the temperature used to crystallize the glass specimens. In addition, Figure 10.14 shows a SEM micrograph of the $Na_{3.9}Sm_{0.6}P_{0.3}Si_{2.7}O_9$ specimen microstructure heated at 900 °C using pattern (C). The grain size of this specimen was approximately 3–5 μm. The state of grain growth was promoted by increasing the crystallization

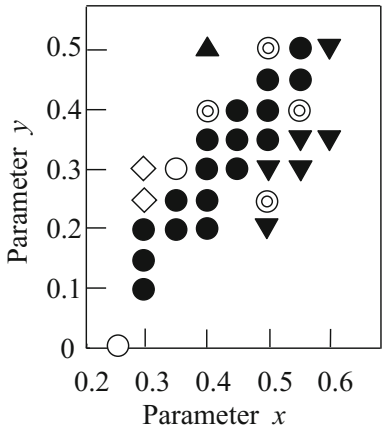

Fig. 10.13 Phase-composition diagram of the Sm-Narpsio glass-ceramics crystallized at 900 °C [17]. • N5, ▲ N3, ▼ N9, ◯N5+N3, ◎N5+N9, ◊N3+N9. Reprinted from J. Ceram. Soc. Jpn. 111 (2003) 257, Copyright 2003

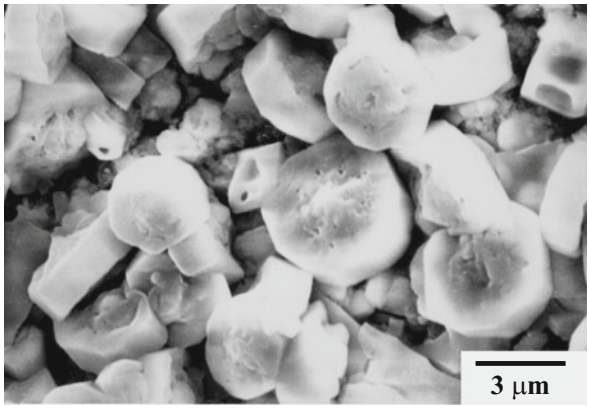

Fig. 10.14 SEM micrograph of the $Na_{3.9}Sm_{0.6}P_{0.3}Si_{2.7}O_9$ specimen heated at 900 °C using heating program (C) [17]. Reprinted from J. Ceram. Soc. Jpn. 111 (2003) 257, Copyright 2003

heating temperature and heating time. Although grain growth can result in high conductivity, crack prevention was difficult in the case of the samples prepared with long heating times. Conduction properties were measured using the alternating current (AC) two-probe method with a low-frequency impedance analyzer. The glass-ceramics for analysis were prepared as cylindrical samples with typical diameters and thicknesses of 15 and 2 mm, respectively. Electrodes were prepared by the sputtering of gold on polished surfaces. The frequency of the applied AC field ranged from 5 to 10 MHz, and the temperature dependence of the conductivity was measured similarly at several temperatures ranging from room temperature to 350 °C. Table 10.3 summarizes the conduction properties of the N5-type glass-ceramic NaSmPSi specimens. It is likely that the low conductivity of Sm-Narpsio (which contained large Sm^{3+} ions) compared to that of Y-Narpsio (containing medium-sized Y^{3+} ions) was due to the particularly small grain sizes of the presented specimens.

Table 10.3 Conduction properties of the N5-type Sm-Narpsio glass-ceramics [17]

Mix proportion			Ea/kJ•mol^{-1}		
x	y	$\sigma_{300}/10^{-1}$ S•cm^{-1}	T	G	G.B.
0.40	0.30	0.238	27.6	17.9	51.4
0.45	0.40	0.408	30.4	18.8	95.7
0.50	0.35	0.352	19.5	15.8	
0.50	0.40	0.478	29.3	16.6	

Heat treatment: 900 °C, 5 h
Reprinted from J. Ceram. Soc. Jpn. 111 (2003) 257, Copyright 2003
σ_{300}: Conductivity at 300 °C
Ea: Activation energy (*T* total, *G* grain, *G.B.* grain boundary)

10.5.2 Composition Control of Silicophosphate Glass-Ceramics

10.5.2.1 Ionic Conductivities of Nasicon-Type Glass-Ceramic Superionic Conductors in the System Na_2O-Y_2O_3-XO_2-SiO_2 (X = Ti, Ge, Te) [37]

Our phosphorus-containing compositions have been confirmed to be superior to the mother composition of N5, especially in the production of single-phase glass-ceramics. Recently, our work has mainly focused on the synthesis of various glass-ceramics with N5 single phase. In the study discussed herein, N5-type glass-ceramics of the titanium-, germanium-, or tellurium-containing Na^+ superionic conductors (N5Y*X*S) were prepared from glasses with the composition $Na_{3+3x}Y_{1-x}X_ySi_{3-y}O_9$ (X = Ti; NYTiS, Ge; NYGeS, Te; NYTeS) ranging in x = 0.1–0.55 and y = 0.1–0.45, and the effect of the X element on phase separation was investigated along with the effect of the sample microstructure on the conduction properties of the glass-ceramics.

The precursor glasses were prepared by melting stoichiometric mixtures of reagent-grade powders of anhydrous Na_2CO_3, Y_2O_3 (TiO_2, GeO_2, or TeO_2), and SiO_2 at 1300–1400 °C for 1 h, followed by annealing for several hours at an optimum temperature. Following crystallization of the obtained glasses, the corresponding N5Y*X*S ionic conductors were successfully produced. Figures 10.15, 10.16, and 10.17 show the diagrams of phase-composition-crystallization temperature of the obtained NYTiS, NYGeS, and NYTeS glass-ceramics, respectively, where it was apparent that N5Y*X*Si was obtained as a stable phase at high temperatures. In addition, the crystallization of a single N5 phase was found to be strongly dependent on the contents of yttrium and (titanium, germanium, or tellurium) ions (or the values x and y in $Na_{3+3x}Y_{1-x}X_ySi_{3-y}O_9$). Furthermore, the N3 and N9 phases were crystallized as high-temperature-stable phases in the regions of higher Y and rather lower Y concentrations, respectively. The combination of x and y gave the

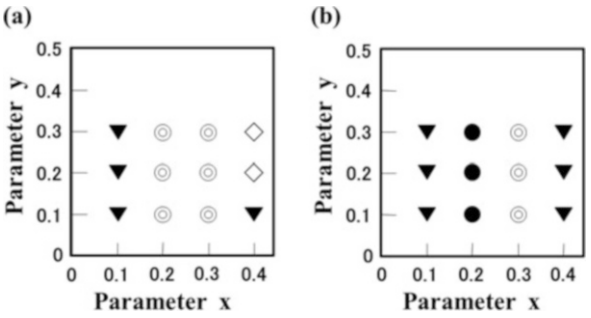

Fig. 10.15
Phase-composition diagrams of the NYTiS glass-ceramics heated at 900 °C (**a**) and 1000 °C (**b**) for 5 h [37]. • N5, ▼ N9, ⊙ N5+N9, ◊ N3+N9. Reprinted from Solid State Ionics 180 (2009) 537, Copyright 2009, with permission from Elsevier

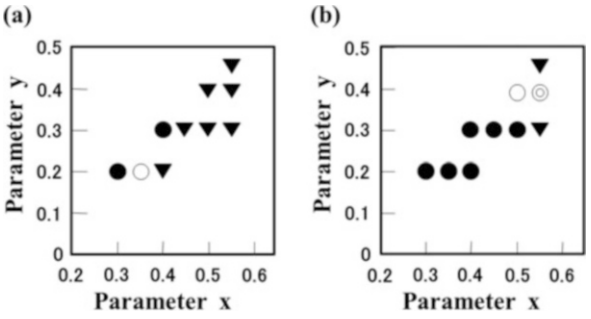

Fig. 10.16
Phase-composition diagrams of the NYGeS glass-ceramics heated at 900 °C (**a**) and 1000 °C (**b**) for 5 h [37]. • N5, ▼ N9, ◯ N5+N3, ⊙ N5+N9. Reprinted from Solid State Ionics 180 (2009) 537, Copyright 2009, with permission from Elsevier

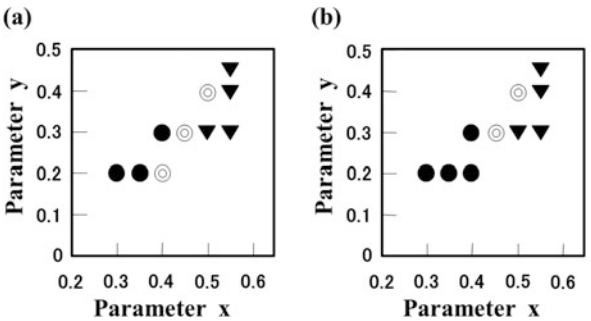

Fig. 10.17
Phase-composition diagrams of the NYTeS glass-ceramics heated at 900 °C (**a**) and 1000 °C (**b**) for 5 h [37]. • N5, ▼ N9, ⊙ N5+N9. Reprinted from Solid State Ionics 180 (2009) 537, Copyright 2009, with permission from Elsevier

greatest variation in N5YGeS but was more limited in the order: N5YTeS > N5YTiS. Moreover, Table 10.4 summarizes the conduction properties of the N5-type glass-ceramics with compositions of $Na_{3.6}Y_{0.8}Ti_{0.2}Si_{2.8}O_9$, $Na_{4.2}Y_{0.6}Ge_{0.3}Si_{2.7}O_9$, and $Na_{4.2}Y_{0.6}Te_{0.3}Si_{2.7}O_9$, respectively. The conductivities and activation energies of these species are in the order of 10^{-2} S/cm at 300 °C and 15–24 kJ/mol, respectively. Interestingly, the conductivity of these samples decreased, giving the order N5YGeS > N5YTeS > N5YTiS. It is considered that this order corresponds to the N5 single-phase region.

Table 10.4 Conduction properties of the N5 glass-ceramics with the $Na_{3.6}Y_{0.8}Ti_{0.2}Si_{2.8}O_9$, $Na_{4.2}Y_{0.6}Ge_{0.3}Si_{2.7}O_9$, and $Na_{4.2}Y_{0.6}Te_{0.3}Si_{2.7}O_9$ compositions [37]

Specimen	Heat treatment		σ_{300}	*E*a/kJ•mol^{-1}		
	Temp.	Time	/10^{-2}•S•cm^{-1}	T	G	G.B.
NYTiS	1000	5	2.5	15.5	19.8	10.0
NYGeS	900	5	4.0	21.1	17.3	44.0
	1000	5	4.5	24.1	19.3	56.6
	1000	24	6.7	22.9	20.6	67.2
NYTeS	900	5	3.2	19.8	18.7	43.7
	1000	5	4.6	21.8	20.5	56.6

Reprinted from Solid State Ionics 180 (2009) 537, Copyright 2009, with permission from Elsevier
σ_{300}: Conductivity at 300 °C
*E*a: Activation energy (*T* total, *G* grain, *G.B.* grain boundary)

10.5.2.2 Synthesis and Na^+ Conduction Properties of Nasicon-Type Glass-Ceramics in the System Na_2O-Y_2O_3-X_2O_3-SiO_2 (X = B, Al, Ga) and Effect of Si Substitution [38]

Following preparation of the glass-ceramics of the boron-, aluminum-, or gallium-containing $Na_5RSi_4O_{12}$-type (R = rare earth; Y) Na^+ superionic conductors obtained from glasses with the $Na_{3+3x+y}Y_{1-x}X_ySi_{3-y}O_9$ composition (X = B; NYBS, X = Al; NYAlS, X = Ga; NYGaS) ($x = 0.2$, $y = 0.1$), the effect of X on the phase separation was investigated in addition to the effect of the microstructure on the conduction properties of glass-ceramics, and the crystallization kinetics of the glasses were examined by DTA.

The precursor glasses were obtained by melting stoichiometric mixtures of reagent-grade powders of anhydrous Na_2CO_3, Y_2O_3 (H_3BO_3, Al_2O_3, or Ga_2O_3), and SiO_2 at 1350 °C for 1 h after calcinations at 900 °C for 1 h. The melts were quickly poured into a graphite cylinder. Crystallization was carried out according to a previous report [14]. The N5-type glass-ceramic NYBS, NYAlS, and NYGaS with the $Na_{3.7}Y_{0.8}B_{0.1}Si_{2.9}O_9$, $Na_{3.7}Y_{0.8}Al_{0.1}Si_{2.9}O_9$, and $Na_{3.7}Y_{0.8}Ga_{0.1}Si_{2.9}O_9$ compositions, respectively, were successfully produced by crystallization of the glasses. The apparent activation energies for crystallization (crystal growth) were determined by employing the non-isothermal-modified Kissinger methods [39, 40], in which some characteristic of the crystallization peak determined by DTA is monitored as a function of the heating rate or temperature. Figure 10.18 shows the modified Kissinger plots for NYBS, NYAlS, and NYGaS glasses. Table 10.5 summarizes the DTA peak temperatures and activation energies of crystal growth obtained from the modified Kissinger equation under non-isothermal condition of the NY*X*S glasses. The activation energies of crystal growth are 410 for NYBS, 392 for NYAlS, and 381 kJ/mol for NYGaS. The activation energy of crystal growth of the NY*X*S glass decreases as the ionic radius of X increases. Table 10.6 summarizes

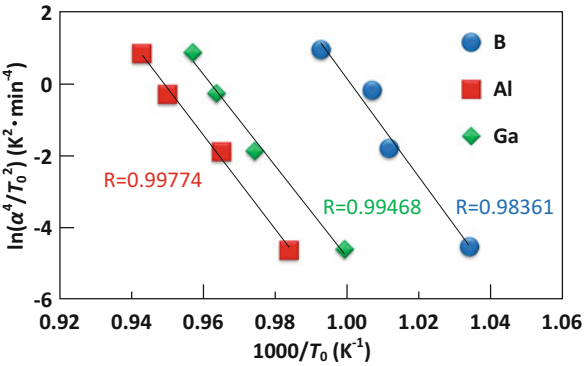

Fig. 10.18 Modified Kissinger plots for the NaYBS, NaYAlS, and NaYGaS glasses [38]. Reprinted from Solid State Ionics 225 (2012) 367, Copyright 2012, with permission from Elsevier

Table 10.5 DTA peak temperatures and activation energies of crystal growth of the NYBS, NYAlS, and NYGaS glasses [38]

	DTA peak temperature (°C)		
Heating rate (°C•min^{-1})	NYBS	NYAlS	NYGaS
10	694	743	728
20	715	763	753
30	720	779	765
40	734	787	772
Activation energy of crystal growth (kJ•mol^{-1})	410	392	382
Ionic radius (nm)	0.025	0.053	0.061

Reprinted from Solid State Ionics 225 (2012) 367, Copyright 2012, with permission from Elsevier

Table 10.6 Conduction properties of the NYBS, NaYAlSi, and NYGaS glass-ceramics [38]

	NYBS	NYAlS	NYGaS
$\sigma_{300\ (G)}$ (S)	5.61×10^{-2}	4.03×10^{-2}	3.79×10^{-2}
$\sigma_{300\ (G.B.)}$ (S)	18.8×10^{-2}	50.4×10^{-2}	33.0×10^{-2}
$\sigma_{300\ (Total)}$ (S)	4.32×10^{-2}	3.73×10^{-2}	3.40×10^{-2}
*E*a $_{(Total)}$ (kJ•mol^{-1})	12.6	12.8	13.2
Ionic radius (nm)	0.025	0.053	0.061

Reprinted from Solid State Ionics 225 (2012) 367, Copyright 2012, with permission from Elsevier
σ_{300}: Conductivity at 300 °C (*T* total, *G* grain, *G.B.* grain boundary)
*E*a: Activation energy at higher temperatures ranging from 250 to 350 °C

the conduction properties of the NY*X*S glass-ceramics. The conductivities of the glass-ceramics NYBS, NYAlS, and NYGaS were 4.32×10^{-2}, 3.73×10^{-2}, and 3.40×10^{-2} S/cm at 300 °C, respectively. The conductivity decreases in the order NYBS > NYAlS > NYGaS. The conductivity of the NY*X*S glass-ceramics decreases as the ionic radius of *X* increases.

10.5.2.3 Effect of Substitution of Si with V and Mo on Ionic Conductivity of $Na_5YSi_4O_{12}$-Type Glass-Ceramics [41]

Glass-ceramics of the vanadium- or molybdenum-containing N5-type Na^+ superionic conductors were prepared by crystallization of glasses with the compositions $Na_{3+3x-y}Y_{1-x}V_ySi_{3-y}O_9$ (NYVS) or $Na_{3+3x-2y}Y_{1-x}Mo_ySi_{3-y}O_9$ (NYMoS) ranging in $x = 0.3$–0.5 and $y = 0.1$–0.4, and the effects of V or Mo elements on the phase separation and the microstructural effects on the conduction properties of glass-ceramics are discussed.

The precursor glasses were made by melting stoichiometric mixtures of reagent-grade powders of anhydrous Na_2CO_3, Y_2O_3, V_2O_5, MoO_3, and SiO_2 at 1400 °C for 1 h, followed by annealing for several hours at an optimum temperature. Figure 10.19 shows the diagrams of phase-composition-crystallization temperature of the glass-ceramic specimens with the $Na_{3.9}Y_{0.6}V_{0.3}Si_{2.7}O_9$ (A) and $Na_{3.7}Y_{0.7}Mo_{0.1}Si_{2.9}O_9$ (B) compositions. N5-type NYVS and NYMoS are obtained as a stable phase at high temperatures. The crystallization of N5 single phase is strongly dependent both on the contents of yttrium and (vanadium or molybdenum) ions (or the values x and y correspond to the composition parameters in $Na_{3+3x-y}Y_{1-x}V_ySi_{3-y}O_9$ or $Na_{3+3x-2y}Y_{1-x}Mo_ySi_{3-y}O_9$). N3 and N9 phases can

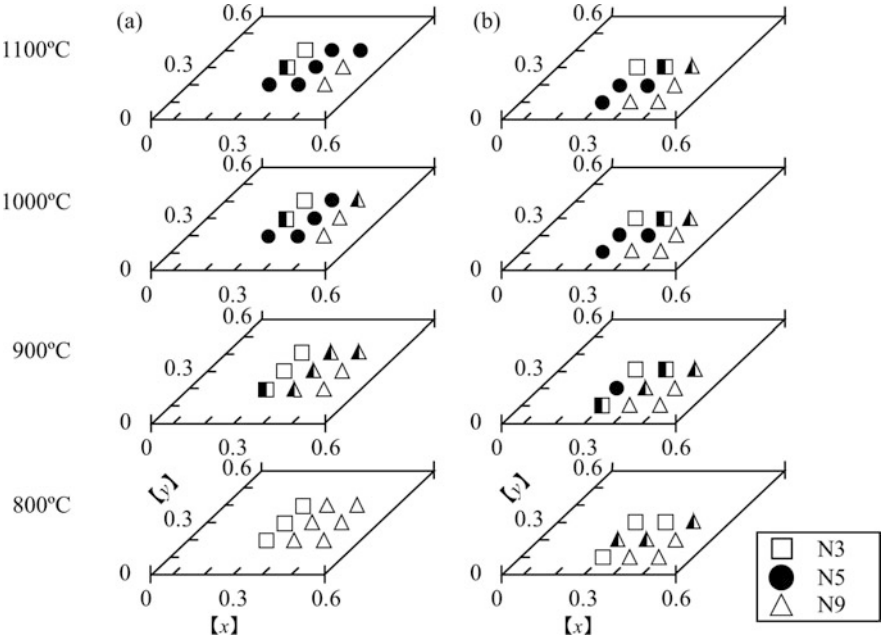

Fig. 10.19 Phase-composition–crystallization temperature diagrams of the NYVS (**a**) and NYMoS (**b**) glass-ceramics crystallized at 800–1100 °C [41]. • N5, □ N3, △ N9, □ $N5^+N3$, △ $N5^+N9$. Reprinted from Solid State Ionics 179 (2008) 1291, Copyright 2008, with permission from Elsevier

Table 10.7 Total conductivities and activation energies of the glass-ceramic specimens $Na_{3.9}Y_{0.6}V_{0.3}Si_{2.7}O_9$ (A) and $Na_{3.7}Y_{0.7}Mo_{0.1}Si_{2.9}O_9$ (B) [41]

(A)						
Temp. (°C)	σ (10^{-2}•S•cm^{-1})			*E*a (kJ•mol^{-1})		
	T	G	G.B.	T	G	G.B.
150	0.13	0.43	0.19			
200	0.28	0.44	0.73	27.5	10.5	47.1
250	0.47	0.62	1.97	——	——	——
300	0.87	1.24	2.93	38.1	40.5	31.7
350	1.63	2.33	5.38			
(B)						
150	0.63	1.24	1.27			
200	1.45	2.11	4.68	29.2		41.1
250	2.46	3.33	9.45	——	22.5	——
300	3.58	4.81	13.91	21.8		19.1
350	4.61	6.49	15.95			

Reprinted from Solid State Ionics 179 (2008) 1291, Copyright 2008, with permission from Elsevier
σ Conductivity, *E*a Activation energy, *T* Total, *G* grain, *G.B.* grain boundary

be crystallized as the high-temperature-stable phases at the regions of rather lower [Y] and higher [Y], respectively. The total conductivities and the activation energies are summarized in Table 10.7. The total conductivities of the specimens (A) and (B) were 0.87×10^{-2} and 3.58×10^{-2} S/cm at 300 °C, respectively, and the activation energies of those specimens were 38.1 and 21.8 kJ/mol, respectively. The combination of x and y was most varied in N5-type NYPS and more limited in N5-type NYVS and NYMoS. The conductivity decreases in the order NYPS > NYMoS > NYVS. It is considered that this order corresponds to the N5 single-phase region. We assume that the effect of the substitution of Si with V or Mo should be to bring about the difference in homogeneity in the N5 ring structure. The total and electronic conductivities and the Na^+ ionic transport numbers of the specimen (A) determined by the Wagner polarization method are summarized in Table 10.8. The ionic transport numbers of specimen (A) were nearly 0.9, and those of specimen (B) were nearly 1. It is considered that approximately 10% of the total conduction is electronic conduction (hopping conduction by transition metal vanadium) in the specimen (A). This result can explain the following fact: the conductivity of the specimen (A) is lower than other N5 conductors.

10.5.2.4 Synthesis and Na^+ Conduction Properties of Nasicon-Type Glass-Ceramics in the System Na_2O-Y_2O_3-R_2O_3-P_2O_5-SiO_2 (R = rare earth) and Effect of Y Substitution [42]

Glass-ceramics of the phosphorus-containing N5-type Na^+-superionic conductors were prepared by the crystallization of glasses of the $Na_{3+3x+y}Y_{1-x-z}R_zP_ySi_{3-y}O_9$

Table 10.8 Total and electronic conductivities and the Na^+ ionic transport numbers of the glass-ceramic specimen $Na_{3.9}Y_{0.6}V_{0.3}Si_{2.7}O_9$ (A) [41]

Temp. (°C)	σ_t (S•cm^{-1})	σ_e (S•cm^{-1})	t_i
150	1.312×10^{-3}	1.582×10^{-5}	0.988
200	2.752×10^{-3}	1.826×10^{-4}	0.934
250	4.728×10^{-3}	4.687×10^{-4}	0.901
300	8.715×10^{-3}	6.582×10^{-4}	0.924
350	1.627×10^{-2}	1.563×10^{-3}	0.904

Reprinted from Solid State Ionics 179 (2008) 1291, Copyright 2008, with permission from Elsevier
σ_t Total conductivity, σ_e Electronic conductivity, t_i Ionic transport number

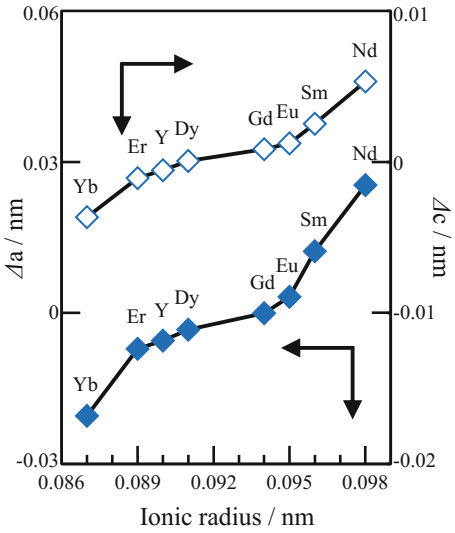

Fig. 10.20 Lattice constants of the NY*R*PS (*R* = Nd, Sm, Eu, Gd, Dy, Er, or Yb) and NYPS (Y-Narpsio) glass-ceramics [42]. Reprinted from Solid State Ionics 262 (2014) 604, Copyright 2014, with permission from Elsevier

composition (NY*R*PS; *R* = Nd, Sm, Eu, Gd, Dy, Er, or Yb, $x = 0.4$, $y = 0.2$, $z = 0.1$), where yttrium was substituted with the various *R* elements. The crystallization kinetics of the glasses were examined by DTA, and the effects of *R* on the phase separation properties of the glass-ceramics were investigated in addition to the effects of the microstructure on the conduction properties.

The precursor glasses were initially prepared by melting stoichiometric mixtures of reagent-grade powders of anhydrous Na_2CO_3, Y_2O_3, R_2O_3 (*R* = Nd, Sm, Eu, Gd, Dy, Er, or Yb), $NH_4H_2PO_4$, and SiO_2 at 1350 °C for 1 h following calcinations at 400 °C for 0.5 h and at 900 °C for 0.5 h. The N5-type glass-ceramics NY*R*PS and NYPS (Y-Narpsio) with the $Na_{4.4}Y_{0.6}P_{0.2}Si_{2.8}O_9$ composition were successfully synthesized by crystallization of the glasses. As indicated in Fig. 10.20, the lattice constants of the glass-ceramic NY*R*PS species increased upon increasing the ionic radius of *R*, whereas the activation energies for crystal growth of the NY*R*PS glass decreased with greater ionic radii (Fig. 10.21). The formation of N5-type structures from the precursor glasses was also found to be dependent on the crystallization kinetics. In this case, the substitution of large *R* ions weakens the bonding of the N3-

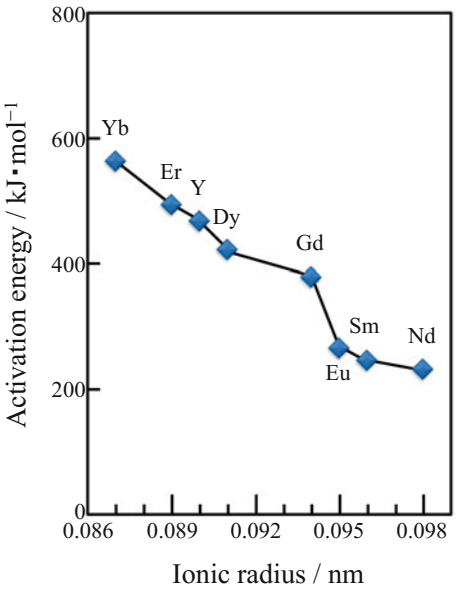

Fig. 10.21 Activation energies (*Ea*) of crystal growth for the NY*R*PS (*R* = Nd, Sm, Eu, Gd, Dy, Er, or Yb) and NYPS (Y-Narpsio) glasses [42]. Reprinted from Solid State Ionics 262 (2014) 604, Copyright 2014, with permission from Elsevier

or N9-type skeleton structure of the 6-membered SiO_4-tetrahedral rings, thereby leading to the formation of stable N5-type 12-membered structure. Furthermore, as shown in Fig. 10.22, the conductivities of the NY*R*PS glass-ceramics increased upon increasing the ionic radius of *R*. Presumably, rare earth ions that are octahedrally coordinated with the non-bridging oxide ions of the 12-membered rings of the silica tetrahedra expand the conduction paths for Na^+ ions along the *c*-axis [4]; this expansion explains the observed dependence of the activation energies on the ionic radius of *R*.

10.5.3 Ionic Conductivities of Na^+ Ion-Implanted Silicophosphate Glass-Ceramics [26]

We consider that a material processing technique to introduce a large number of mobile Na^+ ions into samples is required to realize the superionic conduction in the N5-type Narpsio compounds. Here, we report that a large enhancement in the electrical conductivity, probably due to Na^+ ions, has been obtained in the glass-ceramic Narpsio by ion implantation of Na^+ ions.

Substrate N5-type Narpsio compounds used for ion implantation were the glass-ceramic $Na_{3.9}Y_{0.6}P_{0.3}Si_{2.7}O_9$ and $Na_{3.9}Sm_{0.6}P_{0.3}Si_{2.7}O_9$. Approximately 5-mm-thick glass-ceramic disks were implanted with 200 keV Na^+ ions with flux densities of 10^{14} to 10^{15} ions/cm^2 at room temperature. The current density was 3 $\mu A/cm^2$. The XRD patterns of the Na^+ ion-implanted specimens exhibited

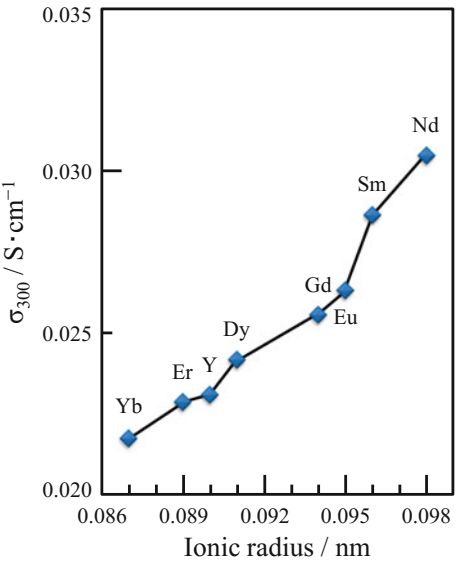

Fig. 10.22 Conductivity at 300 °C of the NY*R*PS (*R* = Nd, Sm, Eu, Gd, Dy, Er, or Yb) and NYPS (Y-Narpsio) glass-ceramics [42]. Reprinted from Solid State Ionics 262 (2014) 604, Copyright 2014, with permission from Elsevier

Table 10.9 Conduction properties of the Na^+-ion-implanted Narpsio glass-ceramics [26]

Dose/ions•cm^{-2}	σ_{300}/10^{-1} S•cm^{-1}	*E*a / kJ•mol^{-1}		
		T	G	G.B.
$Na_{3.9}Y_{0.6}P_{0.3}Si_{2.7}O_9$				
Before implantation	0.201	23.8	18.4	31.3
10^{14}	0.427	18.3	13.3	32.2
10^{15}	0.586	19.3	12.6	40.1
$Na_{3.9}Sm_{0.6}P_{0.3}Si_{2.7}O_9$				
Before implantation	0.238	27.6	17.9	51.4
10^{14}	0.512	36.7	16.9	88.8
10^{15}	0.715	33.3	16.3	104.1

Reprinted from Solid State Ionics 136/137 (2000) 1049, Copyright 2000, with permission from Elsevier

σ_{300}, Conductivity at 300 °C

*E*a Activation energy (*T* total, *G* grain, *G.B.* grain boundary)

N5 single phase. No cracking was perceived for any of the implanted surfaces. Table 10.9 summarizes the conduction properties of the glass-ceramic Narpsio specimens. The samples with the $Na_{3.9}Y_{0.6}P_{0.3}Si_{2.7}O_9$ and $Na_{3.9}Sm_{0.6}P_{0.3}Si_{2.7}O_9$ compositions crystallized at 900 °C for 5 h showed the ionic conductivities of 2.01×10^{-2} and 2.38×10^{-2} S/cm at 300 °C, respectively. It was found that Sm-Narpsio containing the largest Sm^{3+} ions was more conductive than Y-Narpsio with medium Y^{3+} ions under the same heating conditions. The ionic conductivities of the glass-ceramic $Na_{3.9}Y_{0.6}P_{0.3}Si_{2.7}O_9$ and $Na_{3.9}Sm_{0.6}P_{0.3}Si_{2.7}O_9$ at 300 °C were drastically enhanced from 2.01×10^{-2} S/cm to 5.86×10^{-2} S/cm and from

2.38×10^{-2} S/cm to 7.15×10^{-2} S/cm, respectively, upon implantation of 200 keV Na^+ ions with a flux density of 10^{15} ions/cm^2.

10.5.4 Structure and Conduction Properties of $Na_5YSi_4O_{12}$-Type Glass-Ceramics Synthesized by Bias Crystallization of Glass [27]

Glass-ceramics of the phosphorus-containing N5-type Na^+ superionic conductors were prepared by bias crystallization of glasses with the composition $Na_{4.05}Y_{0.55}P_{0.3}Si_{2.7}O_9$ in an electric field. The conditions for bias crystallization are discussed with respect to the microstructure and the conduction properties.

The precursor glasses were made by melting stoichiometric mixtures of reagent-grade powders of anhydrous Na_2CO_3, Y_2O_3, SiO_2, and $NH_4H_2PO_4$ at 1350 °C for 1 h, followed by annealing for several hours at an optimum temperature. The annealed specimens were heated to 900 °C in an electric field for the bias crystallization. The thermostable heating holder was produced in order to do the crystallization in a direct current electric field. This holder is made of alumina and platinum. Glass samples (5 mm × 5 mm × 8 mm) were held between the platinum plates and crystallized in an electrical field of 1 V/mm. The thermal treatment was the same as that used in conventional crystallization without the electric field.

The microstructure was investigated with SEM. The grain length of the cross section parallel with the electric field direction was 10–15 nm, and it was proven to be smaller than the 15–30 nm grain length of the cross section perpendicular to the direction and the specimen crystallized by the conventional method. It was possible to control shape and orientation of crystal grain by the crystallization in the electrical field.

Owing to the bias field, an electric current related to temperature was measured during the crystallization process. Figure 10.23 shows a current profile with respect to temperature during the crystallization process in the electric field. The largest observed current was 250 μA. The current profile exhibits three peaks at approximately 600 °C, 700 °C, and 850 °C. These temperatures correspond to those of nucleation, phase transition from N3 phase to N5 phase, and crystallization of glass specimens determined by DTA analysis, respectively. An electric current with respect to temperature was measured newly by applying the bias voltage only in two limited temperature ranges, because two main peaks were observed in Fig. 10.23. One range is from right before of the first main peak (511–652 °C), and another range is from right before of the second main peak (790–865 °C). The resulting current profile is shown in Fig. 10.24. It was found that the mass transfer in the specimen is generated even in the condition of no applied voltage.

Crystalline phases were identified on the sample after the crystallization in the electric field by XRD in order to consider the possibility of structural changes by the movement of Na^+ ion, which is a carrier. In the several cut sections, no difference in

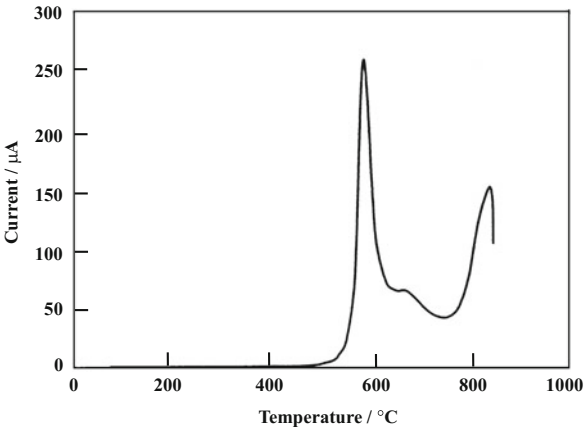

Fig. 10.23 Current profile in relation to temperature during crystallization process in electric field [27]. Reprinted from Solid State Ionics 154 (2002) 361, Copyright 2002, with permission from Elsevier

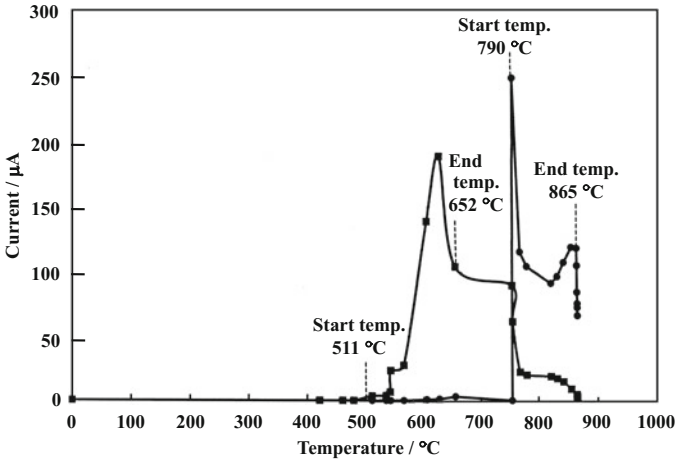

Fig. 10.24 Current profile in relation to temperature measured by applying voltage in two limited temperature ranges [27] Reprinted from Solid State Ionics 154 (2002) 361, Copyright 2002, with permission from Elsevier

the fundamental structure was observed. Judging from the patterns, the N5 single-phase ionic conductors were successfully produced by the bias crystallization of glasses.

Figure 10.25 shows the temperature dependence Arrhenius plots of the conductivities of various specimens. The complex admittances of the measured glass-ceramics consisted of two semicircles below 300 °C. The two intercepting points on the real axis are interpreted as the resistance of the crystallized grains (R_G) and the total resistance of the grains and remaining glassy grain boundaries (R_{GB}). As R_{GB} decreases rapidly with increasing temperature because of high $(Ea)_{GB}$ to a comparable value with R_G at 300 °C, the total conductivities (R_G+R_{GB}) are

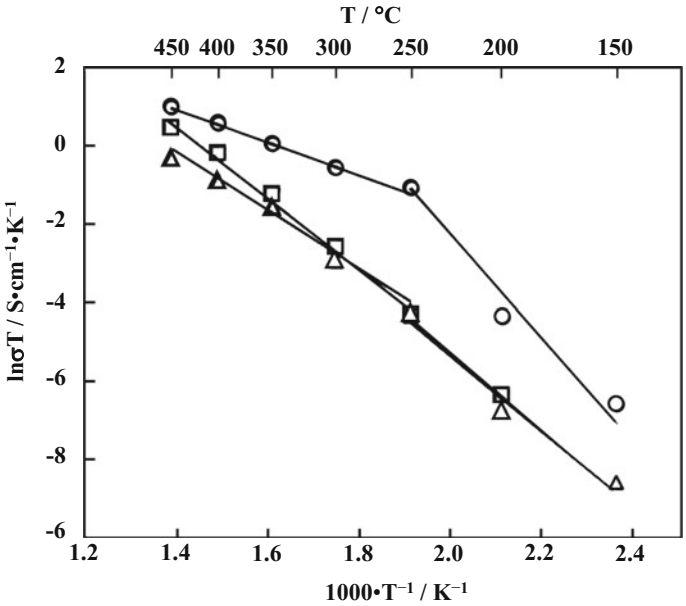

Fig. 10.25 Temperature dependence Arrhenius plots of the conductivities of the bias-crystallized Narpsio glasses [27]. ◯ Conventional, △ Parallel, □ Perpendicular. Reprinted from Solid State Ionics 154 (2002) 361, Copyright 2002, with permission from Elsevier

Table 10.10 Conduction properties of the bias-crystallized Narpsio glasses [27]

	Ea / kJ•mol^{-1}		σ_{300} / mS•cm^{-1}
	Temperature		
	High	Low	
○ Conventional	33.0	99.9	0.9860
△ Parallel	66.6	73.5	0.0923
□ Perpendicular	76.4	82.2	0.1320

Reprinted from Solid State Ionics 154 (2002) 361, Copyright 2002, with permission from Elsevier

dominated by grain boundary conductivity. The effect of the grain boundary is greatly seen on the appearance at lower temperatures. Table 10.10 summarizes the conduction properties obtained from Fig. 10.25. The cross sections parallel and perpendicular to the electric field direction showed the ionic conductivities of 0.0923 and 0.132 mS/cm at 300 °C, respectively. It was found that the bias-crystallized specimens were less conductive than those crystallized by the conventional method. Figure 10.26 shows the temperature dependence of the conductivity of the bias-crystallized specimen. At temperatures over 300 °C, anisotropy in the conductivity was observed. It was also found that the cross section perpendicular to the electric field direction was more conductive than that parallel with the electric field direction. The microstructure and the electric conductivity of the Narpsio glass-

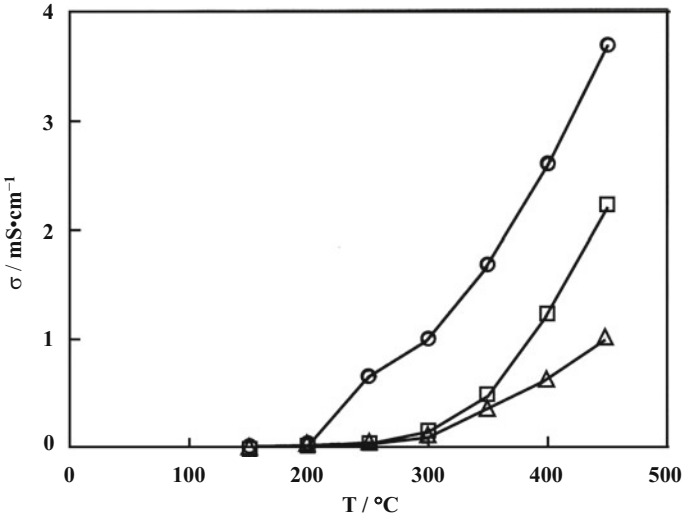

Fig. 10.26 Temperature dependence of conductivity of the bias-crystallized Narpsio glasses [27]. Reprinted from Solid State Ionics 154 (2002) 361, Copyright 2002, with permission from Elsevier

ceramics perpendicular to the electric field direction were significantly different from those in parallel.

10.6 Concluding Remarks

In this article, Na^+ superionic conducting Narpsio glass-ceramics with the $Na_5YSi_4O_{12}$ (N5)-type structure and containing various rare earth elements (R), which were prepared according to the $Na_{3+3x-y}R_{1-x}P_ySi_{3-y}O_9$ composition, were reviewed, and recent research into the structural control of Na^+ superionic conducting glass-ceramics was introduced. The possible combinations of x and y became more limited for the crystallization of the superionic conducting phase as the ionic radius of R increased and the Na^+ conduction properties were more enhanced in the glass-ceramics of larger R. The meaning of the composition formula can be clarified in the thermodynamic and kinetic study of the crystallization and phase transformation of metastable to stable phase in the production of N5-type glass-ceramics. It was demonstrated that the medium value of content product as $[P]\times[R]$ is important in the crystallization of the N5 single phase. The conduction properties of these glass-ceramics were strongly dependent upon the crystallization conditions as well as the compositions. Not only complex impedance analysis but also TEM observations confirmed that this dependence was attributed to the conduction properties of grain boundaries, which were glasses condensed at triple points enclosed by grains.

The Narpsio conductors exhibit great potential and are one of the most important groups of solid electrolytes, not only because they are practically useful for application in advanced batteries but also because they are three-dimensional ionic conductors with a 12-$(SiO_4)^{4-}$-tetrahedra-containing skeleton structure from which, or by analogy with which, various solid electrolyte materials can be derived. In addition, various modified Narpsio glass-ceramics have been synthesized by replacing *R* with Sc, Y, In, La, Nd, Sm, Eu, Gd, Dy, Er, or Yb and/or by substituting tetravalent (Ti^{4+}, Ge^{4+}, Te^{4+}), trivalent (B^{3+}, Al^{3+}, Ga^{3+}), pentavalent (V^{5+}), and hexavalent (Mo^{6+}) ions for P or Si. In this review, the results of Na^+ ion implantation as a material processing technique to introduce a large number of mobile Na^+ ions were presented. A large enhancement in electrical conductivity was observed in the Narpsio glass-ceramics by ion implantation of Na^+ ions. Such glass-making processing is favorable for the fabrication of differently shaped electrolytes, and the microstructures of glass-ceramic electrolytes can be controlled through variation of the crystallization conditions. We have successfully produced anisotropic glass-ceramic conductors by bias crystallization of the glasses in an electric field. The microstructure and the conduction properties were dependent on the current direction in the crystallization process.

10.7 Future Prospects

The Narpsio family has great potential. It is a solid solution in the Na_2O-R_2O_3-P_2O_5-SiO_2 system and is expected to develop a variety of modified Narpsios. Our main work has recently been focused on the synthesis of various glass-ceramics with N5 single phase as shown in Fig. 10.27, which contain 15.6% mobile Na^+ ions and 84.4% bonding Na^+ ions. In the research currently underway, we are trying to synthesize them without *R* elements but with Fe of high abundance and low costs, by melt quenching and glass-crystallization method. Furthermore, mobile Na^+ ions in the N5 phase also can be exchanged for proton or several alkali ions. Our group is advancing the development of new Narpsio family conductors by exchange of carrier mobile Na^+ with Li^+, K^+, or H^+. In the future, we are expecting computational chemistry to elucidate the conduction mechanism in conductors with various kinds of carrier ions.

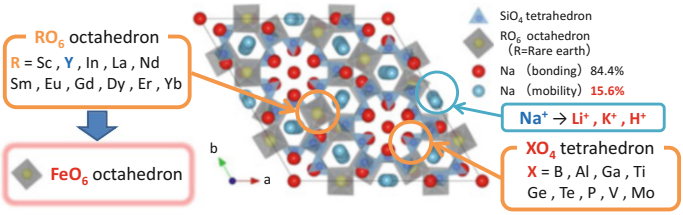

Fig. 10.27 A variety of modified Narpsios

References

1. S. Morimoto, J. Ceram. Soc. Jpn. **97**, 1097 (1989)
2. B.A. Maksimov, Y.A. Kharitonov, A.N.V. Belov, Sov. Phys. Dokl. **18**, 763 (1974)
3. B.A. Maksimov, I.V. Petrov, A. Rabenau, H. Schulz, Solid State Ionics **6**, 195 (1982)
4. T. Okura, N. Yoshida, K. Yamashita, Solid State Ionics **285**, 143 (2016)
5. R.D. Shannon, B.E. Taylor, T.E. Gier, H.Y. Chen, T. Berzins, Inorg. Chem. **17**, 958 (1978)
6. H.U. Beyeler, T. Himba, Solid State Commun. **27**, 641 (1978)
7. H.Y.-P. Hong, J.A. Kafalas, M. Bayard, Mater. Res. Bull. **13**, 757 (1978)
8. E. Banks, C.H. Kim, J. Electrochem. Soc. **132**, 2617 (1985)
9. K. Yamashita, M. Tanaka, T. Umegaki, Solid State Ionics **58**, 231 (1992)
10. K. Yamashita, T. Nojiri, T. Umegaki, T. Kanazawa, Solid State Ionics **35**, 299 (1989)
11. R.D. Shannon, T.E. Gier, C.M. Foris, J.A. Nelen, D.E. Appleman, Phys. Chem. Miner. **5**, 245 (1980)
12. F. Cervantes, L.J. Marr, F.P. Glasser, Ceram. Int. **7**, 43 (1981)
13. C.H. Kim, B. Qiu, E. Banks, J. Electrochem. Soc. **132**, 1340 (1985)
14. K. Yamashita, S. Ohkura, T. Umegaki, T. Kanazawa, Solid State Ionics **26**, 279 (1988)
15. T. Okura, M. Tanaka, G. Sudoh, Mater. Res. Soc. Symp. Proc. **453**, 611 (1997)
16. T. Okura, K. Yamashita, T. Umegaki, Phosphorus Res. Bull. **6**, 237 (1996)
17. T. Okura, M. Tanaka, H. Monma, K. Yamashita, G. Sudoh, J. Ceram. Soc. Jpn. **111**, 257 (2003)
18. K. Yamashita, T. Umegaki, M. Tanaka, T. Kakuta, T. Nojiri, J. Electrochem. Soc. **143**, 2180 (1996)
19. T. Okura, M. Tanaka, H. Kanzawa, G. Sudoh, Solid State Ionics **86–88**, 511 (1996)
20. K. Yamashita, M. Tanaka, T. Kakuta, M. Matsuda, T. Umegaki, J. Alloys Compd. **193**, 283 (1993)
21. K. Yamashita, T. Nojiri, T. Umegaki, T. Kanazawa, Solid State Ionics **40/41**, 48 (1990)
22. K. Yamashita, S. Ohkura, T. Umegaki, T. Kanazawa, J. Ceram. Soc. Jpn. **96**, 967 (1988)
23. W.D. Kingery, H.K. Bowen, D.R. Uhlmann, *Introduction to Ceramics*, 2nd edn. (Wiley, New York, 1976), p. 368
24. T. Okura, H. Monma, K. Yamashita, J. Ceram. Soc. Jpn. **112**, S685 (2004)
25. T. Okura, H. Monma, K. Yamashita, Solid State Ionics **172**, 561 (2004)
26. T. Okura, K. Yamashita, Solid State Ionics **136/137**, 1049 (2000)
27. T. Okura, Y. Inami, H. Monma, S. Nakamura, K. Yamashita, Solid State Ionics **154**, 361 (2002)
28. T. Okura, H. Monma, K. Yamashita, J. Eur. Ceram. Soc. **26**, 619 (2006)
29. S. Suda, K. Yamashita, T. Umegaki, Solid State Ionics **89**, 78 (1996)
30. T. Okura, H. Monma, K. Yamashita, J. Electroceram. **24**, 83 (2010)
31. I.W. Donald, J. Mater. Sci. **30**, 904 (1995)
32. Y.M. Sung, J. Mater. Sci. **31**, 5421 (1996)
33. H.U. Beyler, R.D. Shannon, Appl. Phys. Lett. **37**, 934 (1980)
34. I. Maki, T. Sugimura, J. Ceram. Soc. Jpn. **78**, 129 (1970)
35. P. Mondal, J.W. Jeffery, Acta Crystallogr. **B31**, 689 (1975)
36. M.G. Alexander, Solid State Ionics **22**, 257 (1987)
37. T. Okura, M. Saimaru, H. Monma, K. Yamashita, Solid State Ionics **180**, 537 (2009)
38. T. Okura, K. Kawada, N. Yoshida, H. Monma, K. Yamashita, Solid State Ionics **225**, 367 (2012)
39. I.W. Donald, J. Mater. Sci. **30**, 904 (1995)
40. Y.M. Sung, J. Mater. Sci. **31**, 5421 (1996)
41. T. Okura, T. Takahashi, H. Monma, K. Yamashita, Solid State Ionics **179**, 1291 (2008)
42. T. Okura, K. Kawada, N. Yoshida, H. Monma, K. Yamashita, Solid State Ionics **262**, 604 (2014)

Chapter 11
Surface Characterization of Plasma-Electrolytic Oxidized Coatings by X-Ray Photoelectron Spectroscopy

Elena A. Koblova, Alexander Yu. Ustinov, and Oleg L. Shcheka

Abstract To explain the catalytic properties inherent to a number of coatings formed by the method of plasma-electrolytic oxidation (PEO), a series of Ni- and/or Cu-containing coatings on aluminum were investigated by X-ray photoelectron spectroscopy (XPS). It was determined that the main components of the surface layers of these coatings are a variety of oxide structures of the base and electrolyte elements – oxides of aluminum, nickel, copper, and more complicated composite structures. In this chapter, our experimental results are introduced.

Keywords X-ray photoelectron spectroscopy (XPS) · Surface structure · CO oxidation · Metal oxide coating

11.1 Introduction

Design and investigation of various novel functional materials have been the main objectives in modern material science. It was recently found that coatings formed by the method of plasma-electrolytic oxidation (PEO) and containing 3d element(s) have a pronounced catalytic activity in the oxidation of CO to CO_2 [1–7]. Since the surface plays a decisive role in heterogeneous catalysis, our research has emphasized to investigate the composition and structure of the surface layers of the metal oxide

E. A. Koblova
Institute of Chemistry, Far Eastern Branch of the Russian Academy of Sciences, Russian Federation, Vladivostok, Russia
e-mail: les@ich.dvo.ru

A. Y. Ustinov (✉)
Institute of Chemistry, Far Eastern Branch of the Russian Academy of Sciences, Russian Federation, Vladivostok, Russia

Far Eastern Federal University, Russian Federation, Vladivostok, Russia
e-mail: all_vl@mail.ru

O. L. Shcheka
Far Eastern State Technical Fisheries University, Russian Federation, Vladivostok, Russia

T. Onishi (ed.), *Theoretical Chemistry for Advanced Nanomaterials*,
https://doi.org/10.1007/978-981-15-0006-0_11

PEO-coatings and interrelationships between the surfaces and catalytic properties. A number of Ni- and/or Cu-containing coatings formed by PEO have been investigated by the method of X-ray photoelectron spectroscopy (XPS) [5–7]. It was determined that the main components of the surface layers of these coatings are a variety of oxide structures of the base and electrolyte elements – oxides of aluminum, nickel, copper, and more complicated composite structures. In this chapter, we introduce our recent experimental results on surface coatings on aluminum.

11.2 Composition and Electronic State of Surface Metal Oxide Structure

11.2.1 Experimental Details

The coatings were formed on aluminum (A7 grade) by PEO in water electrolytes containing the basic components (Na_3PO_4, $Na_2B_4O_7$, Na_2WO_4) [8] and nickel and copper acetates in various ratios. A detailed description of the coatings and the process of their formation are in Ref. [5].

The XPS spectra were measured by an ultra-vacuum spectrometer (Specs, Germany) equipped with a 150 mm electrostatic hemispherical Phoibos-150 analyzer [4]. To excite the spectra, we used nonmonochromatized Mg K_α (1253.6 eV) radiation. The vacuum in the analyzer chamber (when measuring the spectra) was about $5 \cdot 10^{-7}$ Pa. The transmission energy of the analyzer was set to 50 eV (which caused the resolution of the spectra in the C 1s band about 1.8 eV). The spectra of the initial surface of the samples (the upper layers of 3–5 nm thickness) and the underlying near-surface layers exposed by ion etching were measured. To remove the upper layer (~3 nm thick), ion etching was used by scanning the sample surface for 5 min at an Ar^+ energy of 5000 eV and current I_{total}= 20 μA. According to our estimation, the etching rate of the studied materials was about 0.1 Å/s. The spectra were calibrated using the hydrocarbon C1*s* lines whose energy was taken to be 285.0 eV.

11.2.2 Experimental Results

According to our previous results [5–7], PEO-coatings have the complicated composition and structure due to the peculiarities of their formation processes. Oxidation of the initial pure aluminum in the base electrolyte (PBW) leads to the oxidation of upper layer metal-base and to the integration of components from electrolyte: Na, P, and W (see Fig. 11.1). Here, as follows from the photoelectron spectra (see Table 11.1), the surface layer of the Al-PBW coating contains not only aluminum oxide and phosphate but also sodium phosphate Na_3PO_4, tungsten

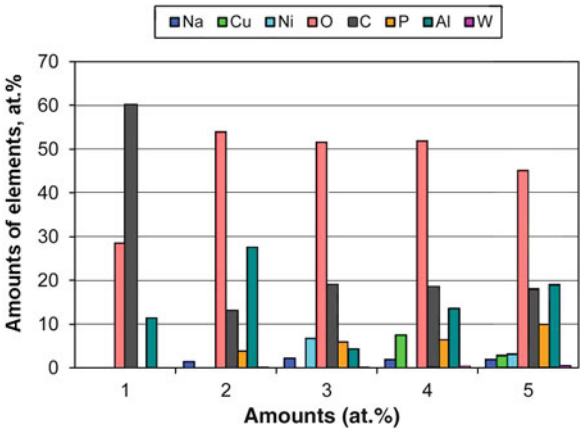

Fig. 11.1 Amounts of the elements in the surface layers of coatings: 1, Al; 2, Al–PBW; 3, Al–$Ni_{0,020}$; 4, Al–$Cu_{0,025}$; 5, Al–$Ni_{0,080}$–$Cu_{0,0125}$

Table 11.1 The binding energy (eV) of the elements and their amounts in the coatings (the upper line is the original sample, the lower one is after etching)

Sample	Na Auger	Cu $2p_{3/2}$	Ni $2p_{3/2}$	O 1s	C 1s	P 2p	Al 2p	W $4f_{7/2}$
1	–	–	–	532,1/28,6 532,3/29,7	285,0/59,9 285,0/1,8	–	74,2/11,5 74,8/68,5	–
2	264,6/1,4 264,1/0,5	–	–	531,9/54,0 531,2/58,5	285,0/12,8 285,0/1,3	134,2/3,9 133,6/1,5	74,7/27,7 74,4/38,1	35,8/0,2 35,2/0,1
3	264,0/2,2 263,7/2,0	–	856,9/6,8 852,8/8,8	531,8/51,6 531,2/55,4	285,0/18,8 285,0/5,0	133,5/6,0 133,0/4,6	74,0/14,4 73,6/24,2	35,2/0,1 35,3/0,1
4	263,9/1,9 263,9/1,2	935,7/7,5 933,7/4,1	–	531,7/51,9 531,6/60,3	285,0/18,3 285,0/1,6	133,3/6,5 133,6/5,8	74,3/13,6 74,5/26,9	36,3/0,4 36,2/0,2
5	264,0/3,2 264,6/1,8	933,6/1,6 933,1/1,0	856,6/4,6 853,4/6,6	531,6/42,9 532,0/46,2	285,0/25,9 285,0/5,6	133,8/9,5 134,4/9,1	74,5/11,8 75,2/28,9	36,0/0,5 36,8/0,8

oxide WO_3, and carbon-containing compounds (see Fig. 11.2a). Coatings formed in electrolytes with the addition of appropriate amounts of nickel and/or copper acetates contain not only the above structural components, oxides, and phosphates of 3d elements, but also more complex spinel-like formations MAl_2O_4, where M = Ni or Cu (see Fig. 11.2b). Depending on the features of the formation (first of all, the composition of the electrolyte, the regime, and the formation time), the proportion of aluminum oxide in the surface layer of coatings can reach 35 at.%; aluminum phosphate, 15 at.% (in the base coating Al-PBW – 60 and 15 at.%, respectively); nickel oxide, 20 at.%; nickel phosphate, 10 at.%; copper oxide, 15 at.%; copper phosphate, 30 at.%. Obviously, the presence of Ni and Cu oxides in a certain quantity and quality determines the observed catalytic activity of the coatings.

In general, the upper layers of nickel- and copper-containing coatings are similar in structure and composition. The main difference is the different occurrence of Ni and Cu in the thickness of the coatings (see Fig. 11.3). Thus, under the transition from the upper to the underlying layers of coatings, an increase in the nickel amount is observed. On the contrary, a decrease in the copper amount indicates the Cu

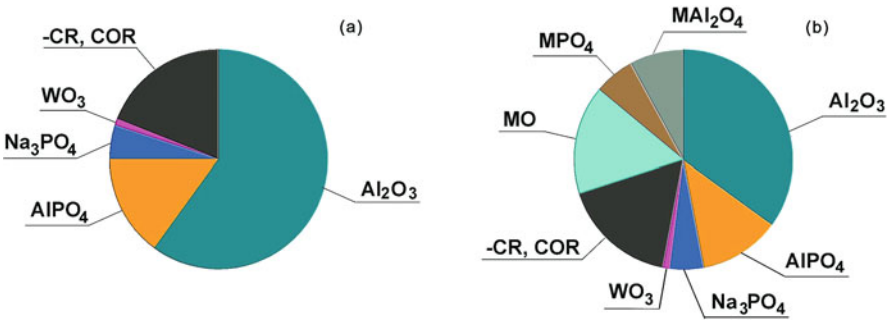

Fig. 11.2 The expected composition of the base coating surface Al–PBW (**a**) and Ni- or Cu-containing coatings (**b**). M = Ni or Cu. MO, MPO_4, and MAl_2O_4 conditionally denote the oxides of 3d elements, their phosphates, and spinel-type structures

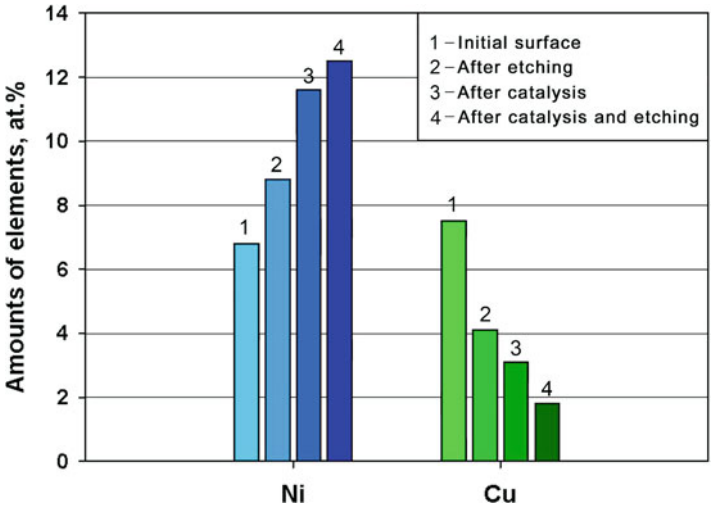

Fig. 11.3 Amounts of Ni 2p and Cu 2p in coatings 3 and 4 according to XPS

concentrating in the surface layers but Ni in the near-surface layers of the coatings. It should be noted the change in the amount of "active" components during the catalytic cycles (with gradual heating and subsequent cooling). An increase in the nickel amount is observed in the upper and lower layers for the nickel-containing coatings, while the copper amount decreases in copper-containing coatings, which characterizes the different orientation of the diffusion processes. As an illustration of these changes, Fig. 11.3 shows the Ni and Cu amounts in coatings 3 and 4, formed in electrolytes with a close amounts of nickel and copper acetates, respectively.

For mixed Ni-, Cu-containing coatings, the presence of both 3d elements in the upper layers is noted. In this case, the composition of the surface of coatings depends significantly on the ratio of components in the electrolyte and the formation time.

Comparing to the "mono" coatings (containing either nickel or copper), there is a larger amount of phosphorus, less amount of oxygen, significantly less nickel and copper in mixed Ni-, Cu-containing coatings (see Fig. 11.1). According to the binding energies (see Table 11.1), the states of the elements in "mono" and in mixed coatings are similar. Also, as for "mono" coatings, for the mixed ones, the concentration of copper in the upper surface layers of the coatings is noted, and nickel is in the deeper layers; an increase in the nickel amount and a decrease in the copper amount in the entire analyzed thickness (about 5 nm) under heating during the catalytic process were found [5].

11.3 Outlook

For deeper understanding of our experimental results, quantum chemical calculation based on density functional theory (DFT) can be applicable [9]. We are investigating catalytic reactions (including the adsorption of carbon monoxide) of the surface metal oxides in case of aluminum (III), nickel(II), and copper(II) oxide clusters. The results of DFT calculations will be summarized in a similar manner after some refinements.

Acknowledgments This work was supported in part by the Russian Ministry of Education and Science (state task 3.6478.2017/6.7)

References

1. N.B. Kondrikov, V.S. Rudnev, M.S. Vasilyeva, L.M. Tyrina, T.P. Yarovaya, A.V. Rozhkov, Chem Sustain Dev **13**(6), 851–853 (2005)
2. I.V. Lukiyanchuk, L.M. Tyrina, V.S. Rudnev, A.Y. Ustinov, P.M. Nedozorov, M.S. Vasilyeva, Kinet Catal **49**(3), 439–445 (2008)
3. M.V. Ved, A.V. Karakurkchi, N.D. Sakhnenko, A.S. Gorohivskiy, Chem Phys Technol Surf **8**(1), 73–79 (2017)
4. A. Karakurkchi, M. Sakhnenko, M. Ved, A. Galak, S. Petrukhin, East Eur J Enterp Technol **89**, 12–18 (2017)
5. E.A. Koblova, A.Y. Ustinov, V.S. Rudnev, I.V. Lukiyanchuk, I.V. Chernyh, J Struct Chem **58**(6), 1175–1183 (2017)
6. E.A. Koblova, A.Y. Ustinov, I.V. Chernyh, I.V. Lukiyanchuk, V.S. Rudnev, FEB RAS Bull **4**, 39–44 (2015)
7. E.A. Koblova, A.Y. Ustinov, I.V. Chernyh, I.V. Lukiyanchuk, V.S. Rudnev, Izvestiya of South-Western State University. Ser Tech Technol **18**(1), 130–138 (2016)
8. Rudnev V.S., Gordienko P.S., Kurnosova A.G., Orlova T.I. Patent 1783004 USSR, MPK C 25 D 11/02. – No. 4757905; appl. 17.10.1989; publ. 23.12.1992, Bul. No. 47
9. E.A. Koblova, A.Y. Ustinov, O.L. Shcheka, J Nano Electron Phys **8**(3), 03003 (2016)

Chapter 12
Inter-spin Interactions of Organic Radical Chains in Organic 1D Nanochannels: An ESR Study of the Molecular Orientations and Dynamics of Guest Radicals

Hirokazu Kobayashi

Abstract Unique inter-spin interaction appears in one-dimensional (1D) organic inclusion compounds which are synthesized by using 2,4,6-tris(4-chlorophenoxy)-1,3,5-triazine (CLPOT) and (*o*-phenylenedioxy) cyclotri phosphazene (TPP). Molecular orientations and dynamics of guest radicals incorporated in CLPOT or TPP nanochannels have been investigated using variable-temperature electron spin resonance (ESR) measurement, together with ESR simulation. When 4-substituted-2,2,6,6-tetramethyl-1-piperidinyloxyl (4-X-TEMPO) is incorporated in 1D CLPOT and TPP nanochannels, they exhibited three-dimensional, temperature-independent or 1D, temperature-dependent exchange interactions. It will be possible to design and develop innovative organic magnet based on these features.

Keywords Inclusion compound · 1D nanochannel · Molecular dynamics · Organic magnet · ESR measurement · ESR simulation

12.1 Introduction of Inclusion Compounds

Various new organic functional materials intended for the development of inclusion compounds (ICs) have been developed over the last few decades [1–13]. The guest molecules in ICs occupy nanosized cavities, nanochannels, molecular sheets or jungle-jim-like frameworks in host lattices [12, 14, 15]. The guest compounds within host compounds are mainly governed by van der Waals interaction. Figure 12.1 demonstrates the images of zero- to three-dimensional nanospaces and the included guest molecules. The nanospaces within the host materials are called as one-dimensional (1D) when their structures are tunnel-like cavities,

H. Kobayashi (✉)
Faculty of Arts and Sciences at Fujiyoshida, Showa University, Yamanashi, Japan
e-mail: hirawk@cas.showa-u.ac.jp

T. Onishi (ed.), *Theoretical Chemistry for Advanced Nanomaterials*,
https://doi.org/10.1007/978-981-15-0006-0_12

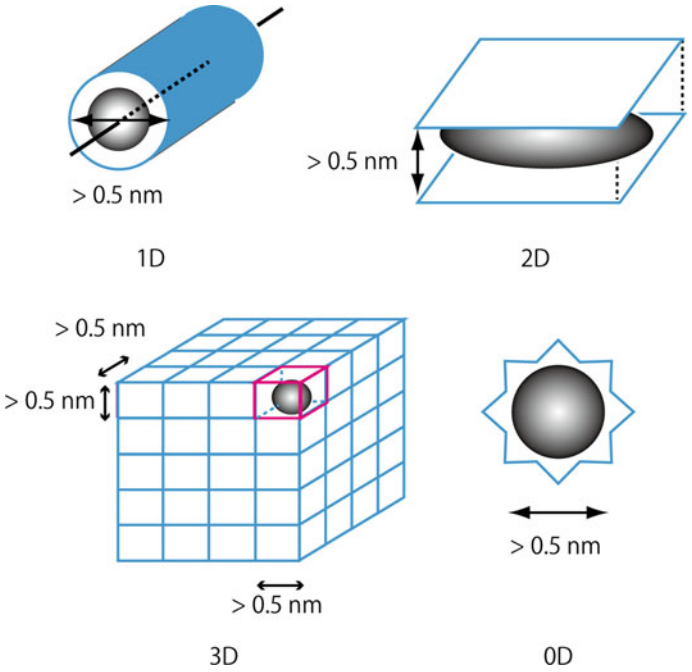

Fig. 12.1 Images of 0–3D nanospaces and the included guest molecules. Black-and-white spherical objects demonstrate guest materials

two-dimensional (2D) in the case sandwiched between molecular sheets, and three-dimensional (3D) in the case stacked jungle-jim-like. On the other hand, when guest molecules are included in the center of circular host molecules, such as crown ether, cyclodextrin, or micelles, they are called as zero-dimensional (0D) for convenience[16]. In 1–3D host materials, when the pores of host materials are kept even in the guest desorption by heating or pH change such as zeolite, they are called as *porous materials*. Many researchers have employed 0–3D host materials with periodic and regular cavities, including 1D nanochannels serving as nanosized molecular templates to align guest molecules [11–13, 17–19]. ICs such as these are expected to exhibit anisotropic physical properties. As an example, the 1D alignment of paramagnetic molecules in 1D nanochannel may generate the array of dimers, trimers, or multi-metric assembly of electron spins and may give rise to anisotropic magnetic characteristics by the intra- or interchain magnetic interactions. Such materials have attracted attention with regard to the fabrication of novel molecular-scale magnets and electric devices [11–13, 17–24] and medications based on magnetic markers [25] and also have applications in magnetic resonance spectroscopy [26, 27].

Crystalline tris(*o*-phenylenedioxy)cyclotriphosphazene (TPP: Scheme 12.1a) has tunnel-like 1D nanochannels in which the walls comprise locally trigonally coordi-

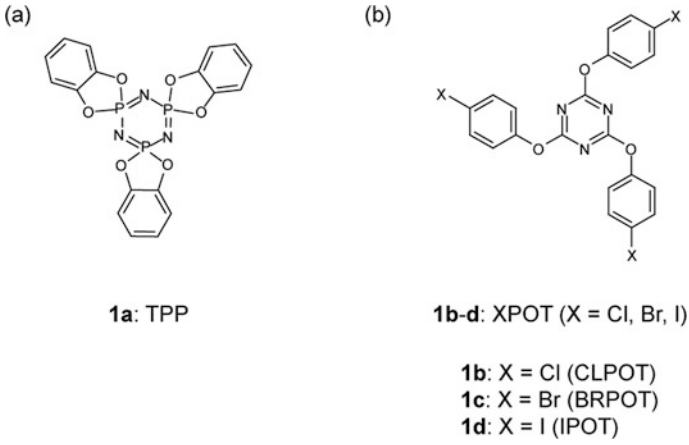

Scheme 12.1 Chemical structures of host compounds described in this review: TPP (**a**) and XPOT (**b–d**)

nated phenyl rings [14, 28]. The pore size of these nanochannels, 0.45 nm in the guest-free state [29], can be expanded to 0.9 nm by including guest molecules. The homogeneity of TPP nanochannels has been examined using hyperpolarized and high-pressure ^{129}Xe nuclear magnetic resonance (NMR) spectroscopy [30–32]. During the recrystallization of TPP, solutes within the solvent and the solvent molecules themselves can be included in TPP nanochannels in a 1D manner to form molecular chains. The extent of inclusion in these nanochannels is decided by the molecular size and the concentration of the guest molecules. If functional molecules having unique electrical characteristics are included in the TPP nanochannels, the resulting ICs may express anisotropic optical, electric, or magnetic properties. As an example, TPP ICs including dye molecules exhibit an anisotropic second harmonic generation effect due to the charge transfer direction in the guest molecules [33, 34] and those including I_2 exhibit anisotropic electron conductivity parallel or perpendicular to the channel axes due to electron donor properties of guest atoms or molecules and the dielectric host structures which separates I_2 chains [35].

TPP-based ICs incorporating sulfur-nitrogen or alkyl stearate radical molecular chains have been assessed by several groups [36, 37]. The formation of 1D molecular chains of 2,2,6,6-tetramethyl-1-piperidinyloxyl (TEMPO; Scheme 12.2a) radicals was achieved using the 1D nanochannels of TPP crystals ([$(TPP)_2$-$(TEMPO)_{1.0}$]; **1a/2a**) [38, 39]. Electron spin resonance (ESR) analyses of **1a/2a** demonstrated isotropic line profiles over all temperature range, in particular intermediate between Lorentzian and Gaussian above 139 K. In addition, a narrowing of the peak-to-peak line width was associated with the 1D spin diffusion behavior in this material ($|J_{intra}| < 1$ K) (see Sects. 12.2.5 and 12.6). On the other hand, the inclusion amount of the guest radicals in nanochannels can be reduced using non-radical molecules such as 2,2,6,6-tetramethylpiperidine (TEMP; Scheme 12.3a), which are similarly sized to the guest radicals. Then, the ICs demonstrate high-

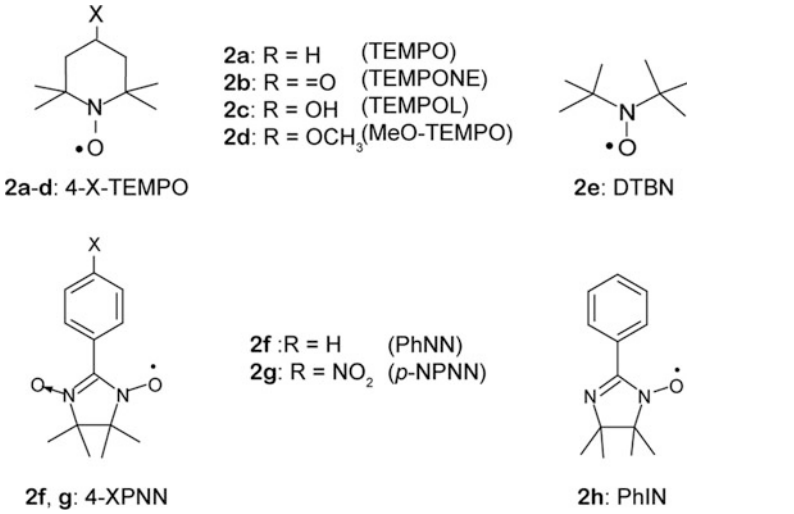

Scheme 12.2 Chemical structures of guest radicals described in this review: 4-substituted-TEMPO derivatives (4-X-TEMPO: **a**–**d**), DTBN (**e**), 4-substitute-PhNN (4-XPNN: **f** and **g**), and PhIN (**h**)

Scheme 12.3 Chemical structures of spacers described in this review: 4-substituted-TEMP derivatives (4-R-TEMP: **a**–**c**), pivalone (**d**), and *N*-PhMI (**e**)

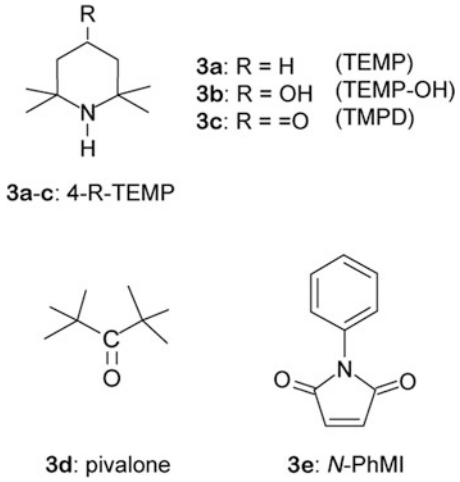

resolved ESR spectra due to the reduction of dipolar broadening. Above 108 K, TEMPO radicals dispersed in TPP nanochannels by TEMP were found to undergo anisotropic rotational diffusion around the principal *y*-axis of the *g* tensors of the radicals, which were perpendicular to the molecular long axis (see Sects. 12.2.3 and 12.5) [40]. These results suggest the possibility of correlating the inter-spin exchange/dipolar interactions of **1a/2a** with the molecular dynamics of TEMPO radicals in TPP nanochannels. **1a/2a** undergo antiferromagnetic exchange interactions at quite low temperatures, indicating that one-dimensional organic

Table 12.1 Host, guest, and spacer described in this chapter

	Roles	Materials	Example
Host	Nanochannel	1–3D porous material	TPP, XPOT
Guest	Magnetic source	Organic radical	4-X-TEMPO (including DTBN), 4-XPNN, PhIN
Spacers	Reduction of guest inclusion in nanochannel	Non-radical molecule	4-R-TEMP, pivalone, *N*-PhMI

inclusion compounds incorporating organic radical (1D OIC-OR) may potentially be synthesized from these compounds. Such materials could be used to probe the magnetic exchange between radicals, based on the appropriate selection of host and guest materials so as to tune the molecular orientations and dynamics of the guest radicals in the nanochannels. In the case of several TPP ICs incorporating organic radicals such as **2a–c** (**2b**: 4-oxo-TEMPO (TEMPONE), **2c**: 4-hydroxy-TEMPO (TEMPOL)), **e** (di-*t*-butyl nitroxide (DTBN)), **f** (phenylnitronylnitroxide (PhNN)), and **h** (phenyl iminonitroxide (PhIN)), the molecular orientation and dynamics of guest molecules in nanochannels have been determined using ESR spectroscopy [41–44] as well as theoretical simulation of spectra [45–47] (see Sects. 12.2.3 and 12.5). These techniques can be employed to determine the molecular orientations and dynamics of organic radicals both in 1D nanochannels and 0D cavities [48, 49]. In Table 12.1, the characters of host, guest, and spacer materials described in this review are summarized.

In other work, the 1D nanochannels of 2,4,6-tris(4-chlorophenoxy)-1,3,5-triazine (CLPOT: Scheme 12.1b) [50] crystals have been used to confine several organic radicals, including 4-substituted-TEMPO derivatives (4-X-TEMPO: Schemes 12.2a–d) [51, 52] and 4-substituted-phenylnitronylnitroxides (4-XPNN: Schemes 12.2f and g) [27]. The 1D rotational diffusion of these radicals in CLPOT nanochannels has been confirmed, based on the ESR spectra of radicals in the nanochannels and numerical simulations (see Sects. 12.2.3 and 12.4). CLPOT ICs incorporating 1D 4-X-TEMPO molecular chains have demonstrated temperature-independent 3D exchange interactions and exchange narrowing in the temperature range from 4.2 to 300 K (see Sect. 12.6) [53]. These results indicate, as predicted, the proper choice of host materials, and guest radicals can control the inter-spin interaction in 1D OIC-OR.

In the synthesis of 1D OIC-OR, CLPOT crystals are preferable to TPP as a host material, as these crystals allow the inclusion of many different types of organic radicals. This is due to the pore diameters in the former, which are comparable to the molecular cross section of many stable nitroxide or NN (nitronylnitroxide) radicals (*ca*. 1.1–1.3 nm in CLPOT but 0.45–0.9 nm in TPP) as well as the suitable polarity of the former (as radicals frequently have polar substituent groups). However, it is possible to include several types of guest radicals in TPP nanochannels by following the appropriate stepwise process [41, 44]. Prior work concerning the determination of the molecular orientations and dynamics of NN or IN (iminonitroxide) radicals in TPP or CLPOT nanochannels using ESR has demonstrated the feasibility of

developing a new ESR spin probe technique based on NN groups [27, 44]. For the reasons described above, 1D OIC-OR represent an important new type of magnetic material.

Both organic porous materials and metal organic frameworks [11, 13] can be used as molecular templates for the array of guest radicals. In addition, 0D, 2D, or 3D porous materials may be employed to produce magnetic inclusion compounds instead of those having 1D nanochannels. As an example, 2,4,6-tris(4-bromophenoxy)-1,3,5-triazine (BRPOT: Scheme 12.1c) [50], one possible derivative of 2,4,6-tris(4-halophenoxy)-1,3,5-triazine (XPOT: Scheme 12.1b–d), can contain several different guest molecules, including Buckminsterfullerenes [54–56]. However, the cavities of XPOT derivatives other than CLPOT do not necessarily have 1D structures. These difference in morphology originate from the inter-atom interactions between halogen atoms in the XPOT crystals [50].

In this review, the molecular orientations and dynamics of various guest radicals, as an example, 4-X-TEMPO, 4-XPNN, or PhIN, in CLPOT or TPP 1D nanochannels are described based on the ESR analyses. In addition, the inter-spin interactions of 4-X-TEMPO radical chains formed in the CLPOT or TPP nanochannels are explained in relation to the molecular dynamics of 4-X-TEMPO in the nanochannels. In Sect. 12.2, theoretical background of ESR and the calculation method in ESR simulation using EasySpin program [46, 47] are introduced. Sample preparation and characterization of 1D OIC-OR are noted in Sect. 12.3. The molecular dynamics of guest radicals in CLPOT- or TPP-based 1D OIC-ORs are explained in Sects. 12.4 and 12.5, respectively. Remarkable exchange interaction in CLPOT- or TPP-based 1D OIC-ORs with 4-X-TEMPO chains are explained in Sect. 12.6. Finally, in Sect. 12.7, the conclusion and outlooks in the future of this study are described.

12.2 Theoretical Background and ESR Simulation

12.2.1 Electron Spin Resonance

In ICs, magnetic resonance spectroscopy is a powerful means of elucidating the molecular structures of host materials and the molecular orientations and the dynamics of guest radicals in host nanochannels, in addition to assessing inter-spin interactions and magnetism of guest radical chains. When the researchers tune into the unpaired electrons in guest radicals or the electric properties of 1D OIC-ORs (as examples, conductivity, dielectric or magnetism), they may use electron spin resonance (ESR) spectroscopy, whereas nuclear magnetic resonance (NMR) spectroscopy is available for the study when they are interested in the molecular structures or the dynamics of non-radical compounds. The reader is referred to several texts that provide detailed discussions of magnetic resonance spectroscopy [57–60].

When a sample with unpaired electrons is inserted into an external magnetic field $\boldsymbol{B_0}$, the magnetic moments of electrons in the material are split into different energy levels, depending on whether these moments are parallel or antiparallel to $\boldsymbol{B_0}$. The electron magnetic moment operators are proportional to the electron spin angular momentum values, and the proportionality constant γ (also referred to as the gyromagnetic ratio) will be negative for electrons. Therefore, the electron magnetic moment will be antiparallel to the angular momentum. In the external magnetic field, the electron spin magnetic moments precess around $\boldsymbol{B_0}$ at the Larmor frequency $\boldsymbol{\omega_0}$, which equals $-\gamma\boldsymbol{B_0}$. The Larmor frequencies of the various electron magnetic moments in a specimen will differ according to the shielding effect of neighboring electrons and/or nuclei. If an electromagnetic wave whose frequency corresponds to the energy difference of the magnetic moments in the field, ($\Delta E = h\nu = \hbar\omega = \gamma\hbar B$) is applied to the sample, the electron spins in the ground states will be excited. This phenomenon is the basis of ESR, which focusses on electron spins. ESR studies employ a magnetic field (generated using an electric magnet) that sweeps over the range of 0–1 T in conjunction with continuous-wave (cw) microwave irradiation (1–100 GHz) of a sample in a cavity resonator. Pulse ESR methods are also used for the clarification of complicated spin-lattice or inter-spin interactions. Variable-temperature ESR over the temperature range from 4.2 to 400 K can be applied to determine the spin concentration of each IC, as well as the molecular orientations and dynamics of organic radicals in 1D nanochannels and the inter-spin interactions and magnetism of 1D organic radical chains constructed in the 1D nanochannels. In this review, the theoretical background of the analysis of free radicals in 1D nanochannels by ESR spectroscopy is described in detail.

12.2.2 Nuclear Magnetic Resonance

When a sample without unpaired electrons is used, electron spins in the description in the prior subsection can be replaced into nuclear magnetic moments (more properly, only in the case of $I = 1/2$ (I: the nuclear spin quantum number of the nuclei). If $I > 1/2$, see Sect. 12.2.3.1 and references [57–59]). However, the proportionality constant γ will be positive for most nuclei. Therefore, the nuclear magnetic moment will typically be parallel to the angular momentum. In modern-day NMR analyses, radio-frequency pulses (ω; in the range of 10^2–10^3 MHz) are applied to a sample surrounded by a coil and subjected to an external magnetic field of approximately 1–15 T in conjunction with a superconducting magnet. In the case of metals or metal nanoparticles, analyses are conducted in a static external magnetic field using a cw radio-frequency source with either a permanent or electric magnet [60, 61]. Room temperature solution ^{1}H NMR spectroscopy is primarily performed for the structural elucidation of host materials such as TPP and CLPOT.

12.2.3 ESR Simulation

12.2.3.1 g Tensor and A Tensor

The ESR spectra for the free radicals in 1D nanochannels is reproducible using EasySpin program for the ESR spectral reproduction under various conditions of electron and nuclear spins [62]. The total spin Hamiltonian used in EasySpin is as follows:

$$\hat{H} = \sum_i \left(\hat{H}_{\mathrm{EZI}}(i) + \hat{H}_{\mathrm{ZFI}}(i) \right) + \sum_i \left(\hat{H}_{\mathrm{NZI}}(k) + \hat{H}_{\mathrm{NQI}}(k) \right) + \sum_i \sum_{j>i} \hat{H}_{\mathrm{EEI}}(i, j) + \sum_i \sum_k \hat{H}_{\mathrm{HFI}}(i, k) \tag{12.1}$$

with the following terms: $\hat{H}_{\mathrm{EZI}}(i)$, electron-Zeeman interaction (EZI) between electron spin i with an external magnetic field; $\hat{H}_{\mathrm{ZFI}}(i)$, zero-field interaction (ZFI) of electron spin i with adjacent electron spins in the case of $S > 1/2$ (S, the total spin quantum number of electrons in the system); $\hat{H}_{\mathrm{NZI}}(i)$, nuclear-Zeeman interaction (NZI) between nuclear spin k with an external field; $\hat{H}_{\mathrm{NQI}}(i)$, nuclear quadrupole interaction (NQI) between nuclear spin k with $I > 1/2$ (I, the nuclear spin quantum number of the nuclei) having an electric quadrupole moment that can interact with the local electric field gradient at the nucleus; $\hat{H}_{\mathrm{EEI}}(i, i)$, electron-electron interaction (EEI) between electron spin i and j as an example, exchange interaction; and $\hat{H}_{\mathrm{HFI}}(i, k)$, hyperfine interaction (HFI) between electron spin i and nuclear spin k at the nucleus. In this review, $\hat{H}_{\mathrm{NZI}}(i)$ and $\hat{H}_{\mathrm{NQI}}(i)$ are ignored due to the small influence in the electron spin system and also $\hat{H}_{\mathrm{ZFI}}(i)$ and $\hat{H}_{\mathrm{EEI}}(i, i)$ due to the quite isolated spin system without zero-field splitting or exchange interaction.

Therefore, the spin Hamiltonian for the free radicals isolated in 1D nanochannels, as examples, 4-X-TEMPO (**2a–e**), 4-XPNN (**2f** and **g**), and PhIN (**2h**), is simplified as follows:

$$\hat{H} = \beta_e \boldsymbol{B} \cdot \boldsymbol{g} \cdot \hat{S} + \hat{S} \cdot \sum_{p=1,2} A_p \cdot \hat{I}_p + \beta_n g_n \boldsymbol{B} \cdot \sum_{p=1,2} A_p \cdot \hat{I}_p \tag{12.2}$$

where β_e, $\boldsymbol{B}$, $\boldsymbol{g}$, $\boldsymbol{A}_p$, β_n, g_n, $\hat{S}$, and $\hat{I}_p$ are the Bohr magneton, the laboratory magnetic flux density vector (corresponding to the external magnetic field), the electron spin g tensor, the hyperfine tensor for the pth ^{14}N nucleus, the nuclear magneton, the nuclear spin g-factor, the electron spin operator, and the nuclear spin operator for the pth ^{14}N nucleus in the radicals, respectively [27, 41–44, 51, 52, 63, 64]. $\boldsymbol{g}$ and $\boldsymbol{A}_p$ are described as diagonal matrices

$$\boldsymbol{g} = \begin{pmatrix} g_{xx} & 0 & 0 \\ 0 & g_{yy} & 0 \\ 0 & 0 & g_{zz} \end{pmatrix} \tag{12.3}$$

$$\boldsymbol{A_p} = \begin{pmatrix} A_{pxx} & 0 & 0 \\ 0 & A_{pyy} & 0 \\ 0 & 0 & A_{pzz} \end{pmatrix} \tag{12.4}$$

via a rotation matrix parameterized by three Euler angle where g_{qq} and A_{qq} ($q = x$, y, z) are the three principal values of the $\boldsymbol{g}$ and $\boldsymbol{A}_p$ matrices [62]. If $p = 1$, the summation sign in Eq. (12.2) may be often omitted for simplification. The isotropic components of $\boldsymbol{g}$ and $\boldsymbol{A}_p$ are defined by $g_{\mathrm{iso}} = (g_{xx} + g_{yy} + g_{zz})/3$, and $(A_p)_{\mathrm{iso}} = (A_{pxx} + A_{pyy} + A_{pzz})/3$.

In the case of 4-X-TEMPO, the single nitrogen atom of the nitroxide (NO) group is considered (i.e., $p = 1$), whereas the nitrogen atoms of the nitronyl and/or imino nitroxide groups (i.e., $p = 1$ or 2) in 4-XPNN and PhIN radicals are considered.

The principal axes of the 4-X-TEMPO radicals are defined such that the z-axis is perpendicular to the NO group, and along the $2p_z$ orbital of the NO group, the x-axis is parallel to the NO bond and the y-axis is perpendicular to the zx plane [65]. The principal axes of the $\boldsymbol{g}$ and $\boldsymbol{A}$ tensors are coincident. The $\boldsymbol{A}$ tensor of the NO radicals is quite anisotropic, such that $A_{zz} > A_{xx}$, A_{yy} [51, 52, 63–65]. To ensure accurate reproduction of the ESR spectra, the A_{xx} and A_{yy} values for 4-X-TEMPO are assumed to be similar, while cylindrical symmetry of the $\boldsymbol{A}$ tensor is not necessarily assumed.

The principal axes of the 4-XPNN radicals are defined such that the z-axis is perpendicular to the molecular plane of the NN group of 4-XPNN, the y-axis is parallel to the bond between the NN group and phenyl ring, and the x-axis is perpendicular to the yz plane [27, 44, 66]. Therefore, the g tensor for the 4-XPNN radical is determined as follows [66]. The unpaired electron of the NN group is associated with a π orbital. As such, the lowest component of the g tensor should be observed perpendicular to the molecular plane of the NN group (i.e., the principal z-axis direction) and should have a value of approximately 2.0023. In molecular orbital calculations, $g_{xx} > g_{yy} > g_{zz}$ for the 4-XPNN radical (i.e., the intensity of the g_{xx} component is observed at the leftmost (lowest magnetic field) side). With respect to the $\boldsymbol{A}$ tensor for the 4-XPNN radical, the unpaired electron occupies the π orbital composed of the $2p_z$ orbitals of the nitrogen atoms (having considerable spin density), such that A_{zz} is major component, with A_{xx} and A_{yy} being minor components. Therefore, the $\boldsymbol{A}$ tensor for NN radicals is also quite anisotropic. Although the local axes of the $\boldsymbol{A}$ tensors of the two nitrogen nuclei of the 4-XPNN radical are expected to be different, it is assumed that the unpaired electron interacts with the two nitrogen nuclei with an averaged $\boldsymbol{A}$ tensor, so as to simplify the analysis. In this approximation, the principal axes of the $\boldsymbol{g}$ and $\boldsymbol{A}$ tensors for the 4-XPNN radical will be coincident.

The principal axes of the g tensor of the PhIN radical are assumed to be similar to those of the 4-XPNN radical and also consistent with NN due to the higher spin density on the NO group [44]. However, it should be noted that $\boldsymbol{A}_1 \neq \boldsymbol{A}_2$ for IN radicals ($(A_1)_{iso} > (A_2)_{iso}$), [44, 67] where $\boldsymbol{A}_1$ is the hyperfine tensor of the NO nitrogen of the IN groups and $\boldsymbol{A}_2$ is that of the 3-position nitrogen. Since the xx and yy components of $\boldsymbol{A}_1$ and $\boldsymbol{A}_2$ are much smaller than the zz component, the principal axes of the $\boldsymbol{g}, \boldsymbol{A}_1$, and $\boldsymbol{A}_2$ tensors for the IN radicals are also assumed to be coincident to allow for simplified calculations, similar to the procedure for 4-XPNN radicals.

12.2.3.2 Calculation Procedure

To the determine the molecular orientations and dynamics of guest radicals in 1D nanochannels, the ESR spectra of isolated radicals must be reproduced in detail, because these spectra provide information concerning the principal values of the $\boldsymbol{g}$ and $\boldsymbol{A}$ tensors. Such spectra can be generated based on theoretical calculations. EasySpin program is a component of the MATLAB software package (MathWorks, Natick, MA, USA), developed by Stoll and intended for the simulation and fitting of a wide range of ESR spectra (EasySpin 5.2.20, ETH Zürich) [46, 47]. EasySpin program provides extensive ESR-related functionality, ranging from spin physics to data analysis. This software also contains routines for the simulation of liquid- and solid-state ESR and electron-nuclear double resonance data. The programming language of MATLAB is based on matrices and very efficient matrix algorithms, and EasySpin program consists of over 80 MATLAB functions that perform a variety of ESR-related tasks. Functions from the larger and more basic category provide the core functionality necessary for computational ESR. Building on this foundation, a small number of general, robust high-level functions for spectral simulation are provided.

This sub-subsection references a number of programs. These include the Pepper, which is used to produce the field-swept and frequency-swept solid-state cw ESR spectra of powders and crystals; Chili, which simulates field- and frequency-swept cw ESR spectra in the slow-motion regime on the ESR time scale; and Garlic, which produces the isotropic or anisotropic fast-motion cw ESR spectra of radicals in solution or nanospaces. Calculations for 4-XPNN and PhIN radicals with two ^{14}N atoms ($I = 1$) based on the interactions of electron spins can be performed using a PC with more than 8 GB of RAM. Chili requires more memory to generate spectral reproductions for 4-XPNN or PhIN radicals, and so the allocation function of Opt within the program parameters, as an example, should be set to Opt.Allocation = [4e7 2e5] [47].

12.2.3.3 Rigid-Limit ESR Spectra

Figure 12.2 presents typical rigid-limit ESR spectra for nitroxide, NN, and IN radicals as simulated using the EasySpin Pepper program to calculate solid-state

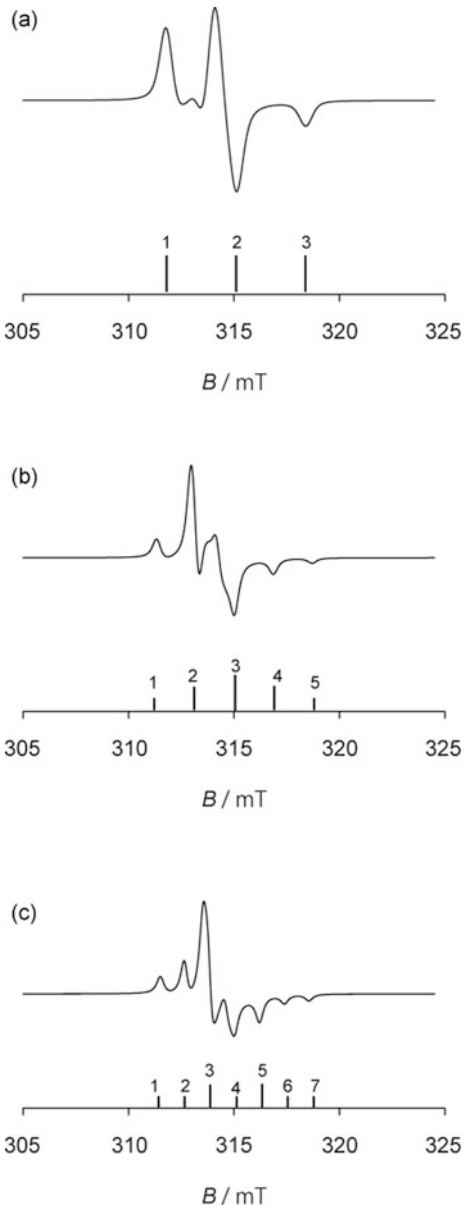

Fig. 12.2 Typical rigid-limit ESR spectra for powder (**a**) nitroxide [52] (**b**) NN [27] and (**c**) IN radicals [44] using the EasySpin Pepper program [46, 47]. Bars on the horizontal axis in each figure indicate the major hyperfine coupling interactions by equivalent or inequivalent nitrogen atoms

cw spectra. In Fig. 12.2a–c, the three, five, or seven major hyperfine interaction lines associated with the equivalent/inequivalent nitrogen atoms having unpaired electrons in the substituent groups are shown on the horizontal axis for convenience. These spectra were reproduced using the principal values of the $\boldsymbol{g}$ and $\boldsymbol{A}$ tensors of unpaired electrons, along with line width parameters and signal amplitudes. The $\boldsymbol{g}$

Table 12.2 Tensor components of the $\boldsymbol{g}$, $\boldsymbol{A}_p$, and line width parameters (G, Gaussian component; L, Lorentzian component) for the reproduced ESR spectra of nitroxide, NN, and IN radicals presented in Fig. 12.2

State of radicals	g_{xx}	g_{yy}	g_{zz}	$A_{1xx}(/A_{2xx})$/mT	$A_{1yy}(/A_{2yy})$ /mT	$A_{1zz}(/A_{2zz})$ /mT	Line width	
							G/mT	L/mT
Fig. 12.2a (nitroxide radicals)[a]	2.0095	2.0066	2.0023	0.06	0.06	3.30	0.50	0.40
Fig. 12.2b (NN radicals)[b]	2.0120	2.0075	2.0028	0.02	0.03	1.84	0.20	0.40
Fig. 12.2c (IN radical)[c]	2.0103	2.0050	2.0028	0.01 0.02	0.01 0.02	2.36 1.16	0.10	0.40

[a]Ref. [52]. [b]Ref. [27]. [c]Ref. [44]

and $\boldsymbol{A}$ tensors for each radical were estimated from experimental data by setting default values for g_{zz} and A_{zz} based on the hyperfine coupling lines associated with isolated radicals acquired at both ends of low-temperature ESR spectra, assuming that the molecular motion of the radicals was frozen. The values of g_{xx} and g_{yy} and of A_{xx} and A_{yy} are difficult to determine directly from ESR spectra, and so these were initially estimated by visual inspection of the simulations of ESR spectra generated using EasySpin program. The final values for each component of the $\boldsymbol{g}$ and $\boldsymbol{A}$ tensors of each radical were estimated via the step-by-step variation of these components or g_{qq} and A_{qq} ($q = x$, y or z) along with the line width parameters and signal amplitudes, so as to minimize the sum of the squares of the difference between the experimental and simulated spectra. The number of the $\boldsymbol{A}$ tensor in Eq. (12.2) will vary according to the number of equivalent/inequivalent nitrogen atoms in substituent groups on which unpaired electron is localized. The principal axis components of the $\boldsymbol{g}$ and $\boldsymbol{A}$ tensors for the reproduced ESR spectra shown in Fig. 12.2 are summarized in Table 12.2.

The EasySpin program expresses the line shape using a Voigt function based on the Gaussian broadening (convolution) of a Lorentzian line [46, 47, 68]. In the present analysis, the full width at half maximum (FWHM) is employed as the line width parameter, and the Gaussian and Lorentzian line width components for the reproduced ESR spectra shown in Fig. 12.2 are also provided in Table 12.2.

The three major hyperfine interaction lines associated with the nitrogen atoms in the NO groups of nitroxide radicals are shown on the horizontal axis in Fig. 12.2a for convenience. These supplementary lines have equivalent peak heights when the ESR spectrum is acquired in dilute solution. In the case of the reproduction of an NN radical spectrum in Fig. 12.2b, the five major hyperfine interaction lines associated with equivalent nitrogen atoms having the same hyperfine coupling constants are included on the horizontal axis. The peak heights of these supplementary lines are proportional to their peak intensities in dilute solution, (i.e., 1:2:3:2:1). Although lines 1, 2, 4, and 5 are well-resolved, the shape of line 3 is more complicated

Table 12.3 Tensor components of the $\boldsymbol{g}$ and $\boldsymbol{A}$ tensors for various organic radicals in the various states. Spacer molecules are abbreviated in each state

State of radicals	g_{xx}	g_{yy}	g_{zz}	$A_{1xx}(/A_{2xx})$/mT	$A_{1yy}(/A_{2yy})$/mT	$A_{1zz}(/A_{2zz})$/mT
TEMPO in TPP[a]	2.0100	2.0070	2.0024	0.60	0.55	3.35
DTBN in TMCB[b]	2.0088	2.0062	2.0027	0.76	0.60	3.18
DTBN in TPP[c]	2.0090	2.0062	2.0022	0.50	0.50	3.48
TEMPOL in TPP[d]	2.0092	2.0061	2.0026	0.83	0.30	3.33
TEMPO in CLPOT[e]	2.0102	2.0062	2.0023	0.73	0.60	3.35
MeO-TEMPO in CLPOT[f]	2.0098	2.0062	2.0024	0.56	0.43	3.43
PhNN in rigid Duco Cement[g]	2.0127	2.0068	2.0028	0.52	0.52	1.80
PhNN in CLPOT[h]	2.0118	2.0075	2.0031	0.34	0.12	1.74
PhNN in TPP[i]	2.0107	2.0086	2.0031	0.01	0.01	2.13
p-NPNN in CLPOT[h]	2.0116	2.0076	2.0030	0.32	0.16	1.77
PhIN glassy toluene[j]	2.00932	2.00604	2.00222	–	–	2.32/1.28
PhIN in TPP[i]	2.0103	2.0050	2.0028	0.02/0.01	0.01/0.02	2.36/1.16

TMBC tetramethyl-1,3-cyclobutanedione
[a]Ref. [40]. [b]Ref. [64]. [c]Ref. [41]. [d]Ref. [43]. [e]Ref. [51]. [f]Ref. [52]. [g]Ref. [66]. [h]Ref. [27]. [i]Ref. [44]. [j]Ref. [67]

[66]. This occurs because the g_{xx} and g_{yy} components are larger than the g_{zz} component and because the $A_{xx}{}^{\mathrm{NN}}$ and $A_{yy}{}^{\mathrm{NN}}$ components are much smaller than the $A_{1zz}{}^{\mathrm{NN}}$ component. In the case of PhIN results in Fig. 12.2c, the seven major hyperfine interaction lines associated with inequivalent nitrogen atoms having different hyperfine coupling constants (typically, $A_{1zz}{}^{\mathrm{IN}} \sim 2A_{2zz}{}^{\mathrm{IN}}$) are included. The peak heights of these lines are proportional to the peak intensities obtained from analyses in dilute solution. Here, lines 1, 2, 5, 6, and 7 are well-resolved, and the spectrum between lines 3 and 4 is more complicated [44]. These results are due to the g_{xx} and g_{yy} components, which are large relative to the g_{zz} components, and to the $A_{1xx}{}^{\mathrm{IN}}$, $A_{1yy}{}^{\mathrm{IN}}$, $A_{2xx}{}^{\mathrm{IN}}$, and $A_{2yy}{}^{\mathrm{IN}}$ components, all of which are much smaller than the $A_{1zz}{}^{\mathrm{IN}}$ or $A_{2zz}{}^{\mathrm{IN}}$ components. The principal axis components of the $\boldsymbol{g}$ and $\boldsymbol{A}$ tensors of several organic radicals in various states are provided in Table 12.3.

12.2.3.4 Anisotropic Rotational Diffusion

When simulating ESR spectra at higher temperatures (at which the molecular motions of radicals in the 1D nanochannels are increased), it is assumed that the rotational axis of each organic radical can be defined by polar and azimuthal angles, θ and ϕ, respectively, in the principal axis system of the g tensor for each radical [27]. As noted, the Chili program within the EasySpin package allows ESR spectra in the slow-motion regime to be generated [46, 47]. These simulations are based on solving the stochastic Liouville equation on the basis of rotational eigenfunctions.

In the case of a molecule that undergoes numerous collisions that cause small random angular reorientations, the resultant anisotropic rotational motion is a Markov process [45]. If Ω is defined as the Euler angle for a tumbling molecular axis with respect to a fixed laboratory axis system, the probability of finding the molecule in direction Ω at time t is defined as $P(\Omega, t)$. In a Markov process, the probability of being in state Ω_1 at time t, if in state Ω_2 at time t-Δt, is both independent of the Ω value at any time earlier than t-Δt and dependent only on Δt rather than t. As such, $P(\Omega, t)$ can be described by the rotational diffusion equation:

$$\frac{\partial P(\Omega, t)}{\partial t} = R\nabla_{\Omega}{}^{2} P(\Omega, t) \tag{12.5}$$

where $\nabla_{\Omega}{}^{2}$is the Laplacian operator on the surface of a unit sphere and R is the rotational diffusion coefficient. If the molecule is approximated by a rigid sphere of radius a rotating in a medium of viscosity η, the rotational Stokes-Einstein relationship yields

$$R = \frac{kT}{8\pi a^3 \eta} \tag{12.6}$$

In an anisotropic liquid, the average rotational diffusion correlation time τ_{R} is given by:

$$\tau_R = \left(6\sqrt{R_{\parallel} R_{\perp}}\right)^{-1} \tag{12.7}$$

where $R_{||}$ and $R_{\perp}$ are defined as the parallel and perpendicular components of R. It is expected that Eqs. (12.5, 12.6, and 12.7) can be applied to anisotropic molecular rotational diffusion in organic 1D nanochannels [27, 44, 51, 52]. Thus, in ESR simulations, highly anisotropic $R_{||}$ and $R_{\perp}$ components, such as $R_{||}/R_{\perp} \approx 1000$, are assumed.

The θ and ϕ values for nitroxide, NN, and IN radicals can be estimated by varying τ_{R} along with the line width parameters and signal amplitudes so as to obtain the best fit to the ESR spectrum at the highest temperature. At elevated temperatures, the molecular motions of guest radicals in the 1D nanochannels will be in the slow-motion regime (10^{-6} s > τ_{R} > 10^{-9} s) on the ESR time scale. Using these θ

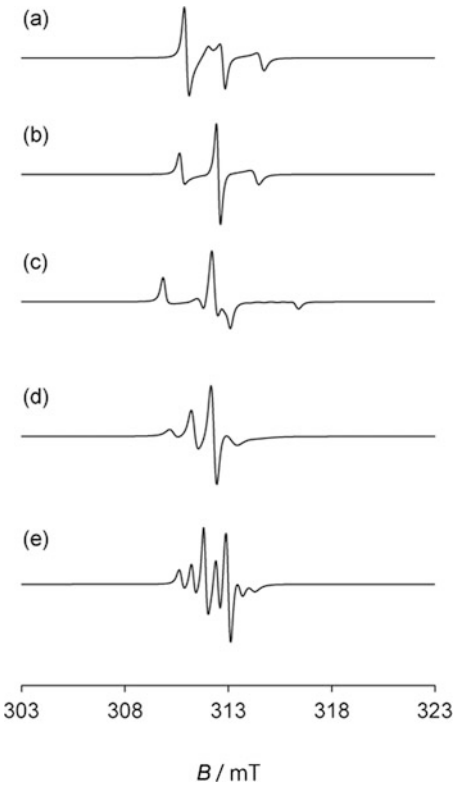

Fig. 12.3 Simulated ESR spectra of nitroxide, NN, and IN radicals, modulated on the basis of anisotropic rotational diffusion around the principal *x*, *y*, and *z* axes of the *g* tensor (**a**–**c**), the principal *y*-axis of the *g* tensor (**d**), and (again) the principal *y*-axis of the *g* tensor (**e**), respectively, using the Chili program within the slow-motion regime with respect to the ESR time scale [27, 41, 44, 52]

and ϕ values, τ_R is similarly estimated at additional temperatures by varying the same factors. Figure 12.3 shows the simulated ESR spectra of nitroxide, NN, and IN radicals, modulated on the basis of anisotropic rotational diffusion around the principal *x*, *y*, and *z* axes of the *g* tensor, the principal *y*-axis of the *g* tensor, and (again) the principal *y*-axis of the *g* tensor, respectively, using the Chili program within the slow-motion regime with respect to the ESR time scale. The associated τ_R values are based on the typical spectra in rotational diffusion of organic radicals in 1D nanochannels and are 6×10^{-9} s for spectra (a)–(c), 3×10^{-8} s for (d), and 9×10^{-9} s for (e) [27, 41, 44, 52]. See Sects. 12.4 and 12.5 about the examples of experimental and simulated ESR spectra of various organic radicals in CLPOT and TPP nanochannel.

12.2.4 Van Vleck's Formula for Rigid Spin Lattices

Sections 12.2.4 and 12.2.5 describe the theoretical background associated with determining the line widths and profiles of broader isotropic ESR spectra in 1D

organic radical chains constructed in 1D nanochannels. This discussion is helpful with regard to clarifying the inter-spin interactions within 1D 4-X-TEMPO chains in 1D nanochannels.

The line profiles of isotropic ESR spectra reflect the type and magnitude of inter-spin dipolar and/or exchange interactions in the specimen, as well as the inter-spin distances between electron spins and other factors. In the absence of exchange interactions (i.e., considering only dipolar interactions in the spin system), the average second moment, M_2, of the rigid spin lattice can be estimated using Van Vleck's formula [39, 44, 59]

$$M_2 = \Delta\omega^2 = \frac{3}{5}\gamma^4\hbar^4 S\,(S+1)\sum_k \frac{1}{r_k} \tag{12.8}$$

where γ, S, and r_k are the electron gyromagnetic ratio, the electron spin quantum number, and the distance between two spins. In this case, the ESR profile becomes a Gaussian function. Generally, the peak-to-peak line width ΔB_{pp} is equal to $2\sqrt{M_2}$ and the FWHM, $\Delta B_{1/2}$ is equal to $2.36\sqrt{M_2}$ [59]. Under the condition of the existence of only dipolar interaction in the spin system, the peak-to-peak line width is described by ${B_{pp}}^D$ in this chapter. It should be noted that the experimental value for ΔB_{pp} may be much narrower than the value estimated using Eq. (12.8), as a result of exchange or motional averaging. Therefore, it is necessary to estimate the inter-spin distance in the system as accurately as possible.

In our previous work regarding [$(TPP)_2$-$(TEMPO)_{1.0}$] (**1a/2a**) and [CLPOT-(4-X-TEMPO)] (**1b/2a–d**), the electron spins on the NO groups of 4-X-TEMPO molecules in TPP or CLPOT nanochannels were found to interact with those of other 4-X-TEMPO molecules in the same or adjacent channels [39]. These interactions are, respectively, defined as "intrachain" or "interchain" inter-spin interaction. In **1a/2a** and **1b/2a–d**, a single 4-X-TEMPO molecule (i.e., one unpaired electron) was determined to be accommodated in a TPP or CLPOT unit cell formed by two molecules. The electron spins of 4-X-TEMPO molecules in the nanochannels were assumed to be located at the center of gravity of the molecules, so as to simplify computation by averaging the uniaxial rotational diffusion of 4-X-TEMPO molecules around the rotational axis (commonly considered to be parallel to the nanochannel axis). In this case, the nearest neighbor intra-channel or interchain inter-spin distance, respectively, corresponds to the cell parameters, such as $c = 1.2$ nm or $a = 0.98$ nm in the case of the TPP frameworks of **1a/2a** [39] and $c = 0.688$ nm or $a = 1.51$ nm in the CLPOT frameworks of **1b/2a** [44]. Therefore, it is convenient to consider **1a/2a** as a spin system having a sixfold symmetric spin lattice with 1.2 nm intra-channel and 0.98 nm inter-channel inter-spin distances. The structures of **1b/2a–d** were interpreted in a similar manner.

However, subsequent studies showed that these assumptions are valid only near room temperature. In this temperature range, 4-X-TEMPO molecules in the TPP or CLPOT nanochannels undergo rotational diffusion in the fast-motion region on the ESR time scale ($\tau_R < 10^{-9}$ s, where τ_R is the correlation time for the rotational

diffusion of 4-X-TEMPO molecules; see Sect. 12.2.3.4). As an example, in **1a/2a** below 112 K, the rotational diffusion of TEMPO molecules in TPP nanochannels is thought to cease, such that the nitroxide groups of TEMPO molecules at different sites are likely disordered [39]. Nevertheless, the relative error associated with the estimations of M_2 using the simple model described in reference [39] and the more precise model taking into account the disorder of nitroxide groups noted above is at most 10%. Similar results are obtained for **1b/2a–d** [44]. Therefore, the simple model based on reference [39], in which the positions of the electron spins of 4-X-TEMPO molecules in the 1D nanochannels are assumed to coincide with the centers of gravity of 4-X-TEMPO molecules, is thought to be suitable as a means of reducing the computational demands when determining M_2.

12.2.5 Dietz's Method for Determination of ESR Line Profiles and Inter-spin Interactions

The ESR line profile [39, 44, 59, 69] is determined by the Fourier transform of the time-dependent relaxation function of transverse magnetization, $\varphi(t)$ expressed as:

$$\varphi(t) = \exp\left[-M_2 \int_0^t (t-\tau)\,\Psi(\tau)\,d\tau\right] \tag{12.9}$$

where $\Psi(\tau)$ is the normalized transverse magnetization correlation function of the local field at the spin. In the absence of an exchange interaction between two electron spins, $\varphi(t)$ can be described by a Gaussian function, resulting in a Gaussian resonance line. In the case of a spin system with 3D interactions due to exchange, or with motional averaging, $\Psi(\tau)$ rapidly decays to zero, leading to an exponential function for $\varphi(t)$ and a Lorentzian resonance line. If $\Psi(\tau)$ decays according to the diffusion equation at the long time region ($\tau_e << \tau$, where τ_e is approximately equal to $1/\omega_e$ where ω_e is the spin fluctuation frequency), $\varphi(t)$ for 1D spin diffusion process can be represented as $\exp[-(\Gamma t)^{3/2}]$ where Γ is a constant. This suggests the presence of exchange interactions between neighboring spins in the 1D system. Since the effect of exchange narrowing becomes weaker than that of 3D exchange interactions between spins in this scenario, the ESR line profile will be intermediate between Lorentzian and Gaussian.

The dimensionality of 1D OIC-OR exchange interactions can be assessed by examining the temperature dependency of the ESR line profile using a Dietz's plot [69], which depicts the inverse of the ESR line profile. In such plots, $I(B_0)/I(B)$ is plotted against $[(B-B_0)/(\Delta B_{1/2}/2)]^2$ (see Figs. 12.14 and 12.15 in Sect. 12.6) where $I(B)$ is the intensity of the ESR resonance line in an external magnetic field B, B_0 is the magnetic field on resonance, and $\Delta B_{1/2}$ is the FWHM of the resonance line (meaning that the term $\Delta B_{1/2}/2$ included in the horizontal axis parameter is the half width at half maximum of the resonance line). Figures 12.14 and 12.15 in Sect. 12.6 present one such plot. The magenta one demonstrates a Gaussian function having

the power index of $\varphi(t)$ is population to $-t^2$. The green line in this same figure depicts a Lorentzian function in which $\varphi(t)$ showing an exponential manner, while the cyan curve is for the case intermediate between Gaussian and Lorentzian observed in 1D spin diffusion systems.

12.3 Experimental Procedure

12.3.1 Sample Preparation and Notation

For the investigation of the molecular orientations and dynamics of organic radicals in 1D nanochannels, the appropriate spacer molecules for the dilution of radicals included in TPP or CLPOT nanochannels were selected. The resulting material comprised needle-like crystallites and was colorless. For the construction of 1D organic radical chains in 1D nanochannels, a solution of the radical species was prepared having an excess concentration and without the spacer species. The resulting material comprised needle-like crystallites and was pale orange or pale pink. The reader is referred to several papers that provide detailed preparation process of 1D OIC-OR [27, 39, 41, 44, 52]. Most of 1D OIC-ORs prepared in this way were stable for at least a year in air.

In this chapter, the notation $[(A)_2-(B)_x/(C)_y]$ is used for 1D OIC-OR. For example, when TPP, 4-X-TEMPO, and 4-R-TEMP are used to as host, guest, and spacer, respectively, the notation becomes $[(TPP)_2\text{-}(4\text{-X-TEMPO})_x/(4\text{-R-TEMP})_y]$. x and y denote the numbers of incorporated units per two host molecules. Throughout the text, the sample names may also be abbreviated simply as "**1a/B/C**" or "**1b/C**." Note that the host to guest ratio notation for each sample has been abbreviated for the sake of simplifying the figure or in the case of focusing only the component materials of 1D OIC-OR (e.g., the notation of [(TPP)-(4-X-TEMPO)/(4-R-TEMP)] is used for $[(TPP)_2\text{-}(4\text{-X-TEMPO})_x/(4\text{-R-TEMP})_y]$).

12.3.2 Sample Characterization

The structures of TPP and CLPOT nanochannels are known to be maintained even after the inclusion of guest radicals. In addition, the space group and cell parameters of CLPOT crystals are similar following inclusion. However, following inclusion, the cell parameters and pore diameters of TPP crystal can be expanded according to the molecular cross section of the guest radical. Figure 12.4 presents the room temperature powder X-ray diffraction (XRD) patterns obtained for guest-free TPP, $[(TPP)_2\text{-}(PhIN)_{0.002}/(N\text{-PhMI})_{1.0}]$ (**1a/2h/3e**) [44], $[(TPP)_2\text{-}(PhNN)_x/(PhIN)_y/(N\text{-PhMI})_{1.0}]$ ($x \approx 5 \times 10^{-4}$ and $y \approx 2 \times 10^{-4}$; (**1a/2f/2h/3e**) [44], $[(TPP)_2\text{-}(DTBN)_x/(pivalone)_{1.1}]$ ($x \approx 4 \times 10^{-4}$; **1a/2e/3d**) [41], $[(TPP)_2\text{-}(TEMPONE)_{0.021}/(TEMP)_{1.1}]$ (**1a/2b/3a**) [41], and $[(TPP)_2\text{-}(TEMPOL)_{0.004}/(TEMP)_{1.2}]$ (**1a/2c/3a**) [43]. In Figs. 12.4a–f, the reflection patterns

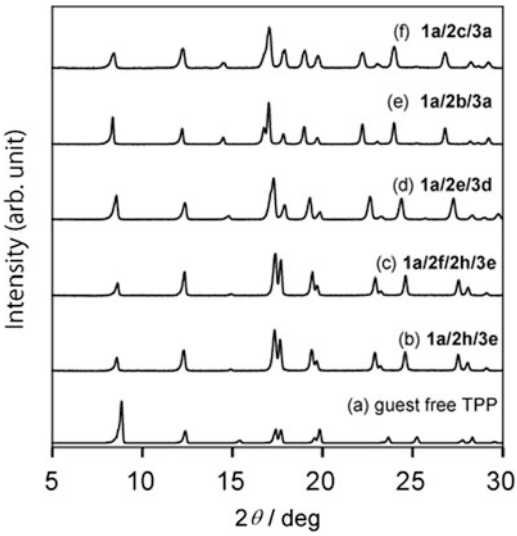

Fig. 12.4 Powder XRD patterns of (**a**) guest-free TPP, (**b**) $[(TPP)_2\text{-}(PhIN)_{0.002}/(N\text{-}PhMI)_{1.0}]$ (**1a/2h/3e**) [44], (**c**) $[(TPP)_2\text{-}(PhNN)_x/(PhIN)_y/(N\text{-}PhMI)_{1.0}]$ ($x \approx 5 \times 10^{-4}$ and $y \approx 2 \times 10^{-4}$; **1a/2f/2h/3e**) [44], (**d**) $[(TPP)_2\text{-}(DTBN)_x/(pivalone)_{1.1}]$ ($x \approx 4 \times 10^{-4}$; **1a/2e/3d**) [41], (**e**) $[(TPP)_2\text{-}(TEMPONE)_{0.021}/(TEMP)_{1.1}]$ (**1a/2b/3a**) [41], and (**f**) $[(TPP)_2\text{-}(TEMPOL)_{0.004}/(TEMP)_{1.2}]$ (**1a/2c/3a**) [43] at room temperature

at small degree values are shifted to the lower degree side as the molecular cross section of the guest radical is increased, demonstrating the expansion of the pore diameters of the TPP nanochannels. The reader is directed to various literature publications that discuss estimation of the cell parameters in various ICs [41–44]. In contrast, the reflection patterns in CLPOT ICs incorporating organic radicals are independent of the presence of guest radicals [51, 52], possibly because of the larger pore diameter of these nanochannels. The inclusion amounts and the composition ratios of guest radicals and spacers in the nanochannels in TPP or CLPOT ICs can be determined according to the ESR spin concentrations, the elemental analysis (EA) results, and the desorption amounts indicated by thermogravimetric analysis – differential thermal analysis (TG-DTA) [27]. The spin concentration in each IC can be obtained from ESR spectra. The composition ratio of guest molecules to host materials or of guest radicals to spacers can be determined from EA data. Finally, in each IC, the possibility of the inclusion of guest molecules in the nanochannels or the adsorption of such species on the host crystal surfaces is given by TG-DTA results. There are several literature reports that provide detailed descriptions of the composition ratios in ICs [39–44, 51–53].

12.4 ESR Analysis of Molecular Orientations and Dynamics of Organic Radicals in CLPOT Nanochannels

As reported in our previous publication [27, 51–53] various organic radicals can be included in CLPOT nanochannels. If these guest organic radicals are adequately dispersed by spacer molecules with sizes similar to those of the guest, or by

vacancies between guest radicals, the molecular orientations and dynamics of the guest radicals can be examined using ESR spectroscopy and spectral simulations. The reader is referred to several papers that provide detailed experimental conditions for ESR analyses [27, 39, 41, 44, 52].

CLPOT nanochannel can include many organic radicals due to its large pore diameters (1.1–1.2 nm in the guest-free state) and minimal polarity. In this section, the ESR spectra of 4-X-TEMPO and 4-XPNN are presented, and the process of spectral reproduction is explained. The results are used to elucidate the molecular orientations and dynamics of guest radicals in the CLPOT nanochannels.

Figure 12.5 shows temperature-dependent ESR spectra acquired from $[(CLPOT)_2$-$(MeO\text{-}TEMPO)_{0.002}/(TEMP\text{-}OH)_{0.50}]$ (**1b/2d/3b**) between 102 and 290 K [52]. All these spectra have been normalized to have the same maximum peak-to-peak height. Green, yellow, and red lines indicate the rotational diffusion, rigid-limit components of the MeO-TEMPO radicals in the CLPOT nanochannels

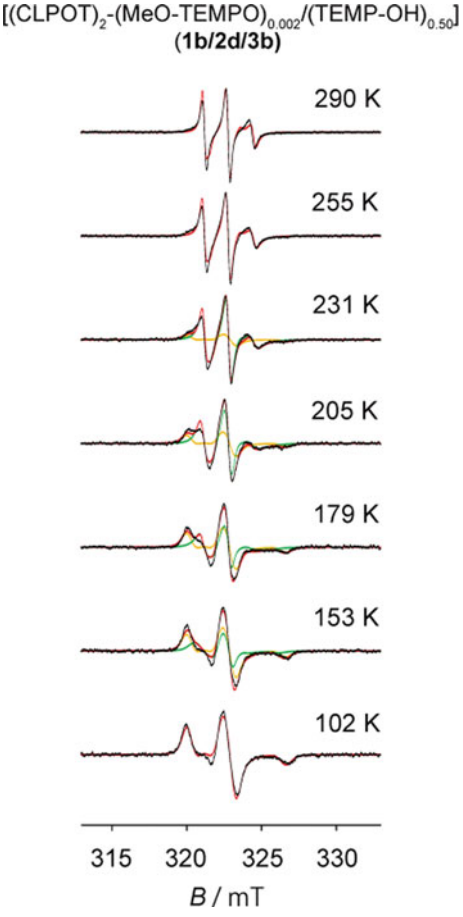

Fig. 12.5 Temperature dependence of the ESR spectra acquired from $[(CLPOT)_2$-$(MeO\text{-}TEMPO)_{0.002}/(TEMP\text{-}OH)_{0.50}]$ (**1b/2d/3b**) [52]. All these spectra have been normalized to have the same maximum peak-to-peak height. A rigid powder pattern of the isolated MeO-TEMPO radical below 102 K, a superposition (red) of a rigid-limit powder pattern (yellow), a slow anisotropic rotational diffusion component (green; 10^{-9} s $< \tau_R < 10^{-6}$ s) in the range of 153–231 K, and a slow anisotropic rotational diffusion component in the range of 255–290 K. (Reprinted with permission from *Magn. Reson Chem.***2016**, *54*, 641. Copyright 2018 Wiley.)

as generated using the EasySpin program (see Sect. 12.2.3.2) [46, 47], and their superpositions, respectively. The spin concentration for each sample remained unchanged after the temperature-dependent ESR analyses. The ESR spectra below 102 K for **1b/2d/3b** were reproduced on the basis of a rigid-limit powder pattern showing an isolated nitroxide radical (see Sect. 12.2.3.3). The ESR spectra in this figure do not include fine structure peaks originating from the formation of radical clusters [37] in the CLPOT nanochannels. Therefore, at these low temperatures, the MeO-TEMPO radicals in **1b/2d/3b** were evidently adequately isolated and did not exhibit molecular motion on the ESR time scale (i.e., $\tau_R > 10^{-6}$ s). The experimental **1b/2d/3b** ESR spectra in Fig. 12.5 were generated using the $\boldsymbol{g}$ and $\boldsymbol{A}$ tensor components in Table 12.3. The Gaussian and Lorentzian line widths of these components were 0.56 and 0.24 mT, respectively. The values for the $\boldsymbol{g}$ and $\boldsymbol{A}$ tensors for **1b/2d/3b** were estimated using the Pepper program within EasySpin program (see Sect. 12.2.3.2 and Table 12.3) and were consistent with values reported previously for different 4-X-TEMPO compounds under other conditions (see Table 12.3).

The ESR spectra for **1b/2d/3b** shown in Fig. 12.5 evidently change with increasing temperature, in accordance with a model for the anisotropic rotational diffusion of nitroxide radicals within the slow-motion region relative to the ESR time scale ($10^{-9} < \tau_R < 10^{-6}$) (see Sect. 12.2.3.4). Over the range of 255–290 K, these spectra can be simulated using the Chili program within EasySpin. The ESR spectra at 290 K were reproduced by assuming rotational diffusion around an axis tilted by $(\theta, \varphi) = (65°, 42°)$ relative to the principal g tensor system, with Gaussian and Lorentzian line width components of 0.011 and 0.19 mT, respectively, and τ_R equal to 6.5×10^{-9} s. The spectra for temperatures above 255 K were also accurately simulated based on the anisotropic rotational diffusion model around the same rotation axis applied in the case of the 290 K data. The results obtained for CLPOT nanochannel incorporated 4-X-TEMPO with a spacer other than TEMP gave similar (θ, φ) values [51, 52]. These results demonstrate that the molecular orientations of guest 4-X-TEMPO molecules in CLPOT nanochannels are independent of the specific 4-position substituent group or spacer molecules.

In contrast, the **1b/2d/3b** spectra obtained in the intermediate-temperature range (153–231 K) were reproduced using a superposition of rigid and anisotropic rotational diffusion (i.e., mobile) components (yellow and green, respectively, in Fig. 12.5). The mobile components in this temperature range were based on the rotational diffusion model previously discussed, around the same rotational axis as had been applied when working with the 290 K data, but with longer τ_R values (Fig. 12.5). With increasing temperature, the peak intensities of the rigid components were reduced, whereas those of the mobile components were increased due to the wide distribution of τ_R resulting from the local inhomogeneity of the host structure and/or guest packing in these ICs.

The procedure applied for **1b/2d/3b** are also available for 4-XPNN radicals, of which molecular orientations and dynamics in nanospaces were not adequately known before [66]. Figure 12.6 presents the temperature-dependent ESR spectra for $[(CLPOT)_2\text{-}(p\text{-NPNN})_{0.04}/(N\text{-PhMI})_{0.5}]$ (**1b/2g/3e**) over the temperature range from 255 to 398 K [27]. The red lines in Fig. 12.6 indicate simulated **1b/2g/3e**

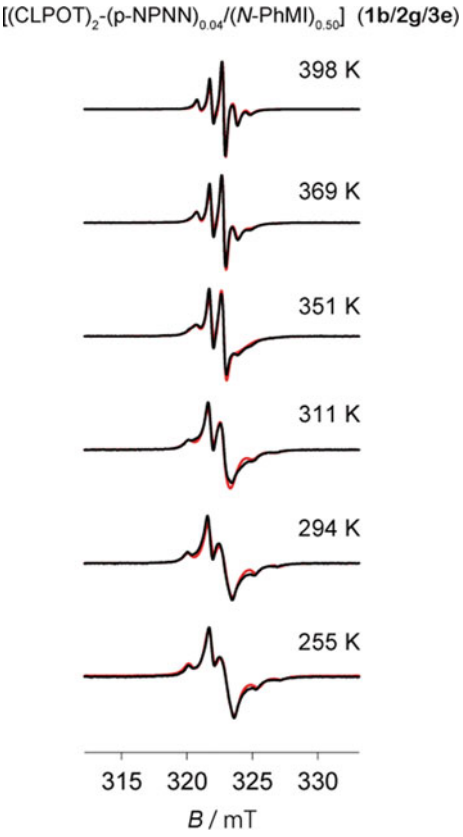

Fig. 12.6 Temperature dependence of the ESR spectra for [(CLPOT)$_2$-(*p*-NPNN)$_{0.04}$/(*N*-PhMI)$_{0.5}$] (**1b/2g/3e**)**.** Each red line indicates the spectrum simulated using the EasySpin program package [46, 47], The ESR spectra for **1b/2g/3e** below 255 K were well-reproduced on the basis of the rigid-limit powder pattern of *p*-NPNN radicals. The spectra for **1b/2g/3e** above 294 K were reproduced an anisotropic rotation diffusion model for *p*-NPNN in CLPOT nanochannels. (Reprinted with permission from *J. Phys Chem. A***2014**, *118*, 4907. Copyright 2018 American Chemical Society.)

spectra generated using EasySpin program. The **1b/2g/3e** spectra were unchanged below 255 K within experimental error and were well-reproduced based on the rigid-limit powder pattern of an isolated NN radical shown in Fig. 12.2b (see Sect. 12.2.3.3). Therefore, it appears that the *p*-NPNN radicals included in the CLPOT nanochannels of **1b/2g/3e** were adequately isolated by spacers and the molecular motion was frozen with respect to the ESR time scale (i.e., $\tau_R > 10^{-6}$ s). The *p*-NPNN spectra at 255 K were simulated using the $\boldsymbol{g}$ and $\boldsymbol{A}$ tensor components in Table 12.3, and the respective Gaussian and Lorentzian line width components were 0.06 and 0.88 mT for **1b/2g/3e**. The values of the $\boldsymbol{g}$ and $\boldsymbol{A}$ tensors for **1b/2g/3e** estimated using the EasySpin program were consistent with the results reported by D'Anna *et al* [66]. Similar results were also obtained for PhNN in CLPOT nanochannels [27]. In the case of isolated NN radicals in CLPOT nanochannels, a change in the ESR spectra from the rigid-limit data was observed above 255 K [51, 52], while temperature was found to affect the ESR spectra of 4-X-TEMPO radicals in CLPOT even above 100 K (see above). The difference in initiation temperature of a change in the ESR spectra is attributed to the fact that the NN radicals have larger molecular size and interaction with the wall of CLPOT than the TEMPO derivatives.

Figure 12.6 shows continuous changes in the ESR spectra with increases in temperature. In the vicinity of 351 K, the **1b/2g/3e** spectra exhibit two narrower peaks between lines 2 and 3 in Fig. 12.2b (see Sect. 12.2.3.4) [27, 66]. In addition, a modulated quintet associated with the two ^{14}N atoms for which $I = 1$ in the NN group appears above 369 K for *p*-NPNN. The temperature-dependent ESR spectra of **1b/2g/3e** were reproducible based on a model for assumption anisotropic rotational diffusion of isolated *p*-NPNN molecules in CLPOT nanochannels within the slow-motion regime with respect to the ESR time scale (10^{-9} s < τ_R < 10^{-6} s) over the entire temperature range in Fig. 12.6. The **1b/2g/3e** spectra at 398 K were obtained by assuming rotational diffusion around the axis tilted by (θ, ϕ) = (74°, 90°) relative to the principal system of the *g* tensor, with Gaussian and Lorentzian line width components and τ_R of 0.11 and 0.30 mT and 1.0×10^{-8} s, respectively. The ESR spectra were also well-reproduced at other temperatures using the anisotropic rotational diffusion model around the same rotation axis.

The rotational axes in **1b/2g/3e** are approximately parallel to the principal *y*-axis of the *g* tensor ($\theta = \phi = 90°$). For this reason, *p*-NPNN molecules are expected to be included in the CLPOT nanochannels with the longest molecular axis parallel to the channel axis, assuming that the rotational axis is parallel to the channel axis. The (θ, ϕ) parameters for the rotational axis relative to the principal axis for *p*-NPNN are larger than those for PhNN ((θ, ϕ) = (68°, 78°)). This difference is likely the result of the ratio of the molecular lengths of the NN radicals relative to the pore diameter for the CLPOT nanochannels (0.9 nm for PhNN, 1.1 nm for *p*-NPNN, and 1.1–1.3 nm for CLPOT).

The effects of temperature on τ_R for various [(CLPOT)-(4-X-TEMPO)] or [(CLPOT)-(4-XPNN)] are shown in Fig. 12.7 [27, 51, 52]. The rotational activation energy, E_a, for 4-X-TEMPO rotation in each [(CLPOT)-(4-X-TEMPO)] was estimated to be in the range of 6–8 kJ mol^{-1}, using the τ_R values plotted in this figure. Thus, all [(CLPOT)-(4-X-TEMPO)] have similar E_a values, and this value is independent of the size or type of the substituent group or the total inclusion amount. This independence may result from the relatively large pore diameter of the CLPOT nanochannels relative to the sizes of the radical molecules. However, the τ_R values for [(CLPOT)-(4-X-TEMPO)] are an order of magnitude greater than the value for **1a/2a/3a**. This result suggests that the pore diameter of the nanochannels is an important factor determining τ_R.

The high-temperature side in Fig. 12.7 demonstrates the temperature dependence of τ_R for [(CLPOT)-(PhNN)/(*N*-PhMI)] (diagonal crosses) and [(CLPOT)-(*p*-NPNN)/(*N*-PhMI)] (yellow circles) [27]. The τ_R values for PhNN or *p*-NPNN rotations in [(CLPOT)-(PhNN)/(*N*-PhMI)] and [(CLPOT)-(*p*-NPNN)/(*N*-PhMI)] are much longer than those for 4-X-TEMPO radicals in these nanochannels at the same temperature. As an example, τ_R for TEMPO or TEMPOL is on the order of 10^{-9} s at room temperature [51], whereas τ_R for the NN radical was approximately 10^{-7} s [27]. The E_a values for PhNN and *p*-NPNN rotations in [(CLPOT)-(PhNN)/(*N*-PhMI)] and [(CLPOT)-(*p*-NPNN)/(*N*-PhMI)] were estimated to be 37 and 54 kJ mol^{-1}, respectively, using the τ_R values in the range of 293–400 K in Fig. 12.7 [27]. These values are several times larger than those for 4-X-TEMPO [51,

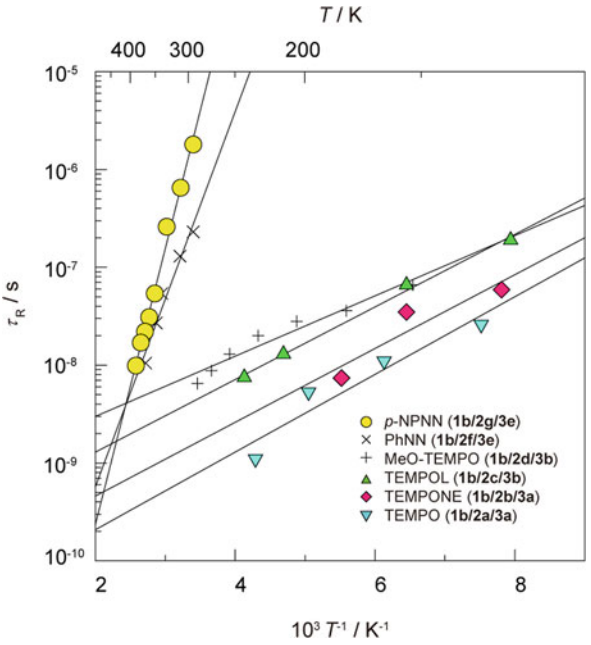

Fig. 12.7 Temperature dependence of the rotation diffusion correlation time τ_R for the isolated organic radicals in the CLPOT nanochannels such as *p*-NPNN (**1b/2g/3e**) [27], PhNN (**1b/2f/3e**) [27], MeO-TEMPO (**1b/2d/3b**) [52], TEMPOL (**1b/2c/3b**) [51], TEMPONE (**1b/2b/3a**) [52], and TEMPO (**1b/2a/3a**) [51]

52]. This difference may be due to the molecular size and weight of the NN radicals (which are larger and heavier than 4-X-TEMPO) as well as stronger interactions between NN radicals and the surrounding host or other guest molecules. Such interactions result from the delocalization of spin density on the nitronylnitroxide group of the NN radical for which, as opposed to 4-X-TEMPO, the spin density is wrapped internally.

12.5 ESR Analysis of Isolated Organic Radical in 1D TPP Nanochannels

The pore diameters of TPP nanochannels are adjustable over the range of 0.45–0.9 nm to the size of guest molecules [14, 28, 29]. The guest radicals in TPP nanochannels undergo uniaxial rotational diffusion motion in the relatively smaller space than the case of CLPOT. Under such conditions, the molecular orientations and dynamics of guest molecules in these nanospaces are dependent on the molecular size [70]. Although the inclusion of guest radicals is limited due to the smaller pore diameter of TPP nanochannels and/or the minimal polarity of TPP molecules, systematic investigations are possible for several 4-X-TEMPO compounds and for simple NN and IN radicals.

Figure 12.8 provides the temperature-dependent ESR spectra acquired for $[(TPP)_2\text{-}(DTBN)_x/(pivalone)_{1.1}]$ ($x = 4 \times 10^{-4}$; **1a/2e/3d**) from 54 to 243 K

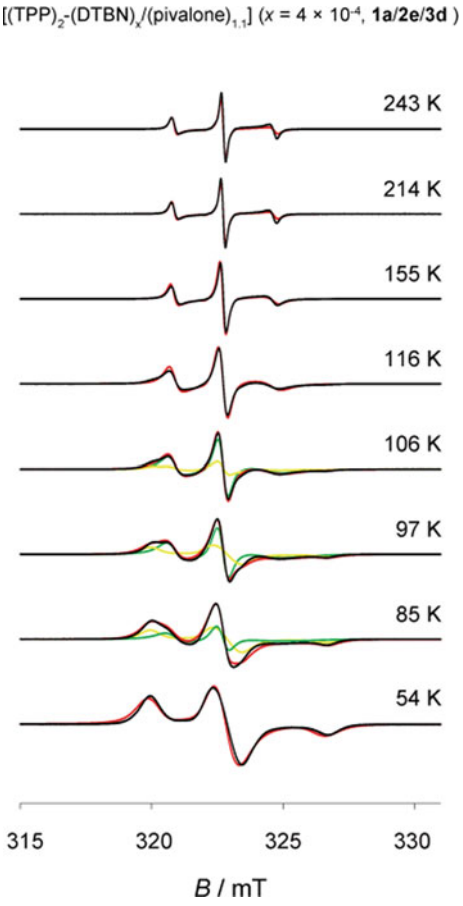

Fig. 12.8 Experimental and reproduced ESR spectra of $[(TPP)_2\text{-}(DTBN)_x/(pivalone)_{1.1}]$ ($x = 4 \times 10^{-4}$; **1a/2e/3d**) [41]. Green, yellow, and red lines of **1a/2e/3d** indicate the rotational diffusion and rigid-limit components of the DTBN radicals in the TPP nanochannels reproduced using the EasySpin program package and their superposition. (Reprinted with permission from *J. Phys Chem. A***2013**, *117*, 2093. Copyright 2018 American Chemical Society.)

[41]. Here, green, yellow, and red lines indicate the rotational diffusion, rigid-limit components of the DTBN radicals in the TPP nanochannels as reproduced using EasySpin program [46, 47], and their superposition. At 54 K, a typical pattern of a rigid-limit nitroxide radical, similar to that in Fig. 12.5 is observed (see Sects. 12.2.3.3 and 12.4). This result demonstrates that the DTBN molecules were adequately isolated in the TPP nanochannels. The narrowed ESR spectra of **1a/2e/3d** at 214 K provide evidence for the uniaxial rotational diffusion of DTBN in the TPP nanochannels within the slow-motion regime with respect to the ESR time scale around the *y*-axis of the *g* tensor of the DTBN molecule. The $\boldsymbol{g}$ and $\boldsymbol{A}$ tensors of the DTBN molecules in the TPP nanochannels were determined, as summarized in Table 12.3, from the 54 K spectrum according to the standard procedure (see Sects. 12.2.3.1, 12.2.3.2, and 12.2.3.3). The calculated $\boldsymbol{g}$ and $\boldsymbol{A}$ tensors are consistent with those of DTBN molecules confined in a tetramethyl-1,3-cyclobutanedione (TMCB) matrix within experimental error [41]. In this simulation, the Gaussian and Lorentzian components of the line width were 0.64 and 0.65 mT, respectively.

The **1a/2e/3d** spectra at 214 K shown in Fig. 12.8 were accurately simulated based on rotation around the axis defined by $(\theta, \phi) = (86°, 89°)$ in the principal axis system of the $\boldsymbol{g}$ and $\boldsymbol{A}$ tensors in Table 12.3. These simulations assumed that $R_{||}/R_{\perp}$ had a value of approximately 1000, τ_R was approximately 7.5×10^{-9} s and that the line widths of the Gaussian and Loretzian components were 0.08 and 0.15 mT, respectively (see Sect. 12.2.3.4). The direction of the rotational axis was estimated to be almost parallel to the principal y-axis ($\theta = 90°$, $\phi = 90°$). That is, the nitroxide groups of uniaxially rotating DTBN molecules confined in TPP nanochannels are considered to be almost perpendicular to the rotational axis, which in turn can be assumed to be parallel to the channel axis. When TEMPO or TEMPONE are dispersed in TPP nanochannels, both the temperature dependency of the ESR spectra and the molecular orientations of the guest radicals in the TPP nanochannels are similar [40, 41]. In the range of 85–106 K, the ESR spectra were reproduced by the superposition of a rigid component and an axially rotational diffusion component, though it was not reproduced by simple rigid or axially rotational diffusion components. These results provide evidence for the coexistence of low- and high-temperature phases, in which the molecular motion of the guest molecules is frozen out and unfrozen, respectively.

When TEMPOL is included as guest radical in TPP nanochannel, molecular orientations and dynamics were quite different from DTBN and other 4-X-TEMPO. Figure 12.9 shows the variable-temperature experimental and simulated ESR spectra for a powdered sample of $[(TPP)_2\text{-}(TEMPOL)_{0.004}/(TEMP)_{1.2}]$ (**1a/2c/3a**) [43]. At 55 K, the ESR spectrum of **1a/2c/3a** demonstrates a rigid-limit for the nitroxide radical that is similar to those of other radicals in the TPP and CLPOT nanochannels (see Figs. 12.5 and 12.8 and Sect. 12.2.3.3). In addition, the principal components of the $\boldsymbol{g}$ and $\boldsymbol{A}$ tensors in this case are comparable to those of other nitroxide radicals (see Table 12.3). However, the spectra of **1a/2c/3a** in the higher temperature region (e.g., at 288 K in Fig. 12.9) are quite different from those in Figs. 12.5 or 12.8. According to the spectral simulation, the rotational axis of the TEMPOL molecules in the TPP nanochannels are tilted by $(\theta, \phi) = (19°, 66°)$ in the principal axis system of the $\boldsymbol{g}$ and $\boldsymbol{A}$ tensors. These values are close to the principal z-axis of the g tensor (corresponding to $\theta = 0°$ and an arbitrary ϕ; see Sect. 12.2.3.4). Thus, it appears that the molecular orientations of guest radicals in TPP nanochannels can be adjusted by the proper selection of guest radicals and spacer molecules, or the co-inclusion of other radicals.

In addition, a rare example of the inclusion of IN or NN radicals in TPP nanochannels has been demonstrated. Figure 12.10 presents the temperature-dependent ESR spectra for $[(TPP)_2\text{-}(PhIN)_{0.002}/(N\text{-}PhMI)_{1.0}]$ (**1a/2h/3e**) [44]. Here, green, yellow, and red lines indicate the rotational diffusion and rigid-limit components of PhIN in **1a/2h/3e** as reproduced using EasySpin program and their superposition. The spectra acquired at less than 165 K were well-reproduced based on a rigid-limit powder pattern for isolated PhIN (see Sect. 12.2.3.3) [68]. The spectrum for **1a/2h/3e** at 56 K shown in Fig. 12.10 was simulated using the $\boldsymbol{g}$ and $\boldsymbol{A}$ tensor components in Table 12.3, and the respective Gaussian and Lorentzian line width components were 0.31 and 0.30 mT. The values of the $\boldsymbol{g}$

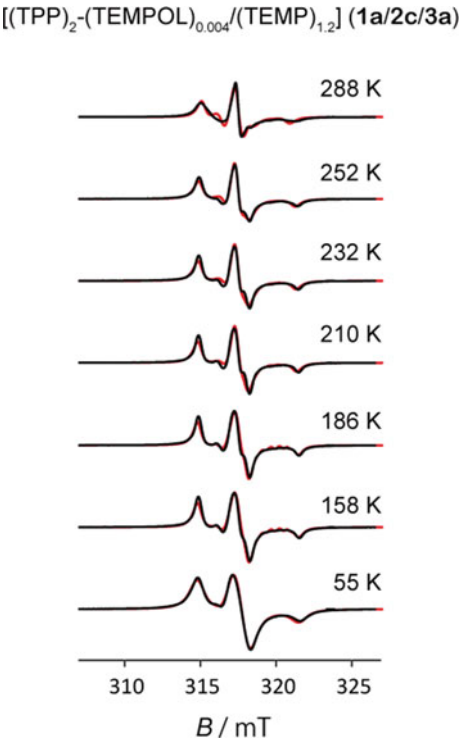

Fig. 12.9 Temperature dependence of the experimental (black) and reproduced (red) ESR spectra of the powder sample of $[(TPP)_2$-$(TEMPOL)_{0.004}/(TEMP)_{1.2}]$ (**1a/2c/3a**) in the temperature range of 55–288 K [43]. (Reprinted with permission from *Chem. Lett***2015**, *44*, 893. Copyright 2018 Chemical Society of Japan.)

and $\boldsymbol{A}$ tensors for **1a/2h/3e** estimated using EasySpin program were consistent with the previous results obtained for PhIN dispersed in glassy toluene (see Table 12.3) [68]. Therefore, in **1a/2h/3e**, the PhIN radicals may be considered to be adequately isolated in the TPP nanochannels as a result of the use of spacers and/or located on the surfaces of the TPP crystals, and the molecular motion is frozen on the ESR time scale (i.e., $\tau_R > 10^{-6}$ s).

The spectra of **1a/2h/3e** above 165 K depicted in Fig. 12.10 were not generated using a single anisotropic rotational diffusion component but by the superposition of anisotropic rotational diffusion and rigid-limit components. From 258 K to room temperature, the rotational diffusion and rigid-limit components were temperature-independent within experimental error. The anisotropic rotational diffusion component of **1a/2h/3e** in the temperature range from 165 to 258 K was reproduced as a septet associated with two ^{14}N atoms (both $I = 1$, but with different hyperfine coupling constants) in the IN group of PhIN modulated by molecular motion in the slow regime with respect to the ESR time scale. These results suggest that some PhIN radicals may be included in the TPP nanochannels, but that additional PhIN radicals may be on the surfaces of the TPP crystals.

In the case of PhIN in diluted solutions or in nanospaces within the fast-motion regime on the ESR time scale, seven major hyperfine splitting lines associated with the inequivalent nitrogen atoms of IN with $A_{1zz}{}^{IN} \sim 2A_{2zz}{}^{IN}$ are observed, with

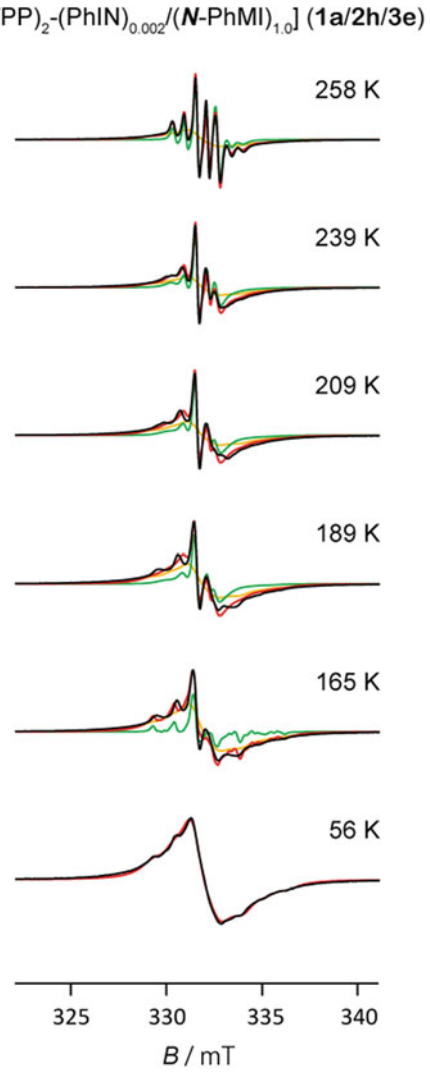

Fig. 12.10 Temperature-dependent ESR spectra for $[(TPP)_2\text{-}(PhIN)_{0.002}/(N\text{-}PhMI)_{1.0}]$ (**1a/2h/3e**) [44]. Green, yellow, and red lines indicate rotational diffusion and rigid-limit components of PhIN in **1a/2h/3e** reproduced using the EasySpin program package [46, 47] and their superposition. (Reprinted with permission from *J. Phys Chem. A***2018**, *122*, 5493. Copyright 2018 American Chemical Society.)

an intensity ratio of 1:1:2:1:2:1:1. However, with the molecular motion around the principal *y*-axis of the *g* tensor in the slow regime on the ESR time scale, the ESR spectra of PhIN radicals are modulated as shown in Fig. 12.3e (see Sect. 12.2.3.4 and reference [44]. When a low-temperature rigid-limit component is superposed, the spectral reproduction at 258 K is improved, as shown in Fig. 12.10. In fact, the modulated septet of the ESR spectrum of **1a/2h/3e** at 258 K is simulated reasonably well assuming that the anisotropic rotational diffusion around the axis is tilted by $(\theta, \phi) = (90°, 73°)$ relative to the principal axis system of the *g* tensor and parallel to the principal *y*-axis, with Gaussian and Lorentzian line width components and

τ_R of 0.17 and 0.036 mT and 1.3×10^{-8} s, respectively. These results show that the rotational axis is also approximately parallel to the molecular long axis of the PhIN molecules (i.e., the molecular long axis is parallel to the channel axis of the TPP nanochannels, if it is assumed that the rotational axis is parallel to the channel axis). Every ESR spectrum collected over the range from 165 to 239 K was also reproduced using this same approach. Based on the spectral reproduction process, it is evident that at least some PhIN radicals are included in the TPP nanochannels, although other PhIN radicals in **1a/2h/3e** may be adsorbed on the surfaces of the TPP crystals.

PhNN radicals can also be included in TPP nanochannels [44]. However, as some PhNN is reduced to PhIN during the synthetic process, $[(TPP)_2(PhNN)_x/(PhIN)_y/(N\text{-PhMI})_{1.0}]$ ($x \approx 5 \times 10^{-4}$ and $y \approx 2 \times 10^{-4}$, **1a/2f/2h/3e**) is produced. According to the ESR results, PhNN radicals included in the TPP nanochannels undergo anisotropic rotational diffusion around a rotational axis tilted by $(\theta, \phi) = (90°, 89°)$ relative to the principal axis system of the g tensor above 253 K.

Figure 12.11 summarizes the effect of temperature on τ_R for isolated organic radicals in TPP nanochannels, including PhNN (**1a/2f/3e**), PhIN (**1a/2h/3e**), TEMPOL (**1a/2c/3a**), TEMPONE (**1a/2b/3a**), TEMPO (**1a/2a/3a**), and DTBN (**1a/2e/3d**) [40, 41, 43, 44] The τ_R of each radical can be approximately determined from the rotational Stokes-Einstein relationship, assuming that the material behaves as an anisotropic liquid (see Sect. 12.2.3.4) [45]. The E_a values of several nitroxide radicals (such as DTBN, TEMPO, and TEMPONE) increase as the substituent groups become larger (with values 3, 5, and 10 kJ mol^{-1}) [40, 41]. In addition,

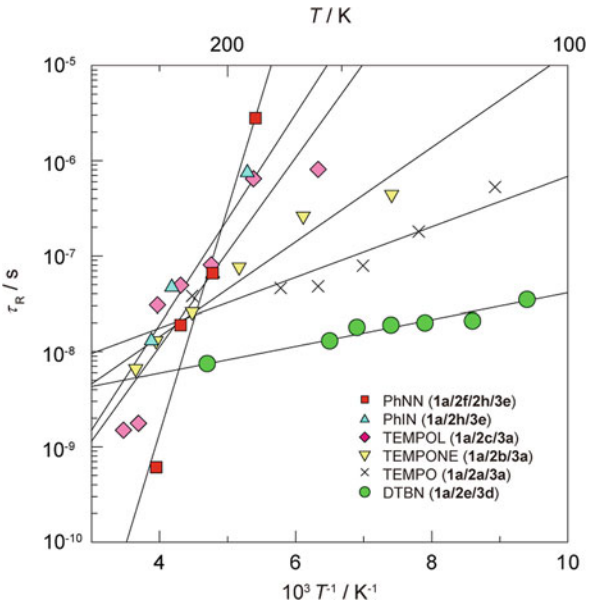

Fig. 12.11 Temperature dependence of the rotational diffusion correlation time τ_R, for the isolated organic radicals in the TPP nanochannels such as DTBN (**1a/2e/3a**), TEMPO (**1a/2a/3a**), TEMPONE (**1a/2b/3a**), TEMPOL (**1a/2c/3a**), PhIN (**1a/2h/3e**), and PhNN (**1a/2f/3e**) [40, 41, 43, 44]

the E_a values for PhIN and PhNN rotations in TPP nanochannel (19 and 45 kJ mol^{-1}) are much greater than those for such nitroxide radicals [44]. These results indicate that the τ_R values in TPP nanochannels are determined by the moment of inertia for guest radicals. Alternatively, these data may result from the strong interactions of PhIN or PhNN with the surrounding host walls formed by the phenyl rings of TPP molecules. Interactions may also occur with neighboring spacers in the TPP nanochannels as a result of the delocalization of the spin density on the iminonitroxide groups of PhIN radicals or the nitronylnitroxide group of NN radicals, in contrast to the behavior of TEMPO (in which the spin density is wrapped inside). However, the E_a value for PhIN rotation is smaller than that for 4-hydroxy-TEMPO (TEMPOL) in TPP nanochannels (26 kJ mol^{-1}) [43]. The E_a for TEMPOL rotation has been reported to be much larger than those for other TEMPO derivatives due to the different molecular orientation of TEMPOL in TPP nanochannels, as shown above (see Fig. 12.9). In the case of PhIN and TEMPOL in TPP nanochannels, the NO groups are approximately perpendicular to the nanochannel axis and also close to the nanochannels walls formed by the phenyl rings of TPP molecules [14, 28, 29], assuming that the rotational axis is parallel to the channel axis. The larger E_a for TEMPOL rotation in TPP nanochannel may be caused by the additional interaction between the OH groups (rather than the NO groups) of TEMPOL and the π-clouds on the phenyl rings of the TPP wall. This is as opposed to hydrogen bridging of the OH groups of TEMPOL with the oxygen atoms or the lone pairs of the nitrogen atoms of the TPP structure.

The molecular orientations of NN radicals in TPP or CLPOT nanochannels is as same each other as discussed in Sects. 12.4 and 12.5, that is, the molecular long axis is parallel to the channel axis. In addition, the E_a value for PhNN rotation in TPP nanochannel is larger than that for PhNN rotation in CLPOT nanochannel (37 kJ mol^{-1}, see Fig. 12.7). This result may be due to the smaller pore diameter of TPP nanochannels compared to those in CLPOT. The E_a value for PhNN rotation in TPP nanochannel is smaller than that for *p*-NPNN in CLPOT nanochannels (54 kJ mol^{-1}, see Fig. 12.7). This outcome is attributed to the smaller moment of inertia for PhNN compared to that for *p*-NPNN. In addition, PhNN rotation gives larger E_a value than PhIN rotation. It may be attributable to the difference in the steric hindrances of NN and IN groups, or to the stronger intermolecular interactions of PhNN with neighboring spacer molecules.

12.6 1D 4-X-TEMPO Chains Constructed in CLPOT and TPP Nanochannels

The ESR measurements for organic radicals in 1D nanochannels dispersed by spacer molecules were conducted in Sects. 12.4 and 12.5. In such systems, dipolar and/or exchange interaction between radicals can be ignored due to the longer intermolecular distance, although 1D molecular chains are formed (see Fig. 12.12a).

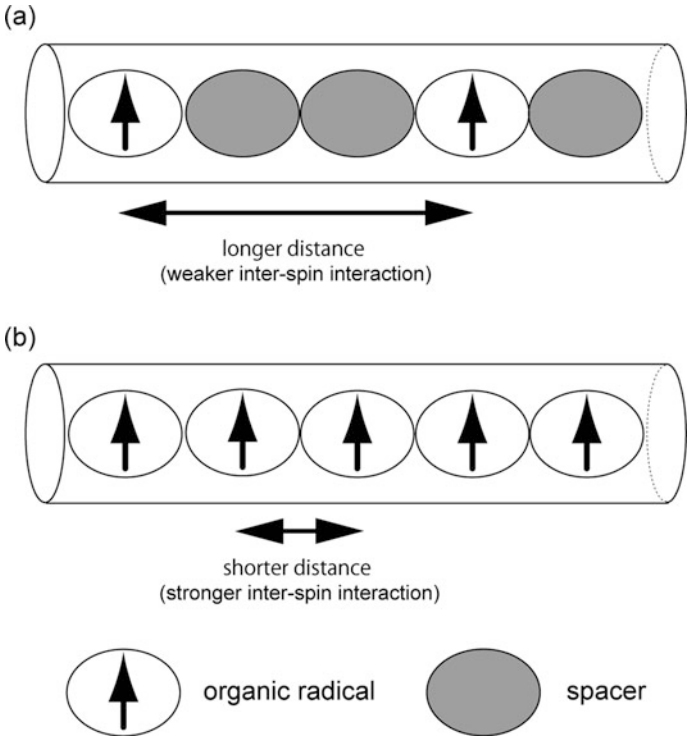

Fig. 12.12 Images of intermolecular distance and inter-spin interaction between radicals included in 1D nanochannel described in Sects. 12.4 and 12.5. (**a**) Isolated radical dispersed by spacer in CLPOT or TPP nanochannel described in Sects. 12.4 and 12.5. (**b**) 1D molecular chain of organic radicals in CLPOT and TPP nanochannel described in this section

In this section, the inter-spin interaction of 1D molecular chains of 4-X-TEMPO constructed in CLPOT and TPP nanochannels (without any spacers; see Fig. 12.12b) is discussed herein, based on the ESR spectra of [(CLPOT)-(4-X-TEMPO)] and [(TPP)-(4-X-TEMPO)]. In particular, the dimensionality and magnitude of these interactions are examined in terms of the molecular dynamics of guest radicals in the CLPOT and TPP nanochannels. Approximately, the inter-spin interactions of organic radical chain in CLPOT nanochannel are independent of the molecular orientations and dynamics of guest radicals, whereas those in TPP nanochannel are affected by the molecular dynamics of guest radicals described in Sects. 12.4 and 12.5.

Figure 12.13 summarizes the effect of temperature on the peak-to-peak line width ΔB_{pp} values (see Sect. 12.2.4) associated with the ESR spectra of $[(TPP)_2\text{-}(TEMPO)_{1.0}]$ (**1a/2a**; diagonal crosses), $[(CLPOT)_2\text{-}(TEMPO)_{1.0})]$ (**1b/2a**; yellow triangles), $[(CLPOT)_2\text{-}(TEMPOL)_{1.0})]$ (**1a/2c**; empty circles), $[(CLPOT)_2\text{-}(TEMPONE)_{1.1})]$ (**1a/2b**; magenta diamonds), and $[(CLPOT)_2\text{-}(MeO\text{-}TEMPOL)_{0.91})]$ (**1a/2d**; cyan squares) over the temperature range from 4.2 to

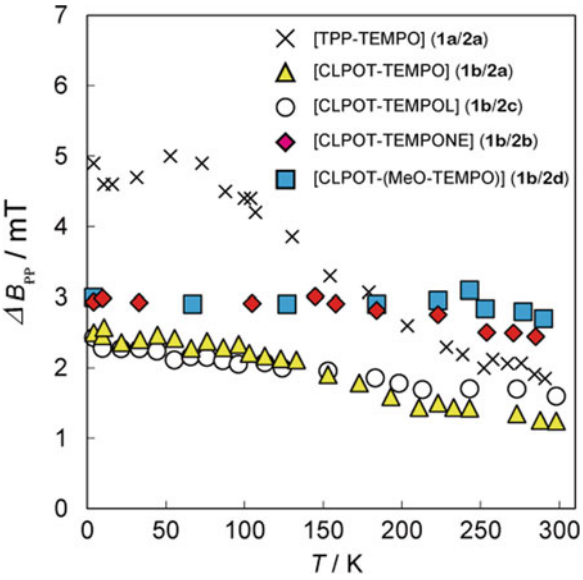

Fig. 12.13 Temperature dependency of the ESR spectra of the ΔB_{pp} of isotropic ESR spectra of $[(TPP)_2\text{-}(TEMPO)_{1.0}]$ (diagonal crosses; **1a/2a**), $[(CLPOT)_2\text{-}(TEMPO)_{1.0})]$ (yellow triangles; **1b/2a**), $[(CLPOT)_2\text{-}(TEMPOL)_{1.0})]$ (empty circles; **1a/2c**), $[(CLPOT)_2\text{-}(TEMPONE)_{1.1})]$ (magenta diamonds; **1a/2b**), and $[(CLPOT)_2\text{-}(MeO\text{-}TEMPOL)_{0.91})]$ (**1a/2d**; cyan squares) in the temperature range from 4.2 to 300 K [41, 53]. Note that the composition ratio of host to guest of each sample in the figure was abbreviated in the figure for simplification. (Reprinted with permission from *Bull. Chem. Soc. Jpn.***2018**, *91*, 375. Copyright 2018 Chemical Society of Japan.)

300 K [53]. Note that the composition ratio of host to guest in each sample has been abbreviated in this figure for simplification. Isolated 4-X-TEMPO radicals in the 1D TPP or CLPOT nanochannels generate anisotropic ESR signals, as discussed in Sects. 12.4 and 12.5. However, in the case of spin systems having spin concentrations greater than those for isolated radicals (as shown in this section), the ESR spectra appear isotropic because the line width of the 4-X-TEMPO absorption line becomes broader than the hyperfine coupling of the nitroxide. This occurs due to significant dipole interactions and minimal exchange narrowing.

The effect of temperature on the ΔB_{pp} values of $[(TPP)_2\text{-}(TEMPO)_{1.0}]$ (**1a/2a**) are summarized as follows. These effects are related to the molecular motions of TEMPO radicals in TPP nanochannels [39, 40, 53]. The essentially steady value of ΔB_{pp} of approximately 4.8 mT below 100 K reflects the termination of the molecular motion of TEMPO radicals in the TPP nanochannels. In addition, the gradual decrease of ΔB_{pp} with increasing temperature in the range of 100–253 K reflects the rotational diffusion of these radicals in the nanochannels within the slow-motion regime on the ESR time scale (10^{-9} s $< \tau_R < 10^{-6}$ s). The almost constant value ($\Delta B_{pp} = 1.8$ mT) above 253 K indicates rotational diffusion within the fast-motion regime on the ESR time scale ($\tau_R < 10^{-9}$ s). The variations in ΔB_{pp} values

between the highest and lowest temperatures are close to 3.6 mT. Above 100 K, the experimental ΔB_{pp} values for **1a/2a** are smaller than the estimated dipolar peak-to-peak line width ($\Delta B_{pp}{}^{D}$; see Sect. 12.2.4) based on Van Vleck's formula for a rigid spin lattice (Eq. (12.8) in Sect. 12.2.4), indicating exchange narrowing due to the temperature dependency of the ESR line profile (see below and Fig. 12.15).

On the other hand, the effect of temperature on the ΔB_{pp} values of **1b/2a–d** is evidently more gradual than that for **1a/2a**, although there is a slight decrease with increases in temperature. The magnitude of the ΔB_{pp} values for **1b/2a–d** was at most 2–3 mT even at low temperature, and the variation with increasing in temperature was less than 1.4 mT, even at 300 K. The ΔB_{pp} value is also somewhat larger when the 4-position substituent group on the TEMPO molecule is bulkier. Because the crystal structure of the CLPOT nanochannels and the quantity of guest radicals per unit cell in each [CLPOT-(4-X-TEMPO)] are similar to the values for **1a/2a** (see Sect. 12.3.2), the dipolar peak-to-peak line width ($\Delta B_{pp}{}^{D}$, see Sect. 12.2.4) for **1b/2a–d** was estimated assuming a hexagonal rigid spin lattice formed by positioning the electron spin in the CLPOT nanochannels at the center of gravity of the TEMPO molecule [39, 53] (see Sect. 12.2.4). Using this model, the $\Delta B_{pp}{}^{D}$ value for **1b/2a–d** was estimated to be 11.2 or 11.3 mT. A significantly larger $\Delta B_{pp}{}^{D}$ was evidently obtained from the shorter c (*i.e.*, shorter intra-channel inter-spin distance of 0.7 nm) [50] of **1b/2a–d** as compared to **1a/2a**. These results indicate the narrowing of ESR line width of **1b/2a–d** due to molecular motion or exchange interaction.

The ESR line profiles were determined according to the theory described in Sect. 12.2.5. Figure 12.14 shows the effect of temperature on the line profiles of [$(TPP)_2$-$(TEMPO)_{1.0}$] (**1a/2a**; diagonal crosses) and of [CLPOT-(4-X-TEMPO)], such as [$(CLPOT)_2$-$(TEMPO)_{1.0}$)] (**1b/2a**, yellow triangles), [$(CLPOT)_2$-$(TEMPOL)_{1.0}$)] (**1a/2c**, empty circles), [$(CLPOT)_2$-$(TEMPONE)_{1.1}$)] (**1a/2b**, magenta diamonds), and [$(CLPOT)_2$-$(MeO\text{-}TEMPOL)_{0.91}$)] (**1a/2d**, cyan squares) according to Dietz's method (see Sect. 12.2.5) at 4.2, 155 K, and 290 K [39, 53]. Note that the host to guest ratio notation for each sample in Fig. 12.14 has been abbreviated for the sake of simplifying the figure.

In the case of **1b/2a–d**, the molecular motions of guest radicals in CLPOT nanochannels are temperature-dependent, as shown in Sect. 12.4, with a rigid-limit under about 120 K. With increases in temperature (above 200–240 K), the rotational diffusion motion originally in the slow-motion regime on the ESR time scale changed such that τ_R moved into the fast-motion region of the ESR time scale. In addition, τ_R of **1b/2a–d** was shorter than the value for TEMPO in the TPP nanochannels in the same temperature range (see Figs. 12.7 and 12.11) [41, 43, 52]. The **1b/2a–d** line profiles were almost independent of temperature, as seen in Fig. 12.14a–c, indicating different results compared to those obtained for **1a/2a** (see below and Fig. 12.15). These data suggest that the molecular motions and/or substituent groups of guest radicals in the CLPOT nanochannels are not correlated with the inter-spin interactions of **1b/2a–d**. Therefore, the narrower ESR line width for **1b/2a–d** may be considered to originate not from motional narrowing but rather than 3D exchange interactions. This finding demonstrates that 3D exchange

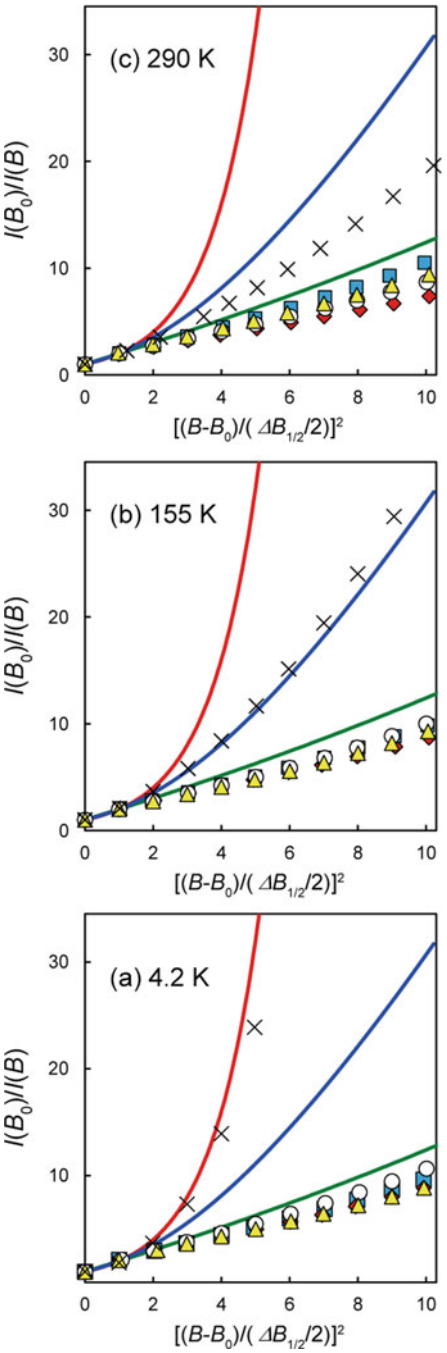

Fig. 12.14 Dietz's plot of isotropic ESR spectra of $[(TPP)_2\text{-}(TEMPO)_{1.0}]$ (**1a/2a**; diagonal crosses) and the [CLPOT-(4-X-TEMPO)] (**1b/2a**, yellow triangles; **1b/2c** empty circles; **1b/2b**, magenta diamonds; and **1b/2d**, cyan squares) according to Dietz's method at (**a**) 4.2, (**b**) 155 K, and (**c**) 290 K [41, 53]. Note that the composition ratio of host to guest of each sample in the figure was abbreviated in the figure for simplification. (Reprinted with permission from *Bull. Chem. Soc. Jpn.***2018**, *91*, 375. Copyright 2018 Chemical Society of Japan.)

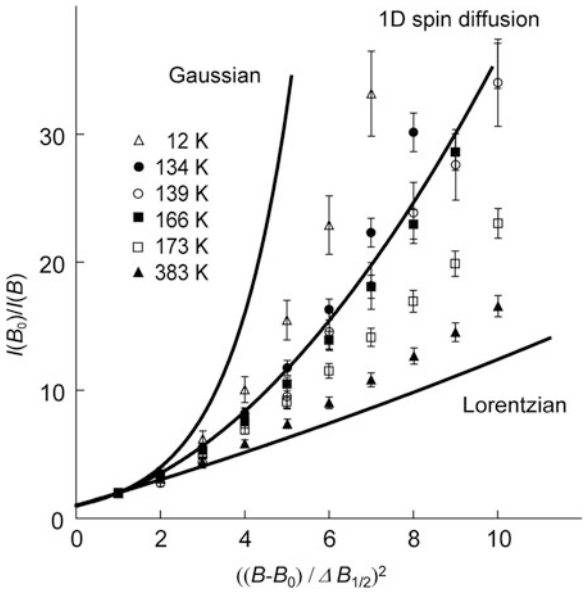

Fig. 12.15 Temperature dependency of line shape of $[(TPP)_2\text{-}(TEMPO)_{1.0}]$ (**1a/2a**) in 12–383 K using Dietz' method. (Reprinted with permission from *Bull. Chem. Soc. Jpn.***2007**, *80*, 711. Copyright 2018 Chemical Society of Japan.)

interactions can be observed even in 1D OIC-OR by selecting the optimal host and/or guest compounds. The 3D exchange interactions of organic radical chains in [CLPOT-(4-X-TEMPO)] may result from the formation of an imperfect 1D electron spin array due to the disordered orientation of the nitroxide groups of guest 4-X-TEMPO molecules in the CLPOT nanochannels, which have larger pore diameters than those in TPP.

Figure 12.15 shows the effect of temperature on the ESR line profiles of $[(TPP)_2\text{-}(TEMPO)_{1.0}]$ (**1a/2a**), as determined using Dietz's method (see Sect. 12.2.5). In the temperature range from 12 to 139 K, approximately corresponding to the rigid-limit of TEMPO in TPP nanochannels, the line shape exhibits characteristics intermediate between those expected from the pure Gaussian and 1D spin diffusion models. Therefore, the 1D spin diffusion mechanism occurs even at fairly low temperature, where TEMPO rotation is frozen in TPP nanochannel. Over the range of 139–166 K, corresponding to τ_R values of approximately 10^{-7} s for TEMPO in TPP nanochannels, the **1a/2a** line shape is in good agreement with that expected from the pseudo-1D-spin diffusion model. This result obviously indicates that exchange narrowing explains the narrowing seen in Fig. 12.13. At temperatures greater than 166 K (corresponding to $\tau_R < 10^{-8}$ s), the resonance peak become more Lorentzian with increases in temperature, although a pure Lorentzian line shape never appears, even at 383 K. This increase in the Lorentzian character suggests that anisotropic exchange interactions occur between interchain spins. These interchain interactions cut off $\Psi(\tau)$ after a characteristic time (see Sect. 12.2.5). The line shape at 383 K roughly reflects the ratio of intrachain exchange interactions, J_{intra}, to interchain exchange interactions, J_{inter}, giving a J_{inter}/J_{intra} ratio in the range of 10^{-2}–10^{-3} [71,

72]. The average molecular orientation of TEMPO in TPP nanochannel by rotational diffusion provides homogeneous interaction between unpaired electrons in adjacent TEMPOs. This scenario produces a large exchange integral, thus increasing the efficiency of exchange narrowing. The exchange integral in this system may be calculated based on the wavefunction perturbed by molecular motion of guest radicals in TPP nanochannel. For these reasons, **1a/2a** is a remarkable material, as the dimensionality of the exchange interactions changes from 1D to 3D with increasing temperature (compare this result to that in CLPOT above).

In other [TPP-(4-X-TEMPO)], a few interesting experimental results are known. [$(TPP)_2$-$(DTBN)_{1.3}$] (**1a/2e)** exhibits a similar effect of temperature on ΔB_{pp} to **1a/2a [**42]. However, the $\Delta B_{pp}{}^{D}$ value for **1a/2e** estimated from Eq. (12.8) (approximately 9 mT) is significantly larger than that for **1a/2a**. Therefore, the line width of **1a/2e** is thought to be much narrower than that for **1a/2a**. In addition, the ESR line profiles for [$(TPP)_2$-$(DTBN)_{1.3}$] (**1a/2e)** are also temperature-dependent, but 1D spin diffusion behavior is observed around room temperature [42], while [TPP-TEMPONE] (**1a/2b**) shows temperature-dependent anisotropic exchange interaction even in the vicinity of 4.2 K. Thus, [TPP-(4-X-TEMPO)] is unique among the various 1D OIC-OR.

12.7 Concluding Remarks and Outlook

In CLPOT and TPP nanochannels, incorporated organic radicals form 1D organic radical chain. To examine the 1D or 3D exchange interactions in 1D organic radical chain, molecular dynamics of organic radicals in the nanochannels were assessed by experimental and theoretical ESR analyses.

It was found that molecular dynamics of 4-X-TEMPO radical in CLPOT nanochannel is independent of the substituent groups of the guest radicals and/or the type of spacer. From ESR adsorption line profiles and the molecular dynamics of 4-X-TEMPO radicals in CLPOT nanochannels, it was found that [CLPOT-(4-X-TEMPO)] exhibits temperature-independent 3D exchange interactions. The existence of 3D exchange interaction in [CLPOT-(4-X-TEMPO)] may be the first step to express magnetic phase transition in 1D OIC-OR.

On the other hand, [TPP-(4-X-TEMPO)] exhibited temperature-dependent anisotropic exchange interaction. It may be correlated with temperature dependency on molecular dynamics of guest radical in TPP nanochannel with a small pore diameter. These different exchange interaction in CLPOT and TPP nanochannels will be a key to design and develop a new organic magnet.

The molecular dynamics of 4-XPNN and PhIN radicals in CLPOT or TPP nanochannels was clarified using ESR analyses. These results may be available to the development of a new ESR spin probe technique using NN or IN radicals for the clarification of the structure of nanospaces in polymer, liquid crystal, and membrane. It is expected that spin system based on 4-XPNN or PhIN radicals will be formed in 1D OIC-OR by the increase of the guest inclusion amount.

The relationship between exchange interactions of organic radical chain and molecular dynamics should be further elucidated in order to design and develop innovative organic magnet. This work is underway.

Acknowledgments These works were partially supported by the Strategic Research Base Development program for Private Universities of the Ministry of Education, Culture, Sports, Science and Technology of Japan (MEXT), 2009–2013. These works were also partially supported by the Common Research Funding by Showa University, 2017–2018. The authors wish to thank Professor T. Asaji of Nihon University for assistance with the ESR analyses, Professor T. Hashimoto of Nihon University for assistance with the TG-DTA measurements, Prof. S. Stoll of the University of Washington for assistance with the EasySpin calculations, and the Organic Elemental Analysis Research Center, Kyoto University, for performing the elemental analyses.

References

1. Z. Rinkevicius, B. Frecus, N.A. Murugan, O. Vahtras, J. Kongsted, H. Ågren, Encapsulation influence on EPR parameters of spin-labels: 2,2,6,6-tetramethyl-4-methoxypiperidine-1-oxyl in cucurbit[8]uril. J Chem Theory Comput **8**, 257 (2012)
2. S.M. Neville, G.J. Halder, K.W. Chapman, M.B. Duriska, B. Moubaraki, K.S. Murray, C.J. Kepert, Guest tunable structure and spin crossover properties in a nanoporous coordination framework material. J Am Chem Soc **131**, 12106 (2009)
3. G.J. Halder, C.J. Kepert, B. Moubaraki, K.S. Murray, J.D. Cashion, Guest-dependent spin crossover in a nanoporous molecular framework material. Science **298**, 1762 (2002)
4. D. Tanaka, S. Kitagawa, Template effects in porous coordination polymers. Chem Mater **20**, 922 (2008)
5. M. David, T. Kishi, M. Kisaku, H. Nakanishi, H. Kasai, Carbon nanoarch encapsulating Fe nanowire on Ni(111). Jpn J Appl Phys **45**, 2869 (2006)
6. R. Kulasekharan, N. Jayaraj, M. Porel, R. Choudhury, A.K. Sundaresan, A. Parthasarathy, M.F. Ottaviani, S. Jockusch, N.J. Turro, V. Ramamurthy, Guest rotations within a capsuleplex probed by NMR and EPR techniques. Langmuir **26**, 6943 (2010)
7. N. Jayaraj, M. Porel, M.F. Ottaviani, M.V.S.N. Maddipatla, A. Modeli, J.P. Da Silva, B.R. Bhogala, B. Captain, S. Jockusch, N.J. Turro, V. Ramamurthy, Self aggregation of supramolecules of nitroxides@cucurbit[8]uril revealed by EPR spectra. Langmuir **25**, 13820 (2009)
8. D. Fujita, Y. Ueda, S. Sato, N. Mizuno, T. Kumasaka, M. Fujita, Self-assembly of tetravalent Goldberg polyhedra from 144 small components. Nature **540**, 563 (2016)
9. V.I. Nikolayenko, L.J. Barbour, A. Arauzo, J. Campo, J.M. Rawson, D.A. Haynes, Inclusion of a dithiadiazolyl radical in a seemingly non-porous solid. Chem Commun, 11310 (2017)
10. Q.F. Sun, J. Iwasa, D. Ogawa, Y. Ishido, S. Sato, T. Ozeki, Y. Sei, K. Yamaguchi, M. Fujita, Self-assembled $M_{24}L_{48}$ polyhedra and their sharp structural switch upon subtle ligand variation. Science **328**, 1144 (2010)
11. R. Kitaura, K. Seki, G. Akiyama, S. Kitagawa, Porous coordination-polymer crystals with gated channels specific for supercritical gases. Angew Chem Int Ed **42**, 428 (2003)
12. G. Couderc, J. Hulliger, Channel forming organic crystals: guest alignment and properties. *Chem Soc Rev***39**, 1545 (2010)
13. R. Kitaura, S. Kitagawa, Y. Kubota, T.C. Kobayashi, K. Kindo, Y. Mita, A. Matsuo, M. Kobayashi, H.-C. Chang, T.C. Ozawa, M. Suzuki, M. Sakata, M. Takata, Formation of a one-dimensional array of oxygen in a microporous matal-organic solid. Science **298**, 2358 (2002)
14. H.R. Allcock, Cyclophosphazene clathlates-exploring the adjustable tunnel. Acc Chem Res **11**, 81 (1978)

15. M. Fanina, G. di Silvestro, P. Sozzani, Perhydrotriphenylene: D_3 symmeric host, in *Comprehensive supramolecular chemistry*, ed. by D. D. MacNicol, F. Toda, R. Bishop, vol. 6, (Pergamon, Oxford, 1996), pp. 371–419
16. R.T. Morrison, R.N. Boyd, *Organic chemistry*, 6th edn. (Prentice-Hall, Inc, 1992)
17. B. Ye, M.L. Trudeau, D.M. Antonelli, Observation of a double maximum in the dependence of conductivity on oxidation state in potassium fulleride nanowires supported by a mesoporous niobium oxide host lattice. Adv Mater **13**, 561 (2001)
18. F. Marlow, M. Wübbenhorst, J. Caro, Pyroelectric effects on molecular sieve crystals loaded with dipole molecules. J Phys Chem **98**, 12315 (1994)
19. B. Zhou, A. Kobayashi, H. Kobayashi, Dielectric properties of one-dimensional water clusters confined in the porous crystal, $[Co_3(2,4\text{-pyde})_2(\mu_3\text{-OH})_2]\bullet 9H_2O$ (2,4-pyde: pyridine-2,4-dicarboxylate). Chem Lett **42**, 1131 (2013)
20. T. Fukino, H. Joo, Y. Hisada, M. Obana, H. Yamagishi, T. Hikima, M. Takata, N. Fujita, T. Aida, Manipulation of discrete nanostructures by selective modulation of noncovalent forces. Science **344**, 499 (2014)
21. A.C. Soegiarto, W. Yan, A.D. Kent, M.D. Ward, Regulating low-dimensional magnetic behavior of organic radicals in crystalline hydrogen-bonded host frameworks. J Mater Chem **21**, 2204 (2011)
22. D. Bardelang, M. Giorgi, V. Hornebecq, A. Stepanov, M. Hardy, E. Rizzato, V. Monnier, M.B. Zaman, G. Chan, K. Udachin, Hosting various guests including fullerenes and free radicals in versatile organic paramagnetic bTbk open frameworks. Cryst Growth Des **14**, 467 (2014)
23. A.R. Albunia, C. D'Aniello, G. Guerra, D. Gatteschi, M. Mannini, L. Sorace, Ordering magnetic molecules within nanoporous crystalline polymers. Chem Mater **21**, 4750 (2009)
24. M. Mon, A. Pascual-Alvarez, T. Grancha, J. Cano, J. Ferrando-Soria, F. Lloret, J. Gascon, J. Pasan, D. Armentano, E. Pardo, Solid-state molecular nanomagnet inclusion into a magnetic metal–organic framework: interplay of the magnetic properties. Chem Eur J **22**, 539 (2016)
25. J.X. Huang, C.D. Luo, W.B. Li, Y. Li, Y.S. Zhang, J.H. Zhou, Q. Jiang, Eccentric magnetic microcapsules for orientation-specific and dual stimuli-responsive drug release. J Mater Chem B **3**, 4530 (2015)
26. K. Tateishi, M. Negoro, S. Nishida, A. Kagawa, Y. Morita, M. Kitagawa, Proc Natl Acad Sci U S A **111**, 7527 (2014)
27. H. Kobayashi, Y. Morinaga, E. Fujimori, T. Asaji, ESR study of molecular orientation and dynamics of nitronyl nitroxide radicals in CLPOT 1D nanochannels. J Phys Chem A **118**, 4907 (2014)
28. H.R. Allcock, L.A. Siegel, Phosphonitrilic compounds. III.1 Molecular inclusion compounds of Tris(o-phenylenedioxy)phosphonitrile trimer. J Am Chem Soc **86**, 5140 (1964)
29. P. Sozzani, S. Bracco, A. Comotti, L. Ferrentti, R. Simonutti, Methane and carbon dioxide storage in a porous van der Waals Crystal. Angew Chem Int Ed **44**, 1816 (2005)
30. T. Meersmann, J.W. Logan, R. Simonutti, S. Caldarelli, A. Comotti, P. Sozzani, L.G. Kaiser, A. Pines, J Phys Chem A **104**, 11665 (2000)
31. P. Sozzani, A. Comotti, R. Simonutti, T. Meersmann, J.W. Logan, A. Pines, Angew Chem Int Ed **39**, 2695 (2000)
32. H. Kobayashi, T. Ueda, K. Miyakubo, T. Eguchi, Z Naturforsch **58a**, 727 (2003)
33. T. Hertzsch, S. Kluge, E. Weber, F. Budde, J. Hulliger, Adv Mater **13**, 1864 (2001)
34. C. Gervais, T. Hertzsch, J. Hulliger, Insertion of dipolar molecules in channels of a centrosymmetric organic zeolite: molecular modeling and experimental investigation on diffusion and polarity formation. J Phys Chem B **109**, 7961 (2005)
35. T. Hertzsch, F. Budde, E. Weber, J. Hulliger, Angew Chem Int Ed **41**, 2281 (2002)
36. H.I. Süss, T. Wuest, A. Sieber, R. Althaus, F. Budde, H.-P. Lüthi, G.D. McManus, J. Rawson, J. Hulliger, CrystEngComm **4**, 432 (2002)
37. A. Barbon, A. Zoleo, M. Brustolon, A. Comotti, P. Sozzani, One-dimensional clusters of 16-doxyl-stearate radicals in organic nanochannels as studied by electron paramagnetic resonance (EPR). Inorg Chim Acta **361**, 4122 (2008)

38. H. Kobayashi, T. Ueda, K. Miyakubo, J. Toyoda, T. Eguchi, A. Tani, Preparation and characterization of new inclusion compound with 1D molecular arrangement of organic radicals using a one-dimensional organic homogeneous nanochannel template. J Mater Chem **15**, 872 (2005)
39. H. Kobayashi, T. Ueda, K. Miyakubo, T. Eguchi, A. Tani, Spin-spin interaction of TEMPO molecular chains formed in an organic one-dimensional nanochannel as studied by electron spin resonance (ESR). Bull Chem Soc Jpn **80**, 711 (2007)
40. H. Kobayashi, T. Ueda, K. Miyakubo, T. Eguchi, A. Tani, ESR study of molecular dynamics and orientation of TEMPO included in organic one-dimensional nanochannel. Phys Chem Chem Phys **10**, 1263 (2008)
41. H. Kobayashi, K. Takeuchi, T. Asaji, Molecular orientation and dynamics of different sized radicals included in organic 1-D nanochannels. J Phys Chem A **117**, 2093 (2013)
42. H. Kobayashi, T. Asaji, A. Tani, Preparation and characterization of new inclusion compounds using stable nitroxide radicals and an organic 1-D nanochannel as a template. Materials **3**, 3625 (2010)
43. H. Kobayashi, K. Aoki, T. Asaji, Dynamics of TEMPOL radicals in TPP 1D nanochannels and different molecular orientation from other TEMPO derivatives. Chem Lett **44**, 893 (2015)
44. H. Kobayashi, T. Mori, Y. Morinaga, E. Fujimori, K. Akiniwa, F. Iwahori, Electron spin resonance study of molecular orientation and dynamics of phenyl imino and nitronyl nitroxide radicals in organic 1D nanochannels of Tris(*o*-phenylenedioxy)cyclotriphosphazene. J Phys Chem A **122**, 5493 (2018)
45. J.H Freed*, Spin labeling, theory and applications*, ed. by L. J Berliner (Academic, New York, 1976)
46. S. Stoll, A. Schweiger, EasySpin, a comprehensive software package for spectral simulation and analysis in EPR. J Magn Reson **178**, 42 (2006)
47. http://www.easyspin.org/: see the manual of Chili (2018–12–07)
48. B. Dzikovski, D. Tipikin, V. Livshits, K. Earle, J. Freed, Multifrequency ESR study of spin-labeled molecules in inclusion compounds with cyclodextrins. Phys Chem Chem Phys **11**, 6676 (2009)
49. C. Aliaga, F. Bravo-Moraga, D. Gonzalez-Nilo, S. Márquez, S. Lühr, G. Mena, M.C. Rezende, Location of TEMPO derivatives in micelles: subtle effect of the probe orientation. Food Chem **192**, 395 (2016)
50. R.K.R. Jetti, P.K. Thallapally, F. Xue, T.C.W. Mak, A. Nangia, Hexagonal nanoporous host structures based on 2,4,6-tris-4-(halo-phenoxy)-1,3,5-triazines (halo = chloro, bromo). Tetrahedron **56**, 6707 (2000)
51. H. Kobayashi, T. Asaji, A. Tani, ESR study of the molecular orientation and dynamics of stable organic radicals included in the 1-D organic nanochannels of 2,4,6-tris-4-(chlorophenoxy)-1,3,5-triazine. Magn Reson Chem **50**, 221 (2012)
52. H. Kobayashi, Y. Furuhashi, H. Nakagawa, T. Asaji, ESR study of molecular orientation and dynamics of TEMPO derivatives in CLPOT 1D nanochannels. Magn Reson Chem **54**, 641 (2016)
53. H. Kobayashi, H. Takamisawa, Y. Furuhashi, H. Nakagawa, K. Nakatsugawa, K. Takeuchi, Y. Morinaga, Inter-spin interaction of CLPOT inclusion compounds with 1D molecular chains of 4-X-TEMPO radicals in the temperature range of 4.2-300 K. Bull Chem Soc Jpn **91**, 375 (2018)
54. M. Bonin, G. Labat, G. Couderc, T.A. Lüthi, K. Reichenbächer, J. Hulliger, H.–.B. Bürgi, Novel host-guest structures of 2,4,6-*Tris*(4-Halophenoxy)-1,3,5-Triazines (XPOT): inclusion of C_{60} and pyridine. J Chem Crystllogr **42**, 645 (2012)
55. H.I. Süss, J. Hulliger, Organic channel inclusion compound featuring an open pore size of 12 Å. Microporous Mesoporous Mater **78**, 23 (2005)
56. B. Naydenov, C. Spudat, W. Harneit, H.I. Süss, J. Hulliger, J. Nuss, M. Jansen, Ordered inclusion of endohedral fullerenes N@C_{60} and P@C_{60} in a crystalline matrix. Chem. Phys. Lett **424**, 327 (2006). S.D. Bruce, J. Higinbotham, I. Marshall, P.H. Beswick, An Analytical Derivation of a Popular Approximation of the Voigt Function for Quantification of NMR Spectra. J Magn Reson **142**, 57 (2000)

57. H.M. Levitt, *Spin dynamics*, 2nd edn. (Wiley, 2008)
58. C.P. Slichter, *Principles of magnetic resonance*, 3rd edn. (Spiringer, Heidelberg, 1996)
59. A. Abragam, *Principles of nuclear magnetism* (Oxford/New York, 1961)
60. G.E. Pake, T.L. Estle, *The physical principle of electron paramagnetic resonance*, 2nd edn. (W. A. Benjamin, Inc., New York, 1973)
61. T.T. Tong, T. Yonezawa, N. Toshima, J.J. van der Klink, ^{195}Pt NMR of polymer-protected Pt/Pd bimetallic catalysts. J Phys Chem B **100**, 730 (1996)
62. The Spin Hamitonian (EasySpin), http://easyspin.org/easyspin/documentation/hamiltonian.html (2018–12–07).
63. L.J. Libertini, O.H. Griffith, Orientation dependence of the electron spin resonance spectrum of Di-*t*-butyl nitroxide. J Chem Phys **53**, 1359 (1970)
64. B.G. Birrell, S.P. Van, O.H. Griffith, Electron spin resonance of spin labels in organic inclusion crystals. Models for anisotropic motion in biological membranes. J Am Chem Soc **95**, 2451 (1973)
65. V.F. Tarasov, I.A. Shkrob, A.D. Trifunac, Spin-polarized nitroxide radicals in organic glasses. J Phys Chem A **106**, 4838 (2002)
66. J.A. D'Anna, J.H. Wharton, Electron spin resonance spectra of α-nitronylnitroxide radicals; solvent effects; nitrogen hyperfine tensor; *g* anisotropy. J Chem Phys **53**, 4047 (1970)
67. S.A. Dikanov, V.I. Gulin, Y.D. Tsvetkov, I.A. Grigor'ev, 2 mm Electron paramagnetic resonance studies of the new types of imidazoline nitroxide radicals. J. Chem. Soc. Faraday Trans. **86**, 3201 (1990)
68. S.D. Bruce, J. Higinbotham, I. Marshall, P.H. Beswick, An analytical derivation of a popular approximation of the voigt function for quantification of NMR spectra. J. Magn. Reson. **142**, 57–63 (2000). https://doi.org/10.1006/jmre.1999.1911
69. R.E. Dietz, F.R. Merritt, R. Dingle, D. Hone, B.G. Silbernagel, P.M. Richards, Exchange narrowing in one-dimensional systems. Phys Rev Lett **26**, 1186 (1971)
70. J.A. Villaunueva-Garibay, K. Müller, Solid-state ^{2}H NMR studies of cyclophosphazene inclusion compounds: order and dynamics of the benzene guests. J Phys Chem B **108**, 15057 (2004)
71. M.J. Hennessy, C.D. McElwee, P.M. Richards, Effect of interchain coupling on electron-spin resonance in nearly one-dimensional system. Phys Rev B **7**, 930 (1973)
72. T.T.P. Cheung, Z.G. Soos, R.E. Dietz, F.R. Merritt, Temperature dependence of exchange narrowing in the one-dimensional antiferromagnet $N(CH_3)_4MnCl_3$. *Phys*. Rev B **17**, 1266 (1978)

Part V
Forthcoming Theoretical Approach

Chapter 13
If *Truncated* Wave Functions of Excited State Energy Saddle Points Are Computed as Energy *Minima*, Where Is the Saddle Point?

N.C. Bacalis

Abstract Theoretical computations tend to compute electronic properties of increasingly larger systems. To understand the properties, we should rather need small truncated but concise and comprehensible wave functions. For electronic processes, in particular charge transfer, which occur in excited states, we need both the energy and the wave function in order to draw and predict correct conclusions. But the excited states are saddle points in the Hilbert space, and, as shown here, the standard methods for excited states, based on the Hylleraas-Undheim and MacDonald (HUM) theorem, compute indeed the correct energy but may give misleadingly incorrect truncated wave functions, because they search for ***an energy minimum, not a saddle point*** (many functions can have the correct energy). Then, **where is the saddle point?** We shall see the use of a functional F_n of the wave function that has a local minimum **at** the excited state saddle point, without using orthogonality to approximants of lower-lying states, provided these approximants are reasonable, even if they are crude. Therefore F_n finds a correct, albeit small and concise, thus comprehensible truncated wave function, approximant of the desired excited state saddle point, allowing correct predictions for the electronic process. This could also lead to computational developments of more appropriate (to excited state) truncated basis sets. It is further shown that, via a correct approximant of the 1st excited state, we can improve the ground state. Finally it is shown that, in iterative computations, in cases of "root flipping" (which would deflect the computation), we can use F_n to identify the flipped root. For all the above, demonstrations are given for excited states of He and Li. The grand apophthegm is that HUM finds an energy **minimum** which, only if the expansion is increased, can approach the excited state saddle point, whereas F_n has local minimum **at** the saddle point, so it finds it independently of the size of the expansion.

N. C. Bacalis (✉)
Theoretical and Physical Chemistry Institute, National Hellenic Research Foundation, Athens, Greece
e-mail: nbacalis@eie.gr

T. Onishi (ed.), *Theoretical Chemistry for Advanced Nanomaterials*,
https://doi.org/10.1007/978-981-15-0006-0_13

Keywords Configuration interaction · Excited states · Saddle point by minimization · Truncated wave function · LUMO

13.1 Introductory Remark

Suppose that we want to know the behavior of some material when we bring atoms close together, for example, we want to know the behavior of a catalyst or we want to invent a new battery. After the contact of the atoms, where will the electrons go? Will they be excited? How will they drive the surrounded nuclei? Will they go to the lowest unoccupied orbital of the ground state or to the highest occupied orbital of the excited state? When the charge transfer occurs in appropriate excited electronic states, the electrons are transferred to appropriate orbitals of the surrounding species. Therefore, we must know not only the excitation energy **but also the wave function of the excited state**. But, the excited states are saddle points in the Hilbert space, and the standard computational methods (except for some that aim to the saddle nature of the answer), based on the Hylleraas-Undheim and MacDonald (HUM) theorem [1], minimize the energy of the desired root of the secular equation, since in optimizing the "desired root," the other roots, all mutually orthogonal, get deteriorated. **However**, **a local minimum** (i.e., HUM) **cannot be simultaneously saddle point *in the same* restricted subspace**; therefore, the standard methods, finding a local energy minimum, do not find the saddle point sought, with a danger, if they use small truncated, supposedly easily comprehensible expansions, to get probably a deceiving answer. For this reason the standard methods resort to approaching the saddle point using huge expansions (rather inappropriate for large systems). We can use a proposed functional [2] that, even within small expansions, has minimum **at** the saddle point, successfully tested, up to now, by direct multidimensional minimization, which is hard to use and time-consuming. It will be much more beneficial to the scientific community, both theoretical and practical, if we try to transform it, so that it is solved, faster and safer, self-consistently, as we shall see below, but this has not been done yet. Presently we shall see the presentation of the functional along with some computational applications due to it, e.g., (i) immediately improving a ground state approximant if we know a better excited state saddle point approximant and (ii) avoiding "root flipping." Then, we shall see demonstrations, for excited He, using both Hylleraas coordinates and configuration interaction (CI) in standard coordinates, and for Li using CI.

13.2 Overview

In order to study electronic processes occurring via excited states, we must know not only the excitation energy but also the wave function of the excited state, which, as is well known, is a saddle point in the Hilbert space. The correct wave function

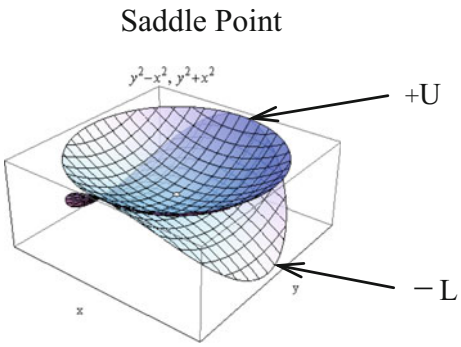

Fig. 13.1 E_n is a saddle point

is needed because if the computed wave function is away from the saddle point, incorrect conclusions may be deduced, concerning the physical process of charge transfer, i.e., of the main information needed both for the understanding of the electronic process and for the prediction of the path of the process, desired by any interested social-minded organization, private or public. This danger exists because we expand the wave functions in truncated bases, mimicking an ideal expansion in the complete orthonormal basis of the unknown exact Hamiltonian eigenfunctions, $\psi_0, \psi_1, \ldots (|0\rangle, |1\rangle, \ldots)$ with energies $E_0 < E_1 < \ldots$ (assumed in the present analysis normalized real and non-degenerate). That is, if these were known, we could expand in terms of them any normalized wave function, in particular an approximant $|\phi_n\rangle$ of the n^{th} excited state, as

$$|\phi_n\rangle = \sum_{i \neq n} |i\rangle \langle i|\phi_n\rangle + |n\rangle \sqrt{1 - \sum_{i \neq n} \langle i|\phi_n\rangle^2},$$

where the expansion coefficients $\langle i|\, \phi_n\rangle$ would be small. Then the energy would be

$$\langle \phi_n | H |\phi_n\rangle = E[\phi_n] = E = E_n - L + U \tag{13.1}$$

where the lower term, L, and the higher term, U, would be

$$L = \sum_{i<n} (E_n - E_i) \langle i|\phi_n\rangle^2 > 0, \quad U = \sum_{i>n} (E_i - E_n) \langle i|\phi_n\rangle^2 > 0, \tag{13.2}$$

which, in the Hilbert space (of the wave functions), are parabolas, the L downward and the U upward. In other words, the unknown sought exact eigenfunction, ψ_n, i.e., the stationary point of the parabolas, is a saddle point with n downward parabolas as indicated pictorially in Fig. 13.1.

Thus, the ground state, ψ_0 ($n = 0$), where the term L (with $n = 0$) does not exist, can be computed by minimizing the energy, $E = E_0 + U$, of a trial normalized approximant ϕ_0. And also, if the term L (with $n \neq 0$) were artificially absent, the excited states, ψ_n, could be computed similarly by minimizing the energy of

a normalized trial approximant ϕ_n, by orthogonalizing the trial function ϕ_n to all lower **exact** ψ_i, $i < n$ (if they were known), that would nullify all coefficients in L, $\langle i|\,\phi_n\rangle$=0, and would leave only the remaining term U to be minimized.

However, when, in the absence of the **exact** eigenfunctions, ψ_n, we have only normalized **approximants** ϕ_n (expanded in truncated bases, e.g., Gaussians), we cannot use orthogonalization to a **known** ϕ_0, approximant of ψ_0, not even to approach the 1st excited state ψ_1: Because, if (most probably) the – known – normalized approximant ϕ_0 is not exactly orthogonal to the – unknown – ψ_1, the orthogonal to ϕ_0 subspace (call this subspace $\{\backslash\Phi_0\}$) *does not contain* ψ_1 (see Fig. 13.2). Therefore, ψ_1 cannot be found orthogonally to the normalized **approximant** ϕ_0. So, the best achievement of a normalized trial ϕ_1 varied orthogonally to ϕ_0 (i.e. belonging to the subspace $\{\backslash\Phi_0\}$) is to be *closest* to ψ_1 in the subspace $\{\backslash\Phi_0\}$, i.e. with the largest overlap $\langle 1|\,\phi_1\rangle$. At the *closest,* here called ϕ_1^+, it has no other components out of the 2D space of $\{\phi_0, \psi_1\}$ (because any other components would diminish the largest overlap $\langle 1|\,\phi_1\rangle$), i.e. ϕ_1^+ is the Gram-Schmidt orthogonal to ϕ_0 in the 2D space of $\{\phi_0, \psi_1\}$:

$$\left|\phi_1^+\right\rangle = \frac{|1\rangle - |\phi_0\rangle\,\langle\phi_0|1\rangle}{\sqrt{1-\langle 1|\phi_0\rangle^2}};\quad \text{with}\quad E\left[\phi_1^+\right] = E_1 - \frac{E_1 - E\left[\phi_0\right]}{1-\langle 1|\phi_0\rangle^2}\langle 1|\phi_0\rangle^2. \tag{13.3}$$

Observe, however, that (if ϕ_0 is a reasonable approximant of ψ_0 with $E[\phi_0] < E_1$) the last (subtracted) energy term in Eq. (13.3), is positive, and ϕ_1^+, the *closest to the saddle point* ψ_1 in the orthogonal to ϕ_0 subspace, has **lower** energy than the exact E_1, without being any stationary point. Therefore, the minimization of the energy of ϕ_1 orthogonally to the known normalized **approximant** ϕ_0 will end up even lower, departing even more from the saddle point (of the sought excited ψ_1), farther than ϕ_1^+. The final (converged in minimization) function, being orthogonal to a reasonable ground state approximant, will not be collapsed to the ground state, but it will simply be veered away from the saddle point ψ_1. This problem has been known since the early application tries of quantum mechanics.

However, fortunately (for the energy – but "unfortunately" for the wave function) the theorem of Hylleraas-Undheim and MacDonald (HUM) [1] ensures that the $(n+1)^{\text{th}}$ root (eigenvalue) of the secular equation of the expansion coefficients in *truncated* basis, when varied, cannot take values below the **exact** (unknown) Hamiltonian eigenvalue, i.e., it has a **minimum** at (or just above) the exact value E_n. Thus, almost all computational methods of excited states (except some that aim to the saddle nature of the excited states, cf. [3–9]) are based on the HUM theorem, cf. [3–5, 10–65], achieving correct energies by **minimizing** the energy of the desired root. But **the finally converged point, being a *minimum, cannot be simultaneously a saddle point* in the same, restricted, subspace**; thus, only when the expansions are huge can the wave functions approach the exact excited state saddle point eigenfunctions (the larger, the closer to the exact). If they are truncated, not huge, "unfortunately," the HUM wave functions (themselves – not their energies) *avoid the saddle points* of the exact and unknown eigenfunctions, ψ_n, many times deceivingly.

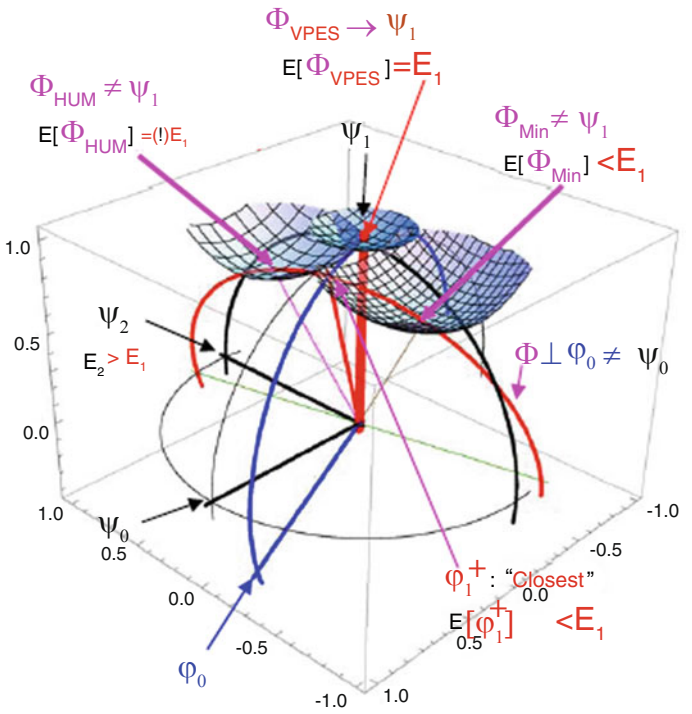

Fig. 13.2 Schematic representation of states. All states are assumed normalized: ψ_0, ψ_1, ψ_2, ... with energies $E_0 < E_1 < E_2 <$ ... are the unknown exact eigenstates; φ_0 is a known approximant of ψ_0. The subspace $S = \{\Phi, \varphi_1^+\}$ (red circle orthogonal to the blue circle of $\{\varphi_0, \psi_1\}$) is orthogonal to φ_0, and if φ_0 is not (accidentally) orthogonal to the unknown ψ_1, the subspace $S = \{\Phi, \varphi_1^+\}$ does not contain ψ_1. In the subspace $S = \{\Phi, \varphi_1^+\}$, the closest approximant to ψ_1 is φ_1^+ (the trace of the red on the blue cycle), and, as explained in the text, φ_1^+ lies below ψ_1: $E[\varphi_1^+] < E_1$. In going, while in S, orthogonally to φ_0, from φ_1^+ toward a state near ψ_2 (the green vector near ψ_2), i.e., in going, in S, from $E[\varphi_1^+] < E_1$ toward $E \approx E_2 > E_1$, one passes from E_1, i.e., from states, φ_1, of S, orthogonal to φ_0, but having energy $E[\varphi_1] = E_1$. If, in optimizing φ_1 by HUM theorem, φ_0 is the lowest (deteriorated, as explained in the text) root of the secular equation, then the 2nd "root," $\varphi_1 = \Phi_{HUM}$, is one of these states, "φ_1," with lowest possible energy $E[\varphi_1] = E[\Phi_{HUM}] = E_1$. But it is not ψ_1. It might be desirable to continue optimization in S toward, at least, φ_1^+, the closest, in S, to ψ_1. But HUM theorem forbids such a continuation, since the 2nd root must always be higher than E_1. In an attempt to approach, as much as possible, ψ_1, one might try, by other means, i.e., by direct minimization, to minimize the energy, in S, orthogonally to φ_0, toward φ_1^+. But φ_1^+ is not a critical point, and the minimum in S, orthogonal to φ_0, lies even lower: $E[\Phi_{Min}] < E_1$. Φ_{Min} does not suffer from variational collapse, since it is orthogonal to φ_0. Φ_{Min} is not a "bad" approximant of ψ_0: it is an approximant of ψ_1, probably as good (or as bad) as Φ_{HUM}. Both Φ_{HUM} and Φ_{Min} are veered away from φ_1^+, in S, and, therefore, from ψ_1. On the other hand, the here reported "variational principle for excited states" F_n (VPES) approaches ψ_1 (in general the exact excited states ψ_n), $\Phi_{VPES} \rightarrow \psi_1$, independently of the orthogonality to φ_0 (to lower lying approximants), and regardless of the accuracy of the latter, i.e., of their closeness to the exact saddle point, provided that the lower approximants, used in VPES F_n, are reasonable approximants, as explained in the text

Why "unfortunately"? Because by optimizing one root of the secular equation, all others get deteriorated: For example, the expansion of ψ_0 in the *truncated* basis of the roots – all mutually orthogonal to each other – Φ_0,Φ_1, ..., Φ_N, leaves an unknown remainder Y; therefore, even if we optimize ***at will*** one of them, say Φ_1, $\langle\psi_1|\,\Phi_1\rangle^2 \to 1$, we shall have

$$\langle\psi_0|\Phi_0\rangle^2 + \langle\psi_0|\Phi_1\rangle^2 + \langle\psi_0|\Phi_2\rangle^2 + \cdots + \langle\psi_0|\Phi_N\rangle^2 \leq 1 - Y^2$$
$$\Rightarrow \langle\psi_0|\Phi_0\rangle^2 < 1 - \langle\psi_0|\Phi_2\rangle^2 - \cdots - \langle\psi_0|\Phi_N\rangle^2 < 1$$

i.e., Φ_0 will be deteriorated, *without being able to approach* ψ_0 ***at will***, and the optimized Φ_1 will be orthogonal to a *deteriorated* Φ_0. So, if the expansion is large, then it tends to the exact eigenfunction, but if the expansion is small (necessarily for large systems, like molecules, catalysts, etc.), then, in a *truncated* basis, it is worse than just always being "$\Phi_1 \neq \psi_1$." For example, in a subspace of mainly two configurations, if the *deteriorated* normalized function is $\Phi_0 = \alpha\psi_0 + \beta\psi_1$ (+corrections), where β is not negligible, $\alpha < \sqrt{1-\beta^2}$, then the HUM-*optimized* (i.e., with $E[\Phi_1] > E_1$) $\Phi_1 = \alpha\psi_1 - \beta\psi_0$ (+corrections) *is equally deteriorated*, and the worse, it is not even close to Φ_1^+, which is *the closest to the saddle point* ψ_1, among all normalized functions orthogonal to Φ_0: $\Phi_1^+ = \left(\left(1-\beta^2\right)\psi_1 - \alpha\beta\psi_0\right)/\sqrt{1-\beta^2}$ (+corrections) with $E\left[\Phi_1^+\right] < E_1$, because the HUM theorem necessitates that the *optimized* root Φ_1 shall *not go below* E_1 (in order to try to approach Φ_1^+).

Therefore, the HUM-optimized root Φ_1 is much more away from the saddle point ψ_1, although its energy approaches E_1. (Since there are normalized functions Φ orthogonal to ϕ_0 with $E[\Phi] < E_1$, it will eventually lead to one of the infinitely many normalized functions having $E[\Phi] = E_1$. Indeed, doing the analysis from any function Ψ if we consider a normalized function $\phi_1^{\perp+}$ orthogonal to both ϕ_0 and $\phi_1{}^+$ and diagonalize the Hamiltonian operator between $\phi_1^{\perp+}$ and $\phi_1{}^+$, this will open their energy gap, giving eigenfunctions Ψ^- and Ψ^+ (both orthogonal to ϕ_0). Then the function

$$\Phi = \Psi^- \sqrt{\frac{E\left[\Psi^+\right] - E_1}{E\left[\Psi^+\right] - E\left[\Psi^-\right]}} \pm \Psi^+ \sqrt{\frac{E_1 - E\left[\Psi^-\right]}{E\left[\Psi^+\right] - E\left[\Psi^-\right]}}$$

is orthogonal to ϕ_0 and has ***equal to*** $\boldsymbol{E_1}$ energy $E[\Phi] = E_1$, **without being** $\boldsymbol{\psi_1}$. Even worse, from any Ψ, consider a normalized function $\Psi_\perp$ orthogonal to both ψ_0 and ψ_1. Then the function

$$\Phi = \sqrt{\frac{E\left[\Psi_\perp\right] - E_1}{E\left[\Psi_\perp\right] - E_0}}\psi_0 + 0\psi_1 - \sqrt{\frac{E_1 - E_0}{E\left[\Psi_\perp\right] - E_0}}\Psi_\perp$$

has ***equal*** *to* E_1 **energy:** $E[\Phi] = E_1$, but is **orthogonal, to** $\boldsymbol{\psi_1}$.) Thus, the only rescue of HUM optimization of a higher root, in order to approach the excited state

saddle point, is to use huge expansions ($\alpha \to 1$) (impracticable for large systems). The above are explained pictorially in Fig. 13.2.

However, in order to correctly comprehend charge transfer that will enable us to guide the applied research toward the correct and not (as seen below) toward a deceiving direction, we must find the *saddle point*, ψ_n, and, as explained above, with *truncated bases, this cannot be approached by neither orthogonal optimization (OO) nor by HUM optimization.* On the contrary, by both of these methods (OO, HUM), with *truncated* bases, *the saddle point* ψ_n, is avoided! (At least, by HUM the correct energy is approached). **For this reason, a safe approach of the saddle point, $\boldsymbol{\psi_n}$, is needed, using *truncated* bases, thus, allowing both an understanding and a correct prediction, of practical interest, about the behavior of the electrons concerning charge transfer.** Specifically:

Because, by HUM, the space spanned by a *small* basis is not completely exploitable, since, **necessarily**, normalized functions that are closer to the *saddle point* ψ_1 – and in general to ψ_n (i.e., with lower energy than the HUM answer, toward Φ_n^+) – are **excluded** (**forbidden**) by HUM, we shall see a developed functional, F_n [2], which has ***local minimum at the saddle points,*** ψ_n, which uses lower-lying normalized approximants Φ_i, $i < n$, but, practically, **does not depend on Φ_i's accuracy** (provided only that the Φ_is are reasonable):

$$F_n[\Phi_0, \Phi_1, \ldots; \Phi_n] \equiv E[\Phi_n] + 2\sum_{i<n} \frac{\langle \Phi_i | H - E[\Phi_n] | \Phi_n \rangle^2}{E[\Phi_n] - E[\Phi_i]} \left[1 - \sum_{i<n} \langle \Phi_i | \Phi_n \rangle^2\right]^{-1}. \tag{13.4}$$

As shown below, F_n has a *minimum* at each excited energy saddle point, even in pathological cases where at the excited eigenvalue there is no definite Hessian (to count its negative eigenvalues). As a "difficult" check, F_n easily passes the pathological Rellich test [5] of the Hermitian matrix:

$$\begin{pmatrix} -\sin x & \sin y \\ \sin y & \sin x \end{pmatrix} \begin{pmatrix} X \\ Y \end{pmatrix} = E \begin{pmatrix} X \\ Y \end{pmatrix} \Rightarrow E_{0,1} = \pm\sqrt{\sin^2 x + \sin^2 y}.$$

The "excited" E_1 has minimum at $x = 0$, $y = 0$ (as parameters), with indefinite Hessian there. The eigenvectors ψ_0, ψ_1 are easily computed:

$$\frac{Y_{0,1}}{X_{0,1}} = \frac{\pm\sqrt{\sin^2 x + \sin^2 y} + \sin x}{\sin y}, \quad \psi_{0,1}(x, y) = \begin{pmatrix} X_{0,1} \\ Y_{0,1} \end{pmatrix} / \sqrt{X_{0,1}^2 + Y_{0,1}^2}.$$

If we choose in F_1 (i.e., for $n = 1$), as fixed function, a **crude but reasonable** "ground state" expansion, in terms of $\{\psi_0, \psi_1\}$, namely, $\Phi_0 = 0.1\ \psi_1 + \psi_0\sqrt{1 - 0.1^2}$ (where 0.1 is "close" to 0, but, obviously, not too close) and if, by using this fixed function Φ_0, we minimize F_1 by optimizing $\Phi_1 = a\ \psi_1 +$

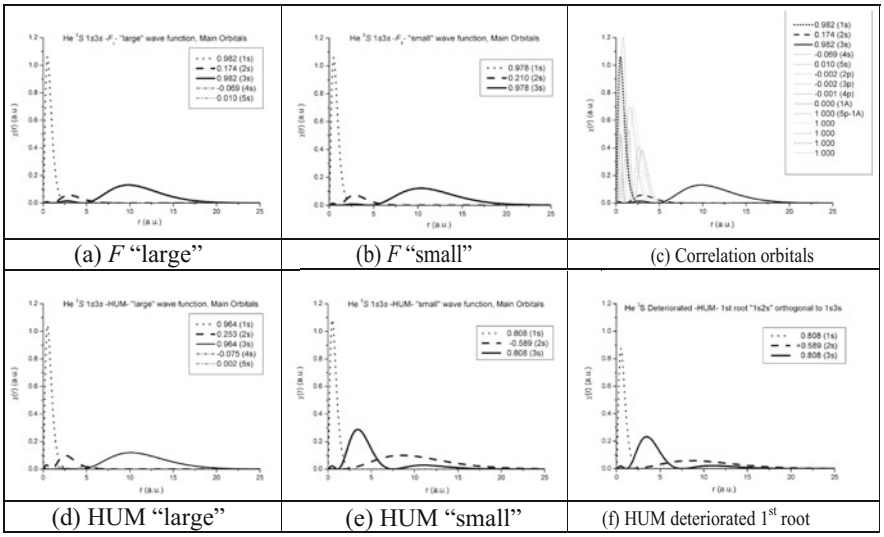

Fig. 13.3 CI wave functions (main orbitals): for $\mathbf{He^3}\boldsymbol{S1s3s}$. Dotted: 1*s*. Dashed: 2*s*. Solid: 3*s*. Clearly, the "large" expansions, either "*F*" (**a**) or HUM (**d**), are equivalent and have the same main orbitals as the *F* "small" (**b**), i.e., 1*s*3*s*, and the 2*s* just serves for dynamic correlation. However, the HUM "small" (**e**) is, incorrectly, mainly 1*s*2*s*, and the 3*s* "tries to improve" the wave function (and the energy) as static correlation, but by no means can 3*s* be taken as "LUMO" (and 2*s* as "HOMO") orbital. Note its orthogonal deteriorated HUM 1st "root" (**f**): they have the same main orbitals but with different signs. Note also that the "large" expansion needs static correlation corrections (from other CI terms) (**c**), to "split" electrons in areas where they are compacted together in the core. The diffuse orbital 3s essentially is not affected

$\psi_0\sqrt{1-a^2}$ with respect to the parameters $\{a, x, y\}$ around $(a, x, y) \sim (1, 0, 0)$, the resulting minimum is easily obtained correctly at $x = 0$, $y = 0$ (for any a).

The above F_1 has been successfully tested for excited states of the atoms He and C [2, 66] using large basis sets, where it agrees with bibliography and with our HUM – *large*-bases – computations, as well as *using small bases* for He, where, for example, it gives correct excited wave functions $1s3s\,(+\text{corrections})^1S\,or^3S$, whereas, on the contrary, small-bases-HUM gives, incorrectly, $1s\mathbf{2}s\,(+\text{corrections})^1S\,or^3S$ [2]. See also Fig. 13.3, where it is shown that, in optimizing the 2nd HUM root, the 1st root, Φ_0, is indeed deteriorated: It is *neither* $1s^2$ *nor* $1s2s$, the nodes are at unexpected "unphysical" distances from the nucleus, and the energy deviates significantly from the ground state energy. Its orthogonal **optimized** 2nd HUM root consists of the same "main" orbitals but with different signs, i.e., mainly $(\beta, -\alpha)$, although its energy **approaches** E_1, but remains above it, $E[\Phi] > E_1$, in accordance with the HUM theorem. It is not allowed to approach even Φ_1^+, *the closest to the saddle point* ψ_1 in the space orthogonal to the *deteriorated* Φ_0 (because Φ_1^+ has energy $E\left[\Phi_1^+\right] < E_1$). Thus, the optimized 2nd HUM root ***avoids*** *the exact saddle point eigenfunction* $\psi_1 = 1s3s$. This is clearly shown in Fig. 13.4, where the functional F_n [2], with a small basis, finds the

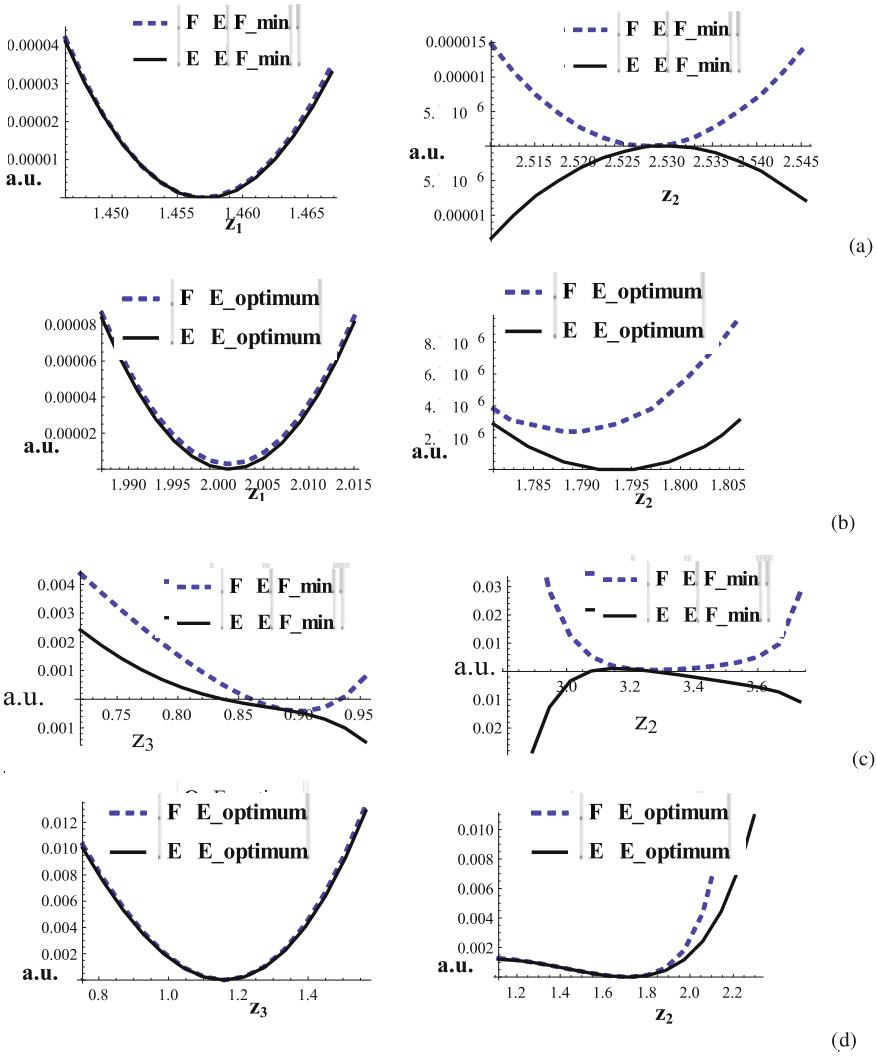

Fig. 13.4 **He^{3}S 1*s*3*s*.** (**a**) F_1 "small" expansion: Saddle point of energy at the F minimum. (**b**) HUM "small" expansion: Although the optimized 2nd root has "perfect" energy, it is not a saddle point and, of course, does not correspond to an F minimum. (**c**) F_1 "large" expansion: Saddle point of energy at the F minimum. (**d**) HUM "large" expansion: Although the optimized 2nd root has more "perfect" energy, it is not a saddle point

excited state saddle point, whereas the HUM optimization, with a small basis, does not find it, while, with a large basis, although HUM finds a minimum – as expected, not the saddle point – it approaches it more reasonably (the larger the basis, the better the approximation).

From Fig. 13.3 it is shown that the HUM optimization tries to correct the 2nd root as much as possible, via other orbitals (in the same small basis) as static (just descriptive) correlation corrections. Thus, although the **energy** may approach the correct eigenvalue E_1, the normalized **wave function** remains orthogonal to the *deteriorated* Φ_0, and far from Φ_1^+, and much farther from the saddle point ψ_1.

Similar results are found for Li ^{2}S and ^{4}S low-lying excited states (cf. Table 13.1).

Since the optimization of higher HUM roots fails for the *smallest atoms* He and Li, it does not provide any guarantee for larger systems, where, most probably, small basis sets are needed.

Presently, the direct minimization of the functional F_n has been tested by varying the parameters of the trial normalized expansion Φ_n (while the lower normalized approximants $\Phi_{i<n}$ must be kept unvaried), but this procedure is hard to use and is time-consuming. It is desirable, by nullifying (setting equal to 0) the derivatives of F_n with respect to the parameters, to reduce the minimization to an eigenvalue problem, so that the lowest eigenvalue would be used. This would be immediately accomplishable if the differentiation yielded a set of linear equations.

However, because of the form of F_n in the denominator, the Rayleigh-Ritz quotient yields a nonlinear system of equations of higher degree. Thus, there should be a plan to solve the problem self-consistently, i.e., to consider Φ_n in certain locations in the formula of the Rayleigh-Ritz quotient, except one location, as constant (initial guess), so as, by nullifying the (varied) derivatives, to use the lowest root as a new guess Φ_n in the other (artificially un-varied) locations, hoping to converge. A choice that has not been yet exhaustively tested, but seems to work efficiently, is to consider as initial guess (ig) all locations of the 2nd term of the F_n formula, except inside the quadratic term (because this term always converges quadratically), i.e., specifically,

$$F_n\left[\Phi_{ig},\Phi_n\right] \equiv E\left[\Phi_n\right] + 2\sum_{i<n} \frac{\langle \Phi_i | H - E\left[\Phi_{ig}\right] | \Phi_n\rangle^2}{E\left[\Phi_{ig}\right] - E\left[\Phi_i\right]} \left[1 - \sum_{i<n} \left\langle \Phi_i | \Phi_{ig}\right\rangle^2\right]^{-1}$$

which is of the form

$$F_n\left[\Phi_{ig},\Phi_n\right] \equiv \frac{\langle \Phi_n | H | \Phi_n\rangle}{\langle \Phi_n | \Phi_n\rangle} + 2Z\left[\Phi_{ig}\right] \sum_{i<n} \frac{\langle \Phi_i | H - E\left[\Phi_{ig}\right] | \Phi_n / \sqrt{\langle \Phi_n | \Phi_n\rangle}\rangle^2}{E\left[\Phi_{ig}\right] - E\left[\Phi_i\right]},$$

where Φ_n is yet unnormalized, and which reduces to a standard generalized eigenvalue problem:

$$F_n\left[\Phi_{ig},\Phi_n\right] \langle \Phi_n | \Phi_n\rangle \equiv \langle \Phi_n | H | \Phi_n\rangle + 2Z\left[\Phi_{ig}\right] \sum_{i<n} \frac{\langle \Phi_i | H - E\left[\Phi_{ig}\right] | \Phi_n\rangle^2}{E\left[\Phi_{ig}\right] - E\left[\Phi_i\right]}.$$

Table 13.1 The CI expansion of various excited states of Li ^{2}S and ^{4}S. The n^{th} optimized HUM root is indicated by n**r;** the n^{th} excited state saddle point, local minimum of F_n, is indicated by **f***n*; <*r*> is the RMS extent of the indicated orbital; **<f|r>**/NCI is the overlap of the corresponding wave functions consisting of NCI configurations. A 2nd derivative $E[\Phi]_{z_i z_i}$ (**<0** for the saddle point, >0 for the HUM root **minimum**) is shown with respect to the indicated variation parameter in the eighth column

Φ	Main configurations	$F_n[\Phi]$ (a.u.)	$E[\Phi]$ (a.u.)	<*r*> (a.u.)	<*r*> (a.u.)	<*r*> (a.u.)	$E[\Phi]_{z_i z_i}$ [a]	$\lvert\langle \mathbf{f}\rvert \mathbf{r}\rangle\rvert$/NCI
Li^2*S*								
f0 $1s^2 2s(= 1\mathbf{r})$	$0.996\ 1s^2 2s - 0.053\ 1s^2 3s$	−7.45	−7.45	1s: 0.69	2s: 4.13	3s: 1.29		1/18
$2\mathbf{r}1s^2 3s$	$0.838\ 1s^2\mathbf{2s} - 0.545\ 1s^2 3s$	−7.295	−7.296	1s: 0.64	3s: 4.93	2s: 11.3		[b]
f1 $1s^2 3s$	$0.935\ 1s^2 3s - 0.354\ 1s3s2s$	−7.31	−7.33	1s: 0.49	3s: 14.4	2s: 1.12	$\mathbf{z_3}$**: −0.003**	0.89/8
$2\mathbf{r}1s^2 3s$	$0.964\ 1s^2 3s - 0.264\ 1s^2 2s$	−7.298	−7.299	1s: 0.64	3s: 11.6	2s: 2.94	z_3: +0.002	[c]
$3\mathbf{r}1s^2 4s$	$0.820\ 1s^2\mathbf{3s} - 0.44\ 1s^2 4s$ -...	−7.25	−7.260	1s: 0.64	4s: 7.71	3s: 18.5		
f2 $1s^2 4s$	$0.974\ 1s^2 4s - 0.222\ 1s4s2s$	−7.285	−7.290	1s: 0.55	4s: 22.9	2s: 1.26	$\mathbf{z_4}$**: −0.016**	0.94/20
$3\mathbf{r}1s^2 4s$	$0.979\ 1s^2 4s + 0.188\ 1s^2 2s$	−7.264	−7.265	1s: 0.64	4s: 21.5	2s: 2.68	z_4: +0.020	
f3 $1s^2 5s$	$0.863\ 1s^2 5s - 0.490\ 1s^2 4s$	−7.250	−7.250	1s: 0.64	5s: 32.6	4s: 28.5	$\mathbf{z_3}$**: −0.0002**	0.99[d]/40
$4\mathbf{r}1s^2 5s$	$0.981\ 1s^2 5s + 0.165\ 1s^2 2s$	−7.248	−7.250	1s: 0.64	5s: 35.1	2s: 2.54	z_3: +0.0001	
Li^4*S*								
f0 1s2s3s(= 1**r**)	$0.993\ 1s2s3s + 0.112\ 1s2s4s$	−5.204	−5.204	1s: 0,58	2s: 2.56	3s: 8.95		1
2r 1s2s4s	$0.836\ 1s2s\mathbf{3}s - 0.547\ 1s2s4s$	−5.153	−5.154	1s: 0,57	2s: 2.70	3s: 18.6		[b]
f1 1s2s4s	$0.999\ 1s2s4s - 0.030\ 1s4s5s$	−5.147	−5.156	1s: 0,58	2s: 2.67	4s: 21.8	$\mathbf{z_2}$**: −0.624**	0.90/10
2r 1s2s4s	$0.961\ 1s2s4s + 0.273\ 1s2s3s$	−5.154	−5.154	1s: 0,58	2s: 2.58	4s: 18.8	z_2: +0.193	[c]
3r 1s2s5s	$0.580\ 1s2s\mathbf{3}s - 0.547\ 1s3s\mathbf{4}s$	−5.120	−5.123	1s: 0,57	2s: 5.17	3s: 39.5		
f2 1s2s5s	$0.999\ 1s2s5s + 0.035\ 1s4s5s$	−5.130	−5.136	1s: 0.58	2s: 2.66	5s: 39.3	$\mathbf{z_3}$**: −0.009**	0.79/10
3r 1s2s5s	$0.980\ 1s2s5s + 0.188\ 1s2s3s$	−5.134	−5.134	1s: 0.58	2s: 2.55	5s: 29.9	z_3: +0.156	

[a] 2nd derivative $E[\Phi]_{z_i z_i}$ at the **optimal point** with respect to the parameter z_i, indicated in each case, to check whether it is **saddle** for **f**n, or **minimum** for n**r** (indicating that the HUM root, n**r**, is **not** the **saddle point**)

[b] Initially we found this "optimized" 2nd root (for ^{2}S: $1s^2\mathbf{2}s$ instead of the expected $1s^2 3s$ – and similarly for the ^{4}S). These parameters are more appropriate to the ground state basis functions. Starting from this we minimized F_1 that changed the basis functions more appropriate to the excited state, getting $f1$; then, starting from $f1$ we found a better 2nd root, $2r$, more appropriate to the excited state basis functions, which we used for the comparisons

[c] Similarly for the 3rd root (for ^{2}S:$1s^2\mathbf{3}s$ instead of the expected $1s^2 4s$ – and similarly for the ^{4}S)

[d] The CI expansion is already large

After normalization, the normalized Φ_n is used as a new $\Phi_{ig} \leftarrow \Phi_n$, until convergence. Note that, this way, we need only the extra computation of $\langle \Phi_i | \Phi_n \rangle$ and $\langle \Phi_i | H | \Phi_n \rangle$, which is standard feature in most standard electronic structure codes, with Φ_n expanded in the chosen (presumably small) basis.

In other words, this would extend the known MCSCF (multi-configuration self-consistent field) methodology with a Rayleigh-Ritz quotient of not only the energy (of the 1st term of F_n) under the normalizing condition of the trial function but of the whole functional F_n. Note that now, having used the $\Phi_{i<n}$ lower, rather crude, approximants, the desired root of the resulting secular equation is the *lowest* root above the (n^{th} HUM root – δE) where δE should be a reasonably small quantity. (This precaution should be taken especially for the initial guess.)

Since the above self-consistency is presently still being tested, in the following demonstrations, for the linear part of the process, the optimization of the expansion coefficients minimizing F_n is performed on the 1st term of F_n while checking whether the 2nd term vanishes (being essentially Schrodinger's equation "dotted" on the unvaried $\Phi_{i<n}$). Thus, the lowest (not the n^{th}) HUM root, if it is above all lower-lying (crude) energies and if it does not nullify the 2nd term and is not a saddle point, is rejected. But, in this way (by checking every time), the correct local minimum may be missed, that is why a targeted but self-consistent nullification of the derivatives of the Rayleigh-Ritz quotient from F_n itself is rather needed.

If the method succeeds for larger atoms, then it could be extended to molecules and larger systems using CI expansions in standard Gaussian bases, so that it may be proven useful for large systems demanding small bases, appropriate for both time saving and easy understanding of the (small and comprehensible) wave functions. These, however, are future plans; here we shall see a presentation of F_n and some demonstrations of its applications.

13.3 The Construction of F_n

The central idea is to invert the sign of L in Eq. 13.1, in order to have all parabolas upward and then to make a continuation from the unknown exact set of $\{\psi_i\}$ to known approximants $\phi_{i<n}$.

Consider the energy (Eq. 13.1) of a normalized approximant ϕ_n of the n^{th} excited state, expanded in the exact eigenfunctions $\{\psi_i\}$

$$E[\phi_n] = E_n - L + U,$$

where L and U are the downward and upward paraboloids defined in Eq. 13.2.

Invert the sign of L to introduce the functional

$$F[\phi_n] = E_n + L + U;$$

now all parabolas are upward and $F[\phi_n]$ has a local minimum at ψ_n: $F[\phi_n] = E_n$.

Substitute from Eq. 13.1 the unknown quantities $E_n + U = E[\phi_n] + L$:

$$F\left[\phi_n\right] = E\left[\phi_n\right] + 2L; \tag{13.5}$$

now $F[\phi_n]$ is expressed in terms of only the lower exact eigenfunctions $\psi_{i<n}$ in paraboloid L, inverted upward. But all $\psi_{i<n}$ are unknown; suppose, however, that we already have computed normalized approximants $\phi_{i<n}$ for all $\psi_{i<n}$. Then make a continuation of $F[\phi_n]$ from $\psi_{i<n}$ to $\phi_{i<n}$.

Expand each $\phi_{i<n}$ in the $\{\psi_i\}$ basis, and obtain to leading order in coefficients

$$\begin{aligned} \langle\phi_i|\phi_n\rangle &= \langle i|\phi_n\rangle + \langle n|\phi_i\rangle + \cdots \\ \langle\phi_i|\,H\,|\phi_n\rangle &= E_i\,\langle i|\phi_n\rangle + E_n\,\langle n|\phi_i\rangle + \cdots\ . \end{aligned} \tag{13.6}$$

Solve Eq. 13.6 for $\langle i|\,\phi_n\rangle$, and substitute to each term of $L = \sum\limits_{i<n}(E_n - E_i)\,\langle i|\phi_n\rangle^2$ in Eq. 13.5 to get, to leading order, $L = \sum_{i<n}(E_n\langle\phi_i|\,\phi_n\rangle - \langle\phi_i|H|\phi_n\rangle)^2/(E_n - E_i)$, which suggests an examination, in terms the known *approximants* $\phi_{i<n}$, of the expression

$$S \equiv \sum_{i<n} \frac{\left(E\left[\phi_n\right]\langle\phi_i|\phi_n\rangle - \langle\phi_i|\,H\,|\phi_n\rangle\right)^2}{E\left[\phi_n\right] - E\left[\phi_i\right]}\ . \tag{13.7}$$

When both $\phi_i = \psi_\iota$ and [in Eq. (13.1)] $U = \sum\limits_{i>n}(E_i - E_n)\,\langle i|\phi_n\rangle^2 \to 0$, the quantity S of Eq. 13.7 reduces, as directly verified, to

$$S \equiv L\left(1 - \sum_{i<n}\langle\phi_i|\phi_n\rangle^2\right) \Rightarrow L = \frac{S}{1 - \sum\limits_{i<n}\langle\phi_i|\phi_n\rangle^2}.$$

Then, for $U \neq 0$ and for ϕ_n close to ψ_n, the functional $F[\phi_n]$ in Eq. 13.5 adequately behaves as

$$F_n\left[\phi_0, \phi_1, \ldots; \phi_n\right] \equiv E\left[\phi_n\right] + 2\sum_{i<n}\frac{\langle\phi_i|\,H - E\left[\phi_n\right]|\phi_n\rangle^2}{E\left[\phi_n\right] - E\left[\phi_i\right]}\left[1 - \sum_{i<n}\langle\phi_i|\phi_n\rangle^2\right]^{-1},$$

where the adequacy depends on the Hessian determinant, A_n^n, and its principal minors along the main diagonal, $A_n^{k<n}$, at $\phi_n = \psi_n$. According to the standard theorems of calculus (cf. Sylvester theorem), if ψ_n is still a critical point and $A_n^{k<n} > 0$, $A_n^n > 0$, then $F[\phi_n]$ has a local minimum at $\phi_n = \psi_n$.

Indeed, at $\phi_n = \psi_n$, $E[\phi_n] = E_n$, and the 2nd term vanishes because the operator becomes $(H - E[\phi_n])\phi_n = (H - E_n)\psi_n = 0$, (i.e., Schrödinger's equation) so that

$$F_n\,[\phi_0, \phi_1, \ldots; \psi_n] = E_n,$$

i.e., ψ_n *is* a critical point, the saddle point, ***regardless*** **of the quality of** $\phi_{i<n}$.

Incidentally, notice that, since E_n is a saddle point, the energy $E[\phi_n]$ of an approximant ϕ_n **is not necessarily an upper bound of** E_n; it must only be **an upper bound of** $(\boldsymbol{E_n - L})$: Since $E[\phi_n] + L - E_n = U > 0$, then $E_n - L < E[\phi_n]$, or

$$E_n - \sum_{i<n} (E_n - E_i)\,\langle i|\phi_n\rangle^2 < E\,[\phi_n]\,, \tag{13.8}$$

i.e., it may be *below* E_n (that is why the aforementioned "orthogonal" minimization (OO) does not "collapse"). This means that since, in practice, with a truncated expansion, the minimization procedure of F_n, within a tolerance, stops around (but not exactly at) ψ_n, if it stops at a side of upward parabola, we will have $E_n < E[\phi_n] < F_n$, but if it stops at a side of downward parabola, we will have $E_n - L < E[\phi_n] < E_n < F_n$. In this case, the final (converged) ϕ_n, although slightly below E[HUM] (by $\leq L$), will be certainly acceptable. The value of L could be estimated using accurate approximants $\phi_{i<n}$ and checked to be of the order of the tolerance.

Further, at $\phi_n = \psi_n$, if we denote by $\left|\phi_i^{\perp\{n\}}\right\rangle$ the projection of $|\phi_i\rangle$ on the subspace of the higher than-n eigenfunctions, the Hessian determinant is

$$A_n^n = 2^{n+1} \prod_{i=0}^{n-1} (E_n - E_i) \left(E\left[\phi_n^{\perp\{n\}}\right] - E_n\right) \times$$
$$\times \left\{ 1 + 2 \left[\begin{array}{l} n \sum\limits_{i=0}^{n-1} \langle n|\phi_i\rangle^2 + \\ + \sum\limits_{i=0}^{n-1} \dfrac{\left(E\left[\phi_n^{\perp\{n\}}\right] - E_n\right)\left(E\left[\phi_i^{\perp\{n\}}\right] - E_n\right) - \left(\left\langle \phi_i^{\perp\{n\}} \middle| H - E_n \middle| \phi_n^{\perp\{n\}} \right\rangle\right)^2}{(E_n - E_i)\left(E\left[\phi_i^{\perp\{n\}}\right] - E_n\right)} \left\langle \phi_i^{\perp\{n\}} | \phi_i \right\rangle^2 \\ - 2 \sum\limits_{i=0}^{n-1} \sum\limits_{j=i+1}^{n-1} \dfrac{\left((E_n - E_j)\langle j|\phi_i\rangle + (E_n - E_i)\langle i|\phi_j\rangle\right)^2}{(E_n - E_i)(E_n - E_j)} + O[\text{coefficients}]^3 \end{array} \right] \right\}, \tag{13.9}$$

and its principal minors are

$$A_n^{k<n} = 2^{k+1} \prod_{i=0}^{k} (E_n - E_i) \times$$
$$\times \left\{ 1 + 2 \left[\begin{array}{l} (k+1) \sum\limits_{i=0}^{n-1} \langle n|\phi_i\rangle^2 + \sum\limits_{j=k+1}^{n-1} \sum\limits_{i=0}^{k} \frac{E_n - E_i}{E_n - E_j} \langle i|\phi_j\rangle^2 + \sum\limits_{i=0}^{k} \dfrac{E\left[\phi_i^{\perp\{n\}}\right] - E_n}{E_n - E_i} \left\langle \phi_i^{\perp\{n\}} | \phi_i \right\rangle^2 \\ - \sum\limits_{j=k+1}^{n-1} \sum\limits_{i=0}^{k} \frac{E_n - E_j}{E_n - E_i} \langle j|\phi_i\rangle^2 - 2 \sum\limits_{i=0}^{k} \sum\limits_{j=i+1}^{k} \dfrac{\left((E_n - E_j)\langle j|\phi_i\rangle + (E_n - E_i)\langle i|\phi_j\rangle\right)^2}{(E_n - E_i)(E_n - E_j)} \end{array} \right] \right\}$$
$$+ O[\text{coefficients}]^3. \tag{13.10}$$

(For clarity in the above expressions, care has been taken to be expressed in terms of positive quantities.) In these expressions, if the lower approximants $\phi_{i<n}$ are accurate enough, the coefficients inside the "2[square brackets]" are normally small (squared: even smaller), and the factor of "1," before them, normally dominates over them, so that $A_n^{k<n} > 0$, $A_n^n > 0$. Therefore, if the lower approximants $\phi_{i<n}$, **without being very accurate**, fulfill the conditions $A_n^{k<n} > 0$, $A_n^n > 0$, the functional $F[\phi_n]$ has a local minimum at $\phi_n = \psi_n$. (In practice, if these conditions are not fulfilled, $F[\phi_n]$ drops down to $-\infty$).

It is important to note that **no orthogonality to the lower approximants $\phi_{i<n}$ has been assumed**, whatsoever; it is not needed, the functional $F[\phi_n]$ has a local minimum at $\phi_n = \psi_n$ for any **reasonable** $\phi_{i<n}$ (that would satisfy Eqs. 13.9 and 13.10). Also, as mentioned before, it is not necessary to compute and diagonalize the Hessian and count its negative eigenvalues to identify the saddleness at $\phi_n = \psi_n$.

However, a simple criterion of being at the saddle point is to compute the 2nd derivative of the energy $E[\phi_n]$ with respect to the parameters: There should be n down-parabolas. Of course, the corresponding 2nd derivatives of F_n would be positive.

13.4 Improving a Ground State Approximant ϕ_0 Via an Accurate ϕ_1

The central idea is that: if our approximant ϕ_1 is more accurate than an approximant ϕ_0, then diagonalizing the Hamiltonian between the two, opens their energy gap and improves ϕ_0 more than ϕ_1 (since ϕ_1 is more accurate than ϕ_0). Then repeat the process by working in the space orthogonal to ϕ_1, by diagonalizing between the new ϕ_0 and any function orthogonal to both ϕ_1 and the new ϕ_0, and so on, until no further improvement.

13.4.1 Improving ϕ_0 Orthogonally to the Exact ψ_1 (Analysis)

First, if we had the exact ψ_1, then we could immediately improve an approximant ϕ_0 orthogonally to ψ_1 [2]: In the subspace of $\{\phi_0, \psi_1,\}$, the highest Hamiltonian eigenvector, Ψ^+, is ψ_1 itself:

$$\Psi^+ = \psi_1. \tag{13.11}$$

The lowest, Ψ^-, is orthogonal to ψ_1,

$$\Psi^- = \phi_0^+ \equiv \frac{\phi_0 - \psi_1 \langle \psi_1 | \phi_0 \rangle}{\sqrt{1 - \langle \psi_1 | \phi_0 \rangle^2}}, \tag{13.12}$$

with energy

$$E\left[\phi_0^+\right] = E\left[\phi_0\right] - \frac{\left(E\left[\psi_1\right] - E\left[\phi_0\right]\right)\langle\psi_1|\phi_0\rangle^2}{1-\langle\psi_1|\phi_0\rangle^2} \leq E\left[\phi_0\right] \tag{13.13}$$

(i.e., Ψ^- is same or better than ϕ_0). Further, rotating ϕ_0^+ around ψ_1 would improve ϕ_0^+ as follows: Introduce (e.g., by one more configuration) a function $\phi_0^{(2+)}$ orthogonal to both $\{\phi_0^+, \psi_1\}$. Then, in the subspace of $\{\phi_0^+, \phi_0^{(2+)}\}$, (both orthogonal to ψ_1), the Hamiltonian opens their energy gap, so the lowest eigenvector $\Psi^- \equiv \phi_0^-$ has energy $E\left[\phi_0^-\right] \leq E\left[\phi_0^+\right]$, closer to $E[\psi_0]$ (in a three-dimensional function space $\{\psi_0, \psi_1, \psi_k\}$, this would be exactly $E[\psi_0]$ as directly verified). $E\left[\phi_0^-\right]$ could be further improved by further rotating around ψ_1 similarly: i.e., after introducing another function $\phi_0^{(3+)}$ orthogonal to both $\{\phi_0^-, \psi_1\}$ in the subspace of $\{\phi_0^-, \phi_0^{(3+)}\}$ (both orthogonal to ψ_1), the lowest Hamiltonian eigenvector is $\Psi^- \equiv \phi_0^{(2-)}$ with energy $E\left[\phi_0^{(2-)}\right] \leq E\left[\phi_0^-\right]$(even closer to $E[\psi_0]$) and so on.

Now let us consider the approximants.

13.4.2 Improving ϕ_0 Orthogonally to ϕ_1

Since ψ_1 is never exactly known, we can still improve ϕ_0 orthogonally to ϕ_1, our **best** approximant of ψ_1 (obtained either via F_1 or via a "large" HUM expansion), by first computing ϕ_0^+ orthogonal to our ϕ_1,

$$\phi_0^+ \equiv \frac{\phi_0 - \phi_1\langle\phi_1|\phi_0\rangle}{\sqrt{1-\langle\phi_1|\phi_0\rangle^2}}, \tag{13.14}$$

if the condition $E\left[\phi_0^+\right] \leq E\left[\phi_0\right]$ is attainable: Indeed, by expanding about ϕ_1, as directly verified, the condition $E\left[\phi_0^+\right] \leq E\left[\phi_0\right]$, to leading order, reads $(E_1 - E_0)\left(1-\langle\psi_1|\phi_0\rangle^2\right) \geq \left(E\left[\phi_0^{\perp\{1\}}\right] - E_0\right)\left\langle\phi_0^{\perp\{1\}}|\phi_0\right\rangle^2$, which is not impossible. Here, as defined in Eqs. (13.9) and (13.10), $\phi_0^{\perp\{1\}}$ is the normalized function, orthogonal to both $\{\psi_0, \psi_1\}$, collecting all higher than ψ_1 terms (the last terms forming U) of Eqs. (13.1) and (13.2) for $\phi_n = \phi_0$. For ϕ_0,ϕ_1 very close to ψ_0,ψ_1, as directly verified by expanding about ϕ_0 as well, the condition is satisfied when $\langle\psi_0|\phi_1\rangle^2 \leq \langle\psi_1|\phi_0\rangle^2$, i.e., when ϕ_1 attains better orthogonality to ψ_0 than ϕ_0 to ψ_1, which is essentially the original assumption that our ϕ_1 is more accurate than our ϕ_0.

In fact, if our ϕ_1 is close to ψ_1, then a 2×2 diagonalization of the Hamiltonian between ϕ_1 and ϕ_0 (or ϕ_0^+) should give as a higher eigenvector $\phi_1 \approx \psi_1$ unaffected

and as a lower eigenvector ϕ_0^+ itself as improved ϕ_0. This, by just a 2×2 diagonalization, is another simple criterion of being at the saddle point.

Incidentally, all other (small) components are less relevant, so that the opposite procedure of optimizing ϕ_1 orthogonally to ϕ_0 can lead to ϕ_1^{MIN}, unpredictably *far from* ψ_1, even orthogonal to ψ_1, with *still* $E\left[\phi_1^{\text{MIN}}\right] \underset{\sim}{<} E\left[\psi_1\right]$, as shown (as analysis) in the following counterexample: Even in the subspace $\{\psi_0, \psi_1, \psi_2\}$ (supposedly known for the present counterexample), the orthonormal trial functions $\phi_0 = a\psi_0 + 0\psi_1 + b\psi_2$ and $\phi_1 = b\psi_0 - a\psi_2$ with $a = \sqrt{\frac{(E_1-\varepsilon)-E_0}{E_2-E_0}}$, $b = \sqrt{\frac{E_2-(E_1-\varepsilon)}{E_2-E_0}}$, (small ε), where, by construction, ϕ_0 is orthogonal to ψ_1 and ϕ_1 is orthogonal to both ψ_1 and ϕ_0, have energies $\langle\phi_0|H|\phi_0\rangle = a^2E_0 + b^2E_2 =$, $E[\phi_0] = E_0 + E_2 - (E_1 - \varepsilon) > E_0$, and $E[\phi_1] = E_1 - \varepsilon$, while ϕ_0 may approximate ψ_0. (To make the counterexample numerical, consider He ^{1}S, for which it is known that, in a.u., $E_0 = -2.903$, $E_1 = -2.146$, $E_2 = -2.06$. In terms of $\{\psi_0\ (=1s^2)$, $\psi_1(=1s2s)$, $\psi_2(=1s3s)\}$ (supposedly known for the present counterexample), the function $\phi_0 = 0.9476\ \psi_0 + 0.3194\ \psi_2$ would have $E[\phi_0] = -2.832$, and the function $\phi_1 = 0.3194\ \psi_0 - 0.9476\ \psi_2$ *chosen orthogonal to both* ψ_1 *and* ϕ_0 would have $E[\phi_1] = -2.146 = E_1$ (i.e., it would be a function with the **energy** of ψ_1, although ***orthogonal*** to ψ_1), so that, any function orthogonal to the same ϕ_0, between this ϕ_1 and ${\phi_1}^+ = \psi_1$ (if ϕ_0 is orthogonal to ψ_1, the "closest" to ψ_1 is ψ_1 itself), could be a minimization result, ϕ_1^{MIN}, with arbitrary $\left\langle\psi_1|\phi_1^{\text{MIN}}\right\rangle$ and with $E_1 - \varepsilon \leq E\left[\phi_1^{\text{MIN}}\right] \leq E_1$. In this counterexample, *using* F_1 this danger would not exist: Minimization of F_1, for the same, not particularly accurate, unvaried ϕ_0 (0.3194 is not very small), by varying $\phi_1 = c\ \psi_0 + d\ \psi_2 + \psi_1\sqrt{1 - c^2 - d^2}$, yields: $c <$ tol$(=10^{-8})$ and $d <$ tol, i.e., $\phi_1 = \psi_1$, with $E[\phi_1] = -2.146$ [so that, from Eq. 13.14, $\phi_0^+ = \phi_0$]. Below we shall see an actual demonstration.

13.4.3 Further Improvement of ϕ_0

If $E\left[\phi_0^+\right] \leq E\left[\phi_0\right]$, then, by rotating around ϕ_1, as described above [after Eq. 13.13], since the Hamiltonian always opens the energy gap between mutually orthogonal functions (all orthogonal to ϕ_1), ϕ_0^+ can be further improved (until $\langle\psi_0|\,\phi_1\rangle^2 > \langle\psi_1|\,\phi_0\rangle^2$), by always computing the 2×2 eigenfunctions (both orthogonal to ϕ_1) and taking the lowest current eigenfunction Ψ^- as: $\phi_0^{(m-)} = \Psi^-$. (At any step, $\phi_0^{(m-)}$ could be used as a new ϕ_0 to improve ϕ_1 via F_1 of Eq. 13.4.) In the above example (using the above He values), rotating ϕ_0 around ϕ_1 immediately gives $\phi_0^{(1-)} = \Psi^- = \psi_0$ (and $\Psi^+ = \psi_2$). Below we shall see an actual demonstration, performing a few "rotating" cycles.

13.5 Identifying a Flipped Root Around an Avoided Crossing

When atoms approach each other, then at a certain nuclear separation for each pair of molecular electronic states (of the same symmetry), the Hamiltonian opens their energy gap, and an avoided crossing may occur, changing their order: In passing the crossing, the continuation of the ground state becomes excited, and the continuation of the excited state becomes lowest. At a **fixed** nuclear separation, **near** the crossing, the (avoided) exact and sought eigenstates ψ_0 and ψ_1 are **distinct**. However, their approximants ϕ_0 and ϕ_1 are computed by varying their (truncated) expansion parameters, and in the parameter space, also an avoided crossing occurs, because, for any set of their parameters, the Hamiltonian opens their energy gap. However, there is a significant difference between avoided crossing in the parameter space and avoided crossing in the nuclear separation space. In the nuclear separation space, the wave function in the united-atom limit is completely different than in the separated-atom limit. However, in the parameter space, if $\phi_1 \approx \psi_1$ is, say 1s2s, then, just beyond the crossing and away from the sought ψ_1, ϕ_1 is still 1s2s, but with slightly different values of the same parameters (i.e., of the exponents, of the expansion coefficients, etc.). Thus, during optimization, the new (last suggested by the optimization method) trial parameters do not provide any information as to whether they are beyond or before the crossing. And if, toward convergence, we consider as ϕ_1 the ϕ_0 (instead of ϕ_1, erroneously), just because, with the new (last suggested) trial parameters, ϕ_0 has flipped to be higher, i.e., beyond the crossing, then the computation gets lost. We should feed ϕ_1 **with the orbitals of $\boldsymbol{\phi_1}$** at the new (last suggested) trial parameters beyond the crossing, despite their flipping [9, 61, 64, 65, 67–78], i.e., **in spite of the fact that** at the new (last suggested) trial parameters, $\boldsymbol{\phi_1}$ **is lower than $\boldsymbol{\phi_0}$**. Root flipping may be avoided by an appropriate representation of the excited state, [65] but this may not be known in advance. If we do not know where the crossing is, we cannot identify the flipped functions by looking at the values of their parameters, but we can, by checking their (individually computed) F_1 using an **unvaried** (at least crude but reasonable) lower approximant of ψ_0, say Φ_0 (presumably unambiguously known from nearby nuclear separations): We shall see that: independently of whether ϕ_1 is, the 2nd (correct) or the 1st (flipped) root, by computing the two functionals $F_1[\Phi_0;\phi_1]$ and $F_1[\Phi_0;\phi_0]$, we will have

$$F_1\,[\Phi_0;\,\phi_1\,] < F_1[\,\Phi_0;\,\phi_0]\,. \tag{13.15}$$

Indeed: Consider the two lowest states [see also Ref. 75]. The eigenfunctions of the secular equation, "roots," depend on variational parameters $\mathbf{p}$ (both linear and nonlinear) to be optimized, and say the **optimal** functions are $\phi_0(\mathbf{p}_0)$, $\phi_1(\mathbf{p}_1)$. For example, in 1-electron hydrogen-like S-states $\phi_0(r) \sim e^{-\alpha Zr}$, $\phi_1(r) \sim (1 - \gamma Zr/2)e^{-\beta Zr/2}$, $\mathbf{p} = (\alpha, \beta, \gamma)$, so that at their F_1 minimum $\mathbf{p}_0 = (1, 0, 0)$, $\mathbf{p}_1 = (0, 1, 1)$. At the specified nuclear positions, under examination, ϕ_0, ϕ_1 are continuous functions of their parameters; their characteristics are maintained at

the region of any value of $\mathbf{p}$. Of course, we are seeking the **optimal** positions, in the parameter space, i.e., $\mathbf{p}_0$ for ϕ_0 and $\mathbf{p}_1$ for ϕ_1, ***not*** the position of the crossing, which is not the optimal. Now, it is important to realize that if there is no other crossing closer to $\mathbf{p}_0$ and $\mathbf{p}_1$ (otherwise we would consider the closest, judged by the overlap $\langle\Phi_0|\,\phi_0\rangle$), the **optimal** functions ϕ_0 (lower), ϕ_1 (higher) are unflipped *both* at $\mathbf{p}_0$ (where $\phi_0(\mathbf{p_0})$ is the lowest and all other roots (deteriorated) including $\phi_1(\mathbf{p}_0)$ are above it) **and** at $\mathbf{p}_1$ (where $\phi_1(\mathbf{p}_1)$ is excited, having the lower root(s) (deteriorated) below it, including $\phi_0(\mathbf{p}_1)$): Since $E_0 < E_1$, and at $\mathbf{p}_0$, $\phi_0(\mathbf{p}_0) \simeq \psi_0$ is the lowest lying, then every other root, including $\phi_1(\mathbf{p_0})$**,** lies higher, i.e., at $\mathbf{p}_0$, $E_0 \approx E[\phi_0(\mathbf{p}_0)] < E[\phi_1(\mathbf{p}_0)]$; also, at $\mathbf{p}_1$, $\phi_1(\mathbf{p}_1) \simeq \psi_1$, $E_1 \approx E[\phi_1(\mathbf{p}_1)] > E_0$, and any lower-lying root must describe (well or badly) the only lower-lying exact ψ_0 (or, in general, one of the lower lying $\psi_{i<n}$), i.e., it is the deteriorated approximant $\phi_0(\mathbf{p}_1)$, so, also, $E_0 < E[\phi_0(\mathbf{p}_1)] < E[\phi_1(\mathbf{p}_1)] \approx E_1$; otherwise, if we had $E[\phi_1(\mathbf{p}_1) \simeq \psi_1] < E[\phi_0(\mathbf{p}_1)]$, then $\phi_1(\mathbf{p}_1) \simeq \psi_1$ would not be excited, contrary to our assumption. Thus, the order $E[\phi_0(\mathbf{p})] < E[\phi_1(\mathbf{p})]$ holds at *both* ***optimal*** *positions* $\mathbf{p}_0$ (of ϕ_0) and $\mathbf{p}_1$ (of ϕ_1). Let us call the whole union of the $\mathbf{p}$-regions where $E[\phi_0(\mathbf{p})] < E[\phi_1(\mathbf{p})]$: "*in front of*" the crossing or "*before*" root flipping. Thus, both optimal positions $\mathbf{p}_0$ and $\mathbf{p}_1$ are located "*before*" root flipping. At the (closest) crossing (say at some value $\mathbf{p_c}$), since there is no other crossing in between, the characteristics of the roots $\phi_0(\mathbf{p}_0)$, $\phi_1(\mathbf{p}_1)$ in the region of $\mathbf{p_c}$ are maintained, i.e., they are continuous at $\mathbf{p_c}$. In the variational parameter $\mathbf{p}$-space, "root flipping" $E[\phi_0(\mathbf{p})] > E[\phi_1(\mathbf{p})]$ means that the parameters $\mathbf{p}$ are such that the continuation *behind* the crossing of the sought excited state ϕ_1 lies lower than the continuation of ϕ_0, *behind* the crossing, i.e., the **lower** "root" *behind* the crossing consists mainly, i.e., has, *behind* the crossing, mainly the characteristics, of the **sought excited** state wave function which we must detect and recognize, in order to extrapolate ***it*** (i.e., the "root" that is lower *behind* the crossing) by some method, e.g., by quasi-Newton, to regions *in front of* the crossing, close to $\mathbf{p}_1$ (where the unknown optimal $E[\phi_1(\mathbf{p}_1)]$ must occur – higher than $E[\phi_0(\mathbf{p}_1)]$), while the other root, that is higher beyond the crossing, must, beyond the crossing, mostly resemble the crude approximant $\Phi_0 \sim \phi_0(\mathbf{p}_0)$.

Near the crossing, let the indices "$-$"/"$+$" indicate "just before"/"just behind" the crossing, so that, while ϕ_0 and ϕ_1 are **continuous** near the crossing, i.e., $\phi_{0-} = \phi_{0+} = \phi_0$ and $\phi_{1-} = \phi_{1+} = \phi_1$, the higher (blindly taken) "2nd root," $\Phi_1^{\text{"}2r\text{"}}$, "just before" (unflipped) is $\Phi_{1-}^{\text{"}2r\text{"}} = \phi_{1-}$ and "just behind" (flipped) is $\Phi_{1+}^{\text{"}2r\text{"}} = \phi_{0+}$, whereas the lower (blindly taken) "1st root," $\Phi_0^{\text{"}1r\text{"}}$, "just before" (unflipped) is $\Phi_{0-}^{\text{"}1r\text{"}} = \phi_{0-}$ and "just behind" (flipped) is $\Phi_{0+}^{\text{"}1r\text{"}} = \phi_{1+}$. Now, near the crossing, by computing the two functionals $F_1[\Phi_0;\phi_1]$ and $F_1[\Phi_0;\phi_0]$, we have for the higher (blindly taken) "2nd root": $F_1\left[\Phi_0;\Phi_{1-}^{\text{"}2r\text{"}}\right] = F_1\left[\Phi_0;\phi_{1-}\right]$ and $F_1\left[\Phi_0;\Phi_{1+}^{\text{"}2r\text{"}}\right] = F_1\left[\Phi_0;\phi_{0+}\right]$, similarly for the lower (blindly taken) 1st root: $F_1\left[\Phi_0;\Phi_{0-}^{\text{"}1r\text{"}}\right] = F_1\left[\Phi_0;\phi_{0-}\right]$ and $F_1\left[\Phi_0;\Phi_{0+}^{\text{"}1r\text{"}}\right] = F_1\left[\Phi_0;\phi_{1+}\right]$. (These could be anyway recognizable from known $\mathbf{p}$-points a little away from the crossing, i.e., where unambiguously $F_1\left[\Phi_0;\Phi_1^{\text{"}2r\text{"}}\right] = F_1\left[\Phi_0;\phi_1\right]$ and $F_1\left[\Phi_0;\Phi_0^{\text{"}1r\text{"}}\right] = F_1\left[\Phi_0;\phi_0\right]$.) Now, the fixed Φ_0, independent of the presently

varied parameters, already optimized at its own energy minimum, is close to ϕ_0, i.e., $\langle\phi_0|\,\Phi_0\rangle^2 \sim 1 > \langle\phi_1|\,\Phi_0\rangle^2 \sim 0$, so, near the crossing, the denominators in Eq. 13.4 are $[1-\langle\phi_1|\,\Phi_0\rangle^2]^{-1} < [1-\langle\phi_0|\,\Phi_0\rangle^2]^{-1}$ (for the two lowest states $\ll$ holds), while the numerators in Eq. 13.4, $\langle\Phi_0|H-E[\phi_0]|\phi_0\rangle^2$, $\langle\Phi_0|H-E[\phi_1]|\phi_1\rangle^2$, remain finite. But, in optimizing the 2nd "root," the 1st "root" deteriorates. So, if the (supposedly good) lower approximant Φ_0 is better than the deteriorated $\Phi_0^{"1r"}$ near the crossing, i.e., if $E[\Phi_0] < E\left[\Phi_0^{"1r"}\right] \sim E\left[\Phi_1^{"2r"}\right]$, then the 2nd terms (i.e., the sums $2\sum \ldots$ – the "annexations," so to speak, to the energy) of both individually computed $F_1\left[\Phi_0;\Phi_1^{"2r"}\right]$ and $F_1\left[\Phi_0;\Phi_0^{"1r"}\right]$ are positive (cf. Eq. 13.4), and, due to the smaller denominator, the F_1 of (the continuous) ϕ_0 is normally **larger** than the F_1 of (the continuous) ϕ_1. Therefore, in passing the crossing, for the blindly taken 2nd root, we have that $F_1\left[\Phi_0;\Phi_1^{"2r"}\right]$ jumps up from $F_1\left[\Phi_0;\Phi_{1-}^{"2r"}\right] = F_1[\Phi_0;\phi_{1-}] = F_1[\Phi_0;\phi_1]$ to $F_1\left[\Phi_0;\Phi_{1+}^{"2r"}\right] = F_1[\Phi_0;\phi_{0+}] = F_1[\Phi_0;\phi_0]$:

$$F_1\left[\Phi_0;\Phi_{1-}^{"2r"}\right] = F_1[\Phi_0;\phi_1] < F_1[\Phi_0;\phi_0] = F_1\left[\Phi_0;\Phi_{1+}^{"2r"}\right], \tag{13.16}$$

while for the blindly taken 1st root, we have that $F_1\left[\Phi_0;\Phi_0^{"1r"}\right]$ jumps down from $F_1\left[\Phi_0;\Phi_{0-}^{"1r"}\right] = F_1[\Phi_0;\phi_{0-}] = F_1[\Phi_0;\phi_0]$ to $F_1\left[\Phi_0;\Phi_{0+}^{"1r"}\right] = F_1[\Phi_0;\phi_{1+}] = F_1[\Phi_0;\phi_1]$:

$$F_1\left[\Phi_0;\Phi_{0-}^{"1r"}\right] = F_1[\Phi_0;\phi_0] > F_1[\Phi_0;\phi_{1+}] = F_1\left[\Phi_0;\Phi_{0+}^{"1r"}\right]. \tag{13.17}$$

In both cases

$$F_1[\Phi_0;\phi_1] < F_1[\Phi_0;\phi_0].$$

Hence, near the crossing, if $E[\Phi_0] < E\left[\Phi_0^{"1r"}\right] \sim E\left[\Phi_1^{"2r"}\right]$, ***we can recognize ϕ_1: It is the (blindly taken) "root" that has the lowest (individually computed) F_1.*** Of course, it is a continuation of an unambiguous value of $F_1[\Phi_0;\phi_1]$ well before the crossing – if it is known. It might be possible to just check the closeness to Φ_0, or, for the n^{th} state, to check $\prod_{i<n}(1-\langle\Phi_i|\,\phi_n\rangle^2)^{-1}$ vs. $\prod_{i<n}(1-\langle\Phi_i|\,\phi_{n-1}\rangle^2)^{-1}$ because all terms are close to 1, except the one resembling some lower crude approximant $\Phi_{i<n}$, that would make it close to 0^{-1}, but this possibility needs future investigation. (Generally, the recognition of ϕ_1 could be used in MCSCF to feed the next iteration.)

Yet, by just recognizing ϕ_1 **at** the crossing, we have not found the sought **optimal** position of $\mathbf{p_1}$, which is "**before**" the crossing. Therefore, at every quasi-Newton cycle, we must "suggest" new trial **p** values that are "**before**" the crossing, without being stuck at the crossing. To ensure that we are not stuck at the crossing, we can use the procedure shown in Table 13.2, which extrapolates the quasi-Newton **p** values every three steps by twice the final step – or more if convergence is slow, the question being to decide, via F_1, whether a given value of **p**, near the crossing, is "before" or "beyond" the crossing.

Table 13.2 Three-step quasi-Newton (qN) extrapolation

```
if F1[Φ0;Φ^1st root(p)]< F1[Φ0;Φ^2nd root(p)] then
     n(p) ← 1
else
     n(p) ← 2.

if |p3-p2|>|p2-p1| then
     h ← p3
else
     h ← p3+(p3-p2).

if n(p1)≡1 then
     { p2 ← qN(p1) and
     if n(p2)≡1 then
            [ p3 ← qN(p2) and
            if n(p3)≡1 then
                  p ← h
            else if n(p3)(≡2)≠1 then
                  p ← qN(p3)
            ]
     else if n(p2)(≡2)≠1 then
            p ← qN(p2)
     }
else if n(p1)(≡2)≠1 then
     p ← qN(p1).
```

(Incidentally, note that **"state averaging"** ***at*** the crossing does not provide any information about the correct, and sought, optimal points $\mathbf{p}_0$ and $\mathbf{p}_1$ that must be located "***before***" the crossing.) The recognition is demonstrated below for 1-electron atomic ion S-states.

13.6 Demonstrations

Below demonstrations of the above are presented for He ^1S ($1s^2$ and $1s2s$), by using Hylleraas variables $s = r_1 + r_2$, $t = r_1 - r_2$ and $u = \left|\overrightarrow{r}_1 - \overrightarrow{r}_2\right|$ [1], so as to establish rather accurate basis-functions out of variationally optimized state-specific Laguerre-type orbitals [79], where the polynomial coefficients and exponents are optimized, allowing few term (small-size) series expansions in terms of $s^i(t^2)^j u^k$: For example, by selecting 24 terms up to 0.001 $s^2(t^2)^2u^3$, the obtained energy is $E_0 \simeq -2.90372$ a.u. However, for demonstration reasons, all 27 terms up to $s^2(t^2)^2u^2$ are used ($E_0 \simeq -2.90371$ a.u., $E_1 \simeq -2.14584$ a.u.), along with all 8 terms up to $s^1(t^2)^1u^1$ whose ϕ_0 will be immediately improved via the 27-term ϕ_1. (Pekeris' 9-term ϕ_1 is still unbound; he reports larger than 95 terms wave functions [80] – indicating that the present optimized Laguerre-type orbitals reduce the size efficiently.) Evidently, if E_1 were minimized, instead of F_1, the $2s$ Laguerre-type orbital $(1 - ar)\,\mathrm{e}^{-\zeta_1 r}$ would collapse to $1s$ ($a \to 0$, $\zeta_1 \to \zeta_0$), transparently showing E_1's "saddleness" at $|\phi_1\rangle = |1\rangle$.

In the next section, the formalism will be described (see [81] for *matrix elements of* $\langle\phi_i|\,\phi_n\rangle$, $\langle\phi_i|H|\phi_n\rangle$ *in Hylleraas coordinates*). Then, the results will be presented, including the immediate improvement of ϕ_0 via a more accurate ϕ_1. And then, a demonstration of recognizing a "flipped root" near the crossing will follow. After the demonstrations using the *Hylleraas coordinates* demonstrations for He and Li by conventional CI computation, appropriate for any number of electrons, will be presented.

13.6.1 Formalism in Hylleraas Coordinates

For two-electron atomic ions of nuclear charge Z, the wave function will consist of a single Slater determinant multiplied by a truncated power series of $s = r_1 + r_2$, $t = r_1 - r_2$, and $u = \left|\overrightarrow{r}_1 - \overrightarrow{r}_2\right|$: $\sum_{i_s,i_t,i_u=0}^{n_s,n_t,n_u} c_{i_s,i_t,i_u} s^{i_s} t^{2i_t} u^{i_u}$. Due to the spin antisymmetry, the Slater determinant is reduced to a symmetric sum of products and the power series to a symmetric function of t, i.e., of t^2. And since the Hamiltonian is also symmetric, the t-integrals could be evaluated only for $t > 0$ (eventually multiplied by 2), so that, with volume element $2\pi^2(s^2 - t^2)u\,dt\,du\,ds$, the limits of integration be $0 < t \le u \le s < \infty$ [82].

The spin-orbitals are composed of Laguerre-type radial orbitals, where their polynomial coefficients are treated as variational parameters [79]. For low-lying *singlet* states, only s- such orbitals will be considered. Thus, the spatial orbitals will be

$$\chi\left(n, r; z_n, \left\{a_{n,k}\right\}\right) = \frac{4\sqrt{\pi}\sqrt{(n-1)!n!}}{n^2} z_n^{3/2} \sum_{k=0}^{n-1} \frac{a_{n,k}(-2rz_n/n)^k \mathrm{e}^{-rz_n/n}}{k!\,(k+1)!\,(n-k-1)!}$$

where the variational parameters are z_n and $a_{n,k}$ factors [the latter are expected to have values near 1 (for $k = 0$, $a_{n,0} \equiv 1$)] for state-specific functions, allowing also the possibility for non-state-specific description: $a_{n,0} \equiv 1$, $a_{n,k>0} = 0$. (In wider parameter space, the free non-state-specific functions turn out to be slightly more accurate than the state-specific.) The prefactors assert orbital orthonormality for one-electron ions (all $z_n = \mathrm{Z}$ and all $a_{n,k} = 1$). The power series will be truncated at most up to the 2nd power, $s^2(t^2)^2u^2$, sufficient for the purposes of the present demonstrations.

The two-electron Hamiltonian in terms of the s, t, u variables is given, e.g., in Refs. [82] or [83], but:

(i) by selecting r_1 or r_2 via the sum $(1 - q)r_1 + qr_2$, $(q = 0, 1)$, (so that the symmetric sum of products be expressed as a monomial sum, e.g., $\sum_{q=0}^{1} \psi\left((1-q)\,r_1 + qr_2\right)\chi\left(qr_1 + (1-q)\,r_2\right)$),

(ii) by binomial expanding $r_{1,2}^k \sim (s \pm t)^k$,

(iii) by using $\left(s^2 - t^2\right)\varphi = \sum_{p=0}^{1} (-1)^p s^{2(1-p)} t^{2p} \varphi$, and,

(iv) by writing the required derivatives as $\frac{\mathrm{d}}{\mathrm{d}x}\left(x^n \mathrm{e}^{-zx}\right) = \sum_{b=0}^{1} [n\,(1-b) - zb]\, x^{n-1+b} \mathrm{e}^{-zx}$,

all terms can be reduced to monomial sums, so that the total symmetric two-electron function be written as

$$\phi\left(\overrightarrow{r}_1, \overrightarrow{r}_2\right) = \Phi^{\left(n_{1\Phi}, n_{2\Phi}, n_{s_\Phi}, n_{t_\Phi}, n_{u_\Phi}\right)}(s,t,u) = \frac{1}{\pi}\sqrt{\left(n_{1\Phi}-1\right)! n_{1\Phi}!}\,\sqrt{\left(n_{2\Phi}-1\right)! n_{2\Phi}!}\left(1 - \tfrac{1}{2}\delta_{n_{1\Phi}, n_{2\Phi}}\right)$$
$$\sum_{i_{s_\Phi}=0}^{n_{s_\Phi}} \sum_{i_{t_\Phi}=0}^{n_{t_\Phi}} \sum_{i_{u_\Phi}=0}^{n_{u_\Phi}} \sum_{k_{2\Phi}=0}^{n_{2\Phi}-1} \sum_{k_{1\Phi}=0}^{n_{1\Phi}-1} \sum_{q_\Phi=0}^{1} \sum_{j_{2\Phi}=0}^{k_{2\Phi}} \sum_{j_{1\Phi}=0}^{k_{1\Phi}} \Big[(-1)^{j_{1\Phi}+k_{1\Phi}+k_{2\Phi}}$$
$$(2q_\Phi - 1)^{j_{1\Phi}+j_{2\Phi}} n_{1\Phi}^{-2-k_{1\Phi}} n_{2\Phi}^{-2-k_{2\Phi}} z_{\Phi,n_{1\Phi}}^{\frac{3}{2}+k_{1\Phi}} z_{\Phi,n_{2\Phi}}^{\frac{3}{2}+k_{2\Phi}} \mathrm{e}^{-s\left(\frac{z_{\Phi,n_{1\Phi}}}{2n_{1\Phi}} + \frac{z_{\Phi,n_{2\Phi}}}{2n_{2\Phi}}\right)}$$
$$- t\left(\tfrac{1}{2} - q_\Phi\right)\left(\frac{z_{\Phi,n_{1\Phi}}}{n_{1\Phi}} - \frac{z_{\Phi,n_{2\Phi}}}{n_{2\Phi}}\right) s^{i_{s_\Phi} - j_{1\Phi} - j_{2\Phi} + k_{1\Phi} + k_{2\Phi}} t^{2i_{t_\Phi} + j_{1\Phi}}$$
$$+ j_{2\Phi} u^{i_{u_\Phi}} a_{\Phi,n_{1\Phi},k_{1\Phi}} a_{\Phi,n_{2\Phi},k_{2\Phi}} c_{\Phi,i_{s_\Phi},2i_{t_\Phi},i_{u_\Phi}}\Big] /$$
$$\left[j_{1\Phi}!\, j_{2\Phi}!\,(k_{1\Phi}+1)!(k_{1\Phi}-j_{1\Phi})!\,(k_{2\Phi}+1)!(k_{2\Phi}-j_{2\Phi})!\,(n_{1\Phi}-1-k_{1\Phi})!\,(n_{2\Phi}-1-k_{2\Phi})!\right]$$

where n_{i_Φ} is the degree of the associated Laguerre polynomial of the i^{th} spin-orbital in the Φ-Slater determinant (which is multiplied by the power series expansion). Hence, the total wave function is characterized by the set of integers $(n_1, n_2, n_s, n_t, n_u)$ (where $n_i - 1$ is the number of nodes of the i^{th} polynomial). Thus, the ground state's, $1s^2$, approximant is characterized by $(1, 1, n_s, n_t, n_u)$ and the 1st excited state's, $1s2s$, approximant, by $(1, 2, n_s, n_t, n_u)$ or equivalently by $(n_1 = 2, n_2 = 1, n_s, n_t, n_u)$, in state-specific description, or also by the 2nd root of "$(1, 1, n_s, n_t, n_u)a = 0$" in non-state-specific description (where "$a = 0$" means that all parameters $a_{n,k \neq 0} = 0$), and these can be calculated either by using (minimizing) the F functional – indicated by an index F, or not.

By applying Green's theorem in the integrals, in order to deal with first derivatives, Φ_s, Φ_t, Φ_u, instead of Laplacians, the Hamiltonian and overlap matrix elements are:

$$\langle \Phi | H | \Psi \rangle = 2\pi^2 \int_0^\infty \int_0^s \int_0^u \Big[-4Z\, s\, u\, \Phi\, \Psi + \sum_{p=0}^{1} (-1)^p (s^{2(1-p)} t^{2p} u\, (\Phi_s \Psi_s$$
$$+ \Phi_t \Psi_t + \Phi_u \Psi_u) + u^{2(1-p)} t^{2p} s\, (\Phi_u \Psi_s + \Phi_s \Psi_u) + s^{2(1-p)} u^{2p} t\, (\Phi_u \Psi_t + \Phi_t \Psi_u)$$
$$+ s^{2(1-p)} t^{2p} \Phi\, \Psi)\Big]\, \mathrm{d}t\, \mathrm{d}u\, \mathrm{d}s$$

and

$$\langle \Phi | \Psi \rangle = 2\pi^2 \int_0^{\infty} \int_0^{s} \int_0^{u} \sum_{p=0}^{1} (-1)^p s^{2(1-p)} t^{2p} u \ \Phi \ \Psi \ \mathrm{d}t \ \mathrm{d}u \ \mathrm{d}s$$

The integrals, of the form $J(z_s, z_t; n_s, n_t, n_u) = \int_0^{\infty} \int_0^{s} \int_0^{u} \mathrm{e}^{-z_s s - z_t t} s^{n_s} t^{n_t} u^{n_u} \mathrm{d}t \ \mathrm{d}u \ \mathrm{d}s$, are reported in [81].

13.6.1.1 F_n Minimization Procedure

To minimize F_n, the fixed lower approximants $\{\phi_i, i < n\}$ (that can be crude, but reasonable, needed to compute F_n) have been computed (independently of each other, and not necessarily orthogonal to each other, since, in F_n, Schrödinger's equation is "dotted" into them). For each (varied) value of the parameters z_n and $a_{n,k}$, the critical points of F_n (saddle points of E_n) are found, and F_n is minimized (*without* demanding orthogonality to the lower approximants .$\{\phi_i, i < n\}$ Orthogonality, among the functions that minimize each F_i, $i < n$, should be an outcome). In finding the saddle points of E_n, for certain trial values of the parameters z_n and $a_{n,k}$, the linear part, $\partial \langle \phi_n | H | \phi_n \rangle / \partial c_{i_s, 2i_t, i_u} = 0$, can be solved either by direct variation of the c-coefficients or, preferably, by reducing to a generalized eigenvalue problem (requiring $\langle \phi_n | \phi_n \rangle$ for normalization). Thus, the *lowest* eigenvalue (1*st root*) *above the known* (highest) $E[\phi_{n-1}]$ and the c-coefficients of its eigenvector are substituted in Eq. 13.4 of F_n, and improved values of z_n and $a_{n,k}$ are sought until minimization of F_n.

13.6.1.2 Establishing "Exact" Wave Functions ψ_0, ψ_1 and Truncated Approximants ϕ_0, ϕ_1

First a reliable wave function basis $|\psi_0\rangle \cong |0\rangle$, $|\psi_1\rangle \cong |1\rangle$ is established by taking 27 terms, i.e., up to $s^2(t^2)^2u^2$, $(n_s, n_t, n_u) = (2, 2, 2)$, adequate to achieve coincidence of the HUM and F_1 minima: ($E[\phi_0 \sim \psi_0] = -2.90371$ a.u., $z_0 = 1.9549$), ($E\left[\psi_1^{\mathrm{HUM}}\right] = -2.14584$, $z_{1,1} = 1.8348$, $z_{1,2} = 1.9745$, $a_{1,2,1} = 0$; or $E\left[\psi_1^{F_1}\right] = -2.14577$, $z_{1,1} = 1.930501$, $z_{1,2} = 1.827298$, $a_{1,2,1} = 0.799760$; $\left\langle \psi_1^{F_1} | \psi_1^{\mathrm{HUM}} \right\rangle = 0.99996$) – thus, going up to $(n_s, n_t, n_u) = (2, 2, 2)$ is sufficient. Then, in order to exhibit the aforesaid demonstrations, truncations up to $s^1(t^2)^1u^1$, $(n_s, n_t, n_u) = (1, 1, 1)$, i.e., 8 terms, will be used.

In F_1, a fixed 1-term normalized ϕ_0, i.e., up to $s^0(t^2)^0u^0$, $(n_s, n_t, n_u) = (0, 0, 0)$ ($z_0 = 1.6875$, $E[\phi_0] = -2.84766$ a.u.), is used.

13.6.1.3 Results

For He ($Z = 2$) ^1S, the exact eigenvalues are [80] $E_0 = -2.90372$ a.u., $E_1 = -2.14597$ a.u., $E_2 = -2.06127$ a.u.

The Lowest Orthogonal to ϕ_0 (OO)

Before proceeding to HUM and F_n results and their comparisons, it will be demonstrated that minimizing the excited state energy while keeping orthogonality to a normalized *approximant*, ϕ_0, of the ground state (e.g., the 1-term "fixed," used in F_1) leads to a function, ϕ_1^{LE}, lying lower than the exact, therefore veered away from the exact.

From a trial function ϕ (unnormalized), subtract its projection to (normalized) ϕ_0, to obtain the required normalized orthogonal, and its energy:

$$\phi_\perp \equiv \Phi_1 = \frac{\phi - \phi_0 \langle\phi_0|\phi\rangle}{\sqrt{\langle\phi|\phi\rangle - |\langle\phi_0|\phi\rangle|^2}} \; ;$$
$$\langle\Phi_1|\, H\, |\Phi_1\rangle = \frac{\langle\phi|\, H\, |\phi\rangle - 2\,\langle\phi_0|\, H\, |\phi\rangle\,\langle\phi_0|\phi\rangle + \langle\phi_0|\, H\, |\phi_0\rangle\,|\langle\phi_0|\phi\rangle|^2}{\langle\phi|\phi\rangle - |\langle\phi_0|\phi\rangle|^2}, \tag{13.18}$$

which will be used as a Rayleigh-Ritz quotient.

To obtain the energy minimum, either all parameters ({z},{a},{c's}) of the trial function ϕ can be varied, or only the nonlinear ({z},{a}) can be varied, while (for every trial {z},{a}) the linear part, {c}, can be reduced to a generalized eigenvalue problem $(\mathbf{A} - \lambda\mathbf{B}) \cdot \mathbf{c} = 0$, where $\mathbf{A}_{ij}$ are the coefficients of $c_i c_j$ of the numerator and $\mathbf{B}_{ij}$ of the denominator of the Rayleigh-Ritz quotient and where λ is a Lagrange multiplier, whose lowest value (1st root) is minimized by varying ({z},{a}). The corresponding lowest-lying eigenvector {c} provides the coefficients of ϕ, which, along with ({z},{a}), minimize $\langle\Phi_1|\mathrm{H}|\Phi_1\rangle$, to obtain the final ϕ_1^{LE}, by normalizing the function $\phi - \phi_0\langle\phi_0|\,\phi\rangle$.

After minimization of the above Rayleigh-Ritz quotient, (without using ψ_1 or $\phi_1{}^+$) ϕ_1^{LE} has energy -2.14762 a.u., certainly below the exact or of the above 27-term ψ_1, -2.14584. The 27-term minimizing function ϕ forms $\phi - \phi_0\langle\phi_0|\,\phi\rangle$, whose main orbital part has the form $(\upsilon(r_1)\chi(r_2) + \upsilon(r_2)\chi(r_1) - 1)\omega(r_1)\omega(r_2)$, where $\omega(r)$ is the 1s orbital of ϕ_0 (after normalization) and $\upsilon(r)$ and $\chi(r)$ are shown in Fig. 13.5. They remind 1s and 2s (where the 2s is more remote), which means that ϕ_1^{LE}, despite its lower energy, is not collapsed but, of course, is veered away from the exact.

(n_s, n_t, n_u) = (2, 2, 2): 27 Terms

First establish a reliable basis $|\psi_0\rangle \cong |0\rangle$, $|\psi_1\rangle \cong |1\rangle$, (27 terms) in order to compare (project on it) the truncated $(n_\mathrm{s}, n_\mathrm{t}, n_\mathrm{u}) = (1, 1, 1)$ 8-term approximants:

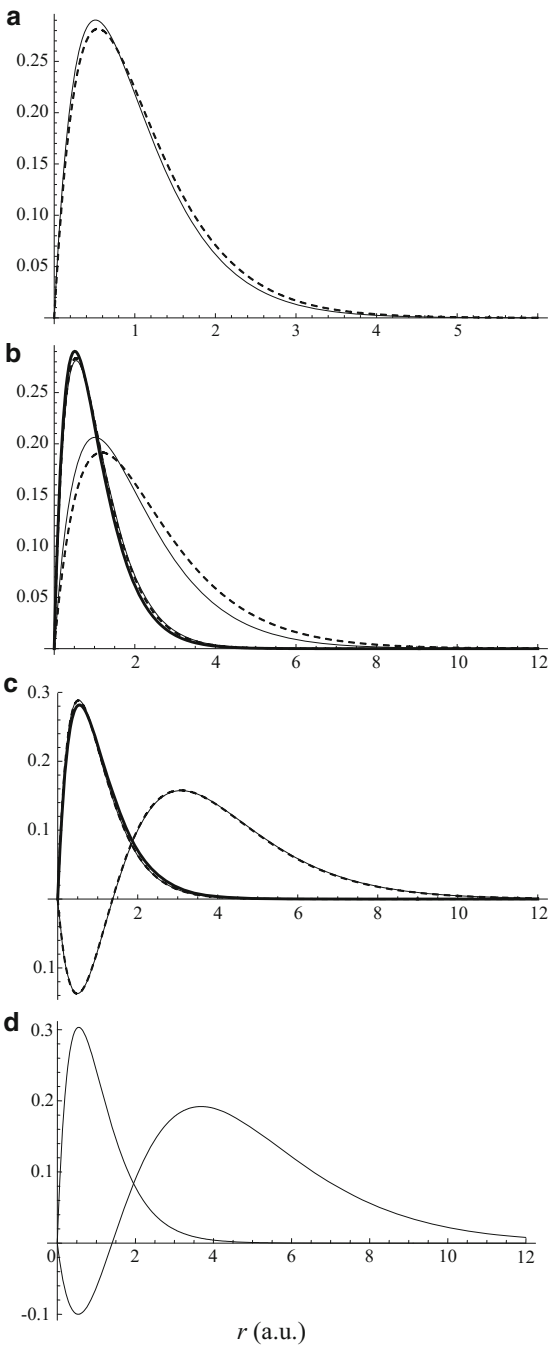

Fig. 13.5 Main orbitals of the 27-term (solid line) and 8-term (dashed line) optimal wave functions. (**a**) Ground state $1s^2$. (**b**) HUM excited state $1s1s'$ (either $a = 0$, or $a \approx 0$ as explained in the text, compared to $1s^2$. (**c**) F_1 excited state $1s2s$ compared to $1s^2$. (**d**) Lowest orthogonal to ϕ_0 (OO)

Table 13.3 Energies and overlaps of the computed states. Notation "tSzaR": $t = \{\psi$: 27 terms, Φ: 8 terms$\}$, $S = \{$via optimization of: 0: ground state, 1: excited state$\}$, $z = \{0: z_1$ only, 1: $z_1, z_2\}$, $a = \{0: a = 0, 1: a \neq 0\}$, $R = \{$0: 1st root, 1: 2nd root, H: HUM, F: $F_1\}$

Φ = tSzaR	E (a.u.)	$(\boldsymbol{\psi_0}\|\Phi)$	$(\boldsymbol{\psi_1}\|\Phi)$	$(\boldsymbol{\Phi 010H}\|\Phi)$
$\psi 0000 \rightarrow \boldsymbol{\psi_0}$	**−2.90371**			
($\psi 0001$)	(−2.1391)			
$\psi 0100$	−2.90371	1		
($\psi 0101$)	(−2.1306)			
$\psi 110H \rightarrow \boldsymbol{\psi_1}$	**−2.14584**	0.000172		
($\psi 1100$)	(−2.90327)			
$\psi 111F$	−2.14577	0.000457	0.99996	
$\boldsymbol{\phi_0}$ (1-term)	−2.84766	0.993		
$\Phi 0000$	−2.903121	0.999958	$1.3\ 10^{-5}$	
($\Phi 0001$)	(−2.01016)			
$\Phi 100H$	−2.07215	$1.97\ 10^{-5}$	0.875	
($\Phi 1000$)	(−2.89748)			
$\Phi 100F$	−2.07215			
$\Phi 010H$	**−2.903123**			
($\Phi 0101$)	(−2.0196)			
$\Phi 110H$	−2.14449			0.0026
($\Phi 1100$)	(−2.8886)			
$\Phi 110F$	−2.14449			
$\Phi 111H \rightarrow \boldsymbol{1s1s'}$	**−2.14449**	**0.0033**	**0.9986**	
$\Phi 111F \rightarrow \boldsymbol{1s2s}$	**−2.145152**	**0.00490**	**0.999807**	0.0186

Ground State 27 Terms

The optimized ground state approximant $0^{(1,1,2,2,2)}$ [cf. monosyllabic "tSzaR" = $\psi 0000$ in Table 13.3] has lowest root energy $E[0^{(1,1,2,2,2)}] = -2.90371$ a.u. and parameters $z_{0,1} = 1.954881$, and the 27 c-expansion coefficients are given in Ref. [81]. (The optimized 2nd root with the same $z_{0,1}$ is rather high: (tSzaR = $\psi 0001$), $E = -2.1391$ a.u.)

Also, by including the $z_{1,2}$ parameter, but $a_{1,2,1} = 0$, the optimized 1st root $0^{(1,2,2,2,2)a=0}$ (tSzaR = $\psi 0100$) has $E[0^{(1,2,2,2,2)a=0}] = -2.90371$ a.u., $z_{1,1} = 1.93945$, $z_{1,2} = 3.8926$ and corresponding c-expansion coefficients as given in Ref. [81]. (The optimized 2nd root with the same $z_{1,1}$, $z_{1,2}$ is rather high again: (tSzaR = $\psi 0101$) $E = -2.1306$ a.u.)

As seen in Fig. 13.6, the minimum is very flat, but indeed, within the accuracy of the computation ($\sim$ 6 digits[1]), the 2nd function has, as expected, $z_{1,2} = 2z_{1,1}$, i.e., both represent the same 1s orbital, with $\{c\}$ coefficients very similar to the 1st, and $\langle 0^{(1,1,2,2,2)}|\, 0^{(1,2,2,2,2)a=0}\rangle$=1. = ($\psi 0000|\psi 0100$). Among the above

[1]The computation is performed in 15 digit "double precision," but the coexistence in the secular matrix of very large numbers with small ones reduces the accuracy to $\sim$ 6 digits

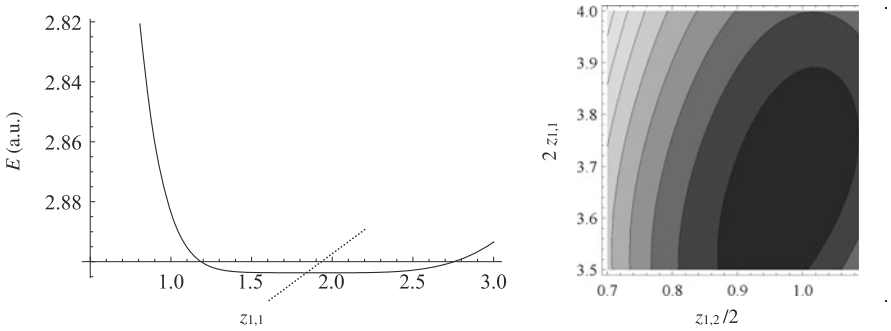

Fig. 13.6 1st root's energy (in a.u.) v.s. $z_{1,1}$ (left) and 2nd root's energy v.s. $z_{1,1}$, $z_{1,2}$ (right). Dotted line: Some other property might not have 0 slope at the (flat) energy minimum

two approximants representing the same unique ground state the simplest is used, $0^{(1,1,2,2,2)}$, (tSzaR = ψ0000), as a quite reliable approximant of ψ_0.

Incidentally, because of the flatness of the minimum, any traditional convergence criterion (e.g., $\delta E < \varepsilon = 10^{-6}$) can be easily satisfied anywhere between $1.5 < z_{1,1}$, < 2.3, so that any other property not having extremum at ψ_0 but rather would pass from it with a finite slope would be computed arbitrarily incorrectly; some reference could give it positive, while others would give it negative. The same comment holds also for the 1st excited state – [cf. below and Fig. 13.6] – which is also quite flat in varying the $z_{1,1}$, $z_{1,2}$ parameters. Thus the exact F minimum is required.

2nd HUM Root 27 Terms

The optimized 2nd HUM root $1^{(1,2,2,2,2)a=0}$ has (tSzaR = ψ110H) $E[1^{(1,2,2,2,2)a=0}]$ $= -2.14584$ a.u., $z_{1,1} = 1.8348$, $z_{1,2} = 1.9745$ and corresponding c-expansion coefficients as given in Ref. [81]. (Of course, this is orthogonal to its deteriorated 1st root Φ_0^{1r}, (tSzaR = ψ1100) $E = -2.90327$ compared to $E[0^{(1,1,2,2,2)}] = -2.90371$).

Its overlap is $\langle 0^{(1,1,2,2,2)} | 1^{(1,2,2,2,2)a=0} \rangle$=0.000172 = ($\psi$0000|$\psi$110H), and its main two orbitals are as in Fig. 13.5. However, these resemble 1s,**1s'**, rather than 1s,2s, but since its F-value is the same ($F - E = 3 \times 10^{-9}$), because its 27-term series is large, it can be considered close to the excited state saddle point.

Also, by allowing $a_{1,2,1} \neq 0$, the optimized 2nd HUM root has $a_{1,2,1} \approx 0$, introducing a node very far from the nucleus (rendering it *literally* "2"s!, but *essentially* 1s'), and its energy is negligibly better than the above with $a_{1,2,1} = 0$. Actually there is also another minimum at $a_{1,2,1} = 0.539$, with $E[1^{(1,2,2,2,2)}] = -2.126$ a.u. Although $z_{1,1} = 2.106$, $z_{1,2} = 2.478$, i.e., the *main* (without the series expansion) orbital 2s is orthogonal to the *main* 1s, this high lying function is rejected. This suggests that using a (perhaps habitual) criterion *of orthogonality of the* ***main*** *orbitals,* in computing excited states, ***is not sufficient***, because many random functions may have mutually orthogonal *main* orbitals.

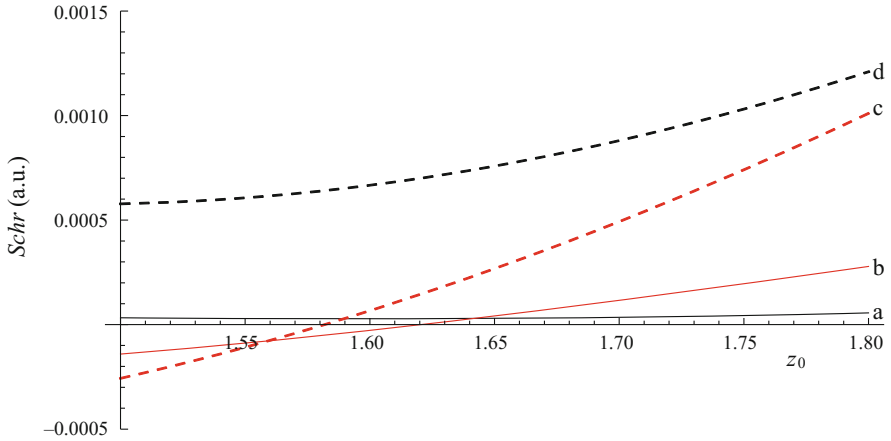

Fig. 13.7 The difference Schr $\equiv \langle 0^{(1,1,0,0,0)}|(H - E[\Phi])|\Phi\rangle$ vs. the exponent z_0 of normalized $0^{(1,1,0,0,0)}$, for optimized $\Phi = (a)$: $1^{(1,2,2,2,2)a=0}$ HUM 2nd root, (b) $1^{(1,2,2,2,2)F,a}$, (c) $1^{(1,2,1,1,1)F,a}$, (d) $1^{(1,2,1,1,1)a=0}$ HUM 2nd root

"F_1" Root, 27 Terms

The optimized "F_1" root $\Phi_1^F \Phi_1{}^{\rm F}$ (the 1st above the fixed $E[\phi_0] = -2.84766$ a.u.) has (tSzaR = ψ111F) $E[1^{(1,2,2,2,2)\rm F}] = -2.14577$ a.u., $(F - E = 3 \times 10^{-8})$ a.u., $z_{1,1} = 1.930501$, $z_{1,2} = 1.827298$, $a_{1,2,1} = 0.799760$, and corresponding c-expansion coefficients as given in Ref. [81]. Its main orbitals are as in Fig. 13.5, resembling $1s$, $2s$. It has overlap $\langle 0^{(1,1,2,2,2)}|\, 1^{(1,2,2,2,2)F}\rangle = 0.000457 = (\psi 0000|\psi 111\rm F)$ and $\langle 1^{(1,2,2,2,2)a=0}|\, 1^{(1,2,2,2,2)F}\rangle = 0.99996 = (\psi 110\rm H|\psi 111\rm F)$. Although their main orbitals differ, their series expansions, up to $(n_s, n_t, n_u) = (2, 2, 2)$**,** are large, and the two wave functions essentially coincide.

Checking the Satisfaction of Schrödinger's Equation

If these two functions Φ_1^{2r} and Φ_1^F are close to the exact, they should satisfy Schrödinger's equation for any normalized "ϕ_0" not orthogonal to Φ_1:

$$\text{Schr} \equiv \langle \phi_0 | \left(H\,|\Phi_1\rangle - E\,[\Phi_1]\,|\Phi_1\rangle \right) = \langle \phi_0|\, H\,|\Phi_1\rangle - E\,[\Phi_1]\,\langle \phi_0|\Phi_1\rangle \sim 0.$$

(In principle it might be possible for some $\langle\phi_0|$ to be accidentally almost orthogonal to *both* $|\Phi_1\rangle$ *and* $H|\Phi_1\rangle$, making Schr artificially small without Φ_1 being close to the exact, that could pull F_1 below E_1: $E < F_1 < E_1$. To avoid this, just use some other ϕ_0 for the same Φ_1.)

Using the above fixed ϕ_0, the Schr difference equals $\sim 3 \times 10^{-5}$ for Φ_1^{2r} and $\sim 8 \times 10^{-5}$ for Φ_1^F. Figure 13.7 shows the Schr difference for both Φ_1^{2r} and Φ_1^F, along with their more truncated versions (cf. below) $1^{(1,2,1,1,1)a=0}$ (Schr $\sim 8 \times 10^{-4}$) and $1^{(1,2,1,1,1)F}$ (Schr $\sim 4 \times 10^{-4}$), for various ϕ_0s, i.e., various values

of the exponent z_0. Indeed, Φ_1^{2r} has slightly better Schr values than Φ_1^F, contrary to the more truncated versions.

Thus, a quite reliable basis (27 terms) has been established, adequate for the attempted demonstration, by adopting $\{\psi_0 = 0^{(1,1,2,2,2)}, \psi_1 = 1^{(1,2,2,2,2)a=0}\}$, since the state-specific expansion, despite its more reasonable main orbitals, is slightly inferior in Schr than the expansion of the (large) HUM 2nd root.

$(n_s, n_t, n_u) = (1, 1, 1)$: 8 Terms

Minimal Basis

Ground State 8 Terms

The optimized ground state 8-term approximant $0^{(1,1,1,1,1)}$ has lowest root energy (cf. Table 13.3: tSzaR = Φ0000) $E[0^{(1,1,1,1,1)}] = -2.903121$ a.u. and parameters $z_{0,1} = 1.84250$, $c_{0,0,0,0} = 1$, $c_{0,0,0,1} = 0.290798$, $c_{0,0,1,0} = 0.190212$, $c_{0,0,1,1} = -0.0765151$, $c_{0,1,0,0} = 0.00688611$, $c_{0,1,0,1} = 0.0139948$, $c_{0,1,1,0} = 0.016833$, $c_{0,1,1,1} = 0.0120625$, normalization constant $N = 1/1.47861$, while its orthogonal 2nd root $1^{[0^{(1,1,1,1,1)}]}$ (same $z_{0,1}$) lies too high: (tSzaR = Φ0001) $E[1]^{[0^{(1,1,1,1,1)}]} = -2.01016$ a.u. Since $0^{(1,1,1,1,1)}$ has $\langle\psi_0|\, 0^{(1,1,1,1,1)}\rangle = 0.999958$ and $\langle\psi_1|\, 0^{(1,1,1,1,1)}\rangle = 1.3 \times 10^{-5}$, it is nearly "perfect." However, for the 1st excited state, as seen below, this truncation (1,1,1,1,1) is not adequate: A richer function (1,2,1,1,1) is needed.

2nd HUM Root and "F_1" Root 8 Terms

The optimized 8-term 2nd HUM root $1^{(1,1,1,1,1)}$ (see also Fig. 13.5) has (tSzaR = Φ100H) $E[1^{(1,1,1,1,1)}] = -2.07215$ a.u., $z_{1,1} = 1.44234$, and corresponding c-expansion coefficients $\{c\} = \{1, 0.199163, 0.0540545, 0.0273041, -0.418026, -0.0402484, -0.0720681, -0.040584\}$, $N = 1/1.3566$, while its orthogonal 1st root $0^{[1^{(1,1,1,1,1)}]}$ (same $z_{1,1}$) is, of course, deteriorated: (tSzaR = Φ1000) $E[0]^{[1^{(1,1,1,1,1)}]} = -2.89748$ a.u., $\{c\} = \{1, 0.145873, 0.160241, -0.0416745, -0.245673, -0.00154526, -0.0197971, 0.00659241\}$. The overlap between the normalized independently optimized approximants is $\langle 0^{(1,1,1,1,1)}|\, 1^{(1,1,1,1,1)}\rangle = -1.97349 \times 10^{-5} = (\psi_0|\Phi100H)$, meaning that the **HUM root** $1^{(1,1,1,1,1)}$ has contributions from other higher states orthogonal to the 1st root (its energy is close to the 3rd). The overlap with the above established $\psi_1 = 1^{(1,2,2,2,2)}$ is $\langle\psi_1|\, 1^{(1,1,1,1,1)}\rangle = 0.875$. By using F_1 the optimized "F" root $1^{(1,1,1,1,1)F}$ (tSzaR = Φ100F), in lack of other parameters, nearly coincides with the 2nd HUM root near the minimum.

Richer Basis

In a richer parameter space, including $z_{1,2}$ and, optionally, $a_{1,2,1} \neq 0$ (state-specific description), the optimized 8-term functions are as follows:

$a_{1,2,1} = 0$

HUM 1st Root 8 Terms, $a_{1,2,1} = 0$

The optimized 8-term HUM 1st root $0^{(1,2,1,1,1)}$ has (tSzaR = Φ010H) $E = -2.903123$ a.u, $z_{0,1} = 1.93393$, $z_{0,2} = 3.50164$, {c} = {1, 0.290154, 0.184912, −0.077204, 0.006390, 0.014435, 0.017008, 0.011521}, N = 1/2.94444, with 2nd root severely deteriorated (tSzaR = Φ0101), E = −2.0196 a.u. Thus, the 8-term $0^{(1,2,1,1,1)}$ is not essentially improved over the above simpler 8-term $0^{(1,1,1,1,1)}$.

HUM 2nd Root 8 Terms, $a_{1,2,1} = 0$

However, the optimized 8-term HUM 2nd root $1^{(1,2,1,1,1)}$ has (tSzaR = Φ110H) $E = -2.14449$ a.u., $z_{1,1} = 0.851359$, $z_{1,2} = 3.73405$ (or $z_{1,1} = 1.86703$, $z_{1,2} = 1.70272$), {c} = {1, 0.180637, −0.127452, 0.019460, −0.367640, −0.065135, −0.046299, −0.003814}, N = 1/3.19489, with 1st root deteriorated (tSzaR = Φ1100), E = −2.8886 a.u. The overlap $\langle 0^{(1,2,1,1,1)}|\, 1^{(1,2,1,1,1)}\rangle = 0.0026$ =(Φ010H|Φ110H).

"F_1" Root 8 Terms, $a_{1,2,1} = 0$

By minimizing F_1 (using the above fixed 1-term ϕ_0) first with $a_{1,2,1} = 0$, the same function is obtained, because the 1st root lies below ϕ_0 – and the lowest root above $E[\phi_0]$ is the 2nd root. [With $a_{1,2,1} = 0$ there are no other parameters to vary, and, as seen in the next subsection, with $a_{1,2,1} \neq 0$, a minimum of F_1 is obtained with the same ϕ_0 above; so, it is not necessary to use any lower (fixed) ϕ_0.]

$a_{1,2,1} \neq 0$

HUM 2nd Root, 8 Terms, $a_{1,2,1} \neq 0$

Using $a_{1,2,1} \neq 0$, the optimized 8-term HUM 2nd root $1^{(1,2,1,1,1)a}$, having $a_{1,2,1} = 1.5773 \times 10^{-7}$, remains essentially the same: (tSzaR = Φ111H) $E = -2.14449$, $z_{1,1} = 1.86703$, $z_{1,2} = 1.70272$. The main orbitals resemble $\mathbf{1}s\mathbf{1}s'$ (cf. Fig. 13.5). The overlaps with the above established $\psi_0 = 0^{(1,2,2,2,2)}$ and $\psi_1 = 1^{(1,2,2,2,2)}$ are $\langle\psi_0|\, 1^{(1,2,1,1,1)}\rangle = 0.0033$, and $\langle\psi_1|\, 1^{(1,2,1,1,1)}\rangle = 0.9986$.

Generally, in a complete (**infinite**) space, both HUM and F should yield the same wave function, but in a truncated space, the 2nd HUM root may be worse than the lowest root above the known (highest) $E[\phi_{n-1}]$. Indeed, in 8-term He_2 ^1S, *at* the F_1 minimum, the lowest three roots above the known 1-term $E[\phi_0] = -2.824$ are {−2.145, −2.028, −1.898}, whereas in optimizing the 2nd HUM root, the lowest three HUM roots are {−2.889, −2.144, −1.993} (As seen later in detail, F_1 yields $E[\phi_1] = -2.1452$, much closer to the exact −2.1459 than the 2nd HUM root $E\left[\phi_1^{2r}\right] = -2.144$, while its 1st HUM root, $E\left[\phi_1^{1r}\right] = -2.889$, is much deteriorated).

Obviously, fulfilling the inherent restrictions of the HUM functions [84], the 8-term 2nd HUM root $1^{(1,1,1,1,1)}$ has lower quality than $0^{(1,1,1,1,1)}$ ($\approx 0^{(1,2,1,1,1)}$) since $0.875^2 < (1 - (1.3 \times 10^{-5})^2)$, but also the optimized HUM 2nd root $1^{(1,2,1,1,1)a}$ has lower quality as well, since $0.9986^2 < 1 - (1.3 \times 10^{-5})^2$ – assuming near orthogonality (0.0026) to the optimized HUM 1st root.

"F_1"Root 8 Terms, $a_{1,2,1} \neq 0$

In contrast, by minimizing F_1, with the same set of parameters, ($z_{1,1}$, $z_{1,2}$, $a_{1,2,1}$), a much better 8-term approximant $1^{(1,2,1,1,1)F,a}$ is obtained: (tSzaR = Φ111F) $E = -2.145152$, $F = -2.145151$, $F - E = 5.3 \times 10^{-7}$, $z_{1,1} = 1.938718$, $z_{1,2} = 1.817736$, $a_{1,2,1} = 0.799286$, {c} = {1., 0.196506, 0.086316, −0.026204, 0.043226, 0.016366, 0.015810, 0.002479}, $N = 1/3.637910$, **where the main orbitals resemble 1*s*2*s*** [cf. Figure 13.5]. The overlap with the optimized 8-term HUM 1st root is $\langle 0^{(1,2,1,1,1)} | \, 1^{(1,2,1,1,1)F,a} \rangle = 0.0186 =$ (Φ010H|Φ111F). The corresponding overlaps with the above-established basis are $\langle \psi_0 | \, 1^{(1,2,1,1,1)F,a} \rangle = 0.00490$, and $\langle \psi_1 | \, 1^{(1,2,1,1,1)F,a} \rangle = 0.999807$. Clearly, the F_1-minimizing function, although truncated (to 8 terms), is much closer to the exact saddle point. This is also depicted in Fig. 13.7, where *it satisfies the Schrödinger equation better* (−0.0003 < Schr < 0.0009) *than the 8-term HUM 2nd root* (0.0006 < Schr < 0.0012).

13.6.1.4 The Main Orbitals: F_1 (and OO) Give 1*s*2*s*; HUM Gives 1*s*1*s*′

Observe that the HUM 2nd root's main orbitals are **1*s*1*s*′** and it is "corrected" by the c-series, the (OO) function, although veered away and below the saddle point (thus, abandoned) has correct main orbitals 1s2s (cf. Eq. 13.18 ff), whereas F_1 directly finds physically correct main orbitals **1*s*2*s*** (and better energy in truncated space). If this HUM phenomenon emerges already in a system of two-electrons, or three-electrons as foresaid and will be seen for Li (cf. Table 13.1), there is no guarantee (and might be more important) in **large systems**, where **small truncated space is unavoidable** and where the nature of the main (HOMO/LUMO) orbitals is decisive in order to **predict** or **cause** desired reactions; **then, the *F* functional will be needed**. The above energies and overlaps are summarized in Table 13.3.

13.6.1.5 Fulfillment of the Saddle Point Criteria by F_1 and Immediate Improvement of Φ_0

The functions obtained by F_1, fulfill the saddle point **criteria** mentioned in the introduction:

Firstly, to check ***the 27-term approximant* ψ_1**, a 2×2 ($H_{ij} - ES_{ij}$) generalized diagonalization between ψ_1 and the 1-term Φ_0 indeed leaves ψ_1 practically unaffected, as "high 2×2 root" $\phi_1 = (\psi_1 - 4.7 \times 10^{-5} \, \Phi_0)$, with energy changed by only 1.57×10^{-9} a.u, while, by opening their energy "gap," improves Φ_0

to the "low 2 × 2 root" $\phi_0 = (0.999\ \Phi_0 - 0.048\ \psi_1)$, with (indeed lower than $E[\Phi_0] = -2.84766$) energy: $E[\phi_0] = -2.84926$ a.u. differing from the energy of *the exact orthogonal to* ψ_1 (in the $\{\Phi_0, \psi_1\}$ subspace [cf. Eq. 13.13]) by -1.57×10^{-9} a.u. (which means that the "low 2 × 2 root" ϕ_0 is actually orthogonal to ψ_1). This verifies that ψ_1 is indeed very close to the exact excited saddle point eigenfunction and that ϕ_0, in order to further approach ψ_0, needs be rotated only orthogonally to ψ_1.

Similarly, a 2 × 2 diagonalization between ***the F_1 27-term Φ_1*** and the 1-term Φ_0 yields: $\phi_1 = (\psi_1 - 1.4 \times 10^{-4}\ \Phi_0)$, $E[\phi_1] - E[\Phi_1] = -1.34 \times 10^{-8}$ a.u., $\phi_0 = (0.999\ \Phi_0 - 0.048\ \psi_1)$, with lower energy: $E[\phi_0] = -2.84934$ a.u. differing from the energy of *the exact orthogonal to* Φ_1 (in the $\{\Phi_0, \Phi_1\}$ subspace [cf. Eq. 13.13]) by -1.34×10^{-8} a.u., which verifies that the F_1 27-term Φ_1 is also very close to the exact saddle point, as expected.

Now, to check F_1, a 2 × 2 diagonalization between **the *8-term Φ_1*** and the 1-term Φ_0 indeed leaves Φ_1 also almost unaffected, as "high root" $\phi_1 = (\psi_1 - 6.2 \times 10^{-4}\ \Phi_0)$, $E[\phi_1] - E[\Phi_1] = -2.69 \times 10^{-7}$ a.u., and, by opening their "gap," improves Φ_0 to the "low root" $\phi_0 = (0.999\ \Phi_0 - 0.052\ \psi_1)$, with lower energy: $E[\phi_0] = -2.84957$ a.u. differing from the energy of *the exact orthogonal to* Φ_1 (in the $\{\Phi_0, \Phi_1\}$ subspace [cf. Eq. 13.13]) by -2.69×10^{-7} a.u., which means that the "low 2 × 2 root" ϕ_0 is practically orthogonal to Φ_1 and verifies that Φ_1 $1s2s$ is indeed very close to the exact excited saddle point eigenfunction; ϕ_0 could still be further improved by rotating it orthogonally to Φ_1.

Repeating the check with ***the 8-term HUM 2nd root*** $1s1s'$ and the 1-term Φ_0, yields: $\phi_1 = (0.999\ \psi_1 - 1.2 \times 10^{-3}\ \Phi_0)$, $E[\phi_1] - E[\Phi_1] = -1.02 \times 10^{-6}$ a.u., $\phi_0 = (0.999\ \Phi_0 - 0.049\ \psi_1)$, with lower energy: $E[\phi_0] = -2.84937$ a.u. differing from the energy of *the exact orthogonal to* Φ_1 (in the $\{\Phi_0, \Phi_1\}$ subspace [cf. Eq. 13.13]) by -1.02×10^{-6} a.u., which verifies that 8-term HUM 2nd root $1s1s'$ is indeed **inferior** than the F_1 8-term $1s2s$ function.

Secondly, as shown in Fig. 13.8, ***F_1* has local minimum**, always above the energy, while (*thirdly*) the energy $E[\Phi_1]$ is a **saddle point at the minimum of *F_1***, showing that it has approached the exact excited state $1s2s$. For some parameters (z, c, etc.), the energy has local minimum, while for others ($a_{1,2}$) it has local maximum.

13.6.1.6 Quick Check of Reasonableness via the Main Orbitals and via 2nd Derivatives

Figure 13.5 shows the main orbitals of both the 27-term and the 8-term optimized wave functions of the HUM 2nd root and also of ϕ_1^{LE} (the lowest orthogonal to ϕ_0) and of F_1 excited state solutions, compared to the ground state. Observe that the HUM answer is $1s1s'$, instead of $1s2s$ (because $a_{1,2} \approx 0$, as mentioned above), and the HUM 8-term function deviates from the 27-term ψ_1, as anticipated in the introduction (also the HUM $1s$ orbital is, unexpectedly, slightly more *diffuse* than $1s^2$); therefore the HUM function is veered away from the exact, whereas the F_1 answer is indeed $1s2s$, the F_1 8-term function already almost coincides with the

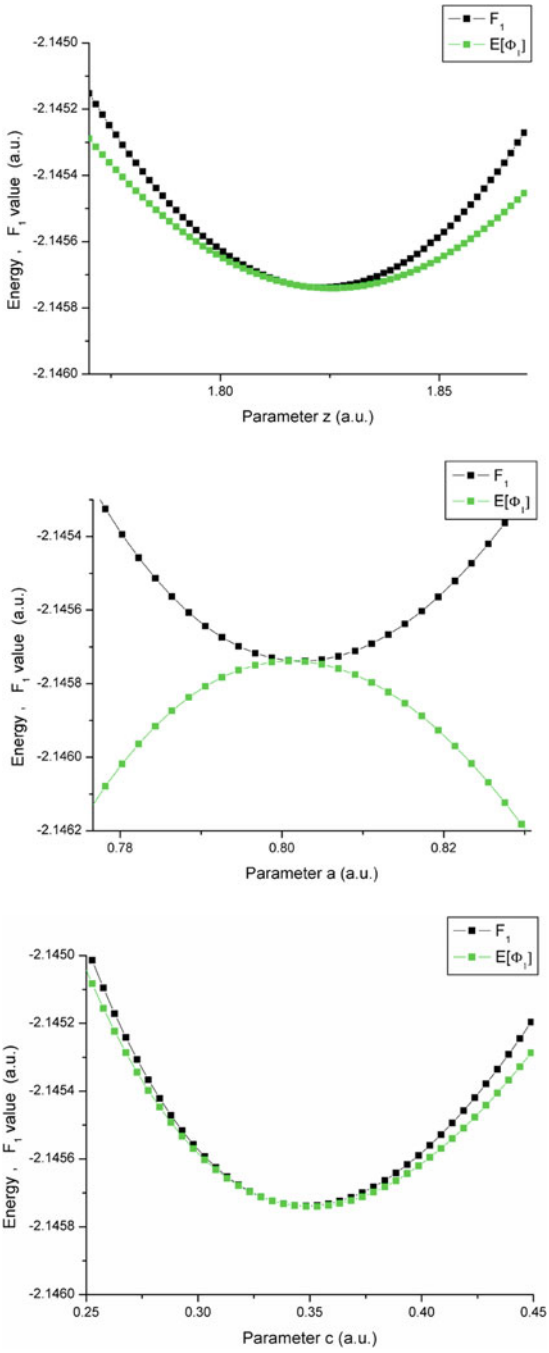

Fig. 13.8 The 27-term energy and the F_1 values (a.u.) near the minimum of F_1, versus: Top: a z-parameter ($z_{1,2}$). Middle: an $a \neq 1$-parameter ($a_{1,2}$). Bottom: a c-parameter ($c_{0,0,1}$). Always: $F_1 \geq E_1$

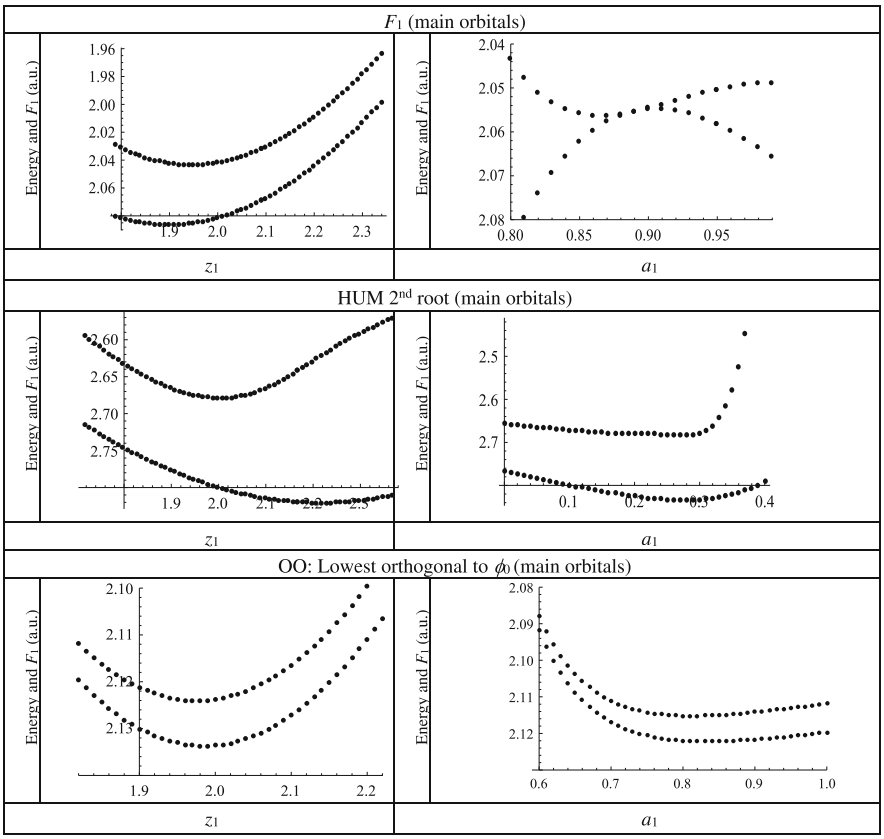

Fig. 13.9 The behavior of F_1 (upper curves in each frame) above the energy due to the *main-orbitals* (lower curves in each frame) (in a.u.) in varying z_1 (left frames) and a_1 (right frames). Upper frames: F_1 $1s2s$ approximant. Middle frames: HUM $1s1s'$ approximant. Lower frames: OO: the lowest orthogonal to ϕ_0, whose behavior (at the minimum) was expected, i.e., both F_1 and energy have minimum. But note that the HUM energies (and F_1) also have minimum (not saddle)

exact, and the F_1 $1s$ orbital is indeed more *compact* than $1s^2$, pushed toward the nucleus by the $2s$ electron, as intuitively expected.

Using F_1 we can quickly decide about the quality of the main orbitals. If the function of the main orbitals is close to the saddle point, then F_1 will have a minimum above it. Fig. 13.9 shows that F_1 behaves "reasonably" around the F_1 $1s2s$ 8-term main orbitals (i.e., without the series expansion), but neither HUM $1s1s'$ 8-term nor the 27-term (OO) lowest orthogonal to ϕ_0 behave "reasonably."

We shall see that similar results hold also for Li (cf. Table 13.1) where the 2nd derivative is also displayed, (positive for HUM, negative with respect to one parameter for F_n).

13.6.1.7 The Energy of ϕ_1^+ (the Closest to ψ_1 Orthogonal to ϕ_0)

Now, by using the above-established Φ_1^{2r} as ψ_1 and a truncated approximant of ψ_0 as ϕ_0, it is demonstrated that the corresponding $|\phi_1^+\rangle$ [cf. Eq. 13.3], i.e., the closest to ψ_1 while orthogonal to ϕ_0, lies lower than $E[\psi_1]$ (actually, than $E[\Phi_1^{2r}]$). Since the 8-term HUM 1st root $0^{(1,1,1,1,1)}$ is, as seen above, "almost perfect," $\langle\phi_0|\,1\rangle^2 = 10^{-10}$, $E\left[\phi_1^+\right]$ is lower than $E_1 = -2.14584$ by only 10^{-10} a.u., well beyond the accuracy of the present demonstration, so, a less accurate ϕ_0 will be used in the demonstration, e.g., the 1-term "fixed," used in F_1, with $\langle\phi_0|\,1\rangle = 0.04786$; then by replacing ψ_1 by Φ_1^{2r} in $|\phi_1^+\rangle$: $\langle\phi_1^+|\,H\,|\phi_1^+\rangle = -2.15470$ a.u., whereas by replacing it in the exact formula [cf. Eq. 13.3]: $E\left[\phi_1^+\right] = -2.14745$ a.u. The 0.3% discrepancy is due to the inexactness of Φ_1^{2r}. We expect that if the energy were further minimized while keeping orthogonality to this 1-term $\phi_0 = 0^{(0,1,0,0,0)}$, we should end up with a function orthogonal to this ϕ_0, lying lower than -2.15470 a.u. (if this were the correct value based on the exact ψ_1), veered well away from ψ_1. This is demonstrated below. If the deteriorated HUM 1st root, orthogonal to the optimized HUM 2nd root $1^{(12111)a=0}$, is used as ϕ_0, with $\langle\phi_0|\,1\rangle = -0.00405$, then the corresponding $\langle\phi_1^+|\,H\,|\phi_1^+\rangle = -2.14591$ a.u. (and by the exact Eq. 13.3: $E\left[\phi_1^+\right] = -2.14585$ a.u.), which is slightly below $E[\Phi_1^{2r}]$, while the exact eigenvalue is slightly even lower, which confirms that it is not necessary for the 1st root to approach ψ_0, $\phi_0 \to \psi_0$, although deteriorated, **only orthogonality to ψ_1,** $\langle\phi_0|\,\psi_1\rangle \to 0$**, is adequate**.

13.6.1.8 Comparison Between *F*, HUM, and the Lowest Orthogonal to ϕ_0 (OO)

Up to now it has been demonstrated that the optimized HUM 2nd root Φ_1^{2r} is veered away from the exact saddle point because it must be orthogonal to a deteriorated approximant of the ground state while lying higher than the exact (in accordance with the HUM theorem). Also, previously it was demonstrated that (OO) minimizing the excited state energy orthogonally to a normalized *approximant* ϕ_0, of ψ_0, leads to a function, ϕ_1^{LE}, lying lower than the exact (not collapsed), therefore, also veered away from the exact. Thus the F_1-minimizing function, $\phi_1^{F_1}$, is the most reliable truncated approximant among the three $\{\phi_1^{F_1}, \phi_1^{\mathrm{LE}}$, and $\Phi_1^{2r}\}$.

13.6.1.9 Remarks

1. If $\langle 1|\,\phi_0\rangle = 0$, then the three functions $\{\phi_1^{F_1}, \phi_1^{\mathrm{LE}}$, and $\Phi_1^{2r}\}$ coincide with ψ_1 and ϕ_1^+, because the orthogonal to ϕ_0 subspace will contain ψ_1; hence ϕ_1^+ will coincide with ψ_1: not lying lower. Thus the minimizing function ϕ_1^{LE} will coincide with ϕ_1^+ and, therefore, with ψ_1. Also, Φ_1^{2r}, having ϕ_0 as 1st root, will

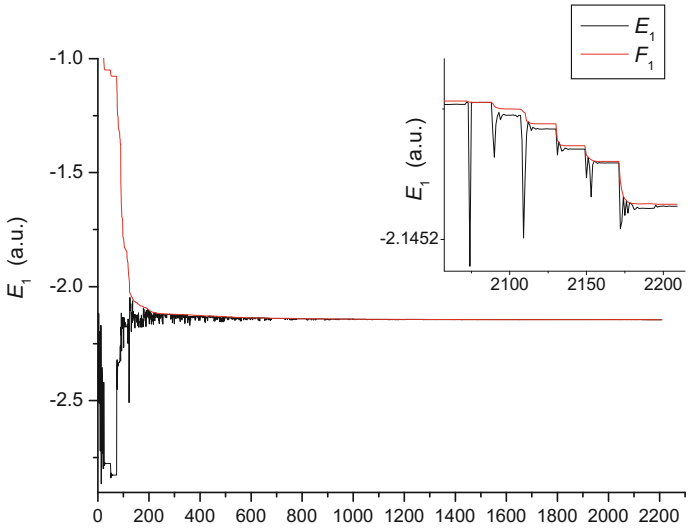

Fig. 13.10 The various (E,F) values visited in F_1-minimization, sorted by descending F_1. Observe that many E values are deceptively low, having large F_1 (the first points). Those having good F_1, e.g., the 2074th or the 2010th zoomed in the inset, may have acceptable wave function (see text). The correct is the last one

belong to the orthogonal subspace that contains ψ_1, and, since there is no other minimum than that of $\phi_1^{\mathrm{LE}} = \psi_1$, it will coincide with ψ_1. Therefore, for the three functions to coincide the condition $\langle 1|\,\phi_0\rangle \to 0$ suffices; it is not necessary to meet the condition $\phi_0 \to \psi_0$.

2. Finding the minimum of F_n is necessary: Fig. 13.10 shows all computed 8-term energy values, $E[\phi_1]$, in this work along their F_1 values, sorted by F. Of course, the first points have large F and low E, and the last points tend to the minimum of F_1. Nevertheless, some of the last points, as shown in the inset, have reasonable F_1, but rather low $E[\phi_1]$. The correct point is the last one at the minimum of F_1, where the E and F values coincide.
3. Since E_n is a saddle point, some wave functions ϕ_n near the F_n minimum are still acceptable even if they lie below E_n, as long as they lie above $E_n - L$ [cf. Eq. 13.8], or, in general, above the convex combination of all lower eigenvalues up to E_n, which is of the form $(1 - \sum_i a_i)E_n + \sum_i a_i E_i$; if the expansion coefficients (weights $a_i = \langle i|\,\phi_n\rangle^2$) are small, or $L < \varepsilon$ (an acceptable tolerance), the point is near E_n and ϕ_n is acceptably near ψ_n [79]. The value of L, already at such accuracies near the F_n minimum, can be easily checked. This criterion of validity holds for any ϕ_n, not necessarily obtained via F_n. For example, ϕ_1^{LE}, above, has $L = (E_1 - E_0)\left\langle 0|\phi_1^{\mathrm{LE}}\right\rangle^2 = 0.0018$, which is a quite large tolerance; therefore, ϕ_1^{LE} is rather unacceptable.

13.6.2 Demonstration of Identifying a "Flipped Root"

Let the ground and 1st excited state wave functions of a hydrogen-like ion be parametrized as

$$\psi_0(z_0; r) = a_0(z_0)\, \mathrm{e}^{-Z\, r\, z_0},\ \psi_1(z_1, g; r) = a_1(z_1, g)\, \mathrm{e}^{-z_1 Z\, r/2}\,(1 - g\ Z\ r/2)$$

where Z is the nuclear charge, z_0, z_1, g are variational parameters, and $a_0(z_0)$, $a_1(z_1, g)$ are normalization constants. These functions are not orthonormal, unless $z_0 = 1, z_1 = 1, g = 1$, when they form eigenfunctions of the Hamiltonian $H\psi_j(r) = -\psi_j''(r)/2 - \psi_j'(r)/r - Z\psi_j(r)/r$.

In their 2×2 subspace create an orthonormal basis

$$\Psi_0(r) = \psi_0(r), \quad \Psi_1(r) = (\psi_1(r) - \psi_0(r)\,\langle\psi_0|\psi_1\rangle)\,/\sqrt{1 - \langle\psi_0|\psi_1\rangle^2},$$

whose overlap matrix is $\delta_{i,j}$. In diagonalizing their Hamiltonian matrix $H_{i,j} = \int_0^\infty 4\pi r^2\, \Psi_i(r) H \Psi_j(r) \mathrm{d}r$, let the two normalized eigenfunctions be $\Phi^{1r}(r)$, $\Phi^{2r}(r)$, with their eigenvalues ("roots") depending on z_0, z_1, g.

Now, around $z_0 \approx 2$ a root crossing occurs for a wide range around $z_1 \approx 1$ and $g \approx 1$. Near and "before" the crossing the continuation of $\psi_0(z_0; r)$ is $\Phi^{1r}(r)$ and the continuation of $\psi_1(z_1, g; r)$ is $\Phi^{2r}(r)$, whereas "beyond" the crossing the continuation of $\psi_1(z_1, g; r)$ is $\Phi^{1r}(r)$ and the continuation of $\psi_0(z_0; r)$ is $\Phi^{2r}(r)$. The question is to decide, via F_1, whether a given value ("point") of (z_0, z_1, g), near the crossing, is "before" or "beyond" the crossing, in order to use the continuation, ε, of (always) $E[\psi_1(z_1, g; r)]$ in an optimization algorithm. (In the present demonstration Newton-Raphson (NR) is used: $\boldsymbol{\varepsilon}' := (\partial\varepsilon/\partial z_0, \partial\varepsilon/\partial z_1, \partial\varepsilon/\partial g) = 0$ is solved by proceeding iteratively to a new point $\mathbf{p} + \delta\mathbf{p} = \mathbf{p} - \mathbf{J}^{-1} \cdot \boldsymbol{\varepsilon}'$ – or less if the method diverges – having started at some point $\mathbf{p} = (z_0, z_1, g)$, where $\mathbf{J}$ is the Jacobian matrix, Hessian of ε [85].)

Thus, consider

$$F_1\left[\phi_0; \Phi^{nr}\right] = E\left[\Phi^{nr}\right] + 2\frac{(\langle\phi_0|\, H\, |\Phi^{nr}\rangle - E\left[\Phi^{nr}\right]\langle\phi_0|\Phi^{nr}\rangle)^2}{(E\left[\Phi^{nr}\right] - E\left[\phi_0\right])\left(1 - \langle\phi_0|\Phi^{nr}\rangle^2\right)}, \quad n = 1, 2$$

where the fixed predetermined (deliberately not very accurate) ground state approximant is $\phi_0\left(z_0^0; r\right) = a_0\left(z_0^0\right)\mathrm{e}^{-Z\, r\, z_0^0}$ with $z_0^0 = 1$–0.05. (By direct minimization, $F_1[\phi_0; \Phi^{2r}]$ is minimized to $F_1 \to E[\Phi^{2r}(r)] = E[\psi_1(1, 1; r)] = -0.125$ at $z_1 = 1$, $g = 1$, ($z_0 \approx 1$).) As explained above in the theory (cf. Eq. 13.15), among the two "roots," the continuation of the excited state, near the crossing, is the one with the lowest F_1. Indeed, for $Z = 1$, using (first traditionally) blindly the "2nd root," i.e., keeping ε to $E[\Phi^{2r}(r)]$, i.e., regardless of which n (n^{th} root) the lowest F_1 suggests, "root flipping" occurs: The sequence of Table 13.4 is obtained, even by using half NR-step.

Table 13.4 Root flipping: no convergence of the 2nd root

			n	E^{2r} (a.u.)
2.7	0.95	0.8	1	1.09915
1.89975	0.657935	0.618574	1	0.0312309
1.79561	0.457167	0.5843	2	−0.05816
1.81109	0.303372	0.471712	2	−0.0491109
1.88811	0.0253053	0.0834495	2	−0.0056792
−4.64705	1.13597	3.82639	1	14.4125
−4.64705	1.13597	3.82639	1	14.4125
−1.79846	0.463128	1.53227	1	3.19065
0.416586	−0.117902	−0.379791	2	0.0138916
0.647726	−0.168901	−0.60433	2	0.0232773
0.913718	−0.21854	−0.88652	2	0.0336386
1.15883	−0.254786	−1.19969	2	0.0428655
...	...	...	...	...

Table 13.5 Same as Table 13.4, but by consulting F_1

z_0	z_1	g	n	ε (a.u.)
2.7	0.95	0.8	**1**	−0.142331
2.62754	0.95588	0.907362	1	−0.127151
2.37234	0.971824	0.98181	1	−0.124935
1.92938	0.992178	1.00683	1	−0.125094
1.3233	1.02512	0.953813	**2**	−0.124875
1.18358	1.01644	0.958059	2	−0.12496
1.07193	1.01041	0.964645	2	−0.124988
0.980565	1.00646	0.97107	2	−0.124997
0.905827	1.00399	0.976612	2	−0.124999
0.844753	1.00248	0.981153	2	−0.125

On the contrary, by consulting F_1 the continuation of the excited state is recognized near the crossing and is used (until finally, at convergence, only $n = 2$, the 2nd root, is suggested by the lowest F_1) [cf. Table 13.5].

Observe that at the beginning, "beyond" the crossing, the lowest F_1 dictates to use, for the next step, the (**lower than E_1**) value of $\varepsilon = E[\Phi^{1r}(r)]$ ($n = 1$, the lowest function at that point).

Similarly, using blindly only the 2nd root (regardless of which n is dictated by the lowest F_1) and starting again "beyond" the crossing ($n = 1$), Table 13.6 is obtained. In this case, despite the original irregularities due to root flipping, the 2nd root finally happened to remain "before" the crossing ($n = 2$) and converged (0.3 of NR-step was used.)

By starting from the same point but by consulting F_1 no irregularities occurred [cf. Table 13.7].

Note that finally, near the minimum of the 2nd root where $E[\Psi_1(\mathbf{p}_1)] > E[\Psi_0(\mathbf{p}_1)]$, "before" the crossing, the convergence *should* use the 2nd root. If (and when), while in $n = 1$, it were stuck approaching a point of the 1st root, i.e., "beyond" the crossing, the NR-step should be increased somewhat in the direction of the last

Table 13.6 Accidental convergence of the 2nd root

z_0	z_1	g	n	E^{2r} (a.u.)
2.7	1.2	1.1	1	0.99477
2.20242	0.940034	0.917342	1	0.256091
1.89495	0.731999	0.818135	1	−0.0551044
1.58749	0.523964	0.718929	2	−0.0866029
−3.05737	−10.9139	−12.3444	1	69.042
−2.07399	−7.38161	−8.30417	1	33.6488
−1.38465	−4.90769	−5.47902	1	16.3024
−0.695314	−2.43378	−2.65387	1	5.07481
−0.695314	−2.43378	−2.65387	1	5.07481
−0.414382	−1.43604	−1.53652	1	2.2856
−0.214196	−0.731385	−0.76036	1	0.910672
−0.0140099	−0.0267279	0.0157957	2	0.0214185
0.164968	0.31467	−0.18661	2	−0.0598432
0.326748	0.626253	−0.334901	2	−0.103163
0.401263	0.771636	−0.381191	2	−0.116354
...	...	...	...	...
0.518132	1.00162	−0.429903	2	−0.124998
0.516411	0.998281	−0.42876	2	−0.125

Table 13.7 Same as in Table 13.5, but by consulting F_1

z_0	z_1	g	n	ε(a.u.)
2.7	1.2	1.1	**1**	−0.119716
1.93961	1.03415	0.976157	1	0.126188
1.76764	0.886719	1.08156	**2**	−0.121279
1.61807	0.892447	1.16453	2	−0.121751
1.41702	0.918759	1.21697	2	−0.123372
1.20892	0.9443	1.21744	2	−0.124476
1.04199	0.963778	1.18615	2	−0.12487
0.924215	0.977699	1.15139	2	0.124969
0.841179	0.986541	1.12222	2	0.124992
0.780975	0.991767	1.09888	2	0.124998
0.735948	0.994853	1.0804	2	−0.124999
0.701294	0.996712	1.06577	2	−0.125

Table 13.8 Overpassing a false convergence

z_0	z_1	g	n	E (a.u.)
2.5	1.2	0.9	1	−0.138096
2.62454	1.03587	0.935687	1	−0.127460
2.48591	0.989487	0.976356	1	−0.125154
2.34727	0.943106	1.01703	**1**	−0.124859
1.41343	1.02160	0.963025	**2**	−0.124868
1.25337	1.01623	0.964009	2	−0.124954
1.12615	1.01049	0.968734	2	−0.124986
1.02330	1.00655	0.974106	2	−0.124996
0.939738	1.00405	0.978974	2	−0.124999
0.871820	1.00250	0.983044	2	−0.125

"false"-converged $\delta\mathbf{p}$ in order to send it farther to $n = 2$, i.e., "before" the crossing where the real minimum should be [cf. Table 13.8]. (Such a "false" convergence should always be checked). While being in $n = 1$, it approached p = (2.34, 0.94, 1.01); in order to send it farther to $n = 2$ "before" the crossing, p was extrapolated every three steps by twice the final step – or more if convergence is slow, according to the logical code exposed in Table 13.2. Such an extrapolation was also used in the first example above; in the second it was not needed.

Note that the graphs of all converged functions, above,

$$\begin{aligned}
\Phi^{2r}(r) &= -0.0074983\, \mathrm{e}^{-0.844753\, r} + (0.206437 - 0.101273\, r)\ \mathrm{e}^{-0.50124\, r},\\
\Phi^{2r}(r) &= 0.615983\, \mathrm{e}^{-0.516411\, r} - (0.416497 + 0.0892886\, r)\ \mathrm{e}^{-0.499141\, r},\\
\Phi^{2r}(r) &= 0.0178076\, \mathrm{e}^{-0.701294\, r} + (0.182078 - 0.0970265\, r)\ \mathrm{e}^{-0.498356\, r},\\
\Phi^{2r}(r) &= -0.00706569\, \mathrm{e}^{-0.87182\, r} + (0.205952 - 0.10123\, r)\ \mathrm{e}^{-0.50125\, r}
\end{aligned}$$

are practically identical to the exact

$$\psi_1\,(1,\,1;\,r) = (1 - r/2)\,\mathrm{e}^{-r/2}/\sqrt{8\pi} = (0.199471 - 0.0997356\, r)\,\mathrm{e}^{-r/2};$$

they differ by at most 0.001 at $r = 0$ (the second differs at most by $1.5\ 10^{-5}$).

13.6.3 Application to Conventional Configuration Interaction Treatment

The functional F_n has been preliminarily [2, 66] used for the computation of atomic excited states in standard coordinates (r, θ, φ) by configuration interaction (CI), where the configurations are symmetry-adapted linear combinations of Slater determinants (SD) composed of analytic Laguerre-type orbitals, whose polynomial prefactors are variationally optimized (AVOLTOs), thus providing small, concise, and comprehensible analytic wave functions, with accuracy comparable to numerical MCSCF [79]:

$$\langle r|n,\,\ell,\,m\rangle = A^{n,\ell,m} L_{n,\ell}(r) Y^{\ell,m}\,(\theta,\,\phi)\,,$$

where $A^{n,\,\ell,\,m}$ are normalization factors, $Y^{\ell,\,m}(\theta,\phi)$ are spherical harmonics, and $L_{n,\,\ell}(r)$ are the AVOLTOs,

$$L_{n,\ell}(r) = \sum_{k=0}^{n-\ell-1} c_k^{n,\ell}\, g_k^{n,\ell}\, r^{(\ell+k)} \mathrm{e}^{-z_{n,\ell}\frac{r}{n}} + b^{n,\ell} \mathrm{e}^{-q^{n,\ell} z_{n,\ell}\frac{r}{n}} \delta_{\ell,0}. \tag{13.19}$$

Here $c_k^{n,\ell}$ are the usual associated Laguerre polynomial coefficients, $z_{n,\ell}$, $b^{n,\ell}$, $q^{n,\ell}$ are variational parameters, and $g_k^{n,\ell}$ are factors determined by orthogonalization to desired, only, orbitals, i.e., by solving (for $g_k^{n,\ell}$) the relations $\langle n_i,\ \ell,\ m|\, n_j,\ \ell,\ m\rangle = \delta_{i,j}$, so that not all orbitals are mutually orthogonal. Therefore the general formalism is non-orthogonal, which allows spin unrestricted as well as open shell computation.

Thus, for an atom with nuclear charge Z_{nuc} and N electrons, with space and spin coordinates $\mathbf{r}_1 s_1$, ..., $\mathbf{r}_N s_N$, and for a given symmetry type and electron occupancy, the desired $N-$ electron normalized wave function, of the n^{th} excited state, consisting of N_{conf} (predetermined) configurations, out of N_{det} SDs, is written as

$$\phi_n\left(\mathbf{r}_1 s_1, \ldots, \mathbf{r}_N s_N\right) = \sum_{p=1}^{N_{\text{conf}}} d_p \sum_{a=1}^{N_{\text{det}}} f_{p,a} D_a;\ \ |\phi_n|^2 = 1 \tag{13.20}$$

and is obtained by minimization of F_n, with Hamiltonian

$$H = -\frac{1}{2}\sum_{i=1}^{N}\left(\nabla_i^2 + \frac{Z_{\text{nuc}}}{|\ r_i\ |}\right) + \sum_{i>j}^{N}\frac{1}{|\ r_i - r_j\ |} \equiv \sum_{i=1}^{N} h_i + \sum_{i>j}^{N} g_{i,j}.$$

In Eq. 13.20, if N_{det} is the number of SDs, D_α, consistent with the desired electronic state, N_{orb} is the predetermined number of spinorbitals, a_i, under optimization, and $f_{p,a}$ are all ($N_{\text{conf}} \times N_{\text{det}}$) consistent corresponding coefficients, then, the linear parameters d_p are determined from a desired root of the secular equation ($N_{\text{conf}} \times N_{\text{conf}}$) with ($p$,$q$) matrix elements

$$\sum_{a,b=1}^{N_{\text{det}}} f_{p,a} f_{q,b} \left\langle D_a\right| H - E\left|\ D_b\right\rangle,$$

and ϕ_n is a critical point of both the energy and F_n, while all ϕ_i $i < n$, remain unvaried, rather crude, approximants of the lower states.

The one- and two-electron terms between SDs are computed by

$$\langle D_a| \sum_{i=1}^{N} h_i\ |D_b\rangle = \frac{1}{\sqrt{D_{aa} D_{bb}}} \sum_{i,j=1}^{N} \left\langle a_i\right| h\left|\ b_j\right\rangle D_{ab}\left(a_i b_j\right)$$

where $D_{ab} =$ det $|\ \langle a_1|\, b_1\rangle\langle a_2|\, b_2\rangle \cdots \langle a_n|\, b_n\rangle|$, a_i (and b_j, etc.) are the spin-orbitals, and where $D_{ab}(a_i b_j)$ is the cofactor of the element $\langle a_i|\, b_j\rangle$ in the determinant D_{ab}, and D_{aa}, D_{bb} are similar normalization factors. Also,

$$\langle D_a | \sum_{i>j}^{N} g_{i,j} \, | D_b \rangle = \frac{1}{\sqrt{D_{aa} D_{bb}}} \sum_{j>l}^{N} \sum_{i>t}^{N} \langle a_i a_t \, | g | \, b_j b_l \rangle \, D_{ab} \left(a_i a_t b_j b_l \right)$$

where $D_{ab}(a_i a_t b_j b_l)$ is the cofactor of D_{ab} defined by deleting the rows and columns containing $\langle a_i | \, b_j \rangle$ and $\langle a_t | \, b_l \rangle$ and attaching a factor $(-1)^{i+j+t+l}$ to the resultant minor. The determinant cofactors are most efficiently computed via the inverse matrix, after adding to all matrix elements small random numbers of the order of machine accuracy, in order to avoid occasional (but harmless) vanishing of the determinant.

13.6.3.1 Results

He

To check the reliability of the CI computation, before demonstrating comparisons between F_n and HUM – small and large – expansions, a comparison with the literature is shown:

For the 1st excited state of He ^1S $1s2s$, using, in ϕ_1, 11 AVOLTOs forming 76 SDs and 22 configurations and a fixed crude ϕ_0 approximant of $1s^2$ of only two AVOLTOs in a 2×2 CI ($\mathrm{E}[\phi_0] = -2.88$ a.u.), then $\mathrm{E}[\phi_1] = -2.1458140$ a.u. ($F_1 = -2.1458139$ a.u.). The wave function is primarily $\phi_1 = 0.9993$ ($1sB \; 2sA - 1sA \; 2sB$) + 0.0190 ($2p_1A \; 3p_{-1}B - 2p_1B \; 3p_{-1}A - 2p_0A \; 3p_0B + 2p_0B \; 3p_0A + 2p_{-1}A \; 3p_1B - 2p_{-1}B \; 3p_1A$) + 0.0178 $3s^2$, where A,B denote the spin, the {r_{rms} distance from the nucleus (a.u.); and $z_{n,\ell}$, $b^{n,\ell}$, $q^{n,\ell}$ values} are, respectively, for $1s$: {0.8699666; 1.9690983, 0.0881525, 1.2060984}, for $2s$: {5.6429592; 1.1248561, 0, 1}, for $2p$: {1.1438142; 4.7885604, 0, 1}, and for $3s$: {1.0879814; 5.6155136, 0, 1}, the g_k-factors are for $2s$: (0.8186816, 1) and for $3s$: (4.0287651, 2.0322568, 1), making them both orthogonal to another $1s$, a little more diffuse: {1.0374887; 3.0931600, −0.9341100, 0.9519696}. This energy value can be compared to (i) −2.1457316 a.u., with 10 AVOLTOs forming 68 SDs and 18 configurations, exactly orthogonal to a quite accurate ϕ_0 of $E = -2.9031501$ a.u. with 15 AVOLTOs, 157 SDs, and 40 configurations and to (ii) −2.145873 a.u. using 10 numerical MCHF orbitals, with a comparably highly accurate ground state of $E = -2.9031173$ $\mathrm{E_h}$ [86].

For the 2nd excited state of He ^1S $1s3s$, using, in ϕ_2, 11 AVOLTOs, 77 SDs, 23 configurations, and again 2×2 ϕ_0 and ϕ_1, then $\mathrm{E}[\phi_2] = -2.0612263$ a.u. ($F_1 = -2.0611758$ a.u.). The wave function is primarily $\phi_2 = 0.9788$ ($1sA \; 3sB - 1sB \; 3sA$) + 0.2035 ($3sA \; 2sB - 3sB \; 2sA$) + 0.0170 ($1sA \; 2sB - 1sB \; 2sA$); the {r_{rms}; z, b, q} values are for $1s$: {1.1051964; 1.61507, 2.0564, 0.95729}, for $3s$: {12.9875477; 1.09458, 0, 1}, and for $2s$: {1.6490337; 3.49456, 0, 1}; the g_k-factors are for $3s$: (0.7660135, 0.9277702, 1), making it orthogonal to $1s$ and to the previous $2s$, and for $2s$: (1.5813926, 1), making it orthogonal to $1s$. This energy value can be compared to −2.0612681, obtained by *B-splines* [87]. By increasing to 19 AVOLTOs, 263

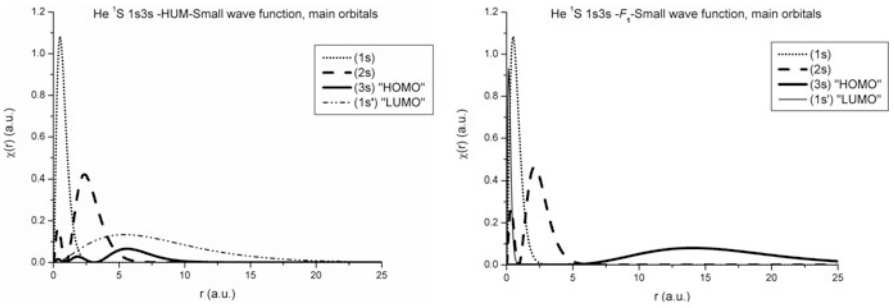

(a) HUM 2nd root (b) F_1

Fig. 13.11 CI wave functions (main orbitals): for **He^1*S*1*s*3*s***. Dotted: 1*s*. Dashed: 2*s*. Solid: 3*s*. The HUM main orbitals (**a**) are, incorrectly, **1*s*,1$\underline{s}'$**, whereas the *F* main orbitals (**b**) are, correctly, 1*s*3*s*. Notice that the "LUMO" is just a static correlation orbital very close to the nucleus, not an excitation orbital

SDs, 53 configurations, the improved energy is $E[\phi_2] = -2.0612522$ a.u. $(= F_1)$ [88].

Therefore, the CI computation is reliable. To compare with HUM, as "exact" ψ_n a "large" expansion in **1*s*, 2*s*, 3*s*, 4*s*, 5*s*, 2*p*, 3*p*, 4*p*, 5*p*, 3*d*, 4*d*, 5*d*, 4*f*, 5*f*** was used. For ^1S: $E_0 \approx -2.90324$ a.u., $E_1 \approx -2.14594$ a.u., $E_2 \approx -2.06125$ a.u. (exact: -2.06127 a.u [80].), for ^3S: $E_0 \approx -2.17521$ a.u. (compared to -2.17516 of ref. [89]), $E_1 \approx -2.06869$ a.u. (exact: -2.17536, -2.06881 a.u [80]). As "truncated" trial functions ϕ_n a "small" expansion in **1*s*, 2*s*,** and **3*s*** was used.

He ^1S

He ^1S 1s2s (1st Excited State ϕ_1)

As found above with Hylleraas coordinates, for He ^1S 1*s*2*s* the "small" HUM and *F* functions, in lack of other parameters, are essentially the same. There is nothing interesting to compare.

He ^1S 1s3s (2nd Excited State ϕ_2)

For the singlet **He ^{1}*S* 1*s*3*s***, the comparison is shown in Fig. 13.11. *F* "small" is, correctly, mainly 1*s*3*s*, whereas HUM "small" is, **misleadingly**, mainly 1*s***$\underline{s}'$**, instead of 1*s*3*s*. Notice that the lowest unoccupied orbital, "LUMO," acts as a static correlation orbital, improving the *total* wave function *near the nucleus*. By no means should it be considered as the first candidate orbital to be occupied by an excited electron. For details see Ref. [90].

He ^3S

He ^3S 1s3s (1st Excited State ϕ_1)

The lowest state of He ^3S is 1s2s, obtainable by simply minimizing the energy. For the 1st excited state ϕ_1, as seen in Fig. 13.3 (a), again it is demonstrated that "large" functions, HUM and F, are practically equivalent. The F "small" function (b) has the same main orbitals, 1s and 3s, as both the "large" functions F (a) and HUM (d), where the 2s just adds some static correlation correction near the nucleus (as well as all higher orbitals of the "large" expansion (c)). But the HUM "small" expansion (e), orthogonal to a deteriorated 1st root ^3S "1s2s" (f), **has main orbitals 1s2$\underline{s}$** (with opposite sign), while the 3s orbital acts as a static correlation correction of the total wave function, to approach the correct energy. Thus, the HUM solution **incorrectly** predicts, as "HOMO" orbital, the 2s instead of the 3s; therefore, it **is misleading**. Of course, blindly considering as "LUMO" the 1st higher "unoccupied" orbital, i.e., the HUM 3s, is completely out of question.

The above conclusions are clearly confirmed by Fig. 13.4, where all HUM functions have minimum, whereas all F functions, either "large" or "small," have energy saddle point. (Of course, the larger the expansion, the better is the approximation, but for larger systems this is not feasible; rather "small" but reliable functions are needed.)

Li

Similar results are found for Li: Several low-lying excited states of Li ^{2}S and ^{4}S are shown in Table 13.1, where the main configuration, the energy E and the F_n value are displayed, along with the RMS extent of the main orbitals. The low-lying HUM "small" functions were misleading. However, by appropriately changing the basis, guided by the F_n functional, much better HUM "small" functions were found, used for final comparisons with the F_n functions. This, as well as the corresponding aforementioned results for He, suggests that small expansions for excited states would be more correctly described in terms of more appropriate basis functions. The last (9th) column shows the number of configurations along with the overlap $\langle HUM|\, F_n\rangle$ of the corresponding functions. Clearly, the larger the expansion, the better the approximation; nevertheless, the 2nd derivatives in the eighth column assert that the HUM functions always have energy minimum and therefore are **not** the excited state saddle points, whereas the F_n functions are saddle points.

13.6.4 Immediate Improvement of a Lowest State Approximant

A very accurate ϕ_1 approximant of ψ_1 was used for He ^1S 1s2s, in terms of 19 AVOLTOs up to 5 g with unrestricted s orbitals up to 4s, 53 CI terms, 263 SDs,

with $E[\phi_1] = -2.14593739906107$ a.u., $F_1 = -2.14593739906075$, and, as ϕ_0, a crude approximant $1s^2$, restricted s, with $E[\phi_0] = -2.847656$ a.u. In their 2D space their 2×2 overlap matrix, s_{ij}, and Hamiltonian matrix, h_{ij}, are $s_{11} = 1.0$; $s_{12} = s_{21} = -0.047857$; $s_{22} = 1.0$ and $h_{11} = -2.847656$; $h_{12} = h_{21} = 0.102699$; $h_{22} = -2.145937$, as expected, since ϕ_1 is very close to ψ_1 and $(s_{12}\ h_{22} - h_{12}) = 5 \times 10^{-8}$ (i.e., in other words: $\langle\phi_0|\mathrm{H}|\phi_1\rangle = E_1\langle\phi_0|\,\phi_1\rangle$).

The (orthonormal) eigenvectors are indeed $\Psi^+ = 1.2\ 10^{-6}\ \phi_0 + 1.00\ \phi_1 = \psi_1$, $E^+ = E_1 = -2.145937$ a.u. (unchanged, since it was already essentially a Hamiltonian eigenfunction) and the improved $\Psi^- = 1.0011471\ \phi_0 + 0.047910626\ \phi_1$, $E^- = -2.8492667$ a.u. This is equal to [also computed independently via Eq. (13.14)] ϕ_0^+ exactly orthogonal to $\phi_1 = \psi_1$. By using a partially optimized wave function $\mathbf{f_2} = \mathbf{2s3s}$, a function $\phi_0^{(2+)}$ orthogonal to both $\{\phi_0^+,\ \psi_1\}$ was obtained, then, in the 2×2 subspace of $\{\phi_0^+, \phi_0^{(2+)}\}$ (both orthogonal to ψ_1), the lowest Hamiltonian eigenvector $\Psi^- \equiv \phi_0^- = 0.09305114\ \phi_1 + 0.29149129\ \phi_0 + 0.715803\ \mathrm{f}_2$ has energy $E\left[\phi_0^-\right] = -2.8673305$ a.u. By further introducing an individually optimized wave function $\mathbf{f_3} = \mathbf{4s^2}$, then $\Psi^- \equiv \phi_0^{2-} = 0.093057191\ \phi_1 + 0.29149218\ \phi_0 + 0.71580519\ \mathrm{f}_2 - 0.0025808019\ \mathrm{f}_3$ was obtained with ${E_0}^{2-} = -2.8673481$ a.u. By repeating with an individually optimized wave function $\mathbf{f_4} = \mathbf{2p3p}$, then $\Psi^- \equiv \phi_0^{3-} = 0.09284577\ \phi_1 + 0.29145852\ \phi_0 + 0.71572254\ \mathrm{f}_2 - 0.0025805039\ \mathrm{f}_3 - 0.013914576\ \mathrm{f}_4$ was obtained with ${E_0}^{3-} = -2.8677801$ a.u., and so on. All these improvements were done immediately within negligible time.

13.7 Final Remark

The excited states are energy saddle points in the Hilbert space of wave functions. To compute excited states with **truncated** wave functions, most standard methods are based on HUM theorem, which says that, optimizing the desired higher root of the secular equation approaches the correct energy from above; it does not say anything about the quality of the wave function. However, the wave function is needed if we want to understand the behavior of the electrons and to compute other properties besides the energy. For large systems we need rather small and comprehensible (truncated) wave functions. We have seen that using small wave function expansions, HUM theorem, allows us to approach the energy (from above, i.e., by minimization), **but it prevents us from approaching the exact excited state saddle point wave function**. Thus, based on HUM theorem, we must use large expansions (the larger, the better), which is impracticable for large systems. We have also seen that **the functional F_n (Eq. 13.4) has local minimum at the excited state saddle point, regardless of the size of the expansion**. Therefore, it could be used for large systems with small wave functions. We saw that it has been tested for small atoms and demonstrated the above statements. So, it is worth trying it for larger systems. The implementation needs the computation, beyond the energy $\langle\phi_n|H|\phi_n\rangle$, of simple matrix elements $\langle\phi_{i<n}|\,\phi_n\rangle$ and $\langle\phi_{i<n}|H|\phi_n\rangle$, that

are standard subroutines of most of the common computational codes. The lower lying approximants $\phi_{i<n}$ need not be very accurate; it is sufficient to be **crude** but reasonable. F_n can be also used to identify a "flipped root," a usual problem near an avoided energy crossing in the variational parameter space. It can also be used to immediately improve a ground state approximant if the 1st excited state is more accurately known.

Acknowledgments The present work was supported in part by the project "Advanced Materials and Devices" (MIS 5002409) implemented under the "Action for the Strategic Development on the Research and Technological Sector," funded by the Operational Programme "Competitiveness, Entrepreneurship and Innovation" (NSRF 2014–2020) and co-financed by Greece and the European Union (European Regional Development Fund).

References

1. E.A. Hylleraas, B. Undheim, Z. Phys. **65**, 759 (1930); J.K.L. McDonald, Phys. Rev. **43**, 830 (1933)
2. N.C. Bacalis, Z. Xiong, J. Zang, D. Karaoulanis, AIP Conference Proceedings, **1790** UNSP 020007 (2016) https://doi.org/10.1063/1.4968633; N.C. Bacalis, Z. Xiong, Z.X. Wang, Int. J. Quantum Chem (2017) (submitted)
3. J. Golab, D. Yeager, P. Jørgensen, Chem. Phys. **93**, 83 (1985)
4. P. Jørgensen, J. Olsen, D. Yeager, J. Chem. Phys. **75**, 5802 (1981)
5. M. Reed, B. Simon, *Methods of Modern Mathematical Physics. Analysis of Operators*, vol IV (Academic, New York, 1978)
6. P. Jørgensen, P. Swanstrøm, D. Yeager, J. Chem. Phys. **78**, 347 (1983)
7. H. Jensen, P. Jørgensen, J. Chem. Phys. **80**, 1204 (1984)
8. H. Jensen, Electron correlation in molecules using direct second order MCSCF, in *Relativistic and Electron Correlation Effects in Molecules and Solids* (Plenum, New York, 1994), pp. 179–206
9. E. Cancès, H. Galicher, M. Lewin, J. Comput. Phys. **212**, 73 (2006)
10. H. Nakatsuji, K. Hirao, J. Chem. Phys. **68**, 2053 (1978)
11. D. Hegarthy, M.A. Robb, Mol. Phys. **38**, 1795 (1979)
12. R.H.E. Eade, M.A. Robb, Chem. Phys. Lett. **83**, 362 (1981)
13. O. Christiansen, H. Koch, P. Jørgensen, J. Chem. Phys. **103**, 7429 (1995)
14. H. Koch, O. Christiansen, P. Jørgensen, T. Helgaker, A.S. de Meras, J. Chem. Phys. **106**, 1808 (1997)
15. C. Haettig, F. Weigend, J. Chem. Phys. **113**, 5154 (2000)
16. C. Haettig, Adv. Quantum Chem. **50**, 37 (2005)
17. E.S. Nielsen, P. Jørgensen, J. Oddershede, J. Chem. Phys. **73**, 6238 (1980)
18. S.P.A. Sauer, J. Phys. B **30**, 3773 (1997)
19. J.J. Eriksen, S. Sauer, K.V. Mikkelsen, H.J.A. Jensen, J. Kongsted, J. Comput. Chem. **33**, 2012 (2013)
20. J. Schirmer, Phys. Rev. A **26**, 2395 (1982)
21. A.B. Trofimov, J. Schirmer, J. Phys. B **28**, 2299 (1995)
22. J.H. Starcke, M. Wormit, A. Dreuw, J. Chem. Phys. **130**, 024104 (2009)
23. M. Tassi, I. Theophilou, S. Thanos, Int. J. Quantum Chem. **113**, 690 (2013)
24. D.H. Weinstein, Proc. Natl. Acad. Sci. U. S. A. **20**, 529 (1934)
25. J.E. Subotnik, J. Chem. Phys. **135**, 071104 (2011)
26. A. Dreuw, M. Head-Gordon, J. Am. Chem. Soc. **126**, 4007 (2004)

27. J. Autschbach, ChemPhysChem **10**, 1757 (2009)
28. S. Grimme, F. Neese, J. Chem. Phys. **127**, 154116 (2007)
29. H.J. Monkhorst, Int. J. Quantum Chem. Symp. **11**, 421 (1977)
30. E. Dalgaard, H.J. Monkhorst, Phys. Rev. A **28**, 1217 (1983)
31. H. Koch, P. Jørgensen, J. Chem. Phys. **93**, 3333 (1990)
32. H. Koch, H.J.A. Jensen, P. Jørgensen, T. Helgaker, J. Chem. Phys. **93**, 3345 (1990)
33. K. Emrich, Nucl. Phys. A **351**, 397 (1981)
34. H. Sekino, R.J. Bartlett, Int. J. Quantum Chem. Symp. **18**, 255 (1984)
35. J. Geertsen, M. Rittby, R.J. Bartlett, Chem. Phys. Lett. **164**, 57 (1989)
36. J.F. Stanton, R.J. Bartlett, J. Chem. Phys. **98**, 7029 (1993)
37. D.C. Comeau, R.J. Bartlett, Chem. Phys. Lett. **207**, 414 (1993)
38. R.J. Rico, M. Head-Gordon, Chem. Phys. Lett. **213**, 224 (1993)
39. J.D. Watts, An introduction to equation-of-motion and linear-response coupled-cluster methods for electronically excited states of molecules, in *Radiation Induced Molecular Phenomena in Nucleic Acids*, ed. by M. K. Shukla, J. Leszczynski (Springer, Dordrecht, 2008), pp. 65–92
40. M. Nooijen, R.J. Bartlett, J. Chem. Phys. **107**, 6812 (1997)
41. J.F. Stanton, J. Chem. Phys. **101**, 8928 (1994)
42. M. Musial, R.J. Bartlett, J. Chem. Phys. **134**, 034106 (2011)
43. C. Hättig, A. Hellweg, A. Köhn, J. Am. Chem. Soc. **128**, 15672 (2006)
44. B.M. Wong, J.G. Cordaro, J. Chem. Phys. **129**, 214703 (2008)
45. A.I. Krylov, Chem. Phys. Lett. **350**, 522 (2001)
46. Y. Shao, M. Head-Gordon, A.I. Krylov, J. Chem. Phys. **118**, 4807 (2003)
47. S.V. Levchenko, A.I. Krylov, J. Chem. Phys. **120**, 175 (2004)
48. E.J. Sundstrom, M. Head-Gordon, J. Chem. Phys. **140**, 114103 (2014)
49. B.O. Roos, Ab initio methods, in *Quantum Chemistry, Part 2, Advances in Chemical Physics*, ed. by K. P. Lawley, vol. 69 (Wiley, Hoboken, 1987), pp. 399–442
50. K. Andersson, P.-A. Malmqvist, B.O. Roos, J. Chem. Phys. **96**, 1218 (1992)
51. P.M. Zimmerman, F. Bell, M. Goldey, A.T. Bell, M. Head-Gordon, J. Chem. Phys. **137**, 164110 (2012)
52. D. Casanova, J. Chem. Phys. **137**, 084105 (2012)
53. M. Wormit, D.R. Rehn, P.H.P. Harbach, J. Wenzel, C.M. Krauter, E. Epifanovsky, A. Dreuw, Mol. Phys. **112**, 774–784 (2014)
54. P.-O. Löwdin, Phys. Rev. **97**, 1509 (1955)
55. P.-O. Löwdin, Adv. Chem. Phys. **2**, 207 (1959)
56. R. Shepard, Adv. Chem. Phys. **69**, 63 (1987)
57. M. Born, R. Oppenheimer, Ann. Phys. **84**, 457 (1927)
58. H.-J. Werner, Adv. Chem. Phys. **69**, 1 (1987)
59. H.-J. Werner, W. Meyer, J. Chem. Phys. **73**, 342 (1980)
60. M. Frisch, I. Ragazos, M. Robb, H. Schlegel, Chem. Phys. Lett. **189**, 524 (1992)
61. K. Ruedenberg, L.M. Cheung, S.T. Elbert, Int. J. Quantum Chem. **16**, 1069 (1979)
62. K. Docken, J. Hinze, J. Chem. Phys. **57**, 4928 (1972)
63. H.-J. Werner, W. Meyer, J. Chem. Phys. **74**, 5794 (1981)
64. D. Yeager, D. Lynch, J. Nichols, P. Jørgensen, J. Olsen, J. Phys. Chem. **86**, 2140 (1982)
65. J. Olsen, P. Jørgensen, D. Yeager, J. Chem. Phys. **76**, 527 (1982)
66. Z. Xiong, N.C. Bacalis, Chin. Phys. B **19**, 023601 (2010). https://doi.org/10.1088/1674-1056/19/2/023601
67. T.C. Chang, W.H.E. Schwarz, Theor. Chim. Acta (Berl) **44**, 45 (1977)
68. S. Matsumoto, M. Toyama, Y. Yasuda, T. Uchide, R. Ueno, Chem. Phys. Lett. **157**, 142 (1989)
69. M.R. Hoffmann, C.D. Sherrill, M.L. Leininger, H.F. Schaefer III, Chem. Phys. Lett. **355**, 183 (2002)
70. J.J. Dorando, J. Hachmann, G.K.-L. Chan, J. Chem. Phys. **127**, 084109 (2007)
71. M. McCourt, J.W. McIver Jr., J. Comput. Chem. **8**, 454 (1987)
72. E.R. Davidson, L.Z. Stenkamp, Int. J. Quantum Chem. Symp. **10**, 21 (1976)
73. C.S. Sharma, S. Srirankanathan, Mol. Phys. **40**, 1021 (1980)

74. H.G. Miller, R.M. Dreizler, Nucl. Phys. A **316**, 32 (1979)
75. G.J. Atchity, S.S. Xantheas, K. Ruedenberg, J. Chem. Phys. **95**, 1862 (1991)
76. P.J. Knowles, H.-J. Werner, Theor. Chim. Acta **84**, 95 (1992)
77. M. Lewin, J. Math. Chem. **44**, 967 (2008)
78. J. Liu, W. Liang, J. Chem. Phys. **135**, 014113 (2011)
79. Z. Xiong, N.C. Bacalis, Commun. Math. Comput. Chem. 53, 283 (2005); Z. Xiong, M. Velgakis, N.C. Bacalis, Int. J. Quantum Chem. **104**, 418 (2005); Chin Phys. **15**, 992 (2006)
80. C.L. Pekeris, Phys. Rev. **126**, 1470 (1962)
81. N.C. Bacalis, J. Comput. Methods Sci. Eng. **16**, 253 (2016)
82. H.A. Bethe, E.E. Salpeter, *Quantum Mechanics of One- and Two-Electron Atoms* (Plenum, New York, 1977), pp. 146–162
83. M.B. Ruiz, Int. J. Quantum Chem. **101**, 246 (2005)
84. N.C. Bacalis, Z. Xiong, D. Karaoulanis, J. Comput. Methods Sci. Eng. **8**, 277 (2008). http://iospress.metapress.com/content/9270636750564km0/
85. W.H. Press, S.A. Teukolsky, W.T. Vetterling, B.P. Flannery, *Numerical Recipes in FORTRAN 77: The Art of Scientific Computing* (Cambridge University Press, Cambridge, 1992), p. 374
86. C. Froese Fischer, T. Brage, P. Jönsson, *Computational Atomic Structure: An MCHF Approach* (Institute of Physics Publishing, Bristol, 1997), pp. 92–96
87. M.-K. Chen, J. Phys. B Atomic Mol. Phys. **27**, 865 (1994)
88. Z. Xiong, Z.-X. Wang, N.C. Bacalis, Acta Phys. Sin. **63**, 053104 (2014)
89. A. Sarsa, E. Buendía, F.J. Gálvez, J. Phys. BQ At. Mol. Phys. **49**, 145003 (2016)
90. Z. Xiong, J. Zang, H.J. Liu, D. Karaoulanis, Q. Zhou, N.C. Bacalis, J. Comput. Methods Sci. Eng. **17**(3), 347–361 (2017)

Chapter 14
Simulating Quantum Dynamics in Classical Nanoscale Environments

Gabriel Hanna and Alessandro Sergi

Abstract In this chapter, we describe a mixed quantum-classical approach for simulating the dynamics of quantum mechanical phenomena occurring in nanoscale systems. This approach is based on the quantum-classical Liouville equation (QCLE), which prescribes the dynamics of a quantum subsystem coupled to a classical environment. We explain how the QCLE can be solved using a stochastic surface-hopping algorithm and how expectation values of observables can be computed. Schemes for reducing the number of trajectories required in these computations and for ensuring the continuous evolution of the quantum subsystem states along the trajectories are also outlined. To demonstrate the utility of these techniques, we describe two recent applications: vibrational energy transfer in an alpha-helical polypeptide and the field-driven dynamics of a plasmonic metamolecule.

Keywords Mixed quantum-classical dynamics · Quantum-classical Liouville equation · Nonadiabatic transitions · Surface hopping · Vibrational energy transfer · Plasmonic metamolecule

G. Hanna (✉)
Department of Chemistry, University of Alberta, Edmonton, AB, Canada
e-mail: gabriel.hanna@ualberta.ca

A. Sergi
Dipartimento di Scienze Matematiche e Informatiche, Scienze Fisiche e Scienze della Terra, Università degli Studi di Messina, Messina, Italy

Institute of Systems Science, Durban University of Technology, Durban, South Africa

Istituto Nazionale di Fisica Nucleare, Sez. di Catania, Catania, Italy
e-mail: asergi@unime.it

T. Onishi (ed.), *Theoretical Chemistry for Advanced Nanomaterials*,
https://doi.org/10.1007/978-981-15-0006-0_14

14.1 Introduction

Nanotechnologies have attracted the attention of many over the last several decades due to their versatility and advanced functionality. Optoelectronics [24, 88], molecular electronics [62] and quantum computing/information [8, 58, 59] are just a few prominent examples of fields that have benefitted tremendously from nanotechnologies. Nowadays, researchers are faced with the challenge of designing high-performance, efficient and environmentally friendly materials and devices. This challenge could translate into, for example, constructing devices that are capable of highly efficient transfer of energy [43, 57], charge [30, 54] or quantum information [58, 59] in complex nanostructures. To achieve such goals, however, one must gain a fundamental understanding of the dynamical processes involved and how these processes are influenced by their nanoscale environments. In this regard, molecular simulation has proven to be an indispensable tool for probing the structure and dynamics of nanoscale systems.

When the process under study is of a quantum nature and occurs in a complex, many-particle system such as a nanomaterial, a fully quantum approach to modelling the dynamics will be computationally intractable. In this case, an approximate treatment of the dynamics is required to gain insight into the process. Mixed quantum-classical dynamics methods, which treat a subsystem of interest quantum mechanically and the particles in its environment (or bath) in a classical-like fashion, can provide tremendous computational savings over fully quantum methods. For example, the subsystem could be a key proton/electron in a charge transfer reaction, a chromophore involved in a vibrational/electronic energy transfer process or an exciton in a light-harvesting system, while the environment could be a molecule, solvent or crystal.

The partitioning of a system into different sets of degrees of freedom (DOF) lies at the heart of the Born–Oppenheimer (BO) approximation, which assumes a time/energy scale separation between the motions of the nuclei and electrons. In quantum chemistry, the BO approximation greatly simplifies calculations of molecular energies and wave functions by enabling one to solve the electronic Schrödinger equation for a fixed configuration of the nuclei to obtain electronic energies and wave functions that depend on the nuclear configuration. By repeating this calculation for a sufficiently large number of nuclear configurations, one can then construct the potential energy surfaces (PESs) of the electronic subsystem. These PESs give rise to forces (known as Hellmann-Feynman forces) that act on the nuclei over the course of their dynamics. When the energy scale separation between the nuclei and electrons is sufficiently large, the nuclei will evolve subject to the forces obtained from the PES corresponding to the current state of the electrons (which will not change because the electrons will not have enough energy to hop to another PES). This is known as *adiabatic* dynamics. However, when their energy scales become comparable, the nuclei can evolve subject to the forces obtained from another PES (because the electrons may acquire enough energy from the nuclei to hop to another PES). This breakdown of the BO approximation is

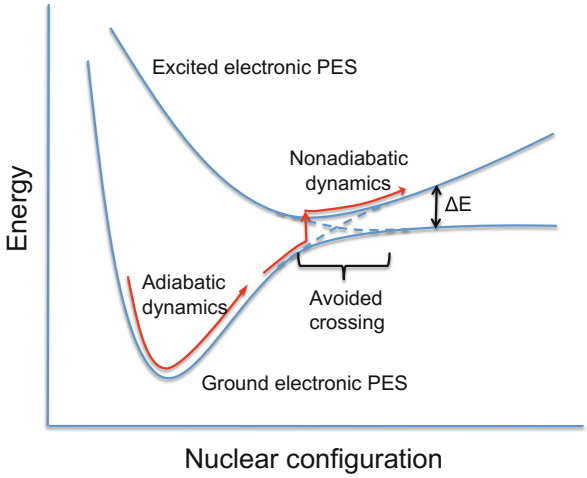

Fig. 14.1 A schematic representation of the ground and excited electronic PESs of a system. In adiabatic dynamics, the nuclei evolve on a single PES. However, in the vicinity of an avoided crossing, a nonadiabatic transition can occur, which causes the nuclei to evolve on another PES

known as *nonadiabatic* dynamics. It typically occurs in the vicinity of an avoided crossing or conical intersection between PESs. (See Fig. 14.1 for an illustration of the aforementioned concepts.)

In general, adiabatic dynamics arises whenever one set of DOF changes slowly compared to another set, as in the case of nuclei and electrons in the BO approximation. If one is able to partition a system into a subsystem containing fast DOF of interest and an environment containing slow DOF, then the dynamics of the environmental DOF will be governed by a single PES corresponding to the state of the subsystem. However, when the time scales of motion of the subsystem and environmental DOF become comparable, motion on a single PES is no longer able to accurately capture the dynamics of the slower DOF. Many important processes in physics, chemistry and biology involve this nonadiabatic dynamics. Examples include intersystem crossings and internal conversions in photochemistry, electron transfer reactions in electrochemistry, ion–molecule reactions, reactions at metal surfaces, photo-induced dynamics of molecules adsorbed to semiconductor substrates (as in a photovoltaic cell) and photo-induced dynamics in quantum dots.

Due to the importance of nonadiabatic dynamics, a great deal of effort has been devoted to developing simulation methods over the years that take nonadiabatic effects into account. In particular, many mixed quantum-classical methods have been proposed for simulating nonadiabatic dynamics, which essentially differ in the way they couple the subsystem and bath DOF [1, 3, 25, 27, 33, 35, 39, 41, 48, 50, 61, 70, 74, 76, 81, 84, 85]. The two most widely used methods are mean-field (or Ehrenfest) and fewest switches surface-hopping (FSSH) dynamics [5–7, 10, 20, 29, 60, 67–69, 71, 75, 77, 86]. Mean-field dynamics is based on the assumption that the environmental motions are governed by a single effective PES, which is a weighted average over the adiabatic PESs of the subsystem. On the other hand, surface-hopping methods evolve the environmental DOF on a single adiabatic PES at any given time, with instantaneous hops to other PESs at times when the BO

approximation breaks down. However, mean-field and FSSH dynamics suffer from several drawbacks. Both methods do not correctly describe the "quantum back-reaction", i.e. the effect due to the subsystem-environment coupling, whereby a change in the environmental DOF modifies the subsystem Hamiltonian, which in turn modifies the forces governing the motion of the environmental DOF. Mean-field dynamics is not capable of capturing decoherence, while FSSH can do so after incorporating some ad hoc corrections [68, 71]. Both methods also struggle to satisfy detailed balance. Due to the incorrect nature of the energy transfer between the subsystem and environment, it is possible for the subsystem to approach unrealistically high temperatures in mean-field dynamics [55]; in such cases, one can employ quantum correction factors that modify the dynamics in such a way that detailed balance is enforced [4]. In FSSH, it is possible to satisfy detailed balance in certain limits if the so-called frustrated hops are allowed [64].

In this chapter, we focus on a mixed quantum-classical dynamics approach that is based on the quantum-classical Liouville equation (QCLE) [2, 22, 33, 89], which can be derived from the quantum Liouville equation by first taking its partial Wigner transform [87] over the bath DOF (leading to a description of the subsystem and bath DOF in terms of operators and phase space variables, respectively) and then truncating the resulting equation after first order in $\hbar$. The QCLE constitutes an ideal starting point [31, 32] for deriving mixed quantum-classical dynamics algorithms because (i) it can be rigorously derived from the more fundamental quantum Liouville equation based on a well-defined and physically reasonable approximation, and (ii) it yields the exact quantum dynamics for quantum subsystems that are bilinearly coupled to harmonic environments [45], which are frequently used models in chemical and condensed matter physics research. A large number of QCLE-based algorithms have been developed over the years [16–18, 23, 26–28, 34, 36, 37, 40, 41, 44, 46, 47, 49, 53, 63, 82, 83]. This chapter will deal with a particular algorithm known as sequential short-time propagation (SSTP) [23, 47], due to its favourable compromise between accuracy and ease of implementation. SSTP is a hybrid molecular dynamics/Monte Carlo algorithm, which relies on the so-called momentum jump approximation [23, 65] and solves the QCLE in terms of an ensemble of *surface-hopping* trajectories. However, a direct application of this algorithm has proven to be very challenging due to severe numerical instabilities that arise beyond short times when the subsystem-bath coupling strength is not very weak. In this case, the statistical weights associated with the Monte Carlo sampling of the nonadiabatic transitions (and that enter into the calculation of the observable) grow very rapidly in time, thereby necessitating very large numbers of trajectories to obtain converged expectation values. Transition filtering schemes [12, 13, 15, 23, 66, 79, 80], which impede the growth of these weights by filtering out the low-probability nonadiabatic transitions, have been shown to significantly alleviate the numerical instabilities. We will discuss one such scheme [12, 13] in this chapter.

In most mixed quantum-classical surface-hopping approaches (including the SSTP algorithm), one must evaluate the adiabatic states and nonadiabatic couplings between them at each time step of the simulation. In most cases, they are evaluated

numerically, which first entails a numerical diagonalization of the Hamiltonian matrix. However, the resulting eigenvectors are determined uniquely up to a sign, which leads to an arbitrariness in the signs of the nonadiabatic coupling vectors. These signs must be corrected by requiring that the eigenvectors change continuously from one point to the next along a trajectory in configuration space. However, the situation is further complicated when one is interested in computing time-dependent expectation values based on an ensemble of trajectories (which are typically initialized at different points in the configuration space). In this chapter, we outline a recently proposed method [14] for ensuring eigenvector sign continuity across an ensemble of trajectories in surface-hopping simulations.

To illustrate the utility of the aforementioned methods for simulating the dynamics of mixed quantum-classical systems, we present two applications. The first one demonstrates how transition filtering can be used to facilitate the calculation of amide I mode populations in a six-site model of an alpha-helical polypeptide, after a vibrational excitation at one end of the chain. The second one involves calculations of populations and coherences in a reduced model of a plasmonic metamolecule in an external field, using a generalized version of the SSTP algorithm for simulations of systems with time-dependent Hamiltonians.

The chapter is organized as follows. In Sect. 14.2, we present the QCLE, discuss how it can be solved via the SSTP algorithm, and explain how expectation values of observables can be computed. Recently proposed schemes for transition filtering and eigenvector sign correction are also outlined in this section. In Sect. 14.3, we present two recent applications of the aforementioned techniques to simulating vibrational energy transfer in an alpha-helical polypeptide and the field-driven dynamics of a plasmonic metamolecule. Our summary and future outlook are given in Sect. 14.4.

14.2 Mixed Quantum-Classical Liouville Dynamics

14.2.1 The Quantum-Classical Liouville Equation

We begin by considering a quantum subsystem, whose Hamiltonian operator is $\hat{H}_{\mathrm{S}}$, embedded in a classical environment, whose Hamiltonian function is $H_{\mathrm{B}}(Q, P) = \frac{P^2}{2M} + V(Q)$. The coordinates (Q, P) denote the positions and momenta, respectively, of the atoms or molecular fragments (characterized by masses M and interacting according to the potential energy function $V(Q)$) in the environment. The coupling between the quantum subsystem and classical environment is governed by the operator $\hat{H}_{\mathrm{C}}(Q)$, which is also a function of the configuration of the environment. (In this chapter, we do not consider situations where the subsystem interacts with a magnetic field, such that the coupling Hamiltonian depends only on the configuration.) Hence, the Hamiltonian of the total system is given by

$$\hat{H}(Q, P) = \hat{H}_{\mathrm{S}} + H_{\mathrm{B}}(Q, P) + \hat{H}_{\mathrm{C}}(Q) \,, \tag{14.1}$$

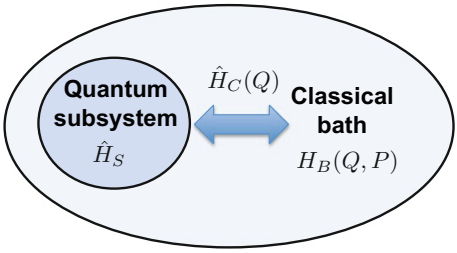

Fig. 14.2 A schematic representation of the total system and its components. The Hamiltonian of the total system is the sum of the subsystem ($\hat{H}_S$), bath (H_B) and coupling ($\hat{H}_C$) Hamiltonians

where S, B and C stand for subsystem, bath and coupling, respectively (see Fig. 14.2 for a schematic representation of the total system). The statistical and dynamical properties of the hybrid quantum-classical system defined by the Hamiltonian in Eq. (14.1) can be obtained in terms of the system's time-dependent density matrix $\hat{\rho}(Q, P, t)$, which is also a function of the phase space coordinates (Q, P). The mixed quantum-classical dynamics of $\hat{\rho}(Q, P, t)$ is governed by the QCLE:

$$\frac{\partial}{\partial t}\hat{\rho}(Q,P,t) = -\frac{i}{\hbar}\left[\hat{H},\hat{\rho}(Q,P,t)\right] + \frac{1}{2}\left\{\hat{H},\hat{\rho}(Q,P,t)\right\} - \frac{1}{2}\left\{\hat{\rho}(Q,P,t),\hat{H}\right\}\ , \tag{14.2}$$

where $[\cdot,\cdot]$ and $\{\cdot,\cdot\}$ denote the commutator and Poisson bracket, respectively. The QCLE can either be postulated by requiring energy conservation (i.e. the antisymmetry of the right-hand side guarantees that the time derivative of the Hamiltonian $\hat{H}(Q, P)$ is identically zero) or derived from a fully quantum dynamical description of the total system in the limit that the particles in the environment are much heavier than those in the subsystem. This derivation first involves a representation of the heavy coordinates in Wigner phase space, followed by a linearization of the resulting equation in the smallness parameter $\mu = \sqrt{m/M}$, where m is a characteristic mass of the quantum DOF and M is a characteristic mass of the classical DOF. By coupling the dynamics of the quantum and classical DOF in this fashion, the QCLE consistently describes the back-and-forth exchange of energy between the quantum subsystem and classical environment.

Knowledge of $\hat{\rho}(Q, P, t)$ allows one to calculate the average of any observable property of the system, which is represented in this formalism by a *microscopic* Hermitian operator that depends on the phase space point, i.e. $\hat{\chi}(Q, P) = \hat{\chi}^{\dagger}(Q, P)$. Finally, the value of a *macroscopic* observable at time t is given by

$$\langle\hat{\chi}(t)\rangle = \mathrm{Tr}' \int dQdP\,\hat{\chi}(Q,P)\hat{\rho}(Q,P,t)\ , \tag{14.3}$$

where Tr' denotes a partial trace over the quantum DOF. It is also possible to evaluate the average in the Heisenberg picture,

$$\langle \hat{\chi}(t) \rangle = \mathrm{Tr}' \int dQ dP \hat{\rho}(Q, P) \hat{\chi}(Q, P, t) \,, \tag{14.4}$$

where the mixed quantum-classical equation of motion of $\hat{\chi}(Q, P, t)$ is given by

$$\frac{\partial}{\partial t} \hat{\chi}(Q, P, t) = \frac{i}{\hbar} \left[\hat{H}, \hat{\chi}(Q, P, t) \right] - \frac{1}{2} \left\{ \hat{H}, \hat{\chi}(Q, P, t) \right\} + \frac{1}{2} \left\{ \hat{\chi}(Q, P, t), \hat{H} \right\} \,. \tag{14.5}$$

14.2.2 Representing the QCLE in the Adiabatic Basis

To arrive at a surface-hopping algorithm for solving the QCLE, one must first represent it in the adiabatic basis defined by the following eigenvalue problem (i.e. the time-independent Schrödinger equation):

$$\hat{H}_{\mathrm{ad}}(Q) |\Phi_k(Q)\rangle = \epsilon_k |\Phi_k(Q)\rangle \,, \tag{14.6}$$

where $\hat{H}_{\mathrm{ad}}(Q) = \hat{H}_S + \hat{H}_C(Q) + V(Q)$ is the so-called adiabatic Hamiltonian operator, $|\Phi_k(Q)\rangle$ is the kth adiabatic basis state, and ϵ_k is the energy of that state. In this basis, the QCLE becomes [34]

$$\begin{aligned} \frac{\partial}{\partial t} \rho_{kk'}(Q, P, t) = &- \sum_{jj'} \delta_{kj} \delta_{k'j'} \left(i\omega_{kk'} + iL_{kk'} \right) \rho_{jj'}(Q, P, t) \\ &- \sum_{jj'} \mathcal{K}_{kk',jj'} \rho_{jj'}(Q, P, t) \,, \end{aligned} \tag{14.7}$$

where $\rho_{kk'}(Q, P, t) = \langle \Phi_k | \hat{\rho}(Q, P, t) | \Phi_{k'} \rangle$ are the density matrix elements, $\omega_{kk'} = [\epsilon_k(Q) - \epsilon_{k'}(Q)]/\hbar$ are the Bohr frequencies, $iL_{kk'}$ are the matrix elements of a classical-like Liouville operator

$$iL_{kk'} = \frac{P}{M} \frac{\partial}{\partial Q} + \frac{F_k(Q) + F_{k'}(Q)}{2} \frac{\partial}{\partial P} \,, \tag{14.8}$$

with Hellmann-Feynman forces $F_k = -\partial \epsilon_k / \partial Q$, and $\mathcal{K}_{kk',jj'}$ are the matrix elements of a nonadiabatic transition super-operator

$$\begin{aligned} \mathcal{K}_{kk',jj'} = &\, \delta_{k'j'} c_{kj}(Q, P) \left(1 + \frac{1}{2} \frac{\hbar \omega_{kj}}{c_{kj}(Q, P)} d_{kj}(Q) \cdot \frac{\partial}{\partial P} \right) \\ &+ \delta_{kj} c^*_{k'j'}(Q, P) \left(1 + \frac{1}{2} \frac{\hbar \omega_{k'j'}}{c^*_{k'j'}(Q, P)} d^*_{k'j'}(Q) \cdot \frac{\partial}{\partial P} \right) \,, \end{aligned} \tag{14.9}$$

with $d_{kj} = \langle \Phi_k | \partial \Phi_j / \partial Q \rangle$ the nonadiabatic coupling vector and $c_{kj} = P/M \cdot d_{kj}$.

14.2.3 The Sequential Short-Time Propagation Algorithm

Now, we demonstrate how one can obtain a numerical algorithm for solving the QCLE in terms of a swarm of stochastic trajectories, where each trajectory is composed of piecewise deterministic segments interspersed with stochastic transitions of the quantum subsystem between different adiabatic states.

The sequential short-time propagation (SSTP) solution to Eq. (14.7) for $\rho_{kk'}(Q, P, t)$ is [47]

$$\rho_{kk'}(Q, P, t) = \sum_{(k_1 k_1')\ldots(k_N k_N')} \Big[\prod_{j=1}^{N} (e^{-i\hat{\mathcal{L}}\Delta t_j})_{k_{j-1}k'_{j-1},k_j k'_j} \Big] \rho_{k_N k'_N}(Q, P), \tag{14.10}$$

where the time interval t is divided into N segments and $\Delta t_j = t_j - t_{j-1}$. In the limit that Δt_j is sufficiently small, the propagator for segment j may be approximated by

$$(e^{-i\hat{\mathcal{L}}\Delta t_j})_{k_{j-1}k'_{j-1},k_j k'_j} \approx \mathcal{W}_{k_{j-1}k'_{j-1}}(t_{j-1}, t_j) e^{-iL_{k_{j-1}k'_{j-1}}\Delta t_j} \times \Big(\delta_{k_{j-1}k_j}\delta_{k'_{j-1}k'_j} - \Delta t \mathcal{K}_{k_{j-1}k'_{j-1},k_j k'_j} \Big), \tag{14.11}$$

where $\mathcal{W}_{k_{j-1}k'_{j-1}}(t_{j-1}, t_j) = e^{-i\omega_{k_{j-1}k'_{j-1}}\Delta t_j}$ is the phase factor associated with that segment. To simulate the action of $\mathcal{K}_{kk',jj'}$ on functions of the momenta, the momentum-jump approximation (MJA) [23, 65] is invoked, namely,

$$\begin{aligned} \Big(1 + \frac{\hbar\omega_{kj}}{2} \frac{d_{kj}}{c_{kj}} \cdot \frac{\partial}{\partial P} \Big) f(P) &= \Big(1 + \hbar\omega_{kj} \frac{\partial}{\partial(\bar{P} \cdot \bar{\hat{d}}_{kj})^2} \Big) f(P) \\ &\approx e^{\hbar\omega_{kj}\partial/\partial(\bar{P}\cdot\bar{\hat{d}}_{kj})^2} f(P) \\ &= f(P + \Delta P), \end{aligned} \tag{14.12}$$

where $\bar{P} = P/\sqrt{M}$, $\bar{\hat{d}}_{kj} = \bar{d}_{kj}/|\bar{d}_{kj}|$, $\bar{d}_{kj} = d_{kj}/\sqrt{M}$, and the momentum shift, ΔP, is given by

$$\Delta P = \sqrt{M}\bar{\hat{d}}_{kj} \Big[\mathrm{sgn}(\bar{P} \cdot \bar{\hat{d}}_{kj}) \sqrt{(\bar{P} \cdot \bar{\hat{d}}_{kj})^2 + \Delta\epsilon_{kj}} - (\bar{P} \cdot \bar{\hat{d}}_{kj}) \Big] . \tag{14.13}$$

(N.B.: $d_{kj}/\sqrt{M} = d_{kj}^T M^{-1/2}$, where T stands for the transpose and $M^{-1/2}$ is a diagonal matrix containing the inverse square root of the masses.) According to Eq. (14.13), if $\Delta\epsilon_{kj} < 0$ (i.e. an upward transition from $k \to j$) and $(\bar{P} \cdot \bar{\hat{d}}_{kj})^2 < |\Delta\epsilon_{kj}|$ (i.e. there is insufficient kinetic energy from the bath momenta along $\bar{\hat{d}}_{kj}$ for the nonadiabatic transition to occur), then the argument of the square root is negative

leading to imaginary momentum changes. If this occurs, the nonadiabatic transition is forbidden, and the trajectory is continued adiabatically. It should be noted that the approximation made in the second line of Eq. (14.12) relies on $|\hbar\omega_{kj} d_{kj} c_{kj}^{-1}/2|$ being small. Also, the total energy of the system is conserved along a trajectory under the MJA.

The expectation value of $\hat{\chi}(Q, P, t)$ is given by

$$\begin{aligned}\langle\hat{\chi}(t)\rangle &= \sum_{kk'} \int dQdP \chi_{k'k}(Q, P)\rho_{kk'}(Q, P, t) \\ &= \sum_{(k_0k_0')\ldots(k_Nk_N')} \int dQdP \chi_{k_0'k_0}(Q, P)\Big[\prod_{j=1}^{N} (e^{-i\hat{\mathcal{L}}\Delta t_j})_{k_{j-1}k_{j-1}', k_jk_j'}\Big]\rho_{k_Nk_N'}(Q, P),\end{aligned} \tag{14.14}$$

or, in the Heisenberg representation, by

$$\begin{aligned}\langle\hat{\chi}(t)\rangle &= \sum_{kk'} \int dQdP \chi_{kk'}(Q, P, t)\rho_{k'k}(Q, P) \\ &= \sum_{(k_0k_0')\ldots(k_Nk_N')} \int dQdP \rho_{k_0'k_0}(Q, P)\Big[\prod_{j=1}^{N} (e^{i\hat{\mathcal{L}}\Delta t_j})_{k_{j-1}k_{j-1}', k_jk_j'}\Big]\chi_{k_Nk_N'}(Q, P).\end{aligned} \tag{14.15}$$

The SSTP algorithm evaluates Eq. (14.15) via a hybrid molecular dynamics (MD)/Monte Carlo (MC) approach, whereby the multidimensional sums over the state indices are evaluated using MC sampling, the initial conditions of the subsystem and bath are determined from $\rho_{k_0'k_0}(Q, P)$, and $\chi_{kk'}(Q, P, t)$ is propagated in time using MD simulation.

We now detail the steps of the SSTP algorithm for evaluating Eq. (14.15) by considering the evolution through a single time step (i.e. $N = 1$):

$$\begin{aligned}\langle\hat{\chi}(\Delta t)\rangle &= \sum_{(k_0k_0')(k_1k_1')} \int dQdP \rho_{k_0'k_0}(Q, P)(e^{i\hat{\mathcal{L}}\Delta t_j})_{k_0k_0', k_1k_1'}\chi_{k_1k_1'}(Q, P). \\ &= \sum_{(k_0k_0')(k_1k_1')} \int dQdP \rho_{k_0'k_0}(Q, P)\mathcal{W}_{k_0'k_0}(t_0, t_1)e^{iL_{k_0k_0'}\Delta t_1} \\ &\times \left(\delta_{k_0k_1}\delta_{k_0'k_1'} + \Delta t\mathcal{K}_{k_0k_0', k_1k_1'}\right)\chi_{k_1k_1'}(Q, P).\end{aligned} \tag{14.16}$$

1. After specifying the initial density matrix, $\rho_{k_0' k_0}(Q, P)$, of the system, sample the initial conditions from $|\rho_{k_0' k_0}(Q, P)|$ using an appropriate scheme.
2. Propagate the bath DOF adiabatically on the adiabatic PES corresponding to the pair of indices $(k_0 k_0')$, i.e. $(\epsilon_{k_0} + \epsilon_{k_0'})/2$, for a time interval Δt, and calculate the phase factor $\mathcal{W}_{k_0' k_0}(0, \Delta t)$ for this interval.
3. According to Eq. (14.9) for $\mathcal{K}_{k_0 k_0' k_1 k_1'}$, determine stochastically whether or not a nonadiabatic transition $(k_0 k_0') \rightarrow (k_1 k_1')$ takes place. One way of sampling the nonadiabatic transitions involves first identifying which of the two terms in the expression for $\mathcal{K}_{k_0 k_0', k_1 k_1'}$ acts (viz. the first term changes the index $k_0 \rightarrow k_1$, while the second changes the index $k_0' \rightarrow k_1'$). This can be accomplished using MC by assigning a 50% probability to selecting each term. Once one of these terms has been selected, the actual transition is MC sampled with a probability

$$\mathcal{P}_{kj} = \frac{\Delta t |d_{kj} \cdot \frac{P}{M}|}{1 + \Delta t |d_{kj} \cdot \frac{P}{M}|}. \tag{14.17}$$

The probability of remaining in the same adiabatic state (i.e. no nonadiabatic transition) is therefore

$$\mathcal{Q}_{kj} = \frac{1}{1 + \Delta t |d_{kj} \cdot \frac{P}{M}|}, \tag{14.18}$$

satisfying $\mathcal{P}_{kj} + \mathcal{Q}_{kj} = 1$. If the transition is accepted, then the momenta are shifted according to Eqs. (14.12) and (14.13), and the value of the observable becomes

$$\chi_{k_1 k_1'}(\Delta t) = 2\mathcal{W}_{k_0 k_0'}(0, \Delta t) d_{kj} \frac{P_{\Delta t}}{M} \chi_{k_0 k_0'}(Q_{\Delta t}, P_{\Delta t} + \Delta P) \frac{1}{\mathcal{P}_{kj}}. \tag{14.19}$$

In the above equation, the factor of 2 is the MC weight associated with the sampling of the $k_0 \rightarrow k_1$ or $k_0' \rightarrow k_1'$ term in $\mathcal{K}_{k_0 k_0', k_1 k_1'}$ (which each occur with a probability of 50%), and $1/\mathcal{P}_{kj}$ is the MC weight associated with the sampling of the transition. On the other hand, if the transition is rejected, there is no momentum shift, and the value of the observable becomes

$$\chi_{k_1 k_1'}(\Delta t) = \mathcal{W}_{k_0 k_0'}(0, \Delta t) \chi_{k_0 k_0'}(Q_{\Delta t}, P_{\Delta t}) \frac{1}{\mathcal{Q}_{kj}}, \tag{14.20}$$

where $1/\mathcal{Q}_{kj}$ is the MC weight associated with no transition.
4. Repeat steps 2–3 until time t to calculate $\chi_{k_N k_N'}(t)$.
5. Multiply $\chi_{k_N k_N'}(t)$ by the sign of the density matrix, and average the resulting value over the initial conditions to obtain $\langle \hat{\chi}(t) \rangle$.

14.2.4 Transition Filtering

To obtain reliable expectation values beyond short times using the SSTP algorithm, experience has shown that one requires extremely large ensembles of trajectories. This is mainly due to the fact that the statistical weights associated with the MC sampling of the nonadiabatic transitions grow very rapidly in time, making it extremely difficult to obtain converged expectation values at longer times. More specifically, each trajectory acquires a statistical weight, $\prod_{j=1}^{N} \mathcal{W}_j$ (where $\mathcal{W}_j$ is the MC weight for time step j), which factors into the expectation value. In practice, these weights grow exponentially with time [12], thereby requiring an exponentially growing number of trajectories to converge expectation values at longer times. To slow down the growth of these weights and thereby reduce the number of trajectories required for convergence at longer times, observable cutting [23] and transition filtering [12, 13, 15, 66, 79, 80] schemes have been used, both separately and together, with varying degrees of success.

In observable cutting, one sets an upper bound on the magnitude of the weight at each time step of the simulation, thereby ensuring that the magnitude of the weight never becomes too large. Then, one computes the expectation value subject to this upper bound. To determine the value of the upper bound that will yield a satisfactory expectation value, one must repeat the calculation with increasingly larger values of the upper bound. Using this scheme, however, it is difficult to know if one has converged to the true result. In other words, if the upper bound is too small, the result may appear stable but may be inaccurate. Conversely, if the upper bound is too large, the result may be too noisy to be interpretable.

In contrast, transition filtering reduces the statistical noise by disallowing those nonadiabatic transitions that would lead to large statistical weights. In this subsection, we will outline the transition filtering approach proposed and implemented by Hanna et al. in Refs. [12, 13, 15]. In Refs. [12, 13], the scheme was laid out and applied to two relatively simple systems (viz. 2 quantum states coupled to 20 classical DOF and 3 quantum states coupled to 1 classical DOF), yielding substantial reductions in the numbers of trajectories required for convergence and smoother and more accurate results than those obtained with observable cutting. In Ref. [15], the scheme was applied to a model containing six quantum and six classical DOF, in order to investigate the feasibility and efficacy of the scheme for treating subsystems with larger numbers of states (as the number of trajectories scales with the number of states in the quantum subsystem). In this case, it was possible to obtain numerically stable results with more than one order of magnitude fewer trajectories than the number of trajectories used to generate the results without any filtering. This application will be discussed in more detail in Sect. 14.3.1.

We now outline the transition filtering scheme. To begin with, we define the following transition probability for the MC sampling of nonadiabatic transitions along an SSTP trajectory [12]

$$\Pi = \frac{\Delta t |A(Q,P)| w(\kappa_{\alpha\beta}, \Delta E_{\alpha\beta})}{1 + \Delta t |A(Q,P)| w(\kappa_{\alpha\beta}, \Delta E_{\alpha\beta})}, \tag{14.21}$$

where Δt is the time step and

$$w(\kappa_{\alpha\beta}, \Delta E_{\alpha\beta}) = \begin{cases} 1, & \text{if} |\Delta E_{\alpha\beta}| \leq \kappa_{\alpha\beta}, \\ 0, & \text{otherwise.} \end{cases} \tag{14.22}$$

As can be seen, this transition probability restricts nonadiabatic transitions between adiabatic PESs α and β to occur when the magnitude of the energy gap between the surfaces is sufficiently small, i.e. less than a threshold value $\kappa_{\alpha\beta}$. The functional form of $A(Q, P)$ should be chosen in such a way to minimize the statistical noise in the expectation value. One form that has been shown to work relatively well is [12]

$$A(Q,P) = \frac{P}{M} \cdot d_{\alpha\beta} \frac{\Delta E_{\alpha\beta}^{\min}}{\Delta E_{\alpha\beta}}, \tag{14.23}$$

where $\Delta E_{\alpha\beta}^{\min}$ is the smallest energy gap between the α and β surfaces. In practice, $\Delta E_{\alpha\beta}^{\min}$ may be extracted from a $\Delta E_{\alpha\beta}$ histogram, generated by evolving the system adiabatically on its ground-state PES for a sufficiently long time. By filtering out nonadiabatic transitions with large $\Delta E_{\alpha\beta}$'s according to w and placing $\Delta E_{\alpha\beta}$ in the denominator of $A(Q, P)$, one favours the high-probability transitions and thereby slows down the temporal growth of the statistical weights.

For an n-state quantum subsystem, one must specify the values of $n(n-1)/2$ $\Delta E_{\alpha\beta}^{\min}$'s and $\kappa_{\alpha\beta}$'s (because there are $n(n-1)/2$ possible $\alpha \leftrightarrow \beta$ nonadiabatic transitions). The $\Delta E_{\alpha\beta}^{\min}$ values may be obtained as explained in the previous paragraph, while sensible initial trial values for the $\kappa_{\alpha\beta}$'s are the mean values of the $\Delta E_{\alpha\beta}$'s. Using the SSTP algorithm, one then computes a time-dependent expectation value out to some time t, using a reasonably large number of trajectories. If the result is noisy, one may converge the expectation value according to the following steps:

1. Reduce the value of κ_{1n} (relative to its previous value) to filter the $1 \leftrightarrow n$ transitions and recompute the expectation value out to time t.
2. If the result is noisy, then further reduce the values of $\kappa_{\alpha\beta}$ to filter the transitions between states for which $|\alpha - \beta| = n - 2$ (e.g. in the $n = 4$ case, the $1 \leftrightarrow 3$ and $2 \leftrightarrow 4$ transitions) and recompute the expectation value out to time t.
3. If $n > 3$, then repeat the previous step for the transitions with $|\alpha - \beta| = n - k$ (where $k = 3 \ldots n - 1$).
4. If the result is noisy, repeat steps 1 to 3.

14.2.5 Eigenvector Sign Correction

In nonadiabatic dynamics methods such as the SSTP algorithm, the adiabatic states and nonadiabatic couplings between them must be evaluated on-the-fly. Typically, they are evaluated numerically, which first involves a numerical diagonalization of the Hamiltonian matrix (represented in a convenient basis). The diagonalization results in eigenvectors that are uniquely determined up to a sign, which leads to arbitrary signs of the nonadiabatic coupling vectors. The signs may be corrected by requiring that the eigenvectors change continuously from one time step to the next. However, when a system is in the vicinity of an avoided crossing or conical intersection between two PESs, it becomes more complicated to correctly distinguish between physical and unphysical sign changes in the eigenvectors. Previously, Errea et al. proposed a procedure for correcting the sign of an electronic state, which involves tracking the sign of the overlap between the state evaluated at neighbouring points in a grid of nuclear positions [19]. This procedure also accounts for situations in which the system is in the vicinity of an avoided crossing or conical intersections.

The procedure put forward in Ref. [19] focuses on ensuring the continuous evolution of eigenvectors and nonadiabatic coupling vectors along a single trajectory in configuration space. However, when computing time-dependent expectation values based on an ensemble of trajectories (which are typically initialized at different points in configuration space), one is faced with the issue of how to ensure eigenvector sign continuity within the ensemble. In Ref. [14], building upon elements of Errea et al.'s method, Hanna et al. proposed a simple procedure that accomplishes this within the context of mixed quantum-classical surface-hopping dynamics simulations. The utility of this procedure was demonstrated by calculating both adiabatic state populations in a reduced model of a condensed phase proton-coupled electron transfer reaction and subsystem state populations in an excitonic model of an alpha-helical chain undergoing vibrational energy transport, using the SSTP algorithm. More specifically, the results showed that ensuring eigenvector sign continuity across the ensemble leads to minor (but significant) improvements in the accuracy of expectation values in some cases and to drastic improvements in other cases.

We now outline the procedure proposed in Ref. [14]. To properly evaluate the expression for a time-dependent expectation value in Eq. (14.15), the sign continuity of the eigenvectors must be preserved across all of the points in the configurational space (of the classical DOF) visited by an ensemble of trajectories, as opposed to the points within a single trajectory. This may be accomplished by first sampling the initial conditions of the classical DOF for the first microcanonical (i.e. NVE) trajectory from a canonical (i.e. NVT) trajectory, in which the eigenvector signs are tracked and corrected at each time step according to the following steps:

1. Compute $O_{\alpha\alpha}(t) = \langle \alpha; Q_t | \alpha; Q_{t-\Delta t} \rangle$ (i.e. the overlap of eigenvector α with eigenvector α of the previous time step) for each α. When the classical configuration $Q_{t-\Delta t}$ is not close to an avoided crossing or conical intersection

and the time step is sufficiently small, the eigenvectors are not expected to rotate by much. In this case, the $O_{\alpha\alpha}$'s will be close to 1 (assuming that the eigenvectors are normalized). However, if an eigenvector undergoes an arbitrary sign flip, then the $O_{\alpha\alpha}$'s will be close to -1. In contrast, when $Q_{t-\Delta t}$ is close to an avoided crossing or conical intersection, the eigenvectors may vary rapidly, leading to $O_{\alpha\alpha}$'s that are substantially lower than 1 and possibly even negative. In this case, if an eigenvector undergoes an arbitrary sign flip, then $O_{\alpha\alpha}$ could lie in the interval $-\delta < O_{\alpha\alpha} < \delta$, where $|\delta|$ is substantially lower than 1 (e.g. 0.7 or lower).

2. Determine the value of $m_t(\alpha)$ for all α's, according to

$$m_t(\alpha) = \begin{cases} 0 \text{ if } |O_{\alpha\alpha}(t) - 1| < \epsilon \\ 1 \text{ if } |O_{\alpha\alpha}(t) + 1| < \epsilon \\ 2 \text{ otherwise} \end{cases} \tag{14.24}$$

where ϵ is a threshold parameter (with $0 < \epsilon < 1$) that depends on the size of the time step, Δt, and the details of the PESs. The $m_t(\alpha) = 0$ and 1 cases would typically arise when $Q_{t-\Delta t}$ is not in the vicinity of an avoided crossing or conical intersection and the eigenvector undergoes a physical rotation and unphysical sign flip, respectively. The $m_t(\alpha) = 2$ case would typically arise when $Q_{t-\Delta t}$ is in the vicinity of an avoided crossing or conical intersection. In this case, one must return the system to the end of the previous time step, divide the current time step in half, and evolve the system with the reduced time step. This process is repeated until $m_t(\alpha)$ becomes either 0 or 1. A sensible choice of ϵ (in combination with a sufficiently small Δt) should yield $m_t(\alpha) = 0, 1$ most of the time (in order to minimize the number of time steps needed).

3. Correct the signs of all eigenvectors according to

$$|\alpha; Q_t\rangle^c = (-1)^{m_t(\alpha)} |\alpha; Q_t\rangle, \tag{14.25}$$

i.e. if $m_t(\alpha) = 0$, then the sign is not changed, and if $m_t(\alpha) = 1$, then the sign is flipped to ensure the continuous evolution of the eigenvector.

At the end of this NVT dynamics phase, the eigenvectors are stored in memory (i) to continue the sign tracking and correction during the first NVE trajectory in the ensemble and (ii) to continue the sign tracking and correction during the second NVT dynamics phase preceding the second NVE trajectory. This procedure is repeated for the remaining trajectories in the ensemble (see Fig. 14.3 for an illustration of this procedure). In this way, the basis coefficients in $|\alpha; Q\rangle = \sum_i c_i^\alpha(Q)|\phi_i\rangle$ (where $\{|\phi_i\rangle\}$ is a basis set of choice), which may enter explicitly into the sampling of $\rho_{\alpha'\alpha}(Q, P)$ and into the dynamics of $\chi_{\alpha\alpha'}(Q, P, t)$, will evolve continuously throughout the configurational space.

For systems that do not spend a significant amount of time in the vicinity of an avoided crossing or conical intersection, one can reduce the computational time

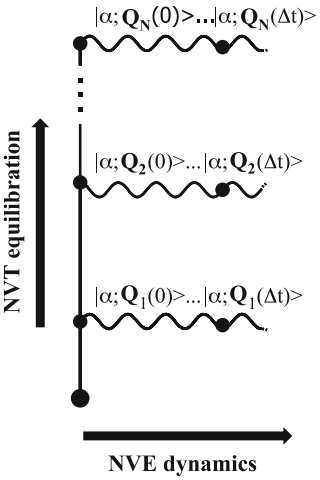

Fig. 14.3 A pictorial depiction of the procedure for ensuring sign continuity within an ensemble of trajectories

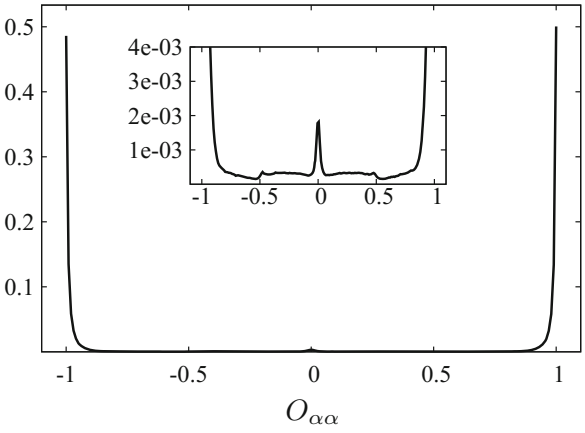

Fig. 14.4 Histogram of all eigenvector overlap values, $O_{\alpha\alpha}$, for the PCET model considered in Ref. [14]. The inset portrays a zoomed in portion of the histogram

associated with implementing the $m_t(\alpha) = 2$ case by neglecting it altogether, i.e. one does not change the sign of the eigenvector (based on the assumption that any sign change is physical in this region of the configurational space). In such situations, one must choose the value of ϵ with great care. If ϵ is too large, then one could erroneously change the eigenvector signs and, in turn, distort the results. We now discuss a way of choosing appropriate ϵ values for a given system and time step size (in general, the optimal value of ϵ will depend on these factors). To determine which value or range of values would be appropriate, it is instructive to first generate a histogram of the $O_{\alpha\alpha}$ values. In Fig. 14.4, we present the histogram of $O_{\alpha\alpha}$ values for the proton-coupled electron transfer (PCET) model considered in Ref. [14], which was calculated based on a sufficiently large ensemble of "sign-uncorrected" trajectories. As can be seen, the most probable values of $O_{\alpha\alpha}$ occur in the ranges $-1 < O_{\alpha\alpha} < -0.9$ and $0.9 < O_{\alpha\alpha} < 1$, with the remaining $O_{\alpha\alpha}$ values having very low probabilities. Zooming in on the region at low ordinate values (see inset of

Fig. 14.4), one sees continuous decays starting from $O_{\alpha\alpha} = \pm 1$, followed by two blips centred at $O_{\alpha\alpha} \approx \pm 0.5$, and a peak centred at $O_{\alpha\alpha} = 0$ (which is presumably due to character switches in the eigenstates after a nonadiabatic transition). The discontinuities at $O_{\alpha\alpha} \approx \pm 0.5$ are suggestive of the onset of eigenvector rotations near an avoided crossing or conical intersection and thereby point to an optimal ϵ value that is slightly less than ≈ 0.5.

To validate the accuracy of the expectation values calculated using the streamlined version of the eigenvector sign correction procedure, one could repeat the calculation with a reduced time step and compare the results to those obtained with the larger time step. (For the system considered in Ref. [14], it was found that the percentage of the total time that the $m_t(\alpha) = 2$ case arises for a particular choice of ϵ decreases by about two orders of magnitude when the time step is decreased by at least a factor of ten.) If there is no significant change in the results, then the streamlined method is justified.

Finally, to speed up the generation of the ensemble of trajectories, one can split up the work onto many computer processors. As a result, however, one can no longer easily ensure eigenvector sign continuity across the entire ensemble, but only within the sub-ensemble of trajectories generated on a given processor. In Ref. [14], the authors confirmed that the final expectation values were not adversely affected by the parallelization by checking what happens after randomizing the initial eigenvector signs every n trajectories on each processor. This check revealed that for the system considered, one must run at least $\approx$400 trajectories per processor to recover the fully sign-corrected results.

14.3 Applications

14.3.1 Vibrational Energy Transfer in an Alpha-Helical Polypeptide

We now present an application in which the utility of the previously discussed transition filtering scheme is demonstrated for simulating vibrational energy transfer in a six-state model of an alpha-helical polypeptide [15]. In this case, the vibrational energy transfer is monitored by computing the time-dependent amide I mode populations, following a vibrational excitation at one end of the polypeptide.

The aforementioned model, portrayed in Fig. 14.5, involves a one-dimensional chain of hydrogen-bonded (H-bonded) peptide groups, constituting one of the three peptide chains in an alpha-helical polypeptide. Adopting a mixed quantum-classical description, the high-frequency amide I modes are treated quantum mechanically, while the low-frequency H-bond displacement coordinates to which the amide I modes are coupled are treated classically. The Hamiltonian of this system is given by

$$H = H_0|0\rangle\langle 0| + \sum_{m,n} H_{mn}|\phi_m\rangle\langle\phi_n|, \tag{14.26}$$

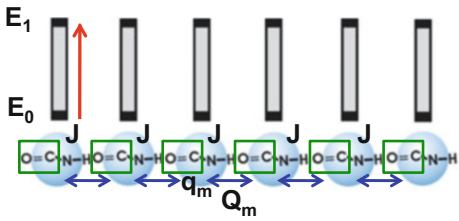

Fig. 14.5 One-dimensional chain model of H-bonded peptide groups (blue spheres) in an alpha-helical polypeptide. The position of the mth amide I mode (green rectangles) is denoted by q_m, while the longitudinal displacement of the mth unit (blue double-sided arrows) is denoted by Q_m. Initially, the first amide I mode in the chain is vibrationally excited (as indicated by the red arrow) with energy E_1, and the remainder of the amide I modes are in their ground states with energies E_0

where $|\phi_m\rangle = |\chi_{m1}\rangle \prod_{n\neq m} |\chi_{n0}\rangle$ is the mth singly excited state and $|0\rangle = \prod_m |\chi_{m0}\rangle$ is the ground state of a chain of amide I modes. (N.B.: $|\chi_{m0}\rangle$ and $|\chi_{m1}\rangle$ denote the ground and first excited states, respectively, of the mth amide I mode). The ground-state matrix element is given by $H_0 = T + \mathcal{E}_0(Q)$, where $T = \Sigma_i \frac{P_i^2}{2M}$ is the kinetic energy associated with the motion of the H-bond lattice displacements and the potential energy has the following form:

$$\mathcal{E}_0(Q) = \sum_m \left[E_{m0} + (1 - \delta_{m,1}) \frac{W}{2} (Q_m - Q_{m-1})^2 + w_{m0}(Q) \right]. \tag{14.27}$$

The excited state matrix elements are given by

$$\begin{aligned} H_{mn} = {} & \delta_{m,n} \left[H_0 + E_{m1} - E_{m0} + w_{m1}(Q) - w_{m0}(Q) \right] \\ & - J \left[\delta_{m-1,n} \langle \phi_m | q_m q_{m-1} | \phi_{m-1} \rangle \right. \\ & \left. + \delta_{m,n-1} \langle \phi_n | q_n q_{n-1} | \phi_{n-1} \rangle \right], \end{aligned} \tag{14.28}$$

where $\delta_{i,j}$ is the Kronecker delta function, J is the parameter governing the strength of the transition dipole moment coupling between neighbouring amide I modes, W is the force constant governing the motion of the H-bond lattice displacements, $E_{m1} - E_{m0}$ is the energy gap between the ground and first excited states of the mth amide I mode, q_m is the position of the mth amide I mode, and $Q = \{Q_m\}$ corresponds to the set of H-bond lengths. The term $w_{m\nu}(Q)$, which describes the coupling between the H-bond displacements and the amide I modes, is given by

$$w_{m\nu}(Q) = (1 - \delta_{m,1}) \frac{\chi}{2} (Q_m - Q_{m-1}) \langle \chi_{m\nu} | q_m^2 | \chi_{m\nu} \rangle, \tag{14.29}$$

where χ is the coupling strength. The values of the various matrix elements of q_m and q_m^2 are taken from Table 2 in Ref. [73], while the values of the parameters

$E_{m1} - E_{m0}$, J, W, χ and M are taken from Table 1 in Ref. [73] and are given by 1660 cm^{-1}, 7.8 cm^{-1}, 13 N/m, 62 pN and 87 m_p, respectively.

The quantum subsystem of amide I modes and classical environment of H-bond lattice displacements are uncorrelated initially, which yields the following factorized initial density matrix:

$$\hat{\rho}(0) = \hat{\rho}_q(0)\,\rho_e(Q, P), \tag{14.30}$$

where $\hat{\rho}_q(0)$ and $\rho_e(Q, P)$ correspond to the initial densities of the quantum subsystem and classical environment, respectively. Following a vibrational excitation of the first amide I mode in the chain, the initial density matrix of the quantum subsystem, represented in the subsystem basis of singly excited states, is given by

$$\hat{\rho}_q(0) = \begin{pmatrix} 1\,0 & \cdots & 0 \\ 0\,0 & \cdots & 0 \\ \vdots\,\vdots & \ddots & 0 \\ 0\,0 & \cdots & 0 \end{pmatrix}. \tag{14.31}$$

The positions and momenta of the classical oscillators are initialized by first treating them as a collection of uncoupled harmonic oscillators at thermal equilibrium at 300 K, whose equilibrium Wigner distribution $\rho_e(Q, P)$ can be well approximated by

$$\rho_e(Q, P) \approx \frac{1}{Z}\prod_{j=1}^{M}\exp\left[-\beta\left\{\frac{P_j^2}{2} + \frac{1}{2}W^2Q_j^2\right\}\right], \tag{14.32}$$

where M is the number of oscillators and $Z = \int dQ\,dP\,\exp\left[-\frac{\beta}{2}\sum_j(P_j^2 + W^2Q_j^2)\right]$ is the partition function. The correct thermal equilibrium distribution at 300 K (in the absence of any amide I excitation) is then achieved by equilibrating the coupled harmonic oscillators for 2 ps using the ground-state potential found in Eq. (14.27) with a Nosé-Hoover thermostat and a time step of 0.25 fs. (In Ref. [21], the ergodicity of the Nosé-Hoover thermostat was confirmed by comparing the results to those generated with a Nosé-Hoover chain thermostat.) The initial state of the quantum oscillators is sampled by first transforming $\hat{\rho}_q(0)$ to the adiabatic basis (see details of the transformation and sampling in Appendix A of Ref. [21]). Following the classical equilibration and sampling of the initial quantum state, a 50-fs microcanonical SSTP trajectory is generated using a time step of 1 fs. The arbitrary sign flips in the eigenvectors upon numerical diagonalization of the Hamiltonian matrix are corrected at each time step using the procedure described in Sect. 14.2.5.

Before presenting the results for the time-dependent populations of the amide I modes, one must describe how the optimal values of $\Delta E_{\alpha\beta}^{\min}$ and $\kappa_{\alpha\beta}$ are determined (see Sect. 14.2.4 for the definitions of these quantities). Because the basis set

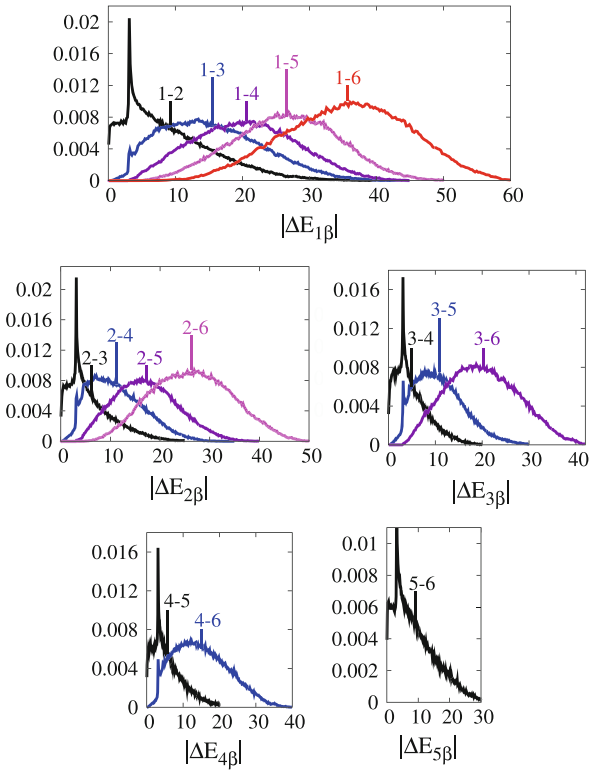

Fig. 14.6 Histograms of $|\Delta E_{\alpha\beta}|$ values (in units of 10^{-22} J) for all 15 possible energy gaps between the adiabatic states. The mean value of each histogram is denoted by a vertical arrow. Each colour corresponds to energy gaps with the same value of $|\alpha - \beta|$

contains six singly excited states (one per amide I mode), the number of adiabatic states involved in the dynamics is $n = 6$, and, therefore, one has to determine 15 $\Delta E_{\alpha\beta}^{\min}$ values and 15 $\kappa_{\alpha\beta}$ values. To accomplish this, the system is evolved adiabatically on its ground-state PES for a sufficiently long time (i.e. to explore the important regions of the configuration space of the classical DOF), and 15 $|\Delta E_{\alpha\beta}|$ histograms are generated based on the $\Delta E_{\alpha\beta}$ values calculated at each time step (see histograms in Fig. 14.6). The first, second and third columns of Table 14.1 show the $\Delta E_{\alpha\beta}^{\min}$ values corresponding to the smallest $\Delta E_{\alpha\beta}$ values with a non-zero probability density in the histograms, the mean values of each $|\Delta E_{\alpha\beta}|$ histogram and the optimal $\kappa_{\alpha\beta}$ values used to generate the results, respectively. It should be noted that the $|\alpha - \beta| = 1$ transitions (whose $|\Delta E_{\alpha\beta}|$ histograms have substantial probability densities at lower $|\Delta E_{\alpha\beta}|$ values) are not filtered in an effort to minimize the errors introduced by filtering out transitions.

Figure 14.7 shows the time-dependent populations of the amide I modes out to 50 fs, generated using the transition filtering scheme, 10^9 trajectories and a time step of 1 fs. Comparing these results to the unfiltered ones [14] generated using 5×10^{10} trajectories, one sees that it is possible to obtain smoother and comparably accurate results with more than an order of magnitude fewer trajectories when transition filtering is used.

Table 14.1 The values of the transition filtering parameters used in the simulations. All values are in units of 10^{-22} J

$\alpha \leftrightarrow \beta$	$\Delta E_{\alpha\beta}^{\min}$	$\overline{\Delta E}_{\alpha\beta}$	$\kappa_{\alpha\beta}$
1↔2	0.00182	9.3	–
1↔3	0.255	15.53	8
1↔4	3.117	20.57	12
1↔5	5.103	26.55	20
1↔6	6.327	35.72	23
2↔3	0.00035	6.19	–
2↔4	0.229	11.27	8
2↔5	3.117	17.27	12
2↔6	4.826	26.42	20
3↔4	0.0004	5.02	–
3↔5	0.181	11.01	8
3↔6	3.119	20.19	12
4↔5	0.000577	5.76	–
4↔6	0.234	15.15	8
5↔6	0.00119	8.98	–

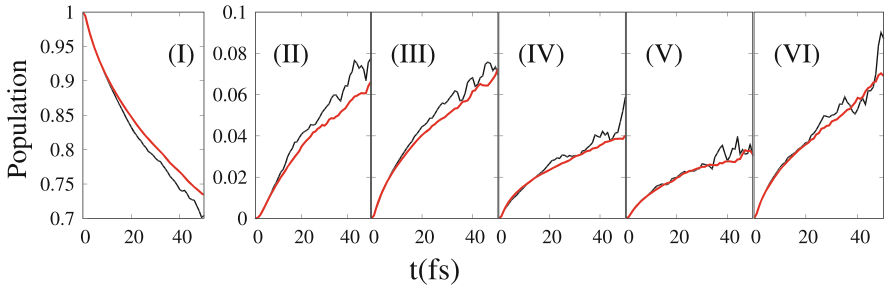

Fig. 14.7 Comparison of the time-dependent populations of the six amide I modes, generated with the transition filtering scheme (red lines) and without any filter (black lines). (The unfiltered results are taken from Ref. [14])

14.3.2 Field-Driven Dynamics of a Plasmonic Metamolecule

We next present an application in which the SSTP algorithm is generalized for simulating the dynamics of a metamolecule subjected to a time-dependent driving field [78]. In this case, because the Hamiltonian is time-dependent, a time-dependent basis is used. Metamolecules are important in the field of quantum plasmonics [9, 11, 72, 90], which studies the interactions of surface plasmons with quantum emitters (a metamolecule collectively refers to the surface plasmon and quantum emitter). At the nanometre scale, metamolecules can operate at optical frequencies [38, 42, 52, 56]. A typical example of such a metamolecule is a quantum dot coupled to a surface plasmon in a metal nanoparticle [51].

A metamolecule can be modelled by a two-level system, representing the quantum dot, coupled to a resonant mode, representing the surface plasmon in

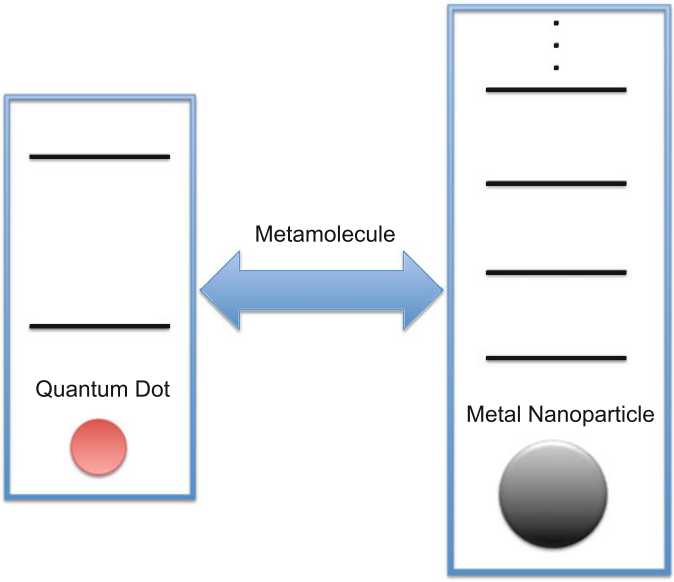

Fig. 14.8 A schematic illustration of a model metamolecule. The metamolecule is composed of a quantum dot, represented by a two-level system, coupled to a surface plasmon in a metal nanoparticle and represented by a quantum harmonic oscillator (with a manifold of equispaced energy levels)

the metal nanoparticle (see Fig. 14.8 for a schematic illustration) [72]. In addition, the effect of a time-dependent driving field on the dynamics of the metamolecule can be considered. In this section, we present a study in which the two-level system is treated quantum mechanically and the resonant mode and driving field are treated classically. The time-dependent Hamiltonian of this mixed quantum-classical system, written in terms of adimensional quantities (whose definitions are given in the Appendix), is given by

$$\hat{H}(t) = -\frac{\Omega}{2}\hat{\sigma}_z + \frac{P^2}{2} + \frac{1}{2}\omega^2 Q^2 - cQ\hat{\sigma}_x + g\cos(\omega_d t)\hat{\sigma}_x\,, \qquad (14.33)$$

where Ω is the frequency associated with the two-level system, ω is the frequency associated with the resonant mode, c is a coupling constant, g denotes the subsystem-field coupling strength, ω_d is the driving frequency, and $\hat{\sigma}_{x/z}$ denote the Pauli matrices. The composite system is initialized in the factorized state $\hat{\rho}(Q, P) = \hat{\rho}_S \rho_B(Q, P)$, where the density matrix of the subsystem (i.e. the two-level quantum dot), expressed in the subsystem basis, is given by

$$\hat{\rho}_S = \begin{pmatrix} 0 & 0 \\ 0 & 1 \end{pmatrix}, \qquad (14.34)$$

and $\rho_{\mathrm{B}}(Q,P)$, the Wigner distribution function of the bath (i.e. the resonant harmonic mode), is given by

$$\rho_{\mathrm{B}}(Q,P)=\frac{\tanh(\beta\omega/2)}{\pi}\exp\left[-\frac{2\tanh(\beta\omega/2)}{\omega}\left(\frac{P^2}{2}+\frac{\omega^2Q^2}{2}\right)\right]. \quad (14.35)$$

To simulate the quantum-classical Liouville dynamics of the Hamiltonian in Eq. (14.33), a generalization of the SSTP algorithm to time-dependent Hamiltonians is needed. To this end, one can introduce a time-dependent basis in terms of the eigenstates of $\hat{h}(Q,t)=\hat{H}(Q,P,t)-P^2/2M$ (defined by $\hat{h}(Q,t)|\alpha;Q,t\rangle=E_\alpha(Q,t)|\alpha;Q,t\rangle$, where $|\alpha;Q,t\rangle$ and $E_\alpha(Q,t)$ are the αth eigenstate and eigenvalue, respectively). In this basis, the evolution of an observable χ takes the form

$$\chi_{\alpha\alpha'}(Q,P,t)=\mathcal{T}\left\{\sum_{\beta\beta'}\left(e^{i\int_{t_0}^{t}d\tau\mathcal{L}^t(\tau)}\right)_{\alpha\alpha',\beta\beta'}\right\}\chi_{\beta\beta'}(Q,P,t_0), \quad (14.36)$$

where t_0 is the initial time, $\mathcal{T}$ is the time-ordering operator and

$$i\mathcal{L}^t_{\alpha\alpha',\beta\beta'}(t)=i\tilde{\mathcal{L}}_{\alpha\alpha',\beta\beta'}(t)+\mathcal{K}^t_{\alpha\alpha',\beta\beta'}(t). \quad (14.37)$$

In the above equation, the operator $\mathcal{K}^t$ is responsible for the nonadiabatic transitions in the subsystem due to the interaction with the external field, and its matrix elements are given by

$$\mathcal{K}^t_{\alpha\alpha',\beta\beta'}=\langle\dot{\alpha}|\beta\rangle\delta_{\alpha'\beta'}+\langle\beta|\dot{\alpha}'\rangle\delta_{\alpha\beta}, \quad (14.38)$$

where the dot denotes a time derivative. The matrix elements of the operator $i\tilde{\mathcal{L}}$ have a similar form to those implied in Eq. (14.7) and are given by

$$i\tilde{\mathcal{L}}_{\alpha\alpha',\beta\beta'}(t)=i\tilde{\mathcal{L}}^0_{\alpha\alpha'}(t)\delta_{\alpha\beta}\delta_{\alpha'\beta'}+\tilde{\mathcal{K}}_{\alpha\alpha',\beta\beta'}(t), \quad (14.39)$$

where $i\tilde{\mathcal{L}}^0_{\alpha\alpha'}(t)=i\tilde{\omega}_{\alpha\alpha'}(t)+i\tilde{L}_{\alpha\alpha'}(t)$, with the Bohr frequency $\tilde{\omega}_{\alpha\alpha'}(Q,t)=[E_\alpha(Q,t)-E_{\alpha'}(Q,t)]/\hbar$ and the classical-like Liouville operator $i\tilde{L}_{\alpha\alpha'}=(P/M)\cdot(\partial/\partial Q)+(1/2)[\tilde{F}^{\alpha}_{\mathrm{W}}(t)+\tilde{F}^{\alpha'}_{\mathrm{W}}(t)]\cdot\partial/\partial P$ ($\tilde{F}^{\alpha}_{\mathrm{W}}(Q,t)$, is the time-dependent Hellman-Feynman force derived from the adiabatic energy surface $E_\alpha(Q,t)$); the operator $\tilde{\mathcal{K}}$ is responsible for nonadiabatic transitions in the subsystem due to the interaction with the bath and its matrix elements are given by

$$\tilde{\mathcal{K}}_{\alpha\alpha',\beta\beta'}(t)=\tilde{\mathcal{T}}_{\alpha\to\beta}(t)\delta_{\alpha'\beta'}+\tilde{\mathcal{T}}^*_{\alpha'\to\beta'}(t)\delta_{\alpha\beta}, \quad (14.40)$$

where

$$\tilde{\mathcal{T}}_{\alpha\to\beta}(t)=\frac{P}{M}\cdot d_{\alpha\beta}(Q,t)\left(1+\frac{1}{2}\frac{\Delta E_{\alpha\beta}(t)d_{\alpha\beta}(Q,t)}{\frac{P}{M}\cdot d_{\alpha\beta}(Q,t)}\frac{\partial}{\partial P}\right), \quad (14.41)$$

$$\tilde{\mathcal{T}}^{*}_{\alpha'\to\beta'}(t) = \frac{P}{M}\cdot d^{*}_{\alpha'\beta'}(Q,t)\left(1+\frac{1}{2}\frac{\Delta E_{\alpha'\beta'}(t)d^{*}_{\alpha'\beta'}(Q,t)}{\frac{P}{M}\cdot d^{*}_{\alpha\beta}(Q,t)}\frac{\partial}{\partial P}\right), \quad (14.42)$$

with $\Delta E_{\alpha\beta}(t) = E_{\alpha}(Q,t) - E_{\beta}(Q,t)$ and $d_{\alpha\beta}(Q,t) = \langle\alpha;\, Q,t|\partial/\partial Q|\beta;\, Q,t\rangle$ is the nonadiabatic coupling vector between the time-dependent states α and β.

To arrive at an algorithm for computing $\chi_{\alpha\alpha'}(t)$, one starts by discretizing the time to obtain

$$\chi_{\alpha\alpha'}(t) = \sum_{\beta\beta'}\mathcal{T}\left\{\exp\left[i\sum_{n}\tau_n\mathcal{L}^{t}(\tau_n)\right]\right\}_{\alpha\alpha',\beta\beta'}\chi_{\beta\beta'}(t_0)\,, \quad (14.43)$$

where $\sum_n \tau_n = t - t_0$. As in the derivation of the SSTP algorithm [47], one then assumes very small time steps τ_n and applies the Dyson identity to obtain

$$\begin{aligned}\chi_{\alpha\alpha'}(t) = \sum_{\beta\beta'}\mathcal{T}\prod_{n}\Big\{&\exp\left[i\tau_n\tilde{\mathcal{L}}^{0}_{\alpha\alpha'}(\tau_n)\right]\\ &\times\left(1+\tau_n\tilde{\mathcal{K}}_{\alpha\alpha',\beta\beta'}+\tau_n\mathcal{K}^{t}_{\alpha\alpha',\beta\beta'}\right)\Big\}\chi_{\beta\beta'}(t_0)\,. \quad (14.44)\end{aligned}$$

In what follows, it will be assumed that the subsystem-bath coupling is sufficiently weak that the action of $\tilde{\mathcal{K}}_{\alpha\alpha',\beta\beta'}$ can be disregarded. Thus, if $\tau_n = \tau$ for every n, then one obtains

$$\chi_{\alpha\alpha'}(t) = \sum_{\beta\beta'}\mathcal{T}\prod_{n}\left\{\exp\left[i\tau\tilde{\mathcal{L}}^{0}_{\alpha\alpha'}(\tau)\right]\left(1+\tau\mathcal{K}^{t}_{\alpha\alpha',\beta\beta'}\right)\right\}\chi_{\beta\beta'}(t_0)\,. \quad (14.45)$$

In practice, Eq. (14.45) can be evaluated using an analogous procedure to that described in Sect. 14.2.3. At the beginning of each time step, one propagates the phase space point deterministically using $i\tilde{\mathcal{L}}^{0}_{\alpha\alpha',\beta\beta'}(t)$. Then, at the end of the step, one samples stochastically the nonadiabatic transition due to the driving field. This is done by first sampling with probability 1/2 one of the two terms of $\mathcal{K}^{t}_{\alpha\alpha',\beta\beta'}$ in Eq. (14.38). The probability of accepting the transition is defined as

$$\mathcal{P}_{\beta\to\alpha} = \frac{\tau|\langle\dot{\alpha}|\beta\rangle|}{1+\tau|\langle\dot{\alpha}|\beta\rangle|}\,, \quad (14.46)$$

while the probability of rejecting the transition is given by

$$\mathcal{Q}_{\beta\to\alpha} = \frac{1}{1+\tau|\langle\dot{\alpha}|\beta\rangle|}\,. \quad (14.47)$$

As described in Sect. 14.2.3, the observable is then multiplied by the appropriate MC weight, depending on whether or not the transition is accepted. Finally, the

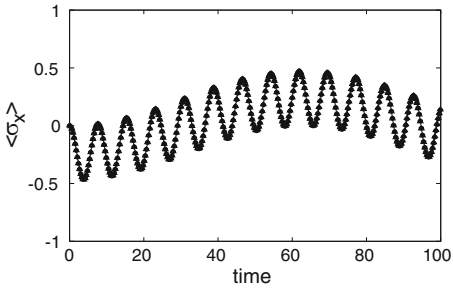

Fig. 14.9 Plot of the time-dependent coherence, $\langle \sigma_x(t) \rangle$, for the weak subsystem-field case ($g = 0.1$)

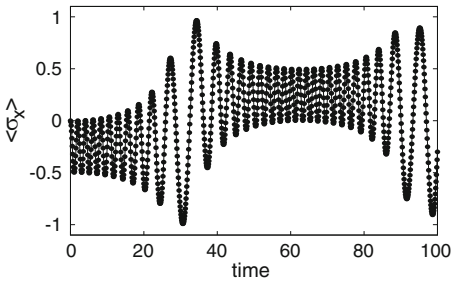

Fig. 14.10 Plot of the time-dependent coherence, $\langle \sigma_x(t) \rangle$, for the strong subsystem-field coupling case ($g = 1.5$)

average value of the observable is calculated according to Eq. (14.15), with the use of the time-dependent basis as opposed to the time-independent one.

The results of the simulations are now presented and discussed. A time step of $\tau = 0.1$ and 10^5 trajectories were used to obtain all the results. First, the influence of the driving field on the metamolecule is investigated by varying the subsystem-field coupling from $g = 0.1$ to $g = 1.5$ while keeping the system parameters fixed at $\beta = 12.5$, $c = 0.01$, $\Omega = 0.8$, $\omega = 0.5$ and $\omega_d = 0.05$. For this set of parameter values, the coupling between the quantum dot and resonant mode is weak, and, therefore, the effect of nonadiabatic transitions (due to this coupling) on the dynamics is expected to be minor. Figure 14.9 shows the results for the time-dependent subsystem coherence, $\langle \sigma_x(t) \rangle$, in the $g = 0.1$ case. We see that $\langle \sigma_x(t) \rangle$ exhibits both high- and low-frequency oscillatory modes, with the values of $\langle \sigma_x(t) \rangle$ ranging between -0.5 and 0.5. The fast mode (with angular frequency ≈ 0.81) is superimposed on the slow mode (with angular frequency ≈ 0.05). The low frequency corresponds to that of the driving field, while the high frequency corresponds to that of the tunnel splitting, shifted by a very small amount due to the weak coupling to the bath and field. As expected, in the case of weak coupling to the driving field, the tunnel splitting dominates the time evolution of $\langle \sigma_x(t) \rangle$.

Figure 14.10 shows the results for the time-dependent subsystem coherence, $\langle \sigma_x(t) \rangle$, in the $g = 1.5$ case. When strongly coupled to the driving field, the time evolution of $\langle \sigma_x(t) \rangle$ displays an irregular pattern, viz. it starts by rapidly oscillating around $\langle \sigma_x \rangle = -0.25$ between $t = 0$ and $t \approx 20$; it undergoes large oscillations from $t \approx 20$ to $t \approx 40$ and then switches to oscillating rapidly around $\langle \sigma_x \rangle = 0.25$ until $t = 80$; and finally, it undergoes large oscillations again. Based on these

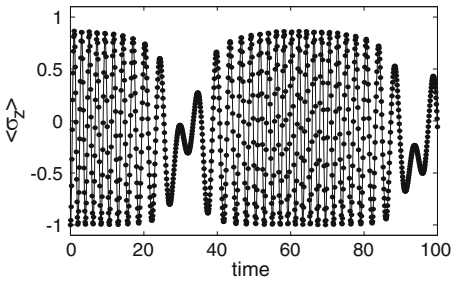

Fig. 14.11 Plot of the time-dependent population difference, $\langle\sigma_z(t)\rangle$, for the strong subsystem-field coupling case ($g = 1.5$)

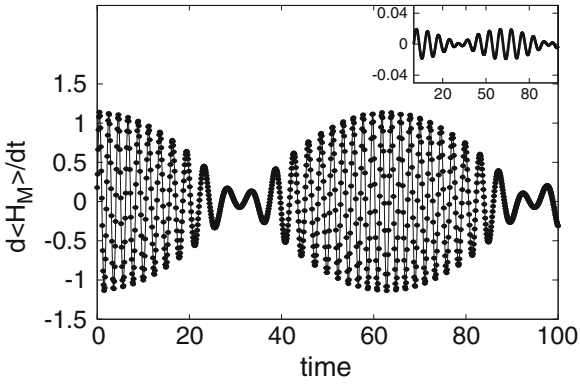

Fig. 14.12 Rate of change of the expectation value of the Hamiltonian of the metamolecule, $d\langle H_M\rangle/dt$, as a function of time. The main figure displays the result for the strong driving field case, while the inset shows the result for the weak driving field case

results, one can conclude that the quantum dot switches between two different dynamical regimes, one in which the coherence is positive and the other in which it is negative. Because of the strong coupling to the driving field, the frequency of the fast oscillations is $\approx 200\%$ greater than that obtained in the weak subsystem-field coupling case.

Figure 14.11 shows the time evolution of the subsystem population difference, $\langle\sigma_z(t)\rangle$, in the strong driving regime. It also exhibits an irregular pattern, with regions of large and fast oscillations separated by regions of small and slow oscillations. In the weak driving regime, such a behaviour is not observed, and the amplitude of the oscillations is much smaller (result not shown). This is simply a reflection of the fact that a smaller fraction of the trajectories is driven into the excited state by the driving field in this regime.

Figure 14.12 shows the rate of change of the expectation value of the energy of the metamolecule for the $g = 0.1$ and $g = 1.5$ cases. For $g = 1.5$, we see that $d\langle H_M(t)\rangle/dt$ exhibits regions of large and fast oscillations about zero separated by regions of small and slow oscillations about zero, in the same time intervals where $\langle\sigma_x(t)\rangle$ and $\langle\sigma_z(t)\rangle$ do. Instead, for $g = 0.1$, $d\langle H_M(t)\rangle/dt$ exhibits much smaller oscillations about zero.

14.4 Summary and Future Outlook

Quantum dynamical modelling of nanoscale systems containing large numbers of DOF is essential for understanding their microscopic and macroscopic properties. Adiabatic mixed quantum-classical dynamics simulations, which rely on the Born-Oppenheimer approximation, may be performed when there is a large separation between the timescales of the quantum subsystem and classical environment. However, for many chemical and biological processes of interest, this is not the case, and, as a result, the dynamics is not confined to a single state of the quantum subsystem. This has prompted the development of mixed quantum-classical methods for simulating nonadiabatic dynamics.

In this chapter, we discussed a hybrid MD/MC method known as the SSTP algorithm, which is based on a solution of the QCLE. This method has been shown to perform quite well on relatively simple model systems, but its extension to systems containing multiple (i.e. >2) quantum DOF and strong subsystem-bath coupling has proven to be challenging. This is primarily due to the rapid growth of MC weights (associated with the stochastic sampling of the nonadiabatic transitions) in time, which render the expectation values difficult to converge. To alleviate this problem, observable cutting and transition filtering techniques have been put forward, which significantly reduce the number of trajectories required for convergence of the expectation values. In this chapter, we discussed one transition filtering scheme, which is designed to filter out the low-probability transitions (which lead to the large MC weights) and thereby slow down the growth of the weights. This scheme has been shown to yield substantial improvements in accuracy, as compared to the other schemes, and to generate results with at least one order of magnitude fewer trajectories than what would be required without the scheme. We also discussed a simple procedure for ensuring sign continuity/consistency in the evolution of eigenvectors within an ensemble of surface-hopping trajectories. This is required because the on-the-fly numerical diagonalization of the Hamiltonian matrix can yield eigenvectors with arbitrary signs. Without such a scheme, trajectory-based calculations of expectation values in the adiabatic representation can be adversely affected.

This chapter also covered two recent applications of the SSTP algorithm. The first one demonstrated the efficacy of the aforementioned transition filtering scheme for simulating vibrational energy transfer dynamics in systems with higher dimensional Hilbert spaces and phase spaces. In particular, the time-dependent populations of the amide I modes in a model of an alpha-helical polypeptide (containing six quantum and six classical coordinates) were presented. The results showed that it is possible to obtain smooth, reliable profiles with more than one order of magnitude fewer trajectories compared to those obtained without any filtering. In the second application, we presented a dynamical study of a model for a plasmonic metamolecule interacting with an oscillatory driving field. In this case, the Hamiltonian is explicitly time-dependent, and, thus, the SSTP algorithm had to be generalized to account for this fact. Results showing the effects of the

driving strength on the population and coherence dynamics of the quantum dot, as well as on the rate of change of the metamolecule energy, were presented and discussed. Interestingly, in the strong subsystem-field coupling case, large and irregular variations in the populations and coherences of the quantum dot were observed.

The QCLE-based approach to modelling quantum dynamics in classical environments has proven to be successful in studying a variety of quantum processes at the nanoscale. Nevertheless, the currently available algorithms present significant challenges, necessitating the need for further improvements and developments. Thus, we hope that this chapter will stimulate research along this direction. In addition, we are interested in broadening the scope of applications studied by the methods discussed herein. In particular, we believe that these methods can be effectively used to study energy and charge transfer dynamics in nanoscale devices.

Appendix

The following adimensional coordinates and parameters were used to express the metamolecule Hamiltonian in Eq. (14.33):

$$\Omega = \frac{\Omega'}{\omega'_{\mathrm{a}}} , \tag{14.48}$$

$$P = \frac{P'}{\sqrt{M'\hbar\omega'_{\mathrm{a}}}} , \tag{14.49}$$

$$Q = \sqrt{\frac{\hbar\omega'_{\mathrm{a}}}{\hbar}}\, Q' , \tag{14.50}$$

$$\omega = \frac{\omega'}{\omega'_{\mathrm{a}}} , \tag{14.51}$$

$$c = \frac{c'}{\sqrt{\hbar\omega'^{3}_{\mathrm{a}} M'}} , \tag{14.52}$$

$$g = \frac{g'}{\hbar\omega'_{\mathrm{a}}} , \tag{14.53}$$

$$\beta = \hbar\omega'_{\mathrm{a}}\beta' , \tag{14.54}$$

where the primed quantities denote coordinates and parameters with dimensions and M' is the inertial parameter of the resonant mode (which has been set to unity). In the above equations, the energy scale $\hbar\omega'_{\mathrm{a}}$ has been introduced. ω'_{a} is chosen in such a way that the frequency $\omega = 0.5$ of the resonant mode corresponds to $\omega' = 8.9 \times 10^{12}$ Hz (which is typical of metal nanoparticles [51]) and a total simulation time of 5.62×10^{-12} s.

References

1. F. Agostini, S.K. Min, A. Abedi, E.K.U. Gross, J. Chem. Theory Comput. **12**, 2127 (2016)
2. I.V. Aleksandrov, Z. Naturforsch. A **36**, 902 (1981)
3. S.M. Bai, W.W. Xie, Q. Shi, J. Phys. Chem. A **118**, 9262 (2014)
4. A. Bastida, C. Cruz, J. Zúñiga, A. Requena, B. Miguel, The Ehrenfest method with quantum corrections to simulate the relaxation of molecules in solution: equilibrium and dynamics. J. Chem. Phys. **126**(1), 014503 (2007)
5. M.J. Bedard-Hearn, R.E. Larsen, B.J. Schwartz, J. Chem. Phys. **123**, 234106 (2005)
6. E.R. Bittner, P.J. Rossky, Quantum decoherence in mixed quantum-classical systems: nonadiabatic processes. J. Chem. Phys. **103**, 8130–8143 (1995)
7. E.R. Bittner, B.J. Schwartz, P.J. Rossky, Quantum decoherence: a consistent histories treatment of condensed phase non-adiabatic quantum molecular dynamics. J. Mol. Struct. Theochem **389**, 203–216 (1997)
8. S. Bose, Quantum communication through an unmodulated spin chain. Phys. Rev. Lett. **91**(20), 207901 (2003)
9. J.G. Bouillard, W. Dickson, D.P. O'Connor, G.A. Wurtz, A.V. Zayats, Low-temperature plasmonics of metallic nanostructures. Nano Lett. **12**, 1561 (2012)
10. C. Brooksby, O.V. Prezhdo, Quantized mean-field approximation. Chem. Phys. Lett. **346**, 463–469 (2001)
11. X. Chen, S. Li, C. Xue, M.J. Banholzer, G.C. Schatz, C.A. Mirkin, Plasmonic focusing in rod-sheath heteronanostructures. ACS Nano **3**, 87 (2009)
12. D. Dell'Angelo, G. Hanna, Self-consistent filtering scheme for efficient calculations of observables via the mixed quantum-classical liouville approach. J. Chem. Theory Comput. **12**, 477–485 (2016)
13. D. Dell'Angelo, G. Hanna, Using multi-state transition filtering to improve the accuracy of expectation values via mixed quantum-classical Liouville dynamics. AIP Conf. Proc. **1790**, 020009(1)–020009(4) (2016)
14. D. Dell'Angelo, G. Hanna, Importance of eigenvector sign consistency in computations of expectation values via mixed quantum-classical surface-hopping dynamics. Theor. Chem. Acc. **136**, 75 (2017)
15. D. Dell'Angelo, G. Hanna, On the performance of multi-state transition filtering in mixed quantum-classical Liouville surface-hopping simulations: beyond two- and three-state quantum subsystems. Theor. Chem. Acc. **137**, 15 (2018)
16. A. Donoso, D. Kohen, C.C. Martens, Simulation of nonadiabatic wave packet interferometry using classical trajectories. J. Chem. Phys. **112**, 7345 (2000)
17. A. Donoso, C.C. Martens, Simulation of coherent nonadiabatic dynamics using classical trajectories. J. Phys. Chem. A **102**, 4291–4300 (1998)
18. A. Donoso, C.C. Martens, Semiclassical multistate Liouville dynamics in the adiabatic representation. J. Chem. Phys. **112**, 3980 (2000)
19. L.F. Errea, L. Fernández, A. Macías, L. Méndez, I. Rabadán, A. Riera, Sign-consistent dynamical couplings between ab initio three-center wave functions. J. Chem. Phys. **121**(4), 1663–1669 (2004)
20. S.A. Fischer, C.T. Chapman, X. Li, J. Chem. Phys. **135**, 144102 (2011)
21. H. Freedman, G. Hanna, Mixed quantum-classical Liouville simulation of vibrational energy transfer in a model alpha-helix at 300 K. Chem. Phys. **477**, 74–87 (2016)
22. V.I. Gerasimenko, Theor. Math. Phys. **50**, 77 (1982)
23. G. Hanna, R. Kapral, Quantum-classical Liouville dynamics of nonadiabatic proton transfer. J. Chem. Phys. **122**, 244505 (2005)
24. G.J. Hedley, A. Ruseckas, I.D. Samuel, Light harvesting for organic photovoltaics. Chem. Rev. **117**(2), 796–837 (2016)
25. I. Horenko, C. Salzmann, B. Schmidt, C. Schütte, J. Chem. Phys. **117**, 11075 (2002)

26. I. Horenko, C. Salzmann, B. Schmidt, C. Schütte, Quantum-classical Liouville approach to molecular dynamics: surface hopping Gaussian phase-space packets. J. Chem. Phys. **117**, 11075–11088 (2002)
27. C.Y. Hsieh, R. Kapral, J. Chem. Phys. **137**, 22A507 (2012)
28. C.Y. Hsieh, R. Kapral, Analysis of the forward-backward trajectory solution for the mixed quantum-classical Liouville equation. J. Chem. Phys. **138**(13), 134110 (2013)
29. A.W. Jasper, C. Zhu, S. Nangia, D.G. Truhlar, Faraday Discuss. **127**, 1 (2004)
30. C. Joachim, M.A. Ratner, Molecular electronics: some views on transport junctions and beyond. Proc. Natl. Acad. Sci. U. S. A **102**(25), 8801–8808 (2005)
31. R. Kapral, J. Phys. Condens. Matter. **27**, 073201 (2015)
32. R. Kapral, Chem. Phys. **481**, 77 (2016)
33. R. Kapral, G. Ciccotti, J. Chem. Phys. **110**, 8919–8929 (1999)
34. R. Kapral, G. Ciccotti, Mixed quantum-classical dynamics. J. Chem. Phys. **110**, 8919–8929 (1999)
35. A. Kelly, T.E. Markland, J. Chem. Phys. **139**, 014104 (2013)
36. A. Kelly, T.E. Markland, Efficient and accurate surface hopping for long time nonadiabatic quantum dynamics. J. Chem. Phys. **139**(1), 014104 (2013)
37. A. Kelly, R. van Zon, J.M. Schofield, R. Kapral, J. Chem. Phys. **136**, 084101 (2012)
38. K.L. Kelly, E. Coronado, L.L. Zhao, G.C. Schatz, The optical properties of metal nanoparticles: the influence of size, shape, and dielectric environment. J. Phys. Chem. B **107**, 668 (2003)
39. H. Kim, R. Kapral, Chem. Phys. Chem. **9**, 470 (2008)
40. H. Kim, A. Nassimi, R. Kapral, J. Chem. Phys. **129**, 084102 (2008)
41. H.W. Kim, Y.M. Rhee, J. Chem. Phys. **140**, 184106 (2014)
42. S. Lal, S. Link, N.J. Halas, Nano-optics from sensing to waveguiding. Nat. Photon. **1**, 641 (2007)
43. Z. Lin, I.V. Rubtsov, Constant-speed vibrational signaling along polyethyleneglycol chain up to 60-Å distance. Proc. Natl. Acad. Sci. U. S. A. **109**(5), 1413–1418 (2012)
44. J. Liu, G. Hanna, J. Phys. Chem. Lett. **9**, 3928 (2018)
45. D. MacKernan, G. Ciccotti, R. Kapral, J. Chem. Phys. **116**, 2346–2353 (2002)
46. D. MacKernan, G. Ciccotti, R. Kapral, Trotter-based simulation of quantum-classical dynamics. J. Phys. Chem. B **112**, 424 (2008)
47. D. MacKernan, R. Kapral, G. Ciccotti, Sequential short-time propagation of quantum-classical dynamics. J. Phys. Condens. Matter. **14**, 9069–9076 (2002)
48. C.C. Martens, J. Phys. Chem. Lett. **7**, 2610 (2016)
49. C.C. Martens, J. Fang, Semiclassical-limit molecular dynamics on multiple electronic surfaces. J. Chem. Phys. **106**, 4918 (1997)
50. C.C. Martens, J.Y. Fang, J. Chem. Phys. **106**, 4918 (1997)
51. K.R. McEnery, M.S. Tame, S.A. Maier, M.S. Kim, Tunable negative permeability in a quantum plasmonic metamaterial. Phys. Rev. A **89**, 013822 (2014)
52. C.L. Nehl, J.H. Hafner, Shape-dependent plasmon resonances of gold nanoparticles. J. Mater. Chem. **18**, 2415 (2008)
53. S. Nielsen, R. Kapral, G. Ciccotti, Non-adiabatic dynamics in mixed quantum-classical systems. J. Stat. Phys. **101**, 225–242 (2000)
54. A. Nitzan, M.A. Ratner, Electron transport in molecular wire junctions. Science **300**(5624), 1384–1389 (2003)
55. P.V. Parandekar, J.C. Tully, Detailed balance in Ehrenfest mixed quantum-classical dynamics. J. Chem. Theory Comput. **2**(2), 229–235 (2006)
56. M. Pelton, J. Aizpurua, G. Bryant, Metal-nanoparticle plasmonics. Laser Photon. Rev. **2**, 136 (2008)
57. V. Pouthier, Energy transfer in finite-size exciton-phonon systems: confinement-enhanced quantum decoherence. J. Chem. Phys. **137**(11), 114702 (2012)
58. V. Pouthier, Vibrational exciton mediated quantum state transfer: simple model. Phys. Rev. B **85**(21), 214303 (2012)

59. V. Pouthier, Vibrons in finite size molecular lattices: a route for high-fidelity quantum state transfer at room temperature. J. Phys. Condens. Matter. **24**(44), 445401 (2012)
60. O.V. Prezhdo, Mean field approximation for the stochastic Schrödinger equation. J. Chem. Phys. **111**, 8366–8377 (1999)
61. O.V. Prezhdo, V.V. Kisil, Phys. Rev. A **56**, 162 (1997)
62. M. Ratner, A brief history of molecular electronics. Nat. Nanotechnol. **8**(6), 378 (2013)
63. M. Santer, U. Manthe, G. Stock, Quantum-classical Liouville description of multi-dimensional nonadiabatic molecular dynamics. J. Chem. Phys. **114**, 2001 (2001)
64. J.R. Schmidt, P.V. Parandekar, J.C. Tully, Mixed quantum-classical equilibrium: surface hopping. J. Chem. Phys. **129**(4), 044104 (2008)
65. A. Sergi, D. MacKernan, G. Ciccotti, R. Kapral, Simulating quantum dynamics in classical environments. Theor. Chem. Acc. **110**, 49–58 (2003)
66. A. Sergi, F. Petruccione, Phys. Rev. E **81**, 032101 (2010)
67. N. Shenvi, J.E. Subotnik, W. Yang, Phase-corrected surface hopping: Correcting the phase evolution of the electronic wavefunction. J. Chem. Phys. **135**(2), 024101 (2011)
68. N. Shenvi, J.E. Subotnik, W. Yang, Simultaneous-trajectory surface hopping: a parameter-free algorithm for implementing decoherence in nonadiabatic dynamics. J. Chem. Phys. **134**(14), 144102 (2011)
69. J.E. Subotnik, Augmented Ehrenfest dynamics yields a rate for surface hopping. J. Chem. Phys. **132**(13), 134112 (2010)
70. J.E. Subotnik, A. Jain, B. Landry, A. Petit, W. Ouyang, N. Bellonzi, Annu. Rev. Phys. Chem. **67**, 387 (2016)
71. J.E. Subotnik, N. Shenvi, A new approach to decoherence and momentum rescaling in the surface hopping algorithm. J. Chem. Phys. **134**(2), 024105 (2011)
72. M.F. Tame, K.R. McEnery, S.K. Özdemir, J. Lee, S.A. Maier, M.S. Kim, Quantum plasmonics. Nat. Phys. **9**, 329 (2013)
73. D.V. Tsivlin, V. May, Multidimensional wave packet dynamics in polypeptides: coupled amide-exciton chain-vibrational motion in an α-helix. Chem. Phys. **338**(2–3), 150–159 (2007)
74. J.C. Tully, J. Chem. Phys. **93**, 1061–1071 (1990)
75. J.C. Tully, Molecular dynamics with electronic transitions. J. Chem. Phys. **93**, 1061 (1990)
76. J.C. Tully, Faraday Discuss. **110**, 407–419 (1998)
77. J.C. Tully, Nonadiabatic dynamics, in *Modern Methods for Multidimensional Dynamics Computations in Chemistry*, ed. by D.L. Thompson (World Scientific, New York, 1998), p. 34
78. D.A. Uken, A. Sergi, Quantum dynamics of a plasmonic metamolecule with a time-dependent driving. Theor. Chem. Acc. **134**, 141 (2015)
79. D.A. Uken, A. Sergi, F. Petruccione, Phys. Scr. **T143**, 014024 (2011)
80. D.A. Uken, A. Sergi, F. Petruccione, Filtering schemes in the quantum-classical Liouville approach to nonadiabatic dynamics. Phys. Rev. E **88**, 033301 (2013)
81. C. Wan, J. Schofield, J. Chem. Phys. **113**, 7047 (2000)
82. C. Wan, J. Schofield, Exact and asymptotic solutions of the mixed quantum-classical Liouville equation. J. Chem. Phys. **112**, 4447 (2000)
83. C. Wan, J. Schofield, Mixed quantum-classical molecular dynamics: aspects of multithreads algorithms. J. Chem. Phys. **113**, 7047 (2000)
84. L.J. Wang, A. Akimov, O.V. Prezhdo, J. Phys. Chem. Lett. **7**, 2100–2112 (2016)
85. L.J. Wang, A.E. Sifain, O.V. Prezhdo, J. Phys. Chem. Lett. **6**, 3827–3833 (2015)
86. F. Webster, E.T. Wang, P.J. Rossky, R.A. Friesner, Stationary-phase surface hopping for nonadiabatic dynamics – two-state systems. J. Chem. Phys. **100**, 4835–4847 (1994)
87. E. Wigner, Phys. Rev. **40**, 749 (1932)
88. R.P. Xu, Y.Q. Li, J.X. Tang, Recent advances in flexible organic light-emitting diodes. J. Mater. Chem. C **4**(39), 9116–9142 (2016)
89. W.Y. Zhang, R. Balescu, J. Plasma Phys. **40**, 199 (1988)
90. J. Zuloaga, E. Prodan, P. Nordlander, Quantum plasmonics: nonlinear effects in the field enhancement of a plasmonic nanoparticle dimer. ACS Nano **4**, 5269 (2010)